

Solid Propellant Chemistry, Combustion, and Motor Interior Ballistics

Edited by

Vigor Yang

Pennsylvania State University

University Park, Pennsylvania

Thomas B. Brill

University of Delaware

Newark, Delaware

Wu-Zhen Ren

China Ordnance Society

Beijing, People's Republic of China

Volume 185

PROGRESS IN

ASTRONAUTICS AND AERONAUTICS

Paul Zarchan, Editor-in-Chief

Charles Stark Draper Laboratory, Inc.

Cambridge, Massachusetts

Published by the

American Institute of Aeronautics and Astronautics, Inc.

1801 Alexander Bell Drive, Reston, Virginia 20191-4344

Copyright © 2000 by the American Institute of Aeronautics and Astronautics, Inc. Printed in the United States of America. All rights reserved. Reproduction or translation of any part of this work beyond that permitted by Sections 107 and 108 of the U.S. Copyright Law without the permission of the copyright owner is unlawful. The code following this statement indicates the copyright owner's consent that copies of articles in this volume may be made for personal or internal use, on condition that the copier pay the per-copy fee (\$2.00) plus the per-page fee (\$0.50) through the Copyright Clearance Center, Inc., 222 Rosewood Drive, Danvers, Massachusetts 01923. This consent does not extend to other kinds of copying, for which permission requests should be addressed to the publisher. Users should employ the following code when reporting copying from the volume to the Copyright Clearance Center:

1-56347-442-5/00 \$2.50 + .50

Data and information appearing in this book are for informational purposes only. AIAA is not responsible for any injury or damage resulting from use or reliance, nor does AIAA warrant that use or reliance will be free from privately owned rights.

ISBN 1-56347-442-5

Preface

We hope that readers will be interested in and will benefit from the international collection of high quality research papers and overviews presented in this Progress Series volume. The authors are among the most highly regarded scientists in the field of solid rocket propulsion, and come from the countries of Australia, Canada, China, France, Japan, Russia, and the United States. The volume embraces three subject areas: 1) solid propellant chemistry, synthesis, and formulation, 2) combustion of solid energetic materials, and 3) motor interior ballistics. A total of 39 papers have been included in the compilation, which is structured in such a manner as to provide a well-rounded balance of basic scientific research and applied technology.

Putting together this issue was not easy. We were reminded of the emotional tone poem entitled "Tod und Verklärung" ("Death and Transfiguration") by the 19th century German composer Richard Strauss. While composing this volume, we wondered on several occasions whether world events and national policies had doomed the effort to the trash bin, but we found in the end that the healthier course of transfiguration enabled it to come to fruition. Originally imagined, this was to be a special issue of the *Journal of Propulsion and Power* that compiled recent fundamental advancements in the chemistry and physics related to solid-propellant rocket motors. At the same time, Chinese scientists were in the process of organizing a symposium largely based on the papers presented herein. Owing to several unfortunate world events that were completely outside the spheres of everyone involved in the technical effort, the best-laid plans had to be scuttled and the meeting canceled. This archival effort could be salvaged, however, if in a modified form. The papers contained in this volume are therefore in large part those originally planned, although several could not be included, for reasons beyond the editors' control.

From a technical point of view, a wide range of topics is covered in some depth. Most of the papers deal with advanced materials and nontraditional formulations. The chemical aspects of organic and inorganic components in relation to decomposition mechanisms, kinetics, combustion, and modeling are a primary focus of Parts I and II of this volume. It is not possible to practice these fields without carefully attending to the safety issues, and so we have included several contributions on hazards and explosive characteristics. The field of experimental and computational interior ballistics research, overviewed in Part III, is moving quickly to include chemical information and the physics of the complex flowfield. One motivation for melding the areas of chemistry and turbulent flows is the hope of eventually learning how to control combustion dynamics in solid rocket motors through the use of chemical effects. We hope that this Progress Series volume will stimulate interest in continuing toward this goal.

The editors sincerely appreciate the patience and hard work of the scholars who contributed to this volume. We owe a large debt of gratitude to Woody Waesche for his extremely valuable support and encouragement throughout this effort. Enabling financial support was provided by the Pennsylvania State University, the American Institute of Aeronautics and Astronautics, and the China International Culture Exchange Center.

Finally, we wish to express our thanks to Mary Newby and Fengqi Zhao for handling voluminous correspondence among editors, authors, reviewers, and the AIAA. Anna Creese deserves special acknowledgment for her outstanding effort in the technical editing of the manuscripts. We are also grateful to Quinn Brewster, Rong-Jie Yang, Eun Kim, Robert Glick, Aiyu Zhang, and Danning You for proof-reading manuscripts and providing technical drawing services. The friendly and professional assistance of Rodger Williams, Heather Brennan, and Brian Haefs of the AIAA in publishing the volume is sincerely appreciated.

The individuals who provided their time and expertise toward reviewing the papers in this volume deserve special recognition. Their names appear below.

William Anderson	Gary Flandro	Bernard Matkowsky
Merrill Beckstead	Robert Frey	Martin Miller
Richard Behrens	Robert Geisler	John Murdock
Fred Blomshield	Robert Glick	Jamie Neidert
M. Quinn Brewster	Donna Hanson-Parr	Vitali Nesterenko
Thomas Brill	Paul Harris	Yoshio Oyumi
Robert Brown	Thomas Highsmith	Timothy Parr
Victor Burnley	Merrill K. King	Joseph Powers
Rodney Burton	Naminosuke Kubota	Edward Price
P. Barry Butler	Ellis Landsbaum	Ron Simmons
Weidong Cai	Shui-Chi Li	Steven F. Son
Robert Chapman	Yeong-Cherng Liau	Al Stern
May Chen	Ming-Chang Lin	Stefan Thynell
Paul Clavin	Tom Litzinger	John Vanderhoff
Norman Cohen	John Lyman	Francois Vuillot
Fred Culick	Joe Majdalani	R.H. Woodward Waesche
Joe Flanagan	Stephen Margolis	Saburo Yuasa

Vigor Yang
Thomas B. Brill
Wu-Zhen Ren
 April 2000

Color Reproductions for Chapter 2.15 (courtesy of Defence Science and Technology Organization, Salisbury, Australia)

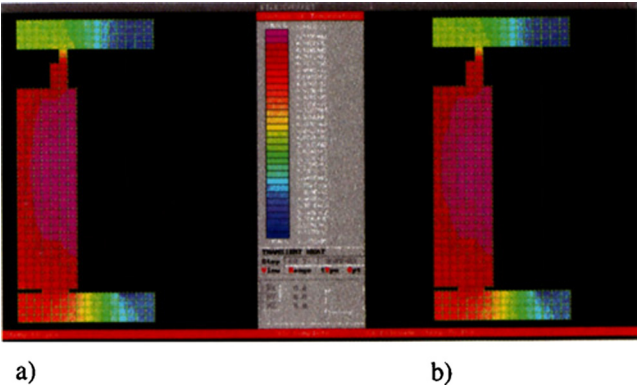


Fig. 2 Temperature distribution in SSCB at a) time = 1360 s (before ignition) and b) time = 1520 s (during combustion).

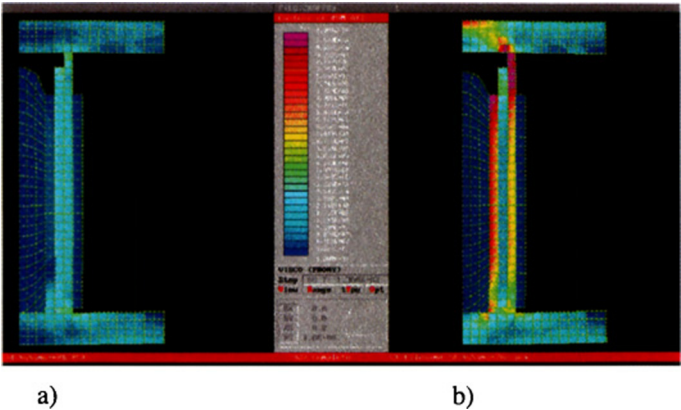


Fig. 3 Von Mises stress contours in SSCB at a) time = 1360 s (before ignition) and b) time = 1520 s (during combustion).

Color Reproductions for Chapter 3.4 (courtesy of ONERA and Societe Nationale des Poudres et Explosifs [Fig. 19], Châtillon, France)



Fig. 2 Aluminum droplets in combustion immediately above propellant surface, AP/Al/HTPB propellant, chamber pressure = 0.6 MPa.

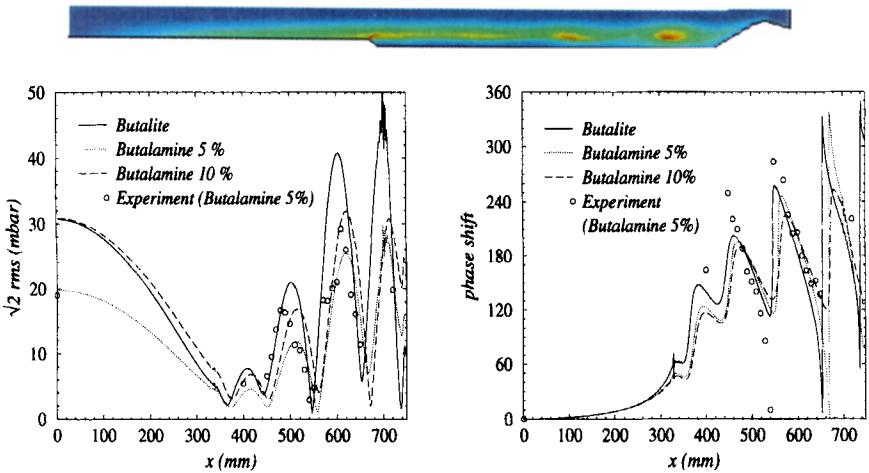


Fig. 7 Vorticity contour plot for the Butalite computation and Fourier coefficients of the first mode along the chamber axis.

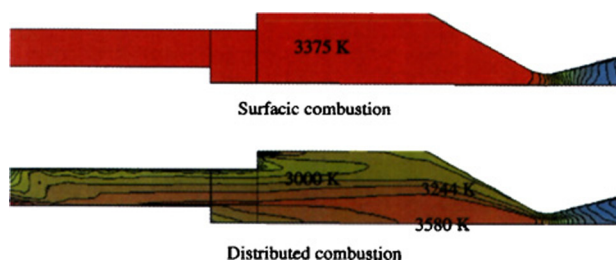


Fig. 10 Temperature fields for the two approaches.

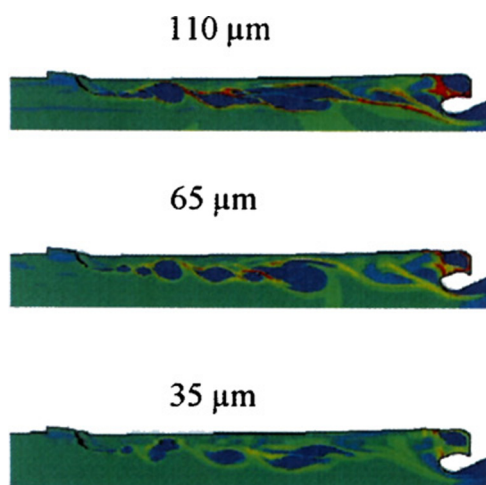
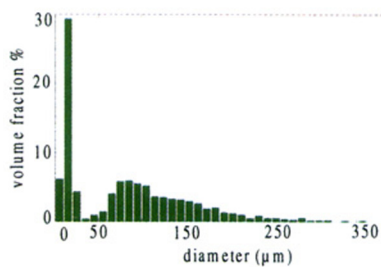
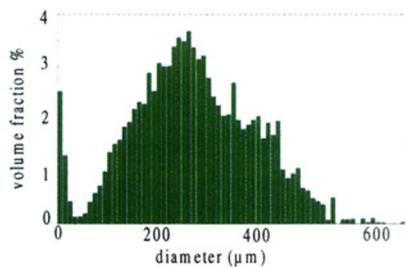


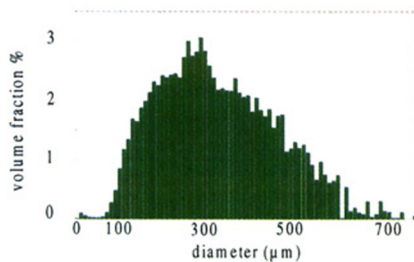
Fig. 19 Droplet volume fraction in the aft segment of the motor for three droplet sizes.



Section 1

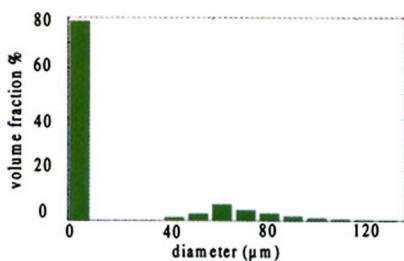


Section 2

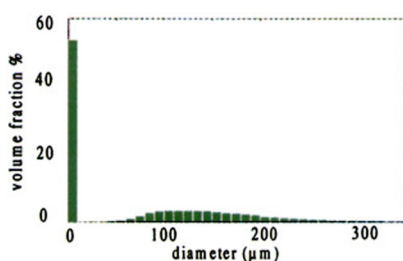


Section 3

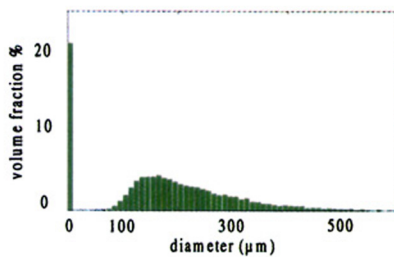
Fig. 13 Droplet size distributions in different sections (model 1).



Section 1



Section 2



Section 3

Fig. 14 Droplet size distributions in different sections (model 2).

Table of Contents

Preface	xxiii
----------------------	--------------

I. Propellant Chemistry, Synthesis, and Formulation

Chapter 1.1 Flash Pyrolysis of Ammonium Perchlorate-Hydroxyl-Terminated-Polybutadiene Mixtures Including Selected Additives	3
T. B. Brill and B. T. Budenz <i>University of Delaware, Newark, Delaware</i>	
Introduction	3
Flash Thermolysis Experiments	4
Decomposition of the Pure Materials	6
Pure AP.	6
HTPB	10
AP-HTPB Mixture	11
Thermal Stability of the Mixture	12
Gaseous Products	13
Effect of Pressure	18
AP-HTPB with TiO ₂ and Melamine.	20
Conclusions	22
References	23
 Chapter 1.2 Gas-Phase Chemical Kinetics of [C, H, N, O] Systems Relevant to Combustion of Nitramines	 33
D. Chakraborty and M. C. Lin <i>Emory University, Atlanta, Georgia</i>	
Introduction	33
Computational Methods.	34
Potential-Energy Profile and Reaction Mechanisms	34
Rate Constant Calculations	35
Results and Discussions.	36
Systems Relevant to the Early-Stage Combustion of ADN.	36
Systems Relevant to the Early-Stage Decomposition of RDX/HMX	51
Conclusions	64
References	65
 Chapter 1.3 Reactivity of Azide Polymer Propellants	 73
Yoshio Oyumi <i>Japan Defence Agency, Tokyo, Japan</i>	
Introduction	73
Experiments	73
Structural Analysis	73
Thermal Analysis	73
Burning-Rate and Temperature-Profile Measurements	74

Results and Discussion	74
Microstructure of BAMO/NMMO Copolymer	74
Thermal Decomposition	75
BAMO Copolymers	76
Improvement of Mechanical Properties	81
Burning Rate	82
BAMO/NMMO/AP Propellants	82
BAMO/AMMO/AN Propellants	87
GAP/AN Propellants	92
BAMO/NMMO/AN Propellants	93
Conclusions	94
References	95
 Chapter 1.4 Effect of Molecular Structure on Combustion of Polynitrogen Energetic Materials	 99
V. P. Sinditskii, A. E. Fogelzang, V. Yu. Egorshhev, V. V. Serushkin, and V. I. Kolesov <i>Mendeleev University of Chemical Technology, Moscow, Russia</i>	
Nomenclature	99
Introduction	100
Experimental Methods	100
Results and Discussion	101
Combustion of Hydrazoic Acid and its Onium Salts	101
Combustion of Organic Azides	106
Combustion of Tetrazoles	114
Comparison with Nitrocompounds	120
Conclusions	125
References	125
 Chapter 1.5 Molecular Structure Tailoring of Binders in Solid Propellants	 129
Huimin Tan, Yingquan Duo, and Futai Chen <i>Beijing Institute of Technology, Beijing, People's Republic of China</i>	
Nomenclature	129
Introduction	130
Molecular Structure Tailoring for Prepolymers in NEPE Propellant Binder	130
Molecular Structure Tailoring of Binders in TPE Propellants	134
Hard-Segment Domain Structure Selection	134
Chemical Structure Selection of Soft Segments	135
Microphase Separation Estimation	137
TPE Propellant	139
Conclusions	139
References	140
 Chapter 1.6 Effects of Microstructure on Explosive Behavior	 141
Philip M. Howe <i>Los Alamos National Laboratory, Los Alamos, New Mexico</i>	
Introduction	141
Shock Sensitivity and Microstructural Effects	142
Nature of Hot Spots	142

Compressive Heating of Occluded Gas	142
Localized Shock Interactions and Hydrodynamic Flow	144
Viscoplastic Flow	145
Effect of Porosity Upon Shock Sensitivity	151
Particle Size Effects on Shock Initiation	156
Microstructure and Initiation by Shear	161
Friction and Shear Heating in Explosives	161
Evidence for Shear Band Formation in Explosives	161
Effects of Microstructure on Shear Band Formation	163
Shear Band Formation in the Drop Weight Impact Experiments	165
Other Shear Experiments	168
Effects of Microstructure on Friction Initiation	170
Conclusions	174
References	174

Chapter 1.7 Advances in Solid Propellant Formulations 185

May L. Chan, Russ Reed Jr., and David A. Ciaramitaro *Naval Air Warfare Center,
China Lake, California*

Nomenclature	185
Introduction	185
Background—High Performance	186
Background—Insensitive Munitions	186
Background—Pollution Prevention	187
Experimental Results and Discussion	188
High Performance	188
Insensitive Munitions	195
Pollution Prevention	198
Conclusions	203
References	204

Chapter 1.8 Synthesis and Characterization of Dinitramidic Acid and Its Salts 207

Oleg A. Luk'yanov and Vladimir A. Tartakovsky *Russian Academy of Sciences,
Moscow, Russia*

Introduction	207
Methods for the Synthesis of Dinitramide and Its Salts	208
Structure and Properties of Dinitramide and Its Salts	212
Chemical Properties of DNA and Its Salts	215
Conclusions	218
References	218

Chapter 1.9 Hazards Associated with Solid Propellants 221

T. L. Boggs, A. I. Atwood, and A. J. Lindfors *Naval Air Warfare Center Weapons
Division, China Lake, California*; E. J. Mulder *John Hopkins University/
Chemical Propulsion Information Agency, Columbia, Maryland* and R. W.
Pritchard *Naval Air Warfare Center Weapons Division, China Lake, California*

Introduction	221
Hazard Classification	222

Critical Diameter/Shock Sensitivity	223
Bore Effect	226
Delayed Detonation (XDT)	227
IM Fragment and Bullet Impact Tests and Sympathetic Detonation Tests . .	227
Ignition.	228
Ignition due to Electrostatic Discharge (ESD).	233
Ignition due to Impact and Friction.	234
Other Ignition Hazard Considerations.	234
Combustion	235
Burning Rates of Energetic Materials	235
Burning Area	236
Effect of Strain on the Burning Rates of High-Energy Solid Propellants.	237
DDT.	238
Cookoff	240
Conclusions	242
Appendix	242
References	262

II. Combustion of Solid Energetic Materials

Chapter 2.1 Overview of Combustion Mechanisms and Flame Structures for Advanced Solid Propellants 267

M. W. Beckstead *Brigham Young University, Provo, Utah*

Introduction	267
Monopropellant Burning Characteristics.	268
Solid-Propellant Combustion Characteristics	273
Solid-Propellant Combustion Mechanisms	275
Phenomenological Concepts	275
AP Composite Propellants.	276
HMX Composite Propellants	277
Summary.	280
Combustion Characteristics of Advanced Propellants	280
Conclusions	282
References	283

Chapter 2.2 Physico-Chemical Mechanisms of Solid Propellant Combustion 287

G. Lengellé, J. Duterque, and J. F. Trubert *ONERA, Châtillon, France*

Introduction	287
Combustion of DB Propellants and Active Binders	288
Introduction	288
Flame Structure.	291
Condensed-Phase Processes	293
Flame Zone	298
Active Binders	302
Mechanisms of Action of Additives	303
Pyrolysis of Inert Binders	305

Combustion of AP	307
Condensed-Phase Behavior	307
Energetics of AP Combustion	308
Surface Pyrolysis of AP	309
Flame Structure of AP Combustion	310
Combustion of HMX	313
Condensed-Phase Processes	313
Gas-Phase Behavior	317
Combustion of Composite Propellants	319
Comparison of Composite Propellant Combustion Behaviors	319
Propellant Burning Rate Resulting from Component Rates	320
HMX-Active Binder Propellants	323
AP-Inert Binder Propellants	326
Conclusions	330
References	332

Chapter 2.3 Flame Structure of Solid Propellants 335

Oleg P. Korobeinichev *Russian Academy of Sciences, Novosibirsk, Russia*

Introduction	335
Experimental	337
Substantiation of the Method of Probing Flames	
with Narrow Combustion Zones	339
SP Flame Structure: Results and Discussion	341
Flame Structure of AP and Composite Propellants Based on It	341
RDX and HMX Flame Structure	343
ADN Flame Structure	344
Flame Structure of Propellants Based on ADN and HTPB	347
Double-Based Propellant Flame Structure at High Pressure	349
Conclusions	350
References	350

Chapter 2.4 Experimental Studies of Nitramine/Azide Propellant Combustion 355

Thomas A. Litzinger, YoungJoo Lee, and Ching-Jen Tang *Pennsylvania State
University, University Park, Pennsylvania*

Introduction	355
Previous Studies	355
Research Objectives	357
Experimental Approach	357
Results and Discussion	360
RDX/BAMO	360
RDX/GAP	364
HMX/GAP	368
Overall Chemical Structure	373
Effect of Azide Polymer Structure	374
Effect of Oxidizer Structure	375
Effects of Heat Flux on Pseudopropellant Combustion	376
Conclusions	377
References	378

Chapter 2.5 Optical Diagnostics of Solid-Propellant Flame Structures	381
Timothy Parr and Donna Hanson-Parr <i>Naval Air Warfare Center Weapons Division, China Lake, California</i>	
Introduction	381
Experimental Techniques	381
Description	381
Uncertainties in Concentration and Temperature Measurements	384
Results	384
Laser-Supported Deflagration of RDX and HMX at 0.094 Megapascal (1 Atmosphere)	384
Effect of Pressure on HMX Flame Structure	386
Self-Deflagration of RDX at 0.1 Megapascal (1 Atmosphere)	386
HMX Self-Deflagration at 0.1 Megapascal (1 Atmosphere)	388
Ignition of HMX and RDX	389
Comparison Between HMX and RDX	390
TNAZ	391
HNF Neat Self-Deflagration Flame Microstructure at 0.094 Megapascal (0.92 Atmosphere)	391
Diffusion Flame Studies via Sandwiches	393
Counterflow Diffusion Flames	400
Formulated Propellants: XM39 Self-Deflagration at 0.094 Megapascal (0.92 Atmosphere)	402
Metal Combustion	405
Conclusions	408
References	409
Chapter 2.6 Thermal Decomposition and Combustion of GAP/AN/Nitrate Ester Propellants	413
Xiao-Bin Zhao, Lin-Fa Hou, and Xiao-Ping Zhang <i>Red-Star Institute of Chemistry, Xiangfen, Hubei, People's Republic of China</i>	
Nomenclature	413
Introduction	413
Experimental Methods	414
Discussion of Results	415
Thermal Decomposition of AN and MNE	415
Thermal Decomposition Kinetics of GAP and PSAN	416
Mechanism of MO Catalyzing Decomposition of AN	417
Temperature Profile of Combustion Wave	418
Flame Structure	419
Correlation of Thermal Decomposition and Burning-Rate Characteristics	422
Conclusions	423
References	424
Chapter 2.7 Thermal Decomposition of Potassium Dinitramide at Elevated Pressure	425
Cuimei Yin, Ziru Liu, Yanghui Kong, Fengqi Zhao, Yuan Wang, Ming Lei, Yang Luo, Pei Zhang, Yinghui Shao, and Shangwen Li <i>Xi'an Modern Chemistry Research Institute, Xi'an, People's Republic of China</i>	

Nomenclature	425
Introduction	425
Experimental Techniques	426
Results and Discussion	427
Decomposition of Solid KDN	427
Thermal Decomposition of Liquid KDN	430
Decomposition Mechanisms of KDN	431
Phase Stabilization of KDN	434
Eutectic System of KDN	435
Conclusions	436
References	436

Chapter 2.8 Combustion Mechanism of 3-Azidomethyl-3-Methyloxetane (AMMO)

Composite Propellants 439

Hakobu Bazaki Asahi Chemical Industry Company, Ltd., Oita, Japan

Nomenclature	439
Introduction	440
Experimental Methods	440
Results and Discussion	442
Combustion Characteristics of AMMO	442
Theoretical Rocket Performance of AP/AMMO and AP/HTPB Propellants	444
Combustion Characteristics of AP/AMMO and AP/HTPB Propellants	444
Combustion Characteristics of Catalyzed AP/AMMO and AP/HTPB Propellants	447
Temperature Sensitivity Analysis of AP/AMMO Composite Propellants	449
Conclusions	453
References	453

Chapter 2.9 Burning Rate Characteristics of Glycidyl Azide

Polymer (GAP) Fuels and Propellants 455

Iwai Komai, Koh Kobayashi, and Kazushige Kato NOF Corporation, Aichi, Japan

Nomenclature	455
Introduction	455
Theoretical Performance	456
GAP Fuels	456
GAP Propellants	457
Burning Rate Characteristics	458
GAP Fuels	458
GAP Propellants	460
Conclusions	463
References	463

Chapter 2.10 Effects of Carbon Substances on Combustion

Properties of Catalyzed RDX-CMDB Propellants 465

*Fengqi Zhao, Shangwen Li, Wengang Shan, and Dianlin Lu Xi'an Modern
Chemistry Research Institute, Xi'an, People's Republic of China and
Shufen Li China University of Science and Technology, Hefei, People's
Republic of China*

Nomenclature	465
Introduction	465
Effect of Carbon and Potential of C_{60} in Solid Propellants	466
Experimental Results on the Burning Rate Enhancement of C_{60} , FS, and CB.	468
Experimental Methods	468
Burning Rate Enhancement of C_{60} , FS, and CB.	468
Effect of FS or CB Content on the Combustion Properties	470
Discussion of Burning Rate Enhancement by Various Carbon Substances	471
Conclusions	474
References	474

Chapter 2.11 Modeling of RDX/GAP Propellant Combustion with Detailed Chemical Kinetics. 477

Yeong-Cherng Liao *Los Alamos National Laboratory, Los Alamos, New Mexico*
and Vigor Yang and Stefan T. Thynell *Pennsylvania State University,
University Park, Pennsylvania*

Nomenclature	477
Introduction	478
Theoretical Formulation	479
Solid-Phase Region	481
Subsurface Multiphase Region.	481
Gas-Phase Region	485
Boundary Conditions	487
Numerical Method	489
Results and Discussion	489
Conclusions	499
References	500

Chapter 2.12 Energetic-Material Combustion Modeling with Elementary Gas-Phase Reactions: A Practical Approach. 501

Martin S. Miller and William R. Anderson *U.S. Army Research Laboratory,
Aberdeen Proving Ground, Maryland*

Introduction	501
Conceptual Framework	503
Mathematical Framework	504
Example: Frozen Ozone	507
Example: RDX	509
Example: Nitroglycerine	513
Effect of Chemical Additives on the Burning Rate	519
Speculations on Practical Burning-Rate Modifiers.	521
Conclusions	522
Appendix: Reaction Mechanism (DB11) for Nitroglycerine.	523
References	528

Chapter 2.13 Burning-Rate Prediction of Double-Base Plateau Propellants	533
Dong Yang and Hongchang Song <i>Nanjing University of Science and Technology, Nanjing, People's Republic of China</i> and Fengqi Zhao and Shangwen Li <i>Xi'an Modern Chemistry Research Institute, Xi'an, People's Republic of China</i>	
Nomenclature	533
Introduction	534
Theoretical Background	535
Mechanism of Plateau Combustion	537
Effects of Catalysts on Burning Surface Physico-Chemistry	537
Hypothesis on the Reaction of [CHO] Near Burning Surface	538
Effect of Nitramines	539
Burning Rate Equation of DB and RDX-CMDB Propellants	540
Influence Level of Catalysts on the Reaction of [CHO]	540
Burning-Rate Equation	541
Burning-Rate Pressure Exponent	541
Results and Discussion	542
Calculated Results	542
Plateau Combustion Phenomena	542
Effect of Chemical Structure Factors on Plateau Combustion	545
Conclusions	546
References	547
Chapter 2.14 Structure and Stability of Deflagrations in Porous Energetic Materials	549
Stephen B. Margolis <i>Sandia National Laboratories, Livermore, California</i> and Forman A. Williams <i>University of California at San Diego, La Jolla, California</i>	
Introduction	549
Formulation	551
Nondimensionalizations and Further Approximations	555
Burning-Rate Eigenvalue for Steady, Planar Combustion	558
Preliminary Analysis	559
Burning-Rate Eigenvalue	562
Analysis of the Gas-Permeation Layer	566
Asymptotic Model for Nonsteady, Nonplanar Burning	569
Outer Problem	570
Reaction-Zone Solutions	574
Summary of Asymptotic Model	576
Basic Solution and Its Linear Stability	578
Analysis of Dispersion Relation	581
Conclusions	587
References	588
Chapter 2.15 Modeling of Cook-Off Reaction Violence of Confined Energetic Materials	591
Sook-Ying Ho <i>Defence Science and Technology Organisation, Salisbury, South Australia, Australia</i>	

Nomenclature	591
Introduction	592
Coupled Thermal/Structural Analysis	593
Thermomechanical Properties and Temperature-Dependent Viscoelastic Models	595
Energy Release from Dynamic Combustion	597
Failure Analysis of Confinement	598
Fragmentation Analysis	599
Conclusions	603
References	603

**Chapter 2.16 Solid Propellant Combustion Response:
Quasi-Steady (QSHOD) Theory Development and Validation 607**

M. Q. Brewster *University of Illinois at Urbana-Champaign, Urbana, Illinois*

Nomenclature	607
Introduction	608
Synopsis of QSHOD Theory Development	610
Nonlinear QSHOD Response (ZN).	611
Linearized QSHOD Response Function (ZN)	613
Condensed Phase Kinetics (FM)	615
Gas Phase Kinetics (FM)	618
Experimental and Theoretical Response for NC/NG	619
Experimental and Theoretical Response for HMX.	625
Non-QSHOD Response	629
Homogeneous, Non-Quasi-Steady Response.	629
Nonhomogeneous, Quasi-Steady Response	631
Conclusions	632
References	634

**Chapter 2.17 Burning-Rate Response Functions
of Composite-Modified Double-Base Propellants and HMX. 639**

Anatoli A. Zenin and Sergei V. Finjakov *Russian Academy of Sciences, Moscow,
Russia*

Nomenclature	639
Introduction	640
Investigated Substances and Experimental Results	640
Pressure and Temperature Sensitivities of Burning Rate and Burning Surface Temperature	641
Theory of Burning-Rate Response Functions	646
Solid Layer on the Burning Surface	646
Melting Layer on the Burning Surface	647
Burning-Rate Response Functions for HMX and CMDB Propellants	650
HMX Response Functions.	650
Propellant Response Functions.	654
Conclusions	658
References	660

Chapter 2.18 Combustion of Aluminized Solid Propellants. 663

E. W. Price and R. K. Sigman *Georgia Institute of Technology, Atlanta, Georgia*

Introduction	663
History	665
Aluminum	665
Thermal Response of Aluminum Powders	666
Droplet Burning	669
Accumulation and Agglomeration	670
Particle Packing	671
Retention of Aluminum on the Burning Surface	672
Susceptibility of Al Particles to Ignition	672
Connective Processes Among Concentrating Particles	673
Evolution of the Local Environment	673
Formation of Agglomerates	674
Burning Aluminum Agglomerates	676
Al ₂ O ₃ Product Population	681
Conclusions	683
References	684

Chapter 2.19 Detailed Studies on the Flame Structure of Aluminum Particle Combustion

689

P. Bucher, L. Ernst, and F. L. Dryer *Princeton University, Princeton, New Jersey;*
 R. A. Yetter *Pennsylvania State University, University Park, Pennsylvania* and
 T. P. Parr and D. M. Hanson-Parr *Naval Air Warfare Center Weapons Division,*
China Lake, California

Introduction	689
Isolated Aluminum Particle Combustion Experiments	692
Modeling of Single-Aluminum Particle Combustion	693
Experimental Approach	695
Particle Generation and Ignition	695
Photographic and Emission Measurements	697
Condensed-Phase Species Measurements	697
Gas-Phase Species and Temperature Measurements	700
Experimental Results	703
Modeling Approach	712
Modeling Results	716
Conclusions	718
References	719

Chapter 2.20 Combustion of Aluminum Particles in Solid-Rocket Motor Flows

723

John C. Melcher, Rodney L. Burton, and Herman Krier *University of Illinois at*
Urbana-Champaign, Urbana, Illinois

Nomenclature	723
Introduction and Background	724
Research Motivation and Objective	724
Aluminum Particle Combustion	724
Experimental Apparatus	726
Chamber Design	726

Chamber Conditions	728
Aluminized Propellant Description	729
Particle Quench Tests	730
Experiment Optics	732
Oxidizer Study Control	733
Data Reduction Technique	734
Image Analysis	734
Mathematical Analysis	735
Uncertainty Analysis	737
Results and Discussion	738
Burn-Time Dependence on Particle Diameter	738
Effect of Oxidizer Concentration	739
Effect of Pressure	741
Conclusions	743
References	744
 Chapter 2.21 Formation of Condensed Combustion Products at the Burning Surface of Solid Rocket Propellant	 749
V. A. Babuk, V. A. Vassiliev, and V. V. Sviridov <i>Baltic State Technical University, Saint Petersburg, Russia</i>	
Nomenclature	749
Introduction	750
Experimental Technique	750
Visualization of the Combustion Zone and Temperature Measurements	750
Surface Layer Study	751
Propellant Structure Study	753
Quench Collection of CCP Particles	754
Agglomeration Behavior	755
Agglomerate Structure	755
Agglomerate Formation Conditions	759
Influence of Propellant Composition and Combustion Conditions on	
Agglomeration Behavior	762
Formation of Smoke Oxide Particles	766
CCP Formation at the Propellant Burning Surface	768
Agglomerate Formation	768
Formation of Smoke Oxide Particles	772
Conclusions	773
References	774
 Chapter 2.22 Measurements of the Physico-Chemical Properties of Liquid Alumina Using Contactless Techniques.	 777
Francis Millot, Benoît Glorieux, and Jean Claude Rifflet <i>Centre National de la Recherche Scientifique, Orléans, France</i>	
Introduction	777
Physico-Chemical Properties of Liquid Alumina	778
Density	778
Surface Tension	779

Viscosity	781
Aluminum Self Diffusion	782
Electrical Conductivity	782
Radiative Properties	783
Conclusions	785
References	785

III. Motor Interior Ballistics

Chapter 3.1 Effect of Acoustic Oscillation on Flow Development in a Simulated Nozzleless Rocket Motor 791

Sourabh Apte and Vigor Yang *Pennsylvania State University, University Park,
Pennsylvania*

Nomenclature	791
Introduction	792
Theoretical Formulation	795
Numerical Method and Error Analysis	798
Stationary Flowfield	801
Vorticity Field.	802
Mean Flow Properties	802
Turbulence Energy Spectrum and Transport Properties	805
Motor Flow Development	806
Effect of Acoustic Oscillation on Flow Evolution	809
Decomposition and Averaging	809
Vorticity Field.	810
Acoustic Field	812
Effect of Acoustic Oscillation on Turbulence Properties	813
Effect of Turbulence on the Acoustic Flowfield	815
Conclusions	817
Appendix	818
References	819

Chapter 3.2 Stability and Acoustic Resonance of Internal Flows Generated by Side Injection 823

B. Ugurtas, G. Avalon, and N. Lupoglazoff *ONERA, Palaiseau, France*; F. Vuillot
ONERA, Châtillon, France and G. Casalis *ONERA, Toulouse, France*

Nomenclature	823
Introduction	823
Experimental Facility	824
Linear Stability Theory	826
Numerical Approach	827
Discussion of Results	829
Flow Stability.	829
Acoustic Resonance.	832
Conclusions	834
References	835

Chapter 3.3 Turbulent Transport in Rocket Motor**Unsteady Flowfield 837**

G. A. Flandro *University of Tennessee Space Institute, Tullahoma, Tennessee* and
Weidong Cai and V. Yang *Pennsylvania State University, University Park,
Pennsylvania*

Nomenclature	837
Introduction	838
Analysis	839
Mean Flowfield with Turbulence	840
Formulation of Unsteady Viscous Flow Model	842
Unsteady Vorticity	844
Rotational Velocity Vector Corrections	849
Effects of Turbulence on Organized Unsteady Flow	850
Effect of Turbulence on Vorticity Production and Transport	853
Effect of Turbulence on System Stability Integrals	855
Conclusions	856
References	857

Chapter 3.4 Some Aspects of Two-Phase Flows in Solid-Propellant**Rocket Motors 859**

J. Dupays, Y. Fabignon, P. Villedieu, G. Lavergne, and J. L. Estivalezes *ONERA,
Châtillon, France*

Nomenclature	859
Introduction	860
Aluminum Oxide Formation	861
Interactions Between Droplets and Gas Flowfield	862
Interactions Between Inert Particles and Vortex Shedding	863
Interactions Between Vaporizing Droplets and Acoustic Waves	867
Interactions Between Burning Droplets and Mean Gas Flowfield	868
Slag Accumulation	870
Two-Phase Flowfields	870
Effect of Droplet Coalescence	871
Capture Rules, Droplet–Wall Interactions, and Liquid Film Formation.	874
Effect of Vortices.	877
Conclusions	879
References	879

Chapter 3.5 Combustion Dynamics of Homogenous Solid**Propellants in a Rocket Motor with Acoustic Excitations. 885**

Tae-Seong Roh, Sourabh Apte, and Vigor Yang *Pennsylvania State University,
University Park, Pennsylvania*

Nomenclature	885
Introduction	886
Theoretical Formulation	887
Gas-Phase Process	887
Chemical Kinetics Model	889
Condensed-Phase Process	889

Interfacial Conditions	889
Turbulence Closure	890
Turbulence/Chemistry Interaction	892
Boundary Conditions	892
Numerical Method	893
Results and Discussion	893
Steady-State Flowfield	893
Interaction Between Acoustic Wave and Propellant Combustion	896
Conclusions	905
References	905

Chapter 3.6 Combustion Characteristics of Aluminized HTPB/AP Propellants in Acceleration Fields. 907

Peijuan Yang, Zhen Huo, and Zhongquan Tang *46th Institute of China Aerospace
Corporation, Huhhot, People's Republic of China*

Nomenclature	907
Introduction	907
Experimental Apparatus	908
Data Reduction	909
Experiment	909
Results and Discussion	909
Acceleration Effects: Baseline Formulation	909
Influence of Aluminum Content	912
Influence of Aluminum Particle Size	913
Influence of Solid Content.	913
Influence of Oxidizer Particle Size	913
Influence of Oxidizer Type	914
Influence of Static Burning Rate.	915
Influence of Static Pressure	916
Residue Retention	917
Conclusions	918
References	919

Chapter 3.7 Pulsed Motor Firings 921

Fred S. Blomshield *Naval Air Warfare Center, China Lake, California*

Introduction	921
Pressure.	924
Stability Additives	924
Stability Calculations	925
Geometry.	925
Pulsing	925
Nonlinear Effects	925
Motor Firing Details	926
Propellants	926
Test Matrix.	927
Pulsers	927
Instrumentation	927

Motor Failures	931
Motor Hardware	931
Firing Results and Analysis of Motors 3–5	932
Motor 3	933
Motor 4	933
Motor 5	936
Linear Stability	938
Nonlinear Instability	942
Firing Results and Analysis of Motors 6–10	945
Stability Boundaries	950
Stability Additives	951
Waveform Shape and Phase Relationships	951
Frequency Content	952
Motor 10 Failure Analysis	955
Conclusions	956
References	957

Chapter 3.8 Transverse Waves in Solid-Propellant Rocket Motors: Pulse-Triggered Unstable Mode 959

P. G. Harris *Defence Research Establishment Valcartier, Val Bélair, Québec,
Canada* and A. De Champlain *Laval University, Québec, Québec, Canada*

Introduction	959
Test Matrix	962
Experimental Technique	963
New Data Analysis Method	965
Transverse Waves: Presence and Nature	967
Detailed Analysis	968
Generalized Analysis	971
Transverse Waves: Source	974
Transverse Waves: Effect	982
Conclusions	986
References	987

Author Index 989

I. Propellant Chemistry, Synthesis, and Formulation

Flash Pyrolysis of Ammonium Perchlorate–Hydroxyl-Terminated-Polybutadiene Mixtures Including Selected Additives

T. B. Brill* and B. T. Budenz†

University of Delaware, Newark, Delaware

I. Introduction

WORLDWIDE, ammonium perchlorate (AP, NH_4ClO_4) and hydroxyl-terminated-polybutadiene (HTPB) composite mixtures, usually also containing aluminum powder and ballistic modifiers, are the most frequently used formulations in solid rocket propellants. In terms of publications, AP has been the most extensively investigated solid oxidizer since its introduction into propellants, probably in the late 1940s¹ by the Jet Propulsion Laboratory. A large number of publications appeared in 1950–1970, and, by comparison, a relatively lesser number have appeared since then. The impressive review by Jacobs and Whitehead² was quite extensive in range and depth at the time of publication in 1969. The falloff in research interest after this time is reflected in the additional information reviewed 10–15 years later,³ but subsequent reviews of various aspects of decomposition, ignition,⁴ and combustion^{5–8} of AP-composite propellants have appeared. A modest resurgence of new interest in AP-composite propellant decomposition and combustion is motivated in part by the availability of advanced methods of diagnostics,^{9–13} by new kinetics data and methods of modeling,^{14–16} and by intriguing plateau-burning behavior of some AP-HTPB formulations.^{17,18}

Despite the widespread use and long investigative history of AP-fuel mixtures, it still can be said that AP alone and AP-fuel composites remain among the most confounding materials in the research setting. From the point of view of chemistry, one reason is that the full range of formal oxidation states of nitrogen and chlorine can apparently become involved, for example, the formal oxidation state of Cl in ClO_4^- is +7, whereas that of HCl is –1; N in NH_4^+ is –3, whereas that of N in NO_2^+ (Ref. 19) and HNO_3 (Ref. 20) is +5. When all of the various combinations of

Copyright © 1999 by the American Institute of Aeronautics and Astronautics, Inc. All rights reserved.

*Professor, Dept. of Chemistry and Biochemistry.

†Graduate Research Assistant, Dept. of Chemistry and Biochemistry.

N-, H-, O-, and Cl-containing compounds are considered together, in excess of 1000 chemical reactions become possible.⁹ Likewise, the thermal decomposition of pure HTPB involves a number of processes and potentially leads to a large number of hydrocarbon products.²¹⁻²⁴ Because of the interactions between AP and HTPB during the decomposition process, the products from the pure materials will be altered in quantity or completely changed to different products. The diffusion flame structure that results from the pyrolysis of the heterogeneous composite surface is a feature that imparts a strong combustion dependence on the pressure, the AP particle size, and the oxidizer/fuel ratio.^{16,25-28} Furthermore, a highly complex surface structure exists²⁹⁻³¹ with three phases present at least below 50 atm (Ref. 32).

Given the extraordinarily intertwined and complex processes involved in the decomposition and combustion of AP-HTPB mixtures, it is reasonable to wonder if adding another drop to the voluminous bucket of literature could possibly make any difference. After examining many open-literature papers in this field and conducting a large number of flash pyrolysis experiments in our laboratory, we decided to try to amalgamate our findings with many of those previously reported in the hope of contributing some useful insights. Our initial objective was to contribute something more quantitative about the condensed-phase chemistry dimension of the overall process. Given the complexity, however, this ambitious goal had to be scaled back to a more empirical set of mechanistic observations. The literature used is extensive, but is hardly comprehensive. The emphasis was placed on the chemistry of the heterogeneous AP-HTPB mixture in Sec. IV. To discuss this mixture in context, it is first necessary to summarize the experimental methods in Sec. II and some of the relevant features of the pure materials in Sec. III.

II. Flash Thermolysis Experiments

The condensed-phase chemistry at a burning surface is extremely difficult to study.^{33,34} In an attempt to learn more about rates and mechanisms, we have developed several spectroscopically accessible flash thermolysis methods³⁵ culminating in the currently used method of temperature-jump (T-jump) Fourier transform infrared (FTIR) spectroscopy.¹¹ The assumption is that flash pyrolysis of a thin film of material is a snapshot simulation of the burning surface provided that the heating rate and temperature are high enough. The unique feature of this device is the use of a high-gain, fast-response, power supply to adjust the temperature of a Pt filament extremely rapidly to accommodate the endothermic and exothermic events of the sample. Thereby, an essentially constant, but high, temperature is maintained during the experiment.

The concept of T-jump/FTIR spectroscopy^{11,36,37} is shown in Fig. 1. Approximately 200 μg of material was thinly spread on the center of a polished Pt ribbon filament. The filament was arranged inside of a closed gas cell so that the infrared (IR) beam of a rapid-scanning FTIR spectrometer passed about 3 mm above the surface. The cell was purged with Ar and pressurized at any desired pressure up to 70 atm, although 50 atm was the highest pressure used in this work. By using the high-performance power supply, the filament and sample were heated at about 800°C s^{-1} and then held at the chosen temperature in the $400\text{--}600^\circ\text{C}$ range for the

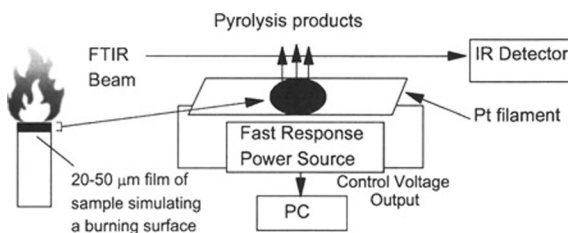


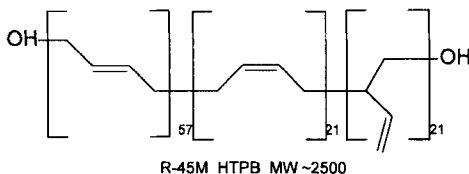
Fig. 1 Basic design of the T-jump/FTIR spectroscopy experiment to give a snapshot simulation of the burning propellant surface.

duration of the experiment. Data up to 500°C are given in this work. The relation between the applied voltage and the resulting filament temperature was calibrated for all experimental conditions by using melting point standards.

Because of limitations in the rate of heat transfer between the filament and sample,^{36,37} the data at <0.5 s are not necessarily isothermal. After this time the characteristic thermal diffusion time, which is the time required for one of the film faces to sense 60% of the temperature change at the other, is about 25 μ s in this experiment.³⁶ This time is much faster than the data collection rate. Once equilibrated, the temperature is known to about $\pm 2^\circ\text{C}$. As a result, the small changes in control voltage applied to the filament can be used to track the endothermic and exothermic events of the sample. An exotherm produces a sharp spike in the control voltage vs time trace. This marks the time to the exothermic event. Transmission IR spectra of the gaseous products are recorded every 100 ms at 4-cm^{-1} resolution simultaneously with the control voltage measurement. These data help outline the chemistry that takes place within the simulated surface reaction zone without the additional complicating contribution of the flame zone.

At least three concerns arise about this simulation. First, the configuration of the experiment is not the same as the burning propellant in that the sample is heated from the underside by the filament rather than the topside by the near-surface primary flame reactions. As the reactions accelerate in the experiment, however, a very thin gas layer may develop between the steady heat source of the filament and the material. This process resembles film boiling, but is more transient because of the reacting dynamic surface. In some sense, however, the configuration of heat source to reactive gas layer to sample in the T-jump experiment resembles the configuration of flame to reactive gas layer to sample that exists during propellant burning. Second, during steady combustion of a propellant, the gaseous products flow against the chamber pressure. To simulate this condition in the snapshot T-jump experiment, argon gas was added to raise the internal pressure in the cell. Third, the film can not replicate all of the events of the burning surface. Connections seem to exist, however, between rapid heating of a film and steady combusting of a bulk energetic material. For example, the rate of mass loss from these mesoscopic films at fast heating rates resembles that calculated from the burning rate of a bulk material at the same (low) pressure.³³ On balance we know that the laboratory simulation of the burning surface by rapidly heating a film cannot be a perfect replication of the combustion conditions, but it is hoped that it offers some useful guidance for current and future propellant modeling efforts.

Four nominal particle diameters of AP (1.4, 8, 18, and 44 μm) were obtained from the Thiokol Corporation. The HTPB used was propellant-grade R45M, whose structure is as follows:



TiO_2 (anatase, 0.5 μm) and melamine (1, 3, 5-triamino-2, 4, 6-triazine) were obtained from Aldrich Chemical Company.

Mixtures were made on a weight percentage basis by thoroughly mixing them with an agate mortar and pestle. These uncured materials were then spread as a film of about 50 μm thickness onto the center of the Pt filament. Multiple data sets were recorded in search of reproducibility. It was found that the results in the first day after mixing were less reproducible than those taken at least a month after mixing. Thus, the slightly aged samples were used for this work. The IR spectra were converted into species concentrations by methods described before.³⁵

III. Decomposition of the Pure Materials

Although no new work on pure AP and pure HTPB was conducted in this project, the behavior of the AP-HTPB mixtures is difficult to appreciate without the context of the pure ingredients. In addition, some comments and cautionary notes about the pure materials may enhance the understanding of their pyrolysis and combustion.

A. Pure AP

Note that the purity of AP used in rocket propellants is 99.3–99.8% (Ref. 38), which raises the question about the role of the impurities in the various, sometimes contradictory, results reported for decomposition and combustion of AP. For example, it has long been known³⁹ that the burning rate of AP depends on the sample purity. This is vividly shown by the burning-rate behavior of single crystals of AP that have been isomorphously doped with <1% quantities of other ions.^{38,40} Very dramatic effects are produced by both redox-active and nonactive ions. The most pronounced effect is with NO_2^+ , which has been shown to increase the burning rate by about 50% when it is present in the crystal lattice at about the 0.01% level.^{19,40} The amount of H_2O incorporated in the crystal lattice can also vary. This potentially affects the experimental decomposition and combustion results because H_2O is known to suppress the burning rate, perhaps by decreasing the amount of radical chemistry associated with HClO_4 (Ref. 41) or perhaps by decomposing the proposed $\text{NO}_2^+\text{ClO}_4^-$ intermediate¹⁹ to which the burning rate is very sensitive.⁴⁰ An additional complication is that $\text{Ca}_3(\text{PO}_4)_2$ is used to coat fine AP crystals to prevent caking.⁴² Discussion of the extent that adventitious impurities might affect experimental results on AP is rare, and this factor may be a variable in some of the differing findings and opinions that have been published. This is particularly an

issue in light of the dramatic effects that the purposeful addition of salts can have on the decomposition and combustion of AP.^{2,3,19,38,40,43,44}

The earliest molecular event in hot AP is the orthorhombic-to-cubic solid-solid phase transition at about 240°C (Ref. 45). This transition occurs beneath the burning surface^{30,46,47} and results from the transition of the ClO_4^- ion from restricted to unrestricted tumbling on the vibrational timescale.⁴⁸ The ensuing destabilization of the AP crystal effectively facilitates the partial conversion from the ionic state to the neutral NH_3 and HClO_4 molecules in the condensed phase. These molecular forms are not thermodynamically favored in the presence of one another and should be thought of as minor species that are in equilibrium with the ions. As the temperature is further raised, the crystal lattice is no longer stable and progressively liquefies,^{30,38,46,49,50} in part because of depression of the melting point by the presence of reaction products. The thickness of the liquid layer during burning is at most about 10 μm at lower pressures based on scanning electron microscopy of quenched samples.^{29,30} Chemical reactions concurrently take place in the liquid layer making it a mixture of components rather than a true AP melt. Attempts to characterize the liquid AP by spectroscopy resulted in an explosion, which is contrary to the more successful experience with liquefied RDX and HMX (Ref. 51). Hence, the chemical details of liquid AP to our knowledge remain unknown.

The initial proton transfer step leading to NH_3 and HClO_4 in the decomposition of pure AP is widely accepted,^{10,12,41,50,52-57} and is highly endothermic ($\Delta H_{\text{dissn}} = 58 \pm 2 \text{ kcal/mol}$) (Ref. 52) with an activation energy E_a of about half this value in the 200–250°C range.⁵⁸⁻⁶² An alternative point of view is that electron transfer occurs to form NH_4 and ClO_4 radicals, and this predominates above 350°C (Refs. 3, 44, 58, and 63). The basis for competing pathways is primarily the comparative values of E_a for the proton and electron transfer processes relative to the E_a value for AP decomposition. In the 250–350°C range, $E_a = 18.5 \text{ kcal/mol}$ for electron transfer whereas $E_a = 30 \text{ kcal/mol}$ for proton transfer.³ E_a for global decomposition in this range is about 20 kcal/mol (Ref. 3), which compares best with the electron transfer process. It is risky, however, to compare E_a values for specific reactions to global decomposition rates⁶⁴ in a process as complicated as the thermal decomposition of AP. For example, $\Delta H_{\text{dissn}} = 58 \text{ kcal/mol}$, which was measured below 250°C, will decrease as the temperature increases. In tandem, E_a will also decrease bringing the proton and electron transfer rates more into line with one another at higher temperatures. Thus, it is probable that both proton and electron transfer rates compete to a degree that depends on the temperature, defect number, and purity of the AP crystal. Electron transfer will be strongly influenced by the presence of intentionally added or adventitiously present redox-active impurities. Redox-active catalysts acting in the condensed phase should primarily alter this mechanism as opposed to the proton-transfer mechanism. For AP used in rocket propellants, however, this initiating reaction may be a moot issue for the combustion of so-called pure AP because the secondary exothermic reactions resulting from the initial, endothermically formed products by the two processes rapidly become indistinguishable.

The secondary reactions involving the initial products of the AP decomposition are very complex and are different from most other energetic materials because of the involvement of chlorine oxides. It is widely accepted that exothermic chemistry begins immediately after the crystal lattice begins to break down,^{41,43,50,54,56} and

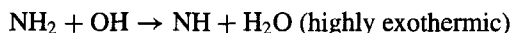
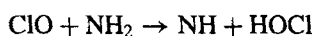
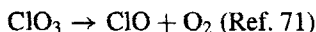
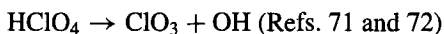
Table 1 Examples of surface temperatures reported for burning AP

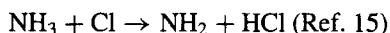
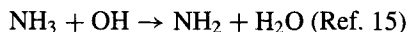
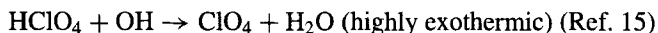
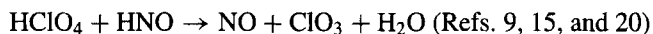
T_s , °C	Pressure, atm	Remarks	Reference
330	1	Thermocouple	65
440	13	Optical pyrometry	66
650	20	IR pyrometry	53
680	33	IR pyrometry	53
720	66	IR pyrometry	53
525–600	20–66	Phase transition	46
442 ± 30	20–66	Reanalysis of Ref. 46	67

that the liquid layer formed during combustion is frothy as a result of the formation of the gaseous products. The degree of exothermicity is not sufficient to sustain the burning of AP below about 15-atm pressure. Heat feedback from the flame zone is needed, and an estimate of the amount of heat released at the surface is as high as 70% (Ref. 57). The thickness of the liquid layer decreases with increasing pressure, and the layer appears gone by about 60 atm (Refs. 3, 29, and 30).

The surface temperature of burning AP has been estimated by several methods and a few of the values are given in Table 1 (Refs. 46, 53, and 65–67). As is the case with many other energetic materials, the agreement among these data is poor, which reflects the difficulty of making an accurate measurement on a transient, multiphase, reaction surface.

The details of the heterogeneous reactions involving the gaseous and liquid phases remain a murky and hopelessly complex subject. Numerous parallel and consecutive reactions occur that are affected by the pressure, temperature, and spatial location in the froth. It is generally agreed, however, that HClO_4 accelerates the decomposition,^{41,44,50,68,69} whereas NH_3 retards the rate at lower temperatures,⁴⁴ but accelerates it at higher temperatures.⁵⁰ Obviously, the relative roles of the heterogeneous reactions change with pressure and formulation, but the occurrence of reactions in the condensed phase is difficult to avoid. For example, assuming an average unit cell dimension of 7.5 Å for AP (Ref. 70), a 1 μm -thick surface reaction zone corresponds to about 1300 unit cell lengths. Given the time estimate for reactions of about 10^{-3} s (Ref. 67) and the surface temperatures in Table 1, there is ample time for many reactions to take place in the condensed phase. Unfortunately, the rate constants have not been measured for many of the possible reactions, especially when mediated by the heterogeneous condensed phase, and so there is little value in speculating further. Some of the reactions that provide radical chain carriers, for example, ClO , and species known to be important in other reaction schemes are listed as follows:





Although radicals such as OH, ClO, and NH are detected after laser pyrolysis,^{10,13} most of the products detected by other methods are stable molecules with mostly even, but some odd, electron counts^{2,9,20,55,59,73,74}: N₂O, NO, NO₂, NOCl, HNO₃, HClO₄, HCl, ClO₂, NH₃, H₂O, Cl₂, O₂, N₂, H₂, and hydrated HCl and HClO₄. For example, the IR spectrum over AP flash heated at 800°C s⁻¹ to 500°C under 4 atm of Ar is shown in Fig. 2 and reveals some of these products. The species just listed are later-stage products from the numerous elementary reactions between N, H, O, and Cl. Many of these products, along with some of the more reactive radicals, escape the surface and initiate the AP flame. Discussion of the flame structure is not the subject of this paper, but closure of this section is aided by summarizing the flame zone chemistry modeling efforts. Kishore⁶ reviewed some of the models devised before 1976.

Models of the combustion process reflect the wisdom and available experimental data at the time of development. Understandably, the earlier models emphasize physical processes. Chemistry and energetics were sometimes incorporated globally, whereas the later models incorporate detailed chemistry. Physical observations about the burning process of AP led to the earliest models based on the conservation equations and management of heat transfer.⁷⁵⁻⁷⁹ Although these models were successful in fitting features such as the burning rate, the low-pressure deflagration limit, and some of the ignition behavior, it was difficult to extend them to include the binder, temperature sensitivity, and the details of the flame structure. Inclusion of chemistry was, therefore, needed.

Manelis and Strunin⁴¹ brought to light the probable behavior of the initial products NH₃ and HClO₄ during the burning of AP and, thereby, focused attention on the

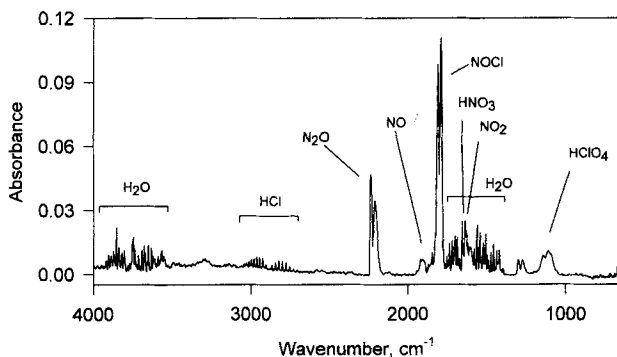


Fig. 2 IR spectrum of the gaseous products from solid AP heated at 800°C s⁻¹ and held at 500°C under 4 atm Ar.

role of chemical processes. In fact they asserted that the condensed phase chemistry dominates in the combustion processes. Comments of this type appeared along side the earliest chemistry-based model of AP combustion by Guirao and Williams,⁵⁷ who used a 14-step gas-phase reaction mechanism to fit the burning-rate curve and also proposed that 70% of the heat is released in a global surface process. In another pioneering chemistry-based effort, Ermolin et al.⁹ devised an 80-step mechanism with 24 species that was motivated by an attempt to fit the species profiles in the gas phase of AP burning at low pressure.⁷⁴ A subsequent more limited mechanism having 22 steps and 8 species⁸⁰ has been criticized by Cohen,⁷² who updated several earlier mechanisms with 136 steps and 35 species.¹⁴ He obtained reasonable agreement with the flame temperature. Tanaka and Beckstead¹⁵ devised a combined gas-liquid-solid phase model of AP combustion in which the gas phase consisted of 107 steps and 32 species. They concluded that the condensed-phase kinetics much more strongly influenced the combustion characteristics than did physical properties, such as the thermal conductivity and density of the solid. The minor role played by heat conduction has been noted elsewhere.⁸¹

B. HTPB

The use of HTPB as a binder in solid rocket propellants appears to date from about 1962 in work by the Aerojet Corporation.⁴² Many structures of HTPB exist, and the most commonly used type (R45M, whose structure was shown in Sec. II) can be thought of as a terpolymer of *cis*-, *trans*-, and vinyl-linked butadiene units. In addition, the terminal groups, that are $-\text{OH}$ in R45M are an additional variable. Also, $-\text{CO}_2\text{H}$ has been used as a terminal group (called CTPB), but is no longer used as a propellant binder in the United States. The copolymer of polybutadiene and acrylic acid (PBAA) and terpolymer of polybutadiene, acrylic acid, and acrylonitrile (PBAN) also have application as propellant binders. Several detailed reviews^{27,82} and more specialized summaries^{3,6,24,83} of polybutadienes, including their use in rocket propellant formulations, are available.

Studies of the thermal decomposition of HTPB and related polymers at fast heating rates^{24,83-89} and at slow heating rates^{21-23,90-104} are rather extensive. The decomposition process has a distinguishable, mildly exothermic component because bond forming processes occur along side of the bond-breaking processes.^{83,89,102,104} Numerous fragments of the polymer have been detected, but the main species are the butadiene monomer, dimer (4-vinylcyclohexene), and *trans*-butadiene oligomers. Figure 3 shows the mole fractions of the major products from flash heating of a thin film of R45M at 800°C s^{-1} under 2 atm of Ar to the constant temperatures shown.²⁴ These species primarily indicate that random chain cleavage occurs along the polymer backbone followed by subsequent vaporization of the fragments. The presence of a high percentage of oligomers of butadiene relative to the monomer indicates that the zip length of HTPB is relatively small. That is, the formation of a radical due to bond cleavage in the polymer backbone does not result in an extensive propagation of the radical sites along the chain and, thus, liberates a comparatively low percentage of the monomer.

The kinetics of formation of each of the products shown in Fig. 3 has been established recently at a high heating rate.⁸³ The behavior observed suggests that the process that controls the rate of appearance of the species in the gaseous

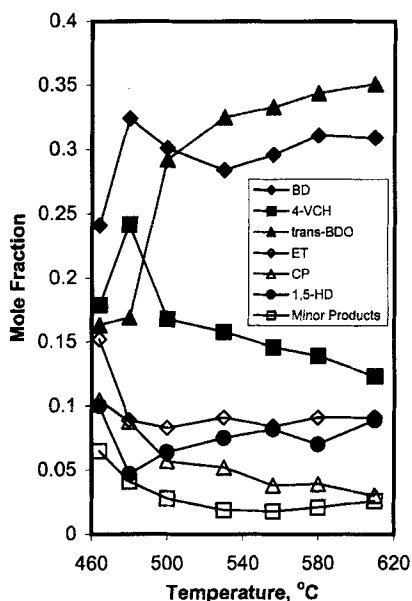


Fig. 3 Quantified gaseous product concentration profiles from flash heating of HTPB (R45M) to the temperature shown under 2 atm Ar (Ref. 24): BD = butadiene; 4-VCH = 4-vinylcyclohexene; ET = ethylene; CP = cyclopentene; 1,5-HD = 1,5-hexadiene; trans-BDO = transbutadiene oligomers.

phase shifts from one of bulk-phase chemical reaction control below 500–530°C to one of desorption/evaporation control above this temperature range. It has also been shown that urethane cross-linked HTPB upon fast heating regenerates the cross-linking agent that then vaporizes before the polymer fragments appear.⁸⁹ This has been used to justify the use of uncross-linked HTPB to identify potential hydrocarbon fragments released when the surface of an AP-HTPB mixture pyrolyzes.^{24,83} The physical properties of the polymer-rich region of the mixture can be expected to differ depending on whether the cross-linking agent is present or not, but the focal chemistry question for this work was the extent to which the decomposition products of AP affect the decomposition process of HTPB. One study has suggested that there is little effect,¹⁰⁵ perhaps because AP mainly controls the burning rate of AP-HTPB mixtures,³ especially above 70 atm (Ref. 106). Other studies indicate that the AP and HTPB interact during decomposition of the mixture.^{27,107–109}

IV. AP-HTPB Mixture

The complexity of the pyrolysis and combustion of pure AP and pure HTPB alone is magnified when the two are combined as a heterogeneous mixture. The overall event becomes a three-dimensional combination of homogeneous and heterogeneous chemical and physical processes whose balance depends on the intrinsic variables that are in play.^{29,110,111} A few of the general concepts expressed

about this process in the past 50 years are summarized next in the context of the present experiments. In some instances the fuel used by others was not HTPB, but the comments apply in general terms to AP mixed with any hydrocarbon fuel.

First, one of the main themes of this section is the evidence that AP and HTPB interact during fast decomposition of the mixture. By design, the T-jump/FTIR spectroscopy experiment is intended for study of the condensed-phase chemical processes without the flame zone. Decomposition of energetic materials in the condensed phase is inherently made complicated, however, because gaseous products form that leads to phase interfaces. In the case of AP-HTPB composite mixtures, additional interfaces also exist between the ingredients. Throughout this section the term interfacial is intended to group together these ill-defined reaction interfaces because they cannot be distinguished in the experiment.

Second, a wide range of opinions exists with regard to the relative roles of the condensed and gas phases during combustion of propellants containing AP. Some believe that the condensed-phase chemistry almost totally controls the burning process,^{41,57,112} whereas others merely favor an important role for the condensed phase.^{25,31,32,50,54,108,113–119} The other extreme is that the gas phase primarily controls the combustion process^{68,70,76,77,88,120} and that interfacial chemistry in the condensed phase is not apparent.¹²⁰ Some of these distinctions may be primarily semantic given the unclear distinction of what the condensed phase is and where it becomes the gas phase. That is, if a liquid layer containing bubbles exists,^{32,71,111,121} then the gas and condensed phases coexist. To complicate matters further, particles may be able to enter the gaseous phase.^{112,122} The surface structure of AP crystals is also highly nonuniform with ridges and valleys present.^{29–32}

Third, it is generally accepted that the near-surface edge of the AP–fuel diffusion flame is an important site in the combustion process because it is the location of a large amount of exothermic redox chemistry. This concept enables features such as the dependence of the burning rate on the pressure and the AP particle size to be understood.^{25,26,28,123,124}

Fourth, during the ignition stage, heterogeneous gas–condensed-phase reactions are believed to dominate,^{54,106,125–127} as opposed to an entirely gas-phase ignition event, but this view requires careful interpretation.¹²⁸ Thus, it has been widely stated^{12,26,31,54,81,88,115,118,129–131} that interfacial chemistry plays a major role in the condensed-phase, surface, and near-field gas-phase processes of AP–binder mixtures, although agreement is not universal.^{67,132} The problem is to define what reactions occur under what conditions.

We accepted that elucidation of the chemical details of the condensed phase of AP-HTPB mixtures at combustion-like conditions was probably beyond the present ability of chemical diagnostics, although this issue is recognized to be perhaps the major deficiency in understanding in this field.^{8,15} This project was undertaken with the hope of adding additional insights at fast heating rates because most past chemistry studies on the AP-HTPB mixtures have been undertaken at low (<100°C/min) heating rate conditions.^{2,44,55,58,59,61–63,73,113,114,132–134}

A. Thermal Stability of the Mixture

T-jump/FTIR spectroscopy makes it possible to measure the time to exotherm at relatively high temperatures, because flash heating to a controlled set temperature is

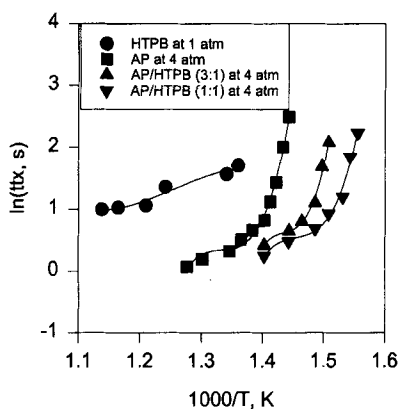


Fig. 4 Times-to-exotherm data for films of the samples (44- μm AP) heated at 800°C s^{-1} to the temperature shown under 4-atm Ar; HTPB was studied at 1-atm pressure of Ar.

performed. By monitoring the control voltage trace of the Pt filament that maintains this constant set temperature as a function of time, the time to exotherm at a series of temperatures can be obtained. The temperature range was chosen with an eye on the T_s values in Table 1, although practical considerations dictated the use of the lower end of the range ($375\text{--}500^\circ\text{C}$).

Figure 4 shows the time-to-exotherm plot for pure HTPB, pure AP, and two physical mixtures of AP with different weight ratios of HTPB. The theoretical basis of this type of plot has been discussed³⁶ including that the curvature is related to the changing role of heat transfer as a function of temperature. This is not the main point of interest here. The relevant point is the relative positions of the curves. Figure 4 shows that pure HTPB and pure AP are both more stable in terms of the time to exotherm at a given temperature than either of the physical mixtures of AP-HTPB. This finding is consistent with previous studies that found AP-fuel mixtures to be less thermally stable^{25,108,109,135} and to burn faster³⁹ than the pure components and is evidence that interfacial, exothermic, free-radical chemistry in the condensed phase contributes to the early stages of pyrolysis of AP-HTPB mixtures. This is despite the initial decomposition reaction, which is proton transfer involving the AP, being highly endothermic. The rapid, highly exothermic, secondary redox reactions quickly destabilize the mixture compared to the pure components. Thus, these results are consistent with the existence of exothermic surface reactions for AP-HTPB, as has been postulated before.^{28,108,110,126,133}

B. Gaseous Products

In accordance with the apparent occurrence of some interactive chemistry of the AP-fuel mixture in the condensed phase, the gaseous products from flash heating of a thin film of the 3:1 AP-HTPB mixture (Fig. 5) are dramatically different from those of pure AP (Fig. 2) and HTPB (Fig. 3). An interesting observation is the nature of the hydrocarbon products detected. Unlike pure HTPB, the highest molecular weight hydrocarbon observed is C_2H_2 . This implies that radicals formed when AP decomposes cause extensive radical chain cleavage of the HTPB backbone

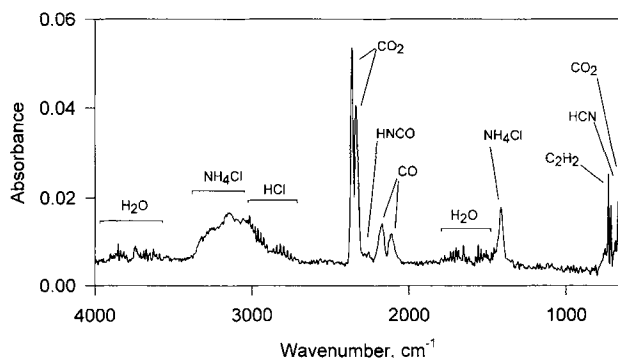


Fig. 5 IR spectrum from 1.4- μm AP-HTPB at a 3:1 weight-weight ratio flash heated at 800°C s^{-1} to 410°C under 4-atm Ar.

resulting in extremely fast disintegration of the polymer and liberation of only the most stable low molecular weight hydrocarbons. It is believed that HClO_4 and its derived radicals attack the polymer.^{125,136} The absence of high molecular weight hydrocarbons from pyrolysis of AP-fuel mixtures has been observed by others using a variety of diagnostic and heating methods.^{12,116,118,131,132,136} As has been done recently, this makes low molecular weight hydrocarbons the most relevant for use in studying and modeling the diffusion flame structure of an AP-fuel mixture.¹⁶

Other major differences are apparent when Figs. 2 and 5 are compared. Pure AP in Fig. 2 liberates NO , NOCl , N_2O , NO_2 , HNO_3 , and HClO_4 , which reflect only partially completed redox chemistry because an insufficient amount of fuel (NH_3) is present. Hence, various oxides of nitrogen form with intermediate formal oxidation states of N. On the other hand, when the hydrocarbon fuel is available, the needed fuel, as well as the ease of oxidizing the hydrocarbons compared to NH_3 , is apparent in the fraction of carbon oxides, as opposed to nitrogen oxides, that dominate. In fact, no nitrogen oxides at all are detected from the AP-HTPB mixture by IR spectroscopy. Discussion of several further details about the product ratios is deferred until later in this section.

Figures 6 and 7 show the trends in the mole fractions as a function of the pyrolysis temperature for 1.4- and 44- μm -diam AP, respectively, in a 3:1 AP-HTPB mixture. The main difference in this case is the different amount of contact between the AP and HTPB because the surface area of the AP particles scales as $1/r^2$. In Fig. 6, the products from 1.4- μm AP exhibit a mild dependence on the temperature, especially at the lower end of the range. This is not so much the case with the other AP particle sizes used (8, 18, and 44 μm). For example, Fig. 7 for 44- μm AP shows less dependence of the gaseous product concentrations on the pyrolysis temperature. An additional manifestation of the larger AP surface area of 1.4- μm AP is that the 3:1 weight-weight ratio sample has a cakey appearance, whereas the samples with larger particles are thick fluids. Apparently the higher surface area of 1.4- μm AP enables more complete wetting by HTPB and, thus, has less free HTPB to act as a fluidizing medium. The more intimate contact of the HTPB with the smaller AP crystals enhances the opportunity for radical reactions to occur between the binder and oxidizer. Bakhman earlier arrived at the same conclusion.¹³⁷ This maximizes the opportunity for the AP-binder reaction over a wide range of conditions and leads to the dependence of the product

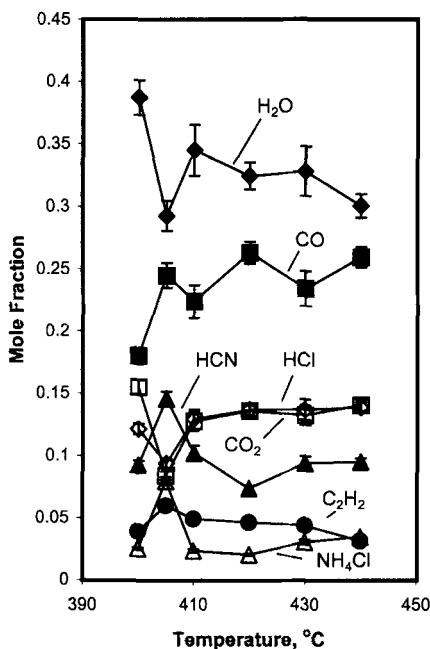


Fig. 6 Mole fractions of the gaseous products from flash heating of 3:1 AP (1.4 μm)-HTPB at 800°C s^{-1} to the temperatures shown under 4-atm Ar.

ratios on the pyrolysis temperature shown in Fig. 6. Earlier experimental findings and modeling principles are consonant with this result. For example, it is known that the binder type plays a lesser role in the burning rate for larger AP particle sizes,¹²¹ which suggests that the amount of interfacial chemistry is less. Models of composite propellant burning^{6,26,28,71,115,123,138} have paid attention to larger AP particles in composite propellants tending to give lower burning rates, especially at higher pressures^{39,40,128,139,140} because the diffusion flame develops farther from the pyrolysis surface. Smaller AP particles, on the other hand, lead to better fuel-oxidizer mixing closer to the surface.^{28,137} Some chemical details of the diffusion flame are beginning to emerge.¹⁶

The gaseous product ratios shown in Fig. 6 compare quite well with those found by Korobeinichev et al.,¹¹⁶ who determined them by probing the flame of a 5:1 AP-CTPB mixture at a subatmospheric pressure by TOF mass spectrometry (Table 2). In constructing Table 2, their data at about 2 mm above the surface were used and were normalized to ours by removing the small amounts (<3%) of Cl₂, O₂, N₂, H₂, and HOCl that were not detected with the IR spectroscopy method. We verified by separate mass spectrometry and Raman spectroscopy experiments that small amounts of Cl₂, N₂, and H₂ are indeed present in our experiment. HOCl was not detected. In view of the different fuel-oxidizer ratio and the different end groups used in the fuel in the comparison in Table 2, the agreement is satisfactory. One obvious difference is that we detected NH₄Cl. This is an artifact of quenching by the cool Ar atmosphere that enables NH₃ and HCl to recombine. This recombination is not favored in the flame and contributes to the higher quantity of HCl reported by Korobeinichev et al.¹¹⁶

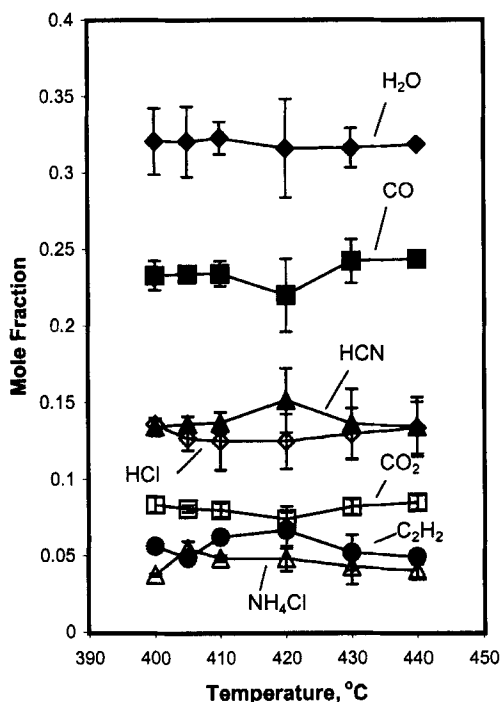


Fig. 7 Mole fractions of the gaseous products from flash heating of 3:1 AP ($44\ \mu\text{m}$)-HTPB at $800^\circ\text{C}\ \text{s}^{-1}$ to the temperatures shown under 4-atm Ar.

As a method to summarize the effect of the AP particle size on the mole fractions of the gaseous products, the data for each particle size were averaged over the 400–440°C range and plotted as a function of the particle size. The result is shown in Fig. 8. As discussed earlier and shown in Fig. 6, the results for $1.4\text{-}\mu\text{m}$ AP are somewhat atypical, and so attention is mainly focused on the trends for $\geq 8\ \mu\text{m}$ particle sizes of AP. The trends are that the concentrations of HCN and C_2H_2 tend to decrease whereas CO_2 and CO tend to increase with increasing particle

Table 2 Comparison of the mole fractions of gaseous products from AP-polybutadiene mixtures

Product	Ref. 116	This work
H ₂ O	29	33
CO	23	24
HCl	23	12
HCN	7	13
CO ₂	11	8
C ₂ H ₂	5	5
NH ₃	3	5 ^a

^aAs NH_4Cl .

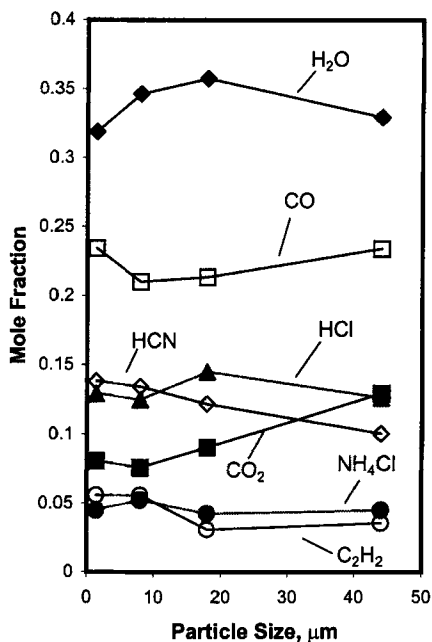


Fig. 8 Mole fractions of the gaseous products averaged over 400–440°C as a function of the AP particle size; data were taken at 4-atm Ar.

size. Various explanations can be imagined, but one that is consistent with the experimental design is suggested here. The HCN and C₂H₂ contain carbon in lower oxidation states and, thus, reflect incomplete oxidation of the hydrocarbon fuel. This suggests that less interfacial AP–fuel chemistry occurs with the larger AP crystals, which is consistent with their lower surface area. As a result, more of the AP-based decomposition products have not reacted with the binder at the interface in the condensed phase and are, instead, able to form the gaseous phase, where they can then react. Hence, there is proportionally more gas-phase redox chemistry possible with the larger particle sizes that results in larger amounts of CO₂ and CO.

Figure 9 shows the trend in the ratio of C₂H₂ to CO₂ as a function of the ratio of AP to HTPB. The C₂H₂/CO₂ ratio partly reflects the relative extents of cleavage of the polymer backbone vs oxidation of the fragments. At low AP–HTPB ratios, where the mixture is strongly fuel rich, a small amount of ethylene, C₂H₄, was also detected, but the predominate hydrocarbon is still C₂H₂. Hence, even in a fuel-rich mixture, the fuel pyrolysis process is completely unlike that of pure HTPB (Fig. 3) because the AP-based radicals attack the polymer backbone and cause radical chain cleavage. Not surprisingly, however, the C₂H₂/CO₂ ratio decreases as the AP–HTPB ratio increases because more hydrocarbon oxidation can occur. There is possibly a dependence of the C₂H₂/CO₂ ratio on the AP particle size in Fig. 9, which becomes more pronounced with the larger particle sizes.

Widely used combustion models of composite propellants that emphasize control of combustion by the leading edge of the diffusion flame handle the relative balance between the fuel and oxidizer species in the gas phase by an adjustable parameter β_F (Refs. 28 and 138). Other approaches over the years use the concept

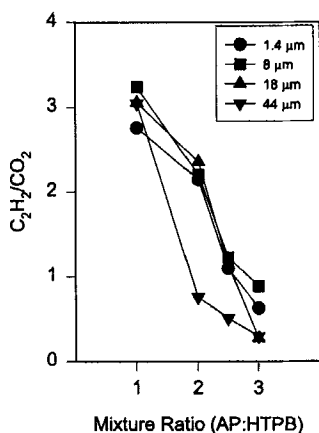


Fig. 9 $\text{C}_2\text{H}_2/\text{CO}_2$ ratio as a function of AP particle size in 3:1 AP-HTPB mixtures flash heated to 440°C under 4-atm Ar.

of two temperatures^{39,141,142} and different activation energies¹⁴³ at the surface of a burning AP-composite propellant. That is, one temperature or activation energy applies to pyrolysis of the binder whereas another applies to pyrolysis of the AP crystal. The conclusion we would draw from the current chemistry study is that the two-temperature concept would be most appropriate for larger AP particle sizes and for AP-fuel mixtures that are somewhat less than stoichiometric.

As noted earlier in the products from pure AP (Fig. 2) compared to those from the AP-fuel mixtures (Figs. 6 and 7), an important difference is the presence of NH_4Cl in the latter. NH_4Cl has been seen before as a product of the AP-fuel mixture at slow heating rates.¹⁴⁴ The formation of NH_4Cl reflects the competitive oxidation rates of NH_3 and the hydrocarbons in which the hydrocarbons win.^{145,146} The hydrocarbon fragments, except possibly C_2H_2 , are more easily oxidized than NH_3 , which results in the liberation of some unreacted NH_3 in the AP decomposition process. The appearance of C_2H_2 in the gas phase reflects that C_2H_2 is oxidized more slowly than are the other hydrocarbons.¹⁴⁵ Figure 10 shows the $\text{NH}_4\text{Cl}/\text{C}_2\text{H}_2$ ratio as a function of temperature when the data are averaged for the four AP particle sizes. At lower temperatures, less of the NH_3 is oxidized relative to the hydrocarbons so that the ratio is higher compared to that at higher temperatures. The rather large error bars of Fig. 10 result from the averaging of the different particle sizes, rather than the true error in an individual measurement. The trend shown was found in all of the data.

C. Effect of Pressure

These flash pyrolysis studies to establish some of the chemical features of AP-HTPB mixtures were conducted at 1–5 atm of Ar so that the reaction zones would be stretched with the hope of seeing more than just the thermodynamically stable final products. These pressures do not apply to steady combustion conditions of a rocket motor. Therefore, 8- μm -diam AP particles in a 3:1 AP-HTPB mixture were flash pyrolyzed at different static pressures at 4–50 atm Ar. Figure 11 shows the trends observed. Although the behavior of H_2O is not easily understood, the trends

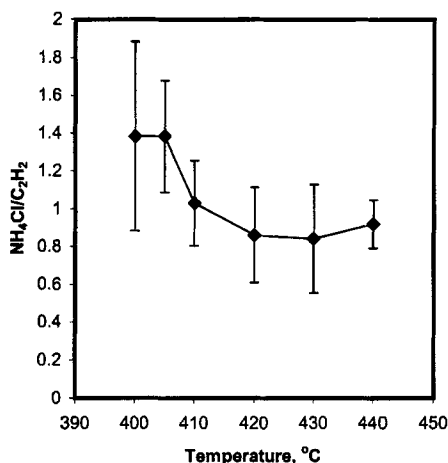


Fig. 10 $\text{NH}_4\text{Cl}/\text{C}_2\text{H}_2$ ratio from 3:1 AP-HTPB mixtures flash heated to the temperatures shown under 4-atm Ar; concentrations for all particle sizes were averaged.

of the other products can be explained in terms of past work of this type.¹⁴⁷ As the pressure is increased, the CO , CO_2 , and NH_4Cl products appear with larger concentration, whereas C_2H_2 and HCN are decreased in concentration. Consequently, the application of higher pressures advances the extent of the AP-fuel reaction by forcing the products to remain longer in the reaction zone close to the heat source. That more NH_4Cl forms at the higher pressures is consistent with an increase in the amount of HClO_4 -hydrocarbon chemistry relative to HClO_4 - NH_3 chemistry. This is a direct result of the greater reactivity of the hydrocarbons toward HClO_4 compared to NH_3 (Refs. 125, 136, 145, and 146).

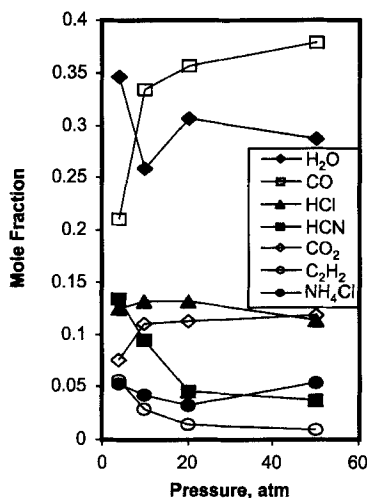


Fig. 11 Mole fractions as a function of the static cell pressure of Ar for 3:1 AP (8 μm)-HTPB flash heated to 440°C.

V. AP-HTPB with TiO_2 and Melamine

As complicated as the AP-HTPB interfacial chemistry is, the addition of a burning-rate modifier adds yet another dimension of complexity. Several reviews of such additives have appeared over the years.^{2,3,43,44,148} The most commonly used class of modifiers has been the inorganic oxides, although interesting results can also be produced with organic additives.¹⁴⁹ Many studies propose that the ballistic modifier is active primarily in the condensed phase at the AP-binder interface,^{110,135,150,151} where electron transfer is important,^{44,135} whereas others propose that the action primarily takes place in the gas phase.^{65,152}

In this section the properties of TiO_2 in the AP-HTPB matrix are the main focus in view of the recently discovered plateau burning behavior of AP-HTPB propellants in the 50–100 atm pressure range when 0.5–5% TiO_2 has been added.^{17,18} Prior to this discovery, TiO_2 had been studied frequently as an additive with the results being somewhat contradictory. It had been described variously as inactive,^{44,153} less active,⁵⁶ a suppressant to the burning rate,⁴³ and as an acoustic dampener that stabilizes combustion.¹⁵⁴ On the other hand, the addition of an ultrafine mixture of the anatase and rutile polymorphs of TiO_2 promotes plateau burning in the AP-HTPB propellant.¹⁷ The mechanism of action is not yet agreed upon, although thermogravimetric analysis (TGA) measurements indicate that the weight loss is faster when TiO_2 is present,¹⁸ which suggests that some additional chemical reactivity has been introduced. As a sidelight, we explored the behavior of melamine in the AP-HTPB mixture. To our knowledge, past work on this additive has been limited, but is potentially interesting as a burning-rate suppressant.¹⁴⁹

Flash pyrolysis of small quantities of a three-component mixture understandably has more potential problems with the sample uniformity than the single- and two-component systems. Consequently, completely reproducible results were difficult to obtain, and many repeated experiments were conducted to acquire a representative set of results. With the caveat that some outlying results were obtained, Figure 12 shows the time sequence of the product evolution from a 3:1 AP-HTPB mixture with 8- μm AP that had been heated at 800°C s^{-1} to 405°C under 4 atm of Ar. Figure 13 shows the results of an equivalent experiment in which 5% TiO_2 had been added to the sample. Figure 14 is the same as the experiment shown in Fig. 12,

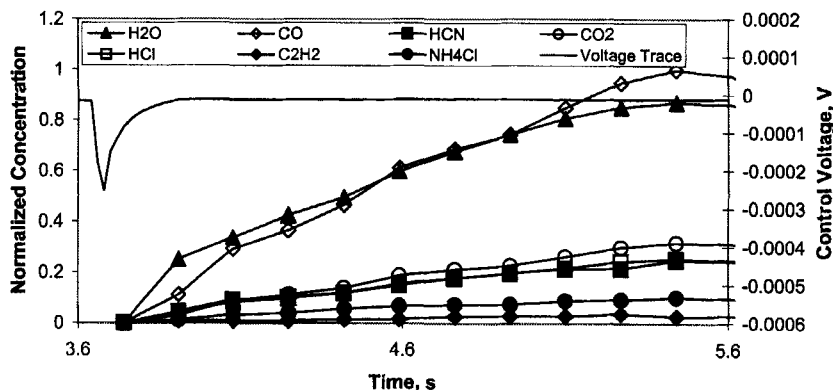


Fig. 12 Rate for formation of products and the Pt filament control voltage trace for 3:1 AP (8 μm)-HTPB flash heated at 800°C s^{-1} to 405°C under 4-atm Ar.

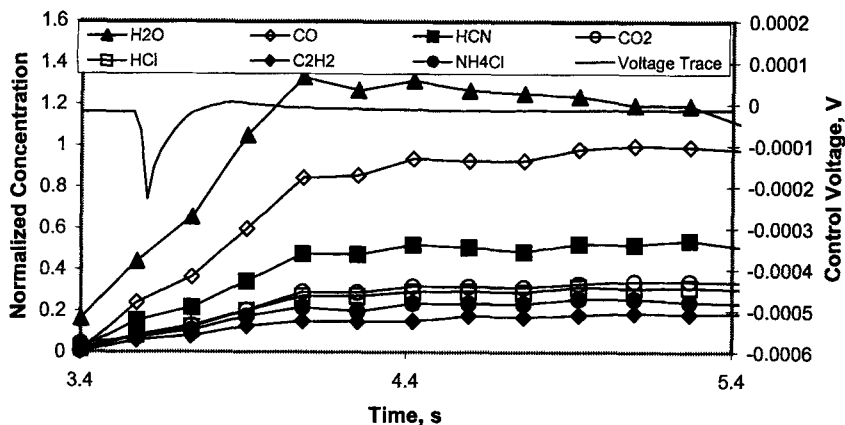


Fig. 13 Rate of formation of gaseous products and the Pt filament control voltage trace for 3:1 AP (8 μ m)-HTPB containing 5% TiO₂ (anatase) flash heated to 405°C under 4-atm Ar.

except that 5% melamine was present in the sample. Comparing Figs. 12 and 13, the time to exotherm (the negative spike in the control voltage difference trace) is affected little by the addition of the TiO₂, but TiO₂ accelerates the rate of evolution of the gaseous products. This finding is consistent with TGA data¹⁸ that revealed faster weight loss in a TiO₂-containing AP-HTPB propellant sample. In contrast, Fig. 14 shows that melamine lengthens the time to exotherm, but has a small effect on the formation rate of the products. Consequently, we conclude that TiO₂, but not melamine, is a positive catalyst for decomposition under the conditions used here. TiO₂ does not destabilize the mixture in terms of the time-to-exotherm criterion of Fig. 4. Thus, it is probable that the surface temperature during combustion is similar with and without the TiO₂ additive, which is consistent with the notion that the surface temperature is not generally a strong function of the catalyst.¹¹⁰

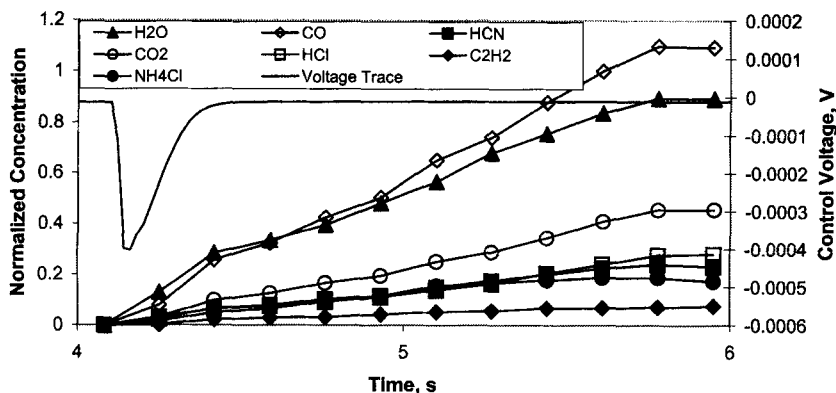


Fig. 14 Rate of formation of the gaseous products and the Pt filament control voltage trace for 3:1 AP (8 μ m)-HTPB containing 5% melamine flash heated to 405°C under 4-atm Ar.

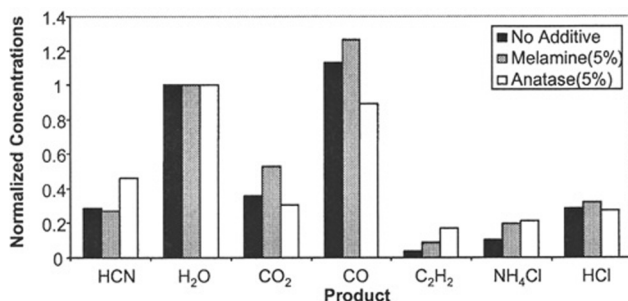


Fig. 15 Comparison of the maximum mole fractions of the gaseous products normalized to H₂O for Figs. 12–14.

Melamine, on the other hand, seems to stabilize the mixture somewhat in the context of Fig. 4 without affecting the decomposition rate. As a result, it may slightly decrease the surface temperature during combustion.

Figure 15 is a bar graph that compares the mole fractions of the gaseous products from the three formulations at their maximum point normalized to the mole fraction of H₂O. These data were obtained on 8- μ m AP, but the features shown also qualitatively apply to the other particle sizes. The presence of TiO₂ increases the relative amounts of HCN, C₂H₂, and NH₄Cl, which is the same effect seen in Fig. 8, caused by reducing the AP particle size. That is, the relative proportion of condensed phase interfacial chemistry is somewhat higher when TiO₂ is present. This seems to be consistent with the higher rate of product evolution shown in Fig. 13. The amount of CO₂ and CO are about the same or somewhat less, suggesting that the redox chemistry may be reduced to some extent by the presence of TiO₂. Because these experiments were conducted at a pressure well below that where plateau burning is observed (50–100 atm) (Ref. 17), it is not at all certain that they have any relation to the mechanism of this phenomenon. If this observation is valid at higher pressures, however, TiO₂ may dampen the amount of heat released and possibly contribute to a slowing of the burning rate.

The effect of 5% melamine on the product ratios is small compared to the AP-HTPB mixture without the additives. This observation is consistent with the similarity of the product formation rates in Figs. 12 and 14. The main effect is to increase the amounts of CO₂, CO, and NH₃ (NH₄Cl), which is understandable because decomposition of melamine itself by the AP radicals will produce CO, CO₂, and NH₃. Thus, the product distribution is somewhat skewed, but in an understandable way. The behavior of melamine is consistent with the hypothesis¹⁴⁹ that the melamine suppresses the burning rate of the AP-HTPB mixture by affecting the heat transfer process rather than by altering the chemistry of the AP-HTPB system.

VI. Conclusions

Superatmospheric pressure, flash-heated, physical mixtures of AP and HTPB may provide insight into behavior at combustionlike conditions and provide a context for past studies conducted at other conditions. Some of the mechanistic features may help refine several details in modeling efforts.

It was clearly found that the AP-HTPB mixture is less thermally stable than the pure components, which is a strong indication that radical chain cleavage of the HTPB polymer is induced, and that the AP radical products are formed at a higher rate in the presence of hydrocarbons. These reactions become highly exothermic in the heterogeneous gas-condensed phase region as a result of oxidation-reduction processes. One useful observation is that C_2H_2 is the highest molecular-weight hydrocarbon to survive the condensed-phase reactions in a measurable concentration. Its survival in part reflects that C_2H_2 is the least readily oxidized of the available hydrocarbons. The remaining hydrocarbons are also oxidized faster than NH_3 , which leads to the liberation of some NH_3 (detected as the recombination product of NH_3 and HCl in the gas phase). The gaseous product ratios observed agree reasonably well with studies by Korobeinichev et al.¹⁴⁵ on the combustion of AP-binder mixtures at low pressure.

The AP particle size effect can be seen clearly in the flash decomposition products of the AP-HTPB mixture. More AP-fuel interfacial chemistry is apparent with the smaller particle sizes. The effect of increasing the pressure is to drive the reactions further toward the more thermodynamically stable products.

The addition of TiO_2 , which creates plateau burning in the AP composite propellant, had no effect on the thermal stability in terms of the time to exotherm. Instead, it acted as a catalyst, as evidenced by the faster rate of gaseous product evolution and a higher concentration of products resulting from the AP-HTPB interfacial chemistry. A lower concentration of the products from the more exothermic gas-phase redox reactions was generated that might have the effect of decreasing the burning rate. In contrast, the addition of melamine stabilized the AP-HTPB mixture by producing a longer time to exotherm, but did not significantly affect the AP-HTPB interfacial chemistry. This finding is consistent with the notion that melamine affects heat transfer by forming polymeric materials in addition to lower molecular-weight decomposition products.¹⁴⁹ The provocative question arises as to whether T-jump/FTIR spectroscopy might be used to provide more insight into the mechanisms of burning rate modifiers than has been available from other methods.

Acknowledgments

We are grateful for support of this work by the Ballistic Missile Defense Office through the Office of Naval Research (ONR) on the Multidisciplinary University Research Initiative program as a subcontract from California Institute of Technology. The Program Monitor is Judah Goldwasser on ONR N00014-95-1-1338. Thiokol Corporation generously provided samples of AP and R45M.

References

- ¹Price, E. W., "History of Solid Rocket Motors (1940-1960)," AIAA Paper 98-3978, 1998.
- ²Jacobs, P. W. M., and Whitehead, H. M., "Decomposition and Combustion of Ammonium Perchlorate," *Chemical Reviews*, Vol. 69, No. 4, 1969, pp. 551-590.
- ³Kishore, K., and Prasad, G., "A Review on Decomposition/Deflagration of Oxidizer and Binder in Composite Solid Propellants," *Defence Science Journal*, Vol. 29, 1979, pp. 39-54.

⁴Kishore, K., and Gayathri, V., "Chemistry of Ignition and Combustion of Ammonium-Perchlorate-Based Propellants," *Fundamentals of Solid-Propellant Combustion*, edited by K. K. Kuo and M. Summerfield, Vol. 90, Progress in Astronautics and Aeronautics, AIAA, New York, 1984, pp. 53–106.

⁵Lengellé, G., Brulard, J., and Moutet, H., "Combustion Mechanisms of Composite Solid Propellants," *Proceedings of the 16th Symposium (International) on Combustion*, Combustion Inst., Pittsburgh, PA, 1976, pp. 1257–1270.

⁶Kishore, K., "Comprehensive View of the Combustion Models of Composite Solid Propellants," *AIAA Journal*, Vol. 17, No. 11, 1979, pp. 1216–1224.

⁷Ramohalli, K., "Technologies and Techniques for Instability Suppression in Motors," *Nonsteady Burning and Combustion Stability of Solid Propellants*, edited by L. De Luca, E. W. Price, and M. Summerfield, Vol. 143, Progress in Astronautics and Aeronautics, AIAA, Washington, DC, 1989, pp. 805–848.

⁸Beckstead, M. W., "Solid Propellant Combustion Mechanisms and Flame Structure," *Pure and Applied Chemistry*, Vol. 65, No. 2, 1993, pp. 297–307.

⁹Ermolin, N. E., Korobeinichev, O. P., Tereschenko, A. G., and Fomin, V. M., "Kinetic Calculations and Mechanism Definition for Reactions in an Ammonium Perchlorate Flame," *Combustion, Explosion, and Shock Waves*, Vol. 18, No. 2, 1982, pp. 180–189.

¹⁰Chen, K. M., Wang, G. P., Kuo, C. N., Shyy, I. N., and Chang, Y. M., "Laser-Induced Decomposition of Ammonium Perchlorate. Identification of Nascent Products from Emission Spectroscopy," *Chemical Physics Letters*, Vol. 167, No. 4, 1990, pp. 351–355.

¹¹Brill, T. B., Brush, P. J., James, J. E., Shepherd, J. E., and Pfeiffer, K. J., "T-Jump/FTIR Spectroscopy. A New Entry into the Rapid, Isothermal Pyrolysis Chemistry of Solids and Liquids," *Applied Spectroscopy*, Vol. 46, No. 6, 1992, pp. 900–911.

¹²Klotz, S., Thynell, S. T., Huang, I. T., and Kuo, K. K., "Analysis of Plumes of Solid Propellant Combustion Using a Fourier Transform-Infrared Spectrometer," *Journal of Propulsion and Power*, Vol. 8, No. 3, 1992, pp. 537, 538.

¹³Parr, T., and Hanson-Parr, D., "Solid Propellant Flame Chemistry and Structure," *Non-Intrusive Combustion Diagnostics*, edited by K. K. Kuo and T. P. Parr, Begell House, New York, 1994, pp. 571–599.

¹⁴Cohen, N., "A Review of Kinetic Models for the High Temperature Gas Phase Decomposition of Ammonium Perchlorate," Aerospace Rept. ATR-92(9558)-3, The Aerospace Corp., El Segundo, CA, Sept. 1992.

¹⁵Tanaka, M., and Beckstead, M. W., "A Three Phase Combustion Model of Ammonium Perchlorate," AIAA Paper 96-2888, 1996.

¹⁶Parr, T. P., Hanson-Parr, D., Smooke, M., Ilincic, N., Tanoff, M., and Yetter, R., "AP Diffusion Flame Structure," CPIA Publ. 662, Vol. 2, Chemical Propulsion Information Agency, Laurel, MD, 1997, pp. 13–22.

¹⁷Taylor, R. H., Use of Controlled Burn Rate, Reduced Smoke, Biplateau Solid Propellant Formulations, U.S. Patent 5,579,634, 3 Dec. 1996.

¹⁸Freeman, J. M., Price, E. W., Chakravarthy, S. R., and Sigman, R. K., "Contribution of Monomodal AP/HC Propellants to Bimodal Plateau-Burning Propellants," AIAA Paper 98-3388, 1998.

¹⁹Galwey, A. K., Herley, P. J., and Mohamed, M. A., "Role of Additives in the Thermal Decomposition of Ammonium Perchlorate and Evidence Supporting the Identification of Nitryl Perchlorate as the Essential Reaction Intermediate," *Thermochimica Acta*, Vol. 132, No. 1, 1988, pp. 205–215.

²⁰Brill, T. B., Brush, P. J., and Patil, D. G., "Thermal Decomposition of Energetic Materials 60. Major Reaction Stages of a Simulated Burning Surface of AP," *Combustion and Flame*, Vol. 94, No. 1/2, 1993, pp. 70–76.

- ²¹Braun, D., and Canji, E., "Pyrolysis-Gas Chromatography of Diene Polymers," *Angewandte Makromolekulare Chemie*, Vol. 29/30, No. 3, 1973, pp. 491–505.
- ²²Beck, W. H., "Pyrolysis Studies of Polymeric Materials Used as Binders in Composite Propellants: A Review," *Combustion and Flame*, Vol. 70, No. 2, 1987, pp. 171–190.
- ²³Rama Rao, M., and Radhakrishnan, T. S., "Thermal Degradation of Functionally-Terminated Polybutadienes: Pyrolysis Gas Chromatography and Thermogravimetric Studies," *Journal of Applied Polymer Science*, Vol. 41, No. 9/10, 1990, pp. 2251–2263.
- ²⁴Arisawa, H., and Brill, T. B., "Flash Pyrolysis of Hydroxyl-Terminated Polybutadiene I: Analysis and Implications of the Gaseous Products," *Combustion and Flame*, Vol. 106, No. 1/2, 1996, pp. 131–143.
- ²⁵Vandenkerckhove, J., and Jaumotte, A., "Remarks on the Burning Mechanism and Erosive Burning of Ammonium Perchlorate Propellants," *Proceedings of the 8th Symposium (International) on Combustion*, Combustion Inst., Pittsburgh, PA, 1960, pp. 689–693.
- ²⁶Fenn, J. B., "A Phalanx Flame Model for the Combustion of Composite Solid Propellants," *Combustion and Flame*, Vol. 12, No. 3, 1968, pp. 201–216.
- ²⁷Timnat, Y. M., *Advanced Chemical Rocket Propulsion*, Academic, New York, 1987, pp. 48–62.
- ²⁸Beckstead, M. W., Derr, R. L., and Price, C. F., "A Model of Composite Solid-Propellant Combustion Based on Multiple Flames," *AIAA Journal*, Vol. 8, No. 12, 1970, pp. 2200–2207.
- ²⁹Boggs, T. L., and Kraeutle, K. J., "Role of Scanning Electron Microscope in the Study of Solid Rocket Propellant Combustion, I. Ammonium Perchlorate Decomposition and Deflagration," *Combustion Science and Technology*, Vol. 1, No. 2, 1969, pp. 75–93.
- ³⁰Boggs, T. L., "Deflagration Rate, Surface Structure, and Subsurface Profile of Self-Deflagrating Single Crystals of Ammonium Perchlorate," *AIAA Journal*, Vol. 8, No. 5, 1970, pp. 867–873.
- ³¹Krishnan, S., and Swami, R. D., "Effect of Catalyst Mixing Procedure on Subatmospheric Combustion Characteristics of Composite Propellants," *Journal of Propulsion and Power*, Vol. 13, No. 2, 1997, pp. 207–212.
- ³²Boggs, T. L., Derr, R. L., and Beckstead, M. W., "Surface Structure of Ammonium Perchlorate Composite Propellants," *AIAA Journal*, Vol. 8, No. 2, 1970, pp. 370–372.
- ³³Brill, T. B., Arisawa, H., Brush, P. J., Gongwer, P. E., and Williams, G. K., "Surface Chemistry of Burning Explosives and Propellants," *Journal of Physical Chemistry*, Vol. 99, No. 5, 1995, pp. 1384–1392.
- ³⁴Brill, T. B., "Multiphase Chemistry Considerations at the Surface of Burning Nitramine Monopropellants," *Journal of Propulsion and Power*, Vol. 11, No. 4, 1995, pp. 740–751.
- ³⁵Brill, T. B., "Connecting the Chemical Composition of a Material to its Combustion Characteristics," *Progress in Energy and Combustion Science*, Vol. 18, No. 2, 1992, pp. 91–116.
- ³⁶Shepherd, J. E., and Brill, T. B., "Interpretation of Time-to-Explosion Tests," *Proceedings of the 10th International Detonation Symposium*, Office of Naval Research, ONR 33395-12, 1993, pp. 849–855.
- ³⁷Thynell, S. T., Gongwer, P. E., and Brill, T. B., "Condensed-Phase Kinetics of Cyclotrimethylenetrinitramine by Modeling the T-Jump/Infrared Spectroscopy Experiment," *Journal of Propulsion and Power*, Vol. 12, No. 5, 1996, pp. 933–939.
- ³⁸Boggs, T. L., Price, E. W., and Zurn, D. E., "The Deflagration of Pure and Isomorphously Doped Ammonium Perchlorate," *Proceedings of the 13th Symposium (International) on Combustion*, Combustion Inst., Pittsburgh, PA, 1971, pp. 995–1008.
- ³⁹Adams, G. K., Newman, B. H., and Robins, A. B., "The Combustion of Propellants Based Upon Ammonium Perchlorate," *Proceedings of the 8th Symposium (International) on Combustion*, Combustion Inst., Pittsburgh, PA, 1960, pp. 693–705.

⁴⁰Hackman, E. E., III, and Beachell, H. C., "Combustion Characteristics of Crystalline Oxidizers," *AIAA Journal*, Vol. 6, No. 3, 1968, pp. 561-564.

⁴¹Manelis, G. B., and Strunin, V. A., "The Mechanism of Ammonium Perchlorate Burning," *Combustion and Flame*, Vol. 17, 1971, pp. 69-77.

⁴²Sobczak, R. R., "Ammonium Perchlorate Composite Basics," *Journal of Pyrotechnics*, Vol. 3, Summer, 1996, pp. 35-46.

⁴³Boggs, T. L., Zurn, D. E., Cordes, H. F., and Covino, J., "Combustion of Ammonium Perchlorate and Various Inorganic Additives," *Journal of Propulsion and Power*, Vol. 4, No. 1, 1988, pp. 27-40.

⁴⁴Ramamurthy, S., and Shrotri, P. G., "Catalytic Decomposition of Ammonium Perchlorate," *Journal of Energetic Materials*, Vol. 14, No. 2, 1996, pp. 97-126.

⁴⁵Brill, T. B., and Goetz, F., "Laser Raman Studies of Solid Oxidizer Behavior," *Experimental Diagnostics in Combustion of Solids*, edited by T. L. Boggs and B. T. Zinn, Vol. 63, Progress in Astronautics and Aeronautics, AIAA, New York, 1978, pp. 3-19.

⁴⁶Beckstead, M. W., and Hightower, J. D., "Surface Temperature of Deflagrating Ammonium Perchlorate Crystals," *AIAA Journal*, Vol. 5, No. 10, 1967, pp. 1785-1790.

⁴⁷Selzer, H., "The Decomposition of Ammonium Perchlorate in the Condensed Phase," DLR, German Aerospace Research Center, Rept. 73-59, Lampoldshausen, Germany, 1973.

⁴⁸Brill, T. B., and Goetz, F., "Laser Raman Study of the Thermal Decomposition of Solid AP," *Journal of Chemical Physics*, Vol. 65, No. 3, 1976, pp. 1217-1219.

⁴⁹Hightower, J. D., and Price, E. W., "Combustion of Ammonium Perchlorate," *Proceedings of the 11th Symposium (International) on Combustion*, Combustion Inst., Pittsburgh, PA, 1967, pp. 463-472.

⁵⁰Manelis, G. B., and Strunin, V. A., "Mechanism and Elementary Theory of Burning of the Composite Solid Propellants," *Proceedings of the 11th International Symposium of Space Technology and Science*, 1975, pp. 97-104.

⁵¹Karpowicz, R. J., and Brill, T. B., "In Situ Characterization of the 'Melt' Phase of RDX and HMX by Rapid-Scan FTIR Spectroscopy," *Combustion and Flame*, Vol. 56, No. 3, 1984, pp. 317-325.

⁵²Inami, S. H., Rosser, W. A., and Wise, H., "Dissociation Pressure of Ammonium Perchlorate," *Journal of Physical Chemistry*, Vol. 67, No. 5, 1963, pp. 1077-1083.

⁵³Powling, J., and Smith, W. A. W., "The Surface Temperature of Ammonium Perchlorate Burning at Elevated Pressures," *Proceedings of the 10th Symposium (International) on Combustion*, Combustion Inst., Pittsburgh, PA, 1965, pp. 1373-1380.

⁵⁴Powling, J., "Experiments Relating to the Combustion of Ammonium Perchlorate-Based Propellants," *Proceedings of the 11th Symposium (International) on Combustion*, Combustion Inst., Pittsburgh, PA, 1967, pp. 447-456.

⁵⁵Boldyrev, V. V., Alexandrov, V. V., Boldyreva, A. V., Gritsan, V. I., Karpenko, Y. Y., Korobeinichev, O. P., Panfilov, V. N., and Khairtdinov, E. F., "On the Mechanism of the Thermal Decomposition of Ammonium Perchlorate," *Combustion and Flame*, Vol. 15, No. 1, 1970, pp. 71-78.

⁵⁶Pearson, G. S., "The Role of Catalysts in the Ignition and Combustion of Solid Propellants," *Combustion Science and Technology*, Vol. 3, June 1971, pp. 155-163.

⁵⁷Guirao, C., and Williams, F. A., "A Model for Ammonium Perchlorate Deflagration Between 20 and 100 ATM," *AIAA Journal*, Vol. 9, No. 7, 1971, pp. 1345-1356.

⁵⁸Bircumshaw, L. L., and Newman, B. H., "The Thermal Decomposition of Ammonium Perchlorate I. Introduction, Experimental, Analysis of Gaseous Products, and Thermal Decomposition Experiments," *Proceedings of the Royal Society of London, Series A: Mathematical and Physical Sciences*, Vol. 227, 1954, pp. 115-132.

⁵⁹Pai Verneker, V. R., and Maycock, J. N., "Mass-Spectrometric Study of the Thermal Decomposition of Ammonium Perchlorate," *Journal of Chemical Physics*, Vol. 47, No. 7, 1967, pp. 3618–3621.

⁶⁰Jacobs, P. W. M., and Russell-Jones, A., "Sublimation of Ammonium Perchlorate," *Journal of Physical Chemistry*, Vol. 72, No. 1, 1968, pp. 202–207.

⁶¹Kraeulte, K. J., "The Response of Ammonium Perchlorate to Thermal Stimulus," U.S. Naval Weapons Center, NWC-TP-7053, China Lake, CA, 1990, pp. 43–75

⁶²Oxley, J. C., Kaushik, S. M., and Gilson, N. S., "Ammonium Perchlorate Thermal Stability in the Presence of Hydrocarbons," U.S. Naval Weapons Center, NWC-TP-7053, China Lake, CA, 1990, pp. 43–75.

⁶³Maycock, J. N., and Pai Verneker, V. R., "Role of Point Defects in the Thermal Decomposition of Ammonium Perchlorate," *Proceedings of the Royal Society of London, Series A: Mathematical and Physical Sciences*, Vol. 307, 1968, pp. 303–315.

⁶⁴Brill, T. B., Gongwer, P. E., and Williams, G. K., "Thermal Decomposition of Energetic Materials, 66. Kinetic Compensation Effects in HMX, RDX, and NTO," *Journal of Physical Chemistry*, Vol. 98, No. 24, 1994, pp. 12242–12247.

⁶⁵Yano, Y., Miyata, K., Kubota, N., and Sakamoto, S., "Combustion Wave Structure of AP Composite Propellants," *Propellants, Explosives, and Pyrotechnics*, Vol. 12, No. 4, 1987, pp. 137–140.

⁶⁶Seleznev, V. A., Pokhil, P. F., Maltsev, V. M., and Bavykin, I. B., "An Optical Method of Measuring the Burning-Surface Temperature of Condensed Systems," *Combustion and Flame*, Vol. 13, No. 2, 1969, pp. 139–142.

⁶⁷Caveny, L. H., and Pittman, C. U., Jr., "Contribution of Solid-Phase Heat Release to AP Composite Propellant Burning Rate," *AIAA Journal*, Vol. 6, No. 8, 1968, pp. 1461–1467.

⁶⁸Pittman, C. U., "Location of Action of Burning-Rate Catalysts in Composite Propellant Combustion," *AIAA Journal*, Vol. 7, No. 2, 1969, pp. 328–334.

⁶⁹Osada, H., and Kakinouchi, N., "Initiation of Ignition of Solid Composite Propellants," *Kogyo Kayaku Kyokaishi*, Vol. 26, 1965, pp. 200–211; T.I.L. translation T/5669, Ministry of Aviation, 1966.

⁷⁰Choi, C. S., Prask, H. J., and Prince, E., "Crystal Structure of NH_4ClO_4 at 298°, 77°, and 10°K by Neutron Diffraction," *Journal of Chemical Physics*, Vol. 61, No. 9, 1974, pp. 3523–3529.

⁷¹Wengan, X., Baoxuan, L., and Kexiu, W., "Mechanism of Steady-State Burning of Composite solid Propellants Including Those with Negative Pressure-Exponents," *Acta Astronautica*, Vol. 15, No. 2, 1987, pp. 83–96.

⁷²Cohen, N., "Comment on 'Novel Kinetic Scheme for the Ammonium Perchlorate Gas Phase,'" *Journal of Physical Chemistry*, Vol. 96, No. 14, 1992, pp. 5668, 5669.

⁷³Maycock, J. N., Pai Verneker, V. R., and Jacobs, P. W. M., "Mass-Spectrometric Study of the Thermal Decomposition of Ammonium Perchlorate," *Journal of Chemical Physics*, Vol. 46, No. 7, 1967, pp. 2857, 2858.

⁷⁴Ermolin, N. E., Korobeinichev, O. P., Tereschenko, A. G., and Fomin, V. M., "Measurement of the Concentration Profiles of Reacting Components and Temperature in an Ammonium Perchlorate Flame," *Combustion, Explosion, and Shock Waves*, Vol. 18, 1982, pp. 46–49.

⁷⁵Smith, J. M., "Burning Rates of Solid Propellants," *AIChE Journal*, Vol. 6, No. 2, 1960, pp. 299–304.

⁷⁶Nachbar, W., "A Theoretical Study of the Burning of a Solid Propellant Sandwich," *Solid Propellant Rocket Research*, edited by M. Summerfield, Vol. 1, Progress in Astronautics and Rocketry, Academic, New York, 1960, pp. 207–226.

⁷⁷Summerfield, M., Sutherland, G. S., Webb, M. S., Taback, H. J., and Hall, K. P., "Burning Mechanism of Ammonium Perchlorate Propellants," *Solid Propellant Rocket Research*, edited by M. Summerfield, Vol. 1, Progress in Astronautics and Rocketry, Academic, New York, 1960, pp. 141-182.

⁷⁸Sohn, H. Y., "A Unified Theory of Ammonium Perchlorate Deflagration and the Low-Pressure Deflagration Limit," *Combustion Science and Technology*, Vol. 10, No. 1, 1975, pp. 137-154.

⁷⁹Beckstead, M. W., Derr, R. L., and Price, C. F., "The Combustion of Solid Monopropellants and Composite Propellants," *Proceedings of the 13th Symposium (International) on Combustion*, Combustion Inst., Pittsburgh, PA, 1971, pp. 1047-1056.

⁸⁰Sahu, H., Sheshadri, T. S., and Jain, V. K., "Novel Kinetic Scheme for the Ammonium Perchlorate Gas Phase," *Journal of Physical Chemistry*, Vol. 94, No. 1, 1990, pp. 294, 295.

⁸¹Selzer, H., "The Temperature Profile Beneath the Burning Surface of a Composite Ammonium Perchlorate Propellant," *Proceedings of the 11th Symposium (International) on Combustion*, Combustion Inst., Pittsburgh, PA, 1967, pp. 439-445.

⁸²Ajaz, A. G., "Hydroxyl-Terminated Polybutadiene Telechelic Polymer: Binder for Solid Rocket Propellants," *Rubber Chemistry and Technology*, Vol. 68, No. 3, 1995, pp. 481-506.

⁸³Arisawa, H., and Brill, T. B., "Flash Pyrolysis of Hydroxyl-Terminated Polybutadiene II: Implications of the Kinetics to Combustion of Organic Polymers," *Combustion and Flame*, Vol. 106, No. 1/2, 1996, pp. 144-154.

⁸⁴Bouck, L. S., Baer, A. D., and Ryan, N. W., "Pyrolysis and Oxidation of Polymers at High Heating Rates," *Proceedings of the 14th Symposium (International) on Combustion*, Combustion Inst., Pittsburgh, PA, 1973, pp. 1165-1176.

⁸⁵Blazowski, W. S., Cole, R. B., and McAlevy, R. F., III, "Linear Pyrolysis of Various Polymers Under Combustion Conditions," *Proceedings of the 14th Symposium (International) on Combustion*, Combustion Inst., Pittsburgh, PA, 1973, pp. 1177-1186.

⁸⁶Hansel, J. G., and McAlevy, R. F., III, "Energetics and Chemical Kinetics of Polystyrene Surface Degradation in Inert and Chemically Reactive Environments," *AIAA Journal*, Vol. 4, No. 5, 1966, pp. 841-848.

⁸⁷Ericsson, I., "Sequential Pyrolysis Gas Chromatographic Study of the Decomposition Kinetics of Cis-1,4-Polybutadiene," *Journal of Chromatographic Science*, Vol. 16, No. 8, 1978, pp. 340-344.

⁸⁸Cohen, N. S., Fleming, R. W., and Derr, R. L., "Role of Binders in Solid Propellant Combustion," *AIAA Journal*, Vol. 12, No. 2, 1974, pp. 212-218.

⁸⁹Chen, J. K., and Brill, T. B., "Chemistry and Kinetics of Hydroxyl-Terminated Polybutadiene and Diisocyanate-HTPB Polymers During Slow Decomposition and Combustion-Like Conditions," *Combustion and Flame*, Vol. 87, No. 3/4, 1991, pp. 217-232.

⁹⁰Shono, T., and Shina, K., "Determination of the Microstructure of Polybutadiene by Pyrolysis-Gas Chromatography," *Analytica Chimica Acta*, Vol. 56, No. 2, 1971, pp. 303-307.

⁹¹Haeusler, K. G., Schroeder, E., and Wege, F. W., "Light Beam and Curie Point Pyrolysis of Polymers II. Curie Point Pyrolysis of Polybutadiene," *Plaste und Kautschuk*, Vol. 24, 1977, pp. 175-179.

⁹²Tamura, S., and Gillham, J. K., "Pyrolysis-Molecular Weight Chromatography-Vapor Phase Infrared Spectrophotometry: An On-Line System for Analysis of Polymers IV. Influence of cis/trans Ratio on the Thermal Degradation of 1,4-Polybutadienes," *Journal of Applied Polymer Science*, Vol. 22, No. 7, 1978, pp. 1867-1884.

⁹³Radhakrishnan, T. S., and Rama Rao, M., "Thermal Decomposition of Polybutadienes by Pyrolysis Gas Chromatography," *Journal of Polymer Science, Polymer Chemistry*, Vol. 19, No. 12, 1981, pp. 3197–3208.

⁹⁴Rama Rao, M., Sebastian, T. V., Radhakrishnan, T. S., and Ravindran, P. V., "Correlation of Binder Mechanical Properties with Microstructure for Poly-(Butadiene–Acrylonitrile–Methacrylic Acid) Terpolymer: Carbon-13 NMR and Pyrolysis Gas Chromatography Studies," *Journal of Applied Polymer Science*, Vol. 42, No. 3, 1991, pp. 753–766.

⁹⁵Thomas, T. J., Krishnamurthy, V. N., and Nandi, U. S., "Thermogravimetric and Mass-Spectrometric Study of Thermal Decomposition of PBCT Resins," *Journal of Applied Polymer Science*, Vol. 24, No. 8, 1979, pp. 1797–1808.

⁹⁶Golub, M. A., and Gargiulo, R. J., "Thermal Degradation of 1,4-Polyisoprene and 1,4-Polybutadiene," *Journal of Polymer Science, Polymer Letters Edition*, Vol. 10, No. 1, 1972, pp. 41–49.

⁹⁷Schneider, B., Doskocilova, D., Stokr, J., and Svoboda, M., "Study of Thermal Degradation of Polybutadiene in Inert Atmospheres I. Evidence of Temperature and Time of Heating in Infrared and NMR Spectra," *Polymer*, Vol. 34, 1993, pp. 432–436.

⁹⁸Grassie, N., and Heaney, A., "Thermal Reaction of Pendent Vinyl Groups in Polybutadiene and Copolymers of Butadiene and Acrylonitrile," *Journal of Polymer Science, Polymer Letters Edition*, Vol. 12, No. 2, 1974, pp. 89–94.

⁹⁹Brazier, D. W., and Schwartz, D. W., "The Effect of Heating Rate on the Thermal Degradation of Polybutadiene," *Journal of Applied Polymer Science*, Vol. 22, No. 1, 1978, pp. 113–124.

¹⁰⁰Coffman, J. A., "Highly Crosslinked Polybutadiene," *Industrial Engineering and Chemistry*, Vol. 44, 1952, pp. 1421–1428.

¹⁰¹McCreedy, K., and Keskkula, H., "Effect of Thermal Crosslinking on Decomposition of Polybutadiene," *Polymer*, Vol. 20, No. 9, 1979, pp. 1155–1159.

¹⁰²Du, T., "Thermal Decomposition Studies of Solid Propellant Binder HTPB," *Thermochimica Acta*, Vol. 138, No. 2, 1989, pp. 189–197.

¹⁰³Golub, M. A., and Sung, M., "Thermal Cyclization of 1,2-Polybutadiene and 3,4-Polyisoprene," *Journal of Polymer Science, Polymer Letters Edition*, Vol. 11, No. 2, 1973, pp. 129–138.

¹⁰⁴Lu, Y. C., and Kuo, K. K., "Thermal Decomposition Study of Hydroxyl-Terminated Polybutadiene Solid Fuel," *Thermochimica Acta*, Vol. 275, No. 2, 1996, pp. 181–191.

¹⁰⁵Narahari, H. K., Mukunda, H. S., and Jain, V. K., "A Model of Combustion Monopropellants (AP) with Complex Gas Phase Kinetics," *Proceedings of the 20th Symposium (International) on Combustion*, Combustion Inst., Pittsburgh, PA, 1985, pp. 2073–2082.

¹⁰⁶Price, E. W., Sambamurthi, J. K., Sigman, R. K., and Panyam, R. R., "Combustion of Ammonium Perchlorate-Polymer Sandwiches," *Combustion and Flame*, Vol. 63, No. 3, 1986, pp. 381–413.

¹⁰⁷Rabinovitch, B., "Regression Rates and the Kinetics of Polymer Degradation," *Proceedings of the 10th Symposium (International) on Combustion*, Combustion Inst., Pittsburgh, PA, 1965, pp. 1395–1404.

¹⁰⁸Inami, S. H., Rosser, W. A., Jr., and Wise, H., "Heat-Release Kinetics of Ammonium Perchlorate in the Presence of Catalysts and Fuel," *Combustion and Flame*, Vol. 12, No. 1, 1968, pp. 41–44.

¹⁰⁹Brill, T. B., Gongwer, P. E., and Budenz, B., "Oxidizer-Binder Interactions from T-Jump/FTIR Flash Pyrolysis," *Proceedings of the 28th ICT International Annual Conference*, Fraunhofer Institute of Chemical Technology, 1997, pp. 14/1–14/10.

¹¹⁰Wise, H., Inami, S. H., and McCulley, L., "Role of Condensed-Phase Reactions in Ignition and Deflagration of Ammonium Perchlorate Propellants," *Combustion and Flame*, Vol. 11, No. 6, 1967, pp. 483–488.

¹¹¹Price, E. W., Handley, J. C., Panyam, R. R., Sigman, R. K., and Ghosh, A., "Combustion of Ammonium Perchlorate-Polymer Sandwiches," *AIAA Journal*, Vol. 19, No. 3, 1981, pp. 380–386.

¹¹²Kumar, R. N., "Condensed Phase Details in the Time-Independent Combustion of AP/Composite Propellants," *Combustion Science and Technology*, Vol. 8, March 1973, pp. 133–148.

¹¹³Kishore, K., Pai Verneker, V. R., Sunitha, M. R., and Prasad, G., "Contribution of the Condensed-Phase Reactions in the Combustion of Solid Rocket Fuels," *Fuel*, Vol. 56, No. 7, 1977, pp. 347, 348.

¹¹⁴Kishore, K., Pai Verneker, V. R., and Gayathri, V., "Reaction Intermediates During Combustion and Decomposition of Some Model Solid Rocket Fuels," *Fuel*, Vol. 60, No. 2, 1981, pp. 164–167.

¹¹⁵Hermance, C. E., "A Model of Composite Propellant Combustion Including Surface Heterogeneity and Heat Generation," *AIAA Journal*, Vol. 4, No. 9, 1966, pp. 1629–1637.

¹¹⁶Korobeinichev, O. P., Kuibida, L. V., Paletsky, A. A., Chernov, A. A., and Ermolin, N. E., "Chemistry of Solid Propellant Combustion Studied by Mass Spectrometry and Modeling," *American Chemical Society Division of Fuel Chemistry, Preprinted Papers*, Vol. 36, American Chemical Society Publications, Washington, DC, 1991, pp. 1582–1587.

¹¹⁷Kishore, K., and Sridhara, K., "Influence of Structure of Polymeric Fuels on the Combustion Behaviour of Composite Solid Propellants," *Fuel*, Vol. 75, No. 7, 1996, pp. 912–918.

¹¹⁸Law, R. J., Baer, A. D., and Ryan, N. W., "Preignition Reactions of AP-HTPB Propellants Studied by Infrared Spectrometry," *Proceedings of the 16th Symposium (International) on Combustion*, Combustion Inst., Pittsburgh, PA, 1976, pp. 1271–1277.

¹¹⁹Zhang, W., Zhu, H., and Zhang, R., "Correlation Between Thermal Decomposition and Burning Rate in AP/HTPB Propellants," *Proceedings of the 22nd ICT International Annual Conference*, Fraunhofer Institute of Chemical Technology, 1991, pp. 62/1–62/6.

¹²⁰Hightower, J. D., and Price, E. W., "Experimental Studies Relating to the Combustion Mechanism of Composite Propellants," *Astronautica Acta*, Vol. 14, No. 1, 1968, pp. 11–21.

¹²¹Kuwahara, T., and Kubota, N., "Low Pressure Burning of Ammonium Perchlorate Composite Propellants," *Combustion Science and Technology*, Vol. 47, No. 1/2, 1986, pp. 81–91.

¹²²Ohlenmiller, T. J., and Summerfield, M., "Radiation Augmented Burning of a Solid Propellant," *Aerospace and Mechanical Sciences Rept. 799*, Princeton Univ., Princeton, NJ, April 1967.

¹²³Barrere, M., and Nadaud, L., "Combustion of Ammonium Perchlorate Spheres in a Flowing Gaseous Fuel," *Proceedings of the 10th Symposium (International) on Combustion*, Combustion Inst., Pittsburgh, PA, 1965, pp. 1381–1394.

¹²⁴Tanoff, M. A., Ilincic, N., Smooke, M. D., Yetter, R. A., Parr, T. P., and Hanson-Parr, D. M., "Computational and Experimental Study of Ammonium Perchlorate Combustion in Counterflow Diffusion Flames," *27th Symposium (International) on Combustion*, Vol. 2, The Combustion Inst., Pittsburgh, PA, pp. 2397–2404.

¹²⁵Pearson, G. S., and Sutton, D., "Composite Solid Propellant Ignition: Ignition of Ammonia and Other Fuels by Perchloric Acid Vapors," *AIAA Journal*, Vol. 5, No. 2, 1967, pp. 344–346.

- ¹²⁶Fishman, N., "Surface Exotherm During Ignition of Ammonium Perchlorate Propellants," *AIAA Journal*, Vol. 5, No. 8, 1967, pp. 1500, 1501.
- ¹²⁷Anderson, R., Brown, R. S., and Shannon, L. J., "Heterogeneous Reactions in Ignition and Combustion of Solid Propellants," *AIAA Journal*, Vol. 2, No. 1, 1964, pp. 179, 180.
- ¹²⁸Price, E. W., Bradley, H. H., Jr., Dehority, G. L., and Ibiricu, M. M., "Theory of Ignition of Solid Propellants," *AIAA Journal*, Vol. 4, 1966, pp. 1153–1181.
- ¹²⁹Derr, R. L., and Boggs, T. L., "Role of Scanning Electron Microscopy in the Study of Solid Propellant Combustion: Part III. The Surface Structure and Profile Characteristics of Burning Composite Propellant," *Combustion Science and Technology*, Vol. 1, No. 3, 1970, pp. 369–384.
- ¹³⁰Brown, R. S., Muzzy, R. J., and Steinle, M. E., "Surface Reaction Effects on the Acoustic Response of Composite Solid Propellants," *AIAA Journal*, Vol. 6, No. 3, 1968, pp. 479–488.
- ¹³¹Druet, L. M., Ahmed, S., and Pandey, R. N., "Application of Curie Point Pyrolysis-Gas Chromatography for the Characterization of Rocket Propellants," *Proceedings of the 22nd ICT International Annual Conference*, 1991, pp. 64/1–64/14.
- ¹³²Radhakrishnan, T. S., and Rama Rao, M., "Thermo-Oxidative Degradation of Polybutadiene Binders," *Propellants, Explosives, and Pyrotechnics*, Vol. 20, No. 1, 1995, pp. 32–35.
- ¹³³Kishore, K., and Pai Verneker, V. R., "Condensed Phase Reactions in Solid Propellants," *AIAA Journal*, Vol. 13, No. 9, 1975, pp. 1240–1242.
- ¹³⁴Waesche, R. H. W., Wenograd, J., and Feinauer, L. R., "Investigation of Solid Propellant Decomposition Characteristics and Their Relation to Observed Burning Rates," *ICRPG/AIAA Solid Propulsion Conference*, 1967, pp. 136–147.
- ¹³⁵Rosser, W. A., Fishman, N., and Wise, H., "Ignition of Simulated Propellants Based on Ammonium Perchlorate," *AIAA Journal*, Vol. 4, No. 9, 1966, pp. 1615–1622.
- ¹³⁶Ermolin, N. E., "Kinetic Parameters of Overall Gas-Phase Reactions for Propellants Based on Ammonium Perchlorate and Polybutadiene Rubber," *Fizika Goreniya i Vzryva*, Vol. 29, No. 4, 1993, pp. 508–515.
- ¹³⁷Bakhman, N. N., "Dependence of Burning Rate on Oxidizer Particle Size," *Combustion and Flame*, Vol. 17, No. 3, 1971, pp. 383–389.
- ¹³⁸Cohen, N. S., and Strand, L. D., "An Improved Model for the Combustion of AP Composite Propellants," *AIAA Journal*, Vol. 20, No. 12, 1982, pp. 1739–1746.
- ¹³⁹Fong, C. W., and Smith, R. F., "The Relationship Between Plateau Burning Behavior and Ammonium Perchlorate Particle Size in HTPB-AP Composite Propellants," *Combustion and Flame*, Vol. 67, No. 3, 1987, pp. 235–247.
- ¹⁴⁰Green, L., Jr., "Some Effects of Oxidizer Concentration and Particle Size on Resonance Burning of Composite Solid Propellants," *Jet Propulsion*, Vol. 28, No. 3, 1958, pp. 159–164.
- ¹⁴¹Schultz, R. D., Green, L., and Penner, S. S., "Studies of the Decomposition Mechanism, Erosive Burning, Sonance and Resonance for Solid Composite Propellants," *Combustion and Propulsion*, Pergamon, New York, 1958, pp. 367–420.
- ¹⁴²Chaiken, R. F., and Andersen, W. H., "The Role of Binder in Composite Propellant Combustion," *Solid Propellant Rocket Research*, edited by M. Summerfield, Vol. 1, Progress in Astronautics and Rocketry, Academic, New York, 1960, pp. 227–249.
- ¹⁴³King, M. K., "Examination of Chemical Approaches to Stabilizing Composite-Propellant Combustion," *Journal of Propulsion and Power*, Vol. 12, No. 3, 1996, pp. 554–563.
- ¹⁴⁴Kishore, K., Pai Verneker, V. R., Shubha, K. R., and Sankaralingam, S., "Some Features of Solid Propellant Chemistry," *Combustion and Flame*, Vol. 46, No. 3, 1982, pp. 323, 324.

¹⁴⁵Chemov, A. A., Shvartsberg, V. M., Ermolin, N. E., Korobeinichev, O. P., and Fomin, V. M., "Flame Structure of Sandwich Systems Based on Ammonium Perchlorate, HMX, and Polybutadiene Rubber Studied by Probe Mass-Spectrometry and Modeling," *American Chemical Society Division of Fuel Chemistry, Preprinted Papers*, Vol. 39, American Chemical Society Publications, Washington, DC, 1994, pp. 188–192.

¹⁴⁶Inami, S. H., Rajapakse, Y., Shaw, R., and Wise, H., "Solid Propellant Kinetics I. The Ammonium Perchlorate–Copper Chromite–Fuel System," *Combustion and Flame*, Vol. 17, No. 2, 1971, pp. 189–196.

¹⁴⁷Oyumi, Y., and Brill, T. B., "Thermal Decomposition of Energetic Materials 22. The Contrasting Effects of Pressure on the High-Rate Thermolysis of 34 Energetic Compounds," *Combustion and Flame*, Vol. 68, No. 2, 1987, pp. 209–216.

¹⁴⁸Rudy, T. P., Anderson, W. S., Valerga, A. J., and Weyland, H. H., "Copper Burn Rate Additives," U.S. Air Force Rocket Propulsion Lab., Rept. AFRPL-TR-82-85, Edwards AFB, CA, Oct. 1982.

¹⁴⁹Stoner, C. E., Jr., and Brill, T. B., "Thermal Decomposition of Energetic Materials 46. The Formation of Melamine-like Cyclic Azines as a Mechanism for Ballistic Modification of Composite Propellants by DCD, DAG, and DAF," *Combustion and Flame*, Vol. 83, No. 3/4, 1991, pp. 302–308.

¹⁵⁰Strahle, W. C., Handley, J. C., and Milkie, T. T., "Catalytic Effect in the Combustion of AP-HTPB Sandwiches to 3200 PSIA," *Combustion Science and Technology*, Vol. 8, No. 5/6, 1974, pp. 297–304.

¹⁵¹Chakravarthy, S. R., Price, E. W., and Sigman, R. K., "Mechanism of Burning Rate Enhancement of Composite Solid Propellants by Ferric Oxide," *Journal of Propulsion and Power*, Vol. 13, No. 4, 1997, pp. 471–480.

¹⁵²Coates, R. L., Myers, G. E., and Stapleton, W. G., "Combustion Mechanism Studies," *Proceedings of the 2nd ICRPG Combustion Conference*, CPIA Publ. 105, Vol. 1, Chemical Propulsion Information Agency, Laurel, MD, 1966, p. 443.

¹⁵³Solymosi, F., and Fonagy, K., "Effect of Cadmium Oxide and Cadmium Perchlorate on the Decomposition of Ammonium Perchlorate," *Proceedings of the 11th Symposium (International) on Combustion*, Combustion Inst., Pittsburgh, PA, 1967, pp. 429–435.

¹⁵⁴Gould, R. D., "Combustion Instability of Solid Propellants: Effect of Oxidizer Particle Size, Oxidizer/Fuel Ratio, and Addition of Titanium Dioxide to Plastic Propellants," Rocket Propulsion Establishment, NTIS Rept. AD684244, National Technical Information Service, Springfield, VA, 1968.

I. Propellant Chemistry, Synthesis, and Formulation

Flash Pyrolysis of Ammonium Perchlorate–Hydroxyl-Terminated-Polybutadiene Mixtures Including Selected Additives

T. B. Brill* and B. T. Budenz†

University of Delaware, Newark, Delaware

I. Introduction

WORLDWIDE, ammonium perchlorate (AP, NH_4ClO_4) and hydroxyl-terminated-polybutadiene (HTPB) composite mixtures, usually also containing aluminum powder and ballistic modifiers, are the most frequently used formulations in solid rocket propellants. In terms of publications, AP has been the most extensively investigated solid oxidizer since its introduction into propellants, probably in the late 1940s¹ by the Jet Propulsion Laboratory. A large number of publications appeared in 1950–1970, and, by comparison, a relatively lesser number have appeared since then. The impressive review by Jacobs and Whitehead² was quite extensive in range and depth at the time of publication in 1969. The falloff in research interest after this time is reflected in the additional information reviewed 10–15 years later,³ but subsequent reviews of various aspects of decomposition, ignition,⁴ and combustion^{5–8} of AP-composite propellants have appeared. A modest resurgence of new interest in AP-composite propellant decomposition and combustion is motivated in part by the availability of advanced methods of diagnostics,^{9–13} by new kinetics data and methods of modeling,^{14–16} and by intriguing plateau-burning behavior of some AP-HTPB formulations.^{17,18}

Despite the widespread use and long investigative history of AP-fuel mixtures, it still can be said that AP alone and AP-fuel composites remain among the most confounding materials in the research setting. From the point of view of chemistry, one reason is that the full range of formal oxidation states of nitrogen and chlorine can apparently become involved, for example, the formal oxidation state of Cl in ClO_4^- is +7, whereas that of HCl is –1; N in NH_4^+ is –3, whereas that of N in NO_2^+ (Ref. 19) and HNO_3 (Ref. 20) is +5. When all of the various combinations of

Copyright © 1999 by the American Institute of Aeronautics and Astronautics, Inc. All rights reserved.

*Professor, Dept. of Chemistry and Biochemistry.

†Graduate Research Assistant, Dept. of Chemistry and Biochemistry.

N-, H-, O-, and Cl-containing compounds are considered together, in excess of 1000 chemical reactions become possible.⁹ Likewise, the thermal decomposition of pure HTPB involves a number of processes and potentially leads to a large number of hydrocarbon products.²¹⁻²⁴ Because of the interactions between AP and HTPB during the decomposition process, the products from the pure materials will be altered in quantity or completely changed to different products. The diffusion flame structure that results from the pyrolysis of the heterogeneous composite surface is a feature that imparts a strong combustion dependence on the pressure, the AP particle size, and the oxidizer/fuel ratio.^{16,25-28} Furthermore, a highly complex surface structure exists²⁹⁻³¹ with three phases present at least below 50 atm (Ref. 32).

Given the extraordinarily intertwined and complex processes involved in the decomposition and combustion of AP-HTPB mixtures, it is reasonable to wonder if adding another drop to the voluminous bucket of literature could possibly make any difference. After examining many open-literature papers in this field and conducting a large number of flash pyrolysis experiments in our laboratory, we decided to try to amalgamate our findings with many of those previously reported in the hope of contributing some useful insights. Our initial objective was to contribute something more quantitative about the condensed-phase chemistry dimension of the overall process. Given the complexity, however, this ambitious goal had to be scaled back to a more empirical set of mechanistic observations. The literature used is extensive, but is hardly comprehensive. The emphasis was placed on the chemistry of the heterogeneous AP-HTPB mixture in Sec. IV. To discuss this mixture in context, it is first necessary to summarize the experimental methods in Sec. II and some of the relevant features of the pure materials in Sec. III.

II. Flash Thermolysis Experiments

The condensed-phase chemistry at a burning surface is extremely difficult to study.^{33,34} In an attempt to learn more about rates and mechanisms, we have developed several spectroscopically accessible flash thermolysis methods³⁵ culminating in the currently used method of temperature-jump (T-jump) Fourier transform infrared (FTIR) spectroscopy.¹¹ The assumption is that flash pyrolysis of a thin film of material is a snapshot simulation of the burning surface provided that the heating rate and temperature are high enough. The unique feature of this device is the use of a high-gain, fast-response, power supply to adjust the temperature of a Pt filament extremely rapidly to accommodate the endothermic and exothermic events of the sample. Thereby, an essentially constant, but high, temperature is maintained during the experiment.

The concept of T-jump/FTIR spectroscopy^{11,36,37} is shown in Fig. 1. Approximately 200 μg of material was thinly spread on the center of a polished Pt ribbon filament. The filament was arranged inside of a closed gas cell so that the infrared (IR) beam of a rapid-scanning FTIR spectrometer passed about 3 mm above the surface. The cell was purged with Ar and pressurized at any desired pressure up to 70 atm, although 50 atm was the highest pressure used in this work. By using the high-performance power supply, the filament and sample were heated at about 800°C s^{-1} and then held at the chosen temperature in the $400\text{--}600^\circ\text{C}$ range for the

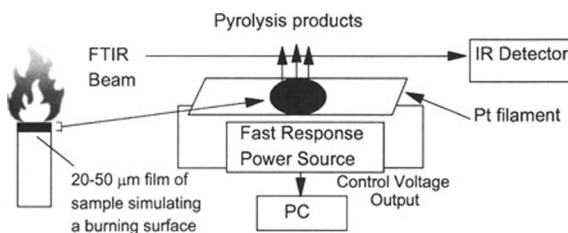


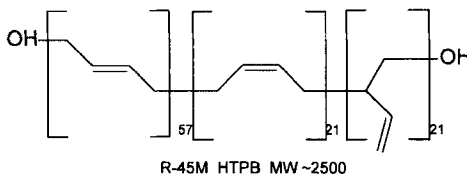
Fig. 1 Basic design of the T-jump/FTIR spectroscopy experiment to give a snapshot simulation of the burning propellant surface.

duration of the experiment. Data up to 500°C are given in this work. The relation between the applied voltage and the resulting filament temperature was calibrated for all experimental conditions by using melting point standards.

Because of limitations in the rate of heat transfer between the filament and sample,^{36,37} the data at <0.5 s are not necessarily isothermal. After this time the characteristic thermal diffusion time, which is the time required for one of the film faces to sense 60% of the temperature change at the other, is about $25\ \mu\text{s}$ in this experiment.³⁶ This time is much faster than the data collection rate. Once equilibrated, the temperature is known to about $\pm 2^{\circ}\text{C}$. As a result, the small changes in control voltage applied to the filament can be used to track the endothermic and exothermic events of the sample. An exotherm produces a sharp spike in the control voltage vs time trace. This marks the time to the exothermic event. Transmission IR spectra of the gaseous products are recorded every 100 ms at 4-cm^{-1} resolution simultaneously with the control voltage measurement. These data help outline the chemistry that takes place within the simulated surface reaction zone without the additional complicating contribution of the flame zone.

At least three concerns arise about this simulation. First, the configuration of the experiment is not the same as the burning propellant in that the sample is heated from the underside by the filament rather than the topside by the near-surface primary flame reactions. As the reactions accelerate in the experiment, however, a very thin gas layer may develop between the steady heat source of the filament and the material. This process resembles film boiling, but is more transient because of the reacting dynamic surface. In some sense, however, the configuration of heat source to reactive gas layer to sample in the T-jump experiment resembles the configuration of flame to reactive gas layer to sample that exists during propellant burning. Second, during steady combustion of a propellant, the gaseous products flow against the chamber pressure. To simulate this condition in the snapshot T-jump experiment, argon gas was added to raise the internal pressure in the cell. Third, the film can not replicate all of the events of the burning surface. Connections seem to exist, however, between rapid heating of a film and steady combusting of a bulk energetic material. For example, the rate of mass loss from these mesoscopic films at fast heating rates resembles that calculated from the burning rate of a bulk material at the same (low) pressure.³³ On balance we know that the laboratory simulation of the burning surface by rapidly heating a film cannot be a perfect replication of the combustion conditions, but it is hoped that it offers some useful guidance for current and future propellant modeling efforts.

Four nominal particle diameters of AP (1.4, 8, 18, and 44 μm) were obtained from the Thiokol Corporation. The HTPB used was propellant-grade R45M, whose structure is as follows:



TiO_2 (anatase, 0.5 μm) and melamine (1, 3, 5-triamino-2, 4, 6-triazine) were obtained from Aldrich Chemical Company.

Mixtures were made on a weight percentage basis by thoroughly mixing them with an agate mortar and pestle. These uncured materials were then spread as a film of about 50 μm thickness onto the center of the Pt filament. Multiple data sets were recorded in search of reproducibility. It was found that the results in the first day after mixing were less reproducible than those taken at least a month after mixing. Thus, the slightly aged samples were used for this work. The IR spectra were converted into species concentrations by methods described before.³⁵

III. Decomposition of the Pure Materials

Although no new work on pure AP and pure HTPB was conducted in this project, the behavior of the AP-HTPB mixtures is difficult to appreciate without the context of the pure ingredients. In addition, some comments and cautionary notes about the pure materials may enhance the understanding of their pyrolysis and combustion.

A. Pure AP

Note that the purity of AP used in rocket propellants is 99.3–99.8% (Ref. 38), which raises the question about the role of the impurities in the various, sometimes contradictory, results reported for decomposition and combustion of AP. For example, it has long been known³⁹ that the burning rate of AP depends on the sample purity. This is vividly shown by the burning-rate behavior of single crystals of AP that have been isomorphously doped with <1% quantities of other ions.^{38,40} Very dramatic effects are produced by both redox-active and nonactive ions. The most pronounced effect is with NO_2^+ , which has been shown to increase the burning rate by about 50% when it is present in the crystal lattice at about the 0.01% level.^{19,40} The amount of H_2O incorporated in the crystal lattice can also vary. This potentially affects the experimental decomposition and combustion results because H_2O is known to suppress the burning rate, perhaps by decreasing the amount of radical chemistry associated with HClO_4 (Ref. 41) or perhaps by decomposing the proposed $\text{NO}_2^+\text{ClO}_4^-$ intermediate¹⁹ to which the burning rate is very sensitive.⁴⁰ An additional complication is that $\text{Ca}_3(\text{PO}_4)_2$ is used to coat fine AP crystals to prevent caking.⁴² Discussion of the extent that adventitious impurities might affect experimental results on AP is rare, and this factor may be a variable in some of the differing findings and opinions that have been published. This is particularly an

issue in light of the dramatic effects that the purposeful addition of salts can have on the decomposition and combustion of AP.^{2,3,19,38,40,43,44}

The earliest molecular event in hot AP is the orthorhombic-to-cubic solid-solid phase transition at about 240°C (Ref. 45). This transition occurs beneath the burning surface^{30,46,47} and results from the transition of the ClO_4^- ion from restricted to unrestricted tumbling on the vibrational timescale.⁴⁸ The ensuing destabilization of the AP crystal effectively facilitates the partial conversion from the ionic state to the neutral NH_3 and HClO_4 molecules in the condensed phase. These molecular forms are not thermodynamically favored in the presence of one another and should be thought of as minor species that are in equilibrium with the ions. As the temperature is further raised, the crystal lattice is no longer stable and progressively liquefies,^{30,38,46,49,50} in part because of depression of the melting point by the presence of reaction products. The thickness of the liquid layer during burning is at most about 10 μm at lower pressures based on scanning electron microscopy of quenched samples.^{29,30} Chemical reactions concurrently take place in the liquid layer making it a mixture of components rather than a true AP melt. Attempts to characterize the liquid AP by spectroscopy resulted in an explosion, which is contrary to the more successful experience with liquefied RDX and HMX (Ref. 51). Hence, the chemical details of liquid AP to our knowledge remain unknown.

The initial proton transfer step leading to NH_3 and HClO_4 in the decomposition of pure AP is widely accepted,^{10,12,41,50,52-57} and is highly endothermic ($\Delta H_{\text{dissn}} = 58 \pm 2 \text{ kcal/mol}$) (Ref. 52) with an activation energy E_a of about half this value in the 200–250°C range.⁵⁸⁻⁶² An alternative point of view is that electron transfer occurs to form NH_4 and ClO_4 radicals, and this predominates above 350°C (Refs. 3, 44, 58, and 63). The basis for competing pathways is primarily the comparative values of E_a for the proton and electron transfer processes relative to the E_a value for AP decomposition. In the 250–350°C range, $E_a = 18.5 \text{ kcal/mol}$ for electron transfer whereas $E_a = 30 \text{ kcal/mol}$ for proton transfer.³ E_a for global decomposition in this range is about 20 kcal/mol (Ref. 3), which compares best with the electron transfer process. It is risky, however, to compare E_a values for specific reactions to global decomposition rates⁶⁴ in a process as complicated as the thermal decomposition of AP. For example, $\Delta H_{\text{dissn}} = 58 \text{ kcal/mol}$, which was measured below 250°C, will decrease as the temperature increases. In tandem, E_a will also decrease bringing the proton and electron transfer rates more into line with one another at higher temperatures. Thus, it is probable that both proton and electron transfer rates compete to a degree that depends on the temperature, defect number, and purity of the AP crystal. Electron transfer will be strongly influenced by the presence of intentionally added or adventitiously present redox-active impurities. Redox-active catalysts acting in the condensed phase should primarily alter this mechanism as opposed to the proton-transfer mechanism. For AP used in rocket propellants, however, this initiating reaction may be a moot issue for the combustion of so-called pure AP because the secondary exothermic reactions resulting from the initial, endothermically formed products by the two processes rapidly become indistinguishable.

The secondary reactions involving the initial products of the AP decomposition are very complex and are different from most other energetic materials because of the involvement of chlorine oxides. It is widely accepted that exothermic chemistry begins immediately after the crystal lattice begins to break down,^{41,43,50,54,56} and

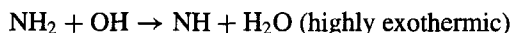
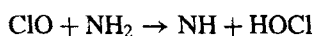
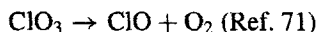
Table 1 Examples of surface temperatures reported for burning AP

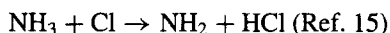
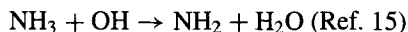
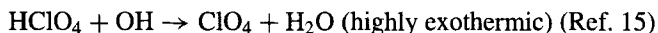
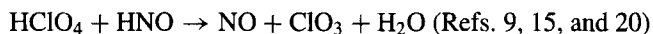
T_s , °C	Pressure, atm	Remarks	Reference
330	1	Thermocouple	65
440	13	Optical pyrometry	66
650	20	IR pyrometry	53
680	33	IR pyrometry	53
720	66	IR pyrometry	53
525–600	20–66	Phase transition	46
442 ± 30	20–66	Reanalysis of Ref. 46	67

that the liquid layer formed during combustion is frothy as a result of the formation of the gaseous products. The degree of exothermicity is not sufficient to sustain the burning of AP below about 15-atm pressure. Heat feedback from the flame zone is needed, and an estimate of the amount of heat released at the surface is as high as 70% (Ref. 57). The thickness of the liquid layer decreases with increasing pressure, and the layer appears gone by about 60 atm (Refs. 3, 29, and 30).

The surface temperature of burning AP has been estimated by several methods and a few of the values are given in Table 1 (Refs. 46, 53, and 65–67). As is the case with many other energetic materials, the agreement among these data is poor, which reflects the difficulty of making an accurate measurement on a transient, multiphase, reaction surface.

The details of the heterogeneous reactions involving the gaseous and liquid phases remain a murky and hopelessly complex subject. Numerous parallel and consecutive reactions occur that are affected by the pressure, temperature, and spatial location in the froth. It is generally agreed, however, that HClO_4 accelerates the decomposition,^{41,44,50,68,69} whereas NH_3 retards the rate at lower temperatures,⁴⁴ but accelerates it at higher temperatures.⁵⁰ Obviously, the relative roles of the heterogeneous reactions change with pressure and formulation, but the occurrence of reactions in the condensed phase is difficult to avoid. For example, assuming an average unit cell dimension of 7.5 Å for AP (Ref. 70), a 1 μm -thick surface reaction zone corresponds to about 1300 unit cell lengths. Given the time estimate for reactions of about 10^{-3} s (Ref. 67) and the surface temperatures in Table 1, there is ample time for many reactions to take place in the condensed phase. Unfortunately, the rate constants have not been measured for many of the possible reactions, especially when mediated by the heterogeneous condensed phase, and so there is little value in speculating further. Some of the reactions that provide radical chain carriers, for example, ClO , and species known to be important in other reaction schemes are listed as follows:





Although radicals such as OH, ClO, and NH are detected after laser pyrolysis,^{10,13} most of the products detected by other methods are stable molecules with mostly even, but some odd, electron counts^{2,9,20,55,59,73,74}: N₂O, NO, NO₂, NOCl, HNO₃, HClO₄, HCl, ClO₂, NH₃, H₂O, Cl₂, O₂, N₂, H₂, and hydrated HCl and HClO₄. For example, the IR spectrum over AP flash heated at 800°C s⁻¹ to 500°C under 4 atm of Ar is shown in Fig. 2 and reveals some of these products. The species just listed are later-stage products from the numerous elementary reactions between N, H, O, and Cl. Many of these products, along with some of the more reactive radicals, escape the surface and initiate the AP flame. Discussion of the flame structure is not the subject of this paper, but closure of this section is aided by summarizing the flame zone chemistry modeling efforts. Kishore⁶ reviewed some of the models devised before 1976.

Models of the combustion process reflect the wisdom and available experimental data at the time of development. Understandably, the earlier models emphasize physical processes. Chemistry and energetics were sometimes incorporated globally, whereas the later models incorporate detailed chemistry. Physical observations about the burning process of AP led to the earliest models based on the conservation equations and management of heat transfer.⁷⁵⁻⁷⁹ Although these models were successful in fitting features such as the burning rate, the low-pressure deflagration limit, and some of the ignition behavior, it was difficult to extend them to include the binder, temperature sensitivity, and the details of the flame structure. Inclusion of chemistry was, therefore, needed.

Manelis and Strunin⁴¹ brought to light the probable behavior of the initial products NH₃ and HClO₄ during the burning of AP and, thereby, focused attention on the

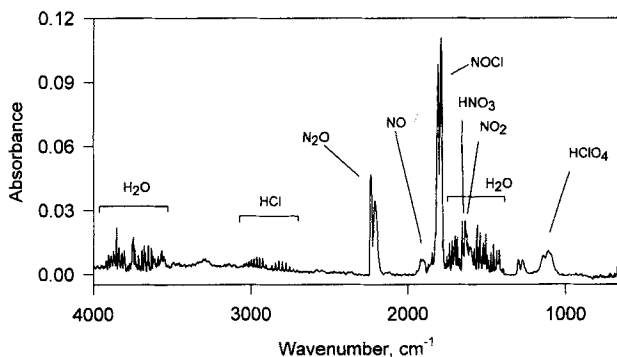


Fig. 2 IR spectrum of the gaseous products from solid AP heated at 800°C s⁻¹ and held at 500°C under 4 atm Ar.

role of chemical processes. In fact they asserted that the condensed phase chemistry dominates in the combustion processes. Comments of this type appeared along side the earliest chemistry-based model of AP combustion by Guirao and Williams,⁵⁷ who used a 14-step gas-phase reaction mechanism to fit the burning-rate curve and also proposed that 70% of the heat is released in a global surface process. In another pioneering chemistry-based effort, Ermolin et al.⁹ devised an 80-step mechanism with 24 species that was motivated by an attempt to fit the species profiles in the gas phase of AP burning at low pressure.⁷⁴ A subsequent more limited mechanism having 22 steps and 8 species⁸⁰ has been criticized by Cohen,⁷² who updated several earlier mechanisms with 136 steps and 35 species.¹⁴ He obtained reasonable agreement with the flame temperature. Tanaka and Beckstead¹⁵ devised a combined gas-liquid-solid phase model of AP combustion in which the gas phase consisted of 107 steps and 32 species. They concluded that the condensed-phase kinetics much more strongly influenced the combustion characteristics than did physical properties, such as the thermal conductivity and density of the solid. The minor role played by heat conduction has been noted elsewhere.⁸¹

B. HTPB

The use of HTPB as a binder in solid rocket propellants appears to date from about 1962 in work by the Aerojet Corporation.⁴² Many structures of HTPB exist, and the most commonly used type (R45M, whose structure was shown in Sec. II) can be thought of as a terpolymer of *cis*-, *trans*-, and vinyl-linked butadiene units. In addition, the terminal groups, that are $-\text{OH}$ in R45M are an additional variable. Also, $-\text{CO}_2\text{H}$ has been used as a terminal group (called CTPB), but is no longer used as a propellant binder in the United States. The copolymer of polybutadiene and acrylic acid (PBAA) and terpolymer of polybutadiene, acrylic acid, and acrylonitrile (PBAN) also have application as propellant binders. Several detailed reviews^{27,82} and more specialized summaries^{3,6,24,83} of polybutadienes, including their use in rocket propellant formulations, are available.

Studies of the thermal decomposition of HTPB and related polymers at fast heating rates^{24,83-89} and at slow heating rates^{21-23,90-104} are rather extensive. The decomposition process has a distinguishable, mildly exothermic component because bond forming processes occur along side of the bond-breaking processes.^{83,89,102,104} Numerous fragments of the polymer have been detected, but the main species are the butadiene monomer, dimer (4-vinylcyclohexene), and *trans*-butadiene oligomers. Figure 3 shows the mole fractions of the major products from flash heating of a thin film of R45M at 800°C s^{-1} under 2 atm of Ar to the constant temperatures shown.²⁴ These species primarily indicate that random chain cleavage occurs along the polymer backbone followed by subsequent vaporization of the fragments. The presence of a high percentage of oligomers of butadiene relative to the monomer indicates that the zip length of HTPB is relatively small. That is, the formation of a radical due to bond cleavage in the polymer backbone does not result in an extensive propagation of the radical sites along the chain and, thus, liberates a comparatively low percentage of the monomer.

The kinetics of formation of each of the products shown in Fig. 3 has been established recently at a high heating rate.⁸³ The behavior observed suggests that the process that controls the rate of appearance of the species in the gaseous

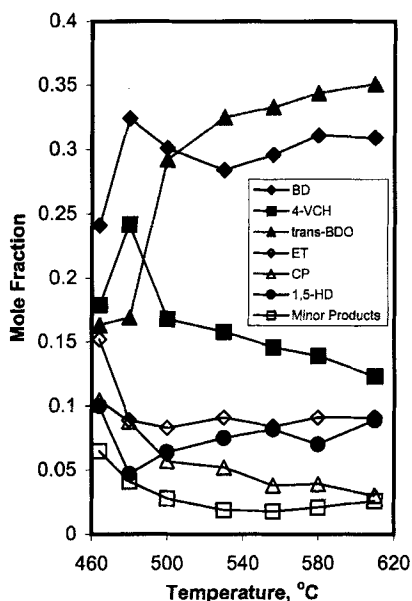


Fig. 3 Quantified gaseous product concentration profiles from flash heating of HTPB (R45M) to the temperature shown under 2 atm Ar (Ref. 24): BD = butadiene; 4-VCH = 4-vinylcyclohexene; ET = ethylene; CP = cyclopentene; 1,5-HD = 1,5-hexadiene; trans-BDO = transbutadiene oligomers.

phase shifts from one of bulk-phase chemical reaction control below 500–530°C to one of desorption/evaporation control above this temperature range. It has also been shown that urethane cross-linked HTPB upon fast heating regenerates the cross-linking agent that then vaporizes before the polymer fragments appear.⁸⁹ This has been used to justify the use of uncross-linked HTPB to identify potential hydrocarbon fragments released when the surface of an AP-HTPB mixture pyrolyzes.^{24,83} The physical properties of the polymer-rich region of the mixture can be expected to differ depending on whether the cross-linking agent is present or not, but the focal chemistry question for this work was the extent to which the decomposition products of AP affect the decomposition process of HTPB. One study has suggested that there is little effect,¹⁰⁵ perhaps because AP mainly controls the burning rate of AP-HTPB mixtures,³ especially above 70 atm (Ref. 106). Other studies indicate that the AP and HTPB interact during decomposition of the mixture.^{27, 107–109}

IV. AP-HTPB Mixture

The complexity of the pyrolysis and combustion of pure AP and pure HTPB alone is magnified when the two are combined as a heterogeneous mixture. The overall event becomes a three-dimensional combination of homogeneous and heterogeneous chemical and physical processes whose balance depends on the intrinsic variables that are in play.^{29,110,111} A few of the general concepts expressed

about this process in the past 50 years are summarized next in the context of the present experiments. In some instances the fuel used by others was not HTPB, but the comments apply in general terms to AP mixed with any hydrocarbon fuel.

First, one of the main themes of this section is the evidence that AP and HTPB interact during fast decomposition of the mixture. By design, the T-jump/FTIR spectroscopy experiment is intended for study of the condensed-phase chemical processes without the flame zone. Decomposition of energetic materials in the condensed phase is inherently made complicated, however, because gaseous products form that leads to phase interfaces. In the case of AP-HTPB composite mixtures, additional interfaces also exist between the ingredients. Throughout this section the term interfacial is intended to group together these ill-defined reaction interfaces because they cannot be distinguished in the experiment.

Second, a wide range of opinions exists with regard to the relative roles of the condensed and gas phases during combustion of propellants containing AP. Some believe that the condensed-phase chemistry almost totally controls the burning process,^{41,57,112} whereas others merely favor an important role for the condensed phase.^{25,31,32,50,54,108,113–119} The other extreme is that the gas phase primarily controls the combustion process^{68,70,76,77,88,120} and that interfacial chemistry in the condensed phase is not apparent.¹²⁰ Some of these distinctions may be primarily semantic given the unclear distinction of what the condensed phase is and where it becomes the gas phase. That is, if a liquid layer containing bubbles exists,^{32,71,111,121} then the gas and condensed phases coexist. To complicate matters further, particles may be able to enter the gaseous phase.^{112,122} The surface structure of AP crystals is also highly nonuniform with ridges and valleys present.^{29–32}

Third, it is generally accepted that the near-surface edge of the AP–fuel diffusion flame is an important site in the combustion process because it is the location of a large amount of exothermic redox chemistry. This concept enables features such as the dependence of the burning rate on the pressure and the AP particle size to be understood.^{25,26,28,123,124}

Fourth, during the ignition stage, heterogeneous gas–condensed-phase reactions are believed to dominate,^{54,106,125–127} as opposed to an entirely gas-phase ignition event, but this view requires careful interpretation.¹²⁸ Thus, it has been widely stated^{12,26,31,54,81,88,115,118,129–131} that interfacial chemistry plays a major role in the condensed-phase, surface, and near-field gas-phase processes of AP–binder mixtures, although agreement is not universal.^{67,132} The problem is to define what reactions occur under what conditions.

We accepted that elucidation of the chemical details of the condensed phase of AP-HTPB mixtures at combustion-like conditions was probably beyond the present ability of chemical diagnostics, although this issue is recognized to be perhaps the major deficiency in understanding in this field.^{8,15} This project was undertaken with the hope of adding additional insights at fast heating rates because most past chemistry studies on the AP-HTPB mixtures have been undertaken at low (<100°C/min) heating rate conditions.^{2,44,55,58,59,61–63,73,113,114,132–134}

A. Thermal Stability of the Mixture

T-jump/FTIR spectroscopy makes it possible to measure the time to exotherm at relatively high temperatures, because flash heating to a controlled set temperature is

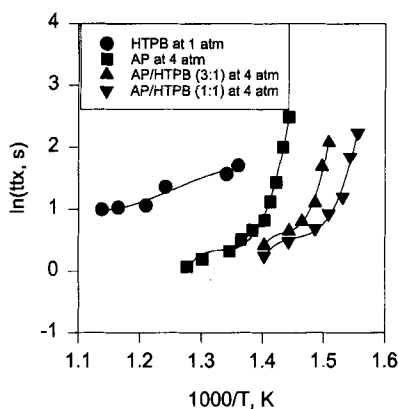


Fig. 4 Times-to-exotherm data for films of the samples (44- μm AP) heated at 800°C s^{-1} to the temperature shown under 4-atm Ar; HTPB was studied at 1-atm pressure of Ar.

performed. By monitoring the control voltage trace of the Pt filament that maintains this constant set temperature as a function of time, the time to exotherm at a series of temperatures can be obtained. The temperature range was chosen with an eye on the T_s values in Table 1, although practical considerations dictated the use of the lower end of the range ($375\text{--}500^\circ\text{C}$).

Figure 4 shows the time-to-exotherm plot for pure HTPB, pure AP, and two physical mixtures of AP with different weight ratios of HTPB. The theoretical basis of this type of plot has been discussed³⁶ including that the curvature is related to the changing role of heat transfer as a function of temperature. This is not the main point of interest here. The relevant point is the relative positions of the curves. Figure 4 shows that pure HTPB and pure AP are both more stable in terms of the time to exotherm at a given temperature than either of the physical mixtures of AP-HTPB. This finding is consistent with previous studies that found AP-fuel mixtures to be less thermally stable^{25,108,109,135} and to burn faster³⁹ than the pure components and is evidence that interfacial, exothermic, free-radical chemistry in the condensed phase contributes to the early stages of pyrolysis of AP-HTPB mixtures. This is despite the initial decomposition reaction, which is proton transfer involving the AP, being highly endothermic. The rapid, highly exothermic, secondary redox reactions quickly destabilize the mixture compared to the pure components. Thus, these results are consistent with the existence of exothermic surface reactions for AP-HTPB, as has been postulated before.^{28,108,110,126,133}

B. Gaseous Products

In accordance with the apparent occurrence of some interactive chemistry of the AP-fuel mixture in the condensed phase, the gaseous products from flash heating of a thin film of the 3:1 AP-HTPB mixture (Fig. 5) are dramatically different from those of pure AP (Fig. 2) and HTPB (Fig. 3). An interesting observation is the nature of the hydrocarbon products detected. Unlike pure HTPB, the highest molecular weight hydrocarbon observed is C_2H_2 . This implies that radicals formed when AP decomposes cause extensive radical chain cleavage of the HTPB backbone

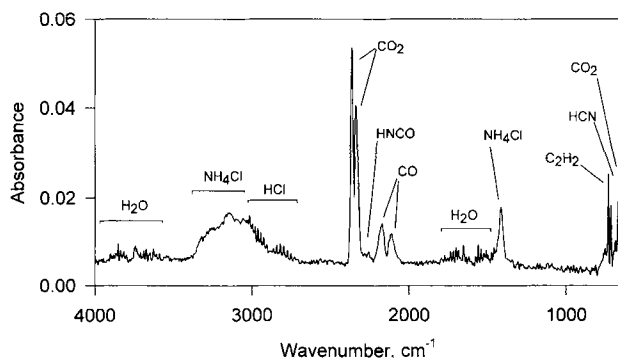


Fig. 5 IR spectrum from 1.4- μm AP-HTPB at a 3:1 weight-weight ratio flash heated at 800°C s^{-1} to 410°C under 4-atm Ar.

resulting in extremely fast disintegration of the polymer and liberation of only the most stable low molecular weight hydrocarbons. It is believed that HClO_4 and its derived radicals attack the polymer.^{125,136} The absence of high molecular weight hydrocarbons from pyrolysis of AP-fuel mixtures has been observed by others using a variety of diagnostic and heating methods.^{12,116,118,131,132,136} As has been done recently, this makes low molecular weight hydrocarbons the most relevant for use in studying and modeling the diffusion flame structure of an AP-fuel mixture.¹⁶

Other major differences are apparent when Figs. 2 and 5 are compared. Pure AP in Fig. 2 liberates NO , NOCl , N_2O , NO_2 , HNO_3 , and HClO_4 , which reflect only partially completed redox chemistry because an insufficient amount of fuel (NH_3) is present. Hence, various oxides of nitrogen form with intermediate formal oxidation states of N. On the other hand, when the hydrocarbon fuel is available, the needed fuel, as well as the ease of oxidizing the hydrocarbons compared to NH_3 , is apparent in the fraction of carbon oxides, as opposed to nitrogen oxides, that dominate. In fact, no nitrogen oxides at all are detected from the AP-HTPB mixture by IR spectroscopy. Discussion of several further details about the product ratios is deferred until later in this section.

Figures 6 and 7 show the trends in the mole fractions as a function of the pyrolysis temperature for 1.4- and 44- μm -diam AP, respectively, in a 3:1 AP-HTPB mixture. The main difference in this case is the different amount of contact between the AP and HTPB because the surface area of the AP particles scales as $1/r^2$. In Fig. 6, the products from 1.4- μm AP exhibit a mild dependence on the temperature, especially at the lower end of the range. This is not so much the case with the other AP particle sizes used (8, 18, and 44 μm). For example, Fig. 7 for 44- μm AP shows less dependence of the gaseous product concentrations on the pyrolysis temperature. An additional manifestation of the larger AP surface area of 1.4- μm AP is that the 3:1 weight-weight ratio sample has a cakey appearance, whereas the samples with larger particles are thick fluids. Apparently the higher surface area of 1.4- μm AP enables more complete wetting by HTPB and, thus, has less free HTPB to act as a fluidizing medium. The more intimate contact of the HTPB with the smaller AP crystals enhances the opportunity for radical reactions to occur between the binder and oxidizer. Bakhman earlier arrived at the same conclusion.¹³⁷ This maximizes the opportunity for the AP-binder reaction over a wide range of conditions and leads to the dependence of the product

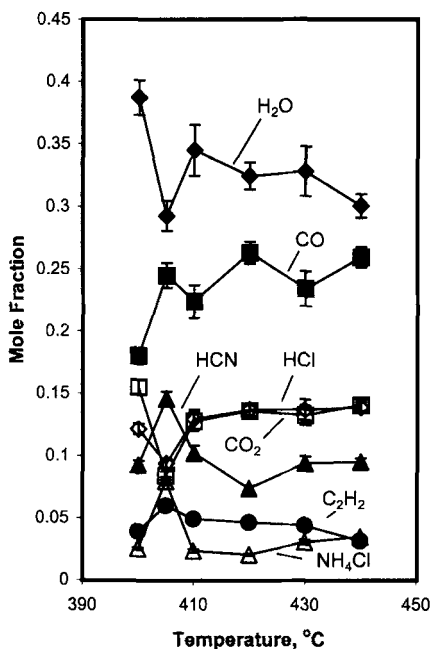


Fig. 6 Mole fractions of the gaseous products from flash heating of 3:1 AP (1.4 μm)-HTPB at 800°C s^{-1} to the temperatures shown under 4-atm Ar.

ratios on the pyrolysis temperature shown in Fig. 6. Earlier experimental findings and modeling principles are consonant with this result. For example, it is known that the binder type plays a lesser role in the burning rate for larger AP particle sizes,¹²¹ which suggests that the amount of interfacial chemistry is less. Models of composite propellant burning^{6,26,28,71,115,123,138} have paid attention to larger AP particles in composite propellants tending to give lower burning rates, especially at higher pressures^{39,40,128,139,140} because the diffusion flame develops farther from the pyrolysis surface. Smaller AP particles, on the other hand, lead to better fuel-oxidizer mixing closer to the surface.^{28,137} Some chemical details of the diffusion flame are beginning to emerge.¹⁶

The gaseous product ratios shown in Fig. 6 compare quite well with those found by Korobeinichev et al.,¹¹⁶ who determined them by probing the flame of a 5:1 AP-CTPB mixture at a subatmospheric pressure by TOF mass spectrometry (Table 2). In constructing Table 2, their data at about 2 mm above the surface were used and were normalized to ours by removing the small amounts (<3%) of Cl₂, O₂, N₂, H₂, and HOCl that were not detected with the IR spectroscopy method. We verified by separate mass spectrometry and Raman spectroscopy experiments that small amounts of Cl₂, N₂, and H₂ are indeed present in our experiment. HOCl was not detected. In view of the different fuel-oxidizer ratio and the different end groups used in the fuel in the comparison in Table 2, the agreement is satisfactory. One obvious difference is that we detected NH₄Cl. This is an artifact of quenching by the cool Ar atmosphere that enables NH₃ and HCl to recombine. This recombination is not favored in the flame and contributes to the higher quantity of HCl reported by Korobeinichev et al.¹¹⁶

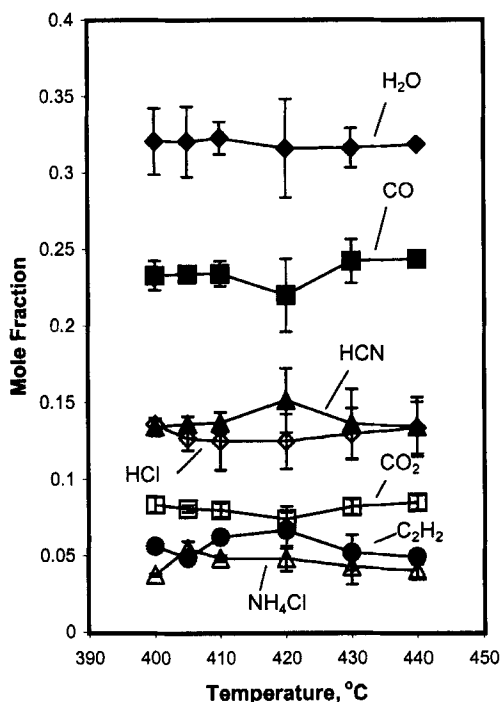


Fig. 7 Mole fractions of the gaseous products from flash heating of 3:1 AP ($44\ \mu\text{m}$)-HTPB at $800^\circ\text{C}\ \text{s}^{-1}$ to the temperatures shown under 4-atm Ar.

As a method to summarize the effect of the AP particle size on the mole fractions of the gaseous products, the data for each particle size were averaged over the 400–440°C range and plotted as a function of the particle size. The result is shown in Fig. 8. As discussed earlier and shown in Fig. 6, the results for $1.4\text{-}\mu\text{m}$ AP are somewhat atypical, and so attention is mainly focused on the trends for $\geq 8\ \mu\text{m}$ particle sizes of AP. The trends are that the concentrations of HCN and C_2H_2 tend to decrease whereas CO_2 and CO tend to increase with increasing particle

Table 2 Comparison of the mole fractions of gaseous products from AP-polybutadiene mixtures

Product	Ref. 116	This work
H ₂ O	29	33
CO	23	24
HCl	23	12
HCN	7	13
CO ₂	11	8
C ₂ H ₂	5	5
NH ₃	3	5 ^a

^aAs NH_4Cl .

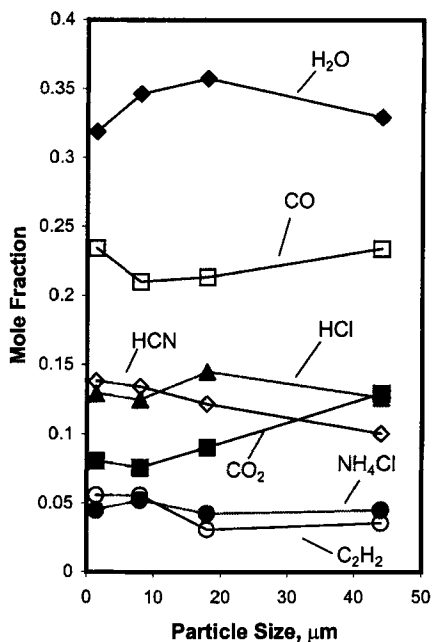


Fig. 8 Mole fractions of the gaseous products averaged over 400–440°C as a function of the AP particle size; data were taken at 4-atm Ar.

size. Various explanations can be imagined, but one that is consistent with the experimental design is suggested here. The HCN and C₂H₂ contain carbon in lower oxidation states and, thus, reflect incomplete oxidation of the hydrocarbon fuel. This suggests that less interfacial AP–fuel chemistry occurs with the larger AP crystals, which is consistent with their lower surface area. As a result, more of the AP-based decomposition products have not reacted with the binder at the interface in the condensed phase and are, instead, able to form the gaseous phase, where they can then react. Hence, there is proportionally more gas-phase redox chemistry possible with the larger particle sizes that results in larger amounts of CO₂ and CO.

Figure 9 shows the trend in the ratio of C₂H₂ to CO₂ as a function of the ratio of AP to HTPB. The C₂H₂/CO₂ ratio partly reflects the relative extents of cleavage of the polymer backbone vs oxidation of the fragments. At low AP–HTPB ratios, where the mixture is strongly fuel rich, a small amount of ethylene, C₂H₄, was also detected, but the predominate hydrocarbon is still C₂H₂. Hence, even in a fuel-rich mixture, the fuel pyrolysis process is completely unlike that of pure HTPB (Fig. 3) because the AP-based radicals attack the polymer backbone and cause radical chain cleavage. Not surprisingly, however, the C₂H₂/CO₂ ratio decreases as the AP–HTPB ratio increases because more hydrocarbon oxidation can occur. There is possibly a dependence of the C₂H₂/CO₂ ratio on the AP particle size in Fig. 9, which becomes more pronounced with the larger particle sizes.

Widely used combustion models of composite propellants that emphasize control of combustion by the leading edge of the diffusion flame handle the relative balance between the fuel and oxidizer species in the gas phase by an adjustable parameter β_F (Refs. 28 and 138). Other approaches over the years use the concept

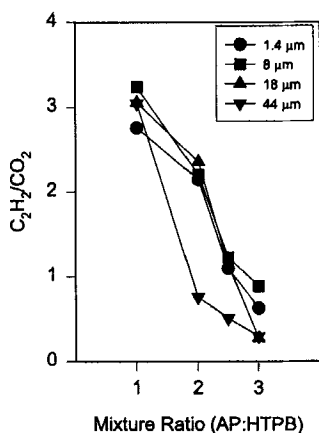


Fig. 9 $\text{C}_2\text{H}_2/\text{CO}_2$ ratio as a function of AP particle size in 3:1 AP-HTPB mixtures flash heated to 440°C under 4-atm Ar.

of two temperatures^{39,141,142} and different activation energies¹⁴³ at the surface of a burning AP-composite propellant. That is, one temperature or activation energy applies to pyrolysis of the binder whereas another applies to pyrolysis of the AP crystal. The conclusion we would draw from the current chemistry study is that the two-temperature concept would be most appropriate for larger AP particle sizes and for AP-fuel mixtures that are somewhat less than stoichiometric.

As noted earlier in the products from pure AP (Fig. 2) compared to those from the AP-fuel mixtures (Figs. 6 and 7), an important difference is the presence of NH_4Cl in the latter. NH_4Cl has been seen before as a product of the AP-fuel mixture at slow heating rates.¹⁴⁴ The formation of NH_4Cl reflects the competitive oxidation rates of NH_3 and the hydrocarbons in which the hydrocarbons win.^{145,146} The hydrocarbon fragments, except possibly C_2H_2 , are more easily oxidized than NH_3 , which results in the liberation of some unreacted NH_3 in the AP decomposition process. The appearance of C_2H_2 in the gas phase reflects that C_2H_2 is oxidized more slowly than are the other hydrocarbons.¹⁴⁵ Figure 10 shows the $\text{NH}_4\text{Cl}/\text{C}_2\text{H}_2$ ratio as a function of temperature when the data are averaged for the four AP particle sizes. At lower temperatures, less of the NH_3 is oxidized relative to the hydrocarbons so that the ratio is higher compared to that at higher temperatures. The rather large error bars of Fig. 10 result from the averaging of the different particle sizes, rather than the true error in an individual measurement. The trend shown was found in all of the data.

C. Effect of Pressure

These flash pyrolysis studies to establish some of the chemical features of AP-HTPB mixtures were conducted at 1–5 atm of Ar so that the reaction zones would be stretched with the hope of seeing more than just the thermodynamically stable final products. These pressures do not apply to steady combustion conditions of a rocket motor. Therefore, 8- μm -diam AP particles in a 3:1 AP-HTPB mixture were flash pyrolyzed at different static pressures at 4–50 atm Ar. Figure 11 shows the trends observed. Although the behavior of H_2O is not easily understood, the trends

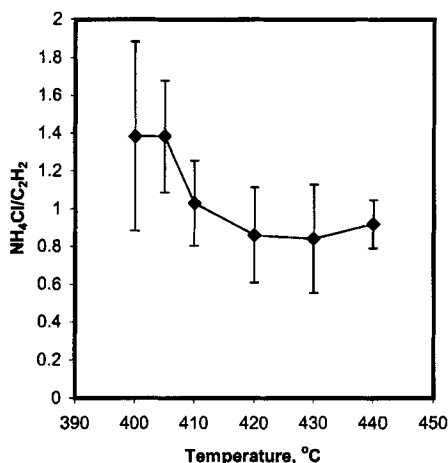


Fig. 10 $\text{NH}_4\text{Cl}/\text{C}_2\text{H}_2$ ratio from 3:1 AP-HTPB mixtures flash heated to the temperatures shown under 4-atm Ar; concentrations for all particle sizes were averaged.

of the other products can be explained in terms of past work of this type.¹⁴⁷ As the pressure is increased, the CO , CO_2 , and NH_4Cl products appear with larger concentration, whereas C_2H_2 and HCN are decreased in concentration. Consequently, the application of higher pressures advances the extent of the AP-fuel reaction by forcing the products to remain longer in the reaction zone close to the heat source. That more NH_4Cl forms at the higher pressures is consistent with an increase in the amount of HClO_4 -hydrocarbon chemistry relative to HClO_4 - NH_3 chemistry. This is a direct result of the greater reactivity of the hydrocarbons toward HClO_4 compared to NH_3 (Refs. 125, 136, 145, and 146).

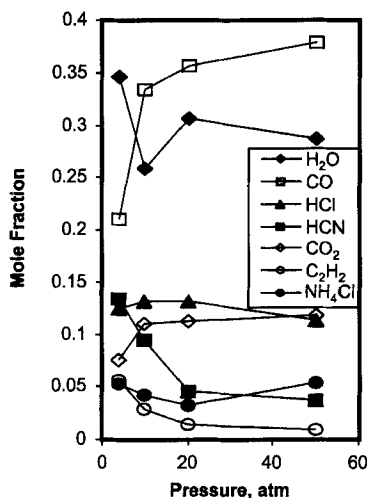


Fig. 11 Mole fractions as a function of the static cell pressure of Ar for 3:1 AP (8 μm)-HTPB flash heated to 440°C.

V. AP-HTPB with TiO_2 and Melamine

As complicated as the AP-HTPB interfacial chemistry is, the addition of a burning-rate modifier adds yet another dimension of complexity. Several reviews of such additives have appeared over the years.^{2,3,43,44,148} The most commonly used class of modifiers has been the inorganic oxides, although interesting results can also be produced with organic additives.¹⁴⁹ Many studies propose that the ballistic modifier is active primarily in the condensed phase at the AP-binder interface,^{110,135,150,151} where electron transfer is important,^{44,135} whereas others propose that the action primarily takes place in the gas phase.^{65,152}

In this section the properties of TiO_2 in the AP-HTPB matrix are the main focus in view of the recently discovered plateau burning behavior of AP-HTPB propellants in the 50–100 atm pressure range when 0.5–5% TiO_2 has been added.^{17,18} Prior to this discovery, TiO_2 had been studied frequently as an additive with the results being somewhat contradictory. It had been described variously as inactive,^{44,153} less active,⁵⁶ a suppressant to the burning rate,⁴³ and as an acoustic dampener that stabilizes combustion.¹⁵⁴ On the other hand, the addition of an ultrafine mixture of the anatase and rutile polymorphs of TiO_2 promotes plateau burning in the AP-HTPB propellant.¹⁷ The mechanism of action is not yet agreed upon, although thermogravimetric analysis (TGA) measurements indicate that the weight loss is faster when TiO_2 is present,¹⁸ which suggests that some additional chemical reactivity has been introduced. As a sidelight, we explored the behavior of melamine in the AP-HTPB mixture. To our knowledge, past work on this additive has been limited, but is potentially interesting as a burning-rate suppressant.¹⁴⁹

Flash pyrolysis of small quantities of a three-component mixture understandably has more potential problems with the sample uniformity than the single- and two-component systems. Consequently, completely reproducible results were difficult to obtain, and many repeated experiments were conducted to acquire a representative set of results. With the caveat that some outlying results were obtained, Figure 12 shows the time sequence of the product evolution from a 3:1 AP-HTPB mixture with 8- μm AP that had been heated at 800°C s^{-1} to 405°C under 4 atm of Ar. Figure 13 shows the results of an equivalent experiment in which 5% TiO_2 had been added to the sample. Figure 14 is the same as the experiment shown in Fig. 12,

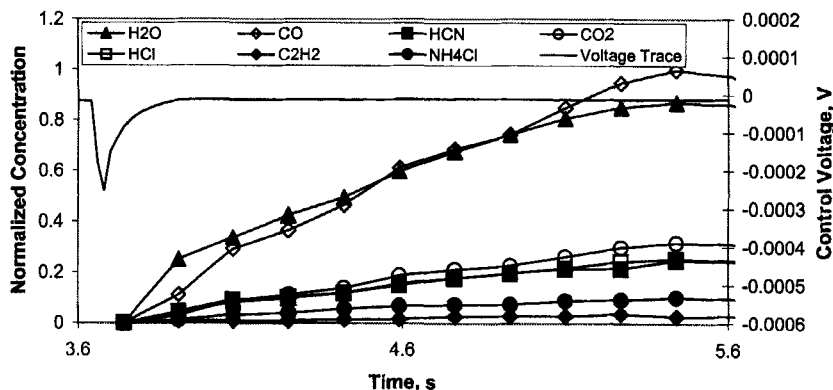


Fig. 12 Rate for formation of products and the Pt filament control voltage trace for 3:1 AP (8 μm)-HTPB flash heated at 800°C s^{-1} to 405°C under 4-atm Ar.

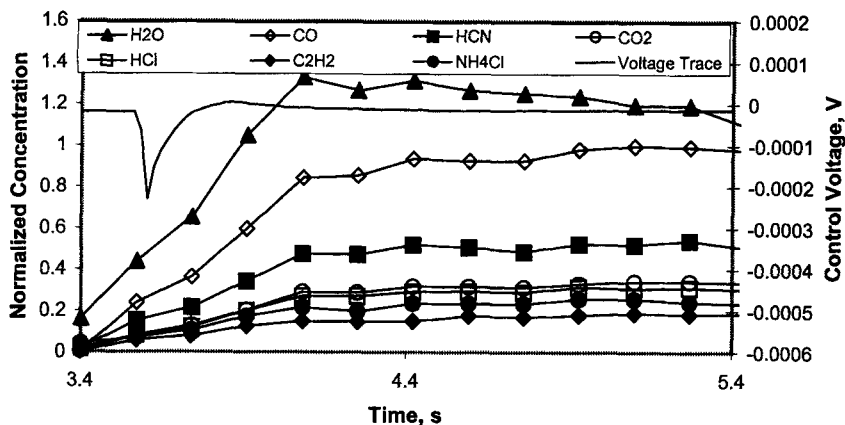


Fig. 13 Rate of formation of gaseous products and the Pt filament control voltage trace for 3:1 AP (8 μm)-HTPB containing 5% TiO_2 (anatase) flash heated to 405°C under 4-atm Ar.

except that 5% melamine was present in the sample. Comparing Figs. 12 and 13, the time to exotherm (the negative spike in the control voltage difference trace) is affected little by the addition of the TiO_2 , but TiO_2 accelerates the rate of evolution of the gaseous products. This finding is consistent with TGA data¹⁸ that revealed faster weight loss in a TiO_2 -containing AP-HTPB propellant sample. In contrast, Fig. 14 shows that melamine lengthens the time to exotherm, but has a small effect on the formation rate of the products. Consequently, we conclude that TiO_2 , but not melamine, is a positive catalyst for decomposition under the conditions used here. TiO_2 does not destabilize the mixture in terms of the time-to-exotherm criterion of Fig. 4. Thus, it is probable that the surface temperature during combustion is similar with and without the TiO_2 additive, which is consistent with the notion that the surface temperature is not generally a strong function of the catalyst.¹¹⁰

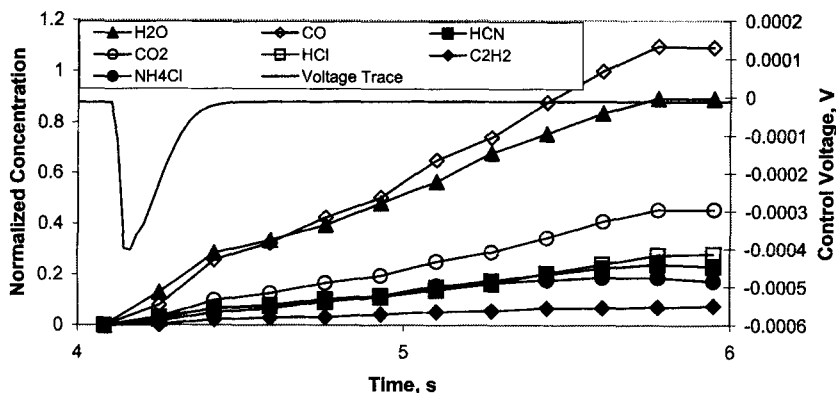


Fig. 14 Rate of formation of the gaseous products and the Pt filament control voltage trace for 3:1 AP (8 μm)-HTPB containing 5% melamine flash heated to 405°C under 4-atm Ar.

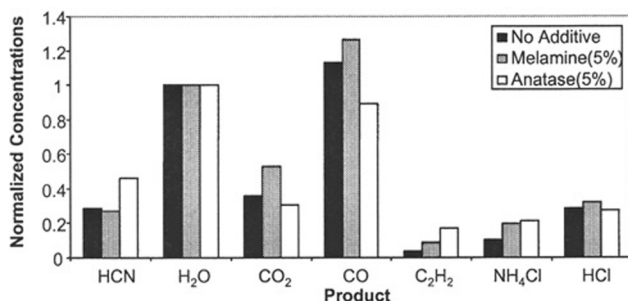


Fig. 15 Comparison of the maximum mole fractions of the gaseous products normalized to H₂O for Figs. 12–14.

Melamine, on the other hand, seems to stabilize the mixture somewhat in the context of Fig. 4 without affecting the decomposition rate. As a result, it may slightly decrease the surface temperature during combustion.

Figure 15 is a bar graph that compares the mole fractions of the gaseous products from the three formulations at their maximum point normalized to the mole fraction of H₂O. These data were obtained on 8- μ m AP, but the features shown also qualitatively apply to the other particle sizes. The presence of TiO₂ increases the relative amounts of HCN, C₂H₂, and NH₄Cl, which is the same effect seen in Fig. 8, caused by reducing the AP particle size. That is, the relative proportion of condensed phase interfacial chemistry is somewhat higher when TiO₂ is present. This seems to be consistent with the higher rate of product evolution shown in Fig. 13. The amount of CO₂ and CO are about the same or somewhat less, suggesting that the redox chemistry may be reduced to some extent by the presence of TiO₂. Because these experiments were conducted at a pressure well below that where plateau burning is observed (50–100 atm) (Ref. 17), it is not at all certain that they have any relation to the mechanism of this phenomenon. If this observation is valid at higher pressures, however, TiO₂ may dampen the amount of heat released and possibly contribute to a slowing of the burning rate.

The effect of 5% melamine on the product ratios is small compared to the AP-HTPB mixture without the additives. This observation is consistent with the similarity of the product formation rates in Figs. 12 and 14. The main effect is to increase the amounts of CO₂, CO, and NH₃ (NH₄Cl), which is understandable because decomposition of melamine itself by the AP radicals will produce CO, CO₂, and NH₃. Thus, the product distribution is somewhat skewed, but in an understandable way. The behavior of melamine is consistent with the hypothesis¹⁴⁹ that the melamine suppresses the burning rate of the AP-HTPB mixture by affecting the heat transfer process rather than by altering the chemistry of the AP-HTPB system.

VI. Conclusions

Superatmospheric pressure, flash-heated, physical mixtures of AP and HTPB may provide insight into behavior at combustionlike conditions and provide a context for past studies conducted at other conditions. Some of the mechanistic features may help refine several details in modeling efforts.

It was clearly found that the AP-HTPB mixture is less thermally stable than the pure components, which is a strong indication that radical chain cleavage of the HTPB polymer is induced, and that the AP radical products are formed at a higher rate in the presence of hydrocarbons. These reactions become highly exothermic in the heterogeneous gas-condensed phase region as a result of oxidation-reduction processes. One useful observation is that C_2H_2 is the highest molecular-weight hydrocarbon to survive the condensed-phase reactions in a measurable concentration. Its survival in part reflects that C_2H_2 is the least readily oxidized of the available hydrocarbons. The remaining hydrocarbons are also oxidized faster than NH_3 , which leads to the liberation of some NH_3 (detected as the recombination product of NH_3 and HCl in the gas phase). The gaseous product ratios observed agree reasonably well with studies by Korobeinichev et al.¹⁴⁵ on the combustion of AP-binder mixtures at low pressure.

The AP particle size effect can be seen clearly in the flash decomposition products of the AP-HTPB mixture. More AP-fuel interfacial chemistry is apparent with the smaller particle sizes. The effect of increasing the pressure is to drive the reactions further toward the more thermodynamically stable products.

The addition of TiO_2 , which creates plateau burning in the AP composite propellant, had no effect on the thermal stability in terms of the time to exotherm. Instead, it acted as a catalyst, as evidenced by the faster rate of gaseous product evolution and a higher concentration of products resulting from the AP-HTPB interfacial chemistry. A lower concentration of the products from the more exothermic gas-phase redox reactions was generated that might have the effect of decreasing the burning rate. In contrast, the addition of melamine stabilized the AP-HTPB mixture by producing a longer time to exotherm, but did not significantly affect the AP-HTPB interfacial chemistry. This finding is consistent with the notion that melamine affects heat transfer by forming polymeric materials in addition to lower molecular-weight decomposition products.¹⁴⁹ The provocative question arises as to whether T-jump/FTIR spectroscopy might be used to provide more insight into the mechanisms of burning rate modifiers than has been available from other methods.

Acknowledgments

We are grateful for support of this work by the Ballistic Missile Defense Office through the Office of Naval Research (ONR) on the Multidisciplinary University Research Initiative program as a subcontract from California Institute of Technology. The Program Monitor is Judah Goldwasser on ONR N00014-95-1-1338. Thiokol Corporation generously provided samples of AP and R45M.

References

- ¹Price, E. W., "History of Solid Rocket Motors (1940-1960)," AIAA Paper 98-3978, 1998.
- ²Jacobs, P. W. M., and Whitehead, H. M., "Decomposition and Combustion of Ammonium Perchlorate," *Chemical Reviews*, Vol. 69, No. 4, 1969, pp. 551-590.
- ³Kishore, K., and Prasad, G., "A Review on Decomposition/Deflagration of Oxidizer and Binder in Composite Solid Propellants," *Defence Science Journal*, Vol. 29, 1979, pp. 39-54.

⁴Kishore, K., and Gayathri, V., "Chemistry of Ignition and Combustion of Ammonium-Perchlorate-Based Propellants," *Fundamentals of Solid-Propellant Combustion*, edited by K. K. Kuo and M. Summerfield, Vol. 90, Progress in Astronautics and Aeronautics, AIAA, New York, 1984, pp. 53–106.

⁵Lengellé, G., Brulard, J., and Moutet, H., "Combustion Mechanisms of Composite Solid Propellants," *Proceedings of the 16th Symposium (International) on Combustion*, Combustion Inst., Pittsburgh, PA, 1976, pp. 1257–1270.

⁶Kishore, K., "Comprehensive View of the Combustion Models of Composite Solid Propellants," *AIAA Journal*, Vol. 17, No. 11, 1979, pp. 1216–1224.

⁷Ramohalli, K., "Technologies and Techniques for Instability Suppression in Motors," *Nonsteady Burning and Combustion Stability of Solid Propellants*, edited by L. De Luca, E. W. Price, and M. Summerfield, Vol. 143, Progress in Astronautics and Aeronautics, AIAA, Washington, DC, 1989, pp. 805–848.

⁸Beckstead, M. W., "Solid Propellant Combustion Mechanisms and Flame Structure," *Pure and Applied Chemistry*, Vol. 65, No. 2, 1993, pp. 297–307.

⁹Ermolin, N. E., Korobeinichev, O. P., Tereschenko, A. G., and Fomin, V. M., "Kinetic Calculations and Mechanism Definition for Reactions in an Ammonium Perchlorate Flame," *Combustion, Explosion, and Shock Waves*, Vol. 18, No. 2, 1982, pp. 180–189.

¹⁰Chen, K. M., Wang, G. P., Kuo, C. N., Shyy, I. N., and Chang, Y. M., "Laser-Induced Decomposition of Ammonium Perchlorate. Identification of Nascent Products from Emission Spectroscopy," *Chemical Physics Letters*, Vol. 167, No. 4, 1990, pp. 351–355.

¹¹Brill, T. B., Brush, P. J., James, J. E., Shepherd, J. E., and Pfeiffer, K. J., "T-Jump/FTIR Spectroscopy. A New Entry into the Rapid, Isothermal Pyrolysis Chemistry of Solids and Liquids," *Applied Spectroscopy*, Vol. 46, No. 6, 1992, pp. 900–911.

¹²Klotz, S., Thynell, S. T., Huang, I. T., and Kuo, K. K., "Analysis of Plumes of Solid Propellant Combustion Using a Fourier Transform-Infrared Spectrometer," *Journal of Propulsion and Power*, Vol. 8, No. 3, 1992, pp. 537, 538.

¹³Parr, T., and Hanson-Parr, D., "Solid Propellant Flame Chemistry and Structure," *Non-Intrusive Combustion Diagnostics*, edited by K. K. Kuo and T. P. Parr, Begell House, New York, 1994, pp. 571–599.

¹⁴Cohen, N., "A Review of Kinetic Models for the High Temperature Gas Phase Decomposition of Ammonium Perchlorate," Aerospace Rept. ATR-92(9558)-3, The Aerospace Corp., El Segundo, CA, Sept. 1992.

¹⁵Tanaka, M., and Beckstead, M. W., "A Three Phase Combustion Model of Ammonium Perchlorate," AIAA Paper 96-2888, 1996.

¹⁶Parr, T. P., Hanson-Parr, D., Smooke, M., Ilincic, N., Tanoff, M., and Yetter, R., "AP Diffusion Flame Structure," CPIA Publ. 662, Vol. 2, Chemical Propulsion Information Agency, Laurel, MD, 1997, pp. 13–22.

¹⁷Taylor, R. H., Use of Controlled Burn Rate, Reduced Smoke, Biplateau Solid Propellant Formulations, U.S. Patent 5,579,634, 3 Dec. 1996.

¹⁸Freeman, J. M., Price, E. W., Chakravarthy, S. R., and Sigman, R. K., "Contribution of Monomodal AP/HC Propellants to Bimodal Plateau-Burning Propellants," AIAA Paper 98-3388, 1998.

¹⁹Galwey, A. K., Herley, P. J., and Mohamed, M. A., "Role of Additives in the Thermal Decomposition of Ammonium Perchlorate and Evidence Supporting the Identification of Nitryl Perchlorate as the Essential Reaction Intermediate," *Thermochimica Acta*, Vol. 132, No. 1, 1988, pp. 205–215.

²⁰Brill, T. B., Brush, P. J., and Patil, D. G., "Thermal Decomposition of Energetic Materials 60. Major Reaction Stages of a Simulated Burning Surface of AP," *Combustion and Flame*, Vol. 94, No. 1/2, 1993, pp. 70–76.

- ²¹Braun, D., and Canji, E., "Pyrolysis-Gas Chromatography of Diene Polymers," *Angewandte Makromolekulare Chemie*, Vol. 29/30, No. 3, 1973, pp. 491–505.
- ²²Beck, W. H., "Pyrolysis Studies of Polymeric Materials Used as Binders in Composite Propellants: A Review," *Combustion and Flame*, Vol. 70, No. 2, 1987, pp. 171–190.
- ²³Rama Rao, M., and Radhakrishnan, T. S., "Thermal Degradation of Functionally-Terminated Polybutadienes: Pyrolysis Gas Chromatography and Thermogravimetric Studies," *Journal of Applied Polymer Science*, Vol. 41, No. 9/10, 1990, pp. 2251–2263.
- ²⁴Arisawa, H., and Brill, T. B., "Flash Pyrolysis of Hydroxyl-Terminated Polybutadiene I: Analysis and Implications of the Gaseous Products," *Combustion and Flame*, Vol. 106, No. 1/2, 1996, pp. 131–143.
- ²⁵Vandenkerckhove, J., and Jaumotte, A., "Remarks on the Burning Mechanism and Erosive Burning of Ammonium Perchlorate Propellants," *Proceedings of the 8th Symposium (International) on Combustion*, Combustion Inst., Pittsburgh, PA, 1960, pp. 689–693.
- ²⁶Fenn, J. B., "A Phalanx Flame Model for the Combustion of Composite Solid Propellants," *Combustion and Flame*, Vol. 12, No. 3, 1968, pp. 201–216.
- ²⁷Timnat, Y. M., *Advanced Chemical Rocket Propulsion*, Academic, New York, 1987, pp. 48–62.
- ²⁸Beckstead, M. W., Derr, R. L., and Price, C. F., "A Model of Composite Solid-Propellant Combustion Based on Multiple Flames," *AIAA Journal*, Vol. 8, No. 12, 1970, pp. 2200–2207.
- ²⁹Boggs, T. L., and Kraeutle, K. J., "Role of Scanning Electron Microscope in the Study of Solid Rocket Propellant Combustion, I. Ammonium Perchlorate Decomposition and Deflagration," *Combustion Science and Technology*, Vol. 1, No. 2, 1969, pp. 75–93.
- ³⁰Boggs, T. L., "Deflagration Rate, Surface Structure, and Subsurface Profile of Self-Deflagrating Single Crystals of Ammonium Perchlorate," *AIAA Journal*, Vol. 8, No. 5, 1970, pp. 867–873.
- ³¹Krishnan, S., and Swami, R. D., "Effect of Catalyst Mixing Procedure on Subatmospheric Combustion Characteristics of Composite Propellants," *Journal of Propulsion and Power*, Vol. 13, No. 2, 1997, pp. 207–212.
- ³²Boggs, T. L., Derr, R. L., and Beckstead, M. W., "Surface Structure of Ammonium Perchlorate Composite Propellants," *AIAA Journal*, Vol. 8, No. 2, 1970, pp. 370–372.
- ³³Brill, T. B., Arisawa, H., Brush, P. J., Gongwer, P. E., and Williams, G. K., "Surface Chemistry of Burning Explosives and Propellants," *Journal of Physical Chemistry*, Vol. 99, No. 5, 1995, pp. 1384–1392.
- ³⁴Brill, T. B., "Multiphase Chemistry Considerations at the Surface of Burning Nitramine Monopropellants," *Journal of Propulsion and Power*, Vol. 11, No. 4, 1995, pp. 740–751.
- ³⁵Brill, T. B., "Connecting the Chemical Composition of a Material to its Combustion Characteristics," *Progress in Energy and Combustion Science*, Vol. 18, No. 2, 1992, pp. 91–116.
- ³⁶Shepherd, J. E., and Brill, T. B., "Interpretation of Time-to-Explosion Tests," *Proceedings of the 10th International Detonation Symposium*, Office of Naval Research, ONR 33395-12, 1993, pp. 849–855.
- ³⁷Thynell, S. T., Gongwer, P. E., and Brill, T. B., "Condensed-Phase Kinetics of Cyclotrimethylenetrinitramine by Modeling the T-Jump/Infrared Spectroscopy Experiment," *Journal of Propulsion and Power*, Vol. 12, No. 5, 1996, pp. 933–939.
- ³⁸Boggs, T. L., Price, E. W., and Zurn, D. E., "The Deflagration of Pure and Isomorphously Doped Ammonium Perchlorate," *Proceedings of the 13th Symposium (International) on Combustion*, Combustion Inst., Pittsburgh, PA, 1971, pp. 995–1008.
- ³⁹Adams, G. K., Newman, B. H., and Robins, A. B., "The Combustion of Propellants Based Upon Ammonium Perchlorate," *Proceedings of the 8th Symposium (International) on Combustion*, Combustion Inst., Pittsburgh, PA, 1960, pp. 693–705.

⁴⁰Hackman, E. E., III, and Beachell, H. C., "Combustion Characteristics of Crystalline Oxidizers," *AIAA Journal*, Vol. 6, No. 3, 1968, pp. 561-564.

⁴¹Manelis, G. B., and Strunin, V. A., "The Mechanism of Ammonium Perchlorate Burning," *Combustion and Flame*, Vol. 17, 1971, pp. 69-77.

⁴²Sobczak, R. R., "Ammonium Perchlorate Composite Basics," *Journal of Pyrotechnics*, Vol. 3, Summer, 1996, pp. 35-46.

⁴³Boggs, T. L., Zurn, D. E., Cordes, H. F., and Covino, J., "Combustion of Ammonium Perchlorate and Various Inorganic Additives," *Journal of Propulsion and Power*, Vol. 4, No. 1, 1988, pp. 27-40.

⁴⁴Ramamurthy, S., and Shrotri, P. G., "Catalytic Decomposition of Ammonium Perchlorate," *Journal of Energetic Materials*, Vol. 14, No. 2, 1996, pp. 97-126.

⁴⁵Brill, T. B., and Goetz, F., "Laser Raman Studies of Solid Oxidizer Behavior," *Experimental Diagnostics in Combustion of Solids*, edited by T. L. Boggs and B. T. Zinn, Vol. 63, Progress in Astronautics and Aeronautics, AIAA, New York, 1978, pp. 3-19.

⁴⁶Beckstead, M. W., and Hightower, J. D., "Surface Temperature of Deflagrating Ammonium Perchlorate Crystals," *AIAA Journal*, Vol. 5, No. 10, 1967, pp. 1785-1790.

⁴⁷Selzer, H., "The Decomposition of Ammonium Perchlorate in the Condensed Phase," DLR, German Aerospace Research Center, Rept. 73-59, Lampoldshausen, Germany, 1973.

⁴⁸Brill, T. B., and Goetz, F., "Laser Raman Study of the Thermal Decomposition of Solid AP," *Journal of Chemical Physics*, Vol. 65, No. 3, 1976, pp. 1217-1219.

⁴⁹Hightower, J. D., and Price, E. W., "Combustion of Ammonium Perchlorate," *Proceedings of the 11th Symposium (International) on Combustion*, Combustion Inst., Pittsburgh, PA, 1967, pp. 463-472.

⁵⁰Manelis, G. B., and Strunin, V. A., "Mechanism and Elementary Theory of Burning of the Composite Solid Propellants," *Proceedings of the 11th International Symposium of Space Technology and Science*, 1975, pp. 97-104.

⁵¹Karpowicz, R. J., and Brill, T. B., "In Situ Characterization of the 'Melt' Phase of RDX and HMX by Rapid-Scan FTIR Spectroscopy," *Combustion and Flame*, Vol. 56, No. 3, 1984, pp. 317-325.

⁵²Inami, S. H., Rosser, W. A., and Wise, H., "Dissociation Pressure of Ammonium Perchlorate," *Journal of Physical Chemistry*, Vol. 67, No. 5, 1963, pp. 1077-1083.

⁵³Powling, J., and Smith, W. A. W., "The Surface Temperature of Ammonium Perchlorate Burning at Elevated Pressures," *Proceedings of the 10th Symposium (International) on Combustion*, Combustion Inst., Pittsburgh, PA, 1965, pp. 1373-1380.

⁵⁴Powling, J., "Experiments Relating to the Combustion of Ammonium Perchlorate-Based Propellants," *Proceedings of the 11th Symposium (International) on Combustion*, Combustion Inst., Pittsburgh, PA, 1967, pp. 447-456.

⁵⁵Boldyrev, V. V., Alexandrov, V. V., Boldyreva, A. V., Gritsan, V. I., Karpenko, Y. Y., Korobeinichev, O. P., Panfilov, V. N., and Khairtdinov, E. F., "On the Mechanism of the Thermal Decomposition of Ammonium Perchlorate," *Combustion and Flame*, Vol. 15, No. 1, 1970, pp. 71-78.

⁵⁶Pearson, G. S., "The Role of Catalysts in the Ignition and Combustion of Solid Propellants," *Combustion Science and Technology*, Vol. 3, June 1971, pp. 155-163.

⁵⁷Guirao, C., and Williams, F. A., "A Model for Ammonium Perchlorate Deflagration Between 20 and 100 ATM," *AIAA Journal*, Vol. 9, No. 7, 1971, pp. 1345-1356.

⁵⁸Bircumshaw, L. L., and Newman, B. H., "The Thermal Decomposition of Ammonium Perchlorate I. Introduction, Experimental, Analysis of Gaseous Products, and Thermal Decomposition Experiments," *Proceedings of the Royal Society of London, Series A: Mathematical and Physical Sciences*, Vol. 227, 1954, pp. 115-132.

⁵⁹Pai Verneker, V. R., and Maycock, J. N., "Mass-Spectrometric Study of the Thermal Decomposition of Ammonium Perchlorate," *Journal of Chemical Physics*, Vol. 47, No. 7, 1967, pp. 3618–3621.

⁶⁰Jacobs, P. W. M., and Russell-Jones, A., "Sublimation of Ammonium Perchlorate," *Journal of Physical Chemistry*, Vol. 72, No. 1, 1968, pp. 202–207.

⁶¹Kraeulte, K. J., "The Response of Ammonium Perchlorate to Thermal Stimulus," U.S. Naval Weapons Center, NWC-TP-7053, China Lake, CA, 1990, pp. 43–75.

⁶²Oxley, J. C., Kaushik, S. M., and Gilson, N. S., "Ammonium Perchlorate Thermal Stability in the Presence of Hydrocarbons," U.S. Naval Weapons Center, NWC-TP-7053, China Lake, CA, 1990, pp. 43–75.

⁶³Maycock, J. N., and Pai Verneker, V. R., "Role of Point Defects in the Thermal Decomposition of Ammonium Perchlorate," *Proceedings of the Royal Society of London, Series A: Mathematical and Physical Sciences*, Vol. 307, 1968, pp. 303–315.

⁶⁴Brill, T. B., Gongwer, P. E., and Williams, G. K., "Thermal Decomposition of Energetic Materials, 66. Kinetic Compensation Effects in HMX, RDX, and NTO," *Journal of Physical Chemistry*, Vol. 98, No. 24, 1994, pp. 12242–12247.

⁶⁵Yano, Y., Miyata, K., Kubota, N., and Sakamoto, S., "Combustion Wave Structure of AP Composite Propellants," *Propellants, Explosives, and Pyrotechnics*, Vol. 12, No. 4, 1987, pp. 137–140.

⁶⁶Seleznev, V. A., Pokhil, P. F., Maltsev, V. M., and Bavykin, I. B., "An Optical Method of Measuring the Burning-Surface Temperature of Condensed Systems," *Combustion and Flame*, Vol. 13, No. 2, 1969, pp. 139–142.

⁶⁷Caveny, L. H., and Pittman, C. U., Jr., "Contribution of Solid-Phase Heat Release to AP Composite Propellant Burning Rate," *AIAA Journal*, Vol. 6, No. 8, 1968, pp. 1461–1467.

⁶⁸Pittman, C. U., "Location of Action of Burning-Rate Catalysts in Composite Propellant Combustion," *AIAA Journal*, Vol. 7, No. 2, 1969, pp. 328–334.

⁶⁹Osada, H., and Kakinouchi, N., "Initiation of Ignition of Solid Composite Propellants," *Kogyo Kayaku Kyokaishi*, Vol. 26, 1965, pp. 200–211; T.I.L. translation T/5669, Ministry of Aviation, 1966.

⁷⁰Choi, C. S., Prask, H. J., and Prince, E., "Crystal Structure of NH_4ClO_4 at 298°, 77°, and 10°K by Neutron Diffraction," *Journal of Chemical Physics*, Vol. 61, No. 9, 1974, pp. 3523–3529.

⁷¹Wengan, X., Baoxuan, L., and Kexiu, W., "Mechanism of Steady-State Burning of Composite solid Propellants Including Those with Negative Pressure-Exponents," *Acta Astronautica*, Vol. 15, No. 2, 1987, pp. 83–96.

⁷²Cohen, N., "Comment on 'Novel Kinetic Scheme for the Ammonium Perchlorate Gas Phase,'" *Journal of Physical Chemistry*, Vol. 96, No. 14, 1992, pp. 5668, 5669.

⁷³Maycock, J. N., Pai Verneker, V. R., and Jacobs, P. W. M., "Mass-Spectrometric Study of the Thermal Decomposition of Ammonium Perchlorate," *Journal of Chemical Physics*, Vol. 46, No. 7, 1967, pp. 2857, 2858.

⁷⁴Ermolin, N. E., Korobeinichev, O. P., Tereschenko, A. G., and Fomin, V. M., "Measurement of the Concentration Profiles of Reacting Components and Temperature in an Ammonium Perchlorate Flame," *Combustion, Explosion, and Shock Waves*, Vol. 18, 1982, pp. 46–49.

⁷⁵Smith, J. M., "Burning Rates of Solid Propellants," *AIChE Journal*, Vol. 6, No. 2, 1960, pp. 299–304.

⁷⁶Nachbar, W., "A Theoretical Study of the Burning of a Solid Propellant Sandwich," *Solid Propellant Rocket Research*, edited by M. Summerfield, Vol. 1, Progress in Astronautics and Rocketry, Academic, New York, 1960, pp. 207–226.

⁷⁷Summerfield, M., Sutherland, G. S., Webb, M. S., Taback, H. J., and Hall, K. P., "Burning Mechanism of Ammonium Perchlorate Propellants," *Solid Propellant Rocket Research*, edited by M. Summerfield, Vol. 1, Progress in Astronautics and Rocketry, Academic, New York, 1960, pp. 141-182.

⁷⁸Sohn, H. Y., "A Unified Theory of Ammonium Perchlorate Deflagration and the Low-Pressure Deflagration Limit," *Combustion Science and Technology*, Vol. 10, No. 1, 1975, pp. 137-154.

⁷⁹Beckstead, M. W., Derr, R. L., and Price, C. F., "The Combustion of Solid Monopropellants and Composite Propellants," *Proceedings of the 13th Symposium (International) on Combustion*, Combustion Inst., Pittsburgh, PA, 1971, pp. 1047-1056.

⁸⁰Sahu, H., Sheshadri, T. S., and Jain, V. K., "Novel Kinetic Scheme for the Ammonium Perchlorate Gas Phase," *Journal of Physical Chemistry*, Vol. 94, No. 1, 1990, pp. 294, 295.

⁸¹Selzer, H., "The Temperature Profile Beneath the Burning Surface of a Composite Ammonium Perchlorate Propellant," *Proceedings of the 11th Symposium (International) on Combustion*, Combustion Inst., Pittsburgh, PA, 1967, pp. 439-445.

⁸²Ajaz, A. G., "Hydroxyl-Terminated Polybutadiene Telechelic Polymer: Binder for Solid Rocket Propellants," *Rubber Chemistry and Technology*, Vol. 68, No. 3, 1995, pp. 481-506.

⁸³Arisawa, H., and Brill, T. B., "Flash Pyrolysis of Hydroxyl-Terminated Polybutadiene II: Implications of the Kinetics to Combustion of Organic Polymers," *Combustion and Flame*, Vol. 106, No. 1/2, 1996, pp. 144-154.

⁸⁴Bouck, L. S., Baer, A. D., and Ryan, N. W., "Pyrolysis and Oxidation of Polymers at High Heating Rates," *Proceedings of the 14th Symposium (International) on Combustion*, Combustion Inst., Pittsburgh, PA, 1973, pp. 1165-1176.

⁸⁵Blazowski, W. S., Cole, R. B., and McAlevy, R. F., III, "Linear Pyrolysis of Various Polymers Under Combustion Conditions," *Proceedings of the 14th Symposium (International) on Combustion*, Combustion Inst., Pittsburgh, PA, 1973, pp. 1177-1186.

⁸⁶Hansel, J. G., and McAlevy, R. F., III, "Energetics and Chemical Kinetics of Polystyrene Surface Degradation in Inert and Chemically Reactive Environments," *AIAA Journal*, Vol. 4, No. 5, 1966, pp. 841-848.

⁸⁷Ericsson, I., "Sequential Pyrolysis Gas Chromatographic Study of the Decomposition Kinetics of Cis-1,4-Polybutadiene," *Journal of Chromatographic Science*, Vol. 16, No. 8, 1978, pp. 340-344.

⁸⁸Cohen, N. S., Fleming, R. W., and Derr, R. L., "Role of Binders in Solid Propellant Combustion," *AIAA Journal*, Vol. 12, No. 2, 1974, pp. 212-218.

⁸⁹Chen, J. K., and Brill, T. B., "Chemistry and Kinetics of Hydroxyl-Terminated Polybutadiene and Diisocyanate-HTPB Polymers During Slow Decomposition and Combustion-Like Conditions," *Combustion and Flame*, Vol. 87, No. 3/4, 1991, pp. 217-232.

⁹⁰Shono, T., and Shina, K., "Determination of the Microstructure of Polybutadiene by Pyrolysis-Gas Chromatography," *Analytica Chimica Acta*, Vol. 56, No. 2, 1971, pp. 303-307.

⁹¹Haeusler, K. G., Schroeder, E., and Wege, F. W., "Light Beam and Curie Point Pyrolysis of Polymers II. Curie Point Pyrolysis of Polybutadiene," *Plaste und Kautschuk*, Vol. 24, 1977, pp. 175-179.

⁹²Tamura, S., and Gillham, J. K., "Pyrolysis-Molecular Weight Chromatography-Vapor Phase Infrared Spectrophotometry: An On-Line System for Analysis of Polymers IV. Influence of *cis/trans* Ratio on the Thermal Degradation of 1,4-Polybutadienes," *Journal of Applied Polymer Science*, Vol. 22, No. 7, 1978, pp. 1867-1884.

⁹³Radhakrishnan, T. S., and Rama Rao, M., "Thermal Decomposition of Polybutadienes by Pyrolysis Gas Chromatography," *Journal of Polymer Science, Polymer Chemistry*, Vol. 19, No. 12, 1981, pp. 3197–3208.

⁹⁴Rama Rao, M., Sebastian, T. V., Radhakrishnan, T. S., and Ravindran, P. V., "Correlation of Binder Mechanical Properties with Microstructure for Poly-(Butadiene–Acrylonitrile–Methacrylic Acid) Terpolymer: Carbon-13 NMR and Pyrolysis Gas Chromatography Studies," *Journal of Applied Polymer Science*, Vol. 42, No. 3, 1991, pp. 753–766.

⁹⁵Thomas, T. J., Krishnamurthy, V. N., and Nandi, U. S., "Thermogravimetric and Mass-Spectrometric Study of Thermal Decomposition of PBCT Resins," *Journal of Applied Polymer Science*, Vol. 24, No. 8, 1979, pp. 1797–1808.

⁹⁶Golub, M. A., and Gargiulo, R. J., "Thermal Degradation of 1,4-Polyisoprene and 1,4-Polybutadiene," *Journal of Polymer Science, Polymer Letters Edition*, Vol. 10, No. 1, 1972, pp. 41–49.

⁹⁷Schneider, B., Doskocilova, D., Stokr, J., and Svoboda, M., "Study of Thermal Degradation of Polybutadiene in Inert Atmospheres I. Evidence of Temperature and Time of Heating in Infrared and NMR Spectra," *Polymer*, Vol. 34, 1993, pp. 432–436.

⁹⁸Grassie, N., and Heaney, A., "Thermal Reaction of Pendent Vinyl Groups in Polybutadiene and Copolymers of Butadiene and Acrylonitrile," *Journal of Polymer Science, Polymer Letters Edition*, Vol. 12, No. 2, 1974, pp. 89–94.

⁹⁹Brazier, D. W., and Schwartz, D. W., "The Effect of Heating Rate on the Thermal Degradation of Polybutadiene," *Journal of Applied Polymer Science*, Vol. 22, No. 1, 1978, pp. 113–124.

¹⁰⁰Coffman, J. A., "Highly Crosslinked Polybutadiene," *Industrial Engineering and Chemistry*, Vol. 44, 1952, pp. 1421–1428.

¹⁰¹McCreedy, K., and Keskkula, H., "Effect of Thermal Crosslinking on Decomposition of Polybutadiene," *Polymer*, Vol. 20, No. 9, 1979, pp. 1155–1159.

¹⁰²Du, T., "Thermal Decomposition Studies of Solid Propellant Binder HTPB," *Thermochimica Acta*, Vol. 138, No. 2, 1989, pp. 189–197.

¹⁰³Golub, M. A., and Sung, M., "Thermal Cyclization of 1,2-Polybutadiene and 3,4-Polyisoprene," *Journal of Polymer Science, Polymer Letters Edition*, Vol. 11, No. 2, 1973, pp. 129–138.

¹⁰⁴Lu, Y. C., and Kuo, K. K., "Thermal Decomposition Study of Hydroxyl-Terminated Polybutadiene Solid Fuel," *Thermochimica Acta*, Vol. 275, No. 2, 1996, pp. 181–191.

¹⁰⁵Narahari, H. K., Mukunda, H. S., and Jain, V. K., "A Model of Combustion Monopropellants (AP) with Complex Gas Phase Kinetics," *Proceedings of the 20th Symposium (International) on Combustion*, Combustion Inst., Pittsburgh, PA, 1985, pp. 2073–2082.

¹⁰⁶Price, E. W., Sambamurthi, J. K., Sigman, R. K., and Panyam, R. R., "Combustion of Ammonium Perchlorate-Polymer Sandwiches," *Combustion and Flame*, Vol. 63, No. 3, 1986, pp. 381–413.

¹⁰⁷Rabinovitch, B., "Regression Rates and the Kinetics of Polymer Degradation," *Proceedings of the 10th Symposium (International) on Combustion*, Combustion Inst., Pittsburgh, PA, 1965, pp. 1395–1404.

¹⁰⁸Inami, S. H., Rosser, W. A., Jr., and Wise, H., "Heat-Release Kinetics of Ammonium Perchlorate in the Presence of Catalysts and Fuel," *Combustion and Flame*, Vol. 12, No. 1, 1968, pp. 41–44.

¹⁰⁹Brill, T. B., Gongwer, P. E., and Budenz, B., "Oxidizer-Binder Interactions from T-Jump/FTIR Flash Pyrolysis," *Proceedings of the 28th ICT International Annual Conference*, Fraunhofer Institute of Chemical Technology, 1997, pp. 14/1–14/10.

¹¹⁰Wise, H., Inami, S. H., and McCulley, L., "Role of Condensed-Phase Reactions in Ignition and Deflagration of Ammonium Perchlorate Propellants," *Combustion and Flame*, Vol. 11, No. 6, 1967, pp. 483–488.

¹¹¹Price, E. W., Handley, J. C., Panyam, R. R., Sigman, R. K., and Ghosh, A., "Combustion of Ammonium Perchlorate-Polymer Sandwiches," *AIAA Journal*, Vol. 19, No. 3, 1981, pp. 380–386.

¹¹²Kumar, R. N., "Condensed Phase Details in the Time-Independent Combustion of AP/Composite Propellants," *Combustion Science and Technology*, Vol. 8, March 1973, pp. 133–148.

¹¹³Kishore, K., Pai Verneker, V. R., Sunitha, M. R., and Prasad, G., "Contribution of the Condensed-Phase Reactions in the Combustion of Solid Rocket Fuels," *Fuel*, Vol. 56, No. 7, 1977, pp. 347, 348.

¹¹⁴Kishore, K., Pai Verneker, V. R., and Gayathri, V., "Reaction Intermediates During Combustion and Decomposition of Some Model Solid Rocket Fuels," *Fuel*, Vol. 60, No. 2, 1981, pp. 164–167.

¹¹⁵Hermance, C. E., "A Model of Composite Propellant Combustion Including Surface Heterogeneity and Heat Generation," *AIAA Journal*, Vol. 4, No. 9, 1966, pp. 1629–1637.

¹¹⁶Korobeinichev, O. P., Kuibida, L. V., Paletsky, A. A., Chernov, A. A., and Ermolin, N. E., "Chemistry of Solid Propellant Combustion Studied by Mass Spectrometry and Modeling," *American Chemical Society Division of Fuel Chemistry, Preprinted Papers*, Vol. 36, American Chemical Society Publications, Washington, DC, 1991, pp. 1582–1587.

¹¹⁷Kishore, K., and Sridhara, K., "Influence of Structure of Polymeric Fuels on the Combustion Behaviour of Composite Solid Propellants," *Fuel*, Vol. 75, No. 7, 1996, pp. 912–918.

¹¹⁸Law, R. J., Baer, A. D., and Ryan, N. W., "Preignition Reactions of AP-HTPB Propellants Studied by Infrared Spectrometry," *Proceedings of the 16th Symposium (International) on Combustion*, Combustion Inst., Pittsburgh, PA, 1976, pp. 1271–1277.

¹¹⁹Zhang, W., Zhu, H., and Zhang, R., "Correlation Between Thermal Decomposition and Burning Rate in AP/HTPB Propellants," *Proceedings of the 22nd ICT International Annual Conference*, Fraunhofer Institute of Chemical Technology, 1991, pp. 62/1–62/6.

¹²⁰Hightower, J. D., and Price, E. W., "Experimental Studies Relating to the Combustion Mechanism of Composite Propellants," *Astronautica Acta*, Vol. 14, No. 1, 1968, pp. 11–21.

¹²¹Kuwahara, T., and Kubota, N., "Low Pressure Burning of Ammonium Perchlorate Composite Propellants," *Combustion Science and Technology*, Vol. 47, No. 1/2, 1986, pp. 81–91.

¹²²Ohlenmiller, T. J., and Summerfield, M., "Radiation Augmented Burning of a Solid Propellant," *Aerospace and Mechanical Sciences Rept. 799*, Princeton Univ., Princeton, NJ, April 1967.

¹²³Barrere, M., and Nadaud, L., "Combustion of Ammonium Perchlorate Spheres in a Flowing Gaseous Fuel," *Proceedings of the 10th Symposium (International) on Combustion*, Combustion Inst., Pittsburgh, PA, 1965, pp. 1381–1394.

¹²⁴Tanoff, M. A., Ilincic, N., Smooke, M. D., Yetter, R. A., Parr, T. P., and Hanson-Parr, D. M., "Computational and Experimental Study of Ammonium Perchlorate Combustion in Counterflow Diffusion Flames," *27th Symposium (International) on Combustion*, Vol. 2, The Combustion Inst., Pittsburgh, PA, pp. 2397–2404.

¹²⁵Pearson, G. S., and Sutton, D., "Composite Solid Propellant Ignition: Ignition of Ammonia and Other Fuels by Perchloric Acid Vapors," *AIAA Journal*, Vol. 5, No. 2, 1967, pp. 344–346.

- ¹²⁶Fishman, N., "Surface Exotherm During Ignition of Ammonium Perchlorate Propellants," *AIAA Journal*, Vol. 5, No. 8, 1967, pp. 1500, 1501.
- ¹²⁷Anderson, R., Brown, R. S., and Shannon, L. J., "Heterogeneous Reactions in Ignition and Combustion of Solid Propellants," *AIAA Journal*, Vol. 2, No. 1, 1964, pp. 179, 180.
- ¹²⁸Price, E. W., Bradley, H. H., Jr., Dehority, G. L., and Ibiricu, M. M., "Theory of Ignition of Solid Propellants," *AIAA Journal*, Vol. 4, 1966, pp. 1153–1181.
- ¹²⁹Derr, R. L., and Boggs, T. L., "Role of Scanning Electron Microscopy in the Study of Solid Propellant Combustion: Part III. The Surface Structure and Profile Characteristics of Burning Composite Propellant," *Combustion Science and Technology*, Vol. 1, No. 3, 1970, pp. 369–384.
- ¹³⁰Brown, R. S., Muzzy, R. J., and Steinle, M. E., "Surface Reaction Effects on the Acoustic Response of Composite Solid Propellants," *AIAA Journal*, Vol. 6, No. 3, 1968, pp. 479–488.
- ¹³¹Druet, L. M., Ahmed, S., and Pandey, R. N., "Application of Curie Point Pyrolysis-Gas Chromatography for the Characterization of Rocket Propellants," *Proceedings of the 22nd ICT International Annual Conference*, 1991, pp. 64/1–64/14.
- ¹³²Radhakrishnan, T. S., and Rama Rao, M., "Thermo-Oxidative Degradation of Polybutadiene Binders," *Propellants, Explosives, and Pyrotechnics*, Vol. 20, No. 1, 1995, pp. 32–35.
- ¹³³Kishore, K., and Pai Verneker, V. R., "Condensed Phase Reactions in Solid Propellants," *AIAA Journal*, Vol. 13, No. 9, 1975, pp. 1240–1242.
- ¹³⁴Waesche, R. H. W., Wenograd, J., and Feinauer, L. R., "Investigation of Solid Propellant Decomposition Characteristics and Their Relation to Observed Burning Rates," *ICRPG/AIAA Solid Propulsion Conference*, 1967, pp. 136–147.
- ¹³⁵Rosser, W. A., Fishman, N., and Wise, H., "Ignition of Simulated Propellants Based on Ammonium Perchlorate," *AIAA Journal*, Vol. 4, No. 9, 1966, pp. 1615–1622.
- ¹³⁶Ermolin, N. E., "Kinetic Parameters of Overall Gas-Phase Reactions for Propellants Based on Ammonium Perchlorate and Polybutadiene Rubber," *Fizika Goreniya i Vzryva*, Vol. 29, No. 4, 1993, pp. 508–515.
- ¹³⁷Bakhman, N. N., "Dependence of Burning Rate on Oxidizer Particle Size," *Combustion and Flame*, Vol. 17, No. 3, 1971, pp. 383–389.
- ¹³⁸Cohen, N. S., and Strand, L. D., "An Improved Model for the Combustion of AP Composite Propellants," *AIAA Journal*, Vol. 20, No. 12, 1982, pp. 1739–1746.
- ¹³⁹Fong, C. W., and Smith, R. F., "The Relationship Between Plateau Burning Behavior and Ammonium Perchlorate Particle Size in HTPB-AP Composite Propellants," *Combustion and Flame*, Vol. 67, No. 3, 1987, pp. 235–247.
- ¹⁴⁰Green, L., Jr., "Some Effects of Oxidizer Concentration and Particle Size on Resonance Burning of Composite Solid Propellants," *Jet Propulsion*, Vol. 28, No. 3, 1958, pp. 159–164.
- ¹⁴¹Schultz, R. D., Green, L., and Penner, S. S., "Studies of the Decomposition Mechanism, Erosive Burning, Sonance and Resonance for Solid Composite Propellants," *Combustion and Propulsion*, Pergamon, New York, 1958, pp. 367–420.
- ¹⁴²Chaiken, R. F., and Andersen, W. H., "The Role of Binder in Composite Propellant Combustion," *Solid Propellant Rocket Research*, edited by M. Summerfield, Vol. 1, Progress in Astronautics and Rocketry, Academic, New York, 1960, pp. 227–249.
- ¹⁴³King, M. K., "Examination of Chemical Approaches to Stabilizing Composite-Propellant Combustion," *Journal of Propulsion and Power*, Vol. 12, No. 3, 1996, pp. 554–563.
- ¹⁴⁴Kishore, K., Pai Verneker, V. R., Shubha, K. R., and Sankaralingam, S., "Some Features of Solid Propellant Chemistry," *Combustion and Flame*, Vol. 46, No. 3, 1982, pp. 323, 324.

¹⁴⁵Chemov, A. A., Shvartsberg, V. M., Ermolin, N. E., Korobeinichev, O. P., and Fomin, V. M., "Flame Structure of Sandwich Systems Based on Ammonium Perchlorate, HMX, and Polybutadiene Rubber Studied by Probe Mass-Spectrometry and Modeling," *American Chemical Society Division of Fuel Chemistry, Preprinted Papers*, Vol. 39, American Chemical Society Publications, Washington, DC, 1994, pp. 188–192.

¹⁴⁶Inami, S. H., Rajapakse, Y., Shaw, R., and Wise, H., "Solid Propellant Kinetics I. The Ammonium Perchlorate–Copper Chromite–Fuel System," *Combustion and Flame*, Vol. 17, No. 2, 1971, pp. 189–196.

¹⁴⁷Oyumi, Y., and Brill, T. B., "Thermal Decomposition of Energetic Materials 22. The Contrasting Effects of Pressure on the High-Rate Thermolysis of 34 Energetic Compounds," *Combustion and Flame*, Vol. 68, No. 2, 1987, pp. 209–216.

¹⁴⁸Rudy, T. P., Anderson, W. S., Valerga, A. J., and Weyland, H. H., "Copper Burn Rate Additives," U.S. Air Force Rocket Propulsion Lab., Rept. AFRPL-TR-82-85, Edwards AFB, CA, Oct. 1982.

¹⁴⁹Stoner, C. E., Jr., and Brill, T. B., "Thermal Decomposition of Energetic Materials 46. The Formation of Melamine-like Cyclic Azines as a Mechanism for Ballistic Modification of Composite Propellants by DCD, DAG, and DAF," *Combustion and Flame*, Vol. 83, No. 3/4, 1991, pp. 302–308.

¹⁵⁰Strahle, W. C., Handley, J. C., and Milkie, T. T., "Catalytic Effect in the Combustion of AP-HTPB Sandwiches to 3200 PSIA," *Combustion Science and Technology*, Vol. 8, No. 5/6, 1974, pp. 297–304.

¹⁵¹Chakravarthy, S. R., Price, E. W., and Sigman, R. K., "Mechanism of Burning Rate Enhancement of Composite Solid Propellants by Ferric Oxide," *Journal of Propulsion and Power*, Vol. 13, No. 4, 1997, pp. 471–480.

¹⁵²Coates, R. L., Myers, G. E., and Stapleton, W. G., "Combustion Mechanism Studies," *Proceedings of the 2nd ICRPG Combustion Conference*, CPIA Publ. 105, Vol. 1, Chemical Propulsion Information Agency, Laurel, MD, 1966, p. 443.

¹⁵³Solymosi, F., and Fonagy, K., "Effect of Cadmium Oxide and Cadmium Perchlorate on the Decomposition of Ammonium Perchlorate," *Proceedings of the 11th Symposium (International) on Combustion*, Combustion Inst., Pittsburgh, PA, 1967, pp. 429–435.

¹⁵⁴Gould, R. D., "Combustion Instability of Solid Propellants: Effect of Oxidizer Particle Size, Oxidizer/Fuel Ratio, and Addition of Titanium Dioxide to Plastic Propellants," Rocket Propulsion Establishment, NTIS Rept. AD684244, National Technical Information Service, Springfield, VA, 1968.

Chapter 1.2

Gas-Phase Chemical Kinetics of [C, H, N, O] Systems Relevant to Combustion of Nitramines

D. Chakraborty* and M. C. Lin[†]
Emory University, Atlanta, Georgia

I. Introduction

SIGNIFICANT progress has been made in recent years in modeling the combustion of nitramines, particularly hexahydro-1,3,5-trinitro-1,3,5-triazine (RDX) and, to some extent, tetranitrotetraazacyclooctone (HMX).¹⁻⁸ In most of these computer simulation studies, the burning rate of RDX and, in some cases, species concentration profiles above the propellant surface can be reasonably accounted for. However, the agreement depends largely on an assumed condensed-phase mechanism that provides an estimated initial gas-phase species composition, possibly containing RDX, CH_2NNO_2 , CH_2N , CH_2O , HCN, NO_x , and N_2O , among others. The decomposition of larger molecular and radical species (e.g., RDX, CH_2NNO_2 , CH_2NO , and CH_2N) produces key chain carriers such as H and OH, whose reactions lead to the release of the available energy.

The rate constants for the fragmentation of these large molecules and radicals are not known because of the inherent experimental difficulty in producing and monitoring them in the gas phase. Consider the CH_2N radical (a pivotal radical in the dark zone) for example. The lack of a known fluorescing state of this radical makes its direct probing by such sensitive techniques as laser-induced fluorescence impossible.

To minimize the uncertainty and the subjectivity in these modeling studies and to improve our understanding of complex combustion chemistry, we have recently carried out a series of theoretical investigations on the kinetics and the mechanisms of several [C, H, N, O] systems relevant to the combustion of nitramines such as ammonium dinitramide (ADN) and RDX by using high-level

Copyright © 2000 by D. Chakraborty and M. C. Lin. Published by the American Institute of Aeronautics and Astronautics, Inc., with permission.

*Postdoctoral Research Associate, Dept. of Chemistry.

[†]R. W. Woodruff Professor of Chemistry, Dept. of Chemistry.

ab initio molecular orbital (MO) and statistical theory calculations. In this initial effort, we focus our calculations on mid-sized molecular and radical species containing 4–5 heavy atoms; for example, HNNO , HNNO_2 , CH_2NO , CH_2NNO , CH_2NNO_2 , and $\text{CH}_2\text{NN}_2\text{O}$. These species are the intermediates of the bimolecular reactions of NH with NO_x and CH_2N with NO_x and N_2O , which are important to the combustion of ADN and/or RDX/HMX nitramines near their burning surfaces.

Our discussion of these near-field chemical reactions centers on $[\text{H}, \text{N}, \text{O}]$ and $[\text{C}, \text{H}, \text{N}, \text{O}]$ systems; both chemical systems are closely linked, particularly after the binder chemistry is introduced to simulate the combustion of the two major classes of energetic materials (ADN and RDX/HMX).

II. Computational Methods

A. Potential-Energy Profile and Reaction Mechanisms

A reliable ab initio MO prediction of the potential-energy surfaces (PESs) of chemical reactions, such as primary and secondary reactions occurring in ADN or RDX/HMX combustion considered in this review, is a prerequisite to the accurate calculation of their rate constants. Because of the significant progress made in the field of computational chemistry in recent years, it is now possible to perform calculations of PESs for the reactions between small molecules and radicals to chemical accuracy. The Gaussian- X (GX) ($X = 1, 2, 3$) series of methods developed by Pople et al.⁹ and Curtiss et al.^{10–13} are aimed at achieving the prediction of molecular energies to within 1–2 kcal/mol. The more reliable G2 methodology uses a series of quadratic configuration interaction with single, double (triple) substitutions¹⁴ [QCISD(T)] and Møller-Plesset MP4 and MP2 (Ref. 15) calculations with various basis sets to approximate a QCISD(T)/6–311+ $G(3df,2p)$ calculation with an additional empirical higher-level correction based on the number of paired and unpaired electrons. The geometry in G2 is optimized at the MP2/6–31 $G(d,p)$ level and vibrational frequencies are calculated at the Hartree-Fock HF/6–31 $G(d)$ level of theory. Before the submission of this study, the third improved version in this series, G3, appeared in the literature.¹³

Various modifications of the G2 scheme, with the goal of improving its performance for transition states (TSs) and for radical species, have been proposed.^{16,17} In the present calculations we use the modified G2 (G2M) scheme developed at Emory University.¹⁷ The scheme uses a series of restricted coupled-cluster with single, double (triple) substitutions^{18–21} [RCCSD(T)], MP2, and MP4 calculations to approximate an RCCSD(T)/6–311+ $G(3df,2p)$ energy based on the geometries and vibrational frequencies calculated at the B3LYP/6–311 $G(d,p)$ level of theory, that is, Becke's three-parameter nonlocal exchange functional^{22–24} in conjunction with the nonlocal correlation functional of Lee, Yang, and Parr.²⁵ Three different versions of the scheme have been proposed for varying molecular sizes.¹⁷ Depending on the size of the molecules involved in the chemical reactions considered in this study, an appropriate version of this scheme is implemented. All three versions of the method are briefly summarized below.

In all three versions, the base energy, $E_{\text{bas}} = E[\text{PMP4/6-311G}(d,p)]$, and the B3LYP/6-311G(d,p) zero point energy (ZPE) correction are used:

1) $E[\text{G2M(RCC)}] = E_{\text{bas}} + \Delta E(+) + \Delta E(2df) + \Delta E(\text{RCC}) + \Delta' + \Delta E(\text{HLC, RCC2}) + \text{ZPE}$ where

$$\Delta E(+) = E[\text{PMP4/6-311+G}(d,p)] - E_{\text{bas}}$$

$$\Delta E(2df) = E[\text{PMP4/6-311G}(2df,p)] - E_{\text{bas}}$$

$$\Delta E(\text{RCC}) = E[\text{RCCSD}(T)/6-311G(d,p)] - E_{\text{bas}}$$

$$\Delta' = E[\text{MP2/6-311G}(3df,2p)] - E[\text{MP2/6-311G}(2df,2p)] \\ - E[\text{MP2/6-311+G}(d,p) + E[\text{MP2/6-311G}(d,p)]]$$

$\Delta E(\text{HLC,RCC2}) = -5.71n_{\beta} - 0.19n_{\alpha}$, where n_{α} and n_{β} are the number of α and β valence electrons, respectively. This version is used for systems containing three to four heavy atoms.

2) $E[\text{G2M(Rcc,MP2)}] = E_{\text{bas}} + \Delta E(+3df,2p) + \Delta E(\text{RCC}) + \Delta E(\text{HLC, RCC5}) + \text{ZPE}$ where

$$\Delta E(+3df,2p) = E[\text{MP2/6-311+G}(3df,2p)] - E[\text{MP2/6-311G}(d,p)]$$

$$\Delta E(\text{RCC}) = E[\text{RCCSD}(T)/6-311G(d,p)] - E_{\text{bas}}$$

$$\Delta E(\text{HLC,RCC5}) = -5.25n_{\beta} - 0.19n_{\alpha}$$

This version is used for systems containing five to six heavy atoms.

3) $E[\text{G2M(rcc,MP2)}] = E_{\text{bas}} + \Delta E(+3df,2p) + \Delta' E(\text{RCC}) + \Delta E(\text{HLC, RCC6}) + \text{ZPE}$ where

$$\Delta E(+3df,2p) = E[\text{MP2/6-311+G}(3df,2p)] - E[\text{MP2/6-311G}(d,p)]$$

$$\Delta' E(\text{RCC}) = E[\text{RCCSD}(T)/6-31G(d,p)] - E[\text{PMP4/6-31G}(d,p)]$$

$$\Delta E(\text{HLC,RCC5}) = -4.93n_{\beta} - 0.19n_{\alpha}$$

This version is used for systems containing up to seven heavy atoms.

In all three versions, the geometries and the vibrational frequencies of the systems studied are obtained at the B3LYP/6-311G(d,p) level. All the stationary points have been positively identified for local minima (with the number of imaginary frequencies $\text{NIMAG} = 0$), TSs ($\text{NIMAG} = 1$), or higher-order tops ($\text{NIMAG} > 1$). To confirm that the TSs connect between designated intermediates, we also performed intrinsic reaction coordinate calculations²⁶ at the B3LYP/6-311G(d,p) level. All calculations were carried out with Gaussian 94 (Ref. 27) and MOLPRO 96 (Ref. 28) programs.

B. Rate Constant Calculations

Because many of the reactions considered in this review do not have a well-defined TS because of the absence of a reaction barrier, canonical variational Rice-Ramsperger-Kassel-Marcus (cVRRKM) calculations²⁹ have been carried out. According to the canonical variational theory^{30,31} (CVT), the rate constant

k^{CVT} at T is obtained by maximizing $\Delta G(T, s)$ with respect to the reaction coordinate s . The position of the dividing surface associated with the maximum $\Delta G(T, s)$ is denoted by s^\ddagger . Depending on the nature of the system, the reaction coordinate is varied to reach the dissociation limit (in general 2.0–4.0 Å), and the $3N - 7$ vibrational frequencies projected out of the gradient direction are calculated for each point in reaction coordinate. To obtain more reliable energy along the reaction path, the B3LYP-computed energy at each point is generally scaled to fit the corresponding G2M energy. These G2M-calculated energies at each point along the reaction path were used to evaluate the Morse potential-energy function. The resulting potential-energy function $E(R)$ is given by

$$E(R) = \text{De} \left[1 - e^{-\beta(R - \text{Re})} \right]^2$$

where De is the dissociation energy, β is the Morse parameter, and Re is the equilibrium value of the reaction coordinate.

The Morse potential energy, computed moments of inertia, and the vibrational frequencies were then used to search for the maximum $\Delta G(T, s^\ddagger)$, or ΔG^\ddagger , at temperatures in the range of 300–3000 K. The accurate position of the maximum for each temperature was calculated on the basis of the parabolic fit of the three largest ΔG values.^{29,32} All the molecular parameters corresponding to the structure with a maximum ΔG^\ddagger for each temperature were then used in the RRKM calculation for the association or the dissociation rate.^{29,32} In the RRKM calculation, we assume Ar as a third body by using uniform Lennard–Jones parameters: $\sigma_{\text{Ar}-M} = 4.24$ Å and $\epsilon_{\text{Ar}-M} = 324$ K, where M represents the molecular collision partner.

III. Results and Discussions

A. Systems Relevant to the Early-Stage Combustion of ADN

1. Unimolecular Decomposition of $\text{HN}(\text{NO}_2)_2$ and Related Bimolecular Reactions

The structure and the energetics of gaseous ADN [$\text{NH}_4\text{N}(\text{NO}_2)_2$] were theoretically calculated by Mebel et al., who used different ab initio MO approaches; they proposed a realistic decomposition mechanism of ADN based on the theoretical results.³³ ADN, similar to other ammonium salts, was concluded to be unstable in its ionic form, $\text{NH}_4^+\text{N}(\text{NO}_2)_2^-$, in the gas phase. Its sublimation should lead to the formation of two molecular complexes, $\text{H}_3\text{N} \cdot \text{HN}(\text{NO}_2)_2$ and $\text{H}_3\text{N} \cdot \text{HON}(\text{O})\text{NNO}_2$, which are more stable than the dissociated states, $\text{H}_3\text{N} + \text{HN}(\text{NO}_2)_2$ and $\text{H}_3\text{N} + \text{HON}(\text{O})\text{NNO}_2$, by 12.4 and 14.1 kcal/mol, respectively, at the MP4(SDQ)/6–31+G(d,p)/MP2/6–31G(d) level. The former $\text{HN}(\text{NO}_2)_2$ (DN) isomer was calculated at the G1 level of theory to have 38.4-kcal/mol dissociation energy, producing $\text{NO}_2 + \text{HNNO}_2$, whereas the latter $\text{HON}(\text{O})\text{NNO}_2$ (DN') isomer has a dissociation energy of 40.1 kcal/mol, yielding $\text{NO}_2 + \text{HON}(\text{O})\text{N}$. The overall energy difference for the formation of DN and DN' from ADN was predicted to be 4.2 kcal/mol. Earlier, Politzer and Seminario predicted the N–N bond cleavage in $\text{HN}(\text{NO}_2)_2$ to be 44.0 kcal/mol at their DF-GGA/DZVPP/MP2–6–31G* level of theory.³⁴ The BAC-MP4 calculations also reported a higher value (46.6 kcal/mol) of dissociation energy. We recalculated the dissociation energy at the G2M level as 37.9 kcal/mol (Ref. 35), which agrees very well with the earlier G1 result of Mebel et al.³³ The G2M results were used

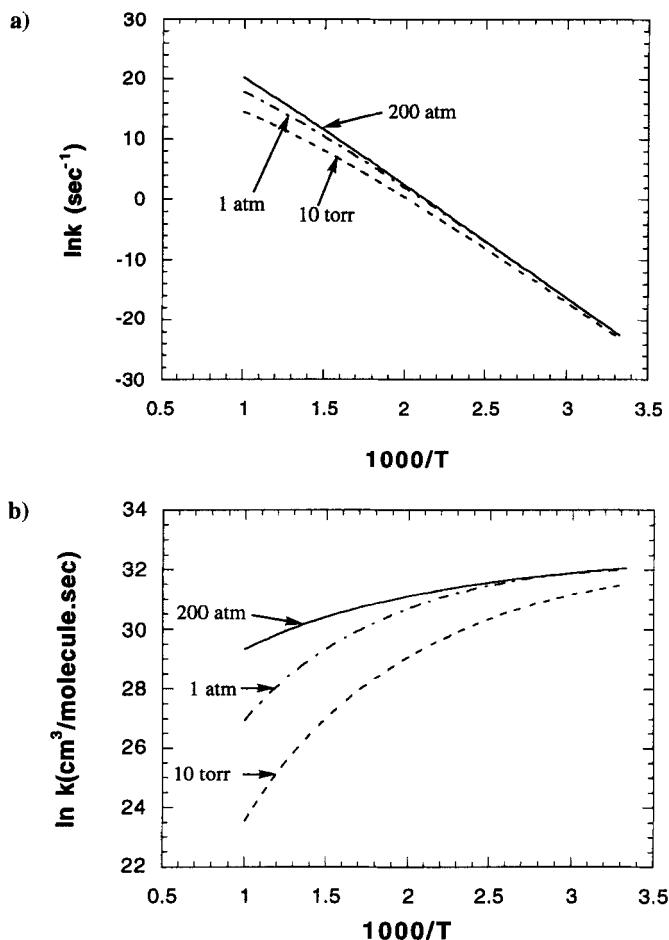


Fig. 1 Arrhenius plots for a) DN decomposition and b) its reverse association reaction.

for the theoretical prediction of the unimolecular decomposition or the reverse bimolecular association reaction rate constant of $\text{HN}(\text{NO}_2)_2$. The calculated cVRRKM rate constants for the decomposition of DN and reverse association of HNNO_2 with NO_2 are shown in Fig. 1. A least-squares analysis of rate constants for the decomposition process at the high-pressure limit, 200 atm, 1 atm, and 1.32×10^{-2} atm (10 torr) for He or Ar, respectively, as diluent can be represented by the following expressions:

$$k_1^\infty = 1.92 \times 10^{17} \exp(-18,300/T) \text{ s}^{-1}$$

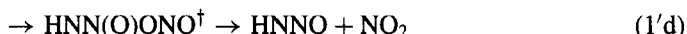
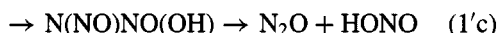
$$k_1(200 \text{ atm}) = 6.88 \times 10^{16} \exp(-18,300/T) \text{ s}^{-1}$$

$$k_1(1 \text{ atm}) = 1.90 \times 10^{41} T^{-8.1} \exp(-21,500/T) \text{ s}^{-1}$$

$$k_1(10 \text{ torr}) = 6.79 \times 10^{48} T^{-11.0} \exp(-21,800/T) \text{ s}^{-1}$$

for the temperature range 300–1000 K. When used in the mechanism containing 152 reactions, k_1 (10 torr) could satisfactorily model the kinetics of our experimental result of the thermal decomposition of ADN by pyrolysis/mass spectrometry under the low-pressure conditions.³⁵

The bimolecular reactions of HNNO_2 with NO_x ($x = 1, 2$) and OH are considered to be very important for the combustion of ADN under high-pressure conditions. Theoretical calculations are underway for the HNNO_2 reaction with NO_2 and OH. The reactions are expected to give $\text{HONO} + 2\text{NO}$ and $\text{HNOH} + \text{NO}_2$, respectively. Recently we have calculated the PES for the $\text{HNNO}_2 + \text{NO}$ reaction at the G2M level of theory and the following low-energy pathways have been identified for this reaction:



The major product of this reaction, $\text{HNNO} + \text{NO}_2$, can be reached by the association of NO to both the N and the O radical sites of HNNO_2 followed by decomposition of the vibrationally excited intermediates. A coupled-channel RRKM calculation for these reactions leads to the following rate expressions in the temperature range of 500–2000 K and two different pressures (1 and 200 atm):

$$k_{1'a}(1 \text{ atm}) = 8.67 \times 10^{34} T^{-6.6} \exp(-8400/T)$$

$$k_{1'a}(200 \text{ atm}) = 6.08 \times 10^{18} T^{1.88} \exp(-7300/T)$$

$$k_{1'b}(1 \text{ atm}) = 9.88 \times 10^{32} T^{-6.08} \exp(-7800/T)$$

$$k_{1'b}(200 \text{ atm}) = 3.18 \times 10^{15} T^{-0.96} \exp(-6500/T)$$

$$k_{1'd}(1 \text{ atm}) = 7.95 \times 10^4 T^{1.51} \exp(2600/T)$$

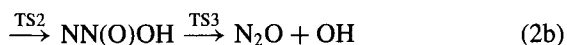
$$k_{1'd}(200 \text{ atm}) = 1.70 \times 10^{15} T^{-1.24} \exp(-3100/T)$$

in units of cubic centimeters per (mole times second). The HONO formation reaction has a higher barrier and thus cannot compete with the other three channels.

2. Unimolecular Decomposition of HNNO_2

As HNNO_2 , the key radical species directly formed in the decomposition of DN, was found to be responsible for chain initiation in the combustion of ADN,^{35–37} we recently studied the kinetics of the unimolecular decomposition of HNNO_2 and the bimolecular association of $\text{NH} + \text{NO}_2$ in detail by using ab initio MO and statistical theory calculations.³⁸ Earlier, several efforts were made to characterize the PES of the $\text{NH} + \text{NO}_2$ reaction, emphasizing primarily the isomerization and the decomposition of the HNNO_2 radical intermediate.^{39–42} On the basis of the potential-energy profile and the mechanism for the formation and fragmentation of HNNO_2 discussed in our recent paper,³⁸ the following two low-energy paths

are expected to be dominant:



The G2M-calculated N–N bond dissociation energy in HNNO_2 (38.1 kcal/mol) is quite close to our earlier predicted results at the G1 (39.1 kcal/mol) and G2 (38.9 kcal/mol) levels of theory.³³ On the other hand, the exothermic $\text{N}_2\text{O} + \text{OH}$ products (with the exothermicity of 65.9 kcal/mol with respect to $\text{NH} + \text{NO}_2$ at the G2M level of theory) are more favorably formed in this decomposition by means of the 1,3-H shift transition state (TS2), intermediate NN(O)OH , and TS3, with a maximum barrier of 31.5 kcal/mol at TS2 (Ref. 38). The G2M-calculated potential-energy profile for the $\text{NH} + \text{NO}_2$ reaction is presented in Fig 2. Transition state theory (TST) calculations for individual decomposition reactions (2a) and (2b)

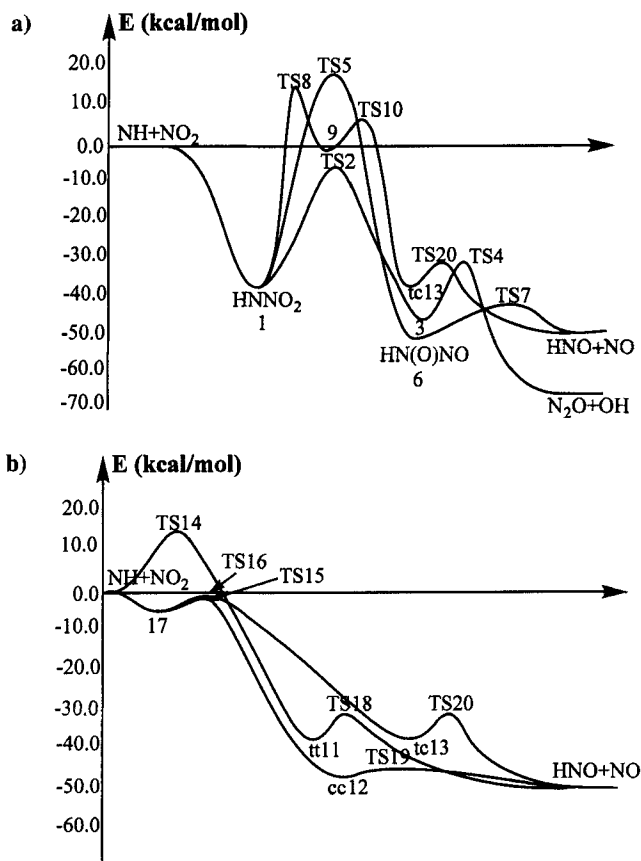


Fig. 2 Potential-energy profiles for the reaction $\text{NH} + \text{NO}_2$ by means of a) HNNO_2 and b) HNONO based on the G2M calculation.

controlled by VTS1 and TS2, respectively, give their high-pressure rate constants,

$$k_{2a}^{\infty} = 1.00 \times 10^{15} \exp(-19,200/T) \text{ s}^{-1}$$

$$k_{2b}^{\infty} = 7.43 \times 10^{12} \exp(-16,200/T) \text{ s}^{-1}$$

and the corresponding rate constants at the low-pressure limit are

$$k_{2a}^0 = 2.65 \times 10^6 T \exp(-15,800/T) \text{ cm}^3/(\text{mol} \cdot \text{s})$$

$$k_{2b}^0 = 1.62 \times 10^{26} T^{-3.42} \exp(-8700/T) \text{ cm}^3/(\text{mol} \cdot \text{s})$$

For practical applications under varying temperature and pressure conditions, our coupled, dual-channel RRKM calculations for reactions (2a) and (2b), by solving the master equation,⁴³ give rise to the rate constants for the temperature range 500–2000 K at two different pressures for the formation of NO₂ and N₂O, respectively:

$$k_{2a}(200 \text{ atm}) = 7.29 \times 10^{44} (T)^{-9.27} \exp(-24,100/T) \text{ s}^{-1}$$

$$k_{2b}(200 \text{ atm}) = 1.45 \times 10^{41} (T)^{-8.89} \exp(-20,500/T) \text{ s}^{-1}$$

$$k_{2a}(1 \text{ atm}) = 6.09 \times 10^{44} (T)^{-9.92} \exp(-23,600/T) \text{ s}^{-1}$$

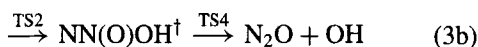
$$k_{2b}(1 \text{ atm}) = 1.36 \times 10^{54} (T)^{-13.16} \exp(-22,300/T) \text{ s}^{-1}$$

These results are graphically presented in Fig. 3.

In our RRKM calculations, we have also investigated the effect of tunneling for reaction (2b), as shown in Fig. 3b. The tunneling correction enhances the rate of N₂O formation, as expected from the nature of the TS (TS2). Contrary to the commonly observed tunneling effect, the noticeable decrease in the rate of N₂O formation in the absence of tunneling at high temperatures and lower pressures results from the increasing rate of the backdissociation to the reactants.

3. Bimolecular Reactions of NH with NO₂

The bimolecular reaction of NH with NO₂ is more complex because of the possibility of forming concurrently both HNNO₂ and HNONO; the latter has three different conformers, as shown in Fig. 2. The dominant reaction paths occur without reaction barriers:



where † stands for internal excitation, cc stands for *cis-cis*, and tc stands for *trans-cis*.

Our coupled-channel RRKM calculated rate constants for the formation of HNNO₂ from NH + NO₂ by collisional deactivation reaction (3a) and for the production of N₂O and OH by reaction (3b) at the high-pressure and the low-pressure

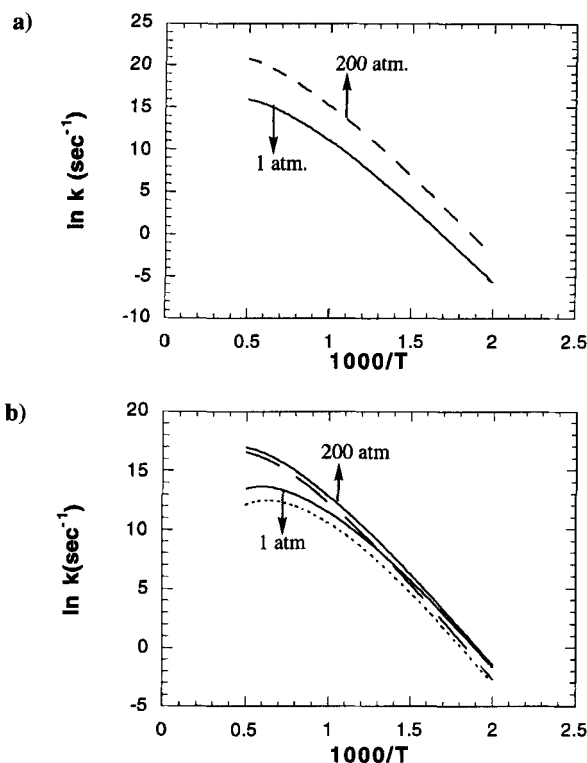


Fig. 3 Arrhenius plots for the unimolecular decomposition rate constants of HNNO_2 to form a) $\text{NH} + \text{NO}_2$ and b) $\text{N}_2\text{O} + \text{OH}$ at 1- and 200-atm pressures and over the temperature range of 500–2000 K. The broken curves represent reaction rate constants without tunneling corrections.

limits in the temperature range 300–3000 K are

$$k_{3a}^{\infty} = 1.42 \times 10^{16} (T)^{-0.75} \exp(-617/T) \text{ cm}^3/(\text{mol} \cdot \text{s})$$

$$k_{3b}^{\infty} = 0 \quad (\text{no production of } \text{N}_2\text{O})$$

$$k_{3a}^0 = 0 \quad (\text{no stabilization})$$

$$k_{3b}^0 = 2.08 \times 10^{13} (T)^{-0.49} \exp(360/T) \text{ cm}^3/(\text{mol} \cdot \text{s})$$

As discussed in detail in our earlier paper,³⁸ the common initial association complex $\text{HN}-\text{ONO}$ (4.9 kcal/mol more stable than the reactants), formed in the bimolecular association of NH and ONO [reaction path (3'a) and (3'b)], plays an important role in determining the formation rate constant of $\text{HNO} + \text{NO}$. By using the approach of Hirschfelder and Wigner⁴⁴ and Miller⁴⁵ to compute the overall probability of the flux's passing through individual transition barriers involving multiple reflections in the shallow well of the complex in conjunction with the canonical variational TST calculation for the formation of the initial association complex, we obtained an overall pressure-independent ($P \leq 200$ atm) rate

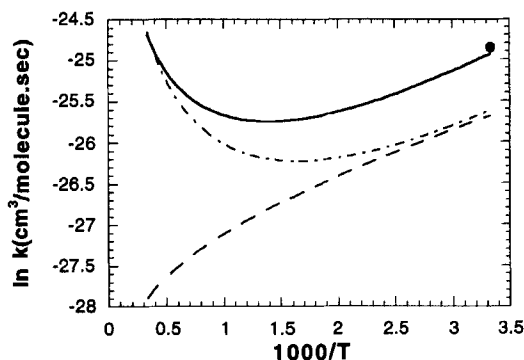


Fig. 4a Arrhenius plots of the bimolecular rate constants for the $\text{NH} + \text{NO}_2$ reaction at 1-torr pressure: ---, $\text{N}_2\text{O} + \text{OH}$; - · -, $\text{HNO} + \text{NO}$; —, total rate constant; and •, total rate constant taken from Ref. 46.

constant of

$$k_3 = 1.25 \times 10^6 (T)^{1.96} \exp(1180/T) \text{ cm}^3/(\text{mol} \cdot \text{s})$$

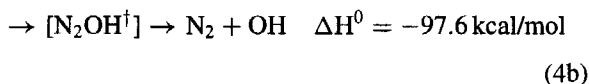
by means of reaction paths (3'a) and (3'b), leading to the formation of $\text{HNO} + \text{NO}$, over the temperature range 300–3000 K.

The total rate constant for the bimolecular reaction of NH with NO_2 reported by Harrison et al.,⁴⁶ $k_{\text{tot}} = 9.64 \pm 0.14 \times 10^{12} \text{ cm}^3/\text{mol} \cdot \text{s}$, was determined experimentally at 300 K and 1-torr pressure. Under the same conditions, the total rate constant predicted by our cVRRKM calculations is the sum of k_{3a} , k_{3b} , and k_3 ; $k_{\text{tot}} = 7.95 \times 10^{12} \text{ cm}^3/\text{mol} \cdot \text{s}$. The agreement is quite satisfactory. The bimolecular rate constants for the N_2O and HNO forming channels at 1-torr experimental pressure over the temperature range of 300–3000 K are shown in Fig. 4a.

The branching ratios for the formation of N_2O and HNO from $\text{NH} + \text{NO}_2$ at room temperature and 3-torr pressure have been reported recently by Quandt and Hershberger⁴⁷: 0.41 ± 0.15 for N_2O and 0.59 ± 0.15 for HNO productions. These ratios agree satisfactorily with the predicted values: $k_{3b}/(k_3 + k_3') = 0.46$ and $k_3'/(k_3 + k_3') = 0.54$, respectively, under the same conditions. Figure 4b shows the calculated branching probability of the formation of HNO as a function of temperature and pressure. The lowering of the branching probability for the formation of HNO with pressure, as is evident from Fig. 4b, can be accounted for by the increase in the rate constant k_{3a} with pressure.

4. $\text{NH} + \text{NO}$ System

There are two main exothermic product channels for the $\text{NH} + \text{NO}$ reaction:



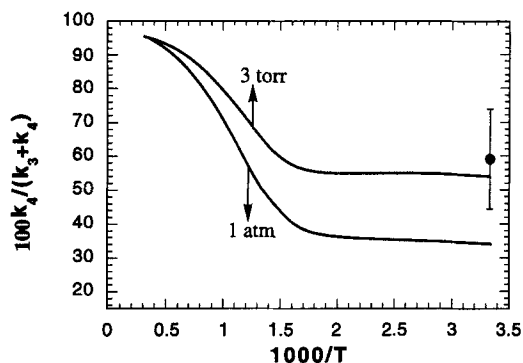


Fig. 4b Calculated branching ratios for HNO formation, $k_4/(k_3 + k_4)$; and ●, the experimental branching ratio taken from Ref. 47.

The energetics of the $\text{NH} + \text{NO}$ system have been investigated in a number of studies,^{48–52} but the most recent and most detailed description of the PES was given by Walch, who used a high-quality multireference configuration interaction (MRCI) method.⁵² A schematic diagram of the PES is provided in Fig. 5. The initial reaction involves the association of HN with NO to form HNNO on the barrierless $^2A''$ surface. The association on the $^2A'$ surface provides a more stable ($\Delta H^0 = -51.5$ kcal/mol vs -21.1 kcal/mol) HNNO species but must proceed over a 3.2-kcal/mol barrier. The coupling between these two states is expected to be strong as they are of same symmetry for out-of-plane motions. It was thus assumed

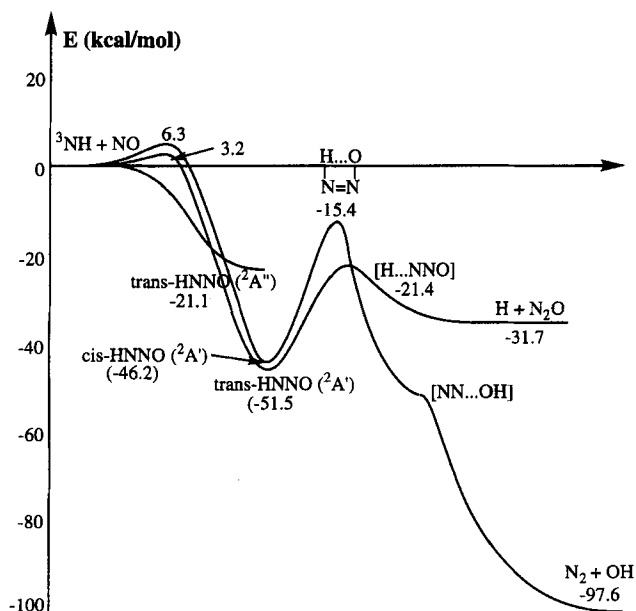


Fig. 5 Schematic PES for the HNNO system.

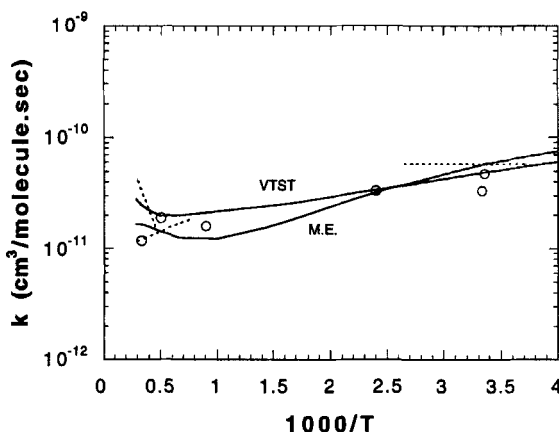


Fig. 6a High-pressure limit rate constant for the $\text{NH} + \text{NO}$ reaction. M.E.: VRRKM microscopic rates with analytical solution of master equation, VTST: variational TS rate constants. All experimental points and symbols are as described in Fig. 2 of Ref. 54.

that the initially formed $\text{HNNO} (^2A'')$ rapidly converts to $\text{HNNO} (^2A')$ and that the progression to products occurs from the $^2A'$ state.

Several research groups worldwide have attempted to determine experimentally the total reaction rate and the branching ratios for H and OH production. Values published to date vary widely.⁵³ Only very recently have we made an attempt to reconcile the data with a high-level statistical theory calculation on the effects of temperature and pressure on the total rate constants and branching ratios.⁵⁴ The barrierless $\text{NH} + \text{NO}$ association process was treated by micro-cVRRKM theory^{55,56} and the competitive decomposition as well as the deactivation process were determined by solving the master equation analytically,⁵⁷ with the incorporation of tunneling effect present in both processes (4a) and (4b). Figure 6a shows the high-pressure loss rate from $\text{NH} + \text{NO}$ by this master equation solution as well as the

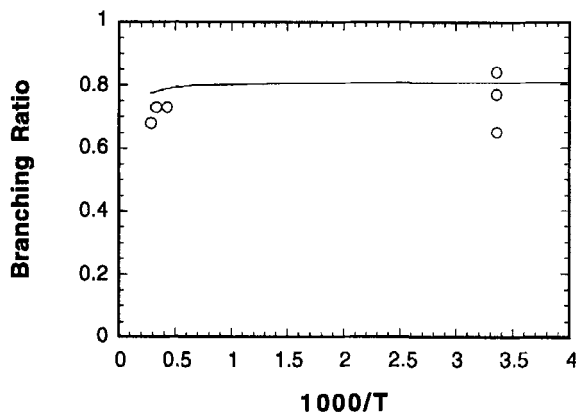


Fig. 6b Branching ratios for the two products of the reaction $\text{NH} + \text{NO} \rightarrow \text{H} + \text{N}_2\text{O}$ or $\text{OH} + \text{N}_2$. All experimental points and symbols are as described in Fig. 3 of Ref. 54.

conventional variational TST (VTST) approach in the temperature range of 300–3000 K. The result obtained by solving the master equation could be expressed by the following three-parameter expression:

$$k_4 = 8.85 \times 10^9 T^{0.83} \exp(1100/T)$$

The experimental loss rates are also presented in Fig. 6a.^{53,54} The branching ratio obtained by the master equation solution is shown in Fig. 6b in comparison with experimental data.^{53,54}

5. $\text{NH}_2 + \text{NO}_x$ ($x = 1$ and 2) Systems

The reactions of NH_2 with NO and NO_2 are very critical to the combustion of ADN and AN. The reactions are also very important to the EXXON deNO_x process, in which NH_3 is used as an NO_x reducing agent. The key processes involved in the deNO_x system are



There have been many studies on the rate constants and product branching ratios of the two reactions; most of these studies, including our detailed theoretical investigations of the processes, have been reviewed by Mebel and Lin.⁴⁸ The total rate constants of the reactions have been most reliably measured by means of pulsed laser photolysis/mass spectrometry carried out in Refs. 58–62; they can be represented by the following expressions in units of cubic centimeters per (mole times seconds):

$$k_5 = 8.3 \times 10^{13} T^{-0.57} \exp(300/T)$$

$$k_{5'} = 8.1 \times 10^{16} T^{-1.44} \exp(-135/T)$$

for the temperature range 300–1000 K. The branching rate constants for the two key product channels given above, measured by mass spectrometry aided by kinetic modeling over the same temperature range, can be given by

$$k_{5a} = 1.4 \times 10^7 T^{1.4} \exp(894/T)$$

$$k_{5b} = 1.2 \times 10^{17} T^{-1.61} \exp(-150/T)$$

$$k_{5'a} = 1.5 \times 10^{16} T^{-1.44} \exp(-135/T)$$

$$k_{5'b} = 6.6 \times 10^{16} T^{-1.44} \exp(-135/T)$$

For reaction (5'), the branching ratio $k_{5'b}/k_{5'}$ was found to be temperature independent, with a constant value of 0.19 ± 0.02 . For reaction (5), the branching ratio for reaction (5b) has been reevaluated with our newly modeled values and the recent results of Glarborg et al.⁶³ and Votsmeier et al.⁶⁴ These branching rate constants may be used for kinetic modeling of ADN, AN, and AP.

6. $\text{NH}_3 + \text{NO}_x$ Systems

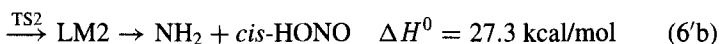
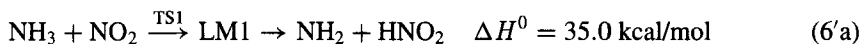
The only reaction between NH_3 and NO proceeds by the direct abstraction of a hydrogen atom of NH_3 by NO to form the NH_2 radical and HNO ; the reaction was computed to have a high endothermicity of 57.5 kcal/mol at the G2(PU) level of theory, which is close to the experimental value of 58.5 kcal/mol (Ref. 65). A small barrier had been predicted for the reverse reaction.⁶⁵ The VTST calculated rate constants for the forward and the reverse reactions in the temperature range 300–5000 K are given by

$$k_{6a} = 1.04 \times 10^7 T^{1.73} \exp(-28,500/T) \text{ cm}^3/(\text{mol} \cdot \text{s})$$

$$k_{-6a} = 3.62 \times 10^6 T^{1.63} \exp(630/T) \text{ cm}^3/(\text{mol} \cdot \text{s})$$

The calculated rate constant for the forward reaction is significantly lower than the experimental shock tube measurement of Roose et al. because a low transition barrier (50.0 kcal/mol) was assumed in the latter.⁶⁶

Three main endothermic product channels have been identified at the G1(PU) level of theory in the $\text{NH}_3 + \text{NO}_2$ reaction^{65,67}:



All three channels were found to go through weak molecular complexes before product formation.⁵⁷ The reaction channel leading to the formation of $\text{NH}_2 + \text{cis-HONO}$ is the dominant step. VTST-calculated rate constants gave rise to the following three-parameter expressions fitted in the temperature range of 300–5000 K (Refs. 57 and 59):

$$k_{6'b} = 7.35 T^{3.30} \exp(-11,200/T) \text{ cm}^3/(\text{mol} \cdot \text{s}) \text{ (with UMP2 parameters)}$$

$$k_{6'b} = 1.18 \times 10^1 T^{3.41} \exp(-11,300/T) \text{ cm}^3/(\text{mol} \cdot \text{s}) \text{ (with B3LYP parameters)}$$

We have also evaluated the rate constant $k_{6'b}$ through the kinetic modeling⁶⁷ of the photometrically measured NO_2 decay rates available in the literature,^{68,69} based on the proposed mechanism containing 47 reactions. The following expression was obtained in a narrow range of experimental temperatures (600–800 K):

$$k_{6'b} = 10^{11.39 \pm 0.16} \exp[-(12,620 \pm 240)/T] \text{ cm}^3/(\text{mol} \cdot \text{s})$$

This modeled rate constant agrees quantitatively with the computed rate constant obtained with the G2M PES.⁶⁷

The other two reaction paths by means of TS1 and TS3 were reported to have higher activation barriers at the G1(PU) level of theory and the recommended rate coefficients in the temperature range of 300–5000 K are as follows:

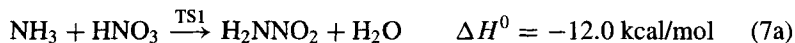
$$k_{6'a} = 2.45 T^{3.41} \exp(-15,000/T) \text{ cm}^3/(\text{mol} \cdot \text{s})$$

$$k_{6'c} = 1.88 \times 10^1 T^{3.52} \exp(-16,400/T) \text{ cm}^3/(\text{mol} \cdot \text{s})$$

where the necessary tunneling correction was included in $k_{6'c}$.

7. $\text{NH}_3 + \text{HNO}_x$ ($x = 2, 3$) Reactions

Two nonionic molecular product channels have been theoretically identified with similar barriers (~ 46.0 kcal/mol) for the $\text{NH}_3 + \text{HNO}_3$ reaction⁷⁰



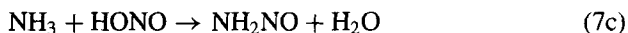
The first channel occurs by means of a four-member-ring TS with an activation barrier of 45.7 kcal/mol. The other takes place by means of a five-member-ring TS whose barrier is 46.0 kcal/mol. TST calculations with tunneling corrections that used the predicted energies and molecular parameters gave rise to the following rate constants:

$$k_{7a} = 0.81 T^{3.47} \exp(-21,670/T) \text{ cm}^3/(\text{mol} \cdot \text{s})$$

$$k_{7b} = 23.2 T^{3.50} \exp(-22,600/T) \text{ cm}^3/(\text{mol} \cdot \text{s})$$

for the temperature range 300–3000 K. The tunneling correction for the first reaction amounts to 48% at 500 K and 12% at 1000 K; the correction for the latter reaction is, however, negligible (<1%) because of its low imaginary frequency.

We recently performed a similar calculation for the analogous reaction



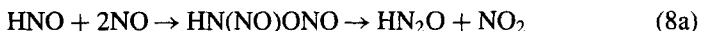
at the G2M//B3LYP/6–311G(*d,p*) level of theory.⁷¹ A TST calculation based on the computed energetics and the TS structure for the lowest-energy path gives rise to

$$k_7 = 1.15 \times 10^{12} \exp(-18,000/T) \text{ cm}^3/(\text{mol} \cdot \text{s})$$

for the temperature range 300–3000 K.

8. HNO Reactions with $\text{NO}/\text{HNO}/\text{NO}_2$

HNO undergoes bimolecular and termolecular reactions with NO, depending on the concentration of NO and the temperature of the system. Under low-temperature and NO-rich conditions, the termolecular process takes place readily with a small activation barrier by means of a short-lived intermediate⁷²:



A BAC-MP4 calculation for this termolecular reaction showed the presence of a relatively high barrier ($E_a > 14.0$ kcal/mol) for the formation of the endothermic products $\text{H} + \text{N}_2 + \text{NO}_3$ through a five-centered intermediate,⁷³ which would prevent it from occurring at room temperature, contrary to earlier experimental findings. We recommended an approximate Arrhenius equation,

$$k_{8a} = 10^{11.2 \pm 0.3} \exp[-(1050 \pm 200)/T] \text{ cm}^6/(\text{mol}^2 \cdot \text{s})$$

in the temperature range of 450–520 K by detailed product measurements made with Fourier transform infrared spectroscopy⁷⁴ combined with those derived from modeling of the data of Cheskis et al.⁷⁵

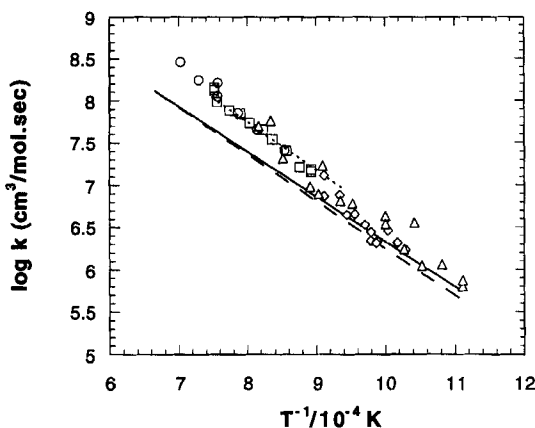


Fig. 7 Arrhenius plots of the rate constant for the reaction $\text{HNO} + \text{NO} \rightarrow \text{OH} + \text{N}_2\text{O}$. The solid and the dotted lines are the results of RRKM calculations with and without tunneling corrections, respectively, based on the PES in the G2 level.⁷⁶ The dashed line is Wilde's modeled result.⁸³ All other experimental data are as described in Fig. 4 of Ref. 72.

At higher-temperature conditions ($900 \text{ K} < T < 1500 \text{ K}$), the reaction of HNO with NO is dominated by the bimolecular process, which occurs through the rate-limiting H migration step:



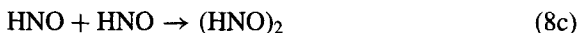
The PES of this reaction was reported at the G2 and the QCISD levels of theory.^{76,77} The barriers for H migration were calculated to be 23 and 25 kcal/mol at the G2 and the QCISD/6-311 + G(2df,2p)//QCISD/6-31g(d,p) levels of theory, respectively. They are somewhat lower than the value of 29.0 kcal/mol kinetically modeled with several sets of experimental data,⁷⁸⁻⁸⁰ which used a mechanism containing 60 elementary reactions with the CHEMKIN program⁸¹ in conjunction with sensitivity analyses.⁸² Figure 7 summarizes the modeled result. A least-squares analysis of these results gives rise to the expression

$$k_{8b} = 10^{12.84 \pm 0.06} \exp[-(14,740 \pm 180)/T] \text{ cm}^3/(\text{mol} \cdot \text{s})$$

which agrees well with the earlier modeled result of Wilde.⁸³ The difference between the calculated and the kinetically modeled activation energies (~ 3 –5 kcal/mol) is, however, puzzling at present. We plan to remodel our kinetic data by including additional higher barrier reactions such as $\text{HNO} + \text{NO} \rightarrow \text{NH} + \text{NO}_2$, whose reverse rate constant has been calculated by us,³⁸ as mentioned in the preceding subsection.

The bimolecular self-reaction of HNO is very complicated because of the presence of numerous geometric isomers of HNO dimers with comparable thermal stability.⁷³ The lowest-energy paths found theoretically led to either the dimeric products by collisional stabilization or to the decomposition products, $\text{N}_2\text{O} + \text{H}_2\text{O}$ and $\text{HNOH} + \text{NO}$, depending on the temperature regime.⁷³ These theoretical results led us to conclude that the rate of HNO decay measures at low temperatures ($T < 420 \text{ K}$) were controlled entirely by the association-stabilization reaction producing *cis*- and *trans*- $(\text{HNO})_2$ instead of the formation of the commonly

assumed products, $\text{N}_2\text{O} + \text{H}_2\text{O}$. A least-squares fit to the calculated rate constants for the dimerization of HNO,

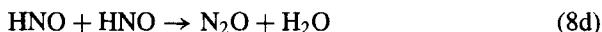


computed with BAC-MP4-predicted parameters for 710-torr H_2 or He within the 80–420 K temperature range gives

$$k_{8c} = 10^{16.2} T^{-2.40} \exp(-590/T) \text{ cm}^3/(\text{mol} \cdot \text{s})$$

which satisfactorily reconciles the fast rates of HNO decay measured by Callear and Carr⁸⁴ and the slow rates of N_2O formation reported by He and Lin.⁷⁴

At higher temperatures, the thermal decomposition channel producing $\text{N}_2\text{O} + \text{H}_2\text{O}$ becomes important. From the modeling of N_2O formation by the overall mechanistic scheme of H/N/O reactions,⁷² an apparent rate constant for this reaction,



$$k_{8d} = 10^{8.93 \pm 0.30} \exp[-(1550 \pm 150)/T] \text{ cm}^3/(\text{mol} \cdot \text{s})$$

was obtained for the temperature range of 450–700 K under NO lean conditions and recommended for combustion modeling.

The theoretical calculation of the $\text{HNO} + \text{NO}_2$ reaction at the G2M(RCC,MP2) level of theory by Mebel et al.⁸⁵ showed that the direct H abstraction leading to the $\text{NO} + \text{cis-HONO}$ products should be the most significant reaction mechanism. Direct H abstraction giving $\text{NO} + \text{trans-HONO}$ has a high barrier on the PES, and the reaction would rather occur by the addition/1,3-H shift by means of the HN(O)NO_2 intermediate or by the secondary isomerization of *cis*-HONO, giving the *trans*-isomer. The formation of $\text{NO} + \text{HNO}_2$ from $\text{HNO} + \text{NO}_2$ can take place by direct H transfer with a barrier that is 3 kcal/mol higher than that for the $\text{NO} + \text{cis-HONO}$ channel. The formation of HNO_2 by oxygen abstraction from NO_2 by HNO is predicted to be the least-significant reaction channel. The rate constants calculated in the temperature range 300–5000 K for the lowest-energy path producing $\text{NO} + \text{cis-HONO}$,

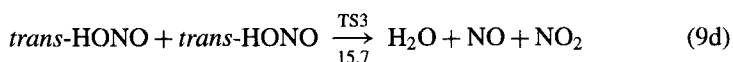
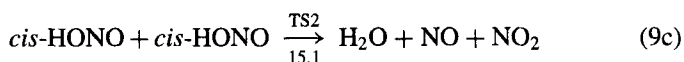
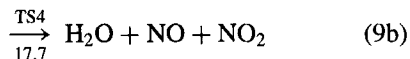
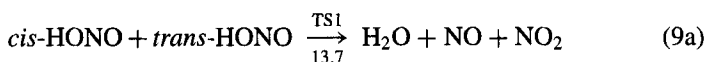


gave rise to

$$k_{8e} = 4.42 \times 10^4 T^{2.64} \exp(-2034/T) \text{ cm}^3/(\text{mol} \cdot \text{s})$$

9. HONO + HONO Reaction

Four reaction channels with comparable energy barriers were found to be important in our recent theoretical study of the bimolecular decomposition of HONO^{86} :



where the numerical values represent the computed reaction barriers at 0 K given in units of kilocalories per mole.

The total rate constant including all four channels, calculated with our ab initio MO results, can be represented by the three-parameter expression for the 300–5000 K temperature range:

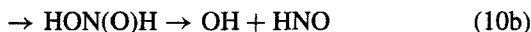
$$k_9 = 3.49 \times 10^{-1} T^{3.64} \exp(-6100/T) \text{ cm}^3/(\text{mol} \cdot \text{s})$$

which includes the correction of the equilibrium concentration of the *cis*-isomer. This recommended rate constant is, however, considerably lower than the available experimental results^{87–90} but is consistent with the upper limit set at 300 K by Kaiser and Wu.⁹¹ The high values of measured rate constants are believed to have suffered from deleterious surface effects.⁹¹

Similar calculations are underway on the reactions of HONO with NO₂ and HNO, which are expected to produce HNO₃ + NO and H₂O + 2NO, respectively.

10. H + HONO Reaction

The ab initio MO calculations made with G2 and BAC-MP4 methods⁹² predicted three major reaction channels for the H + HONO reaction (for which no experimental data are available), leading to the formation of exothermic products NO + H₂O, H₂ + NO₂, and HNO + OH:



The reaction occurs predominantly by two indirect metathetical processes unknown before this study. One produces OH + HNO [reaction (10b)] and H₂O + NO [reaction (10c)] from the decomposition of the vibrationally excited hydroxyl nitroxide, HON(O)H, formed by H atom addition to the N atom of HONO. The other also produces H₂O + NO [reaction (10d)] from the decomposition of the dihydroxylamino radical, N(OH)₂, formed by H atom addition to the terminal O atom of HONO. These indirect displacement processes are much more efficient than the commonly assumed, direct H abstraction reaction that produces H₂ + NO₂. A TST calculation for the direct abstraction reaction and RRKM calculations for the two indirect displacement processes gave rise to the following recommended rate expressions in units of cubic centimeters per (mole times seconds) for the 300–3500 K temperature range under atmospheric conditions⁹²:

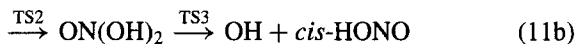
$$k_{10a} = 2.01 \times 10^8 T^{1.55} \exp(-3300/T)$$

$$k_{10b} = 5.64 \times 10^{10} T^{0.86} \exp(-2500/T)$$

$$k_{10c+10d} = 8.13 \times 10^6 T^{1.89} \exp(-1900/T)$$

11. $H + HNO_3$ Reaction

Three reaction channels have been identified for the bimolecular reaction between H and HNO_3 at the G2M(RCC,MP2) level of theory⁹³:



Similar to that of $H + HONO$, the reaction is dominated by the indirect metathetical process, producing $OH + cis\text{-}HONO$ by means of $TS2$, intermediate $ON(OH)_2$, and $TS3$. The direct H abstraction reaction by means of $TS1$ was found to be the least important one. A TST calculation for this direct abstraction in the temperature range 300–3000 K gave rise to the following expression:

$$k_{11a} = 5.56 \times 10^8 T^{1.53} \exp(-8200/T) \text{ cm}^3/(\text{mol} \cdot \text{s})$$

Rate constants for both the indirect processes were obtained by solving the master equation,⁴³ which includes RRKM microscopic rate constants and tunneling correction. At atmospheric pressure and the same temperature range given above, the following rate expressions are recommended for these two indirect metathetical reactions:

$$k_{11b} = 3.82 \times 10^5 T^{2.30} \exp(-3500/T) \text{ cm}^3/(\text{mol} \cdot \text{s})$$

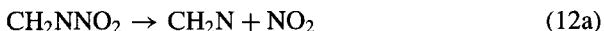
$$k_{11c} = 6.08 \times 10^1 T^{3.29} \exp(-3200/T) \text{ cm}^3/(\text{mol} \cdot \text{s})$$

These rate constants agree well with the available experimental data^{94–96} at room temperature.

B. Systems Relevant to the Early-Stage Decomposition of RDX/HMX

1. Unimolecular Decomposition of CH_2NNO_2

The thermal decomposition of methylene nitramine (MN), CH_2NNO_2 , is an important mechanistic step in RDX and HMX decomposition reactions.^{97–99} Three unimolecular decomposition channels of MN were identified as secondary reactions in the RDX decomposition by Zhao et al., who used the infrared multiphoton dissociation technique⁹⁷:



Reported theoretical studies include ab initio MO calculations^{100,101} and unimolecular decomposition dynamics simulations,^{102,103} emphasizing mainly the competitive fragmentation processes, N–N bond dissociation vs HONO elimination reaction. Mowrey et al.,¹⁰⁰ from their MCSCF-MO calculation and error estimation on such calculations, recommended the activation barrier for the HONO elimination path to be 31 ± 4 kcal/mol and the N–N bond dissociation energy to be

35 ± 4 kcal/mol. Our G2M-calculated energies (TS for HONO elimination = 32.7 and N–N bond scission = 35.9 kcal/mol) agree very well with their recommended values. The BAC-MP4 values reported by Melius and Binkley gave a reverse energetic ordering (TS1 = 41.2 and NN scission = 28.6 kcal/mol).¹⁰¹ The most exothermic products $\text{CH}_2\text{O} + \text{N}_2\text{O}$ ($\Delta H^0 = -75.3$) can be reached by means of the formation and the decomposition of a four-member cyclic intermediate, whose maximum barrier is 38.1 kcal/mol higher than the reactant at the G2M level. Thus both the higher barrier and the much tighter TS structure of this channel make it noncompetitive with the other two decomposition channels at low temperatures.

To our knowledge, no experimental rate constants are available for the thermal unimolecular decomposition of MN. The classical dynamics simulation by Rice et al.¹⁰² showed that the N–N dissociation is the dominant reaction path and only at higher energies does the HONO elimination process become competitive. They reported an activation energy and an A factor of 31.8 kcal/mol and $4 \times 10^{13} \text{ s}^{-1}$, respectively, for the latter reaction in the temperature range of 300–1500 K based on their conventional TST calculations. Our coupled three-channel RRKM calculations, including a tunneling correction for reaction (12b) by solving the master equation,⁴³ gave rise to the following rate expressions in the temperature range 500–1500 K and at two different pressures (1 and 200 atm):

$$k_{12a}(1 \text{ atm}) = 2.35 \times 10^{56} T^{-13.26} \exp(-24,550/T) \text{ s}^{-1}$$

$$k_{12a}(200 \text{ atm}) = 7.33 \times 10^{57} T^{-13.01} \exp(-26,100/T) \text{ s}^{-1}$$

$$k_{12b}(1 \text{ atm}) = 2.87 \times 10^{39} T^{-9.37} \exp(-17,800/T) \text{ s}^{-1}$$

$$k_{12b}(200 \text{ atm}) = 1.45 \times 10^{11} \exp(-14,200/T) \text{ s}^{-1}$$

$$k_{12c}(1 \text{ atm}) = 1.38 \times 10^4 \exp(-12,100/T) \text{ s}^{-1}$$

$$k_{12c}(200 \text{ atm}) = 2.88 \times 10^9 \exp(-16,400/T) \text{ s}^{-1}$$

These results are graphically presented in Fig. 8. It is clearly evident from the figure that the NN bond dissociation reaction is the dominant channel, and only

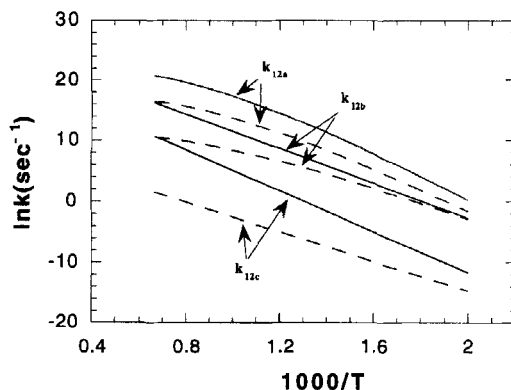


Fig. 8 Arrhenius plots of the rate constant for the unimolecular decomposition of CH_2NNO_2 : —, 200-atm pressure and ---, 1-atm pressure.

at low temperature and low pressure does the concerted HONO formation reaction becomes competitive. At the high-pressure limit, our calculation gives the following Arrhenius expressions:

$$k_{12a} = 2.46 \times 10^{15} \exp(-17,200/T) \text{ s}^{-1}$$

$$k_{12b} = 6.21 \times 10^{12} \exp(-16,350/T) \text{ s}^{-1}$$

$$k_{12c} = 4.52 \times 10^{11} \exp(-19,300/T) \text{ s}^{-1}$$

and the corresponding rate expressions at the low-pressure limit are

$$k_{12a} = 1.15 \times 10^{12} T \exp(-17,700/T) \text{ cm}^3/(\text{mol} \cdot \text{s})$$

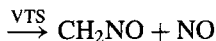
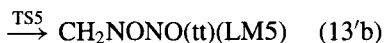
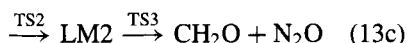
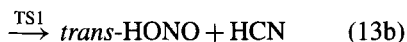
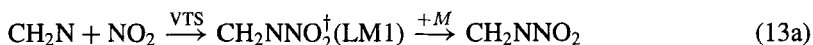
$$k_{12b} = 4.54 \times 10^{43} T^{-8.36} \exp(-14,7000/T) \text{ cm}^3/(\text{mol} \cdot \text{s})$$

$$k_{12c} = 9.48 \times 10^{72} T^{-19.8} \exp(-28,520/T) \text{ cm}^3/(\text{mol} \cdot \text{s})$$

For the HONO formation channel, our calculated rate constant is somewhat lower than that of Rice et al., as alluded to above.¹⁰²

2. Bimolecular Reaction of CH_2N with NO_2

The following two low-energy paths are identified for the bimolecular reaction between CH_2N and NO_2 by means of CH_2NNO_2 and CH_2NONO intermediates:



A complete PES for the $\text{CH}_2\text{N} + \text{NO}_2$ reaction is presented in Figs. 9a and 9b for the nitro and the nitrite channels, respectively, corresponding to the NN association and decomposition and the NO association and decomposition reactions. The initial NN association does not have an activation barrier and can form the MN molecule by collisional stabilization or the exothermic decomposition products HONO and CH_2O by means of respective TSs. We perform here coupled-channel RRKM calculations for these reaction paths in the temperature range of 300–2500 K at two different pressure (1 and 200 atm). The results, as shown in Fig. 10, clearly indicate that at low temperatures the collisional stabilization to form MN is the most dominant path but at higher temperatures ($T > 1200$ K) the HONO formation is equally probable. The third channel forming CH_2O and N_2O becomes competitive only at very high temperatures ($T > 2000$ K). The following rate expressions in

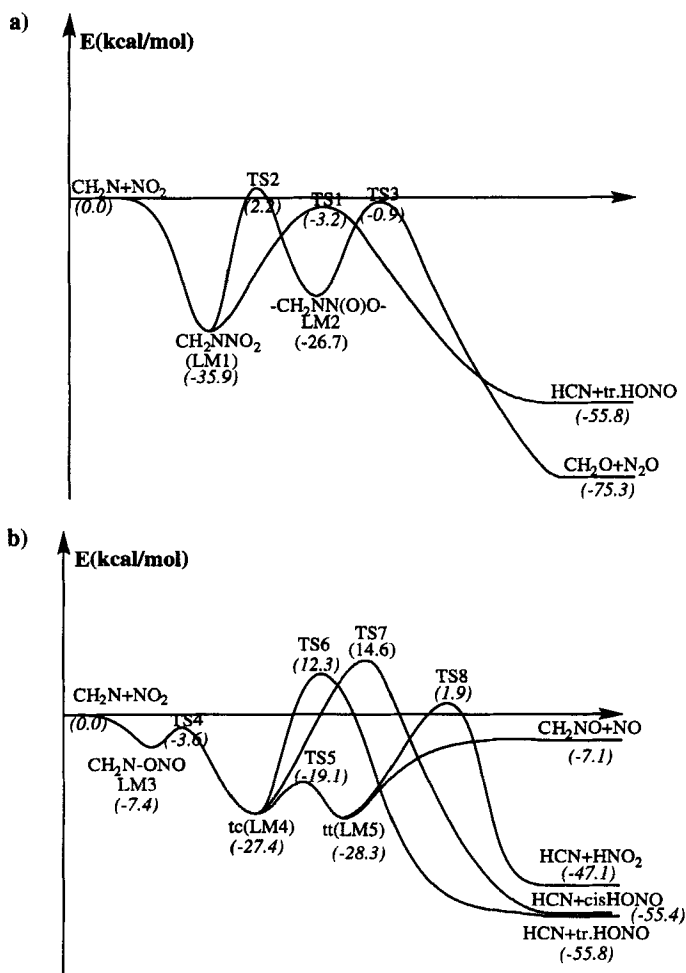


Fig. 9 Potential-energy profiles for the reaction $\text{CH}_2\text{N} + \text{NO}_2$ based on the G2M method: a) the formation and decomposition of the nitro (CH_2NNO_2) intermediate and b) the formation and decomposition of the nitrite (CH_2NONO) intermediate.

units of cubic centimeters per mole times second are recommended for the kinetic modeling of this reaction:

$$k_{13a} (1 \text{ atm}) = 5.43 \times 10^{39} T^{-9.09} \exp(-3100/T)$$

$$k_{13a} (200 \text{ atm}) = 1.04 \times 10^{33} T^{-6.49} \exp(-2800/T)$$

$$k_{13b} (1 \text{ atm}) = 5.16 \times 10^5 T^{1.54} \exp(630/T)$$

$$k_{13b} (200 \text{ atm}) = 3.62 \times 10^6 T^{1.39} \exp(-1050/T)$$

$$k_{13c} (1 \text{ atm}) = 3.78 \times 10^4 T^{1.57} \exp(-1100/T)$$

$$k_{13c} (200 \text{ atm}) = 1.52 \times 10^4 T^{1.66} \exp(-3700/T)$$

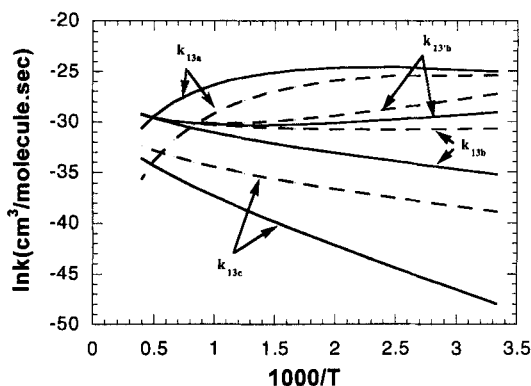


Fig. 10 Arrhenius plots of the rate constants for the bimolecular reaction between CH_2N and NO_2 : —, 200-atm pressure and ---, 1-atm pressure.

The ONO association reaction is more complex because of the presence of a very loose association complex, $\text{CH}_2\text{N} \cdots \text{ONO}$ (LM3), and two different nitrite isomers [*trans-cis* (tc) and *trans-trans* (tt)] with comparable energy, as shown in Fig. 9b. At the G2M level the tt isomer is 0.9 kcal/mol more stable. The initial association to LM3 leads to the formation of the tc isomer by means of TS4, which is 3.6 kcal/mol lower than the reactants. The tc isomer can then isomerize to the more stable tt structure by means of TS5. The direct association to the tt isomer always leads to the formation of the more stable CH_2NNO_2 (MN) along the reaction path. The dissociated $\text{CH}_2\text{NO} + \text{NO}$ products are more preferably formed by splitting the ON bond of the tt isomer than that of the tc isomer. A cVRRKM calculation coupled with multiple-reflection probability (as used in Ref. 38) in the shallow well of LM3 was performed to calculate the bimolecular rate constants for this reaction under the same temperature and pressure conditions as those used for reactions (13a–13c). We did not find any appreciable reduction in the rate constant by the multiple reflections. This may be attributed to the relatively low energy of TS4 (–3.6 kcal/mol) compared with its analog in the $\text{NH} + \text{NO}_2$ reaction, as shown in Fig. 2. The collisional stabilization to form the CH_2NONO isomers are negligible compared with their dissociation to $\text{CH}_2\text{NO} + \text{NO}$, except at very high pressures. The calculated rate constants under the same temperature and pressure conditions (300–2500 K at 1 and 200 atm) for the bimolecular formation of $\text{CH}_2\text{NO} + \text{NO}$ are shown in Fig. 10 along with the other reaction path rate constants; they can be expressed with the following three-parameter rate expressions:

$$k_{13b}(1 \text{ atm}) = 3.97 \times 10^1 T^{2.65} \exp(2600/T) \text{ cm}^3/(\text{mol} \cdot \text{s})$$

$$k_{13b}(200 \text{ atm}) = 3.74 \times 10^3 T^{2.12} \exp(1600/T) \text{ cm}^3/(\text{mol} \cdot \text{s})$$

At temperatures below 2000 K, the bimolecular reaction of CH_2N with NO_2 is clearly dominated by the recombination process, producing CH_2NNO_2 at $P \geq 1$ atm. This result suggests that the destruction of CH_2NNO_2 by H and OH is critical under high-pressure combustion conditions and should be studied theoretically.

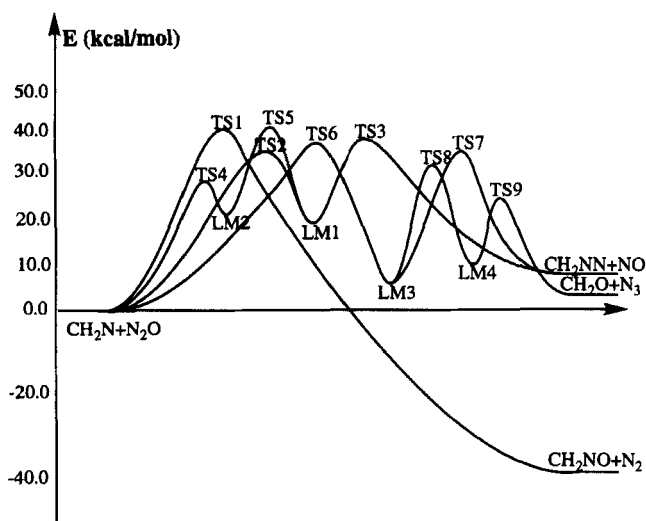
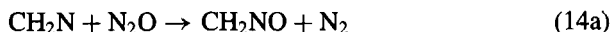


Fig. 11 Potential-energy profile for the reaction $\text{CH}_2\text{N} + \text{N}_2\text{O}$ based on the G2M method. See Ref. 104 for the structures of intermediates and TSs.

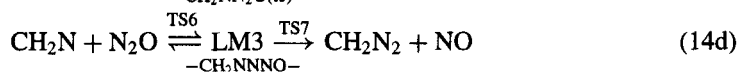
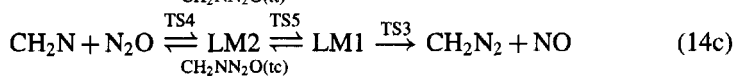
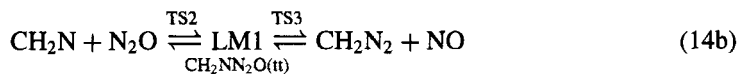
3. $\text{CH}_2\text{N} + \text{N}_2\text{O}$ Reaction

Three different product channels have been identified for the bimolecular reaction between CH_2N and N_2O , producing $\text{CH}_2\text{NO} + \text{N}_2$, $\text{CH}_2\text{N}_2 + \text{NO}$, and $\text{CH}_2\text{O} + \text{N}_3$ (Ref. 104). The G2M PES of the system is shown in Fig. 11. The direct abstraction reaction,



which occurs by means of transition state TS1 yielding most exothermic products CH_2NO and N_2 , has an activation barrier of 42.4 kcal/mol at the G2M level. This is identified as a minor channel in this reaction, contrary to the previous assumption of its importance in the kinetic modeling of RDX combustion.²⁻⁴ A TST calculation for which the predicted energies and molecular parameters were used gave rise to rate constant $k(\text{CH}_2\text{NO}) = k_{14a} = 1.71 \times 10^{13} \exp(-24,900/T) \text{ cm}^3/(\text{mol} \cdot \text{s})$ in the temperature range of 1000–3000 K.

The other two product channels are endothermic; they can be reached in only a stepwise manner by means of the formation and decomposition of different intermediates. As is evident from Fig. 11, the $\text{CH}_2\text{N}_2 + \text{NO}$ products can be reached by three different reaction paths:



We used our coupled-channel RRKM programs to calculate the individual and the overall rates of formation of the products in the temperature range of

1000–3000 K; the results can be expressed as

$$k_{14b} = 5.37 \times 10^{12} \exp(-21,900/T) \text{ cm}^3/(\text{mol} \cdot \text{s})$$

$$k_{14c} = 1.22 \times 10^{12} \exp(-25,100/T) \text{ cm}^3/(\text{mol} \cdot \text{s})$$

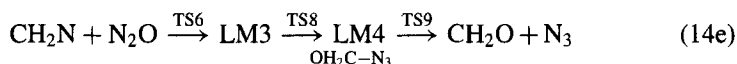
$$k_{14d} = 2.40 \times 10^{10} \exp(-24,900/T) \text{ cm}^3/(\text{mol} \cdot \text{s})$$

$$k(\text{CH}_2\text{N}_2) = k_{14b} + k_{14c} + k_{14d}$$

$$= 5.98 \times 10^{12} \exp(-22,000/T) \text{ cm}^3/(\text{mol} \cdot \text{s})$$

It is evident from these calculated rate constants that the formation of $\text{CH}_2\text{N}_2 + \text{NO}$ is dominated by reaction channel (14b), and only at very high temperatures would other channels become accessible. The results of the calculation indicate that the predicted rate constants are pressure independent in the range of 10 torr–200 atm. For coupled channels (14b) and (14c), for example, the rates of deactivation of the activated intermediates to potential wells LM1 and LM2 are significantly less important compared with their rates of disproportionation through the individual product channels.

The reaction channel leading to the formation of CH_2O and N_3 ,



is connected with channel (14d), as already mentioned. Our coupled dual-channel RRKM calculation (incorporating the loss of LM3 by TS7) yielded the bimolecular formation rate constant in the same temperature and pressure ranges:

$$k(\text{CH}_2\text{O}) = k_{14e} = 2.76 \times 10^{11} \exp(-21,800/T) \text{ cm}^3/(\text{mol} \cdot \text{s})$$

These results are presented in Fig. 12. At higher temperatures, the rates of formation of CH_2NO and CH_2N_2 become comparable, although at lower temperatures the formation rate of CH_2NO is much less because of the presence of a higher activation barrier for this process. As is also evident from the figure, the rate of formation of $\text{CH}_2\text{O} + \text{N}_3$ is less important compared with that of the other individual channels.

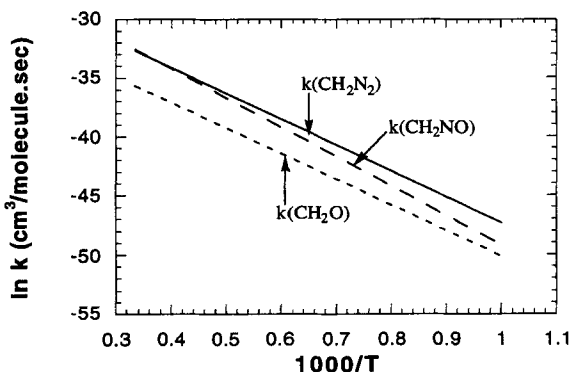


Fig. 12 Arrhenius plots of the bimolecular rate constants for the formation of $\text{CH}_2\text{NO} + \text{N}_2$, $\text{CH}_2\text{N}_2 + \text{NO}$, and $\text{CH}_2\text{O} + \text{N}_3$ from $\text{CH}_2\text{N} + \text{N}_2\text{O}$.

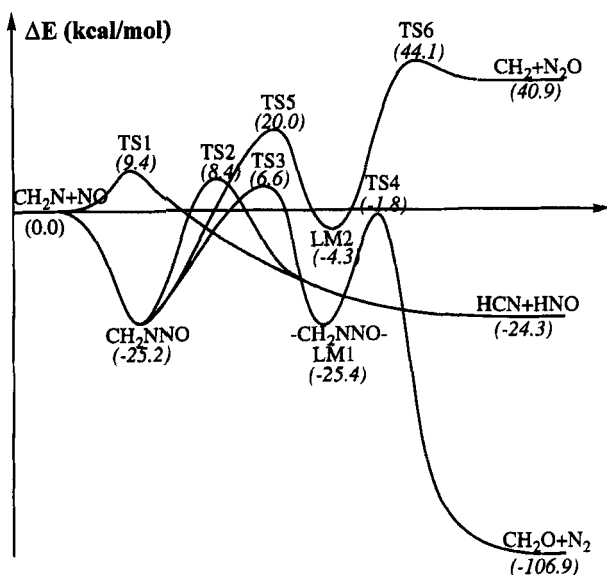
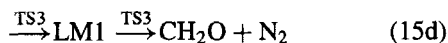


Fig. 13 Potential-energy profile for the reaction $\text{CH}_2\text{N} + \text{NO}$ based on the G2M method.

4. $\text{CH}_2\text{N} + \text{NO}$ Reaction

The PES of the bimolecular reaction of CH_2N and NO is obtained at the same G2M(RCC,MP2) level of theory and is presented in Fig. 13. Three different product channels have been identified for this reaction. The formation of the most endothermic products, $\text{CH}_2 + \text{N}_2\text{O}$, requires a very high activation barrier and may not be reached even at higher temperatures, but two exothermic products, $\text{HCN} + \text{HNO}$ and $\text{CH}_2\text{O} + \text{N}_2$, could be formed by the following three possible reaction paths:



Direct abstraction reaction (15a), which leads to $\text{HCN} + \text{HNO}$, has a barrier of 9.4 kcal/mol at the G2M level and a TST calculation with tunneling corrections for this channel in the temperature range of 300–3000 K, giving rise to

$$k_{15\text{a}} = 7.28T^{2.13} \exp(-3700/T) \text{ cm}^3/(\text{mol} \cdot \text{s})$$

Because both the reaction channels that occur by means of TS2 and TS3 have activation barriers above the reactants, the collisional stabilization of the vibrationally excited CH_2NNO intermediate will be the dominant reaction channel and only at very high temperatures will the other two channels become competitive,

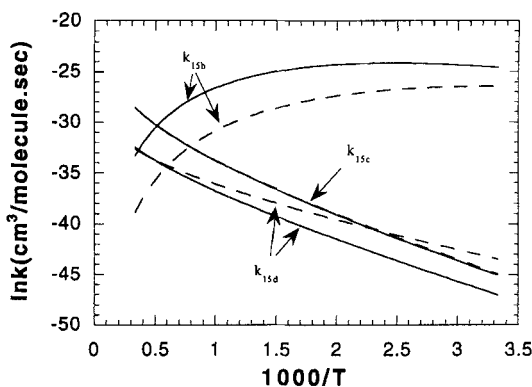


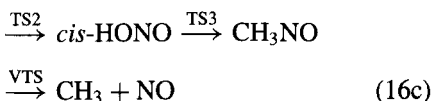
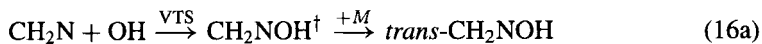
Fig. 14 Arrhenius plots of the rate constants for the formation of different products from the bimolecular reaction between CH_2N and NO : —, 200-atm pressure and ---, 1-atm pressure.

as shown in Fig. 14. A coupled-channel RRKM calculation has been used to calculate the respective rate constants in the temperature range of 300–3000 K at two different pressures (1 atm and 200 atm); these rate constants could be expressed in units of cubic centimeters per (mole times seconds) as follows:

$$\begin{aligned}
 k_{15b}(1 \text{ atm}) &= 1.24 \times 10^{38} T^{-8.86} \exp(-2700/T) \\
 k_{15b}(200 \text{ atm}) &= 1.07 \times 10^{38} T^{-8.12} \exp(-3300/T) \\
 k_{15c}(1 \text{ atm}) &= 3.99 \times 10^2 T^{2.66} \exp(-3400/T) \\
 k_{15c}(200 \text{ atm}) &= 4.02 \times 10^2 T^{2.66} \exp(-3450/T) \\
 k_{15d}(1 \text{ atm}) &= 4.68 \times 10^3 T^{1.80} \exp(-2200/T) \\
 k_{15d}(200 \text{ atm}) &= 6.02 \times 10^3 T^{1.84} \exp(-3400/T)
 \end{aligned}$$

5. $\text{CH}_2\text{N} + \text{OH}$ Reaction

The following two major reaction paths have been identified in the bimolecular reaction of CH_2N and OH at the G2M level of theory:



The G2M-calculated PES for this reaction is presented in Fig. 15. The thermal decomposition and isomerization of formaldoxime, CH_2NOH , has been studied with a reflected-shock-wave experiment and ab initio MO calculations by Saito et al.¹⁰⁵ They found that the main thermal decomposition reaction proceeded by means of $\text{CH}_2\text{NOH} \rightarrow \text{HCN} + \text{H}_2\text{O}$ and that the alternative isomerization

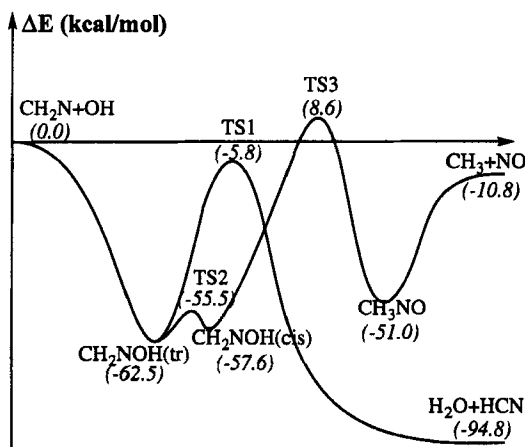


Fig. 15 Potential-energy profile for the reaction $\text{CH}_2\text{N} + \text{OH}$ based on the G2M method.

reaction $\text{CH}_2\text{NOH} \rightarrow \text{CH}_3\text{NO}$ was negligible. Their *ab initio* MO calculations at the MP2/3-21G level reported a barrier of 50.6 kcal/mol for HCN formation and 72.9 kcal/mol for the isomerization step from the most stable *trans*-isomer of formaldoxime. The G2M-calculated barrier for the former is 56.7 kcal/mol and for the latter is 71.1 kcal/mol. Over the narrow temperature range of 1050–1300 K their shock-wave experiment gave rise to the decomposition rate constant that leads to the formation of HCN (monitored with vacuum UV absorption of the reactant and IR emission from HCN): $k_{\text{HCN}} = 10^{12.65} \exp(-24,200/T) \text{ s}^{-1}$. They also concluded that there is a very slight pressure dependence over their experimental region.

We performed here a coupled-channel RRKM calculation for the unimolecular decomposition of CH_2NOH as well as the bimolecular reaction of $\text{CH}_2\text{N} + \text{OH}$. We also observed that the isomerization reaction cannot compete with the decomposition reaction that leads to the formation of $\text{HCN} + \text{H}_2\text{O}$, but the reverse decomposition of the *trans*-formaldoxime to $\text{CH}_2\text{N} + \text{OH}$ has a comparable rate in the experimental temperature regime. The calculated forward and reverse decomposition rate constants (in units of inverse seconds) that produce $\text{HCN} + \text{H}_2\text{O}$ and $\text{CH}_2\text{N} + \text{OH}$ from CH_2NOH in the temperature range of 500–2000 K at two different pressures, 1 and 200 atm, could be expressed as follows:

$$k_f (1 \text{ atm}) = 3.01 \times 10^{11} \exp(-25,000/T)$$

$$k_f (200 \text{ atm}) = 3.97 \times 10^{12} \exp(-26,100/T)$$

$$k_r (1 \text{ atm}) = 6.44 \times 10^{11} \exp(-27,600/T)$$

$$k_r (200 \text{ atm}) = 3.58 \times 10^{14} \exp(-30,300/T)$$

A tunneling correction has been included in the forward decomposition reaction. Our calculation shows a significant pressure effect at higher temperatures, in contrast to the earlier observation.¹⁰⁵ The calculated forward decomposition rate is

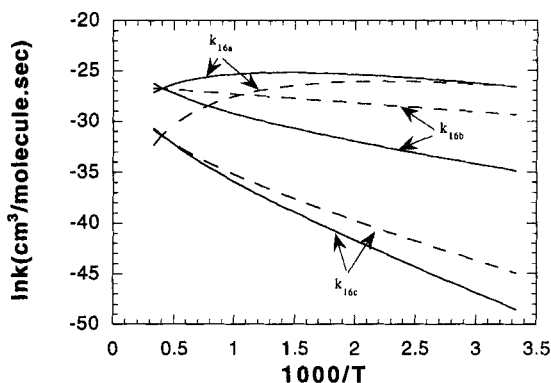


Fig. 16 Arrhenius plots of the rate constants for the formation of different products from the bimolecular reaction between CH_2N and OH : —, 200-atm pressure and ---, 1-atm pressure.

somewhat lower than the experimental and theoretical results of Saito et al.¹⁰⁵ in their experimental temperature range. The higher value of HCN formation data obtained experimentally may result from the secondary contribution from CH_2N decomposition, which was not included in the kinetic analysis by Saito et al.¹⁰⁵

The bimolecular reaction rate is dominated mainly by the collisional stabilization to form CH_2NOH , and only at very high temperatures ($T > 2500$ K) does the formation of $\text{HCN} + \text{H}_2\text{O}$ become competitive, as shown in Fig. 16. The following three-parameter expressions for the respective reactions in the temperature range of 300–3000 K at two different pressures, 1 and 200 atm, are recommended for kinetic modeling;

$$k_{16a}(1 \text{ atm}) = 6.93 \times 10^{30} T^{-5.96} \exp(-2700/T)$$

$$k_{16a}(200 \text{ atm}) = 2.36 \times 10^{22} T^{-2.91} \exp(-2100/T)$$

$$k_{16b}(1 \text{ atm}) = 1.98 \times 10^{11} \exp(-890/T)$$

$$k_{16b}(200 \text{ atm}) = 1.67 \times 10^6 T^{1.83} \exp(-1500/T)$$

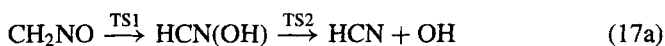
$$k_{16c}(1 \text{ atm}) = 1.70 \times 10^2 T^{2.1} \exp(-3100/T)$$

$$k_{16c}(200 \text{ atm}) = 1.76 \times 10^3 T^{2.2} \exp(-4300/T)$$

in units of cubic centimeters per mole times seconds.

6. Unimolecular Decomposition of CH_2NO

The unimolecular decomposition of CH_2NO has been studied at the G2M level of theory, and the PES is shown in Fig. 17. Two major reaction paths have been identified for this decomposition reaction:



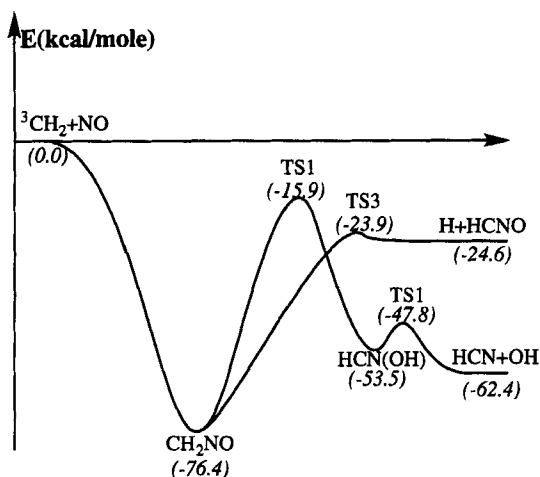


Fig. 17 Potential-energy profile for the unimolecular decomposition of CH_2NO based on the G2M method.

The decomposition of CH_2NO to $^3\text{CH}_2 + \text{NO}$ is less important compared with these two reaction paths because of the larger endothermicity, as shown in Fig. 17. The reverse association ($\text{CH}_2 + \text{NO}$) reaction is, however, important and well studied experimentally; it is not included in this review because of its irrelevance to the RDX/HMX decomposition reactions. The barrier of TS3 (52.5 kcal/mol) is less than that of TS1 (60.5 kcal/mol), which makes $\text{H} + \text{HCNO}$ the major product channel of this decomposition reaction. The production of $\text{HCN} + \text{OH}$ occurs through the formation and the decomposition of another intermediate, $\text{HCN}(\text{OH})$, which is 22.9 kcal/mol above CH_2NO . The predicted decomposition rate constants (in inverse seconds) for these two channels (Fig. 18) in the temperature range of 500–2000 K at two different pressures, 1 and 200 atm, could be expressed by the

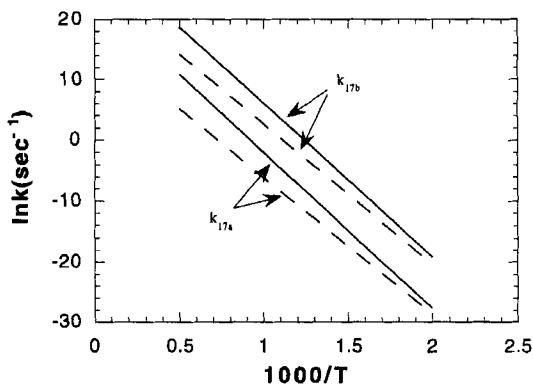


Fig. 18 Arrhenius plots of the rate constants for the unimolecular decomposition of CH_2NO producing different products: —, 200-atm pressure and ---, 1-atm pressure.

following Arrhenius expressions:

$$k_{17a} (1 \text{ atm}) = 1.21 \times 10^7 \exp(-22,450/T)$$

$$k_{17a} (200 \text{ atm}) = 1.77 \times 10^{10} \exp(-25,600/T)$$

$$k_{17b} (1 \text{ atm}) = 1.39 \times 10^{11} \exp(-23,000/T)$$

$$k_{17b} (200 \text{ atm}) = 3.53 \times 10^{13} \exp(-25,100/T)$$

The corresponding rate constants at the high- and the low-pressure limits can be expressed by the following Arrhenius expressions:

$$k_{17a}^{\infty} = 2.08 \times 10^{13} \exp(-29,450/T) \text{ s}^{-1}$$

$$k_{17b}^{\infty} = 3.13 \times 10^{15} \exp(-27,700/T) \text{ s}^{-1}$$

$$k_{17a}^0 = 2.0 \times 10^{13} T \exp(-19,650/T) \text{ cm}^3/(\text{mol} \cdot \text{s})$$

$$k_{17b}^0 = 8.49 \times 10^{10} T \exp(-22,700/T) \text{ cm}^3/(\text{mol} \cdot \text{s})$$

7. Unimolecular Decomposition of CH_2N

The isomerization and the decomposition of CH_2N and its related bimolecular processes in its doublet and quartet PESs, have been studied in detail recently by Sumathi and Nguyen.¹⁰⁶ They reported a dissociation energy of 23.3 kcal/mol for the decomposition channel,



at their best CCSD(T)/6-311++G(3df, 3dp)//CCSD(T)/6-311++G(d, p) level of theory. Their calculated decomposition transition state has a barrier of 32.0 kcal/mol with respect to CH_2N at the same level of theory. In both the cases, their calculation indicates an overestimation made by the earlier ab initio calculations of Bair and Dunning on the rate of CH_2N decomposition.¹⁰⁷ Furthermore, because of the existence of scattered experimental results for the heat of formation of CH_2N , from their calculated energetics, they recommended a value of 56–57 kcal/mol at 298 K (or 57–58 kcal/mol at 0 K) for the heat of formation of CH_2N . Our calculated dissociation energy, 23.9 kcal/mol, and the decomposition transition barrier, 30.5 kcal/mol, at the G2M(RCC,MP2) level of theory agree quite well with their calculated values and thus the heat of formation of CH_2N . The structure of the TS at the B3LYP/6-311g(d, p) level is loose (with the dissociating HC bond, 1.91 Å) compared with their UMP2 (1.638-Å) and CCSD(T) (1.794-Å) calculated structures. The isomerization of CH_2N to HCNH has a higher barrier of 45.1 kcal/mol, as they reported, and thus cannot compete with the decomposition reaction. Because our aim is to obtain the rate constant for the unimolecular reaction of CH_2N radical, we performed an RRKM calculation for the dominant decomposition channel with tunneling corrections by using our calculated molecular parameters and energies; the resulting Arrhenius expressions,

$$k_{18} (1 \text{ atm}) = 5.54 \times 10^9 \exp(-12,800/T) \text{ s}^{-1}$$

$$k_{18} (200 \text{ atm}) = 1.47 \times 10^{12} \exp(-14,000/T) \text{ s}^{-1}$$

are obtained in the temperature range of 500–2000 K. At the high- and the low-pressure limits these rate constants can be expressed as

$$k_{18}^{\infty} = 1.32 \times 10^{14} \exp(-16,200/T) \text{ s}^{-1}$$
$$k_{18}^0 = 3.75 \times 10^{11} T \exp(-10,800/T) \text{ cm}^3/(\text{mol} \cdot \text{s})$$

IV. Conclusions

In this chapter we have summarized the results of our recent theoretical studies on the reactions of some [C, H, N, O]-containing systems relevant to the combustion of nitramines, specifically ADN and RDX/HMX, in their early stages. In all these reactions, detailed information on the kinetics and mechanisms for barrierless radical–radical association processes as well as the subsequent isomerization and decomposition of excited association products are presented. Most of our theoretical results related to RDX/HMX systems are based on the recently calculated G2M (modified Gaussian-2) potential-energy profiles of these reactions. For reactions related to ADN combustion, a comprehensive description of the theoretical results obtained at our laboratory in the recent past with reference to other existing theoretical and experimental data has been made. Many of these processes have been mechanistically elucidated by us for the first time in this and earlier studies.

For many exothermic radical–radical reactions that cannot be readily measured experimentally, a key challenge is to predict quantitatively the absolute rate constants for the initial association reactions as well as for the formation of various products as a function of temperature and pressure. In this initial effort, we have attempted to address the problem quantitatively for several important reactions (such as $\text{NH} + \text{NO}_x$, $\text{CH}_2\text{N} + \text{NO}_x$, etc.) by using a canonical variational RRKM approach in conjunction with the G2M potential-energy profiles and the molecular parameters predicted by the hybrid density functional method. In this regard, further improvement may be achieved by performing a more rigorous and computationally more expensive treatment of microcanonical variational RRKM theory for the initial association processes as well as by introducing a more detailed treatment for isomerization/decomposition and energy transfer processes by solving the coupled master equations.

Most of the rate constants summarized here that are related to the RDX/HMX systems are computed for the first time. The accuracy of these values is difficult to assess because of the lack of experimental data. However, our successful prediction of the overall rate constants and product branching ratios in several analogous systems allows us to recommend with some confidence these calculated rate constants for the kinetic modeling of RDX/HMX combustion in their early stages.

Acknowledgments

The authors gratefully acknowledge the partial support of this work by the Caltech MURI project under the U.S. Office of Naval Research Grant N00014-95-1338, J. Goldwasser, program manager. We thank the Cherry L. Emerson Center for Scientific Computation for the use of computing facilities and various programs.

References

- ¹Ermolin, N. E., Korobeinichev, O. P., Kuibida, L. V., and Fomin, V. M., "Analysis of Chemical Processes in a Hexogen Flame," *Combustion, Explosion, and Shock Waves*, Vol. 24, No. 4, 1988, pp. 400–407.
- ²Davidson, J. E., and Beckstead, M. W., "A Three Phase Model of HMX Combustion," *Twenty-Sixth Symposium (International) on Combustion*, Vol. 2, Combustion Inst., Pittsburgh, PA, 1996, pp. 1989–1996.
- ³Melius, C. F., "Thermomechanical Modeling II. Application to Ignition and Combustion of Energetic Materials," *Chemistry and Physics of Energetic Materials*, edited by S. N. Bulusu, Kluwer Academic, Dordrecht, The Netherlands, 1990, pp. 51–78.
- ⁴Yetter, R. A., Dryer, F. L., Allen, M. T., and Gatto, L. J., "Development of Gas Phase Reaction Mechanisms for Nitramine Combustion," *Journal of Propulsion and Power*, Vol. 11, No. 4, 1995, pp. 683–697.
- ⁵Liau, Y.-C., and Yang, V., "Analysis of RDX Monopropellant Combustion with Two-Phase Subsurface Reactions," *Journal of Propulsion and Power*, Vol. 11, No. 4, 1995, pp. 729–739.
- ⁶Li, S. C., and Williams, F. A., "Nitramine Deflagration: Reduced Chemical Mechanism for Primary Flame Facilitating Simplified Asymptotic Analysis," *Journal of Propulsion and Power*, Vol. 12, No. 2, 1996, pp. 302–309.
- ⁷Davidson, J. E., and Beckstead, M. W., "Improvements to Steady-State Combustion Modeling of Cyclotrimethylenetrinitramine," *Journal of Propulsion and Power*, Vol. 13, No. 3, 1997, pp. 375–383.
- ⁸Prasad, K., Yetter, R. A., and Smooke, M. D., "An Eigenvalue Method for Computing the Burning Rates of RDX Propellants," *Combustion Science and Technology*, Vol. 124, No. 1–6, 1997, pp. 35–82.
- ⁹Pople, J. A., Head-Gordon, M., Fox, D. J., Raghavachari, K., and Curtiss, L. A., "Gaussian-1 Theory: A General Procedure for Prediction of Molecular Energies," *Journal of Chemical Physics*, Vol. 90, No. 10, 1989, pp. 5622–5629.
- ¹⁰Curtiss, L. A., Jones, C., Trucks, G. W., Raghavachari, K., and Pople, J. A., "Gaussian-1 Theory of Molecular Energies for Second-Row Compounds," *Journal of Chemical Physics*, Vol. 93, No. 4, 1990, pp. 2537–2545.
- ¹¹Curtiss, L. A., Raghavachari, K., Trucks, G. W., and Pople, J. A., "Gaussian-2 Theory for Molecular Energies of First- and Second-Row Compounds," *Journal of Chemical Physics*, Vol. 94, No. 11, 1991, pp. 7221–7230.
- ¹²Curtiss, L. A., Redfern, P. C., Raghavachari, K., and Pople, J. A., "Assessment of Gaussian-2 and Density Functional Theories for the Computation of Enthalpies of Formation," *Journal of Chemical Physics*, Vol. 106, No. 3, 1997, pp. 1063–1079.
- ¹³Curtiss, L. A., Raghavachari, K., Redfern, P. C., Rassolov, V., and Pople, J. A., "Gaussian-3 (G3) Theory for Molecules Containing First- and Second-Row Atoms," *Journal of Chemical Physics*, Vol. 109, No. 18, 1998, pp. 7764–7776.
- ¹⁴Pople, J. A., Head-Gordon, M., and Raghavachari, K., "Quadratic Configuration Interaction. A General Technique for Determining Electron Correlation Energies," *Journal of Chemical Physics*, Vol. 87, No. 10, 1987, pp. 5968–5975.
- ¹⁵Hehre, W., Radom, L., Schleyer, P. V. R., and Pople, J. A., *Ab Initio Molecular Orbital Theory*, Wiley, New York, 1986.
- ¹⁶Durant, L. J., and Rohlfing, C. M., "Transition State Structures and Energetics Using Gaussian-2 Theory," *Journal of Chemical Physics*, Vol. 98, No. 10, 1993, pp. 8031–8036.
- ¹⁷Mebel, A. M., Morokuma, K., and Lin, M. C., "Modification of the Gaussian-2 Theoretical Model: The Use of Coupled-Cluster Energies, Density Functional Geometries

and Frequencies," *Journal of Chemical Physics*, Vol. 103, No. 17, 1995, pp. 7414–7421.

¹⁸Purvis, G. D., and Bartlett, R. J., "A Full Coupled-Cluster Singles and Doubles Model: The Inclusion of Disconnected Triples," *Journal of Chemical Physics*, Vol. 76, No. 4, 1982, pp. 1910–1918.

¹⁹Hampel, C., Peterson, K. A., and Warner, H.-J., "A Comparison of the Efficiency and Accuracy of the Quadratic Configuration Interaction (QCISD), Coupled-Cluster (CCSD), and Brueckner Coupled-Cluster (BCCD) Methods," *Chemical Physics Letters*, Vol. 190, No. 1, 1992, pp. 1–12.

²⁰Knowels, P. J., Hampel, C., and Warner, H.-J., "Coupled-Cluster Theory for High Spin, Open Shell Reference Wave Functions," *Journal of Chemical Physics*, Vol. 99, No. 7, 1994, pp. 5219–5227.

²¹Degan, M. O. J., and Knowels, P. J., "Perturbative Corrections to Account for Tripple Excitations in Closed and Open Shell Coupled-Cluster Theories," *Chemical Physics Letters*, Vol. 227, No. 3, 1994, pp. 321–326.

²²Becke, A. D., "Density Functional Thermochemistry I. The Effect of the Exchange and Gradient Correction," *Journal of Chemical Physics*, Vol. 96, No. 3, 1992, pp. 2155–2160.

²³Becke, A. D., "Density Functional Thermochemistry II. The Effect of the Perdew-Wang Generalized-Gradient Correlation Correction," *Journal of Chemical Physics*, Vol. 97, No. 12, 1992, pp. 9173–9177.

²⁴Becke, A. D., "Density Functional Thermochemistry III. The Role of Exact Exchange," *Journal of Chemical Physics*, Vol. 98, No. 7, 1995, pp. 5648–5652.

²⁵Lee, C., Yang, W., and Parr, R. G., "Development of the Colle-Salvetti Correlation-Energy Formula into a Functional of the Electron Density," *Physical Review B*, Vol. 37, No. 2, 1988, pp. 785–789.

²⁶Gonzalez, C., and Schlegel, H. B., "An Improved Algorithm for Reaction Path Following," *Journal of Chemical Physics*, Vol. 90, No. 4, 1989, pp. 2154–2161.

²⁷Frisch, M. J., Trucks, G. W., Schlegel, H. B., Gill, P. M. W., Johnson, B. G., Robb, M. A., Cheeseman, J. R., Keith, T., Petersson, G. A., Montgomery, J. A., Raghavachari, K., Al-Laham, M. A., Zakrzewski, V. G., Ortiz, J. V., Foresman, J. B., Cioslowski, J., Stefanov, B. B., Nanayakkara, A., Challacombe, M., Peng, C. Y., Ayala, P. Y., Chen, W., Wong, M. W., Andres, J. L., Replogle, E. S., Gomperts, R., Martin, R. L., Fox, D. J., Binkley, J. S., Defrees, D. J., Baker, J., Stewart, J. P., Head-Gordon, M., Gonzalez, C., and Pople, J. A., "GAUSSIAN 94, Revision B.2," Gaussian, Inc., Pittsburgh, PA, 1995.

²⁸MOLPRO is a package of ab initio programs written by Werner, H.-J. and Knowels, P. J., with contributions from Almlöf, J., Amos, R. D., Deegan, M. J. O., Elbert, S. T., Hampel, C., Meyer, W., Peterson, K., Pitzer, R., Stone, A. J., Taylor, P. R., and Lindh, R.

²⁹Hsu, C. C., Mebel, A. M., and Lin, M. C., "Ab Initio Molecular Orbital Study of the HCO + O₂ Reaction. Direct Versus Indirect Abstraction Channels," *Journal of Chemical Physics*, Vol. 105, No. 6, 1996, pp. 2346–2352.

³⁰Garrett, B. C., and Truhlar, D. G., "Generalized Transition State Theory. Classical Mechanical Theory and Applications to Collinear Reactions of Hydrogen Molecules," *Journal of Physical Chemistry*, Vol. 83, No. 8, 1979, pp. 1052–1079.

³¹Garrett, B. C., and Truhlar, D. G., "Criterion of Minimum State Density in the Transition State Theory of Bimolecular Reactions," *Journal of Chemical Physics*, Vol. 70, No. 4, 1979, pp. 1593–1598.

³²Chakraborty, D., Park, J., and Lin, M. C., "Theoretical Study of the OH + NO₂ Reaction: Formation of Nitric Acid and the Hydroperoxy Radical," *Chemical Physics*, Vol. 231, No. 1, 1998, pp. 39–49.

³³Mebel, A. M., Lin, M. C., Morokuma, K., and Melius, C. F., "Theoretical Study of the Gas Phase Structure, Thermochemistry and Decomposition of NH_4NO_2 and $\text{NH}_4(\text{NO}_2)_2$," *Journal of Physical Chemistry*, Vol. 99, No. 18, 1995, pp. 6842–6848.

³⁴Politzer, P., and Seminario, J. M., "Computational Study of the Structure of Dinitraminic Acid, $\text{HN}(\text{NO}_2)_2$ and Energetics of Some Possible Decomposition Steps," *Chemical Physics Letters*, Vol. 216, No. 3, 1993, pp. 348–352.

³⁵Park, J., Chakraborty, D., and Lin, M. C., "Thermal Decomposition of Gaseous Ammonium Dinitramide at Low Pressure: Kinetic Modeling of Product Formation with Ab Initio MO/cVRRKM Calculations," *Twenty-Seventh Symposium (International) on Combustion*, Combustion Inst., Pittsburgh, PA, 1998, pp. 2351–2357.

³⁶Rossi, M. J., Bottaro, J. C., and McMillen, D. F., "The Thermal Decomposition of New Energetic Material Ammoniumdinitramide $\text{NH}_4\text{N}(\text{NO}_2)_2$ in Relation to Nitramide NH_4NO_2 and NH_4NO_3 ," *International Journal of Chemical Kinetics*, Vol. 25, No. 7, 1993, pp. 549–575.

³⁷Lin, M. C., and Park, J., "Kinetic Modeling of the Decomposition of Sublimed ADN Under Low-Pressure Conditions," *Proceedings of 1997 JANNAF Combustion Meeting*, CPIA Publ. 622, Vol. 2, Chemical Propulsion Information Agency, Columbia, MD, pp. 427–437.

³⁸Chakraborty, D., Hsu, C.-C., and Lin, M. C., "Theoretical Studies of Nitroamino Radical Reactions. Rate Constants for the Unimolecular Decomposition of $\text{HN}(\text{NO}_2)_2$ and Related Bimolecular Processes," *Journal of Chemical Physics*, Vol. 109, No. 20, 1998, pp. 8887–8896.

³⁹Harrison, J. A., and Maclagan, R. G. A. R., "Structures, Energies and Harmonic Vibrational Frequencies for the Reaction of NH with NO and NO_2 ," *Journal of the Chemical Society, Faraday Transactions*, Vol. 86, No. 21, 1990, pp. 3519–3523.

⁴⁰Melius, C. F., and Binkley, J. S., "Thermochemistry of the Decomposition of Nitramines in the Gas Phase," *Proceedings of the 21st Symposium on Combustion*, Combustion Inst., Pittsburgh, PA, 1988, pp. 1953–1963.

⁴¹Melius, C. F., "Thermomechanical Modeling II. Application to Ignition and Combustion of Energetic Materials," *Chemistry and Physics of Energetic Materials*, edited by S. N. Bulusu, Kluwer Academic, Dordrecht, The Netherlands, 1990, pp. 21–78.

⁴²Mebel, A. M., Morokuma, K., and Lin, M. C., "Ab Initio Molecular Orbital Study of Potential Energy Surface for the $\text{NH} + \text{NO}_2$ Reaction," *Journal of Chemical Physics*, Vol. 101, No. 5, 1994, pp. 3916–3922.

⁴³Diau, E. W. G., and Lin, M. C., "Theoretical Study of $\text{H}(\text{D}) + \text{N}_2\text{O}$: Effect of Pressure, Temperature and Quantum Mechanical Tunneling on $\text{H}(\text{D})$ -Atom Decay and $\text{OH}(\text{D})$ -Radical Productions," *Journal of Physical Chemistry*, Vol. 99, No. 17, 1995, pp. 6589–6594.

⁴⁴Hirschfelder, J. O., and Wigner, E., "Some Quantum Mechanical Considerations in the Theory of Reactions Involving an Activation Energy," *Journal of Chemical Physics*, Vol. 7, No. 1–12, 1939, pp. 616–628.

⁴⁵Miller, W. H., "Unified Statistical Model for 'Complex' and 'Direct' Reaction Mechanisms," *Journal of Chemical Physics*, Vol. 65, No. 6, 1976, pp. 2216–2223.

⁴⁶Harrison, J. A., Wayte, A. R., and Phillips, L. F., "Kinetics of Reaction of NH with NO and NO_2 ," *Chemical Physics Letters*, Vol. 129, No. 4, 1986, pp. 346–352.

⁴⁷Quandt, R. W., Hershberger, J. F., "Product Branching Ratios of the $\text{NH}({}^3\Sigma^-) + \text{NO}$ and $\text{NH}({}^3\Sigma^-) + \text{NO}_2$ Reactions," *Journal of Physical Chemistry*, Vol. 99, No. 46, 1995, pp. 16939–16944.

⁴⁸Mebel, A. M., and Lin, M. C., "Reactions of NO_x with Nitrogen Hydrides," *International Reviews in Physical Chemistry*, Vol. 16, No. 2, 1997, pp. 249–266.

⁴⁹Melius, C. F., and Binkley, J. S., "Energetics of the Reaction Pathways for Amidogen + Nitric Oxide \rightarrow Products and Imidogen + Nitric Oxide \rightarrow Products," *Proceedings of the 20th Symposium (International) on Combustion*, Combustion Inst., Pittsburgh, PA, 1985, pp. 575–583.

⁵⁰Marshall, P., Fontijn, A., and Melius, C. F., "High-Temperature Photochemistry and BAC-MP4 Studies of the Reaction Between Ground-State H Atoms and N_2O ," *Journal of Chemical Physics*, Vol. 86, No. 10, 1987, pp. 5540–5549.

⁵¹Durant, J. L., "Product Branching Fractions in the Reaction of $\text{NH}(\text{ND})$ ($^3\Sigma^-$) with NO ," *Journal of Physical Chemistry*, Vol. 98, No. 2, 1994, pp. 518–521.

⁵²Walch, S. P., "Theoretical Characterization of the Potential Energy Surface for $\text{NH} + \text{NO}$," *Journal of Chemical Physics*, Vol. 98, No. 2, 1993, pp. 1170–1177.

⁵³Baulch, D. L., Cobos, C. J., Cox, R. A., Esser, C., Frank, P., Just, Th., Kerr, J. A., Pilling, M. J., Troe, J., Walker, R. W., and Warnatz, J. J., "Evaluated Kinetic Data for Combustion Modelling," *Journal of Physical and Chemical Reference Data*, Vol. 21, No. 3, 1992, pp. 411–734.

⁵⁴Kristyan, S., and Lin, M. C., "Theoretical Calculations for Kinetics of the $\text{NH} + \text{NO}$ Reaction," *Chemical Physics Letters*, Vol. 297, No. 3–4, 1998, pp. 200–204.

⁵⁵Klippenstein, S. J., "An Efficient Procedure for Evaluating the No. of Available States Within a Variably Defined Reaction Coordinate Frame Work," *Journal of Physical Chemistry*, Vol. 98, No. 44, 1994, pp. 11459–11464.

⁵⁶Klippenstein, S. J., "Variational Optimization in the Rice–Ramsberger–Kassel–Marcus Theory Calculations for Unimolecular Dissociations with No Reverse Barrier," *Journal of Chemical Physics*, Vol. 96, No. 1, 1992, pp. 367–371.

⁵⁷Bedanov, V. M., Tsang, W., and Zachariah, M. R., "Master Equation Analysis of Thermal Activation Reactions: Reversible Isomerization and Decomposition," *Journal of Physical Chemistry*, Vol. 99, No. 29, 1995, pp. 11452–11457.

⁵⁸Park, J., and Lin, M. C., "Direct Determination of Product Branching for the $\text{NH}_2 + \text{NO}$ Reaction at Temperatures Between 302 and 1060 K," *Journal of Physical Chemistry*, Vol. 100, No. 9, 1996, pp. 3317–3319.

⁵⁹Park, J., and Lin, M. C., "Laser-Initiated NO Reduction by NH_3 : Total Rate Constant and Product Branching Ratio Measurements for the $\text{NH}_2 + \text{NO}$ Reaction," *Journal of Physical Chemistry A*, Vol. 101, No. 1, 1997, pp. 5–13.

⁶⁰Park, J., and Lin, M. C., "Mass-Spectrometric Determination of Product Branching Probabilities in the $\text{NH}_2 + \text{NO}_2$ Reaction at Temperatures Between 300 and 990 K," *International Journal of Chemical Kinetics*, Vol. 28, No. 12, 1996, pp. 879–883.

⁶¹Park, J., and Lin, M. C., "A Mass-Spectrometric Study of the $\text{NH}_2 + \text{NO}_2$ Reaction," *Journal of Physical Chemistry A*, Vol. 101, No. 14, 1997, pp. 2643–2647.

⁶²Park, J., and Lin, M. C., "Product Branching Ratios in the $\text{NH}_2 + \text{NO}$ Reactions: A Reevaluation," *Journal of Physical Chemistry A*, 1999 (to be published).

⁶³Glarborg, R. W., Dam-Johansen, K., and Miller, J. A., "The Reaction of Ammonia with Nitrogen Dioxide in a Flow Reactor: Implications for the $\text{NH}_2 + \text{NO}_2$ Reaction," *International Journal of Chemical Kinetics*, Vol. 27, No. 12, 1995, pp. 1207–1220.

⁶⁴Votsmeier, M., Song, S., Hanson, R. K., and Bowman, C. T., "A Shock Tube Study of the Product Branching Ratio for the Reaction $\text{NH}_2 + \text{NO}$ Using Frequency-Modulation Detection of NH_2 ," *Journal of Physical Chemistry A*, Vol. 103, No. 11, 1999, pp. 1566–1571.

⁶⁵Mebel, A. M., Diau, E. W. G., Lin, M. C., and Morokuma, K., "Theoretical Rate Constants for the $\text{NH}_3 + \text{NO}_x \rightarrow \text{NH}_2 + \text{HNO}_x$ ($x = 1, 2$) Reactions by Ab Initio MO/VTST Calculations," *Journal of Physical Chemistry*, Vol. 100, No. 18, 1996, pp. 7517–7525.

⁶⁶Roose, T. R., Hanson, R. K., and Kruger, C. H., "Decomposition of Nitric Oxide in the Presence of Ammonia," *Shock Tube Shock Wave Research, Proceedings of 11th International Symposium*, 1977, pp. 245–253.

⁶⁷Thaxton, A. G., Hsu, C.-C., and Lin, M. C., "Rate Constant for the $\text{NH}_3 + \text{NO}_2 \rightarrow \text{NH}_2 + \text{HONO}$ Reaction: Comparison of Kinetically Modelled and Predicted Results," *International Journal of Chemical Kinetics*, Vol. 29, No. 4, 1997, pp. 245–251.

⁶⁸Rosser, W. A., Jr., and Wise, H., "Gas-Phase Oxidation of Ammonia by Nitrogen Dioxide," *Journal of Chemical Physics*, Vol. 25, No. 5, 1956, pp. 1078, 1079.

⁶⁹Bedford, G., and Thomas, J. H., "Reaction Between Ammonia and Nitrogen Dioxide," *Journal of the Chemical Society, Faraday Transactions I*, Vol. 68, No. 12, 1972, pp. 2163–2170.

⁷⁰Musin, R. N., and Lin, M. C., "Novel Bimolecular Reaction Between NH_3 and HNO_3 in the Gas Phase," *Journal of Physical Chemistry*, Vol. 102, No. 10, 1998, pp. 1808–1814.

⁷¹Musin, R. N., and Lin, M. C., Manuscript under preparation.

⁷²Diau, E. W. G., Lin, M. C., He, Y., and Melius, C. F., "Theoretical Aspects of H/N/O-Chemistry Relevant to the Thermal Reduction of NO by H_2 ," *Progress in Energy Combustion Science*, Vol. 21, 1995, pp. 1–23.

⁷³Lin, M. C., He, Y., and Melius, C. F., "Theoretical Interpretation of the Kinetics and Mechanisms of the $\text{HNO} + \text{HNO}$ and $\text{HNO} + 2\text{NO}$ Reactions with a Unified Model," *International Journal of Chemical Kinetics*, Vol. 24, No. 5, 1992, pp. 489–516.

⁷⁴He, Y., and Lin, M. C., "Effects of Nitric Oxide on the Thermal Decomposition of Methoxy Nitrite: Overall Kinetics and Rate Constants for the $\text{HNO} + \text{HNO}$ and $\text{HNO} + 2\text{NO}$ Reactions," *International Journal of Chemical Kinetics*, Vol. 24, No. 8, 1992, pp. 743–760.

⁷⁵Cheskis, S. G., Nadochenko, V. A., and Sarkisov, O. M., "Study of the $\text{HNO} + \text{HNO}$ and $\text{HNO} + \text{NO}$ Reactions by Intracavity Laser Spectroscopy," *International Journal of Chemical Kinetics*, Vol. 13, No. 10, 1981, pp. 1041–1050.

⁷⁶Mebel, A. M., Morokuma, K., Lin, M. C., and Melius, C. F., "Potential Energy Surface of the $\text{HNO} + \text{NO}$ Reaction. An Ab Initio Molecular Orbital Study," *Journal of Physical Chemistry*, Vol. 99, No. 7, 1995, pp. 1901–1908.

⁷⁷Bunte, S. W., Rice, B. M., and Chabalowski, C. F., "An Ab Initio QCISD Study of the Potential Energy Surface for the Reaction $\text{HNO} + \text{NO} \rightarrow \text{N}_2\text{O} + \text{OH}$," *Journal of Physical Chemistry A*, Vol. 101, 1997, pp. 9430–9438.

⁷⁸Hinshelwood, C. N., and Mitchell, J. W., "The Reaction of Nitric Oxide with Hydrogen and with Deuterium," *Journal of the Chemical Society*, 1936, pp. 378–384.

⁷⁹Kaufman, F., and Decker, L. J., "Effect of Oxygen on the Thermal Decomposition of Nitric Oxide at High Temperatures," *Proceedings of Symposium (International) on Combustion*, Vol. 8, Combustion Inst., Pittsburgh, PA, 1959, p. 139.

⁸⁰Graven W. M., "Kinetics of the Homogeneous Reaction of NO and H_2 ," *Journal of the American Chemical Society*, Vol. 79, No. 13, 1957, pp. 3697–3700.

⁸¹Kee, R. J., Rupely, F. M., and Miller, J. A., "CHEMKIN-II, A Fortran Chemical Kinetics Package for the Analysis of Gas Phase Chemical Kinetics," Sandia National Lab., Rept. SAND87-8248, Albuquerque, NM, 1988.

⁸²Lutz, A. E., Kee, R. J., and Miller, J. A., "SENKIN, A Fortran Program for Predicting Homogeneous Gas Phase Chemical Kinetics with Sensitivity Analysis," Sandia National Lab., Rept. SAND87-8248, Albuquerque, NM, 1988.

⁸³Wilde, K. A., "Role of HNO in the Hydrogen-Nitric Oxide Reaction," *Combustion and Flame*, Vol. 13, No. 2, 1969, pp. 173–180.

⁸⁴Callear, A. B., and Carr, R. W., "Thermal Decomposition of Nitrosylhydride," *Journal of the Chemical Society, Faraday Transactions 2*, Vol. 71, No. 9, 1975, pp. 1603–1609.

⁸⁵Mebel, A. M., Lin, M. C., and Morokuma, K., "Ab Initio MO and TST Calculations for the Rate Constant of the $\text{HNO} + \text{NO}_2 \rightarrow \text{HONO} + \text{NO}$ Reaction," *International Journal of Chemical Kinetics*, Vol. 30, No. 9, 1998, pp. 729–736.

⁸⁶Mebel, A. M., Lin, M. C., and Melius, C. F., "Rate Constant of the $\text{HONO} + \text{HONO} \rightarrow \text{H}_2\text{O} + \text{NO} + \text{NO}_2$ Reaction from Ab Initio MO and TST Calculations," *Journal of Physical Chemistry A*, Vol. 102, No. 10, 1998, pp. 1803–1807.

⁸⁷Wayne, L. G., and Yost, D. M., "Kinetics of the Rapid Gas Phase Reaction Between NO , NO_2 and H_2O ," *Journal of Chemical Physics*, Vol. 19, No. 1, 1951, pp. 41–47.

⁸⁸Graham, R. F., and Tyler, B. J., "Formation of Nitrous Acid in a Gas-Phase Stirred Flow Reactor," *Journal of the Chemical Society, Faraday Transactions I*, Vol. 68, No. 4, 1972, pp. 683–688.

⁸⁹Cox, R. A., and Derwent, R. G., "The Ultraviolet Absorption Spectrum of Gaseous Nitrous Acid," *Journal of Photochemistry*, Vol. 6, No. 1, 1976, pp. 23–34.

⁹⁰Chan, W. H., Nordstrom, R. J., Calvert, J. G., and Shaw, J. H., "An IRFTS Spectroscopic Study of the Kinetics and the Mechanism of the Reactions in the Gaseous System HONO , NO , NO_2 , H_2O ," *Chemical Physics Letters*, Vol. 37, No. 3, 1976, pp. 441–446.

⁹¹Kaiser, E. W., and Wu, C. H., "A Kinetic Study of the Gas Phase Formation and Decomposition Reactions of Nitrous Acid," *Journal of Physical Chemistry*, Vol. 81, No. 18, 1977, pp. 1701–1706.

⁹²Hsu, C.-C., Lin, M. C., Mebel, A. M., and Melius, C. F., "Ab Initio Study of the $\text{H} + \text{HONO}$ Reaction: Direct Abstraction Versus Indirect Exchange Processes," *Journal of Physical Chemistry A*, Vol. 101, No. 1, 1997, pp. 60–66.

⁹³Boughton, J. W., Kristyan, S., and Lin, M. C., "Theoretical Study of the Reaction of Hydrogen with Nitric Acid: Ab Initio MO and TST/RRKM Calculations," *Chemical Physics*, Vol. 214, No. 2–3, 1997, pp. 219–227.

⁹⁴Berces, T., Forgeteg, S., and Marta, F., "Kinetics of Photolysis of Nitric Acid Vapour," *Transactions of the Faraday Society*, Vol. 66, No. 567, Pt. 3, 1970, pp. 648–655.

⁹⁵Morris, E. D., and Niki, H., "Mass Spectrometric Study of the Reactions of Nitric Acid with O Atoms and H Atoms," *Journal of Physical Chemistry*, Vol. 75, No. 20, 1971, pp. 3193, 3194.

⁹⁶Chapman, C. J., and Wayne, R. P., "The Reaction of Atomic Oxygen and Hydrogen with Nitric Acid," *International Journal of Chemical Kinetics*, Vol. 6, 1974, pp. 617–630.

⁹⁷Zhao, X., Hinsta, E. J., and Lee, Y. T., "Infrared Multiphoton Dissociation of RDX in a Molecular Beam," *Journal of Chemical Physics*, Vol. 88, No. 2, 1988, pp. 801–810.

⁹⁸Alexander, M. H., Dagdigian, P. J., Jacox, M. E., Kolb, C. E., and Melius, C. F., "Nitramine Propellant Ignition and Combustion Research," *Progress in Energy Combustion Science*, Vol. 17, No. 4, 1991, pp. 263–296.

⁹⁹Adams, G. F., and Shaw, R. W., Jr., "Chemical Reactions in Energetic Materials," *Annual Review of Physical Chemistry*, Vol. 43, 1992, pp. 311–340.

¹⁰⁰Mowrey, R. C., Page, M., Adams, G. F., and Lengsfeld, B. H., III, "Ab Initio Multireference Configuration Interaction Study of CH_2NNO_2 . HONO Elimination vs. NN Bond Fragmentation," *Journal of Chemical Physics*, Vol. 93, No. 3, 1990, pp. 1857–1864.

¹⁰¹Melius, C. F., and Binkley, J. S., "Thermochemistry of the Decomposition of Nitramines in the Gas Phase," *Twenty-First Symposium (International) on Combustion*, Combustion Inst., Pittsburgh, PA, 1986, pp. 1953–1963.

¹⁰²Rice, B. M., Adams, G. F., Page, M., and Thompson, D. L., "Classical Dynamics Simulations of Unimolecular Decomposition of CH_2NNO_2 : HONO Elimination vs

N–N Bond Scission,” *Journal of Physical Chemistry*, Vol. 99, No. 14, 1995, pp. 5016–5028.

¹⁰³Rice, B. M., Grosh, J., and Thompson, D. L., “Vibrational Mode Selectivity in the Unimolecular Decomposition of CH_2NNO_2 ,” *Journal of Chemical Physics*, Vol. 102, No. 22, 1995, pp. 8790–8799.

¹⁰⁴Chakraborty, D., and Lin, M. C., “Theoretical Studies of Methyleneamino (CH_2N) Radical Reactions. 1. Rate Constants and Product Branching Ratios for the $\text{CH}_2\text{N} + \text{N}_2\text{O}$ Process by Ab Initio Molecular Orbital/Statistical Theory Calculations,” *Journal of Physical Chemistry A*, Vol. 103, No. 5, 1999, pp. 601–606.

¹⁰⁵Saito, K., Makishita, K., Kakumoto, T., Sasaki, T., and Imamura, A., “Unimolecular Thermal Reaction of Formaldoxime at High Temperatures: Experiments and Calculations,” *Journal of Physical Chemistry*, Vol. 92, No. 15, 1988, pp. 4371–4374.

¹⁰⁶Sumathi, R., and Nguyen, M. T., “A Theoretical Study of the CH_2N System: Reactions in Both Lowest Lying Doublet and Quartet States,” *Journal of Physical Chemistry A*, Vol. 102, No. 41, 1998, pp. 8013–8020.

¹⁰⁷Bair, R. A., and Dunning, T. H., Jr., “Theoretical Studies of the Reactions of HCN with Atomic Hydrogen,” *Journal of Chemical Physics*, Vol. 82, No. 5, 1985, pp. 2280–2294.

Reactivity of Azide Polymer Propellants

Yoshio Oyumi*

Japan Defence Agency, Tokyo, Japan

I. Introduction

THE synthesis processes¹⁻¹⁰ and the properties¹¹⁻¹⁵ of azide polymers have recently been investigated to improve the performance of advanced solid rocket propellant. Although 3,3-bis(azidomethyl)oxetane (BAMO) is one of the most energetic polymers, polyBAMO shows relatively poor mechanical properties as a binder of solid rocket propellants because of its crystalline chain. So copolymerization with tetrahydrofuran (THF), 3-azidomethyl-3-methyloxetane (AMMO), or 3-nitratomethyl-3-methyloxetane (NMMO) has been studied to improve the mechanical properties at low temperatures and the burning-rate characteristics. The effect of the soft segment in the initiator system was studied in BAMO/NMMO copolymer (B/N), glycidyl azide polymer (GAP), and GAP/THF copolymer (G/T). The microstructure of B/N, thermal decomposition of copolymers, mechanical properties, and burning-rate characteristics are reported here.

II. Experiments

A. Structural Analysis

The ¹H-NMR and ¹³C-NMR spectra were obtained at 400 MHz using a JEOL JNM-GX400 spectrometer equipped with a Fourier transfer accessory. All spectra were collected at room temperature in a solution of CDCl₃ with an internal standard of tetramethyl silane.

B. Thermal Analysis

Thermogravimetric analysis (TGA) data were obtained using a Seiko SSC5200 TG/DTA220 with a helium flow rate of 150 ml/min. For isothermal runs the samples were heated to the experimental temperatures with a heating rate of 80 K/min and

Copyright © 1999 by the American Institute of Aeronautics and Astronautics, Inc. All rights reserved.

*Chief, Rocket Propulsion Research Function, Third Research Center, Technical Research and Development Institute.

then were kept at constant temperature for 30–240 min. The isothermal condition was obtained within 3 min after the heating was started. Each sample (1 mg) was unconfined in a small aluminum cell. Differential scanning calorimetric analysis (DSC) was made on a Seiko SSC5200 DSC120 with a 10 K/min heating rate. Each sample (0.5 mg) was confined in a small aluminum cell.

C. Burning-Rate and Temperature-Profile Measurements

The burning rates of the propellants were measured with a chimney-type strand burner pressurized with nitrogen. The size of the propellant strand was 7×7 mm in cross section and 70 mm in length. Three fuse wires were passed through the propellant strand in 15-mm intervals. The ignition of the strand was conducted by an electrically heated nichrome wire attached on the top of the propellant strand. To determine the process of heat feedback from the gas phase to the burning surface of the propellants, the temperature profile in a combustion wave was measured at 2 MPa with microthermocouples made of Pt-Pt10%Rh wires 5 μ m in diameter.

III. Results and Discussion

A. Microstructure of BAMO/NMMO Copolymer

One of the most promising polymers in this context is polyBAMO containing 50 wt% of nitrogen. BAMO is known to polymerize cationically, and its polymerization has already been studied.³ PolyBAMO was also thoroughly investigated for its crystallization behavior and the different ways to prevent it.¹⁶ Copolymerization of BAMO with substituted oxetanes containing azide groups is the most effective way to obtain a reduction of the crystallization tendency and the glass transition temperature of polyBAMO at the same time without decreasing the azide content of the copolymer.⁶ However, it is quite reasonable to expect that the polymer properties are affected not only by the composition of copolymer structures but also by their distribution and the arrangement of the BAMO units and NMMO units. Analysis of the bulk polymer microstructure by NMR methods is unsurpassed in its information content. Sequence distribution information can be studied in polyoxetane systems.

The ^1H -NMR spectrum of BAMO exhibited two peaks corresponding to the methylene proton belonging to the azidomethyl group ($\delta = 3.7$) and to the oxetane ring ($\delta = 4.4$) (Ref. 13). In the NMMO spectrum characteristic signals were observed at $\delta = 1.4$ (3H, singlet), 4.4 (4H, doublet), and 4.6 (2H, singlet).¹³ The spectrum of B/N(7/3), with molar ratio of monomer feed depicted in parenthesis, exhibited various peaks corresponding to the monomer unit, namely, $\delta = 1.0$ ($-\text{C}-\text{C}-\text{CH}_3$), 3.3 ($-\text{C}-\text{CH}_2\text{N}_3$, side group), 3.5 ($-\text{O}-\text{CH}_2-\text{C}-$, main chain), 3.7 ($-\text{C}-\text{CH}_2-\text{OH}$, terminal hydroxyl group), and 4.4 ($-\text{C}-\text{CH}_2-\text{ONO}_2$, nitratomethyl group).¹³ According to the proton signal intensities, the molar ratio observed in the NMR spectrum of B/N(7/3) was 68/32 (Ref. 13). The experimental molar ratios of B/N(8/2) and B/N(6/4) were 81/19 and 60/40, respectively. These results support the assumption that the copolymerization behaved like an ideal system, in the sense that the copolymer had approximately the same composition as the monomer feed. Although it was reported that the reactivity of NMMO is higher than that of BAMO,^{2,8} there was no difference in the reactivity of the monomers in the copolymerization.

Table 1 Relative compositions of triad microstructures for the BAMO units and the NMMO units (signals used for analysis were at $\delta = 70.2$ for BAMO and at 17.3 for NMMO)¹³

Copolymer	Triad	Measured, %	Theoretical, %
B/N(8/2)	BBB ^a	61	64
	BBN ^b	36	32
	NBN ^c	3	4
B/N(7/3)	BBB	48	49
	BBN	45	42
	NBN	7	9
B/N(6/4)	BBB	34	36
	BBN	51	48
	NBN	15	16
B/N(8/2)	BNB ^d	65	64
	NNB ^e	32	32
	NNN ^f	3	4
B/N(7/3)	BNB	56	49
	NNB	39	42
	NNN	6	9
B/N(6/4)	BNB	42	36
	NNB	47	48
	NNN	11	16

^aBBB: triad microstructure of BAMO–BAMO–BAMO.

^bBBN: triad microstructure of BAMO–BAMO–NMMO.

^cNBN: triad microstructure of NMMO–BAMO–NMMO.

^dBNB: triad microstructure of BAMO–NMMO–BAMO.

^eNNB: triad microstructure of NMMO–NMMO–BAMO.

^fNNN: triad microstructure of NMMO–NMMO–NMMO.

Triad distribution information is available in the ¹³C-NMR spectra.¹³ The relative composition of the microstructures of copolymers were analyzed using the ¹³C-NMR signal at $\delta = 70.2$ for the BAMO units and at 17.3 for the NMMO units. The triad microstructures were well separated to measure the intensities in these peaks.¹³ The relative compositions of the BAMO triads and the NMMO triads for three copolymers are indicated in Table 1.¹³ Experimental triad distributions are compared to those calculated for perfectly random polymers. The reactivity of NMMO is not equal to that of BAMO, but we assumed them to be equal in order to calculate the theoretical relative compositions. The relative compositions of triad microstructures for the copolymers are listed in Table 2.¹³ The arrangement of the monomer units in the copolymer chain was found to be almost the ideal system. All copolymers used here were random polymers. To improve the mechanical properties at low temperatures, a soft segment was applied in an initiator system of the BAMO or GAP copolymers. Even with a different initiator system, random structures were observed.¹⁷ Any block polymers were not used in this study, but have been applied to thermoplastic explosives.^{4,5,7,10}

B. Thermal Decomposition

Thermal decomposition studies on the azide polymers have been reported.^{18,19} Farber et al.¹⁸ determined the kinetics of decomposition of the azide group by

Table 2 Relative compositions of triad microstructures for the copolymers (Theoretical values are in parenthesis.)¹³

Triad	B/N(8/2)	B/N(7/3)	B/N(6/4)
BBB	48.8 (51.2)	33.6 (34.3)	20.4 (21.6)
BBN	28.8 (25.6)	31.5 (29.4)	30.6 (28.8)
NBN	2.4 (3.2)	4.9 (6.3)	9.0 (9.6)
BNB	13.0 (12.8)	16.8 (14.7)	16.8 (14.4)
NNB	6.4 (6.4)	11.7 (12.6)	18.8 (19.2)
NNN	0.6 (0.8)	1.8 (2.7)	4.4 (6.4)

monitoring the N₂ evolution from 5–50 mg of sample slowly heated in a vacuum effusion cell connected to a quadruple mass spectrometer. Rapid-scanning Fourier transform infrared spectroscopy (10 scans/s) was used to characterize the slow (5 K/min) and rapid (50–255 K/s) thermolysis of azide polymers at the applied pressure (1–1000 psi Ar) (Ref. 19). However, unlike C-nitro and N-nitro compounds, pressure and heating rate were found to exert relatively little influence on the product concentration of azide decomposition. The azide group decomposes before the polymer backbone does.¹⁹ However, polyBAMO was found to undergo simultaneous decomposition of its backbone structure, as indicated by the release of high concentrations of CH₂O, H₂O, and CO, and of side chains, by the large amounts of N₂, HCN, and some larger molecules.²⁰ In the flash pyrolysis of GAP mono-ol, GAP di-ol, GAP tri-ol, and GAP poly-ol, the volatile products identified from the condensed phase were CH₄, HCN, CO, C₂H₄, NH₃, CH₂O, CH₂CO, H₂O, and GAP oligomers.²¹ The NH₃ content increased with the –OH content, which suggested that NH₃ is primarily formed by the reaction of the end-chain azide groups.²¹ The initial step in the azide polymers is decomposition of the azide group producing N₂, and the initial decomposition process has been reported as first-order kinetics.^{12,18,19} However, for GAP tri-ol it was found using both variable heating rate and isothermal techniques that the decomposition kinetics was not a first-order process.²² Though the azide polymers contain relatively small amounts of oxygen, the heat release is considered to be because of the scission of the –N₃ bond structure to form N₂. Thermal decomposition of the polymer binder plays an important role in the combustion of solid propellants.

C. BAMO Copolymers

Effects of the soft segment on the decomposition kinetics of BAMO copolymers were studied by using THF, AMMO, and NMMO, which were selected as an inert unit, azide unit, and nitrate ester unit, respectively.²³ Three different molar ratios, 5/5, 6/4, and 7/3, were also studied in BAMO/THF copolymers (B/T).^{12,13} Azide group terminated GAP (GAPN₃) was compared with GAP.¹²

The kinetic parameters for thermal decomposition are listed in Table 3.^{12,13} The Arrhenius plots of the polymers are shown in Fig. 1. PolyBAMO and B/A(7/3) show exactly the same rates of decomposition. This shows that the reactivity of the BAMO unit was equal to that of the AMMO unit. B/T(7/3) showed a relatively

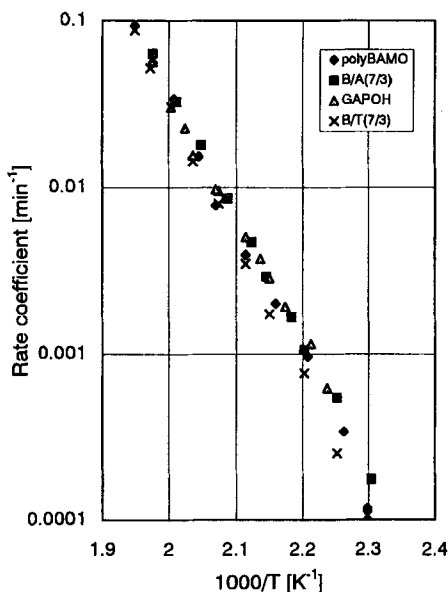
Table 3 Kinetic parameters for thermal decomposition of azidopolymers^{12,23}

Azidopolymer	Kinetic parameters
polyBAMO	$\ln k = 39.9 - 150700/RT$ (435–513 K)
B/A(7/3)	$\ln k = 40.9 - 154100/RT$ (425–516 K)
B/T(7/3)	$\ln k = 42.2 - 161000/RT$ (435–513 K)
B/T(6/4)	$\ln k = 40.7 - 156200/RT$ (456–511 K)
B/T(5/5)	$\ln k = 36.9 - 141300/RT$ (458–510 K)
GAP	$\ln k = 36.2 - 135700/RT$ (447–506 K)
GAPN ₃	$\ln k = 37.1 - 136700/RT$ (433–490 K)
B/N(7/3)	$\ln k_1 = 38.5 - 139700/RT$ (424–514 K) $\ln k_2 = 35.2 - 130700/RT$ (424–514 K)
polyNMMO	$\ln k = 42.1 - 149100/RT$ (425–503 K)

The dimension of activation energy E_a is in J/mol and the temperature ranges of isothermal decomposition are shown in parentheses.

slower rate of decomposition than polyBAMO. This indicates that the THF unit acted as a relatively inert and stable material in the polymer chain. GAP had the same rate of decomposition as polyBAMO with a relatively lower E_a . Because the thermal decomposition of the polymers is initiated by the decomposition of the azide group producing N_2 , almost exactly the same rate of decomposition was observed, as shown in Fig. 1.

The Arrhenius plots of B/T(5/5), B/T(6/4), and B/T(7/3) are shown in Fig. 2. The rate of decomposition of B/T(6/4) is almost the same as that of B/T(5/5)


Fig. 1 Arrhenius plots of the polymers.

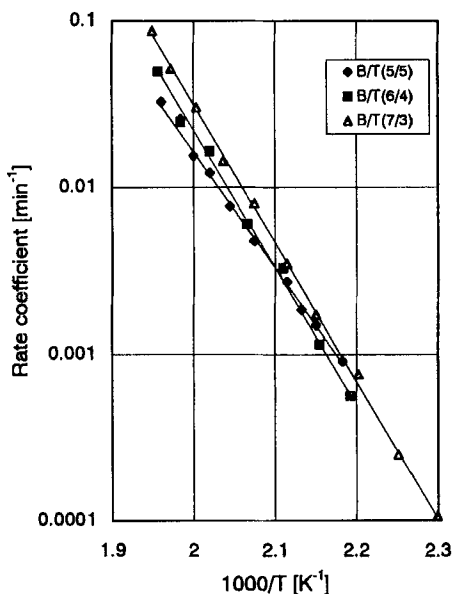


Fig. 2 Arrhenius plots of BAMO/THF copolymers.

with a slightly higher value of E_a . This shows that the additional azide groups in the main chain altered the decomposition kinetics of polymer sample. The azide group decomposed before the polymer backbone did at high-rate thermolysis, with heating rates of 50–255 K/s (Ref. 19), but simultaneous decomposition of its backbone structure was observed in rapid pyrolysis with a CO₂ laser²⁰ and heat fluxes of 100 and 400 W/cm². In this isothermal condition the decomposition characteristics of the azide group depend on that of the polymer backbone. B/T(6/4) has 10% more azide groups in the polymer chain than B/T(5/5). Although there were energy differences between the two, the rates of decomposition of B/T(5/5) and B/T(6/4) were almost the same. B/T(7/3) also showed a similar tendency. E_a increased with an increase in the BAMO content in the B/T.

The effect of the terminal structure of GAP on decomposition kinetics was examined.¹² The Arrhenius plots of GAP and GAPN₃ are shown in Fig. 3. Because of the presence of another azide group at the terminal position of the polymer chain, GAPN₃ showed a faster rate of decomposition than GAP. GAPN₃ has 10% more azide groups in the molecule than GAP, as in B/T(6/4) and B/T(5/5). However they had almost the same value of E_a . This result indicates that the azide groups at the terminal position of polymer chain decomposed independently of the polymer chain and other azide groups on the main chain.

PolyNMMO showed much faster rate of decomposition than polyBAMO, as shown in Fig. 4. The thermal stability of polyNMMO was much lower than that of polyBAMO in the temperature range between 425 and 513 K (Ref. 23). The decomposition reactions of polyNMMO occur in the condensed phase and initially produce highly reactive gases that percolate through the condensed phase before they reach the gas phase.²⁴ The azidomethyl group is also highly reactive and

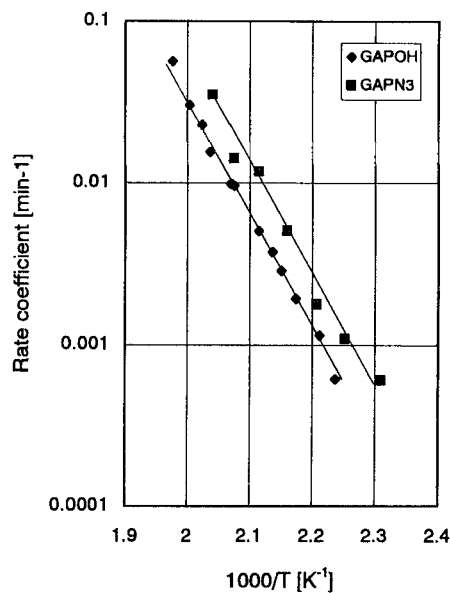


Fig. 3 Arrhenius plots of GAP.

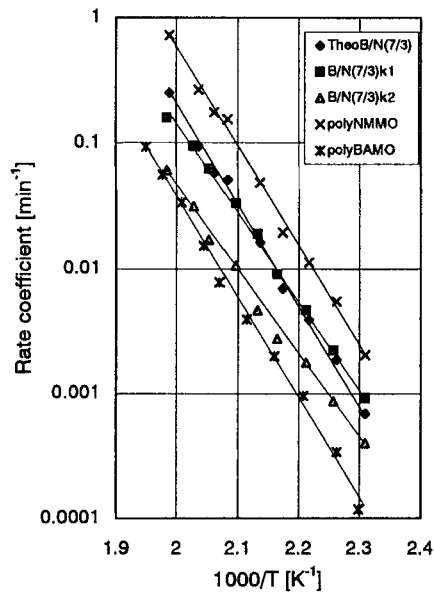


Fig. 4 Arrhenius plots of BAMO/NMMO copolymers.

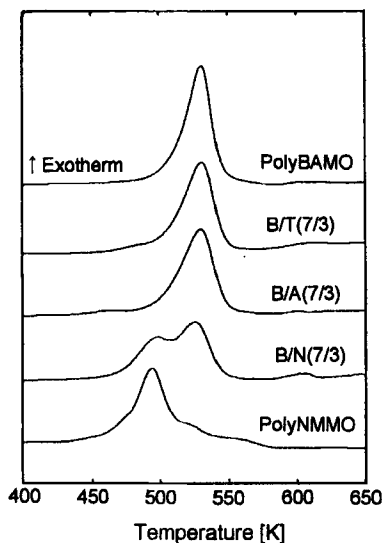


Fig. 5 DSC thermograms of the polymers.

produces N_2 and HCN. Both N_2 and HCN, however, are less reactive, and the rest of the molecule of the BAMO unit may also be less reactive with HONO and CH_2O , which are generated by the NMMO unit decomposition. Therefore, the BAMO unit and the NMMO unit decompose independently in the copolymer.^{13,23}

The kinetic parameter calculated by the equation of 0.7 polyBAMO + 0.3 polyNMMO [TheoB/N(7/3)] was $\ln k = 40.6 - 150200/RT$, and its curve overlapped with that of $\ln k_1$ for B/N(7/3), as shown in Fig. 4. The theoretical rate of decomposition curve shows that the reactions which are related to the NMMO unit decomposition dominate the copolymer decomposition over the whole temperature region. The decomposition of the nitratomethyl group initiated the backbone decomposition, and the bond cleavage of the oxetane chain was accelerated by the copolymerization with NMMO.

DSC thermograms of polymer samples are shown in Fig. 5. The peak temperatures were polyNMMO: 494 K; B/N(7/3): 498 and 526 K; B/A(7/3): 530 K; B/T(7/3): 531 K; and polyBAMO: 531 K (Ref. 23). The azide polymers show the same decomposition peak temperatures. This indicates that the decomposition reactions of the BAMO unit dominate those of the copolymers B/T and B/A. PolyAMMO shows its DSC exotherm peak temperature at 542 K, and its decomposition exotherm overlaps the BAMO exotherm. AMMO decomposition reactions were found to be accelerated by the heat generated by the BAMO unit decomposition. The decomposition peak temperature of polyNMMO was 37° lower than that of polyBAMO. The combination of 70% polyBAMO exotherm and 30% polyNMMO exotherm indicates that the heat generated by the NMMO unit decomposition activates the decomposition of the BAMO unit.¹³ On the other hand, the THF and AMMO units did not affect the thermal decomposition of the BAMO unit. The thermochemical characteristics of BAMO copolymers polymerized with THF or AMMO were the same as those of polyBAMO. THF and AMMO are,

therefore, good candidates for improving the physical properties, such as viscosity and glass transition temperature, of polyBAMO. AMMO is preferred from the energetic point of view, whereas THF is recommended from the viewpoint of mechanical properties.

D. Improvement of Mechanical Properties

B/T showed good mechanical properties at low temperature,⁷ but an increase in the amount of THF soft segment decreased the energy level of the copolymer. NMMO became an alternative soft segment of the BAMO copolymer, and B/N(7/3) showed relatively better thermal properties and sensitivity characteristics.¹³ 1,4-Butandiol/BF₃(C₂H₅)₂O was used as an initiator system. In this study more soft segment of the initiator system, hydroxyl-terminated polyester (PE)/BF₃(C₂H₅)₂O, was applied to improve the mechanical properties of B/N, and the compound was designated B/N/PE.

According to the ¹H-NMR spectrum analysis of B/N/PE,¹⁷ the molar ratio of each composition in the copolymer was B/N/PE = 7.4/2.6/0.39. The result indicates that the copolymer had approximately the same composition as the monomer fed, which was 7.0/3.0/0.33. ¹³C-NMR analysis showed that the arrangement of the monomer units in the copolymer chain was very nearly ideal, or a perfectly random conformation.

The tensile strength (TS) and the tensile elongation (TE) of the composite propellants, whose composition was 77% ammonium perchlorate (AP) and 23% binder for both copolymers, are shown in Fig. 6.¹⁷ The TE of B/N/PE propellant in the low-temperature region was larger than that of B/N propellant. The mechanical properties at low temperature were significantly improved by the PE application. The theoretical specific impulse (*I*_{sp}) of the B/N/PE propellant as calculated by the NASA code²⁵ was 2545 N · s at 10 MPa and 2566 N · s for the other propellant. The *I*_{sp} was decreased slightly, but the improvement of TE below 253 K played an important role in the case-bonding processability and the propellant grain design.^{26,27}

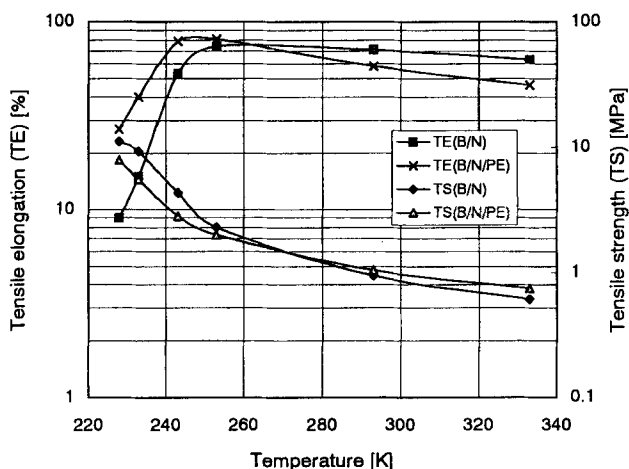


Fig. 6 Effect of soft segment in initiator system.¹⁷

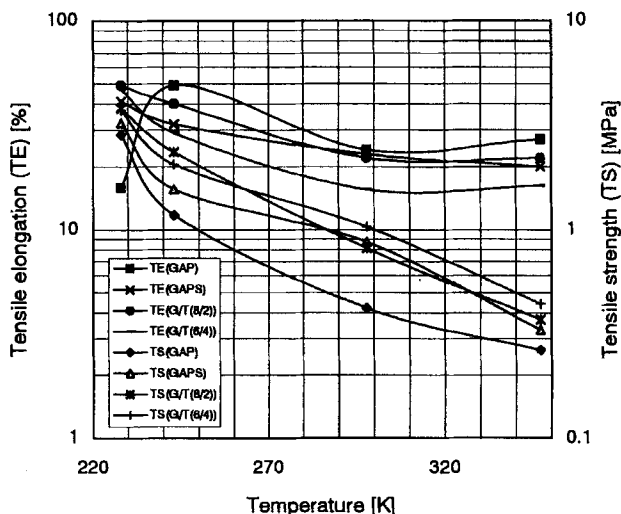


Fig. 7 Effect of soft segment in GAP.

The detailed viscoelasticity²⁸ and the properties at high strain rate²⁹ up to 2937 mm/min were also reported.

A similar technique was applied to GAP, which showed less of the plateau burning property but was cost effective. In addition to the soft segment in the initiator system (GAPS), the soft segment of THF was also copolymerized in the main chain with molar ratios of 8/2 and 6/4 for the GAP/THF copolymer (G/T), making G/T(8/2) and G/T(6/4) (Ref. 30). Each propellant composition was 75% AP, 11.9% binder, and 13.1% plasticizer. TE and TS are shown in Fig. 7 as a function of temperature. The structural modification and the plasticizer were very effective in the TE improvement at 228 K. Although GAP propellant had maximum TE at 243 K, other propellants with modified binder had maximum TE below 228 K. The modification significantly altered the glassification characteristic of the propellant viscoelasticity. G/T(8/2) showed a better TE property than G/T(6/4) in the temperature region tested, but G/T(6/4) was expected to have better TE below 228 K.

The mechanical properties at a strain rate of 50 mm/min were not related to the impact sensitivity of the solid rocket propellants.³¹⁻³⁵ Only fragmentation was observed at lower impact velocity, up to 172 m/s, even with 1-kg impactor.³⁴ Most of the propellants showed a linear relation between the impact velocity and the fragmented fraction. The critical impact velocity depended on the amount of the binder but not on the chemical structure.

IV. Burning Rate

A. BAMO/NMMO/AP Propellants

Although AP-based propellant shows high flammability in the insensitive-munitions characteristics,³⁵ its combustion characteristics are well understood,³⁶⁻⁴¹ and it is relatively easy to obtain a high burning rate, which is necessary for a high-performance rocket motor. AP-based composite propellants show

Table 4 Propellant compositions⁴¹

Sample	B/N ^a	AP ^b	Fe ₂ O ₃ ^f	Fe ₃ O ₄ ^f	ZrC ^g
1	20.0	80.0 ^c	—	—	—
2	20.0	79.9 ^c	0.1	—	—
3	19.8	79.2 ^c	1.0	—	—
4	19.4	77.7 ^c	2.9	—	—
5	19.4	77.7 ^c	—	2.9	—
6	21.9	73.3 ^c	2.9	—	1.9
7	22.1	74.0 ^d	1.9	—	1.9
8	22.5	75.4 ^e	0.1	—	2.0

^aBAMO/NMMO(7/3) binder.

^bAmmonium perchlorate, average diameter.

^c106 μm . ^d63 μm . ^e11 μm . ^fIron oxide. ^gZirconium carbide.

a complex flame structure.^{36–40} The heat release responsible for sustained burning occurs in three different kinds of reaction stages: 1) oxidizer exothermic decomposition at the burning surface reactions, 2) a leading edge of the oxidizer-fuel diffusion flame,³⁹ and 3) diffusion-limited flames between mixing oxidizer and fuel vapors. Some catalyzed AP-based azide composite propellants have a very low-pressure exponent of the burning rate. The site and mechanism of the plateau burning is currently a subject of controversy.

The burning-rate behavior of AP-based azide composite propellants and the condensed-phase chemistry were studied to elucidate the catalytic effect. The compositions of AP-based B/N (B/N/AP) propellants are listed in Table 4.⁴¹ Uncatalysed B/N/AP propellant strand showed unstable combustion at below 11 MPa, as shown Fig. 8. The propellant strand ignited by the electrically heated nichrome

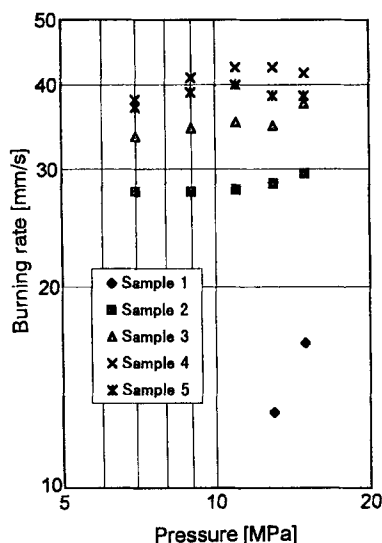


Fig. 8 Burning rate vs pressure for B/N/AP propellants with and without iron oxides (see Table 4 for propellant compositions).

wire burned 30 mm from the heating wire at pressures of 11–9 MPa and 10 mm at 7 MPa. Such an unfavorable characteristic disappeared when iron oxides were used as a burning rate catalyst. The suggestion was made that the burning rate was controlled by gas-phase reactions at high pressures because of the gas-phase heat release close to the burning surface.^{36–38} However, azide polymer exothermically decomposes at the burning surface, and the reaction scheme in the combustion wave structure might become complicated. Several investigators continue to emphasize the possibility that subsurface reactions might control or contribute measurably to the propellant burning rate.^{42,43} The catalyzed propellants studied here showed plateau-burning behavior.

The burning-rate augmentation was observed at 0.1% addition of Fe_2O_3 to the base propellant, as shown in Fig. 8. The burning rate increased with the increase in iron oxide content. Iron oxide became an increasingly effective catalyst as the weight percent of AP in the propellant was increased. At the higher pressures more gas-phase collisions between the catalyst and oxidizer, which was generated by AP decomposition, occurred in the region close to the burning surface. If iron oxide acted to increase only the reaction rate in the gas phase, therefore, the catalyst would be more effective at the higher pressures. However, catalyzed B/N/AP composite propellants showed plateau-burning characteristics, in which burning-rate augmentation was diminished at the higher pressures. Although the pressure limitation on the nitrogen-pressurized strand burner prevented burning-rate measurements above 15 MPa, catalyzed propellant showed a mesa-burning between 15 and 20 MPa in 80-mm-diam microrocket motor experiments.⁴¹

Fe_3O_4 also enhanced the burning rate but was less effective in the burning rate augmentation than Fe_2O_3 . However, the Fe_3O_4 -catalyzed propellant showed a lower pressure exponent of strand burning rate. The quantitative comparison of relative catalytic effectiveness in mechanistic terms is difficult when dealing with solid catalysts because the particle size and state of aggregation of each catalyst is different. Therefore, the same submicron-order particle size and the same propellant processing procedures were used for Fe_2O_3 and Fe_3O_4 -catalyzed propellant samples.

The TGA results of B/N/AP propellants with and without iron oxide are shown in Fig. 9. The TGA thermogram of sample 1 shows a slope break at around 10% weight loss, and the reaction mechanism changes at around 570 K. The initial stage of the thermal decomposition of sample 1 was dominated by B/N binder decomposition reaction, which was initiated by the nitrogen gas evolution from the azidomethyl group and NO_2 from the nitratomethyl group. The calculated weight loss for evolution of N_2 and NO_2 is 8%. The slope of the TGA thermogram from 10 to 40% and the weight-loss temperature region were significantly altered by the addition of iron oxide. This catalyst became increasingly effective as the iron oxide percent was increased. The onset temperature of the second-stage reaction, in which AP decomposition dominated, was lowered by the catalyst. Fe_3O_4 was more effective at the onset temperature of the second-stage reaction. However, there were no differences between the activation energies, which were 190 kJ/mol.

DSC thermograms of the propellant samples are shown in Fig. 10. The exotherm peak shifted to the lower-temperature region with an increase in the catalyst amount. The heats of decomposition measured by DSC were the following: sample 1, 7.5 kJ/mol; sample 2, 8.5 kJ/mol; sample 3, 9.1 kJ/mol; sample 4, 9.1 kJ/mol; and sample 5, 8.5 kJ/mol, respectively. The heat generated in the condensed phase

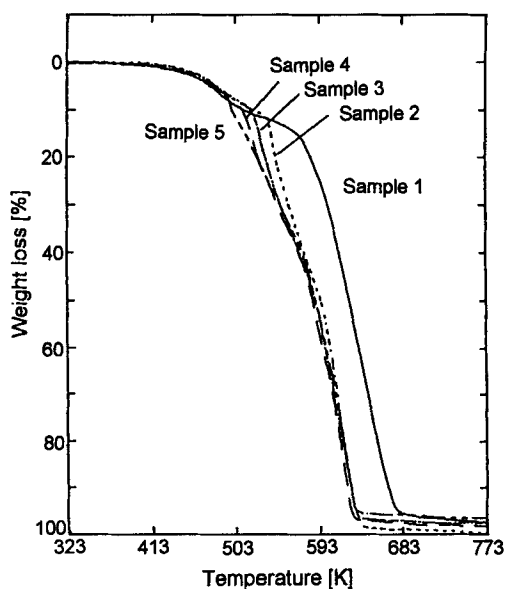


Fig. 9 TGA thermograms of B/N/AP propellants with and without iron oxides (see Table 4 for propellant compositions).

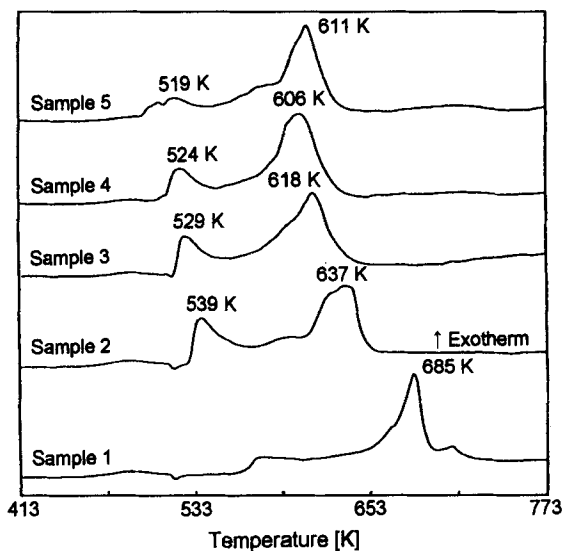


Fig. 10 DSC thermograms of B/N/AP propellants with and without iron oxides (see Table 4 for propellant compositions).

increased with the catalytic effect. Although the heat of decomposition measured by DSC is not identical to the heat value of the solid phase near the burning surface, it is expected that the trend of the magnitudes given by DSC measurement will be the same as the heat value. Taking account of the thermal equilibrium on the burning surface, these results indicate that the condensed phase plays an important role in the burning-rate equation.

The isothermal decompositions for the B/N prepolymer with Fe_2O_3 provide kinetic parameters of $\ln k_1 = 38.5 - 139800/RT$ and $\ln k_2 = 35.2 - 130800/RT$ in the temperature range of 424–514 K. The activation energy unit is in J/mol. These results indicate that the B/N binder decomposition reaction was only slightly affected by the addition of Fe_2O_3 (Refs. 23 and 41).

In the evolved gases of thermal decomposition, CO_2 was increased by the catalyst. This result indicates that Fe_2O_3 accelerated the oxidation of the binder. Infrared spectra of the gases in the final decomposition stage showed that oxidation of AP and fuel binder was significantly enhanced to produce CO. These results suggest that the accelerated oxidation reaction occurred in the condensed phase. A similar reaction mechanism was observed in AMMO/AP composite propellants.⁴⁴ Although Fe_2O_3 did not affect the onset temperature of the weight loss, it changed the profile of the TGA curve below the 25% weight-loss point⁴⁴ and showed a rapid weight loss between 520 and 560 K. Because Fe_2O_3 did not accelerate the thermal decomposition of the AMMO prepolymer,⁴⁵ the rapid weight loss was caused by the reaction between decomposed AMMO and AP. Fe_2O_3 catalyzed the AP decomposition or reaction of decomposed AMMO binder with AP.

The effect of AP particle size on the burning rate of B/N/AP propellant is shown in Fig. 11.²⁷ Although 106- and 63- μm propellants showed plateau-mesa burning and almost the same burning rate, very fine AP (11 μm) diminished the plateau burning at a pressure range between 9 and 15 MPa. This result indicates that the combustion mechanism of the propellant tested here was dominated by the particle size of AP. The structure of the combustion wave near the burning surface was influenced by the modification of AP particle size.

Plateau burning was observed even after accelerated aging of B/N/AP propellant at 333 K for 32 weeks.⁴⁶ The pressure range of the plateau burning moved to a higher pressure region with aging, which indicated that the reactions between AP

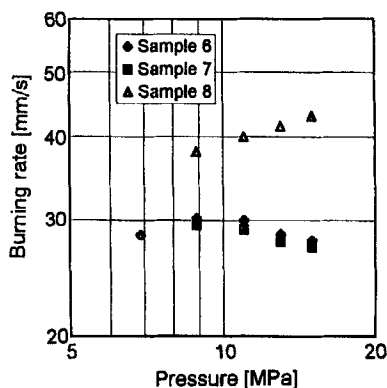


Fig. 11 Effect of AP particle size on the burning rate of B/N/AP propellants (see Table 4 for propellant compositions).²⁷

and the decomposed binder products that occurred in the condensed phase were altered by the change in binder reaction chemistry, which was generated by the aging.

B. BAMO/AMMO/AN Propellants

In the solid rocket propellant arena the desire for minimum signature (smoke and flame) has eliminated AP from consideration in a wide variety of applications. For increased specific impulse at reduced flame temperatures, a cyclic nitramine (HMX) was selected as an energetic material in the propellant ingredients.⁴⁷ The insensitivity of the solid rocket motor to several stimuli (e.g., bullet impact, cook-off) is also desired. From this point of view, ammonium nitrate (AN) is one of the strong candidates as solid oxidizer. However, HMX and AN have low burning rates coupled with a relatively high burning-rate exponent problem.^{47–50} The objective of this research program was to increase the burning rate of HMX and AN via the use of an energetic-binder material containing azide side chains and the addition of modifiers.⁵¹

The relation between the propellant burning rate and pressure at 293 K is shown in Fig. 12, where good linearity in the log scale, except in the case of sample 10, is seen. The compositions are listed in Table 5. The combination of ammonium dichromate and copper chromite was most effective at increasing the burning rate and lowering the pressure exponent.

The effects of the initial temperature of the propellant on the burning rate were measured at 243 and 343 K. The temperature sensitivities of the burning rate at 2 MPa in %/K were 0.425 for sample 9, 0.183 for samples 10 and 11, and 0.085 for sample 12. The catalytic effects were also observed on the temperature sensitivities, as shown in Fig. 13. The combined additive had the most effect on lowering the temperature sensitivity.

The TGA results of AN/HMX-based propellants with a heating rate of 0.17 K/s in helium are shown in Fig. 14. All propellants decomposed in the temperature range of 390–550 K. Observed weight losses in this region were 88% for sample 9, 91% for sample 10, 87% for sample 11, and 83% for sample 12. The slope of the

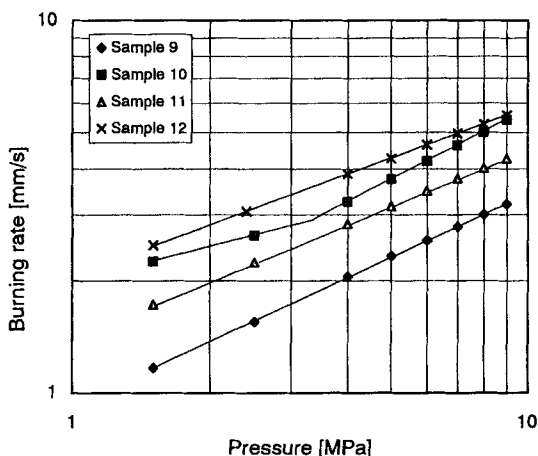


Fig. 12 Burning rate of BAMO/AMMO propellants (see Table 5 for propellant compositions).

Table 5 Propellant compositions

Sample	B/A ^a	AN ^b	HMX ^c	Cat. 1 ^d	Cat. 2 ^e
9	25.0	60.0	15.0	—	—
10	24.5	58.8	14.7	2.0	—
11	24.5	58.8	14.7	—	2.0
12	24.0	57.7	14.4	1.9	1.9
13	25.0	60.0	15.0	—	—

^aBAMO/AMMO(7/3) binder.^bAmmonium nitrate.^cCycrotetramethylene tetranitramine.^dAmmonium dichromate.^eCopper chromite.

weight-loss curve around 400 K was steeper in sample 12 than in sample 9 and was gentle in samples 10 and 11. All samples showed a slope break at a weight loss of 65%. This temperature region was consistent with that of AN decomposition reactions.^{52,53}

The DSC thermograms are shown in Fig. 15. There was no apparent exotherm in the 70% weight-loss temperature region shown in Fig. 14. Urbanski⁵² states that AN has six modes of decomposition and that these are all exothermic reactions, except the decomposition reaction to ammonia and nitric acid of scheme 6.

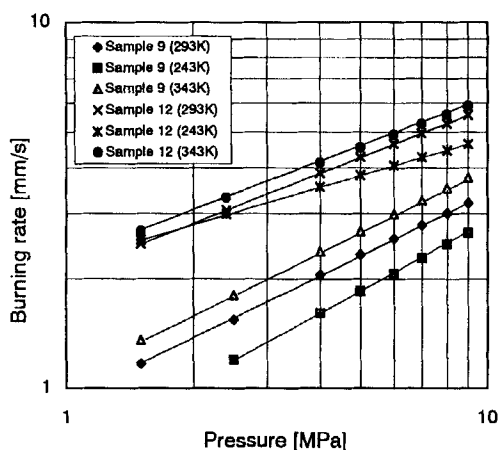
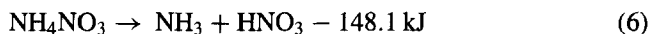
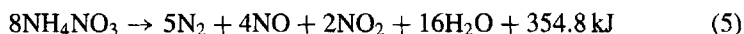
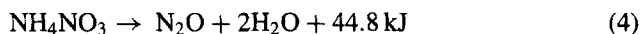
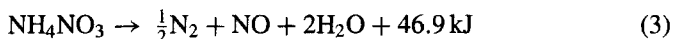
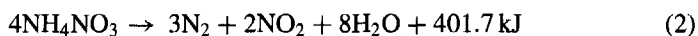
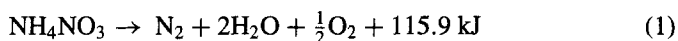


Fig. 13 Temperature sensitivity of BAMO/AMMO propellants (see Table 5 for propellant compositions).

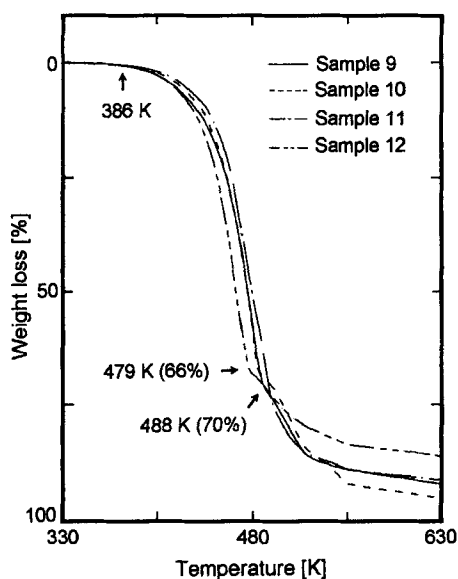


Fig. 14 TGA thermograms of B/A/AN propellants with and without additives (see Table 5 for propellant compositions).

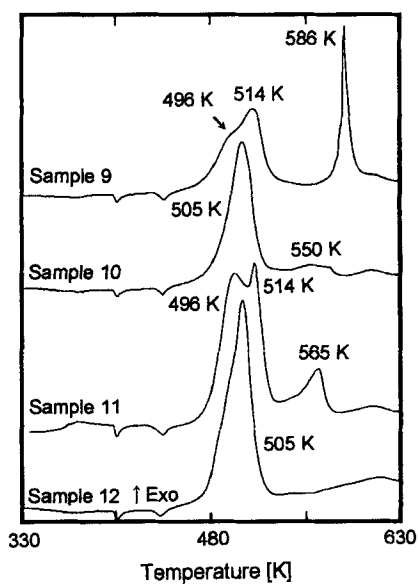


Fig. 15 DSC thermograms of B/A/AN propellants with and without additives (see Table 5 for propellant compositions).

Scheme 4 occurs above the melting point of 443 K, and scheme 3 only starts at 493 K. Fedoroff⁵³ reported 10 modes of decomposition reactions and states that the decomposition reaction of AN was significantly affected by the condition of the heating rate, confinement of sample cell, amount of sample, pressure, etc., and turned into a complicated reaction, which was the combination of several modes of the proposed reaction schemes. In sample 9 the endotherm and exotherm were relatively balanced in the solid phase and then more exothermic reaction occurred in the gas phase, showing a peak temperature at 505 K. Sample 9 showed two endotherms related to the phase transition of AN at 406 K and to the melting of AN at 443 K and two exotherms at around 500 and 586 K. According to the TGA thermogram, these exotherms mainly occurred in the gas-phase reaction. The exotherm at 586 K was removed by the additives used here. The additives also altered the shape of the peak at around 500 K. Especially in samples 10 and 12, ammonium dichromate sharpened this exotherm. The two exotherms were merged into single peak by the combination of ammonium dichromate and copper chromite.

The heats of decomposition measured by DSC for AN/HMX-based propellants were 2.88 kJ/mol for sample 9, 2.80 kJ/mol for sample 10, 2.89 kJ/mol for sample 11, and 2.84 kJ/mol for sample 12. There was no difference in the heat of decomposition of the propellants with and without catalysts.

AN and HMX interaction in the decomposition reaction is depicted in Figs. 16 and 17. The amount of the oxidizer was HMX/AN(65/10) and HMX/AN(15/60). Figure 16 shows AN separately decomposed from HMX, and the first stage was related to the decomposition of AN. In this temperature region the exothermic reactions mainly occurred in the gas phase.

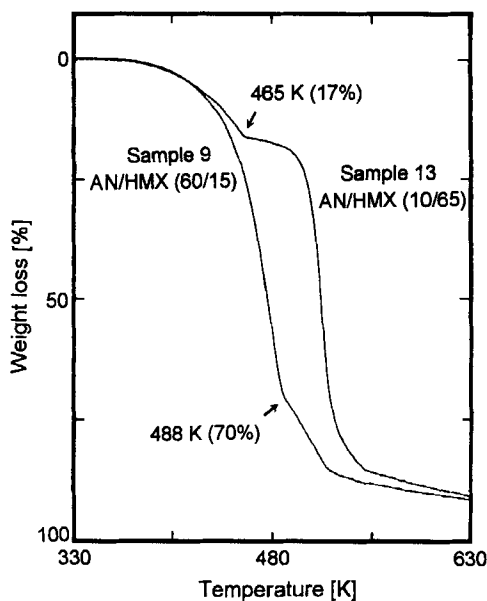


Fig. 16 Effect of AN/HMX concentration on the TGA thermogram.

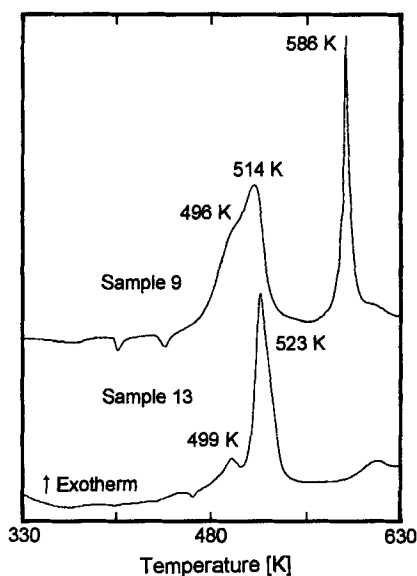


Fig. 17 Effect of AN/HMX concentration on the DSC thermogram.

The average burning-surface temperature T_s and the temperature gradients in the close-to-surface area of the gas phase $(dT/dx)_s$ are listed in Table 6. The $(dT/dx)_s$ of sample 9 was twice that of sample 13. According to the gas composition, the heat conductivity in the gas phase of sample 9 was not the same as that of sample 13. Therefore, the large $(dT/dx)_s$ might not be related to the large heat feedback to the burning surface. The melting of AN at the burning surface is also related to its slow burning rate. The T_s and $(dT/dx)_s$ were increased by the addition of ammonium dichromate. The observed increase in the burning rate agreed well with the increase in the heat flux into the condensed phase. The combined catalyst of ammonium dichromate with copper chromite was the most effective for the burning-rate augmentation. The $(dT/dx)_s$ of sample 12 was, however, similar to that of sample 9. This result indicates that the combined catalyst activated not only the gas-phase reactions but also the reactions occurring in the condensed phase.

Table 6 Average burning-surface temperatures and temperature gradients at 2 MPa

Sample	T_s , K	$(dT/dx)_s$, K/m
9	690	3.1×10^6
10	870	11.4×10^6
11	770	1.8×10^6
12	820	3.8×10^6

Table 7 Propellant compositions

Sample	GAP ^a	TMETN ^b	AN	NC ^c	HMX
14	20	20	60	—	—
15	15	15	70	—	—
16	15	15	60	10	—
17	15	15	40	30	—
18	15	15	40	—	30

^aGAP binder.^bTrimethylolethane trinitrate.^cNitrocellulose microsphere.

C. GAP/AN Propellants

GAP and AN were chosen as an energetic binder and main oxidizer.⁵⁴ HMX, nitrate esters (NC and TMETN), and AP were used as co-oxidizers. Sample propellant compositions are listed in Table 7. The effects of nitrate esters on the burning rate of GAP/AN propellant were evaluated here. The strand burning rates are shown in Fig. 18. The higher AN content propellant, sample 15, showed a lower burning rate than sample 14. The I_{sp} of sample 15, calculated by the NASA-SP-273 code,²⁵ was 2453 N · s at 10 MPa and 2406 N · s for sample 14. Although a higher I_{sp} propellant tends to show higher burning rate, the endotherm at the burning surface, which was caused by the melting and sublimation of AN, played an important role in the lower burning rate of the AN composite propellants. The effect of NC was observed in samples 16 and 17. The burning rate became higher

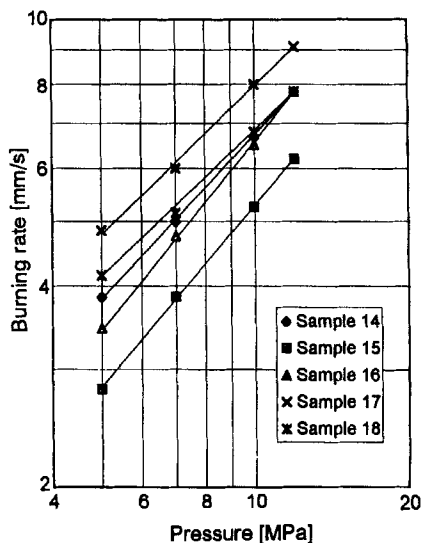


Fig. 18 Burning rate of GAP/AN propellants co-oxidized by nitrate ester or HMX (see Table 7 for propellant compositions).

Table 8 Propellant compositions

Sample	B/N	AN	HMX	AP	Fe ₃ O ₄	Cat. 2	Cat. 3 ^a	Cat. 4 ^b
19	24.5	58.8	14.7	—	—	—	2.0	—
20	23.8	57.1	14.7	—	—	2.9	—	1.9
21	23.8	57.1	9.5	4.8	—	2.9	—	1.9
22	26.7	52.5	14.9	5.0	1.0	—	—	—

^aChromium oxide.

^bButacene, ferrocenyl grafted hydroxyl terminated polybutadiene.

with the replacement of AN with NC. Casting powder was also a very effective ballistic modifier that provided useable burning rates and pressure exponent (~ 0.5) for minimum signature propellant based on AN.⁵⁴ The addition of HMX was effective on the I_{sp} increase, and the I_{sp} of sample 17, 2345 N · s at 10 MPa, was changed to 2512 N · s by the replacement of NC with HMX, sample 18. The burning rate decreased, however, with the increase in HMX. The nitrate ester plasticizer TMETN increased the burning rate of GAP/AN propellants. NC was also effective in augmenting the propellant burning rate.

D. BAMO/NMMO/AN Propellants

The burning rates of BAMO/NMMO/AN (B/N/AN) propellants, whose compositions are listed in Table 8, are shown in Fig. 19. Chromium oxide is a common burning rate modifier for AN-based propellants. The combined catalyst of

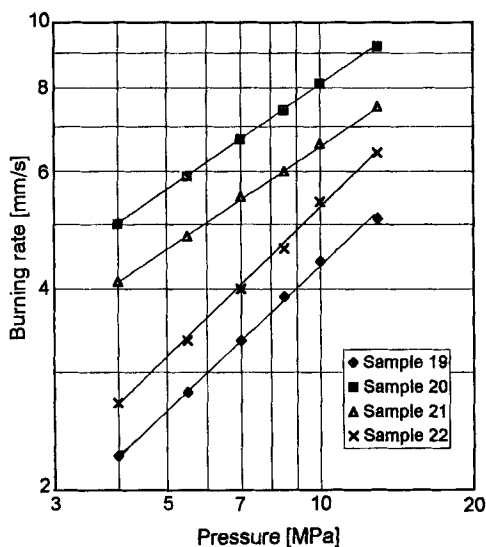


Fig. 19 Burning rates of B/N/AN propellants (see Table 8 for propellant compositions).

copper chromite and butacene was effective in increasing the burning rates. The ammonium dichromate with copper chromite was also effective in the B/A/AN propellants,⁵¹ in which the combined catalyst activated not only the gas-phase reactions but also the reactions occurring in the condensed phase. The replacement of HMX with AP altered the reaction mechanism of the combined catalyst, and the burning rate was decreased by approximately 15% at 10 MPa. The pressure exponent was increased approximately 0.08 by the replacement. These results indicate that the reaction mechanisms of the burning rate of AN propellants were influenced by AP reactions.

A higher BAMO ratio in the binder caused a faster burning rate in the HMX-based B/N propellants.⁵⁵ The burning rate was proportional to the calculated energy level of the propellant, but AN-based propellant showed complicated burning characteristics. A linear relationship between the critical shock pressure in the Card Gap test and the oxygen balance was found in solid rocket propellants.⁵⁶ However, various types of azide polymer binders can effect the burning rates of AN propellant differently.

V. Conclusions

1) The copolymerization of BAMO with NMMO behaved like an ideal system, in the sense that the copolymer had approximately the same composition as the monomer fed during synthesis. The microstructures of copolymers were shown to be truly random.

2) Because the thermochemical characteristics of BAMO copolymers with THF or AMMO were the same as those of polyBAMO, we conclude that the thermal stability of the BAMO unit controls the thermal characteristics of the copolymers.

3) The main chain cleavage of the NMMO unit occurred in the B/N, but both units independently decomposed. The theoretical rate coefficient of decomposition showed that the reactions related to the NMMO unit decomposition played a dominant role in the copolymer decomposition over the whole temperature range used.

4) The additional azide groups at the terminal position or main chain position in the molecular structure produced about a 10% energy increase. The additional azide at terminal position decomposed independently and increased the overall rate of decomposition of the polymer. However, azide groups in the main chain altered the decomposition kinetics of the polymer.

5) A soft segment in the initiator system and/or main chain was very effective in improving the mechanical properties at low temperature.

6) The heat balance at the burning surface of B/N/AP propellants was shown to be unstable below 11 MPa. However, the addition of iron oxide catalysts altered the burning property of the propellant and enhanced the burning rate with plateau-mesa burning characteristics. Such pressure insensitiveness of the burning rate indicates that the condensed-phase chemistry played an important role in the catalytic activity of iron oxides.

7) The ammonium dichromate with copper chromite significantly increased the burning rate of B/A/AN propellant, with a favorable decrease in the pressure exponent. It is possible that the catalyst not only participates in the gas-phase reactions but also enhances the condensed-phase reactivity.

8) TMETN acted as an excellent energetic plasticizer to GAP/AN propellant and was also effective on the burning-rate augmentation in combination with NC.

References

- ¹Frankel, M. B., Wilson, E. R., Wooley, D. O., and Hamermesh, C. L., "Energetic Azido Compounds," National Technical Information Service Final Rept. to Office of Naval Research, AD-A110292, Arlington, VA, Jan. 1982.
- ²Manser, G. H., Fletcher, R. W., and Knight, M. R., "High Energy Binders," Final Rept. to Office of Naval Research, ONR Contract N00014- 82-C-0800, Arlington, VA, May 1985.
- ³Manser, G. H., and Ross, D. L., "Synthesis of Energetic Polymer," Office of Naval Research Rept. AD-A107498, Arlington, VA, Oct. 1981.
- ⁴Xu, B., Lin, Y. G., and Chien, J. C. W., "Energetic ABA and (AB)_n Thermoplastic Elastomers," *Journal of Applied Polymer Science*, Vol. 46, 1992, pp. 1603-1608.
- ⁵Talukder, M. A. H., and Lindsay, G. A., "Synthesis and the Preliminary Analysis of Block Copolymers of 3,3-Bis(azidomethyl)-Oxetane and 3-Nitratomethyl-3'-Methyloxetane," *Journal of Polymer Science, Part A: Polymer Chemistry*, Vol. 28, 1990, pp. 2393-2402.
- ⁶Cheradame, H., and Gojon, E., "Synthesis of Polymers Containing Pseudohalide Groups by Cationic Polymerization. 2. Copolymerization of 3,3-Bis(azidomethyl)Oxetane with Substituted Oxetanes Containing Azide Groups," *Macromolecular Chemistry*, Vol. 192, 1991, pp. 919-927.
- ⁷Ling, L. Y., Ho, H. G., and Chum, C. Y., "Preparation and Properties of BAMO/THF Triblock Copolymers," *Proceedings of 24th International Annual Conference of Institute of Chemical Technology*, Fraunhofer-Institut für Chemische Technologies, Pfinztal-Berghausen, Germany, 1993, pp. 10.1-10.11.
- ⁸Xu, B., Lillya, C. P., and Chien, J. C. W., "Spiro(benzoxasilole) Catalized Polymerization of Oxetanes," *Journal of Polymer Science, Part A: Polymer Chemistry*, Vol. 30, 1992, pp. 1899-1904.
- ⁹Manser, G. E., "The Development of Energetic Oxetane Polymers," *Proceedings of 21st International Annual Conference of Institute of Chemical Technology*, Fraunhofer-Institut für Chemische Technologies, Pfinztal-Berghausen, Germany, 1990, pp. 50.1-50.13.
- ¹⁰Hsiue, G.-H., Liu, Y.-L., and Chiu, Y.-S., "Triblock Copolymers Based on Cyclic Ethers: Preparation and Properties of Tetrahydrofuran and 3,3-Bis(azidomethyl)Oxetane Triblock Copolymers," *Journal of Polymer Science, Part A: Polymer Chemistry*, Vol. 32, 1994, pp. 2155-2166.
- ¹¹Chen, J. K., and Brill, T. B., "Thermal Decomposition of Energetic Materials 54. Kinetics and Near-Surface Products of Azide Polymers AMMO, BAMO, and GAP in Simulated Combustion," *Combustion and Flame*, Vol. 87, No. 2, 1991, pp. 157-168.
- ¹²Oyumi, Y., "Thermal Decomposition of Azide Polymer," *Propellant, Explosives, Pyrotechnics*, Vol. 17, No. 4, 1992, pp. 226-231.
- ¹³Kimura, E., Oyumi, Y., Kawasaki, H., Maeda, Y., and Anan, T., "Characterization of BAMO/NMMO Copolymers," *Propellant, Explosives, Pyrotechnics*, Vol. 19, No. 5, 1994, pp. 270-275.
- ¹⁴Brill, T. B., and Brush, P. J., "Condensed Phase Chemistry of Explosives and Propellants at High Temperature: HMX, RDX and BAMO," *Philosophical Transactions of the Royal Society of London, Series A: Mathematical and Physical Science*, Vol. 339, 1992, pp. 377-385.

¹⁵Hsieh, W. H., Peretz, A., Huang, I. T., and Kuo, K. K., "Combustion Behavior of Boron-Based BAMO/NMMO Fuel-Rich Solid Propellants," *Journal of Propulsion*, Vol. 7, No. 2, 1991, pp. 497–504.

¹⁶Hardenstine, K. E., Henderson, G. V. S., Sperling, L. H., Murphy, C. J., and Manser, G. E., "Crystallization Behavior of Poly[3,3-bis(ethoxymethyl)oxetane] and Poly[3,3-bis(azidomethyl)oxetane]," *Journal of Polymer Science, Polymer Physics Edition*, Vol. 23, 1985, pp. 1597–1608.

¹⁷Kawasaki, H., Anan, T., Kimura, E., and Oyumi, Y., "BAMO/NMMO Copolymer with Polyester Initiation," *Propellants, Explosives, Pyrotechnics*, Vol. 22, 1997, pp. 87–92.

¹⁸Farber, M., Harris, S. P., and Srivastava, R. D., "Mass Spectrometric Kinetic Studies on Several Azido Polymers," *Combustion and Flame*, Vol. 55, No. 2, 1984, pp. 203–211.

¹⁹Oyumi, Y., and Brill, T. B., "Thermal Decomposition of Energetic Materials 12. Infrared Spectral and Rapid Thermolysis Studies of Azide-Containing Monomers and Polymers," *Combustion and Flame*, Vol. 65, No. 2, 1986, pp. 127–135.

²⁰Lee, Y. J., Tang, C.-J., Kudva, G., and Litzinger, T. A., "Thermal Decomposition of 3,3'-Bis-Azidomethyl-Oxetane," *Journal of Propulsion and Power*, Vol. 14, No. 1, 1998, pp. 37–44.

²¹Arisawa, H., and Brill, T. B., "Thermal Decomposition of Energetic Materials 71: Structure-Decomposition and Kinetic Relationships in Flash Pyrolysis of Glycidyl Azide Polymer (GAP)," *Combustion and Flame*, Vol. 112, No. 4, 1998, pp. 533–544.

²²Jones, D. E. G., Malechaux, L., and Augsten, R. A., "Thermal Analysis of GAPTRIOL, An Energetic Azide Polymer," *Thermochimica Acta*, Vol. 242, No. 2, 1994, pp. 187–197.

²³Kimura, E., and Oyumi, Y., "Thermal Decomposition of BAMO Copolymers," *Propellants, Explosives, Pyrotechnics*, Vol. 20, No. 6, 1995, pp. 322–326.

²⁴Oyumi, Y., and Brill, T. B., "Thermal Decomposition of Energetic Materials 22. The Contrasting Effects of Pressure on the High-Rate Thermolysis of 34 Energetic Compounds," *Combustion and Flame*, Vol. 68, No. 2, 1987, pp. 209–216.

²⁵Gordon, S., and McBride, B. J., "Computer Program for Calculation of Complex Chemical Equilibrium Compositions, Rocket Performance, Incident and Reflected Shocks, and Chapman-Jouguet Detonations," NASA SP-273, N71-37775, 1971.

²⁶Nagayama, K., and Oyumi, Y., "Combustion Characteristics of High Burn Rate Azide Polymer Propellant," *Propellants, Explosives, Pyrotechnics*, Vol. 21, 1996, pp. 74–78.

²⁷Oyumi, Y., and Nagayama, K., "Development of High Burn Rate Azide Polymer Propellant," *Journal of Energetic Materials*, Vol. 15, No. 1/2, 1997, pp. 59–69.

²⁸Oyumi, Y., "Mechanical Properties of Plateau Burn Azide Composite Propellants," *Journal of Energetic Materials* (to be published).

²⁹Nagayama, K., and Oyumi, Y., "Mechanical Properties of Azide Polymer Propellant at Ignition Stage," *Journal of Energetic Materials*, Vol. 15, No. 1/2, 1997, pp. 47–57.

³⁰Tanaka, T., and Hirata, T., "Characterization of GAP/AN Composite Propellants," *Kayaku Gakkaishi* (to be published).

³¹Oyumi, Y., Kimura, E., and Nagayama, K., "Initiation and Detonation Properties of Azide Polymer Propellants," *Kayaku Gakkaishi*, Vol. 55, No. 5, 1994, pp. 194–201.

³²Oyumi, Y., and Kimura, E., "IM Characteristics of GAP/AN Composite Propellants," *Kayaku Gakkaishi*, Vol. 57, No. 1, 1996, pp. 9–13.

³³Kimura, E., and Oyumi, Y., "IM Characteristics of BAMO/NMMO Composite Propellants," *Kayaku Gakkaishi*, Vol. 57, No. 1, 1996, pp. 14–20.

³⁴Oyumi, Y., Kimura, E., and Nagayama, K., "Impact Sensitivity of Azide Polymer Composite Propellants," *Propellants, Explosives, Pyrotechnics*, Vol. 23, No. 3, 1998, pp. 123–127.

³⁵Kimura, E., and Oyumi, Y., "Sensitivity of Azide Polymer Propellants in Fast Cook-off, Card Gap, and Bullet Impact Tests," *Journal of Energetic Materials*, Vol. 15, No. 3/4, 1997, pp. 163-178.

³⁶Summerfield, M., Sutherland, G. S., Webb, M. J., Taback, H. J., and Hall, K. P., *Burning Mechanism of Ammonium Perchlorate Propellants*, edited by M. Summerfield, Vol. 1, ARS Progress in Astronautics and Rocketry: Solid Propellant Rocket Research, Academic International Press, New York, 1960, pp. 141-182.

³⁷Bastress, E. K., Hall, K. P., and Summerfield, M., "Modification of the Burning Rates of Solid Propellants by Oxidizer Particle Size Control," American Rocket Society Paper 1597-61, 1961.

³⁸Adams, G. K., Newman, B. H., and Robins, A. B., "The Combustion of Propellants Based Upon Ammonium Perchlorate," *Proceedings of Eighth Symposium (International) on Combustion*, Williams and Wilkins, Baltimore, MD, 1962, pp. 693-705.

³⁹Price, E. W., Sambamurthi, J. K., Sigman, R. K., and Panyam, R. R., "Combustion of Ammonium Perchlorate-Polymer Sandwiches," *Combustion and Flame*, Vol. 63, No. 3, 1986, pp. 381-413.

⁴⁰DeLuca, L., Price, E. W., and Summerfield, M., *Nonsteady Burning and Combustion Stability of Solid Propellants*, edited by K. K. Kuo, Vol. 143, Progress in Astronautics and Aeronautics, AIAA, Washington, DC, 1992.

⁴¹Oyumi, Y., Anan, T., Bazaki, H., and Harada, T., "Plateau Burning Characteristics of AP Based Azide Composite Propellants," *Propellants, Explosives, Pyrotechnics*, Vol. 20, No. 3, 1995, pp. 150-155.

⁴²Pittman, C. U., "Location of Action of Burning Rate Catalysts in Composite Propellant Combustion," *AIAA Journal*, Vol. 7, No. 2, 1969, pp. 328-334.

⁴³Brown, R. S., Muzzy, R. J., and Steinle, M. E., "Surface Reactions on the Acoustic Response of Composite Solid Propellants," *AIAA Journal*, Vol. 6, No. 3, 1968, pp. 479-488.

⁴⁴Oyumi, Y., Mitarai, Y., and Bazaki, H., "Thermal Decomposition of AMMO/AP Composite Propellants," *Propellants, Explosives, Pyrotechnics*, Vol. 18, No. 3, 1993, pp. 168-172.

⁴⁵Oyumi, Y., and Yamazaki, A., "Thermal Decomposition of Azido Prepolymers. Part 1: Effects of Metal Compounds," Japan Defense Agency, TR to TRDI, TRDI-TR-6030, Tokyo, July 1991.

⁴⁶Oyumi, Y., Kimura, E., and Nagayama, K., "Accelerated Aging of Plateau Burn Composite Propellant," *Propellants, Explosives, Pyrotechnics*, Vol. 22, No. 5, 1997, pp. 263-268.

⁴⁷Flanagan, J. E., Frankel, M. B., and Woolery, D. O., "HMX Combustion Modification," Final Rept. to Air Force Propulsion Lab., AFRPL-TR-84-044, AD-A145071, Edwards AFB, CA, Aug. 1984.

⁴⁸Schroeder, M. A., "Critical Analysis of Nitramine Decomposition Data: Product Distributions from HMX and RDX Decomposition," TR to U.S. Army Ballistic Research Lab., BRL-TR-2659, AD-A159325, Aberdeen Proving Ground, MD, June 1985.

⁴⁹Kaste, P. J., "Studies of the Effect of Hivelite and Other Boron Compounds on Nitramine Decomposition by Pyrolysis GC-FTIR," TR to U.S. Army Ballistic Research Lab., BRL-TR-2973, AD-A206802, Aberdeen Proving Ground, MD, Dec. 1988.

⁵⁰Schroeder, M. A., "Borohydride Catalysis of Nitramine Thermal Decomposition and Combustion. II. Thermal Decomposition of Catalyzed and Uncatalyzed HMX Propellant Formulations," TR to U.S. Army Ballistic Research Lab., BRL-TR-3078, AD-A220303, Aberdeen Proving Ground, MD, Feb. 1990.

⁵¹Oyumi, Y., Inokami, K., Yamazaki, K., and Matsumoto, K., "Burning Rate Augmentation of BAMO Based Propellants," *Propellants, Explosives, Pyrotechnics*, Vol. 19, No. 4, 1994, pp. 180-186.

⁵²Urbanski, T., *Chemistry and Technology of Explosives*, Vol. 2, Pergamon, New York, 1965, p. 455.

⁵³Fedoroff, B. T., *Encyclopedia of Explosives and Related Items*, Vol. 1, Picatinny Arsenal, NJ, 1960, pp. A311–379.

⁵⁴Oyumi, Y., Kimura, E., Hayakawa, S., Nakashita, G., and Kato, K., “Insensitive Munitions (IM) and Combustion Characteristics of GAP/AN Composite Propellants,” *Propellants, Explosives, Pyrotechnics*, Vol. 21, No. 5, 1996, pp. 271–275.

⁵⁵Kimura, E., and Oyumi, Y., “Effects of Copolymerization Ratio of BAMO/NMMO and Catalyst on Sensitivity and Burning Rate of HMX Propellant,” *Propellants, Explosives, Pyrotechnics*, Vol. 20, 1995, pp. 215–221.

⁵⁶Kimura, E., and Oyumi, Y., “Sensitivity of Solid Rocket Propellants for Card Gap Test,” *Propellants, Explosives, Pyrotechnics* Vol. 24, No. 2, 1999, pp. 90–94.

Chapter 1.4

Effect of Molecular Structure on Combustion of Polynitrogen Energetic Materials

V. P. Sinditskii,* A. E. Fogelzang,[†] V. Yu. Egorshv,[‡]

V. V. Serushkin,* and V. I. Kolesov[‡]

Mendeleev University of Chemical Technology, Moscow, Russia

Nomenclature

A_n	= preexponential factor for n -order reaction
C	= concentration
C^0	= initial concentration
c_p	= average specific heat of the gas/condensed phase
E	= activation energy
k	= reaction rate coefficient
L_d	= heat of dissociation
L_m	= heat of melting
m	= temperature exponent in the Arrhenius equation
\dot{m}	= mass burning rate
n	= formal order of reaction
p	= pressure
pK_a	= equilibrium constant of proton transfer
p_0	= constant in the van't Hoff equation
Q	= heat of reaction
T_b	= boiling temperature
T_{eq}	= adiabatic flame temperature
T_f	= flame temperature
T_{HCN}	= combustion temperature calculated for nonequilibrium = composition of combustion products (frozen HCN)
T_m	= melting point
T_{max}	= maximal combustion temperature
T_s	= surface temperature

Copyright © 1999 by the American Institute of Aeronautics and Astronautics, Inc. All rights reserved.

*Associate Professor, Dept. of Chemical Engineering.

[†]Professor, Dept. of Chemical Engineering.

[‡]Scientist, Dept. of Chemical Engineering.

T_0	= initial temperature
T_1	= temperature above the burning surface
Ze	= Zel'dovich number
ΔH_d^0	= standard enthalpy of dissociation
ΔH_f^0	= standard enthalpy of formation
ΔH_{rn}	= molar reaction enthalpy
η	= mole fraction of hydrazoic acid in the gas phase
λ	= average thermal conductivity of the gas/condensed phase
μ	= molecule weight
σ_p	= temperature sensitivity
$\tau_{1/2}$	= time of releasing one-half heat of decomposition
ρ	= density

I. Introduction

ENERGETIC materials (EMs) can be generally divided into two classes: substances capable of deflagration at the expense of the heat produced during redox reactions between the fuel and the oxidizing parts of the molecule, and substances that burn through the release of heat in the decomposition of endothermic groups or fragments of the energetic molecule. Most explosives and propellant formulations of practical significance belong to redox-type systems, so that essentially all studies on the combustion of EMs have been devoted to this type of compounds rather than to endothermic-type EMs. At the same time, over the past decade there has been an increasing interest in the combustion of endothermic EMs, predominantly azides and tetrazoles, considered as components of promising propellant and composite formulations, as well as clean-burning emergency gas generators.

This chapter presents a short overview of the steady-state combustion of endothermic polynitrogen compounds: salts of hydrazoic acid (HN_3), organic azides, and tetrazole derivatives, in which burning propagates through the decomposition reactions of the endothermic groups or fragments. Because it is the decomposition reaction that is considered to play a key role in combustion, our main goal in this work was to examine the relationship between the decomposition kinetics and the burning rate of EM, as well as to elucidate the chemical structure effect and the reasons for the burning-rate level.

II. Experimental Methods

We obtained most of the experimental data on the burning of endothermic-type EM presented in this work by using the strand burner technique. Parameters of steady-state combustion of both pressed strands and liquid samples of the substances under investigation were photographically measured in a constant-pressure window vessel of 2-liter volume in the pressure range of 0.1–36 MPa (Ref. 1). A vacuum bomb of 40-liter volume was used for experiments at subatmospheric pressures.

The combustion strands were prepared by compacting thoroughly comminuted substances in transparent acrylic tubes with internal diameters of 4, 7, or 10 mm. The height of the ready strands compacted under pressure of 200–250 MPa never exceeded two diameters, which ensured a uniform distribution of the strand density

with height. The resulting strands had densities of 95–99% theoretical maximum density. This method enabled steady-state combustion of the substances and prevented flame penetration between the particles into the strand and its propagation along the side surface. Liquid materials were tested in transparent quartz or acrylic tubes.

A microthermocouple technique was extensively used to measure temperature profiles during combustion. The thermocouples were welded from 80% W + 20% Re and 95% W + 5% Re wires 25 or 50 μm in diameter and rolled in bands 5 and 20 μm thick, respectively. The thermocouple was embedded in the center of the strand so that the section with the junction was parallel to the combustion front.² The thermocouples with a 20- μm thickness were used in measuring only the maximum flame temperature.

The condensed combustion products were collected and then analyzed by means of infrared (IR) spectroscopy. The compositions of the gaseous combustion products (N_2 , NO, CO, and CO_2) were analyzed on a gas chromatograph. In this case the strands were burned in a 0.25-liter bomb filled with He. NH_3 was absorbed by a concentrated H_3BO_3 solution present in the bottom of the bomb, and its concentration was measured acidometrically.³

III. Results and Discussion

A. Combustion of Hydrazoic Acid and its Onium Salts

HN_3 is one of the most energetic, while chemically simplest, EM representatives. Experimental determinations of the burning rate of liquid HN_3 have not been carried out until now because of its extremely high explosiveness. Only the combustion of HN_3 vapors at low pressures has been studied.⁴ Extrapolation of the combustion velocity ($960 \text{ cm} \cdot \text{s}^{-1}$ or $0.11 \text{ g} \cdot \text{cm}^{-2} \cdot \text{s}^{-1}$ at 50-mm Hg pressure) to 0.1 MPa, under the assumption that it is in direct proportion to pressure, gives $1.7 \text{ g} \cdot \text{cm}^{-2} \cdot \text{s}^{-1}$. This value agrees well with the value of $1.9 \text{ g} \cdot \text{cm}^{-2} \cdot \text{s}^{-1}$, calculated on the basis of the well-known models of combustion of volatile explosives, for which the kinetic parameters of the decomposition reaction of HN_3 at the combustion temperature are used.⁵

Onium salts of HN_3 , with such bases as ammonium, hydrazine, and organic amines, are not nearly so dangerous as liquid HN_3 and are capable of sustained steady-state burning.⁵ Energetic parameters of these salts are less than those of the parent HN_3 , owing to the heat of salt formation as well as the lower molar concentration of HN_3 , in which the decomposition reaction is the major source of heat. It is no wonder therefore that the salts under study showed lower burning rates than the estimated value for liquid HN_3 at atmospheric pressure (Fig. 1). Ethylenediamine and aminoguanidine salts, unlike the other salts, start burning at high pressures: 10 and 30 MPa, respectively. An interesting combustion peculiarity is demonstrated by triaminoguanidine azide: there is a pressure region 2.6–23.0 MPa within which the salt will not burn in the form of a 7-mm-diam pressed strand.

Inspection of ammonium azide temperature profiles has shown⁵ that the surface temperature is determined by the dissociation of the salt and that all the heat required for the warming up and dissociation of ammonium azide comes from the gas phase. The burning rate in this situation may be considered to be governed by gas-phase reactions at the maximal flame temperature provided by the HN_3 decomposition. The nature of the second constituent of an onium salt, the base, determines

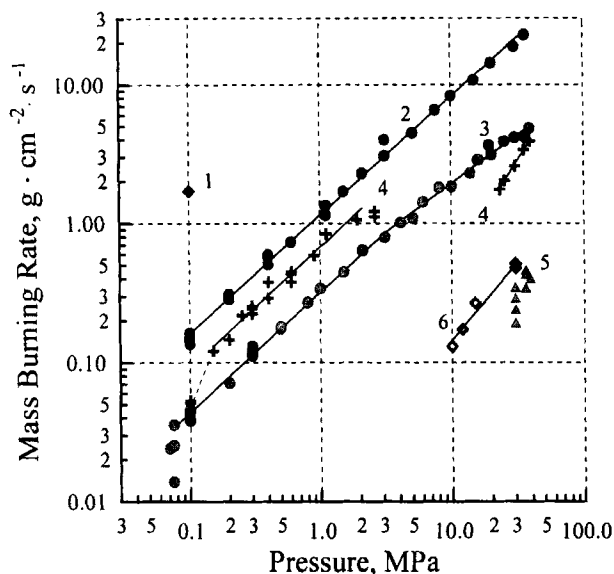


Fig. 1 Mass burning rate vs pressure for 1, HN_3 and its salts with 2, hydrazine; 3, ammonium; 4, triaminoguanidine; 5, aminoguanidine; and 6, ethylenediamine.

the surface temperature. The point is that the higher the basicity, the stronger the binding between basic and acid components of the molecule and the higher the dissociation enthalpy of the salt. The dissociation temperature, which determines the temperature at the burning surface T_s , is dependent on the salt dissociation enthalpy ΔH_d^0 , according to the van't Hoff equation, $p = p_0 e^{-\Delta H_d^0/RT_s}$, where p is the equilibrium vapor pressure above the solid or the liquid phase. Varying the base can also affect the flame temperature: decrease it through dilution of HN_3 vapors and heat consumption for salt formation on the one hand, or contribute to the combustion temperature if an endothermic base is taken, on the other.

Measured surface temperatures of the salts are moderate (400–500 K) (Ref. 5), because HN_3 is a weak acid ($\text{pK}_a = 4.8$) and its onium salts have correspondingly low dissociation enthalpies (31–37 kcal · mol⁻¹). Calculations show that decomposition reactions in the condensed phase at these temperatures can be ignored.

A correlation between the burning rate and maximal flame temperature can be seen from Table 1. The salt of more basic amines (those having lower pK_a values), other conditions being the same, may be pointed out to reveal a tendency to decreased combustion stability. Methylammonium azide, for example, appeared to be incapable of sustained burning in the whole pressure interval investigated, and triaminoguanidine azide reveals a lack of combustion within a large pressure region. Such behavior is believed to be connected with the condensed-phase heat imbalance, i.e., the heat supply from the gas is insufficient to heat the salt to the surface temperature and produce dissociation. A comparison between two similar salts, methylamine azide ($\text{CH}_3\text{NH}_2 \cdot \text{HN}_3$) and ethylenediamine diazide [$(\text{CH}_2\text{NH}_2 \cdot \text{HN}_3)_2$], both containing practically the same amount of HN_3 in the molecule (58.1 and 58.9%, respectively) and hence having very similar energy characteristics, substantiates this conclusion. The second amino group of

Table 1 Characteristics of burning of HN_3 salts and basicity of protonated amines, expressed in terms of pK_a values

Base	pK_a^6	Adiabatic flame temperature at 0.1 MPa, K	Measured (calculated) ^b flame temperature at 0.1 MPa, K	Burning rate, $\text{g} \cdot \text{cm}^{-2} \cdot \text{s}^{-1}$	
				0.1 MPa	30 MPa
Hydrazine	8.5	1849	2080	0.15	18.76
Triaminoguanidine	—	1730	1820	0.05 ^c	2.57 ^c
Ammonium	9.25	1285	1660	0.04	4.13
Ethylenediamine	10.07, 6.99 ^a	1343	(1500)	—	0.49
Methylamine	10.66	1263	(1460)	Will not burn	
Aminoguanidine	11.0	1211	(1130)	—	0.33
Guanidine	13.6	936	(610)	Will not burn	

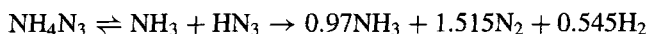
^aThe second step of dissociation.

^bCalculated for nonequilibrium composition of combustion products (frozen NH_3 and/or HCN).

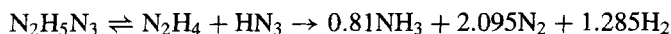
^cValues corresponds to unstable combustion (pressure exponent is more than unity).

ethylenediamine is far less basic than methylamine. The difference in the basicity accounts for the fact that, of the two substances, it is one capable of burning, which requires less heat for warming up and dissociation.

Calculated adiabatic flame temperatures of hydrazine, triaminoguanidine, and ammonium azides are significantly different from experimentally obtained ones, suggesting that the composition of the combustion products does not reach its equilibrium state. Indeed, our experiments showed that at 0.1 MPa the combustion products of ammonium and hydrazine salts contain large amounts of NH_3 : 0.97 and 0.81 moles per mole of the salt, respectively.⁵ NH_3 is present in the former case because there is insufficient time for it to be destroyed in the front of the flame, whereas radical products of HN_3 decomposition (mainly nitrene HN and H atoms) scarcely react with ammonia at all, being turned to N_2 and H_2 :



As for NH_3 in the ammonium azide flame, hydrazine also has not enough time to decompose in the hydrazine azide flame, as is clear from a comparison with burning of liquid hydrazine.⁷ The formation of NH_3 during combustion of hydrazine azide therefore may be attributed to the substantial reaction of hydrazine with the radical decomposition products of HN_3 :



Related reactions indubitably occur with the other hydrazine derivatives: aminoguanidine and triaminoguanidine.

Because of the presence of large quantities of NH_3 that have a negative enthalpy of formation in the combustion products, combustion temperatures of ammonium, hydrazine, and triaminoguanidine salts prove to be substantially higher than the calculated values (see Table 1). In the case of guanidine, aminoguanidine, and triaminoguanidine, decomposition of the bases induced by radical products of HN_3 destruction may result in the formation of ammonia along with another stable

molecule, HCN. Unlike NH_3 , HCN has a positive enthalpy of formation and is responsible for decreasing flame temperature.

The thermal decomposition of HN_3 diluted in Ar has been studied in shock tubes, but the data reported are in disagreement. According to Kajimoto et al.⁸ and Dupré et al.⁹ the primary process of decomposition is a bimolecular reaction, whereas Zaslonko et al.¹⁰ proposed that above 1250 K the primary process is a unimolecular reaction.

Assuming no reaction in the condensed phase during combustion and by using a combustion model of volatile explosives,¹¹ one can easily calculate the formal kinetics of a gas-phase reaction that is responsible for heat generation in the gas and controls the burning rate. Hereafter this reaction is referred to as the dominant combustion reaction. The combustion model used links the kinetics of the dominant reaction under flame conditions with the rate of burning:

$$\dot{m} = \sqrt{\frac{2\lambda\mu}{c_p(T_f - T_0)} \left(\frac{RT_f^2}{E}\right)^{n+1} \frac{n!}{(T_f - T_{01})^n} \left(\frac{\eta \cdot p}{RT_f}\right)^n A_n e^{-E/RT_f}} \quad (1)$$

where \dot{m} is the mass burning rate; T_f is the flame temperature; μ is the molecular weight of a salt; p is pressure; η is the mole fraction of HN_3 in the gas; E , A_n , and n are the activation energy, preexponential factor, and the formal order of the leading reaction, respectively; and c_p and λ are the average specific heat and the thermal conductivity of the gas phase, respectively. The value of $T_{01} = T_0 - (L_m + L_d)/c_p$ stands for initial temperature T_0 with allowance for the heat consumed for melting L_m and dissociation L_d .

The product $A_n \exp(-E/RT_f)$ of Eq. (1) represents the rate constant of the dominant reaction at flame temperature and can be derived from the equation by substituting the experimental burn rate and flame temperature data into it. The rate constants of the dominant reaction in combustion of ammonium, hydrazine, and triaminoguanidine azides at atmospheric pressure, as well as pure⁴ and diluted¹² HN_3 vapors at 50-mm Hg, have been calculated in this way, assuming either the first- or the second-order reaction of HN_3 decomposition in the flame and by use of corresponding values of the activation energy. The results obtained have been plotted in the Arrhenius coordinates along with apparent first-order¹⁰ and second-order^{8,9} rate constants for HN_3 decomposition reactions obtained previously by a shock-wave decomposition procedure (Fig. 2).

Reasonable agreement between the rate constants of HN_3 decomposition and those derived from burn-rate data is observed for the first-order reaction (Fig. 2a), whereas the assumption of the second order gives rate constants ~ 100 times greater than the shock-wave decomposition experimental data^{8,9} (Fig. 2b). However, the calculated rate constants for the second-order dominant combustion reaction of both hydrazoic acid salts and HN_3 vapors agree closely with Rice–Ramsperger–Kassel–Marcus (RRKM) calculations of the decomposition rate constants for the triplet pathway,⁸ assuming that the reaction probability factor is equal to unity.

The first order of the HN_3 decomposition reaction, in spite of its fair consistency with corresponding data from the literature, can hardly be unconditionally accepted for describing the combustion of HN_3 salts because it implies that the burning rate is proportional to the one-half power of the pressure as it follows from Eq. (1) with $n = 1$. What actually happens is that the pressure exponent for the salts proves to be close to unity, at least at low pressures (0.99, 0.96, and 0.78 for ammonium, hydrazine, and triaminoguanidine azides, respectively).

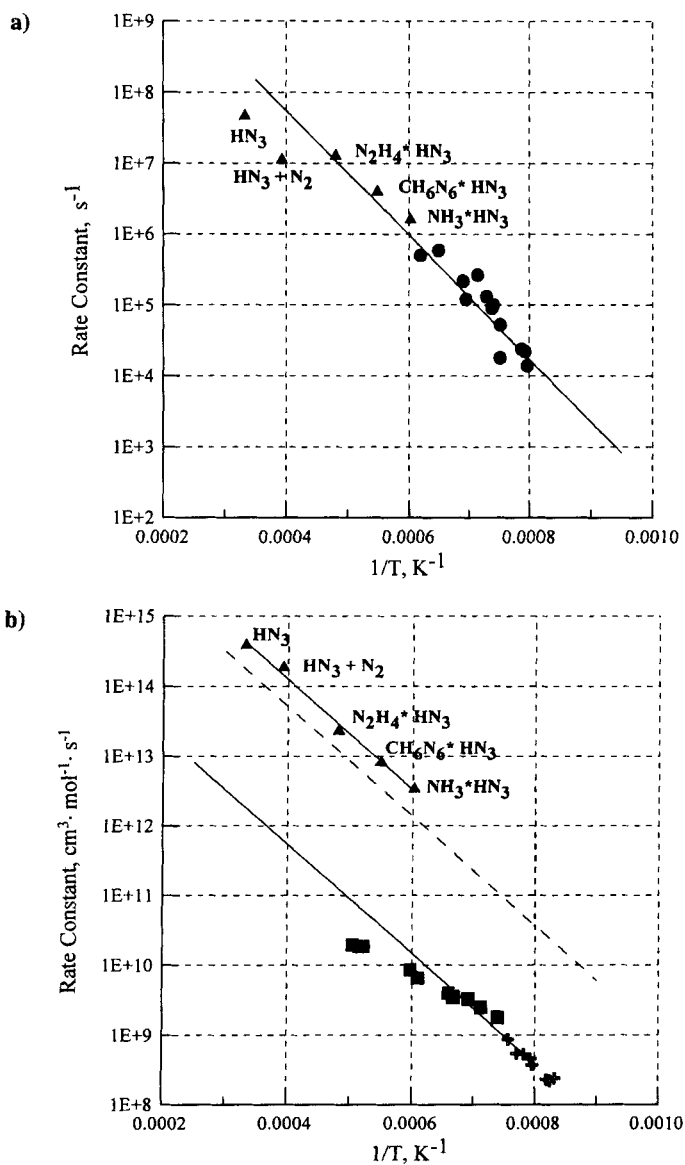


Fig. 2 Arrhenius plot of apparent a) first-order and b) second-order rate constants obtained by Zaslanko et al.¹⁰ (solid line and circles in a), Kajimoto et al.⁸ (solid line and crosses, experiment; dashed line; RRM calculations in b), and Dupré et al.⁹ (squares in b) for the decomposition reaction of HN_3 , compared with calculated rate constants for the dominant reaction during combustion of HN_3 and its salts (triangles).

Adoption of the second order of the reaction results in the preexponential factor $10^{17.25} \text{ cm}^3 \cdot \text{mol}^{-1} \cdot \text{s}^{-1}$, which is consistent with the values for the decomposition of normal four-atom molecules,⁸ and almost the same value of the activation energy obtainable from the slope of the fitting line ($36.14 \text{ kcal} \cdot \text{mol}^{-1}$), which matches well the calculated RRKM activation energy of HN_3 decomposition ($36.0 \text{ kcal} \cdot \text{mol}^{-1}$) (Ref. 8). Finally, mention may be made of that low-pressure flame studies of pure and diluted HN_3 vapors¹² were indicative of the overall reaction order of ~ 2 and activation energy equal to $30 \text{ kcal} \cdot \text{mol}^{-1}$.

Thus the combustion behavior of both HN_3 and its salts may be assumed to depend on a common gas-phase reaction, namely, the HN_3 decomposition reaction. One conceivable reason for the observed discrepancy between HN_3 decomposition kinetics in flame conditions and shock tubes is that in the latter case the decomposition may be subjected to the effect of vibrational nonequilibrium,⁹ with a consequent deviation from the Arrhenius law.

B. Combustion of Organic Azides

A change from HN_3 and its salts to organic azides opens up another class of endothermic compounds with a wide structural diversity, among which are found primary explosives (cyanurotriazide and similar heterocyclic azides), high explosives (trinitroazidobenzene and related compounds), and energetic binders and plasticizers {poly(3-azidemethyl-3-methyloxetane) (AMMO), poly[bis(3-azidomethyl)oxetane] (BAMO), glycidyl azide polymer (GAP), and other azide polymers}.

Organic azides are only slightly different from HN_3 in terms of their thermal decomposition mechanism: Likewise, the nitrogen molecule is released to form nitrene intermediate $\text{R}\ddot{\text{N}}$, which reacts further by C–H and C–C bonds to produce imines and nitriles.^{13–15} As with those of HN_3 , the secondary reactions of nitrene $\text{R}\ddot{\text{N}}$ are also considered to take place very fast; it has even been suggested that a rearrangement of the nitrene skeleton proceeds concurrently with liberation of the nitrogen molecule.¹³

The thermal stability of the azides decreases in going from alkyl to aryl azides, which is associated with the resonance stabilization of forming nitrene by the aromatic ring. The least stable are aryl azides that have an *ortho*-substituent in the ring, which can participate in the decomposition reaction to form heterocyclic systems.¹³

1. Aliphatic Azides

Most alkyl azides are liquids under standard conditions and can easily change their combustion regime from laminar to turbulent as the pressure increases. Laminar combustion of the azides has been observed in the subatmospheric pressure region.^{16,17} All of them have low boiling points (from 470 to 520 K at atmospheric pressure), allowing the use of the combustion model for volatile explosives.¹¹ As the alkyl radical chemical structure has only a slight effect on the decomposition kinetics of alkyl azides,¹⁴ the available decomposition data of any one of them, such as methyl azide, for example, can be used for comparison purposes. Unfortunately, experimental data on combustion temperatures are rare in the literature. Combustion data for two azides, 1,3-diazidopropanol-2, $[\text{N}_3\text{CH}_2\text{CH}(\text{OH})\text{CH}_2\text{N}_3]$ and acetate of 1,3-diazidopropanol-2 $[\text{N}_3\text{CH}_2\text{CH}(\text{OCOCH}_3)\text{CH}_2\text{N}_3]$ have¹⁷ been

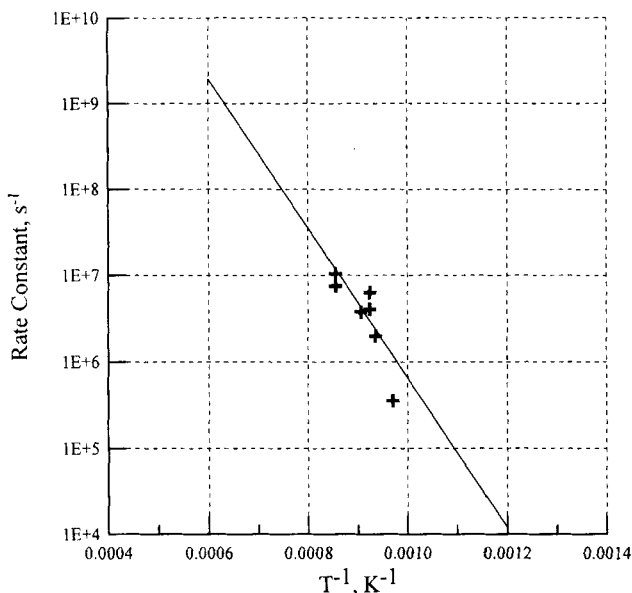


Fig. 3 Arrhenius plot of apparent first-order rate constants for the decomposition reaction of methyl azide (solid line) and rate constants for the dominant combustion reaction of alkyl azides at subatmospheric pressure (crosses).

taken for calculations of rate constants from Eq. (1), and the results appeared to agree satisfactorily with first-order rate constants for the decomposition reaction of methyl azide¹⁴ (Fig. 3). Thus, as with that of HN_3 onium salts, the burning rate of volatile alkyl azides is determined by the rate of azide decomposition reaction at the flame temperature.

An interesting combustion feature of some alkyl azides, such as 1,5-diazidopentane, 1,3-diazidopropanol-2, and acetate and propionate of 1,3-diazidopropanol-2, is the presence of breaks on the burn rate vs pressure curves, i.e. some pressure interval within which the azides are incapable of self-sustained burning.¹⁷ At low pressures the azides burn in the laminar regime, and after the break they start burning in the turbulent one. This phenomenon was first observed for the combustion of nitroglycerine.¹⁸ The noted behavior does not appear to be a result of peculiar chemical structure of the energetic materials but is conditioned by the Landau instability effect,¹⁹ the disturbance of the liquid-vapor interface (the burning surface becomes distorted). The disturbance appears and progresses after the burning rate has reached a critical value, which depends on the viscosity of the liquid. Calculations of the critical burn-rate values¹⁷ showed that the viscosity of the liquid alkyl azides under study could not provide stable burning at pressures above atmospheric.

The solid representatives of the alkyl azides, the azide polymers, unlike their liquid analogs, appear to be capable of self-sustained burning within a wide pressure range. Typical azide polymers, such as the well-known GAP, AMMO, BAMO, and others, are produced by curing and crosslinking of the corresponding azide oligomers with a molecular weight of 2000–5000. These polymers are used as

energetic binders and plasticizers in rocket propellants with reduced smoke and vulnerability, as well as in composite explosives with low sensitivity. A number of thermochemical and burn rate studies on azide polymers have been conducted that describe the thermal decomposition chemistry and combustion mechanism.^{15,20–27} Thermolysis of the azide polymers leads to the formation of solid polymeric material containing $-\text{CH}=\text{NH}$ groups and gaseous N_2 , H_2 , CO , C_2H_4 , CH_4 , and HCN . The results are consistent with the initial rupture of the $\text{N}-\text{N}_2$ bond of the azide to produce reactive nitrene, which gives rise to the final gaseous and solid products. It is interesting to note that the ratio of the solid polymeric products decreases and the amount of HCN formed increases as the thermolysis conditions near those of combustion.²³

The composition of the combustion products of azide polymers is different from the thermodynamical equilibrium composition because of the presence of large amounts of HCN , C_2H_4 , and CH_4 , resulting in an actual flame temperature that is considerably lower than the calculated adiabatic temperature. Very high values of the surface temperature measured with thin Pt–Pt/Rh thermocouples [700–730 K at 0.4–0.8 MPa (Ref. 20), 700–800 K at 1.5–10 MPa (Ref. 26) for GAP, 720–750 K at 3 MPa for the BAMO/tetrahydrofuran (THF) copolymer²⁵] and compared with known kinetic data on thermolysis of the azide polymers¹⁵ suggest that the dominant combustion reaction proceeds in the condensed phase. This suggestion is also supported by the Zel'dovich number $Ze = \sigma_p(T_s - T_0) \approx 5$ for the BAMO/THF copolymer, where σ_p is the burning-rate temperature sensitivity, 0.0112 K^{-1} at 3 MPa (Ref. 25), which is five times greater than the Zel'dovich number for volatile alkyl azides with the dominant reaction in the gas phase¹⁷ ($Ze = 0.8\text{--}1.1$).

Because the main heat source for combustion of azide polymers is the azide group decomposition reaction and because kinetic parameters of the decomposition vary only slightly,¹⁴ the burning rate may be correlated with the azide group density in related materials, for example within copolymers of BAMO and THF.²² Chen and Brill showed that the decomposition kinetics match the burning rate of GAP extrapolated to the same pressure and temperature ranges.¹⁵ Rate constants of the dominant combustion reaction of azide polymers can be obtained from a combustion model based on a dominant role of the condensed-phase chemistry²⁸:

$$\dot{m} = \sqrt{\frac{2\lambda\rho}{c_p} \frac{(T_f - T_0)}{(T_s - T_0)^2} \frac{RT_s^2}{E} A e^{-E/RT_s}} \quad (2)$$

where T_f and T_s are the flame and the surface temperatures, respectively, E and A are the activation energy and the preexponential factor of the dominant reaction, respectively, and c_p and λ are the average specific heat and thermal conductivity of the condensed phase, respectively.

Experimental data on surface temperatures for GAP and BAMO/THF were used to calculate rate constants from Eq. (2) and were compared with rate constants for the decomposition reaction of GAP.¹⁵ As seen in Fig. 4, the results derived from the combustion model are in satisfactory agreement with the kinetics of GAP slow thermal decomposition. Also presented in the figure are rate constants for volatile alkyl azides, calculated in the preceding section from Eq. (1) on the assumption of gas-phase priority. As can readily be observed, the burning rate of all

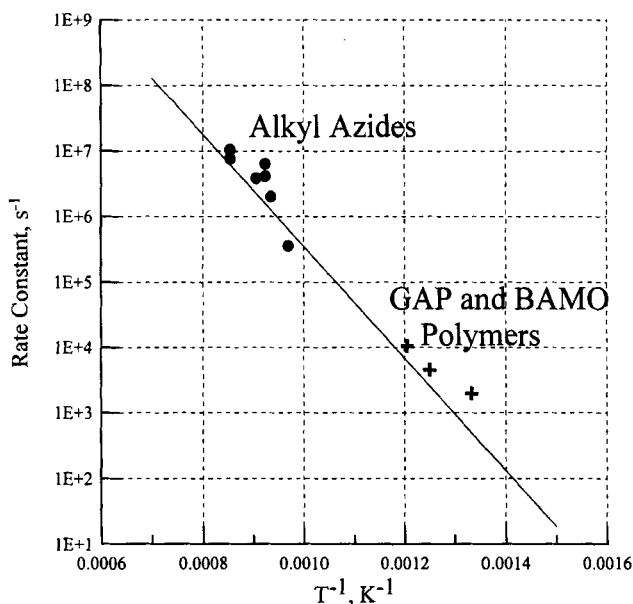


Fig. 4 Arrhenius plot of apparent first-order rate constants for decomposition reaction of GAP (solid line) and rate constants of the dominant combustion reaction of GAP and BAM/THF polymers (crosses) and alkyl azides (circles).

the considered azides is governed by the kinetics of the decomposition, irrespective of whether it occurs in the condensed or the gas phase.

The most probable contributor of heat evolution in the gas phase during combustion of azide polymers is thought to be the decomposition of small fragments of the azide polymer, formed by means of partial depolymerization and removed to the gas phase through either evaporation or carrying over with the gas flow. Alternative possibilities for heat release in the gas are unlikely because the polymer itself is not volatile and there are no other channels giving rise to gaseous endothermic compounds, as elimination of HN_3 , for example, is not typical for organic azides.¹⁴ Oxidation of the polymer backbone by ether oxygen atoms could add only a few tens of degrees to the combustion temperature, rather than 200 or 300, as has been proposed elsewhere.²⁶

2. Aromatic Azides

The main combustion features of aromatic azides basically repeat those of aliphatic azides: An increase in the number of azide groups in the molecular leads to a regular increase in the burning rate. Some of the azides reveal a gap in the burn rate–pressure dependence (Figs. 5 and 6).

Studying the combustion behavior of aryl azides is also of interest because the aromatic ring allows introducing the nitro group along with the azide group into the molecule, thereby giving a comparative correlation between them with respect to influence on the burning rate. In studies of combustion of nitroazidobenzenes¹ (NABs), the position of the nitro group in the NAB molecule was found to have a strong effect on the burning rate as well as on thermal stability.²⁹ However, the

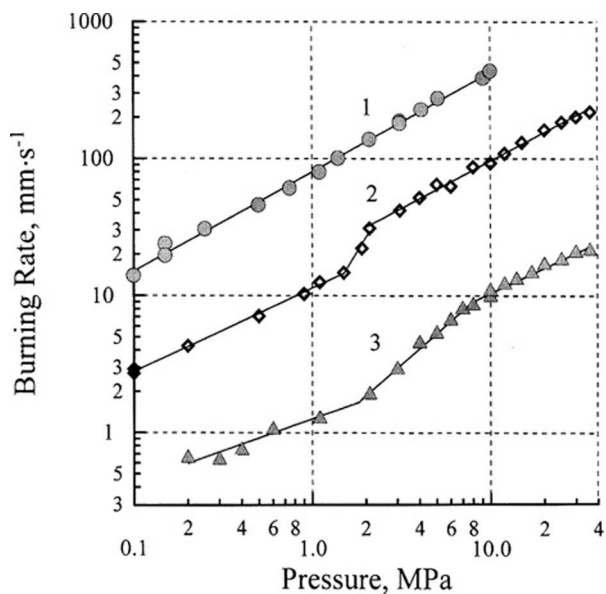


Fig. 5 Effect of azide group content on burn-rate characteristics of 1, cyanurotri-azide; 2, aminodiazidotriazine; and 3, azidobenzoic acid.

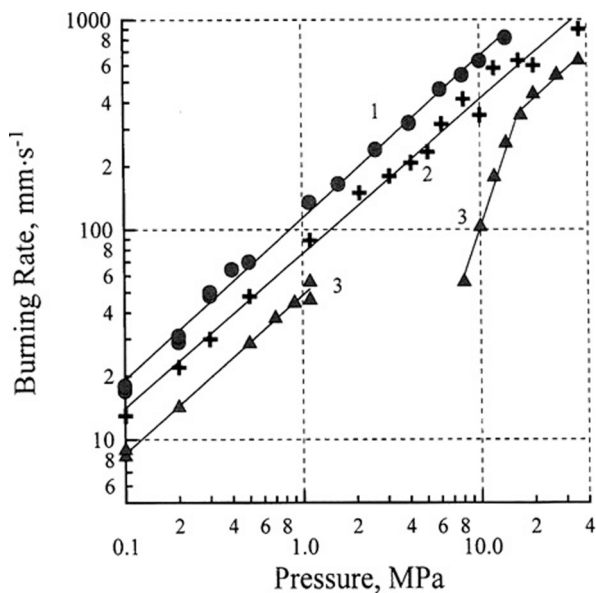


Fig. 6 Effect of azide group content on burn-rate characteristics of azides of the phthalazine series: 3, diazidophthalazine; 2, triazidophthalazine; and 1, tetrazidophthalazine.

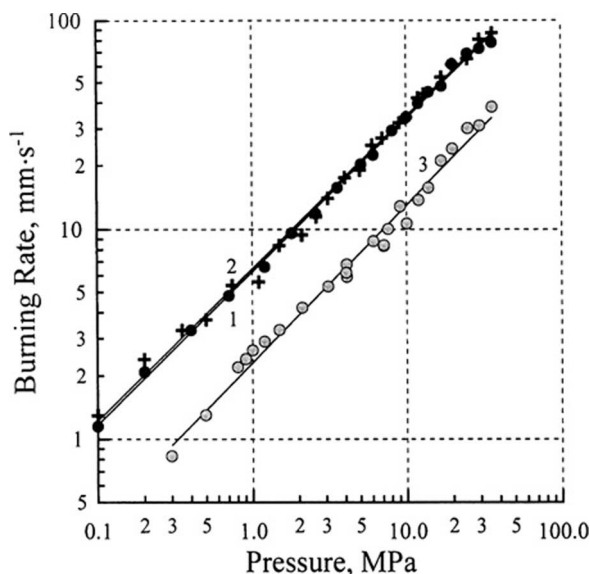


Fig. 7 Comparison of burn-rate characteristics of three isomers of NAB: 1, *para*; 2, *meta*; and 3, *ortho*.

expected correlation between the thermal stability of the compounds and their burning rates was not directly observed: The least stable compound among the three isomers of NAB, *ortho*-NAB, showed a burning rate that was 60–70% lower than that of more stable *meta*- and *para*-isomers (Fig. 7).

The introduction of each additional nitro group into the molecule of a regular nitro compound is known to raise its burning rate by a factor of 2–3 (Ref. 30). Quite a different picture was observed with NABs when the second nitro group was introduced. 2,4-dinitroazidobenzene burns at the same rate as *ortho*-NAB, whereas 3,5-dinitroazidobenzene burns almost at the same rate as *meta*-NAB (Fig. 8). Here the second nitro group does not markedly affect the burning rate if it is introduced in the *meta* or the *para* positions to the azide group. When introduced in the *ortho* position, the nitro group, however, reduces the burning rate, as exemplified by a comparison of *para*-NAB and 2,4-dinitroazidobenzene.

Thermocouple-aided measurements in the combustion wave of the NAB isomers allowed proposing the combustion mechanism and an explanation of the unusual correlation between the burning rate and thermal stability. Typical temperature profiles for *ortho*-NABs and *para*-NABs are presented in Fig. 9. The temperature at the surface T_s and the temperature of the primary flame T_1 reached in close proximity to the burning surface are always lower, under equal conditions, for the *ortho*-isomer than for the *meta*- and the *para*-isomers. The temperature profiles for the *ortho*-isomer at 4 and 7 MPa clearly indicate the presence of two flames, but there is no such clear-cut separation in the flames from the *meta*- and the *para*-isomers. At high pressures the maximal flame temperatures T_f , measured for the *ortho*- and the *para*-isomers, are virtually identical, but they are 300–400 K lower than the adiabatic flame temperature calculated on the assumption of thermodynamic equilibrium in the combustion products ($T_{eq} = 2170$ K at 10 MPa).

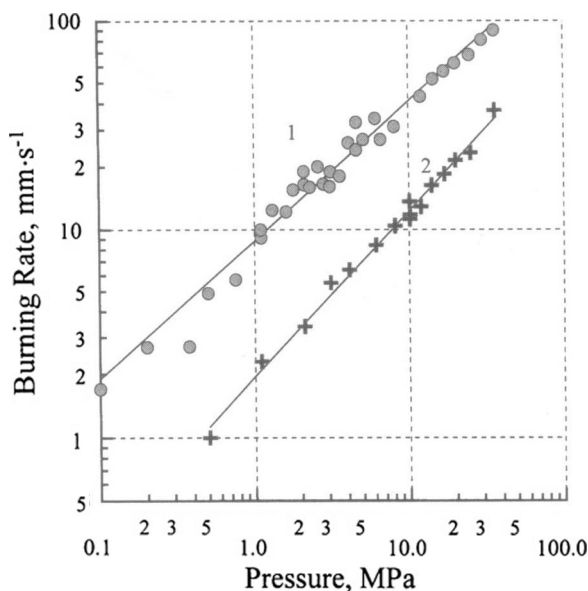


Fig. 8 Comparison of burn-rate characteristics of dinitroazidobenzene isomers: 1, 3,5-dinitroazidobenzene and 2, 2,4-dinitroazidobenzene.

The discrepancy between the T_{eq} and the measured maximal flame temperatures may be caused either by incomplete reduction of the active oxygen contained in the molecule or by incomplete release of the energy stored in the azide group. An analysis of the gaseous combustion products from *para*-NAB indicates that nitrogen oxides were not present in the combustion products, even at atmospheric pressure. At the same time, the measured and the calculated T_f are in good agreement if the calculations are made on the assumption that one of the nitrogen atoms

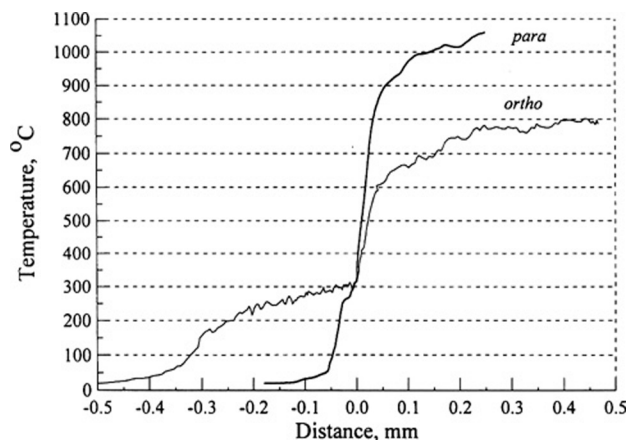
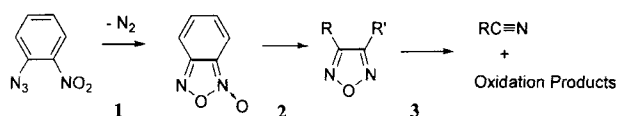


Fig. 9 Temperature profiles for *ortho*-NABs and *para*-NABs at 1.0 MPa.

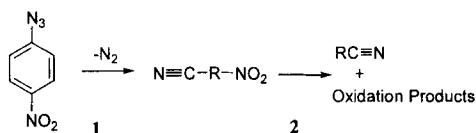
of the azide group has remained in the form of endothermic nitrile moiety in the combustion products, resulting in incomplete combustion heat release.

Distinctions in temperature profiles among the NAB isomers was assumed to be connected with different pathways of the azide chemical conversion in the combustion wave. The first step of *ortho*-NAB combustion (in the condensed phase and near the surface) involves the elimination of the nitrogen molecule to form furoxan. After that, furoxan undergoes reduction to furazan, followed by degradation and oxidation reactions, yielding a nitrile derivative:



The temperature rise corresponding to the first step can be distinctly seen in temperature profiles at low pressures. At higher pressures the first two steps become hardly discernible, but the third step makes its appearance because of oxidation reactions involving all of the oxygen in the molecule.

The pathway for the conversion of *meta*-NABs and *para*-NABs is slightly different. In the first step, the azide group undergoes decomposition with the formation of a nitrile derivative containing the unreacted nitro group. The nitro group then undergoes reduction, but the nitrile group, as before, does not decompose:



By and large, surface and T_1 temperatures in the combustion wave of *ortho*-NAB are less than those for *meta*- and *para*-isomers and could be responsible for the slower burning of the former. A comparison among decomposition kinetics of the isomers shows that the decomposition rate of the *ortho*-isomer exceeds that of the other isomers at low temperatures (below 700 K) and is less in the high-temperature region typical for the flame zone. It is of prime importance therefore to know exactly the combustion zone in which the rate-controlling reaction mainly proceeds in order to use the known decomposition kinetics in modeling combustion.

The heat balance calculated for the condensed phase indicates that the maximum fraction of NAB decomposed is 30% for *para*-NAB and *meta*-NAB and 60% for *ortho*-NAB. This fact, along with the Zel'dovich number of 1.9 obtained for the combustion of *para*-NAB,³¹ supports the priority of the condensed phase in the burning of such azides.

We calculated the rate constants of the dominant combustion reaction of both *ortho*-NAB and *para*-NAB from Eq. (2), assuming that this reaction occurred in the condensed phase and substituting experimental data on the surface temperature. The calculated values proved to agree closely with first-order rate constants for the decomposition reaction of the *ortho*-isomer (Fig. 10) but noticeably exceeded the decomposition kinetics data³⁰ for the *para*-isomer. However, calculations for

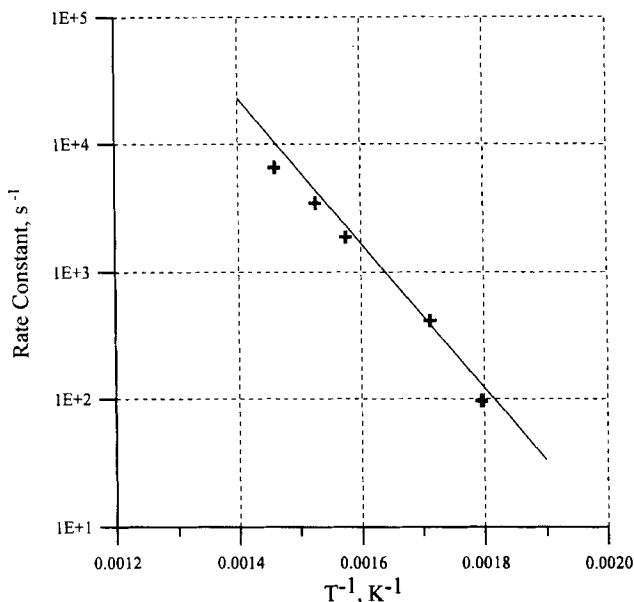


Fig. 10 Arrhenius plot of apparent first-order rate constants for the decomposition reaction of *ortho*-NAB (solid line) compared with calculated rate constants for the dominant combustion reaction of *ortho*-NAB (crosses).

para-NAB, based on the gas-phase combustion model [Eq. (1)], failed even further to match the thermal decomposition kinetics extrapolated to the high-temperature area. Therefore the combustion process of *para*-NAB (and *meta*-isomer) is not likely to be described satisfactorily by the condensed-phase model alone, but should include a contribution from heat evolution in the gas phase as well.

Nevertheless, it may be safely stated that the heat produced in the condensed phase is of primary importance in controlling the burning rate of NAB and that the rate of the heat evolution process is in general agreement with the decomposition kinetics of the azides. The mutual arrangement of the azide and nitro groups in the NAB molecule (chemical structure) will influence the burning rate as far as it exerts an effect on the kinetics of azide decomposition.

C. Combustion of Tetrazoles

Tetrazoles, high-nitrogen heterocyclic compounds, are of special interest as energetic components of propellants and gas-generating systems. Chemically, tetrazoles can be viewed as cyclic tautomers of azidoimines $N_3-CR=NR$. Having a high-internal-energy content, many tetrazole derivatives are capable of sustained burning (Figs. 11 and 12) at the expense of heat produced during the thermal decomposition of the heterocyclic ring.^{33,34}

The stationary combustion of the parent compound tetrazole and the temperature distribution in its combustion wave at atmospheric pressure have been investigated previously,³³⁻³⁶ and some of their thermophysical characteristics were determined.³⁵

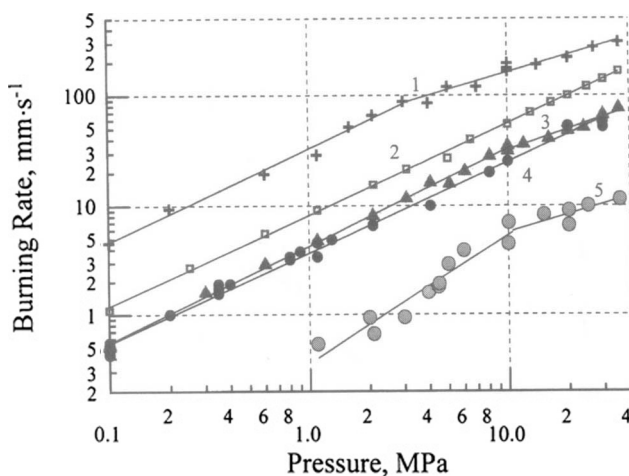


Fig. 11 Linear burning rate vs pressure for 5-substituted tetrazoles: 1, bistetrazole; 2, cyanotetrazole; 3, bis(tetrazolyl-5)amine; 4, tetrazole; and 5, aminotetrazole.

At atmospheric and near-atmospheric pressures, tetrazole burns under a nitrogen atmosphere with crackling, forming copious white vapors, which condense as fine yellowish drops inside a tube and on the cold surfaces of the bomb. As pressure increases above 2 MPa, the gases flowing off become almost transparent, with no condensed combustion products observed. The IR spectroscopy data on the condensed combustion products indicate a wideband in the range $3080\text{--}3330\text{ cm}^{-1}$ ($\nu\text{N-H}$), a strong band in the range $2130\text{--}2245\text{ cm}^{-1}$ ($\nu\text{C}\equiv\text{N}$), and absorbances in the range $1400\text{--}1620\text{ cm}^{-1}$ (δNH_2 and $\nu\text{C}=\text{N}$), allowing the conclusion that the condensed products consist of a mixture of cyanamide and its condensation

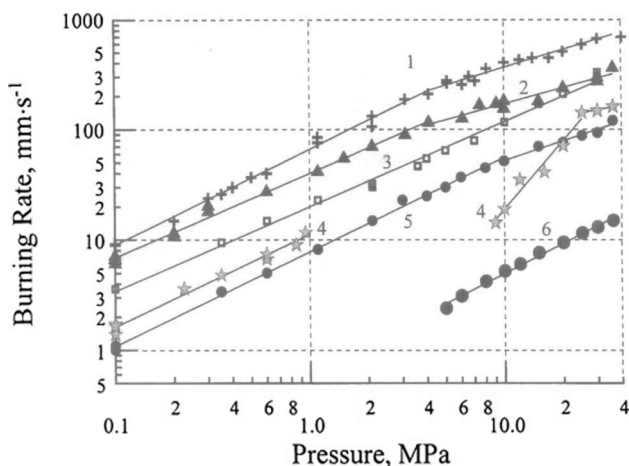


Fig. 12 Linear burning rate vs pressure for 5-substituted tetrazoles: 1, tetrazene; 2, nitraminotetrazole; 3, nitrotetrazole; 4, chlorotetrazole; 5, bromotetrazole; and 6, hydroxytetrazole.

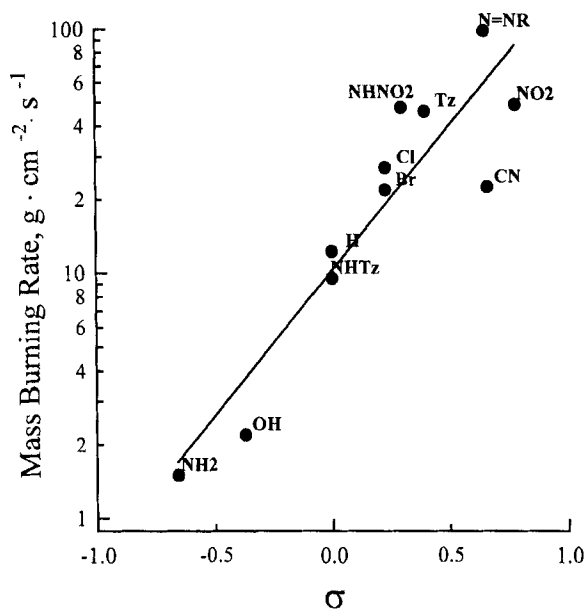


Fig. 13 Correlation between the mass burning rate of 5-substituted tetrazoles at 30 MPa and Hammett's σ values for the substituents.

products: dicyandiamide and, probably, melamine. Burning of amino, hydroxy, and cyano derivatives is also accompanied by formation of condensed combustion products, whereas chloro, bromo, nitro, and some other derivatives do not form condensed products in combustion.

As with triaminoguanidine azide, chlorotetrazole appeared to be incapable of sustained burning in a certain pressure interval (Fig. 12). The introduction of electron-withdrawing groups into the tetrazole molecule raises the burning rate. Inspection of the experimental data reveals an interesting correlation between Hammett's σ values for the substituents and mass burning rates of the tetrazoles (Fig. 13). The Hammett's σ value of a substituent is known to affect the kinetics of a thermal opening of the tetrazole cycle to a substituted guanilazide.^{37,38} The correlation shown in Fig. 13 is believed to be indicative of an important role of tetrazole cycle decomposition reactions in combustion.

Thermocouple-aided measurements have been extensively carried out with tetrazole and 5-chlorotetrazole.^{34,36} Temperature profiles of tetrazole (Fig. 14a) demonstrate the following peculiarities:

- 1) The length of the molten layer extending from the melting point T_m to the surface temperature T_s and the value of T_s are both subject to significant variations at the same pressure.

- 2) As pressure increases from 0.1 to 0.8 MPa, somewhat regular drops in the temperature are observed in the gas phase (Fig. 14a), whereas at 1.3 and 30 MPa the profiles are quite smooth.

A different flame structure is typical on chlorotetrazole combustion (Fig. 14b); in contrast to tetrazole, the scatter in the measured lengths of zones and T_s is significantly less; there are no temperature falls in the gas-phase region.

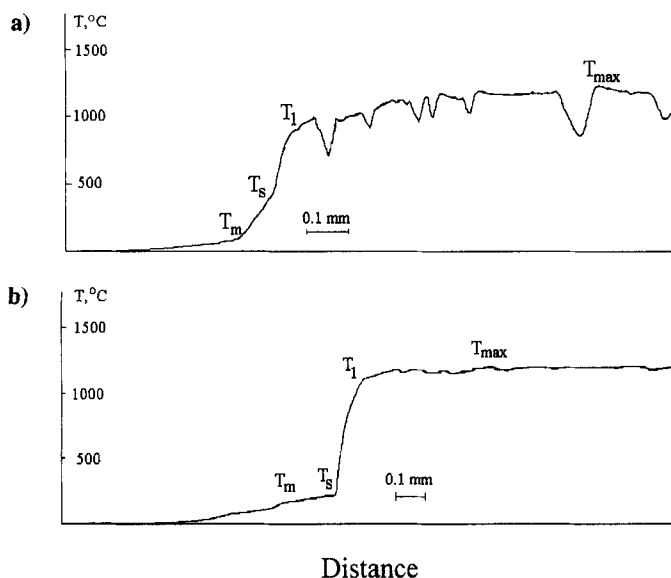


Fig. 14 Temperature distribution in the combustion wave of a) tetrazole at 0.8 MPa and b) chlorotetrazole at atmospheric pressure.

All data of temperature measurements for tetrazole are collected in Fig. 15. It is interesting to note that temperature above the burning surface T_l varies very little with pressure, whereas the maximal combustion temperature T_{max} shows a peculiar behavior: As pressure increases from 0.1 to 0.8 MPa it rises and then falls by 120–160°C in the pressure interval 0.8–30 MPa. The dependence of the tetrazole boiling temperature T_b on pressure calculated from Nernst's equation³⁹ is also presented in Fig. 15. The heat of evaporation of 19.0 kcal · mol⁻¹ was obtained as the difference between the sublimation heat of 23.3 kcal · mol⁻¹ (Ref. 40) and the melting heat of 4.2 kcal · mol⁻¹ (Ref. 35). Minimal measured values of T_s turn out to lie virtually on the calculated line of the tetrazole boiling temperature, whereas the maximal T_s values exceed it more and more as pressure rises. With the kinetic parameters of tetrazole thermal decomposition⁴¹ and assuming that the measured surface temperature at atmospheric pressure corresponds to the boiling temperature, it has been calculated that no more than 3% of tetrazole undergoes decomposition in the surface reactive zone during combustion at 0.1 MPa.

Variations in the surface temperature can be explained by a periodic process that involves a gradual accumulation of decomposition products with a high decomposition/boiling temperature on the burning surface, followed by ejection of the products in the gas and clearing of the surface. Formation of thermostable products of tetrazole decomposition has been observed elsewhere.^{42,43}

It is essential that the maximal measured temperatures of combustion of both tetrazole and chlorotetrazole at all studied pressures are much below calculated adiabatic ones. At 0.1 MPa, for example, measured and calculated temperatures are 1140 and 1925°C, respectively, for tetrazole, and 1260 and 2180°C, respectively, for chlorotetrazole. As in the case with organic azides, the difference between

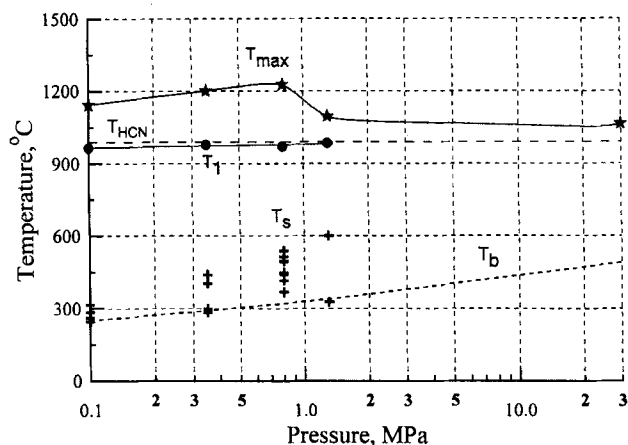
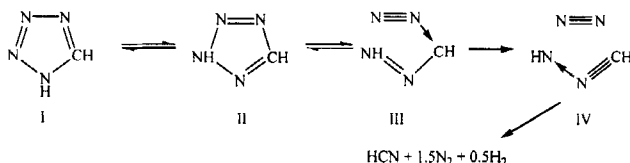


Fig. 15 Pressure dependence of surface temperature T_s , temperature above the surface T_1 , and maximal temperature T_{\max} , in the combustion of tetrazole. Dashed lines are calculated boiling temperatures of tetrazole T_b and tetrazole combustion temperatures assuming frozen HCN, H_2 , and N_2 in the combustion products T_{HCN} .

calculated and measured temperatures could be attributed either to a nonequilibrium composition of the combustion products or to the incompleteness of the combustion process because of the dispersal of the initial substances from the surface. However, the latter assumption was not proved by analysis of the condensed combustion products, in which there was no initial tetrazole detected. A correlation between combustion temperatures calculated for various tetrazole decomposition channels and measured combustion temperatures was made and allowed choosing between possible decomposition routes: The temperature in the gas phase directly above the surface T_1 appeared to be in good agreement with the calculated temperature achievable in tetrazole decomposition to form HCN, H_2 , and N_2 .

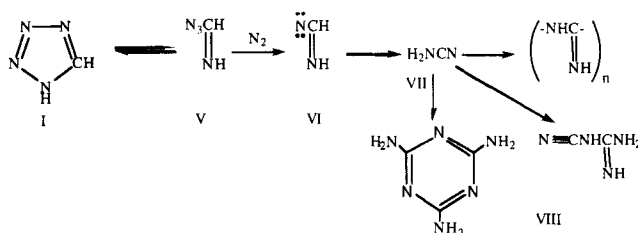
This decomposition is likely to proceed in the gas phase, because the composition of the main combustion products is similar to that found during gas thermolysis of tetrazole.⁴³ The decomposition mechanism includes the fast reversible transformation of 1*H*-tetrazole I into 2*H*-tautomer II, which dominates in gas phase,⁴⁴ followed by the formation and subsequent decomposition of intermediate azodiazocompound III and nitrilimine IV:



The concerted single-stage decomposition of tetrazole to give HCN and HN_3 was reported to have a high activation barrier⁴⁵ and thus be unlikely, although rapid thermal decomposition of 5-aminotetrazole in the interval 25–300°C, studied with rapid-scan Fourier transform IR spectroscopy,⁴² resulted in the formation of HN_3

and H_2NCN in the gas phase at the beginning of degradation, followed by the appearance of a condensation product that was identified as melamine (trimer of cyanamide).

Under decomposition in the condensed phase, tetrazole affords only insignificant amounts of HCN formed ($\sim 5\%$) (Ref. 43). The decomposition scheme includes isomerization of the *1H*-form I into azidoazomethyne V, followed by the formation of nitrene VI. This scheme is based on the fact that tetrazole thermolysis leads to the formation of high-thermostable compounds VIII representing polymerization products of cyanamide VII:



Small amounts of cyanamide VII and its polymerization products found experimentally in the tetrazole combustion products suggest a partial decomposition reaction of I in the condensed phase. The contribution of this decomposition route at low pressure has been estimated to be ~ 10 – 20% , that is, more than the calculated contribution for the thermolysis at boiling temperature. This is likely to be connected with the accumulation of high-boiling decomposition products in the tetrazole molten layer, resulting in an increased surface temperature and thus enhancing the proportion of tetrazole decomposed in the condensed phase. The accumulated layer of high-boiling condensed products is ejected at times by gases flowing off the surface. A portion of the condensed products, having been thrown into the high-temperature zone as small drops, undergoes endothermic decomposition to form NH_2CN and then HCN. At low pressures, however, the drops do not all have time to be decomposed. Small, regular temperature decreases, which are seen on profiles in the pressure region 0.1 – 0.8 MPa, are likely to result from colder drops hitting the thermocouple. Because the formation of both cyanamide and its condensation products (dicyandiamide and melamine) is more favorable than HCN formation from the energetic standpoint, the maximal combustion temperature T_{max} exceeds that achievable in the decomposition pathway to form HCN. Besides, if a part of the condensed droplets passes through the flame zone accessible to the thermocouple without evaporating, it will also promote overestimating the gas-phase temperature. Increasing pressure, being favorable for more effective evaporation of the flying droplets, results in the homogeneous gas-phase zone observed in profiles at high pressures. At the same time, the maximal temperature is reduced and approaches the tetrazole combustion temperature, calculated on the assumption that HCN is produced.

The combustion of 5-chlorotetrazole has much in common with the burning of tetrazole. The measured combustion temperature matches closely the calculated temperature of chlorotetrazole conversion to nitrile-containing products of dicyan type. In contrast to tetrazole, the decomposition of chlorotetrazole does not result in formation of high-boiling or thermostable products. Cyanuric chloride $(\text{ClCN})_3$, a possible condensation product, has a boiling temperature of 190°C , which is

below the measured surface temperature. The smooth appearance of chlorotetrazole temperature profiles confirms this suggestion.

Which reaction of the proposed decomposition scheme can be thought of as playing the dominant role in combustion? There is no apparent correlation between the kinetics of the initial reaction of tetrazole decomposition and the burning rate. For example, tetrazole and bistetrazole have very similar parameters of thermal decomposition,⁴¹ and quite different burning rates (Fig. 11); only a slight influence of the 5-substituent on the decomposition rate is observed on the thermolysis of tetrazole derivatives,^{41,45} whereas it is quite noticeable in combustion (Fig. 13).

Such different behaviors of tetrazoles in thermolysis and combustion could be explained by a change in the dominant reaction in passing from thermolysis (150–200°C; decomposition through nitrene) to combustion (above 1000°C; decomposition through HCN and HN₃).³⁶ There is, however, another possible explanation. The shift of the tautomeric equilibrium to 2*H*-tetrazole is facilitated not only by phase transition into gas but also by the withdrawing power of the 5-substituent.⁴⁶ Solvents used in a thermolysis study of dissolved tetrazoles⁴¹ promoted shifting the equilibrium to 1*H*-tetrazole, thus compensating for the withdrawing effect of 5-substituents. Considering that most of the material decomposes during combustion in the gas phase, where the 2*H*-form dominates, an increase in the withdrawing properties of the 5-substituent will cause the equilibrium concentration of this form in the gas to increase, with the resulting enhancement in rates of heat production and burning. In either case, the burning rate of 5-substituted tetrazoles will be controlled by the primary decomposition reaction of the tetrazole cycle, although kinetics parameters of this reaction in conditions of slow thermal decomposition at 150–250°C may differ from those in combustion.

D. Comparison with Nitrocompounds

The combustion of practically all kinds of EM has its origins in the initial endothermic reaction of decomposition with the high activation energy to give active intermediate products, followed by secondary reactions of the lower activation energy, giving rise to the heat evolution. Analysis of the combustion behavior of redox systems indicates that the burning rate is greatly affected by the activity of the oxidizer formed in the decomposition of the initial compound (NO, NO₂, ClO₂, HNO₃, HClO₄, HClO₃, HBrO₃, etc.), whereas a correlation between burning rate and thermal stability is not obvious for this type of EM.⁴⁷

Investigations of the combustion of the other types of EM, such endothermic compounds as organic azides, salts of HN₃, and tetrazole derivatives, show that, unlike in redox systems, it is the decomposition reaction that determines the burning rate.^{5,34,47}

For better visualization of the reasons for the above-mentioned distinction between the combustion of the two types of EM, the kinetics of the heat production process in the gas phase have been considered for two model systems: nitromethane (CH₃NO₂) and HN₃. The reaction mechanisms for the decomposition of gaseous CH₃NO₂ and HN₃ have been determined in several studies,^{8,48,49} and so rate coefficients for elementary reactions are well known. Because the main objective of modeling was to find the reason why the two types of EM had different dominant combustion reactions, the number of reactions used was reduced to 3 for the HN₃ flame (Table 2) and 18 for CH₃NO₂ flame (Table 3).

Table 2 Elementary chemical reaction rate coefficients in the form $k = A_n T^m \exp(-E/RT)$ ($\text{cm}^3 \cdot \text{mol}^{-1} \cdot \text{s}^{-1}$) and molar reaction enthalpy ΔH_{rn} used in modeling HN_3 flame

Number	Reaction	$\ell_n A_n$	m	$E, \text{kcal} \cdot \text{mol}^{-1}$	$\Delta H_{rn}, \text{kcal} \cdot \text{mol}^{-1}$
1	$\text{HN}_3 + \text{M} = \text{NH} + \text{N}_2 + \text{M}$	14.88	0.0	36.2	17.5
2	$\text{NH} + \text{NH} = \text{H} + \text{N}_2 + \text{H}$	13.4	0.0	0.0	-77.0
3	$\text{H} + \text{H} + \text{M} = \text{H}_2 + \text{M}$	17.8	-1.0	0.0	-103.3

The solution of differential kinetic equations for these models allows time-varying species profiles at a given temperature in the interval 800–3500 K. The heat of reaction is calculated then as the difference in the enthalpies of formation between initial and formed species at each instant of time:

$$Q = \Delta H_f^0(\text{CH}_3\text{NO}_2/\text{HN}_3) \cdot (C_{\text{CH}_3\text{NO}_2/\text{HN}_3}^0 - C_{\text{CH}_3\text{NO}_2/\text{HN}_3}) - \sum \Delta H_f^0(\text{products}) C_{\text{products}}$$

Heat evolution profiles have been obtained as the result of the calculations. Typical profiles are presented in Figs. 16 and 17. The distinction in the decomposition mechanism between these representatives of two types of EM is immediately obvious, even from Tables 2 and 3: the endothermic compound (HN_3) can release the heat in fewer elementary stages compared with the redox system (CH_3NO_2).

Table 3 Elementary chemical reaction rate coefficients in the form $k = A_n T^m \exp(-E/RT)$, ($\text{cm}^3 \cdot \text{mol}^{-1} \cdot \text{s}^{-1}$) and molar reaction enthalpy ΔH_{rn} used in modeling nitromethane flame

Number	Reaction	$\ell_n A_n$	m	$E, \text{kcal} \cdot \text{mol}^{-1}$	$\Delta H_{rn}, \text{kcal} \cdot \text{mol}^{-1}$
1	$\text{CH}_3\text{NO}_2 + \text{M} = \text{CH}_3 + \text{NO}_2 + \text{M}$	17.0	0.0	44.0	70.1
2	$\text{CH}_3 + \text{NO}_2 = \text{CH}_3\text{O} + \text{NO}$	13.1	0.0	0.0	-18.2
3	$\text{CH}_3\text{O} + \text{M} = \text{CH}_2\text{O} + \text{H} + \text{M}$	26.3	-2.7	30.6	23.0
4	$\text{CH}_2\text{O} + \text{OH} = \text{HCO} + \text{H}_2\text{O}$	4.8	2.7	-1.9	-31.2
5	$\text{CH}_2\text{O} + \text{H} = \text{HCO} + \text{H}_2$	9.4	1.3	2.6	-16.1
6	$\text{HCO} + \text{M} = \text{H} + \text{CO} + \text{M}$	14.2	0.0	14.7	15.6
7	$\text{HCO} + \text{NO} = \text{CO} + \text{HNO}$	11.3	0.5	2.0	-29.8
8	$\text{NO}_2 + \text{H} = \text{NO} + \text{OH}$	14.5	0.0	0.8	-29.0
9	$\text{HNO} + \text{HNO} = \text{N}_2\text{O} + \text{H}_2\text{O}$	11.5	0.0	3.5	-10.5
10	$\text{CH}_3\text{O} + \text{HNO} = \text{CH}_3\text{OH} + \text{NO}$	13.5	0.0	0.0	-1.3
11	$\text{HCO} + \text{H} = \text{H}_2 + \text{CO}$	13.0	0.3	0.0	-88.6
12	$\text{HNO} + \text{NO} = \text{N}_2\text{O} + \text{OH}$	12.3	0.0	25.0	-17.4
13	$\text{H}_2 + \text{OH} = \text{H}_2\text{O} + \text{H}$	9.0	1.3	3.6	-15.1
14	$\text{CH}_3 + \text{CH}_2\text{O} = \text{CH}_4 + \text{HCO}$	8.4	1.8	3.0	-19.1
15	$\text{CH}_3 + \text{OH} = \text{CH}_2 + \text{H}_2\text{O}$	6.9	2.0	5.0	-11.2
16	$\text{CH}_3 + \text{NO} = \text{HCN} + \text{H}_2\text{O}$	11.0	0.0	15.0	-28.3
17	$\text{CH}_2 + \text{OH} = \text{CH}_2\text{O} + \text{H}$	13.4	0.0	0.0	-74.2
18	$\text{H} + \text{H} + \text{M} = \text{H}_2 + \text{M}$	18.0	-1.0	0.0	-103.3

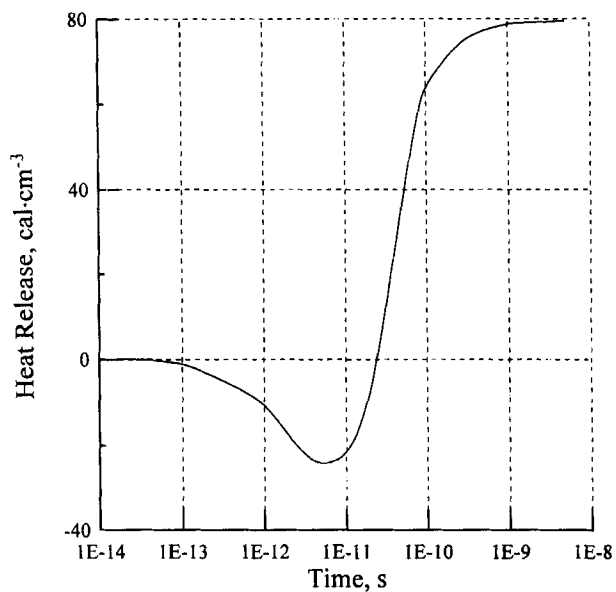


Fig. 16 Heat release profile for CH_3NO_2 decomposition at 1500 K.

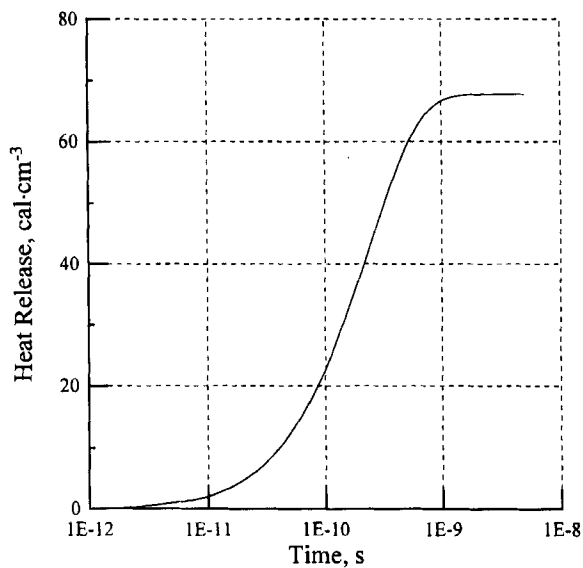


Fig. 17 Heat release profile for HN_3 decomposition at 1500 K.

Heat release profiles are also different. Typical profiles for CH_3NO_2 at temperatures above 1000 K invariably reveal a region where the heat is taken up (Fig. 16). This means that the rate of decomposition of the initial CH_3NO_2 molecule is superior to the rates of secondary exothermic reactions to consume formed radicals. At temperatures below 1000 K, however, the profile acquires the S-shaped curve form typical of a single-stage Arrhenius-type process. A noticeable time delay in the secondary heat-release reactions was experimentally observed in methylnitrate decomposition in shock waves at temperatures above 1000 K (Ref. 50). On the other hand, the HN_3 heat-release profile is characterized by an S-shaped curve (Fig. 17), and the heat-absorption region does not appear until 4000 K.

The profiles obtained can be used for determining the rate constants of the pseudo-first-order reaction responsible for the heat evolution process: $k = (1/\tau_{1/2}) \text{ s}^{-1}$, where $\tau_{1/2}$ is the time taken to release one-half heat of decomposition. The rate constants thus obtained and divided by the initial reagent concentrations can also be useful for comparing with rate constants for second-order elementary reactions.

Results of the calculations are presented in Figs. 18 and 19. Shown here are also thermal decomposition kinetic data for CH_3NO_2 (Fig. 18) and HN_3 (Fig. 19), as well as data for two reactions of recombination chosen from Tables 2 and 3, in such a way that both are best suited to the calculated rate constants. These reactions proved to be a recombination of HNO , in the case of CH_3NO_2 and a recombination of NH , in the case of HN_3 .

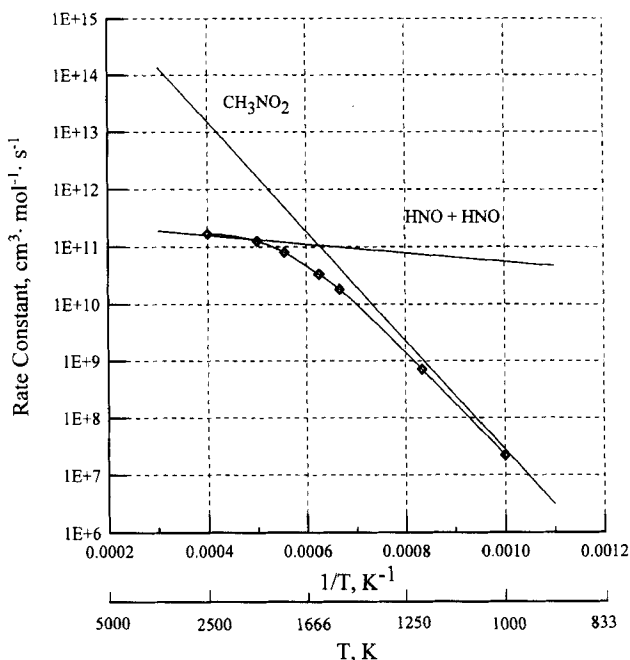


Fig. 18 Arrhenius plot of calculated rate constants for heat-release process in the decomposition of CH_3NO_2 (points) compared with kinetics of CH_3NO_2 thermal decomposition and HNO elementary reaction.

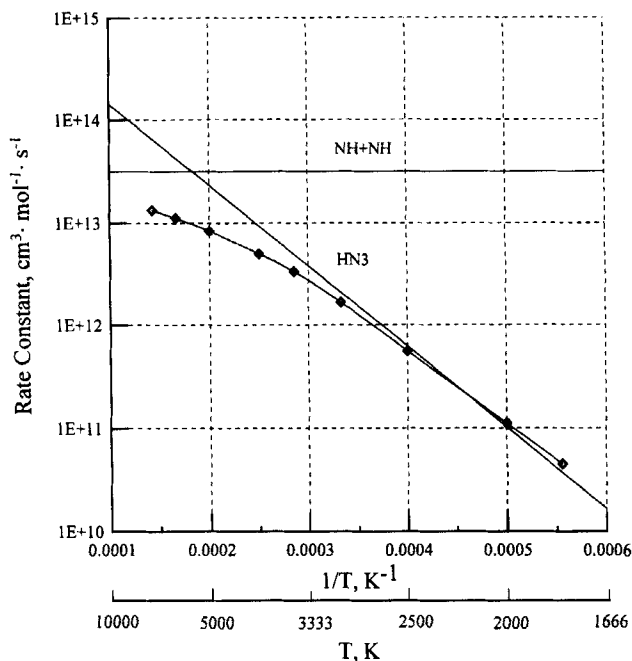


Fig. 19 Arrhenius plot of calculated rate constants for heat release process in decomposition of HN_3 (points) compared with kinetics of HN_3 thermal decomposition and NH elementary reaction.

The two plots are similar in appearance: at low temperatures the heat release is defined by the endothermic decomposition of the initial molecule, whereas at high temperatures it is controlled by secondary exothermic reactions of recombination. The main difference is in the temperature of transition: Nitromethane makes the transition at 1400 K, whereas for HN_3 the changeover is not observed until 3300 K. Other representatives of nitrocompounds and azides will be likely to demonstrate different transition temperatures, but these differences are not expected to be considerable, because the kinetic parameters of decomposition of EM of any given class normally differ only slightly.

An unexpected outcome of this kinetic analysis is that the rate of the heat generation process is seen to be dependent on the kinetics of both initial decomposition and secondary reactions within a rather wide temperature interval: 1500–2000 K for nitrocompounds and 3500–4500 K for azides. Within these intervals, the reaction rates are comparable, and neither should be disregarded.

Combustion temperatures of most of the HN_3 salts, organic azides, and tetrazoles fall in the range between 1000 and 2000 K and are confined to the HN_3 combustion temperature of ~ 3300 K. On the other hand, the majority of redox-type EMs have a combustion temperature above 1500 K. It is evident therefore why the burning rate of redox systems is mainly dependent on the kinetics of secondary reactions of recombination involving oxidizer-containing species, whereas for endothermic compounds it is determined by decomposition reactions.

IV. Conclusions

The combustion mechanism of energetic materials in which burning proceeds at the expense of the heat produced during decomposition reactions has been shown to differ significantly from the combustion mechanism of redox systems. The initial decomposition reaction, with high activation energy and the subsequent secondary exothermic reactions with lower activation energy provide the basis for the combustion process of both redox systems and endothermic compounds. The burning rate of endothermic EMs, however, unlike redox systems, is determined by only the decomposition kinetics. The reason for this is that the transition from combustion dominated by thermal decomposition to combustion dominated by the secondary reactions takes place in endothermic EMs at only high flame temperatures (above 3500 K), whereas the combustion temperatures of these materials are usually lower.

Incorporation of nitro groups into the aryl azide molecule, giving rise to increased combustion temperature, does not generally result in an increased rate of burning, as the rate of heat release in redox reactions involving NO₂ groups is much lower than the rate of heat evolution during decomposition of the energetic azide group. The exception is the case in which the introduction of the nitro group will influence the decomposition kinetics, as with *ortho*-NAB. In this case too the burning rate is determined by the kinetics of decomposition of the endothermic group.

It is significant that the kinetic parameters of the dominant reaction that controls the burning rate in the high-temperature gas zone may well be different from the kinetics of slow thermal decomposition at 150–250°C.

An important feature of the burning of organic azides and related tetrazoles is in the preferred formation of thermostable high-energy nitrile derivatives among the combustion products, resulting in incomplete heat release. On the other hand, in the presence of NH₃ or related groups (amino or hydrazino) in the molecule, NH₃ may remain in the combustion products, giving rise to elevated temperatures, because of its negative enthalpy of formation.

Acknowledgments

The authors gratefully acknowledge support from the Russian Fund for Fundamental Research (Grant 97-03-32402).

References

- ¹Fogelzang, A. E., Egorshv, V. Y., Sinditskii, V. P., and Dutov, M. D., "Combustion of Nitro Derivatives of Azidobenzenes and Benzofuroxans," *Combustion and Flame*, Vol. 87, No. 2, 1991, pp. 123–135.
- ²Bakhman, N. N., Kichin, Y. S., Kolyasov, S. M., and Fogelzang, A. E., "Investigation of the Thermal Structure of the Burning in Condensed Mixtures by Fine Thermocouples," *Combustion and Flame*, Vol. 26, No. 2, 1976, pp. 235–248.
- ³Skoog, D. A., and West, D. M., *Fundamentals of Analytical Chemistry*, Holt, Rinehart and Winston, New York, 1976, pp. 265–283.

⁴Laffitte, P., Hajal, I., and Combourieu, J., "Hydrogen Azide Decomposition Flame," *Proceedings of the 10th Symposium (International) on Combustion*, The Combustion Inst., Pittsburgh, PA, 1965, pp. 79–85.

⁵Fogelzang, A. E., Egorshv, V. Yu., Sinditskii, V. P., and Kolesov, B. I., "Combustion of Ammonium and Hydrazine Azides," *Combustion and Flame*, Vol. 90, No. 3–4, 1992, pp. 289–294.

⁶Gordon, A. J., and Ford, R. A., *The Chemist's Companion. A Handbook of Practical Data, Techniques and References*, Wiley, New York, 1972, pp. 72, 73.

⁷Alekseev, A. P., and Manelis, G. B., "Study of Liquid Hydrazine Combustion with Sampling of Gaseous Products Directly from the Flame," *Fizika Goreniya i Vzryva [Detonation and Shock Waves]*, Vol. 16, No. 4, 1980, pp. 54–60.

⁸Kajimoto, O., Yamamoto, T., and Fueno, T., "Kinetic Studies of the Thermal Decomposition of Hydrazoic Acid in Shock Waves," *Journal of Chemical Physics*, Vol. 83, No. 4, 1979, pp. 429–435.

⁹Dupré, G., Paillard, C., Combourieu, J., Fomin, N. A., and Soloukhin, R. I., "Decomposition of Hydrogen Azide in Shock Waves," *Proceeding of the 13th International Symposium on Shock Tubes and Waves*, Niagara Falls, NY, 1982, pp. 626–634.

¹⁰Zaslanko, I. S., Kogarko, S. M., and Mozhukhin, E. V., "Thermal Decomposition Mechanism of Hydrazoic Acid," *Zhurnal Kinetika i Kataliz [Russian Journal of Kinetics and Catalysis]*, Vol. 13, No. 4, 1972, pp. 829–835.

¹¹Zeldovich, Y. B., and Frank-Kamenetskii, D. A., "The Theory of Thermal Propagation of a Flame," *Zhurnal Fizicheskoi Khimii [Russian Journal of Physical Chemistry]*, Vol. 12, No. 1, 1938, pp. 100–105.

¹²Dupré, G., Paillard, C., and Combourieu, J., "A Study of the Decomposition Flame of Gaseous Azides by Time-of-Flight Mass Spectroscopy," *Dynamic Mass Spectrometry*, edited by D. Price and T. F. T. Todd, Vol. 4, Heyden and Sons, London, 1975, pp. 233–245.

¹³Barton, D., and Ollis, W. D., *Comprehensive Organic Chemistry. Nitrogen Compounds*, Vol. 2, Pergamon, New York, 1979, Chap. 6.5, pp. 313–326.

¹⁴Manelis, G. B., Nazin, G. M., Rubtsov, Yu. I., and Strunin, V. A., *Thermal Decomposition and Combustion of Explosives and Propellants*, Nauka, Moscow, 1996, pp. 70–75.

¹⁵Chen, J. K., and Brill, T. B., "Thermal Decomposition of Energetic Materials 54. Kinetics and Near-Surface Products of Azide Polymers AMMO, BAMO, and GAP in Simulated Combustion," *Combustion and Flame*, Vol. 87, No. 2, 1991, pp. 157–168.

¹⁶Sergeev, V. V., and Kozhukh, M. S., "On Combustion of 1,3-diazidopropanol-2," *Fizika Goreniya i Vzryva [Detonation and Shock Waves]*, Vol. 11, No. 3, 1975, pp. 403–412.

¹⁷Kozhukh, M. S., and Sergeev, V. V., "Limit Burning Conditions of Some Organic Azides," *Fizika Goreniya i Vzryva [Detonation and Shock Waves]*, Vol. 13, No. 5, 1977, pp. 690–698.

¹⁸Andreev, K. K., and Bespalov, G. N., "Combustion of Nitroglycerine," *Book of Articles on the Theory of Explosives*, Oborongiz, Moscow, 1963, pp. 430–443.

¹⁹Landau, L. D., and Livshits, E. M., *Mechanics of Continuous Mediums*, Gostekhteorizdat, Moscow, 1953, pp. 326–355.

²⁰Kubota, N., and Sonobe, T., "Combustion Mechanism of Azide Polymer," *Propellants, Explosives, Pyrotechnics*, Vol. 13, No. 4, 1988, pp. 172–177.

²¹Nakashita, G., and Kubota, N., "Energetics of Nitro/Azide Propellants," *Propellants, Explosives, Pyrotechnics*, Vol. 16, No. 4, 1991, pp. 177–181.

²²Miyazaki, T., and Kubota, N., "Energetics of BAMO," *Propellants, Explosives, Pyrotechnics*, Vol. 17, No. 1, 1992, pp. 5–9.

²³Haas, Y., Eliahu, Y. B., and Welner, S., "Infrared Laser-Induced Decomposition of GAP," *Combustion and Flame*, Vol. 96, No. 3, 1994, pp. 212–220.

²⁴Kimura, E., and Oyumi, Y., "Thermal Decomposition of BAMO Copolymers," *Propellants, Explosives, Pyrotechnics*, Vol. 20, No. 6, 1995, pp. 322–326.

²⁵Kubota, N., "Combustion of Energetic Azide Polymers," *Journal of Propulsion and Power*, Vol. 11, No. 4, 1995, pp. 677–682.

²⁶Hori, K., and Kimura, M., "Combustion Mechanism of Glycidyl Azide Polymer," *Propellants, Explosives, Pyrotechnics*, Vol. 21, No. 4, 1996, pp. 160–165.

²⁷Arisawa, H., and Brill, T. B., "Thermal Decomposition of Energetic Materials 71. Structure-Decomposition and Kinetic Relationships in Flash Pyrolysis of Glycidyl Azide Polymer (GAP)," *Combustion and Flame*, Vol. 112, No. 4, 1998, pp. 533–544.

²⁸Zel'dovich, Y. B., "Theory of Combustion of Propellants and Explosives," *Zhurnal Eksperimental'noy i Teoreticheskoy Fiziki [Journal of Experimental and Theoretical Physics]*, Vol. 12, No. 11–12, 1942, pp. 498–524.

²⁹Khmelnitsky, L. I., Novikov, S. S., and Godovikova, T. I., *Chemistry of Furoxans. Structure and Synthesis*, Nauka, Moscow, 1996, pp. 269–303.

³⁰Kondrikov, B. N., Raikova, V. M., and Samsonov, B. S., "On Kinetics of Burning Reactions of Nitrocompounds at a High Pressure," *Fizika Goreniya i Vzryva [Detonation and Shock Waves]*, Vol. 9, No. 1, 1973, pp. 84–76.

³¹Fogelzang, A. E., Egorshv, V. Y., Sinditskii, V. P., and Dutov, M. D., "Influence of Chemical Structure of Organic Azides on Their Combustion Behavior," *Fizika Goreniya i Vzryva [Detonation and Shock Waves]*, Vol. 26, No. 5, 1990, pp. 69–76.

³²Dyall, L. K., and Kemp, J. E., "Neighboring-Group Participation in Pyrolysis of Aryl Azides," *Journal of the Chemical Society, Sec. B*, No. 9, 1968, pp. 976–979.

³³Fogelzang, A. E., Egorshv, V. Y., Sinditskii, V. P., Dutov, M. D., and Solov'ev, M. Y., "Research of Combustion of Tetrazole and Its Derivatives," *Proceedings of the 9th All-Union Symposium on Combustion and Explosion. Combustion of Condensed System*, Institut Khimicheskoy Fiziki, Chernogolovka, 1989, pp. 3–5, 129–131.

³⁴Fogelzang, A. E., Egorshv, V. Y., and Sinditskii, V. P., "Influence of Chemical Nature of Substituent on the Burning Rate of 5-Substituent Tetrazoles," *Proceedings of the 17th International Pyrotechnic Seminar Combined with 2nd Beijing International Symposium on Pyrotechnics and Explosives*, Vol. 2, Beijing Inst. of Technology Press, Beijing, China, 1991, pp. 618–623.

³⁵Lesnikovich, A. I., Printsev, G. V., Ivachkevich, O. A., Lutsko, V. A., and Kovalenko, K. K., "Combustion of Tetrazole," *Fizika Gorenia i Vzryva [Detonation and Shock Waves]*, Vol. 24, No. 5, 1988, pp. 48–51.

³⁶Sinditskii, V. P., Egorshv, V. Y., Fogelzang, A. E., Serushkin, V. V., and Kolesov, V. I., "Combustion Behavior and Flame Structure of Tetrazole Derivatives," *29th International Conference of the Fraunhofer-Institut Chemische Technologie*, Verlag GmbH, Karlsruhe, Germany, 1998, Paper 171, pp. 1–15.

³⁷Henry, R. A., Finnegan, W. G., and Lieber, E., "Thermal Isomerization of Substituted 5-Aminotetrazoles," *Journal of the American Chemical Society*, Vol. 76, No. 1, 1954, pp. 88–93.

³⁸Henry, R. A., Finnegan, W. G., and Lieber, E., "Kinetics of the Isomerization of Substituted 5-Aminotetrazoles," *Journal of the American Chemical Society*, Vol. 77, No. 8, 1955, pp. 2264–2270.

³⁹Brodskii, A. I., *Physical Chemistry*, Vol. 1, Nauka, Moscow, 1948, pp. 273–290.

⁴⁰McEvan, M. S., and Rigg, M. W., “The Heats of Combustion of Compounds Containing the Tetrazole Ring,” *Journal of the American Chemical Society*, Vol. 73, No. 10, 1951, pp. 4725–4727.

⁴¹Prokudin, V. G., Poplavsky, V. S., and Ostrovsky, V. A., “The Mechanism of Monomolecular Thermal Decomposition of Tetrazole and Its 5-Substituted Derivatives,” *Izvestiya Akademii Nauk, Seriya Khimicheskaya*, [Russian Bulletin of the Academy of Sciences, Chemistry Series], No. 9, 1996, pp. 2216–2219.

⁴²Gao, A., Oyumi, Y., and Brill, T. B., “Thermal Decomposition of Energetic Materials 49. Thermolysis Routes of Mono- and Diaminotetrazoles,” *Combustion and Flame*, Vol. 83, No. 3–4, 1991, pp. 345–352.

⁴³Ivachkevich, O. A., Krasitsky, V. A., Lesnikovich, A. I., Astashinsky, V. M., Kostyukevich, E. A., Khusid, B. M., and Mansurov, V. A., “Liquid-Flame Combustion II,” *Combustion and Flame*, Vol. 110, No. 1–2, 1997, pp. 113–126.

⁴⁴Wong, M. W., Leung-Toung, R., and Wentrup, C., “Tautomeric Equilibrium and Hydrogen Shifts of Tetrazole in Gas Phase and in Solution,” *Journal of the American Chemical Society*, Vol. 115, No. 6, 1993, pp. 2465–2472.

⁴⁵Prokudin, V. G., Poplavsky, V. S., and Ostrovsky, V. A., “The Mechanism of Monomolecular Thermal Decomposition of 1,5- and 2,5-Disubstituted Tetrazoles,” *Izvestiya Akademii Nauk, Seriya Khimicheskaya* [Russian Bulletin of the Academy of Sciences, Chemistry Series], No. 9, 1996, pp. 2209–2215.

⁴⁶Koldobskii, G. I., and Ostrovskii, V. A., “Tetrazoles,” *Uspekhy Khimii* [Russian Chemistry Review], Vol. 63, No. 10, 1994, pp. 847–865.

⁴⁷Fogelzang, A. E., Sinditskii, V. P., Egorshv, V. Y., and Serushkin, V. V., “Effect of Structure of Energetic Materials on Burning Rate,” *Decomposition, Combustion, and Detonation Chemistry of Energetic Materials*, MRS Symposium Proceedings, Vol. 418, Materials Research Society, Pittsburgh, PA, 1996, pp. 151–161.

⁴⁸Melius, C. F., “Thermochemical Modeling: II. Application to Decomposition of Energetic Materials,” *Chemistry and Physics of Energetic Materials*, edited by S. Bulusu, Kluwer Academic, Dordrecht, The Netherlands, 1990, pp. 51–78.

⁴⁹Melius, C. F., “Thermochemistry and Reaction Mechanism of Nitromethane Ignition,” *Journal de Physique IV (Paris)* Vol. 5, May 1995, pp. C4-535–C4-551.

⁵⁰Zaslanko, I. S., Smirnov, V. N., Tereza, A. M., and Tsyganov, S. A., “Kinetics of Energy Release by Thermal Decomposition of Nitrates in Shock Waves,” *Fizika Goreniya i Vzryva* [Detonation and Shock Waves], Vol. 24, No. 2, 1988, pp. 137–141.

Chapter 1.5

Molecular Structure Tailoring of Binders in Solid Propellants

Huimin Tan,* Yingquan Duo,[†] and Futai Chen[†]

Beijing Institute of Technology, Beijing, People's Republic of China

Nomenclature

H	= fraction of hard segment in thermoplastic elastomer (TPE) by mass, Eq. (3)
N_E	= average sequence length of ethylene oxide (EO) unit
N_T	= average sequence length of tetrahydrofuran (THF) unit
T_g	= measured glass transition temperature of soft segments in TPE
T_{g1}	= glass transition temperature of soft segments of TPE
T_{g2}	= glass transition temperature of hard segments of TPE
W	= fraction of weight
γ_E	= rate of competition of EO monomer
γ_T	= rate of competition of THF monomer
ΔT_g	= changes of the glass transition temperature
ε_m	= elongation at peak
σ_m	= tensile strength at peak
χ_c	= molar ratio of ether oxygen units in soft segments forming hydrogen bonds

Subscripts

BTTN	= 1, 2, 4-butanetriol trinitrate
NG	= nitroglycerin
PL	= polymer
1	= soft segments
2	= hard segments

This material is declared a work of the U.S. Government and is not subject to copyright protection in the United States.

*Professor, School of Chemical Engineering and Materials Science.

[†]Graduate Student, School of Chemical Engineering and Materials Science.

I. Introduction

IT IS well understood that binders play a very important role in solid propellants, in which filler particles and other additives are bound together to form a composite grain with satisfactory mechanical properties. During propellant combustion, the binder reacts with the oxidizer and acts as an important part of the fuel to provide energy release and working mass (fluid). Therefore, the properties of a given solid propellant are determined, to a great extent, by the selected binder system. For this reason, optimizing the molecular design and tailoring of binders has been the subject of considerable study.

To meet application requirements, a solid propellant binder should possess the following properties: 1) good mechanical properties over a wide temperature range, typically from -40 to 60°C ; 2) good compatibility with other ingredients in the formulation; 3) good thermal and aging stability; 4) fulfillment of casting or extrusion processing requirements; and 5) low toxicity and high level of safety during propellant manufacturing.

Therefore, an ideal molecule for thermoset binder should be a liquid prepolymer that 1) exhibits low- (or non) crystallization potential at low temperatures, 2) is capable of providing low viscosity in high solid loading mixtures and has a reasonable relative molecular weight (i.e., 2000–6000) and preferably a narrow molecular weight distribution, and 3) possesses two (or more) functional groups that are able to complete the curing reaction with suitable kinetic reaction rate to ensure sufficient pot life.

Usually, a telechelic prepolymer is preferable. In this class of prepolymer, the cured network parameters, that is, cross-link density and average network molecular weight can be adjusted in a relatively wide range to meet different mechanical property requirements of propellants.

On the other hand, the prepolymer should not contain any active functional groups other than those necessary to meet the curing requirement. Functional groups, such as double bonds, tertiary hydrogens, and alkylene-alcohols, are not suitable for these molecule chains.

To ensure low viscosity for casting slurry, low hydrogen bonding between binder chains is desirable. Currently, the binders used in solid propellants do not have optimum chemical structures. Therefore, a reasonable molecular design, or a tailoring of binder systems, is an important field of study in solid propellants. This paper describes an optimum molecular design for thermoset binders in nitrate ester plasticized polyether (NEPE) propellants, based on chain structure and mechanical property tailoring.

For thermoplastic elastomers (TPEs), there are additional requirements for the design of the proper microdomain in these binders so that they can provide the proper melting temperature and mechanical properties for the resulting propellants. As the result of our study, we have obtained a correlation of binder chemical structure and the required propellant properties. These results could be useful for optimizing binder chemical structure for propellant applications.

II. Molecular Structure Tailoring for Prepolymers in NEPE Propellant Binder

In polymers, the chains' symmetry and regularity are the main factors affecting crystallization and are, therefore, the main problems in obtaining good mechanical

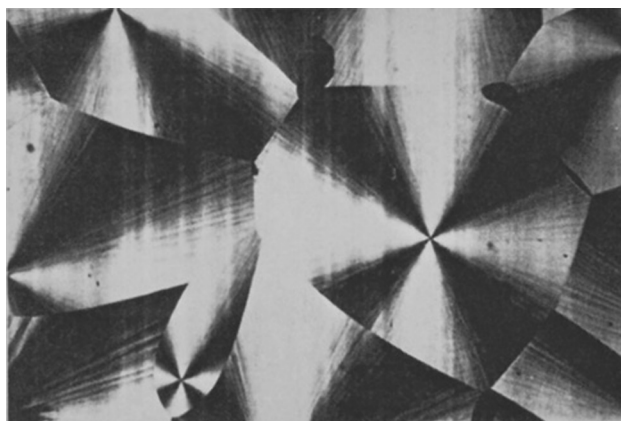


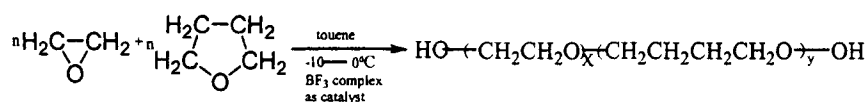
Fig. 1 Orthogonal polarizing micrograph of PEG (\overline{M}_n 8000), obtained by heating to 70°C and crystallizing at room temperature.

properties for propellants within the applications temperature range, that is, from -50 to 70°C. It is well understood that flexible chains consisting of symmetrical structure units and/or highly regular sequence arrangements show a tendency to crystallize at temperatures below the melting point due to the decrease of free energy and system entropy. As a rule, the better the flexibility is, the easier the crystallization is. A chain's conformation in crystals may be zigzag or helical. Crystals appear to be either spherulite or lamellar in structure.

It is known that the polyethylene glycol (PEG) prepolymer used in NEPE propellant tends to form crystals.¹ Orthogonal polarizing microscopic observations revealed that these crystals are mainly spherulites (see Fig. 1). X-ray diffraction results indicate that PEG spherulite still exists in the NEPE propellant binder, but the crystallization tendency is suppressed by adding large amounts of nitrate ester (see Fig. 2). The tendency of PEG to crystallize at low temperatures is responsible for the low-strain capability of the propellant in the low-temperature range. As reported in Ref. 2, the elongation of this type of NEPE propellant is only about 20% at -40°C. Therefore, decreasing the binders' chain stereo regularity would be an effective way to reduce its crystallization tendency and to improve its low-temperature mechanical properties.

It is possible in polymer synthesis to introduce another structure unit in the polymer chains to reduce the structure symmetry, thereby decreasing the crystallization tendency. If proper chemical units are chosen, then good properties of a highly plasticized binder can be maintained. Tetramethylene oxide is such an ideal structural unit. Using ethylene oxide (EO) and tetrahydrofuran (THF) as monomers and ethylene glycol as the initiator, a random distributed copolymer of polyether can be synthesized by bulk polymerization with a BF_3 complex as catalyst.³

The alternate extent of the structure units, their sequence length, and their rate of competition are summarized in Table 1.



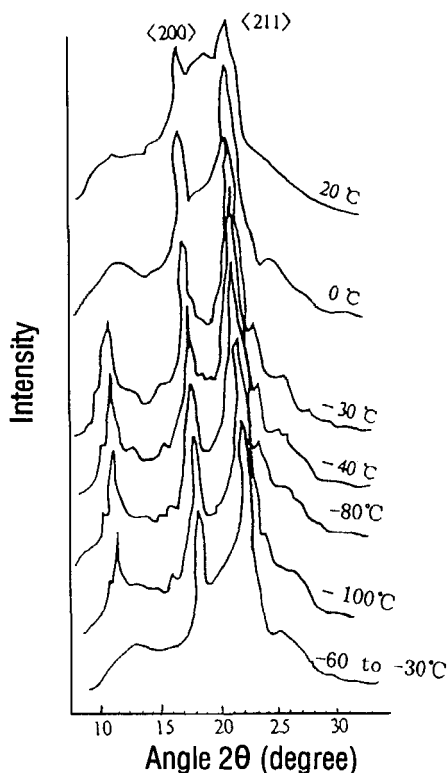


Fig. 2 WAXD spectrum of nitrate ester plasticized PEG (8000) cured with TDI, plasticizing ratio $W_{PL}/W_{PO} = 7/3$, plasticizer NG/BTTN = 1/1.

Theoretically, a truly random polymer can be obtained with a monomer change of THF/EO (50/50), where the extent of alternation of the structural units approaches 50% and the sequence lengths of these two structural units are close to 2. This means that a randomly distributed chain is achieved. As a result, the cured binders with this prepolymer exhibit a low crystallization tendency. Wide angle x-ray diffraction analysis of isophorone diisocyanate (IPDI) cured, nitrate ester plasticized P(E/T) binder indicated a noncrystalline morphology (Fig. 3).

Table 1 Chain composition of EO and THF copolymer P(E/T)

Molar ratio of feeding THF/EO	Alternate extent, %	Average sequence length		Rate of competition		
		THF unit N_T	EO units N_E	γ_T	γ_E	$\gamma_T \cdot \gamma_E$
70/30	44.96	2.87	1.58	0.8014	1.3500	1.0818
60/40	48.30	2.37	1.79	0.9000	1.1830	1.0665
50/50	50.22	1.97	2.01	0.9700	1.0100	0.9797
40/60	48.33	1.74	2.39	1.1000	0.7942	0.8815
30/70	46.40	1.38	2.93	0.8866	0.8271	0.7333

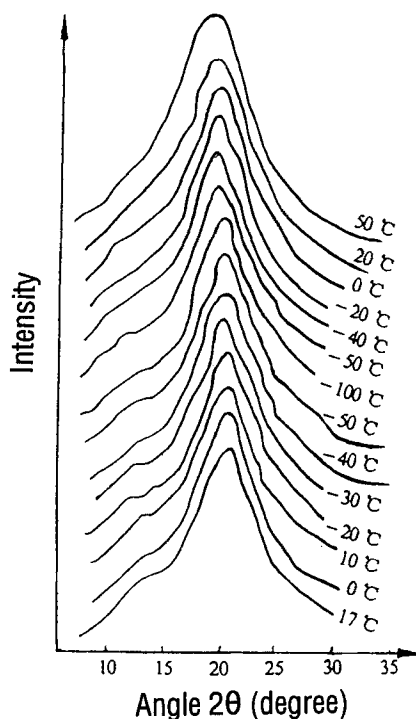


Fig. 3 WAXD spectrum of nitrate ester plasticized P(E/T), monomer unit ratio E:T = 50/50, plasticizing ratio $W_{PL}/W_{PO} = 1.50$, plasticizer NG/BTTN = 1/1.

Propellants based on the copolymer P(E/T) with ammonium perchlorate (AP), Al, and octogen (HMX) as solid filler and plasticized with nitrate ester NG/BTTN (1:1) were also prepared. With isocyanate N-100 as the curing and cross-linking agent, as shown in Table 2, P(E/T) propellants exhibited excellent mechanical properties. As compared with PEG propellant, elongation at low temperature is significantly improved from 20 to 107%. This is undoubtedly attributed to the molecular design and the built-in flexible random distributed copolymer chains in the binder. Results reveal that P(E/T) propellant is capable of providing excellent

Table 2 Mechanical properties of P(E/T) propellant^a

Temperature, °C	Stress strength σ_m , MPa	Elongation ε_m , %
70	0.642	62
20	0.945	67
-40	1.86	107

^aSolid content, 75%; plasticizer, NG/BTTN = 1/1; plasticizing ratio, $W_{PL}/W_{PO} = 2.80$.

mechanical properties in a wide temperature range, between -40 and 70°C . Consequently, great potential for applications not only in strategic but also in tactical missiles can be seen.

III. Molecular Structure Tailoring of Binders in TPE Propellants

TPEs are made up with a combination of hard segments and soft segments in a polymer chain. Rubber elasticity and plasticity are both present in the polymer. TPEs can be easily melted in processing and maintain rubber elasticity at room temperature. Therefore, highly efficient processing techniques of plastics, that is, extrusion, also can be employed. Attempts have been made in the propellant industry to obtain low-vulnerability ammunition propellants with TPEs. In this way, extrusion techniques can be applied in producing composite propellants, and the excess and expired propellants can be remelted and reproduced. This is the reason that TPE has attracted considerable attention from propellant chemists. Several types of TPEs have been investigated in the preparation of solid propellant. They are all block copolymers, such as Kraton G1652 (styrene-butadiene-styrene block copolymer),^{4,5} Kyeas 40-04 (copolymer of ethylene and acrylic acid or acrylate), Estome 5712 (a kind of polyurethane), and Kratone 1107 (copolymer consisting of 15% polystyrene and 85% polyisoprene). TPE binders have already been used in rocket motors and gas generators. Like all other TPE polymer materials, the properties of TPE propellants are determined by their chemical structure (short-range structure), morphology (long-range structure), supermolecular structure (i.e., phase separation structure or microdomains), and to a great extent, the interactions and distributions of fillers and additives in the materials (the so-called textile structure). In an $(AB)_n$ -type TPE, the hard segments A (crystalline phase) tend to aggregate to form microdomains of physically cross-linked regions that are distributed throughout the soft segments B (continuous phase). The constitution of A and B in this linear block copolymer and their sequence length play an important role in the physical properties of TPEs. The chemical structure of the hard and soft segments and their ratio are an integral part of the molecular design of the optimum TPE binder. When applied to propellant manufacturing, the TPE must exhibit the following specific characteristics.

1) The TPE should consist of linear chains with high relative molecular weight, that is, $\overline{M}_n > 10^5$.

2) The TPE gumstock should exhibit $\sigma_m > 4$ MPa and $\varepsilon_m > 500\%$ to be considered for propellant applications. These excellent mechanical properties can be achieved by the proper selection of A and B blocks and tailoring of their ratios.

3) The TPE should be capable of being plasticized with energetic plasticizers, that is, nitrate esters, at high levels of retention.

4) The processing temperature (mixing extrusion) must be within the safety limit of the propellant mixture: $353\sim 393$ K is preferable.

5) To obtain high elongation (usually 30% is required) at low temperature, the glass transition temperature of the soft segments should be lower than 223 K.

IV. Hard-Segment Domain Structure Selection

There are four types of hard-segment domains defined according to the chemical structure feature in linear TPE: 1) glass state domain, where the hard segments

serve as cross-linking points (polystyrene polybutadiene polystyrene TPE of Kratone G16562 is a representative of this type); 2) ionic complex domain, such as Kyeas 40-04 of polyethylene-acrylic acid (or acrylate) TPE; 3) crystalline domain, for example, polyurethane TPE Estome 5712; and 4) chemical cross-linked domain, partly cured EPDM or reversible covalent bond cross-linked polyurethanes.

In reversible covalent bond cross-linked TPE, the melting temperature is usually above 140°C, which is too high for the propellant to be mixed safely. Furthermore, chemically cross-linked TPE has the drawback of having poor processing properties, so that it is eliminated from consideration. On the other hand, TPE with ionic complex domains, of which soft segments are mainly vinyl polymers, are not miscible with nitrate esters. As a consequence, energetic performance of propellants made of this kind of TPE would be reduced. Polystyrene (such as Kratone G) typically exhibits glass state microdomains, with a typical glass transition temperature of usually up to 100°C. As a result, within the application temperature range, the required propellant mechanical properties appear to be characteristic of a glass state. The most likely candidate for the crystalline block is polyurethane because its melting temperature is lower than 120°C and it supports a good melting behavior because of its crystalline domain structure.

V. Chemical Structure Selection of Soft Segments

The rubber elasticity of TPE mainly comes from the soft segments that serve as the continuous phase in the matrix. We used the following criteria to select the soft segment for synthesis of polyurethane TPE.

- 1) It must have a highly flexible chain with low glass transition temperature ($T_g < -50^\circ\text{C}$) and high elasticity. Moreover, high molecular weight, such as $\overline{M}_n > 2000 \sim 3000$, has to be maintained.
- 2) It must possess proper crystallization ability that will support a sharp melting behavior.
- 3) It is able to form fairly low hydrogen bonding with hard segments.
- 4) It should be miscible with nitrate esters.

Our investigation indicated that prepolymers able to meet the listed requirements are hydroxy-terminated polyesters or polyethers, that is, polyethylene adipate, hydroxy-terminated polyethers, that is, polyethylene glycol, polytetramethylene oxide (PTMO), and copolymer of ethylene oxide and THF [P(E/T)]. Their properties are given in Table 3.

According to the data in Table 3, random distributed copolyether P(E/T) is the best choice for soft-segment prepolymer. In addition, an ideal TPE with proper hard- and soft-segment ratio can be obtained through its reaction with diisocyanate:

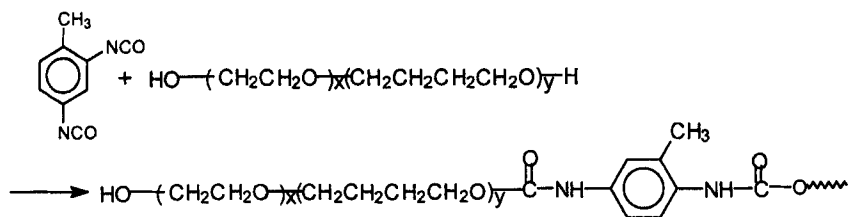


Table 3 Properties of aliphatic polyesters and polyethers

Polymer	Miscibility with nitrate ester		Potential for crystallization (melting point, °C)	T_g , °C
	W_{NG}/W_{PL}	W_{BTN}/W_{PL}		
PTMO	0.46	0.24	Strong (28)	-76
PEG	>4.0	>4.0	Strong (53)	-53
Polyethylene adipate	>4.0	>4.0	Medium (65)	-40
Copolyether P(T/E)				
70/30	1.18	0.64	Medium	—
60/40	1.64	0.92	Weak	-58
50/50	2.26	1.46	No	—
40/60	2.74	1.90	Strong	—

To obtain a high molecular weight TPE, a chain extender has to be used in the reaction. Because the cohesion energy for different chain extenders varies, different secondary cross-linking extents (caused by hydrogen bonding) will be exhibited in the synthesized TPE. When different chain extenders are used, mechanical property changes to the final products are evident, as shown in Table 4.

Results shown in Table 4 indicate the following.

1) TPEs with ethylene glycol (EDO) as chain extender bring excellent mechanical properties to the products. This is attributed to the existence of more hydrogen bonding. Processing temperature is also increased, generally to above 393 K (measured from differential scanning calorimetry).

2) In addition to the chain extender, the weight percent of the hard segment in the synthesized TPE also plays an important role in determining the mechanical properties. The higher the weight percent of the hard segments, the better the ability to withstand stress and strain.

3) The processing transition temperature can be brought down to below 393 K by using 1,4-butanediol (BDO) as chain extender, while keeping the hard-segment

Table 4 Chain extender effects on TPE matrix

Molecular weight of P(E/T)	Chain extender ^a	Hard segment content, %	Tensile strength σ_m , MPa	Elongation ϵ_m , %	Modulus, MPa	σ at 250% elongation, MPa
3600	BDO	37	1.3	>439	22	—
3600	BDO	40	4.97	692	30	1.98
3600	BDO	45	8.34	639	35	3.96
1400	BDO	40	0.2	149	1.0	—
1400	BDO	46	0.2	370	1.1	—
3600	EDO	23	1.7	196	4.1	—
3600	EDO	35	6.6	316	15.3	—
3600	EDO	38	14.7	>439	19.3	—
3600	EDO	43	20.4	>439	22.0	—

^aBDO: 1,4-butanediol, EDO: ethylene glycol.

content within 40~45%. In this situation, a desirable coincidence of mechanical properties and propellant processing temperature was reached.

4) Molecular weight of P(E/T) exhibits significant effects on the matrix mechanical properties. A sharp drop in ability to withstand stress and strain occurs when the molecular weight of P(E/T) is below 1400.

VI. Microphase Separation Estimation

Microphase separation is an important physical property for all TPEs. According to published work,^{6,7} the microphase separation in a TPE is essentially an equilibrium process, in which certain hard segments will be dissolved in the soft segments and vice versa. Usually, only the dissolution of the hard-segment phase material into the soft-segment phase material is considered because much less soft-segment phase is dissolved in the hard-segment phase. As a consequence, the glass transition temperature T_g changes in accordance with the Gordon-Taylor equation⁸:

$$1/T_g = W_1/T_{g1} + W_2/T_{g2} \quad (1)$$

where T_{g1} is 198 K and T_{g2} is 390 K as reported in Ref. 9.

Furthermore, it is known that the formation of hydrogen bonding is the driving force of aggregation in the hard-segment phase, where the hydrogen in the $-\text{NH}-$ group is the donor of the proton and the carbonyl and ether oxygen is the acceptor. Usually 95% of $-\text{NH}-$ are involved in hydrogen bonding. Of course, hydrogen bondings exist between hard and soft segments. As a result, the movements of soft segments are restricted. Therefore, T_g is affected. This kind of physical cross-linking effect should also account for T_g changes, which can be estimated with the DiBenedetto-Dimarzio equation¹⁰:

$$(T_g - T_{g1})/T_{g1} = k\chi_c/(1 - \chi_c) \quad (2)$$

where k is constant, generally 1.5.

The combination of Eqs. (1) and (2) gives a quantitative estimation of the percentage of hard segments dissolved into soft segments:

$$\frac{T_g - T_{g1}}{T_{g1}} = \frac{1.05H \cdot W}{1 - H + 0.136H \cdot W} \quad (3)$$

By means of DSC measurements of T_g variations in the soft segments, the extent of hard segments dissolved into soft segments will be estimated using Eq. (3). Results are summarized in Table 5. Data in Table 5 indicate that excellent microphase

Table 5 Percentage of hard segments dissolved into soft segments in TPE

Hard-segment content of TPE, %	ΔT_g , K	Dissolved extent W , %
40	13.8	6.28
45	13.1	6.01
48	13.4	6.11
50	11.8	5.42

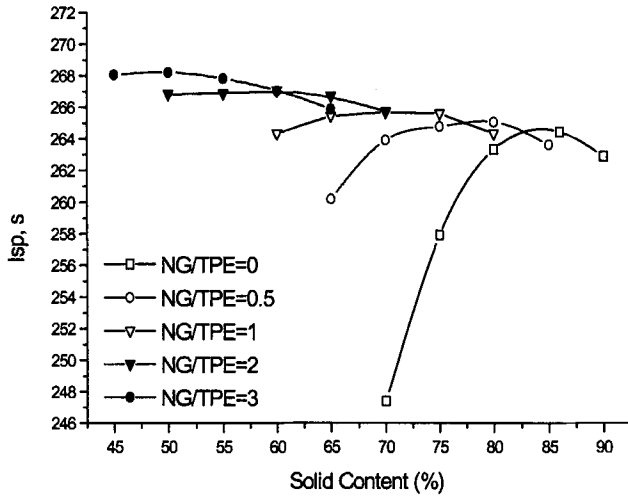


Fig. 4 Relationship of specific impulse vs solid content for different plasticizing ratios in TPE propellants.

Table 6 Maximum theoretical specific impulse of TPE propellants

Plasticizing ratio NG/TPE	Composition, %				Solid content, %	Maximum theoretical specific impulse	
	TPE	NG	AP	AL		$N \cdot S/\text{kg}$	s
0	13.8	0	62.3	23.9	86.2	2591.4	264.4
0.5	13.3	6.6	55.2	24.9	80.1	2598.3	265.1
1.0	14.9	14.9	48.4	21.8	70.2	2604.1	265.7
2.0	13.3	26.6	39.6	20.5	60.1	2617.8	267.1
3.0	12.5	37.5	28.4	21.6	50.0	2628.6	268.2

Table 7 Composition of nitrate ester plasticized TPE propellant

Formulation	TPE, %	NG, %	AP, %	Al, %
A	14.9	14.9	48.4	21.8
B	20.0	10.0	49.3	20.7

Table 8 Mechanical properties of TPE propellant

Formulation	20°C		-40°C	
	σ_m , MPa	ε_m , %	σ_m , MPa	ε_m , %
A	0.66	183.3	9.94	46.5
B	1.14	388.5	14.80	30.1

separation exists in all of the investigated TPE (containing 40~50% hard segment) because the dissolving extent for all of the samples is less than 10%. Therefore, as an ideal propellant binder, a polyurethane TPE molecule is selected with the following structural features: soft segment consists of P(E/T) [E:T = 50/50] and PEG with molecular weights of 3600 and 4000, respectively, and PEG content is 6%. The hard segment consists of IPDI and BDO, where 40~45% hard-segment content is preferred. The overall molecular weights of the synthesized TPEs are in the range of 10^5 – 1.2×10^5 .

VII. TPE Propellant

Propellant samples were made from this newly synthesized TPE binder. We have evaluated these samples for their mechanical processing and combustion properties. A conventional absorption–rolling–extrusion process was used to prepare the TPE propellant. A special procedure was also adopted for the addition of water soluble AP. That is, part of the TPE was dissolved in an assistant solvent (THF) and slurry was formed in a mixer with AP. A prerolling was then applied to evaporate most of the solvent. Finally, the mixture was put into a rolling machine to combine with the dehydrated paste.

Results of thermodynamic calculations are shown in Fig. 4 and Table 6. The maximum theoretical impulse reaches $2628.6 \text{ N} \cdot \text{S/kg}$, where the solid content is 50% and plasticizing ratio NG/TPE equals 3.0.

Formulations chosen for the evaluation of propellant mechanical and combustion behaviors are given in Table 7. The results are listed in Table 8.

The combustion properties of TPE propellant (formulation A) are as follows: at 4, 6, 7, 9, and 11 MPa pressure the burning rate is 11.1, 11.7, 13.7, 14.1, and $16.0 \text{ mm} \cdot \text{s}^{-1}$, respectively. Measured results reveal that the TPE propellant candidates are promising. Note that an attractive feature is that, without the addition of a burn rate catalyst, the burn rate pressure exponent was as low as 0.36, which will contribute to easy control in propellant combustion.

VIII. Conclusions

1) For flexible chain prepolymers, the high regularity of structural units tends to result in high crystallinity. The introduction of secondary structural units into the polymer to increase the degree of randomness suppresses the crystallization at low temperature. A copolymer formed from ring opening polymerization of ethylene oxide and THF is shown to be a random copolymer. When the monomer ratio EO/THF approaches 50/50, NEPE propellants with this binder possess excellent mechanical properties in a wide temperature range. The elongation at -40°C , as high as 100%, implies the potential of this NEPE propellant to be applied to not only strategic, but also tactical missiles.

2) A new thermoplastic elastomer was successfully synthesized through the molecular structure design of the hard and soft segments. By using the copolyether, P(E/T), as the soft segment and IPDI as the hard segment and BDO (or EDO) as chain extender, the propellant material made with this new polyurethane TPE showed good processing temperature ($<393 \text{ K}$) and excellent mechanical properties.

References

- ¹Kovacs, A. J., and Straupe, C., "Isothermal Growth, Thickening and Melting of Poly(ethylene-oxide) Single Crystals in Bulks," *Journal of Crystal Growth*, Vol. 48, 1980, pp. 216–226.
- ²Li, Y. M., "NEPE Propellant," *Foreign Weapons Technology*, Vol. 5, No. 4, 1984, pp. 1–13.
- ³Zhou, J. Y., Wu, Y., Xu, B. G., Yang, Z. Y., and Zhao, Z. G., "Synthesis of Ethylene Oxide and Tetrahydrofuran Copolymer," *Journal of Beijing Institute of Technology*, Vol. 12, No. 1, 1992, pp. 30–38.
- ⁴Henry, C. A., "Thermoplastic Composite Rocket Propellant," U.S. Patent 4361526, 1982.
- ⁵Ernie, D. B., "Process for Preparing Solid Propellant Grains Using Thermoplastic Binders and Products Thereof," U.S. Patent 4764816, 1986.
- ⁶Hesketh, T. R., and Cooper, S. L., "DSC Analysis of Morphological Change in Segmented Elastomers," *Polymer Engineering and Science*, Vol. 20, No. 3, 1980, pp. 190–197.
- ⁷Krause, S., "Microphase Separation in Block Copolymers: Zeroth Approximation Including Surface Free Energies," *Macromolecules*, Vol. 3, No. 1, 1970, pp. 84–86.
- ⁸Gordon, J. M., Rouse, G. B., Gibbs, J. H., and Risen, W. M., "The Composition Dependence of Glass Transition Properties," *Journal of Chemical Physics*, Vol. 66, No. 11, 1977, pp. 4971–4976.
- ⁹Tan, H. M., Zhang, B. Y., and Lu, C. S., "Synthesis and Properties of Thermoplastic Polyurethanes," *Journal of Beijing Institute of Technology*, Vol. 15, No. 6, 1995, pp. 105–110.
- ¹⁰Dimarzio, E. A., "The Second-Order Transition of Rubber," *Journal of Research of the National Bureau of Standards, Section A*, Vol. 68, No. 6, 1964, pp. 611–617.

Chapter 1.6

Effects of Microstructure on Explosive Behavior

Philip M. Howe*

Los Alamos National Laboratory, Los Alamos, New Mexico

I. Introduction

IT is almost axiomatic that the macroscopic behavior of a material is strongly dependent on its microstructure. This is especially true for explosives, where variations in microstructure have a marked effect on many aspects of reactivity that affect safety, handling, and performance. Although the importance of effects of microstructure on certain aspects of explosive behavior has been well known for many years, a thorough and accurate description of the relationship between explosive behavior and microstructure still eludes us. This review is intended to summarize our current understanding of this relationship and to indicate directions for further research. Although the review is intended to focus primarily on the influence of microstructures on macroscopic behaviors, there are certain behaviors in between the microstructural and macrostructural that need to be addressed, and these are discussed as well. Further, some attention is given to the macroscopic behaviors that are believed to be sensitive to microstructural effects.

Examples of explosive behaviors that are believed to be quite sensitive to microstructural effects are shock sensitivity, fragment impact sensitivity, thermal (cookoff) response, friction response, and response to low-velocity impact. In this chapter, we address each of these in turn, although not at the same level of detail. The level of detail will be partly driven by the extent to which researchers have explored microstructural effects and partly by the importance of microstructures to the explosive behavior. (The role of microstructure in shock initiation behavior has been much more thoroughly investigated than the role of microstructure in cookoff behavior, for example. Also, the influence of microstructural features on various forms of sensitivity is typically much greater than its influence on performance.)

Copyright © 1999 by the American Institute of Aeronautics and Astronautics, Inc. All rights reserved.

*Senior Project Leader, Explosives Research.

II. Shock Sensitivity and Microstructural Effects

A. Nature of Hot Spots

That microstructure variations are important to impact initiation has been recognized since the late 1940s, when Apin and Bobolev¹ published their work on the influence of physical structure and of aggregate state on hot spot formation and subsequently Bowden and McOnie² and Bowden and Yoffe³ published their work on hot spots. The hot spot concept was motivated by the realization that, if the impact energy were converted to heat and distributed uniformly throughout the impacted sample, the resulting temperature rise would be far too small to cause ignition within experimentally observed times. The work of Bowden and others demonstrated that hot spots could be formed in impact processes by compression of interstitial gas, intergranular friction, and high-velocity flow.

It was a natural extension to apply the hot spot concept to shock initiation, and similar heating processes have been postulated. Thus, it has been proposed that hot spots can be formed in shock initiation by compression of interstitial gases,⁴ shock interactions with grains,² intergranular friction,⁵ spallation,⁶ jetting,^{1,7,8} and stagnation.⁹ Cheret has classified these mechanisms into three major groups: those involving gas compression sources, those involving localized shock interactions and consequent hydrodynamic flow, and those involving viscous dissipation and mechanical working.¹⁰ This is a useful approach and will be followed here.

B. Compressive Heating of Occluded Gas

Experiments designed to assess the importance of compression of interstitial gas to hot spot formation have given mixed results. Seay and Seely examined the shock response of low-density penta erythrytol tetranitrate (PETN) using wedge test configurations.¹¹ They found that there was no significant difference in the shock response of the compacts with interstitial air, argon, and methane and concluded that the temperature of the included gas had nothing to do with the initiation mechanism. They also performed an experiment where the sample was evacuated to a pressure of nominally 50 μm of Hg. No change in sensitivity was observed. This was in direct contradistinction to the earlier work of Bowden and McOnie,² Bowden and Yoffe,³ and Bowden and Gurton,¹² who had explored effects of gas content on the drop weight impact response of liquid and solid explosives. The difference is evidently a result of different timescales of interest. Shock rise times (and pore collapse times) are typically of the order of a fraction of a microsecond, and heat transfer is unimportant in influencing the temperature of surrounding material, for bubbles sizes of interest. In the drop weight impact experiments, timescales are significantly longer, often extending over several hundred microseconds, and heat transfer can become important.

Chick conducted experiments using a small-scale gap test and examined the effect of pressure and composition of gases on gap sensitivity in low-density octahydro-1,3,5,7-tetranitro-1,3,5,7-tetrazocine (HMX) and PETN.¹³ The gas pressure was varied from atmospheric to a maximum pressure of 1000 psi. He found that the shock sensitivity of all of the pressed compacts decreased with increasing gas pressure. The rate of decrease was faster for gases of greater molecular complexity. The desensitizing effect was greater for compacts made with coarse particles than those made with fine particles. Chick concluded that the high shock

sensitivity of low-density compacts is due to geometrical features at the grain size level and that the interstitial gas simply reduced the effect: "The compact is sensitive in spite of the gas and not because of it."¹³ In this case, the gas apparently serves to reduce the rate of cavity collapse. That there was an effect of molecular weight of the gas on the rate at which sensitivity changed with gas pressure suggests that flow of the gas through the porous compacts was part of the collapse dynamics. Higher molecular weight materials, with higher viscosities, would be expected to offer more resistance to flow through the compact and, thus, would be more effective in retarding collapse of pores. This effect has apparently not been modeled in the shock initiation literature.

Chick's results were obtained using a gap test geometry and were threshold data, that is, gap thicknesses were determined for which an explosion would occur 50% of the time.¹³ Marshall extended this work to measure initiation delay times.¹⁴ He first determined the shim thickness in the gap test for which the probability of detonation was 50% and then conducted a second series, with shim thicknesses up to and including the 90% probability point. The difference between the actual shock transit time and the time for a detonation wave to transit the sample was reported as lost time. This lost time is a measure of the shock acceleration rate and is proportional to the times to detonation reported from wedge test experiments.¹⁵ Marshall's gap test results¹⁴ showed that the shock sensitivity, as measured by the 50% point, was a strong function of gas type and pressure and confirmed Chick's results.¹³ However, Marshall¹⁴ found that the lost times were independent of gas type and pressure. Marshall postulated two contributing processes. One process, which he asserted would determine whether the charge would detonate or fail, is strongly affected by interstitial gas type and pressure. The second process he attributed to the shock acceleration phase that consumes most of the time and distance in the transition to detonation. This second process was found to be independent of the nature and pressure of interstitial gas.

Starkenbergs conducted experiments and analysis showing that, under certain circumstances, compressive heating of occluded gas could be quite important to ignition.¹⁶ He was particularly interested in the response of explosive-filled artillery shells to gun launch setback forces. Strictly speaking, this is not a shock initiation problem, inasmuch as the compression rate is much too slow for shock formation. Nonetheless, it is important work and serves as an excellent reminder that explosive behaviors can be quite sensitive to the nature of the stimulus and that there is no paucity of potential ignition mechanisms. His analysis showed quite clearly that there are domains where heat transfer could be very important and domains where it was essentially irrelevant to ignition.

The regime Starkenberg investigated involved times long compared to typical shock initiation times.¹⁶ Typical shock initiation experiments using wedge test geometry and 100-mm-diam projectiles are limited to times of about 15 μ s. Starkenberg's experiments involved times of multiple milliseconds. Heat transfer from hot gas to relatively cool explosive was, thus, a viable mechanism in his experiments. (The characteristic time for the cooling of the surface of a sphere is given by

$$t_c = A^2 \rho C / K$$

where A is the cavity radius, C is the heat capacity, K is the thermal conductivity, and ρ is the density. For a 1- μ m cavity, t_c is of the order of 10 μ s for typical

explosive properties¹⁷). The microstructure surrounding the gas-filled void was found to exert a very strong effect. For example, precompression of the explosive material near the void greatly lowered the ignition threshold. Frey postulated that the as-cast and polished surfaces contained significant amounts of microporosity that tended to reduce the amount of hot gas available to heat the explosive. Precompression eliminated this porosity and rendered the sample more sensitive. Apparently, there was sufficient porosity to allow evacuation of the gas in the bubble on the timescale of the compression process, thus, preventing the occluded gas from reaching maximum pressure (and temperature). If this were not the case, the availability of the additional surface area in the as-cast and polished samples would be sensitizing. The result should be quite sensitive to cavity size. Larger cavities should eliminate the effect, and smaller ones should exacerbate it.

C. Localized Shock Interactions and Hydrodynamic Flow

The members of this group of mechanisms depend strongly on the nature of local shock interactions and consequent flow, somewhat independent of the nature of the material in the void or of its size. Mader^{18–20} and Mader and Kershner²¹ pioneered the numerical modeling of this type of hot spot mechanism, treating the material surrounding the void as an inviscid liquid. It was applied first to liquid explosives containing bubbles and high-density inclusions and later to porous solid explosives assumed to obey an elastic–plastic constitutive behavior. Both shock focusing and pore collapse processes were found to be important. In the modeling, it was found that hot spots originate from the very strongly asymmetric pore collapse process and from further energy focusing as the result of microshock interactions with each other. Many of the mechanisms associated by earlier authors with pore collapse were observed in Mader's numerical results.^{1,5,7–9,22}

Dear and Field,^{23,24} Dear et al.,²⁵ and Bourne and Field^{26,27} have conducted experiments that provide considerable support for the hydrodynamic hot spot model. In their experiments, they cut arrays of cavities into moderately thin layers of gels.^{23–27} These perforated gel layers were placed between transparent windows, thus, providing a quasi-two-dimensional array of cavities. Shock loading was introduced into the gel layer either by impact or from a plane wave generator. High-speed photography was used to monitor cavity motion and deformation and shock interactions. Clear evidence of shock interactions and asymmetric bubble collapse with associated jet formation was obtained. Indeed, much of the phenomenology described by Mader was directly observed in these experiments. Field has summarized this work and studies of some of the other mechanisms in a review paper.²⁸ Khasainov et al. have pointed out that Mader's calculations did not include effects of viscosity and are, therefore, appropriate only for conditions of high Reynolds number flow in regions with sufficiently small velocity gradients.²⁹ They also make the point that, because of the size of the cavities in the experiments of Refs. 23–27 and because of the materials used, the flow in their experiments is in the high Reynolds number domain. Using similar reasoning, Zababakhin and Nechaev noted that void collapse processes could be divided into two regimes, depending on Reynolds number.³⁰ At high Reynolds number, the viscosity of the surrounding material does not affect void collapse; the pores collapse quickly to essentially zero volume, with a consequent pressure overshoot;

and the process is essentially hydrodynamic. At low Reynolds number, the void never collapses fully, there is no significant overshoot, and viscous heating effects dominate.

D. Viscoplastic Flow

Jacobs et al. suggested that hot spots were formed as the result of shock-induced micro-shear or micro-fracture at or near voids as the shock passed over them.³¹ Eyring et al. proposed that reaction would be initiated at points of contacts between crystals where hot spots were formed as a result of intergranular friction during the compression by the shock wave.³² Carroll and Holt developed a one-dimensional viscoplastic pore collapse model, for hot spot formation, based on a spherical shell.³³ They obtained a dynamic compaction equation with inertial effects. The porosity and the average pore size of the real material were approximated by the porosity and the initial inner radius of the model sphere. Solution of the resulting differential equations provided a description of the kinetic energy, plastic work, and shock structure. The viscosity coefficient and the yield strength were assumed to be temperature independent to facilitate analysis. This model has served as the basis for many modeling efforts. Thus, Carroll et al. extended this work to include temperature effects explicitly.³⁴ Frey modified this model to conduct a sensitivity analysis of the relative importance of inviscid plastic work, viscoplastic work, gas phase heating, and solid phase compression.¹⁷ Frey found that each of the mechanisms considered could dominate under certain conditions. He also showed that, if viscous heating was included, the hot spot temperature was not limited to the melting temperature of the solid explosive. He included a viscosity that was dependent on both temperature and pressure. Many of the concepts discussed by Frey were pursued independently by Khasainov et al.³⁵⁻³⁷ and were extended by many others.³⁸⁻⁴⁴

The Carroll and Holt model³³ and the models based on it describe a process involving one-dimensional spherical void collapse. This is a severe idealization. Other factors, such as nonaxisymmetric collapse, particle (or void) geometry, void size distribution, and rearrangement of particles during the shock compaction process are likely to play significant roles. Nonetheless, the viscoplastic hot spot model has had considerable success in explaining trends in shock initiation. Conley has conducted a careful study of spherical and cylindrical void collapse and has considered the relative importance of plastic work, viscous heating, compressive heating of the gas, heat transfer, and bulk compression.*

It is interesting that, in nearly all of the papers discussed so far, the emphasis has been on pore collapse rather than on particle deformation (necessary to effect a pore collapse). This is presumably a result simply of historical precedent, stemming from Bowden's work demonstrating the effectiveness of bubbles serving as hot spots in nitroglycerine and other liquid explosives. An alternative approach would be to focus on the grains in granular flows or compacts. This approach has been taken by the shock compaction community, who have been interested in forming a wide variety of materials with improved properties, using a variety of dynamic

*Conley, P., University of California, San Diego, private communication, May 1998.

compaction processes. A major benefit of these shock compaction approaches as a processing technique is that the heating can be localized to the periphery of the grains, allowing sintering without loss of properties due to bulk heating. Materials of interest include diamond compacts,⁴⁵ metals^{46,47} intermetallics,⁴⁸ ceramics,⁴⁹ fiber-reinforced composites,⁵⁰ and materials doped with organics.⁵¹ Indeed, the range of materials is so broad that the material behaviors encompass most of the (inert) material behaviors of explosives. Thus, these results can be used to shed light on the mechanisms of hot spot formation relevant to explosive behaviors.

The earliest theories of shock compaction assume that shock compression causes particle surfaces to be heated and melted, provided that sufficiently strong shock loading is delivered. Some time after shock passage, the melt region cools and solidifies, providing bonding between particles. All of the models assume that the shock-induced thermal energy can be deposited in a surface layer. For example, Belyakov et al. assumed that the net shock energy was deposited at particle interfaces as a uniform, constant flux during the rise time of the shock.⁵² This hypothesis was also advanced by Raybould⁵³ and by Goudin.^{54,55} Kondo and Sawai proposed a model in which the shock thermal energy is deposited into a skin surrounding each particle.⁵⁶ A comparison of these models was provided by Nesterenko and Muzykantov.⁵⁷ Schwartz et al. also proposed a similar model.⁵⁸ In each of these models, the thickness of the heated layer is a function of the material properties, the porosity, and the shock strength.

There is considerable experimental evidence that, for weak shock inputs, the principal heating is in a surface layer.^{59,60} In each of the early models, however, the thickness of the hot layer is assumed. An unanswered question is how this thickness quantitatively depends on material properties, microstructure, and shock strength. Schwartz et al.⁵⁸ noted that optical micrographs of polished and etched iron-based powder compacts showed that increasing shock pressures caused the original grain boundaries to become less distinct and also caused a reduction in density of internal fractures. They concluded that the increase in shock pressure caused an increase in the mass fraction of material heated to a temperature. This conclusion has been confirmed computationally by Conley et al.⁶¹ Conley et al. did not examine a wide range of constitutive behavior, however, and it is unknown how general the conclusion is, or how sensitive it is to the nature of the constitutive behavior.

The experimental evidence suggests that, whereas the skin models provide a useful first approximation for some conditions, the actual situation is considerably more complex. Matsumoto et al.⁶² and Matsumoto and Kondo⁶³ have performed experiments that allowed them to identify three major mechanisms involved in shock compaction of powders. Because shock compaction relies on localized heating for interparticle bond formation, these same mechanisms should be important in hot spot formation in explosives. The three mechanisms identified by Matsumoto et al.⁶² and Matsumoto and Kondo⁶³ are 1) dynamic friction between particles, 2) plastic deformation about voids, and 3) generation and trapping of molten jet material. Matsumoto et al.⁶² used equiatomic Ni Ti alloy powders for their experiments. The powder particles were generally spherical with particle sizes ranging from about 50 to 200 μm . Some experiments were performed with somewhat smaller particle size ranges. The samples were compacted quasi-statically to a density of about 70% of maximum theoretical density and then shock loaded with a flying plate launched from a powder gun.

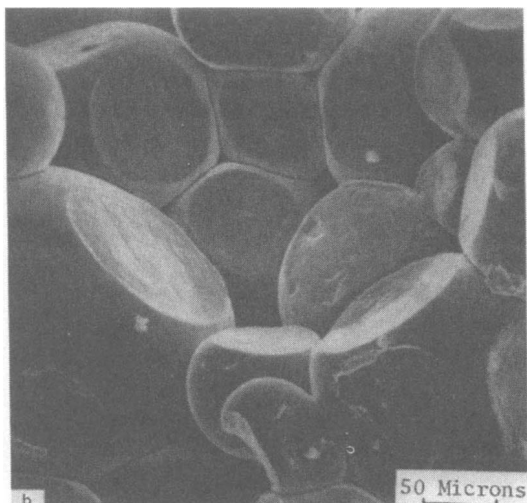


Fig. 1a Compaction geometry of spherical Ti alloy particles at low shock strengths; negligible interparticle motion has occurred, and negligible frictional heating has occurred. (Reprinted from Ref. 68, p. 44, courtesy of Marcel Dekker.)

Although all three mechanisms were apparent in micrographs of Refs. 62 and 63 for experiments conducted at a single impact velocity, review of the literature indicates that the importance of each mechanism is a function of shock and material strength. Here, the trends are shown qualitatively in Figs. 1a–1f. Thus, at low shock strengths and for strong materials, localized deformation and mutual indentation are most important. As the ratio of shock strength to material strength is increased, localized shear deformations and viscous heating at particle interfaces become

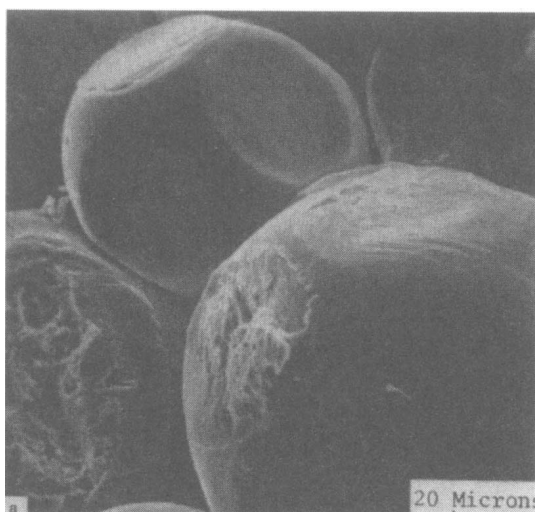


Fig. 1b Frictional heating and localized shear flow; note evidence of interparticle bonding. (Reprinted from Ref. 70, p. 297, courtesy of Marcel Dekker.)

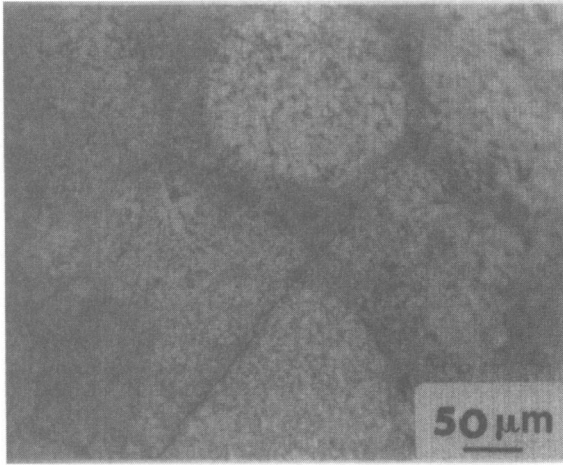


Fig. 1c Photomicrograph of shock compacted Ti3Al showing surface melting of particles. (Reprinted from Ref. 75, p. 497, with permission of the author.)

important. At higher values of the ratio of shock strength to material strength, plastic deformation becomes more important, although heating is still greatest near the surface of the grains. At even higher ratios of shock strength to material strength, plastic deformation dominates, and a characteristic fish scale appearance to the microstructure occurs. At very high ratios of shock strength to dynamic material strength, significant rotational flow occurs. (The word strength is used rather loosely here. This author believes that the nature of the yield surface will have a strong influence on the relative importance of each mechanism at any particular

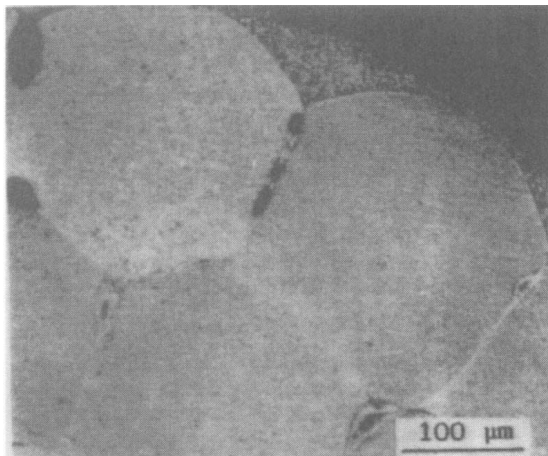


Fig. 1d Microphotograph of a cross section of shock compacted low carbon steel wires. The white, thin layer surrounding particles have melted; shock propagation direction from upper right to lower left. (Reprinted from Ref. 68, p. 7554, © 1991, courtesy of the American Institute of Physics.)

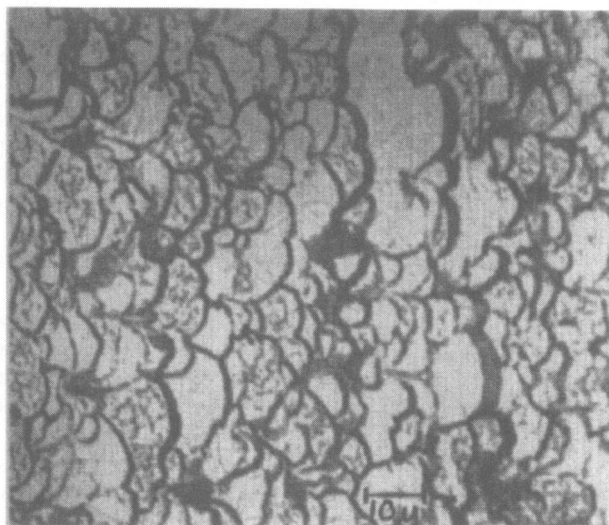


Fig. 1e Fish scale appearance of shock compacted Pb^4 ; arrow indicates direction of shock propagation. (Reprinted from Ref. 71, p. 297, courtesy of Marcel Dekker.)

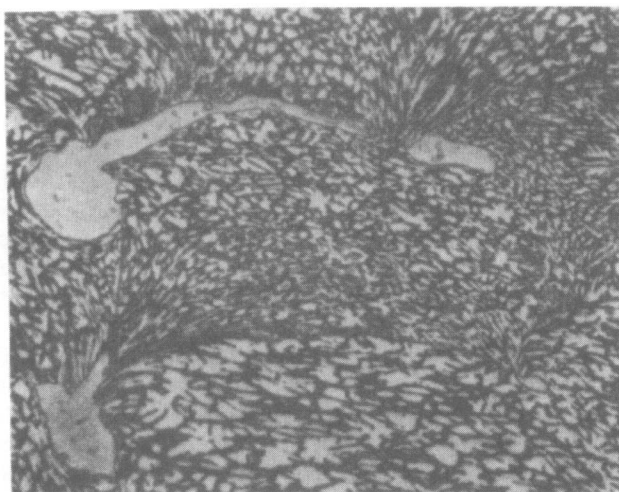


Fig. 1f Rotational flow in shock compacted Al-Si alloy: Melting has occurred in the regions of highest vorticity; shock propagation direction is from upper right to lower left. (Reprinted from Ref. 72, p. 116, courtesy of Marcel Dekker.)

input shock strength. Yield surface influences will be especially important in making material-to-material comparisons.) These trends do not seem to have been codified in the literature. Nesterenko has broached the topic with his "microkinetic energy" construct,⁶⁴ Benson and Nellis have shown the trend of increasing rotational flow with increasing impact velocity (shock strength) for shocked porous copper,⁴⁶ and Benson et al. have addressed some of the issues.⁶⁵ The deformation behavior and the consequent local heating changes quite dramatically as shock strength is increased relative to material strength. The photomicrographs are from various sources.⁶⁶⁻⁷¹ Unfortunately, the micrographs are not all of the same material. However, numerical predictions of a major part of the sequence are given by Benson et al.⁶⁵

In Fig. 1a, the shock loading was insufficiently strong to cause compaction to full density. There is no evidence of particle-particle relative motion and no evidence of melting resulting from either interparticle friction or from localized flow. Note that the contours of the indentations on the particles visible in the picture form a sphere that presumably fits the contour of a large particle no longer present. This supports the idea that the smaller particles tend to undergo greater deformation than the larger ones.

Figure 1b shows the same material under conditions that provide some degree of material bonding. For this material and these conditions, there is no evidence of one particle sliding past another (note the symmetry of the bond areas). Evidently, the high temperatures that led to melting and interparticle bonding resulted from very localized deformation and flow at the contact surface. This behavior is discussed and modeled by Ahrens et al.⁷² Frey has shown that, in such viscous flows, temperatures can greatly exceed the melting point of the material.⁷³ This type of flow, then, provides a viable mechanism for hot spot formation in explosives.

Evidence of widespread melting to form a surface layer and of significant flow leading to formation of a solid compact is shown in Fig. 1c, where the spherical symmetry is still retained, at least for the particle interior regions where melting did not occur. Figure 1d shows more stringent conditions, where melting at the interfaces is still very clear, although the particles have been plastically deformed to the point where their original geometry is almost entirely lost.

Progressively more severe deformations are shown in Fig. 1e and 1f. In Fig. 1e, most of the particle interfaces are still very clearly delineated. (The samples were polished and etched, prior to being photographed. The etch marks indicate melting has occurred in a thin layer at the interfaces.) However, there are instances where particles have appeared to fuse together with loss of interface sensitivity to the etchant.

Figure 1f shows a microstructure where shock compaction has caused significant local deformation to occur as part of the flow pattern. Because melting occurred in regions of highest flow, no flow lines are present to define the rotation in these regions. However, the envelope is characteristic of the incipient vortex formation. Careful examination of this photograph allows identification of several other regions of less severe shear deformation, as well as delineation of particle boundaries. Benson et al. have performed numerical calculations of these phenomena.⁶⁵

The models just discussed are appropriate first-order theories for the situations where the principal heating occurs as a result of viscous work confined to a layer that is thin relative to the particle diameter. The other two mechanisms require significant contributions of bulk heating. Nesterenko,⁶⁴ Ferreira and Meyers,⁷⁴ and Potter and Ahrens^{75,76} have developed models that address the plastic work

contributions. Nesterenko⁶⁴ has modified the single pore shell model of Carroll and Holt³³ by introducing a nondeformable central core. The presence of the core prevents complete axisymmetric collapse of the outer shell and separates the dissipation process into two states: a pore collapse and postcollapse flow. Nesterenko associates the first phase with quasi-static processes and the second phase with purely dynamic processes and notes that the quasi-static compaction does not lead to interparticle bonding, even at high pressures.⁶⁴ He also introduced the concept of microkinetic energy, which he defines as the localized energy dissipated by the viscoplastic flow of the material after the pore collapse. The criterion separating the two stages is based on the ratio of the minimum plastic work necessary for the collapse of the spherical pore to the total internal shock energy. Low values of this ratio imply a large microkinetic energy and consequent dynamic behavior. Low values of this ratio also lead to qualitatively different behaviors from those observed when interparticle frictional heating is the only controlling mechanism. Thus, as the ratio decreases, the microstructure shifts from one where the grains retain much of their original geometry, to a regime where there is significant plastic flow and the grain boundaries form a fish scale appearance, to a regime where significant vorticity appears. Benson et al. have conducted a rather thorough two-dimensional numerical analysis of these behaviors.⁶⁵

Williamson et al.,⁷⁷ Williamson,⁷⁸ and Williamson et al.,⁷⁹ using finite difference techniques, have also modeled shock compaction processes and have noted (as had Nesterenko earlier⁸⁰) that, in bimodal mixtures of particles, the smaller particles typically suffer the largest amount of deformation and, thus, get heated to the highest temperatures. Because most explosives have bimodal or multimodal particle size distributions to maximize solids loading, this conclusion should be of considerable importance in initiation modeling. Models to date have not explicitly considered this.

So far, we have discussed only hot spot formation. Additional mechanisms need be included to describe the evolution of reaction after hot spot formation. The first indications of the importance of microstructure to postignition behavior in explosives came from studies of critical detonation diameters (the critical detonation diameter is the smallest diameter of an unconfined explosive cylindrical charge that will support a steady-state detonation wave). It was found that explosive particle sizes had a strong effect on the critical diameter, and various grain burning mechanisms were proposed.^{3,32}

The grain burning mechanisms have been quite effective in explaining critical diameter effects. For a recent analysis of grain burning and surface area effects on shock initiation and detonation wave propagation, see Khasainov et al.³⁷ They have been less successful in describing shock initiation behaviors, although the concept is well established and forms the basis for numerous shock initiation models.⁸¹⁻⁸³

Because of the difficulties in direct observation of hot spot formation and the subsequent reaction evolution, most of the models rely on correlations with trends in macroscopic initiation data for validation. The two major trends that have been examined are tied to effects of porosity and effects of particle size.

E. Effect of Porosity Upon Shock Sensitivity

Porosity is a macroscopic quantity, yet it is coupled to the pore size distribution through the particle size distribution and the intrinsic intraparticle pore size

distribution. That is, given a particle size distribution containing a distribution of internal pores, specification of porosity determines the overall pore size distribution. Numerous studies over the years have shown that the presence of porosity in an explosive sensitizes it to shock loading. Nearly all of these studies have involved long-duration step shocks.

Introduction of porosity has two effects. One effect is to introduce an additional amplification/focusing mechanism not present in the absence of any porosity. This is consistent with the idea that hot spots are formed by local high-temperature excursions, and that the local high temperature is related to the input internal energy through whatever amplification or focusing mechanisms are involved in the hot spot formation process. This can be a large and important effect. The second effect is to change the shock Hugoniot for the material and greatly reduce the shock pressure corresponding to a given internal energy state. This can also be a large and important effect. A recent analysis of literature data has demonstrated that most of the effect is not due to changes in the microstructure, but rather to changes in the bulk properties, that is, Hugoniot effects that change the relationships between various state variables.⁸⁴

Pores can occur in the binder material (if present), at the binder-explosive crystal interface, and within the explosive crystals themselves. Few systematic studies have been conducted to quantify the relative importance of each type of void. Typically, when explosives are manufactured, considerable effort is made to control the presence of voids external to the explosive crystals, that is, intergranular voids. However, intragranular voids typically are not well controlled. In military explosives, the emphasis is usually placed on elimination of as much porosity as possible, to reduce sensitivity. In commercial explosives, especially the relatively insensitive nonideal explosives, considerable effort is expended to provide a porosity and pore size distribution that yields sensitivity and performance characteristics tailored for specific applications.

Borne has conducted studies of the effects of explosive microstructure, particularly intragranular voidage, on shock sensitivity of HMX formulations. In a series of studies, he examined effects of morphology, surface properties, and presence and concentration of intragranular voids.⁸⁵⁻⁸⁷ Of the parameters examined, intragranular porosity showed the strongest effect. No control was exercised over the size of the internal voids. Other parameters of the experiments were carefully controlled. Materials with narrow, monomodal particle size distributions and with very small density variations (less than 0.5%) were used. Formulations were prepared using 70% by weight solids loading and a wax as a binder. Flat-ended projectile impact experiments and plane wave step shock experiments were conducted. Three porosities were addressed, ranging from 0.1% intragranular void content to 0.45% intragranular void content.

There is some ambiguity in regard to the amount of the extragranular porosity present and its relative importance in his studies.⁸⁵⁻⁸⁷ The statement is made that a formulation density close to the theoretical maximum is achieved (>99.5%) and that the formulations were essentially free of extragranular voids. However, actual values were not presented. Nonetheless, a clear and unambiguous trend in shock sensitivity with intragranular porosity was observed. Not surprisingly, the formulation with the highest internal void content was found to be the most sensitive. The total porosity of the materials examined in these studies was very small and would have a negligible effect on the shock Hugoniots except, perhaps, at very low shock strengths. Hence, the voids are affecting sensitivity primarily through

hot spot formation and reactivity, rather than through changes in the equation of state of the material.

Similar studies on hexa-hydro-1,3,5-trinitro-1,3,5-triazine (RDX) were reported by Baillou et al.⁸⁸ They found a correlation between shock sensitivity and the magnitude of the intragranular porosity. They found that the chemical nature of the impurities contained within the intragranular pores exerted only a second-order effect. This suggests that the temperature amplification mechanisms associated with hot spot formation through pore collapse overwhelm any chemical effect associated with the impurities. (Note that Ref. 88, in common with many others, has a major weakness in that the sensitivity data are reported in a log pressure vs log distance to detonation plane, without error bars. The combination of use of log-log plots and absence of error bars makes the analysis of the data very susceptible to misinterpretation.)

During manufacture, considerable effort is often expended to eliminate porosity in plastic-bonded explosives. Skidmore et al. have shown that a common process used to press an HMX-based plastic bonded explosive (PBX 9501) can introduce considerable fracture to the HMX crystals.⁸⁹ They found that, as porosity is decreased, the first step in quasistatic compaction was elimination of large voids by deformation of prills. Little fracture of the HMX crystals occurred under these conditions. The little amount of fracture that did occur was a result of severe deformation of individual prills. However, fracture was not really extensive except for the sample with the lowest porosity (0.6%). In this case, nearly all large HMX crystals were fractured. Several representative photomicrographs are shown in Fig. 2.

Both fracture and porosity might be expected to play a role in establishing shock sensitivity. Whereas elimination of porosity will reduce the explosive shock sensitivity, crystal fracture would be expected to sensitize, if it were to have any effect at all. Because, typically, removal of the intragranular porosity requires fracturing the crystals, desired changes in sensitivity might not be realized. This would depend on whether or not each fractured crystal behaves as one or as several during the

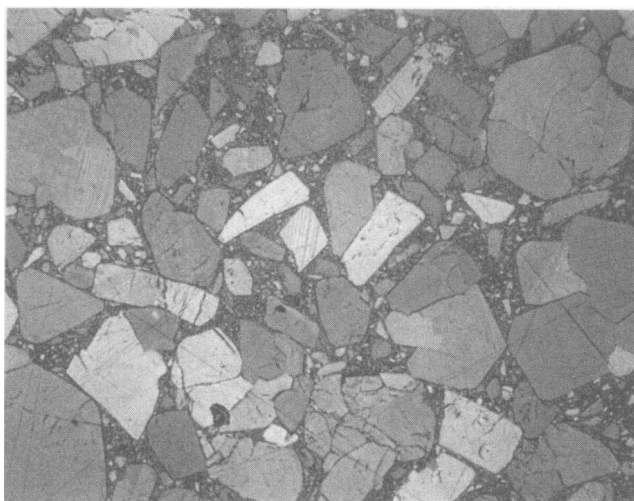


Fig. 2a PBX 9501 pressed to 0.6% porosity. (Photomicrograph courtesy of Cary A. Skidmore and David Phillips, Los Alamos National Lab.)

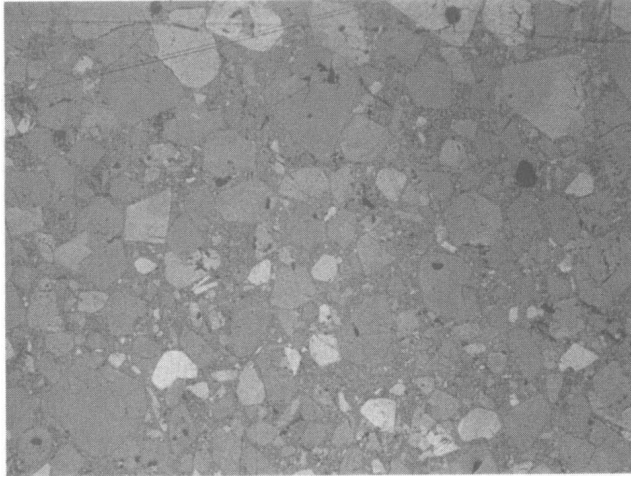


Fig. 2b PBX 9501 pressed to 1.0% porosity. (Photomicrograph courtesy of Cary A. Skidmore and David Phillips, Los Alamos National Lab.)

initiation process. Data for both PBX 9501 and PBX 9404 [a plastic bonded explosive composed of 94-wt% HMX, 3-wt% nitrocellulose, and 3-wt% tris (β -chloroethyl) phosphate] were examined.⁸⁴ The acceleration histories were not affected by porosity, within the precision of the data. As shown in Fig. 3, the threshold material velocity for initiation dropped significantly with the introduction of a small amount of porosity and then became independent of porosity for larger porosities.

The pedigree of the samples whose data are shown in Fig. 3 is unknown. If these samples were pressed using HMX with significant amounts of intragranular porosity, the lowest porosity samples would quite likely contain significant fracture

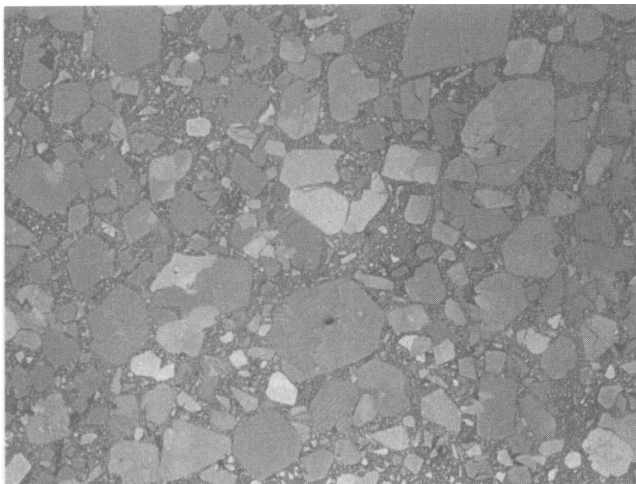


Fig. 2c PBX 9501 pressed to 7.0% porosity. (Photomicrograph courtesy of Cary A. Skidmore and David Phillips, Los Alamos National Lab.)

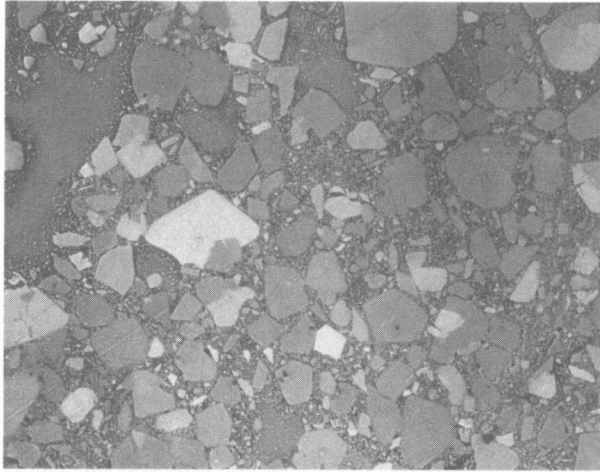


Fig. 2d PBX 9501 pressed to 11.0% porosity. (Photomicrograph courtesy of Cary A. Skidmore and David Phillips, Los Alamos National Lab.)

damage. In this case, one could conclude that any effect of fracture introduced by elimination of porosity is overwhelmed by the effect of the reduction in porosity. There is a small chance, however, that the lowest porosity samples were prepared from lots of HMX with very small amounts of intragranular porosity. This makes the conclusion somewhat suspect.

Porosity should have an effect on the sensitivity of explosives to short-duration shocks and to ramp waves, where the thickness of the shock in the former and the thickness of the shock front in the latter are commensurate with or smaller than

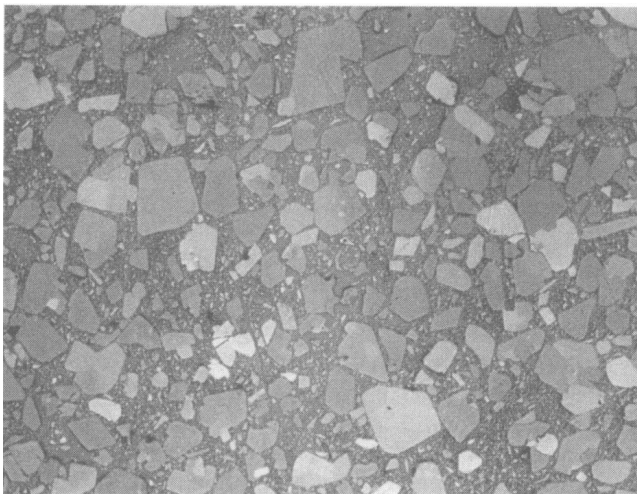


Fig. 2e PBK 9501 pressed to 21% porosity. (Photomicrograph courtesy of Cary A. Skidmore and David Phillips, Los Alamos National Lab.)

Chapter 1.7

Advances in Solid Propellant Formulations

May L. Chan,* Russ Reed Jr.,* and David A. Ciaramitaro†
Naval Air Warfare Center, China Lake, California

Nomenclature

F	= thrust, N
g	= gravity constant, 9.806 m/s^2
H_c	= enthalpy in the chamber, J/kg
H_{exit}	= enthalpy at the nozzle exit, J/kg
I_{sp}	= specific impulse, lbf-s/lbm or s
\dot{m}	= mass flow rate, kg/s
P_c	= chamber pressure, Pa
P_{exit}	= exit pressure, Pa
R	= gas constant, J/g-mol/K
T_c	= adiabatic chamber temperature, K
u_{exit}	= propellant jet speed at the nozzle exit, m/s
γ	= ratio of the specific heats, C_p/C_v
ΔH	= change in enthalpy during the expansion process, J/kg
ΔH_f	= heat of formation, cal/g
ρ	= density, g/cm^3

I. Introduction

OVER the years, high performance, insensitive munitions, and pollution prevention issues in relation to solid rocket propellants have grown in importance. The authors describe the rationale that was used in the selection of propellant formulation ingredients to maximize I_{sp} and to meet insensitive munitions and pollution prevention goals. Experimental results for these efforts are provided along with a discussion of some of the most pertinent aspects related to these topics.

This material is declared a work of the U.S. Government and is not subject to copyright protection in the United States.

*Senior Research Chemist, Research Dept., Weapons Division.

†Research Chemist, Weapons/Targets Dept., Weapons Division.

A. Background—High Performance

The fundamental merit of performance for a propellant is the I_{sp} . I_{sp} can be interpreted as the thrust delivered per unit weight flow of propellant, or, more important, to the propellant chemist, the enthalpy release converted into kinetic energy of the exhaust jet. Application of the energy balance, assuming adiabatic conditions, results in the relationship given by Eq. (1). I_{sp} simply is the jet velocity divided by the gravity constant as seen in Eq. (2):

$$u_{\text{exit}} = [2(H_c - H_{\text{exit}})]^{\frac{1}{2}} = (-2\Delta H)^{\frac{1}{2}} \quad (1)$$

$$I_{sp} = u_{\text{exit}}/g \quad (2)$$

If it is further assumed that the expansion process from the chamber to the nozzle exit is isentropic as well as adiabatic, then Eq. (3) is the result. Equation (3) shows two items of interest: the specific impulse is proportional to the square root of the adiabatic chamber temperature T_c and inversely proportional to the square root of the molecular weight (MW). Thus, it is evident that propellant formulations having high adiabatic combustion temperatures and low molecular weights are highly desirable:

$$I_{sp} = 1/g \{ 2 \cdot \gamma / (\gamma - 1) \cdot R \cdot T_c / \text{MW} [1 - (P_{\text{exit}}/P_c)^{\gamma/(\gamma-1)}] \}^{\frac{1}{2}} \quad (3)$$

Because the I_{sp} also is sensitive to the pressure ratio (P_{exit}/P_c), comparison of I_{sp} values must be made at standard conditions that are defined as optimum expansion from 1000 psia (6.895 MPa) to 14.7 psia (0.1 MPa). Under fixed pressure ratio conditions, the I_{sp} is invariant for any propellant system and is the basic chemical comparison parameter used in evaluations.¹⁻⁶

One of the primary ways of improving the I_{sp} of propellant compositions is by increasing the enthalpy release and lowering the average molecular weight of the exhaust gases to attain more working fluid.

B. Background—Insensitive Munitions

Propulsion systems in operational missiles can produce catastrophic responses when subjected to the thermal and ballistic impact hazards that are present in shipping, handling, storage, and operational environments. Therefore, to reduce the threat to personnel and to minimize the consequences of these adverse responses, the United States military services have established a requirement that operational missiles exhibit no greater than a burning reaction when subjected to the hazardous environments defined by MIL-STD-2105B (Ref. 7). For the past 15 years, the military services have made great progress in research conducted to improve the safety properties of weapons. Through the efforts of the Insensitive Munitions (IM) Program, many of these safety improvements will be applied to various weapon systems in the future.

Systems that yield high performance and that incorporate highly energetic compounds typically release energy easily. For example, tactical rocket motors loaded with propellants that contain ammonium perchlorate (AP) and polybutadiene binders can undergo violent reactions on heating, impact, or shock. Thus, these motors have failed from one to as many as four of the required IM tests. Accordingly, the technical challenge is to develop insensitive propellant formulations that will meet the IM requirements and, at the same time, retain or exceed the

performance characteristics of conventional hydroxyl-terminated polybutadiene (HTPB)/AP propellants.

This chapter describes the development of a hydroxyl-terminated polyether (HTPE) propellant that passes all IM tests. In addition, a version of hexanitrohexaazaisowurtzitane (CL-20) propellant that is substantially less shock sensitive than the current Class 1.1 minimum-signature propellant is discussed.

C. Background—Pollution Prevention

Historically, demilitarization of rocket motor grains has been accomplished by open burning/open denotation (OB/OD). Although the material values of the items destroyed by this method were lost, this technique had the virtues of simplicity and a minimal expenditure of time, effort, and capital. However, with the enactment of the Clean Air Act, increasing attention to the environmental hazards of OB/OD has created a climate of steadily rising costs and restricted use of this technique. (A comprehensive review of the Code of Federal Regulations relating to the manufacturing, shipping, and disposal of energetic materials is contained in Ref. 8.) A logical extrapolation of the increasingly strict environmental regulations indicates that, at some time in the future, OB/OD will be judged an environmentally unacceptable practice and will be banned.

In generating alternative methods for the demilitarization of rocket motors, designers must consider the high energy content of formulations and their sensitivity to shock, friction, and impact. The grain must be removed from the case and decomposed in a way that does not create a hazard or cause damage to the environment, the required equipment, or personnel. Generally, complying with these precautions requires a process that is excessively time consuming and hazardous for use in the demilitarization of large numbers of rocket motors on a routine basis. To date, most of the development efforts have been devoted to methods that involve cutting the propellant out of the case with high-pressure jets of water, solvents, or cryogenic liquids and caustic solutions.^{9,10} Then, the fragments are carefully macerated (typically, by slow grinding or kneading under the liquid), and the soluble materials are leached from the finely divided fragments of binder.

This problem is caused by binders composed of cross-linked rubbers. These binders, typically hydrocarbon chains cured with diisocyanates that form urethane linkages, form a matrix that is impervious to penetration, dissolution, or decomposition by most solvents, especially water. Thus, even though the cutting-macerating-leaching method removes much of the water-soluble oxidizers, such as AP or ammonium nitrate (AN), and some of the organic-soluble energetic materials, such as cyclotetramethylene tetranitramine (HMX), this process fails to completely remove these materials. In addition, insoluble fuels, such as aluminum (Al), will still be coated by the binder. The binder left, though reduced in weight and volume, remains a hazardous waste and still represents a disposal problem. This method is labor and capital intensive. Moreover, without a viable recycling plan, large quantities of contaminated water or solvent are generated during the process. Therefore, viable alternative methods that provide for the recovery, recycling, and easy removal of energetic components are of primary interest.

Efforts are being made with newly developed propellants to incorporate a hydrolyzable binder that dissolves in dilute acid or base but not in water. This binder allows the recovery of the other propellant ingredients for reuse.

II. Experimental Results and Discussion

Increases in performance beyond the current state of the art have been difficult to achieve because of the resulting increases in cost and hazards. Generally, past increases have been attained by the addition of more energetic ingredients such as AP or Al, additives that gave acceptable increase in hazardous properties. Nitramines (e.g., HMX, CL-20), as well as energetic plasticizers, have provided gains in propellant energy, but these additives increase the sensitivity of the compositions along with their performance. However, energetic polymeric binders such as bis(azidomethyl)oxetane and nitratomethyl methyl oxetane (BAMO/NMMO) copolymers may yield enhanced performance-sensitivity relationships because a portion of the energetic groups is contained in a soft rubbery matrix that acts as a desensitizer. Another promising ingredient is ammonium dinitramide (ADN), an oxidizer that increases performance when used to replace AP. These new ingredients have stimulated work in high-performance propellants.

A. High Performance

Enthalpy release and working fluid are maximized when propellant compositions of fuel and oxidizer contain light elements such as hydrogen (H), beryllium (Be), boron (B), carbon (C), nitrogen (N), oxygen (O), and fluorine (F). Fuel/oxidizer properties largely determine the energetic, sensitivity, ballistic, and processing properties of most classes of propellants. In the past, a number of ingredients that increase performance suffered from instability problems as well as incompatibility with binders. Still others, especially oxidizers, were hygroscopic and became strongly acidic on absorbing moisture. In addition, many compounds were hazardous because of their extreme sensitivity.

The first oxidizer used in composite propellants was potassium perchlorate (KP). KP is stable, compatible, and relatively insensitive but contributes little energy. Thus, it was soon replaced by AP, which is more energetic and is now the most commonly used oxidizer in composite propellants. This chapter, therefore, compares other oxidizers to AP.

An oxidizer's energy contribution is determined by the heat and gas volume that is produced by the oxidation of binders of metallic fuels. In general, the potential for enthalpy release increases as O content increases but decreases as negative heat of formation increases. For example, AN has a high O content, but its enthalpy release is relatively low as a result of its comparatively high negative heat of formation. Hydrazinium nitrate (HN) has a gas yield equivalent to AN but with a lower O content. Yet, HN is much more energetic because its heat of formation is less negative than that of AN.

Because AP evolves hydrogen chloride (HCl), which acts to increase average molecular weight, and because AP has a relatively high (-602 cal/g) negative heat of formation, it is only moderately energetic. Thus, in the 1960s there was an effort to enhance propellant performance by incorporating more energetic oxidizers with an O content similar to that of AP but with a lower negative heat of formation. Energetic oxidizers were investigated, including those containing a hydrazinium moiety like HN, hydrazinium monoperchlorate (HP), and hydrazinium dperchlorate (HP2). Hydroxylammonium perchlorate (HAP) was also studied because of its high O content. These oxidizers exhibited lower heats of formation than AP but produced energetic propellants that were detonable in addition to being friction and impact sensitive. HAP, HP, and HN were all quite hygroscopic, while

Table 1 Properties of oxidizers

Oxidizer	Oxygen content, wt %	Density, g/cm ³	ΔH_f , cal/g
ADN	51.6	1.80	-298
FDNEN	54.1	1.93	-355
HNF	52.5	1.87	-94
AN	59.6	1.73	-1090
HN	50.5	1.65	-531
AP	54.5	1.95	-602
HP2	55.1	2.21	-296
HAP	59.70	2.12	-497

HP2 slowly lost perchlorate acid and was marginally compatible with binders in extended tests. In addition, many had undesirable combustion characteristics.

The successful synthesis of new oxidizers and binders¹¹ has led to the creation of oxidizers such as CL-20 (Ref. 12) and ADN¹³⁻¹⁵ and binders such as the BAMO/NMMO (70/30) copolymer, also known as BN-7 (Ref. 16), for advanced propellant applications. All of these ingredients show very desirable characteristics. Hydrazinium nitroformate (HNF) was evaluated in the United States and later in The Netherlands.^{17,18} HNF is incompatible with some binder curatives. Furthermore, ADN as a propellant additive was investigated by Russian scientists in the early to mid 1970s. However, information was not released to the public until the presentation of Pak's work¹⁹ in 1993.

The performance of the most significant oxidizers is compared in Table 1 and Fig. 1. The oxidizers are measured by their contribution to I_{sp} , which is determined by such factors as O content and heat of formation (Table 1) and their contribution to working fluids (Fig. 2). A product of density (ρ^n) and I_{sp} is a figure of merit for the total impulse of volume-limited systems (i.e., small rocket motors), and this $\rho^n I_{sp}$ is influenced by the density of the oxidizer (Table 1).

The O content and the heat of formation of the oxidizer essentially determine the propellant composition's enthalpy release. Of those oxidizers compared in Fig. 1,

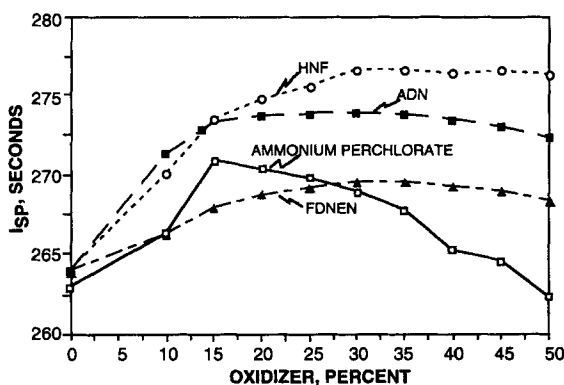


Fig. 1 Specific impulse of propellants containing BN-7/BTTN, Al, and various oxidizers.

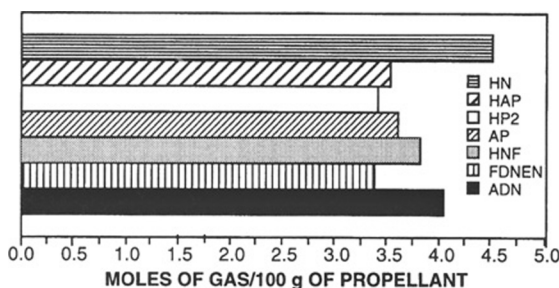


Fig. 2 Yields of working fluid based on a monopropellant.

HP2 and HNF are superior to ADN in O content. However, as seen in Table 1, only HNF is greatly superior in heat of formation. Thus, the calculated values of I_{sp} for HNF are higher than ADN, AP, and bis(fluorodinitroethyl) nitramine (FDNEN). The relationship of enthalpy release and I_{sp} is denoted by Eq. (4):

$$I_{sp} \propto (\Delta H)^{\frac{1}{2}} (\text{gas volume})^{\frac{1}{2}} \quad (4)$$

The I_{sp} values obtained from aluminized formulations that contain 20% Al and oxidizers such as AP, HNF, FDNEN, and ADN in a BN-7/butanetriol trinitrate (BTTN) binder were compared. As indicated in Fig. 1, the results show that HNF produced the highest performance at 276.1 lbf-s/lbm, followed by ADN at 274.0 lbf-s/lbm, AP at 270.9 lbf-s/lbm, and FDNEN at 269.9 lbf-s/lbm. Optimized performance occurred in formulations that contained 15% AP and 30% HNF, FDNEN, and ADN. Thus total solid levels are low at 35% for the AP formulation and 50% for the other three formulations, respectively. While HNF is more energetic than ADN, the former tends to be incompatible with binder curatives and nitrate ester plasticizers. Thus, ADN appears to be the most appropriate oxidizer for compositions containing a BN-7 energetic binder, a BTTN plasticizer, and Al.

The contribution to working fluid volume was estimated by calculating the I_{sp} for those oxidizers considered as monopropellants (Fig. 2). For CHON oxidizers, the yield of gas generally depends on the H content, and, while HN has the highest yield of gas (4.49 mol), it is not a useful oxidizer. ADN has a relatively high yield (4.03 mol) because of its NH_4 moiety. Thus, ADN's yield working fluid combined with its O content (Table 2) and relatively low heat of formation make ADN a comparatively attractive energetic oxidizer.

Earlier, the contributions to performance of different types of binders used in similar aluminized-propellant formulations were quantified and compared. BN-7 exhibits higher calculated values of I_{sp} than polycyanodifluoroaminoethylene oxide (PCDE),²⁰ polyglycidyl nitrate (PGN),^{21,22} and bis(nitratomethyl) oxetane (BNMO).²³ As the oxidizer content increases, polyethylene glycol (PEG) compositions improve rapidly until a 45% oxidizer content is reached, a point at which PEG maximizes to an I_{sp} just above that of PCDE (Fig. 3). Moreover, BN-7 exhibits a high I_{sp} because of its positive heat of formation and high yield of working fluid.

In Table 2, other properties of ADN are also compared with those of AP. Whereas ADN is lower in O content, 51.6% as compared to 54.5% for AP, the former has a more favorable heat of formation, -298 as compared with -602 cal/g. This

Table 2 Comparative properties of ADN and AP

Property	ADN	AP
Oxygen content, %	51.6	54.5
ΔH_f , cal/g	-298	-602
Melting point, °C	92-94	300-350
Density, g/cm ³	1.80	1.95
Yield of gas, moles/100 g	4.03	3.58
Stability/compatibility	Adequate stability/ compatibility	Superior stability/ compatibility
Crystal shape	Needles/leaflets with ability to form spherical prills	Spherical shape as received
Cost	Moderately high	Low
Sensitivity	Sensitivity greater than AP	Sensitivity less than ADN
Contribution to I_{sp}	3-5 s higher than AP	3-5 s lower than ADN
Environmental aspects	Inability to evolve corrosive gas	Ability to evolve HCl gas
Ability to oxidize Al	Less than AP	More than ADN

condition is due to the relatively weak N—N and N—O bonds in ADN as compared with the stabilized chlorine—O bonds in AP. Moreover, the yield of gas (working fluid) from ADN is higher, 4.03 as compared with only 3.58 mol/100 g for AP, owing to the relatively high molecular weight of the HCl produced by AP. The lower heat of formation (which enhances enthalpy release) and the greater volume of gas generated (which enhances the working fluid) cause ADN formulations to have a higher I_{sp} than corresponding AP compositions (Table 2).

The use of metals such as B, Be, and Al contributed to the highest increases in enthalpy release. Whereas nonmetallic energetic materials typically release less than 1.3 kcal/g, the oxidation of Al increases the yield to over 2 kcal/g. These high enthalpy releases are obtained when metal oxides form during combustion, as shown in Table 3. Metal fluorides also form when there is F present in the oxidizer or binder. The data in Table 3 clearly indicate that Be and Al (either as

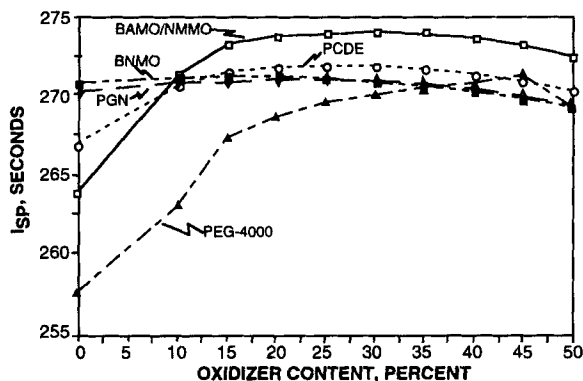
**Fig. 3** Specific impulse of propellants containing ADN, Al, and various binders.

Table 3 Comparison of enthalpy release of metal to metal oxides and fluorides

Metal	Oxide	ΔH_f		Fluoride	ΔH_f	
		kcal/mole	kcal/g		kcal/mole	kcal/g
Be	BeO	-145	-5.8	BeF ₂	-245	-5.2
B	B ₂ O ₃	-304	-4.4	BF ₃ (g)	-272	-4.0
				BOF (g)	-145	-3.2
Mg	MgO	-144	-1.3	MgF ₂	-26	-4.3
Al	Al ₂ O ₃	-401	-3.9	AlOF (g)	-140	-2.3
				AlOF ₂	-265	-3.3
				AlF ₃	-361	-4.3
				AlF ₃ (g)	-289	-3.4
H	H ₂ O (g)	-58	-3.2	HF (g)	-65	-3.2
	H ₂ O (l)	-68	-3.8	HF (l)	-72	-3.6

oxides or fluorides) yield the highest enthalpy release. This high yield is the reason that the performance of aluminum propellant is superior to that of nonaluminized propellant, especially because enthalpy release is the major driver for high I_{sp} and high flame temperature. Both conditions more than compensate for the modest loss of working fluid due to the formation of condensable aluminum oxide (Al₂O₃). However, because Be is toxic and B is difficult to burn with common oxidizers, Al is used most commonly as fuel, even though its atomic weight is higher than that of the light metals mentioned (Be and B).

Replacing metals with metal hydrides is another particularly attractive alternative because both enthalpy release and working fluid are increased. In addition, the H evolved lowers flame temperature. This is especially true for AlH₃. The I_{sp} of propellants containing AlH₃ is typically 1–4 s higher than that of propellants containing Be. However, propellants that contain high levels of AlH₃ (>20–25%) are difficult to process. At present, the use of metal hydrides such as AlH₃ is precluded by their extreme reactivity and safety problems when combined with other plasticizers and oxidizers. Research is underway on stabilizers and binder materials that may be more compatible.

Additional H to lower the product molecular weight can be found in the CH linkages in the binder/plasticizer and in the NH linkages in the oxidizers and nitramines. However, the molecular weight reduction is limited and only achieved at the expense of diminishing enthalpy values because of the relatively strong C–H and N–H bonds. However, these sources of H are critical in metallized propellants in which the addition of metals tends to reduce the sources of working fluid. Thus, in earlier metallized compositions, replacing KP with the H-containing AP resulted in a significant increase in I_{sp} .

To further clarify these points, a typical high-energy propellant [I_{sp} at 1000 psi (6.895 MPa) → 14.5 psi (0.09997 MPa) over 270 lbf-s/lbm] contains a binder such as PEG, a nitrate ester plasticizer, an oxidizer, a nitramine, and Al. While PEG is inert and has a relatively high negative heat of formation (>-1 kcal/g), the addition of an energetic plasticizer renders the binder energetic because of the reduction in the relative level of inert polymers. Cyclic nitramines such as CL-20 and HMX have positive heats of formation and also contribute to a relatively low

Table 4 Calculated specific impulse for energetic compositions

Binder	Plasticizer	Oxidizer	Additive	Metal	I_{sp} , lbf-s/lbm
PEG	NG ^c	—	HMX	Al	274
PEG	NG ^c	AP	HMX	Al	270
BN-7	BTTN	—	HMX	Al	277
PEG	BTTN	ADN	—	Al	277
PEG	BTTN	ADN	—	AlH ₃	291
BN-7	BTTN	ADN	—	AlH ₃	294
BN-7	BTTN	ADN	—	Be	290
NC	NG	AP	HMX/TAZ	Be	298
BN-7	BTTN	ADN	—	BeH ₂	>310
BN-7	BTTN	—	HNFX ^a	BeH ₂	>310
NF binder ^b	—	—	—	BeH ₂	>310
OF binder	—	—	—	BeH ₂	>310

^aHNFX = 3,3,7,7-tetrakis(difluoramino)-octahydro-1,5-dinitro-1,5-diazonine.

^bNF = fluoro amino.

^cNG = nitroglycerine.

molecular weight. The use of AP in these compositions can decrease I_{sp} because of its high negative heat of formation (-606 cal/g). However, because of its high density, AP can also effectively increase the density I_{sp} (1.95 g/cm³). Furthermore, the addition of AP is necessary to tailor the burning rates and enhance the metal combustion of the propellant material.

The energy of the propellants shown in Table 4 can be further increased by replacing the polyether binder, PEG, with BN-7, which has a positive heat of formation ($+330$ cal/g). The replacement of AP with an oxidizer such as ADN that has a lower negative heat of formation (-298 cal/g), will produce further I_{sp} gains. Performance gains can also be achieved by replacing Al with Be, a composition that produces a significant gain in performance (to >280 lbf-s/lbm I_{sp}) because of BeO's high heat of combustion (5.8 kcal/g). Adding conventional ingredients such as HMX, nitrate ester, and triaminoguanidinium azide (TAZ)²⁴ to the propellants shown in Table 4 increases I_{sp} to >298 lbf-s/lbm.

The most energetic combination of ingredients may be created by the addition of Be and ADN in an energetically plasticized binder such as PEG or BN-7. This composition will produce an I_{sp} that exceeds 290 lbf-s/lbm. Replacement of Al with the most energetic fuel reported herein, BeH₂, will yield a further I_{sp} gain, up to 310 lbf-s/lbm or more. This fuel makes a superior contribution to enthalpy release and working fluid. This approach may yield only inert BeO because no chlorine is available (in the absence of AP) to form the soluble and toxic BeCl₂. This toxicity issue has precluded the use of Be in formulations. However, if a nontoxic combustion product of Be could be ensured, the energy yields would be significantly increased.

Compositions containing binders or solids having NF groups^{25,26} and BeH₂ can be exceptionally energetic. This enhanced energy level is based on the favorable combination of enthalpy release and working fluid that is produced from the formation of BeF₂, HF, and H. Furthermore, NF compounds tend to be high in density and, thus, partially offset the low density of BeH₂. Perhaps the ultimate

combination of ingredients is BeH_2 and an OF-containing fluorocarbon binder. Because O—F bonds are weaker than N—F bonds, enthalpy release may be enhanced. However, the reactivity of the COF moiety may preclude the existence of binders containing C—C bonds. In any event, at present, this long-term approach is highly speculative.

Although compositions containing HMX, Al, and AP are effective in achieving a high $\rho^* I_{\text{sp}}$ in long-range strategic missiles, those combinations cannot be used in many short-range tactical missiles. This limitation exists because Al_2O_3 and HCl droplets cause the formation of a visible plume that decreases effectiveness in many engagements. However, the absence of Al causes a decrease in performance in both density and impulse. Thus, the more energetic tactical missiles contain minimum-signature propellants having energetically plasticized polyether–polyester binders filled with cyclic nitramines. However, conventional reduced-smoke propellants containing HTPB binder and AP oxidizer have only modest performance.

Reduced-smoke propellant performance can also be enhanced by the addition of ADN and dense nitramines such as HMX and CL-20. ADN is an oxidizer that contributes to a lower molecular weight and to a higher enthalpy release than AP. Moreover, high-energy, minimum-smoke propellants can be made with ADN or CL-20.

CL-20, first synthesized by Nielsen in 1987,¹² has a greater density than HMX and cyclotrimethylene trinitramine (RDX), as indicated in Table 5. In addition, CL-20's positive heat of formation value is higher, an indication that CL-20 is thermodynamically less stable and, hence, more energetic than HMX.

As a propellant ingredient, CL-20 (based on its high density and high positive heat of formation) can significantly enhance the performance of rocket propellants.

Thus far, I_{sp} has been the principal figure of merit used to characterize propellant performance. However, as mentioned before, to address the performance associated with systems, density to a power times I_{sp} , $\rho^* I_{\text{sp}}$, should be used as the measure of merit. For a volume-limited system, an exponent of 0.75 is used, while for a weight-limited missile system, a value of 0.15 is applied. Thus, $\rho^{0.75} I_{\text{sp}}$ is used for volume-limited systems and $\rho^{0.15} I_{\text{sp}}$ is used for weight-limited systems. This measure is used with the understanding that the performance of an actual system may have an exponent between these two extremes. Tables 6 and 7 show a comparison of propellants made with conventional binders and with AP, HMX, or CL-20 as the sole oxidizer. The results indicate that the propellant containing CL-20 provided higher performance than those made with AP or HMX. This

Table 5 Properties of CL-20, HMX, and RDX

Properties	CL-20	HMX	RDX
Molecular formula	$\text{C}_6\text{H}_6\text{O}_{12}\text{N}_{12}$	$\text{C}_4\text{H}_8\text{N}_8\text{O}_8$	$\text{C}_3\text{H}_6\text{N}_6\text{O}_6$
Melting point, °C ^a	260	285	205
Density, g/cm ³	2.04	1.9	1.82
ΔH_f , cal/g	228	61	66
Standard I_{sp} , lbf-s/lbm ^b	273	265	265.5

^aDecomposition temperature.

^bCalculated from standard condition: 1000–14.5 psia (6.895–0.09997 MPa).

Table 6 Volume-limited system propellant performance comparison

Propellant	$\rho^{0.75} I_{sp}$	Exhaust temperature, K
Metallized conventional Al/AP	427.8	2324
Metallized conventional Al/HMX	430.2	2313
Metallized conventional Al/CL-20	431.8	2314
Nonmetallized HMX high energy	409.7	1509
Nonmetallized CL-20 high energy	429.8	1950

performance enhancement was even more dramatic in nonmetallized formulations, that is, reduced- and minimum-smoke propellants.

In summary, the criteria for the selection of ingredients that enhance performance for composite propellants are described in terms of the contribution to enthalpy release and gas volume (working fluid) generated. The ingredients, in their descending order of contribution to enthalpy release, are as follows: 1) metals and metal hydrides, 2) nitramines (with chemical energy equal to or higher than HMX), 3) nitrate esters, 4) energetic binders, and 5) inert binders.

The oxidizers, in their decreasing order of ability to increase working fluid, are as follows: 1) HN, 2) ADN, 3) HNF, 4) AP, 5) HAP, 6) HP2, and 7) FDNEN.

Although all of these ingredients are important in the investigation of future propellant applications, the most practical combinations of ingredients are those that have the highest performance and the greatest stability: Al, ADN, and energetic binders. Compositions that contain the most energetic ingredients such as metal hydrides and HNF suffer from sensitivity, compatibility, and aging instability problems brought about by the extreme reactivity of these ingredients.

B. Insensitive Munitions

A new class of reduced-smoke propellants has been developed by Alliant Techsystems.^{27,28} Full-scale rocket motors loaded with these propellants passed all the IM-required tests, which included slow cookoff, fast cookoff, fragment impact, and bullet impact. This accomplishment was remarkable inasmuch as conventional HTPB/AP propellants often fail one or more of these tests and exhibit violent reactions. Because the principal cause of these failures is inclusion of energetic materials within the formulations prepared for the munitions, incorporation of less

Table 7 Weight-limited system propellant performance comparison

Propellant	I_{sp} , lbf-s/lbm	$\rho^{0.15} I_{sp}$	Exhaust temperature, K
1.3 Reduced smoke	247.9	270.3	1455
1.3 Minimum smoke	243.5	262.7	1339
1.1 Minimum smoke	246.6	267.4	1249
1.1 CL-20 high energy	270.4	296.7	1950

Table 8 Properties of HTPB and HTPE propellant characteristics

Characteristics	HTPB	HTPE
$I_{sp} \times \text{density}$	~ 15	~ 15
Burning rate at 1000 psi (6.895 MPa), in./s (cm/s)	0.39 (0.99)	0.40 (1.01)
Pressure exponent	0.44	0.50
π_k , %/°F	0.11	0.10
77°F stress, psi (MPa)	120 (0.827)	174 (1.199)
77°F strain, %	56	44
77°F modulus, psi (MPa)	628 (4.33)	588 (4.05)
-65°F ignition strain, %	15	21
-65°F thermal strain, %	30	40
Shock sensitivity	Zero card	Zero card

sensitive ingredients is the most crucial step toward successfully achieving IM goals.

These new propellants are based on a binder containing a HTPE polymer, an energetic plasticizer, and an AP oxidizer. The mechanical and ballistic properties of these HTPE propellants are very similar to those of the HTPB/AP propellants used in tactical systems. A comparison between these propellants is shown in Table 8.

The introduction of this new HTPE binder provided substantial differences in the propellant's behavior when exposed to external stimuli (heat, shock, and mechanical impact). Graphite composite case demonstration motors, 10 in. in diameter, that contained approximately 60 lb of HTPE propellant were subjected to all four of the IM tests mentioned. The results are compared with those motors loaded with conventional HTPB propellants in Table 9. The motors loaded with HTPE propellant passed all four IM tests, but the motors loaded with HTPB propellant passed only one. The successful development of this reduced-smoke propellant was further utilized in evolving an aluminized version of HTPE propellant.

Studies conducted over the years indicated that AP was not usable for minimum-signature propellant applications, thus the incorporation of CL-20 in more recent compositions. The use of high-explosive solids such as HMX or CL-20 in minimum-signature propellant compositions to obtain high performance was described earlier in this paper. However, these solids tended to be shock sensitive

Table 9 IM test results in 10-in. demonstration motors

IM test	HTPB propellant	HTPE propellant
Slow cookoff	Explosion (fail)	Burning (pass)
Fast cookoff	Burning (pass)	Burning (pass)
Bullet impact	Deflagration (fail)	Burning (pass)
Fragment impact	Explosion (fail)	Extinguished (pass)
overpressure	78 psi (0.537 MPa)	0 psi (0 MPa)

Table 10 Shock sensitivity test results of CL-20 propellants

CL-20 type in propellant	NOL card gap test, 50% point, no. card (<i>p</i>)
200 μm in ε form (poor crystal quality, high levels of defects)	>170 cards (<30 kbar)
7.6 μm (FEM ground)	90 cards (60 kbar)
3 μm (SWECO ground)	58 cards (70 kbar)

Note: All sizes of CL-20 are in ε form.

because they possessed high chemical energies. On the other hand, propellant formulations containing AN, while less shock sensitive, exhibited intolerable performance losses (typically, less than 200 lbf-s/lbm in delivered I_{sp}). Recent work has shown that when both AN and CL-20 are used together to formulate a minimum-signature propellant²⁹ the result is a less sensitive composition with improved performance characteristics.

To continue the progress in the areas of decreased sensitivity with increased energy, new ingredients must be of higher quality as well as of increased energy. Three CL-20 minimum-signature propellant samples were produced to evaluate the effect of crystal quality and size on the shock sensitivity of the propellant. The results of the Naval Ordnance Laboratory (NOL) card gap test³⁰ are summarized in Table 10. These results indicate that samples made with an unground CL-20 production lot contained the highest amount of crystalline defects, a condition that translated into higher sensitivity to shock initiation. When this CL-20 material was ground, the shock sensitivity of the propellant sample improved significantly. The difference between the fluid-energy-milled (FEM) and the vibro-energy-milled (SWECO) materials was that this FEM-ground material retained larger particles with crystalline defects (i.e., >50 μm), a condition that contributed to the shock sensitivity of 90 cards. This value is not acceptable because it is higher than the 70-card limit for classification as Class 1.3 material. In later work, the FEM process was refined to produce particles that were uniformly fine and equivalent in sensitivity to the SWECO-ground material.

The experience showed that crystal quality is important in obtaining the least shock sensitive formulation. When crystalline defects are removed through mechanical grinding, it is possible to achieve a Class 1.3 minimum-signature propellant that incorporates a significant percentage of a very high-energy ingredient. Thus, a method that uses CL-20 or HMX to boost the energy of AN propellants without degrading their desirable insensitivity to shock has been successfully developed. It should be reemphasized that the data clearly showed that the crystal quality of CL-20 and HMX materials plays an important role in shock initiation.^{31,32}

High-density additives, such as burning-rate modifiers or combustion instability additives, can increase the shock sensitivity of AN propellant. Therefore, one important aspect of the formulation work was to choose burning-rate modifiers that support the burning of the propellant and yet do not increase shock sensitivity. An experimental propellant [glycidyl azide polymer (GAP)/BTTN/AN/RDX] was prepared with two different types of lead-containing additives to boost burning

Table 11 Shock sensitivity test results of propellant GAP/BT/N/TMETN/AN/RDX

Lead additives	NOL card gap test	
	Cards 50% point	Pressure (kbar) in PMMA ^a
Propellant without lead additive	58	75
Lead carbonate	80	70
Lead citrate	58	75
A ^b	141–173	41–30

^aPMMA = polymethyl methacrylate.^bA = conventional minimum-signature propellant.

rates. When lead carbonate, an insoluble, dense material, was added to this composition, shock sensitivity was increased from 58 to 80 cards (Table 11). However, the soluble compound, lead citrate, not only enhanced burning rate but also preserved the low shock sensitivity of the propellant.

There is a growing body of evidence indicating that the crystal defects residing within high explosives are one of the major causes of shock sensitization in energetic composite materials. Therefore, methods that remove or minimize these imperfections (proper recrystallization or mechanical grounding) can greatly improve shock sensitivity of the filled material.

Related to this phenomenon, hot spot initiation has been studied and documented.³³ CL-20, because of its exceptionally high chemical energy content, is probably more prone to sensitization when large amounts of crystalline imperfections exist in the sample. The studies documented in this paper have helped formulators prepare CL-20 so that it can be incorporated into propellants to enhance energy yet still maintain low shock sensitivity properties. Combustion additives, such as lead catalysts or zirconium carbides, can also sensitize the propellant to shock initiation. However, care must be taken when such additives are used. To maximize the yield of energy while reducing sensitivity, the chemical structure, the reactivity and compatibility with other ingredients, and even the physical form of the ingredients must be carefully scrutinized.

C. Pollution Prevention

The desirability of developing a new propellant that can facilitate the demilitarization and regeneration of ingredients was described in an earlier section of this chapter. A technique has been successfully demonstrated that incorporates a hydrolyzable binder into an energetic formulation. Thus, demilitarization is only a matter of dissolving the binder into oligomeric compounds and molecular constituents by solvolysis in dilute aqueous acid or alkali. This method allows recycling of the solid ingredients by either filtration or recrystallization from the aqueous solution.³⁴

Few polymers have the potential for facile ability to hydrolyze combined with the ability to meet the stringent requirements of binders for tactical rocket motors.

Hydrocarbon chains meet the latter requirements but not the former. Moreover, as mentioned earlier, these chains are insoluble and unreactive to conditions applicable to the demilitarization and recycling of energetic munitions and their components.

The most promising polymers for acid- or base-catalyzed hydrolytic degradation are hydroxyl-terminated polyesters cured with isocyanates to form urethane cross links.^{35,36} In principle, both ester and urethane linkages are hydrolyzable in dilute aqueous acid and base solutions, although normally the process is slow. However, if the polymer backbones of such materials also contain hydrophilic polyester segments that allow the aqueous medium to penetrate to the cure linkages, and if these polyether moieties are optimized for length, the rate of hydrolysis of the polyester linkages increases under mild conditions. If, in addition, the urethane linkages are modified with electron-withdrawing groups, the rate of hydrolysis of these linkages increases. Hydrolysis of such a polymer results in a dilute aqueous solution of a diamine, a diacid, and a short PEG chain.

The development of hydrolyzable binders for explosive formulations has been ongoing for over 20 years. However, only recently has the development been expanded to include propellant formulations.³⁷ In the 1970s, polyglycol adipate esters³⁸ with PEGs of varying molecular weights were used to attain degradable PBXs. The ester hydrolysis rates were found to increase markedly as the length of the glycol chain increased. Lengthening the polyether chain enhanced the affinity to water and rate of hydrolysis. The rates were also increased by the assistance of the neighboring ether O. A PEG of about 400 daltons was selected and a hydroxyl-terminated polyethylene glycol adipate (PEGA) was developed from this PEG. Synthesis of the PEGA is shown schematically in Fig. 4. Trimethylolpropane was added in small quantities to provide a functionality greater than two.

Laboratory-scale samples of propellant formulations that utilize PEGA cross linked with hexamethylene diisocyanate (HMDI) can be hydrolyzed in dilute acid or base in a day's time if the aqueous solution is warmed. Compositions containing Al are treated with ammonium hydroxide, which, unlike dilute acid, does not dissolve the Al. Potassium carbonate was also used in hydrolysis. This method enabled the AP to convert to the slightly soluble KP, which could be recovered by filtration. A further increase in the binder degradation rate was afforded by curing the PEGA with a diisocyanate bearing an electron-withdrawing group. Lysine diisocyanate methyl ester (LDIM) contains a carbomethoxy group on its α -carbon atom. Urethanes formed by a reaction of this α -isocyanato group are more readily hydrolyzed than are urethanes formed from a conventional isocyanate such as HMDI. Samples cured with LDIM or lysine triisocyanate (LTI) were shown to

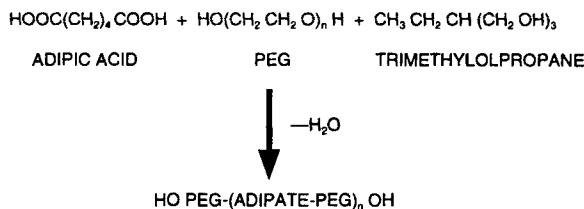


Fig. 4 Preparation of polyethylene glycol adipate.

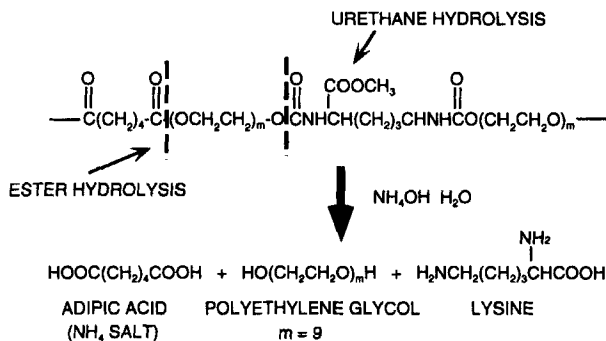


Fig. 5 Binder hydrolysis.

hydrolyze in room temperature aqueous acid or base in a few hours. The formation of the binder and its hydrolysis are shown in Fig. 5. LDIM used as the curative enhances the environmental innocuousness of the demilitarization process because other isocyanates are hydrolyzed to form toxic amines. The lysine formed from LDIM on hydrolysis is a nontoxic essential amino acid.

With the utilization of binders such as PEGA, demilitarization of rocket motors generates a clear, nonviscous supernatant hydrolysate from which insoluble ingredients such as HMX and Al can be recovered easily by filtration. These solids can then be sold for reuse in commercial explosives and alternative energetic formulations. Soluble ingredients such as AP can be crystallized out, and the aqueous acid or base solution recycled. Left over is a liquid hydrolysate containing nontoxic compounds that can be easily and cheaply treated for proper disposal. Under this demilitarization scheme, the value of the ingredients can be saved, and the environmental burdens involved in manufacturing new replacement materials can be alleviated. Moreover, concerns about air and water pollution involved in the demilitarization of these formulations can be allayed.

The hydrolyzable binder PEGA has properties significantly different from the common binder HTPB (as shown in Table 12). Thus, changes in formulation of PEGA are necessary.

Because PEGA has a higher O content than HTPB, the former is also higher in density. Consequently, the volume percentage of binder per unit weight is reduced when PEGA is used as a binder. Thus, relatively high percentage levels of binders are required to attain good processibility. Fortunately, the high O content permits the use of high levels of Al. Typical formulations can contain up to 22% Al, an amount that tends to produce a density impulse equivalent to that of an aluminized

Table 12 Comparison of the properties of hydrolyzable binders (PEGA) and HTPB (R-45M)

	Viscosity, cP	Density, g/cm ³	ΔH_f , cal/g	Oxygen, %	MW	Functionality
PEGA	8500	1.2	-1100	37	3500	2.33
HTPB	6000	0.9	-5.0	2	2800	2.2-2.4

HTPB propellant. A typical propellant is composed of a PEGA polymer, an LDIM curative, an acetyltriethyl citrate plasticizer, AP (2, 20, and 200 μm), a Fe_2O_3 burning rate catalyst, and Al (30 μm).

Propellants were then optimized to exhibit adequate mechanical properties. The burning rates were varied by changing the particle size of AP, as well as by adding iron oxide. These propellants typically exhibited rates between 0.55 and 0.88 in./s (1.4–2.23 cm/s) at 1000 psia (6.895 MPa). The pressure exponent was as low as 0.47 between 1000 and 3000 psia (6.895–20.685 MPa).

An ideal hydrolyzable binder would be resistant to ambient moisture exposure during storage. Thus, another critical issue addressed was long-term aging in humid environments. In the presence of moisture, AP becomes a catalyst that enhances hydrolysis of polyesters.^{35,36} Preliminary aging results indicated that the propellant incorporating PEGA survived well at 50% relative humidity at ambient temperature for six weeks. However, additional aging experiments are currently being conducted in a more stringent environment because of the following concerns.

Thus far, hydrolyzable binders in propellant formulations have been limited to experimental applications in small gun-launched systems. Future development of this hydrolyzable binder concept must address the more stringent requirements for aging in humid environments to which larger, more exposed propulsion systems are subjected. Although the PEGA binder is insoluble in water, trace quantities of acidic or basic compounds in conjunction with moisture tend to degrade the mechanical properties of formulations unless they are manufactured under dry conditions and protected, to some extent, from the environment. The present situation is analogous to the early days in the development of biodegradable packaging, in which the first products on the market began to biodegrade before the end of their service lives. Modifications of the polyether chains and variations of the structure of the diacid moiety in the polyether–polyester structure are under investigation and may result in polyesters that are hydrolyzable under more specific conditions than the prototypical PEGA binder described earlier. Such variant binders would be applicable to propulsion systems that have to endure long exposures to humid environments, for example, on the wing of a plane on a carrier deck at sea.

Another technique for a viable demilitarization recycling plan currently under investigation is a binder that can be melted or dissolved from the motor case and divested of its solids content by filtration or solvent washing. This binder can then be reconstituted, reformulated with the solid ingredients, and replaced in the case. This method has the virtue of enabling the recycling of virtually everything in the rocket motor with minimal additions of new material. In addition, the binder can itself be an energetic ingredient, a condition that allows large increases in performance with only slight increases in sensitivity. A great deal of developmental work to this end has been done on the copolymer BAMO/azidomethyl methyl oxetane (AMMO)^{37,39} (Fig. 6), which is an energetic thermoplastic elastomer (TPE). Although this TPE is not a true hard-soft-hard (ABA) triblock polymer, the polymer is thermoplastic and has elastomeric properties.^{40,41}

Any usable binder in this demilitarization scheme must be thermoplastic or soluble in organic solvents, or both, like BAMO/AMMO. Because fugitive emissions of volatile organic compounds and solvent vapors in the workplace are under heavy regulatory attention and require strict engineering controls, the use of thermoplastics is by far the most attractive alternative.

The dilemma for this option is thermoplastics' reliance on the physical entanglements and chemical associations of polymer chains for their mechanical

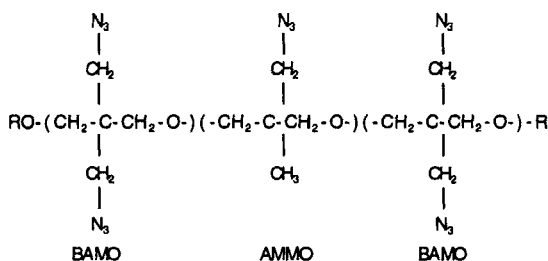


Fig. 6 Structure of BAMO/AMMO.

properties.^{39,40} The associations of the hard polymer blocks and the chain entanglements form virtual cross links that are weakened when heat energy is added to the polymer and when molecular motion increases. These cross-links are strengthened when the material is cooled and the motion decreases. Thus, at a higher temperature, any given thermoplastic will always have lower stress and higher strain than at a lower temperature. This reduction in mechanical properties continues to the point of the polymer melting and running if the temperature is high enough. On the other hand, at a given temperature, the binder with the greater number of entanglements and associations (brought on by greater length, more branching, or more associative moieties in the polymer chains) will have better mechanical properties. Thus, the mechanical properties of a given thermoplastic polymer structure are very dependent on the temperature at which they are measured. Furthermore, this mechanical behavior tends to change in direct proportion to a change in temperature.

To be a successful meltout recycling scheme, a propellant formulation that utilizes a thermoplastic binder must melt to a low-viscosity liquid (similar to light oil) at a temperature below that of the thermal decomposition of the propellant formulation. In addition, the solids must be filtered relatively rapidly without clogging the filter. However, this temperature cannot be higher than 100–125°C so that serious risk of decomposition with ingredients such as nitrate ester plasticizers or ADN can be avoided. At the same time, the thermoplastic must have adequate mechanical properties for storage and use at temperatures as high as 60°C yet not be overly brittle or glassy at temperatures as low as –50°C. Generally, the systematic reaction of thermoplastics to structure and temperature dictates that a thermoplastic that does not soften, slump, or creep at 60°C will not melt to a low-viscosity liquid at 100°C and will be brittle or glassy at –50°C. The addition of plasticizers improves low-temperature mechanical properties, but at the same time is liable to degrade high-temperature properties. Thus, the challenge is either to find the perfect compromise of molecular weight and degree of branching for the polymer or to discover substitutes that both attach to the binder and have a nonsystematic association as the temperature increases.

Another approach is to design the block polymer so that the center (soft) block has a more fluid structure than AMMO. AMMO has a pendant, rodlike azido group that is more characteristic of a hard block. Polyethers of ethylene–propylene copolymers and fluoropolyethers have relatively low viscosities at a given chain length and are more appropriate substances for the soft block in an ABA block thermoplastic elastomer. Polar nitramino or tetrazolyl groups are efficient hard

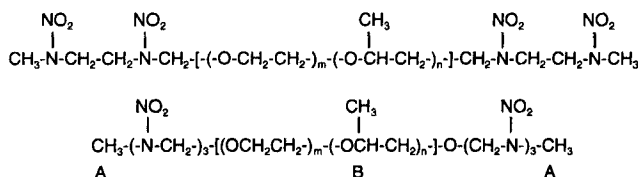


Fig. 7 Proposed structures of thermoplastic elastomers.

blocks for the associative parts of the molecule. An example of such a structure is shown in Fig. 7.

Because thermoplastics are not cross linked, it is possible to dissolve them in the appropriate organic solvent. The limitation in the length of the chains for ease of solubility also limits the mechanical properties of the binder across the appropriate temperature range. The demilitarization of a rocket motor under these conditions somewhat resembles the cryogenic or water washout method described earlier, except that the dissolution of the binder is complete and all of the ingredients are recovered. The binder must be reconstituted by evaporation of the solvent, and degradation of mechanical properties may occur if any solvent is retained in the thermoplastic or if the heat necessary to evaporate the last traces of solvent degrades the binder chains. Engineering controls are required to curtail emissions of solvent vapors during the washout, evaporation, and vapor recovery processes. Nevertheless, within the context of these challenges, demilitarization of thermoplastic binder propellants is feasible.

III. Conclusions

In summary, ingredients containing light chemical elements such as H, Al, Be, B, C, N, O, and F are the most useful for high-energy propellant compositions. Generally, these elements enhance enthalpy release per unit weight while reducing the average molecular weight of gases. Oxidizers such as CL-20, ADN, and HNF have been identified as the most energetic ingredients for achieving high-performance propellants. Metal fuels such as Be and metal hydrides such as AlH_3 and BeH_2 contribute to even greater performance enhancements, especially when used with energetic binders such as azido and nitrate polyoxetanes.

The requirement for insensitive high-energy propellants that pass all IM tests when loaded in rocket motors is of primary interest to the user community. This consideration is especially vital because insensitive propellants greatly reduce the hazardous properties of munitions. Among numerous approaches, only the HTPE propellant passed all IM tests. Therefore, additional innovative ideas are definitely needed in this area, especially a new, insensitive, minimum-smoke propellant because it is the most detonable propellant material.

Hydrolyzable propellant is another excellent approach for incorporating a simplified demilitarization process into the design of formulation. Thus, binders can be easily removed and ingredients reused. However, other techniques such as the use of TPEs are attractive. With a TPE, the binder is designed to be remelted and recast into a reusable propellant grain.

Ultimately, the environmental impact of propellant formulation must be addressed at each step in the manufacturing process. Energetic formulation

ingredients such as HMX and nitroester plasticizers are produced in conjunction with large quantities of hazardous waste products in the form of spent acids, solvents, and contaminated water. Additional environmental pollution occurs when the motor goes through the demilitarization process by conventional methods. Therefore, the most desirable scenario is to address the environmental damage potential in the early stages of the formulation so that the manufacturing and demilitarization phases cause less pollution. Developmental efforts that address all of the phases in a propellant's life cycle must be emphasized.

Efforts ranging from feasibility studies to demonstrations are being made in the following fields: modifications of ingredient synthesis to reduce the hazards of the reaction byproducts, recycling of synthetic reaction solvents and reagent byproducts, reduction of hazardous ingredients in propellant formulations, reduction of solvent usage, and replacement of hazardous solvents with more innocuous solvents in propellant manufacture. Ultimately, all these efforts will combine to reduce the environmental hazards of propellant formulations throughout their service lives.

Acknowledgments

The authors wish to gratefully acknowledge the research grants generously supported by the Air and Surface Weapons Technology Program under the auspices of the Office of Naval Research (James Chew, OCNR-351, cognizant technology manager) and by the Insensitive Munitions Advanced Development Program and the Green Energetics Materials Program under the cognizance of Don Porada, SEA91M1.

References

- ¹Farber, M., "Fluorine Solid Propellants," *Astronautics*, Aug. 1960, p. 39.
- ²Kubota, N., "Survey of Rocket Propellants and Their Combustion Characteristics," *Fundamentals of Solid-Propellant Combustion*, edited by K. K. Kuo and M. Summerfield, Progress in Astronautics and Aeronautics, Vol. 90, AIAA, New York, 1984, pp. 1-52.
- ³Sutton, G. P., *Rocket Propulsion Elements*, 5th ed., Wiley, New York, 1986.
- ⁴Sarner, S. P., *Propellant Chemistry*, Reinhold, New York, 1966.
- ⁵Siegel, B., and Schieler, L., *Energetics of Propellant Chemistry*, Wiley, New York, 1964.
- ⁶Cruise, D. R., "Theoretical Computations of Equilibrium Compositions, Thermodynamic Properties and Performance Characteristics of Propellant Systems," Technical Publ. 6037, Naval Weapons Center, China Lake, CA, April 1979.
- ⁷"Insensitive Munitions: Hazard Assessment Tests for Non-Nuclear Munitions," MIL-STD-2105B, U.S. Dept. of Defense, Jan. 1994.
- ⁸Farley, K. D., and Swartz, D., "Environmental Analysis for Solid Rocket Motor Operation," Solid Rocket Lecture Series, 32nd AIAA/ASME/SAE/ASEE Joint Propulsion Conference, Orlando, FL, July 1996.
- ⁹Munson, W. O., "Large Rocket Motor Demilitarization," *Proceedings of the 4th Global Demilitarization Symposium and Exhibition*, American Defense Preparedness Association, Reno, Nevada, 1996, p. 331.
- ¹⁰Borcherding, R., "An Alternative to Open Burning Treatment of Solid Propellant Manufacturing Wastes," *Proceedings of the 1998 Life Cycles of Energetic Materials*, Del Mar, CA, 1998, p. 87.

¹¹Miller, R. S., "Research on New Energetic Materials," *Proceedings of Materials Research Society Symposium*, Vol. 418, 1996, p. 3.

¹²Nielsen, A., "Caged Polynitramine Compound," U.S. Patent 5,693,794, Dec. 1997.

¹³Tartakovsky, V. A., and Luk'yanov, O. A., "Synthesis of Dinitramide Salts," *Proceedings of the 25th International Annual Conference of ICT*, 1994.

¹⁴Schmidt, R. J., Bottaro, J. C., Ross, D. S., and Penwell, P. E., "Dinitramide Salts and Method of Making Same," International Patent Application WO 91/19669, June 1990; U.S. Patent 5,254,324, Oct. 1993.

¹⁵Schmidt, R. J., Bottaro, J. C., Penwell, P. E., and Bomberger, D. C., "Process for Forming Ammonium Dinitramide Salt by Reaction Between Ammonia and A Nitronium-Containing Compound," U.S. Patent 5,316,749, May 1994.

¹⁶Manser, G. E., "Energetic Copolymers and Method of Making Same," U.S. Patent 4,483,978, Nov. 1987.

¹⁷Schoyer, H. F. R., Schnorhk, A. J., Korting, P. A. O. G., and Van Lit, P. J., "First Experimental Results of an HNF/Al/GAP Solid Propellant," 33rd AIAA/ASME/SAE/ASEE Joint Propulsion Conf. and Exhibit, Seattle, WA, July 1997.

¹⁸Schoyer, H. F. R., Schnorhk, A. J., Korting, P. A. O. G., Van Lit, P. J., Mul, J. M., Gadiot, G. M. H. J. L., and Meulenbrugge, J. J., "High-Performance Propellants Based on Hydrazinium Nitroformate," *Journal of Propulsion and Power*, Vol. 11, No. 4, 1995, pp. 856-859.

¹⁹Pak, Z., "Some Ways to Higher Environmental Safety of Solid Rocket Propellant Application," AIAA/SAE/ASME/ASEE 29th Joint Propulsion Conf. and Exhibit, Monterey, CA, June 1993.

²⁰Hunter, L., and Pety, W. L., "Polycyanodifluoroaminoethers," U.S. Patent 4,055,516, Oct. 1977.

²¹Willer, R. L., and Day, R. S., "Poly(glycidyl Nitrate) Revisited, *Proceedings of American Defense Preparedness Association International Symposium on Compatibility of Plastics and other Materials with Explosives, Propellants and Pyrotechnics and Processing Propellants, Explosives and Ingredients*, ADPA, 1989, p. 257.

²²Agrawal, J. P., "Recent Trends in High Energy Materials," *Progress in Energy and Combustion Science*, Vol. 24, 1998, pp. 1-340.

²³Manser, G. E., "The Development of Energetic Oxetane Polymers," *Proceedings of the 21st International Annual Conference of ICT*, 1990.

²⁴Rains, W. A., Fox, R. D., and Flynn, J. P., "Composite Double Base Propellant with Triaminoguanidinium Azide," U.S. Patent 3,971,681.

²⁵Eremenko, L. T., "Interrelationship Between Density and Structure in An Explosive," *Proceedings of the 11th Symposium on Explosives and Pyrotechnics*, Franklin Research Center, Philadelphia, 1981.

²⁶Chapman, R. D., Gilardi, R. D., Welker, M. F., and Kreutzberger, C. B., "Nitrolysis of a Highly Deactivated Amide by Protonitronium. Synthesis and Structure of HNF_x," *Journal of Organic Chemistry*, Vol. 64, 1999, pp. 960-965.

²⁷Goleniewski, J. R., and Roberts, J. A., "Solid Propellant with Non-Crystalline Polyether/Energetic Plasticizer Binder," U.S. Patent 5,783,769, July 1998.

²⁸Comfort, T. F., Steckman, R. M., and Hartman, K. O., "Insensitive HTPPE Propellants," *Proceedings of the American Defense Preparedness Meeting, Insensitive Munitions Technology*, 1994.

²⁹Atwod, A., Curran, P. O., Chan, M. L., Reed, R., Boggs, T. L., and Wilknich, J., "Combustion of CL-20 and CL-20 Propellant Formulations," *Proceedings of the American*

Defense Preparedness Association, International Symposium on Energetic Materials Technology, ADPA, 1994, pp. 70–75.

³⁰Erkman, J. O., Edwards, D. J., Clairmont, A. R., Jr., and Price, D., “Calibration of the NOL Large-Scale Gap Test; Hugoniot Data for Polymethyl Methacrylate,” NOTLR 73-15, April 1973.

³¹Baillou, F., Dartyge, J. M., Spyckerelle, M., and Mala, J., “Influence of Crystal Defects on Sensitivity of Explosives,” *Proceedings of the Tenth International Detonation Symposium*, 1993.

³²van der Steen, A., de Jong, E., Prinse, W., Hordijk, A., and Duvalios, W., “Crystal Quality and Shock Sensitivity of RDX-Based PBXs,” *Proceedings of the Tenth International Detonation Symposium*, 1993.

³³Coffey, C. S., “Localization of Energy and Plastic Deformation in Crystalline Solids During Shock or Impact,” *Journal of Applied Physics*, Vol. 70, No. 8, 1991, p. 4248.

³⁴Reed, R., Jr., Lee, B. Y. S., and Miller, R. L., “Degradable Binder Explosives,” U.S. Patent 4,293,352, Oct. 1981.

³⁵Cohen, J. L., and Van Aartsen, J. J., “The Hydrolytic Degradation of Polyurethanes,” *Journal of Polymer Science*, Symposium 42, 1973, pp. 1325–1338.

³⁶Brown, D. W., Lowry, R. E., and Smith, L. E., “Equilibrium Acid Concentrations in Hydrolyzed Polyesters and Polyester—Polyurethane Elastomers,” *Journal of Applied Polymer Science*, Vol. 28, 1983, pp. 3779–3792.

³⁷Manser, G. E., Fletcher, R. W., and Shaw, G. C., *High Energy Binders*, Rept. NR659-792, Office of Naval Research, Arlington, VA, Jan. 1984.

³⁸Reed, R., Jr., Ciaramitaro, D. A., and Brady, V. L., “The Role of Binder Chemistry in the Demilling of Rocket Propellants,” *Proceedings of the 1998 Life Cycle of Energetic Materials*, Fullerton, CA, 1998.

³⁹Cannizo, L. F., Wardle, R. B., Hamilton, R. S., and Edwards, W. W., “Oxetane Thermoplastic Elastomeric as Solid Propellant Binders” *Proceedings of 1994 Life Cycles Of Energetic Materials Conference*, Del Mar, CA, 1994.

⁴⁰Cannizo, L. F., Wardle, R. B., Hamilton, R. S., and Edwards, W. W., “Poly (BAMO/AMMO) TPE Composite Propellant,” *Proceedings of American Defense Preparedness Association Meeting on International Symposium on Energetic Materials Technology*, ADPA, 1995.

⁴¹Sanderson, A. J., Edwards, W. W., Wardle, R. B., Cannizzo, L. F., and Hamilton, R. S., “Improvements in the Physical Properties of Energetic Thermoplastic Elastomers,” *Proceedings of 1998 National Defense Industrial Association Meeting on the Insensitive Munitions and Energetics Materials Technology Symposium*, San Diego, CA, Nov. 1998.

Chapter 1.8

Synthesis and Characterization of Dinitramidic Acid and Its Salts

Oleg A. Luk'yanov* and Vladimir A. Tartakovsky†
Russian Academy of Sciences, Moscow, Russia

I. Introduction

DINITRAMIDIC acid (DNA) and its salts were discovered for the first time at the N.D. Zelinsky Institute of Organic Chemistry of the Russian Academy of Sciences in May 1971 by the authors, working jointly with S. S. Novikov and V. P. Gorelic. This discovery was not published at the time because of the potential usefulness of DNA derivatives, particularly in rocket propellant formulations. In 1993, Russian delegates made a presentation at the meeting of the American Institute of Aeronautics and Astronautics on the use of the ammonium salt (ADN) as a high-performance and ecologically friendly oxidizer for rocket propellants.¹ A year before that, a patent was published in the United States in which ADN salts were suggested for use as solid rocket propellant components.² A number of publications have appeared subsequently that dealt with various aspects of the use of ADN salts in highly energetic formulations with diverse applications.³⁻⁵ The pioneering Russian publication appeared only in 1994.⁶

This new class of compounds is based on the anion with the following composition: N_3O_4^- or $\text{N}(\text{NO}_2)_2^-$. The corresponding acid HN_3O_4 belongs to the family of simple inorganic acids that are among the universal reagents of chemistry. Perhaps the most amazing aspect of this discovery is that it was made so recently. Indeed, the simplest combinations of nitrogen and oxygen atoms, for example, NO , N_2O , N_2O_3 , N_2O_4 , and N_2O_5 have been known throughout the 20th century. Respective carbon and oxygen analogs of the anion $\text{N}(\text{NO}_2)_2^-$, such as $\text{C}(\text{NO}_2)_3^-$, and ONO_2^- , are also well known. The discovery of HN_3O_4 may be, therefore, compared with encountering a new island, not in the vast Pacific Ocean but somewhere in the English Channel. In our opinion, this area of chemistry seemed so widely explored that nothing new was expected of it. In addition, the prospects may have seemed discouraging because the first nitro derivative of ammonia (nitramide

Copyright © 2000 by O. A. Luk'yanov and V. A. Tartakovsky. Published by the American Institute of Aeronautics and Astronautics, Inc., with permission.

*Professor, N.D. Zelinsky Institute of Organic Chemistry.

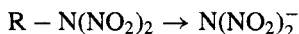
†Professor, Director of N.D. Zelinsky Institute of Organic Chemistry.

NH_2NO_2) is known to be an unstable compound that is decomposed readily by base. Furthermore, organic compounds with the $\text{N}(\text{NO}_2)_2$ fragment, for example, methyl dinitramine, have low stability and are good nitrating agents because cleavage of the nitrogen central atom bond leads to the formation of stable fragments: the cation of NO_2 and the anion CH_3NNO_2 . We assumed that a similar reaction of the $\text{N}(\text{NO}_2)_2$ system should not proceed because it would result in the formation of the dianion $\text{N}(\text{NO}_2)_2^{2-}$ and involve a great energy loss. Meanwhile, it was evident that the anion $\text{N}(\text{NO}_2)_2^-$ should be a rather stable fragment because a high degree of negative charge delocalization would be achieved among the seven atoms. This assumption was confirmed and the period of 1971–1975 at this Institute was marked by the development of 20 synthesis options for the nitrogen–oxygen system N_3O_4 . We synthesized DNA and over a hundred of its various organic and inorganic salts and obtained their structures, spectra, and physical and chemical properties.

The synthesis of the same class of compounds was duplicated independently by U.S. chemists in 1989.² In this connection, the terminology for this type of compounds is worth discussing. American researchers suggested that the first member of this series should be termed dinitramide and, respectively, its derivatives termed dinitramide salts. To our mind, this nomenclature is incorrect, because amide is the name for a compound in which only one hydrogen atom on N is substituted by the functional group, for example, CH_3CONH_2 acetamide. The compounds with two hydrogen atoms substituted by functional groups have a general name imide, for example, $(\text{CH}_3\text{CO})_2\text{NH}$ –acetimide. Hence, a more appropriate name for this class of compound should be dinitrimide salts. Because $\text{HN}(\text{NO}_2)_2$ is among the strongest inorganic acids, we called this compound dinitrasous acid or DNA in our publications of the 1970s. Note that the abbreviation DNA is the same in both Russian and English. For consistency with current nomenclature, we defer to the name dinitramide in this paper. Finally, the abbreviation DNA is used here with due respect for its more familiar meaning outside of the present field of rocket propulsion.

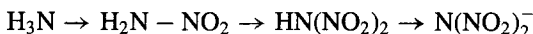
II. Methods for the Synthesis of Dinitramide and Its Salts

Methods for the synthesis of DNA salts may be divided into three groups, of which some are more complex than others. Principles of the synthesis of ADN salts developed by us in 1971–1975, with the largest part of this work published in 1994–1996, chiefly coincide with those put forward in American, Swedish, and Japanese publications and differ merely in the details. For this reason we will discuss these principles with reference to papers and patents best known to us. Briefly overviewed, the first category of reactions is characterized by that the organic N,N-dinitro derivative $\text{RN}(\text{NO}_2)_2$ is first synthesized. The R–N bond breaks in the course of further reaction, leading to the thermodynamically stable DNA anion:

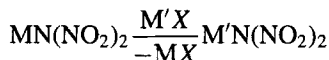


Methods of organic chemistry form in the basis of the generation of $\text{RN}(\text{NO}_2)_2$ compounds and their subsequent transformations. Therefore, these methods may be called organic in origin. The other two methods of synthesis are inorganic. Formally, the most feasible synthesis techniques of DNA salts are those based on direct

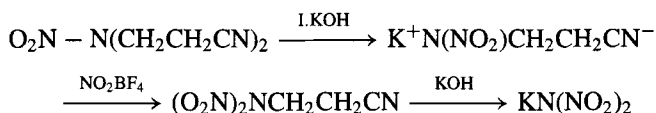
nitration of ammonia or nitramide followed by the reaction of DNA with bases:



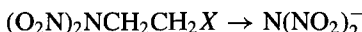
The third group consists of the reactions where already synthesized DNA and its salts are used as starting reagents:



As already mentioned, DNA salts, being inorganic compounds, historically were obtained by an organic method.⁶ An organic method was chosen as most reliable for DNA synthesis for two reasons. First, we took into account the instability of the potential precursor nitramide (H_2NNO_2) in base media, thus excluding its alkaline nitration, for instance, by tetranitromethane. Furthermore, there was a sound basis for assuming that DNA would be unstable in strongly acidic media, just as are primary nitramines and numerous primary nitramides. Therefore, we used the reaction of organic N,N-dinitramines with bases as the starting point in the first approach to the synthesis of DNA salts, that is, we formed the DNA anion in a basic medium and avoided the dinitramide formation step. As DNA-specific precursors, we selected, among others, compounds of the $(\text{NO}_2)_2\text{NCH}_2\text{CH}_2\text{X}$ type, where X was an electron-accepting group that activates the α -hydrogen atoms with respect to the attack by bases, and thus creates the anion center in the position β to the dinitramine fragment. We presumed that the most probable means of stabilizing such an anion center should be splitting off of the DNA anion, which is a low-energy process (due to charge delocalization). This presumption was then proven experimentally. DNA salts were obtained the first time through the following scheme:



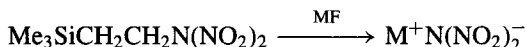
It is possible to employ ammonia, instead of inorganic bases, in the decyanoethylation step, thus yielding the ammonium salt of DNA directly. The preceding reaction, being a special case of the retro-Michael's reaction, is rather general to the series of $(\text{O}_2\text{N})_2\text{NCH}_2\text{CH}_2\text{X}$ compounds and may serve as a general synthesis technique for the DNA salts, not only with propionitrile but also with the analogous esters, aldehydes, and ketones⁷⁻⁹:



where



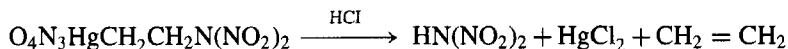
Note that in the United States, DNA salts were also synthesized by an organic method and a β -substituted alkyl-N,N-dinitramine (although the latter had a different structure, namely, 2-(trimethylsilylethyl)-N,N-dinitramine).^{2-5,7-10} The general strategy of formation of a carbanion and its stabilization through splitting off of the $\text{N}(\text{NO}_2)_2$ anion is similar to our approach:



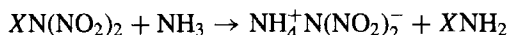
where



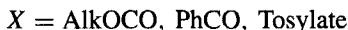
Transformation of β -Hg derivatives of alkyl-N,N-dinitramines is also chemically very similar to the latter reaction¹¹:



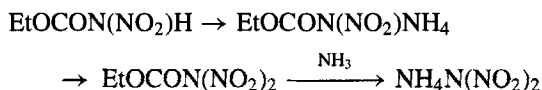
Another general method for the synthesis of DNA salts is the reaction of N,N-dinitramides with bases,^{10,12,13}



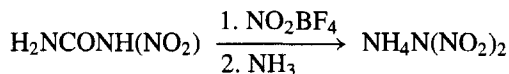
where



These reactions are analogous to the retro-Michael's reactions discussed earlier, with the only difference being that the anion center in the DNA anion precursors is formed in the β position to the dinitramine grouping on oxygen atoms of C=O or SO₂ groups, rather than on the carbon atom. N,N-dinitramides, which are used as intermediate reagents, are best obtained through nitration of corresponding nitramides by nitronium salts. They are highly labile compounds (especially N,N-dinitrobenzamide and N,N-dinitro-*n*-toluenesulfamide) and, therefore, should be handled at low temperatures of -65 to 75°C . N,N-dinitro derivatives of alkyl urethanes are more stable, although it is also advisable to handle them at temperatures of about -35 to 45°C . In a number of cases rather high yields ($\sim 60\%$) are achievable at -5°C . Three centers of the nucleophilic attack (amide nitrogen atom and oxygen atoms of the nitro groups) are available in the initial nitro urethane salt, and three centers of the nucleophilic attack (carbonyl group and nitro groups) are available in the intermediate dinitro urethane that lead to nitro urethane transformation to the DNA salt. This variety causes the process to depend on many factors (such as nitronium salt character, temperature, time, medium, reagent mixing technique, ratio of reagents, and nucleophilic reagent specifics). When all of these factors are considered, it is possible to synthesize DNA from nitro urethane in 75–85% yields:

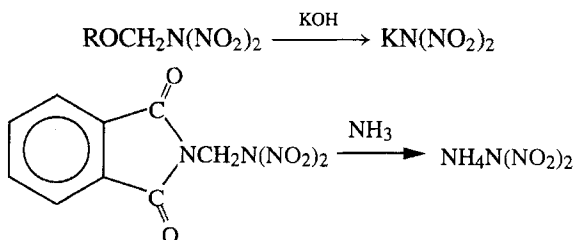


The reaction of nitro urea with nitronium tetrafluoroborate^{14,15}



resembles, at least outwardly, the preceding reactions for obtaining DNA salts by nitration of N-nitramide salts with nitronium salts. Nevertheless, these attempts in a similar fashion¹² failed to produce DNA salts from the potassium salts of N-nitro cyanamide and N-nitro urea, and the dipotassium salt of N-nitrocarbamic acid. Finally, we should mention that DNA salts can be synthesized from α derivatives of alkyl dinitramine having the atom with the unshared electron pair (oxygen or nitrogen atom) in the β position.¹⁶ This facilitates the N–C bond breakage through

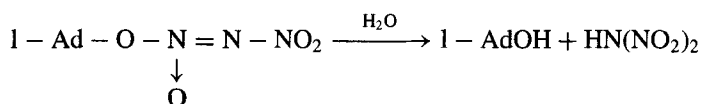
stabilization of the carbocation formed by this electron pair.



where

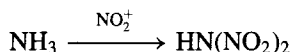


Hydrolysis of N-adamantyloxy-N'-nitrodiazene-N-oxide (Ref. 16) (1-Ad) represents a special organic reaction yielding DNA, but is so far only of theoretical interest:

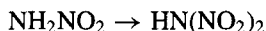


In contrast to these reactions, the starting reactant here contains the DNA fragment in the aci-form. The availability of the tertiary alkyl radical at the oxygen atom is likely to be necessary because analogous derivatives with primary and secondary radicals are reasonably stable in water, and so the reaction acquires another pathway in the alkaline medium.

Inorganic methods for producing DNA are less diverse than the organic. The most feasible and attractive technique is nitration of ammonia^{10,17,18}:

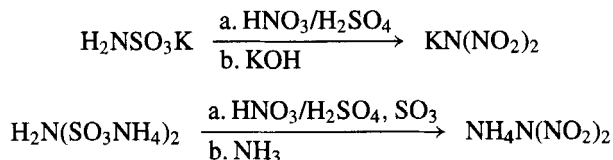


Unfortunately, the low DNA yields, the high cost of some nitrating agents, the low concentration of target substances in the salt mixtures formed, and the challenges of isolating and purifying the DNA salts obtained in this way currently prevent us from recommending this method as more fruitful than the others. Another inorganic method for synthesizing DNA salts involves nitramide nitration^{3,10,19}:



Both the possibility of synthesizing DNA in this manner and the yield depend dramatically on the characteristics of the nitrating agent, the medium, the temperature, and the reaction time.¹⁹ Nitration proceeds most smoothly when nitronium fluoro-sulfonate is employed as the nitrating agent and acetonitrile is the solvent. Under these conditions, nitramide can be transformed into DNA quantitatively in 5 min at 0–20°C. Acidic or neutral nitronium pyrosulfates may also be used as nitrating agents, but the reaction should be carried out in CH_2Cl_2 . This method provides a 27–50% yield of DNA. When mixtures of HNO_3 with organic acid anhydrides or N_2O_5 are used rather than nitronium salts, DNA is generated in trace amounts at best. About 80% yield of DNA is achievable by nitration of nitramide by sulfuric–nitric acid mixtures.²⁰ The same patent describes a technique for producing DNA

salts from the ammonia-sulfate derivatives $\text{H}_2\text{NSO}_3\text{H}$ and $\text{HN}(\text{SO}_3\text{H})_2$ with a standard set of nitrating agents²⁰:

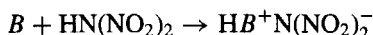


The patent cited here is novel because it also contains a pioneering DNA absorption-desorption purification technique.

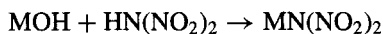
All of the described methods were utilized to synthesize chiefly ADN and potassium dinitramide (KDN). DNA and its salts act as bases when they are employed as starting reagents.^{21,22} Ionic salt exchange was the most frequently used option to produce other salts:



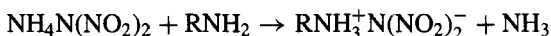
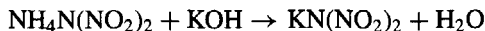
In laboratory practice it is convenient to use $\text{AgN}(\text{NO}_2)_2$ as the starting DNA salt and the M' halide or hydrochloride of the nitrogenous base. $\text{KN}(\text{NO}_2)_2$ also gives good results in a number of cases. The most feasible technique for synthesizing many stable salts with bases is neutralization of these bases B with DNA solutions^{10,21,22}:



Metal oxides or carbonates are equally applicable in place of the metal hydroxides:



Aqueous solutions with 7–10% $\text{HN}(\text{NO}_2)_2$ are easy and safe to prepare by passing a $\text{KN}(\text{NO}_2)_2$ solution in water through a column filled with cation-exchange resin in the H^+ form. Nonaqueous DNA solutions were prepared by passing gaseous dry HCl into a $\text{KN}(\text{NO}_2)_2$ suspension stirring in absolute ether, followed by evaporation of the excess HCl and ether at 0°C . This procedure, however, should be used only in the rarest of cases, due to the danger of explosion.²¹ To produce DNA with strong and nonvolatile bases, including organic, it is possible to employ ADN instead of DNA.

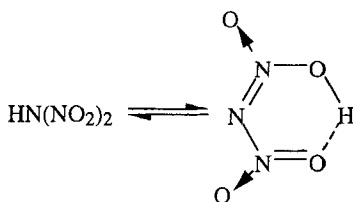


These methods were employed to synthesize DNA salts with mono- and divalent metals of the groups I, II, VII and VIII of the periodic table and several dozen DNA salts with ammonium bases, such as ammonia, hydrazine, hydroxylamine, formamidine, and their alkyl and amino derivatives.

III. Structure and Properties of Dinitramide and Its Salts

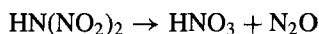
Depending on the method of synthesis and the medium, DNA can have three forms: one ionic and two covalent.²³ According to quantum chemistry²⁴ covalent DNA should predominantly have the N-H form, but in equilibrium with the

aci-form having an intramolecular hydrogen bond:



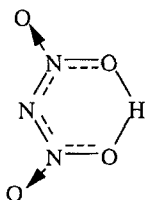
Experiments at least partially verify this result.²³ Indeed, after treatment of the K^+ salt of DNA suspension with excess HCl in nonpolar solvents, followed by removal of the excess HCl and solvent, a substance remains whose infrared (IR) spectrum has absorptions at 1255, 1625, and $3245\text{--}3295\text{ cm}^{-1}$ that are characteristic of alkyl- N,N -dinitramines ($1250, 1255, 1600\text{--}1615, 1640\text{--}1655\text{ cm}^{-1}$) and of N-H compounds. It transforms again to the DNA salt upon treatment with base. This served as the basis for assigning the structure to a true dinitramine form $\text{HN}(\text{NO}_2)_2$ (Ref. 24).

DNA in the individual state is a colorless, rather mobile, unstable liquid. When it is obtained in a few tenths of a gram, extensive decomposition accompanied by the generation of initially colorless and then grayish nitrogen oxides occurs promptly after solvent removal at 0°C . The key decomposition product is nitric acid,²¹



If a larger amount of free DNA is isolated, then decomposition ends with an explosion. On the other hand, DNA solutions in water or organic solvents can be kept for a long time. DNA is one of the strongest mineral acids ($\text{pK}_a = -5.62$), greatly exceeding in this respect nitric and sulfuric acids and being inferior only to several hydrogen halides and perchloric acid.²⁵

Another covalent form of DNA was detected from dichloroethane-extraction of water solutions generated by the reaction of 65% H_2SO_4 with $\text{KN}(\text{NO}_2)_2$ (Ref. 14). The extracted substance treated with KOH also yielded $\text{KN}(\text{NO}_2)_2$, although it had a UV spectrum ($\lambda_{\text{max}} = 243\text{--}250\text{ nm}$) and an IR spectrum ($1515, 1190\text{ cm}^{-1}$) different from true DNA ($\lambda_{\text{max}} = 223\text{ nm}$) and DNA salts ($\lambda_{\text{max}} = 285\text{ nm}$). The absence of absorption in the IR spectrum of this DNA form in the region of nitramines with electron-acceptor substituents ($1150\text{--}1650\text{ cm}^{-1}$) indicates that it is not the trivial aci-form. By analogy with the acetylacetone structure and with respect for some regularities in spectral characteristics, this DNA form was assigned a cyclic structure of the aci-form but with the proton equally bound to two oxygen atoms of separate nitro groups²³:



DNA salts of metal ions (with the exception of the mercury derivative) have the ionic structure. Each possesses characteristic absorptions in the IR spectrum (1520–1540, 1430, 1180–1210, 1010–1035 cm^{-1}) and UV spectrum [$\lambda_{\text{max}} = 223, 285$ (ϵ 5640 l mol^{-1}), shoulder 335 nm] (Refs. 10 and 22). Quantum chemical calculations for the free anion $\text{N}(\text{NO}_2)_2^-$ point to the structure with equal negative charge distribution between two nitro groups.²⁶ On dissolution, however, the initial anion structure distorts^{22,27} as a result of the low-energy barrier to rotation around the N–N bond.²⁷ The nature of counter ion strongly influences the anion structure in the crystal lattice and, hence, the distribution of the negative charge. Judging from bond lengths and angles, the negative charge in the crystalline ammonium and hydrazinium salts of DNA is delocalized over the two conjugated nitro groups, whereas in the K^+ salt it is chiefly concentrated on one of the NO_2 groups.²⁵

The counter ion greatly affects not only the anion structure but also the properties and the very possibility of synthesis. As mentioned earlier, DNA forms salts with mono- and divalent metals of the I, II, VII, and VIII groups. They normally represent crystalline substances stable at ambient temperature with rather low melting (50–130°C) and decomposition (60–160°C) points. Attempts to obtain individual DNA salts with Cu^{I} , Al^{III} , Cr^{III} , and Fe^{III} failed, apparently due to their low thermal stability. DNA salts are normally readily soluble in water, alcohols, acetonitrile, and other polar solvents.²¹

A special place in the series of DNA metal derivatives (as well as in the series of metal derivatives of polynitro alkyl compounds) is occupied by the mercury derivative. This compound is covalent in the crystal state and nonpolar solvents and, according to the UV spectrum ($\lambda_{\text{max}} = 250$ and 217 nm), IR spectrum (1610, 1530, 1285, and 1220 cm^{-1}), and Raman spectrum (1590–1620, 1518–1438, and 1214–1220 cm^{-1}), the mercury atom is bound to oxygen atoms.²⁸ The mercury derivative has the dissociated ionic structure (UV spectrum: $\lambda_{\text{max}} = 285$ nm) in dilute aqueous solutions. DNA yielded stable salts with most of the nitrogenous bases studied, including ammonia; hydrazine; hydroxylamine; primary, secondary, and tertiary amines; quaternary aliphatic bases; various aromatic and heterocyclic amines; amidines; guanidines; and aromatic diazo compounds.²² Like the salts of metal ions, as a rule they are also colorless crystalline substances with low melting (15–150°C) and decomposition points. Salts of primary aliphatic amines decompose at 120–140°C. The highest melting and decomposition points (175–228°C) are specific to the quaternary ammonium and hydrazonium salts. Alternatively, salts with weak bases (urea, double salts with methylene diamine and hydrazine, aminotetrazole, and diaminofurazan) could not be synthesized in the pure state due to their instability. Ammonium salts of DNA dissolve readily in water and polar solvents. Some salts are highly hygroscopic whereas others are not. The mechanical impact sensitivity of these salts varies over a wide range, from insensitive to rather dangerous to handle. The latter category primarily consists of the hydrazine and triaminoguanidine salts.²²

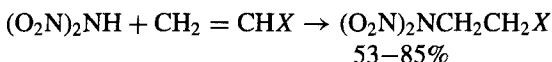
ADN, which is most important for practical use, occupies a somewhat bothersome position with respect to safety. Its melting point is 92–94°C, density is 1.83–1.84 g/cm^3 (Refs. 25 and 29), and decomposition onset temperature is $\sim 135^\circ\text{C}$. However, ADN is rather sensitive to impact and in this sense is a typical secondary explosive. Therefore, it should be handled with a high degree of caution, particularly in the presence of organic solvents having high salt concentration.

IV. Chemical Properties of DNA and Its Salts

We have already discussed the most practically significant reactions of DNA and its salts. These are the reaction of DNA with bases resulting in DNA salts, reaction of DNA salts with acids producing DNA, and reactions with salts and bases leading to cation substitution in the starting DNA salt. Reactions of free DNA were investigated with diazomethane and with olefins having an activated multiple bond. Diazomethane reacts readily with DNA in ether solution to produce the N-methylation product with a 30% yield¹⁶:



The reaction of DNA with activated olefins was explored in more detail. It was found that DNA, like strong acids, easily adds in rather high yield without catalysts to unsaturated carbonyl derivatives (acrolein, vinylmethyl ketone and vinylphenyl ketone) and forms carbonyl-substituted N,N-dinitramines⁷:



where



Additions of DNA to methylacrylate or acrylonitrile, however, have not been achieved, either with or without base catalysts.

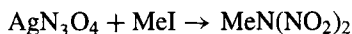
Reactions of DNA salts were studied more systematically than pure DNA. An ability to form hydrates is intrinsic to many salts.²¹ Highly stable hydrates were obtained with copper (II), manganese (II), iron (II), cobalt (II), and nickel (II) salts of DNA. A portion of the water of crystallization remains even after long-term vacuum drying over P_2O_5 . These conditions, however, make it possible to obtain the lithium salt in the water-free state. The ability to complex is generally characteristic of DNA salts, and it should be taken into account even when carrying out reactions in common solvents. The Na^+ salt of DNA, for example, was found to form a stable complex with dioxane, and AgN_3O_4 does the same with acetonitrile (Ref. 21). The formation of complex Ag^+ , Cu^{II} , Ni^{II} , or Hg^{II} salts of DNA with N-donor ligands, namely, ammonia, pyridine, morpholine, and aniline, causes no particular difficulties.^{11,21} Using $\text{Hg}(\text{N}_3\text{O}_4)_2$ as an example, we demonstrated the possibility of introducing trimethylphosphine and dimethylsulfide into such reactions. It is interesting that the mercury–dinitramide bond changes from covalent to ionic on the formation of $\text{Hg}(\text{N}_3\text{O}_4)_2$ complexes with aniline, pyridine, triphenylphosphine, and dimethylsulfide. Yet, while complexing with a weaker donor ligand, for example, diethylmalonate, the character of the bond is not altered.¹¹

A more intricate complex is worth mentioning,³⁰ which features a bond between the metal of a coordination complex and the central nitrogen atom of DNA:

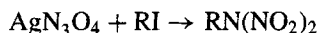


There are several reasons why alkylation stands among the best-understood reactions of DNA salts. The necessity arose for proving the relative positions of

heteroatoms in the DNA anion. For this purpose, and to produce methyl-N,N-dinitramine, which was a known compound at the time, AgN_3O_4 was reacted with methyl iodide. This result showed that the two nitro groups were bound to the nitrogen central atom in anion⁶:



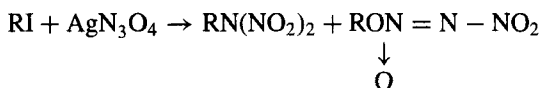
The use of substituted alkyl halides in this reaction made it possible to form previously unknown alkyl-N,N-dinitramine derivatives (ADA). The reaction was of even greater interest for paving the way to a new class of compounds, namely, the N-alkoxy-N'-nitroindazen-N-oxides (ANDO), which were unknown and potentially have high-energy content. The possibility of carrying out alkylation and controlling its direction proved to depend considerably on the DNA salt cation and alkyl halide.¹⁶ AgN_3O_4 reacts with methyl- or allyl iodide yielding respective alkyl-N,N-dinitramines with 16–50% yield:



where



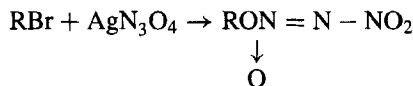
A mixture of ADA and ANDO is formed when EtI and $i\text{-PrI}$ are used, with ADA prevailing in the case of EtI and ADNO in that of $i\text{-PrI}$:



where



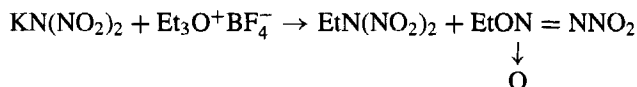
If $i\text{-PrBr}$ and 1-AdBr are used in the reaction, O-alkylation products merely result according to the IR spectrum: $\nu(\text{NO}_2)$ 1620, 1290–1295 cm^{-1} ; $\nu[\text{ON}(\text{O})=\text{N}]$ 1550–1555, 1220–1235 cm^{-1} :



where



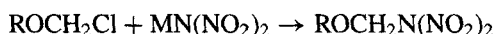
$\text{KN}(\text{NO}_2)_2$ does not react with MeI because of the low nucleophilicity of the DNA anion. This barrier can be overcome by using more activated alkylating agents. For example, $\text{KN}(\text{NO}_2)_2$ reacts vigorously with triethyloxonium tetrafluoroborate, resulting in the mixture of N- and O-alkylation products, the former prevailing¹⁶:



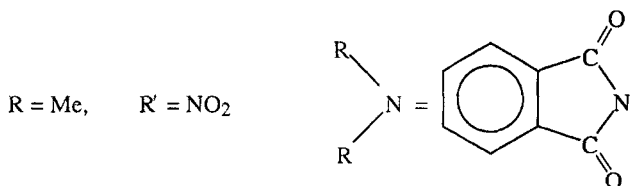
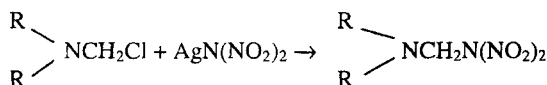
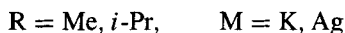
The generation of the N-alkylation product was observed in the reaction of $\text{CsN}(\text{NO}_2)_2$ with methyl triflate as well¹⁰:



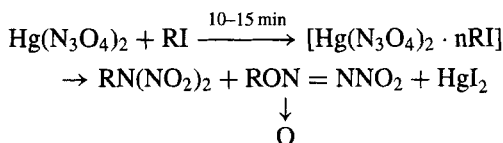
Chloroalkyls react with DNA salts when the atom with the unshared electron pair (oxygen or nitrogen) is in the α position to the halogen atom. The most active derivatives of this type also react with $\text{KN}(\text{NO}_2)_2$. Only N-alkylation products were achievable in all of the mentioned cases.¹⁶



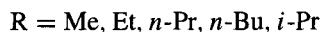
where



Exciting results were obtained in the alkylation of $\text{Hg}(\text{N}_3\text{O}_4)_2$ by alkyl iodides.¹¹ Mixing of these reagents in ether led to the formation of solid or liquid insoluble adducts, which transformed to red HgI_2 and a mixture of N- and O-alkylation products in 10–15 min:



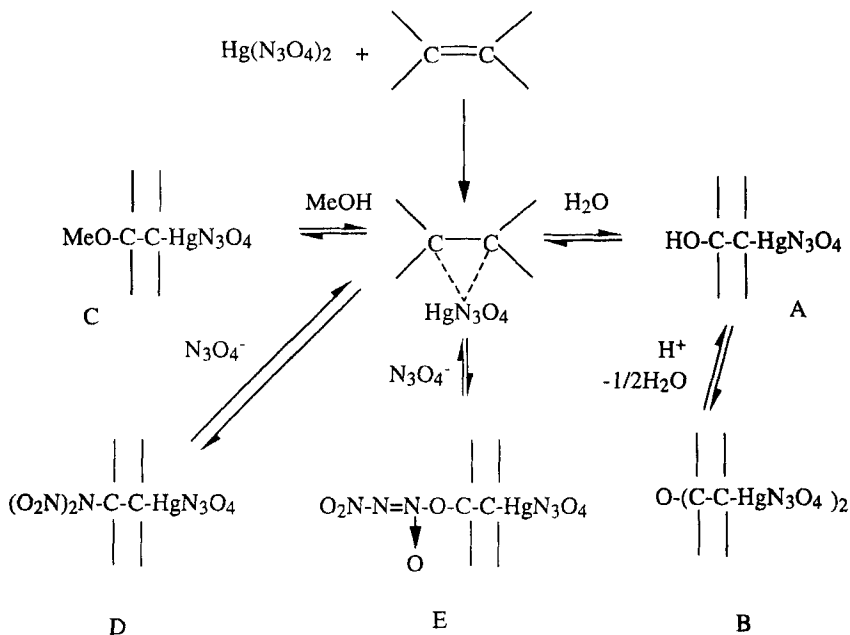
where



Hence, the interaction of alkylating agents with DNA and its salts may result in N- (ADA) and O- (ANDO) alkylation products or their mixture. The DNA anion reveals dual reactivity in these reactions. ADA and ANDO are oillike substances having low stability.

$\text{Hg}(\text{N}_3\text{O}_4)_2$ has rich synthetic potential. In addition to the preceding alkylation and complexing reactions, it readily mercurates aromatic compounds and compounds with mobile hydrogen atoms yielding mercury derivatives of aromatic and aliphatic compounds containing the dinitramide fragment.¹¹ A rather complicated system of consecutive and parallel processes is observed in the reaction of

$\text{Hg}(\text{N}_3\text{O}_4)_2$ with olefins. These processes result in A-, B-, C-, D-, or E-type compounds, depending on the nature of the olefin and medium used.¹¹ The following scheme gives a general picture:



V. Conclusions

DNA salts are important practically as high-performance components for highly energetic formulations, and are theoretically interesting as a new nitrogen–oxygen system. Moreover, they are promising as new reagents that expand opportunities to synthesize previously unknown classes of organic and inorganic substances. The research efforts discussed show that organic and inorganic methods for producing DNA salts, structure of DNA and its salts, and their key physicochemical properties and chemical reactivities have been thus far appropriately and systematically investigated. Yet the practical usability of DNA salts is still evolving, with a view toward cost effectiveness and production safety in the synthesis of DNA salts; the isolation and purification techniques; and the creation of new, efficient, ecologically safe, high-energy formulations in rocket engineering.

References

- ¹Luk'yanov, O. A., Gorelik, V. P., and Tartakovsky, V. A., "Dinitramide and Its Salts. 1. Synthesis of Dinitramide Salts by Decyanoethylation Reaction of N,N-Dinitro- β -Aminopropionitrile," *Russian Chemical Bulletin*, Vol. 43, 1994, pp. 89–92.
- ²Pak, Z. P., "Some Ways to Higher Environmental Safety of Solid Rocket Propellant Application," AIAA Paper 93-1755, 1993.

³Bottaro, J. C., Schmitt, R. J., Penwell, P. E., and Ross, D. S., "Dinitramide Salts and Method of Making Same," *PCT International Application*, WO 91/19669. U.S. Application. 540020, CA, Vol. 116, pp. 217513.

⁴Bormann, S., "Advanced Energetic Materials Emerge for Military and Space Applications," *Chemical and Engineering News*, 1994, Jan. 17, pp. 18–22.

⁵Bottaro, J. C., "Recent Advances in Explosives and Solid Propellants," *Chemistry and Industry*, No. 7, 1 April 1996, pp. 249–252.

⁶Highsmith, T. K., McLeod, C., Wardle, R. B., Schmitt, R., Bottaro, J., Penwell, P., Bomberger, D., and Brough, J., "ADN Manufacturing Technology," *29th International Annual Conference of the ICT (Energetic Materials)*, Vol. 20, 1998, pp. 1–14.

⁷Luk'yanov, O. A., Konnova, Y. V., Klimova, T. A., and Tartakovsky, V. A., "Dinitramide and Its Salts. 2. Dinitramide in Direct and Reverse Michael-Type Reactions," *Russian Chemical Bulletin*, Vol. 43, No. 7, 1994, pp. 1200–1202.

⁸Chung, K.-H., and Sim, H.-H., "A Study on the Synthesis of Dinitramide Salts," *Kongop Hwahak*, Vol. 9, No. 1, 1998, pp. 155–157. C.A., Vol. 129, p. 110952.

⁹Chung, K.-H., and Sim, H.-H., "Study on the Synthesis of Ammonium Dinitramide," *Journal of the Korean Chemistry Society*, Vol. 41, No. 12, 1997, pp. 661–665. C.A., Vol. 128, p. 104058.

¹⁰Bottaro, J. C., Penwell, P. E., and Schmitt, R. J., "1,1,3,3-Tetraoxo-1,2,3-Triazapropene Anion, a New Oxy Anion of Nitrogen: The Dinitramide Anion and Its Salts," *Journal of the American Chemical Society*, Vol. 119, No. 40, 1997, pp. 9405–9410.

¹¹Luk'yanov, O. A., Anikin, O. V., and Tartakovsky, V. A., "Dinitramide and Its Salts. 9. Mercury (II) Dinitramide, New Reagent in the Chemistry of the Organomercury Compounds," *Russian Chemical Bulletin*, Vol. 45, No. 2, 1996, pp. 433–440.

¹²Luk'yanov, O. A., Kozlova, I. K., Shitov, O. P., Konnova, Y. V., Kalinina, I. V., and Tartakovsky, V. A., "Dinitramide and Its Salts. 10. Synthesis of Dinitramide Salts from N,N-Dinitroderivatives of Organic Amides," *Russian Chemical Bulletin*, Vol. 45, No. 4, 1996, pp. 863–867.

¹³Schmitt, R. J., Bottaro, J. C., Penwell, P. E., and Bomberger, D. C., "Manufacture of Dinitramide Salts or Acid as an Oxidizer for Solid Propellant," *PCT International Application*, WO 93/160021, U.S. Application, 827,247. C.A. Vol. 120, pp. 11330c.

¹⁴Suzuki, S., Myazaki, S., Hatano, H., Shiino, K., and Onda, T., "Manufacture of Ammonium Dinitramide (ADN) Useful as Oxidizing Agent," *Japan Kokai Tokkyo Koho*, JP 08325005 A2 961210 *Heisei*, C.A., Vol. 126, pp. 159395.

¹⁵Hatano, H., Onda, T., Shino, K., Miyazaki, S., and Matsuura, S., "New Synthetic Method and Properties of Ammonium Dinitramide," *Kayaku Gakkaishi*, Vol. 57, No. 4, 1996, pp. 160–165. C.A., Vol. 125, pp. 225920z.

¹⁶Luk'yanov, O. A., Shlykova, N. I., and Tartakovsky, V. A., "Dinitramide and Its Salts. 7. Alkylation of Dinitramide and Its Salts," *Russian Chemical Bulletin*, Vol. 43, No. 10, 1994, pp. 1680–1683.

¹⁷Schmitt, R. J., Bottaro, J. C., Penwell, P. E., and Bomberger, D. C., "Manufacture of Ammonium Dinitramide Salt for Rocket Propellant," U.S. Patent 5,316,749. C.A. Vol. 121, pp. 60802g.

¹⁸French, C., Janitschek, W., and Weisweiler, W., "The Reaction of Ammonia with Dinitrogen Pentoxide," *29th International Annual Conference of the ICT (Energetic Materials)*, 1998, pp. 50.1–50.12.

¹⁹Luk'yanov, O. A., Shvedova, S. N., Shepelev, E. V., Varfolomeeva, O. N., Malkina, N. N., and Tartakovsky, V. A., "Dinitramide and Its Salts. 11. Synthesis of Dinitramide by

Nitration of Nitramide with Nitryl Salts," *Russian Chemical Bulletin*, Vol. 45, No. 6, 1996, pp. 1497–1498.

²⁰Langlet, A., Oestmark, H., and Wingborg, N., "Manufacture of Dinitramidic Acid and Its Salts for Solid Propellants," *PCT International Application*, WO 9706099 A 1970220. C.A., Vol. 126, pp. 227269.

²¹Luk'yanov, O. A., Anikin, O. V., Gorelik, V. P., and Tartakovsky, V. A., "Dinitramide and Its Salts. 3. Metallic Salts of Dinitramide," *Russian Chemical Bulletin*, Vol. 43, No. 9, 1994, pp. 1457–1461.

²²Luk'yanov, O. A., Agevnin, A. R., Leichenko, A. A., Seregina, N. M., and Tartakovsky, V. A., "Dinitramide and Its Salts. 6. Dinitramide Salts Derived from Ammonium Bases," *Russian Chemical Bulletin*, Vol. 44, No. 1, 1995, pp. 108–112.

²³Shlyapochnikov, V. A., Cherskaya, N. O., Luk'yanov, O. A., Gorelik, V. P., and Tartakovsky, V. A., "Dinitramide and Its Salts. 4. Molecular Structure of Dinitramide," *Russian Chemical Bulletin*, Vol. 43, No. 9, 1994, pp. 1522–1525.

²⁴Polizer, P., and Seminario, J. M., "Computational Study of the Structure of Dinitraminic Acid, $\text{HN}(\text{NO}_2)_2$, and the Energetics of Some Possible Decomposition Steps," *Chemical Physics Letters*, Vol. 216, No. 3–6, 1993, pp. 348–352.

²⁵Gidaspov, B. V., Tselinskii, I. V., Mel'nikov, V. V., Margolis, N. V., and Grigor'eva, N. V., "Crystal and Molecular Structure and Acid-Base Properties of Dinitramide Salts," *Zhurnal Obshchei Khimii*, Vol. 65, 1995, pp. 995–1002.

²⁶Michels, H. H., and Montgomery, J. A., "On the Structure and Thermochemistry of Hydrogen Dinitramide," *Journal of Physical Chemistry*, Vol. 97, No. 25, 1993, pp. 6602–6608.

²⁷Christe, K. O., Wilson, W. W., Petrie, M. A., Michels, H. H., Bottaro, J. C., and Gilardi, R., "The Dinitramide Anion, $\text{N}(\text{NO}_2)_2^-$," *Inorganic Chemistry*, Vol. 35, No. 17, 1996, pp. 5068–5071.

²⁸Shlyapochnikov, V. A., Cherskaya, N. O., Luk'yanov, O. A., Anikin, O. V., and Tartakovsky, V. A., "Dinitramide and Its Salts. 8. Synthesis, Spectra, and the Structure of Mercury (II) Dinitramide," *Russian Chemical Bulletin*, Vol. 45, No. 2, 1996, pp. 430–432.

²⁹Gilardi, R., Flippen-Anderson, J., George, C., and Buther, R. J., "A New Class of Flexible Energetic Salts: The Crystal Structures of the Ammonium, Lithium, Potassium, and Cesium Salts of Dinitramide," *Journal of the American Chemical Society*, Vol. 119, 1997, pp. 9411–9416.

³⁰Trammell, S., Goodson, P. A., and Sullivan, B. P., "Coordination Chemistry and Photo-reactivity of the Dinitramide Ion," *Inorganic Chemistry*, Vol. 35, No. 6, 1996, pp. 1421–1422.

Chapter 1.9

Hazards Associated with Solid Propellants

T. L. Boggs,* A. I. Atwood,[†] and A. J. Lindfors,[‡]

Naval Air Warfare Center Weapons Division, China Lake, California

E. J. Mulder[§]

*John Hopkins University/Chemical Propulsion Information Agency,
Columbia, Maryland*

and

R. W. Pritchard[¶]

Naval Air Warfare Center Weapons Division, China Lake, California

I. Introduction

SOLID propellants obviously contain significant stored potential energy. If that energy is inadvertently released, whether by inadvertent combustion, explosion, or detonation, significant loss of life and property may occur. The Appendix is a compilation of incidents involving energetic materials. Table A1 shows the tremendous costs associated with incidents.

Hazard of solid propellants is not a new topic: Humans have been concerned with hazards of energetic materials almost with the advent of the earliest gun powders. Indeed the authors, and many others, have published several lengthy works on this topic (for example, see Refs. 1–5). In this chapter we are concerned with the hazards associated with propellants having hazard class 1.1 (mass detonating) and 1.3 (mass fire). Whereas the primary threat to 1.1 propellants is detonation caused by mechanical shock and propagation to adjacent rounds, the major hazard of 1.3 propellants is inadvertent ignition, flame spread, and combustion, occasionally with explosion. Many of the injuries and fatalities associated with solid propellants are due to fire that propagates so fast that people cannot escape. The insensitive munitions (IM) programs have reduced severity of reaction (in some

This material is declared a work of the U.S. Government and is not subject to copyright protection in the United States.

*Head, Engineering Sciences Division, Research Department.

[†]Physical Scientist, Engineering Sciences Division, Research Department.

[‡]Materials Engineer, Engineering Sciences Division, Research Department.

[§]Senior Research Analyst, (dept).

[¶]Supervisor, Product Quality Laboratory, Weapons/Targets Department.

cases from detonation and violent explosions down to burning) and have increased the time for the ship crew to mitigate reactions. However, fire, while passing the IM requirements, remains a major concern. Historically many ships have been lost to fire, often after surviving the blast and fragments from the warhead. The U.S. Navy has lost more ships due to fire than due to blast. Therefore, part of the motivation for presenting this work is to show that a 1.3 hazard classification propellant is neither totally safe nor without hazard.

When considering safety and hazards the following equation must be considered:

$$\text{sample} + \text{stimulus} (i) + \text{environment} \longrightarrow \text{response}$$

Many fields of science and technology make use of this logic: control the sample, stimuli, and environment; change one variable at a time; determine the change in response. Unfortunately, in hazards work, an undesired response occurs, such as fire, explosion, detonation, and one must infer the conditions of sample, stimuli, and environment that produced that response. It is not easy, and often impossible, to discern the causative factor(s), especially if the event destroyed much of the evidence. The problem is made worse if there was loss of life and equipment resulting in litigation and secrecy. If this is not bad enough, it is compounded by the probabilistic nature of hazards where the occurrence of once in a hundred may be a severe risk, but once in a million is frequently felt to be acceptable risk, depending on severity of the accident. Because weapons are expensive, the tendency is to test as few of as possible. This may give a false sense of security because of the probabilistic nature of the hazard response as discussed in Ref. 1.

The following discussions primarily concentrate on the sample, that is, the propellant considerations. However, sight should not be lost of the importance of stimuli and environmental considerations; they are very important.

II. Hazard Classification

Several documents describe the hazard classification of propellants (Refs. 6 and 7, for example). Propellants usually fall within class 1, explosive materials, and usually are either class 1.1 (mass explosion) or 1.3 (mass fire minor blast or fragment). Propellants and explosives are classified primarily for 1) transportation, to protect the public when items are shipped by rail and/or over public highways, and 2) storage, primarily for siting facilities to determine quantity-distance relationships to minimize the level of violence and spread of reaction. Hazard classification is not necessarily a measure of vulnerability or lethality.

The test that usually determines whether a propellant is hazard class 1.1 or 1.3 is a card-gap test. The U.S. standard test for interim hazard classification of propellants is shown in Fig. 1 and consists of the sample contained in a 1.44-in.-diam steel tube. The donor charge is separated from the sample by poly methyl methacrylate (PMMA) cards. Originally the test used playing cards, hence, the term cards. At the other end of the tube is a steel witness plate. A clean hole punched in the witness plate was taken as evidence of a detonation. The standard that has been used in the past has been 70 cards (0.7 in.) of PMMA to differentiate between 1.1 and 1.3. If a hole was punched in the witness plate with a gap of 70 cards or greater, then the sample was considered to be 1.1. If no hole was punched at gaps of 70 cards or less, then the sample was considered to be 1.3. [Note that the latest version of TB-700B/NAVSEA 8020.8B (Ref. 7) requires a zero card configuration and 1.44-, 2.875-, and 8-in.-diam gap tests.] Whereas

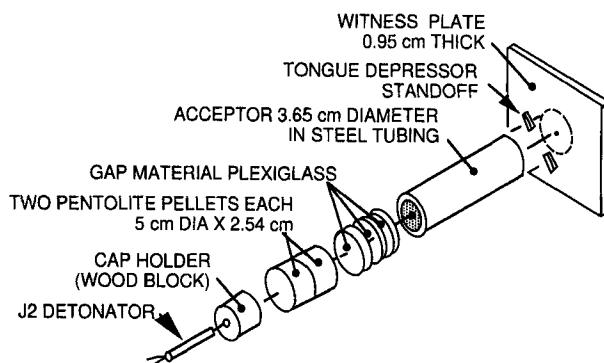


Fig. 1 Standard Naval Ordnance Laboratory gap test.

explosives usually were 1.1, the propellants based on ammonium perchlorate (AP), both metalized and reduced smoke formulations, had no problem passing the card-gap test, even at zero cards because of the large critical diameter (see subsequent discussion) of these formulations. As explosives have become less sensitive, that is, their critical diameters have increased, larger scale (up to 8 in.) gap tests have been used. As will be discussed, the critical diameters of some propellants, primarily high-energy, high-performance propellants, have become modest or small.

What is the relation between the card-gap test, cards, and hazards? As just noted, the card-gap test is used to rank the detonability of propellants and explosives, primarily for storage and handling considerations. Large card gaps indicate higher sensitivity. However, classification for storage and handling almost always assumes the worst case, in which a sufficiently strong mechanical shock stimulus is available. Fortunately for most propellants and explosives, a very high level of mechanical shock (tens of kilobars or greater) is required to initiate detonation. The card-gap test with 70 cards delivers about 70 kbar to the sample. Zero card gap results in approximately 200-kbar input to the sample. The likelihood of a propellant or explosive actually seeing shock levels of this magnitude during manufacturing, shipping, and handling is remote.

III. Critical Diameter/Shock Sensitivity

Although the card-gap test is useful for ranking the sensitivity of explosives, it may give a false sense of security when applied to propellants. This is largely due to critical diameter considerations. The critical diameter is the diameter of the sample that must be shocked at sufficient magnitude for a stable detonation to propagate through the material. If the sample size is bigger than the critical diameter, then a detonation can propagate. If the sample diameter is less than the critical diameter, then the detonation will lose energy and fail to propagate. The critical diameter is affected by confinement; the critical diameter for a heavily confined sample is about one-half that of an unconfined sample. Propellants based on ammonium perchlorate (AP) tend to have large critical diameters that are many times larger than the standard gap test. When tested in the gap test, they do not detonate even at zero cards. This only indicates that they have a larger critical diameter than the test device. However, it does not mean that they are nondetonable.

Almost all propellants are detonable given a large enough sized sample and large enough booster. Tests are, therefore, needed on samples in a size larger than their critical diameter, if practical. This obviously necessitates testing to determine the critical diameter (or at least that the critical diameter is larger than some value of concern). In the past, the critical diameter of the energetic material was determined, and then samples having diameter greater than the critical diameter were tested. This worked well for explosives and double-base propellants that had relatively small critical diameters, but was more difficult for AP-based propellants. The AP-based propellants had large critical diameters, often larger than the tactical motor diameter, so why bother testing for critical diameter? Why bother testing these propellants in the gap test at all?

As the need for performance increased, high-energy ingredients like cyclo-trimethylenetrinitramine (RDX) and cyclotetramethylenetetranitramine (HMX) were added to the AP-based propellants. The addition of nitramines decreased the critical diameter of the propellants. An interesting "game" ensued. Formulators added HMX until they failed the card-gap test, and then decrease the HMX loading until they passed the card-gap test. However, were these propellants truly 1.3? The answer is technically yes, but if they were loaded into a large tactical motor, the motor was often detonable. Some of these gamed propellants also showed interesting nonideal detonation behavior as will be discussed.

There are many ways of testing for critical diameter/critical dimension. One method is to test various sized cylinders and determine which diameters support a detonation and which do not. This may be a costly trial and error method. In an effort to short cut this process, Gibson⁸ developed a tapered wedge technique, as shown in Fig. 2. Graham,⁹ using this technique, studied some of the gamed 1.3 propellants and found the interesting results shown in Fig. 2. He tested 36-, 24-, and 16-in.-long tapered wedges. The 36-in.-long wedge was overdriven with the detonation wave traveling at $8.8 \text{ mm}/\mu\text{s}$. The wave velocity diminished to $2.2 \text{ mm}/\mu\text{s}$ at the 18-in. distance (distance measured from the tip back into the wedge). From 18 to 4 in., the wave traveled at a constant velocity of $2.2 \text{ mm}/\mu\text{s}$ (above sonic speed of $2.05 \text{ mm}/\mu\text{s}$ for this propellant), until it diminished in strength insufficient for the crush gauge to record. This corresponded to an apparent critical dimension of approximately 1 in. When the 24-in. wedge was tested, similar results were seen. The overdriven wave decreased to a velocity of $2.6 \text{ mm}/\mu\text{s}$ (above sonic) and ran at constant velocity from the 18-in. length to the 5-in. length, where again there was insufficient strength to crush the gauge. This corresponded to a critical dimension of 1.1 in. The results for the 16-in. test showed a shock wave of $1.6 \text{ mm}/\mu\text{s}$ running to a critical dimension of 1.26 in. Whereas the reactions for the first two tests were running at velocities barely above sonic, they were more akin to detonations (crushed gauges and removed and flowed metal witness plate)

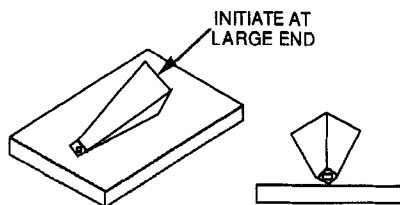


Fig. 2a Critical dimension test.

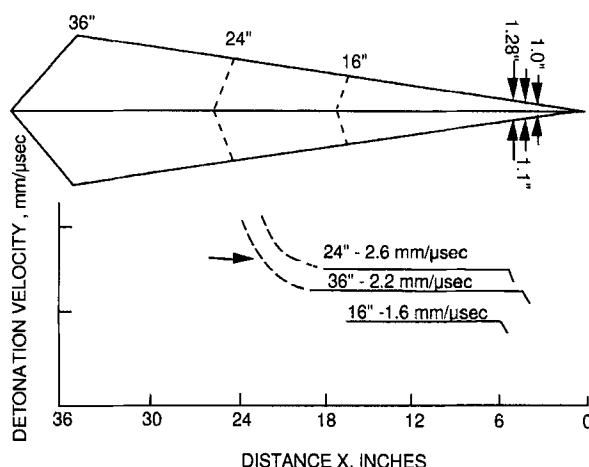


Fig. 2b Test results of high-energy 1.3 propellants.

than to explosions. Obviously these propellants, even though technically 1.3, when loaded into a large diameter motor produced a motor capable of extremely violent reaction.

Before leaving the discussion of response to mechanical shock, the role of damage needs discussion. Work performed that is described in Refs. 9 and 10 showed a marked increase in shock sensitivity of 1.1 propellants that had been slightly damaged (a few void percent), as seen in Fig. 3. Not only was the shock required to initiate the detonation decreased by a factor of 2, but the critical diameter decreased as well. Whereas Graham⁹ and Boggs et al.¹⁰ studied samples that had been previously damaged and then tested, Sandusky did shock experiments on freshly damaged propellant and also found increased sensitivity.

Lindfors performed one-dimensional shock experiments on a 1.3 propellant (88% solids). The material was strained to 5, 10, and 15% resulting in void volumes of 0.2, 0.5, and 1.7%, respectively. The onset of reactivity (shock pressure) was subsequently determined for each void volume, including the pristine material.

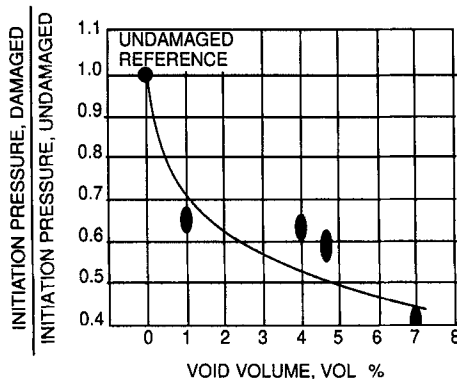


Fig. 3 Effect of damage on shock sensitivity of 1.1 propellant.

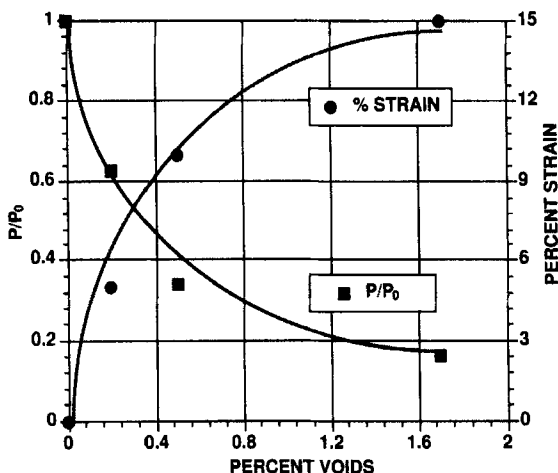


Fig. 4 Normalized reactivity pressure and percent strain with respect to void volume.

The pressure required to induce reactivity was then normalized to the pressure for reactivity in the pristine material. Both normalized pressure and strain are plotted with respect to void volume in Fig. 4.

Figure 4, shows that small strains induce relatively small void volumes in the material, which in turn leads to a drastic reduction in the pressure required to induce reactivity, that is, a 15% strain yields a 1.7% void volume, which reduces the pressure required by a factor of 6.

Though the reactivity measured may not be a classical detonation, it was indeed a steady-state, high-pressure, reactive front. Thus, small amounts of damage may lead to disastrous consequences in a large rocket motor handling accident.

IV. Bore Effect

Propellants often have a center perforation or bore that can have a significant effect depending on whether the propellant was mechanically shocked along or transverse to its bore. Mechanical shock along the axis of the bore can have markedly different effects. Tests were performed in which a solid cylinder of propellant was mechanically shocked. The response was relatively mild. However, when a same diameter cylinder, except with a cylindrical perforation the length of the cylinder, of that same propellant was shocked at the same level, extremely violent reactions occurred. Some of the Project SOPHY (Ref. 11) test results showed a similar bore effect.

Impacts transverse to the bore have been studied by Finnegan in burn to violent reaction tests. Finnegan and coworkers investigated phenomena in an idealized one-dimensional geometry. They fired fragments at a target consisting of metal cover to simulate the motor case, slab of propellant, air gap, propellant, and metal. They found that as the projectile penetrated the first slab of propellant it damaged the propellant, and a debris cloud moved across the air gap. When this debris cloud impacted the second propellant slab, it usually ignited and, depending on the gap and the propellant material, would either burn vigorously or detonate. Finnegan

found that there were three regimes of detonation reaction depending on the bore spacing: one region of prompt, shock-induced reaction and two regions of delayed (50+ ms after debris cloud impacted second surface) reaction. From these studies Finnegan concluded that 1) some confinement (albeit very slight) was necessary to achieve these delayed detonations; 2) the second surface did not have to be live, it could be inert and still cause the delayed detonation; and 3) the reaction required the live debris cloud from the first slab, a second surface that could be inert, and the projectile. Tests with a hole on the second side, so that the debris cloud ahead of the projectile and the projectile, would pass through the hole and not impact the second side, resulted in no delayed detonations. In addition, Finnegan performed a limited number of tests where the second side was either concave or convex.

Finnegan's test is of interest because it mimics responses of ordnance items to bullet and fragment impact. Those items that detonate in the large-scale test also detonate in Finnegan's test, whereas those that violently burn in the large-scale tests also did so in Finnegan's test. When Nouguez et al.¹² fired a bullet through the propellant web, it caused no detonation, whereas when a similar bullet at the same velocity went through the bore, it caused detonation. These phenomena have been incorporated into the bullet/fragment impact hazard assessment protocol.^{3,13,14}

V. Delayed Detonation (XDT)

Finnegan's work and that of Nouguez et al.¹² showed evidence of delayed detonation. Other studies, including some shock input tests (NOL card-gap tests), some impact (shotgun, projectile impact, and multiple impact) initiation tests and piston-driven compaction tests have also shown delayed detonation (XDT). It is called delayed detonation because the resultant detonation occurs at a time later than the normal transit time of the shock through the material. These reactions not only occur at times longer than associated with prompt shock to detonation, but of more significance to hazards and safety, they occur at lower stimuli (as much as 50% lower impact velocity thresholds and an increased number of cards in the card-gap test) and they typically are more violent than corresponding prompt shock to detonation transitions. These effects are shown in Figs. 5 and 6. Other studies have also shown that the velocity threshold required for XDT as being much lower than that required for prompt shock-to-detonation transition (SDT). Also tests in France showed the output pressure of XDT as always greater than that of SDT (generally 30% or more). (It has been suspected that XDT-type reactions have been involved in some large-scale mishaps. In these instances, large rocket motors burst, expelling propellant from the motor and causing it to impact on the adjacent test cell components/walls. Although the impact levels were thought not high enough to cause prompt shock to detonation, it is likely that XDT occurred, causing widespread destruction.)

VI. IM Fragment and Bullet Impact Tests and Sympathetic Detonation Tests

Obviously rocket motors containing 1.1 propellants are more sensitive than their 1.3 counterparts in the IM fragment and bullet impact testing. This is largely due to the 1.1 propellants having smaller critical diameter and lower initiation thresholds than their 1.3 counterparts. This also carries over to the area of sympathetic detonation. However, remember that the IM tests simulate hazards weapons are

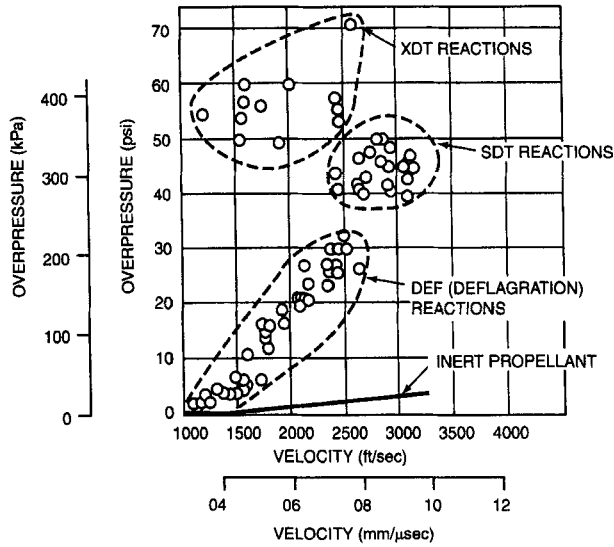


Fig. 5 Overpressure vs impact velocity for direct impact tests (Blommer as cited in Ref. 3).

likely to encounter in operational scenarios. Propellants that pass the IM bullet and fragment tests still may pose significant hazards in their manufacture, handling, and storage. These are primarily in the area of fire.

VII. Ignition

Ignition begins every combustion process and must be properly addressed when a controlled combustion process is to be initiated, and it must be reliably prevented

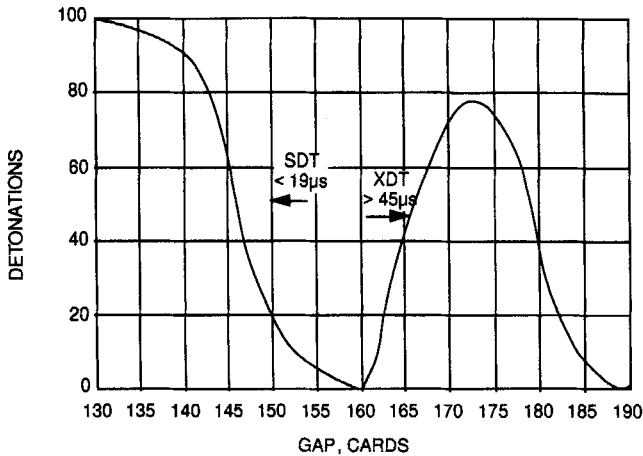


Fig. 6 Card-gap test results showing SDT and XDT (Keefe as cited in Ref. 1).

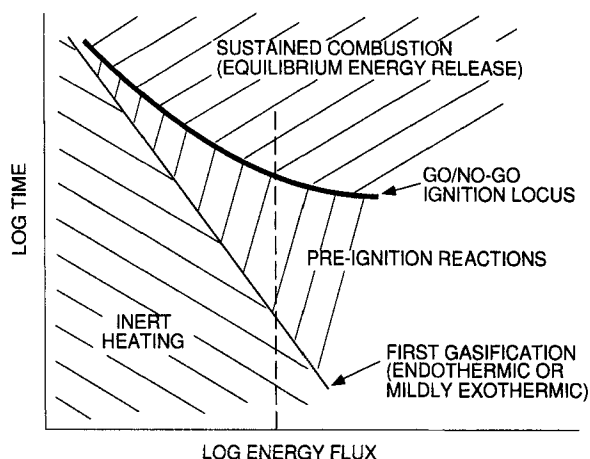


Fig. 7 General log energy flux vs log time plot of ignition process.

if accidental fires and explosions, such as the inadvertent ignition of catocene propellants that caused fatalities, are to be avoided.

Solid propellant ignition is both a process and the successful completion of that process. As a propellant sample is externally heated, the surface temperature increases and a thermal profile builds within the sample. When gasification of the sample begins, the gaseous products begin to react exothermically. This heat release increases the gas temperature and, thus, the reaction rates. With additional heating and accumulation of gas phase species, a flame is established, and the flame will snap back toward the propellant surface. At this point, the flame provides sufficient energy for propellant pyrolysis, the external heat source is no longer necessary, and the ignition process is complete. These processes are graphically illustrated in the general log flux-log time, ignition plot shown in Fig. 7.

For a given energy level (dotted line in Fig. 7), a series of events are shown at various times when the sample is subject to the given flux. For some initial time, nothing appears to be happening. If the energy flux is terminated during this time and the sample examined, no significant decomposition of the exposed surface is seen. Figure 8a shows a sample of a high-energy propellant containing nitramine that was subjected to $200 \text{ cal/cm}^2\text{s}$ for a time just prior to first gasification (evidenced by first light detected by a photodiode). No significant reaction occurred, but a thermal profile was being established within the solid. It is not until the first gasification time is achieved that the sample starts to decompose significantly. The flux established and deepened the thermal profile in the solid until a surface temperature was reached that caused significant ablation/decomposition at the surface. For exposures slightly longer than the time necessary for this initial gasification, the sample continued to gasify but did not ignite in the classical sense. That is, if the external energy flux was removed, the sample would cease gasifying, the temperature profile in the solid would collapse, and the sample would cease regressing. Figure 8b is a sample subjected to $200 \text{ cal/cm}^2\text{s}$ at a time just after first gasification (as evidenced by first light) and shows some decomposition of the surface, whereas Fig. 8c shows another sample at $200 \text{ cal/cm}^2\text{s}$ and a time just less than that required for go/no-go ignition. This sample shows significant

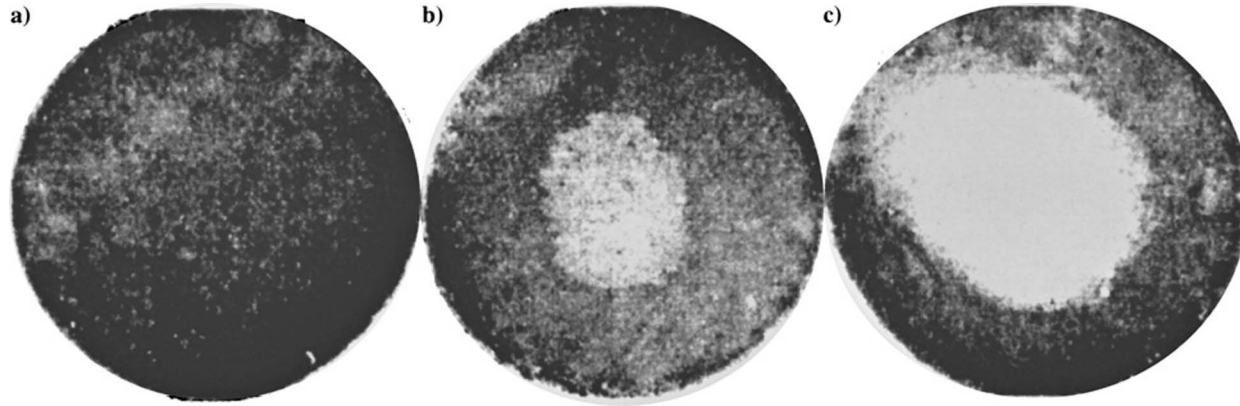


Fig. 8 Nitramine-based propellant exposed to radiant energy flux: a) prior to first light/gasification, b) just after first light/gasification, and c) at a time preceding go/no-go or complete ignition.

decomposition. Ignition was not achieved until the conditions of flux time associated with the line indicated as go/no-go ignition in Fig. 7 were achieved. At this time, and for longer exposure times, the sample was ignited in the sense that if the external energy flux was removed, the sample would continue to burn by itself without the external stimulus.¹⁵ There is another region of overdriven combustion, higher fluxes and steeper thermal profiles, where sudden removal of the flux will also cause the sample to extinguish.¹⁶

Figure 7 is a generalized depiction of the ignition process. It defines three regions separated by two lines: inert heating region, first gasification line, preignition region, go/no-go ignition curve, and self-sustained combustion region. The location of these lines and their relation to the described regions depends on many variables. Propellant formulations, external energy level, and test pressure all affect the time between the establishment of the thermal profile and self-sustained combustion.

Exposing a solid propellant to high-energy levels may not be sufficient to initiate combustion. Some investigators exposed propellant to very high-temperature gases produced by a shock tube. They were surprised when the propellant failed to ignite. While they had high temperatures and high heat flux, they did not have sufficient time. Instead of igniting, the propellant was simply scorched, and the surface layer ablated. The preignition region is important in that it is in this region that the solid has gasified into reactive intermediate species (pyrolysis products), but these intermediate species have not reacted to final products; thus, self-sustained combustion has not been attained. Unfortunately, many investigators view propellant ignition as simply a switch based on a critical surface temperature of the solid. When this ignition criterion is satisfied, these people assumed that an instantaneous change occurs from a nonreacting inert solid to burning at steady state with fully reacted gases at the equilibrium flame temperature. Whereas this criterion may be useful for some AP-rubber propellants where the samples ignite almost immediately after first gasification, it is not reality for all solid propellants and test conditions. Concepts, such as minimum ignition energy or critical ignition temperatures, have been introduced. In some limited instances, they have certain merit despite that their meaning is equivocal and important boundary conditions are usually ignored when applying the data in other situations. In general, AP-based propellants tested at ambient pressures of a few to several atmospheres, even at relatively high flux levels, show little or no detectable difference between go/no-go and first light/first gasification. Nitramine-based propellants under similar conditions, display significant preignition behavior.¹⁷ Preignition behavior can be demonstrated in the AP-based propellants by increasing the flux level and decreasing the test pressure.¹⁷

The effects of heat flux and pressure are shown in Fig. 9 for a predominantly AP-hydroxyl-terminated polybutadiene (HTPB) propellant. The effect of flux is clearly seen for the first gasification line and the various go/no-go lines. The effect of pressure is also clearly shown. Because the first gasification is essentially the ablation of the solid and primarily dependent on surface temperature, pressure should have little or no effect on this line. However, the rate of conversion of pyrolysis products to final reaction products is very pressure dependent, and the go/no-go ignition locus reflects that pressure dependence. The region of preignition reactions discussed earlier (the difference between first gasification and go/no-go lines) is clearly evident for the 50 psia case, as is the diminution of the preignition region with pressure increase to 100 and 200 psia.

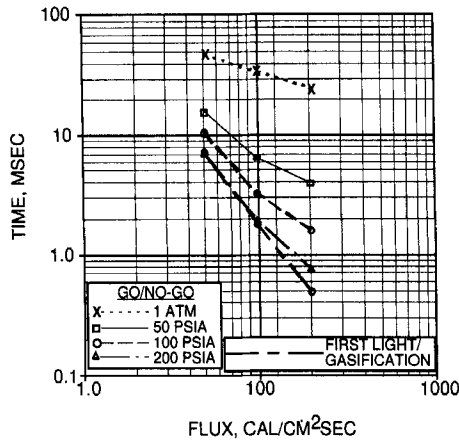


Fig. 9 Effect of flux and pressure on ignition times of AP-HTPB propellant.

Similar behavior, but with even more pronounced preignition, is shown in the ignition map for a composite modified double-base propellant (Fig. 10). Propellants incorporating high nitramine loading also display this pronounced preignition behavior.

The implications of the preignition region on deflagration-to-detonation transition and other transient combustion related hazards has been discussed in Refs. 3–5, 15, and 16 and is shown in the later section on deflagration-to-detonation transition.

This is a general overview of ignition due to thermal flux delivered to the surface (the examples given were for radiant flux).

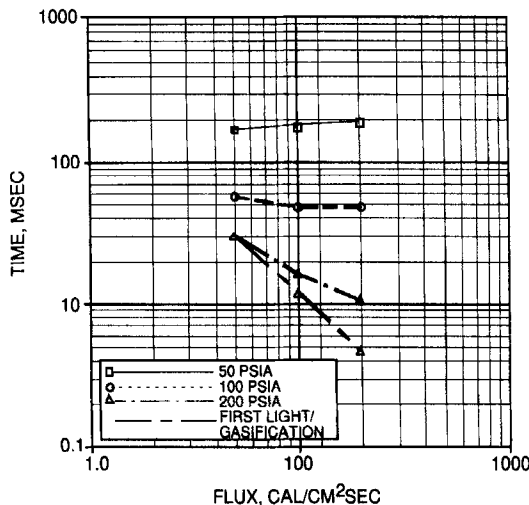


Fig. 10 Effect of flux and pressure on ignition times of composite modified double-base propellant.

VIII. Ignition due to Electrostatic Discharge (ESD)

As shown in Ref. 1, direct thermal ignition is not the only hazard concern. Inadvertent ignition associated with electrostatic discharge (ESD) is discussed next. These materials address ESD hazards in a bit different fashion than the normal laboratory ESD test.

On 11 January 1985, in Heilbron, Germany, a Pershing II missile having an AP/HTPB/Al propellant (1.3 propellant) loaded in a Kevlar[®] case ignited and killed three people. A probable cause was electric charge buildup caused by separation of dissimilar dielectric materials in a cold, dry environment. Another incident, involving the pulling of the mandrel from a large cast HTPB propellant (also 1.3) motor, also resulted in fatalities. This was also attributed to ESD. Recorded electrical potentials on a mandrel core may exceed several thousand volts at the end of the mandrel pulling operation.

Much work has been done to investigate the susceptibility of propellants to ESD, and the works of Kent and Rat, SNPE, France; Hammett of the United Kingdom; Dreitzler of the U.S. Army Missile Command; Lee of the Naval Surface Warfare Center, Raun of Hercules (now Alliant Technology); and others should be consulted. At China Lake, Covino and Hudson performed work summarized in Ref. 18 and discussed next. Much of this work showed that 1.3 propellants (especially those using HTPB binder) were more susceptible to ESD hazards than their 1.1 counterparts.

When a missile motor is charged to a potential where breakdown occurs, or when a change in grounding conditions allows breakdown of the material, electrical discharge can occur. Discharge generates charge carriers, which reduce the impedance of the energetic material, and result in rapid current increase. This can lead to arcing, establishment and growth of further discharge, followed by catastrophic discharge. The discharge releases energy, converting a small volume of propellant to gas. If enough material is converted and enough heat is generated by this decomposition, then the propellant may ignite, often with severe consequences.

The major determinants for ESD sensitivity are volume resistivity, dielectric constant, and dielectric strength. Covino and Hudson¹⁸ measured these parameters for HTPB binder, inert HTPB propellants, and live propellants. The volume resistivities were measured as a function of temperature, voltage, time of voltage application, relative humidity, and sample thickness. The dielectric constant for these materials was measured as a function of temperature, relative humidity, sample thickness, and frequency. Neglecting the effects of breakdown voltage, the higher the dielectric constant, the more energy can be stored in the propellant, and hence increased susceptibility to ESD. This coupled with the low dissipation factor for HTPB (many of the 1.3 propellants use HTPB binder) causes ESD problems. The dielectric breakdown voltage is the voltage that may be sustained across the sample just prior to the transition from nonconductive to conductive. The dielectric strength is the dielectric breakdown voltage divided by the sample thickness.

The results of Covino and Hudson's work¹⁸ was applied using the percolation calculations advocated by Kent and Rat.¹⁹ The results show that the overall electrical properties of the propellant were most influenced by the HTPB binder and to a lesser extent by the concentration and particle size of the aluminum powder. The contribution of the oxidizer particles was primarily in determining

the spacing of the aluminum particles and the thickness of the binder layer between particles.

IX. Ignition due to Impact and Friction

Propellants are routinely tested for their susceptibility of reaction due to friction and impact (for example, see Ref. 6). Although these tests are very important in considering hazards associated with manufacturing and handling of propellants, those tests and the results will not be discussed in this chapter because of space limitations.

X. Other Ignition Hazard Considerations

In addition to a basic understanding of ignition, two rules of thumb are often used.

1) Propellants based on AP often ignite as soon as the stimulus causes rapid gasification of the propellant. Remember, AP propellants usually have less of a preignition region than do double-base or nitramine-based propellants.

2) Within a family of propellants, the faster the burning rate, the easier it is to ignite the propellant. Thus, propellants incorporating burn rate accelerators, such as catocene, may be very easy to ignite.

As with all rules of thumb, the preceding statements have exceptions.

What are some of the hazards based on the preceding discussion of ignition? Obviously propellants that do not ignite at low pressures have some advantages in several hazard areas. It is sometimes stated that class 1.3 propellants are inherently safer than hazard class 1.1 propellants. Although this is true for mechanical shock stimuli of tens of kilobar magnitude, it is not always true for other stimuli. Referring to the sample, stimuli, environment yielding response discussion, and considering the ignition and combustion sections of this chapter, in many instances the 1.3 propellants can be more hazardous than 1.1 propellants. AP-based propellants (almost always class 1.3) are often easier to ignite in terms of the energy flux necessary to cause decomposition and can ignite almost simultaneously with decomposition. In contrast, the nitramine-based propellants (often class 1.1) show large, pressure-dependent delays between decomposition and self-sustained combustion. The AP-based propellants usually burn at 1 atm, whereas nitramine propellants often do not burn well, if at all, at 1 atm.

As discussed earlier, many of the AP/HTPB/Al propellants (usually 1.3 propellants) show high ESD sensitivity and may result in incidents and deaths.

There are other sample types that may have relatively high hazards in some situations, even though they have a hazard class 1.3: for example, some AP-based propellants containing catalysts such as catocene, or some AP-based propellants incorporating fine aluminum fuel.

The purpose of these remarks is not to say that one material is safer than another: there are hazards associated with all propellants, and they must be handled accordingly. Just because a propellant is classed as 1.3 does not mean that it is insensitive to all hazard stimuli. You cannot treat it as if it were inert.

As shown in Ref. 1, propellants with significant preignition behavior, friability, and shock sensitivity are extremely susceptible to deflagration-to-detonation transition (DDT) and other forms of delayed detonation.

XI. Combustion

The pressure–time history of propellant burning in a closed (or semiclosed) container is a function of several considerations and can result in propulsion, explosion, and even transition to detonation. As shown in the fragment impact hazard analysis protocol,^{1,3,4} the balance between gas generation vs gas venting determines whether an explosion can occur. Similarly, a DDT can occur if several conditions, some related to ignition and combustion, are met.

The pressure–time history associated with burning an energetic material in a closed volume is a function of the mass burning rate, which in turn is a function of the propellant density, burning surface area, and surface regression rate (often called the linear burning rate or simply burning rate)

$$p(t) = f(\dot{m}, \dots)$$

where \dot{m} is the density \times surface regression rate \times burn area. However, the surface regression rate r is a function of pressure, often given as $r = Cp^n$. For a vented system such as a rocket motor, the pressure–time curve will be a function of the gas generation rate and the gas discharge rate. There are several factors involved with the combustion of a confined energetic material and how that combustion can lead to hazardous situations. The pressure–time produced from the combustion of the energetic material must be compared to the dynamic mechanical behavior of the case, with proper consideration of the venting, to determine the overall response.

The following sections briefly discuss burning rate and burning area considerations and refer to more detailed discussions.

A. Burning Rates of Energetic Materials

The rate at which a solid is converted to gas during combustion is commonly called the burning rate and is a function of pressure as discussed earlier, initial sample temperature, and boundary considerations, such as flow past the surface (erosive burning). Figure 11, from Atwood and Curran, show burning rates at low pressures for a class 1.3 metallized AP-based propellant and a 1.1 metallized nitramine propellant. The AP-based propellant burns about twice as fast. Not shown on this plot is the behavior at even lower pressure. Whereas the AP-based propellant burned well at 1 atm, the nitramine propellant often did not sustain combustion at 1 atm.

Burning rate data are required for hazard assessment protocol considerations discussed earlier and in other protocols presented in Refs. 1, 3–5, 17, and 18. The data are used in other less obvious ways: 1) The slope of the burning rate–pressure curve, when plotted as log–log is the burning rate exponent (n in the expression $r = Cp^n$) and indicates potential hazards. 2) The temperature and pressure sensitivity of burning rate, coupled with ignition data, can be used to evaluate kinetic parameters that are in turn frozen input variables in transient combustion codes to predict convective combustion and DDT.

Burning rate exponents very near unity and higher are to be avoided because the burning rate is very sensitive to changes in the pressure, and a case failure or explosion may result. Slope breaks as shown in Fig. 12 often occur at high pressures in which the high-pressure portion of the burning rate curve has an exponent very near or slightly greater than unity.

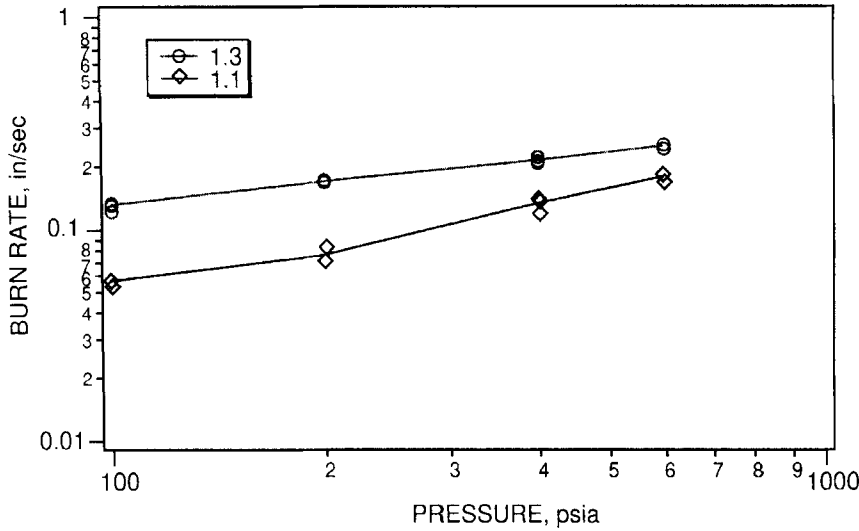


Fig. 11 Low-pressure burning rates for 1.3 propellant (upper curve) and 1.1 propellant (lower curve).

B. Burning Area

Burning area is an extremely important determinant of the hazard severity given inadvertent ignition of the propellant. References 20 and 21 present extensive surveys of combustion into defects in energetic materials. Damage is involved in many hazard scenarios such as bullet fragment impact, ESD, and some slow

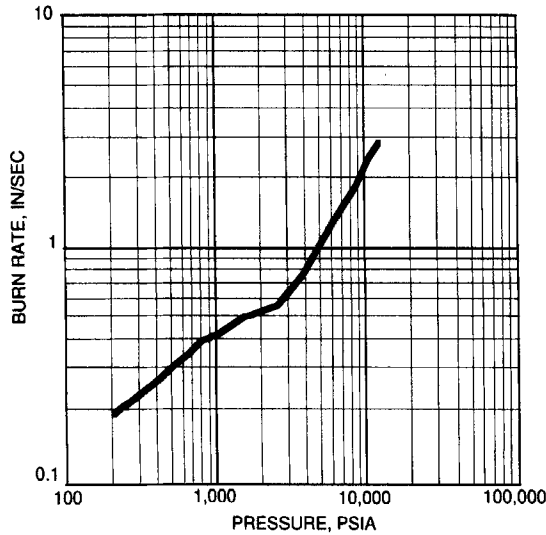


Fig. 12 Burning rate as a function of pressure, showing a slope break.

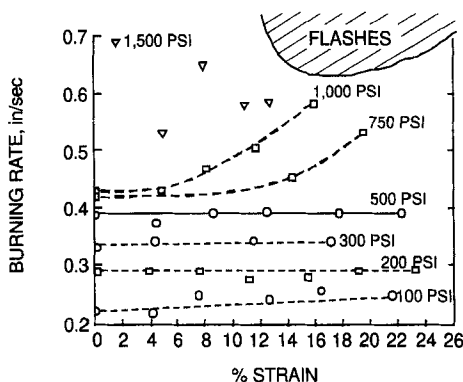


Fig. 13 Burning rate of a high-energy propellant as a function of pressure and strain. (Note that the propellant was strained prior to burning; thus, any damage was preexisting and held open.)

cookoff areas. The damage can exist before ignition/combustion or it may accompany the ignition/combustion. The burning of prestrained (hence, in some cases, predamaged propellant) is described next.

C. Effect of Strain on the Burning Rates of High-Energy Solid Propellants

High-energy propellants usually have a high portion of solid ingredients such as AP, HMX, aluminum, and other ingredients such as solid catalysts. An obvious condition accompanying high solids loading is less polymeric binder to hold the solid particles together and to provide acceptable mechanical properties. It is useful to know how far a propellant can be strained before ballistic anomalies (such as burning rate augmentation) become significant.

The burning rate of a high-energy propellant as a function of strain is presented in Fig. 13. The data show that no significant augmentation of burning rate occurs for pressures below 500 psi regardless of strain (these propellant samples fail at approximately 25% strain). At higher pressures ($p \geq 750$ psi) burn rate augmentation appears for strains above approximately 8%. At 1500 psi and strains above approximately 12%, the sample burns in a vigorous and nonplanar fashion (termed flashing) precluding meaningful measurement of a linear surface regression.

Data for several types of propellants show burning rate increase at pressures and strains greater than some threshold values. The magnitude of the threshold values depends on the propellant. Note that both threshold values (pressure and strain) have to be exceeded, exceeding just one is not sufficient. For example, high strain but low pressure will not cause augmentation, nor will high pressure but low strain.

The mechanical response of the propellants to strain was studied using a binocular microscope. If the propellant of Fig. 13 is used as an example, these studies showed that at 4% strain, debonds (separation, on a microscale, of the solid particle from the polymeric binder) between ingredients occurs. Between 9 and 11% strain, these debonds are often fully developed cracks, with the walls of the crack in close proximity. At approximately 16% strain, these cracks are open voids; that is, the walls of the crack are no longer in contact with one another. At

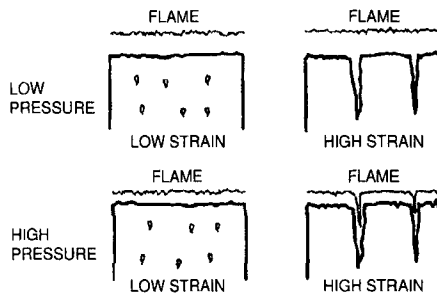


Fig. 14 Mechanism for the augmentation of burning rate due to pressure and strain.

approximately 24% strain, the sample is often riddled with large cracks, and the sample breaks.

The preceding discussion of mechanics, coupled with knowledge of flame stand-off distance decrease with pressure increase, provide a mechanistic understanding for the burning rate augmentation due to strain and pressure. The mechanism is shown in Fig. 14. At low-strain values, the propellant is not significantly damaged, and so regardless of the flame standoff (Fig. 14, left), augmentation will not occur. When the propellant is highly strained and fissured, augmentation occurs if the flames can penetrate into those fissures (Fig. 14, bottom right). At low pressures, the flame stands too far from the surface to allow penetration (Fig. 14, upper right), but at high pressures, the flame is close enough to the surface to penetrate the fissures and cause burning rate augmentation.

Because flame penetration into the defects seems to be required for burning rate enhancement, a study was done using propellants that had been strained almost to failure and then the tension was removed. The voids closed. When these samples with the closed voids were burned, the burning rate was identical to the burning rate of the undamaged propellant burned at that pressure.

These data indicate that under certain conditions strain can cause damage, and if that damage is sufficient and open, and if the pressure is high enough to allow flame penetration into the defects, then burning rate enhancement can occur.

Kuo and Kooker²² have studied the combustion of propellants with various cracks and other defects, observing crack growth during combustion.

In addition to the growth of cracks during combustion, there are other dynamic effects. As burning rate increases, the thermal zone gets thinner and the thermal gradient gets steeper. Under these conditions many samples, and ingredients within samples, crack, allowing combustion into these fissures. Under some conditions the cracking is so severe that the sample actually comes apart. Fifer and his colleagues at the Army Research Laboratory have extensively studied this deconsolidation, and the reader is referred to their works.

If the propellant undergoes significant break-up then DDT or other burning to violent reactions may occur

XII. DDT

DDT has occurred during firing of rocket motors. In the early 1960s at Hercules, Kenil, New Jersey, a 10-lb charge of slurry cast cross-linked composite modified

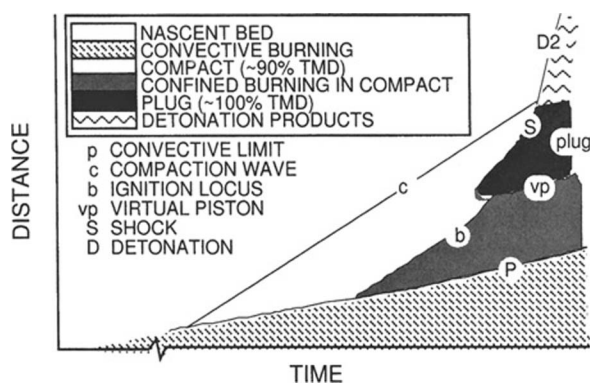


Fig. 15 Schema of the DDT process in granular HMX.

double-base containing AP and HMX was observed to DDT during routine static firing. The cause was attributed to microporosity in the grain (R. L. Simmons, personal communication, 14 February 1996). In May 1974, at Hercules, Bacchus, Utah, a motor underwent DDT during a routine static test firing. The cause was attributed to a region of highly damaged propellant produced when the nozzle blew out and the motor case snapped back shearing the adjacent propellant. DDT has also been observed in granular systems such as gun propellant.

Bernecker²³ listed the stages of DDT mechanism for porous charges as 1) pre-ignition, 2) ignition/conductive burning, 3) convective (reaction) burning, 4) compressive (hot spot) burning, 5) shock formation, 6) compressive burning, and 7) detonation. McAfee et al.²⁴ depicted these stages (combining 1–3 and using slightly different nomenclature) in the distance–time plane as shown in Fig. 15.

Whether or not a propellant reaction can transition from a burning reaction to a detonation is determined by several considerations. The key requirement for this transition to occur is a sufficient surface-to-volume ratio and porosity of the energetic sample either through manufacture and loading, in the case of some gun propellants, or through large-scale damage in the case of missile propellants. For missile propellants the first consideration then is the likelihood of the propellant being damaged either before or during the burn. This is a critical consideration because, with rare exceptions, it is nearly impossible for a consolidated propellant at near theoretical maximum density (TMD) to undergo a DDT reaction.

Figure 16 presents the limits of DDT for granulated propellant samples of a given type (see Ref. 1, p. 97). Figure 16 shows that for this propellant formulation and confinement at least 49% TMD is required for DDT. Although, if the sample is too dense, the DDT reaction will not occur. Similarly a range of surface-to-volume ratio (100–700 in.⁻¹) is required for DDT to occur. If these conditions, or similar conditions for other samples, are not met, then a DDT reaction, for this propellant, is extremely improbable. Although transition to detonation may not be probable, an explosion may still occur. To determine whether an explosion may occur, the pressure and the rate of pressurization caused by gasification must be determined and compared to the rupture characteristics of the motor case.

If the propellant is damaged and if the resulting %TMD and surface-to-volume ratio are in the right range, then DDT is likely. Whether or not the DDT occurs

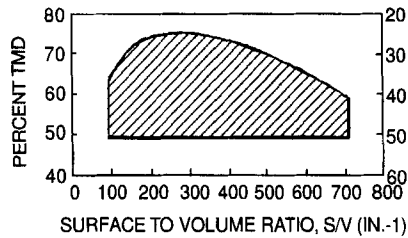


Fig. 16 Limits of DDT or granulated propellant samples.

is determined by the pressure and pressurization rate within the vessel and the rupture characteristics of vessel (motor case). If the motor case ruptures too soon, then confinement is lost, and the DDT reaction becomes unlikely. (The rupture may be a violent explosion.) The rupture characteristics of the vessel need to be determined experimentally and/or analytically, but will not be discussed further.

XIII. Cookoff

As mentioned earlier, fire is a major concern onboard ship, especially for the large aircraft carriers. Operations on a carrier deck are carefully orchestrated events, many of them occurring simultaneously, especially during combat. There is the launching of aircraft with the high-*g* forces associated with catapult launch; there are the hard, high-speed landings on a moving, small deck (when compared to normal landing fields) with rapid deceleration when the tail hook engages the arresting cable (sometimes referred to as controlled crashes); there is the race between launching aircraft and recovering aircraft, often low on fuel, from the previous launches; there are often many planes on deck, in various stages of readiness, some being refueled and some being rearmed; there are often bomb farms (stockpiled weapons stores on the deck) because you do not have time to move enough ordnance from the magazines to the deck and onto the planes without stockpiling the items on deck; there are hot-gas huffers used to start engines; there is handling equipment; and there are people, all on deck, all moving around. The potential for fire is extremely high, and the potential of weapons to be caught in that fire is also relatively high. There is no place to run and hide.

As presented by Beauregard,²⁶ from October 1966 to May 1981 there were four aircraft carrier accidents that resulted in fires and munition explosions: 220 sailors and naval aviators were killed and 708 were injured. In terms of 1990 dollars, there were \$478 million in ship damage, and \$1958 million in aircraft damage.

Cookoff was responsible for the Roseville, California, rail yard fire, and various ammunition dump explosions (also taken from Beauregard²⁶). At Roseville, on 28 April 1973, a boxcar carrying bombs caught fire and caused the bombs to explode. In the next few hours, 18 boxcars exploded in succession. Fortunately no one was killed, but 48 people were injured and there was \$24 million in property damage. In 1965, fire and secondary explosions destroyed the ammunition dump at Bien-Hoa, Vietnam air base. In March 1965, at the munition storage

area at Qui Nhon, fire and secondary explosions killed 3 and injured 34, and many tons of ammunition were destroyed. Also in 1965, fires and secondary explosions at Da Nang destroyed more than \$123 million of ammunition. After the Gulf War there was a fire in a transport vehicle at the Army's Camp Doha in Kuwait. An explosion spread the fire, causing secondary explosions. The Army lost more tanks in that accident than in the entire Desert Storm campaign. In the incident, 52 soldiers were injured, and 3 were killed while clearing damaged ordnance.

There are obviously many cookoff situations to be considered, but much of the attention falls at the two ends of the spectrum: fast cookoff when ordnance is subject to direct fire such as burning aircraft fuel or a bonfire, and slow cookoff. The MIL-STD-2105A defined the fast cookoff and slow cookoff tests for the United States. Whereas the conditions for fast cookoff are widely accepted, those for slow cookoff have been in almost constant debate. The prescribed 6°F/h heating rate (3.3°C/h) has been the topic of heated debate in many cookoff workshops. Many feel that it is not representative of any real threat, that it takes too long to run the test (sometimes days), that the test keeps going until a reaction occurs, regardless of whether that is a realistic time duration, that it gives worst-case reaction (thermal explosion) because of the low-temperature gradient (although some tests, using a higher heating rate, seem to indicate that in some instances a more violent reaction occurred), and that we waste much money trying to design weapons to this unrealistic test. Others defend the test, saying that some criteria are needed, and it has often been said that although it may not be the best test, there is an extensive database. What good is an extensive database, if almost everything fails? For example, of 25 motors tested for slow cookoff at 6°F/h , only 1 passed, and it was an unusual geometry. MIL-STD 2105B allows for a threat hazard assessment (THA) to be made. This THA looks at the weapons system from cradle to grave and tries to describe the environments the weapons system are likely to encounter, the hazards associated with the environment, the stimulus levels likely to be seen in those encounters, the probability of being subject to the event(s), and the likely reactions. From this THA comes recommendations of what stimuli and levels the munition should be tested for. This THA can be used to recommend that some slow cookoff heating rate other than 6°F/h is more realistic for that weapon and its life cycle exposure and that the weapon should be tested at this more realistic condition. Some of the THAs are recommending higher slow cookoff heating rates (e.g., 50°F/h , 53°F/h , and 75°F/h).

Slow cookoff reactions of several propellant types were studied at China Lake using several subscale visualization techniques. There was a rich variety of phenomena, for example, expansion of the propellants, and reaction violence from quiescent-burning- to detonation-type reactions, even between propellants in the same basic family. Some of the most violent reactions were associated with booster type propellants, even though these were 1.3 propellants. (Note that the elastomeric modified cast double-base propellants, hazard class 1.1, also displayed extremely violent reactions.) These boost motors had high burning rate propellants, usually catalyzed with iron oxide burn rate modifier.

Another series of propellants used potassium perchlorate as the oxidizer. These propellants looked extremely good in small-scale tests, having an autoignition

temperature over 500°F. However, when these materials were loaded in small sized motors (about 4–5 lb), the slow cookoff reactions were extremely violent. The violence was mitigated when about 5% of AP was added to these propellants. However, when these propellants were loaded into 8-in.-diam motors, the resultant cookoff reactions were described as detonations: Case fragments went through witness plates. The lessons learned here were that small-scale results do not always scale to the practical size.

Lately promising results have been obtained with propellants that have significant decomposition and reaction at low temperatures (260 and 270°C). In the tests, significant amount of unburned propellant is recovered after the test.

From the many studies, the temperature and time to reaction can be predicted for many materials. However, the ability to predict violence of reaction (case wall movement and fracture and the size, weight, and velocity of the fragments) is still a goal and reflects the complex interaction between the sample, the stimulus, and the environment. For cookoff, the stimulus and environment are obviously intertwined. The sample is also difficult to describe at times because it changes as it decomposes, and the decomposition products may play a significant role.

XIV. Conclusions

1) A hazard class of 1.3 does not mean that the propellant is safe. People have been killed with 1.3 propellants. The 1.3 propellants primarily kill by inadvertent fire.

2) The AP-based propellants (usually 1.3) ignite more readily and burn well at 1 atm.

3) Zero card-gap propellants are not nondetonable. They simply have a critical diameter larger than the sample tested.

4) Very small amounts of damage have a marked increase on shock sensitivity: decreasing the initiating pressure required and decreasing the critical diameter.

5) XDTs occur at lower stimulus levels and have greater blast overpressures than prompt SDTs.

6) The configuration of the propellant can have a marked effect, especially the center perforation or bore effect.

7) Slow cookoff events can be extremely violent, with some 1.3 propellants producing the highest violence.

Appendix: Summary of Accidents Involving Solid Propellants

The information contained in Table A1 has been compiled based on information from published articles, technical reports, media reports, workshops, and personal communications. Table A1 presents the best information available to date, but should not be interpreted as a comprehensive and complete reference source. Table A1 should be considered a work in progress as the authors continue to validate and update information. Corrections and additions can be sent to E. J. Mulder at the Chemical Propulsion Information Agency (CPIA), Johns Hopkins University.

Table A1 Summary of accidents involving solid propellants

Date	Incident description/location	Failure mode, cause (NEW or propellant wt.) and [main ingredients]	Damage or injuries			Ref. no.	Hazard class
			Equipment or facilities	Injuries	Fatalities		
Sept. 1940	Hercules/Kenvil, NJ	Smokeless powder plant explosions, caused by too rapid heating of powder. Firebrands initiated second fire/explosions. Equipment fragments recovered 5-miles away from blast. Heavy barricading was not used prior to accident.	Facility destroyed, 6-mo rebuild	NA	52	27	1.1
June 1948	Hercules/Kenvil, NJ	Nitration house explosion; 3500-lb NG; caused by runaway processing. Blast caused 35-ft crater, heard in New York City 50 miles away, rocked Empire State Building.	Facility destroyed	NA	3	27	1.1
June 1948	Hercules Hercules, CA	Explosion in NG building. Second accident within Hercules Corp. hours apart on June 1948, in a separate Hercules facility 3000 miles apart.	Facility destroyed	NA	2	27	1.1
May 1952	Howard Univ. Washington, D.C.	Chemistry laboratory storage area explosion. ESD/ESE initiated 400-lb container of sodium chlorate when laboratory technician attempted to move the container with a hand truck. When dispensed/stored in damp areas NaClO ₃ hygroscopicity results in very fine, high specific surface area crystal formation. Fine crystals are highly reactive and sensitive to initiation.	Damaged storage facility	Several	4	27	NA
March 1953	Hercules/Kenvil, NJ	Smokeless powder plant explosion.	Facility destroyed	NA	2	27	1.1

(Cont.)

Table A1 Summary of accidents involving solid propellants (continued)

Date	Incident description/location	Failure mode, cause (NEW or propellant wt.) and [main ingredients]	Damage or injuries			Ref. no.	Hazard class
			Equipment or facilities	Injuries	Fatalities		
June 1953	Hercules/Sunflower Ordnance Works, Lawrence, KS	5-in. Zuni (MK16) saw house fire. Fire propagated due to slow sprinkler response. Fire spread through feed door to other areas. Friction of saw against lodged propellant chips caused fire. Accident report states NEW approx. 2500 lb (33.5 lb/motor) [NC/NG].	Saw house and equipment	0	0	—	1.1
Dec. 1954	Indian Head Naval Powder Plant (NPP), Indian Head, MD	Terrier Booster motor postcure mandrel pulling. Mandrel was several inches above grain. Flash fire was seen at the top of the grain before propellant ignited. ESD event. Operator not grounded while wiping grain. Fire did not propagate to other motors in vicinity (800 lb) [NC/NG solvent NG/triacetin].	NA	5 Burned	0	—	1.1
NA	Motor storage building	6-Nike Hercules and 10-Honest John motors. Explosions and fire in motor storage-building lightning strike (25,000 lb) [CMDB].	NA	0	0	—	1.1
NA	Mixer explosion	Composite propellant (98 lb) 20-gal Baker Perkins mixer explosion. Foreign material between mixer blade and bowl.	NA	2	0	—	NA

Oct. 1957	Longhorn Ordnance Works, Marshall, TX	Nike Hercules (X-30) sustainer motors postcure removing motor from cure oven. Hoist and monorail failure. Motor dropped 3 ft and ignited. Fragments sprayed 200 ft. Mandrels, 900 lb each, projected through roof. Fire heat cracked 12-in. RCW. Propagated to 3 motors; all burned (2160 lb/motor) [AP/polysulfide].	NA	2 Burned	0	—	1.1
Oct. 1957	Grand Central Rocket Co., Redlands, CA	While removing mandrel, operator struck mandrel with leather mallet; thin layer of propellant ignited and initiated motor fire. Fire propagated to 25 motors in vicinity. Debris sprayed/scattered 100 ft. Storage bay over loaded (500 lb polysulfide perchlorate; drop test 2 kg = 45 cm).	Postcure work bay destroyed	1 Burned	0	—	1.3
Oct. 1960	Salvage Yard, Phoenix, AZ	HVAR 5-in. motor. Worker using acetylene torch to cut case ignited propellant. Motor went propulsive, traveled 5 blocks landed on home; broke through in exterior walls, and burned hole in living room concrete floor. Motors were supposed to be inert. Five more motors found and removed from yard (15.0 lb UXO) [NC/NG].	NA	1 Burned	0	—	1.1
July 1961	NA—United States	Propellant mixer (200-gal Baker–Perkins) explosion. Polysulfide propellant (1300 lb) detonated. Caused by friction between blades and bowl, or packing glands.	Mixer destroyed, facility damaged	0	0	27	1.1

(Cont.)

Table A1 Summary of accidents involving solid propellants (continued)

Date	Incident description/location	Failure mode, cause (NEW or propellant wt.) and [main ingredients]	Damage or injuries			Ref. no.	Hazard class
			Equipment or facilities	Injuries	Fatalities		
Aug. 1961	Indian Head, MD	Propellant powder mixer explosion. 50-gal Baker-Perkins mixer (10-15 lb) end-of-mix clean up operations. Workmen using shovels/metal hand tools. Friction/impact initiated detonation, mixer fragments found 1000-ft away in another building.	Mixer destroyed, facility damaged	Several	5	27	1.1
Sept. 1961	Thiokol Corp., Brigham City, UT	Quarter-scale Minuteman fire/explosion. Pneumatic grain cutback tool blade impacted propellant. Sparks were seen to propellant surface before motor ignited (12,000 lb) [CTPB/AP/Al].	Destroyed building, equipment, and tooling	1 Burned	NA	—	1.3
1962	NA-United States	Explosion while saw cutting cured composite propellant. Sample prep-area band saw cutting operations with remote vacuum for collecting propellant fine dust. Ignition of fines in band saw guide block transferred to fines in vacuum system.	NA	Several	1	27	NA
July 1962	Rocketdyne Plant, McGregor, TX	Hand cutting propellant laboratory-scale operation. Sparks were seen at blade-propellant interface. Fire propagation limited by deluge system. Building saved adjacent cells and equipment water damaged (92 lb AP/composite).	NA	0	0	—	NA

Oct. 1962	Cape Kennedy, FL Minuteman missile flight test no. 422	<p>Fallback incident class 1.3 propellant high-order explosion. Successful launch T-zero to 3800 ft; after 8.5 s guidance system malfunctioned and destruct action was initiated. Missile stages separated and fell to ground. Free-falling velocity of 500 ft/s at impact (velocity required for stage 3 detonation above 3500 ft/s).</p> <p>Notable results: Effects of fragmentation on 1.3 propellant (<70 card propellant) grain structural integrity can result in a violent reaction upon motor ignition.</p> <p>Stage 1: 1.3 propellant (46,800 lb) [AP/AL/CTPB] impact crater 10 ft deep and 42 ft diam. Report states true crater was considerably larger due to earth and debris fallback in first few seconds after blast is expended. Such destructive results cannot be generated by anything less than a high-order reaction. Partial confinement and high-rate burning resulted in blast pressures equal to a high-order explosion.</p> <p>Stage 3: 1.1 propellant (7309 lb) [CYH or DDP (CMDDB)] impact crater 3 ft deep × 12 ft diam. Prolonged burning, no detonation.</p>	NA	0	0	—	S-3 1.1 S-1 1.3
-----------	--	--	----	---	---	---	--------------------

(Cont.)

Table A1 Summary of accidents involving solid propellants (continued)

Date	Incident description/location	Failure mode, cause (NEW or propellant wt.) and [main ingredients]	Damage or injuries			Ref. no.	Hazard class
			Equipment or facilities	Injuries	Fatalities		
Jan. 1963	NA-United States	Propellant mixer explosion. AP, aluminized composite propellant formulation (100-gal Read mixer) 1300 lb. On reversing mixer-blade direction, mixer exploded. Probable cause 1) foreign materials in mixer, 2) concentration of unmixed perchlorate materials in shaft seal housing.	Mixer destroyed, facility damaged	0	0	27	1.3
1963	NA-United States	Three explosions during solid propellant mix, cast, and cure operations. Explosion consumed 3 rocket motors, plus 4800-lb NG solvent. 30 lb of residual casting solvent in aspirator catch tank. Caused by handling accident while draining aspirator tank, propagated to motors in casting and cure operations.	Facility destroyed	11	3	27	1.1
1964	NA-United States	Explosion during propellant mixer operations. 500–1000 lb propellant consumed in fire/explosion. Additional 2000 lb of combustible materials consumed in fire.	Facility destroyed	8	3	27	NA
NA	NA-United States	Bandsaw fire and explosion, propellant formulation TP-H8126 composite propellant. Ignition of propellant fines in lower guide blocks of bandsaw (7 lb propellant).	NA	2	1	—	NA

April 1963	Allegany Ballistics Lab., Cumberland, MD	Fire and explosion of Large Grain Line Complex. Four A-3 Polaris stage 2 motors. Cause: human error (39,445 lb) [CMDB].	Destroyed buildings	30	3	—	1.1
Feb. 1964	Allegany Ballistics Lab., Cumberland, MD	Minuteman 3rd stage. Remote-operated 72-in. radial saw cutting through motor case to obtain propellant samples. Propellant ignited due to overheating of diamond-dust cutting wheels. Deluge system limited facility damage (1350 lb) [CYH or DDP (CMDB)].	Minimal	0	0	—	1.1
July 1964	Allegany Ballistics Lab., Cumberland, MD	Explosion and fire in casting powder plant. Two explosions occurred one in casting building and second in interstage tower. Propellant ignited due to friction, impingement or ESD/ESE between powder conveying piping and the propellant. Blast propagated through the piping in both directions resulting in two explosions.	Destroyed buildings, equipment, and interstage tower	0	0	—	1.1
1966	U.S.S. Oriskany Viet Nam conflict	Onboard ship fire. Restoring flares from returning aircraft. Sailor dropped flare & it inadvertently ignited. Second sailor picked up flare, threw it in a locker, and closed door. Locker contained 2.75 inch rocket warheads. Warheads cooked-off and detonated. Detonation caused explosion of liquid oxygen tank.	2 helicopters, 4 aircraft destroyed \$15.6 M Ship damage \$48 M	156	44	—	1.1
1967	Allegany Ballistics Lab., Cumberland, MD	Propellant powder fire explosion occurred during transport of propellant powder in slurry dessicator. Dessicator fell off truck explosion and fire occurred.	3 Buildings	Several	8	27	1.1

(Cont.)

Table A1 Summary of accidents involving solid propellants (continued)

Date	Incident description/location	Failure mode, cause (NEW or propellant wt.) and [main ingredients]	Damage or injuries			Ref. no.	Hazard class
			Equipment or facilities	Injuries	Fatalities		
May 1967	Utrecht, The Netherlands	Explosion on a ship loaded with 11,000 kg of ammunition, great damage to surrounding industrial area. Ammunition was obsolete and prepared for dumping. During the handling of pyrotechnic ammunition, one of the items must have activated. Because the ship was loaded with all types of ammunition, deflagration from the pyrotechnic munitions grew to a detonation of the high-explosives munitions also present (Prins Maurits Lab., 1967).	NA	200	2	NA	NA
April 1967	U.S.S. Forrestal	Zuni rocket (Mk-16) accidentally fired from an aircraft being readied for mission. Rocket crossed flight deck struck second aircraft, which ignited a fuel tank. The fire propagated to the aircraft ammunitions that detonated. Detonation ruptured flight deck, fuel spilled to lower decks. Bombs, warheads, and rocket motors reacted. Cookoff incident (33.5 lb/motor) [NC/NG].	21 aircraft, \$758 × 10 ⁶	162	134	NA	1.1

Jan. 1967	Allegany Ballistics Lab., Cumberland, MD	Polaris A2 stage-2 (X-250). Fire and explosion while removing aft dome prior to sectioning propellant grain. Two circumferential cuts were made with 72-in. radial saw. Operators attempted to remove the dome with hydraulic wedge and hand tools, propellant ignited. By (8800 lb) [CMDDB].	Destroyed building and band saw	0	0	—	1.1
June 1967	Hercules/Kenvil, NJ	Propellant handling accident during SOP transfer operation. Operators tilted a 4-wheel hand truck containing 5000 lb of single-base casting powder. Fire and explosion resulted.	Destroyed building	Several	3	27	1.1
1967–1969	Thiokol Corp., Elkton, MD	ZAP motors. Ferrocene propellant. Two incidents occurred while reclaiming motor cases by hydromining propellant. Two motors out of four ignited. B. Gleason, MTI/Elkton, stated these incidents resulted in a change in policy to not hydromine ferrocene propellants due to extreme sensitivity to friction or impact (83 lb/motor) [AP/Al/Fe ₂ O ₃ /HC434/2% ferrocene].	NA	NA	NA	NA	1.3
Jan. 1969	U.S.S. Enterprise	Exhaust from an aircraft engine starter unit impinged onto a pod containing ZUNI (Mk-16) rocket motors; one motor ignited. Fragments ruptured aircraft fuel tanks, and a fire resulted. 1 min after first explosion, three more rocket motors exploded. Flight deck was ruptured spilling fuel to lower deck. 18 munitions detonated, 8 holes in flight deck, and onboard fires. Cookoff incident (33.5 lb/motor) [NC/NG].	15 aircraft destroyed 17 damaged \$57 × 10 ⁶ \$487 × 10 ⁶ ship repair	344	28	NA	1.1

(Cont.)

Table A1 Summary of accidents involving solid propellants (continued)

Date	Incident description/location	Failure mode, cause (NEW or propellant wt.) and [main ingredients]	Damage or injuries			Ref. no.	Hazard class
			Equipment or facilities	Injuries	Fatalities		
Oct. 1972	Thiokol Corp., Brigham City, UT	Minuteman motor. Igniter motor extracting samples during electrochemical milling propellant. Fire and explosion (prop. wt. NA) [AP/Al/CTPB].	NA	0	0	—	1.3
Jan. 1974	Thiokol Corp., Brigham City, UT	Minuteman (MM) 1st stage motor. Hydromining propellant. Automatic washout operation ignited motor. Facility destroyed. Contamination buildup in exhaust duct (45,899 lb) [AP/Al/CTPB].	Destroyed building, equipment tooling, and MM motor case	0	0	—	1.3
March 1974	Edwards AFB, CA	Test area I-21, solid-propellant milling and cutting building 8582. Fire was caused by friction between saw blade and propellant. Burning particles swept into local exhaust duct, where particles exploded. Air Force Rocket Propulsion Lab. contractor's formulation TP-H8219: Oxidizer: ultrafine AP, 6- and 90- μ m AP; fuel: Al 90 μ m, catalyst 1% Fe ₂ O ₃ .	Saw damaged, destroyed exhaust duct work \$5200	0	0	28	1.3
May 1978	SRAM motor failure	Motor case burn through. Motor AHS 1472 blew up at Tonapah. Cause 1) possible manufacturing defect at aft launch lug region, 2) ejection loading caused grain damage and subsequent operational failure (991 lb) 86% total solids [AP/AL/CTPB].	NA	NA	NA	29	1.3

May 1981	U.S.S. Nimitz	A crash landing of aircraft followed by series of explosions. When fuel fire was contained, an order to proceed with clean-up was given. One Sparrow warhead experienced delayed detonation, 3 additional warheads detonated before ensuing fire was contained. 133 pounds of AP/AL/oxamide/CTPB propellant/rocket motor.	3 aircraft destroyed 9 aircraft damaged Ship damage \$150 M total loss	48	14	—	1.3/1.1
1982	Perm, Russia	Hydromining solid propellant. SS-24, 2nd stage rocket motor ignited on a washout stand. On propellant ignition, the motor developed enough thrust to eject the motor from the stand, crashed through the walls of the operations building. Motor went propulsive into a nearby dining hall. Hydromining technology development halted in Russia (76,600 lb) [AP/HMX/ADN/Al/ferrocene/HTPB].	NA	Several	Several	Verbal account, plant manager	1.1
Nov. 1982	U.S.A.F. Arnold Engineering Development Center, Arnold AFB, TN	Fire cell J-4, during MX/Peacekeeper stage 2 propellant cleanup in test cell following motor failure. Cutting of damaged, water-soaked propellant with piano wire (88% solids AP/HTPB/Al 20,000–30,000 lb propellants consumed).	Test cell damaged	NA	4	30	1.3

(Cont.)

Table A1 Summary of accidents involving solid propellants (continued)

Date	Incident description/location	Failure mode, cause (NEW or propellant wt.) and [main ingredients]	Damage or injuries			Ref. no.	Hazard class
			Equipment or facilities	Injuries	Fatalities		
March 1984	Thiokol Corp., Brigham City, UT, south casting pit row	Casting house propellant fire. 7000-lb mix bowl of Shuttle propellant ignited at pit no. 4. Fire propagated to adjacent pit. One forward and one center segment consumed. Cause: previous spilled propellant squeezed between dump station roller and rail. Corrective action: revise safety precautions, training, and cleanup procedures (approx. 500,000–600,000 lb) [AP/Al/PBAN].	Two pits destroyed, local building damage	NA	NA	31	1.3
May 1984	Severomorsk Naval Base, USSR	Fire of unknown origin. Series of fires and explosions lasted for several days.	Multiple tons of munitions	NA	NA	Internet article	NA
Sept. 1984	Atlantic Research, Gainesville, VA	MK-30 cure stand cookoff and explosion (PVC-propellant).	Destroyed building and cure stand equipment	0	0	Verbal account	1.3
Jan. 1985	Waldheide, Heilbronn, Germany (Camp Redleg)	Pershing II 1st stage motor fire during removal from shipping container. Ignition from electrostatic discharge resulting from triboelectric charging of motor case. Attempt 1 off center binding occurred only aft end lifted 5 in. Lift attempt aborted; reset. Attempt 2 reposition boom motor hung-up/released; forward end raised 7-in. Motor shifted aft, striking a steel cross member in the container. Motor ignition occurred ESD/ESE. Local weather conditions contributed to ESD event—air temperature 20°F; motor temperature 10°F; low humidity (7900 lb) [AP/Al/HTPB].	Maintenance tent, crane, and rear of M.A.N. vehicle	9 Injured	3	32	1.3

1985	Pavlograd Chemical Plant, Pavlograd, Ukraine	Sympathetic detonation of six stage-2 SS-24 solid rocket motors. Motors were on cure cycle. Single motor exploded due to impurities in ingredients. (Account discussed with Pavlograd Chemical Officials, 1995) (76,600/motor) [AP/HMX/ADN/Al/ferrocene/HTPB].	Buildings and fatalities	NA	NA	Verbal account	1.1
June 1985	Thiokol Corp., Brigham City, UT	Fire during large-scale propellant mixing operation. Lightning strike caused power interruption. On restart, errant controller function caused mixer blade to scrape mixer bowl resulting in ignition. Deflagration with TNT equivalence of 1400 lb.	M-24 facility	NA	4	—	NA
1985	Thiokol Corp., Brigham City, UT	Mixer fire. Fire started while mixing an AP and ferrocene propellant. (E. Brown, MTI/Wasatch, confirmed SRAM hydromining fires.)	Building and all equipment destroyed	NA	3	NA	1.3
Sept. 1985	Thiokol Corp., Brigham City, UT	Flash fire occurred when a spatula that had been soaked in mineral sprits contacted the propellant samples. Conclusions state: only water to be used on tools contracting ferrocene. Recommend only separate covered buckets containing water to be used for ferrocene disposal.	NA	NA	NA	—	NA
Sept. 1985	Atlantic Research Corp. (ARC), Gainesville, VA	Catocene propellant; fire. 1-gal carton of propellant ignited when container cut by X-acto knife. Fire spread rapidly through propellant testing laboratory containing hundreds of pounds of dog bone samples. One fatality killed by flames traveling through exit path (verbal account confirmed by K. Graham, ARC).	Building and equipment	0	1	—	NA

(Cont.)

Table A1 Summary of accidents involving solid propellants (continued)

Date	Incident description/location	Failure mode, cause (NEW or propellant wt.) and [main ingredients]	Damage or injuries			Ref. no.	Hazard class
			Equipment or facilities	Injuries	Fatalities		
Oct. 1985	NA	Catocene propellant. Dropping 2 × 4 motor case with grain into bucket holding other grains ignited into violent burst of flame, 1 killed, holding bucket.	NA	NA	1	—	NA
Nov. 1985	U.S.A.F. Arnold Engineering Development Center, Arnold AFB, TN	PK, stage III (16,000 lb), Late aft dome failure, propellant pieces detonated on J-5 cell steel walls. Qualification testing a large rocket motor failed, 1100-lb propellant (NEW 1375 lb) [AP/HMX/PEG-NG/Al].	NA	NA	NA	—	1.1
Mid-1980s	Lockheed	Short range attack missiles (SRAM) Lockheed had two fires while hydromining (991 lb/motor) [86% T.S. AP/Al/CTPB/2.5% ferrocene].	NA	NA	NA	—	1.3
Mid-1980s	CSD	One fire while hydromining propellant containing ferrocene. (T. Rudy commented water soaking these propellants prior to hydromining should be investigated.)	NA	NA	NA	—	NA
Mid-1980s	U.K.–Falkland Islands conflict, H.M.S. Sheffield	U.K. lost six ships with damage to others. H.M.S. Sheffield, 4100-ton destroyer, struck by Exocet missile. Amidships strike, penetrated fuel tank and smashed into machinery spaces. Warhead did not detonate. Burning propellant ignited fuel fires, resulting in thick, acrid smoke spreading through the ship's ventilation system. 4.5-h firefight before abandoned ship. Ship sank under tow in heavy seas.	Destroyed ship; sank under tow	NA	20	NA	NA

Mid-1980s	U.K.–Falkland Islands conflict, Atlantic Conveyor	Atlantic Conveyor struck by Exocet missile(s). Warhead did not detonate. Ship was loaded with aluminum freight containers, aircraft, and combustible materials, including munitions and fuel. Burned out and sank 3 days later.	Destroyed ship	NA	12	NA	NA
Mid-1980s	U.K.–Falkland Islands conflict, H.M.S. Glamorgan	Exocet missile strike. 360-lb warhead did not detonate. Burning unspent propellant charge from missile started the ship on fire. A hanger and helicopter were destroyed by fire caused by shrapnel damage and fire.	Destroyed ship	NA	13	NA	NA
Mid-1980s	U.K.–Falkland Islands conflict, H.M.S. Antelope	Bomb strike; bomb did not detonate. Fires caused by the bomb detonating while attempting to defuse it. Runaway munitions fire destroyed ship.	Destroyed ship	NA	NA	NA	NA
Mid-1980s	Fire	Brass on steel. Ferrocene propellant impact/friction initiated fire. 1% ferrocene formulation. One incident reported.	—	0	0	—	NA
Mid-1980s	Explosion	Catocene/nitrate ester, impact initiated explosion, 7% catocene formulation. One incident reported.	—	NA	1	—	NA
Mid-1980s	Fire/Explosion	Hard spatulas/hand tools. Ferrocene sublimate 1% ferrocene, 7% NBF, 5% catocene, 2 and 8% P-XXI, and 7% P-IV formulations. Seven incidents reported.	—	0	6	—	NA
Mid-1980s	Fire	Instron machine fire initiated by impact/friction, ESD. 1% catocene (Zr) formulation. Two incidents reported.	—	0	0	—	NA
Mid-1980s	Fire/Explosion	Machining propellant, friction, pinch initiated. 0.3% catocene formulation. Two incidents reported.	—	0	1	—	NA

(Cont.)

Table A1 Summary of accidents involving solid propellants (continued)

Date	Incident description/location	Failure mode, cause (NEW or propellant wt.) and [main ingredients]	Damage or injuries			Ref. no.	Hazard class
			Equipment or facilities	Injuries	Fatalities		
Mid-1980s	Fire	Moving hardware. Fire initiated by impact. 5% catocene formulation. One incident reported.	—	0	0	—	NA
Mid-1980s	Fire	Waste drop 2%, 3% catocene (Zr), 1% NBF, 1% ferrocene formulations. Five incidents reported.	—			—	NA
Mid-1980s	Fire	Hand cutting propellant. Friction initiated fire. 2% catocene (ZrC) formulation. One incident reported.	—	0	1	—	NA
April 1986	Vandenberg AFB, CA	Titan 34, flight D9 case burst 800 ft above launch pad, many ground craters, propellant debond between insulation and propellant grain (300,000) [AP/Al/PBAN].	Crane	NA	1	NA	1.3
Jan. 1987	Allegany Ballistics Lab., Cumberland, MD	Horizontal bandsaw fire. Sawing operations were complete dry, dry propellant chips contributed to the intensity of the fire (50 lb) [QMZ-1 composite].	Minor damage to bandsaw and building	0	0	27	1.1
April 1987	Thiokol Corp., Brigham City, UT	Disposal waste drop incident. 12-month aging tests were completed on propellant samples. The propellant was aged at 160°F. Plastic bag containing propellant scrapes placed in disposal container (dry metal drum). Fire caused by impact or friction.	NA	NA	NA	—	NA

May 1987	U.S.S. Stark	Hit by Exocet missiles while operating in Persian Gulf. Missile warhead did not detonate. Missile penetrated about 80 ft inboard. Fire resulted 120 lb burning solid-propellant burning at 3000–3500°F. Heat, acid vapors, and smoke filled surrounding area impeding escaping personnel from compartments. Second missile hit, penetrated hull, and detonated 5-ft inboard. Detonation ripped large hole in hull, accelerating combustion of burning materials. Portside fire main lost in blast. Vertical fire spread into compartments directly above main blaze.	NA	Several	37	NA	NA
May 1987	Thiokol Corp., Brigham City, UT	MX/Peacekeeper, Stage I (303), flare followed by natural extinguishment. Occurred during mandrel pulling operation, after cure operators heard crackling noise, saw smoke. No ignition of grain. ESD and friction. 98,462 pounds of AP/Al/HTPB		NA	0	0	1.3
Dec. 1987	Thiokol Corp., Brigham City, UT	MX/Peacekeeper 1st stage (322) fire and case burst during mandrel pulling operation with Peacekeeper ignition from electrostatic discharge resulting from triboelectric (ESD friction combination) charging of tooling/propellant (98,462 lb) [AP/Al/HTPB].	Destroyed facility	NA	5	33	1.3
May 1988	Pepcon AP plant Henderson, NV	More than 8×10^6 lb AP burned and detonated. Local residents included in injured (C&EN, 1988).	Destroyed facility, $\$73 \times 10^6$	350	2	—	1.3

(Cont.)

Table A1 Summary of accidents involving solid propellants (continued)

Date	Incident description/location	Failure mode, cause (NEW or propellant wt.) and [main ingredients]	Damage or injuries			Ref. no.	Hazard class
			Equipment or facilities	Injuries	Fatalities		
March 1989	Hercules, Bacchus, UT	Fire during large-scale propellant mixing operation. Cover of infrared fire detector fell into mixer (26,000 lb) [AP/Al/HTPB].	1800-gal mixer and mix building lost	0	0	—	1.3
May 1989	Aerojet, Sacramento, CA	Fire during high-pressure water-jet propellant removal operation with MM II, 2nd stage. Faulty purge water flow subsystem in water-jet removal system caused friction on propellant that had accumulated in boom bearing block (12,000 lb) [AP/Al/CTPB].	Moderate	0	0	—	1.3
Sept. 1990	Edwards AFB, CA	Titan IV SRMU fire resulted from ground impact during movement by crane near test stand. Crane tipped over due to unstable working surface. Motor impacted the ground and skid down test stand flame bucket. Ignition most likely from impact (AP/HTPB/Al NEW).	Test stand, crane, and nearby buildings destroyed (\$9 × 10 ⁶ loss)	NA	NA	—	1.3
June 1992	Honeywell, Sacramento, CA	Minuteman II, 2nd stage motor. Dropped motor 18 in. to roadway while transferring on forklift (500 lb) 88% total solids [CTPB–AP/AL].	Destroyed forklift	1 Burned	0	—	1.3
June 1992	Indian Head, White Oak, MD	Storage magazine destroyed. Propellant fire and explosion, 4300 lb propellant consumed. Cause: improper storage of materials.	—	—	—	NA	NA

1995	Desert Storm, Persian Gulf, Camp Doha, Kuwait	Transport vehicle fire. Fire spread and secondary explosions resulted. Injuries occurred while clearing damaged ordnance. More tanks were lost in single incident than in the entire Desert Storm conflict (cookoff incident).	U.S. Army tanks and materials	3	52	NA	—
April 1996	U.S. Naval Surface Weapons Center (NSWC), Indian Head, MD	Brick magazine destroyed. Spontaneous combustion. Fragments of asbestos materials scattered to local public neighborhood (cook off incident).	Magazine and contents	0	0	NA	NA
Feb. 1998	NSWC, Indian Head, MD	150-gal, single-blade, vertical mixer fire and explosion during manufacture of an air bag propellant. RDX added by a remotely operated automatic feeder. Small particles falling in a continuous manner generated static charge field. ESD/ESE event.	Building 1026, including 150-gal vertical mixer	0	0	NA	NA
July 1999	NAWC Weapons Div., China Lake, CA	During disposal operation, propellant containing catocene inadvertently ignited when samples removed from wooden box.	None	1	0		1.3L

Acknowledgment

A work of this type incorporates the research and thoughts of many people. Unfortunately there are many instances where a citable reference is not available. The authors would like to acknowledge the many contributions of our colleagues.

References

- ¹Boggs, T. L., and Derr, R. L., (eds.), *Hazard Studies for Solid Propellant Rocket Motors*, NATO AGARDograph 316, 1990.
- ²Mellor, A. M., Boggs, T. L., Covino, J., Dickinson, C. W., Dreitzler, D., Thorn, L. B., Frey, R. B., Gibson, P. W., Roe, W. E., Kirshenbaum, M., and Mann, D. M., "Hazard Initiation in Solid Rocket and Gun Propellants and Explosives," *Progress in Energy and Combustion Science*, Vol. 14, No. 3, 1988, pp. 213–244.
- ³Mellor, A. M., Mann, D. M., Boggs, T. L., Dickinson, C. W., and Roe, W. E., "Hazard Initiation in Energetic Materials: Status of Technology Assessment," *Combustion Science and Technology*, Vol. 54, 1987, pp. 203–215.
- ⁴Boggs, T. L., "Combustion and Safety of Solid Propellant Rocket Motors," *Combustion of Solid Propellants*, NATO, AGARD-LS-180, 1991, pp. 9/1–9/14.
- ⁵Boggs, T. L., "The Hazards of Solid Propellant Combustion," *4th International Symposium on Special Topics in Chemical Propulsion: Challenges in Propellants and Combustion*, 1996.
- ⁶"Transport of Dangerous Goods, Manual of Tests and Criteria," United Nations, ST/SG/AC.10/11/Rev.2, 1995.
- ⁷"Department of Defense Ammunition and Explosives Hazard Classification Procedures," TB 700-2, NAVSEAINST 8020.8B, TO 11A-1-47, DLAR 8220.1, 5 Jan. 1998.
- ⁸Gibson, P. W., *Hazard Studies for Solid Propellant Rocket Motors*, edited by T. L. Boggs and R. L. Derr, NATO AGARDograph 316, 1990, p. 89.
- ⁹Graham, K. J., *Hazard Studies for Solid Propellant Rocket Motors*, edited by T. L. Boggs and R. L. Derr, NATO AGARDograph 316, 1990, pp. 89–90.
- ¹⁰Boggs, T. L., Price, C. F., Richter, H. P., Atwood, A. I., Lepie, A. H., Zwierzchowski, N. G., and Boyer, L. R., "Detonation of Undamaged and Damaged Energetic Materials," *Combustion and Detonation Phenomena, 19th International Annual Conference of ICT*, 1988, pp. 30-1–30-13.
- ¹¹Ewell, R. B., Irwin, O. R., and Vail, R. W., Jr., "Project SOPHY—Solid Propellant Hazards Program, Volume I and II (U)," U.S. Air Force Rocket Propulsion Lab., AFRPL TR 67-211, Vols. 1 and 2. Edwards AFB, CA.
- ¹²Noguez, B., Berger, H., Gondouin, B., and Brunet, J., "An Odd Bore Effect on Bullet Induced Detonation of High Energy Propellant Grains," *American Defense Preparedness Association Symposium on Compatibility of Plastics and Other Materials with Explosives, Propellants and Pyrotechnics*, 1989.
- ¹³Boggs, T. L., Dickinson, C. W., Barrington, L. M., Belanger, C., Connor, J., and Haskins, P. J., "Hazards of Energetic Materials and Their Relation to Munitions Survivability," *Proceedings of the 22nd International Annual Conference of ICT*, 1991.
- ¹⁴James, H., "Final Report, Vol. III—Bullet/Fragment Impact," Technical Cooperation Program W Action Group-11, Hazards of Energetic Materials and their Relation to Survivability, Nov. 1994.

¹⁵Boggs, T. L., Price, C. F., and Derr, R. L., "Transient Combustion: An Important Consideration In Deflagration to Detonation Transition," *Propulsion and Energetics Panel 63(A)th Meeting*, CP-367, AGARD, pp. 12-1-12-2.

¹⁶Boggs, T. L., "Thermal Behavior of RDX and HMX," *Fundamentals of Solid-Propellant Combustion*, Vol. 90, Progress in Astronautics and Aeronautics, AIAA, Washington, DC, 1984, pp. 121-175.

¹⁷Boggs, T. L., Price, C. F., Atwood, A. I., Zurn, D. E., and Derr, R. L., "Role of Gas Phase Reactions in Deflagration-to-Detonation Transition," *Seventh Symposium (International) on Detonation*, Naval Surface Weapons Center, NSWC MP 82-834, 1982, pp. 216-224.

¹⁸Covino, J., and Hudson, F. E., "Current Assessment Methodology for Electrostatic Discharge Hazards of Energetic Materials," *Journal of Propulsion*, Vol. 7, No. 6, 1991, pp. 894-903.

¹⁹Kent, R., and Rat, R. J., *Electrostatics*, Vol. 17, 1985, p. 299.

²⁰Belyaev, A. F., et al., "Transition from Deflagration to Detonation in Condensed Phases," translated by Israel Program for Scientific Translations, Springfield, VA, National Technical Information Service, 1973 (1975 translation).

²¹Bradley, H. H., Jr., and Boggs, T. L., "Convective Burning in Propellant Defects: A Literature Review," Naval Weapons Center, NWC TP 6007, China Lake, CA, 1978, pp. 1-96.

²²Kuo, K. K., and Kooker, D. E., "Coupling Between Nonsteady Burning and Structural Mechanics of Solid Propellant Grains," *Nonsteady Burning and Combustion Instability of Solid Propellants*, Vol. 143, Progress in Astronautics and Aeronautics, AIAA, Washington, DC, 1992, pp. 465-517.

²³Bernecker, R. R., "DDT Studies of a High Energy Spherical Ball Propellant," *Ninth Symposium (International) on Detonation*, Office of the Chief of Naval Research, OCNR 113291-7, Vol. I, pp. 354-362.

²⁴McAfee, J. M., Asay, B. W., and Bdzil, J. B., "Deflagration-to-Detonation in Granulated HMX: Ignition, Kinetics, and Shock Formation," *Tenth International Detonation Symposium*, Office of Naval Research, ONR 33395-12, 1993, pp. 716-723.

²⁵Bernecker, R. R., "The DDT Process in High Energy Propellants," *Hazard Studies for Solid Propellant Rocket Motors*, CP-367, AGARD, 1984, pp. 14-1-14-16.

²⁶Beauregard, R., "Insensitive Munitions—Are They Worth the Cost?"

²⁷Biasutti, G. S., *History of the Accidents in the Explosives Industry*, Jan. 1985 ed.

²⁸Hodson, G. B., Baker, D. E., Arhart, R. W., and Bodrero, T. A., "Hill AFB Bunker 1825 Fire Investigation," *JANNAF Safety and Environmental Protection Subcommittee Meeting*, Chemical Propulsion Information Agency Pub. 543, (CPIA Abstract No. 1992-0078) AD D604 025 U-A Laurel, MD, 1992, pp. 147-155.

²⁹Dunn, B. M., Durbin, A. M. R., Jones, A. L., Lund, E. G., and Partington, R. L., "Short Range Attack Missile (SRM) Propulsion 3-Decades of History," AIAA Paper June 1994; also Chemical Propulsion Information Agency, (CPIA Abstract No. 1996-0941), Laurel, Maryland, 1996.

³⁰Nasser, L. A., "Handling of Damaged Propellant Experiments at AFAL," Final Technical Rept., Sverdrup Technology, Inc., AFAL-TR-87-042, Arnold AFB TN, April-May 1987, available Defense Technical Information Center/National Insts. of Standards and Technology; also Chemical Propulsion Information Agency (CPIA Abstract 1988-0675), Laurel, MD, 1988. AD B117 723 U-A.

³¹Davis, D. B., Macbeth, A. W., Thompson, G. W., Van Dusen, S. A., Kase, D. W., Mckenzie, A. K., Davis, L. E., Thompson, A. R., Johnson, W. B., Loosle, J. W., "Large

Motor Casting Pit Incident Report—2 March 1984,” Morton Thiokol, Inc., Technical Rept. TWR-14335, Brigham City, UT, also Chemical Propulsion Information Agency, (CPIA Abstract No. 1984-5003), U-A Laurel, MD, 1984.

³²Knaur, J. A., “Technical Investigation of 11 January 1985 Pershing II Motor Fire,” 1st-Stage, *DDESB Explosives Safety Seminar*, Vol. I, 1986, Chemical Propulsion Information Agency, pp. 1005–1013 (CPIA Abstract No. 1986-10050), Laurel, MD, 1986. AD P005 343 U-A.

³³Magann, T. F., Davis, L. E., and Campbell, L. A., “Combined Stimuli Solid-Propellant Hazards Testing,” *JANNAF Propulsion Systems Hazards Subcommittee Meeting*, Chemical Propulsion Information Agency Pub. 509, Vol. I, (CPIA Abstract No. 1990-0875) AD D603 997 U-A. Laurel, MD, 1990, pp. 367–374.

II. Combustion of Solid Energetic Materials

Overview of Combustion Mechanisms and Flame Structures for Advanced Solid Propellants

M. W. Beckstead*

Brigham Young University, Provo, Utah

I. Introduction

THE solid ingredients used most often in modern solid propellants are ammonium perchlorate (AP) and cyclotetramethylenetetranitramine (HMX) [or cyclotrimethylenetrinitramine (RDX)]. The two most common binder systems consist of either an inert binder system based on a polybutadiene polymer, typically hydroxy-terminated polybutadiene polymer (HTPB), with various plasticizers, additives, and cross-linking agents, or an active binder system based on energetic components such as nitroglycerin (NG) and nitrocellulose (NC) or with a polyester or polyether polymer (PE). In general, comparing the combustion characteristics of monopropellants with the characteristics that occur when the monopropellants are combined with other ingredients to form propellants can lead to an understanding of the physical mechanisms that are involved. Note that the monopropellant burning rate of AP, HMX, and a typical NG/NC (or NG/PE) double-base propellant are similar. However, when a fuel and oxidizer are mixed together, a diffusion flame usually results. In AP/HTPB this diffusion flame has a huge impact on the combustion process as a function of pressure. Mixing HMX into HTPB to form a composite propellant also has a significant effect on the combustion, but in a different manner than that observed with an AP/HTPB system. Combining HMX with NG and NC or NG/PE to form a composite modified propellant results in little change in the burning rate from that observed with the individual ingredients. Observations such as these have helped to establish an understanding of the combustion mechanisms that determine the burning rate characteristics of typical propellants.

During the past decade the search for more energetic and more environmentally acceptable propellants has led to the development of advanced ingredients such as hexanitrohexaazaisowurtzitane (CL-20), ammonium dinitramide (ADN),

Copyright © 1999 by the American Institute of Aeronautics and Astronautics, Inc. All rights reserved.

*Professor, Chemical Engineering Dept.

hydrazinium nitroformate (HNF), glycidyl azide polymer (GAP), bis-azide methyl oxetane/3-azidemethyl 3'-methyl oxetane (BAMO/AMMO), etc. These are considered advanced in the sense that they are not commonly used in operational motors. The purpose of this study is to relate the observed combustion characteristics of the individual ingredients (as monopropellants) to postulated flame structures and mechanisms, based on observations with AP and HMX propellants. This chapter discusses the combustion and thermodynamic characteristics of the monopropellants and then conjectures the implications of various mechanisms on the potential combustion characteristics of actual propellants. The emphasis is on the qualitative effects of flame structure on combustion mechanisms. Time will not allow a detailed examination of the quantitative aspects of flame structure. For the same reasons, consideration of combustion characteristics has focused on flame temperatures and on burning rate characteristics. Temperature sensitivity, erosive burning, ignition, and unstable combustion are beyond the scope of that considered here.

II. Monopropellant Burning Characteristics

In this section the monopropellant combustion characteristics of several ingredients will be examined to lay a foundation for the understanding of propellants containing these ingredients. Most of our understanding of combustion mechanisms has been based on AP composite propellants, and to a lesser extent HMX composite propellants. Because these two ingredients will be used as a basis for the comparisons to follow, some of their general combustion properties are summarized in Table 1. These property values have typically been taken from previous review articles, for example, those of Kubota¹ and Boggs.² Note that the two compounds are very different in almost every category listed, except burning rate and exponent. The chemical composition, NH_4ClO_4 vs $\text{C}_4\text{H}_8\text{O}_8\text{N}_8$, the melt, surface and flame temperatures, and heats of formation are all very different, and yet the burning rates and exponents are very similar.

The relative burning rates of a large number of typical monopropellant ingredients are shown in Fig. 1. Most of these data (AP, HMX, RDX, ADN, CL-20, and HNF) are summarized in a recent paper by Atwood et al.³ The AN data are from Ref. 4. The azide data (GAP and BAMO) are from Kubota and Sonobe,^{5,6} Kubota,⁷ and Flanagan et al.⁸ The burning rate of the azides depends on the relative concentration of the azide and the material used to solidify and/or plasticize the azide. Typically hexamethylene diisocyanate (HMDI) is used to cure GAP and tetrahydrofuran (TFH) with BAMO. The referenced burning rate data show that the azide burning rate is directly proportional to the N_3 bond density. The data

Table 1 Comparison of AP and HMX combustion properties

Property	AP	HMX
Burning rate at 68 atm, cm/s	0.8	1.1
Pressure exponent	~0.7	~0.8
Chemical formula	NH_4ClO_4	$\text{C}_4\text{H}_8\text{O}_8\text{N}_8$
Adiabatic flame temperature, K	1405	3278
Melt temperature, K	~725–825	553
Surface temperature at 68 atm, K	~825	~750
Heat of formation, Kcal/mole	–70.7	18.1

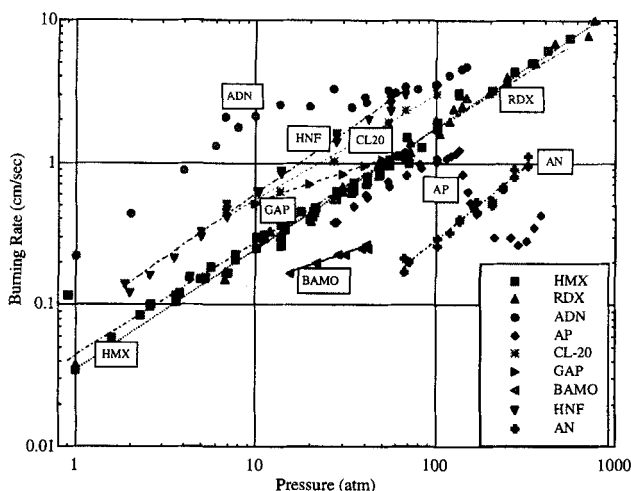


Fig. 1 Burning rate characteristics of ingredients used in solid propellants.

included in Fig. 1 were chosen for materials with $\sim 80:20$ mixture of GAP/HMDI and a $60:40$ mixture of BAMO/TFH as those mixtures were characterized most completely. Monopropellant ingredients used in double-base propellants, that is, nitrate esters, will be discussed later.

Most of the monopropellants examined here exhibit linear characteristics relative to the power law burning rate curve, $r = bP^n$. It is significant that the monopropellant burning rates of HMX and AP are very similar, at least from ~ 30 to ~ 150 atm with HMX having a rate $\sim 20\%$ greater than AP. Above ~ 150 atm the AP burning rate curve has a dip in it that is very uncharacteristic of most monopropellants. However, this behavior is not really applicable to motor operating conditions and, thus, will not be discussed further. ADN has two slope changes indicating rather complex combustion mechanism changes. At a typical operating pressure of 68 atm, ADN and HNF have the highest rates $\sim 3\text{--}4$ cm/s, whereas BAMO and AN are the lowest, approximately a full order of magnitude lower. Most of the ingredients have similar exponents, $\sim 0.8\text{--}1.0$, except for BAMO and GAP (both azides with exponents of ~ 0.5), and ADN, which has a variable exponent.

Table 2 contains a summary of some of the combustion properties of these and other propellant ingredients. Material densities are typically in the range of $1\text{--}2$ g/cm³ (Refs. 1 and 2). Heats of formation vary widely,¹ but are extremely important, because they are a dominant factor in determining flame temperature. The equilibrium conditions were calculated from the given heat of formation, atomic composition, and density of each ingredient. The flame temperature is seen to vary significantly, from a low of 1247 K for AN to a high of ~ 3500 K for CL-20. Most of the ingredients are made up of the CHON atoms. AN and ADN only contain HON atoms. AP is unique because it contains chlorine and produces the environmentally undesirable HCl. AP, ADN, AN, HNF, and CL-20 all produce molecular oxygen in their exhaust products, from 29% for AP decreasing down to 3% for CL-20.

It is informative to examine the burning rates of the various ingredients as a function of their calculated flame temperature. Although it is somewhat intuitive to expect burning rate to be proportional to flame temperature (e.g., Refs. 9 and 10), this is not necessarily the case. This is shown in Fig. 2. There is a general trend,

Table 2 Monopropellant ingredient properties

Ingred.	Density (g/cc)	ΔH_f (Kcal/mole)	Equilibrium products, 1000 psi (mole fractions)								
			T_f , K	MW	O ₂	H ₂ O	CO	CO ₂	H ₂	N ₂	HCl
<i>Nitrates</i>											
ADN	1.72	−35.8	2062	24.8	0.20	0.40				0.40	
AN	1.73	−87.3	1247	22.9	0.14	0.57				0.29	
<i>Perchlorate</i>											
AP	1.95	−70.7	1405	27.9	0.29	0.38				0.12	0.20
<i>Nitramines</i>											
CL-20	1.96	90.0	3571	27.4	0.02	0.14	0.23	0.10	0.03	0.37	
HMX	1.90	18.1	3278	24.3		0.23	0.25	0.09	0.09	0.33	
RDX	1.82	14.7	3286	24.3		0.23	0.25	0.09	0.09	0.33	
HNF	1.86	−17.2	3090	26.4	0.10	0.33	0.02	0.12	0.01	0.35	
<i>Nitrate Esters</i>											
NG	1.60	−90.7	3287	28.9	0.07	0.28	0.11	0.28	0.01	0.18	
TMETN	1.47	−106	2839	23.1		0.26	0.36	0.10	0.14	0.14	
DEGDN	1.39	−103.5	2513	21.8		0.25	0.37	0.08	0.19	0.11	
NC	1.65	−61.4	2425	28.4		0.21	0.43	0.12	0.13	0.11	
<i>Azides</i>											
BAMO	1.28	53.3 ^a	1725	15.2			0.11		0.48	0.39	
GAP	1.27	2.85 ^a	1570	15.7		0.01	0.19		0.43	0.32	
AMMO	1.26	4.32 ^a	1536	12.2		0.01	0.13		0.58	0.23	

^aKcal/100 g

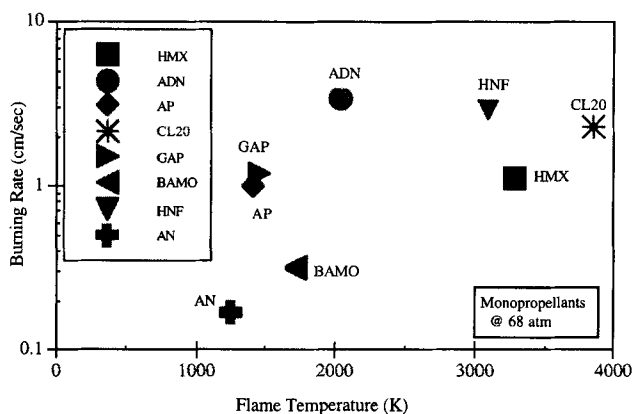


Fig. 2 Dependence of monopropellant burning rate on flame temperature.

but there are many discrepancies. AP, GAP, and HMX all have about the same burning rate, but their flame temperatures differ from 1400 to ~3200 K. ADN has the highest rate, but its flame temperature is a relatively low 2035 K. It appears that burning rates are dependent on many phenomena, including the initial bond breaking steps, concentration of various species leaving the burning surface (which bear on kinetics and the distribution of energetics), and the general mixture of atoms in the products. Although a quantitative prediction of propellant burning rate is beyond the scope of this chapter, it is felt that qualitative generalizations can be made based on the collective properties of the combined ingredients.

Although AP and HMX have very different flame temperatures, they have very similar burning rates. Because of HMX having a higher flame temperature than AP (3200 vs 1400 K), one might expect it to have a much higher burning rate than AP. Thus, it is somewhat surprising that the HMX burning rate is only ~20% greater than that of AP. This is apparently due to a higher reactivity of reactions involving chlorine oxides (i.e., the typical surface products from the condensed phase of the AP) compared to reactions involving nitrogen-containing compounds (i.e., the typical surface products) of HMX. This observation is supported by the much lower burning rate of AN, which has a flame temperature comparable to AP but does not give off the reactive chlorine oxides. The decomposition products from AN are more comparable to those of ADN, and one would expect similar reaction kinetics to be involved with AN and ADN, but not with AP. Therefore, the much lower rate of AN apparently corresponds to the much lower flame temperature of AN compared to that of ADN.

In a similar sense, the AP reaction path follows the reduction of the chlorine atom, whereas all of the other ingredients relate to some kind of a nitrogen reduction path. Although Fig. 2 does not show an obvious correlation between various ingredients, the following paragraphs show that there can be definite correlations within families of ingredients.

Double-base propellants are the classic example of the nitrogen reduction path. A characteristic of double-base propellants is that they burn with a two-stage flame. The inner flame is ~1200–1700 K depending on both pressure and binder energy. A dark zone separates the inner flame from a final flame of ~1500–3000 K, again

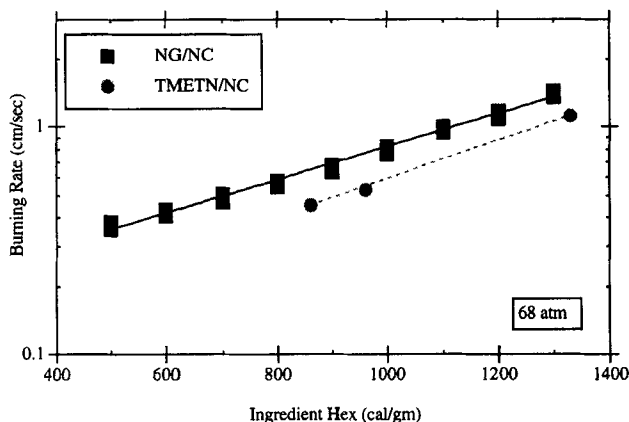


Fig. 3 Burning rate dependence on binder heat of explosion for families of nitrate ester propellants based on both NG/NC and TMETN/NC.

depending on pressure and binder energy. The effect of the heat transfer from the flame on the burning rate of the material is dominated by the inner flame that, in turn, dominates the burning rate. At high pressure (~ 100 atm) the two reaction zones merge, and only one flame is observed at higher pressures. The inner flame is apparently characterized by the reaction of NO_2 to form NO. The NO is relatively stable, leading to the dark zone. The stability of the NO molecule has also been observed in studies of air pollution. The end of the dark zone is characterized by the reaction of NO to react with various intermediates (such as N_2O and NO itself) and ultimately form N_2 .

Because of the dark zone, it is not appropriate to correlate the burning rate with the calculated adiabatic flame temperature. However, the calculated heat of explosion (HEX) is an appropriate correlation parameter and represents the energy available in the combustion process. Figure 3 is a plot of burning rate vs heat of explosion for a classic NC/NG double-base series of propellants, and the corresponding analogs with trimethylolethane trinitrate (TMETN) substituted for NG (Ref. 11). There is a very definite correlation between burning rate and propellant energy. However, the NG-based propellants exhibit a higher rate than the TMETN propellants. NG has more energy than the TMETN, as reflected by a higher flame temperature; thus, one cannot expect the burning rates of all nitrate esters to fall within the same correlation. Cohen and Lo¹² explained this effect of nitrate ester ingredient by the species concentration of NO_2 available for the primary flame zone kinetics.

Note that the burning rate of a typical double-base binder of ~ 1000 HEX, is ~ 0.8 cm/s at 68 atm, compared to that of AP and HMX monopropellants, which are ~ 0.8 and ~ 1.1 cm/s, respectively. There is very little difference in their burning rates, even though the flame structure and chemistry are significantly different.

Some time ago, Fogelzang et al.¹³ obtained data showing a correlation of burning rate vs flame temperature for families of N-nitro (nitramine) and C-nitro (nitrosamine) compounds. These data are presented in Fig. 4. Data were obtained for compounds with varying chemical structure, but with common backbone characteristics. The nitramines include both RDX and HMX. The data were taken at very high pressure (300 atm), but both families show a readily identifiable

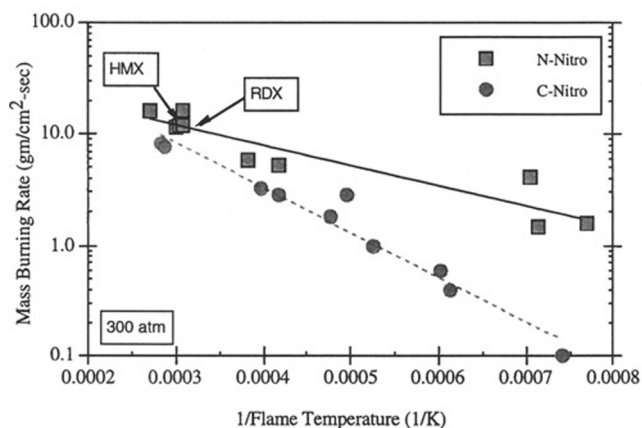


Fig. 4 Comparison of monopropellant burning rate dependence on flame temperature for families of nitramines (N-nitro) and nitrosamines (C-nitro) compounds.

correlation. The intuitive trend of rate increasing with flame temperature is present. Thus, within a given family of ingredients having a common backbone structure, one can expect the rate to correlate with flame temperature.

Having examined the burning rate characteristics of homogeneous ingredients, it is appropriate to consider the combustion characteristics of propellants that result from mixtures of ingredients.

III. Solid-Propellant Combustion Characteristics

The adiabatic flame temperatures for AP, ADN, HMX, and CL-20 in an HTPB binder have been calculated and are shown in Fig. 5 for varying oxidizer concentration. AP and ADN, which are true oxidizers, both show a maximum flame temperature near their stoichiometric mixture ratio. In the range of 80–90% oxidizer,

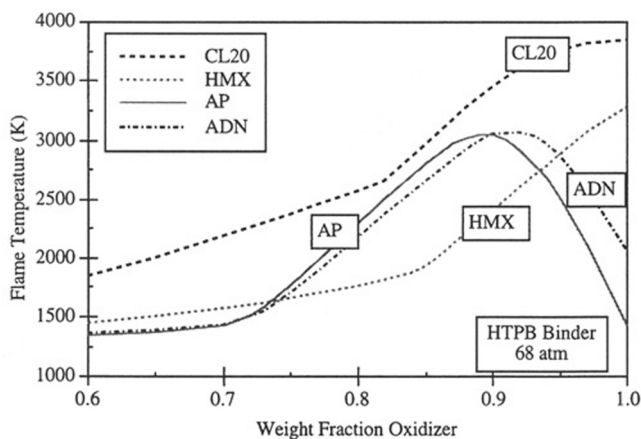


Fig. 5 Calculated flame temperatures for AP, ADN, CL-20, and HMX composite propellants.

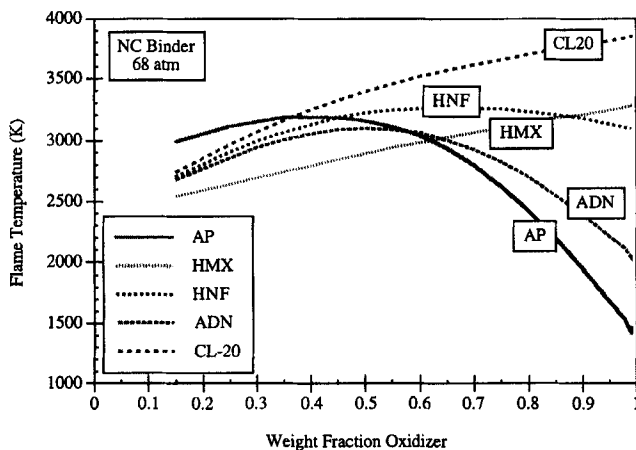


Fig. 6 Calculated flame temperatures for AP, ADN, HNF, CL-20, and HMX in an NC-based propellant.

which is typical of practical propellants, AP, ADN, and CL-20 all have similar flame temperatures, whereas HMX is ~ 1000 K lower. These calculated temperatures should be characteristic of the diffusion flame in propellants that, in turn, relates to the particle size dependence of burning rate. HMX/HTPB propellants typically have a burning rate much lower than HMX monopropellant, whereas AP/HTPB propellants typically have a burning rate higher than the AP monopropellant rate. Apparently the HMX diffusion flame robs energy from the monopropellant flame, suppressing the overall propellant burn rate. Qualitatively this is in agreement with the calculated flame temperature.

The calculated flame temperatures for AP, ADN, HMX, HNF, and CL-20 in an NC binder are shown in Fig. 6. AP, ADN, and HNF all show a maximum flame temperature near their stoichiometric mixture ratio. Up to 50–70%, which is typical of practical propellants, all have similar flame temperatures. Observe that the addition of HMX to a typical double-base propellant usually has little effect on the burning rate of the propellant.^{14,15} As was noted, the relative monopropellant rates of HMX and double-base binders are very similar. Thus, combining two ingredients with comparable monopropellant rates and no effective diffusion flame results in little change in the overall propellant rate.

Figure 7 shows data varying HMX concentration in a double-base binder.¹⁶ The burning rate of the pure HMX is within $\sim 20\%$ of the burning rate of the double-base binder. The rate of the mixtures goes through a minimum between the rates of the two ingredients. Other experimental data,^{17–20} show the same trend and additionally show that adding different-sized HMX particles at concentrations up to $\sim 60\%$ did not significantly alter the burn rate. This is not surprising considering that both HMX and double-base binder each contain CHON elements and similar energy levels. Calculated flame temperatures varying the percent HMX for double-base binders of varying HEX show that for a high-energy binder there is little change in the flame temperature of the propellant, for example, see Fig. 6. For a low-energy binder, adding HMX increases the flame temperature. The calculated temperatures all increase toward the adiabatic flame temperature of HMX, which is higher than any of the double-base flame temperatures.

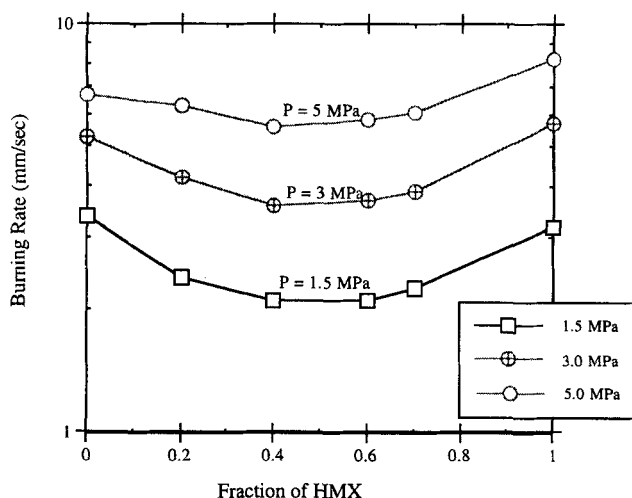


Fig. 7 Burning rate characteristics of HMX in a double-base binder at varying pressures.

However, the addition of AP to a double-base propellant increases the rate significantly, increasingly so for decreasing AP particle size.^{11,15,17,18} Even though the calculated flame temperatures for an AP vs an HMX/double-base propellant are not significantly different, the resultant burning rates are. As noted, the kinetics associated with the chlorine reduction path appear to be significantly faster than those associated with the nitrogen reduction path. Thus, the AP related diffusion flame has a significant effect on the burning rate, whereas the corresponding HMX products diffusing into double-base products are sufficiently similar that there is little change in burning rate.

IV. Solid-Propellant Combustion Mechanisms

The objective of the chapter is to utilize the basic combustion characteristics presented in the preceding sections to project the combustion characteristics of propellants made up of mixtures of advanced ingredients. To develop this logic, a brief review of the physical picture of how older propellants burn will be made.

A. Phenomenological Concepts

Understanding of the combustion mechanisms that determine solid-propellant burning rates have evolved over the past 30 years. In the 1960s, emphasis was determining the critical mechanism that controlled the burning rate and most attention was given to AP composite propellants. A typical example of identifying a single critical mechanism that would describe combustion behavior was the Summerfield granular diffusion flame (GDF) model.²¹ That model was based on the concept that fuel and oxidizer gasify at the burning surface, leaving the surface in pockets of gases that diffuse together, reaction to determine the propellant burning rate. Although this interpretation enjoyed a degree of popularity, it was too narrow in concept to describe the great variation in burning rates observed with AP

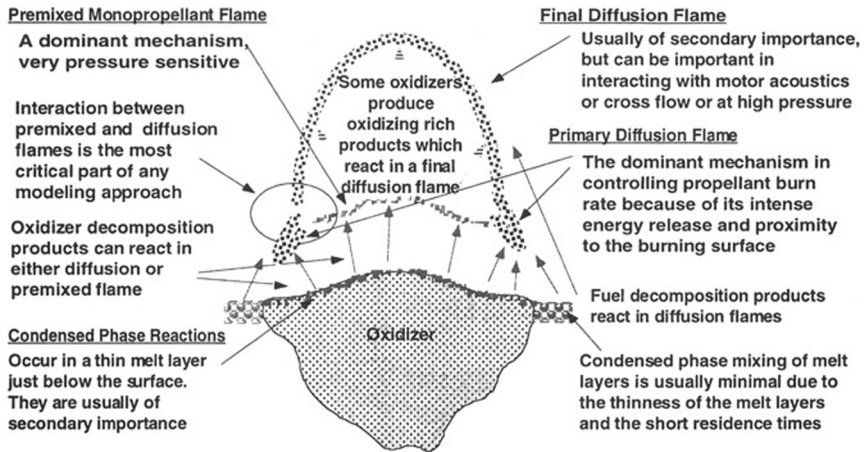


Fig. 8 Conceptual depiction of the BDP model for AP composite propellants.

propellants for varying pressure, oxidizer particle size, and loading. In general, finer AP particle size causes an increase in burning rate, but at very low or high pressures this effect is diminished. Similarly, increased AP concentration tends to increase the burning rate, but this effect is also reduced at extreme pressures. The GDF model was not comprehensive enough to explain such a wide range of behavior.

In the late 1960s Hermance²² proposed a model of heterogeneous reaction at the burning surface between oxidizer and binder, creating an increased, reacting surface area. Although this concept resulted in a mathematical model that correctly gave the increased burning rate with decreasing particle size, Scanning Electron Microscope (SEM) photographs²³ failed to show the postulated undercutting of oxidizer crystals.

In the early 1970s, Beckstead et al. published their multiple-flame [Beckstead, Derr, and Price (BDP)] model.²⁴ This model proposed a complex interaction between the oxidizer monopropellant flame and two different diffusion flames occurring above the oxidizer binder interface. Figure 8 illustrates this. This physical picture was sufficiently comprehensive to be able to explain most of the observed propellant behavior for many years.

B. AP Composite Propellants

Using this model, the burning rate is proposed to be very particle-size dependent due to the primary diffusion flame. For very small particles the diffusion aspect of the primary diffusion flame can be reduced, and the kinetic aspect can become dominant. For these conditions the particles and binder approach a premixed condition. This behavior is illustrated in Fig. 9, adapted from Ref. 25. For increasingly large particles the monopropellant flame dominates and similarly reduces the particle-size effect.

These results indicate that the burning rate can change by an order of magnitude through varying the AP particle size. For lower pressures the curve will shift downward and to the left, and for higher pressures it will shift upward and to the

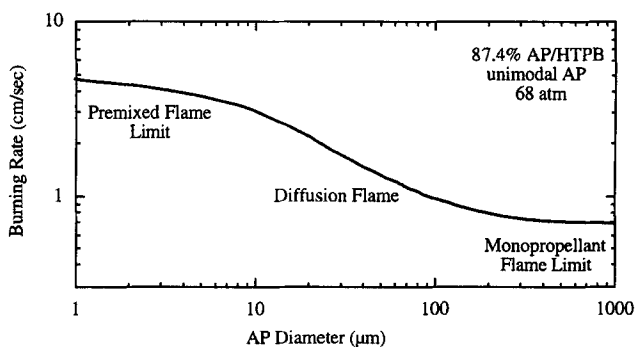


Fig. 9 Variation in burning rate due to varying particle size, as predicted by the BDP model.

right. The conclusion was reached that the primary diffusion flame was the dominant mechanism in determining the burning rate of AP composite propellants. However, it is very apparent that at either low pressures or for very small particles, the kinetic aspect of the primary diffusion flame will be dominant, whereas for high pressures and/or large particles, the monopropellant flame will become dominant.

AP and HMX appear to have similar monopropellant combustion characteristics, but when mixed with a fuel binder into a composite propellant, the resultant burn rates vary by as much as an order of magnitude. The burn rate of AP composite propellants exhibits a very strong particle size dependence (as indicated in Fig. 9). In contrast, the burn rates of HMX composite propellants are much lower than those of AP propellants and show a much smaller particle-size dependence.

Thermochemical calculations for AP composite propellants indicate a primary flame temperature on the order of ~2500–2800 K for typical concentrations as shown in Fig. 5. Thus, the AP diffusion flame is much more energetic than the AP monopropellant flame and leads to higher burning rates. HMX composite propellants have adiabatic flame temperatures on the order of 2000 K implying a less energetic diffusion flame than the monopropellant flame leading to reduced rates. Because of the very large differences in burning rates of the different composite propellants, it was concluded that the dominant mechanism in the propellant combustion must be related to the primary diffusion flame, that is, as opposed to the monopropellant flame.

C. HMX Composite Propellants

Note that sufficiently fine HMX or RDX particles can melt in bulk near the burning surface due to their relatively low melting temperatures, for example, see Ref. 2 and Table 1. In contrast AP has a much higher (apparent) melting temperature that is very close to its surface temperature, resulting in thin layers of surface melt rather than bulk melting, for example, see Table 1 and Refs. 26–28. The melting of propellant ingredients can obscure the heterogeneity effect of the propellant within the combustion zone, affecting diffusion flame structure and reducing dependencies on particle size. This should be kept in mind for advanced ingredients having relatively low melting (or liquifaction) temperatures.

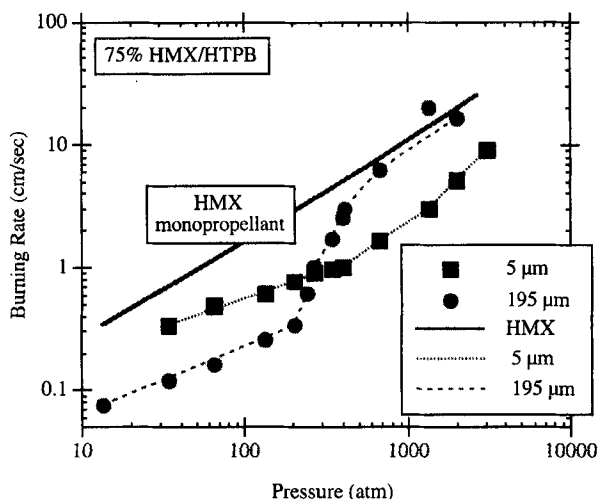


Fig. 10 Example of change in burning rate mechanism in HMX/HTPB propellant.

In the past, certain types of HMX (and RDX) propellants have exhibited a burning rate exponent break,^{29,30} indicative of a change in combustion mechanism. To help identify the mechanism causing the slope break, Cohen³¹ formulated two propellants using very narrow HMX particle-size distributions. Both propellants contained 75% monomodal HMX, one of 5 μm and the other 195 μm . The burning rate data for these propellants are presented in Fig. 10, along with the HMX monopropellant burning rate for reference. The coarse HMX propellant shows a dramatic change in exponent between 200 and 500 atm. At low pressure the rate is approximately one-fifth of the monopropellant rate with an exponent of ~ 0.55 , whereas at very high pressure, the rate and exponent both approach that of the monopropellant, again indicative of another change in combustion mechanism. At ~ 500 atm, the fine HMX propellant shows an upward slope increase from ~ 0.5 to greater than 1. Below about 300 atm, the fine HMX propellant has a rate that is about 2.5 times greater than the coarse HMX, but at high pressure, the coarse HMX propellant rate reaches 4 times that of the fine HMX. These very pronounced characteristics were unique to the Cohen propellants. Most other data for HMX composite propellants show less dramatic changes in burning rate. This is apparently due to the very narrow HMX particle-size distribution. More normal propellants having ingredients with relative broad particle-size distributions, often bimodal and trimodal sizes, seem to blur these effects, making definitive explanations more difficult.

Before the publication of the Cohen data,³¹ various mechanisms were postulated to explain the mechanism change. These included spalling of the HMX crystals due to high heat fluxes, changes in the condensed phase mechanism due to changes in the melt layer thickness,³² mixing of binder and HMX melt layers,³³ changes in kinetic mechanism, etc. However, none of these adequately explained the data. Cohen³¹ reasoned that at high pressure the large HMX did not melt significantly and burned at the monopropellant rate, dominating the overall propellant rate. At low pressure the binder melt was postulated to be sufficiently thick that it could flow and mingle with the adjacent melting HMX crystals inhibiting their burning

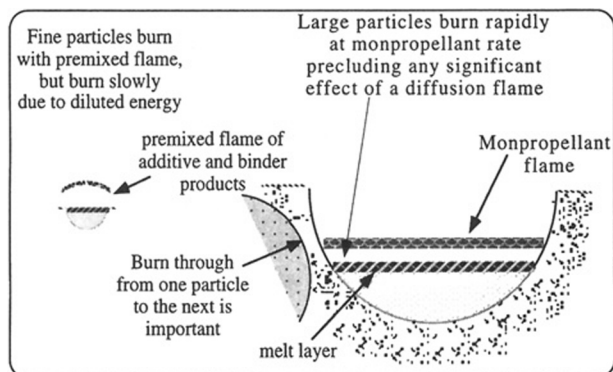


Fig. 11 Postulated combustion mechanism of HMX composite propellants.

rate. With increasing pressure the melt layers become thinner and would be less mobile, leading to the slope break. For the fine particles, Cohen reasoned that they were molten at all pressures tested, and so would not exhibit the dramatic slope breaks. Rates in the melt regime were reduced due to a cooler diffusion flame (as in Fig. 5). Further experiments by McCarty and Beckstead,^{19,20} making propellants with a wax binder that melted at low temperature, did show flowing of the binder over the surface and very sporadic burning as large HMX particles were covered by, or burned through, the layer of molten wax.

In an attempt to model this behavior, Beckstead modified the BDP model and developed a model based on where the overall propellant burning rate was dependent on how individual particles burn through the binder to an adjacent particle.^{34,35} His approach is illustrated in Fig. 11. He postulated that at low pressure large HMX particles burn at the monopropellant rate, burning very little of the binder, leaving a pocket of charred, but unburned, binder. The time to burn through the residual binder and ignite the next particle was postulated to be an important factor in determining the overall rate. Fine particles were postulated to burn in a diffusion-related flame, but approaching a premixed environment similar to the situation shown in Fig. 9. His model did not specifically address the slope breaks nor the very high-pressure behavior.

Considering factors that could potentially cause the slope break, the following seem to be pertinent: the thermal wave depth, the melt layer thickness, the monopropellant rate, the flame standoff distance, and the erosive gas velocity from the monopropellant flame. In going from low pressure to higher pressure, the thermal wave, melt layer thickness, and flame standoff distance all get smaller. Other than the flowing of the binder melt, already mentioned, none of these seem sufficient to explain the slope break. However, an erosive effect of the hot monopropellant gases flowing up over the binder wall formed from where a particle has burned is a concept worth considering. As pressure increases, the depth of a residual pocket could increase due to the increasing monopropellant rate. This would give the hot gases farther to travel, flowing over the binder, before escaping the pocket. The subsequent erosion of the binder would enhance the exposure of adjacent particles and their subsequent ignition. The more rapid exposure and ignition would allow the propellant to approach the monopropellant rate. This mechanism would be much less effective at low pressure, where the pocket depth would be small, but

much more effective with deeper pockets formed at higher pressures. By the same token, a binder that melts more readily would maintain the inhibition by keeping the pockets shallow. In fact, Kubota has published data for a series of HMX composite propellants that showed little change in exponent.³⁶ However, most of his propellants were formulated with binders that melt much more readily than HTPB.

D. Summary

Based on this brief review of mechanistic studies, one concludes that the AP primary diffusion flame is apparently the dominant combustion mechanism in AP-containing propellants, both composite and double base. The effect of the AP diffusion flame is related to the increased temperature of the primary diffusion flame, but is possibly more dependent on the increased reactivity of the chlorine-containing products leaving the burning surface.

In contrast, diffusion related processes seem to be almost absent in HMX containing propellants. In composite propellants, fine particles may burn with a diffusion flame, but the flame is a reduced energy flame and, thus, causes a reduction in rate relative to the monopropellant rate. Also, there is a lack of very reactive species, such as chlorine oxides. Coarse particles essentially burn at the monopropellant rate, but at low pressure the HMX combustion products apparently cannot sweep away the inert binder or the HMX is impeded by molten binder flowing onto the HMX, resulting in a very reduced rate. At high pressures the HMX is able to overcome whichever of these impediments really exists, burn through the binder to an adjacent crystal, and cause the propellant rate to approach the monopropellant rate.

In double-base propellants, the monopropellant rates of the binder and the HMX are very comparable, and the net burning rate of the propellant is usually close to that of the continuous medium, the binder. Stoichiometrically, HMX is not a true oxidizer and decomposition products from HMX and double base are very similar; neither contains a powerful oxidizing species such as chlorine oxides. It appears that the diffusion flame between the HMX and binder is similar enough to the individual monopropellant flames that it only causes small changes in the burning rate. This is very different from the AP/double-base diffusion flame.

V. Combustion Characteristics of Advanced Propellants

The objective of this chapter is to utilize the more or less familiar combustion characteristics of AP- and HMX-containing propellants to project the combustion characteristics of propellants made up of advanced ingredients. An important concept to establish is the role of AP. As mentioned, much of our understanding of combustion mechanisms has been based on AP, AP composite propellants and the BDP flame structure. Comparing the mechanistic aspects of AP and HMX in both composite and double-base propellants, it becomes apparent that the AP primary diffusion flame is the dominant mechanism in AP-containing compounds. This observation is also strongly supported by the work of Parr and Hanson-Parr in their studies of diffusion flames.^{37,38,39} In contrast, HMX-containing propellants seem to be devoid of an effective diffusion flame, apparently due to the lack of the very reactive chlorine species. In extrapolating to advanced propellants, note that none of the advanced ingredients discussed in this chapter contain chlorine. Thus, dominance of a diffusion flame in the combustion of a propellant seems to be an abnormality

associated only with propellants containing AP. Again, this is supported by the results reported in Refs. 37–39. Therefore, in attempting to project the combustion characteristics of advanced ingredients, HMX-related combustion characteristics such as that exemplified in Fig. 11 seem to be more appropriate.

In AP-containing propellants, finer particles or more fine particles lead to a higher burning rate. The conclusions reached in the preceding paragraphs imply that particle-size effects in advanced propellants will most likely be small and mixed, similar to HMX conditions. This was verified by Pak,⁴⁰ when he presented Russian results for ADN propellants showing that propellants with larger particles burned faster than those with smaller particles. Parr and Hanson-Parr⁴¹ have shown a similar result, burning sandwiches of ADN and HTPB. Their data show that the ADN burns very rapidly, leaving the HTPB virtually untouched.

It appears that the burning rates of advanced propellants will depend to a great extent on the relative rates of the monopropellant ingredients. To a lesser extent, both the energy content of the ingredients and potential melting properties can also have an influence. Coarse particles would be expected to burn at approximately the monopropellant rate, but fine particles would burn with a premixed or diffusional flame based on the properties of the mixed ingredients. Thus, the relative monopropellant rates of the propellant ingredients will be important. A high burning rate binder could control the propellant rate, or a high-rate additive, such as ADN, could control it. The size and concentration of fine particles will have an influence, but that influence will probably lead to reduced rates, not the increasing rates normally observed with AP-containing propellants. The propensity for melting, either the solid or the binder, can also influence the rate, particularly at low pressures where the melt layer thickness is greater.

For example, propellants based on a BAMO binder would be expected to have rates approaching the additive monopropellant rate due to the very low rate of BAMO. Therefore, it would be anticipated that the net rate would correlate with the monopropellant rate. Thus, because the monopropellant rates of ADN, CL20, and RDX are ordered $\text{ADN} > \text{CL20} > \text{RDX}$, it would be anticipated that corresponding propellants would fall into the same general trend. At 68 atm, the ratio of monopropellant burning rates is $\sim 3:2:1$ for these three ingredients. Thus it would be anticipated that propellant based on these compounds would have corresponding rates. Furthermore, for a relatively low energy binder, such as BAMO, it would also be anticipated that finer particles, or more fine particles, would tend to reduce the burning rate due to the dilution effect of the premixed flame between binder and particle.

In contrast, GAP has a much higher rate than BAMO, comparable to, or slightly higher than, RDX. ADN and CL20 have higher rates than GAP, so GAP/ADN or GAP/CL20 propellants would probably have rates approaching the ADN or CL20 monopropellant rate, but a GAP/RDX propellant would essentially burn at the GAP monopropellant rate. Thus, it would be anticipated that ADN and CL20/GAP propellants would have similar rates to the BAMO propellants, but the RDX/GAP propellant could have a different rate than the BAMO counterpart. Also, because GAP and BAMO have similar energies, the same trends with particle sizes and concentrations would be anticipated.

Burning rate modifiers have been used effectively in both AP propellants and double-base propellants to modify the burning rate characteristics. These modifiers have not been discussed in this chapter. The use of burning rate modifiers has not been as successful with nitramine propellants.⁴² Nitramine propellants can be catalyzed by catalyzing the binder, but modifying the combustion rate

of the nitramine has generally been unsuccessful. The extrapolation of these observations to advanced-type propellants would be well beyond the scope of this chapter. One very tentative observation might be made. If the general premise is correct, and most advanced ingredients follow the proposed mechanism of HMX propellants, then it may be suspected that the advanced propellants would not be very susceptible to modification by modifiers, similar to the nitramine propellant experience.

VI. Conclusions

A brief review of key mechanistic work has been made. The conclusion is reached that, for propellants containing AP, the primary diffusion flame is the combustion mechanism that dominates the determination of burning rate. Finer particles, or more fine particles, increase the burning rate of AP-containing propellants, and most AP-containing propellant have a rate higher than the AP monopropellant rate. This appears to be true for both composite and double-base (or energetic) propellants.

Using HMX as a typical example of advanced ingredients, one does not reach the same conclusion. In HMX composite propellants, the rate is almost always below the HMX monopropellant rate, and particle-size variation can either increase or decrease the propellant rate. An examination of available data indicates that for a binder that burns at a lower rate than HMX, such as HTPB, large particles will burn at their monopropellant rate, but may not burn through to the next particle in the propellant matrix. This can result in a relatively low propellant rate. At sufficiently high pressure, the HMX seems to be able to burn in a more continuous path, and the propellant rate approaches that of the monopropellant. Fine particles burn in a premixed state, where their decomposition products mix with the HMX decomposition products, diluting the energy of the flame and reducing the rate well below the HMX monopropellant rate. HMX propellants do not appear to have an effective diffusion flame, apparently due to a lack of chlorine containing compounds.

Other advanced ingredients, such as ADN, CL20, BAMO, etc., appear to follow the HMX scenario. Even ADN and CL20, which are true oxidizers with excess oxygen in their combustion products, do not exhibit a reactive diffusion flame. Thus, it is anticipated that large particles will burn at their monopropellant rate, similar to HMX, and if there is a sufficient concentration of large particles in the propellant, the overall rate will approach that of the monopropellant. Also, most active binders are less energetic than the solid component, and thus the fine particles will burn in a diluted energy flame, which will have a negative effect on the burning rate. Fine particles burn in a premixed state, where their decomposition products mix with the binder decomposition products diluting the energy of the flame and reducing the rate, well below the solid's monopropellant rate. Therefore, if a propellant is made up predominantly of fine particles it will most likely have a rate lower than the solid-monopropellant rate, corresponding to the flame temperature of the mixture.

Acknowledgment

This work was sponsored partly by Brigham Young University and partly by the California Institute of Technology Multidisciplinary University Research Initiative

under Office of Naval Research Grant N00014-95-1-1338, Program Manager, Judah Goldwasser.

References

¹Kubota, N., "Survey of Rocket Propellants and Their Combustion Characteristics," Vol. 90, Progress in Astronautics and Aeronautics, edited by K. K. Kuo and M. Summerfield, AIAA, New York, 1984, Chap. 1, pp. 1-52.

²Boggs, T. L., "The Thermal Behavior of Cyclotrimethylenetrinitamine (RDX) and Cyclotetramethylenetetranitramine (HMX)," Vol. 90, Progress in Astronautics and Aeronautics, ed. K. K. Kuo and M. Summerfield, AIAA, New York, 1984, Chap. 3, pp. 121-176.

³Atwood, A. I., Boggs, T. L., Curran, P. O., Parr, T. P., Hanson-Parr, D., and Price, C. F., "Burning Rate of Solid Propellant Ingredients, Part 1: Pressure and Initial Temperature Effects," *Journal of Propulsion and Power*, Vol. 15, No. 6, 1999, pp. 740-747.

⁴Whittaker, A. G., and Barham, D. C., "Surface Temperature Measurements on Burning Solids," *Journal of Physical Chemistry*, Vol. 68, No. 1, 1964, pp. 196-199.

⁵Kubota, N., and Sonobe, T., "Combustion Mechanism of Azide Polymer," *Propellants, Explosives, Pyrotechnics*, Vol. 13, 1988, pp. 172-177.

⁶Kubota, N., and Sonobe, T., "Combustion of GAP Propellants," *Combustion and Detonation Phenomena, 19th International Annual Conference of ICT*, Institute Chemische Technologie, Karlsruhe, Germany, 1988, pp. 2-1-2-12.

⁷Kubota, N., "Combustion of Energetic Azide Polymers," *Journal of Propulsion and Power*, Vol. 11, No. 4, 1995, pp. 677-682.

⁸Flanagan, J. E., Woolery, D. O., and Kistner, R. L., "Fundamental Studies of Azide Decomposition and Combustion," AFRPL TR-86-094, Rockwell International, Canoga Park, CA, 1986.

⁹Simmons, R. L., "Unusual Combustion Behavior of Nitramines and Azides," 4th International Symposium on Special Topics in Chemical Propulsion, Stockholm, Sweden, 1996 Session R = 2, Paper #1.

¹⁰Moy, S., Klingaman, K., and Manning, T., "Burning Rate Characteristics of Some Experimental NC Base Gun Propellant," Publ. 677, Chemical Propulsion Information Agency, Laurel, MD, 1998, pp. 156-165.

¹¹Musso, R. C., Grigor, R., and Yount, R. A., "Combustion Mechanism of Low-Burning Rate Propellant," AFRPL-TR-69-130, Hercules Inc., ABL, Cumberland, MD, 1969.

¹²Cohen, N. S., and Lo, G. A., "Modeling Effects of Composition on the Burn Rates of Nitrate Ester \pm Based Energetic Binders," Publ. 383, Chemical Propulsion Information Agency, Laurel, MD, 1983, pp. 621-628.

¹³Fogelzang, A. E., Suetlov, B. S., Adzhemyan, V. Y., Kolysov, S. M., and Sergienko, O. I., "The Combustion of Nitramines and Nitrosamines," *Doklady Akademii Nauk SSSR [Soviet Physics—Doklady]*, Vol. 216, No. 3, 1974, pp. 603-606.

¹⁴Kubota, N., and Okuhara, H., "Burning Rate Temperature Sensitivity of HMX Propellants," AIAA Paper 86-1593, 1986.

¹⁵Beckstead, M.W., "A Model for Composite Modified Double Base Propellant Combustion," Publ. 529, Vol. 4, Chemical Propulsion Information Agency, Laurel, MD, 1989, pp. 239-254.

¹⁶Yano, Y., and Kubota, N., "Combustion of HMX-CMDB Propellants (II)," *Propellants, Explosives and Pyrotechnics*, Vol. 11, 1986, pp. 1-5.

¹⁷Miller, R. R., Jones, M. L., Foster, R. L., and Condon, J. A., "Ballistic Control of Solid Propellants," Final Rept., Vol. 1, AFRPL-TR-81-058, Air Force Rocket Propulsion Lab., 1982.

¹⁸Miller, R. R., Foster, R. L., Beckstead, M. W., and Jones, M. L., "Ballistic Control of Solid Propellants," Interim Rept., AFRPL-TR-80-10, Air Force Rocket Propulsion Lab., 1980.

¹⁹McCarty, K. P., and Beckstead, M. W., "HMX Propellant Combustion Studies, Final Report," AFRPL-TR-79-61, Air Force Rocket Propulsion Lab., 1979.

²⁰McCarty, K. P., and Beckstead, M. W., "HMX Propellant Combustion Studies, Second Interim Report," AFRPL-TR-78-73, Air Force Rocket Propulsion Lab., 1978.

²¹Summerfield, M., Sutherland, G. S., Webb, W. J., Taback, H. J., and Hall, K. P., "The Burning Mechanism of Ammonium Perchlorate Propellants," *ARS Progress in Astronautics and Rocketry Vol I: Solid Propellant Rocket Research*, Academic, New York, 1960, pp. 141–182.

²²Hermance, C. E., "A Model of Composite Propellant Combustion Including Surface Heterogeneity and Heat Generation," *AIAA Journal*, Vol. 4, No. 9, 1966, pp. 1629–1637.

²³Boggs, T. L., Derr, R. L., and Beckstead, M. W., "Surface Structure of Ammonium Perchlorate Composite Propellants," *AIAA Journal*, Vol. 8, No. 2, 1970, pp. 370–372.

²⁴Beckstead, M. W., Derr, R. L., and Price, C. F., "Model of Composite Solid-Propellant Combustion Based on Multiple Flames," *AIAA Journal*, Vol. 8, No. 12, 1970, pp. 2200–2207.

²⁵Beckstead, M. W., "Combustion Calculations for Composite Solid Propellants," Publ. 281, Vol. 2, Chemical Propulsion Information Agency, Laurel, MD, 1976, pp. 299–312.

²⁶Beckstead, M. W., Tanaka, M., Jing, Q., and Jeppson, M. B., "An Ammonium Perchlorate Model Based on a Detailed Kinetic Mechanism," Publ. 653, Chemical Propulsion Information Agency, Laurel, MD, 1996, pp. 21–34.

²⁷Beckstead, M. W., and Hightower, J. D., "Surface Temperature of Deflagrating Ammonium Perchlorate Crystals," *AIAA Journal*, Vol. 5, No. 10, 1967, pp. 1785–1790.

²⁸Cordes, H. F., "Estimate of the Melting Point of Ammonium Perchlorate," *AIAA Journal*, Vol. 7, No. 6, 1969, pp. 1193–1195.

²⁹Simmons, R. L., "High Pressure Ballistics of Nitramine Gun Propellants," Publ. 231, Vol. 3, Chemical Propulsion Information Agency, Laurel, MD, 1972, pp. 41–59.

³⁰Moy, B. K., "Nitramine Combustion Problems," AFATL-TR-72-190, Air Force Armament Lab., Eglin Air Force Base, FL, 1972.

³¹Cohen, N. S., "Combustion of Nitramine Propellants," Publ. 261, Vol. 1, Chemical Propulsion Information Agency, Laurel, MD, 1974, pp. 267–284.

³²Rocchio, J. J., and Juhasz, A. A., "HMX Thermal Decomposition Chemistry and Its Relation to HMX-Composite Propellant Combustion," Publ. 261, Vol. 1, Chemical Propulsion Information Agency, Laurel, MD, 1974, pp. 247–266.

³³Cohen, N. S., and Price, C. F., "Combustion of Nitramine Propellants," *AIAA Journal*, Vol. 12, No. 10, 1975, pp. 25–42.

³⁴Beckstead, M. W., "A Model for Solid Propellant Combustion," *18th Symposium (International) on Combustion*, Combustion Inst., Pittsburgh, PA, 1981, pp. 175–185.

³⁵Beckstead, M. W., and McCarty, K. P., "Modeling Calculations for HMX Composite Propellants," *AIAA Journal*, Vol. 20, No. 1, 1982, pp. 106–115.

³⁶Kubota, N., "Physicochemical Processes of HMX Propellant Combustion," *19th Symposium (International) on Combustion*, Combustion Inst., Pittsburgh, PA, 1982, pp. 777–785.

³⁷Parr, T., and Hanson-Parr, D., "Solid Propellant Flame Structure," *26th Symp. (International) on Combustion*, The Combustion Institute, 1996, pp. 1981–1987.

³⁸Hanson-Parr, D., and Parr, T. P., "RDX Flame Structure and Chemistry," Publ. 620, Chemical Propulsion Information Agency, Laurel, MD, Vol. II, 1994, pp. 333–344.

³⁹Parr, T., and Hanson-Parr, D., "ADN Propellant Diffusion Flame Structure," Publ. 582, Chemical Propulsion Information Agency, Laurel, MD, Vol. II, 1992, pp. 313–327.

⁴⁰Pak, Z., "Some Ways to Higher Environmental Safety of Solid Rocket Propellant Application," AIAA Paper 93-1755, 1993.

⁴¹Parr, T. P., and Hanson-Parr, D., "ADN Diffusion Flame Structure at Elevated Pressure," Publ. 606, Vol. 2, Chemical Propulsion Information Agency, Laurel, MD, 1993, pp. 1–14.

⁴²Jones, M. L., Elrick, D. E., Herriott, G. E., Muhlfeith, C. M., and McCarty, K. P., "Nitramine Combustion," AFRPL-TR-85-041, Hercules Inc., ABL, Cumberland, MD, 1985.

II. Combustion of Solid Energetic Materials

Overview of Combustion Mechanisms and Flame Structures for Advanced Solid Propellants

M. W. Beckstead*

Brigham Young University, Provo, Utah

I. Introduction

THE solid ingredients used most often in modern solid propellants are ammonium perchlorate (AP) and cyclotetramethylenetetranitramine (HMX) [or cyclotrimethylenetrinitramine (RDX)]. The two most common binder systems consist of either an inert binder system based on a polybutadiene polymer, typically hydroxy-terminated polybutadiene polymer (HTPB), with various plasticizers, additives, and cross-linking agents, or an active binder system based on energetic components such as nitroglycerin (NG) and nitrocellulose (NC) or with a polyester or polyether polymer (PE). In general, comparing the combustion characteristics of monopropellants with the characteristics that occur when the monopropellants are combined with other ingredients to form propellants can lead to an understanding of the physical mechanisms that are involved. Note that the monopropellant burning rate of AP, HMX, and a typical NG/NC (or NG/PE) double-base propellant are similar. However, when a fuel and oxidizer are mixed together, a diffusion flame usually results. In AP/HTPB this diffusion flame has a huge impact on the combustion process as a function of pressure. Mixing HMX into HTPB to form a composite propellant also has a significant effect on the combustion, but in a different manner than that observed with an AP/HTPB system. Combining HMX with NG and NC or NG/PE to form a composite modified propellant results in little change in the burning rate from that observed with the individual ingredients. Observations such as these have helped to establish an understanding of the combustion mechanisms that determine the burning rate characteristics of typical propellants.

During the past decade the search for more energetic and more environmentally acceptable propellants has led to the development of advanced ingredients such as hexanitrohexaazaisowurtzitane (CL-20), ammonium dinitramide (ADN),

Copyright © 1999 by the American Institute of Aeronautics and Astronautics, Inc. All rights reserved.

*Professor, Chemical Engineering Dept.

hydrazinium nitroformate (HNF), glycidyl azide polymer (GAP), bis-azide methyl oxetane/3-azidemethyl 3'-methyl oxetane (BAMO/AMMO), etc. These are considered advanced in the sense that they are not commonly used in operational motors. The purpose of this study is to relate the observed combustion characteristics of the individual ingredients (as monopropellants) to postulated flame structures and mechanisms, based on observations with AP and HMX propellants. This chapter discusses the combustion and thermodynamic characteristics of the monopropellants and then conjectures the implications of various mechanisms on the potential combustion characteristics of actual propellants. The emphasis is on the qualitative effects of flame structure on combustion mechanisms. Time will not allow a detailed examination of the quantitative aspects of flame structure. For the same reasons, consideration of combustion characteristics has focused on flame temperatures and on burning rate characteristics. Temperature sensitivity, erosive burning, ignition, and unstable combustion are beyond the scope of that considered here.

II. Monopropellant Burning Characteristics

In this section the monopropellant combustion characteristics of several ingredients will be examined to lay a foundation for the understanding of propellants containing these ingredients. Most of our understanding of combustion mechanisms has been based on AP composite propellants, and to a lesser extent HMX composite propellants. Because these two ingredients will be used as a basis for the comparisons to follow, some of their general combustion properties are summarized in Table 1. These property values have typically been taken from previous review articles, for example, those of Kubota¹ and Boggs.² Note that the two compounds are very different in almost every category listed, except burning rate and exponent. The chemical composition, NH_4ClO_4 vs $\text{C}_4\text{H}_8\text{O}_8\text{N}_8$, the melt, surface and flame temperatures, and heats of formation are all very different, and yet the burning rates and exponents are very similar.

The relative burning rates of a large number of typical monopropellant ingredients are shown in Fig. 1. Most of these data (AP, HMX, RDX, ADN, CL-20, and HNF) are summarized in a recent paper by Atwood et al.³ The AN data are from Ref. 4. The azide data (GAP and BAMO) are from Kubota and Sonobe,^{5,6} Kubota,⁷ and Flanagan et al.⁸ The burning rate of the azides depends on the relative concentration of the azide and the material used to solidify and/or plasticize the azide. Typically hexamethylene diisocyanate (HMDI) is used to cure GAP and tetrahydrofuran (TFH) with BAMO. The referenced burning rate data show that the azide burning rate is directly proportional to the N_3 bond density. The data

Table 1 Comparison of AP and HMX combustion properties

Property	AP	HMX
Burning rate at 68 atm, cm/s	0.8	1.1
Pressure exponent	~0.7	~0.8
Chemical formula	NH_4ClO_4	$\text{C}_4\text{H}_8\text{O}_8\text{N}_8$
Adiabatic flame temperature, K	1405	3278
Melt temperature, K	~725–825	553
Surface temperature at 68 atm, K	~825	~750
Heat of formation, Kcal/mole	–70.7	18.1

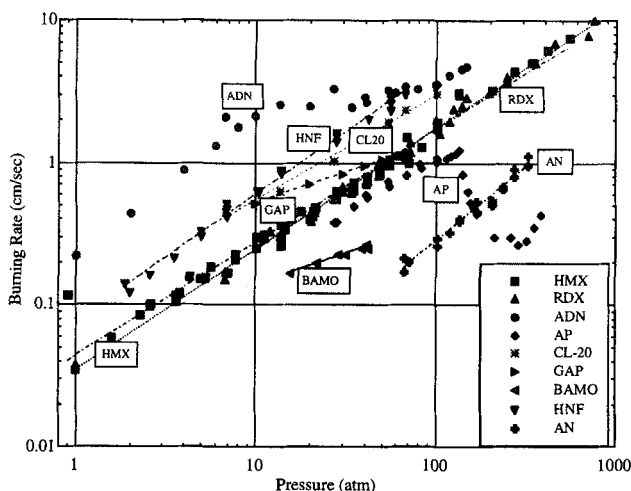


Fig. 1 Burning rate characteristics of ingredients used in solid propellants.

included in Fig. 1 were chosen for materials with $\sim 80:20$ mixture of GAP/HMDI and a $60:40$ mixture of BAMO/TFH as those mixtures were characterized most completely. Monopropellant ingredients used in double-base propellants, that is, nitrate esters, will be discussed later.

Most of the monopropellants examined here exhibit linear characteristics relative to the power law burning rate curve, $r = bP^n$. It is significant that the monopropellant burning rates of HMX and AP are very similar, at least from ~ 30 to ~ 150 atm with HMX having a rate $\sim 20\%$ greater than AP. Above ~ 150 atm the AP burning rate curve has a dip in it that is very uncharacteristic of most monopropellants. However, this behavior is not really applicable to motor operating conditions and, thus, will not be discussed further. ADN has two slope changes indicating rather complex combustion mechanism changes. At a typical operating pressure of 68 atm, ADN and HNF have the highest rates $\sim 3\text{--}4$ cm/s, whereas BAMO and AN are the lowest, approximately a full order of magnitude lower. Most of the ingredients have similar exponents, $\sim 0.8\text{--}1.0$, except for BAMO and GAP (both azides with exponents of ~ 0.5), and ADN, which has a variable exponent.

Table 2 contains a summary of some of the combustion properties of these and other propellant ingredients. Material densities are typically in the range of $1\text{--}2$ g/cm³ (Refs. 1 and 2). Heats of formation vary widely,¹ but are extremely important, because they are a dominant factor in determining flame temperature. The equilibrium conditions were calculated from the given heat of formation, atomic composition, and density of each ingredient. The flame temperature is seen to vary significantly, from a low of 1247 K for AN to a high of ~ 3500 K for CL-20. Most of the ingredients are made up of the CHON atoms. AN and ADN only contain HON atoms. AP is unique because it contains chlorine and produces the environmentally undesirable HCl. AP, ADN, AN, HNF, and CL-20 all produce molecular oxygen in their exhaust products, from 29% for AP decreasing down to 3% for CL-20.

It is informative to examine the burning rates of the various ingredients as a function of their calculated flame temperature. Although it is somewhat intuitive to expect burning rate to be proportional to flame temperature (e.g., Refs. 9 and 10), this is not necessarily the case. This is shown in Fig. 2. There is a general trend,

Table 2 Monopropellant ingredient properties

Ingred.	Density (g/cc)	ΔH_f (Kcal/mole)	Equilibrium products, 1000 psi (mole fractions)								
			T_f , K	MW	O ₂	H ₂ O	CO	CO ₂	H ₂	N ₂	HCl
<i>Nitrates</i>											
ADN	1.72	−35.8	2062	24.8	0.20	0.40				0.40	
AN	1.73	−87.3	1247	22.9	0.14	0.57				0.29	
<i>Perchlorate</i>											
AP	1.95	−70.7	1405	27.9	0.29	0.38				0.12	0.20
<i>Nitramines</i>											
CL-20	1.96	90.0	3571	27.4	0.02	0.14	0.23	0.10	0.03	0.37	
HMX	1.90	18.1	3278	24.3		0.23	0.25	0.09	0.09	0.33	
RDX	1.82	14.7	3286	24.3		0.23	0.25	0.09	0.09	0.33	
HNF	1.86	−17.2	3090	26.4	0.10	0.33	0.02	0.12	0.01	0.35	
<i>Nitrate Esters</i>											
NG	1.60	−90.7	3287	28.9	0.07	0.28	0.11	0.28	0.01	0.18	
TMETN	1.47	−106	2839	23.1		0.26	0.36	0.10	0.14	0.14	
DEGDN	1.39	−103.5	2513	21.8		0.25	0.37	0.08	0.19	0.11	
NC	1.65	−61.4	2425	28.4		0.21	0.43	0.12	0.13	0.11	
<i>Azides</i>											
BAMO	1.28	53.3 ^a	1725	15.2			0.11		0.48	0.39	
GAP	1.27	2.85 ^a	1570	15.7		0.01	0.19		0.43	0.32	
AMMO	1.26	4.32 ^a	1536	12.2		0.01	0.13		0.58	0.23	

^aKcal/100 g

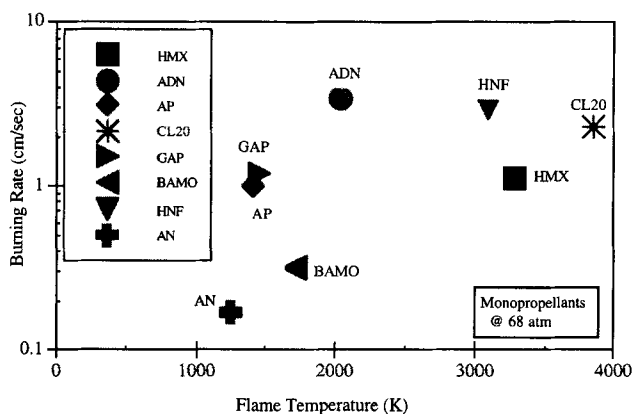


Fig. 2 Dependence of monopropellant burning rate on flame temperature.

but there are many discrepancies. AP, GAP, and HMX all have about the same burning rate, but their flame temperatures differ from 1400 to ~3200 K. ADN has the highest rate, but its flame temperature is a relatively low 2035 K. It appears that burning rates are dependent on many phenomena, including the initial bond breaking steps, concentration of various species leaving the burning surface (which bear on kinetics and the distribution of energetics), and the general mixture of atoms in the products. Although a quantitative prediction of propellant burning rate is beyond the scope of this chapter, it is felt that qualitative generalizations can be made based on the collective properties of the combined ingredients.

Although AP and HMX have very different flame temperatures, they have very similar burning rates. Because of HMX having a higher flame temperature than AP (3200 vs 1400 K), one might expect it to have a much higher burning rate than AP. Thus, it is somewhat surprising that the HMX burning rate is only ~20% greater than that of AP. This is apparently due to a higher reactivity of reactions involving chlorine oxides (i.e., the typical surface products from the condensed phase of the AP) compared to reactions involving nitrogen-containing compounds (i.e., the typical surface products) of HMX. This observation is supported by the much lower burning rate of AN, which has a flame temperature comparable to AP but does not give off the reactive chlorine oxides. The decomposition products from AN are more comparable to those of ADN, and one would expect similar reaction kinetics to be involved with AN and ADN, but not with AP. Therefore, the much lower rate of AN apparently corresponds to the much lower flame temperature of AN compared to that of ADN.

In a similar sense, the AP reaction path follows the reduction of the chlorine atom, whereas all of the other ingredients relate to some kind of a nitrogen reduction path. Although Fig. 2 does not show an obvious correlation between various ingredients, the following paragraphs show that there can be definite correlations within families of ingredients.

Double-base propellants are the classic example of the nitrogen reduction path. A characteristic of double-base propellants is that they burn with a two-stage flame. The inner flame is ~1200–1700 K depending on both pressure and binder energy. A dark zone separates the inner flame from a final flame of ~1500–3000 K, again

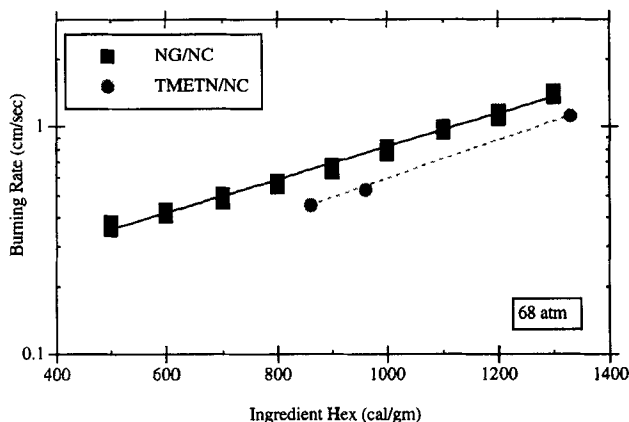


Fig. 3 Burning rate dependence on binder heat of explosion for families of nitrate ester propellants based on both NG/NC and TMETN/NC.

depending on pressure and binder energy. The effect of the heat transfer from the flame on the burning rate of the material is dominated by the inner flame that, in turn, dominates the burning rate. At high pressure (~ 100 atm) the two reaction zones merge, and only one flame is observed at higher pressures. The inner flame is apparently characterized by the reaction of NO_2 to form NO. The NO is relatively stable, leading to the dark zone. The stability of the NO molecule has also been observed in studies of air pollution. The end of the dark zone is characterized by the reaction of NO to react with various intermediates (such as N_2O and NO itself) and ultimately form N_2 .

Because of the dark zone, it is not appropriate to correlate the burning rate with the calculated adiabatic flame temperature. However, the calculated heat of explosion (HEX) is an appropriate correlation parameter and represents the energy available in the combustion process. Figure 3 is a plot of burning rate vs heat of explosion for a classic NC/NG double-base series of propellants, and the corresponding analogs with trimethylolethane trinitrate (TMETN) substituted for NG (Ref. 11). There is a very definite correlation between burning rate and propellant energy. However, the NG-based propellants exhibit a higher rate than the TMETN propellants. NG has more energy than the TMETN, as reflected by a higher flame temperature; thus, one cannot expect the burning rates of all nitrate esters to fall within the same correlation. Cohen and Lo¹² explained this effect of nitrate ester ingredient by the species concentration of NO_2 available for the primary flame zone kinetics.

Note that the burning rate of a typical double-base binder of ~ 1000 HEX, is ~ 0.8 cm/s at 68 atm, compared to that of AP and HMX monopropellants, which are ~ 0.8 and ~ 1.1 cm/s, respectively. There is very little difference in their burning rates, even though the flame structure and chemistry are significantly different.

Some time ago, Fogelzang et al.¹³ obtained data showing a correlation of burning rate vs flame temperature for families of N-nitro (nitramine) and C-nitro (nitrosamine) compounds. These data are presented in Fig. 4. Data were obtained for compounds with varying chemical structure, but with common backbone characteristics. The nitramines include both RDX and HMX. The data were taken at very high pressure (300 atm), but both families show a readily identifiable

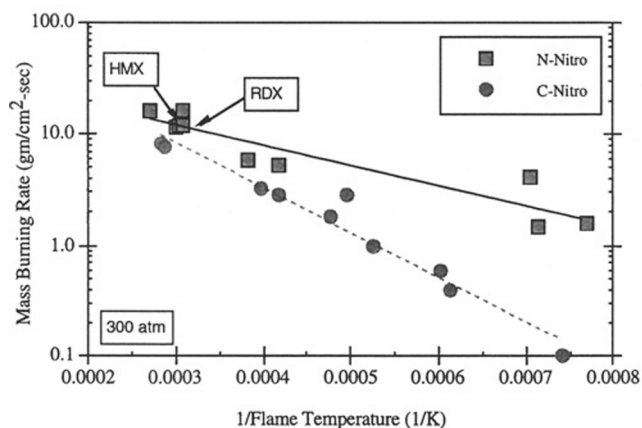


Fig. 4 Comparison of monopropellant burning rate dependence on flame temperature for families of nitramines (N-nitro) and nitrosamines (C-nitro) compounds.

correlation. The intuitive trend of rate increasing with flame temperature is present. Thus, within a given family of ingredients having a common backbone structure, one can expect the rate to correlate with flame temperature.

Having examined the burning rate characteristics of homogeneous ingredients, it is appropriate to consider the combustion characteristics of propellants that result from mixtures of ingredients.

III. Solid-Propellant Combustion Characteristics

The adiabatic flame temperatures for AP, ADN, HMX, and CL-20 in an HTPB binder have been calculated and are shown in Fig. 5 for varying oxidizer concentration. AP and ADN, which are true oxidizers, both show a maximum flame temperature near their stoichiometric mixture ratio. In the range of 80–90% oxidizer,

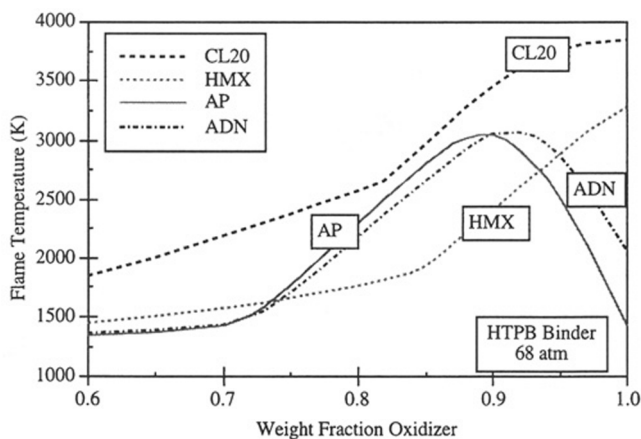


Fig. 5 Calculated flame temperatures for AP, ADN, CL-20, and HMX composite propellants.

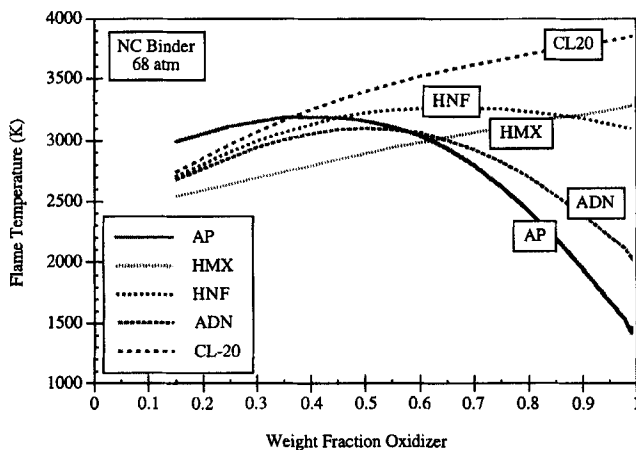


Fig. 6 Calculated flame temperatures for AP, ADN, HNF, CL-20, and HMX in an NC-based propellant.

which is typical of practical propellants, AP, ADN, and CL-20 all have similar flame temperatures, whereas HMX is ~ 1000 K lower. These calculated temperatures should be characteristic of the diffusion flame in propellants that, in turn, relates to the particle size dependence of burning rate. HMX/HTPB propellants typically have a burning rate much lower than HMX monopropellant, whereas AP/HTPB propellants typically have a burning rate higher than the AP monopropellant rate. Apparently the HMX diffusion flame robs energy from the monopropellant flame, suppressing the overall propellant burn rate. Qualitatively this is in agreement with the calculated flame temperature.

The calculated flame temperatures for AP, ADN, HMX, HNF, and CL-20 in an NC binder are shown in Fig. 6. AP, ADN, and HNF all show a maximum flame temperature near their stoichiometric mixture ratio. Up to 50–70%, which is typical of practical propellants, all have similar flame temperatures. Observe that the addition of HMX to a typical double-base propellant usually has little effect on the burning rate of the propellant.^{14,15} As was noted, the relative monopropellant rates of HMX and double-base binders are very similar. Thus, combining two ingredients with comparable monopropellant rates and no effective diffusion flame results in little change in the overall propellant rate.

Figure 7 shows data varying HMX concentration in a double-base binder.¹⁶ The burning rate of the pure HMX is within $\sim 20\%$ of the burning rate of the double-base binder. The rate of the mixtures goes through a minimum between the rates of the two ingredients. Other experimental data,^{17–20} show the same trend and additionally show that adding different-sized HMX particles at concentrations up to $\sim 60\%$ did not significantly alter the burn rate. This is not surprising considering that both HMX and double-base binder each contain CHON elements and similar energy levels. Calculated flame temperatures varying the percent HMX for double-base binders of varying HEX show that for a high-energy binder there is little change in the flame temperature of the propellant, for example, see Fig. 6. For a low-energy binder, adding HMX increases the flame temperature. The calculated temperatures all increase toward the adiabatic flame temperature of HMX, which is higher than any of the double-base flame temperatures.

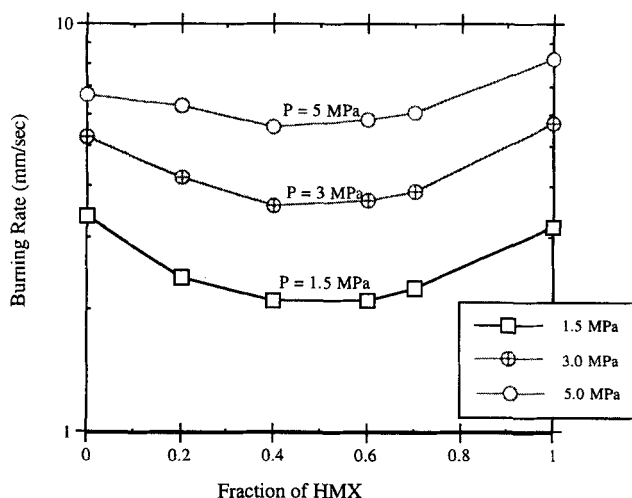


Fig. 7 Burning rate characteristics of HMX in a double-base binder at varying pressures.

However, the addition of AP to a double-base propellant increases the rate significantly, increasingly so for decreasing AP particle size.^{11,15,17,18} Even though the calculated flame temperatures for an AP vs an HMX/double-base propellant are not significantly different, the resultant burning rates are. As noted, the kinetics associated with the chlorine reduction path appear to be significantly faster than those associated with the nitrogen reduction path. Thus, the AP related diffusion flame has a significant effect on the burning rate, whereas the corresponding HMX products diffusing into double-base products are sufficiently similar that there is little change in burning rate.

IV. Solid-Propellant Combustion Mechanisms

The objective of the chapter is to utilize the basic combustion characteristics presented in the preceding sections to project the combustion characteristics of propellants made up of mixtures of advanced ingredients. To develop this logic, a brief review of the physical picture of how older propellants burn will be made.

A. Phenomenological Concepts

Understanding of the combustion mechanisms that determine solid-propellant burning rates have evolved over the past 30 years. In the 1960s, emphasis was determining the critical mechanism that controlled the burning rate and most attention was given to AP composite propellants. A typical example of identifying a single critical mechanism that would describe combustion behavior was the Summerfield granular diffusion flame (GDF) model.²¹ That model was based on the concept that fuel and oxidizer gasify at the burning surface, leaving the surface in pockets of gases that diffuse together, reaction to determine the propellant burning rate. Although this interpretation enjoyed a degree of popularity, it was too narrow in concept to describe the great variation in burning rates observed with AP

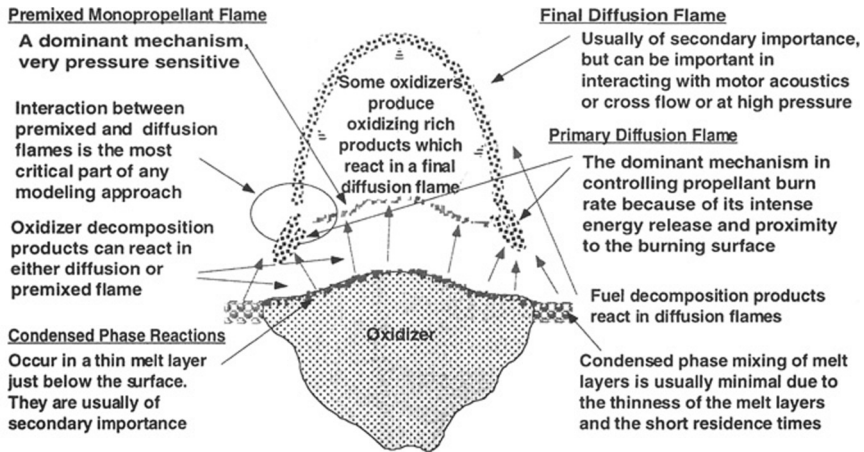


Fig. 8 Conceptual depiction of the BDP model for AP composite propellants.

propellants for varying pressure, oxidizer particle size, and loading. In general, finer AP particle size causes an increase in burning rate, but at very low or high pressures this effect is diminished. Similarly, increased AP concentration tends to increase the burning rate, but this effect is also reduced at extreme pressures. The GDF model was not comprehensive enough to explain such a wide range of behavior.

In the late 1960s Hermance²² proposed a model of heterogeneous reaction at the burning surface between oxidizer and binder, creating an increased, reacting surface area. Although this concept resulted in a mathematical model that correctly gave the increased burning rate with decreasing particle size, Scanning Electron Microscope (SEM) photographs²³ failed to show the postulated undercutting of oxidizer crystals.

In the early 1970s, Beckstead et al. published their multiple-flame [Beckstead, Derr, and Price (BDP)] model.²⁴ This model proposed a complex interaction between the oxidizer monopropellant flame and two different diffusion flames occurring above the oxidizer binder interface. Figure 8 illustrates this. This physical picture was sufficiently comprehensive to be able to explain most of the observed propellant behavior for many years.

B. AP Composite Propellants

Using this model, the burning rate is proposed to be very particle-size dependent due to the primary diffusion flame. For very small particles the diffusion aspect of the primary diffusion flame can be reduced, and the kinetic aspect can become dominant. For these conditions the particles and binder approach a premixed condition. This behavior is illustrated in Fig. 9, adapted from Ref. 25. For increasingly large particles the monopropellant flame dominates and similarly reduces the particle-size effect.

These results indicate that the burning rate can change by an order of magnitude through varying the AP particle size. For lower pressures the curve will shift downward and to the left, and for higher pressures it will shift upward and to the

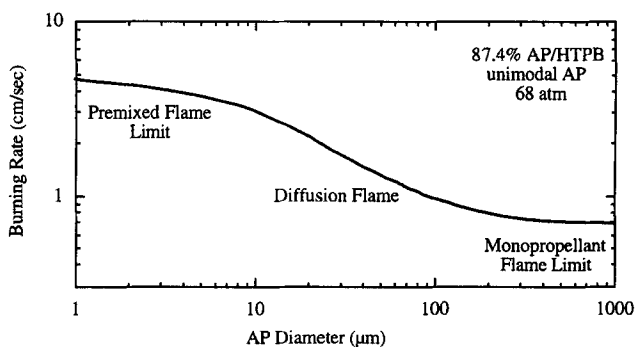


Fig. 9 Variation in burning rate due to varying particle size, as predicted by the BDP model.

right. The conclusion was reached that the primary diffusion flame was the dominant mechanism in determining the burning rate of AP composite propellants. However, it is very apparent that at either low pressures or for very small particles, the kinetic aspect of the primary diffusion flame will be dominant, whereas for high pressures and/or large particles, the monopropellant flame will become dominant.

AP and HMX appear to have similar monopropellant combustion characteristics, but when mixed with a fuel binder into a composite propellant, the resultant burn rates vary by as much as an order of magnitude. The burn rate of AP composite propellants exhibits a very strong particle size dependence (as indicated in Fig. 9). In contrast, the burn rates of HMX composite propellants are much lower than those of AP propellants and show a much smaller particle-size dependence.

Thermochemical calculations for AP composite propellants indicate a primary flame temperature on the order of ~ 2500 – 2800 K for typical concentrations as shown in Fig. 5. Thus, the AP diffusion flame is much more energetic than the AP monopropellant flame and leads to higher burning rates. HMX composite propellants have adiabatic flame temperatures on the order of 2000 K implying a less energetic diffusion flame than the monopropellant flame leading to reduced rates. Because of the very large differences in burning rates of the different composite propellants, it was concluded that the dominant mechanism in the propellant combustion must be related to the primary diffusion flame, that is, as opposed to the monopropellant flame.

C. HMX Composite Propellants

Note that sufficiently fine HMX or RDX particles can melt in bulk near the burning surface due to their relatively low melting temperatures, for example, see Ref. 2 and Table 1. In contrast AP has a much higher (apparent) melting temperature that is very close to its surface temperature, resulting in thin layers of surface melt rather than bulk melting, for example, see Table 1 and Refs. 26–28. The melting of propellant ingredients can obscure the heterogeneity effect of the propellant within the combustion zone, affecting diffusion flame structure and reducing dependencies on particle size. This should be kept in mind for advanced ingredients having relatively low melting (or liquifaction) temperatures.

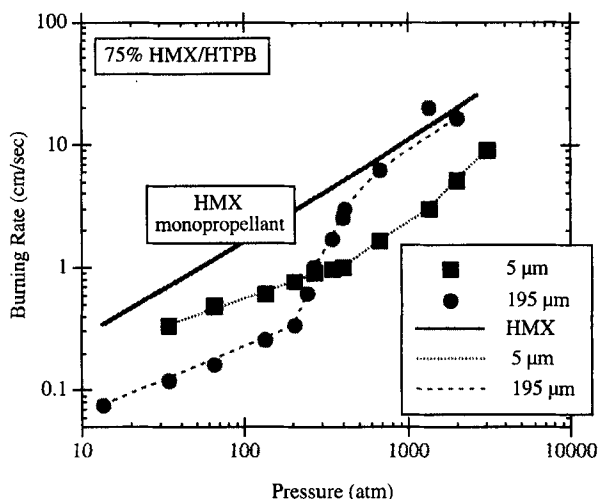


Fig. 10 Example of change in burning rate mechanism in HMX/HTPB propellant.

In the past, certain types of HMX (and RDX) propellants have exhibited a burning rate exponent break,^{29,30} indicative of a change in combustion mechanism. To help identify the mechanism causing the slope break, Cohen³¹ formulated two propellants using very narrow HMX particle-size distributions. Both propellants contained 75% monomodal HMX, one of 5 μm and the other 195 μm . The burning rate data for these propellants are presented in Fig. 10, along with the HMX monopropellant burning rate for reference. The coarse HMX propellant shows a dramatic change in exponent between 200 and 500 atm. At low pressure the rate is approximately one-fifth of the monopropellant rate with an exponent of ~ 0.55 , whereas at very high pressure, the rate and exponent both approach that of the monopropellant, again indicative of another change in combustion mechanism. At ~ 500 atm, the fine HMX propellant shows an upward slope increase from ~ 0.5 to greater than 1. Below about 300 atm, the fine HMX propellant has a rate that is about 2.5 times greater than the coarse HMX, but at high pressure, the coarse HMX propellant rate reaches 4 times that of the fine HMX. These very pronounced characteristics were unique to the Cohen propellants. Most other data for HMX composite propellants show less dramatic changes in burning rate. This is apparently due to the very narrow HMX particle-size distribution. More normal propellants having ingredients with relative broad particle-size distributions, often bimodal and trimodal sizes, seem to blur these effects, making definitive explanations more difficult.

Before the publication of the Cohen data,³¹ various mechanisms were postulated to explain the mechanism change. These included spalling of the HMX crystals due to high heat fluxes, changes in the condensed phase mechanism due to changes in the melt layer thickness,³² mixing of binder and HMX melt layers,³³ changes in kinetic mechanism, etc. However, none of these adequately explained the data. Cohen³¹ reasoned that at high pressure the large HMX did not melt significantly and burned at the monopropellant rate, dominating the overall propellant rate. At low pressure the binder melt was postulated to be sufficiently thick that it could flow and mingle with the adjacent melting HMX crystals inhibiting their burning

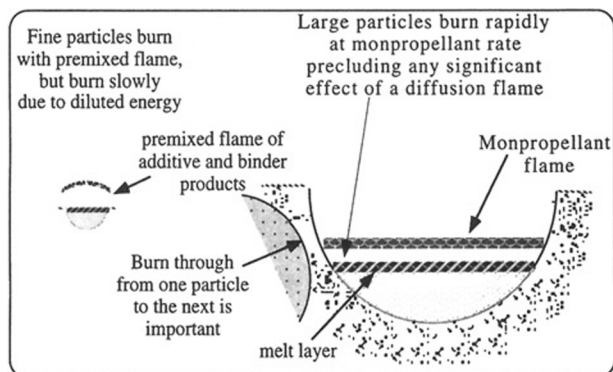


Fig. 11 Postulated combustion mechanism of HMX composite propellants.

rate. With increasing pressure the melt layers become thinner and would be less mobile, leading to the slope break. For the fine particles, Cohen reasoned that they were molten at all pressures tested, and so would not exhibit the dramatic slope breaks. Rates in the melt regime were reduced due to a cooler diffusion flame (as in Fig. 5). Further experiments by McCarty and Beckstead,^{19,20} making propellants with a wax binder that melted at low temperature, did show flowing of the binder over the surface and very sporadic burning as large HMX particles were covered by, or burned through, the layer of molten wax.

In an attempt to model this behavior, Beckstead modified the BDP model and developed a model based on where the overall propellant burning rate was dependent on how individual particles burn through the binder to an adjacent particle.^{34,35} His approach is illustrated in Fig. 11. He postulated that at low pressure large HMX particles burn at the monopropellant rate, burning very little of the binder, leaving a pocket of charred, but unburned, binder. The time to burn through the residual binder and ignite the next particle was postulated to be an important factor in determining the overall rate. Fine particles were postulated to burn in a diffusion-related flame, but approaching a premixed environment similar to the situation shown in Fig. 9. His model did not specifically address the slope breaks nor the very high-pressure behavior.

Considering factors that could potentially cause the slope break, the following seem to be pertinent: the thermal wave depth, the melt layer thickness, the monopropellant rate, the flame standoff distance, and the erosive gas velocity from the monopropellant flame. In going from low pressure to higher pressure, the thermal wave, melt layer thickness, and flame standoff distance all get smaller. Other than the flowing of the binder melt, already mentioned, none of these seem sufficient to explain the slope break. However, an erosive effect of the hot monopropellant gases flowing up over the binder wall formed from where a particle has burned is a concept worth considering. As pressure increases, the depth of a residual pocket could increase due to the increasing monopropellant rate. This would give the hot gases farther to travel, flowing over the binder, before escaping the pocket. The subsequent erosion of the binder would enhance the exposure of adjacent particles and their subsequent ignition. The more rapid exposure and ignition would allow the propellant to approach the monopropellant rate. This mechanism would be much less effective at low pressure, where the pocket depth would be small, but

much more effective with deeper pockets formed at higher pressures. By the same token, a binder that melts more readily would maintain the inhibition by keeping the pockets shallow. In fact, Kubota has published data for a series of HMX composite propellants that showed little change in exponent.³⁶ However, most of his propellants were formulated with binders that melt much more readily than HTPB.

D. Summary

Based on this brief review of mechanistic studies, one concludes that the AP primary diffusion flame is apparently the dominant combustion mechanism in AP-containing propellants, both composite and double base. The effect of the AP diffusion flame is related to the increased temperature of the primary diffusion flame, but is possibly more dependent on the increased reactivity of the chlorine-containing products leaving the burning surface.

In contrast, diffusion related processes seem to be almost absent in HMX containing propellants. In composite propellants, fine particles may burn with a diffusion flame, but the flame is a reduced energy flame and, thus, causes a reduction in rate relative to the monopropellant rate. Also, there is a lack of very reactive species, such as chlorine oxides. Coarse particles essentially burn at the monopropellant rate, but at low pressure the HMX combustion products apparently cannot sweep away the inert binder or the HMX is impeded by molten binder flowing onto the HMX, resulting in a very reduced rate. At high pressures the HMX is able to overcome whichever of these impediments really exists, burn through the binder to an adjacent crystal, and cause the propellant rate to approach the monopropellant rate.

In double-base propellants, the monopropellant rates of the binder and the HMX are very comparable, and the net burning rate of the propellant is usually close to that of the continuous medium, the binder. Stoichiometrically, HMX is not a true oxidizer and decomposition products from HMX and double base are very similar; neither contains a powerful oxidizing species such as chlorine oxides. It appears that the diffusion flame between the HMX and binder is similar enough to the individual monopropellant flames that it only causes small changes in the burning rate. This is very different from the AP/double-base diffusion flame.

V. Combustion Characteristics of Advanced Propellants

The objective of this chapter is to utilize the more or less familiar combustion characteristics of AP- and HMX-containing propellants to project the combustion characteristics of propellants made up of advanced ingredients. An important concept to establish is the role of AP. As mentioned, much of our understanding of combustion mechanisms has been based on AP, AP composite propellants and the BDP flame structure. Comparing the mechanistic aspects of AP and HMX in both composite and double-base propellants, it becomes apparent that the AP primary diffusion flame is the dominant mechanism in AP-containing compounds. This observation is also strongly supported by the work of Parr and Hanson-Parr in their studies of diffusion flames.^{37,38,39} In contrast, HMX-containing propellants seem to be devoid of an effective diffusion flame, apparently due to the lack of the very reactive chlorine species. In extrapolating to advanced propellants, note that none of the advanced ingredients discussed in this chapter contain chlorine. Thus, dominance of a diffusion flame in the combustion of a propellant seems to be an abnormality

associated only with propellants containing AP. Again, this is supported by the results reported in Refs. 37–39. Therefore, in attempting to project the combustion characteristics of advanced ingredients, HMX-related combustion characteristics such as that exemplified in Fig. 11 seem to be more appropriate.

In AP-containing propellants, finer particles or more fine particles lead to a higher burning rate. The conclusions reached in the preceding paragraphs imply that particle-size effects in advanced propellants will most likely be small and mixed, similar to HMX conditions. This was verified by Pak,⁴⁰ when he presented Russian results for ADN propellants showing that propellants with larger particles burned faster than those with smaller particles. Parr and Hanson-Parr⁴¹ have shown a similar result, burning sandwiches of ADN and HTPB. Their data show that the ADN burns very rapidly, leaving the HTPB virtually untouched.

It appears that the burning rates of advanced propellants will depend to a great extent on the relative rates of the monopropellant ingredients. To a lesser extent, both the energy content of the ingredients and potential melting properties can also have an influence. Coarse particles would be expected to burn at approximately the monopropellant rate, but fine particles would burn with a premixed or diffusional flame based on the properties of the mixed ingredients. Thus, the relative monopropellant rates of the propellant ingredients will be important. A high burning rate binder could control the propellant rate, or a high-rate additive, such as ADN, could control it. The size and concentration of fine particles will have an influence, but that influence will probably lead to reduced rates, not the increasing rates normally observed with AP-containing propellants. The propensity for melting, either the solid or the binder, can also influence the rate, particularly at low pressures where the melt layer thickness is greater.

For example, propellants based on a BAMO binder would be expected to have rates approaching the additive monopropellant rate due to the very low rate of BAMO. Therefore, it would be anticipated that the net rate would correlate with the monopropellant rate. Thus, because the monopropellant rates of ADN, CL20, and RDX are ordered $\text{ADN} > \text{CL20} > \text{RDX}$, it would be anticipated that corresponding propellants would fall into the same general trend. At 68 atm, the ratio of monopropellant burning rates is $\sim 3:2:1$ for these three ingredients. Thus it would be anticipated that propellant based on these compounds would have corresponding rates. Furthermore, for a relatively low energy binder, such as BAMO, it would also be anticipated that finer particles, or more fine particles, would tend to reduce the burning rate due to the dilution effect of the premixed flame between binder and particle.

In contrast, GAP has a much higher rate than BAMO, comparable to, or slightly higher than, RDX. ADN and CL20 have higher rates than GAP, so GAP/ADN or GAP/CL20 propellants would probably have rates approaching the ADN or CL20 monopropellant rate, but a GAP/RDX propellant would essentially burn at the GAP monopropellant rate. Thus, it would be anticipated that ADN and CL20/GAP propellants would have similar rates to the BAMO propellants, but the RDX/GAP propellant could have a different rate than the BAMO counterpart. Also, because GAP and BAMO have similar energies, the same trends with particle sizes and concentrations would be anticipated.

Burning rate modifiers have been used effectively in both AP propellants and double-base propellants to modify the burning rate characteristics. These modifiers have not been discussed in this chapter. The use of burning rate modifiers has not been as successful with nitramine propellants.⁴² Nitramine propellants can be catalyzed by catalyzing the binder, but modifying the combustion rate

of the nitramine has generally been unsuccessful. The extrapolation of these observations to advanced-type propellants would be well beyond the scope of this chapter. One very tentative observation might be made. If the general premise is correct, and most advanced ingredients follow the proposed mechanism of HMX propellants, then it may be suspected that the advanced propellants would not be very susceptible to modification by modifiers, similar to the nitramine propellant experience.

VI. Conclusions

A brief review of key mechanistic work has been made. The conclusion is reached that, for propellants containing AP, the primary diffusion flame is the combustion mechanism that dominates the determination of burning rate. Finer particles, or more fine particles, increase the burning rate of AP-containing propellants, and most AP-containing propellant have a rate higher than the AP monopropellant rate. This appears to be true for both composite and double-base (or energetic) propellants.

Using HMX as a typical example of advanced ingredients, one does not reach the same conclusion. In HMX composite propellants, the rate is almost always below the HMX monopropellant rate, and particle-size variation can either increase or decrease the propellant rate. An examination of available data indicates that for a binder that burns at a lower rate than HMX, such as HTPB, large particles will burn at their monopropellant rate, but may not burn through to the next particle in the propellant matrix. This can result in a relatively low propellant rate. At sufficiently high pressure, the HMX seems to be able to burn in a more continuous path, and the propellant rate approaches that of the monopropellant. Fine particles burn in a premixed state, where their decomposition products mix with the HMX decomposition products, diluting the energy of the flame and reducing the rate well below the HMX monopropellant rate. HMX propellants do not appear to have an effective diffusion flame, apparently due to a lack of chlorine containing compounds.

Other advanced ingredients, such as ADN, CL20, BAMO, etc., appear to follow the HMX scenario. Even ADN and CL20, which are true oxidizers with excess oxygen in their combustion products, do not exhibit a reactive diffusion flame. Thus, it is anticipated that large particles will burn at their monopropellant rate, similar to HMX, and if there is a sufficient concentration of large particles in the propellant, the overall rate will approach that of the monopropellant. Also, most active binders are less energetic than the solid component, and thus the fine particles will burn in a diluted energy flame, which will have a negative effect on the burning rate. Fine particles burn in a premixed state, where their decomposition products mix with the binder decomposition products diluting the energy of the flame and reducing the rate, well below the solid's monopropellant rate. Therefore, if a propellant is made up predominantly of fine particles it will most likely have a rate lower than the solid-monopropellant rate, corresponding to the flame temperature of the mixture.

Acknowledgment

This work was sponsored partly by Brigham Young University and partly by the California Institute of Technology Multidisciplinary University Research Initiative

under Office of Naval Research Grant N00014-95-1-1338, Program Manager, Judah Goldwasser.

References

- ¹Kubota, N., "Survey of Rocket Propellants and Their Combustion Characteristics," Vol. 90, Progress in Astronautics and Aeronautics, edited by K. K. Kuo and M. Summerfield, AIAA, New York, 1984, Chap. 1, pp. 1-52.
- ²Boggs, T. L., "The Thermal Behavior of Cyclotrimethylenetrinitamine (RDX) and Cyclotetramethylenetetranitramine (HMX)," Vol. 90, Progress in Astronautics and Aeronautics, ed. K. K. Kuo and M. Summerfield, AIAA, New York, 1984, Chap. 3, pp. 121-176.
- ³Atwood, A. I., Boggs, T. L., Curran, P. O., Parr, T. P., Hanson-Parr, D., and Price, C. F., "Burning Rate of Solid Propellant Ingredients, Part 1: Pressure and Initial Temperature Effects," *Journal of Propulsion and Power*, Vol. 15, No. 6, 1999, pp. 740-747.
- ⁴Whittaker, A. G., and Barham, D. C., "Surface Temperature Measurements on Burning Solids," *Journal of Physical Chemistry*, Vol. 68, No. 1, 1964, pp. 196-199.
- ⁵Kubota, N., and Sonobe, T., "Combustion Mechanism of Azide Polymer," *Propellants, Explosives, Pyrotechnics*, Vol. 13, 1988, pp. 172-177.
- ⁶Kubota, N., and Sonobe, T., "Combustion of GAP Propellants," *Combustion and Detonation Phenomena, 19th International Annual Conference of ICT*, Institute Chemische Technologie, Karlsruhe, Germany, 1988, pp. 2-1-2-12.
- ⁷Kubota, N., "Combustion of Energetic Azide Polymers," *Journal of Propulsion and Power*, Vol. 11, No. 4, 1995, pp. 677-682.
- ⁸Flanagan, J. E., Woolery, D. O., and Kistner, R. L., "Fundamental Studies of Azide Decomposition and Combustion," AFRPL TR-86-094, Rockwell International, Canoga Park, CA, 1986.
- ⁹Simmons, R. L., "Unusual Combustion Behavior of Nitramines and Azides," 4th International Symposium on Special Topics in Chemical Propulsion, Stockholm, Sweden, 1996 Session R = 2, Paper #1.
- ¹⁰Moy, S., Klingaman, K., and Manning, T., "Burning Rate Characteristics of Some Experimental NC Base Gun Propellant," Publ. 677, Chemical Propulsion Information Agency, Laurel, MD, 1998, pp. 156-165.
- ¹¹Musso, R. C., Grigor, R., and Yount, R. A., "Combustion Mechanism of Low-Burning Rate Propellant," AFRPL-TR-69-130, Hercules Inc., ABL, Cumberland, MD, 1969.
- ¹²Cohen, N. S., and Lo, G. A., "Modeling Effects of Composition on the Burn Rates of Nitrate Ester \pm Based Energetic Binders," Publ. 383, Chemical Propulsion Information Agency, Laurel, MD, 1983, pp. 621-628.
- ¹³Fogelzang, A. E., Suetlov, B. S., Adzhemyan, V. Y., Kolysov, S. M., and Sergienko, O. I., "The Combustion of Nitramines and Nitrosamines," *Doklady Akademii Nauk SSSR [Soviet Physics—Doklady]*, Vol. 216, No. 3, 1974, pp. 603-606.
- ¹⁴Kubota, N., and Okuhara, H., "Burning Rate Temperature Sensitivity of HMX Propellants," AIAA Paper 86-1593, 1986.
- ¹⁵Beckstead, M.W., "A Model for Composite Modified Double Base Propellant Combustion," Publ. 529, Vol. 4, Chemical Propulsion Information Agency, Laurel, MD, 1989, pp. 239-254.
- ¹⁶Yano, Y., and Kubota, N., "Combustion of HMX-CMDB Propellants (II)," *Propellants, Explosives and Pyrotechnics*, Vol. 11, 1986, pp. 1-5.
- ¹⁷Miller, R. R., Jones, M. L., Foster, R. L., and Condon, J. A., "Ballistic Control of Solid Propellants," Final Rept., Vol. 1, AFRPL-TR-81-058, Air Force Rocket Propulsion Lab., 1982.

¹⁸Miller, R. R., Foster, R. L., Beckstead, M. W., and Jones, M. L., "Ballistic Control of Solid Propellants," Interim Rept., AFRPL-TR-80-10, Air Force Rocket Propulsion Lab., 1980.

¹⁹McCarty, K. P., and Beckstead, M. W., "HMX Propellant Combustion Studies, Final Report," AFRPL-TR-79-61, Air Force Rocket Propulsion Lab., 1979.

²⁰McCarty, K. P., and Beckstead, M. W., "HMX Propellant Combustion Studies, Second Interim Report," AFRPL-TR-78-73, Air Force Rocket Propulsion Lab., 1978.

²¹Summerfield, M., Sutherland, G. S., Webb, W. J., Taback, H. J., and Hall, K. P., "The Burning Mechanism of Ammonium Perchlorate Propellants," *ARS Progress in Astronautics and Rocketry Vol I: Solid Propellant Rocket Research*, Academic, New York, 1960, pp. 141–182.

²²Hermance, C. E., "A Model of Composite Propellant Combustion Including Surface Heterogeneity and Heat Generation," *AIAA Journal*, Vol. 4, No. 9, 1966, pp. 1629–1637.

²³Boggs, T. L., Derr, R. L., and Beckstead, M. W., "Surface Structure of Ammonium Perchlorate Composite Propellants," *AIAA Journal*, Vol. 8, No. 2, 1970, pp. 370–372.

²⁴Beckstead, M. W., Derr, R. L., and Price, C. F., "Model of Composite Solid-Propellant Combustion Based on Multiple Flames," *AIAA Journal*, Vol. 8, No. 12, 1970, pp. 2200–2207.

²⁵Beckstead, M. W., "Combustion Calculations for Composite Solid Propellants," Publ. 281, Vol. 2, Chemical Propulsion Information Agency, Laurel, MD, 1976, pp. 299–312.

²⁶Beckstead, M. W., Tanaka, M., Jing, Q., and Jeppson, M. B., "An Ammonium Perchlorate Model Based on a Detailed Kinetic Mechanism," Publ. 653, Chemical Propulsion Information Agency, Laurel, MD, 1996, pp. 21–34.

²⁷Beckstead, M. W., and Hightower, J. D., "Surface Temperature of Deflagrating Ammonium Perchlorate Crystals," *AIAA Journal*, Vol. 5, No. 10, 1967, pp. 1785–1790.

²⁸Cordes, H. F., "Estimate of the Melting Point of Ammonium Perchlorate," *AIAA Journal*, Vol. 7, No. 6, 1969, pp. 1193–1195.

²⁹Simmons, R. L., "High Pressure Ballistics of Nitramine Gun Propellants," Publ. 231, Vol. 3, Chemical Propulsion Information Agency, Laurel, MD, 1972, pp. 41–59.

³⁰Moy, B. K., "Nitramine Combustion Problems," AFATL-TR-72-190, Air Force Armament Lab., Eglin Air Force Base, FL, 1972.

³¹Cohen, N. S., "Combustion of Nitramine Propellants," Publ. 261, Vol. 1, Chemical Propulsion Information Agency, Laurel, MD, 1974, pp. 267–284.

³²Rocchio, J. J., and Juhasz, A. A., "HMX Thermal Decomposition Chemistry and Its Relation to HMX-Composite Propellant Combustion," Publ. 261, Vol. 1, Chemical Propulsion Information Agency, Laurel, MD, 1974, pp. 247–266.

³³Cohen, N. S., and Price, C. F., "Combustion of Nitramine Propellants," *AIAA Journal*, Vol. 12, No. 10, 1975, pp. 25–42.

³⁴Beckstead, M. W., "A Model for Solid Propellant Combustion," *18th Symposium (International) on Combustion*, Combustion Inst., Pittsburgh, PA, 1981, pp. 175–185.

³⁵Beckstead, M. W., and McCarty, K. P., "Modeling Calculations for HMX Composite Propellants," *AIAA Journal*, Vol. 20, No. 1, 1982, pp. 106–115.

³⁶Kubota, N., "Physicochemical Processes of HMX Propellant Combustion," *19th Symposium (International) on Combustion*, Combustion Inst., Pittsburgh, PA, 1982, pp. 777–785.

³⁷Parr, T., and Hanson-Parr, D., "Solid Propellant Flame Structure," *26th Symp. (International) on Combustion*, The Combustion Institute, 1996, pp. 1981–1987.

³⁸Hanson-Parr, D., and Parr, T. P., "RDX Flame Structure and Chemistry," Publ. 620, Chemical Propulsion Information Agency, Laurel, MD, Vol. II, 1994, pp. 333–344.

³⁹Parr, T., and Hanson-Parr, D., "ADN Propellant Diffusion Flame Structure," Publ. 582, Chemical Propulsion Information Agency, Laurel, MD, Vol. II, 1992, pp. 313–327.

⁴⁰Pak, Z., "Some Ways to Higher Environmental Safety of Solid Rocket Propellant Application," AIAA Paper 93-1755, 1993.

⁴¹Parr, T. P., and Hanson-Parr, D., "ADN Diffusion Flame Structure at Elevated Pressure," Publ. 606, Vol. 2, Chemical Propulsion Information Agency, Laurel, MD, 1993, pp. 1–14.

⁴²Jones, M. L., Elrick, D. E., Herriott, G. E., Muhlfeith, C. M., and McCarty, K. P., "Nitramine Combustion," AFRPL-TR-85-041, Hercules Inc., ABL, Cumberland, MD, 1985.

Chapter 2.2

Physico-Chemical Mechanisms of Solid Propellant Combustion

G. Lengellé,* J. Duterque,[†] and J. F. Trubert[†]
ONERA, Châtillon, France

I. Introduction

MUCH work has been devoted, in various countries, to investigating the combustion mechanisms of solid propellants. It is timely to bring together the information obtained by the authors and compared with that of the literature on the combustion of the individual components as well as of their combination into propellants. This chapter is about the existing components and propellants: double-base (DB) propellants and active binders, inert binders, ammonium perchlorate (AP), HMX (octogen) and the corresponding composite propellants, ammonium perchlorate—inert binder (plus possibly aluminum), HMX (or RDX hexogen)—active binder.

The viewpoint adopted here is that of the understanding of the combustion behavior of propellants. Therefore, as much information as possible is presented about the fundamentals of the processes (thermal properties, kinetics in the condensed phase and in the gas phase, etc.), and no attempt is made to establish a complete catalog of practical results on various propellants with different particle sizes, catalysts, and variations on the percentage of ingredients. The aim is to give as clear and conclusive a picture as possible. It thus precludes a complete discussion of the various, sometimes contradictory, mechanisms proposed in the literature. The main theme is to compare the different components and the corresponding propellants.

Some attention is given to physico-chemical modeling. The aim is not so much to give the elements of mathematical descriptions that could be used for a priori computations of burning characteristics of propellants (to the extent that such computations are possible). The point is more to put to test the hypotheses made on the mechanisms of combustion by incorporating them into reasonable models and comparing the results thus obtained to experimental data.

Copyright ©1999 by the American Institute of Aeronautics and Astronautics, Inc. All rights reserved.

*Research Director, Fundamental and Applied Energetics Dept.

[†]Research Scientist, Fundamental and Applied Energetics Dept.

These descriptions can also be viewed, alongside the data given for each component or propellant, as useful for understanding the regimes of combustion that go beyond quiescent steady-state burning, that is, erosive burning and unsteady (under pressure excursions or pressure oscillations) combustion responses.

Table 1 gives information about the various types of propellants in actual use.

Double-base propellants (made by the extrusion or powder casting techniques) are used in antitank rockets or missiles and in some tactical missiles. Their main advantage is that they produce a minimum amount of smoke (only from a small amount of additives).

Composite propellants, based on AP without aluminum, generate reduced smoke, although HCl and H₂O vapor will precipitate into droplets in the plume under given temperature and humidity conditions. They are used for various tactical missiles. With aluminum they are widely used in missiles and space launchers. They produce alumina smoke, which, in the case of space launchers, could be considered in the future to be undesirable (along with HCl).

Composite propellants based on nitramines and an active binder (cross-linked polymer with nitroglycerin or other liquid nitrate esters) are used more and more. Without aluminum they are in the minimum smoke category, and they replace DB propellants. With aluminum they reach the highest specific impulse and density and have been used so far for the upper stages of strategic missiles.

The combustion of the components and then of the various propellants will be discussed in the next sections.

II. Combustion of DB Propellants and Active Binders

A. Introduction

It seems appropriate to consider DB propellant combustion mechanisms first because they correspond to relatively simpler premixed processes, which are easier to understand and because they have been investigated for a long time (starting in the 1950s) in the United States, the former Soviet Union, the United Kingdom, Japan, and France in particular.

As will be seen, the mechanisms involved in the combustion of DB propellants also apply to the active binders (\simeq one-third polymer, \simeq two-thirds nitroglycerin, or other liquid nitrate esters). General background on the combustion of DB propellants can be found in Refs. 1–6.

Double-base propellants are made in a number of ways. When they are rolled or extruded, the components are nitrocellulose and nitroglycerin, to which stabilizers such as centralite and plasticizers are added. When they are cast, a casting powder (made of nitrocellulose, some nitroglycerin, and the various additives) is swelled within the mold by a liquid mixture of nitroglycerin and triacetin. The grain thus obtained is then inhibited and used free standing in the motor. The propellant ingredients can also be mixed, cast, cross-linked, and the grain case bonded.

Adjustments to the relative amounts of nitrocellulose and nitroglycerin (Fig. 1) can increase the energetic level of the propellant or, in the usual terminology, its heat of explosion or calorimetric value, that is, the heat evolved in a calorimetric bomb by combustion under an inert atmosphere. One can then talk about cool and hot compositions.

Double-base propellants are used in small- and medium-sized rockets and thus are exposed to varying ambient temperatures. The sensitivity of the motor operation

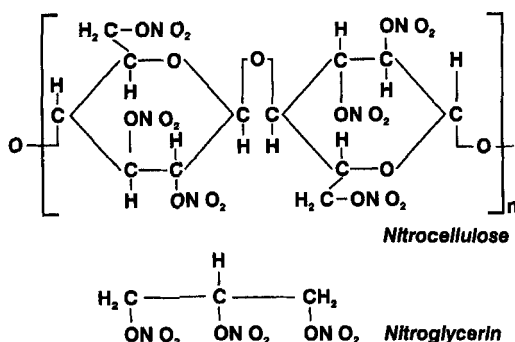
Table 1 Performance/characteristics of various propellants

Propellant	Composition (main ingredients)	ρ_p , g/cm ³	$I_s(70/1)$ theoretical (losses), s	Applications/Characteristics
Extruded DB	Nitrocellulose nitroglycerin	≤ 1.66	≤ 230 ($\simeq -10$)	Antitank rockets and missiles A-S rockets Some tactical missiles (S-A) Minimum smoke
Powder cast DB	Nitrocellulose nitroglycerin	≤ 1.66	≤ 225 ($\simeq -10$)	Antitank missile Some tactical missiles (A-S) Minimum smoke
AP ^a composite	Ex: 88% AP 12% HTPB ^b	1.72	$\simeq 250$ ($\simeq -10$)	Some A-S rockets Some tactical missiles Reduced smoke (HCl-H ₂ O)
AP composite with aluminum	Ex: 68% AP 20% Al 12% HTPB	$\simeq 1.82$	265 ($\simeq -20$)	A-A tactical missiles Antiship missiles (booster) Tactical ballistic missiles Strategic ballistic missiles Apogee motors Boosters for space launchers (Titan III, IV, Space Shuttle, Ariane V, H ₂ , ...) Smokey (Al ₂ O ₃)
HMX (RDX) composite	HMX or RDX and XLDB ^c binder	< 1.75	< 255 ($\simeq -15$)	Antiship missiles (cruise) S-A missiles minimum smoke (without AP)
HMX composite with aluminum	HMX + AP + Al XLDB binder	1.87	273	Strategic ballistic missiles (upper stages) (Trident, MX) Smokey (Al ₂ O ₃)

Sources: *Air et Cosmos*, No. 1000, May 1984; *Annales des Mines*, Jan.-Feb. 1986; *Aéronautique et Astronautique*, No. 138, 1989.

^aAmmonium perchlorate (AP). ^bHydroxyl terminated polybutadiene (HTPB). ^cCross-linked double-base binders (XLDB).

S-A: Surface to air. A-S: Air to surface. A-A: Air to air.



Example of composition :
1100 cal/g, 52.25 % NC, 42.75 % NG, 5 % others

Fig. 1 Components of DB propellants.

to temperature depends upon the propellant burning-rate sensitivity to both the temperature and the pressure. As can be seen in Fig. 2, the pressure exponent, in the usual empirical law $v_b \sim p^n$, is around 0.7 and increases to nearly 1 at high pressure. Super-rate effects (Fig. 3) are created by the use of additives, most often lead and copper salts combined with carbon black. At the end of the super-rate zone, the burning rate falls back to that of the control propellant, with the occurrence of a nearly zero pressure exponent zone, a plateau effect, or a negative exponent zone, a mesa effect. These terms are used by analogy with topographical features. A fairly complete set of results can be found in Ref. 6. It is only in these reduced pressure exponent zones that the propellant is used to minimize the

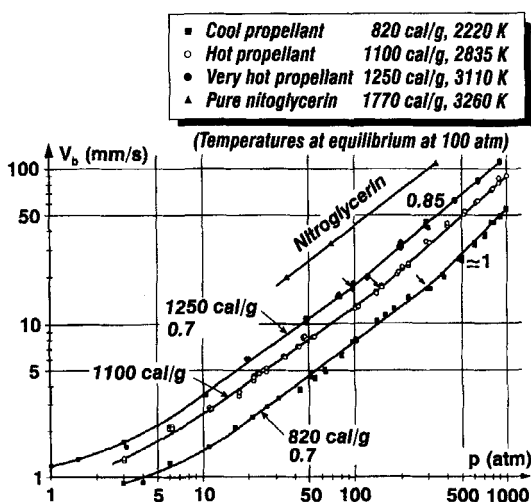


Fig. 2 Burning rate vs pressure laws: DB propellants.

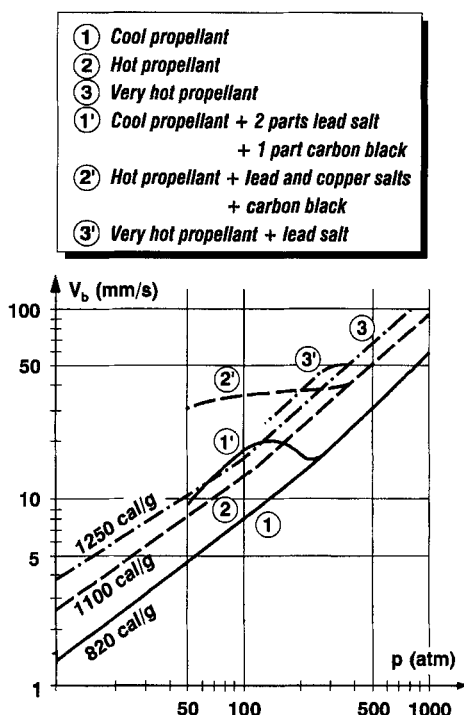


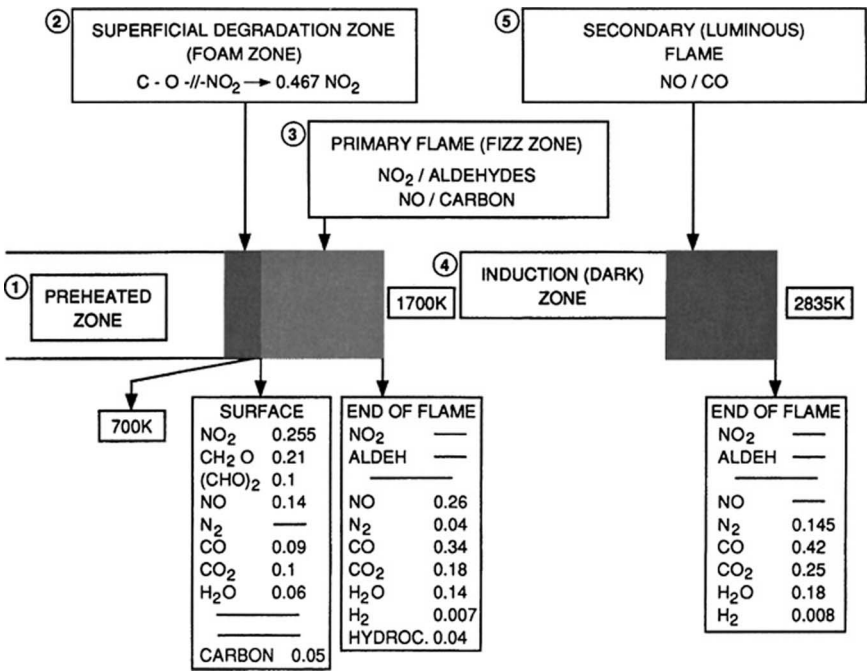
Fig. 3 Super-rate effects: DB propellants.

motor operation sensitivity to ambient temperature. Therefore, the study of the combustion of propellants without additives should be conceived only as a first step toward an understanding of modified (that is, with additives) propellants.

B. Flame Structure

From the works already mentioned, it is possible to describe the combustion wave structure of DB propellants and in particular its chemical processes (see Fig. 4). These various data will be discussed and justified later. Gas analysis results are from Ref. 7; they refer to mass fractions.

The propellant components pass unaffected through a preheated zone of a few tens of micrometers in a few milliseconds and reach a superficial degradation zone (or foam zone in the early literature) where the temperature becomes high enough for the molecular degradation to take place, initiated by the rupture of the C—O—//—NO₂ bond. Simultaneous recombination occurs, so that a mixture of NO₂, aldehydes, but also NO emerges from the surface and so that the net energy balance of the degradation is exothermic. At pressures under about 100 atm (see Fig. 5), a clearly separated primary flame (fizz zone) and a secondary flame (luminous flame) are observed, the first involving NO₂—aldehydes reactions and the second probably NO—CO reactions. In this pressure range the secondary flame is too far away to have any effect on the surface or even to induce a temperature



Figures for an 1100 cal/g propellant. Surface and primary flame (at 11 atm) mass fractions from gas analysis

Fig. 4 Various zones in the combustion of a DB propellant.

gradient into the primary flame. The burning rate is then entirely under the influence of the latter. This corresponds to a burning rate/pressure law with a 0.7 pressure exponent (Fig. 2). As the pressure increases, the secondary flame enhances and then merges into the primary flame, and a transition is observed to a zone with a pressure exponent close to 1. When the secondary flame is fully developed, even at pressures for which it does not yet influence the burning rate, the final products (N₂, CO, CO₂, H₂O, and H₂) and the final temperature (2100–3100 K, depending on the heat of explosion) are attained. Table 2 gives data relative to the various zones of the combustion wave.

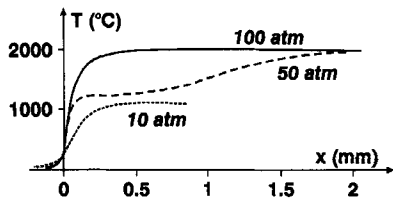


Fig. 5 Temperature profiles at various pressures.

Table 2 Characteristics of the combustion zones

Pressure, atm	v_b , mm/s	T_s , K	Preheated zone, μm (measured/ computed)	Residence time in preheated zone, ms	Superficial degradation zone, μm	Residence time in superficial zone, ms	Flame thickness, μm (measured)
10	1.9	610	140/194	100	11	6	200
50	6.7	662	50/55	8	3	0, 5	75
100	10.6	685	45/35	3	2	0, 2	110 (secondary flame)

Note: Measured results from Zenin.

C. Condensed-Phase Processes

The preheated zone of a regressing propellant is described by the conservation of energy in a coordinate ($x > 0$ in the gas phase) regressing with the surface:

$$\rho_p v_b c_p \left(\frac{dT}{dx} \right) = \frac{d(\lambda_p dT/dx)}{dx} \quad (1)$$

in such a way that a temperature profile

$$(T - T_o)/(T_s - T_o) = \exp(x v_b / d_p), \quad d_p \equiv \lambda_p / \rho_p c_p \quad (2)$$

will progress with the surface into the propellant. From measurements up to 100°C, and from ignition experiments, representative average values of the condensed phase properties for DB propellants are taken as indicated here: $\rho_p = 1.6 \text{ g/cm}^3$, $c_p = 0.4 \text{ cal/g K}$, $\lambda_p = 5.1 \times 10^{-4} \text{ cal/s cm K}$, and $d_p = 0.8 \times 10^{-3} \text{ cm}^2/\text{s}$.

The thickness $e_{\text{cond.}}$ of the conduction zone can be taken conventionally as

$$T(\text{end of cond. zone}) - T_o = 10^{-2} (T_s - T_o) \\ e_{\text{cond.}} = (d_p / v_b) \ell_v 10^2 \quad (3)$$

As an example, for $v_b = 10 \text{ mm/s}$, $e_{\text{cond.}} = 37 \mu\text{m}$, a thickness through which the temperature rises from 293 K to about 700 K. The residence time through this conduction zone is

$$\tau_{\text{cond.}} = (d_p / v_b^2) \ell_v 10^2 \quad (4)$$

about 4 ms in this example, a very short time for a temperature increase of 400 K.

The superficial degradation zone has its thickness ruled by the conservation of the nondegraded propellant mass fraction Y_p :

$$\rho_p v_b \left(\frac{dY_p}{dx} \right) = -\rho_p A_c \exp \left(-\frac{E_c}{RT} \right) \quad (5)$$

with the decomposition represented by an Arrhenius law. Numerous investigations by thermogravimetric analysis (T/A) and differential scanning calorimetry (DSC) on nitrocellulose, nitroglycerin, and other nitrate esters, as well as on DB

propellants, and ignition studies⁵ result in these values for the condensed phase degradation kinetics for DB propellants: decomposition order 0, $A_c = 1 \times 10^{17} \text{ s}^{-1}$ and $E_c = 40 \text{ kcal/mol}$. The thickness of the degradation layer is related to the fast drop in the degradation rate. When this rate is 10^{-2} that at the surface temperature, the lower limit of the reaction layer is conventionally reached:

$$\exp[-\mathcal{E}_c/(1 - \Delta T/T_s)] = 10^{-2} \exp(-\mathcal{E}_c), \quad \mathcal{E}_c \equiv E_c/RT_s$$

The temperature drop is then

$$\Delta T/T_s = 1/(1 + \mathcal{E}_c/\ell_v 10^2) \quad (6)$$

$\Delta T \simeq 100 \text{ K}$ for $T_s = 700 \text{ K}$. Such a temperature drop inserted in Eq. (2) gives an estimation of the reaction-layer thickness

$$e_{\text{reaction}} = -(d_p/v_b)\ell_v[1 - \Delta T/(T_s - T_o)]$$

or, taking into account the magnitude of the reduced activation energy ($\mathcal{E}_c \simeq 30$),

$$e_{\text{reaction}} \simeq e_{\text{cond}} T_s / \mathcal{E}_c (T_s - T_o) \quad (7)$$

For the values just taken, at $v_b = 10 \text{ mm/s}$ then $e_{\text{react}} \simeq 2 \text{ }\mu\text{m}$, with an associated residence time $\tau_{\text{react}} \simeq 0.2 \text{ ms}$.

The summation of Eq. (5) through the degradation layer results in

$$\rho_p v_b (Y_{p,s} - Y_{p,o}) = - \int \rho_p A_c \exp\left(-\frac{E_c}{RT}\right) dx$$

$$v_b \sim A_c \exp\left(-\frac{E_c}{RT_s}\right) e_{\text{reaction}} = A_c \exp(-\mathcal{E}_c) \left(\frac{d_p}{v_b}\right) \ell_v 10^2 \left(\frac{1}{\mathcal{E}_c}\right) \left(\frac{T_s}{T_s - T_o}\right) \quad (8)$$

A more rigorous approach⁸ (which is almost identical to a numerical computation⁹) gives

$$v_b^2 = (d_p/\mathcal{E}_c) A_c \exp(-\mathcal{E}_c) / (1 - T_o/T_s - Q_s/2c_p T_s) \quad (9)$$

This equation indicates a relation between surface temperature and burning rate: the mass flow rate $\rho_p v_b$ emitted from the surface is the result of the decomposition of the propellant into gases throughout the superficial degradation layer Eq. (8). The higher the burning rate v_b , the smaller the residence time $\tau_{\text{react}} \sim 1/v_b^2$, and the higher the surface temperature required for the complete degradation of the propellant.

Traverses with microthermocouples (as already seen, the thickness of the combustion wave is of the order of tens of μm) allow measurements of the surface temperature (see Refs. 2–5). One example is given in Fig. 6. The results from various sources are collected (see Ref. 5), as burning rate vs $1/T_s$, in Fig. 7. Also indicated is the correlation obtained from Eq. (9). Because of the thinness of the conduction zone, a few tens of micrometers, fairly large errors, and scatter should be expected in the measurements of the surface temperature. Nevertheless, some conclusions can be reached (see also Refs. 3 and 10). The initial degradation of the propellant components is controlled by the breaking of the $-C-O-//NO_2$ bond (characterized by the 40 kcal/mol activation energy). This is considered to be a purely temperature sensitive process and irreversible (therefore not influenced by the pressure level). The kinetics of the degradation is the same from thermal

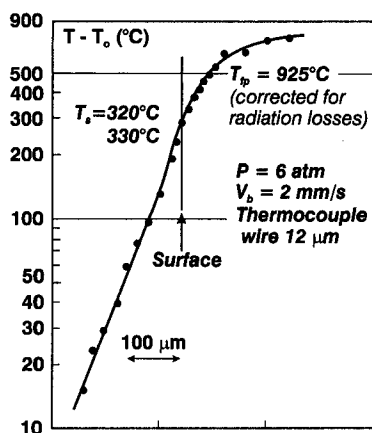
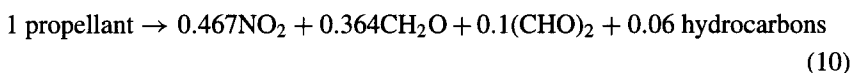


Fig. 6 Temperature profile in the condensed phase.

decomposition [by TGA and DSC] at about 400 K, to ignition from 400 to 500 K (Ref. 5) and combustion at temperatures up to 700 K. Also important is the conclusion, if one looks at the details of Fig. 7, that the presence of super-rate producing additives does not affect the condensed-phase kinetics (although it should be noted that Kubota³ thinks that such an effect exists).

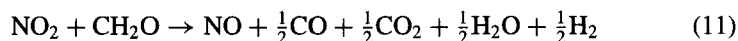
The energetics of the reaction layer is now to be considered. The initial degradation of the propellant, taking into account the assumed decomposition of nitroglycerin into 3NO_2 , $2\text{CH}_2\text{O}$, and $0.5(\text{CHO})_2$, is thought to give (for the example of the 1100 cal/g propellant) the mass balance



with a corresponding endothermic heat of degradation

$$Q_d = -135 \text{ cal/g of propellant}$$

It is thought^{5,9,10} that within the superficial layer the exothermic reaction between NO_2 and aldehydes can start. A plausible mole balance (to match various results, in particular the analysis⁷ of the gases emitted from the surface of regressing propellants) is



with a corresponding exothermic heat of reaction

$$Q_{\text{NO}_2} = 1040 \text{ cal/g of NO}_2$$

Conservation of the species NO_2 (in terms of mass fraction Y) is written (diffusion is not taken into account)

$$\rho_p v_b \left(\frac{dY_{\text{NO}_2}}{dx} \right) = Y_{\text{NO}_2, i} \rho_p A_c \exp \left(-\frac{E_c}{RT} \right) - A_{\text{NO}_2} \left(\frac{pM}{RT} \right) Y_{\text{NO}_2} \exp \left(-\frac{E_{\text{NO}_2}}{RT} \right) \quad (12)$$

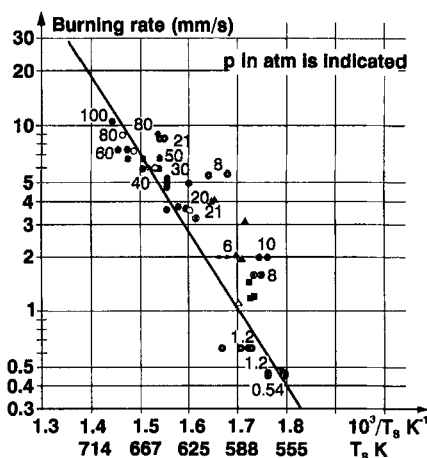
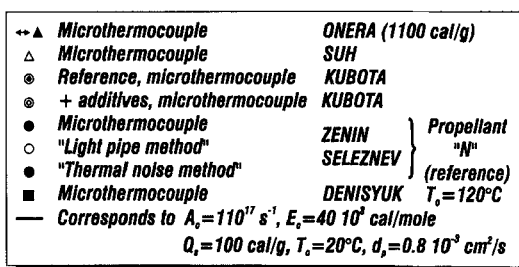


Fig. 7 Pyrolysis law for DB propellants.

if a first-order reaction with respect to the molar concentration of NO_2 is assumed (it will be seen that this is probably the case).

Conservation of energy is written

$$\rho_p v_b c \left(\frac{dT}{dx} \right) - \left[\frac{d(\lambda \frac{dT}{dx})}{dx} \right] = -Q_d \omega_p - Q_{\text{NO}_2} \omega_{\text{NO}_2} \quad (13)$$

with ω_p the rate of reaction of the propellant, as in Eq. (5), and ω_{NO_2} that of NO_2 as in the second term of Eq. (12). The summation of Eqs. (5), (12), and (13) through the condensed phase to the surface leads to

$$\lambda \left(\frac{dT}{dx} \right) \Big|_s = \rho_p v_b (c_g T_s - c_p T_o - Q_s) \equiv \rho_p v_b Q_c \quad (14)$$

$$Q_s \equiv Q_d + Q_{\text{NO}_2} (Y_{\text{NO}_2, i} - Y_{\text{NO}_2, s}) \quad (15)$$

The first equation is the heat balance at the surface, which means that the heat flux from the flame in the gas phase allows the heating and pyrolysis of the propellant. The net heat of decomposition of the propellant Q_s is exothermic, to the extent that some NO_2 already reacts exothermically in the condensed phase.

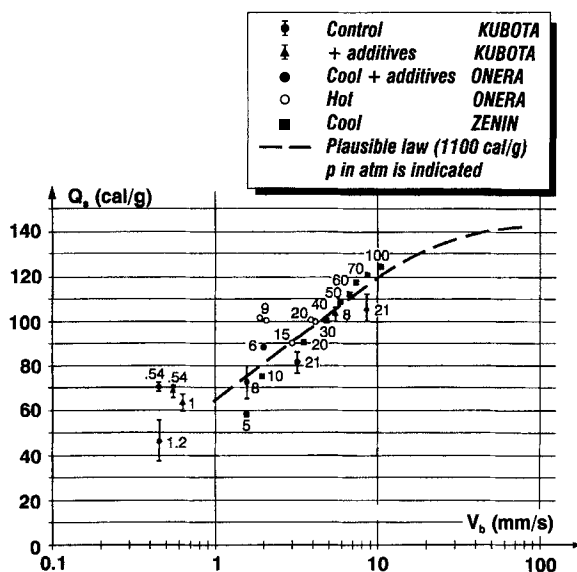


Fig. 8 Heat evolved in the condensed phase of DB propellants.

From thermocouple traverses, such as in Fig. 6, and the balance of Eq. (14), the net heat Q_s can be estimated (again, scatter should be expected). The results from various sources are given in Fig. 8. The net heat of decomposition is seen to be exothermic and increasing with burning rate (because of an increase in pressure). Summation of Eq. (12) yields [with Eq. (5) taken into account]

$$\begin{aligned} \rho_p v_b (Y_{\text{NO}_2, i} - Y_{\text{NO}_2, s}) &= A_{\text{NO}_2} \int \left(\frac{pM}{RT} \right) Y_{\text{NO}_2} \exp \left(-\frac{E_{\text{NO}_2}}{RT} \right) dx \\ &\simeq A_{\text{NO}_2} \left(\frac{pM}{RT_s} \right) Y_{\text{NO}_2} \exp \left(-\frac{E_{\text{NO}_2}}{RT_s} \right) e_{\text{react}}. \end{aligned}$$

and with Eq. (8)

$$Y_{\text{NO}_2, i} - Y_{\text{NO}_2, s} \sim \frac{(pM/RT_s) \exp(-E_{\text{NO}_2}/RT_s)}{\exp(-E_c/RT_s)}$$

This relation indicates that the amount of NO_2 reacting in the condensed phase will increase with pressure, and thus Q_s will increase, if the reaction rate for NO_2 catches up with the decreasing residence time in the degradation layer,

$$\tau_{\text{react}} \sim 1/v_b^2 \sim 1/\exp(-E_c/RT_s)$$

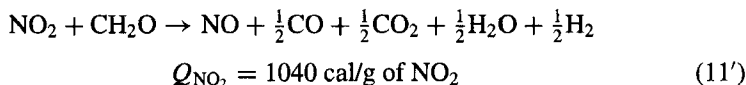
[because of Eq. (9)]. A plausible law is obtained for a first-order NO_2 reaction with an activation energy E_{NO_2} of about 15 kcal/mol.

The observation should be made that the heat evolved in the condensed phase Q_s has to be affected by the amount of NO_2 present in the propellant, that is, by the heat of explosion.

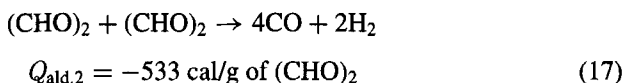
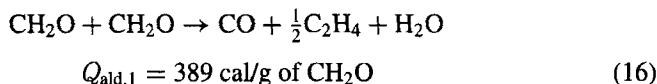
One important feature of Fig. 8 is that the heat evolved in the condensed phase is not affected (considering the scatter) by the presence of additives.

D. Flame Zone

As just seen, the reaction between NO_2 and aldehydes starts in the condensed phase in such a way that the surface gas composition⁷ indicated in Fig. 4 is obtained, with NO_2 being significantly less (0.255) than what results from the initial degradation of the propellant (0.467, in the case of an 1100 cal/g propellant) and with NO already present (0.14). The mole balance of Eq. (11) also allows matching the gas analysis at the end of the primary flame (Ref. 7, measurements at 11 atm):



It is likely that aldehyde-aldehyde reactions also occur following (again to match the gas analysis results)



At low pressure, when probably only reaction (11) can take place, an energy balance between the initial temperature and the end of the primary flame yields

$$c_g T_{\text{fp}} - c_p T_o = Q_d + Q_{\text{NO}_2} Y_{\text{NO}_2,i}, \quad p \leq 1 \text{ atm} \quad (18)$$

because the initial NO_2 is totally consumed in the condensed phase and the primary flame. An evaluation of $T_{\text{fp}} = 1340 \text{ K}$ results. As seen in Fig. 9, measurements with small thermocouples indicate a large increase with pressure of the primary flame temperature from this value. The aldehyde reactions of Eqs. (16) and (17) do not produce significant amounts of energy. The assumption is made⁵ that the NO already present at the surface as well as that produced from the NO_2 -aldehyde reaction react with the layer of carbon residue attached to the surface, which is observed by direct visualization under combustion and after extinction by scanning electron microscopy.

The NO/carbon reaction has been investigated in Ref. 11. If one makes use of the results obtained, the conservation of the species carbon can be written as (knowing that the carbon layer regresses with the surface)

$$v_b \left(\frac{d\rho_c}{dx} \right) = \left(\frac{\mathcal{M}_c}{\mathcal{M}_{\text{NO}}} \right) \omega_{\text{NO}}$$

$$\omega_{\text{NO}} = -A_{\text{NO/C}} \exp \left(-\frac{E_{\text{NO/C}}}{RT} \right) \rho_c S_{s,c} Y_{\text{NO}} p \mathcal{M}, \text{ in g/cm}^3 \text{s} \quad (19)$$

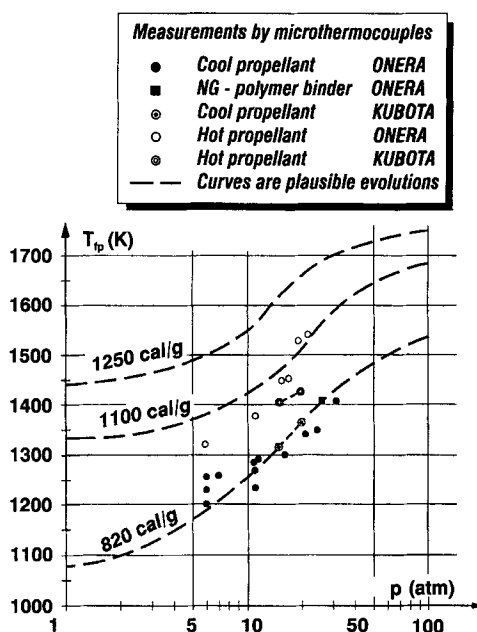


Fig. 9 Primary flame temperature of DB propellants.

(this form resulting from the way the data of Ref. 11 are presented). The reaction balance is assumed to be



and $S_{s,c}$ is the specific surface area of the carbon (at most $10^6 \text{ cm}^2/\text{g}$). Reference 11 produces (after rounding $E_{\text{NO/C}}$)

$$A_{\text{NO/C}} = 2 \times 10^{-3} \text{ mol/s cm}^2 \text{ atm}, \quad E_{\text{NO/C}} = 30 \text{ kcal/mol}$$

A rough estimate of the amount of N_2 produced by reaction (20) through the primary flame is given by (with $m \equiv \rho_p v_b$ the mass-flow rate)

$$m Y_{\text{N}_2, \text{fp}} = -\frac{1}{2} (\mathcal{M}_c / \mathcal{M}_{\text{NO}}) \langle \omega_{\text{NO}} \rangle x_f$$

where $\langle \omega_{\text{NO}} \rangle$ is evaluated at average values through the flame. With $p = 11 \text{ atm}$, $v_b = 0.28 \text{ cm/s}$, $(Y_{\text{NO}}) = 0.2$, $(\rho_c) = 0.5 \text{ g/cm}^3$, $(T_f) = 1400 \text{ K}$, and $x_f = 400 \mu\text{m}$ (from thermocouple measurements), the result is obtained:

$$Y_{\text{N}_2, \text{fp}} \simeq 0.06$$

a reasonable value (with respect to the result shown in Fig. 4). This tends to indicate that the NO/carbon reaction kinetics is indeed fast enough with respect to the residence time allowed in the primary flame.

An energy balance taking into account the NO/carbon reaction is written:

$$c_g T_{\text{fp}} - c_p T_o = Q_d + Q_{\text{NO}_2} Y_{\text{NO}_2, i} + Y_{\text{NO}, \text{cons.}} Q_{\text{NO/C}} + Q_{\text{ald}} Y_{\text{ald}, \text{cons.}} \quad (21)$$

(taking the aldehyde reaction into consideration gives a flame temperature that is cooler by about 80 K). In this balance $Y_{\text{NO,cons.}}$ is the amount of NO consumed in the primary flame:

$$Y_{\text{NO,cons.}} = Y_{\text{NO}_2,i} (\mathcal{M}_{\text{NO}} / \mathcal{M}_{\text{NO}_2}) - Y_{\text{NO,fp}}$$

In the case of the example of Fig. 4 and taking into account the uncertainty on the measurements, $Y_{\text{NO,cons.}} = 0.035\text{--}0.047$, and Eq. (21) results in $T_{\text{fp}} = 1420\text{--}1475$ K, an admissible value when compared to the results shown in Fig. 9.

The temperature profile in the primary flame is controlled by the conservation of energy⁵

$$mc_g \left(\frac{dT}{dx} \right) - \left[\frac{d(\lambda_g dT/dx)}{dx} \right] = -Q_{\text{NO}_2} \omega_{\text{NO}_2} - Q_{\text{NO/C}} \omega_{\text{NO}} - Q_{\text{ald}} \omega_{\text{ald}} \quad (22)$$

Representative values for the gas phase of DB propellants are as follows: $c_g = 0.35$ cal/g K, $\lambda_g = 1.25 \times 10^{-4} (T/700)^{0.7}$ cal/cm s K, and $\mathcal{M} = 30$ g/mol.

The evaluation of the heat flux received at the surface, which controls the burning rate according to Eq. (14), results from the summation of Eq. (22) through the flame zone. Only a true numerical evaluation of the temperature and species profiles will give the proper heat flux. However, conclusions can be drawn from approximate relations. The activation energies of the reactions of Eq. (22) being moderate, the flame is distributed and an approximation of the temperature profile is written as

$$(T_f - T)/(T_f - T_s) = \exp(-3x/x_f) \quad (23)$$

which will produce a shape such as that of Fig. 6. The coefficient of 3 is such that, when $x = x_f$, $T_f - T$ is 5% of $T_f - T_s$, that is, close enough to the final temperature. With Eq. (14)

$$\lambda_{g,s} \left(\frac{dT}{dx} \right) \Big|_s \equiv q_s = m Q_c \equiv \rho_p v_b (c_g T_s - c_p T_o - Q_s)$$

Eq. (23) yields

$$q_s = 3\lambda_{g,s}(T_f - T_s)/x_f, \quad x_f = 3\lambda_{g,s}(T_f - T_s)/m Q_c \quad (24)$$

The summation of Eq. (22) through the flame results in

$$mc_g(T_f - T_s) + q_s = Q_g \langle \omega_g \rangle x_f \quad (\langle \omega_g \rangle \text{ positive is the average rate})$$

or with Eqs. (14) and (24) and taking into account an overall equation for conservation of energy

$$c_g(T_f - T_s) = Q_g - Q_c, \quad m = [3\langle \omega_g \rangle \lambda_{g,s}(T_f - T_s)/Q_c]^{1/2} \quad (25)$$

At very low pressure, ≈ 1 atm, when probably only the NO_2 reaction takes place, the burning rate follows pressure according to [see Eq. (12)]:

$$m \equiv \rho_p v_b \sim (\langle \omega_{\text{NO}_2} \rangle)^{1/2} \sim p^{1/2} \exp(-E_{\text{NO}_2}/2RT_{\text{fp}}) \quad (26)$$

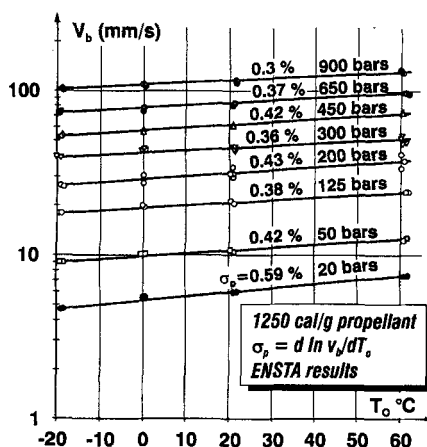


Fig. 10 Temperature sensitivity of DB propellants.

a pressure exponent which is indeed observed (see Fig. 2). As the pressure increases, the NO/carbon reaction takes on more importance, and referring to Eq. (19),

$$m \equiv \rho_p v_b \sim [p \exp(-E_{\text{NO}_2}/RT_{\text{fp}}) + \sim p \exp(-E_{\text{NO/C}}/RT_{\text{fp}})]^{\frac{1}{2}} \quad (27)$$

which, with the increase in flame temperature with pressure (see Fig. 9), accounts for the pressure exponent of 0.7.

At higher pressures, above about 150 atm for the 1100 cal/g propellant for example, a change in the pressure sensitivity (Fig. 2) is observed. This tends to indicate that the secondary flame, probably characterized by a second order, with respect to pressure, reaction for NO, comes into the primary flame and progressively dominates it, with a pressure exponent, according to Eq. (25), increasing to close to 1.

Results shown in Fig. 10 for the 1250 cal/g propellant indicate the temperature sensitivity of the burning rate defined as

$$\sigma_p = \left(\frac{d \ln v_b}{dT_o} \right) \text{ at given } p \quad (28)$$

According to Eq. (27), the burning rate is under the influence of a premixed flame heat flux [noting that the condensed-phase energy balance also contains the effect of T_o , see Eq. (14)] and is therefore very sensitive to changes in the primary flame temperature, in the pressure domain when the two flames are separated. From Eq. (21) any change in initial temperature will affect the primary flame temperature and therefore induce a change in burning rate. As the pressure rises, the primary flame temperature increases (up to 1800 K), and then for higher pressures the burning rate comes under the influence of the final flame (with a temperature reaching 3110 K for the 1250 cal/g propellant). Equation (27) shows that a given change in T_o and therefore in T_f has a smaller impact on the burning rate for

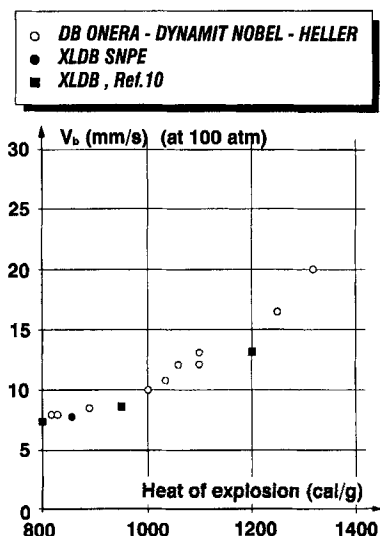


Fig. 11 Burning rate vs heat of explosion: DB propellants and XLDB binders.

higher flame temperatures, that is, for higher pressures, a tendency observed in Fig. 10.

E. Active Binders

Various types of active binders, based on nitrocellulose or an inert binder and nitroglycerin or less energetic liquid nitrates, can be used (see Ref. 10 for a complete description). The cross-linked double-base binders (XLDB), in which the polymer is cured with an isocyanate after mixing with NG, is considered here. These are the values for an XLDB binder: composition is \simeq two-thirds NG, \simeq one-third polyethylene glycol; heat of explosion = 850 cal/g; $T_{ff} = 2000$ K; $\rho_p = 1.42$ g/cm³; $c_p = 0.46$ cal/g K; $\lambda_p = 3.9 \times 10^{-4}$ cal/cm s K; $d_p = 0.6 \times 10^{-3}$ cm²/s; $Y_{NO_2,i} = 0.421$; and $Q_d = -150$ cal/g.

Although the burning rates of the different active binders can be, for a given heat of explosion, somewhat different at low pressures,¹⁰ above 10 atm the differences become small (see Fig. 11). In the case of a DB propellant and of an XLDB binder, with nearly the same heat of explosion, the burning rates for a large range of pressure are very close (Fig. 12).

Measurements of the degradation kinetics, of the surface temperature, of the heat evolved in the condensed phase, as in Fig. 8, and of the primary flame temperature, Fig. 9, for XLDB binders show that these characteristics are very close to those of DB propellants.

Gas analysis at the surface gives results that are qualitatively comparable to those of DB propellants (Fig. 4). The mass fraction of the gases evolved from the surface for an XLDB binder⁷ are listed as follows: NO₂, 0.31; CH₂O, 0.37; (CHO)₂, 0.08; NO, 0.07; CO, 0.03; CO₂, 0.04; H₂O, 0.02; and HC, 0.08. It can then be stated that the combustion mechanisms of the various types of DB propellants and of the active binders are very similar.

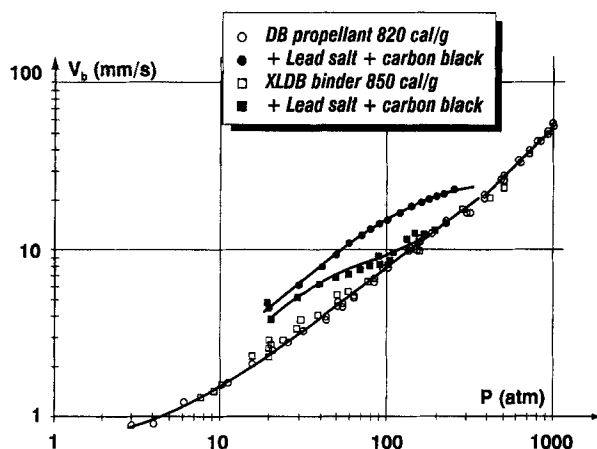


Fig. 12 DB propellant and active binder burning rates.

F. Mechanisms of Action of Additives

The incorporation of a few percent of lead (and copper) salts and carbon black permits the achievement of super-rate effects followed by mesa or plateau effects in the burning rate vs pressure laws of DB propellants (Fig. 3) and of active binders (Fig. 12), although in the latter case these effects are much less pronounced.

What is thought to be the mechanism for the action of the additives has been presented in Refs. 5 and 6 by the authors and in Ref. 12.

The active part of the lead salt has been found to be the oxide of lead that accumulates above the propellant surface after the salt has been trapped in the carbon residue layer, which can be observed, immersed in the primary flame (the decomposition kinetics of the salt is slower than that of the propellant components, and it thus emerges from the surface unchanged). If the propellant (when its heat of explosion increases) or the active binder naturally produces less carbon residue, then the lead-salt particles are in large part ejected from the surface and cannot act. This is probably the case when the amount of nitrocellulose is reduced (hot DB propellants) or almost absent (XLDB binders). In the latter case, however, the inert polymer leaves some carbonaceous residue. Addition of carbon black is probably helpful because it accumulates on the surface in the naturally produced carbon layer.

The authors have found that PbO reacts preferentially with aldehydes to form carbon and CO₂. The observation has been made systematically⁶ that there is a relation between the amount of carbon residue and the magnitude of the super-rate observed (depending, for example, on the fabrication process: solventless extrusion, powder casting, mixing). The primary flame is caused by an NO₂-aldehyde reaction. But NO also starts to react with carbon close to the surface, leading to the increase in primary flame temperature shown in Fig. 9. It is believed that the extra carbon produced in the presence of additives enhances the NO/C reaction (see Ref. 12 for more results on this reaction), depositing extra energy in the primary flame (an increase in primary flame temperature is observed in the presence of additives⁵) and results in a higher heat flux to the surface, and thus a higher burning rate.

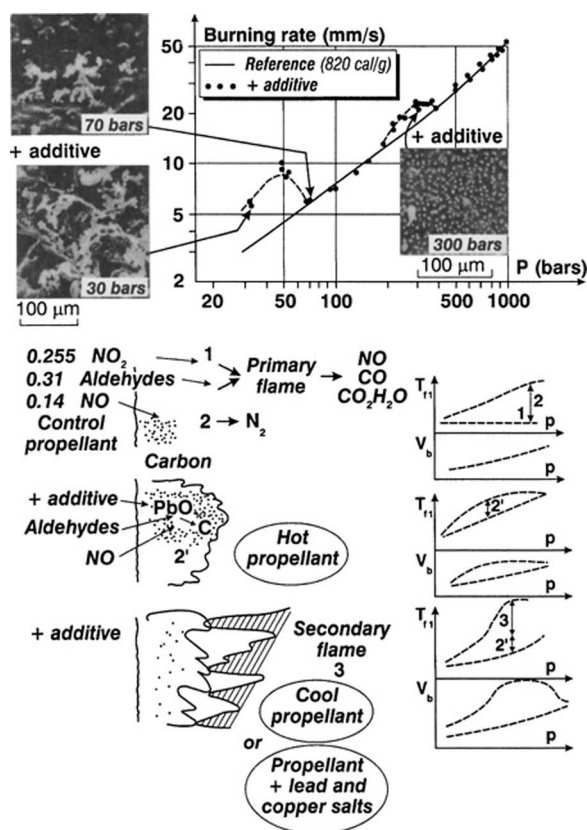


Fig. 13 Super rate effects.

Figure 13 shows surface structures of a cool propellant with a strong super rate and a corresponding thick carbon residue. In this case visualization shows that a physical effect occurs in which the secondary luminous flame attaches in streaks to the carbon layer and brings its high temperature (≈ 2200 K as compared with the ≈ 1400 K of the primary flame) closer to the surface. The abrupt end of the super rate, the mesa effect, is believed to be caused by the too thick carbon residue being expelled from the surface. At the end of the mesa effect, the surface is almost devoid of carbon.

In the case of hot propellants (Fig. 3), the super rate is probably caused only by the chemical effect of the enhanced NO/C reaction. As the pressure increases, the secondary flame, where NO reacts anyway, merges into the primary flame, the modified propellant is progressively caught up by the reference propellant, and a plateau effect results.

When the propellant is ignited, it first behaves like the noncatalyzed propellant, until a carbon residue layer builds up and becomes efficient.

In the high-pressure domain, when the flame system has been reduced to one overall flame, a second super rate occurs (when only lead salt or oxide is added);

see Fig. 13 for the cool propellant and Fig. 3 for a 1250 cal/g propellant. This effect seems to be purely physical, related to the presence of lead oxide particles accumulating and embedding in the surface (Fig. 13) with, for example, an enhancement of the thermal conductivity of the flame zone or more probably a flame-holding effect (the protruding particles perturb the flow from the surface). At higher pressures and burning rates the thickness of the condensed-phase heated zone and reaction layer and flame zone becomes so small that the particles will not attach to the surface or will be too large to perturb the combustion process.

III. Pyrolysis of Inert Binders

A number of books and shorter studies have been devoted to the behavior of polymers, whether or not they are usable as binders, under thermal loads; Refs. 13–17 are examples. Much work has been carried out with TGA or DSC, with the highest heating rates on the order of 0.1°C/s. Under linear pyrolysis (for a binder within a solid propellant), the rate of temperature increase is of the order of 10⁵°C/s. It is far from obvious a priori that the degradation kinetics will be maintained. In Ref. 8 the argument is made that this is indeed the case for a number of polymers.

Although it is hardly a propellant binder, Teflon® is an interesting reference polymer. Its degradation kinetics (obtained by TGA) and thermal properties⁸ ($\lambda_p = 6.34 \times 10^4$ cal/cm K s, $\rho_p = 2.1$ g/cm³, $c_p = 0.25$ cal/g K) are indicated in Fig. 14. To extrapolate these characteristics to the regime of linear pyrolysis (obtained experimentally by pressing the sample on a hot plate), the procedure described in Ref. 8, also explained in the condensed-phase paragraph of the DB propellants section is applied. In the case of a first-order (with respect to the nondegraded polymer) reaction, the relation between regression rate and surface temperature is

$$v_r^2 = \frac{(d_p/\mathcal{E}_c)A_c \exp(-\mathcal{E}_c)}{(-\ell_v Y_{p,s})(1 - T_o/T_s - Q_s/c_p T_s) + Q_s/c_p T_s}$$

$$\mathcal{E}_c \equiv \frac{E_c}{RT_s} \quad (29)$$

Q_s is the heat evolved in the condensed phase, in this case endothermic and about –340 cal/g ($Y_{p,s}$ the mass fraction of the remaining polymer at the surface can be set at 0.01). Numerical computation shows this relation to be accurate to within 1%. Figure 14 shows that there is a good match between the extrapolated law and the measurements. These measurements were obtained under various atmospheres, with no perceptible influence. The conclusion is therefore reached that the pyrolysis of such a polymer is an irreversible thermal mechanism.

In the case of an actual, widely used propellant binder such as hydroxyl terminated polybutadiene (HTPB), the same extrapolation can be made. Figure 15 compares the calculation (thermal properties used: $\lambda_p = 3.6 \times 10^{-4}$ cal/cm K s, $\rho_p = 0.92$ g/cm³, $c_p = 0.39$ cal/g K) with the results of Ref. 15, which were obtained in a hybrid motor with gaseous oxygen on HTPB and with the surface temperature being measured by infrared (IR) pyrometry (with some dispersion). A

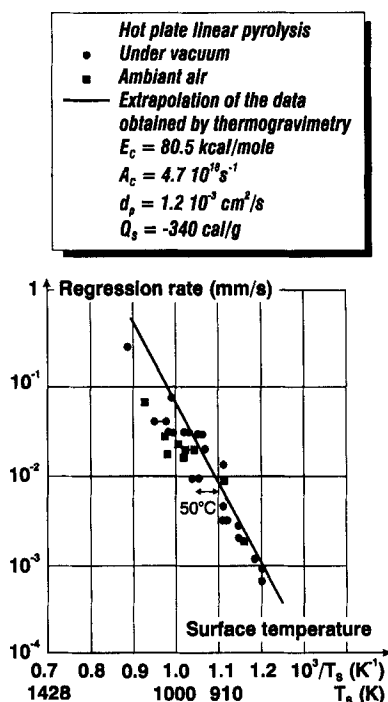


Fig. 14 Linear pyrolysis and extrapolation of thermogravimetric results (example of Teflon®).

measurement obtained by the authors with CO₂ laser heating and IR pyrometer is also indicated. The agreement, considering the extent of the extrapolation, is very satisfactory. Further on, the pyrolysis law based on the TGA and DSC kinetics will be considered to apply.

Equation (29) and Fig. 15 indicate how the surface temperature adjusts itself to allow the polymer to degrade into gases when the regression rate changes. To better understand the binder behavior, the nature of the gases resulting from the pyrolysis and the corresponding heat of degradation should be considered.

The heat of ablation of HTPB was measured in Ref. 16 by relating the mass ablated to the radiation heat flux received by a sample. For a regression rate of 0.4 mm/s (and from Fig. 15, $T_s \approx 1060$ K) the following result is obtained:

$$h_{abl} = c_p(T_s - T_o) - Q_s = 750 \text{ cal/g}, \quad Q_s = -450 \text{ cal/g} \quad (30)$$

This value is compatible with the production of mostly C₄H₆ as pyrolysis gas. Gas analysis at low temperature¹³ reveals a complex set of gases ($\approx 45\%$ in mass butadiene, ethylene, propene) resulting from the degradation of HTPB. If one evaluates the difference in heats of formation of the initial material and butadiene, one can see that

$$\Delta h = h^\circ(\text{C}_4\text{H}_6) - h^\circ(\text{HTPB}) = 496 \text{ cal/g} - 5 \text{ cal/g} \approx 490 \text{ cal/g}$$

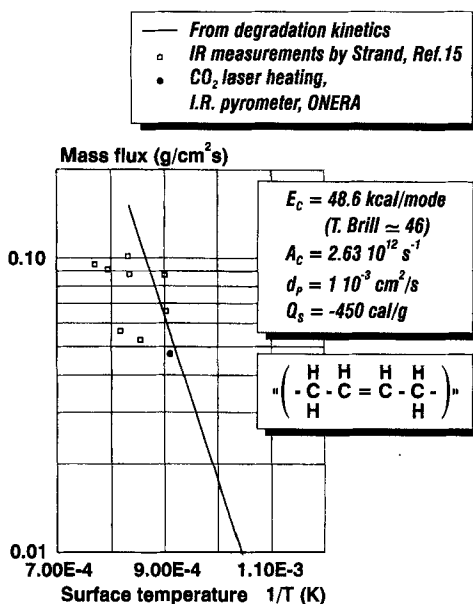


Fig. 15 Pyrolysis law for HTPB.

which is close to the measured heat of degradation. At high heating rates butadiene is probably the major degradation gas.

IV. Combustion of AP

AP, NH_4ClO_4 , is a widely used oxidizer and as such has been the object of numerous investigations. References 18–22 are a sampling, one of them giving a detailed list.²² A viewpoint on the combustion of AP is presented here, attempting to make use as much as possible of the various experimental data available. Because of the large number of works on AP combustion, somewhat contradictory interpretations and corresponding models have been produced. A simplified model is presented, which is considered to represent reasonably the combustion mechanism of AP, although it will not be in agreement with all of the just-mentioned interpretations.

A. Condensed-Phase Behavior

The considerations already presented for the condensed phase of a pyrolyzing monopropellant apply to AP. The conduction zone has a thickness

$$e_{\text{cond.}} = (d_p/v_b) \ell_v 10^2$$

(with the thermal diffusivity²¹ $d_p \approx 1.2 \times 10^{-3} \text{ cm}^2/\text{s}$ at an average temperature in the heat wave) thus equal to $\approx 55 \text{ } \mu\text{m}$ for a burning rate of 10 mm/s . The condensed phase values for AP^{19,21} are listed here: $c_p = 0.31 \text{ cal/g K}$

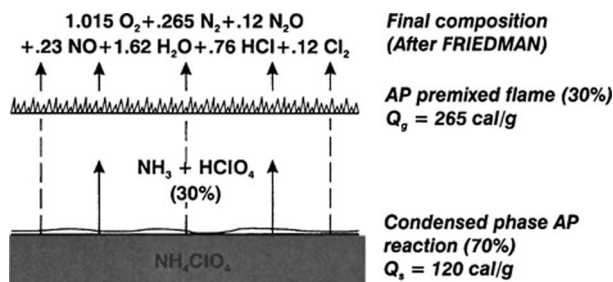


Fig. 16 Autonomous combustion of AP.

(orthorhombic phase < 513 K) = 0.365 cal/g K (cubic phase); $\rho_p = 1.95$ g/cm³; and $d_p = 2.5 \times 10^{-3} - 4.55 \times 10^{-6} T(^{\circ}\text{C})$ cm²/s.

Based on observations by scanning electron microscopy after extinction, the idea has been advanced that the self-deflagration of AP, possible only above 20 atm, requires that a significant exothermic reaction already take place in the condensed phase in a thin liquid layer (above a melting temperature estimated at 835 K).¹⁹⁻²² The original idea of such a liquid layer was proposed by Price in 1967 (see Ref. 19).

B. Energetics of AP Combustion

The model of Ref. 19 is adopted to describe the combustion of pure AP. The AP undergoes a phase transition at 513 K, melts around 835 K, and, in the thin (a few microns) superficial liquid layer thus created, an exothermic reaction affecting 70% of the AP takes place and creates the final combustion gases, O₂ in particular. The remaining 30% of the AP sublimates into NH₃ and HClO₄, which react exothermically in a premixed flame very close to the surface (a few microns) (Fig. 16).

From the data presented in Ref. 19, the change of enthalpy per gram of AP required to heat up the AP to its surface temperature $T_{s,AP}$ is estimated as

$$\begin{aligned} \Delta h_{H,AP} = & 0.31 (513 - 293) + 21 + 0.365 (835 - 513) + 60 \\ & + 0.328 (T_{s,AP} - 835) = 266 + 0.328 (T_{s,AP} - 835) \text{ cal/g} \end{aligned} \quad (31)$$

where the heat of transition and the heat of liquefaction appear. The exothermic condensed-phase degradation involves an enthalpy change of¹⁹

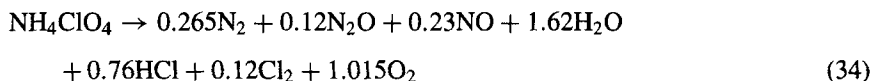
$$\Delta h_{D,AP} \simeq -380 \text{ cal/g of reacting AP} \quad (32)$$

The heat of sublimation is 58 ± 2 kcal/mol or

$$\Delta h_{S,AP} = 476\text{--}510 \text{ cal/g of subliming AP} \quad (33)$$

The adiabatic flame temperature for the combustion of AP alone is estimated in

Ref. 18 to be $T_{f,AP}^{ad} = 1205$ K, corresponding to the reaction



The change of enthalpy $\Delta h_{C,AP}$, corresponding to the combustion of the sublimed NH_3 and HClO_4 [to give the combustion products of Eq. (34)], is obtained from the equation expressing the conservation of enthalpy between the unreacted AP at initial temperature and the combustion products downstream of the flame:

$$0.3\Delta h_{C,AP} + c_g(T_{f,AP}^{ad} - T_{s,AP}) + 0.3\Delta h_{S,AP} + 0.7\Delta h_{D,AP} + \Delta h_{H,AP} = 0 \quad (35)$$

For $c_g \simeq 0.3$, the value given in Ref. 19, it is found that

$$\Delta h_{C,AP} = -850 \text{ to } -885 \text{ cal/g of reacting AP} \quad (36)$$

depending on the value adopted for the heat of sublimation, 476 or 510 cal/g, and independent of the value of $T_{s,AP}$ in the range found in Ref. 19.

The value given here for the transformation of AP into gases [that is, NH_3 and HClO_4 for the subliming 30% and the combustion gases of Eq. (34) for the 70% reacting in the condensed phase], namely

$$-Q_s = 0.3(476 \text{ to } 510) + 0.7(-380) = -123 \text{ to } -113 \text{ cal/g of AP} \quad (37)$$

is also found in Ref. 20, where a model for the combustion of AP similar to that of Ref. 19 is adopted. The heat evolved in the condensed phase Q_s (>0 if exothermic) will be set equal to 120 cal/g.

One last check of consistency can be performed. With the enthalpy of formation of AP at $h_{AP}^0 = -602$ cal/g and that of the combustion products of Eq. (34) $h_{CP}^0 = -877$ cal/g, an overall energy balance between initial AP and combustion products is

$$c_g T_{f,AP}^{ad} + h_{CP}^0 = c_{ortho} T_0 + h_{AP}^0 \quad (38)$$

resulting in $T_{f,AP}^{ad} = 1215$ K, which is close enough to the preceding value.

C. Surface Pyrolysis of AP

Attempts to measure the surface temperature give values between 670 and 973 K. These results, obtained either by using thermocouples imbedded in the AP pellet or by measuring the radiation emitted by the surface, are always associated with some uncertainty because of the operating methods. In effect, the large size of the thermocouples, in relation to the temperature gradients encountered, favors errors; further, the measurement represents an averaging of surrounding conditions. The temperatures thus obtained are therefore probably somewhat lower than the actual temperatures. In the case of experiments using an optical technique, the temperature is deduced from measuring the radiation emitted by the surface and transmitted by the gaseous layer. The disturbance caused by the radiation of the gases and the screening action of the flame limits the application of this method to 60 atm. That is why the original technique suggested by Seleznev,²³

carried out by using a sapphire light guide inserted into the solid substance and by reading the IR emission in the direction of the condensed phase, has the considerable advantage of providing a direct measurement of the radiation emitted by the surface without any hot gases and the reaction of the flame being interposed. Its application can therefore be extended to high pressures, and the measurements appear to be more convincing. These results enable a definition of the AP pyrolysis law.

Further, estimates of the AP melting temperature have been put forward by a number of authors; the values suggested vary from 715 ± 20 K and are useful in interpreting the extinction phenomenon at low pressure.

The pyrolysis law of AP is written as

$$m_{AP} = \rho_{AP} v_{b,AP} = A_{s,AP} \exp(-E_{s,AP}/RT_s) \quad (39)$$

The parameters characterizing the pyrolysis law are determined so as to obtain a good agreement between the rates and the surface temperatures measured by Seleznev²³ (Fig. 17). The activation energy obtained is 20 kcal/mol, a figure compatible with the various estimates encountered. The measurement of the surface temperature made at 40 atm is the only one that deviates from that computed by the pyrolysis law used. On the other hand, for the critical rate of 0.27 cm/s obtained at 20 atm (the AP combustion pressure limit), this law allows for a surface temperature of 830 K, corresponding to the assumed AP melting temperature.¹⁹

D. Flame Structure of AP Combustion

The approach described in Ref. 19 considers 14 different reactions for the flame zone of the AP, involving 30% of the material sublimed into NH_3 and HClO_4 . An

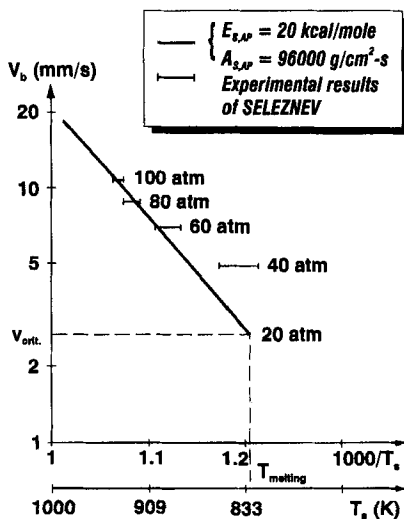
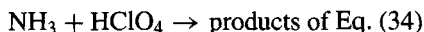


Fig. 17 Pyrolysis law for AP.

overall second-order reaction is then obtained:



with an activation energy of $E_{g,AP} = 15$ kcal/mol.

A simplified model is constructed like the one used in the section on the DB flame. The temperature profile is approximated as

$$\frac{T_{f,AP}^{\text{ad}} - T}{T_{f,AP}^{\text{ad}} - T_{s,AP}} = \exp\left(-\frac{3x}{x_f}\right) \quad (40)$$

with the boundary condition

$$q_s \equiv \lambda_{g,s} \left(\frac{dT}{dx} \right) \Big|_s = m_{AP} Q_c, \quad Q_c = \Delta h_{H,AP} - Q_s \quad (41)$$

Where Q_c is the heat required to bring the AP from T_o to gases at the surface [see Eqs. (31) and (37)].

Combining Eqs. (40) and (41) results in

$$m_{AP} = \frac{3\lambda_{g,s}(T_{f,AP}^{\text{ad}} - T_{s,AP})}{x_f Q_c} \quad (42)$$

Summation of the energy equation from $T_{s,AP}$, $x = 0$, to x_f yields, after using Eqs. (41) and (42) and Eq. (35) written as

$$-Q_g + c_g(T_{f,AP}^{\text{ad}} - T_{s,AP}) + Q_c = 0$$

$$m_{AP} = [3\langle\omega_g\rangle\lambda_{g,s}(T_{f,AP}^{\text{ad}} - T_{s,AP})/Q_c]^{\frac{1}{2}} \quad (43)$$

In this equation the average reaction rate is written as

$$3\langle\omega_g\rangle = p^2 A_{g,AP} \exp(-E_{g,AP}/RT_{f,AP}^{\text{ad}}) \quad (44)$$

expressing a second-order overall rate. The burning rate is then found to follow pressure with an exponent close to 1. Representative values for the AP flame zone are listed here: $\rho_{AP} = 1.95$ g/cm³; $E_{s,AP} = 20$ kcal/mol; $A_{s,AP} = 96,000$ g/cm² s; $E_{g,AP} = 15$ kcal/mol; $A_{g,AP} = 700$ g/cm³ s atm²; $\gamma = 30\%$; $c_g = 0.3$ cal/g K; and $\lambda_g = 1.9 \times 10^{-4}$ cal/cm s K.

Taking into account the various values given for $v_b = 10$ mm/s and $T_{s,AP} \simeq 925$ K the flame stand-off distance is obtained, as given by Eq. (42) and with $Q_c = 175$ cal/g, $x_f \simeq 5$ μ m, the height to reach T_f within 5%.

The only input data that is not defined from outside considerations is the pre-exponential factor $A_{g,AP}$, which is used as a floating parameter for the model. Just by the choice of the prefactor $A_{g,AP}$ adjusted at 700 g/cm³ s atm², the model satisfactorily reproduces variations in the AP burning rate caused by pressure, as well as those caused by the change in the initial temperature of the product. Figure 18 provides a comparison of computed rate curves with experimental points.²¹

At sufficiently high pressures the energy transmitted from the flame toward the surface, to which must be added the effect of the superficial exothermic reactions, maintains the surface temperature above the AP melting point. When the pressure

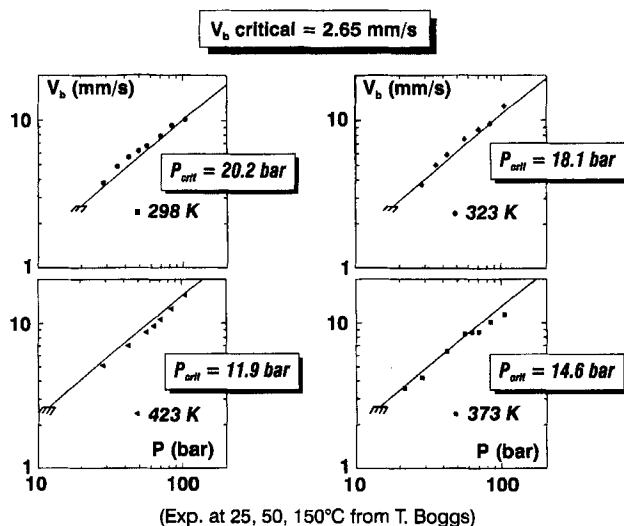


Fig. 18 Burning rate of AP at different initial temperatures.

falls, the premixed flame moves away, and the surface temperature can then drop below the limiting value, thus causing the disappearance of the liquid surface layer, which was enabling the exothermic reactions to occur. The energy from the flame is then much too small to maintain a pyrolysis that has become strongly endothermic, and the AP no longer burns. This minimum pressure, beyond which the combustion cannot propagate itself, sets the pressure limit for AP self-degradation.

On the basis of this hypothesis, the combustion pressure limit is reached when the surface temperature is equal to the AP melting temperature. It is interesting to use the model in order to follow the variation of the computed limiting pressure with the initial temperature. At atmospheric pressure the combustion limit is 20 atm, in agreement with experimental results. The critical rate of 0.27 cm/s and the surface temperature of 830 K, representing the AP melting temperature, correspond to it. The computational method consists, for the initial temperatures between 0 and 200°C, in finding for what pressure the surface temperature is equal to 830 K. A comparison between the computed and experimental pressure limits is very good (Fig. 19) and confirms the soundness of the hypothesis following which AP burns only if the surface temperature exceeds its melting temperature.

One further set of results is presented. Questions have been raised about the combustion of AP at high pressures, above about 100 atm, with many conflicting results. Measurements of burning rates on carefully inhibited samples are presented in Fig. 20. The conclusion can be made that no strong change in the combustion regime is observed. The model based on the preceding hypothesis seems to follow quite well the results up to high pressures. One can argue that the combustion of AP is somewhat helped by some diffusional flame with the degradation gases of the inhibitor material and that the various anomalies seen in noninhibited samples are thus erased.

Chapter 2.3

Flame Structure of Solid Propellants

Oleg P. Korobeinichev*

Russian Academy of Sciences, Novosibirsk, Russia

I. Introduction

IT is generally believed that future progress in the understanding of solid propellant (SP) combustion is to arise from a clearer picture of the chemistry and physics taking place in SP flames. The combustion of SP is a complex multistage process based in the chemical transformations in the condensed- (C-) and in the gas- (G-) phase flame. Much more detailed information about the combustion chemistry of SP is required to enable progress in the understanding of SP combustion. It is important to understand the combustion chemistry because this is the type of information a propellant formulator or a chemist may use to tailor and/or improve the performance of the propellant.¹

The main source of our knowledge of the combustion chemistry of SP comes from the results of flame structure studies: for example, spatial distributions of temperature and species concentration in flame.²⁻⁹ Analysis of the data on SP flame structure provides information on the composition of the C-phase reaction products (gasification products) that are the products of SP thermal decomposition on its burning surface. This, in turn, makes it possible to understand what reactions take place in the C-phase and what their mechanisms are. On the other hand, the chemical structure of the SP flame provides information on the mechanism and kinetics of G-phase chemical reactions of further transformations of gasification products. These reactions are responsible for heat release in the G-phase. The development of SP combustion models requires information on these two reactions, the C-phase and the G-phase. It is impossible to develop a real SP combustion model capable of predicting SP burning rate and other SP ballistic characteristics without this information.

The main methods applied to the investigation of chemical and thermal flame structure of SP are the following: 1) probing mass spectrometry²⁻⁶; 2) spectroscopic methods for absorption and emission,^{1,7,8} including planar laser-induced fluorescence,⁸ spontaneous Raman scattering (SRS), and coherent anti-Stokes Raman spectroscopy,⁹ and 3) the microthermocouple technique.¹⁰ Systematic

studies of SP flame structure using laser spectroscopic methods have been carried out by Parr and Hanson-Parr^{11,12} and Modiano and Vanderhoff.¹³ An essential feature of spectroscopic methods is that they are nonintrusive. However, there are many species (and very often the key species) in a flame that cannot be detected by this method for various reasons. For example, their spectra may be absent from the accessible wave number range, or apparatus sensitivity may not be high enough to provide their detection. Until recently, there were few works on SP flame structure. The improvement of experimental techniques, however, the development of works on flame structure modeling, and the rise of interest in SP combustion chemistry have increased the amount of research in this field.

At present, one of the most effective and universally used experimental techniques for studying SP flame structure is mass spectrometric probing (MSPSPF), which was first presented in Ref. 14. This method allows the detection of all of the species present in the flame as well as determination of their concentrations and spatial distributions, that is, the study of the flame microstructure. The method is as follows: A burning strand of SP moves with a velocity exceeding the burning rate toward a probe, so that the probe is continuously sampling gaseous species from all the zones, including those adjacent to the burning surface. The sample is transported to an ion source of a time-of-flight or quadrupole mass spectrometer. Mass spectra of samples are recorded with simultaneous filming of the probe and the burning surface.

Two types of apparatus have been developed to study flame structure. The sample is transported to an ion source either as a molecular flow using a microprobe with an inlet orifice of 10–20 μm , or as a molecular beam using a sonic probe with an inlet orifice of 20–200 μm . The former setup has high spatial resolution and only slightly disturbs the flame, allowing the study of flames with a narrow combustion zone of up to 0.1 mm. However, in this case, radicals recombine and unstable species can decompose and react on the inner walls of the probe. The latter setup, with molecular beam mass spectrometric (MBMS) sampling, allows detection of radicals and other unstable species but disturbs the flame more strongly and, therefore, has a reduced spatial resolution. The first type of setup and procedure will be referred to as setup 1, the microprobe technique (MPT), and the second type of setup and the corresponding procedure as setup 2, the molecular beam technique (MBT). In the work reported in Ref. 14, the use of MPT to study SP flame structure was first demonstrated by studying the flame structure of a model formulation based on ammonium perchlorate (AP) and polymethylmetacrylate. It was further applied to the study of SP flame structures with narrow combustion zones, or AP and composite propellants based on it. Much later, a similar setup using MPT was developed by Fetherolf and Litzinger⁶ and Lee et al.¹⁵ Its special feature is the use of a triple quadrupole mass spectrometer¹⁵ and a CO_2 laser to study laser-supported combustion (LSC) of SP. The use of a triple quadrupole mass spectrometer makes mass-spectra interpretation easier. The use of a CO_2 laser to heat the SP strand from its face plane widens SP combustion limits toward the lower pressure range. This in turn provides a wider zone of chemical reactions in the SP flame, thus diminishing the error in the flame concentration profile measured by the probe; it is generally believed that the flame zone width should be greater than the probe tip dimensions. Note that research has demonstrated that self-sustaining SP combustion mechanisms often differ from laser-supported ones. Therefore, the application of the results of flame structure studies for SP LSC to self-sustaining

SP combustion can result in erroneous conclusions. Later, an MBMS setup for SP flame structure studies was developed,¹⁶ and with its help the structures of SP flames with burning zones about 1 mm wide were studied.

The objective of this chapter is to describe briefly the MSPSPF method and to present the results of studying the flame structure of monopropellants capable of self-sustaining combustion, such as AP, RDX, HMX, and ADN, as well as some ballistic and composite SP obtained during the two past decades.

II. Experimental

Figure 1 shows the MBMS system²⁻⁴ that has been used to examine the flame structures of RDX, HMX, ADN, and some composite SP. It includes an apparatus for probing a flame, containing a molecular beam sampling system; a time-of-flight mass spectrometer (TOFMS) type MSKh-4 as a detector; a combustion chamber; a scanning system; a data-acquisition system; and an experiment controller based on CAMAC equipment and a computer. The flame is sampled with a probe 3 (Fig. 1), a 25-mm-high cone with a 50-deg external angle, a 40-deg internal angle, and a 50–100- μm -diam orifice at the apex (at 1 atm). The probe produces a molecular beam that passes to an ion source. The ignition spiral 12 is automatically removed from the combustion zone after ignition. To scan the SP flame, a control system and a stepper motor 13 are required. The burning strand 14 is moved by the motor 13. A thermocouple 15 serves to measure temperature profiles in the flame. The strand is moved at a speed of less than 20 mm/s and is driven by a stepper motor with a step of 2.5 μm . The data acquisition and control system consists of an AT486 computer and a CAMAC apparatus. To study the flame structure at high pressure by MBMS, a quartz probe with an inner angle of 40 deg and an orifice of 50 μm at 3 atm, 20 μm at 6 atm, and wall thickness near the probe tip of 25 μm has

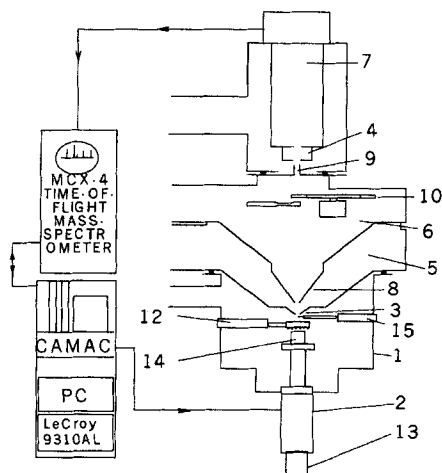


Fig. 1 MBMS system for studying the flame structure of solid propellants with TOFMS: 1) combustion chamber, 2) scanning system, 3) probe, 4) ion source, 5) skim-mer chamber, 6) collimator, 10) slotted disk, 11) electromagnetic chopper, 12) ignition spiral, 13) stepper motor, 14) burning strand, and 15) thermocouple.

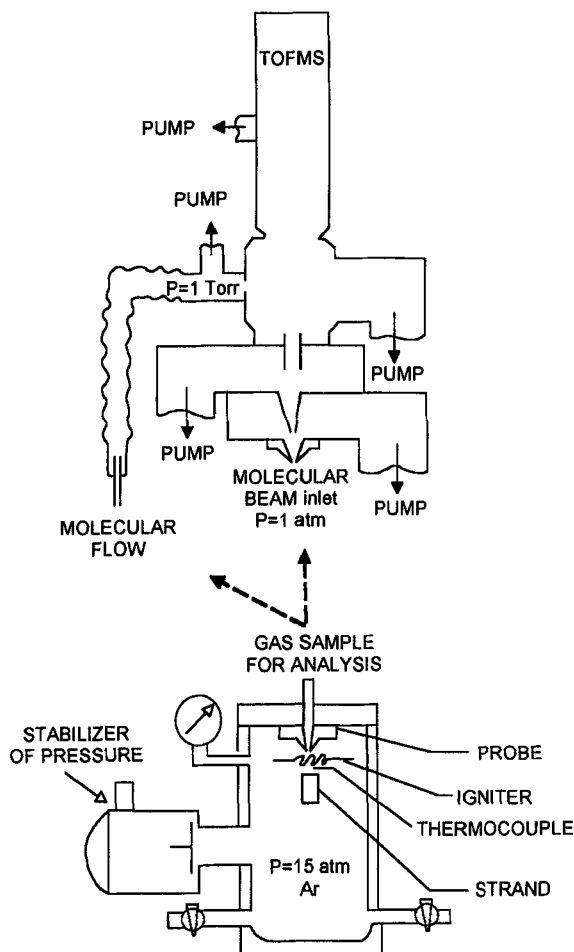


Fig. 3 Microprobe sampling system for investigation of double-base propellant flames at high pressure.

III. Substantiation of the Method of Probing Flames with Narrow Combustion Zones

Quantitative aspects of the results of mass spectrometric (MS) sampling investigations of SP flame structure are substantially defined by the accuracy of the sampling technique. Detailed studies¹⁷⁻²⁰ have been carried out to substantiate the probing method when the ratio of the flame zone width L_b to the probe tip outside diameter d was close to one. This occurs in the case of a preheated ($T = 533$ K) AP flame²¹ where the burning zone is about 0.1 mm wide at 0.6 atm. The distortions can be subdivided into external and internal ones, the external ones being hydrodynamic and thermal. The probe acts as a sink for matter and heat, which results in the distortion of nearby temperature and concentration lines.^{22,23} The errors

have been determined^{17,18,24} by measuring perturbations in the velocity field in one-dimensional gas flow using submicrometer particles and a pulsed laser. The flow starts deviating from a one-dimensional type at a certain distance depending on the sampling factor that is defined by the equation

$$\alpha_0 = 4Q/\pi d_0^2 v_0$$

where Q is the sink flow rate, d_0 is the probe orifice diameter, and v_0 is the flow velocity. The measured field of velocities was in agreement with that calculated from Rosen's disk sink model.²² This model can, therefore, be used to calculate parameters required to evaluate measurement errors.

Probe-error estimates have been also carried out for a real flame. A preheated AP flame with $L_b \sim 0.1$ mm was used, but there were serious experimental difficulties in finding data on the AP chemical structure. Model experiments were, therefore, performed with a methane-air flat flame with an argon additive having a 0.5-mm burning zone width. A special quartz probe was used (subsequently referred to as a macroprobe) with an outside tip diameter equal to the flame zone width of 0.5 mm and with a probe orifice of $d_0 = 0.012$ mm. This probe and flame were similar in such dimensionless parameters as $d_0(\alpha_0)^{0.5}/L_b$, $L_b/d \approx 1$, and $Re_d \approx 1$ to those used in the case of the AP flame (Re_d is the Reynolds number of the flow determined from the probe outside diameter). The following methods were applied to study the structure of the model flame: 1) microthermocouple technique (MT) using Π -shaped platinum-platinum/rhodium thermocouples (wire diameter of 0.02 mm) for measuring temperature profile, 2) probe mass spectrometry measuring methane concentration profile by macroprobe and quartz microprobe with $d_0 = 0.06$ mm, $d = 0.12$ mm, and 3) SRS spectroscopy for measuring methane and nitrogen concentration profiles. Figure 4 shows the dependence of methane molar fraction α , normalized to the maximal values α_{\max} , on the distance L from the burner in methane flame. Points on curve 1 derive from $\alpha/\alpha_{\max} = 1 - T/T_{\max}$,

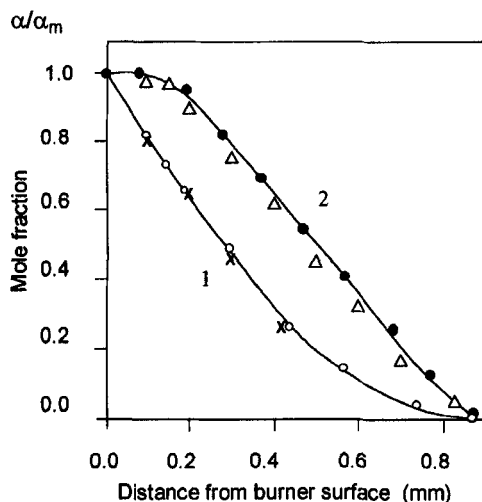


Fig. 4 Mole fraction profiles of methane in methane-air flat flame measured by the different methods: \times , SRS; \bullet , macroprobe; Δ , microprobe; and \circ , thermocouple.

which was obtained on the assumption that temperature and methane concentration curves are similar. The comparison of the results of measuring methane concentration profiles in the model flame by probing methods (curve 2) and nonintrusive diagnostics (curve 1) shows that the error of the probe technique in finding concentrations at the burning surface was less than 10%. When the tip of the probe diameter was reduced seven times, the change in concentration was about 15%. Curve 2 in Fig. 4 coincides within 15% with the undisturbed profiles (curve 1); if curve 2 (from the probe measurements) is shifted toward the burner by a value close to Z_0 , the calculated shift of the sampling point with respect to unperturbed flow. Calculations²³ based on simplified assumptions of the flame and flow preturbations (Rosen's model²²) provided the values $Z_0 \approx 0.4 d_0(\alpha_0)^{0.5}$ and $\Delta \approx 0.3 d_0(\alpha_0)$, where Δ is a sampling zone width representing spatial sampling resolution. MS study of preheated AP flame structure d_0 was 0.012 mm and $\alpha_0 = 75$. After applying appropriate corrections for the sampling point on the concentration profiles (Z_0 shift), the error in finding concentrations by the probe method was less than 15% of its maximal value. This error and sampling zone width were within $\pm 15\%$ of the AP flame zone width, and they were reasonably small for quantitative processing of AP flame structure data.

IV. SP Flame Structure: Results and Discussion

AP, RDX, and ADN are simple propellants belonging to the class of homogeneous condensed systems (monopropellants) that have been examined in detail. They are of simple chemical structure, and so they provide good models for studying combustion mechanisms. They are also the main components of composite SP. The knowledge of their combustion mechanisms is essential to developing composite SP combustion models.

A. Flame Structure of AP and Composite Propellants Based on It

An AP flame preheated to 533 K was studied at 0.6 and 1 atm on the two aforementioned setups. The main experiments were carried out on setup 1 with MPT,²¹ and additional experiments were carried out on setup 2 with MBT.¹⁶ Table 1 represents the results of some peak intensity profile measurements obtained on setup 2 with MBT probing an AP flame preheated to 533 K at 1 atm (see Ref. 16). These experiments provided the first detection of mass peaks with the m/e 83 and 100 characteristics of perchloric acid. Thus, these experiments provided the first

Table 1 Species mass peaks intensities (in relative units) at different L in AP flame (a setup with molecular-beam sampling)

m/e	$L, \mu\text{m}$					
	0	50	100	150	200	250
83	230	140	65	10	0	0
67	290	280	190	90	20	0
52	310	270	230	160	80	0
51	200	180	130	90	30	0

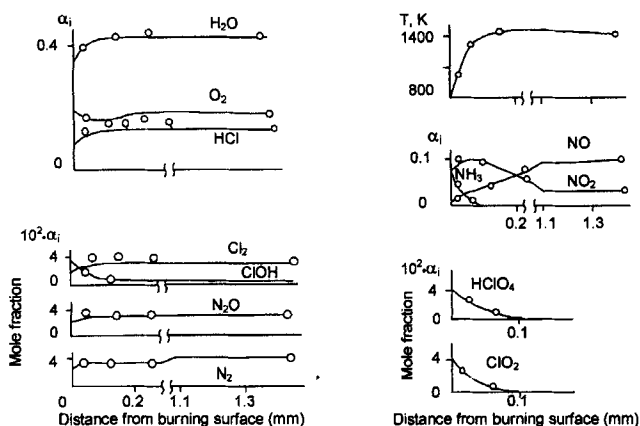


Fig. 5 AP flame structure (points are for experiment and lines are for calculation).

experimental support of the hypothesis that perchloric acid is the main AP gasification product in the combustion wave that plays a key role in the AP combustion mechanisms. This result laid the foundation of modern models of the combustion of AP. The ratio between the intensity of the perchloric acid peaks with m/e 83 and those of chlorine dioxide with m/e 67 (the latter being obtained with regard to the fact that the peaks with m/e 83 from perchloric acid contributes to the peaks with m/e 67) is shown in Table 1.

This ratio (the intensity of the perchloric acid peaks with m/e 83 is equal to those of chlorine dioxide with m/e 67) was used when correlating the data obtained on setup 1, under which conditions chloride dioxide resulting from heterogeneous catalytic decomposition of perchloric acid on the probe walls into ClO_2^+ and HO_2 contributes to a peaks with $m/e = 67$.

By the use of the results of measuring calibration coefficients by individual species and mass peak intensities of the species obtained in the experiments on setup 1, and studying AP flame structure at 0.6 atm (533 K), species concentrations were found. Profiles of species concentrations and temperature vs the distance from the burner surface L are presented in Fig. 5. Concentration profiles in an AP flame show the following two-zone structure: in a narrow (~ 0.1 -mm-wide) zone, NH_3 , HClO_4 , and ClO_2 concentrations fall and NO_2 concentrations rise, and in the next wide (~ 1.5 -mm-wide) zone NO_2 concentrations fall whereas NO and O_2 concentrations rise.

Figure 5 also represents modeling results for the same flame structure (lines)^{25,26} performed using a mechanism incorporating 80 reactions. Satisfactory agreement between the calculation and experimental results provides evidence for the suggested mechanism. Subsequent work provides a revised mechanism.²⁷ The obtained results were used when developing an AP combustion model.²⁸⁻³¹

The flame structure of composite propellants based on AP and HTPB was studied at subatmospheric pressures on setup 1 with MPT and modeling.³²⁻³⁴ In the flame zone, 16 stable species (HCl , H_2O , CO , NH_3 , CO_2 , HClO , NO , O_2 , H_2 , NO_2 , N_2 , C_4H_6 , C_2H_2 , ClO_2 , Cl_2 , and HCN) were detected. No HClO_4 was found, but HClO_4 concentration was determined as it was for the AP flame. The reactions of oxidation of ammonia and HTPB destruction products with perchloric

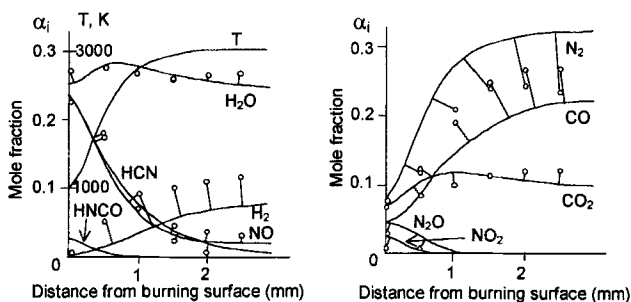


Fig. 6 Temperature and species mole fraction profiles in RDX flame at 0.5 atm (points are for experiment and solid line for modeling).

acid decomposition products (ClO_2 , $ClOH$, ClO , etc.) are the main reactions in the flame of composite propellants based on AP and HTPB. The data analysis of the flame structure of a composite propellant based on AP/HTPB (especially rich formulations) at low pressure indicates that the oxidation of hydrocarbon binder destruction products occurs in the flame much faster than does ammonia oxidation. The obtained data were used when developing a combustion model of AP composite propellants.³⁵

B. RDX and HMX Flame Structure

The results of studying the flame structure in the high-temperature zone of an RDX flame at 0.5 atm (see Ref. 36) using the MBMS technique are shown in Fig. 6. The burning surface was identified, with allowance for the sampling shift Z_0 calculated from the afore-mentioned formula ($\alpha_0 = 70$, $d_0 = 0.1$ mm). These results show that the key species in the RDX high-temperature flame zone are NO and HCN. The main reaction in the high-temperature zone of the RDX flame is the reaction $HCN + NO$ and not $CH_2O + NO_2$ as was previously postulated.³⁷ Figure 6 also shows calculated profiles of mole fraction from the results of Ermolin et al.³⁶ The calculations are in satisfactory agreement with the experimental data. Melius's mechanism³⁸ provided better agreement with the experimental results as compared with that of Ermolin et al.³⁶ The obtained data have also been used by other researchers^{39–41} when developing and validating detailed RDX combustion mechanisms and models. The analysis of experimental data¹⁷ and Melius's model³⁸ predict the existence of a narrow cool flame zone (less than 0.1 mm at 0.5 atm), where RDX vapor decomposition takes place.

Research on low-temperature flame zones in RDX and HMX flames has been carried out by different authors,^{12,42,43} mainly using thin thermocouples. Some investigators reported a plateau on the temperature profile near the burning surface of a temperature of ~ 1000 K. This plateau would provide support for the hypothesis of a narrow zone in cool flame where RDX or HMX vapor decomposition takes place. Other researchers,⁴³ however, did not find evidence to support this hypothesis. The study of a narrow zone (~ 0.1 mm wide) in an RDX flame using MPT with a probe having an orifice of about 0.01 mm could lead to erroneous conclusions. This is because in this case the RDX vapors would hardly be detectable through their possible heterogeneous catalytic decomposition at the

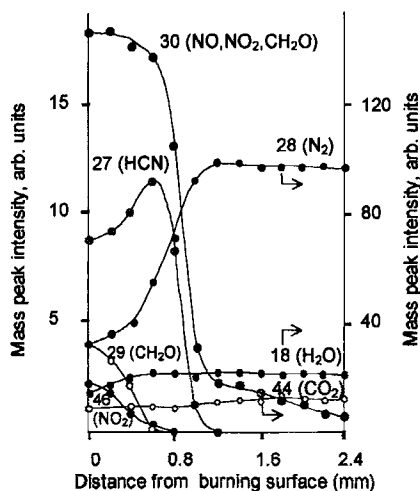


Fig. 7 Profiles of mass peak intensities for HMX flame at 1 atm.

microprobe walls (similarly to HClO_4 decomposition at microprobe walls in an AP flame). Because of the difficulties in an MBMS study of flame zones less than 0.1 mm wide, there is, to date, no direct experimental evidence of the existence of RDX vapor decomposition in an RDX flame. This problem is to be solved in the future. The differences in RDX flame structure in self-sustained³⁶ and laser-supported^{44,45} combustion supports the suggestion that the chemical combustion mechanisms are different in these two processes. There is much that is common to HMX and RDX flame structures, but there are differences as well. Figure 7 represents mass peak intensities in an HMX flame at 1 atm (see Ref. 4). As is apparent from Fig. 7, two clearly defined subzones are seen in the high-temperature zone of the HMX flame. CH_2O and N_2O decomposition takes place in the first one; HCN oxidation with nitrogen oxide, as in the RDX flame, takes place in the second one. Note that NO_2 and CH_2O were also found in the RDX flame at 0.5 and 1 atm. However, mass peaks at intensities of 46 (N_2O) and 29 (CH_2O) were detected in those cases to a much smaller extent. The results obtained for HMX flame structure were used when developing an HMX combustion model.⁴⁶

C. ADN Flame Structure

ADN is a new energetic material that can be used as an oxidizer in solid rocket propellants.⁴⁷ It presents an alternative to AP, being an ecologically pure oxidizer in SP. ADN is a simpler monopropellant than AP and RDX, as defined both by the number of elements as well as by the possible intermediate and final combustion products. In the last few years several works devoted to the study of the ADN combustion mechanisms have been published.^{6,48,49} ADN flame structure was studied at 1–6 atm using an MBMS and MT.⁴⁹ The flame structure was found to involve three zones. At 1–3 atm, a luminous flame zone was not observed. The burning rate at 1–6 atm is controlled by reactions in the condensed phase. At 3 atm a cool flame zone adjacent to the burning surface was found (Fig. 8). The

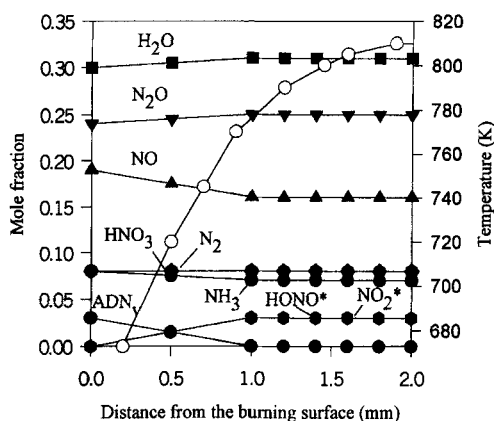


Fig. 8 Temperature and species mole fraction profiles in ADN flame at 3 atm, experimental results.

width of this zone is about 1–1.5 mm. The following mass peaks were found in the mass spectra of samples taken from the area adjacent to the burning surface at 3 atm (ions responsible for these peaks are cited in parentheses): 63 (HNO_3^+), 62 (NH_2NO_2^+ , NO_3^+), 47 (HNO_2^+), 46 (NO_2^+), 45 (HN_2O^+), 44 (N_2O^+), 30 (NO^+), 29 (N_2H^+), 28 (N_2^+), 18 (H_2O^+), and 17 (NH_3^+ , OH^+). Because the HONO mass spectra is not known, we could not take into account these species' contribution to mass peak 46. A sum of the NO_2 and HONO concentration profiles is, therefore, presented in Fig. 8. The ratio between mass peak intensities in the mass spectra of samples taken from the zone close to the ADN burning surface at 3 atm and those of ADN decomposition products⁴⁹ are in reasonable agreement. The results of an MS study of the kinetics and mechanism of ADN evaporation and decomposition in a flow reactor at a low pressure of 1–10 torr has shown that the mechanism of ADN evaporation differs from the mechanism of the evaporation of other ammonium salts. In the case of ADN, evaporation takes place followed by the dissociation of ADN into ammonia and dinitraminic acid (DA):



In the case of AP and ammonium nitrate, dissociative sublimation takes place, yielding ammonia and the corresponding acid. Data analysis provided the ADN molecule mass spectrum, ADN vapor pressure as a function of temperature, and a rate constant for ADN vapor dissociation. The analysis of the mass spectra of the samples taken from the zone near the ADN burning surface at 3 atm has shown that gaseous ADN and DA are the key reactants in the near-surface zone. The product composition near the ADN burning surface has been determined. Gaseous ADN and DA decomposition in the near-surface zone results in a temperature rise of about 150 K. A kinetic model for DA thermal decomposition at low pressure was developed by Park et al.⁵⁰ The second high-temperature zone is found 6–8 mm from the ADN burning surface at 6 atm (Figs. 9 and 10). The main reaction in this zone is ammonia oxidation by nitric acid. The temperature rise in this zone is 500 K. The combustion temperature in this zone is 1400 K, and the combustion products are H_2O , NO , N_2O , and N_2 . The third zone was observed at 40 atm.

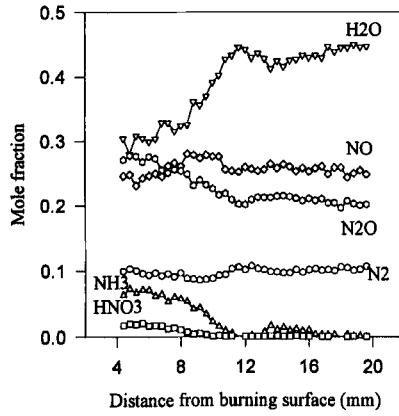


Fig. 9 Species mole fraction profiles in ADN flame at 6 atm, experimental results.

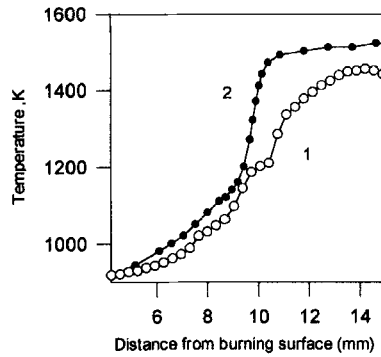


Fig. 10 Temperature profile in ADN flame at 6 atm, 1 represents experiment and 2 represents modeling.

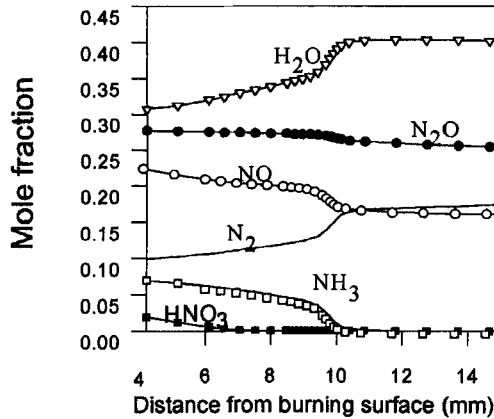


Fig. 11 Species mole fraction profiles in ADN flame at 6 atm, modeling results.

Table 2 Product composition in ADN flame at 3 atm, $L = 0.2$ mm

i	NH ₃	NO	N ₂ O	N ₂	HNO ₃	H ₂ O	ADN _v
α_i	0.08	0.19	0.24	0.08	0.08	0.3	0.03

The measured final temperature of 2000 K is close to the thermodynamically calculated one (2100 K). ADN combustion product compositions at 3 and 6 atm at different distances L from the burning surface are shown in Tables 2 and 3.

The temperature measured at the distance $L = 4.4$ mm at 6 atm with a thin Pt–PtRh thermocouple is 920 K. Product mass flow is 3.4 g/cm² s at 6 atm. With the preceding data representing boundary conditions and making use of the CHEMKIN code,⁵¹ the second zone of the ADN flame at 6 atm was modeled based on the developed⁵² mechanism (98 reactions and 22 species). Part of these reactions and their rate constants have been suggested by Park et al.⁵⁰ The results of temperature and species concentration profile calculations⁵² are shown in Figs. 10 and 11. Correlation between the experimental and calculation results suggests that they are in satisfactory agreement, which would be expected for such a complex system. The calculation has also shown the existence of the third zone at higher pressures, where nitrous oxide decomposes to nitrogen and oxygen with a temperature rise to a value (~ 2000 K) close to the thermodynamic equilibrium temperature. The obtained data are applicable for developing an ADN combustion model.

D. Flame Structure of Propellants Based on ADN and HTPB

The flame structure of propellants based on HTPB (3%) and ADN (97%) at pressures of 0.5–1 and 6 atm was studied by MBMS.⁵³ For propellant HTPB/ADN (3/97) at 6 atm, video recording near the burning surface revealed a dark zone of ~ 0.3 mm that was in agreement with the data obtained when studying the flame structure of ADN-based sandwiches.¹¹ The dark zone width increases up to 1.5 mm as pressure is reduced to 1 atm.

The combustion of HTPB/ADN (3/97) propellant is jetlike in nature. Video recording demonstrated the presence of several brightly luminous jets approximately 0.5–1 mm in diameter at the burning surface, disappearing at one site and appearing at another with a lifetime of 0.2 s. The spatial heterogeneity and nonstationary nature of the propellant combustion process is in agreement with MS and temperature measurements. Thermocouple investigations have shown temperature fluctuations (Fig. 12) of about $\pm 400^\circ\text{C}$ at 1 atm in the flame zone within 1.5–4 mm from the burning surface. Along with the temperature fluctuations, variations in the intensities of mass peaks 17 (NH₃⁺), 28 (CO⁺, N₂⁺), 30 (NO⁺), 46 (HNO₃⁺, NO₂⁺), and 44 (CO₂⁺, N₂O⁺) take place. The values for

Table 3 Product composition in ADN flame at 6 atm, $L = 4.4$ mm

i	NH ₃	NO	N ₂ O	N ₂	HNO ₃	H ₂ O
α_i	0.07	0.23	0.28	0.1	0.02	0.3

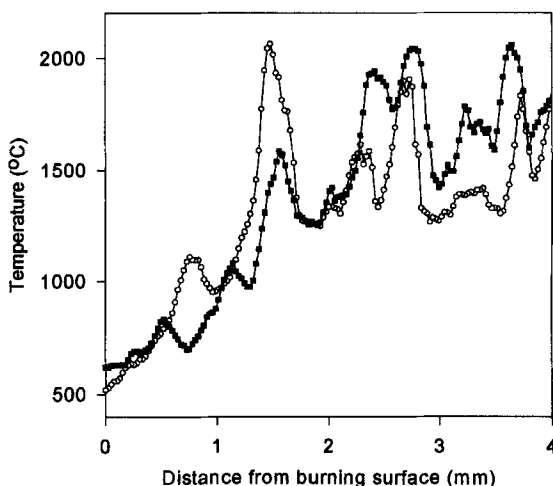


Fig. 12 Temperature profiles in HTPB/ADN flame at 1 atm (two different experiments).

mass peak relative intensities of combustion products near the burning surface of ADN/HTPB 97/3 propellant and pure ADN at 1 atm are close and are presented in Table 4.

One can suggest that pure ADN combustion products are mainly found in the dark zone of propellant combustion and that luminous jets are formed in the G-phase when they are mixed with HTPB decomposition products. One of the explanations of the presence of luminous jets with a mean size of ~ 0.5 – 1 mm at the burning surface, exceeding the size of fuel powder particles (~ 0.04 mm), may be the agglomeration of small ADN particles into large ones at the burning surface. A similar phenomenon has been found when observing ADN particles behavior in noncured HTPB. On heating, melted ADN particles moved together, and on cooling it crystallized into large particles of ~ 1 mm. Similar processes can take place in propellant combustion as well. The combustion product composition of composite propellant ADN/HTPB 97/3 at 1 atm approaches the product composition of pure ADN combustion at 6 atm, in the content of nitrogen-containing components (Table 5).

Thus, the ADN-HTPB interaction in a flame provides an increase in the final temperature and ADN combustion completeness. The main carbon-containing

Table 4 Normalized ($I_i/\Sigma I_j$) mass peak intensities in ADN/HTPB (97%:3%) composite propellant flame at 1 atm (dark zone near the burning surface)

Composition	p , atm	AMU					
		17	18	30	44	46	28
ADN/HTPB	1	0.15	0.10	0.27	0.25	0.12	0.11
ADN	1	0.15	0.07	0.26	0.16	0.23	0.06

Table 5 Comparison of the flame temperature and the final combustion product composition of pure ADN and ADN/HTPB composite propellant

Composition	p , atm	T , K	NH_3	H_2O	N_2	NO	N_2O	CO_2
ADN/HTPB (97/3)	1	2370	0.01	0.35	0.13	0.26	0.18	0.06
ADN	6	1420	0	0.45	0.11	0.25	0.20	—

propellant combustion product at 1 atm is CO_2 . CO was not found in the combustion products.

E. Double-Based Propellant Flame Structure at High Pressure

Probing mass spectrometry and modeling were used to study a double-base propellant flame structure (propellant *N*) at 15 atm (see Ref. 4) using the setup shown in Fig. 3. The composition of propellant *N* is the following: nitrocellulose, 57%; nitroglycerin, 28%; dinitrotoluene, 11%; and stabilizer, plasticizer, 4%. Sampling was performed using a ceramic probe (orifice 300 μm in diameter). The structure of the dark and flame zones was studied at distances more than 2 mm from the burning surface (Fig. 13). In the first zone, situated 2–6 mm from the burning surface, the concentrations of compounds CO_2 , $\text{N}_2 + \text{CO}$, HCN, NO, and H_2 were almost constant. In the second, from 6 to 12 mm, the concentrations of CO_2 , $\text{N}_2 + \text{CO}$, and H_2 varied less drastically. The equations of material balance were used to calculate the concentrations of CO, CO_2 , N_2 , NO, and H_2O in the first and at the end of the second zones. In this case, it was taken into account that the carbon content (up to 5% of the total quantity of carbon) was in the form of soot. The temperature profile was measured with a W/Re thermocouple (50 μm). The composition of products and the temperature in the first zone were used as the boundary conditions to compute the structure of the second flame zone by

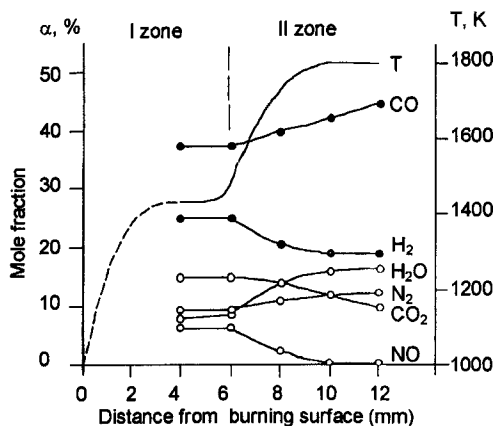


Fig. 13 Profiles of temperature and species concentrations for propellant *N*, $P = 15$ atm, points are for experiment and solid lines are for calculation.

Table 6 Propellant N2 combustion product composition at 20 atm

α_i	α_{CO}	α_{CO_2}	α_{N_2}	α_{H_2}	$\alpha_{\text{H}_2\text{O}}$
Experiment	0.348	0.164	0.135	0.0745	0.279
Calculation	0.35	0.161	0.135	0.073	0.28

a multistage mechanism (81 reactions, 22 components). Satisfactory agreement between the experimental and calculated data of temperature profiles and species concentrations was achieved. Similar calculations modeling the structure of the dark zone of double-base propellant combustion are presented in Ref. 54. Similar studies have been performed at $P = 20$ atm for the double-base propellant N2 (see Ref. 4) that has a higher energy than *N* propellant and the following composition: nitrocellulose, 58%; nitroglycerin, 40%; and centralite, 2%. Satisfactory agreement is observed between the experimentally determined composition of the combustion products of propellant N2 (the final combustion temperature was 2700 K) and the calculated equilibrium composition at 2700 K (Table 6). The data obtained allow this method to be recommended for the study of propellant flame structure at high pressures and the composition of propellant combustion products at high pressure under conditions close to those of SP rocket motors.

V. Conclusions

The probing mass spectrometry procedure has been shown to be an indispensable method providing important information on solid rocket propellant chemical combustion mechanisms, by using the study of the flame structure of AP, RDX, HMX, and ADN, propellants based on these, as well as double-based propellants. Although it is limited to some extent by pressure, flame zone width, and other considerations, the results obtained with its aid have successfully been used to understand the chemical reaction mechanisms of SP combustion and develop combustion models. The further application of this method, as well as other spectroscopic and thermocouple methods, will allow a refined and widened understanding of the SP combustion mechanism.

Acknowledgments

Thanks go to A. G. Tereshchko, L. V. Kuibida, A. A. Paletsky, V. M. Shvartsberg, A. A. Chernov, A. A. Shmakov, and T. A. Bolshova, with whom the author has been working for many years and who have participated in the development and updating of the method of SP flame mass-spectrometric probing, as well as in obtaining the main results reviewed in this chapter.

References

- ¹Edwards, T., "Solid Propellant Flame Spectroscopy," Air Force Astronautics Lab., AFAL-TR-88-076, Edwards AFB, CA, 1988.
- ²Korobeinichev, O. P., "Dynamic Probe Mass Spectrometry of Flames and the Decomposition of Condensed Systems," *Combustion, Explosion and Shock Waves*, Vol. 23, No. 5, 1988, pp. 565-576.

³Korobeinichev, O. P., "A Study of Condensed System Flame Structure," *Pure and Applied Chemistry*, Vol. 65, No. 2, 1993, pp. 269–276.

⁴Korobeinichev, O. P., Kuibida, L. V., Paletsky, A. A., and Chernov, A. A., "Study of Solid Propellant Flame Structure By Mass-Spectrometric Sampling," *Combustion Science and Technology*, Vol. 113–114, 1996, pp. 557–571.

⁵Litzinger, T. A., Lee, Y. J., and Tang, C. J., "A Study of Solid Propellant Combustion Using a Triple Quadruple Mass Spectrometer with Microprobe Sampling," *Proceedings of the Workshop on the Application of Free-Jet, Molecular Beam, Mass Spectrometric Sampling*, National Technical Information Service, U.S. Dept. of Commerce, Springfield, VA, 1994, pp. 128–135.

⁶Fetherolf, B. L., and Litzinger, T. A., "Physical and Chemical Processes Governing the CO₂ Laser-Induced Deflagration of Ammonium Dinitramide (ADN)," *Proceedings of the 29th JANNAF Combustion Subcommittee Meeting*, Vol. 2, 1992, pp. 329–338.

⁷Vanderhoff, J. A., Teague, M. W., and Kotlar, A. J., "Absorption Spectroscopy Through the Dark Zone of Solid Propellant Flame," U.S. Army Ballistic Research Lab., Rept. BRL-TR-3334, Aberdeen Proving Ground, MD, 1992.

⁸Parr, P., and Hanson-Parr, D., "Solid Propellant Flame Chemistry and Structure," *Non-Intrusive Combustion Diagnostics*, edited by K. K. Kuo and T. P. Parr, Begell House, New York, 1994, pp. 517–599.

⁹Stufflebeam, J. H., and Eckbreth, A. C., "CARS Diagnostics of Solid Propellant Combustion at Elevated Pressure," *Combustion Science and Technology*, Vol. 66, 1989, pp. 163–179.

¹⁰Zenin, A. A., "The Temperature Distribution Structure in the Steady Burning of Double-Base Propellants," *Fizika Gorenia i Vzryva*, Vol. 2, No. 3, 1966, pp. 67–76 (in Russian).

¹¹Parr, T. P., and Hanson-Parr, D. M., "Solid Propellant Diffusion Flame Structure," *26th Symposium (International) on Combustion*, Combustion Inst., Pittsburgh, PA, 1996, pp. 1981–1987.

¹²Parr, T. P., and Hanson-Parr, D. M., "Solid Propellant Diffusion Flame Structure," *Decomposition, Combustion and Detonation of Energetic Materials, Proceedings of the Material Research Society Symposium*, edited by T. B. Brill, T. P. Russell, W. C. Tao, and R. B. Wardle, Vol. 418, Material Research Society, Pittsburgh, PA, 1996, pp. 207–219.

¹³Modiano, S. H., and Vanderhoff, J. A., "Propellant Dark Zone Concentration via Multi-channel IR Absorption," *26th Symposium (International) on Combustion*, Combustion Inst., Pittsburgh, PA, 1996, pp. 2017–2023.

¹⁴Korobeinichev, O. P., and Tereshchenko, A. G., "Mass-Spectrometric Study of Distribution of Concentrations in Combustion Zones of Condensed Systems," *Doklady Akademii Nauk USSR*, Vol. 231, No. 5, 1976, pp. 1159–1161 (in Russian).

¹⁵Lee, Y. J., Tang, C. J., and Litzinger, T. A., "A Study of the Chemical and Physical Processes Governing CO₂ Laser-Induced Pyrolysis and Combustion of RDX," *Combustion and Flame*, Vol. 117, 1999, pp. 600–628.

¹⁶Korobeinichev, O. P., and Kuibida, L. V., "Study of Condensed System Flames by Molecular Beam Mass Spectrometry," *Flames, Lasers and Reactive Systems*, edited by J. R. Bowen, N. Manson, A. K. Oppenheim, and R. I. Soloukuin, Vol. 88, Progress in Astronautics and Aeronautics, AIAA, New York, 1982, pp. 197–207.

¹⁷Korobeinichev, O. P., Kuibida, L. V., Orlov, V. N., Tereshchenko, A. G., Kutsenogii, K. P., Mavliev, R. V., Ermolin, N. E., Fomin, V. M., and Emel'yanov, I. D., "Mass-Spectrometric Probe Study of the Flame Structure and Kinetics of the Chemical Reactions in Flames," *Mass-Spektrometriya i Khimika Kinetika*, edited by V. Tal'rose, Nauka, Moscow, 1985, pp. 73–93 (in Russian).

¹⁸Korobeinichev, O. P., Tereshchenko, A. G., Emel'yanov, I. D., Kuibida, L. V., Mavliev, R. V., Kutsenogii, K. P., Rudnitskii, A. L., Fedorov, S. Yu., Ermolin, N. E., and Fomin, V. M., "Probe Mass-Spectrometry for Condensed System Flames Having Narrow Combustion Zones," Preprint 14, Inst. of Chemical Kinetics and Combustion, Siberian Branch, Russian Academy of Sciences, Novosibirsk, Russia, 1985, p. 37 (in Russian).

¹⁹Korobeinichev, O. P., Tereshchenko, A. G., Emel'yanov, I. D., Rudnitskii, A. L., Fedorov, S. Yu., Kuibida, L. V., and Lotov, V. V., "Substantiation of the Probe Mass-Spectrometric Method for Studying the Structure of Flames with Narrow Combustion Zones," *Combustion, Explosion and Shock Waves*, Vol. 21, No. 5, 1985, pp. 524-530.

²⁰Emel'yanov, I. D., Korobeinichev, O. P., Tereshchenko, A. G., and Kuibida, L. V., "Heat Transfer Between Flame and Probe in Mass-Spectrometric Research on Flame Structure," *Combustion, Explosion and Shock Waves*, Vol. 22, No. 2, 1986, pp. 168-175.

²¹Ermolin, N. E., Korobeinichev, O. P., Tereshchenko, A. G., and Fomin, V. M., "Measurements of the Concentration Profiles of Reacting Components and Temperature in an Ammonium Perchlorate Flame," *Combustion, Explosion and Shock Waves*, Vol. 18, No. 1, 1982, pp. 36-38.

²²Rosen, P., "Potential Flow of Fluid into a Sampling Probe," Applied Physics Lab. Rept. CF-2248, Johns Hopkins Univ., Silver Spring, MD 1954.

²³Dubinin, V. V., Kolesnikov, B. Ya., and Ksandopulo, G. I., "Correction of Probe Sampling in Flames," *Fizika Goreniya i Vzryva*, Vol. 13, No. 6, 1977, pp. 920-924.

²⁴Kutsenogii, K. P., Korobeinichev, O. P., Mavliev, R. V., and Tereshchenko, A. G., "Study of Field of Velocities Perturbed by Probe at Mass Spectrometric Investigations of Flame Structure," *Doklady Akademii Nauk USSR*, Vol. 282, No. 6, 1985, pp. 1425-1428 (in Russian).

²⁵Ermolin, N. E., Korobeinichev, O. P., Tereshchenko, A. G., and Fomin, V. M., "Kinetic Calculations and Mechanism Definition for Reactions in an Ammonium Perchlorate Flame," *Combustion, Explosion and Shock Waves*, Vol. 18, No. 2, 1982, pp. 180-189.

²⁶Ermolin, N. E., Korobeinichev, O. P., Tereshchenko, A. G., and Fomin, V. M., "Simulation of Kinetics and Chemical Reaction Mechanism of Ammonium Perchlorate Burning," *Sovetski Jurnal Khimicheskaya Fizika*, Vol. 1, No. 12, 1984, pp. 2872-2883 (in Russian).

²⁷Ermolin, N. E., "Model for Chemical Reaction Kinetics in Perchloric Acid-Ammonia Flames," *Combustion, Explosion and Shock Waves*, Vol. 31, No. 5, 1995, pp. 58-69.

²⁸Tanaka, M., and Beckstead, M. W., "A Three-Phase Combustion Model of Ammonium Perchlorate," AIAA Paper 96-2888, July 1996.

²⁹Beckstead, M. W., Davidson, J. E., and Jing, Q., "A Comparison of Solid Monopropellant Combustion and Modeling," *Challenges in Propellants and Combustion/100 Years After Nobel*, edited by K. K. Kuo, Begell House, New York, 1997, pp. 1116-1132.

³⁰Narahari, H. K., Mukunda, H. S., and Jain, V. K., "A Model of Combustion Monopropellants (AP) with Complex Gas Phase Kinetics," *20th Symposium (International) on Combustion*, Combustion Inst., Pittsburgh, PA, 1984, pp. 2073-2082.

³¹Ilincic, N., Tanoff, M. A., Smooke, M. D., Yetter, R. A., Parr, T. P., and Hanson-Parr, D. M., "Modeling Ammonium Perchlorate Counterflow Diffusion Flames," *Proceedings of the 34th JANNAF Combustion Subcommittee Meeting*, Publ. 662, Vol. 2, Chemical Propulsion Information Agency, Laurel, MD, 1997, pp. 23-33.

³²Korobeinichev, O. P., Ermolin, N. E., Chernov, A. A., and Emel'yanov, I. D., "Flame Structure, Kinetics and Mechanism of Chemical Reactions in Flames of Mixed Composition Based on Ammonium Perchlorate and Polybutadiene Rubber," *Combustion, Explosion and Shock Waves*, Vol. 28, No. 4, 1992, pp. 53-59.

³³Korobeinichev, O. P., Chernov, A. A., Emel'yanov, I. D., Ermolin, N. E., and Trofimychева, T. V., "Investigation of the Kinetics and the Chemical Reaction Mechanism in the Flame of a Mixed Compounds, Based on Ammonium Perchlorate and Polybutadiene Rubber," *Combustion, Explosion and Shock Waves*, Vol. 26, No. 3, 1990, pp. 46–55.

³⁴Korobeinichev, O. P., Kuibida, L. V., Paletsky, A. A., Chernov, A. A., and Ermolin, N. E., "Chemistry of Solid Propellant Combustion Chemistry by Mass Spectrometry and Modeling," Div. of Fuel Chemistry, Preprints 202nd ACS National Meeting, Vol. 36, No. 4, American Chemical Society, Washington, DC, 1991, pp. 1582–1587.

³⁵Jeppson, M. B., Beckstead, M. W., and Jing, Q., "A Kinetic Model for the Premixed Combustion of Fine AP/HTPB Composite Propellant," AIAA Paper 98-0447, Jan. 1998.

³⁶Ermolin, N. E., Korobeinichev, O. P., Kuibida, L. V., and Fomin, V. M., "Processes in Hexogene Flames," *Combustion, Explosion and Shock Waves*, Vol. 24, No. 4, 1985, pp. 400–406.

³⁷Ben-Reuven, M., and Caveny, L. H., "Nitramine Flame Chemistry and Deflagration Interpreted in Terms of Flame Model," *AIAA Journal*, Vol. 19, No. 10, 1981, pp. 1276–1285.

³⁸Melius, C. F., "The Gas-Phase Flame Chemistry of Nitramine Combustion," *Proceedings of the 25th JANNAF Combustion Meeting*, Vol. 2, Chemical Propulsion Information Agency, Hampton, VA, 1988, pp. 155–162.

³⁹Lian, Y.-C., and Yang, V., "Analysis of RDX Monopropellant Combustion with Two-Phase Subsurface Reactions," *Journal of Propulsion and Power*, Vol. 11, No. 4, 1995, pp. 729–739.

⁴⁰Yetter, R. A., Dryer, F. L., Allen, M. T., and Gatto, J. L., "Development of Gas-Phase Reaction Mechanisms for Nitramine Combustion," *Journal of Propulsion and Power*, Vol. 11, No. 4, 1995, pp. 683–697.

⁴¹Cor, J. J., and Branch, J. J., "Structure and Chemical Kinetics of Flames Supported by Solid Propellant Combustion," *Journal of Propulsion and Power*, Vol. 11, No. 4, 1995, pp. 704–716.

⁴²Niioka, T., Mitani, T., Miyajima, H., Saito, N., Sohue, T., Ninomiyya, K., and Aoki, I., "The Fundamental Study of HMX Composite Propellant and its Practical Application," National Aerospace Lab. Rept. TR-875, Japan, 1985.

⁴³Zenin, A., "HMX and RDX: Combustion Mechanism and Influence on Modern Double-Base Propellant Combustion," *Journal of Propulsion and Power*, Vol. 11, No. 4, 1995, pp. 752–758.

⁴⁴Lintzinger, T. A., Fetherolf, B. L., Lee, Y. J., and Tang C.-J., "Study of the Gas-Phase Chemistry of RDX: Experiments and Modeling," *Journal of Propulsion and Power*, Vol. 11, No. 4, 1995, pp. 698–703.

⁴⁵Hanson-Parr, D., and Parr, T., "RDX Flame Structure," *25th Symposium (International) on Combustion*, Combustion Inst., Pittsburg, PA, 1994, pp. 1635–1643.

⁴⁶Bizot, A., and Beckstead, W. M., "A Model for HMX Propellant Combustion," *Flame Structure*, Vol. 1, edited by O. P. Korobeinichev, Nauka, Novosibirsk, Russia, 1991, pp. 230–235.

⁴⁷Pak, Z., "Some Ways to Higher Environmental Safety of Solid Rockets Propellant Application," AIAA Paper 93-1755, 1993.

⁴⁸Fogelzang, A. E., Sinditskii, V. P., Egorshv, V. Y., Levshenkov, A. I., Serushkin, V. V., and Kolesov, V. I., "Combustion Behavior and Flame Structure of Ammonium Dinitramide," *Combustion and Detonation, 28th Annual Conference of ICT*, Vol. 99, DWS Werbeagentur und Verlag GmbH, Karlsruhe, Germany, 1997, pp. 1–14.

⁴⁹Korobeinichev, O. P., Kuibida, L. V., Paletsky, A. A., and Shmakov, A. G., "Development and Application of Molecular Beam Mass-Spectrometry to the Study of ADN

Combustion Chemistry," *Journal of Propulsion and Power*, Vol. 14, No. 6, 1998, pp. 991–1000.

⁵⁰Park, J., Chakraborty, D., and Lin, M. C., "Thermal Decomposition of Gaseous Ammonium Dinitramide at Low Pressure: Kinetic Modeling of Product Formation with AB INITIO MO/c VRRKM Calculations," *27th Symposium (International) on Combustion*, Combustion Inst., Pittsburgh, PA, 1998, pp. 2351–2357.

⁵¹Kee, R. J., Grcar, J. F., Smooke, M. D., and Miller, J. A., "Fortran Program for Modeling Steady Laminar One-Dimensional Premixed Flames," Sandia National Labs., Rept. SAND85-8240, Livermore, CA, Aug. 1989.

⁵²Korobeinichev, O. P., Kuibida, L. V., Paletsky, A. A., and Shmakov, A. G., "Ammonium Dinitramide Combustion Chemistry Studied by MBMS and Modeling," *Proceedings of 21st International Symposium on Space Technology and Sciences*. Vol. 1, Society for Aeronautical and Space Sciences, Tokyo, 1998, pp. 87–95.

⁵³Korobeinichev, O. P., and Paletsky, A. A., "Study of the Flame Structure of ADN/HTPB Composite Propellants Using Molecular-Beam Mass-Spectrometry," *Combustion and Detonation, 29th Annual Conference of ICT*, Vol. 156, DWS Werbeagentur und Verlag GmbH, Karlsruhe, Germany, 1998, pp. 1–7.

⁵⁴Ilincic, N., Anderson, W. R., Sechadri, K., and Meager, N. E., "Simplified Chemical-Kinetic Mechanism for Characterizing the Structure of the Dark Zones of Double Base and Nitramine Propellants," *26th Symposium (International) on Combustion*, Combustion Inst., Pittsburgh, PA, 1996 pp. 1997–2005.

Chapter 2.4

Experimental Studies of Nitramine/Azide Propellant Combustion

Thomas A. Litzinger,* YoungJoo Lee,[†] and Ching-Jen Tang[‡]
Pennsylvania State University, University Park, Pennsylvania

I. Introduction

FOR increased specific impulse at reduced flame temperatures, nitramine compounds such as 1,3,5-trimethylene trinitramine (RDX) and 1,3,5,7-tetramethylene tetranitramine (HMX) have been widely used as energetic materials for the propellant in applications such as guns and rocket motors. In the search for improved performance for nitramine propellants, a great deal of interest has recently centered on azido compounds such as bis-azido methyl oxetane (BAMO) and glycidyl azide polymer (GAP). The structures of RDX and HMX as well as the azide polymers are presented in Fig. 1. These polymers draw considerable interest because they are energetic materials and can serve as binders or plasticizers in nitramine-based propellants, where a relatively low flame temperature and a high mass impetus are desirable. As propellants, they provide a high specific impulse while generating minimum smoke.

II. Previous Studies

In fundamental studies of nitramine/BAMO propellants, two configurations of the oxidizer/binder matrix have been used, heterogeneous mixtures and sandwich configurations. Although the heterogeneous mixture is the form of the propellant used in actual applications, the study of their behavior and decomposition is generally too complex for fundamental studies due to the thin reaction regions and the heterogeneous nature of the propellant. A strategy to alleviate these experimental difficulties is to study the combustion of geometrically simple systems such as an oxidizer/binder sandwich; many such studies have been performed to understand the diffusion flame of ammonium perchlorate- (AP-)

Copyright © 1999 by the American Institute of Aeronautics and Astronautics, Inc. All rights reserved.

*Professor, Dept. of Mechanical and Nuclear Engineering.

[†]Research Associate, Dept. of Mechanical and Nuclear Engineering.

[‡]Postdoctoral Scholar, Dept. of Energy and Geo-Environmental Engineering.

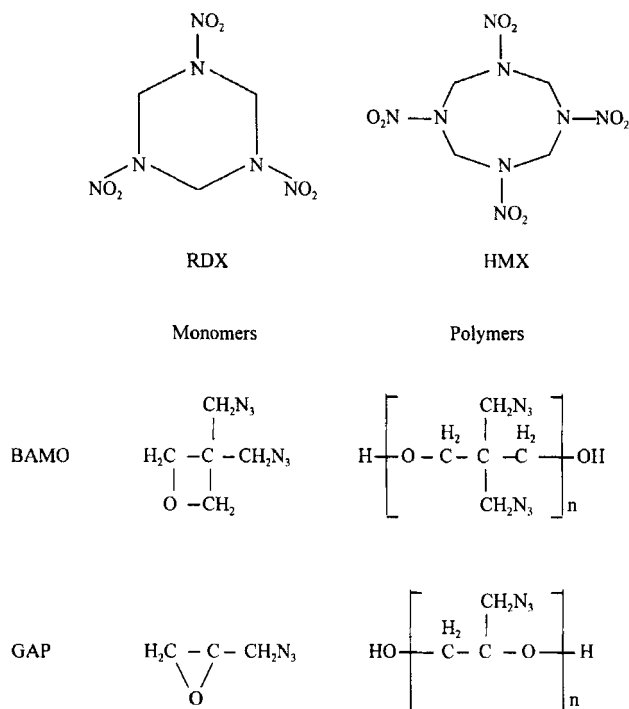


Fig. 1 Chemical structures of RDX, HMX, BAMO, and GAP.

based formulations.¹ Limited research has been conducted on the combustion and decomposition characteristics of nitramine/binder sandwich systems, and they include HMX/carboxyl-terminated polybutadiene,² HMX/hydroxyl-terminated polybutadiene,³ and HMX/BAMO.³ However, the previous studies showed that nitramines had no diffusion flame with nonenergetic binders, while they had very weak diffusion flames with energetic binders at very low pressures. From the previous measurements, no explicit evidence of the flame interaction over the two laminas of nitramine and BAMO was found because the major species measured over each ingredient were almost identical to those of the pure material. Therefore, the study of sandwich configurations between nitramines and BAMO did not provide much information on their chemical interaction or on the effects of each ingredient on the other.

Thermal decomposition of HMX/BAMO propellants was studied by Oyumi et al.⁴ using isothermal thermogravimetric analysis and differential scanning calorimetric analysis. The binder used in the study was a mixture of BAMO and tetrahydrofuran (THF) in a mole ratio of 3 : 2, where THF was used as a cross-linking agent to make the copolymer a three-dimensional network structure. The decomposition of the HMX/BAMO propellant in the study showed overall two-step first-order kinetics; the first-step reaction was considered to be the decomposition of BAMO binder itself because the rate of the first-order reaction was similar to that of the BAMO binder. HMX decomposition was predominant in the second-step reaction and was activated by the binder decomposition. The burning rate of the propellant was larger than that of the pure BAMO binder or HMX. However, the propellant

could not maintain combustion at pressures below approximately 3 MPa, where its burning rate was equal to that of the BAMO binder.

The same research group investigated the burning rate augmentation of BAMO-based propellants with HMX and HMX/ammonium nitrate mixtures, in which the BAMO used was an azide copolymer of BAMO/azidomethyl methyl oxetane (7 : 3, molar ratio).⁵ Based on theoretical calculations, it was reported that the BAMO/HMX propellants showed a relatively low flame temperature (1210–1320 K) and smokeless properties. The burning rate of the propellant was augmented by the addition of lead stearate and AP, which resulted in a decrease of the burning rate exponent. Results for the BAMO-based propellants showed an endotherm of phase transition and an exotherm between 500 and 540 K that exactly coincided with rapid weight loss. From these results, it was concluded that the heat generated by the azide binder decomposition initiated and accelerated the HMX decomposition.

Extensive studies have been performed on individual ingredients of the nitramine/GAP propellants; however, despite the increased interest, only a limited number of results are available on the physical and chemical processes of such propellants. Among the available studies, relatively more complete research results were found in studies of HMX/GAP.^{6–8} Experimental studies of the temperature profile of HMX/GAP suggested that HMX/GAP flames had a two-stage thermal wave structure.⁶ Some preliminary studies have been reported on physical and chemical behavior of RDX/GAP formulations.^{7,8} An evaluation study for the composition of RDX/GAP combustion modified double-base propellants revealed that increasing the amount of GAP increased specific impulse and decreased the pressure exponent marginally.⁸ However, in another study of RDX/GAP with various mixing ratios, a reverse trend was observed.⁷ In that study, final reaction products were measured in both glass vessel and calorimeter bomb experiments; they were found to be N_2 , CO, H_2O , H_2 , and CO_2 .

III. Research Objectives

The research to date with nitramine/azide polymer propellants has not produced a complete understanding of the chemical and physical processes that occur during their combustion. Nor have the interactions of the binder chemistry and the nitramine chemistry been fully explored. To take full advantage of these materials, a more basic understanding of the chemical and physical structure of their reaction zones is needed. Furthermore, if the behavior of these materials is to be modeled with comprehensive numerical models, then experimental data, beyond the burning rate, is needed for validation of such models. The experimental results presented in this chapter include detailed species and temperature measurements in the gas-phase reaction zones above a series of nitramine/azide propellants. They were obtained to identify, and hopefully to understand, unique characteristics of these propellants and the interactions of the nitramines and the azide polymers. In addition, the experiments were carried out with the objective of identifying key similarities and differences in the behavior of these materials that would provide critical tests for numerical models of their burning behavior.

IV. Experimental Approach

All experimental data presented were acquired at a pressure of 0.1 MPa during laser-assisted combustion using a CO_2 laser. At this pressure, continuous energy

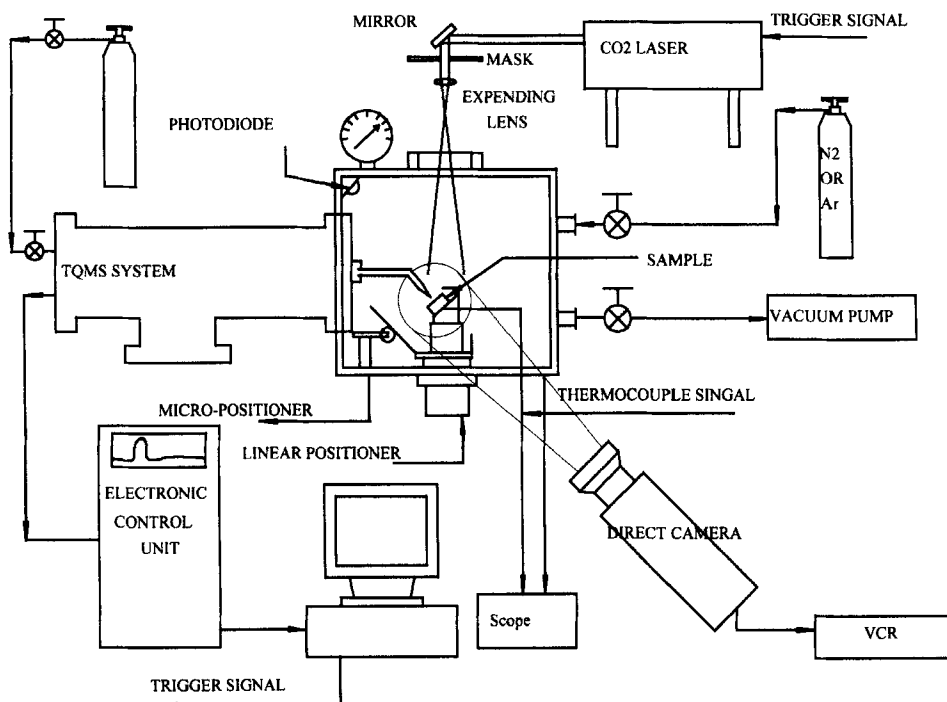


Fig. 2 Overall experimental setup with diagnostic systems.

delivery from the laser was required to sustain combustion. The specific propellants tested were RDX/BAMO, RDX/GAP, and HMX/GAP. Each material was tested at a low heat flux of 100 W/cm^2 and a high heat flux of 300 or 400 W/cm^2 . The difference in high heat flux used was due to variation in the maximum available laser power over the course of the experiments. A schematic diagram of the overall experimental setup is presented in Fig. 2. The remainder of this section summarizes the experimental procedures used; for a more detailed discussion see Refs. 9 and 10.

Mixtures of a nitramine compound and an azide polymer were used to fabricate pseudopropellants. The prefix pseudo is used to emphasize that the propellant used is simply a physical mixture of the two ingredients and that the binder was not cured. The propellants all were made with the nitramine and azide polymer in a weight ratio of 8 : 2; selection of the weight ratio between the two ingredients was made based on the amounts of binders contained in commonly used composite gun propellants. Table 1 presents the elemental composition of the propellants used.

Table 1 Elemental composition and equivalence ratio

Species	C	H	O	N	Equivalence ratio
RDX/GAP	0.169	0.317	0.237	0.277	2.1
HMX/GAP	0.169	0.317	0.237	0.277	2.1
RDX/BAMO	0.168	0.313	0.229	0.289	2.15

Because of the different elemental composition of GAP and BAMO, using the same weight ratio results in different stoichiometry of the pseudopropellants. The RDX/BAMO pseudopropellants are slightly more fuel rich than the nitramine/GAP propellants.

The BAMO used was in the form of a dry powder. It was mixed with military-grade RDX, containing a maximum of 5.5% HMX, and then the mixture was pressed into a cylindrical pellet with a 0.64-cm-diam using a pellet presser. The consolidation pressure was approximately 60 MPa. For the nitramine/GAP propellants, GAP dissolved in methyl ethyl ketone (MEK) was obtained from 3M. To remove the solvent and H₂O from the GAP, the GAP and MEK mixture was dried in a vacuum oven at a temperature of 80°C for more than 24 h. The resulting pure GAP sample was a viscous dark-yellow liquid, with a density of 1.3 g/cm³. The GAP was mixed with the nitramine, and the resulting mixture was a highly viscous gel-type liquid. The HMX used contained a maximum of 0.2% RDX and had a nominal size of 75 μ m. The nitramine/GAP mixture was either hard or soft depending on the amount of mixing that was done. The hard mixtures were formed into a cylindrical shape with a diameter and height of 0.64 cm. However, for the soft material, it was normally impossible to sustain this shape during experiments, and so for both types of material, the propellant was placed in a glass container for testing.

Just prior to a test, the propellant sample was glued to a small sample holder, angled at 45 deg to the incident laser beam so that the sampling microprobe could approach the sample perpendicular to its surface and along its centerline. During the test, the sample was pushed toward the sampling probe by a linear actuator to obtain species profiles vs height from the sample surface. Gas samples were extracted through a quartz microprobe and analyzed using a triple quadrupole mass spectrometer (TQMS).^{9,10} Using the parent and daughter modes of the TQMS and careful calibration, it was possible to differentiate and quantify all species at the same mass-to-charge (m/z) value. Sensitivity coefficients of most stable species were calibrated directly with gas mixtures of known concentration; those of the species for which standards were not readily available were estimated by the ionization cross section method.¹¹ For all of the calibrations and actual tests, an ionization energy of 22 eV was used to minimize fragmentation of molecules while maintaining acceptable intensities.

Temperatures at the surface and in the gas phase were measured using 25- μ m-diam platinum/rhodium (Pt/Rh) and tungsten/rhenium (W/Re) thermocouples, according to the methods suggested by Zenin (Ref. 12 and personal communication). For some materials, surface temperatures were measured separately from gas-phase temperatures to obtain more consistent surface temperatures. The junction of a thermocouple was placed at the center of the sample surface, and two small weights were used to create adequate tension to hold the thermocouple on the surface as the sample burned. In the setup, the weight chosen was in the range of 0.8–2.0 g, and the angle ϕ that the wire made with the lateral edge of the propellant was 10–30 deg. The measurement of a complete temperature profile was performed using the configuration of a side-by-side-divided sample. In this method, the sample was prepared in two pieces shaped like a cylinder split along its centerline, and the thermocouple was embedded in one-half of the sample. A small amount of glue was then applied at the ends of the two thermocouple wires near the sample edges, and the other half of the sample was attached to it without moving the thermocouple. For measuring complete gas-phase temperature profiles, W/Re thermocouples were usually used to reduce the chances of melting

the thermocouple during a test. The thermocouple signals were amplified by a wide-band preamplifier and recorded on a Nicolet NIC-310 digital oscilloscope.

Direct images were acquired using a Pulnix video camera with a macrolens for photography of the flame and the sample surface during combustion and for the identification of sampling heights. Magnification of 30–40 times was normally employed to record the images and obtain the sampling height with a spatial resolution of $\sim 20\ \mu\text{m}$. In addition, a photodiode was used to record light emissions. Its output was recorded simultaneously with the temperature signal to synchronize the video images of the flame to the temperature measurement.

V. Results and Discussion

In this section, the flame and surface behavior, burning rate, species profiles, and temperature profiles will be discussed for each pseudopropellant. Following the presentation and discussion of the data, the characteristics of the pseudopropellants will be compared to the characteristics of the corresponding neat nitramine as well as to each other. Also, the effects of increasing the incident heat flux on the three pseudopropellants will be discussed and contrasted. The goal of the discussion is to identify differences among the three pseudopropellants that might lead to an improved understanding of the binder–nitramine interactions and of trends that may be critical tests for developing detailed models of these materials.

A. RDX/BAMO

Figure 3 shows individual frames taken from the video record to illustrate the burning behavior at 100 and 400 W/cm². The burning RDX/BAMO showed an uneven surface and intermittent glowing particles on the surface during combustion, with a greater number of these particles at the higher heat flux. The glowing particles sometimes left the surface and formed streaks through the gas phase; however, no gas-phase flames were observed during steady-state burning at either heat flux. Transient luminous flames of a distributed nature were sometimes observed for a short time following propellant ignition. The cause of these flames is unclear, but they may be due to buildup of reactive species in the gas phase during the ignition delay period. Similar flames were also observed near the end of the burn at the higher heat flux. The burning rates measured from the videos were ~ 0.35 and ~ 1.4 mm/s at 100 and 400 W/cm², respectively.

Mole fractions of the species evolved in the gas phase of RDX/BAMO pseudopropellants are shown in Fig. 4 at 100 W/cm². Multiple species included at mass/charge ratios of 28, 29, 30, and 44 were differentiated and quantified using the TQMS. Most of the major species were identical to those in pure RDX: H₂O, NO, HCN, H₂CO, N₂, NO₂, N₂O, and CO. The most obvious effects of BAMO are the increased amount of N₂ and H₂CO as well as the presence of NH₃. H₂, a notoriously difficult species to measure, is not shown here due to its highly fluctuating behavior throughout the gas phase. Its mole fraction was estimated to be 1–2% at the surface. The NO₂ profile is indicative of the length of the primary reaction zone, which in this case was approximately 1 mm. The other general characteristic of interest is the height above the surface where the secondary reactions begin. The location of the beginning of the secondary reactions is taken as the height where N₂ and CO begin to increase rapidly. For RDX/BAMO, the beginning of secondary reactions was not observed within the measurement region of 4 mm.

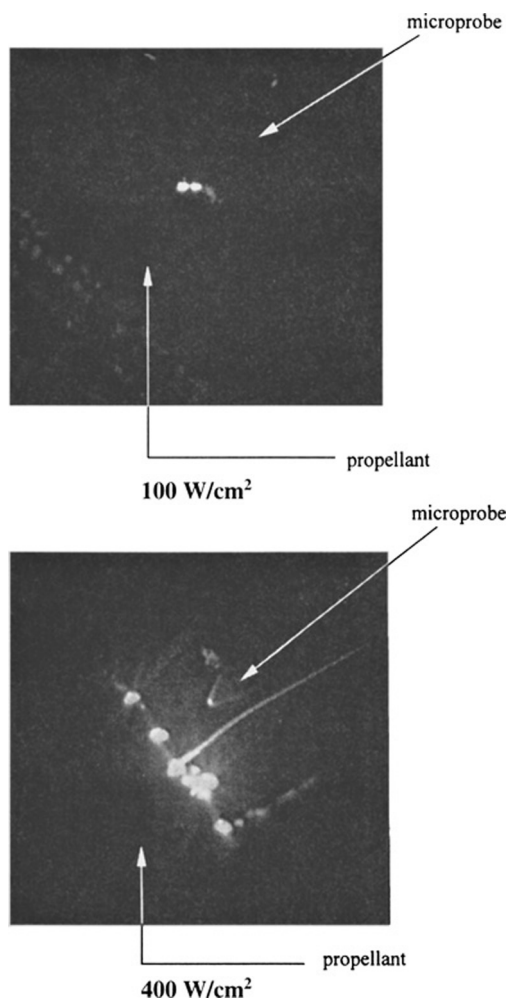


Fig. 3 Typical burning behavior of RDX/BAMO pseudopropellants.

Mole fractions of the species evolved from RDX/BAMO propellants at 400 W/cm^2 are shown in Fig. 5. The major species are the same as those observed at 100 W/cm^2 ; however, some of their mole fractions changed. Among the major species, the mole fraction of HCN increased at the surface, whereas that of N_2O decreased. At this heat flux, the primary reaction zone, as indicated by NO_2 , continues to approximately 2 mm, and the rise in N_2 and CO resulting from secondary reactions begin near 3 mm. Relative to RDX at the same test conditions, only the mole fraction of N_2 is substantially different, at nearly three times the mole fraction for RDX.

The element balances based on the measured species are shown in Figs. 4 and 5. Also shown in Figs. 4 and 5 by dashed lines are the expected element fractions based on the composition of the propellants. In each case the carbon is consistently below the expected value, suggesting that some species composed primarily of carbon may have been missed. Such species could be large unsaturated hydrocarbons or

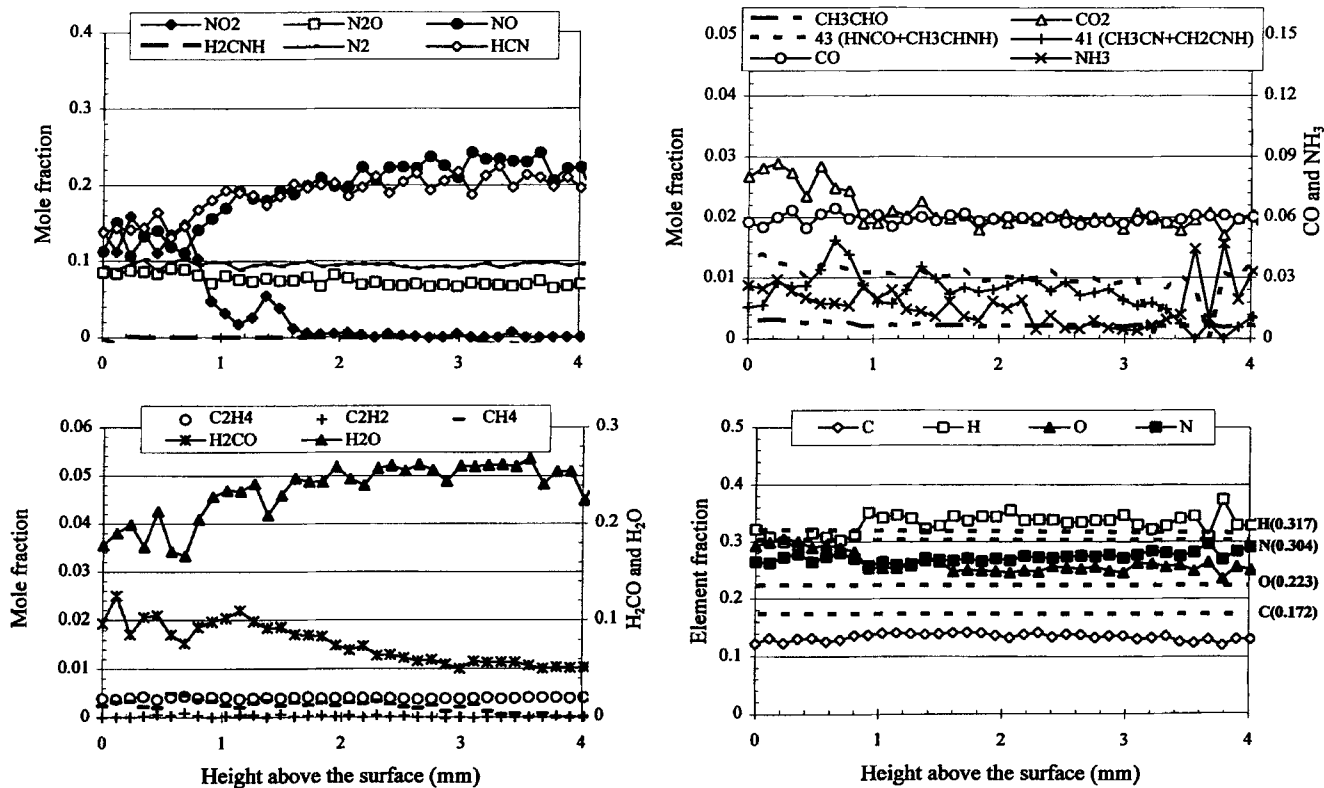


Fig. 4 Species and element fraction profiles for deflagration of RDX/BAMO pseudopropellants at heat flux of 100 W/cm^2 in argon at 1 atm.

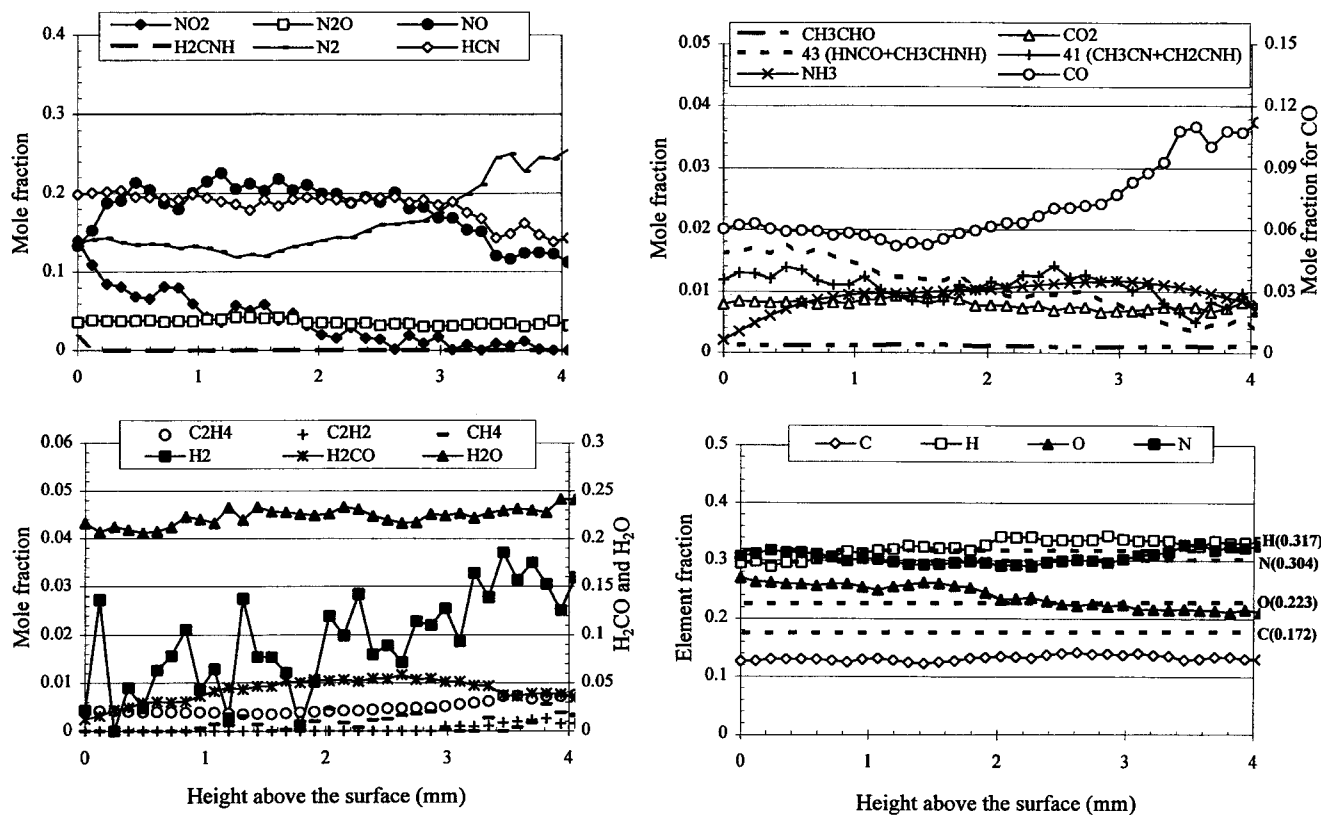


Fig. 5 Species and element fraction profiles for deflagration of RDX/BAMO pseudopropellants at heat flux of 400 W/cm^2 in argon at 1 atm.

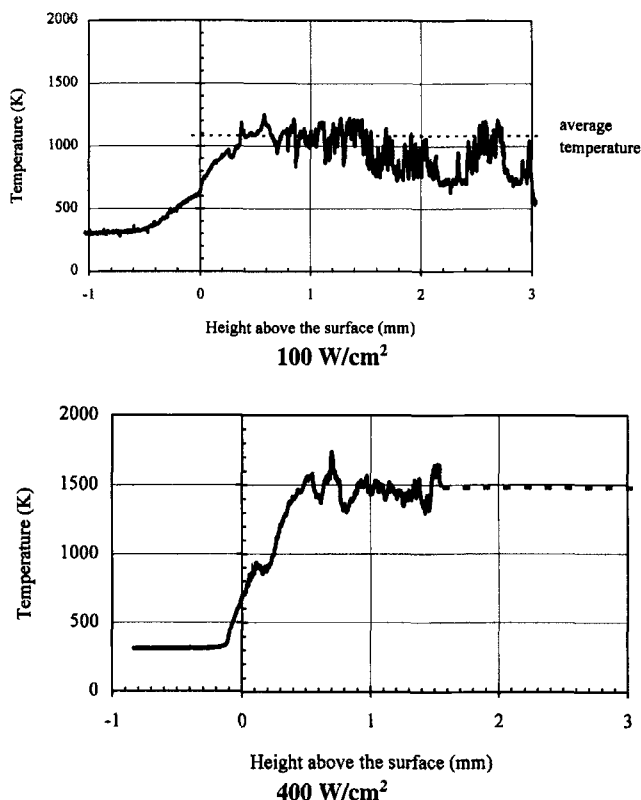


Fig. 6 Temperature profile of RDX/BAMO.

even carbon particles. The other three elements do not show any consistent trends and are close to the expected values.

The temperature profiles at both conditions are shown in Fig. 6 and have essentially the same trends. In both cases the temperature increased from its value at the surface, through a near-surface reaction region, to a nearly isothermal region. This region was called isothermal region in this study because, despite its fluctuating nature, temperature was essentially constant. This region also may be called a dark zone, from the traditional definition for propellant combustion. The temperatures in this region were approximately 1100 and 1500 K at 100 and 400 W/cm², respectively. Such a significant temperature difference with increasing heat flux had not been observed in any other studies in this laboratory, and so an investigation was performed to determine if it was real or an artifact. The investigation led to the conclusion that the difference was real. The surface temperatures of RDX/BAMO were measured as 640 ± 20 K at 100 W/cm² and 670 ± 20 K at 400 W/cm².

B. RDX/GAP

The combustion behavior of RDX/GAP is illustrated in Fig. 7. At 100 W/cm², the propellant underwent an ignition delay period of 150–750 ms during which

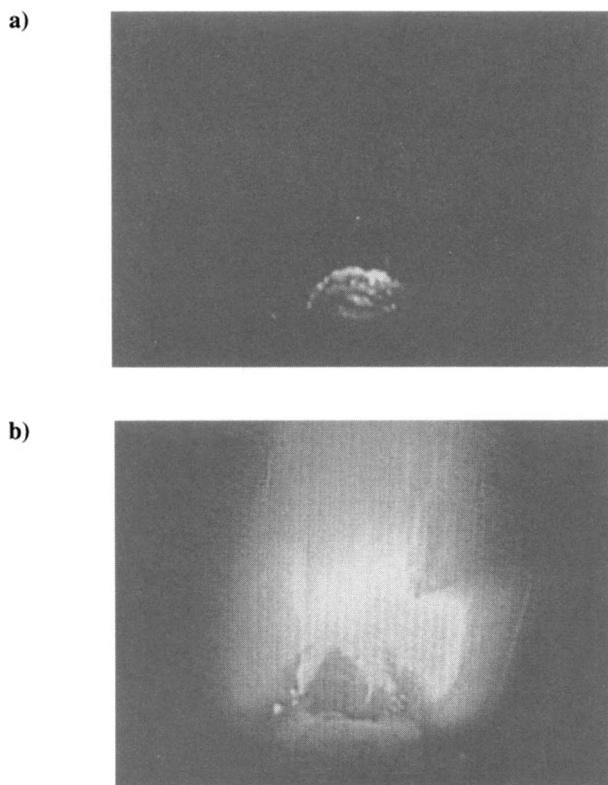


Fig. 7 Typical burning behavior of RDX/GAP pseudopropellants for 100 W/cm^2 at 1 atm.

carbon particles began to form on the surface (Fig. 7a). After the ignition delay, a visible flame evolved (Fig. 7b), most of which consisted of white flames in the center with yellow flames around the periphery of the sample. Finally, the color of the flame changed to a mixture of yellow and red and remained that way for the rest of the burn. The presence of carbonaceous filaments attached to the surface was clear throughout the test, and numerous white flame streaks from burning particles were observed. The streaks are believed to be carbon particles and are most actively produced in the period when the color of the flame was a mixture of yellow and red. At the higher heat flux, no glowing particles were observed prior to ignition; however, the carbonaceous filaments did develop during burning, although they were not as numerous as they were at the lower heat flux. Tests at the higher heat flux yielded a somewhat shorter ignition delay in the range of 50–500 ms. The surface regression rate observed were $\sim 0.8 \text{ mm/s}$ at 100 W/cm^2 and $\sim 1.9 \text{ mm/s}$ at 300 W/cm^2 .

Mole fractions of the major species evolved in the gas phase of RDX/GAP pseudopropellants at 100 W/cm^2 are shown in Fig. 8. As in BAMO/RDX, most of the major species were the same as those from pure RDX. H_2 was not measured in this test due to difficulty in the tuning of the mass spectrometer; however, it

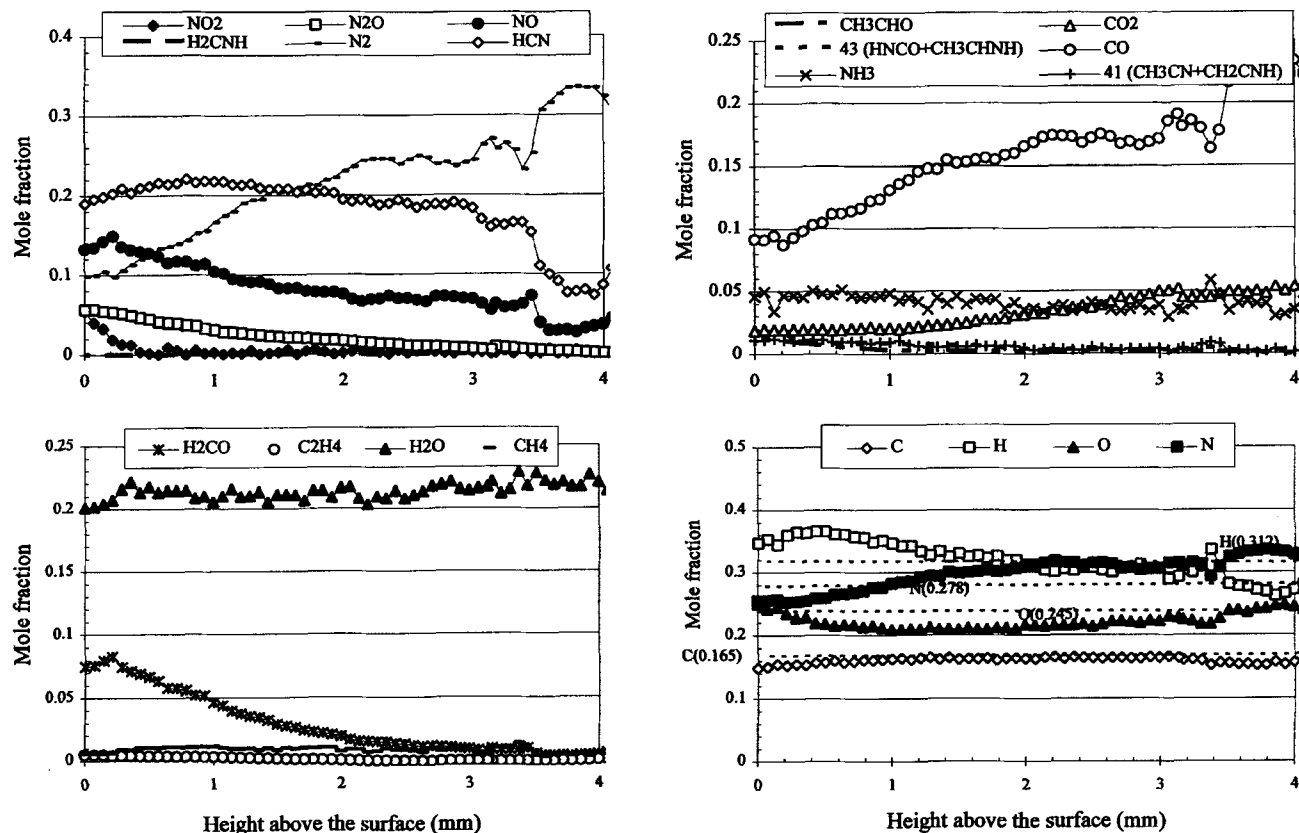


Fig. 8 Species and element fraction profiles for deflagration of RDX/GAP pseudopropellants at heat flux of 100 W/cm² in argon at 1 atm.

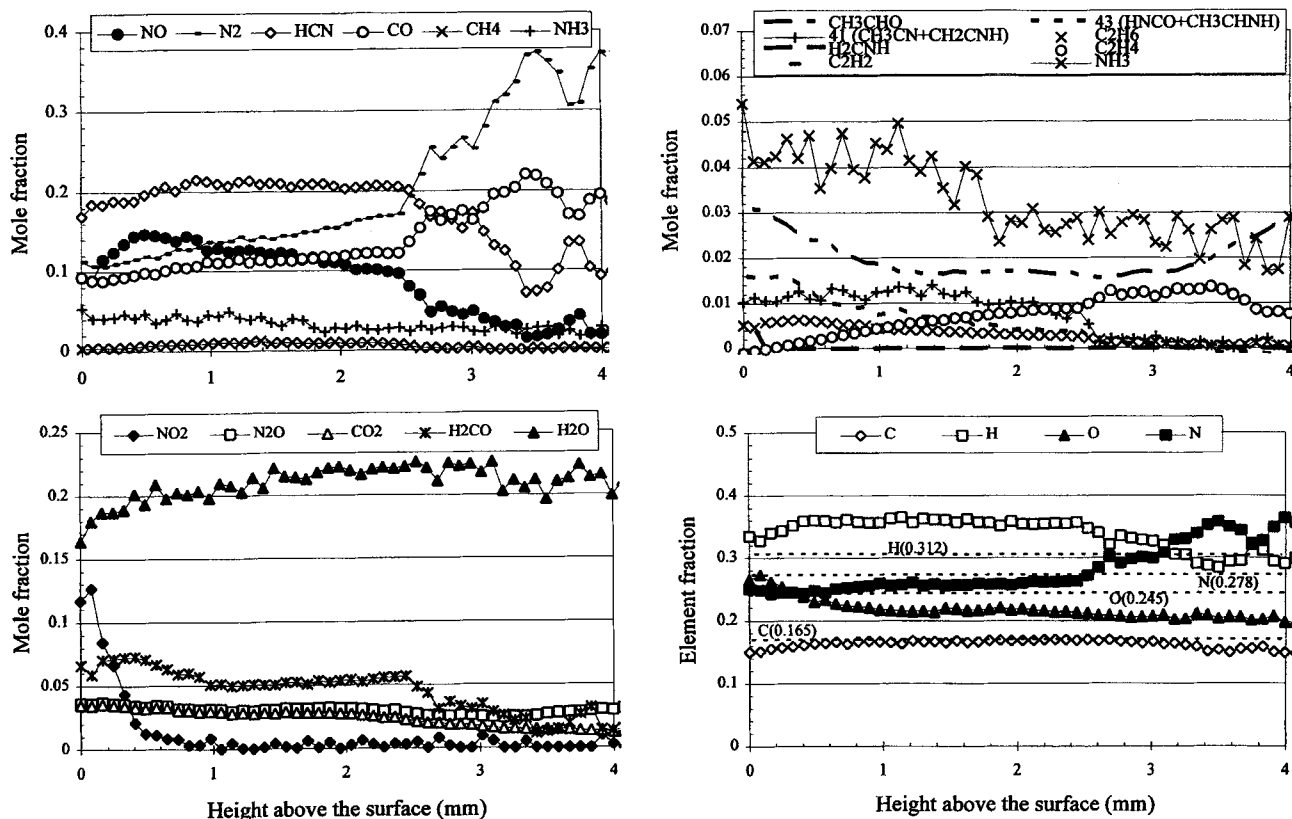


Fig. 9 Species and element fraction profiles for deflagration of RDX/GAP pseudopropellants at heat flux of 300 W/cm² in argon at 1 atm.

was expected because it is found during the combustion of pure RDX. The only species that was solely attributed to GAP and identified as a major species in this study was NH_3 ; it was found to be 3–5% throughout the reaction zones. As for RDX/BAMO, the amount of N_2 and H_2CO increased relative to neat RDX, and CO_2 is observed at the surface where none was detected for RDX.

Species profiles at 300 W/cm^2 are shown in Fig. 9; basically, the same trends of species profiles were obtained as at the lower heat flux condition. However, due to the higher heat flux, the surface mole fraction of NO_2 increased, and the length of the primary reaction zone was increased to approximately 1 mm. The secondary reactions began at approximately 2.5 mm, somewhat closer to the surface than at the lower heat flux.

The element balances at the two heat fluxes are similar. For RDX/GAP, the mole fraction of carbon is very close to the expected value and oxygen is fairly well conserved. However, the mole fractions of nitrogen and hydrogen vary throughout the reaction region. The amount of nitrogen is well above its expected value far from the surface. This may indicate that the amount of N_2 is in error far from the surface, perhaps due to difficulty in separating it from CO during the daughter mode tests.

Temperature measurements in RDX/GAP proved to be quite difficult due to the presence of the carbonaceous residue on the surface that tended to attach to the thermocouples and to confound the measurements. However, multiple profiles were obtained, and typical ones are presented in Fig. 10. For both experimental conditions, the temperature rose from the surface temperature, and then it held constant at a dark zone temperature of approximately 1250 K. The effect of the residue is manifested in the transients present in some of the tests within the dark zone. The surface temperatures were approximately 650 and 700 K at 100 and 300 W/cm^2 , respectively.

C. HMX/GAP

Figure 11 displays two images that were taken before and after ignition at a heat flux of 100 W/cm^2 . Figure 11a shows a significant amount of residue on the propellant surface. Figure 11b shows a broad luminous flame zone separated from the surface by a dark zone. The luminous streaks in the flame appear to indicate that some segments of residue were brought to the flame region from the surface. It was also observed that rapid gas expansion occurred at the beginning of the luminous flame. The flame standoff distance was not very stable at the lower heat flux level and generally decreased with time after ignition. This could be due to the long ignition delay of approximately 1.5 s that built up energy, and perhaps some species, in the condensed phase. The buildup resulted in a higher initial burning rate that stretched the reaction zones. Thus, it is reasonable that the flame standoff was higher just after ignition. The burning rate was calculated to be 1.1 mm/s at a heat flux of 100 W/cm^2 from the video images.

Clearly, the fibrous residue was formed before and after ignition occurred at a heat flux of 100 W/cm^2 . The recovered sample showed many black, carbonaceous fibers tangled together on the surface. The diameter of these fibers was normally less than $10 \mu\text{m}$. These black carbonaceous fibers appeared to be the same fibrous residue observed on the burning surface in the videos. The video images also showed that the carbonaceous fibers grew rapidly after the laser was turned on, much as they did in the case of RDX/GAP.

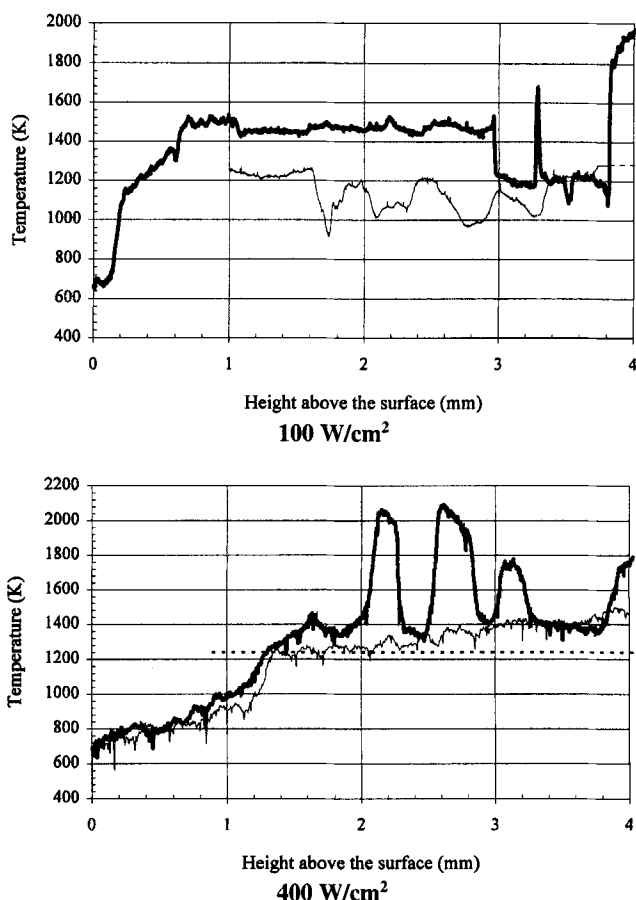
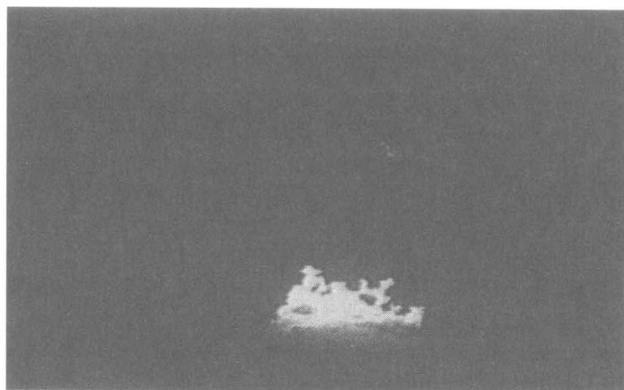


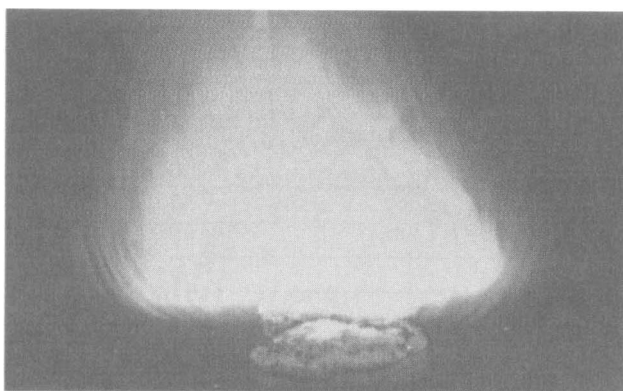
Fig. 10 Temperature profiles of deflagrating RDX/GAP pseudopropellants.

At a heat flux of 300 W/cm^2 , a relatively short ignition delay of 42 ms was observed, and the burning rate was calculated to be 2.4 mm/s. At this heat flux, the distinctive luminous flame zone was not observed in the video, but the test chamber was brightly illuminated. This illumination could indicate that the luminous flame was blown away from the viewing region by the high-velocity gas flow. At this test condition, only a small amount of carbonaceous residue was found at the edge of the propellant. The cause of the reduced level of carbonaceous residue at the higher heat flux is not known.

Figure 12 displays species profiles of the major species measured for GAP/HMX at a heat flux of 100 W/cm^2 . The major species are similar to those found for HMX and RDX. The surface position was difficult to determine because the carbonaceous residue on the surface blocked the view during combustion. Because a sharp temperature rise was observed within approximately 0.5 mm, the burning surface position was assigned at 0.5 mm before the beginning of the region with flat species profiles. H_2 was not included in the species profiles because the setting of the mass spectrometer was not focused on the signal at 2 m/z. Generally, the species profiles



a) During the carbonate accumulation



b) Flame evolution

Fig. 11 Typical burning behavior of the GAP/HMX pseudopropellants for 100 W/cm² and 1 atm.

in Fig. 12 display three distinctive regions: a primary reaction zone, a dark zone, and the secondary reaction zone. The primary reaction zone extends from 0 to 0.5 mm above the surface. The dark zone lasts from 0.5 to approximately 3.5 mm above the surface. In this region, all of the species profiles, except for H₂CO, are relatively flat.

Figure 12 also shows the element fractions for the corresponding species profiles. The theoretical element fractions in HMX/GAP are shown with dotted lines in the Fig. 12. At the surface, H is 14% lower than the theoretical value of H, whereas N is 14% higher than its theoretical value. In the secondary reaction zone, the H fraction shows a significant deficit. The main reason is that H₂ was not measured but was expected to exist in substantial amounts. In general, the element fractions are much closer to the expected values than they were for either of the RDX/azide materials. For neat HMX, the element balances were also better than for neat

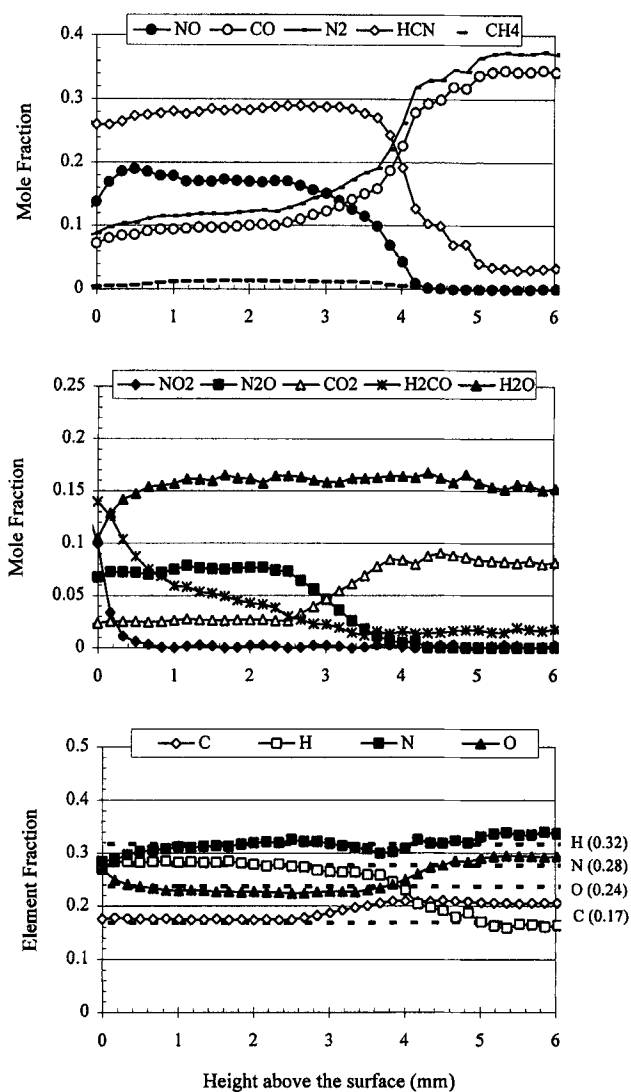


Fig. 12 Species and element fraction profiles for deflagration of HMX/GAP pseudo-propellants at heat flux of 100 W/cm^2 in argon at 1 atm.

RDX.^{13,14} The reason that HMX yields better element balances has never been established, but it may be because HMX burns more rapidly and uniformly than RDX at the conditions used in these tests.

Figure 13 displays species profiles for HMX/GAP at a heat flux of 300 W/cm^2 . The species profiles are similar to those in the dark zone at a heat flux of 100 W/cm^2 . All species remain relatively flat throughout the measurement region, and HCN is the most abundant species followed by H₂O, H₂CO, NO, N₂, CO, and N₂O. The primary reaction region seems to be stretched to approximately 1.5 mm above the

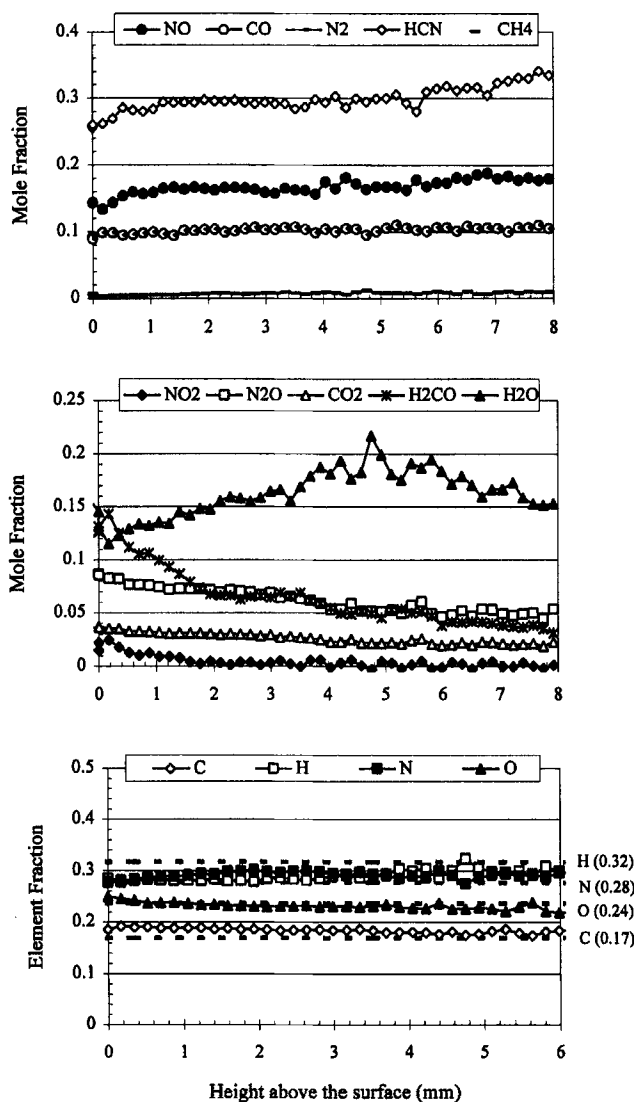


Fig. 13 Species and element fraction profiles for deflagration of HMX/GAP pseudo-propellants at heat flux of 300 W/cm^2 in argon at 1 atm.

surface, followed by a long dark zone. The typical species profiles in the secondary reaction zone were not obtained during these tests. The results were in line with the absence of a distinctive luminous flame at a heat flux of 300 W/cm^2 , probably due to high gas velocity.

The temperature profiles at heat fluxes of 100 and 300 W/cm^2 shown in Fig. 14 are relatively similar. Starting from the surface temperature, ~ 700 and $\sim 750 \text{ K}$ at 100 and 300 W/cm^2 , respectively, the temperature rises sharply near the surface and then flattens out approximately 0.5 mm above the surface. Unfortunately, the

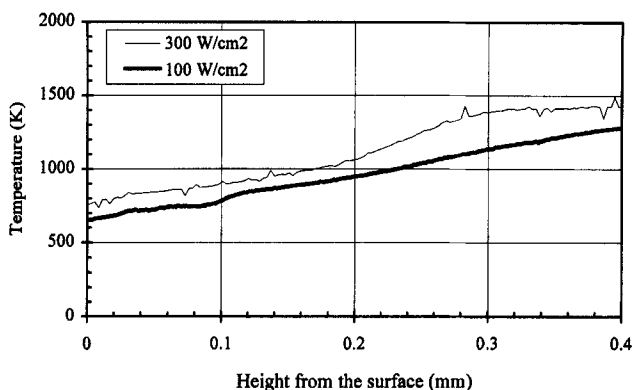
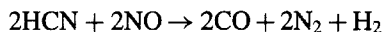


Fig. 14 Temperature profile for deflagration of GAP/HMX pseudopropellants at 100 and 300 W/cm².

thermocouples consistently burned out near this point because the luminous flame came back to the surface. The uncertainties in the exact surface temperature are large due to a steep temperature gradient and a large amount of residue at the surface. Kubota and Sonobe⁶ have measured the temperature profile of the HMX/GAP flame at a pressure of 0.5 MPa. Their results show a two-stage temperature rise. The temperature profile in the present study was very similar to the first stage of their temperature profile.

D. Overall Chemical Structure

Considering all of the species data, it is clear that the reactions in the gas phase are dominated by nitramine chemistry. In all cases, the primary reaction zone near the surface is associated with the consumption of NO₂. In general H₂CO is also consumed in this region; however, it is not completely consumed in the primary reaction zone as it is for the neat nitramines. That H₂CO survives the primary reaction zone is due to its increased mole fraction resulting from the production by the azide polymers. In general, the HCN mole fraction is constant through the primary reaction zone and in the dark zone until the secondary reactions begin. Water increases in the primary reaction zone and then maintains a relatively constant mole fraction through the dark zone and into the secondary reaction zone. This trend is shown most clearly by the HMX/GAP data at 100 W/cm² (Fig. 12). The constant mole fraction of water throughout the secondary reaction zone is explained by the dominant reaction in this region being the HCN/NO reaction typical of nitramines. This reaction can proceed to CO and N₂ without the formation of water through the overall reaction



Unfortunately H₂ was not measured in most of the experiments performed, but it is expected to exist at a high mole fraction in the final products due to the fuel-rich nature of the propellants.

Although the basic structure of these flames is dominated by nitramine chemistry, the influence of the energetic polymers is still clear. As will be discussed

Table 2 Combustion characteristics for nitramines and pseudopropellants at 100 W/cm²

Species	Surface regression rate, mm/s	Length of primary reaction zone, mm	Dark zone present	Beginning of secondary reactions, mm above surface	T_{surface} , K	$T_{\text{dark zone}}$, K
RDX	0.2	~0.5	No	~0.5	610	NA ^a
HMX	0.9	~2.5	No	~2.5	650	NA ^a
RDX/GAP	0.8	~0.5	Yes	~3.5	650	1250
HMX/GAP	1.1	~0.5	Yes	~3.5	700	1300
RDX/BAMO	0.35	~1	Yes	No final flame	640	1200

^aNot applicable.

hereafter in some detail, the addition of the azide polymers affects the length of the primary reaction zone in many cases, as well as the location at which the secondary reactions begin; however, the trends are not consistent among the three propellants. The addition of the polymers also changes surface mole fractions of some of the species associated with nitramine combustion including H₂CO, N₂, and HCN, because these are major products of the decomposition of BAMO¹⁵ and GAP.¹⁶ In addition, species that are only produced by BAMO and GAP are present, including ammonia and acetaldehyde, as well as small hydrocarbons. Also, CO₂ is observed at the propellant surface, whereas it is not present at the surface of the neat nitramines.^{13,14}

E. Effect of Azide Polymer Structure

A comparison of the results for RDX/BAMO and RDX/GAP presents some interesting insight into the effect of the structure of the azide polymer on the chemical and physical processes involved in combustion process. Table 2 presents a summary of the results for key parameters for the three pseudopropellants tested along with those of the neat nitramines at 100 W/cm². Listed in Table 2 are the length of the primary reaction zone, which is estimated from the NO₂ profile, the height above the sample surface at which secondary reactions begin, along with surface regression rates and measured surface temperatures. Choosing the point at which the secondary reactions begin was somewhat arbitrary because the species data often showed a region of gradual increase of CO and N₂ followed by a region where they increased with a much greater slope. Table 2 shows the locations corresponding to the beginning of the larger slope.

RDX/GAP had a much higher regression rate than RDX/BAMO, 0.8 vs 0.35 mm/s; however, the two materials had similar surface temperatures. Even with the much higher regression rate, GAP did not affect the length of the primary reaction zone, whereas the addition of BAMO caused a significant change in the primary reaction zone length as well as the surface concentration of NO₂ and the shape of the NO₂ profile. Clearly, BAMO had a much greater impact on the near surface reaction zones and stretched it substantially.

The location where secondary reactions begin was changed substantially by the addition of GAP to RDX, and the secondary reactions occurred over a larger distance, suggesting that the final reactions occur in a distributed fashion rather than in a thin sheet observed for neat RDX. (The effect of GAP on the secondary reaction

Table 3 Mole fractions of species at sample surface for 100 W/cm²

Species	NO ₂	HCN	N ₂ O	H ₂ CO	NO	N ₂	NH ₃	CO	CO ₂	H ₂ O
RDX	0.04	0.23	0.09	0.03	0.21	0.06	0	0.08	0	0.22
HMX	0.10	0.20	0.09	0.18	0.14	0.08	0	0.06	0	0.15
GAP	0	0.16	0	0.10	0	0.35	0.08	0.10	0	0.01
BAMO	0	0.22	0	0.15	0	0.42	0.05	0.02	0	0.05
RDX/GAP	0.05	0.19	0.06	0.08	0.14	0.10	0.04	0.09	0.02	0.20
HMX/GAP	0.10	0.26	0.07	0.14	0.14	0.08	NM ^a	0.07	0.02	0.10
RDX/BAMO	0.13	0.14	0.08	0.10	0.13	0.10	NM ^a	0.06	0	0.17

^aNot measured.

zone of HMX was similar, and a simple one-dimensional model of this portion of the flame showed that the products entering the dark zone of the HMX/GAP resulted in a distributed secondary reaction zone.¹⁷⁾ The addition of BAMO to RDX again had a more dramatic effect than that of GAP. It pushed the beginning of the secondary reactions beyond 4 mm from the surface where the species measurements ended. The video recordings of the combustion of RDX/BAMO at this condition showed no luminosity characteristic of the secondary flame, suggesting that it was blown off by the addition of BAMO at these experimental conditions.

Additional differences among the propellants can be seen in the near-surface mole fractions of the major products. The surface mole fractions for tests at 100 W/cm² are summarized in Table 3 along with those for the neat materials. Products associated with the initial decomposition of nitramines NO₂, HCN, N₂O, and H₂CO are listed in the first four columns of Table 3. Of the three pseudopropellants, RDX/BAMO shows the greatest impact on these species with substantial increase in NO₂ and H₂CO relative to neat RDX, as well as a significant reduction in HCN. The increase in H₂CO can be partially explained by it being a product of BAMO. The reduction in HCN is not easily explained because both BAMO and RDX produce it at similar levels, and so its reduction may indicate a chemical interaction in the condensed phase. For RDX/GAP, only the increase of H₂CO appears to be significant.

The very different impact of BAMO and GAP on RDX clearly raises the question of what the key physical and chemical processes causing them are. The structure of the gas-phase reaction zone can be affected by a number of factors including 1) increased velocity of products leaving the surface, 2) increased surface temperatures, 3) increased subsurface heat release resulting from the energetic binder, 4) addition of inert N₂ at the surface by the azide binder that could lower reaction rates through dilution effects, 5) changes in the mole fractions of major reactive species leaving the surface, and 6) more fuel-rich stoichiometry that will lower reaction rates and lower the final flame temperature. However, all of these factors are present for both GAP and BAMO, and it is not possible to argue from the present data what interplay of these factors caused the observed trends.

F. Effect of Oxidizer Structure

More interesting questions are raised by comparison of the results for RDX/GAP with those of HMX/GAP to illustrate differences caused by the structure of the nitramine. Previous work with neat nitramines under experimental conditions

Table 4 Effect of increasing heat flux on combustion characteristics^a

Species	Surface regression rate, mm/s	Length of primary reaction zone, mm	Dark zone present	Beginning of secondary reactions, mm above surface	T_{surface} , K	$T_{\text{dark zone}}$, K
RDX	0.7 ↑↑	~1 ↑	No	~1.5 ↑	610 →	NA ^b
HMX	1.2 ↑	~2.5 →	No	~4 ↑	650 →	NA ^b
RDX/GAP	1.9 ↑	~1 ↑	Yes	~2.5 ↓	700 ↑	1250 →
HMX/GAP	2.4 ↑	~1.5 ↑↑	Yes	>8 ↑↑	750 ↑	1400 →
RDX/BAMO	1.4 ↑↑	~2 →	Yes	~3	670 ↑	1500 ↑

^a Arrows indicate change relative to corresponding case at 100 W/cm²; all results for 300 W/cm² except RDX/BAMO at 400.

^b Not applicable.

similar to those used in this study showed distinct differences in their gas-phase chemical structure.^{13,14} Some of these difference are clear in Tables 2 and 4, including that the primary reaction zone length of HMX was much greater than that of RDX at the same experimental conditions. When GAP was added to HMX, it resulted in a shortening of the primary reaction zone at both heat fluxes, whereas the primary reaction zone for RDX/GAP was unchanged relative to that for neat RDX. The effect on the location of the beginning of the secondary reactions was to move it farther from the surface for both nitramines with the addition of GAP. Also, the effect of GAP on the burning rate of RDX was much greater than that for HMX at both heat fluxes, even though the surface temperatures increased by approximately the same amount, 40–50 K, in each case.

G. Effects of Heat Flux on Pseudopropellant Combustion

The arrows included in Table 4 illustrate the direction of the change of each table entry when heat flux was increased. The number of arrows is an attempt to visually indicate the magnitude of the change; an increase of approximately three times was used to delineate the use of one and two arrows. A horizontal arrow indicates that a quantity was unchanged within the uncertainty of the experiments.

For the two nitramine/GAP propellants, the effect of increasing heat flux on the burning rate was of approximately the same order; the burning rate increased by slightly more than a factor of two. For RDX/BAMO, however, the effect of increasing heat flux was nearly a factor of four. Even considering that the high heat flux for RDX/BAMO was 400 W/cm² as opposed to 300 W/cm² for the propellants containing GAP, this is a more substantial effect of heat flux on regression rate. For all of the pseudopropellants, an increase in heat flux resulted in higher measured surface temperatures in contrast to the neat nitramines, for which surface temperature was independent of heat flux.

The effect of increasing heat flux on the reaction zones (Table 4) and surface mole fractions (Table 5) was complex, showing some consistent trends and some opposing trends. For all three propellants, increasing the heat flux caused the primary reaction zone length to increase by a factor of two or more. On the other

Table 5 Mole fractions of species at sample surface for high heat flux

Species	NO ₂	HCN	N ₂ O	H ₂ CO	NO	N ₂	NH ₃	CO	CO ₂	H ₂ O
RDX	0.12	0.23	0.08	0.03	0.16	0.05	0	0.07	0	0.22
HMX	0.12	0.18	0.12	0.10	0.10	0.06	0	0.03	0	0.19
GAP	0	0.16	0	0.11	0	0.36	0.10	0.11	0	0.01
BAMO	0	0.22	0	0.15	0	0.42	0.05	0.02	0	0.05
RDX/GAP	0.12	0.18	0.04	0.07	0.10	0.12	0.04	0.10	0.02	0.16
HMX/GAP	0.03	0.26	0.08	0.15	0.13	0.10	NM ^a	0.10	0.03	0.12
RDX/BAMO	0.14	0.19	0.09	0.02	0.13	0.17	NM ^a	0.06	0.01	0.21

^aNot measured.

hand, the start of secondary reactions showed opposite trends for the two GAP-based propellants. Increasing heat flux caused the start of secondary reactions to move closer to the surface for RDX/GAP, whereas it pushed them beyond 8 mm for HMX/GAP. The effect of increasing heat flux on RDX/BAMO is not entirely clear because of the limited spatial extent of the measurements that were taken only to approximately 3 mm at the high heat flux. The changes in reaction zone structure and burning rate cannot be explained with simple phenomenological arguments.

VI. Conclusions

The species and temperature data for three nitramine/azide pseudopropellants presented must be considered in light of the very challenging nature of the experiments. Although the element balances are not as good as desired, indicating that some species may have been missed, the experiments are among the few in the literature that attempt mass closure in propellant studies. Measurements of surface temperature are notoriously difficult due to the challenge of identifying the surface as well as problems with residue. Independent experiments to confirm the species and temperature data would be very useful to the overall effort to understand and model the behavior of the nitramine/azide propellants. Even so, the data show many fascinating similarities and differences among the three materials in terms of nitramine/azide polymer interactions and also on the effects of increasing heat flux. The trends are too complex to explain with phenomenological arguments and point to the need for detailed numerical modeling of the pseudopropellants. The experimental results presented provide many challenging cases for model validation. Such modeling of nitramine/azide propellants has been started by Liau et al.,¹⁸ but much remains to be done.

Acknowledgments

The authors are most grateful for all of the support, financial and otherwise, that made this work possible. Various parts of the work represented here were supported by the Office of Naval Research (ONR), Mechanics Division, under ONR Contract N00014-93-1-0080, through the California Institute of Technology Multidisciplinary University Research Initiative (MURI) under ONR Grant N00014-95-1-1338, and through an Air Force Office of Scientific Research MURI, Grant F49620-93-0430. The support and encouragement of Richard Miller, Judah

Goldwasser, Len Caveny, and Mitat Birkan are greatly appreciated. This work would not have been possible without the support of three individuals who provided the materials required: Timothy Parr of Naval Air Warfare Center, Gerald Manser of Aerojet, and Anthony Manzara of 3M.

References

- ¹Price, E. W., Sambamurthi, J. K., Sigman, R. K., and Panyam, R. R., "Combustion of Ammonium Perchlorate—Polymer Sandwiches," *Combustion and Flame*, Vol. 63, No. 3, 1986, pp. 381–413.
- ²Korobeinichev, O. P., Tereschenko, A. G., Shvartsberg, V. M., Chernov, A. A., Makhov, G. A., and Zabolotny, A. E., "A Study of Flame Structure of Sandwich Systems Based on Ammonium Perchlorate, HMX, and Polybutadiene Binder," *Flame Structure*, Vol. 1, NAUKA, Novosibirsk, Russia 1991, pp. 262–267.
- ³Parr, T., and Hanson-Parr, D., "Advanced Oxidizer Diffusion Flame Structure," *Proceedings of the 31st JANNAF Combustion Meeting*, Publication 620, Vol. 2, Chemical Propulsion Information Agency, Laurel, MD, 1994, pp. 333–344.
- ⁴Oyumi, Y., Inokami, K., Yamazaki, K., and Matsumoto, K., "Thermal Decomposition of BAMO/HMX Propellants," *Propellants, Explosions, Pyrotechnics*, Vol. 18, No. 1, 1993, pp. 62–68.
- ⁵Oyumi, Y., Inokami, K., Yamazaki, K., and Matsumoto, K., "Burning Rate Augmentation of BAMO-Based Propellants," *Propellants, Explosions, Pyrotechnics*, Vol. 19, No. 4, 1994, pp. 180–186.
- ⁶Kubota, N., and Sonobe, T., "Burning Rate Catalysis of Azide/Nitramine Propellants," *Proceedings of Twenty-Third Symposium (International) on Combustion*, Combustion Inst., Pittsburgh, PA, 1990, pp. 1331–1337.
- ⁷Schedlbauer, F., "LOVA Gun Propellants with GAP Binder," *Propellants, Explosives, Pyrotechnics*, Vol. 17, No. 4, 1992, pp. 164–171.
- ⁸Dhar, S. S., and Singh, H., "Burn Rate and Catalysis Behavior of GAP Based CMDB Propellants," AIAA Paper 95-2589, 1993.
- ⁹Lee, Y. J., Tang, C.-J., Kudva, G. K., and Litzinger, T. A., "Triple Quadrupole Mass Spectrometer System for Studies of Gas-Phase Combustion Chemistry of Energetic Materials," *Measurement Science and Technology*, Vol. 9, No. 9, 1998, pp. 1576–1586.
- ¹⁰Lee, Y. J., "A Study of the Physical and Chemical Processes governing CO₂ Laser-Induced Combustion of RDX, BAMO and RDX/BAMO Pseudo-Propellants," Ph.D. Dissertation, Dept. of Mechanical Engineering, Pennsylvania State Univ., University Park, PA, 1996.
- ¹¹Bobeldijk, M., Van der Sande, W. J., and Kistemaker, P. G., "Simple Models for the Calculation of Photoionization and Electron Impact Ionization Cross-Sections of Polyatomic Molecules," *Chemical Physics*, Vol. 179, No. 2, 1994, pp. 125–130.
- ¹²Zenin, A. A., "Experimental Investigation of the Burning Mechanism of Solid Propellants and Movements of Burning Products," Ph.D. Dissertation, Inst. of Chemical Physics, Russian Academy of Science, Moscow, 1976 (in Russian).
- ¹³Lee, Y., C.-J., Tang, and Litzinger, T., "A Study of the Chemical and Physical Processes Governing the During CO₂ Laser-Assisted Pyrolysis and Combustion of RDX," *Combustion and Flame*, Vol. 117, No. 3, 1999, pp. 600–628.
- ¹⁴Tang, C.-J., Lee, Y. J., Kudva, G. K., and Litzinger, T. A., "A Study of the Gas-Phase Chemical Structure of HMX During CO₂ Laser-Assisted Combustion," *Combustion and Flame*, Vol. 117, No. 1, 1999, pp. 170–188.

¹⁵Lee, Y. J., Tang, C.-J., and Litzinger, T. A., "The Thermal Decomposition of 3,3'-Bis-Azidomethy-Oxetane," *Journal of Propulsion and Power*, Vol. 14, No. 1, 1998, pp. 37-44.

¹⁶Tang, C.-J., Lee, Y. J., Kudva, G. K., and Litzinger, T. A., "Simultaneous Species and Temperature Measurements During Laser-Assisted Combustion of GAP," *Combustion and Flame*, Vol. 117, No. 1, 1999, pp. 244-256.

¹⁷Tang, C. J., "A Study of the Chemical Structure of HMX Propellants and Combustion Response to Oscillatory Radiant Heat Flux," Ph.D. Dissertation, Dept. of Mechanical Engineering, Pennsylvania State Univ., University Park, PA, 1997.

¹⁸Liau, Y.-C., Yang, V., and Thynell, S. T., "Analysis of RDX/GAP Pseudo-Propellants with Detailed Chemistry," *Proceedings of 35th JANNAF Combustion Meeting*, Publication 685, Chemical Propulsion Information Agency, Laurel, MD, 1998, pp. 31-46.

Chapter 2.5

Optical Diagnostics of Solid-Propellant Flame Structures

Timothy Parr* and Donna Hanson-Parr*

Naval Air Warfare Center Weapons Division, China Lake, California

I. Introduction

THIS chapter is a review of results obtained from the authors' experimental work on energetic materials, including solid rocket oxidizers, monopropellants, and fuels at and above atmospheric pressure.^{1–30} Included in these studies were cyclotetramethylene tetranitramine (HMX),^{1–3,5–7,9,10,17,25,27,29} cyclotrimethylene trinitramine (RDX),^{1,2,5,9,17,20,25,27,29,30} 1,3,3-trinitroazetidine (TNAZ),^{3,27} hydrazinium nitroformate [$\text{N}_2\text{H}_5 + \text{C}(\text{NO}_2)_3$] (HNF),^{11,15,17,27,29} ammonium perchlorate (AP),^{3,13,14,16,18,19,21–23,27} ammonium dinitramide (ADN),^{2,3,12,27} and the gun propellant based mostly on RDX, XM39,^{9,17,29} as well as burning aluminum droplets.^{7,24,26,28} A brief general description of the experimental apparatus setups used for various types of experiments, including sample preparation, is presented. This is followed by results for flame structure measurements on various energetic materials. These results show a wide range of behavior for different energetic material families.

The purpose of making spatially and temporally resolved quantitative measurements of species and temperature in solid-propellant flames is to help validate models of propellant combustion based on detailed kinetics. These models will allow a priori prediction of propellant ballistic properties, such as burning rate, pressure exponent, temperature sensitivity, ignition behavior, combustion instability response, and perhaps hazard responses without the costly process of large-scale formulation and testing.

II. Experimental Techniques

A. Description

Samples consisted mostly of pure powders or powder mixtures pressed into solid cylinders. For the sandwich samples, alternating layers of different solid materials

This material is declared a work of the U.S. Government and is not subject to copyright protection in the United States.

*Research Chemist, Research Dept.

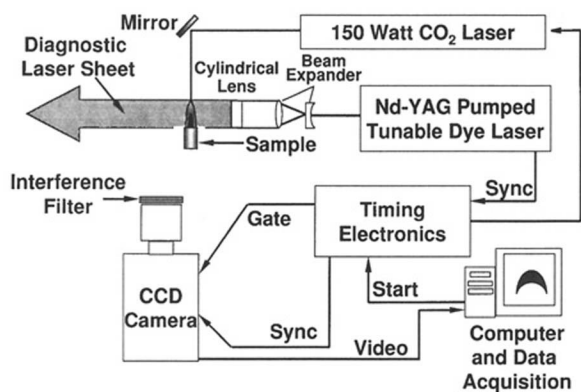


Fig. 1a Apparatus diagram for PLIF experiments.

were pressed firmly against each other in a miniature vise. Formulated propellant samples were cut from as-received material. Oxidizer and monopropellant powders used were HMX, RDX, TNAZ, HNF, AP, and ADN. Fuels were only used in the sandwich experiments and included hydroxyl-terminated polybutadiene (HTPB), polyurethane (PU), glycidylazide polymer (GAP), bis(azidomethyl)oxetane (BAMO), 3-nitratomethyl-3-methyl oxetane (NMMO), and BAMO/NMMO mixture. The HMX and RDX were military grade, and the AP was commercial ultra-pure, low alkali material. The TNAZ, HNF, and ADN were research materials.

Sample cylinders from powders were pressed neat at about 556 MPa to 96–98% theoretical maximum density and were either 6.35 or 10 mm in diameter. For HMX and RDX only, one or two drops of methanol or acetone were used in the pressing process. This was dried out of the sample prior to use. The XM39 samples were 6.35-mm-diam extruded cylinders. For self-deflagration tests, the CO₂ laser ignition source was turned off shortly after the sample was ignited, and the data used were from the time frame of steady-state self-deflagration without CO₂ laser support. In the laser-supported work, the CO₂ laser flux was continued during the entire experiment.

The flame structure was measured using planar laser-induced fluorescence (PLIF) imaging,^{2–7} UV-visible absorption,^{1,2} UV-visible emission, and most recently spontaneous Raman spectroscopy.^{16,17} The apparatus diagrams for the PLIF and absorption spectroscopy setups are shown in Figs. 1a and 1b, respectively, and that for Raman in Fig. 2.

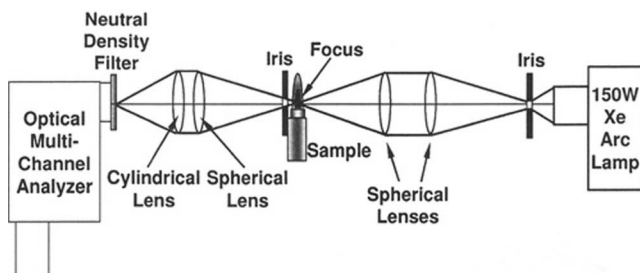


Fig. 1b Apparatus diagram for UV-visible absorption experiments.

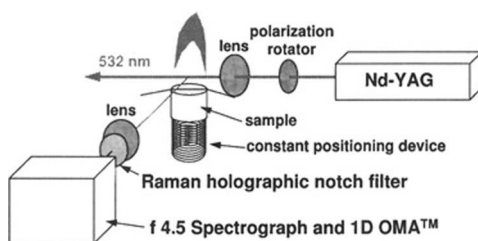


Fig. 2 Raman apparatus diagram.

The laser used to excite PLIF was a Nd-YAG pumped tunable dye laser with nonlinear crystal mixing and doubling into the ultraviolet. The ultraviolet beam was expanded and formed into a sheet and passed through the center of the flame. The camera used to image PLIF was a gated image intensified charge-coupled device with 752×480 pixels. The camera was gated on for about 80 ns only during or just after the diagnostic laser pulse; this discriminated against natural flame emission and monitored only the laser-induced fluorescence.

PLIF provides a narrow planar slice through the flame, whereas emission imaging is a line-of-sight average technique. The thickness of the laser sheet typically was less than $150 \mu\text{m}$, and the resolution of the two-dimensional camera system was from 4 to $9 \mu\text{m}$ per pixel. Such fine resolution was required for the very short RDX and especially HNF flames as well as the fine spatial detail of the sandwich diffusion flames. The camera resolution was determined by imaging a ruler. Species monitored with PLIF included CN, NH, OH, NO, NO_2 , polyaromatic hydrocarbons (PAHs), and AIO. Other species monitored with PLIF but not reported here included H_2CO , C_2 , and CH. Because of quenching, the PLIF technique is not quantitative. However, the measured profiles are placed on an absolute scale by calibration with absorption spectroscopy. Also, because PLIF is quantum state specific, separate levels can be pumped and the resulting signals used to obtain either rotational or vibrational temperature. This was accomplished for CN, NO, OH, and AIO.

The absorption measurements have been described previously.^{1,2} Basically, a light beam, focused at the center of the sample to avoid beam steering, passed through the flame of a deflagrating sample, and the transmitted light was measured spectrally using an intensified linear diode array detector. The absorption spectrum was obtained by ratioing the spectrum obtained with flame to that without flame (I/I_0). Species concentration and temperature (if the spectroscopy of the species is known) are then obtained by comparing with calculated spectra, or (if the spectroscopy is not known) with spectra from the literature. Spatial resolution for absorption measurements was typically $100 \mu\text{m}$ and could be as good as $50 \mu\text{m}$. Species monitored with absorption were NO, OH, CN, NH, H_2CO , HONO, NO_2 , and AIO. The absorption technique is line of sight but quantitative. Absorption path information is obtained from the relevant PLIF results or visible imaging.

Spontaneous Raman is conceptually simple, but in practice is difficult to implement. A full discussion of this technique can be found elsewhere.¹⁶ A laser beam was directed over the sample and focused above the sample, and the Raman signal was detected at 90 deg with a linear diode array camera on a spectrograph. The intensity of the signal is very small, and so great care must be taken to reduce as many sources of noise as possible. The majority of species were detected using

this technique, including HCN, NO, H₂CO, N₂, CO, CO₂, H₂O, H₂, N₂O, and O₂. Although the technique as implemented gives a single point measurement, all of these species are obtained in the spectrum from a single experiment. The spatial resolution for Raman was about 100 μm .

B. Uncertainties in Concentration and Temperature Measurements

The greatest uncertainties in temperature data arise from measurements conducted in the region of the flame close to the sample surface, where there is a steep gradient. Because each OH radical PLIF rotational line measurement was a separate experiment, we used video cameras to verify surface location and flame height. Temperature was obtained from the slope of a type of Boltzmann plot. Temperature measurements for which the correlation coefficient was less than 0.9 were automatically thrown out. For the most part, correlation coefficients of 0.99 were seen, except near the surface, where there is little or no OH. A correlation coefficient of 0.99 yields about a $\pm 8\%$ standard deviation in the slope, or ± 150 K standard deviation in the temperature. The temperatures measured came very close to adiabatic high in the flame, proving the validity of the technique.

Another check of temperature is comparison of the OH radical PLIF-measured temperatures with that obtained from fitting absorption measurements. These appear to overlap well to within 100–200°C. Fitting the absorption spectra for temperature is difficult, however, because of noisy baselines. To obtain concentrations from the absorption results, the temperature is usually taken from the PLIF results, and the fit is compared with the data. Sometimes, vibrational temperatures can be obtained from the absorption measurements (for example, for NO). An error of 150°C in the NO temperature would lead to about a 6–10% error in mole fraction concentration (but not number density).

The other sources of error in absorption measurements involve the pathlength and baseline noise. Absorption is essentially linear with pathlength, so that a 10% error would yield a 10% error in concentration. The pathlength measurement is most uncertain near the secondary flame front because the three-dimensional flame shell around the sample is Gaussian. Near the surface, where the pathlengths are longer, a maximum of 5% error in pathlength would be typical.

Baseline noise is worst for experiments for which little averaging was done and for which the concentration is small and/or the pathlength is short. Typically, the baseline noise was about $\pm 5\%$. Therefore, an estimate of uncertainty in mole fractions, barring gross measurement errors, would be typically 15% near the surface and 25% nearer to the secondary flame front.

III. Results

We start with discussions of RDX and HMX flame structures, including laser-supported deflagration at 0.1 MPa (1 atm), the effect of pressure, steady-state deflagration, transient ignition, and the differences between RDX and HMX. Then we will present results from other neat energetic materials. Diffusion flame structures of composite sandwich samples will be presented. Then results from a complete formulated nonaluminized solid propellant will be shown, and finally metal combustion studies will be summarized. Note that, in all PLIF results color images, red is maximum intensity, and violet to black is minimum.

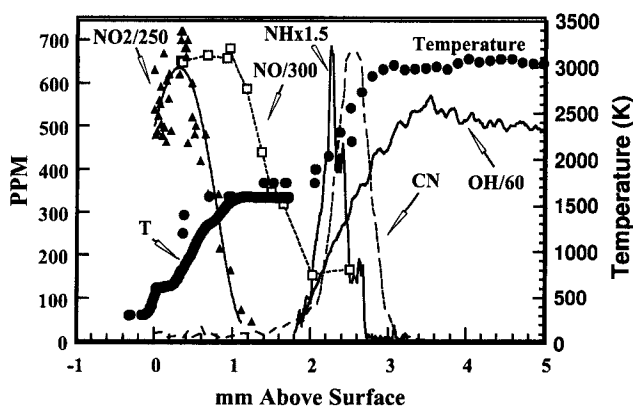


Fig. 3 Temperature and species profiles for laser-supported deflagration of RDX at 1 atm in air; laser flux of 400 W/cm^2 .

A. Laser-Supported Deflagration of RDX and HMX at 0.094 Megapascal (1 Atmosphere)

Work has been conducted to image the flame structure of HMX, RDX, HNF, ADN, and other advanced energetic materials at pressures between 0.094 and 1.84 MPa (0.92 and 18 atm) during the ignition and steady-state deflagration stages using a CO_2 laser as an ignition source.^{1-7,10,20,25} The added CO_2 laser heating was used to enhance the low-pressure burning rate of these neat materials and to simulate more closely the surface heat flux conditions seen by samples self-deflagrating at rocket motorlike pressures. In addition, the external laser flux stretches out the flame zone, making it easier to use diagnostics to resolve the species and temperature profiles. The evolution of the flame during the ignition stage could be studied with PLIF by varying the time between the ignition laser and probe laser. Prior results for HMX have been reviewed previously.² Results for RDX laser-supported deflagration at 0.094 MPa (0.92 atm) are shown in Fig. 3. These profiles were obtained from the PLIF images via selection of a centerline slice and from the UV-visible absorption traces via deconvolution of pathlengths measured from PLIF and emission imaging. RDX shows considerably shorter flame heights than HMX: Under the same conditions of external laser flux, the height to the peak in the CN flamesheet was 2.5 mm for RDX and 4 mm for HMX.

The temperature trace of Fig. 3 is a combination of data from three sources. The temperature within the condensed phase and just above it was obtained from thermocouples with a $5\text{-}\mu\text{m}$ -thick junction. The temperature profile in the dark zone region was obtained from fitting of NO UV absorption spectra, and the temperature profile from the dark zone through the secondary flame and beyond was obtained from OH rotational temperature (OH T_r) PLIF. Several R_1 transitions of the (1, 0) A-X band were excited, and Boltzmann populations were used to obtain rotational temperature. The models of RDX deflagration predict that the temperature should rise above the adiabatic flame temperature in laser-assisted experiments, due to the heat input from the laser, in agreement with our results.

These laser-supported flames were three dimensional rather than one dimensional, due both to the bell-shaped energy profile of the ignition laser and the heat losses from the edges of the flame. Using a flatter energy profile, at lower average

flux, improved the flame structure, but the flame was still far from mathematically one dimensional. Modeling these flames in full three dimensions would obviously be computationally prohibitive, and so we used particle imaging velocimetry to measure the flow streamlines and, therefore, the flame area ratio function. In our geometry, the velocity is nearly constant through the dark zone and secondary flame sheet, so that the energy release of the secondary flame appears mostly to spread out the flame rather than speed up the flow. The area ratio curve was given to modelers to include in their one-dimensional model as a correction factor. When this was included, there was quite good agreement between the model³¹ and our species and temperature profiles, as well as with the burn rate, pressure exponent, and temperature sensitivity measurements of Atwood et al.³² This is the first time that an a priori model with detailed kinetics has been able to predict the ballistic properties of solid-propellant combustion and match the species and temperature profiles. Experimental measurements were important inputs in developing and validating this model.

B. Effect of Pressure on HMX Flame Structure

A study of the change in HMX laser-supported flame structure with pressure⁵ showed that the secondary flamesheet thickness, as monitored with CN radicals, decreases with pressure as $1/P^{0.98}$, and the flame height decreases more or less inversely with pressure as well. The range of pressures covered was 0.094–1.84 MPa (0.92–18 atm). Other PLIF measurements have been done up to 2.5 MPa (25 atm), which is approaching actual rocket motor operating pressures. Loss of signal due to quenching did not seem to be a problem, but Fig. 4 shows that for nitramines the flame structure length scales become exceedingly small at realistic rocket motor pressures. Extrapolation of Fig. 4 to 5.2 MPa (51 atm), a realistic rocket motor operating pressure, results in a flame height of only 24 μm . Virtually no current diagnostic technique can make profile measurements within that length scale. This is why work is done at low pressures of 0.1–1 MPa (1–10 atm).

Nevertheless, modelers wanted some results from a truly one-dimensional flame without added laser flux as a validation. It was also suggested that using added energy from a laser may produce artifacts in the flame, such as liquid spray, which may not be present without the laser. Laser Mie scattering experiments showed that there is indeed a liquid spray above the surface with laser-supported deflagration of RDX or HMX, but also that this spray is present, at a lower number density, for self-deflagration of HMX. The dark zone height of self-deflagrating RDX is so small, even at 0.1 MPa (1 atm), that few liquid droplets survive to be seen. This liquid fuel spray can only be seen under intense laser illumination, as the drops, being nonrefractory, do not incandesce by themselves.

C. Self-Deflagration of RDX at 0.1 Megapascal (1 Atmosphere)

As seen in Fig. 5, the addition of CO_2 laser flux to RDX caused a marked increase in the flame standoff distance. At 0.1-MPa (1-atm) pressure, without the additional flux, the RDX flame height (to the peak in the CN flame sheet) is only about 0.47 mm, and the temperature profile no longer has a plateau region indicative of a dark zone (see Fig. 6). The collapse of the dark zone plateau had also been predicted by model calculations. The reason the dark zone collapsed on removal of the CO_2 laser was that the decomposition rate near the surface slowed

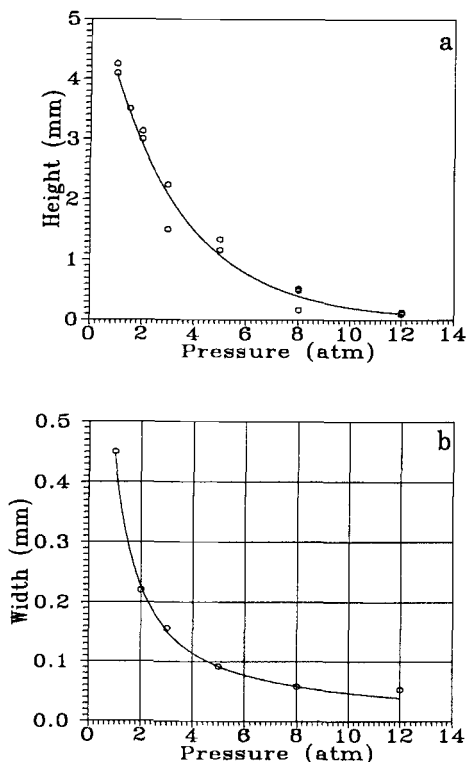


Fig. 4 HMX flame as function of ambient pressure (N_2 atmosphere): a) secondary flame standoff and b) flame thickness.

down, causing a decrease in gas velocity and a diffusive smearing due to the close proximity of the secondary flame radicals.

Measurements of nonlaser-supported deflagration, i.e., self-deflagration, of RDX at 0.094 MPa (0.92 atm) were made using PLIF at down to $4\text{-}\mu\text{m}$ spatial resolution and UV-visible absorption.^{9,29} Despite the much smaller length scales, temperature and many species profiles were measured. Absorption quantified NO, H_2CO , HONO, OH, CN, and NH. The OH concentration shown in Fig. 6 is less than that

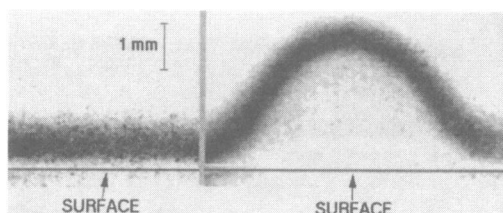


Fig. 5 CN PLIF images using 10-mm-diam RDX pellets at 1 atm for (left) self-deflagration showing an extremely flat flame compared with (right) laser-supported deflagration showing a decidedly nonflat flame.

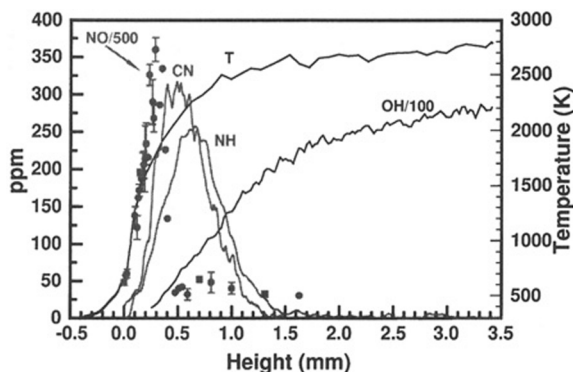


Fig. 6 PLIF measured and absorption calibrated species and temperature profiles for self-deflagration of RDX at 1 atm in air; temperatures below 0.3 mm come from 5- μ m thermocouple.

shown previously^{9,29}; the pathlength used previously for the determination was found to be incorrect. The flame was too short to resolve NO_2 and the 365-nm unknown (possibly a nitrosamine¹) profiles, which die quite close to the surface, even for laser-supported combustion. Peak concentrations were 310 ppm for CN and 260 ppm for NH, and 3.6 mol% for OH, 17 mol% for NO and <1 mol% for H_2CO and HONO. PLIF was used to measure profiles for CN, NH, and OH, and OH rotational temperature. Species concentration and temperatures profiles are shown in Fig. 6. For OH, the $R_1(10)$ line was used and was corrected for the effects of temperature, but it was found that this correction was minor.

D. HMX Self-Deflagration at 0.1 Megapascal (1 Atmosphere)

The flame standoff for self-deflagrating HMX is much higher than for RDX. Without the external laser flux to support the flame, the burn rate and flame height are variable, and this makes comparison of species profiles, each of which are

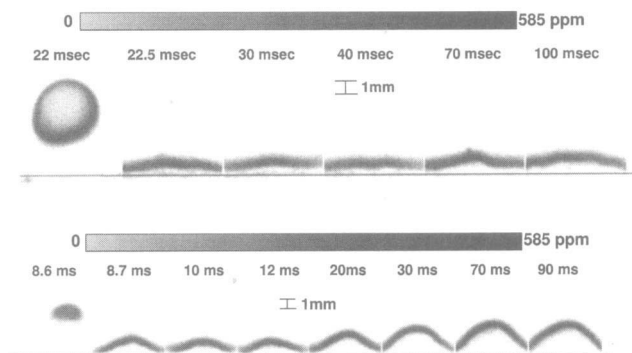


Fig. 7 RDX ignition in air at 1 atm: CN PLIF images of flame structure. Time after start of heating pulse shown above each frame. The top images are low flux ignition and bottom images are medium flux ignition.

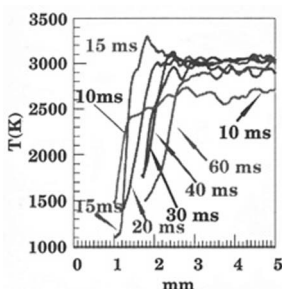


Fig. 8a Temperature ($\text{OH } T_r$) profiles during ignition of RDX in air at 1 atm at medium flux at selected times after the start of heating pulse.

measured in separate experiments, difficult and temperature ratios impossible. We made measurements of HMX deflagration flame structure without laser flux support,^{9,29} but found that the flame was unstable at 0.094 MPa (0.92 atm) and that a fuel spray was present, which interfered especially with the NO measurements. We saw a maximum mole fraction of about 6.5% for both H_2CO and NO_2 , about 210 ppm of CN, and 3.6% OH. The 365-nm nitrosamine was not observed.

E. Ignition of HMX and RDX

Quantitative CN, OH, and OH rotational temperature and velocity two-dimensional profiles were imaged using PLIF or PIV during ignition and deradiative extinguishment of RDX^{20,25} at three different CO_2 laser heat flux levels: low = 195, medium = 402, and high = 807 W/cm^2 . For HMX, only the medium flux was used.^{10,25} Relative NO_2 and NO profiles were also imaged with PLIF. Decomposition products, such as NO and NO_2 , were formed early in the laser heating process for both HMX and RDX, and the gas plume moved away from the surface. Ignition occurred in the gas phase at a later time, as evidenced by radical buildup, such as CN (Fig. 7) and OH. This often appeared as a spherical ignition kernel away from the surface. The flame then transitioned rapidly to a thin flamesheet that moved toward the surface. With longer heating times, laser-supported quasi-steady-state deflagration developed as the flame sheet again moved somewhat farther from the surface. Figure 8a shows the temperature profile as a function of laser heating time, and Fig. 8b shows how the flamesheet height varied with laser

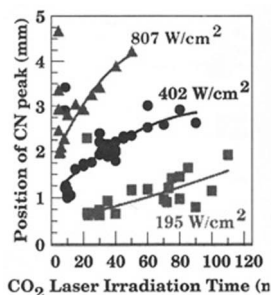


Fig. 8b CN flamesheet height vs time after start of heating flux for various levels of that flux.

heating time. The species and temperature data have been used as an aide in the development of a fully time-dependent RDX combustion model.³³ Such models are useful for not only predicting ignition behavior but also combustion instability response.

Spectra of the preignition gases observed emanating from the surfaces of HMX and RDX during the heat-up phase were measured to look for signs of HONO formation. The spectral region sampled included HONO and NO₂ absorption, averaging from about 1 to 5 mm above the surface. Most or all of what was seen in this spectrum was due to NO₂ absorption, about 10 mol%. Spectra close to the surface were also examined for signs of HONO, but none were observed for either HMX or RDX. Any HONO formed must decay too close to the bubbly surface to be detected.

Concentrations of the radicals CN, NH, and OH appear to be about the same for HMX and RDX during ignition and steady-state combustion (laser-supported or self-deflagration), with possibly 30–40% more CN for RDX during ignition.

When the laser heating flux was shut off, the sample often extinguished (deradiative extinguishment). The condensed phase profile for higher burning rate laser-supported deflagration is steeper (thinner) than that for lower burning rate self-deflagration. At the moment the laser heating flux is removed, the system is not in a steady-state solution. The deflagration continues, but rapidly consumes the thin preheated condensed phase profile, without having the thick profile to draw from. The pyrolysis rate falls off, and the combustion weakens as radical concentrations decay exponentially and the flame cools rapidly (not shown).

Global measurements of the ignition process include establishing the first-light and go/no-go times. First light is the time when visible emission from the gases appears and go/no-go is the time beyond which the sample will remain ignited if the ignition source is removed. These times are, of course, ignition source flux dependent. We have seen that the gas phase flame structure is fully established much earlier than the go/no-go time, and the maximum temperature is already close to adiabatic very soon after first light. After first light, the steep temperature gradient is close to the surface, but then stretches out away from it as time progresses, until steady state is achieved. As the temperature profile stretches away from the surface, less heat feedback is provided by the flame with the complement necessary to sustain combustion coming from the CO₂ laser flux. It appears likely that early on the laser is providing sufficient heat to the surface to sustain combustion, but unless the condensed profile has become fully established that is, at go/no-go, the flame will extinguish if the flux is removed. In addition, we have found that the go/no-go point is dependent on how fast the laser heating flux is removed. Ramping the flux down allows the system to reestablish a solution, whereas instantly removing the flux leaves the system far from a solution.

Because both the gas phase ignition and deradiative extinguishment processes are kinetically sensitive these data will provide good validation of both transient combustion code development and the input kinetic database.

F. Comparison Between HMX and RDX

The following conclusions/speculations were derived from our cited papers for HMX and RDX. Whereas HMX and RDX have virtually identical structures, their combustion properties differ in important ways. The burning rate of HMX at low

pressure and high initial temperature is higher than for RDX. The temperature sensitivity for the HMX burning rate at low pressure is higher than for RDX. Finally, although the molecular structure might imply similar decomposition gases, the flame structure for HMX is different, at low pressures, than for RDX. HMX has a much taller flame when self-deflagrating at 0.1 MPa than RDX does. This implies that the input boundary condition to the gas phase at the surface must differ between HMX and RDX, which implies differences in the condensed phase processes or branching ratios.

HMX and RDX both have high concentrations of NO_2 at the surface: laser-supported results yielded about 9 mol% for HMX and 15% for RDX for the same CO_2 flux. There appears to be as much as 11–16 mol% formaldehyde at the surface during deflagration for HMX (using $T = 660$ K) compared with <1–3% for RDX, with substantial amounts into the dark zone (5–10%). Military-grade RDX contains about 5% HMX, so that it is possible that the formaldehyde seen during RDX deflagration is actually coming from HMX decomposition. Because over an order of magnitude more formaldehyde is seen for HMX at the surface than for RDX during combustion and there is more NO_2 for RDX than for HMX, it appears that HMX decomposes partially via the $\text{N}_2\text{O}/\text{H}_2\text{CO}$ channel, whereas RDX probably proceeds mostly via the NO_2/HCN channel. It is possible that peak concentrations still have not been resolved because these two species (NO_2 and H_2CO) concentrations peak at the surface, which can be ill defined due to the amount of bubbling, especially during self-deflagration.

Although the flame standoffs for HMX are about three times those for RDX during laser-supported deflagration, and 10 or more times during self-deflagration, the trend of flame height vs irradiance has the same slope. It appears that the HMX flame stabilized when the CO_2 laser irradiance was increased from zero. The surface temperature of self-deflagrating RDX, measured at 0.094 MPa using thermocouples was about 610 K, compared with about 660 K for HMX.

It was found that RDX produces a probable nitrosamine not clearly visible in the HMX spectrum. There was about six times as much nitrosamine for RDX as for HMX during rapid thermal decomposition studies. The nitrosamine appearance seemed to be coincident with the liquefying of the material.

G. TNAZ

Neat TNAZ was found to be much harder to ignite than HMX or RDX and self-deflagrated with a visible flame only at pressures above 0.82 MPa (8 atm) (Refs. 3 and 27). Under these conditions the hot flame was very close to the surface, making diagnostics difficult.

H. HNF Neat Self-Deflagration Flame Microstructure^{15,17,29} at 0.094 Megapascal (0.92 Atmosphere)

Some energetic materials have extremely short flame length scales, even at 0.1 MPa (1 atm). Figure 9 shows a video image of HNF deflagration at 0.094 MPa. There is an extremely short dark zone (about 40 μm) with a complex flame structure.

The first visible flame, starting at 40 μm and centered at 180 μm with a full width at half maximum (FWHM) thickness of 180 μm , appears whitish on the

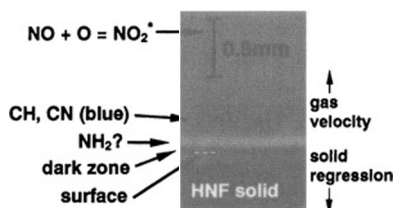


Fig. 9 Video image of HNF self-deflagration at 1 atm in air.

video and has the majority of its spectral emission to the red of 515 nm. A preliminary assignment is the NH_2 radical. Within this flamesheet, and extending beyond, are emissions from CN, NH, and CH. Emission spectroscopy showed that the CH was much stronger than for nitramines. The CN and NH emissions were much weaker than for nitramines, the NH emission being greater than CN, as opposed to nitramines. PLIF showed that the CN profile peaked at $360\text{ }\mu\text{m}$ and the NH at $300\text{ }\mu\text{m}$. Above the bluish flame is broadband orange brown emission, probably $\text{NO} + \text{O} = \text{NO}_2^*$ recombination chemiluminescence, which extends far into the burnt gas region. The OH radical PLIF profile rose rapidly through and outside the CN flamesheet and then transitioned to a more gradual rise in the burned gas region. The OH T_r also rose sharply at the CN flamesheet, but did not reach the adiabatic flame temperature (2766 K) at this point. Instead, it continued to rise at a slower rate. The NO concentration was quite high near the surface and died very gradually above the flame front. As discussed elsewhere,¹⁵ the conversion of NO to N_2 in this system is slow, and this reaction does not add much energy to the flame. Species and temperature profiles from both emission and PLIF imaging are shown in Figs. 10a and 10b. In Figs. 10a and 10b, the (postulated) NH_2 is the Gaussian curve peaking closest to 0 mm, NH is the next Gaussian curve out, CN next (18 ppm at the peak), and CH is the farthest out. The NO profile is from absorption measurements, fit to a curve.

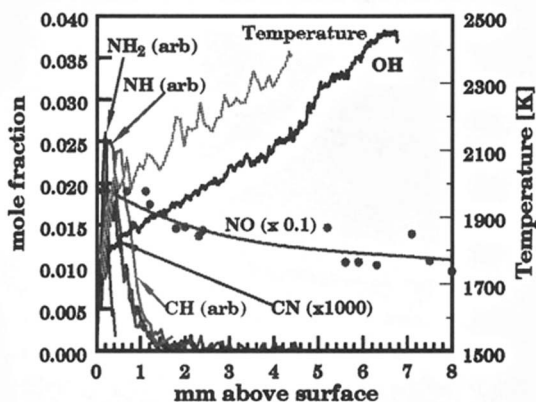


Fig. 10a PLIF measured species and temperature profiles for self-deflagration of HNF at 1 atm in air; also included are selected emission profiles (NH_2^* and CH^*).

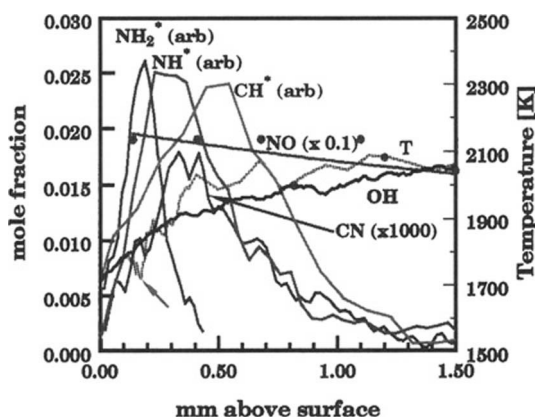


Fig. 10b Same as Fig. 10a, showing only the 0–1.5 mm region.

I. Diffusion Flame Studies via Sandwiches

An actual rocket propellant consists of different materials held together in a binder. Figure 11 is a schematic of a propellant, showing diffusion flames between the decomposition gases of the oxidizer AP with fuel from binder decomposition products. Understanding the interaction between ingredients and diffusion flame structure is important for understanding the effects of particle size on propellant ballistic properties. For example, most AP-based propellants are thought to have diffusion flames between the AP and fuel decomposition products, and such propellants show particle size effects on ballistic properties.^{34,35} Changing the AP particle size in AP composite propellants can lead to nearly a factor of eight change in burn rate. The smallest particles lead to the highest burn rate because the hot primary diffusion flame between AP and fuel dominates the heat feedback to the AP and leads to a high regression rate. Large AP particles experience heat feedback mostly from the cooler AP monopropellant flame, leading to a lower burning rate.³⁸ Much work has already been done in understanding the nature of the propellant diffusion flame structure of AP-based formulations.^{8,36–38}

One method for studying the interaction between ingredients is to use sandwiches^{2,3,8,36–38} consisting of planes or slabs of two ingredients in close contact. This allows imaging of the diffusive flame structure from known geometries.

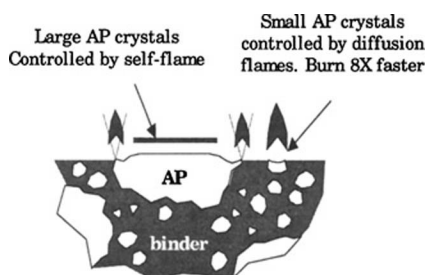


Fig. 11 Solid-propellant matrix.

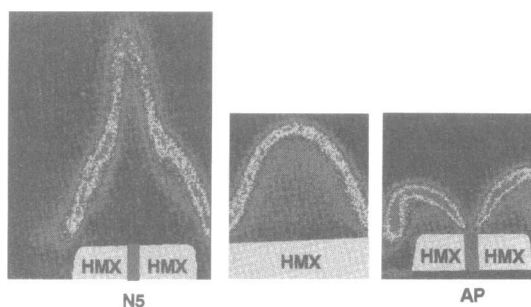


Fig. 12 CN PLIF image HMX/X/HMX sandwich flames, where $X = \text{N5}$ (left, 300- μm thick) and AP (right, 500- μm thick), compared with HMX alone. Sandwich samples were burning at 1 atm in N_2 , and the HMX (middle) was in air.

The approach in our laboratory was to use PLIF to get a two-dimensional image of a particular species in the flame of a sandwich and to study the effects of lamina thickness, lamina type, and pressure on the flame structure. The kinetic delay to significant heat release can be seen by the length of the dark zone in these model propellants. If mixing occurs between the decomposition products of the oxidizer and fuel and the mixture reacts with fast kinetics, then the flame standoff will be short, and if the kinetics is slow, the standoff will be tall. By comparing these standoffs with the neat material one can judge whether there is any positive diffusion flame interaction between the ingredients that might lead to a particle size control of ballistics.

Extensive measurements have been made in our laboratory^{2,3,8,11,12,19,27} of diffusion flame structures of nitramines (HMX, RDX, TNAZ), ADN, HNF, and AP composite sandwich solid propellants. Recent work^{3,19,27} done with AP has shown clear diffusion flames that have persisted at elevated pressures and are located close enough to the surface to supply significant heat feedback and, thereby, to affect burning rates.

The combination of HMX or TNAZ with AP led to obvious flame interactions³. The AP decomposition products accelerated the nitramine dark zone kinetics (see Fig. 12). Other oxidizers, however, even those that have significant excess oxygen, did not show such dramatic diffusion flame effects. For example, measurements were made on ADN/binder sandwiches, and quenched samples are shown in Fig. 13. It was observed that the ADN produced a melt and that the binder (even energetic binders such as N5, a propellant) retarded the combustion of ADN. PLIF imaging of CN radicals clearly showed weak diffusion flames (ADN has no

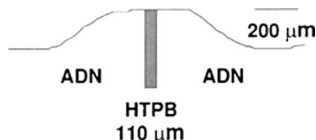


Fig. 13 Deradiatively quenched sandwich sample of ADN/HTPB showing clear evidence of significant melt of ADN; results were for laser-assisted combustion at 2 atm in N_2 .

C atoms and most of the binders had no N atoms, and so CN must have come from interactive chemistry). The diffusion flames were very far from the surface, unlike with AP. The NO_x oxidizer decomposition products of the ADN gave a tall dark zone. The diffusion flames were probably too far from the surface to provide significant heat feedback.

From this work, predictions were made that ADN-based formulations would have weak or no diffusion flame interaction between oxidizer and binder and, therefore, little or inverse particle size control over ballistic properties. This finding was recently corroborated through discussions with Russian scientists who have studied many ADN-based propellants.

Work done in our laboratory³ showed that HMX clearly has no diffusion flame with nonenergetic binders, which is not surprising because HMX and RDX are actually slightly fuel rich by themselves. Figure 12 shows examples: Even with an energetic binder such as N5, the HMX secondary flame sheet is lifted in the diffusive mixing layer, not shortened. In contrast, AP will even oxidize HMX, and rapid AP kinetics holds the flame on the interface region.

Diffusion flames between binder and HNF or AP will be discussed in some detail in the following subsections.

1. HNF Composite Flame Microstructure

PLIF measurements were made on the diffusion flame structure between HNF and various energetic and nonenergetic binders, including HTPB, wax, polyurethane, GAP, and BAMO/NMMO, in sandwich configurations.^{11,27} Unlike ADN, HNF entirely consumes even nonenergetic binders for low flux laser-supported deflagration at 0.1 MPa. ADN did not even consume energetic binders, at 1 MPa (10 atm), for a laser heating flux nearly nine times as large as for the HNF tests. Diffusion flames between the HNF and binder were clearly evident in the emission and PLIF imaging experiments, and these flames had much lower kinetic standoff distances than those seen with ADN sandwiches (Fig. 14).

The HNF and binder regression rate was highest in the interface region, where the diffusion flame heat and chemistry are located. This behavior is understandable: Neat HNF has a relatively hot reactive flame extremely close to the surface, whereas ADN has no visible flame. PLIF measurements of CN, NH, and OH were undertaken for the various binder combinations and binder length scales. These experiments were then extended to elevated pressure to determine if the diffusion flames seen are also important at higher pressures.

It was found that, as with ADN, as the pressure increases the burn rate of the HNF increases, and it starts to leave nonenergetic binders behind. For example, even at

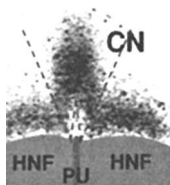


Fig. 14 CN PLIF image of diffusion flame at 1 atm in air between HNF (outer lamina) and polyurethane binder (center); PU is 190 μm thick.

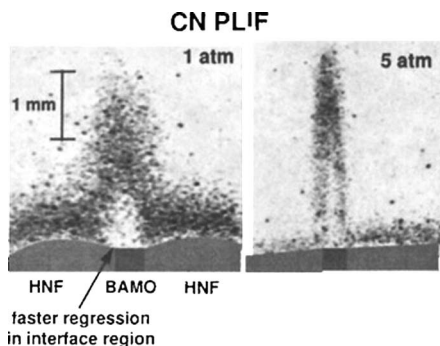


Fig. 15 CN PLIF from HNF/BAMO sandwiches at 1 atm in air (left) and 5 atm in N_2 , to the same scale.

0.1 MPa the HTPB lamina sticks up above the HNF. At 1 MPa, HTPB lamina of $200\ \mu\text{m}$ were recovered only charred. The PLIF images showed weaker diffusion flames at elevated pressures, and HTPB decomposition products (as monitored with the nonresonant portion of the PLIF signal) seemed to pass through the diffusion flame without being totally consumed. In addition, the diffusion flames were much farther from the surface than the hot HNF self-deflagration flame, which, as seen earlier, is very close to the surface. Therefore, the extra energy from the diffusion flame probably does not significantly increase the heat load on the surface.

When HNF was used with energetic binders, such as BAMO/NMMO, the binder was able to keep up with the increasing HNF regression rate at higher pressures, and obvious diffusion flames were seen even at elevated pressures. Figure 15 compares the flame structure of HNF/BAMO sandwiches at 0.094 and 0.51 MPa. Notice that, as per diffusion flame theory, the diffusion flame height is approximately independent of pressure, whereas the HNF flame height decreases dramatically. The diffusion flame height was much taller than the neat HNF flame height. Even in this case, therefore, the diffusion flame is probably not burn rate controlling, and any particle size controllability of HNF propellant ballistics will probably be much weaker than for AP.

HNF with either RDX or HMX as the outer lamina was also studied. Past work³ showed that ADN somewhat accelerated the HMX dark zone chemistry and shortened the HMX secondary flame, whereas AP greatly accelerated it. HNF had the same effect on both the RDX and HMX secondary flames and appeared closer to AP's effectiveness than ADN's. Apparently, the NH_3 decomposition products of ADN and HNF accelerate the slow NO reduction kinetics that are responsible for nitramine dark zones.

2. AP

Besides the experiments with other oxidizers, such as the HMX mentioned earlier, experiments of AP with fuels were also conducted.^{3,19,27} Burn rate controlling composite propellant diffusion flames were imaged at the microscale in AP-based formulations with binder lamina thicknesses down to $18\ \mu\text{m}$. PLIF was used to measure OH and OH rotational temperature and showed that the hot diffusion flame between AP and nonenergetic binders extended very close to the surface in the

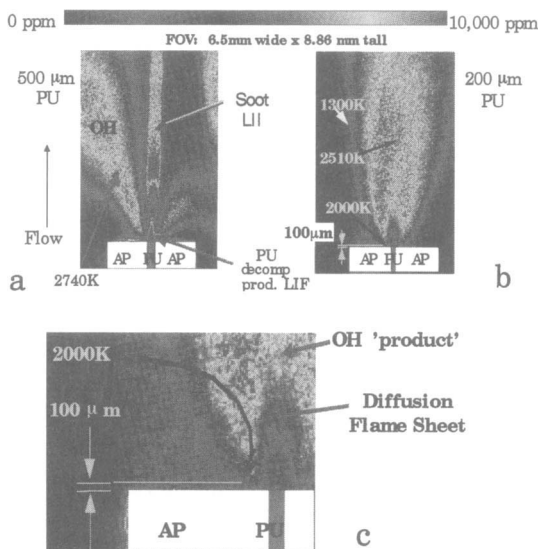


Fig. 16 OH PLIF signal from AP/PU sandwiches, a) 500 μm PU, b) 200 μm PU, c) blown-up version of Fig. 16b near the surface.

interface region, even at 0.1 MPa (2000 K at 100 μm). The measured flame structure and temperature followed expected diffusion flame theoretical dependencies on binder lamina thickness: the smaller the fuel lamina, the shorter the flame. The resulting diffusion flame height and temperature were found to be controlled by fuel flow rate (binder lamina thickness or, for differing binder compositions at constant thickness, binder pyrolysis rate). Binders studied¹⁹ included PU, polyester, HTPB, cellulose, BAMO, and GAP.

Figure 16a shows what happened when too much fuel was used. There are several signals annotated in Fig. 16. The central bar centered over the PU lamina is soot laser-induced incandescence (LII) and is a quantitative measure of soot volume fraction. If the camera is delayed by a few tens of nanoseconds so as to discriminate against LIF emission, all that is left in Fig. 16a is the central LII signal. This LII signal, absent for lamina sizes of 200 μm and below, shows that the higher fuel concentration (wider lamina) causes soot breakthrough in the flame. The tiny triangle sitting directly on the PU surface is the PLIF signal from PU decomposition products: It does not go away when tuning the laser frequency away from the OH resonance (tuning off resonance), but does disappear when the camera gate is delayed, showing that it is not LII. The dark region between the triangle and soot LII is the diffusion flame sheet. The dark region was imaged using a CH and/or C₂ PLIF as discussed later. All of the signal to the right of the centerline, that is, downstream with respect to the diagnostic laser sheet propagation, was affected by absorption in the central soot plume and is spurious.

The fan signal to the left is OH, verified by tuning off resonance, and emanates from the interfacial region. The OH concentration falls off toward the centerline because the flame is rich there. Radial OH rotational temperature profiles peak slightly off the centerline and decrease as radial distance increases into the leaner

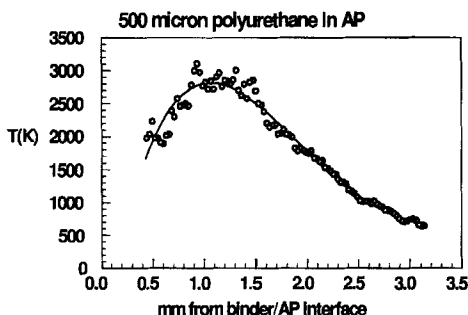


Fig. 17a Radial (horizontal) profile of OH rotational temperature taken 4.1 mm above the surface of the sandwich for the 500- μm PU lamina AP sandwich of Fig. 16a.

portion of the flame or decreases toward the rich side, as seen in Fig. 17a. The abscissa in Fig. 17a is the distance out from the AP/PU interface.

The temperature just beyond 0.5 mm is about 2000 K and rapidly rises to about 2750 K at larger horizontal distance, where the flame is closer to stoichiometric. This is only about 100 K above the maximum adiabatic temperature obtainable from AP/PU (2654 K), but the system is not adiabatic; there is extra heat input from the CO_2 laser. At larger horizontal distances (larger radial distances if the system were cylindrically symmetric instead of planar), the temperature slowly drops as the flame gets leaner due to the presence of more AP and less PU decomposition products. The temperature drops off to below 1000 K in the leanest part of the flame. The temperature here is actually below the adiabatic flame temperature of AP due to heat loss and mixing of external cold air. The temperature above the AP away from the binder was found to be above the adiabatic AP flame temperature (1690 vs 1377 K). This higher temperature could be due to the extra energy from the laser heating flux, heat transfer from the nearby hot diffusion flame, or long distance mass diffusion of a small amount of fuel into the region, which, when reacting with the AP products, would add substantial energy.

Figure 16b shows a quantitative OH radical PLIF image for a 200- μm PU lamina during laser-supported deflagration at 0.094 MPa. OH is both a flame radical

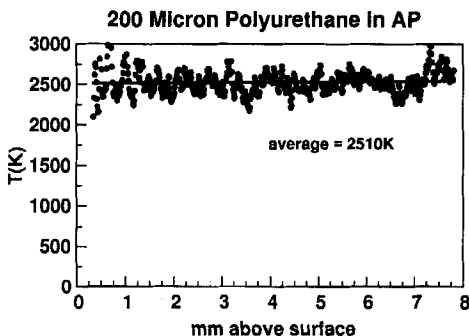


Fig. 17b Axial (vertical) slice profile of OH rotational temperature for AP/200- μm PU/AP sandwich flame.

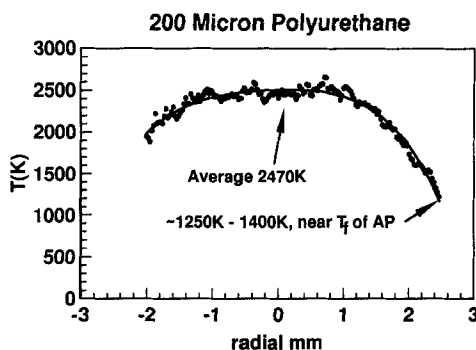


Fig. 17c Radial (horizontal) OH rotational temperature profile taken at 4.1 mm above the surface for the AP/(200- μ m PU)/AP sandwich.

and a product, and its concentration typically peaks on the downstream side of the flamesheet. Even so, the PLIF images show the flame very close to the surface. Analysis of the OH rotational temperature showed that the hot diffusion flame is already 2000 K only 100 μ m from the surface near the binder-AP interface (enlargement in Fig. 16c). If this flame standoff is kinetically controlled, then at realistic rocket motor pressures (7 MPa) it would be on the order of only one-tenth of 1 μ m or 100 nm. It is clear that such a hot diffusion flame so close to the interfacial region would be burn rate controlling and that this is the reason AP composite propellants have such a strong burning rate AP particle size correlation.

Figure 16b shows that for a thinner lamina the flame is shorter and the soot does not break through (no soot LII signal is seen). The OH closes over the binder lamina, and the peak temperature in this region is 2510 K (slightly below the maximum adiabatic AP/PU adiabatic flame temperature of 2654 K). Figure 17b shows the remarkably constant nature of the centerline axial temperature profile for this case. Figure 17c shows a radial, that is, horizontal, temperature profile slice taken at a height of 4.1 mm from the sandwich surface. The abscissa in Fig. 17c is distance from the centerline of the binder lamina, not distance from the interface region. The center of the flame is at a constant temperature (no drop toward the centerline as in Fig. 16a). The OH concentration found in this region (about 1% mole fraction) is below the thermodynamically calculated adiabatic OH concentration of 2.4%. There are two possible explanations for this. First, the temperature is below adiabatic and so the OH concentration would be expected to drop. Second, the OH concentration was calculated by comparison of OH radical PLIF signal strengths with a known OH signal level in an RDX flame. This could be inaccurate for these AP sandwiches because the quenching rate for OH could be substantially higher in AP flames (with high concentrations of polar molecules such as HCl) than in RDX flames. Although the transition is saturated the higher quenching rate could lower the apparent OH concentration. Note in Figs. 16a and 16b, and the corresponding Figs. 17a and 17b that in the outside regions of the flame the OH signal drops and the temperature drops to below 1300 K.

Thinner fuel lamina produced shorter, and at the thinnest dimensions, cooler diffusion flames. For the thin lamina, the contour OH radical PLIF signal around the outside edge of the flame extended down to the AP surface and was nascent OH from the AP self-degradation. The temperature for this region (1690 K, measured

Chapter 2.6

Thermal Decomposition and Combustion of GAP/AN/Nitrate Ester Propellants

Xiao-Bin Zhao,* Lin-Fa Hou,[†] and Xiao-Ping Zhang[‡]*Red-Star Institute of Chemistry, Xiangfen, Hubei, People's Republic of China*

Nomenclature

- E = apparent activation energy
 H = heat release
 K = rate constant
 T_p = peak temperature
 Z = preexponential factor
 β = heating rate

I. Introduction

HIGH energy, low signal, low vulnerability, and low pollution are the current trends in the development of solid propellants.^{1,2} Ammonium perchlorate (AP)/hydroxy terminated polybutadiene (HTPB) propellants, in spite of their broad applications, give rise to toxic hydrogen chloride as part of the combustion products and as such do not meet the requirement of low emission and low pollution. Nitrate ester plasticized polyether (NEPE) propellants and nitramine [cyclotetramethylene tetranitramine (HMX), cyclotrimethylene trinitramine (RDX)] propellants have attained the goal of high energy and reduced smoke or smokelessness, but they have a danger of explosion under intense impact and their safety level is unsatisfactory.

Glycidyl azide polymer (GAP) is a novel energetic binder with positive formation heat (957 kJ/mol) and higher density (1.3 g/cm³). Ammonium nitrate (AN), once applied in the first generation of composite solid propellants, has a series of advantages, such as insensitivity, low signal, easy availability, and low environmental impact. The development of phase stabilized AN has solved the crystal

Copyright © 1999 by the authors. Published by the American Institute of Aeronautics and Astronautics, Inc., with permission.

*Assistant Engineer.

[†]Professor, Director of Science and Technology Council.

[‡]Professor.

transformation problem and avoids volume change resulting from storage temperature. GAP/AN propellant has potential value as a low-cost and low-signal propellant for the next century. Researchers in many countries have investigated GAP/AN propellant, and there has been great progress in many respects. Lessard³ studied GAP/AN propellants plasticized with bisdinitro propylformal/acetal (BDNPF/A).³ The burning rate is 5.2 mm/s at 6.89 MPa and the pressure exponent is 0.63 in the pressure range of 6.89–27.56 MPa. The formulation, including a ballistic modifier, shows a burning rate of 8 mm/s and a pressure exponent of around 0.5. Oyumi studied GAP/AN/nitrocellulose (NC)/trimethylolethane trinitrate (TMETN) low-signal propellants.⁴ NC can provide a high burning rate and low-pressure exponent (about 0.5). CuC and B are very effective as ballistic modifiers, and the combined catalysts are not effective in increasing the burning rate but are effective in decreasing the pressure exponent. Menke⁵ and Weister⁶ investigated the burning-rate characteristics and flame structure of GAP/AN propellants containing different phase stabilizers. The molybdenum/vanadium oxides (MOVO) catalyst proves to be effective for GAP/AN formulations; the burning rate is 7–8 mm/s at 7 MPa and the pressure exponent is 0.50–0.58 (2–20 MPa).

Although GAP/AN propellants have been studied widely, the disadvantages of low burning rate and high-pressure exponent have not yet been resolved, and they become prominent with the introduction of nitrate ester plasticizers. The object of this work is to elucidate the essence of the low burning rate and high-pressure exponent of GAP/AN propellants by means of thermal analysis and modern combustion diagnosis techniques. GAP/AN propellants combined with large doses of nitrate ester plasticizer 1,2,4-butanetriol trinitrate (BTTN), nitroglycerine (NG) were found to achieve a specific impulse of 250 s (70:1, 5%Al) and have good combustion properties with burning-rate modifier transition metal oxide (MO).

II. Experimental Methods

Differential scanning calorimetry and thermogravimetry (TG) experiments were carried out using DSC910S and TGA2950 analyzers. Samples weighing about 1 mg were heated from 30 to 1000°C at a varied heating rate from 5 to 40°C/min in a nitrogen atmosphere. In the TG experiments, two kinds of sample cells made of aluminum and aluminum oxide were used for tests below and above 500°C, respectively. The mass ratio of GAP to mixed nitrate ester (NG/BTTN) (MNE) is 1:2 in the mixtures including GAP and MNE, and the mass fraction of MO is 0.1 in all mixtures including MO.

The compositions of the GAP/AN propellants are listed in Table 1. Phase stabilized ammonium nitrate (PSAN) containing 3.0% NiO is used as phase stabilizer. The molecular weight of GAP is about 3000, and MO is the burning-rate modifier. Propellant ingredients were mixed in a vertical planetary mixer under vacuum and cured at 50°C for five days. Samples of 4 × 4 × 100 mm were prepared for GAP/MNE/AN propellants. The burning rate of propellants was measured in the pressure range of 2.94–8.83 MPa by means of sound emission methods in a nitrogen atmosphere. The burning-rate pressure exponent was calculated with Vieille's equation (see Ref. 7).

Propellant samples were installed on the ignition shelf of a transparent combustion chamber with four-way optical access, which was pressurized with nitrogen to a certain pressure. The samples were ignited from the top with Ni–Cr alloy wire

Table 1 Formulations of GAP/AN propellant (by weight)

Number	GAP	PSAN	BG	Al	AP	MO
ZXB-52	25.0	70.0	0.0	5.0	0	0
ZXB-54	8.30	70.0	16.7	5.0	0	0
ZXB-88	10.0	65.0	20.0	5.0	0	0
ZXB-91	10.0	35.0	20.0	5.0	30	0
ZXB-106	15.0	65.0	15.0	5.0	0	0
ZXB-110	15.0	61.0	15.0	5.0	0	4.0

by 20-V direct current. An oscilloscope was used to record the output signal of the thermocouple, which can be converted to the temperature profile of the combustion wave. The flame structure was photographed by a camera. Experimental methods are discussed in detail in a previous publication.⁸

III. Discussion of Results

A. Thermal Decomposition of AN and MNE

The DSC experiment results, such as peak temperature of decomposition and heat release derived from the DSC curves in which temperature and heat vary with time at different pressures, are listed in Table 2. The decomposition of AN is endothermic at 0.1 MPa and transforms to exothermic with an increase in pressure because of the thermal decomposition characteristics of AN. The decomposition mechanisms of AN have been investigated widely. It is generally agreed that thermal decomposition is initiated by proton transfer.^{9,10} Ionic reaction and free radical reaction mechanisms have recently been advocated.^{11,12} Many possible mechanisms arise because the thermolysis of AN depends greatly on the experimental conditions, including pressure, temperature, state of confinement, and heating rate.

The authors are inclined to favor the proton transfer mechanism of AN decomposition. According to the proton transfer mechanism, AN first decomposes to form nitric acid and ammonia, which are adsorbed on the surface of AN crystal. Subsequently, ammonia and nitric acid desorb from the surface and enter the gas

Table 2 Thermal decomposition behaviors of ingredients (10°C/min)

Sample	0.1 MPa		3 MPa		7 MPa	
	T_p , °C	H , J/g	T_p , °C	H , J/g	T_p , °C	H , J/g
GAP	248.4	2696	251.8	2948	255.9	2600
GAP/MO	230.3	2322	230.8	2664	230.8	2308
GAP/MNE	203.0 ^a /233.3 ^b	1789	204.9/220.1	2541	204.2/220.8	3934
GAP/MNE/MO	202.8 ^a /217.9 ^b	2662	203.6/218.6	2211	203.0/218.9	3823
PSAN	260.7	-1395	323.2	746	323.0	1795
PSAN/MO	234.6	1018	331.2	3563	314.3	4942

^aPeak temperature of MNE. ^bPeak temperature of GAP.

phase at a rate attributed to the ambient pressure.⁹ Ammonia and nitric acid readily desorb and diffuse to the gas phase at low pressure, and the gas products that take further part in the chemical reaction are very minute, so that the heat release can be omitted. The chemical reactions are secondary, and the dissociation of AN is dominant. Simultaneously, solid-state AN sublimates to form gas-state AN.

Both the sublimation and the dissociation require a large amount of heat, which leads to the endothermic nature of AN decomposition at low pressure. The adsorption of ammonia and nitric acid on the surface of AN crystal is a physical adsorption, and the adsorption content is related to temperature and pressure according to the adsorption law. At a given temperature, the adsorption content will be increased as pressure increases until an adsorption balance is set up and the adsorption content is equal to the desorption content at any time. The products of the desorption from the AN crystal surface diffuse to the gas phase, but the diffusion rate is very slow at high pressure. Most of the products desorbed stay near the surface of AN crystal, so that the concentration of gas products will be increased near the AN crystal surface as pressure increases. Nitric acid is not stable and readily decomposes to form nitrogen oxides that can react with ammonia to release significant heat, which in turn leads to the exothermic chemical reaction at high pressure. The heat release is increased drastically with pressure increases.

Pressure also intensely influences the heat release of MNE decomposition, but the peak temperature remains almost unchanged (Table 2). The heat release of GAP/MNE mixtures at 7 MPa is nearly twice that at 3 MPa. However, the mass fraction of GAP is only 0.33 in the GAP/MNE mixtures, and the heat release of GAP is almost the same at different pressures, that is, the heat release of MNE decomposition increases significantly with pressure. This result can be explained by the different decomposition mechanisms of MNE. A little MNE decomposes at low pressure and decomposition progresses slowly with a unimolecular reaction; a large amount of MNE volatilizes, which leads to the endothermic nature of MNE decomposition at low pressure. There is a big endothermic peak in the DSC curve for pure MNE at 0.1 MPa (Ref. 7). At high pressure, however, the decomposition products have full contact with MNE, and the decomposition mechanism transforms from a unimolecular reaction to an autocatalytic reaction. The decomposition products, such as NO_2 , have a strong autocatalytic effect on the decomposition of MNE, the decomposition rate increases violently, and the heat release increases drastically.¹³ Thus, the heat release increase of MNE decomposition is more sensitive to pressure at high pressure. MNE has a negative contribution to the burning-rate increase at low pressure (<5 MPa), but at high pressure (>5 MPa) it has a significant contribution to the burning-rate increase, according to the burning-rate data, which results in an increase of the pressure exponent to a certain extent. It is almost certain that the pressure exponent of the propellant will rise significantly with the introduction of nitrate ester MNE, according to our results. Therefore, the propellant should involve the least possible nitrate ester to meet the energy requirements, or it will be difficult to decrease the burning-rate pressure exponent.

B. Thermal Decomposition Kinetics of GAP and PSAN

Thermal decomposition kinetics of GAP and PSAN were studied by means of differential thermogravimetric data at different heating rates. A plot of $\ln(\beta/T_p^2)$ vs $1/T_p$ was made, according to the Kissinger equation (see Ref. 14). Through a

Table 3 Thermal decomposition kinetics of GAP and PSAN

Parameters	GAP	GAP/MO	PSAN	PSAN/MO
Heating rate, °C/min				
5	505.40	485.53	497.70	462.27
10	513.92	495.52	510.17	467.85
20	524.11	505.96	521.50	472.94
30	531.90	514.72	527.31	477.12
40	543.48	524.13	532.39	491.60
E, kJ/mol	117.99 ^a	108.78	124.54	124.61
	120.37 ^b	111.42	126.43	125.63
Z, min ⁻¹ × 10 ¹²	0.5082	0.1515	3.4130	58.480
K, min ⁻¹ (500 K)	0.2392	0.6543	0.3328	5.6000

^aKissinger's method. ^bOzawa's method.

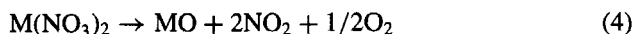
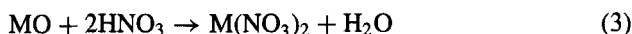
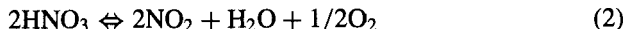
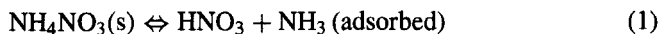
curve fit, the activation energy E and preexponential factor Z can be calculated, and the rate constant K can be obtained from the Arrhenius equation. The activation energies were also calculated according to Ozawa's method, which are a little greater than those derived from Kissinger's method and in agreement with Ref. 7. The thermal decomposition kinetics parameters of GAP and PSAN are given in Table 3. The activation energy of GAP is relatively lower than the values in the literature, but the reason for this is still unknown at present. The decomposition rate of PSAN at 500 K increased 15.7 times with the burning-rate modifier MO and 1.7 times for GAP. The activation energy of PSAN decomposition remains unchanged, indicating that the decomposition mechanism of PSAN with or without the burning-rate modifier MO is the same. The increase in the preexponential factor reveals an increase in the collision probability, which leads to a decomposition rate increase for AN. The burning-rate modifier MO mainly catalyzed the decomposition of AN in the combustion of GAP/AN propellants, according to the kinetics results. The mechanism by which MO acts will be more fully considered hereafter.

C. Mechanism of MO Catalyzing Decomposition of AN

The decomposition rates of GAP and PSAN at 500 K are increased 1.7 and 15.7 times, respectively, by the addition of the burning-rate modifier MO. Furthermore, the decomposition of PSAN changes from endothermic to exothermic at 0.1 MPa, and the heat release of PSAN is increased significantly as compared with PSAN without MO, especially at low pressure. The thermal decomposition of PSAN, AN, PSAN/MO, and AN/MO were studied by means of TG experiments to explore the mechanism by which MO acts. In the TG experiments, thermal decomposition of PSAN was found to have two stages, and the weight loss of the second stage, as calculated from the initial and final weight fractions, is the same as that of nitrate nickel when it decomposes to form NiO. Therefore, it is thought that the second-stage weight loss of PSAN may be attributed to the decomposition of nitrate nickel, that is, NiO reacts with other products to form nitrate nickel in the decomposition of PSAN. The thermal decomposition of PSAN/MO mixtures has three stages, indicating that MO causes a third weight loss. MO, however, is metal oxide and does not lose weight itself, so that it may be that MO reacts with the decomposition products of PSAN and forms a new substance that decomposes again, leading to a

third-stage weight loss. Decomposition of common AN has only one stage, and the weight loss is almost 100%, which demonstrates that the second-stage weight loss of PSAN is due to the decomposition of nitrate nickel. Thermal decomposition of AN/MO mixtures has two stages, so that we can conclude that the second-stage decomposition of AN/MO is initiated by MO. There are surely chemical reactions between NiO or MO and AN, according to the results of TG experiments, and perhaps the chemical reactions of MO and AN promote the decomposition of AN.

AN first decomposes to form nitric acid and ammonia, on the basis of the proton transfer mechanism, and then nitric acid further decomposes to form nitrogen oxides. The two reactions are reversible, that is, AN and nitric acid can be reformed by the decomposition products. Nitrate nickel is formed in the decomposition of PSAN, and it is thought that the phase stabilizer NiO reacts with nitric acid. MO is also a metal oxide, and it is possible that MO reacts with nitric acid in the decomposition of AN. The weight loss of all stages of PSAN or AN were calculated, and the values calculated are close to theoretical values, which reveals that MO has the same reaction mechanism as NiO. Thus, the burning-rate modifier MO first reacts with nitric acid to form nitrate salt, and then nitrate salt decomposes to form a metal oxide, which promotes the proton transfer reaction and increases the decomposition rate of AN. The mechanism of MO's actions is represented by reactions (1–4). According to these mechanisms, MO promotes the proton transfer reaction of AN and consequently increases the burning rate of GAP/AN propellant:



D. Temperature Profile of Combustion Wave

The temperature profile of the combustion wave is an important indicator of the combustion mechanism of the propellant. The burning-rate pressure exponent of GAP/AN propellant rose drastically from 0.69 to 0.91 with the introduction of 16.7% MNE substituting for GAP,⁸ and so it was thought that there should be a significant difference for the two temperature profiles of the combustion wave. The results indicate that there is a dark zone (isothermic zone) in the combustion wave of GAP/AN propellant (Fig. 1), and the thickness of the dark zone increases

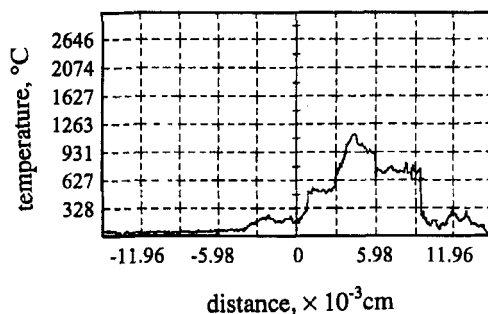


Fig. 1 Temperature profile of combustion wave of ZXB-52 (5 MPa).

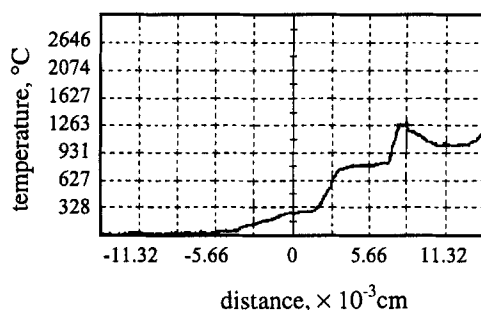


Fig. 2 Temperature profile of combustion wave of ZXB-54 (5 MPa).

significantly with the introduction of MNE for GAP/MNE/AN propellant (Fig. 2). This indicates that the mechanism by which the dark zone is enhanced is related to the introduction of MNE. The burning rate was decreased and the pressure exponent was increased due to the enhancement of the dark zone. For instance, the burning rate and pressure exponent of GAP/AN propellant is 2.99 mm/s (5 MPa) and 0.69 (2.94–8.83 MPa), respectively. They are 2.83 mm/s and 0.91 for GAP/MNE/AN propellant under the same conditions. The relationship between the thickness of the dark zone and the burning-rate characteristics of GAP/AN propellant is listed in Table 4; the thinner the dark zone, the higher the burning rate, and the lower the pressure exponent. The dark zone disappears for GAP/MNE/AN propellant including 30% AP, and it has the highest burning rate and the lowest pressure exponent among the four formulations.⁸ The presence and the thickness of the dark zone are the major factors of influence on the burning-rate characteristics of GAP/MNE/AN propellants. The heat feedback of the gas phase to the burning surface is inhibited due to the presence of the dark zone, and the thickness of the dark zone is closely related to pressure. The dark zone becomes thinner as the pressure increases, which increases the heat feedback of gas phase to the burning surface, and the burning rate is increased. Thus, we can improve the combustion properties of GAP/MNE/AN propellant through regulation of the thickness of the dark zone.

E. Flame Structure

Flame structure is another important indicator of the combustion mechanisms. The length and intensity of the flame, the dark zone and its thickness, and the

Table 4 Relationship between thickness of the dark zone and burning rate characteristics

Characteristic	Sample			
	ZXB-52	ZXB-54	ZXB-88	ZXB-91
Dark zone thickness, μm	22.4	39.5	31.0	0
Burning rate, mm/s (5 MPa)	2.99	2.83	2.30	5.47
Pressure exponent (2.94–8.83 MPa)	0.69	0.91	0.88	0.63



Fig. 3 Flame structure of ZXB-106 (5 MPa).

morphology of the burning surface can be observed from the flame pictures. This is a more direct method of studying the combustion mechanisms of the propellant than temperature profiles of the combustion wave. Figure 3 shows the flame structure of GAP/MNE/AN propellant without any burning-rate modifier. Aluminum particles splash in all directions, and the propellant combusts unstably. The flame is not continuous and not extremely regular, and the length is shorter. There are also some large granular lumps in the flame, indicating that the propellant does not combust fully. The igniter wire was not melted, and plenty of smoke was observed around the flame. There is partial quenching on the combustion surface, which was also found in the static burning-rate testing. Owing to the low combustion temperature and slow decomposition reaction rate of the condensed phase, there is not enough combustible gas mixture to form a gas-phase flame, which results in a partial quenching phenomenon. The phenomenon is called oscillatory combustion, and during the process, the equilibrium of gas content consumed and produced is destroyed.¹⁵ A dark zone is not observed, due to the unstable combustion in the flame structure of GAP/MNE/AN propellant, but there should be a very thick dark zone according to the temperature profile of the combustion wave. The burning rate

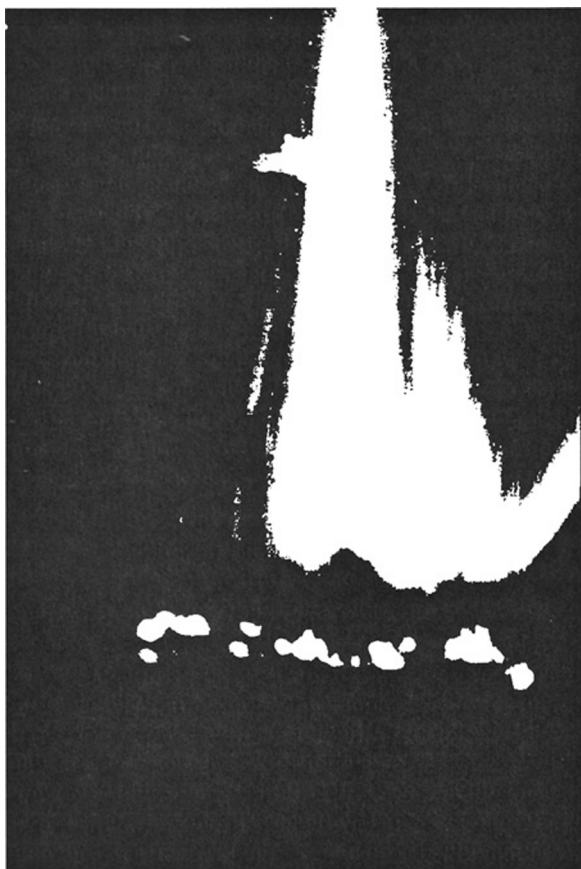


Fig. 4 Flame structure of ZXB-110 (5 MPa).

of GAP/MNE/AN propellant is 4.45 mm/s at 6.86 MPa and the pressure exponent is 0.88 in the pressure range of 2.94–8.83 MPa, respectively.

The flame structure in Fig. 4 is significantly different from that in Fig. 3. In Fig. 4 the flame length increases, and there is no partial quenching. The GAP/MNE/AN propellants containing MO combust stably, and the flame leaves the burning surface to form a distinct dark zone. The flame is very bright, and the igniter wire is melted; the splash of the aluminum is not observed. The burning-rate modifier MO eliminated the oscillatory combustion phenomenon, the combustion efficiency of aluminum particles was increased, and propellant combusted fully. It improves the energy release of the propellant. There is a melt layer under the dark zone that is composed of AN and melted aluminum particles, indicating that the temperature of the burning surface is rising. Dong and Wang found that the near-surface temperature gradient has a strong effect on the burning-rate characteristics of propellants.¹⁶ As the temperature gradient in the near-surface zone rises, the burning rate of the propellant will be increased significantly. In the meantime, the sensitivities of the burning rate to pressure will be decreased, which leads to a decrease in the

Table 5 Heat release of PSAN and PSAN/MO at different pressures, J/g

Sample	0.1 MPa	1 MPa	3 MPa	5 MPa	7 MPa
PSAN	-1395	296	746	1391	1795
PSAN/MO	1018	1927	3563	4040	4942
(PSAN/MO-PSAN)/ PSAN	—	5.51	3.78	1.90	1.75

burning-rate pressure exponent. Dong and Wang had already proven this by means of simulating heat source experiments. We already know that the burning-rate modifier MO speeds up mainly the decomposition of AN in the combustion of GAP/MNE/AN propellant. In the presence of MO, the severe exothermic nature of AN increases the temperature of the burning surface and decreases the thickness of the dark zone, which results in a burning rate increase. It is in accordance with the increase in heat release of AN/MO mixtures at different pressures that the heat release of AN/MO mixtures is far bigger than that of AN at a given pressure (Table 5). The proportional increase is different, however, with a greater increase at low pressure than at high pressure. The heat release increase at low pressure makes a greater contribution to the burning-rate increase than that at high pressure. The enhancement of the burning rate at low pressure is far greater than that at high pressure because the burning-rate modifier MO intensely influences the decomposition of AN at low pressure, and, therefore, the burning-rate pressure exponent is decreased. The burning rate and the pressure exponent of GAP/MNE/AN propellants are 12.7 mm/s (6.86 MPa) and 0.60 (2.94–8.83 MPa), respectively.

F. Correlation of Thermal Decomposition and Burning-Rate Characteristics

In selecting the effective burning-rate modifier by means of thermal analysis, it was found that the burning rates of propellants were closely related to the exothermic peak temperature of AN. To some extent, the lower the exothermic peak temperature of AN is, the higher the burning rate of GAP/MNE/AN propellants. The burning rates of GAP/MNE/AN propellants, including different modifiers, vs

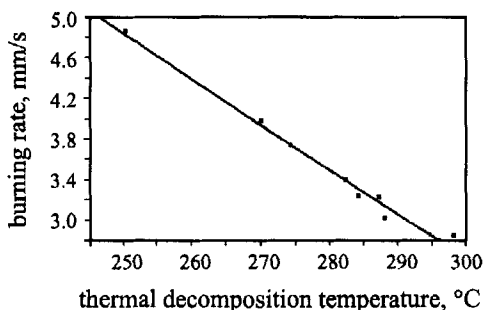


Fig. 5 Relation of AN exothermic peak temperature and burning rate of GAP/MNE/AN propellants.

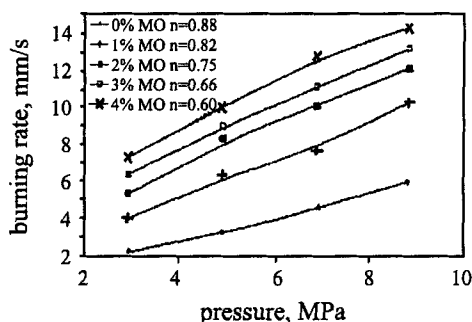


Fig. 6 Influence of MO content on burning rate of GAP/MNE/AN propellants.

the exothermic peak temperature of AN containing the same modifiers are plotted in Fig. 5. The plot shows a good linear curve, indicating that the burning rate of GAP/MNE/AN propellant is closely correlated with the exothermic peak temperature of AN. It is determined by the AN contents and characteristics. AN is the main ingredient of GAP/AN propellant and the mass fraction is 0.7 or bigger, and so the burning-rate characteristics of GAP/AN propellant are largely determined by AN. AN's endotherm of crystal transformation and melt leads to a low burning rate of GAP/AN propellant. There is a degradation of 54°C in the differential thermal analysis curve for the exothermic peak temperature of AN containing MO, which is also most effective at increasing the burning rate of GAP/MNE/AN propellants. The change in exothermic peak temperature of a major ingredient before and after adding the modifier as determined by thermal analysis is used as a criterion for selecting an effective burning-rate modifier.

The influence of MO content on the burning rate of GAP/MNE/AN propellants is shown in Fig. 6. MO not only increased the burning rate drastically, but also decreased the pressure exponent of GAP/MNE/AN propellants from 0.88 to 0.60.

IV. Conclusions

The decomposition of AN and MNE is sensitive to pressure, which leads to a high burning-rate pressure exponent for GAP/MNE/AN propellants. The burning-rate modifier MO can intensely influence the decomposition of AN at low pressure and has some effect on GAP, but does not affect MNE.

There is a dark zone in the combustion wave structure that can significantly influence the burning rate characteristics of GAP/MNE/AN propellants. The thickness of the dark zone is increased with an increase in MNE content. The dark zone does not help increase the burning rate, nor does it decrease the pressure exponent.

The burning-rate modifier MO promotes the decomposition of the condensed phase and increases the heat release of AN while decreasing the thickness of the dark zone and enhancing the heat feedback of the gas phase to the burning surface, which in turn raises the burning rate and decreases the pressure exponent.

The exothermic decomposition peak temperature of AN is closely related to the burning rate of GAP/MNE/AN propellants. The lower the exothermic peak temperature of AN, the higher the burning rate of the propellants, and so the exothermic temperature may serve as a criterion for selecting effective burning-rate modifiers for GAP/MNE/AN propellants.

Acknowledgments

The authors would like to thank Ziru Liu, Cuimei Yin, Yang Luo, Ying Wang, Zhihua Sun, Fengqi Zhao, and Chao Yuan for their support in this project.

References

- ¹Araujo, L., "Thermochemical Characteristics of AN/AP Based Composite Propellants," *25th International Annual Conference of ICT*, Institut Chemische Technologie, Karlsruhe, Germany, 1994, pp. 51-1-51-11.
- ²Li, D.-H., "Dramatic Low Vulnerable Explosive," *Initiators and Pyrotechnics*, No. 5, 1993, pp. 12-15 (in Chinese).
- ³Lessard, P., "Development of a Minimum Smoke Propellant Based on GAP and AN," CP-511, AGARD, May 1991.
- ⁴Oyumi, Y., "Insensitive Munitions (IM) and Combustion Characteristics of GAP/AN Propellants," *Propellants, Explosives, Pyrotechnics*, Vol. 21, No. 5, 1996, pp. 271-275.
- ⁵Menke, K., "Characteristic Properties of GAP/AN Propellants," *Propellants, Explosives, Pyrotechnics*, Vol. 21, No. 3, 1996, pp. 139-145.
- ⁶Weister, V., "Spektroskopische und pyrometrische Untersuchungen des Abbrandverhaltens von AN/GAP-Mischungen mit verschiedenen Phasenstabilisatoren," *25th International Annual Conference of ICT*, Institut Chemische Technologie, Karlsruhe, Germany, 1994, pp. 25-1-25-15.
- ⁷Zhang, R., "Combustion and Catalysis of Solid Propellant," National Univ. of Defense Technology Publishing House, Changsha, PRC, 1992 (in Chinese).
- ⁸Zhao, X.-B., "Study of Application Base of Azide Propellants," M.S. Thesis, Red-Star Inst. of Chemistry, Xiangfan, Hubei; PRC, 1998 (in Chinese).
- ⁹Thomas, P. R., "Thermal Decomposition of Energetic Materials 31-Fast Thermolysis of Ammonium Nitrate, Ethylene Diammonium Dinitrate and Hydrazinium Nitrate and the Relationship to the Burning Rate," *Combustion and Flame*, Vol. 76, No. 7, 1989, pp. 393-401.
- ¹⁰Dilip, G. P., "Thermal Decomposition of Energetic Materials 56. On the Fast Thermolysis Mechanism of Ammonium Nitrate and Its Mixtures with Magnesium and Carbon," *Propellants, Explosives, Pyrotechnics*, Vol. 17, 1992, pp. 99-105.
- ¹¹Brower, K. R., "Evidence for Homolytic Decomposition of Ammonium Nitrate at High Temperature," *Journal of Physical Chemistry*, Vol. 93, No. 10, 1989, pp. 4029-4033.
- ¹²Jimmie, C. O., "Thermal Stability and Compatibility of Ammonium Nitrate Explosives on a Small and Large Scale," *Thermochimica Acta*, Vol. 212, 1992, pp. 77-85.
- ¹³Peng, P.-G., "Properties and Principles of Solid Propellants," National Univ. of Defense Technology Publishing House, Changsha, PRC, 1992 (in Chinese).
- ¹⁴Krishnan, K., "Kinetics of Decomposition of Nitramine Propellant by Differential Scanning Calorimetry," *Defense Science Journal*, Vol. 42, No. 3, 1992, pp. 135-139.
- ¹⁵Wang, Y.-S., "Ignition Characteristic of Low Pollution GAP/AN/AP Propellants at Low Pressure," *Winged Missiles Journal*, No. 11, 1996, pp. 44-49 (in Chinese).
- ¹⁶Dong, C.-S., and Wang, Y., "Study of the Combustion Wave Structure of Solid Propellants with W-Re Microthermocouple Measuring Temperature Technique," *Explosives and Propellants*, No. 2, 1995, pp. 22-26 (in Chinese).

Chapter 2.7

Thermal Decomposition of Potassium Dinitramide at Elevated Pressure

Cuimei Yin,^{*} Ziru Liu,[†] Yanghui Kong,[†] Fengqi Zhao,[‡] Yuan Wang,^{*}
 Ming Lei,[§] Yang Luo,[§] Pei Zhang,[§] Yinghui Shao,^{*} and Shangwen Li[¶]
Xi'an Modern Chemistry Research Institute, Xi'an, People's Republic of China

Nomenclature

A_1, A_2	= preexponent factor of Arrhenius equation for decomposition of potassium dinitramide (KDN), 1/s
E_B	= K^+ electron-binding energy, eV
E_1, E_2	= apparent activation energy for decomposition of KDN, kJ/mol
K	= rate constant, 1/s
^{15}N	= labeled atom of nitrogen
r	= correlative coefficient
T_{m1}, T_{m2}	= decomposition temperature of KDN, °C
ΔH_L	= decomposition enthalpy of liquid KDN, J/g
ΔH_S	= decomposition enthalpy of solid KDN, J/g
ϕ	= heating rate, °C/min

I. Introduction

DINITRAMIDE salts, $M^+N(\text{NO}_2)_2^-$, are a relatively new kind of stabilized energetic inorganic salt compound, including ammonium dinitramide $\text{NH}_4 \cdot \text{N}(\text{NO}_2)_2$ and potassium dinitramide $\text{K} \cdot \text{N}(\text{NO}_2)_2$, which have high oxygen content and free chlorine and stable oxidizers and are considered as potential replacements for ammonium perchlorate (AP) and ammonium nitrate (AN) in propellants. Ammonium dinitramide (ADN) and potassium dinitramide (KDN) would significantly improve the energy density and reduce the signature characteristics of

Copyright © 1999 by the authors. Published by the American Institute of Aeronautics and Astronautics, Inc., with permission.

^{*}Associate Professor, Dept. of Analytical Chemistry.

[†]Professor, Dept. of Analytical Chemistry.

[‡]Associate Professor, National Key Laboratory of Combustion.

[§]Engineer, Dept. of Analytical Chemistry.

[¶]Professor, National Key Laboratory of Combustion.

propellants and would decrease pollution of the environment, so they were known as the candidate oxidizers for the next-generation low-signature characteristic propellant. Propellants containing ADN have been used in various missile systems in Russia.

Many of the thermal behaviors of ADN have been reported in recent years. The melting point of ADN is 91.5°C, and the melting process is accompanied by thermal decomposition. Lobbecke et al.¹ have investigated the additive stabilizers that could restrain the decomposition of ADN under low temperatures to improve its stability. Hexamethylenamine, 2-nitrodiphenylamine, and methyldiphenylurea (akardit) are efficient stabilizers for ADN. ADN produces different decomposition products under various pressures.² Manelis³ found the characteristics of "abnormal decomposition" of solid ADN. The decomposition rate of dried ADN (water content 0.05%) was found to be 1000 times that of ADN containing moisture (water content 0.4%). Russell et al.⁴ discovered reversible phase transition at high pressure, from α -ADN to β -ADN in about 2.0 ± 0.2 GPa, and found that ADN could decompose through two different pathways. The first pathway is the molecular rearrangement reaction, which forms AN and N₂O at low temperatures. The high-temperature decomposition of ADN begins with the cleavage of the N–N bond and produces primarily NO₂. Brill et al.⁵ suggested that dissociation and sublimation to ammonia (NH₃) and dinitraminic acid were one of the main steps of ADN decomposition. Weiser et al.⁶ reported that the burning rate of ADN propellant with an energetic binder was higher than that of AP propellant. Great attention has been paid to ADN as a new energetic oxidizer in many countries.

When the propellants with the low-signature characteristics, low sensitivity, and no contamination were studied, AN had great potential as an oxidizer. However, its disadvantageous phase transition IV→III and greater hygroscopicity limited its application. Although KNO₃, NiO, and CuO, for example, restrain the phase transition IV→III of AN, they decrease the propellant energy by different amounts and pollute the environment. KDN was found to be a new class of energetic phase stabilizer. Its good properties have awakened great interest. KDN and ADN have a similar structure, but KDN is more stable. AN phase stabilized by energetic KDN exhibited unexpected useful properties,⁷ such as a high burning rate and a lower pressure exponent. The decomposition mechanisms of the solid and liquid states of KDN were proposed,^{8,9} but many of the thermal behaviors of KDN have not been reported, especially for elevated pressure. To better understand the combustion mechanisms of KDN, it was very important to determine the thermal decomposition mechanism and primary thermal decomposition stage of KDN, as well as kinetic parameters of these processes under conditions very close to the combustion regime. In this chapter, the thermal decomposition behaviors and mechanisms of KDN are reported for elevated pressures.

II. Experimental Techniques

Two types of KDN samples were synthesized in our institute and recrystallized by methanol with water: sample A, not entirely dried KDN, its melting point 130.9°C, and sample B, entirely dried KDN in vacuum oven. High-pressure thermal decomposition behaviors of KDN were investigated using a TA 910 pressure differential scanning calorimeter (PDSC) at 0.1, 3, and 7 MPa filled with nitrogen. Mass loss tests of KDN were performed by a TA 2950 thermogravimetric analyzer

(TGA) in nitrogen with a flow rate of 40 ml/min. All experiments were performed at a linear heating rate of 10°C/min, with sample mass of 2–4 mg on an aluminum pan. In addition, the thermal decompositions of KDN were studied by PDSC at 0.1 and 6 MPa and heating rates of 5, 10, 20, and 30°C/min, and the kinetic parameters of thermal decomposition for KDN were calculated. An x-ray photoelectron spectroscope, model PE PHI-5400, with Mg target in vacuum 3×10^{-3} Pa, was used to study the structure and characterize the surface of various KDN samples. A Nicolet 60 SXR Fourier transform infrared spectroscope scanning at 18 spectra per min and a cell heating at the rate of 20°C/min were used to follow the thermal decomposition processes of KDN in real time.

III. Results and Discussion

A. Decomposition of Solid KDN

1. Effects of Pressure and Moisture on Decomposition of Solid KDN

In contrast with molten KDN, solid KDN decomposed easily.¹⁰ Processes of the solid-state decomposition and liquifying of KDN were observed by a microscope with a heat stage. The KDN crystal began to crack (decompose partially) when heated to 90°C, and at 97°C the crystal changed from transparent to opaque because of the formation of the decomposition product KNO_3 , which was absorbed on the crystal surface. The solid KDN began to liquify partially at 108°C, and produced a small gas bubble. The liquifying KDN became transparent at 130°C, and its rate of decomposition did not increase until 150°C. This result illustrates that the liquified KDN is more stable. The quantity of gas bubbles increased above 160°C, and the decomposition of liquified KDN began.

The decomposition of solid KDN is very complex, and stored time, grain size, and refinement of KDN may affect its decomposition. In contrast with KDN containing moisture, dried KDN, like ADN,³ decomposes very easily. This is known as “abnormal decomposition” of the solid KDN. In Fig. 1, the dotted lines are the curves of TGA and differential scanning calorimeter (DSC) of KDN containing moisture (sample A), and the solid lines are those of dried KDN (sample B). On the DSC curve of sample A, there is a melting endothermic peak at 130.9°C, and before melt a level straight basis line shows that the decomposition exothermic peak does not occur for solid KDN. The curve corresponding to TGA demonstrates that mass loss of the decomposition of the solid state was very small. For

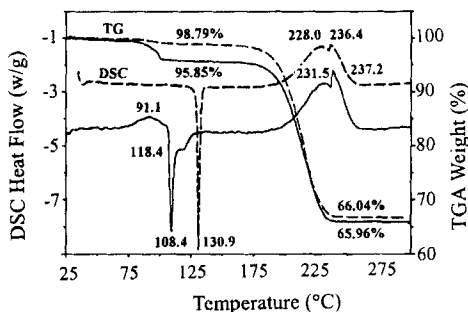


Fig. 1 TGA and DSC curves for KDN at 0.1 MPa: ---, sample A and —, sample B.

Table 1a Results of DSC for KDN (sample B) at various pressures: solid state

Pressure, MPa	Decomposition peak, °C	Decomposition enthalpy ΔH_S , J/g	Eutectic peak, °C	Liquifying peak, °C
0.1	91.1	53.1	108.4	118.4
3	90.0	13.0	107.8	122.1
7	93.7	5.3	108.4	127.1

dried KDN, there is an apparent exothermic peak at about 91°C prior to the two endothermic peaks (the eutectic and liquifying peaks) on the DSC curve of sample B, and an apparent mass loss (about 4%) on its TGA curve. This characteristic of “abnormal decomposition” is very important in the manufacturing and storing process for KDN.

At high pressures, the thermal decomposition for the solid KDN is restrained. In Fig. 2, the DSC curve of KDN shows that the exothermic decomposition peak at about 90°C contracts gradually as the pressure increases. At 7 MPa, it goes flat. It is clear from the data in Table 1a that the decomposition enthalpy ΔH_S of the solid KDN decreases gradually. For example, ΔH_S is equal to 53.1 J/g at 0.1 MPa, but 5.3 J/g at 7 MPa. The larger the pressure, the slower the decomposition of the solid KDN. It is evident that high pressure can improve the stability of the solid KDN. The influence of pressure on the decomposition of solid KDN can be interpreted by the following mechanism. The solid KDN decomposes to form N_2O and KNO_3 . N_2O is adsorbed on the crystal surface. When the concentration of the adsorbed N_2O increases to some extent, N_2O is desorbed or removed from the surface into the gas phase. At the same time, the solid KDN continuously decomposes. However, because pressure prevents the escape of N_2O , the decomposition of the solid KDN is restrained.

2. *Topochemistry of Decomposition for Solid KDN*

The thermal decomposition of solid KDN conforms to the topochemical principle. The crystal decomposition is related to the crystal particle size, moisture content, etc. The decomposition of larger crystals is faster than that of smaller ones. For larger crystal grain sizes, the crystal surface is not smooth, the crystal structure is imperfect, lattice defects, and cracks appear on the crystal surface, the reaction center (“nucleus formation”) forms easily and the reaction rate increases. With decomposition proceeding, the lattice defects and cracks on the crystal surface

Table 1b Results of DSC for KDN (sample B) at various pressures: liquid state

Pressure, MPa	Decomposition peak T_{m1} , °C	Decomposition peak T_{m2} , °C	Decomposition enthalpy ΔH_L , J/g
0.1	231.5	237.2	371.3
3	228.8	238.1	400.4
7	226.3	238.0	447.3

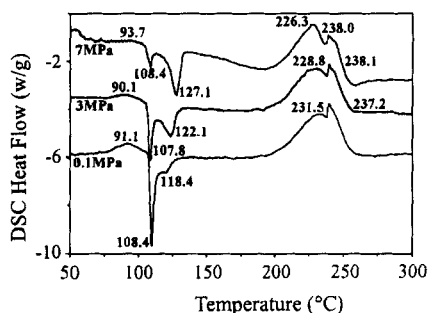


Fig. 2 PDSC curves for KDN (sample B) at various pressures.

expand, and the solidifying product KNO_3 , which is formed from the decomposition of KDN, is absorbed on the crystal surface. Therefore, the crystal produces stress. Then, as the stress increases continuously to some extent, the crystal cracks to form small crystals and generates a new surface, and the reaction occurs continuously on the new surface. Finally, the product KNO_3 completely covers the small crystal surface and eliminates the reaction center, causing the decomposition reaction to stop partially or completely.

At room temperature, the smaller crystals of KDN may decompose partially. When the decomposition product (KNO_3) covers the smaller crystal surface, it restrains the active reaction center. Because the smaller particle size crystal does not easily crack, its topochemistry does not easily proceed, and its thermal stability is better.

Moisture in the KDN can prevent and eliminate the active reaction center, and improve its stability. This may be the reason that KDN containing moisture was found to be more stable than the dried KDN.

The K^+ chemical state on the KDN crystal surface and the ratio of elements K to N were measured by x-ray photoelectron spectroscopy. The results in Table 2 show that the 2P electron-binding energy of K^+ for the KDN crystal surface of sample Nos. 2 and 3, although No. 4, was the same as that of KNO_3 . It is thus clear that these K^+ of the crystal surface of KDN lie mostly in the chemical state of KNO_3 , indicating that the decomposition product KNO_3 almost covers the KDN

Table 2 K^+ electron-binding energy and crystal surface element K/N value in different crystal states

No.	Sample	E_B/eV		
		$2\text{P}_{3/2}$	$2\text{P}_{1/2}$	K/N
1	KNO_3	293.0	295.6	—
2	KDN (larger crystal) ^a	292.9	295.7	0.47
3	KDN (smaller crystal) ^b	292.9	295.7	0.55
4	KDN (new crystal) ^c	292.6	295.4	0.40

^aNot ground.

^bGround and stored for a time.

^cGround and measured immediately.

crystal surface. However, there is not enough time for the decomposition product KNO_3 of KDN to cover the new crystal surface formed in sample No. 4, and internal structure of the KDN crystal is revealed. Its 2P electron-binding energy of K^+ is smaller and close to the K^+ chemical state in KDN structure. The data of Table 2 show that K/N values measured were larger than the K/N theoretical value of 0.33 for KDN. It is thus evident that the decomposition product KNO_3 of KDN could accumulate on the KDN crystal surface. Because the specific area of sample No. 3 was larger and it was stored for a time, its K/N value reached 0.55. Similarly, the new crystal formed from sample No. 4 was not completely covered by the decomposition product KNO_3 , and its K/N value was smaller (0.40). Table 2 shows that the decomposition product KNO_3 of KDN covers the KDN crystal surface, which has an important effect on the thermal behaviors of KDN, such as the topochemistry, thermal stability, and eutectic formation.

B. Thermal Decomposition of Liquid KDN

1. Decomposition Characteristics of Liquid KDN

Pressure has a distinct influence on the thermal decomposition of liquid KDN. At 130–180°C, melting KDN does not essentially decompose, but on the DSC curve of Fig. 2, there are two overlapping exothermic peaks (T_{m1} , T_{m2}) at 180–260°C as the decomposition of liquid KDN occurs. Table 1b shows that, as the pressure increases, the decomposition enthalpy ΔH_L of liquid KDN increases (i.e., ΔH_L increases from 371.3 J/g at 0.1 MPa to 447.3 J/g at 7 MPa). The decomposition of liquid KDN was assigned to two stages. During the first stage of decomposition, with increasing pressure, the decomposition peak temperature T_{m1} on DSC curve (Fig. 2) decreases from 231.5°C at 0.1 MPa to 226.3°C at 7 MPa, dropping by 5.2°C (see Table 1b). The peak shape changes from a gentle slope peak to a sharp peak (Fig. 2). This shows that pressure can change the first stage of decomposition and accelerate the reaction. The second-stage decomposition of liquid KDN is extremely quick and is overlapped by first-stage decomposition, constructing a precipitous sharp peak T_{m2} as shown in Fig. 2. Increasing pressure has little effect on T_{m2} .

2. Decomposition Kinetics for Liquid KDN

Decomposition kinetic parameters for liquid KDN were calculated by Kissinger's method.¹¹ The results are shown in Tables 3 and 4. Figures 3 and 4 are the Arrhenius charts of the decomposition of liquid state KDN of various pressures. It can be seen from Table 3 that, as the pressure increases, the peak temperatures

Table 3 Decomposition results for liquid KDN at 0.1 and 6 MPa

ϕ , °C/min	0.1 MPa		6 MPa	
	T_{m1} , °C	T_{m2} , °C	T_{m1} , °C	T_{m2} , °C
5	223.2	227.6	214.5	227.9
10	231.5	237.3	227.4	237.9
20	238.3	247.6	235.3	247.5
30	243.9	254.7	241.5	254.9

Table 4 Decomposition kinetic parameters for liquid KDN at 0.1 and 6 MPa

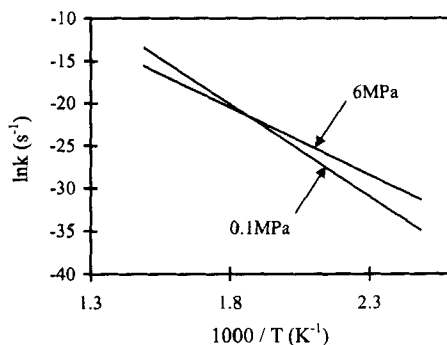
Pressure, MPa	First stage			Second stage		
	E_1^a , kJ/mol	$\text{Log } A_1$, 1/s	r	E_2^a , kJ/mol	$\text{Log } A_2$, 1/s	r
0.1	179.5	8.08	0.9985	137.4	3.65	0.9995
6	131.7	3.43	0.9924	139.2	3.81	0.9991

^a Apparent activation energy.

T_{m1} drop, but T_{m2} does not change at various heating rates. It can be seen from Table 4 that activation energies E_1 of the first-stage decomposition decreases from 179.5 kJ/mol at 0.1 MPa to 131.7 kJ/mol at 6 MPa as the pressure increases. The results in Fig. 3 show that increasing pressure changes the correlation of the first-stage decomposition rate constant with the temperature, the rate constants increase, and the decomposition reaction accelerates. Maybe this is the reason that propellants with KDN possess a high burn rate and a low pressure exponent. The activation energies E_2 of the second-stage decomposition show little difference at 0.1 and 6 MPa, and the relation for the rate constant with temperature shows two very close straight lines (in Fig. 4). It is clear that pressure does not influence second-stage decomposition.

C. Decomposition Mechanisms of KDN

Partial IR spectra, as shown in Fig. 5, were obtained from the decomposition processes of KDN followed by heating in situ cell. It was seen that as the temperature increases, the absorption bands of the vibrations of N-NO₂ (1530, 1431, 1344, and 1178 cm⁻¹) and N-N (1023 cm⁻¹) disappear, and those of -NO₃ (1384 cm⁻¹) and -NO₂ (1249 cm⁻¹) are enhanced gradually. The IR spectra (see Fig. 5) were divided into four groups. From room temperature to 157.2°C (spectra 1-4 in Fig. 5), as the first group corresponding to the solid-state decomposition and liquifying processes of KDN, the spectra of the N-N bond obviously decrease and

**Fig. 3** Arrhenius chart of the first-stage decomposition in liquid KDN at 0.1 and 6 MPa.

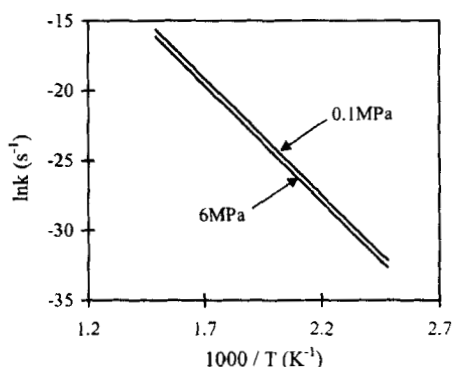


Fig. 4 Arrhenius chart of the second-stage decomposition in liquid KDN at 0.1 and 6 MPa.

do not disappear, but that of $-\text{NO}_3$ appears gradually. From 157.2°C to 190.6°C (spectra 4–7), as the second group, all spectra change very little because molten KDN is a comparatively stable stage. At 190.6–224.3°C (spectra 7–13), as the third group, corresponding to the decomposition of liquid KDN, the spectra of $\text{N}-\text{NO}_2$ and $\text{N}-\text{N}$ contract and disappear, but those of $-\text{NO}_3$ and $-\text{NO}_2$ strengthen gradually. At 224.3–380.9°C (spectra 13–17), the fourth group, corresponding to the final decomposition stage and the total decomposition of KDN, the spectra of $-\text{NO}_3$ and $-\text{NO}_2$ change slightly (the relative quantity of $-\text{NO}_2/-\text{NO}_3$ increase slightly).

From an investigation of the crystal structure of KDN,⁸ it has been believed that the two nitro groups of dinitramide anion $\text{N}(\text{NO}_2)_2^-$ were open and flat and not conjugated, and their negative charges were localized on a nitro group. Because the

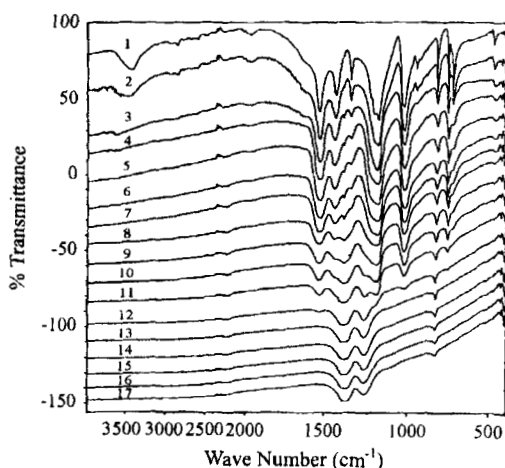


Fig. 5 IR spectra of decomposition of KDN followed by a heating in situ cell: 1, 17.5°C; 2, 71.2°C; 3, 113.1°C; 4, 157.2°C; 5, 168.4°C; 6, 179.4°C; 7, 190.6°C; 8, 201.8°C; 9, 205.2°C; 10, 210.8°C; 11, 215.2°C; 12, 219.7°C; 13, 224.3°C; 14, 269.0°C; 15, 313.8°C; 16, 358.6°C; and 17, 380.9°C.

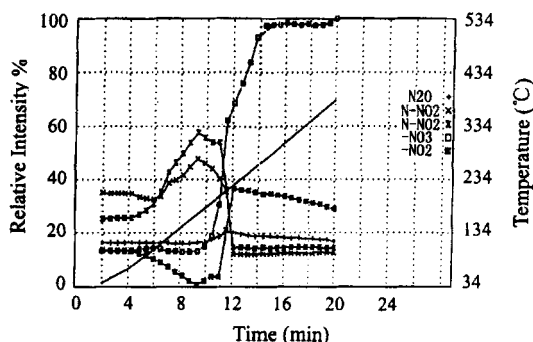


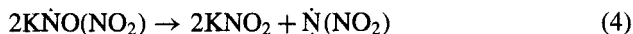
Fig. 6 Relation of relative intensity of IR spectra vs temperature or time.

N-N bond charge was not averaged, $N(NO_2)_2^-$ decomposed into $-NO_3$ and N_2O . Christie et al.¹² suggested that the two nitro groups of KDN crystal were not on the same plane, that their bond angle was 22.6° , and their bond lengths were different and the two nitro groups were asymmetric. Our experimental data show that elevated pressure restrains the decomposition of solid KDN, and demonstrate that the decomposition of solid KDN gives gas products. From this, the decomposition mechanism of solid KDN is



IR spectra recorded by heating in situ cell were integrated to obtain the correlation of the relative intensities of the characteristic peaks of N- NO_2 , $-NO_3$, $-NO_2$, and N_2O to temperature and time (Fig. 6). In the range of 224 – 234°C , the intensities of the mentioned characteristic peaks change suddenly. The peak of N- NO_2 disappears, and the peak of $-NO_3$ gradually reaches its maximum. On the basis of the data and the information in the literature,^{9,13} the decomposition mechanism of liquified KDN is formulated as follows.

The first-stage decomposition (228 – 230°C):



The second-stage decomposition (230 – 238°C):



The thermal decomposition of liquified KDN was investigated by the ^{15}N -labeling technique.⁹ It was found that N-N cleavage primarily removes a nitro group NO_2 with escape of the NO_2 , and a free diradical $\dot{N}(NO_2)$ is formed. At higher temperatures, the decomposition of $\dot{N}(NO_2)$ produces a free radical $[O]$, which is a stronger oxidizer than NO_2 . Therefore, the stronger oxidation reaction

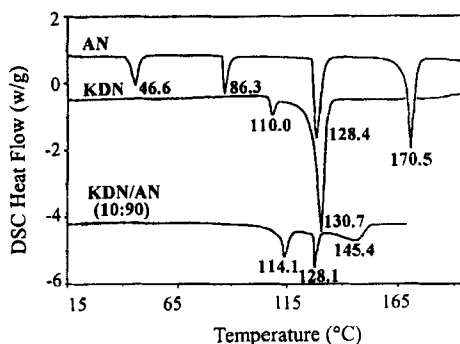


Fig. 7 DSC curves of AN, KDN, and AN/KDN at 0.1 MPa.

between [O] and KNO_2 form KNO_3 , accompanying the quick exothermic process. For this reason, a sharp exothermic peak (T_{m2}) on DSC curve occurs in Fig. 2. In the meantime, although KNO_2 decreases, KNO_3 increases in Fig. 6.

The results from PDSC show that the first-stage decomposition of liquid KDN accelerates with an increase in pressure, which favors increased concentration of the strong oxidant NO_2 in the condensed phase, making the reaction in Eqs. (3) and (5) quick. In the second-stage decomposition of liquid KDN, the reaction products occur mostly in the solid state (because of the formation KNO_2 and KNO_3). Therefore, pressure has no influence on this reaction.

D. Phase Stabilization of KDN

It is shown by the DSC curve at 0.1 MPa in Fig. 7 that AN has four endothermic peaks. The first three peaks are the crystal phase transition of AN, but the last peak is the melting point of AN. The phase IV \rightarrow phase III transition at 46.5°C causes an irreversible increase in the crystal volume of AN as a disadvantageous phase transition. Thus, recycling of the phase IV \rightarrow phase III may cause growth in the charge grain volume and destruction of its integrity. The results show an increase in the probity and loss in the mechanical strength for AN-based propellant. If KDN of about 10 wt% was introduced into the AN crystal lattice, then the IV \rightarrow III phase

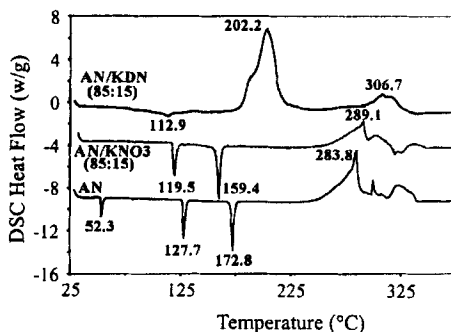


Fig. 8 DSC curves of AN, AN/KDN, and AN/ KNO_3 at 6 MPa.

Table 5 DSC results for AN system at 6 MPa

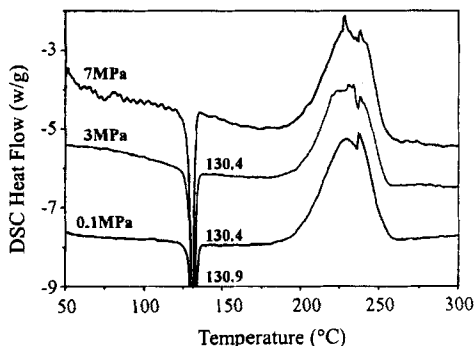
Sample, w/w	Phase transition temperature, °C		Decomposition enthalpy ΔH , J/g
	IV→III	III, II→I	
AN	52.3	127.7	700.5
AN/KNO ₃ (85/15)	—	119.5	362.3
AN/KDN (85/15)	—	112.9	1450.0

transition of AN could be eliminated (see DSC curve of AN/KDN in Fig. 7) in the 25–100°C range.

DSC curves at 6 MPa in Fig. 8 show the phase IV→phase III transition peak of AN at 52.3°C. However, on the DSC curves of AN/KNO₃ and AN/KDN, the phase transition peak is not observable in the 25–100°C range. At 0.1 or 6 MPa, KDN may effectively prevent the defective phase transition. As seen from Table 5, the enthalpy of decomposition for AN/KDN increases largely as compared with that of AN/KNO₃, and KDN not only has a phase-stabilizing effect on AN, but greatly increases AN-based propellant energy. KDN is considered to be a desirable phase-stabilizer of AN.

E. Eutectic System of KDN

The two binary eutectic systems were brought about during its decomposition process. KDN sample A, the decomposition phenomenon that did not appear in the solid phase, had only one endothermic peak, which was the melting point of KDN at 130.9°C in Fig. 1. KDN sample B, the decomposition phenomenon that appeared in the solid phase, had two endothermic peaks at 108 and 118.4°C in Fig. 1, the former being the eutectic peak of formation of KDN with its decomposition product KNO₃, and the latter being the liquifying point of the remaining KDN. It is seen from DSC curves in Fig. 2 that the eutectic peak height decreases, and the liquifying peak height increases as the pressure increases. At 0.1 MPa, the solid-phase KDN decomposes quickly, and forms more of the decomposition product KNO₃. The eutectic peak of the product KNO₃ with KDN becomes larger, and the liquifying peak of the remaining KDN becomes smaller in Fig. 2 and Table 1a. The results in Fig. 9

**Fig. 9** PDSC curves of KDN (sample A) at various pressures.

show that the decomposition of the solid KDN does not all appear at 0.1–7 MPa, so that KDN has only one endothermic peak, which has a melting point of 130.9°C, and the eutectic peak is not present. The results illustrate that KDN, with its decomposition product KNO_3 , can form a binary eutectic system. Another eutectic peak formed by the final decomposition products KNO_3 and KNO_2 for KDN is at about 315°C, and is described in another paper.¹⁴

IV. Conclusions

1) An increase in pressure restrains the thermal decomposition of solid KDN. When processing, using, transporting, and storing KDN, the proper outside pressure should be exerted on KDN. KDN in the smaller grain sizes and containing moisture is more stable, and does not easily decompose.

2) Elevated pressure accelerates the first-stage decomposition of the liquid KDN, to make its decomposition temperature (T_{m1}) and apparent activate energy (E_1) decrease, and its reaction rate constant increase. Generally, the energetic materials possessing the aforementioned characteristics make a greater contribution to the high burn rate and low pressure exponent in the propellant compositions.

3) 10 wt% KDN in AN eliminates the disadvantageous phase IV→phase III transition of AN. The decomposition exothermic enthalpy of AN/KDN is two times greater than that of AN/ KNO_3 . In a word, KDN is an ideal phase-stabilizer for AN.

References

- ¹Lobbecke, S., Krause, H., and Pfeil, A., "Thermal Decomposition and Stabilization of Ammonium Dinitramide (ADN)," *Proceedings of 28th International Annual Conference of Institut Chemische Technologie, (ICT)*, Karlsruhe, Germany, 1997, pp. 112-1–112-8.
- ²Korobeinichev, O. P., Shmakov, A. G., and Paletsky, A. A., "Thermal Decomposition of Ammonium Dinitramide and Ammonium Nitrate," *Proceedings of 28th International Annual Conference of Institut Chemische Technologie, (ICT)*, Karlsruhe, Germany, 1997, pp. 41-1–41-11.
- ³Manelis, G. B., "Thermal Decomposition of Dinitramide Ammonium Salt," *Proceedings of 26th International Annual Conference of Institut Chemische Technologie, (ICT)*, Karlsruhe, Germany, 1995, pp. 15-1–15-17.
- ⁴Russell, T. P., Piermarini, G. J., Block, S., and Miller, P. J., "Pressure, Temperature Reaction Phase Diagram for Ammonium Dinitramide," *Journal of Physical Chemistry*, Vol. 100, No. 8, 1996, pp. 3248–3251.
- ⁵Brill, T. B., Brush, P. J., and Patil, D. G., "Chemistry of Ammonium Nitrate and Ammonium Dinitramide Near the Burning Surface Temperature," *Combustion and Flame*, Vol. 92, No. 2, 1993, pp. 178–186.
- ⁶Weiser, V., Eisenreich, N., and Bayer, A., "Combustion Phenomena of ADN-Base Propellants," *Proceedings of 28th International Annual Conference of Institut Chemische Technologie, (ICT)*, Karlsruhe, Germany, 1997, pp. 8-1–8-14.
- ⁷Highsmith, T. K., Hinshaw, C. J., and Wardle, R. B., "Phase-Stabilized Ammonium Nitrate and Method of Making Same," U.S. Patent 5,292,387, March 1994.
- ⁸Dubovitskii, F. I., and Volkov, G. A., "Thermal Decomposition of KDN in the Solid State," *Doklady Akademii Nauk*, Vol. 348, No. 2, 1996, pp. 205, 206.
- ⁹Dubovitskii, F. I., and Volkov, G. A., "Thermal Decomposition of KDN in the Liquid State," *Doklady Akademii Nauk*, Vol. 347, No. 6, 1996, pp. 763–765.

¹⁰Babkin, S. B., Pavlov, A. N., and Nazin, G. M., "Anomalous Decomposition of Dinitramide Metal Salts in the Solid Phase," *Russian Chemical Bulletin*, Vol. 46, No. 11, 1997, pp. 1844–1847.

¹¹Kissinger, H. E., "Reaction Kinetics in Differential Thermal Analysis," *Analytical Chemistry*, Vol. 29, No. 11, 1957, pp. 1702–1706.

¹²Christe, K. O., William, W. W., Petril, M. A., Michels, H. H., Bottaro, J. C., and Gilardi, R., "The Dinitramide Anion, $\text{N}(\text{NO}_2)^-$," *Inorganic Chemistry*, Vol. 35, 1996, pp. 5068–5071.

¹³Korsounskii, B. L., Matveev, V. G., Nazina, L. D., and Nazin, G. M., "Mechanism of the Primary Stages of Decomposition of Aliphatic Nitro- and Fluoronitramines," *Proceedings of 29th International Annual Conference of Institut Chemische Technologie (ICT)*, Karlsruhe, Germany, 1998, pp. 60-1–60-15.

¹⁴Liu, Z., Kong, Y., and Yin, C., "Thermal Behaviour of KDN," *Proceedings of Symposium on Energetic Materials*, Shandong, Yantai, PRC, 1998, pp. 160–164 (in Chinese).

Chapter 2.8

Combustion Mechanism of 3-Azidomethyl-3-Methyloxetane (AMMO) Composite Propellants

Hakobu Bazaki*

Asahi Chemical Industry Company, Ltd., Oita, Japan

Nomenclature

C	= specific heat
E_s	= activation energy
Q_s	= heat released at the burning surface
R	= universal gas constant
r	= burning rate
r_{Fe}	= burning rate of propellant including ferric oxide
T	= temperature
x	= distance
α_s	= constant
η	= catalytic efficiency
Θ	= heat released at burning surface
Λ	= heat flux transferred back from gas-phase to burning surface
λ	= thermal conductivity
ξ	= fraction of solidified carbon
ρ	= density
σ_p	= temperature sensitivity of burning rate
Φ	= temperature sensitivity of gas-phase reaction
ϕ	= temperature gradient at the burning surface
Ψ	= temperature sensitivity of condensed-phase reaction
ψ	= temperature

Subscripts

c	= carbon
p	= pressure or propellant

Copyright © 1999 by the American Institute of Aeronautics and Astronautics, Inc. All rights reserved.

*Manager, Propellant Group, Explosives Research and Development Center.

- s* = burning surface or solid
- I = zone I, defined in Fig. 2
- II = zone II, defined in Fig. 2
- 0 = initial condition

I. Introduction

THE investigation of organic azide polymers has been conducted for the possible use of such polymers as high-energy plasticizers and binder components of rocket and gun propellants.¹ Typical organic azide polymers that have been studied extensively are glycidyl azide polymer (GAP), 3-azidomethyl-3-methyloxetane polymer (AMMO) and 3,3-bis(azidomethyl) oxetane polymer (BAMO). A number of thermochemical studies on azide polymers have been conducted.²⁻⁸ These azide polymers decompose with high heat release, resulting from the scission of the azide bond, to evolve nitrogen. These decomposition characteristics are significantly different from those of hydroxy-terminated polybutadiene (HTPB). The decomposition products of BAMO, GAP, and AMMO have been determined by simultaneous mass and temperature change/Fourier transform infrared spectroscopy.^{2,5,7} According to the results, CO and HCN are produced by BAMO and GAP, and CH₂O and HCN are produced by AMMO. Because the heat releases from GAP and BAMO are higher than that from AMMO, small molecules are formed by GAP or BAMO, whereas large fragments are evolved by AMMO. Slow heating rate and isothermal decomposition experiments indicate that nitrogen gas is evolved from BAMO at 403 K and from GAP at 393 K. However, the azide absorption of AMMO is still present at 560 K. It is evident that AMMO is more stable than either BAMO or GAP.

The azide polymers burn by themselves without any oxidants because of their high-energy release during decomposition.^{1,3} The kinetic studies revealed that the heat flux transferred back from the high-temperature gas-phase zone to the condensed phase is the major heat determinant of the burning rate. Accordingly, the heat transfer process plays an important role in determining burning rate characteristics, such as pressure and initial temperature effects. Because the azide polymers contain a relatively high concentration of carbon atoms as compared to the concentration of oxygen, the high specific impulse of rockets and impetus of guns could potentially be obtained by the addition of oxidizers such as ammonium perchlorate (AP). During propellant combustion, the AP particles interact with the azide polymer that acts as a base matrix surrounding the individual particles. Large numbers of flamelets are produced from each AP particle on the burning surface of the propellant.¹ Thus, the burning rate appears to be dependent on the physical and chemical mode of the AP particles and the base matrix at the burning surface and/or in the gas phase. In this study, the burning rate and thermochemical measurements were conducted to obtain information on the effects of pressure, initial temperature, and catalyst on AP/AMMO and AP/HTPB propellants.

II. Experimental Methods

The AMMO tested in this study was made by replacing the C-OH bond of 3-methyl 3-oxetane methanol with a C-N₃ bond. The chemical structure and

Table 1 Physico-chemical properties of AMMO

Parameters	Values
Chemical formula	$C_5H_9ON_3$
Molecular structure	$HO \left(\begin{array}{c} CH_2N_3 \\ H \quad \quad H \\ C - C - C - O \\ H \quad \quad H \\ CH_3 \end{array} \right)_n H$
Degree of polymerization, n	30
Molecular weight	3860 kg/kmol
Heat of formation	345.3 kJ/kg
Density	$1.06 \times 10^3 \text{ kg/m}^3$
Adiabatic flame temperature	1283 K at 10 MPa
Combustion ^a products (mole fraction) at 10 MPa	
	C(s), 37.4; N ₂ , 16.2; H ₂ , 26.3;
	CO, 6.8; CO ₂ , 0.5; CH ₄ , 9.6

^aChemical equilibrium calculations.

theoretical combustion properties of AMMO are shown in Table 1. It should be noted that the heat of formation (ΔH_f) of AMMO is a positive value and that the density ρ is relatively high. Both are higher than those of HTPB. The adiabatic flame temperature is 1283 K at 10 MPa. Large amount of C(s), H₂, and N₂ are formed as combustion products.

AP composite propellants composed of 80% AP and 20% binder were burned in a strand burner pressurized with nitrogen. The AP particles were formulated with a trimodal particle-size distribution consisting of a mixture of 10 μm (34%), 200 μm (33%), and 400 μm (33%) in particle diameter. The averaged diameter of the AP particles was 201.4 μm . As a reference to the AP/AMMO propellants tested, AP/HTPB propellants were formulated using the same AP particle distribution. The binders were cured by isophoron diisocyanate. To determine the effect of burning rate catalyst on the AP/AMMO propellants, 1% ferric oxide (Fe₂O₃, 1 μm in diameter) was mixed with the propellants. The propellant compositions tested in this study are shown in Table 2.

Table 2 Composition of AP composite propellants

AP, wt%	AMMO, wt%	HTPB, wt%	Fe ₂ O ₃ , wt%
80	20	—	—
80	20	—	1
80	—	20	—
80	—	20	1

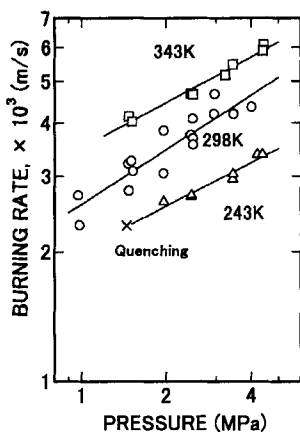


Fig. 1 Burning rate characteristics of AMMO at 243, 298, and 343 K.

III. Results and Discussion

A. Combustion Characteristics of AMMO

Figure 1 shows the combustion characteristics of AMMO polymer without crosslinking and curing at 243, 298, and 343 K. The burning rate of AMMO is as high as the burning rate of conventional double-base propellants. The temperature sensitivity given by the following equation was determined to be 0.0057/K between 243 and 343 K at 2.5 MPa:

$$\sigma_p = \left(\frac{\partial \ln r}{\partial T_0} \right)_p \quad (1)$$

To study the combustion wave structure, microthermocouples made of 50- μ m-diam Pt-Pt13%Rh wires were set into the strand samples. As shown in Fig. 2, the

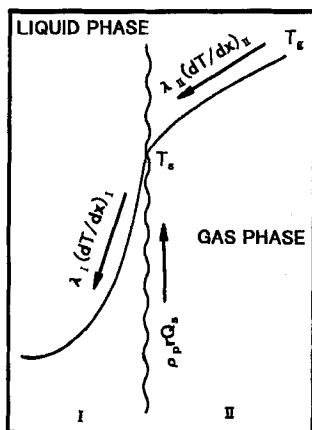


Fig. 2 Schematic representation of the combustion zones of AMMO.

combustion wave structure of AMMO can be divided into two zones: zone I is a nonreactive zone and burning surface and zone II is a gas-phase reaction zone in which final combustion products are formed. Decomposition and gasification occur at the temperature denoted by T_s in zone I. The heat flux transferred back from the gas phase to the burning surface, $\Lambda_{II} = \lambda_{II} (dT/dx)_{II}$, and the heat released at the burning surface, $\Theta_I = \rho_I r Q_I$, are determined by the following one-dimensional heat balance equation¹:

$$\rho_I r C_I (T_s - T_0) = \rho_I r Q_I + \lambda_{II} \left(\frac{dT}{dx} \right)_{II} \quad (2)$$

The value of Q_I was obtained by using Eq. (2), and λ_{II} was obtained by the analysis of combustion products of AMMO. The results showed that 23.4% solidified carbon was formed at the liquid–gas interface and remained in zone II during burning. Thus, the averaged heat conductivity in zone II, λ_{II} , was determined by the following relationship³:

$$\lambda_{II} = \xi \lambda_c + (1 - \xi) \lambda_g \quad (3)$$

In the computation of λ_{II} , $\xi = 0.234$, $\lambda_c = 3.57 \times 10^{-3}$ kW/mK, and $\lambda_g = 6.3 \times 10^{-5}$ kW/mK were used. Using the parameter values $\rho_I = 1.06$ kg/m³ and $C_I = 1.59$ kJ/kgK, and r , T_s , and $(dT/dx)_{II}$ data, the value of Q_I is calculated. The average Q_I was determined to be 668 kJ/kg in the pressure range tested. These results indicate that the exothermic reaction is occurring at the burning surface. The heat flux transferred back from the gas phase to the burning surface and the heat released at the burning surface were calculated. As shown in Fig. 3, both Λ_{II} and Θ_I increase with increasing pressure. The ratio of Λ_{II}/Θ_I was determined to be 0.03 at 2.5 MPa. The results indicate that the exothermic reaction observed at the burning surface is the major heat source of the combustion wave of AMMO.

The results suggest that fragments of hydrocarbon chain accompanied with azide groups are evolved at the burning surface of AMMO. The fragments decompose exothermically near the burning surface by the scission of the N–N₂ bond. Because

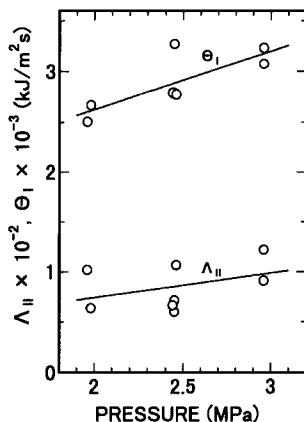


Fig. 3 Heat flux transferred back from zone II to zone I and heat flux produced in zone I of AMMO as a function of pressure.

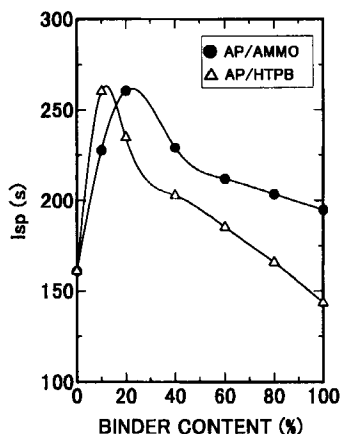


Fig. 4 Relationship between specific impulse and binder contents of AP/AMMO and AP/HTPB propellants.

the heat flux transferred back from the gas phase to the burning surface increases with increasing pressure, the quantities of the fragments increase.

B. Theoretical Rocket Performance of AP/AMMO and AP/HTPB Propellants

The theoretical rocket performance of the propellants composed of AP/AMMO and AP/HTPB was calculated using NASA SP-273.⁹ As shown in Fig. 4, the propellant composed of 20% AMMO and 80% AP indicates the highest specific impulse I_{sp} . I_{sp} decreases rapidly as the concentration of AMMO increases above 20%. The propellant composed of 10% HTPB and 90% AP indicates the highest I_{sp} . The highest I_{sp} of AP/AMMO propellant is as high as that of AP/HTPB propellant.

C. Combustion Characteristics of AP/AMMO and AP/HTPB Propellants

The burning rate characteristics of AP/AMMO propellant and AP/HTPB propellants were measured. As shown in Fig. 5, the burning rate of AP/AMMO propellant is higher than that of AP/HTPB propellant. AP/AMMO propellant shows a plateau burning at pressures between 2 and 4 MPa, and unstable combustion (self-burning interruption) was observed at pressures between 5 and 11 MPa. After the propellant strand burned about 5 mm, a self-burning interruption occurred in the pressure range between 5 and 11 MPa. However, combustion became stable again above 13 MPa. The scanning electron microscope (SEM) photograph revealed that there was a melting layer at the burning surface of the extinct propellant at 5 MPa, as shown in Fig. 6. It has been reported that a molten binder flowed over the AP particles and extinguished the combustion of the propellant.¹⁰ It may, therefore, be suggested that the self-burning interruption of AP/AMMO propellant is caused by a molten layer of AMMO binder.

The effect of initial temperature on the burning rate of AP/AMMO and AP/HTPB propellants was measured. Figures 7 and 8 show the burning rate of AP/AMMO and AP/HTPB propellants at 243, 293, and 343 K. The results indicate that the

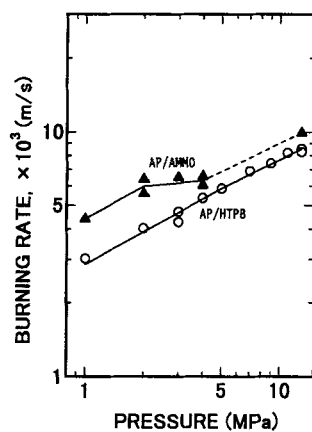


Fig. 5 Comparison of burning rate of AP/AMMO and AP/HTPB propellants.

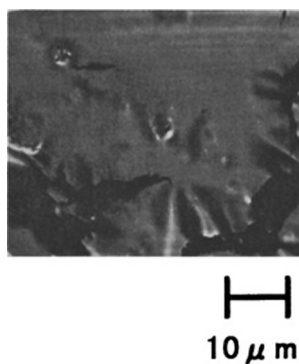


Fig. 6 SEM photograph of burning surface of a quenched AP/AMMO propellant.

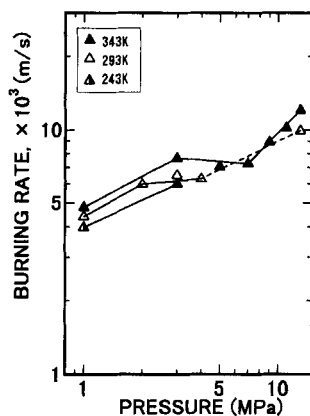


Fig. 7 Burning rate of AP/AMMO propellant at 243, 293, and 343 K.

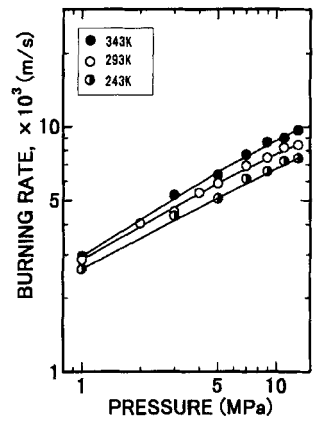


Fig. 8 Burning rate of AP/HTPB propellant at 243, 293, and 343 K.

burning rate of both propellants increases as the initial temperature increases. However, the AP/AMMO composite propellant shows a self-burning interruption above 3 MPa at 243 K. This phenomenon is thought to be due to a molten layer that forms on the burning surface. The molten layer reduces the heat flux feedback from the gas phase to the burning surface. A plateau burning is observed between 3 and 7 MPa at 343 K. Because the heat flux feedback from the gas phase to the burning surface at 343 K is supposed to be higher than that at 293 K, the pressure that indicates the plateau burning at 343 K is higher than the pressure at 293 K. No extinction of the combustion of AP/AMMO propellant was observed in the pressure region tested in this study at 343 K.

The temperature sensitivity of the burning rate σ_p , which was defined in Eq. (1), was obtained from the burning rate results. As shown in Fig. 9, the temperature sensitivity of both AP/AMMO and AP/HTPB propellants increase as pressure increases. The temperature sensitivity of AP/AMMO propellant was higher than

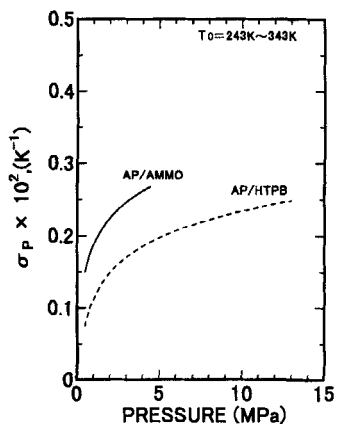


Fig. 9 Temperature sensitivity of AP/AMMO and AP/HTPB propellants.

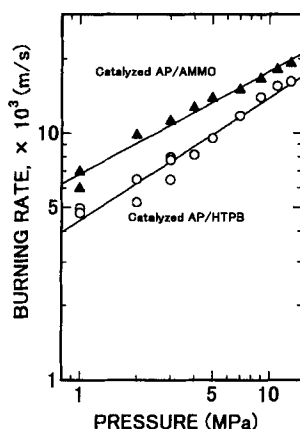


Fig. 10 Burning rate of AP/AMMO and AP/HTPB propellants with ferric oxide.

that of AP/HTPB propellant. From the results, it is thought that the use of AMMO as a binder changes the combustion mode of AP in contrast to the use of HTPB.

D. Combustion Characteristics of Catalyzed AP/AMMO and AP/HTPB Propellants

Metal oxides are widely used to change the combustion mode of AP-based composite propellants. Iron oxides are reported to act as catalysts to accelerate the decomposition of AP particles at the burning surface.¹¹ To understand the effect of the catalyst on the burning rate of AP/AMMO propellant, ferric oxide (Fe_2O_3) was chosen as a catalyst. The burning rate results are shown in Fig. 10. The burning rate and the pressure exponent were both increased by the addition of ferric oxide. The catalytic efficiency, which was defined by Eq. (4), was obtained:

$$\eta = (r_{\text{Fe}}/r) \quad (4)$$

As shown in Fig. 11, though there is some scatter in the data, it is obvious that the catalytic efficiency of AP/AMMO and AP/HTPB propellants was of the same order of magnitude in the pressure range tested. However, the effect of the addition of the catalyst is evident. No burning interruption was observed for the AP/AMMO propellant with ferric oxide between 5 and 11 MPa at 293 K. The results also indicate that ferric oxide acts more effectively to increase the burning rate because the catalytic efficiency increases as pressure increases. The plateau burning was also eliminated by the addition of ferric oxide. It has been reported that ferric oxide acts on the AP decomposition or the reaction of the decomposed AMMO binder with AP.¹² The heat of reaction at the burning surface is increased by the addition of the catalyst, then the heat flux feedback from the gas phase to the burning surface increases. The molten layer observed at the burning surface of the AP/AMMO propellant decreases, the burning rate increases, and the plateau burning is also eliminated.

The effect of the initial temperature on the burning rate of AP/AMMO and AP/HTPB propellants with ferric oxide was also measured at 243, 293, and 343 K.

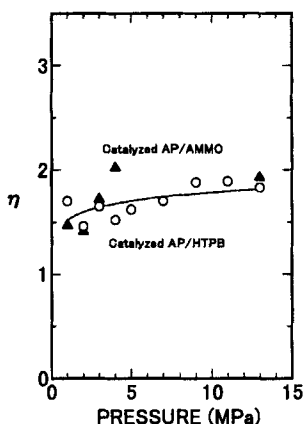


Fig. 11 Catalytic effects on burning rate of AP/AMMO and AP/HTPB propellants.

As shown in Figs. 12 and 13, the burning became stable and no plateau burning was observed when ferric oxide was added. The temperature sensitivity of both AP/AMMO and AP/HTPB propellants increased slightly with increasing pressure, as shown in Fig. 14. The temperature sensitivity of the AP/AMMO propellant with ferric oxide was also higher than that of AP/HTPB propellant with ferric oxide. The pressure dependence of the temperature sensitivity of both propellants was decreased by the addition of ferric oxide.

Price and Sambamurthi reported¹³ that ferric oxide catalyzes not only AP decomposition but also binder decomposition during combustion of AP composite propellants. The results of differential thermal analysis and thermogravimetric measurements indicate that the exothermic reaction and weight loss at the first-stage decomposition of AMMO were accelerated and that the heat of decomposition at about 700 K was increased by the addition of ferric oxide, as shown in

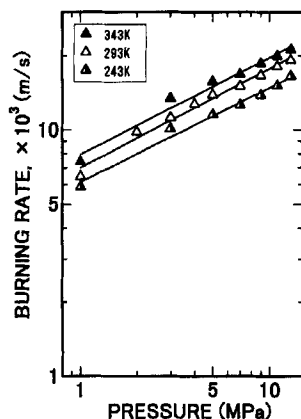


Fig. 12 Burning rate of catalyzed AP/AMMO propellant with ferric oxide at 243, 293, and 343 K.

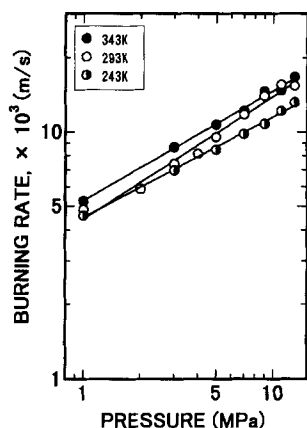


Fig. 13 Burning rate of catalyzed AP/HTPB propellant with ferric oxide at 243, 293, and 343 K.

Fig. 15. The thermal decomposition of HTPB also indicates a similar result, as shown in Fig. 16. A differential scanning calorimeter study showed that the heat of decomposition of AP/azide polymer propellants was increased by the addition of ferric oxide.¹¹ However, no detailed analysis of the action of the catalyst was done in this study.

E. Temperature Sensitivity Analysis of AP/AMMO Composite Propellants

To understand the temperature sensitivity characteristics shown in Figs. 9 and 14, a temperature sensitivity analysis was conducted. The temperature sensitivity of the burning rate was represented by the following equation, which was defined by

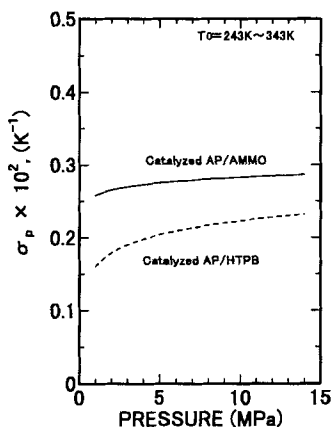


Fig. 14 Comparison of the temperature sensitivity of catalyzed AP/AMMO and AP/HTPB propellants with ferric oxide.

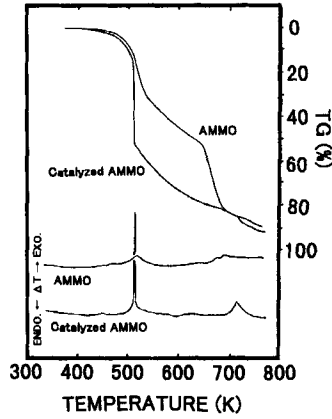


Fig. 15 Effect of ferric oxide on the thermal decomposition of AMMO.

Kubota and Ishihara¹⁴:

$$\sigma_p = \left(\frac{\partial \ln \alpha_s}{\partial T_0} \right)_p + \left(\frac{\partial \ln \phi}{\partial T_0} \right)_p - \left(\frac{\partial \ln \psi}{\partial T_0} \right)_p \quad (5)$$

Because α_s can be assumed to be independent of the initial temperature, Eq. (5) is written in the following form:

$$\sigma_p = \Phi + \Psi \quad (6)$$

Assuming that the burning rate can be expressed by the Arrhenius-type decomposition law at the burning surface, the temperature sensitivity of condensed phase reaction is given by the following equation¹⁴:

$$\Psi = \frac{1 - \sigma_p R T_s^2 / E_s}{T_s - T_0 - Q_s / C_p} \quad (7)$$

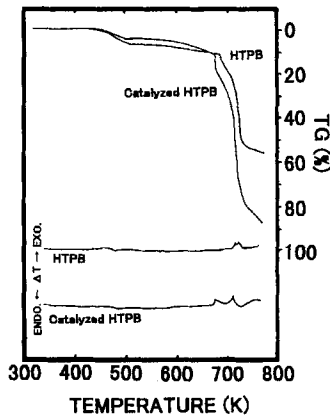


Fig. 16 Effect of ferric oxide on the thermal decomposition of HTPB.

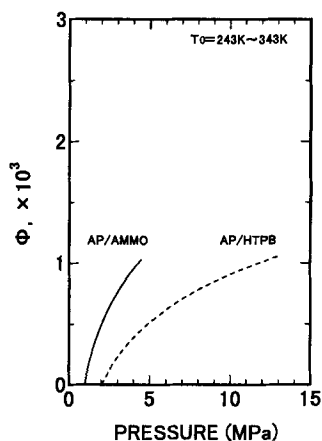


Fig. 17 Comparison of the temperature sensitivity of gas-phase reactions of AP/AMMO and AP/HTPB propellants.

Using Eqs. (6) and (7), the temperature sensitivity of the gas-phase reaction is expressed as

$$\Phi = \sigma_p - \Psi \quad (8)$$

The calculated results of Φ and Ψ of AP/AMMO and AP/HTPB propellants with and without ferric oxide are shown in Figs. 17–20. The temperature sensitivity of gas-phase reaction Φ without ferric oxide increases as pressure increases for both AP/AMMO and AP/HTPB propellants (Fig. 17). The temperature sensitivity of the gas-phase reaction of AP/AMMO propellant was larger than that of AP/HTPB propellant in the pressure range tested. As shown in Fig. 18, the temperature sensitivity of the condensed-phase reaction Ψ for both propellants decreases with

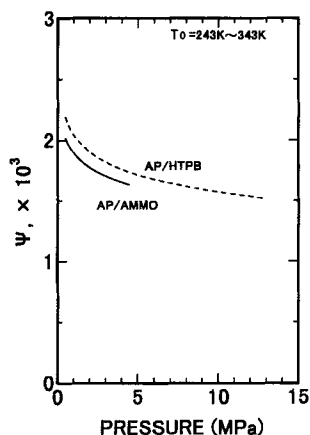


Fig. 18 Comparison of the temperature sensitivity of condensed-phase reactions of AP/AMMO and AP/HTPB propellants.

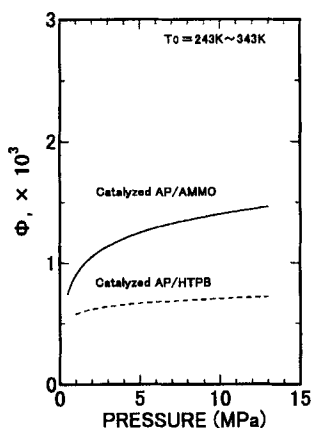


Fig. 19 Comparison of the temperature sensitivity of gas-phase reaction of catalyzed AP/AMMO and AP/HTPB propellants with ferric oxide.

increasing pressure. However, Ψ of both propellants was about the same in the pressure range tested. On the other hand, Φ of AP/AMMO propellant with ferric oxide was larger than that of AP/HTPB propellant with ferric oxide. As shown in Fig. 20, Ψ of both AP/AMMO and AP/HTPB propellants with ferric oxide is approximately the same as that of the propellants without ferric oxide. Though the results indicate that Ψ plays a dominant role in σ_p for both propellants, it is evident from the results shown in Figs. 9 and 17 and Figs. 14 and 19 that Φ is responsible for the type of binder used. As shown in Figs. 17 and 19, Φ of AP/AMMO propellant is higher than that of AP/HTPB propellant. The results indicate that Φ is increased significantly by the use of AMMO binder.

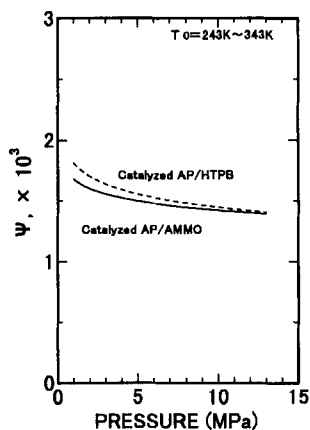


Fig. 20 Comparison of the temperature sensitivity of condensed phase reactions of catalyzed AP/AMMO and AP/HTPB propellants with ferric oxide.

IV. Conclusions

Pressure insensitive burning (i.e., plateau burning) is observed when an HTPB binder is replaced with an AMMO binder for AP composite propellants. This plateau burning is caused by the molten layer that forms on the burning surface. The burning is interrupted between 5 and 13 MPa at 243 K. The temperature sensitivity of the burning rate is higher for AP/AMMO propellant than for AP/HTPB propellant. The temperature sensitivity of both AP/AMMO and AP/HTPB propellants increases as pressure increases. The addition of ferric oxide accelerates the burning rate of both AP/AMMO and AP/HTPB propellants. Though the temperature sensitivity of the burning rate is dominated by the temperature sensitivity of the condensed phase for both AP/AMMO and AP/HTPB propellants, the temperature sensitivity of the gas-phase reaction is increased significantly when the HTPB binder is replaced with an AMMO binder.

Acknowledgment

The author would like to thank Naminosuke Kubota of Mitsubishi Electronic Corporation for the support of these studies.

References

- ¹Kubota, N., Sonobe, T., Yamamoto, A., and Shimizu, H., "Burning Rate Characteristics of GAP Propellants," AIAA Paper 88-3251, 1988.
- ²Oyumi, Y., and Brill, T. B., "Thermal Decomposition of Energetic Materials 22. The Contrasting Effects of Pressure on the High Rate Thermolysis of Energetic Compounds," *Combustion and Flame*, Vol. 68, 1987, pp. 209–216.
- ³Kubota, N., and Sonobe, T., "Combustion Mechanism of Azide Polymer," *Propellants, Explosives, Pyrotechnics*, Vol. 13, 1988, pp. 172–177.
- ⁴Miyazaki, T., and Kubota, N., "Energetics of BAMO," *Propellants, Explosives, Pyrotechnics*, Vol. 17, 1992, pp. 5–9.
- ⁵Chen, J. K., and Brill, T. B., "Thermal Decomposition of Energetic Materials 54. Kinetics and Near Surface Products of Azide Polymers AMMO, BAMO and GAP in Simulated Combustion," *Combustion and Flame*, Vol. 87, 1991, pp. 157–168.
- ⁶Farber, M., Harris, S. P., and Srivastava, R. D., "Mass Spectrometric Kinetic Studies on Several Azide Polymer," *Combustion and Flame*, Vol. 55, 1984, pp. 203–211.
- ⁷Oyumi, Y., and Brill, T. B., "Thermal Decomposition of Energetic Materials 12. Infrared Spectral and Rapid Thermolysis Studies of Azide-Containing Monomers and Polymers," *Combustion and Flame*, Vol. 65, 1986, pp. 127–135.
- ⁸Oyumi, Y., "Thermal Decomposition of Azide Polymers," *Propellants, Explosives, Pyrotechnics*, Vol. 17, 1992, pp. 226–231.
- ⁹Gordon, S., and McBride, B. J., "Computer Program for Calculation of Complex Chemical Equilibrium Compositions, Rocket Performance, Incident and Reflected Shocks, and Chapman–Jouguet Detonations," NASA SP-273, 1971.
- ¹⁰Boggs, T. L., Derr, R. L., and Beckstead, M. W., "Surface Structure of Ammonium Perchlorate Composite Propellants," *AIAA Journal*, Vol. 8, No. 2, 1970, pp. 370–372.
- ¹¹Oyumi, Y., Anan, T., Bazaki, H., and Harada, T., "Plateau Burning Characteristics of AP Based Azide Composite Propellants," *Propellants, Explosives, Pyrotechnics*, Vol. 20, 1995, pp. 150–155.

¹²Oyumi, Y., Mitarai, Y., and Bazaki, H., "Thermal Decomposition of AMMO/AP Composite Propellants," *Propellants, Explosives, Pyrotechnics*, Vol. 18, 1993, pp. 168–172.

¹³Price, E. W., and Sambamurthi, J. K., "Mechanism of Burning Rate Enhancement by Ferric Oxide," *Proceedings of the 21st JANNAF Combustion Meeting*, Publ. 412, Vol. I, Chemical Propulsion Information Agency, Laurel, MD, 1984, pp. 213–231.

¹⁴Kubota, N., and Ishihara, A., "Analysis of the Temperature Sensitivity of Double-Base Propellants," *Twentieth Symposium (International) on Combustion*, Combustion Inst., Pittsburgh, PA, 1984, pp. 2035–2041.

Chapter 2.9

Burning Rate Characteristics of Glycidyl Azide Polymer (GAP) Fuels and Propellants

Iwai Komai,* Koh Kobayashi,* and Kazushige Kato†
NOF Corporation, Aichi, Japan

Nomenclature

g	= acceleration of gravity
I_{sp}	= specific impulse
$I_{sp,g}$	= gross specific impulse
$I_{sp,n}$	= net specific impulse
P	= pressure
Q_s	= heat generation on the combustion surface
r	= burning rate
T	= temperature
T_f	= flame temperature
T_s	= temperature of combustion surface
T_0	= initial temperature of fuel or propellant
u_∞	= air velocity of freestream
x	= distance
ε	= air to fuel ratio
λ_g	= thermal conductivity of gas phase
ρ_p	= fuel or propellant density

I. Introduction

GLYCIDYL azide polymer (GAP)¹ is a well-known energetic polymer that contains azidemethyl groups in the side chain. Because the azide groups release a large amount of heat when they decompose, the enthalpy of formation of GAP is higher than that of the other common polymers.

Copyright © 1999 by the American Institute of Aeronautics and Astronautics, Inc. All rights reserved.

*Senior Engineer, Research and Development Dept.

†Manager, Research and Development Dept.

One application of GAP is as a solid fuel for air-breathing propulsion systems.²⁻⁵ The major ingredient of the fuels is hydroxyl-terminated GAP that is cured with isocyanate. These fuels decompose continuously by themselves without any added oxidizers, and the decomposition product still contains substantial quantities of combustible components. In the air-breathing propulsion systems this combustible gas is burned with the added air. In this kind of system the fuel mass flow rate, which affects the equivalence ratio, is strongly dominated by the burning rate of the fuel.

Another use of GAP is as a fuel binder for composite propellants, which are widely used for rocket motors of tactical missiles. In most case hydroxyl terminated polybutadiene (HTPB) is used as a fuel binder. Other major ingredients are usually ammonium perchlorate (AP) and aluminum powder (Al). However, if Al is mixed in the propellant, the hot plume is easily detected by radar. Also, the trajectory of the missile can be seen with aluminum oxide in the exhaust. Therefore, in some rocket motors Al is not used. Because GAP has higher enthalpy of formation, a higher specific impulse I_{sp} can be obtained by substituting GAP for HTPB.⁶⁻⁸ Furthermore, the burning rate of GAP propellants is higher than that of HTPB propellants.

In this chapter the theoretical performance and the burning rate characteristics and combustion mechanisms of GAP fuels and GAP propellants are evaluated.

II. Theoretical Performance

A. GAP Fuels

The theoretical I_{sp} and flame temperature of GAP fuel in air-breathing propulsion are shown in Fig. 1. The fuel used in this calculation was tetrafunctional GAP cured with hexamethylene diisocyanate. The NASA chemical equilibrium code⁹ was used for the calculation. Because there are some differences between rocket and air-breathing propulsion systems, some extra calculations were needed to obtain the I_{sp} . In this calculation, mixing of the fuel and the air was assumed. The enthalpy of the air varies for the change of velocity of the vehicle (or the relative velocity of the air) and flight altitude. This value can be included in the input data of the chemical equilibrium calculation. In the present study, Mach 2 vehicle velocity and sea-level flight were assumed, and 218.2 kJ/kg was used as

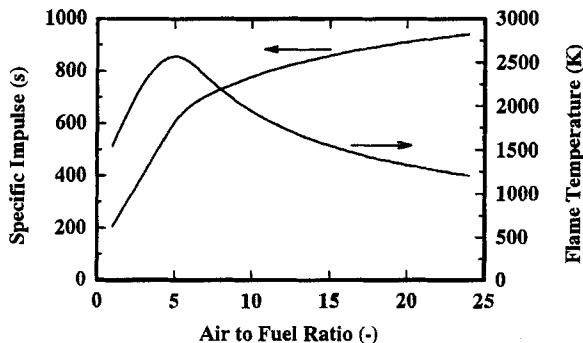


Fig. 1 Specific impulse and flame temperature of GAP fuel.

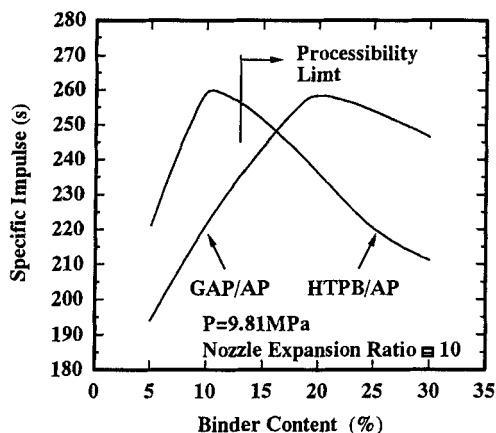


Fig. 2 Specific impulse of GAP/AP and HTPB/AP propellants.

the enthalpy of the air. The calculated I_{sp} in the output was based on the mass flow rate of the fuel and the air, and so it should be reduced to a value based on the mass flow rate of fuel only ($I_{sp,n}$). The reduction was done with the following equation:

$$I_{sp,n} = (1 + \varepsilon)I_{sp,g} - \varepsilon(u_{\infty}/g) \quad (1)$$

It can be seen in Fig. 1 that the stoichiometric air to fuel ratio is around 5, at the maximum T_f . The $I_{sp,n}$ was larger under fuel-lean conditions. It reached about 900 s for the air-to-fuel ratio of 25. However, it has to be noted that even though $I_{sp,n}$ gets higher, the thrust gets lower under fuel-lean conditions.

B. GAP Propellants

Figure 2 shows the theoretical I_{sp} of GAP/AP propellants and HTPB/AP propellants. The chamber pressure and ambient pressure were 9.81 and 0.101 MPa, respectively. The nozzle expansion ratio was 10. For the GAP/AP calculation difunctional GAP with an HMDI curative was used. The maximum theoretical I_{sp} of HTPB/AP propellants is 260 s, at which point the binder content was 10%, whereas the maximum I_{sp} of GAP/AP propellant is 258 s. A major difference between the propellants is the stoichiometric binder content. Because GAP contains a large amount of nitrogen (N), the amount of hydrogen and carbon is relatively smaller. The amount of oxygen required for complete combustion is also smaller. Consequently, the stoichiometric binder content becomes larger. In other words, the stoichiometric oxidizer content is smaller. The maximum I_{sp} of GAP/AP propellant is theoretically smaller than that of HTPB/AP propellant, but the stoichiometric binder content of HTPB/AP propellant is too small for the manufacturing process. Binder content of at least 30% is needed for the process, and so the maximum I_{sp} that can be delivered is about 256 s, which is much lower than the theoretical maximum. The stoichiometric binder content of GAP/AP propellants is, however, in the processible region. Therefore, the I_{sp} of GAP/AP propellants is higher than that of HTPB/AP propellants. In fact, 2 s is a very large difference in I_{sp} .

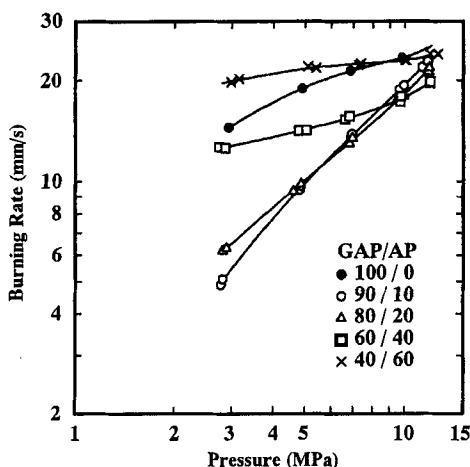


Fig. 3 Relationship between pressure and burning rate in GAP/AP fuels (AP size, $15\ \mu\text{m}$).

III. Burning Rate Characteristics

A chimney-type strand burner¹⁰ was used for the burning rate measurements. The pressure range was from 3 to 12 MPa. Nitrogen gas was used to pressurize the burner. The test pieces were $5 \times 5 \times 80\ \text{mm}$, and the side faces were inhibited. Burning rate measurements were made by timing wires embedded through the test pieces. Burning rate can be calculated by the distance between the wires and the time readings. The estimated measurement error of the distance is 2%, and the accuracy of the time reading is 1%. Thus, the error of burning rate measurement is calculated to be about 2.2%.

A. GAP Fuels

Figures 3 and 4 show the burning rate of GAP fuel with several different quantities of AP. The particle size of AP used in these experiments was $15\ \mu\text{m}$.

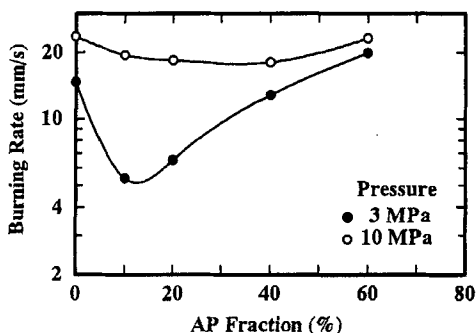


Fig. 4 Relationship between AP fraction and burning rate in GAP/AP fuels (AP size, $15\ \mu\text{m}$).

When AP was not added, the burning rate was relatively high. The burning rate at 3 MPa was about 14 mm/s and at 10 MPa was about 23 mm/s. These are higher than the burning rates of conventional solid propellants.

The heat balance on the combustion surface is written as¹¹

$$\rho_p c_p r (T_s - T_0) = \lambda_g \left(\frac{dT}{dx} \right)_g + \rho_p r Q_s \quad (2)$$

which is reduced to

$$r = \frac{\lambda_g (dT/dx)_g}{\rho_p \{c_p (T_s - T_0) - Q_s\}} \quad (3)$$

It is thought that the high burn rate of GAP fuel is due to the large heat generation Q_s on the combustion surface.^{3,4}

When 10 or 20% of AP was added, the burning rate of the low-pressure region decreased. The minimum burning rate at 3 MPa was about 5 mm/s. When the AP fraction increases the burning rate increases, whereas the burning rate of the high-pressure region decreases just a little.

When a small quantity of AP is added, the amount of heat generated on the combustion surface is reduced. Moreover, AP particles on the surface behave as a heat sink for the heat generation of GAP because the decomposition temperature of AP is much higher than that of GAP. Consequently, the burning rate decreases in the low-pressure region. In the high-pressure region, the gas-phase diffusion flame zone is compressed, and the heat feedback from the gas phase to the combustion surface, which is the numerator in Eq. (3), increases. Therefore, the burning rate does not decrease that much.

When a relatively larger quantity of AP was added, the burning rate was similar to that of GAP fuel without AP addition. This may be because the reduction of the heat generated on the surface is supplemented with the heat feedback from the gas phase to promote decomposition of GAP. In this case, combustion is considered to be driven by heat feedback from the gas phase. This behavior is summarized in Table 1.

Figure 5 shows the effect of cyclo-trimethylene-trinitramin (RDX). The particle size of RDX used in this these experiments was 200 μm . The burning rate of the GAP/RDX fuel is similar to that of the GAP/AP fuel, but the extent of the burning rate reduction was different. The burning rate reduction caused by 30% RDX was about the same as that caused by 10% AP. This is simply because of the particle size. RDX also behaves as a heat sink on the combustion surface, as AP does. When 15- μm RDX was used, the effect was more similar to the GAP/AP case.

Table 1 Combustion behavior summary for GAP fuel with AP

AP fraction	Low-pressure region	High-pressure region
None	Surface driven	Surface driven
Small	Surface driven	Surface driven gas-phase supported
Large	Gas-phase driven	Gas-phase driven

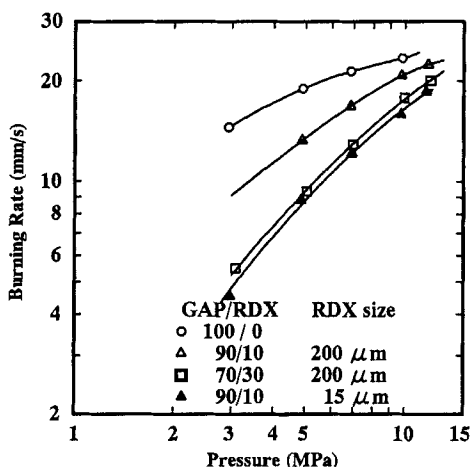


Fig. 5 Relationship between RDX content and burning rate in GAP/RDX fuels.

Another difference is in the burn rate in the high-pressure region. Because RDX is not an oxidizer, there is no diffusion flame in the gas phase. As a result, the heat feedback from the gas phase is smaller than that of GAP/AP fuel.

Some other energetic additives are discussed in Ref. 4. Metals and various other fuel components are under investigation because they may increase I_{sp} .

B. GAP Propellants

1. Effect of Ferric Oxide

Figure 6 shows the burning rate of GAP/AP propellants. The weight ratio of GAP and AP was 20/80, at which the I_{sp} reaches a maximum in these kinds of propellants, as was discussed earlier. The size of the AP particles were 200 and

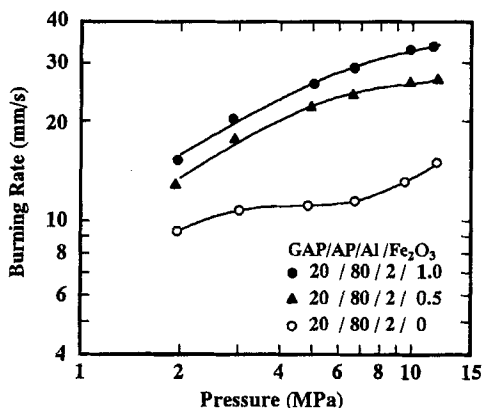


Fig. 6 Burning rate of GAP propellants with Fe_2O_3 .

15 μm . The weight ratio of the AP particles was 70/30. A small quantity of Al was added as an oscillatory combustion suppresser. Because the quantity of Al added is very small, it will not affect the burning rate characteristics of the propellant. Ferric oxide was used as a burning rate modifier that promoted the burning rate. When ferric oxide was not added, the so-called plateau region, in which the burning rate is seldom affected by the pressure, was observed from 3 to 5 MPa. When ferric oxide was added, no plateau region was observed in the tested pressure range. The pressure exponent of the burning rate in the high-pressure region was small, however, which suggests that the plateau region may exist in an even higher pressure region. It seems that ferric oxide may move the plateau region to a higher pressure.

The granular-diffusion-flame (GDF) theory¹² is often used to explain the combustion mechanisms of HTPB/AP propellants. In this theory, the chemical reaction effect and the diffusion effect in the burning rate are separated:

$$1/r = a/P + b/P^{1/3} \quad (4)$$

Equation (4) is rewritten as

$$P/r = a + bP^{2/3} \quad (5)$$

Here, a is a parameter related to the chemical reaction rate in the final diffusion flame, and b is a parameter related to the diffusion rate. If the first term of the right-hand side of the equation is larger, the burning rate is dominated by the chemical reaction. On the other hand, if the second term is larger, the gas-phase diffusion dominates the burning rate.

Figure 7 shows a plot of Eq. (5) for GAP/AP propellant. The horizontal axis is $P^{2/3}$, and the vertical axis is P/r . In Fig. 7 the effect of ferric oxide, a typical burning rate modifier of HTPB/AP propellant, was examined.

If Eq. (5) is applied for the plateau region of the non-ferric oxide added propellant, the value of a becomes negative. Therefore, the GDF theory cannot be applied for this case. For this propellant, the GDF theory can be applied only in the pressure regions below 3 MPa and above 6 MPa. When ferric oxide was added, the experimental data could be fitted with a straight line until the pressure was up to approximately 6 MPa. When the pressure was higher than 6 MPa, P/r became

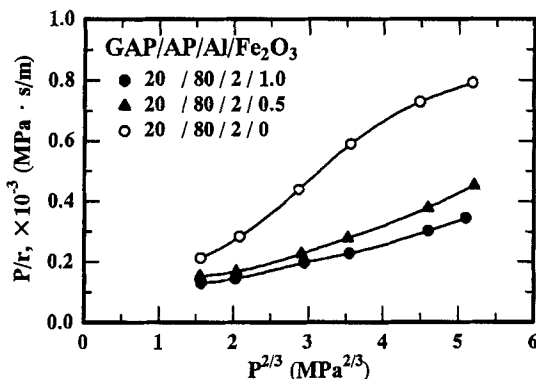


Fig. 7 Relationship between $P^{2/3}$ and P/r of GDF theory in GAP propellants with Fe_2O_3 .

Table 2 Calculated results of a and b in Eq. (4)

Propellant formulation (GAP/AP/Al/Fe ₂ O ₃)	Pressure range, MPa	a , MPa · s/m	b , MPa ^{1/3} · s/m
20/80/2/0	~3	0	135
20/80/2/0.5	~6	43	65
20/80/2/1.0	~6	48	50
20/80/2/1.0 ^a	~13	20	54

^aWeight ratio of 200- and 15- μ m AP = 30/70.

slightly larger. Addition of ferric oxide enlarges the region in which data can be fitted with a straight line.

Parameters a and b in the pressure range in which data could be fitted with a straight line are summarized in Table 2. When ferric oxide was not added, the value of a was very small. In this case, the diffusion is considered to be the rate-determining step. When ferric oxide was added, the value of a increased, whereas the value of b decreased. The addition of ferric oxide is thought to promote the decomposition of AP near the combustion surface¹³ so that the diffusion rate in the gas phase is increased.

2. Effect of AP Particle Size

Figure 8 shows the burning rate of GAP/AP propellant with various AP particle sizes. The weight ratio of 200- and 15- μ m AP were 70/30 and 30/70, respectively. The burning rate increased with the increased amount of fine AP, reaching about 40 mm/s at 10 MPa. In both cases the pressure exponent of the burning rate was relatively small in the high-pressure region. The GDF theory was applied for those propellants. The results are shown in Fig. 9. When a large quantity of fine AP was used, the data could be fitted to a straight line over the entire pressure range tested. The values of a and b are also summarized in Table 2. When the quantity of fine

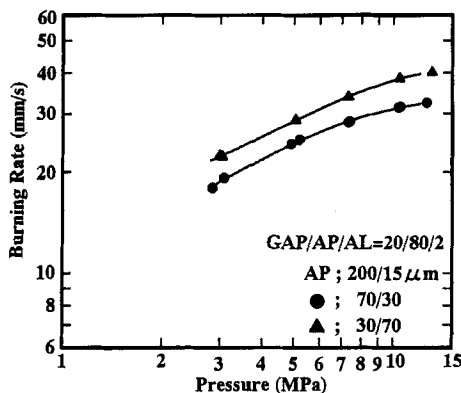


Fig. 8 Burning rate of GAP/AP propellants with various particle size of AP (Fe₂O₃ content, 1.0 part/100 parts GAP/AP).

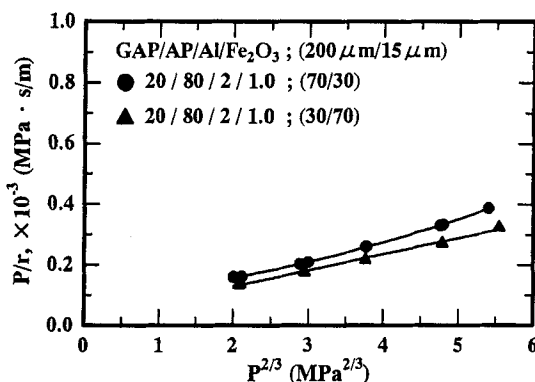


Fig. 9 Relationship between $P^{2/3}$ and P/r of GDF theory in GAP propellants with various AP particle sizes.

AP is larger, the value of a is smaller, and the value of b is larger. These results do not agree with the results reported by Steinz et al.¹² Even though the experimental data fit a straight line, it is difficult to explain the effect of the quantity of fine AP by gas-phase diffusion and chemical reaction.

IV. Conclusions

Theoretical performance and burning rate characteristics of GAP fuels and GAP/AP propellants were evaluated. The I_{sp} of GAP fuel in air-breathing propulsion reached about 900 s. The maximum I_{sp} of GAP/AP propellants was 258 s.

The burning rate of GAP fuels was higher than that of conventional solid propellants. It can be reduced by adding a small quantity (10–30%) of AP or RDX. According to the test results, burning rate of GAP fuels is dominated by the chemical reaction on the combustion surface.

GDF theory, which is often used to explain the combustion mechanisms of HTPB/AP composite propellants, can be applied to GAP/AP propellants. The addition of ferric oxide promotes the condensed phase reaction and diffusion in the gas phase.

When a large quantity of fine AP is used, the data fit the equation. However, the effect of the quantity of fine AP is difficult to explain.

References

- ¹Frankel, M., Grant, L., and Flanigan, J., "Historical Development of GAP," AIAA Paper 89-2307, July 1989.
- ²Helmy, A. M., "GAP Propellant for Gas Generator Application," AIAA Paper 87-1725, June 1987.
- ³Kubota, N., and Sonobe, T., "Combustion Mechanisms of Azide Polymer," *Propellants, Explosives, Pyrotechnics*, Vol. 13, No. 6, 1988, pp. 172–177.
- ⁴Kubota, N., Sonobe, T., Yamamoto, A., and Shimizu, H., "Burning Rate Characteristics of GAP Propellants," *Journal of Propulsion and Power*, Vol. 6, No. 6, 1990, pp. 686–689.
- ⁵Komai, I., Nakashita, G., and Kato, K., "Gas Generator Composition with Azidemethyl Group and Iron Compound Modifier," U.S. Patent 5,834,685, Nov. 1998.

⁶Kato, K., Kobayashi, K., Seike, Y., Sakai, K., and Matsuzawa, Y., "Mechanical Properties of GAP Reduced Smoke Propellants," AIAA Paper 96-3253, July 1996.

⁷Kobayashi, K., and Kato, K., "Burning Rate Characteristics of GAP Propellants," *Proceedings of the Twenty-Third International Pyrotechnics Seminar*, Housei Univ., Tokyo, 1997, pp. 338–345.

⁸Kobayashi, K., and Kato, K., "Burning Rate Characteristics of GAP Propellants," *Journal of the Japan Explosives Society*, Vol. 59, No. 2, 1998, pp. 57–63.

⁹Gordon, S., and McBride, B. J., "Computer Program for Calculation of Complex Chemical Equilibrium Compositions, Rocket Performance, Incident and Reflected Shocks and Chapman–Jouget Detonations," NASA SP-273, 1971.

¹⁰Kubota, N., Ohlemiller, T. J., Caveny, L. H., and Summerfield, M., "The Mechanisms of Super-rate Burning of Catalyzed Double Base Propellants," Dept. of Aerospace and Mechanical Science, Princeton Univ., Rept. 1087 (AD-76376), Princeton, NJ, March 1973.

¹¹Kubota, N., "Survey of Rocket Propellants and Their Combustion Characteristics," *Fundamentals of Solid-Propellant Combustion*, edited by K. K. Kuo and M. Summerfield, Vol. 90, Progress in Astronautics and Aeronautics, AIAA, New York, 1984, pp. 1–52.

¹²Steinz, J. A., Stang, P. L., and Summerfield, M., "Burning Mechanisms of Ammonium Perchlorate-Based Composite Propellants," AIAA Paper 68-658, June 1968.

¹³Price, E. W., and Sambamurthi, J. K., "Mechanisms of Burning Rate Enhancement by Ferric Oxide," *Proceedings of the Twenty-First JANNAF Combustion Meeting*, Publ. 412, Vol. 1, Chemical Propulsion Information Agency, Laurel, MD, 1984, pp. 213–231.

Effects of Carbon Substances on Combustion Properties of Catalyzed RDX–CMDB Propellants

Fengqi Zhao,* Shangwen Li,[†] Wengang Shan,* and Dianlin Lu*
Xi'an Modern Chemistry Research Institute, Xi'an, People's Republic of China
and
Shufen Li[‡]
China University of Science and Technology, Hefei, People's Republic of China

Nomenclature

a	= constant defined in Eq. (2)
d	= diameter, μm
n	= pressure exponent of burning rate
P	= pressure, MPa
r	= burning rate, mm/s
T	= temperature, K
X	= distance, m
Z	= burning rate enhancement efficiency defined in Eq. (1)
Δr	= difference of burning rate, mm/s

Subscripts

c	= condition with carbon substance
0	= initial condition

I. Introduction

USING cyclotrimethylenetrinitramine (RDX) or cyclotetramethylenetetranitramine (HMX) to replace ammonium perchlorate (AP) and aluminum powder in composite modified double-base (CMDB) propellants is an important

Copyright © 1999 by the authors. Published by the American Institute of Aeronautics and Astronautics, Inc., with permission.

*Associate Professor, National Key Laboratory of Combustion.

[†]Professor, National Key Laboratory of Combustion.

[‡]Professor, Dept. of Chemical Physics.

technological method that not only endows the propellant with higher energy, but also provides the minimum smoke characteristics for the exhaust. The addition of RDX or HMX, however, typically lowers the propellant burning rate and increases its pressure sensitivity, that is, produces a high pressure exponent (up to 0.7 or 0.8). Therefore, lowering pressure exponents and enhancing the burning rate of this type of propellant has become a focal point of propellant research.

It is well known that the addition of combustion catalysts is the most effective method to adjust the burning characteristics of propellants. The problem lies in which catalyst can be chosen and how to determine the content and relative proportion of various catalysts. Based on results for double-base (DB) propellants and a minimum smoke RDX-CMDB propellant with a similar flame (combustion wave) structure,¹ it can be concluded that certain kinds of lead salts, copper salts, and carbon black (CB) that are effective for catalyzing the combustion of DB propellants may be effective for RDX-CMDB propellant. Therefore, we have carried out comprehensive research on various combinations of lead salts, copper salts, and CB.^{2,3} It was found that CB plays a very important role in decreasing pressure exponents and increasing burning rates of RDX-CMDB propellants. As is well known, CB is the product of incomplete burning or splitting of many organic compounds, and it is mainly composed of carbon. We were very interested in the effect of CB in carbon substances of diverse types and appearances, especially fullerene, which is being studied extensively, and so we investigated the effects of C₆₀, fullerene soot, and CB on the combustion characteristics of catalyzed RDX-CMDB propellants.

II. Effect of Carbon and Potential of C₆₀ in Solid Propellants

Carbon plays a unique role in the combustion of DB/RDX-CMDB propellants, and it has attracted considerable research attention. Because solid-propellants mixtures have a negative O_x balance and they combust in reduction atmosphere, there is a large amount of carbon formed on the burning surface as well as in the combustion products. In 1965, Preckel⁴ published the results of his early research. It was shown that the addition of a small amount of CB could enhance burning rates and does not harm the plateau effect. When CB had a low concentration (<0.5%), the burning rates of the plateau zone could increase quickly; the finer the CB's particle size was, the higher the burning rates of the propellant were. On the basis that there was a large amount of carbon depositing on the burning surface of nitrate ester-based propellants, Hewkin et al.⁵ first put forward a lead-carbon catalysis theory in 1971 and claimed that carbon accelerated the reaction of NO, whereas the existence of lead salt catalyst activated carbon. Thereafter, Lengellé et al.⁶ indicated clearly that the carbon produced above the burning surface was the key material that enabled the propellant to create the plateau and superrate combustion phenomena. The addition of CB extended the range of the superrate by creating a more cohesive carbon layer in which the lead salt particles are trapped and then decomposed into PbO. Sharma et al.⁷ observed the burning surface and interior surface of suddenly extinguished propellants by x-ray photoelectron spectroscopy (XPS) and found that the samples of the catalyzed propellants quenched at different pressures were altered to a depth of 30–40 μm, and that a fluffy soot with a large concentration of lead in it was the principal constituent. The lead accumulation in the soot showed a maximum at a depth

of about 10 μm below the surface and marked the region of highest catalytic activity. Lead was present both as a metal and as an oxide, and more metallic lead was present in the samples from the superburning regime than from the mesa regime. The Pb/C ratio in the soot, produced at different pressures, showed a sudden decrease coinciding with the onset of the mesa region. Thus, the onset of the mesa regime can be ascribed to the loss of lead in the soot. When Denisjuk et al.⁸ studied the common function of PbO and CB, they discovered that the concentration and slight change of CB would lead to significant changes in PbO's catalytic effect. For a specific surface 800-cm²/g PbO and 50-m²/g CB, the optimum proportion of PbO/CB was (2–3):1, and when CB did not exist, the catalytic effect of PbO became weak. They then observed PbO, carbon particle, and the particles on the extinguished sample surface by high-resolution electron microscope⁹ and found that PbO formed the coagulum on the burning surface of propellants without CB. The accumulation effect made PbO lose its activity, while the sooty shell or carbon frame formed by carbon substances held back the accumulation of PbO and kept the PbO particles close to the burning surface. Li's work¹⁰ on applications of CB also indicated that adding a small amount of CB, e.g., 0.3%, to the formulations would significantly affect the combustion characteristics of propellants. Moreover, the burning rate enhancement of CB derived from different sources and made by different methods differed greatly.

The current literature basically admits that the emergence and disappearance of the superrate burning effect are closely related to the production and disappearance of carbon residues depositing on the burning surface. To sum up, carbon's functions are mainly as follows: 1) The physical action produced by carbon on the catalytic combustion is to prevent lead catalysts from forming coagulum. 2) From the chemical perspective, there are different opinions on the influence of carbon on catalytic combustion. It is generally admitted that carbon is a good catalyst for the reduction of NO and that carbon is also easily oxidized by NO. These reactions produce a large amount of heat. 3) Carbon black changes the optical properties of propellants. 4) The carbon frame (sooty shell or carbon net) formed by burning has higher thermal conductivity that greatly increases the heat flux back to the condensed phase. Furthermore, the carbon frame also hinders the escape of gases like NO and makes NO react fully in the surface zone to release heat.

C₆₀, discovered by Kroto et al.,¹¹ is a special new material with a cage structure and is the third kind of pure carbon shape. It is made up of 60 carbon atoms to form a football molecule whose diameter is 7.1 Å. This unique structure enables C₆₀ to possess many excellent physicochemical characteristics. The application of C₆₀ in some fields has attracted a great amount of attention from the research community. Recently, some articles¹² have discussed the interrelationship among C₆₀, soot, and combustion and indicated that fullerene, or the buckyball, exists in the combustion process. We also did some preliminary work, including detecting C₆₀ in the composition of propellants and determining the influence of soot with C₆₀ on the combustion of DB system propellants. It was found that a kind of carbon black (CB₃) always used as the ingredient of composite catalysts in DB or RDX–CMDB propellants contained a little toluene extract (2–5%). The color and appearance of this kind of toluene extract were similar to those reported for fullerene soot (FS).¹³ A preliminary catalytic combustion experiment using FS (containing about 10% C₆₀) made by the electrical arcing of graphite was also preformed. The results showed that the burning rates of DB propellant and the burning rate enhancement

efficiency increased by 4 mm/s and about 30%, respectively, and that the pressure exponent of the plateau zone and the plateau pressure range remained the same after the FS replaced CB.

There is probably a special relation between fullerene and the catalytic combustion of solid propellants, and fullerene may be a type of key material by which we can further realize the catalytic combustion. Some researchers¹⁴ think that C₆₀ could theoretically be used as the combustible substance of propellants and that, when the carbon cage is destroyed, the extra tension energy and bonding energy could possibly be released, but there have been no reports of experimental studies. Wang and Li¹⁵ succeeded in putting dinitrobenzene and trinitrobenzene on the spherical surface of C₆₀ and tried to press the energetic materials into the holes of C₆₀ under high pressure to increase the density and release much more energy in the course of combustion or explosion.

Our objectives are to study the feasibility of fullerene as burning catalyst in solid propellants and to promote the development of research on the combustion mechanism and the improvement of the combustion characteristics of solid propellants.

III. Experimental Results on the Burning Rate Enhancement of C₆₀, FS, and CB

A. Experimental Methods

The formulation of propellant in the experiment is as follows: 35.6% nitrocellulose (NC) (containing 12% N), 25.8% nitroglycerine (NG), 31.5% RDX, 3% diethylphthalate (DEP), 2% Centralite II (C₂), 0.5% Vaseline, 1.6% Al₂O₃, and catalysts. The samples were prepared by solventless DB propellant extrusion technology including slurry mixing, rolling, and extrusion.

The catalysts were lead phthalate (Φ -Pb), cupric 2,4-dihydroxy-benzoate (β -Cu), CB, C₆₀, and FS. The CB added into propellant is a kind of semireinforcement (SRF) CB and its particle size d_{50} is around 0.07 μ m. The C₆₀ was provided by Wuhan University, People's Republic of China, and its purity was more than 99.9%. FS is the primary product made by the electrical arcing of graphite for preparing C₆₀, contains about 10% C₆₀, and was also provided by Wuhan University.

To study the functions of different carbon substances, a Φ -Pb/C binary catalysis system and a Φ -Pb/ β -Cu/C tribasic catalysis system were designed. Here, tribasic catalysis system means a composite system that consists of three kinds of different catalysts used together.

The burning rates were measured in a strand burner. The appearance of the carbon substances was determined by combining the microanalysis system of a JMS-5800 scanning electronic microscope (Japan Electronic Company) and a LINK ISIS energy spectrum (Oxford, England, United Kingdom).

B. Burning Rate Enhancement of C₆₀, FS, and CB

There was no significant effect on the combustion characteristics of the propellants when the single CB was added into the propellants. Only when CB and lead catalysts were used together was the effect of CB obvious. CB was able to strengthen the catalytic effect of lead compounds. For C₆₀ and FS, the results were similar. To describe clearly the function of the carbon substance in the propellant catalyzed by lead salt, the burning rate enhancement efficiency Z was used to

Table 1 Effect of C₆₀, FS, and CB on combustion characteristics of catalyzed RDX-CMDB propellant

Composition of catalysts	Plateau zone, MPa	<i>n</i>	\bar{r} mm/s, 6–14 MPa	Z, MPa		
				6	10	6–14
2.5% Φ -Pb						
0	4–10	0.071	9.46	1.00	1.00	1.00
0.3% FS	6–16	0.198	12.56	1.36	1.58	1.36
0.3% C ₆₀	8–14	0.240	10.78	1.12	1.33	1.16
0.3% CB	6–12	−0.086	10.71	1.29	1.25	1.15
2.5% Φ -Pb 0.4% β -Cu						
0	4–10	−0.051	9.39	1.00	1.00	1.00
0.3% FS	6–16	0.161	13.05	1.34	1.65	1.42
0.3% C ₆₀	8–14	0.167	11.08	1.14	1.38	1.20
0.3% CB	6–12	−0.188	10.51	1.26	1.19	1.14

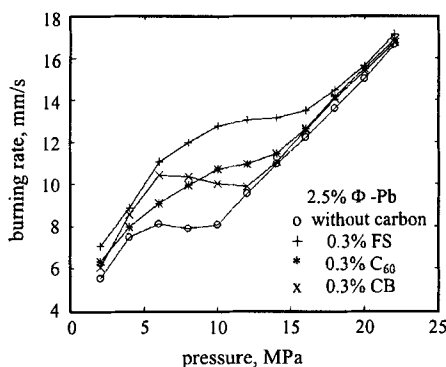
represent the contribution of carbon substance to the burning rate. Z is defined as

$$Z = r_c/r_0 \quad (1)$$

where r_0 is the burning rate of the control (comparative) propellant and r_c is the burning rate of the propellant with carbon substance. The experimental results are shown in Table 1 and Figs. 1 and 2. In Table 1, r is the average burning rate, the burning rate enhancement efficiency at 6–14 MPa is the average zone value of Z at every pressure point, and the pressure exponent n of the plateau zone is obtained by the linear regression of the following equation:

$$r = ap^n \quad (2)$$

The experimental results (Table 1 and Figs. 1 and 2) show that both a binary catalysis system and a tribasic catalysis system can increase the burning rate of propellants when 0.3% carbon substance is added. Compared with C₆₀ and CB, FS

**Fig. 1** Effect of FS, C₆₀, and CB on propellant burning rates.

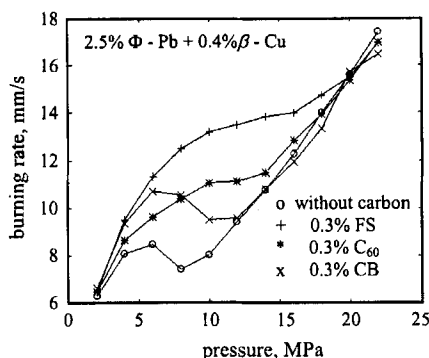


Fig. 2 Relation between burning rate and pressure in tribasic catalysis system.

is the best additive for the burning rate enhancement because the average burning rate of the propellant with FS at 6–14 MPa increases over 3 mm/s, and the Z value is the highest. In the binary system, the Z values for CB and C_{60} are similar. However, the average Z value for C_{60} at 6–14 MPa in the tribasic system is higher than that of CB. CB enhances the burning rate at low pressure, and so its Z value is higher than that of C_{60} at 4–8 MPa, but the burning rates of the propellant with C_{60} are higher at over 8 MPa. This indicates that C_{60} at high pressure is advantageous to enhancing the burning rates of the propellant.

After the addition of different carbon substances, the width of the plateau zone is maintained or even becomes wider, and the plateau zone transfers toward higher pressure. Among the three carbon materials, FS makes the plateau range of the catalyzed propellant widen and the pressure exponent n become large, whereas CB lowers the pressure exponent and makes the pressure exponent of plateau zone become negative. This shows fully that CB is particularly effective in lowering pressure exponent and that C_{60} produces the highest pressure exponent in the plateau zone.

C. Effect of FS or CB Content on the Combustion Properties

FS is most effective in burning rate enhancement, and CB has a significant influence on decreasing pressure exponent n . Therefore, further investigation of the influence of CB or FS content on the combustion properties was performed. The results are shown in Fig. 3 and Table 2. In Fig. 3, $\Delta r = r_c - r_0$, $\Delta r' = r_{FS} - r_{CB}$.

Figure 3 shows that for the pressures measured, the values of Z increase with the addition of FS and reach a maximum at 8 MPa. When the added amount of FS is 1.0%, the burning rate of the propellant is 2.3 times higher than that of the control propellant. This proves that FS has a significant effect on the enhancement of the propellant burning rate. At the same time, the plateau zone becomes wider as the FS content increases, and the plateau burning phenomenon ($n < 0.3$) occurs at 8–22 MPa.

From Table 2 and Fig. 3, it can be seen that increasing the added quantity of CB can enhance the burning rate. However, the burning rate enhancement of CB is far less than that of the same quantity of FS. For example, when the pressure is 10 MPa, the burning rate of the propellant with 0.7% FS is 9.46 mm/s higher

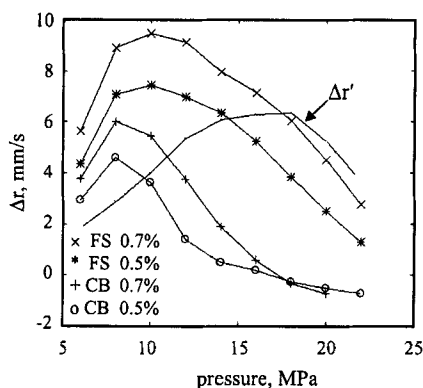


Fig. 3 Burning rate enhancement for various levels of FS and CB content.

than that of the control propellant, whereas the burning rate of the propellant with 0.7% CB is 5.46 mm/s higher than that of the control propellant. In the range of 6–16 MPa, Δr increases with the increase in pressure. When the carbon substance content is 0.7%, the value for $\Delta r'$ at 16 MPa is 6.5 mm/s. This demonstrates that pressure leads to FS having a better burning rate enhancement effect than CB.

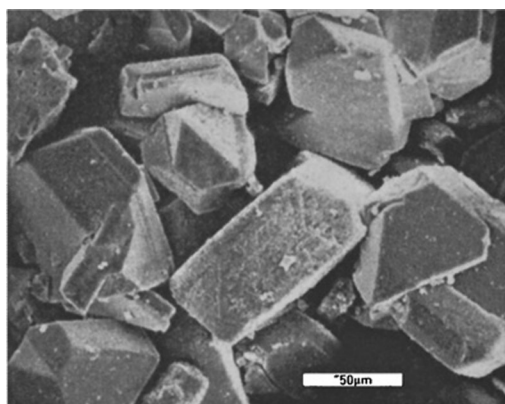
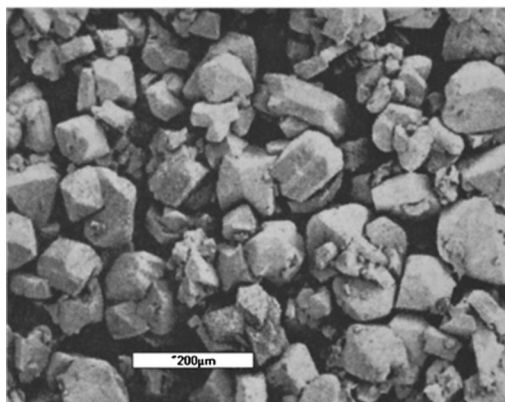
IV. Discussion of Burning Rate Enhancement by Various Carbon Substances

C_{60} , FS, and CB are carbon substances with different morphological properties, and their influences on the burning rate vary greatly. Among the physical and chemical properties of CB, the average particle size and specific surface plays a very important part in improving the burning rate and suppressing the pressure exponent.¹⁰ Thus, the surface appearance of the carbon substance was studied with a scanning electronic microscope (SEM). The results are shown in Fig. 4.

From Fig. 4, it can be stated that most particles of C_{60} 's condensation state are rhomboid and that the particle size is very big ($d_{50} > 50 \mu\text{m}$), whereas CB is a spherical particle whose size is extremely small (about $0.07 \mu\text{m}$). For FS, it is difficult to distinguish the single particle of C_{60} from soot through SEM pictures.

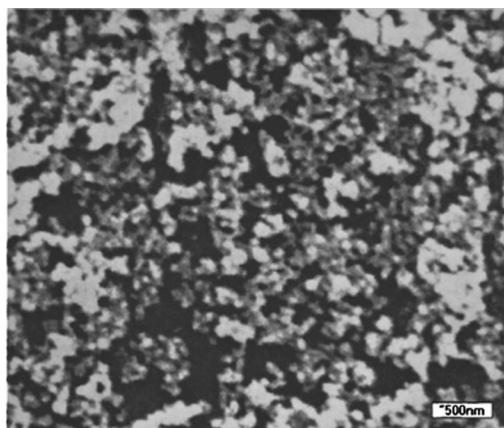
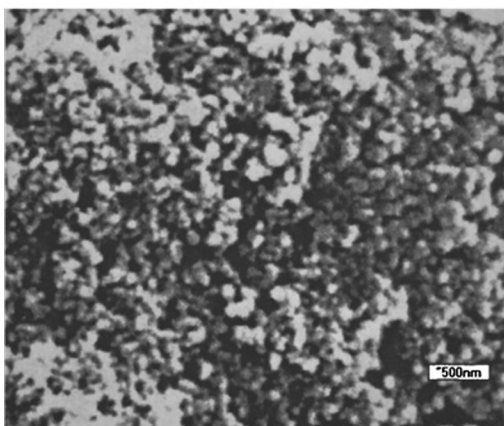
Table 2 Influence of FS content on combustion properties

FS, %	Z/P, MPa								Plateau zone, MPa	$r = ap^n$, mm/s
	4	6	8	10	12	14	16	18		
0	1.00	1.00	1.00	1.00	1.00	1.00	1.00	1.00	4–10	$8.793P^{-0.051}$
0.3	1.18	1.39	1.68	1.65	1.43	1.29	1.14	1.05	8–16	$9.006P^{0.161}$
0.5	1.29	1.52	1.96	1.93	1.74	1.59	1.43	1.29	8–20	$8.918P^{0.241}$
0.7	1.36	1.67	2.20	2.18	1.98	1.74	1.58	1.45	8–22	$10.405P^{0.224}$
1.0	1.43	1.72	2.31	2.30	2.05	1.85	1.64	1.51	8–22	$11.910P^{0.188}$

a) C₆₀ (500×)b) C₆₀ (150×)**Fig. 4 Surface appearance of carbon substances.**

This illustrates that the particle size of C₆₀ in FS is small and C₆₀ is evenly dispersed in soot. The mixture (FS) composed of C₆₀ and soot, in which the particle size of C₆₀ is very different than that of pure C₆₀ and becomes smaller, has a particle size similar to that of CB.

It has been mentioned that the addition of a carbon substance to propellant may result in the formation of a sooty shell on the burning surface, with the sooty shell acting as the concentrating bed for the active composition of catalysts and preventing the accumulation of lead and its oxides. Thus, lead or its oxides catalyze some oxidation and reduction reactions and increase dT/dx on the burning surface. Furthermore, the thermal conductivity of the foam zone containing the sooty shell is about 20 times higher than that of the general gas phase,⁹ which increases the heat feedback toward the condensed phase. The pressure exponent is affected by the disappearance of the sooty shell. When the sooty shell disappears slowly with an increase in pressure, $n > 0$; when the sooty shell disappears fast with an increase in pressure, $n < 0$.

c) CB (30,000 \times)d) FS (30,000 \times)**Fig. 4** Surface appearance of carbon substances (continued).

Because the particle size of CB is extremely small, when the pressure increases it is easy for CB to be oxidized by NO or taken away by the escaping gases. The disappearance of the carbon residues relates closely to the emergence of the mesa effect, and so this may be a reason that CB leads to the appearance of the mesa burning effect. Because the particle size of C_{60} is bigger, and its dispersion on the burning surface is less uniform than that of CB at low pressure, the Z value of C_{60} is lower than that of CB. When pressure increases, however, C_{60} cannot be easily removed by the escaping gases and can still support the catalysis of lead compounds. As a result, the burning rate with C_{60} is higher at high pressure.

The burning rate enhancement effect of FS is the best, which apparently relates closely to the presence of C_{60} . The fullerene molecule is a huge π electron conjugate system, has a high charge capacity, and obtains or loses electrons easily. The numerous double bonds on the surface of fullerene provide many active centers,

especially under high temperatures, where the molecule has striking chemical activity. It has been found that C_{60} has ions of from -5 to $+2$ valence number. Therefore, in propellant combustion, it is possible to produce a coordinate bond and form a C_{60} -Pbx complex between C_{60} and the outer vacant orbit of lead. Then, this complex changes the dispersion of the lead catalyst. Again, because the absorption characteristics of fullerene are better than those of CB, the C_{60} -Pbx complex may form a highly active catalytic center. This catalysis system can absorb certain gases on the burning surface and catalyze these gases to conduct an oxidation or reduction reaction, releasing a large amount of heat to enhance the propellant burning rate. Because the C_{60} -Pbx complex is not easily blown away by the escaping gases, the burning rate of propellants containing FS is higher in the plateau zone.

V. Conclusions

1) Carbon plays a very important part in catalyzing the combustion of minimum smoke propellants. Adding 0.3% C_{60} , FS, or CB can enhance the burning rate of catalyzed RDX-CMDB propellant. Among the three carbon substances, FS most effectively enhances the burning rate.

2) The three carbon substances cause the catalyzed propellant to maintain or even enlarge the width of the plateau zone, and the plateau region drifts toward the direction of high pressure. FS widens the plateau region of the catalyzed propellant, but the pressure exponent increases; CB decreases the pressure exponent (probably to a negative value); C_{60} results in a higher pressure exponent in the plateau zone of the catalyzed propellant.

3) The values of Z increase with an increase in the FS or CB content. However, the burning rate enhancement of CB is far less than that of the same amount of FS.

4) The diversity among the burning rate enhancement effectiveness of the three carbon substances closely relates to the following: the particle size of C_{60} is very big, the particle size of CB is extremely small, and FS has particles similar to CB with C_{60} evenly scattered in FS.

5) The C_{60} -Pbx complex formed between C_{60} and the outer vacant orbit of lead may be a key to the catalysis of certain gases for oxidation or reduction reactions with large heat release.

References

- ¹Kubota, N., "Survey of Rocket Propellants and Their Combustion Characteristics," *Fundamentals of Solid Propellant Combustion*, edited by K. K. Kuo and M. Summerfield, Vol. 90, Progress in Astronautics and Aeronautics, AIAA, Washington, DC, 1984, pp. 1-52.
- ²Meng, X., Zhang, R., and Li, S., "Adjustment on Combustion Properties of RDX-CMDB Propellants," *Tuijinjishu (Journal of Propulsion Technology)*, Vol. 10, No. 3, 1989, pp. 64-69 (in Chinese).
- ³Zhao, F., and Li, S., "An Investigation on Composite Catalysts Used in RDX-CMDB Propellants," *Tuijinjishu (Journal of Propulsion Technology)*, Vol. 13, No. 2, 1992, pp. 57-64 (in Chinese).
- ⁴Preckel, R. F., "Plateau Ballistics in Nitrocellulose Propellants," *AIAA Journal*, Vol. 3, No. 2, 1965, pp. 346, 347.

⁵Hewkin, D. J., Hicks, J. A., Powling, J., and Watts, H., "The Combustion of Nitric Ester-Based Propellants: Ballistic Modification by Lead Compounds," *Combustion Science and Technology*, Vol. 2, No. 2, 1971, pp. 307–327.

⁶Lengellé, G., Bizot, A., Duterque, J., and Trubert, J. F., "Steady-State Burning of Homogeneous Propellants," *Fundamentals of Solid Propellant Combustion*, edited by K. K. Kuo and M. Summerfield, Vol. 90, Progress in Astronautics and Aeronautics, AIAA, Washington, DC, 1984, pp. 361–407.

⁷Sharma, J., Wilmot, G. B., Campolattaro, A. A., and Santiago, F., "XPS Study of Condensed Phase Combustion in Double Base Rocket Propellant With and Without Lead Salt-Burning Rate Modifier," *Combustion and Flame*, Vol. 85, No. 3/4, 1991, pp. 416–426.

⁸Denisyuk, A. P., Margolin, A. D., and Khubaev, G. V., "The Role of Soot in the Combustion of Ballistite Propellants with Lead-Containing Catalysts," *Fizika Goreniya Vzryva (Physics of Combustion and Explosion)*, Vol. 13, No. 4, 1977, pp. 457–584.

⁹Denisyuk, A. P., Denidval, L. A., and Galkin, V. I., "The Primary Zone in the Combustion of Solid Propellants Containing Catalysts," *Combustion, Explosion and Shock Waves*, Vol. 31, No. 2, 1995, pp. 161–167.

¹⁰Li, S., "Influence of CB on Performance of RDX-CMDB Propellants," *Kogyo Kayaku (Journal of the Japan Explosives Society)*, Vol. 47, No. 3, 1986, pp. 6–10.

¹¹Kroto, H. W., Heath, J. R., O'Brien, S. C., Curl, R. F., and Smalley, R. E., "C₆₀: Buckminsterfullerene," *Nature*, Vol. 318, No. 6042, 1985, pp. 162, 163.

¹²Ebert, L. B., "The Interrelationship of C₆₀, Soot and Combustion," *Carbon*, Vol. 31, No. 6, 1993, pp. 999–1001.

¹³Kraetschmer, W., Lamb, L. D., Fostiropoulos, K., and Huffman, D. R., "Solid C₆₀: a New Form of Carbon," *Nature*, Vol. 347, No. 6291, 1990, pp. 354–358.

¹⁴Wen, S., "C₆₀ and M_x C₆₀—A Very Promising New Material," *Kejibaodao (Science and Technology Review)*, No. 7, 1992, pp. 36–40 (in Chinese).

¹⁵Wang, N., and Li, J., "Application Prospect of C₆₀ in Energetic Materials," *Hanneng-cailiao (Energetic Materials)*, Vol. 2, No. 4, 1994, pp. 40–42 (in Chinese).

Chapter 2.11

Modeling of RDX/GAP Propellant Combustion with Detailed Chemical Kinetics

Yeong-Cherng Liau*

Los Alamos National Laboratory, Los Alamos, New Mexico

and

Vigor Yang[†] and Stefan T. Thynell[‡]

Pennsylvania State University, University Park, Pennsylvania

Nomenclature

A	= cross-sectional area of propellant sample
A_g	= fractional cross-sectional area consisting of gas bubbles in two-phase region
A_j	= preexponential factor of rate constant of reaction j
A_s	= interface area between bubbles and liquid per unit volume
B_j	= temperature exponent in rate constant of reaction j
C_i	= molar concentration of species i
c_{pi}	= constant-pressure heat capacity of species i
E_j	= activation energy of reaction j
e	= internal energy
H_v	= enthalpy of vaporization
h	= enthalpy
h_c	= heat transfer coefficient
h_i	= static enthalpy of species i
h_{fi}°	= heat of formation of species i at standard condition
k_j	= rate constant of reaction j
\dot{m}''	= mass flux
N	= total number of species
N_R	= total number of reactions
p	= pressure
p_0	= preexponential factor of vapor pressure in Arrhenius form

Copyright © 2000 by the authors. Published by the American Institute of Aeronautics and Astronautics, Inc., with permission.

*Post-Doctoral Research Associate. Chemical Science and Technology Division. Member AIAA.

[†]Professor, Dept. of Mechanical and Nuclear Engineering. Associate Fellow AIAA.

[‡]Professor, Dept. of Mechanical and Nuclear Engineering. Senior Member AIAA.

R_u	= universal gas constant
T	= temperature
s	= sticking coefficient
t	= time
u	= bulk velocity
V_i	= diffusion velocity of species i
\bar{v}_n	= average normal velocity component of vapor molecule
W_i	= molecular weight of species i
\dot{w}_i	= mass production rate of species i
\dot{w}_{Rj}	= mass production rate of reaction j
X_i	= molar fraction of species i
x	= spatial coordinate
Y_i	= mass fraction of species i

Greek Symbols

ϕ	= void fraction
ρ	= density
λ	= thermal conductivity
$\dot{\omega}$	= molar production rate

Subscripts

0^+	= gas-phase side of propellant surface
0^-	= condensed-phase side of propellant surface
c	= condensed phase
$c-g$	= from condensed to gas phase
cond	= condensation
eq	= equilibrium condition
evap	= evaporation
f	= mass-averaged quantity in subsurface foam layer
g	= gas phase
s	= propellant surface
v	= vapor

I. Introduction

RESEARCH on ignition and combustion mechanisms of solid propellants continues to be of significant interest. It is based on the need to reduce cost, improve safety, increase performance, and minimize emission of harmful pollutants. To reduce emission of hydrochloric acid (HCl), which is formed during the combustion of ammonium perchlorate (AP), consideration has been given to nonchlorine-containing materials such as cyclotrimethylenetrinitramine (RDX), cyclotetramethylenetetranitramine (HMX), and ammonium dinitramide (ADN). To increase performance, attention has been given to various energetic binder ingredients, such as glycidyl azide polymer (GAP), 3,3-bis(azidomethyl)oxetane (BAMO), 3-azidomethyl-3-methyloxetane (AMMO), and 3-nitratomethyl-3-methyloxetane (NMMO). However, the effort involved with the design and formulation of new propellants to meet various stringent performance and environmental requirements

is both challenging and costly. The development of a comprehensive model to predict the detailed combustion characteristics would be of tremendous value to the propellant designer in the fabrication of more energetic and stable systems.

During the past decade, major advances have been made in the development of complex models of the ignition and combustion behavior of solid propellants.¹⁻⁶ These models are one-dimensional and take into account physicochemical phenomena in both the condensed and gas phases. In the model of RDX combustion developed by Melius, a detailed gas-phase reaction mechanism was formulated.¹ Yetter et al. improved the chemical kinetics scheme, but uncertainties still exist about pathways of the reduction and associated rates of large fragments departing from the burning surface of these cyclic nitramines.⁷

Recognizing the important role of the condensed phase, Liao and Yang developed a detailed model of RDX combustion accounting for the foam layer, which is the region between the gas and solid phases.² Such a foam layer consists of two phases: liquefied RDX and bubbles containing gaseous RDX and its decomposition products. With some minor modifications to Liao and Yang's model, Davidson and Beckstead³ concluded that an improved treatment of the near-surface region was needed. The same approach was later extended to study the combustion behavior of HMX.⁴ The lack of experimental data of liquid-phase properties of HMX and the important role of near-surface reactions were identified. Prasad et al. have also studied self-sustained and laser-assisted combustion of RDX and HMX.^{5,6} Their model differs from the ones described in Refs. 2-4 in that bubble formation within the liquid layer is neglected. In general, existing models of RDX and HMX combustion predict burning rates, surface temperature, and melt-layer thickness quite accurately, whereas some disagreements with experimental data in near-surface species profiles and temperature sensitivity are noted.

In view of the success in predicting the burning behavior of RDX and HMX, it appears that attempts should be made to study the effect of binder on nitramine combustion. The objective of this work is to incorporate the available decomposition mechanism of GAP into the existing model of RDX combustion.² Such an attempt is also made based on the availability of highly mature reaction mechanisms of hydrocarbon combustion.*

II. Theoretical Formulation

Figure 1 shows the molecular structures of RDX and GAP. The physical problem of concern is an RDX/GAP pseudo propellant burning in a stagnant environment with or without the assistance of external laser heat flux. The detailed physico-chemical processes involved in RDX/GAP pseudo-propellant combustion are illustrated schematically in Fig. 2. In the solid-phase region, RDX and GAP are physically linked together and heated by conduction. Chemical reactions are absent in the solid-phase region, largely because the temperature is too low. The subsurface multi-phase region begins where the solid RDX melts and becomes liquefied, which occurs at 478 K. Thermal decomposition of RDX and GAP, as well as subsequent reactions, takes place in the liquid layer, generating bubbles and forming a

*Frenklach, M., Bowman, T., Smith, G., and Gardiner, B., "GRI-MECH 1.2," available online at http://euler.berkeley.edu/gri_mech/index.html.

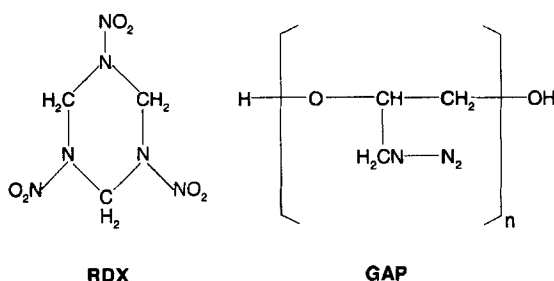


Fig. 1 Molecular structures of RDX and GAP.

multiphase region commonly known as the foam layer. Here, evaporation of RDX occurs at the interface between liquid and gas bubbles. In addition, rapid evaporation of RDX occurs in an infinitesimally thin region immediately above the foam layer,² leaving GAP as an aerosol within the RDX vapor and decomposed gaseous products. In this region, GAP remains as a condensed-phase species and continues to decompose. Oxidation reactions then raise the temperature to its final value.

The entire combustion-wave structure is segmented into three regions: a solid-phase, a near-surface multiphase, and a gas-phase region, as illustrated in Fig. 3. To facilitate the analysis, the coordinate system is fixed at the surface of the propellant, which is defined as the interface between the foam layer and the gas-phase region, as shown in Fig. 3. A pseudo one-dimensional model is formulated as a first approximation to the problem. Both the subsurface and gas-phase

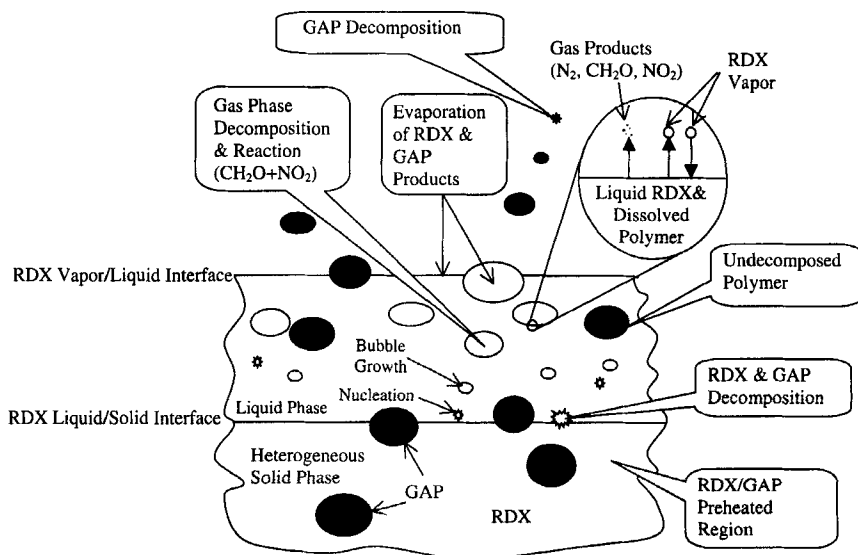


Fig. 2 Condensed and gas-phase processes involved in ignition and combustion of RDX/GAP propellants.

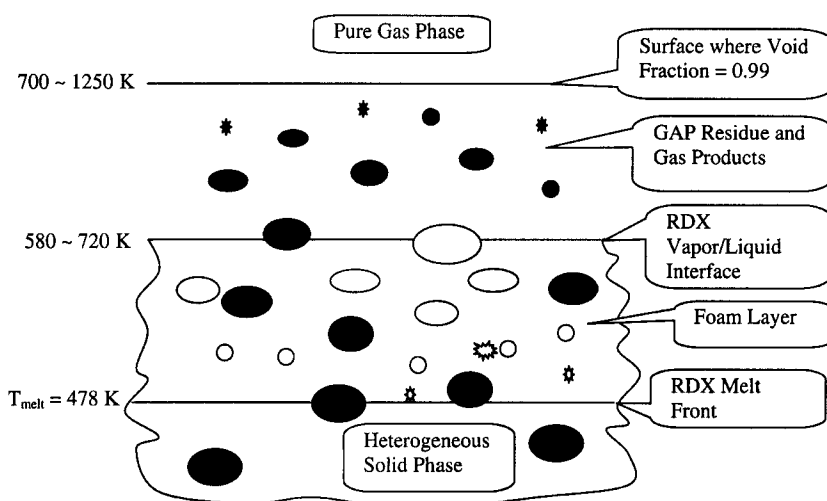


Fig. 3 Combustion-wave structure of RDX/GAP pseudo-propellant combustion.

regions require a multiphase treatment because of the existence of GAP and other condensed-phase species in these zones. A brief summary of the theoretical formulation of physico-chemical processes in various regions follows.

A. Solid-Phase Region

In this work, the propellant is treated as opaque, thus the external laser heat flux is absorbed by a thin surface layer. Here, the solid-phase region involves only heat transport by conduction since the temperature is too low to allow for any extent of chemical reactions. Thus, the governing energy equation is given by

$$\rho_c c_c \frac{\partial T_c}{\partial t} + \rho_c u_c c_c \frac{\partial T_c}{\partial x} = \frac{\partial}{\partial x} \left(\lambda_c \frac{\partial T_c}{\partial x} \right) \quad (1)$$

Standard notations in thermodynamics are used and defined in the nomenclature. The properties of the multicomponent system are averaged based on mass as follows:

$$\rho_c c_c = Y_{\text{RDX}} \rho_{\text{RDX}} c_{\text{RDX}} + Y_{\text{GAP}} \rho_{\text{GAP}} c_{\text{GAP}} \quad (2)$$

$$\lambda_c = Y_{\text{RDX}} \lambda_{\text{RDX}} + Y_{\text{GAP}} \lambda_{\text{GAP}} \quad (3)$$

A closed-form solution for the steady-state condition of Eq. (1) is available subject to appropriate boundary conditions and burning rates.

B. Subsurface Multiphase Region

This region contains a liquid layer of RDX with gas bubbles and other condensed species. The physico-chemical processes are extremely complex, involving an array of intricacies such as thermal decomposition, evaporation, bubble formation, gas-phase reactions in bubbles, interfacial transport of mass and energy between

gas and condensed phases. A two-phase fluid dynamic model using a spatial averaging technique is employed to formulate these complicated phenomena.^{2,8} With the assumption that mass diffusion is negligible, the conservation equations for both the condensed and gas phases can be combined and written as follows.

Mass

$$\frac{\partial[(1 - \phi_f)\rho_c + \phi_f\rho_g]}{\partial t} + \frac{\partial}{\partial x}[(1 - \phi_f)\rho_c u_c + \phi_f\rho_g u_g] = 0 \quad (4)$$

Condensed-Phase Species

$$\frac{\partial[(1 - \phi_f)\rho_c Y_{c_i}]}{\partial t} + \frac{\partial}{\partial x}[(1 - \phi_f)\rho_c u_c Y_{c_i}] = \dot{w}_{c_i} \quad (i = 1, 2, \dots, N_c) \quad (5)$$

Gas-Phase Species

$$\frac{\partial(\phi_f\rho_g Y_{g_i})}{\partial t} + \frac{\partial(\phi_f\rho_g u_g Y_{g_i})}{\partial x} = \dot{w}_{g_i} \quad (i = 1, 2, \dots, N_g) \quad (6)$$

Energy

$$\begin{aligned} \rho_f c_f \frac{\partial T_f}{\partial t} - \frac{\partial p}{\partial t} + \rho_f u_f c_f \frac{\partial T_f}{\partial x} = \frac{\partial}{\partial x} \left(\lambda_f \frac{\partial T_f}{\partial x} \right) - \sum_{j=1}^{N_g} \dot{w}_{g_j} h_{g_j} - \sum_{j=1}^{N_g} \dot{w}_{c_j} h_{c_j} \\ + \sum_{j=1}^{N_g} h_{g_j} Y_{g_j} \dot{w}_{c-g} - \sum_{j=1}^{N_c} h_{c_j} Y_{c_j} \dot{w}_{c-g} \end{aligned} \quad (7)$$

where \dot{w}_{c-g} represents the rate of mass conversion from liquid to gas. The properties are mass-averaged as shown here:

$$\rho_f c_f = [(1 - \phi_f)\rho_c c_c + \phi_f\rho_g c_g] \quad (8)$$

$$\rho_f u_f c_f \equiv [(1 - \phi_f)\rho_c u_c c_c + \phi_f\rho_g u_g c_g] \quad (9)$$

$$\lambda_f = [(1 - \phi_f)\rho_c u_c \lambda_c + \phi_f\rho_g u_g \lambda_g] / [(1 - \phi_f)\rho_c u_c + \phi_f\rho_g u_g] \quad (10)$$

where

$$c_c = \sum_{i=1}^{N_c} c_{c_i} Y_{c_i}, \quad c_g = \sum_{i=1}^{N_g} c_{g_i} Y_{g_i}, \quad \lambda_c = \sum_{i=1}^{N_c} \lambda_{c_i} Y_{c_i}, \quad \lambda_g = \sum_{i=1}^{N_g} \lambda_{g_i} Y_{g_i} \quad (11)$$

The mass and energy production terms depend on the specific chemical reaction mechanisms used and are formulated as follows.

Thermal decomposition of RDX and GAP, evaporation and condensation of RDX, and reactions of gaseous products inside the bubbles are considered in the subsurface foam layer. Two decomposition reactions of RDX are employed as indicated in Table 1. The first (R1) is a water-catalyzed exothermic reaction to form CH_2O and N_2O , and is favored at low heating-rate conditions. The second (R2), initiated with the $\text{N}-\text{NO}_2$ bond cleavage to generate NO_2 , HCN , H_2O , and

Table 1 Subsurface chemical reactions and rate parameters

No.	Reaction	$A^{a,c}$	$E^{b,c}$
R1	$\text{RDX}_{(l)} \rightarrow 3\text{CH}_2\text{O} + 3\text{N}_2\text{O}$	$10^{13.78}$	36,000
R2	$\text{RDX}_{(l)} \rightarrow 3\text{HCN} + 1.5(\text{NO}_2 + \text{NO} + \text{H}_2\text{O})$	$10^{16.4}$	44,100
R3	$\text{GAP56}_{(l)} \rightarrow \text{GAP56}_{(l)}^* + 56\text{N}_2$	5×10^{15}	41,500
R4	$\text{GAP56}_{(l)}^* \rightarrow 25.6\text{HCN} + 15.8\text{CO} + 14.4\text{NH}_3$ $+ 17.8\text{CH}_2\text{O} + 16\text{CH}_3\text{CHO} + \text{H}_2\text{O} + 6.4\text{C}_2\text{H}_3\text{CHO}$ $+ 1.5\text{C}_2\text{H}_4 + 8\text{CH}_3\text{CHNH} + 8\text{CH}_2\text{CHCHNH} + 14.6\text{C}_{(s)}$	$1.28 \times 10^{(19)}$	53,000
R5	$\text{RDX}_{(l)} \rightleftharpoons \text{RDX}_{(g)}$	See Ref. 2	—
R6	$\text{CH}_2\text{O} + \text{NO}_2 \rightarrow \text{CO} + \text{NO} + \text{H}_2\text{O}$	$802 \times T^{2.77}$	13,730
R7	$\text{CH}_3\text{CHO} + \text{M} = \text{CH}_3 + \text{HCO} + \text{M}$	7×10^{15}	81,770
R8	$\text{C}_2\text{H}_3\text{CHO} + \text{M} = \text{C}_2\text{H}_3 + \text{HCO} + \text{M}$	10^{16}	97,600
R9	$\text{CH}_3\text{CHNH} + \text{M} = \text{CH}_3 + \text{H}_2\text{CN} + \text{M}$	10^{16}	63,700
R10	$\text{CH}_2\text{CHCHNH} + \text{M} = \text{C}_2\text{H}_3 + \text{H}_2\text{CN} + \text{M}$	10^{16}	66,900

^aA = pre-exponential factor ^bE = activation energy ^cUnits are in mol, cm, s, K, and cal.

NO, is endothermic and prevails at high heating rates. Within this framework of global reactions, however, the autocatalytic effect of water cannot be considered explicitly. Subsequent reactions among the products of (R1) and (R2) may occur in the bubbles and provide the thermal energy to sustain pyrolysis. Brill⁹ examined several plausible secondary reactions and their reaction rates. Results indicate that reaction (R6) between CH_2O and NO_2 is probably the most important secondary reaction in the foam layer if it indeed does occur. In addition, thermodynamic phase transition consisting of both evaporation and condensation of RDX, (R5), is considered to provide a complete description of the mass transfer process. A detailed description of the treatment is given in Ref. 2.

The GAP sample considered in the present study is composed of 56 monomer units (i.e., $n = 56$ in Fig. 1) and denoted by GAP56. The chemical kinetic details of the decomposition and combustion behavior of GAP are not well known. Most recently, Arisawa and Brill employed a temperature-jump/Fourier transform infrared (T-jump/FTIR) spectroscopy to study the decomposition behavior of GAP.¹⁰ In their study, monol, diol, and triol having one, two, and three end-chain —OH groups were studied to elucidate the role of the —OH end group. Although an IR-inactive N_2 could not be detected by FTIR spectroscopy, GAP decomposition was assumed to be initiated with the bond cleavage of the azide group that releases N_2 . This bond-breaking process proceeds rapidly over a temperature range from 260 to 290°C, and has an activation energy of about 41 kcal/mol. There are, however, some uncertainties as to how the bond-breaking process occurs. Here, we assume a first-order process and use the pre-exponential factor and activation energy deduced by Sysak et al.,¹¹ as shown in Table 1 by reaction (R3).

The subsequent step in the decomposition of GAP releases NH_3 . Its concentration in the gas phase increases with increasing number of —OH end groups in the polymer. It appears that H-atom abstraction involving the —OH end group is an important channel for the NH_3 formation. At this time, there are no mechanistic details that allow one to write the NH_3 evolution as a global reaction, and thus a rate expression cannot be formulated. Since NH_3 is an important source for H-atoms in the gas phase, the deficiency in predicted species concentrations caused

by neglecting this step in the decomposition of GAP must be noted. Finally, the rapid, highly exothermic event takes place and releases HCN, CO, CH₂O, CH₂CO, CH₄, C₂H₄, H₂O, and GAP oligomers, in addition to NH₃.¹⁰

In a laser-assisted combustion study of GAP polyol by Tang et al.,¹² the surface temperature approached 1050 K, which was about 400 K higher than those utilized by Arisawa and Brill.¹⁰ Because this higher temperature and the use of a triple quadrupole mass spectrometer (TQMS), Tang et al. identified several different large molecular species. The major ones were acetaldehyde (CH₃CHO), acrolein (C₂H₃CHO), and different imines (CH₃CHNH and CH₂CHCHNH). In comparing the results of Arisawa and Brill¹⁰ with those of Tang et al.,¹² it appears that the GAP oligomers identified by Arisawa and Brill are likely candidates to form the imines identified by Tang et al. By performing a species balance of the results acquired by Tang et al., it is possible to formulate a global reaction model for the decomposition of GAP56*, which is the polymer unit that has released N₂, as shown in Table 1 as reaction (R4).

Most of the gaseous decomposition products from GAP are hydrocarbons or common gases whose chemical kinetic details are readily available. However, the information about aldehydes (CH₃CHO and C₂H₃CHO) and imines (CH₃CHNH and CH₂CHCHNH), as well as their interactions with either RDX or its decomposition products, appears to be limited. To allow for a reduction of these species, bimolecular decomposition reactions have been formulated, with the activation energies about the difference in enthalpy between products and reactants. The pre-exponential factors are assigned values that are typical for such a process. The considered reactions are listed as reactions (R7-R10) in Table 1.

Note that the condensed species GAP56_(l), GAP56*_(l), and C_(s) are dissolved in the RDX liquid phase, whereas all other species are gaseous and exist in bubbles. Based on the chemical mechanism given by (R1-R6), the species production terms in Eqs. (5) and (6) are listed in Table 2. The forward and backward reactions in (R5) denote the evaporation and condensation processes between liquid and vapor RDX. The production terms for reactions in Table 2 are defined as

$$\dot{w}_{R1} = (1 - \phi_f)\rho_c Y_{c,1} k_1 \quad (12)$$

$$\dot{w}_{R2} = (1 - \phi_f)\rho_c Y_{c,1} k_2 \quad (13)$$

$$\dot{w}_{R3} = (1 - \phi_f)\rho_c Y_{c,2} k_3 \quad (14)$$

$$\dot{w}_{R4} = (1 - \phi_f)\rho_c Y_{c,3} k_4 \quad (15)$$

$$\dot{w}_{R5} = A_s(k_{5f} - k_{5b}) = A_s s \bar{v}_n C_{RDX} \left(\frac{p_{v,eq}}{p} - X_{g,5} \right) \quad (16)$$

where $s = 1$ and

$$p_{v,eq} = P_0 \exp\left(-\frac{H_v}{R_u T}\right), \quad (17)$$

$$\dot{w}_{R6} = \phi_f k_6 \left(\frac{\rho_g Y_{g,6}}{W_6} \right) \left(\frac{\rho_g Y_{g,9}}{W_9} \right) \quad (18)$$

A more detailed discussion of Eq. (16) is given in Refs. 2 and 8.

Table 2 Description of species formation in foam layer

<i>i</i>	Species	\dot{w}_{c_i} or \dot{w}_{g_i}
1	RDX _(l)	$-(\dot{w}_{R1} + \dot{w}_{R2} + \dot{w}_{R5})$
2	GAP56 _(l)	$-\dot{w}_{R3}$
3	GAP56* _(l)	$\dot{w}_{R3} W_3 / W_2 - \dot{w}_{R4}$
4	C _(s)	$14.6 \dot{w}_{R4} W_4 / W_3$
5	RDX _(g)	\dot{w}_{R5}
6	CH ₂ O	$W_6(3 \dot{w}_{R1} / W_1 + 17.8 \dot{w}_{R4} / W_3 - \dot{w}_{R6})$
7	N ₂ O	$W_7(3 \dot{w}_{R1} / W_1)$
8	HCN	$W_8(3 \dot{w}_{R2} / W_1 + 25.6 \dot{w}_{R4} / W_3)$
9	NO ₂	$W_9(1.5 \dot{w}_{R2} / W_1 - \dot{w}_{R6})$
10	NO	$W_{10}(1.5 \dot{w}_{R2} / W_1 + \dot{w}_{R6})$
11	H ₂ O	$W_{11}(1.5 \dot{w}_{R2} / W_1 + \dot{w}_{R4} / W_3 + \dot{w}_{R6})$
12	N ₂	$W_{12}(56 \dot{w}_{R3} / W_2)$
13	CO	$W_{13}(15.8 \dot{w}_{R4} / W_3 + \dot{w}_{R6})$
14	NH ₃	$W_{14}(14.4 \dot{w}_{R4} / W_3)$
15	C ₂ H ₄	$W_{15}(1.5 \dot{w}_{R4} / W_3)$
16	CH ₃ CHO	$W_{16}(16 \dot{w}_{R4} / W_3)$
17	C ₂ H ₃ CHO	$W_{17}(6.4 \dot{w}_{R4} / W_3)$
18	CH ₃ CHNH	$W_{18}(8 \dot{w}_{R4} / W_3)$
19	CH ₂ CHCHNH	$W_{19}(8 \dot{w}_{R4} / W_3)$

C. Gas-Phase Region

The species evolved from the propellant surface into the gas phase include vapor RDX, decomposition products of RDX and GAP, and unreacted GAP. Because condensed and gas species both exist in this region, a two-phase treatment similar to that described in the preceding section is employed to formulate the multiphase problem. With the assumption that body forces, viscous dissipation, and radiation emission/absorption effects are ignored, the isobaric conservation equations for both the condensed and gas phases can be combined and written as follows.

Mass

$$\frac{\partial[(1 - \phi_g)A\rho_c + \phi_g A\rho_g]}{\partial t} + \frac{\partial}{\partial x}[(1 - \phi_g)A\rho_c u_c + \phi_g A\rho_g u_g] = 0 \quad (19)$$

Condensed-Phase Species

$$\frac{\partial[(1 - \phi_g)A\rho_c Y_{c_i}]}{\partial t} + \frac{\partial}{\partial x}[(1 - \phi_g)A\rho_c u_c Y_{c_i}] = A\dot{w}_{c_i} \quad (i = 1, 2, \dots, N_c) \quad (20)$$

Gas-Phase Species

$$\begin{aligned} \phi_g A \rho_g \frac{\partial Y_{g_i}}{\partial t} + \phi_g A \rho_g u_g \frac{\partial Y_{g_i}}{\partial x} + \frac{\partial (\phi_g A \rho_g V_{g_i} Y_{g_i})}{\partial x} \\ = A \dot{w}_{g_i} - Y_{g_i} A \dot{w}_{c-g} \quad (i = 1, 2, \dots, N_g) \end{aligned} \quad (21)$$

Energy

$$\begin{aligned} \rho c_p A \frac{\partial T_g}{\partial t} - \frac{\partial (pA)}{\partial t} + \rho u c_p A \frac{\partial T_g}{\partial x} = \frac{\partial}{\partial x} \left(\lambda A \frac{\partial T_g}{\partial x} \right) - \phi_g A \sum_{j=1}^{N_g} \rho_g Y_{g_j} V_{g_j} c_{p_{g_j}} \frac{\partial T_g}{\partial x} \\ - A \sum_{j=1}^{N_g} \dot{w}_{g_j} h_{g_j} - A \sum_{j=1}^{N_c} \dot{w}_{c_j} h_{c_j} + A \sum_{j=1}^{N_g} h_{g_j} Y_{g_j} \dot{w}_{c-g} - A \sum_{j=1}^{N_c} h_{c_j} Y_{c_j} \dot{w}_{c-g} \end{aligned} \quad (22)$$

The thermophysical properties used in Eq. (22) are mass-averaged as follows:

$$\rho c_p = [(1 - \phi_g) \rho_c c_c + \phi_g \rho_g c_g], \quad (23)$$

$$\rho u c_p = [(1 - \phi_g) \rho_c u_c c_c + \phi_g \rho_g u_g c_g], \quad (24)$$

$$\lambda_g = [(1 - \phi_g) \rho_c u_c \lambda_c + \phi_g \rho_g u_g \lambda_g] / [(1 - \phi_g) \rho_c u_c + \phi_g \rho_g u_g] \quad (25)$$

The enthalpy of gas or condensed species i in Eq. (22) is defined as

$$h_i = \int_{T_{ref}}^T c_{p_i} dT + h_{f_i}^\circ \quad (26)$$

The mass diffusion velocity V_i consists of contributions from both concentration and temperature gradients,

$$V_i = -D_i \frac{1}{X_i} \frac{\partial X_i}{\partial x} + D_i \frac{D_{T_i}}{X_i} \frac{1}{T} \frac{\partial T}{\partial x} \quad (27)$$

Finally, the equation of state for a multicomponent system is used to close the formulation:

$$p = \rho_g R_u T_g \sum_{i=1}^{N_g} \frac{Y_{g_i}}{W_{g_i}} \quad (28)$$

The chemical reactions can be written in the following general form:

$$\sum_{i=1}^{N_g} v'_{ij} M_i \xrightleftharpoons[k_{bj}]{k_{fj}} \sum_{i=1}^{N_g} v''_{ij} M_i, \quad j = 1, 2, \dots, N_R \quad (29)$$

where v'_{ij} and v''_{ij} are the stoichiometric coefficients for i th species appearing as a reactant in j th forward and backward reactions, respectively, and M_i is the chemical symbol for i th species. The reaction rate constant k_j (either k_{fj} or k_{bj}) is given by the Arrhenius expression

$$k_j = A_j T^{B_j} \exp(-E_j / R_u T) \quad (30)$$

The rate of change of molar concentration of species i by reaction j is

$$\dot{C}_{ij} = (v'_{ij} - v''_{ij}) \left(k_{fj} \prod_{i=1}^{N_g} C_i^{v'_{ij}} - k_{bj} \prod_{i=1}^{N_g} C_i^{v''_{ij}} \right) \quad (31)$$

The total mass production rate of gas species i by both gas and condensed species in Eq. (21) is then obtained by summing up the changes due to all gas- and condensed-phase reactions:

$$\dot{w}_{gi} = \phi_g W_{gi} \sum_{j=1}^{N_R} \dot{C}_{ij} + \dot{w}_{c-g,gi} \quad (32)$$

where $\dot{w}_{c-g,gi}$ represents the mass conversion rate from liquid to gas of gas species i .

The gas-phase chemical kinetic scheme is composed of three submodels: 1) the RDX combustion mechanism⁶ containing 45 species and 232 reactions, 2) the initial decomposition reactions of GAP including, among others, aldehydes and imines, and 3) the hydrocarbon combustion mechanism containing 49 species and 279 reactions (see footnote, p. 479). Bimolecular decomposition reactions for the aldehydes (CH_3CHO and $\text{C}_2\text{H}_3\text{CHO}$) and imines (CH_3CHNH and CH_2CHCHNH) are assumed, and their kinetic rates are estimated, as indicated by reactions (R7-R10) in Table 1. In total, the gas-phase chemical kinetic process involves 71 species and 520 reactions.

The mass production rates of gas and condensed species generated by condensed-phase reactions in Eqs. (20) and (21) are described by reactions (R3) and (R4) of condensed species such as GAP and its intermediate product. Thus, the rate expressions of the reactions, except (R1), (R2), (R5), and (R6), listed in Table 2 are used to calculate the mass production rates of species generated from GAP decomposition.

D. Boundary Conditions

The physical processes in the gas phase and foam layer must be matched at the propellant surface to provide the boundary conditions for each region. This procedure requires balances of mass and energy, and eventually determines propellant surface conditions and burning rate. With the neglect of mass diffusion in the condensed phase, the conservation laws at the propellant surface can be written as follows:

Mass

$$[(1 - \phi_f)\rho_c u_c + \phi_f \rho_g u_g]_{0-} = [(1 - \phi_g)\rho_c u_c + \phi_g \rho_g u_g]_{0+} \quad (33)$$

Species

$$[(1 - \phi_f)\rho_c u_c Y_{ci} + \phi_f \rho_g u_g Y_{gi}]_{0-} = [(1 - \phi_g)\rho_c u_c Y_{ci} + \phi_g \rho_g (u_g + V_{gi}) Y_{gi}]_{0+} \quad (34)$$

Energy

$$\left[\lambda_f \frac{\partial T_f}{\partial x} + (1 - \phi_f) \rho_c u_c Y_{\text{RDX}_c} h_{\text{RDX}_{l \rightarrow g}} \right]_{0^-} = \left[\lambda_g \frac{\partial T_g}{\partial x} \right]_{0^+} + \dot{Q}_{\text{laser}}'' \quad (35)$$

The temperature is identical on both sides of the interface; however, the void fraction and species mass fractions might be different.

Since the propellant surface is defined as the interface where rapid phase transition occurs between the foam layer and gas-phase region, the distinct evaporation law of RDX is assumed to prevail at the interface, giving

$$[(1 - \phi_f) \rho_c u_c Y_{\text{RDX}_c}]_{0^-} = \left[s \bar{v}_n C_{\text{RDX}_g} \left(\frac{p_{v,\text{eq}}}{p} - X_{\text{RDX}_g} \right) \right]_{0^+} \quad (36)$$

It has been shown that $\rho_c u_c = \rho_g u_g$ is a good assumption in the two-phase model.⁸ Equation (33) becomes trivial and Eq. (34) can be written as follows when the assumption is applied to both the subsurface and gas-phase regions:

$$[(1 - \phi_f) Y_{c_i} + \phi_f Y_{g_i}]_{0^-} = \left[(1 - \phi_g) Y_{c_i} + \phi_g \left(1 + \frac{V_{g_i}}{u_g} \right) Y_{g_i} \right]_{0^+} \quad (37)$$

Taking summation of the following condensed species $\text{GAP}_{(l)}$, $\text{GAP}_{(l)}^*$, and $\text{C}_{(s)}$ gives that

$$[(1 - \phi_f)(1 - Y_{\text{RDX}_c})]_{0^-} = [(1 - \phi_g)]_{0^+} \quad (38)$$

Equations (35–38) are sufficient to solve the set of unknowns (u , T , Y_i , ϕ) at the propellant surface and provide the boundary conditions for the foam layer and gas phase.

The boundary conditions at the interface (melt front) between the solid phase and foam layer are

$$T_c = T_f = T_{\text{melt}} \quad \text{and} \quad \phi_f = 0 \quad \text{at} \quad x = x_{\text{melt}} \quad (39)$$

$$\left[\lambda_c \frac{\partial T_c}{\partial x} + \rho_c u_c Y_{\text{RDX}_c} h_{\text{RDX}_{s \rightarrow l}} \right]_{x_{\text{melt}}^-} = \left[\lambda_f \frac{\partial T_f}{\partial x} \right]_{x_{\text{melt}}^+} \quad (40)$$

The far-field conditions for the gas phase require the gradients of flow properties to be zero at $x = \infty$:

$$\frac{\partial \rho}{\partial x} = \frac{\partial u}{\partial x} = \frac{\partial Y_i}{\partial x} = \frac{\partial T}{\partial x} = 0 \quad \text{at} \quad x = \infty \quad (41)$$

The condition at the cold boundary for the condensed phase ($x = -\infty$) is

$$T_c = T_i \quad \text{as} \quad x \rightarrow -\infty \quad (42)$$

where T_i is the conditioned initial temperature of the propellant, and the initial compositions of RDX and GAP are also provided as input parameters.

III. Numerical Method

The theoretical formulation established in the previous section requires a robotic numerical method to solve the problem. All of the conservation equations and associated boundary conditions are coupled and solved by a double-iteration procedure that treats the propellant surface temperature T_s and burning rate r_b as eigenvalues. The procedure proceeds with T_s adjusted by an inner loop, while r_b is corrected by the outer iteration. The conservation equations for the subsurface region are first solved and the resulting species concentrations at the surface are used as the boundary conditions for the gas-phase region through the interfacial matching conditions. The next step involves integration of the gas-phase conservation equations to provide the temperature and species-concentration profiles. The nonequilibrium evaporation equation (36) is then employed to check the convergence of T_s . If not successful, another inner iteration is repeated using an updated value of T_s . The outer iteration follows the same procedure as the inner loop, except that r_b is used as the eigenvalue to check the interfacial energy continuity [Eq. (35)]. Because only the burning rate and surface temperature, but not interfacial species composition, are involved in the iterative procedure, the present algorithm performs quite well and significantly reduces the computational burden.

The conservation equations (4–7) for the subsurface region are fully coupled. However, they are solved by an uncoupled-iteration method. The method starts with an estimated temperature profile obtained by solving an inert energy equation, and then the conservation equations except the energy equation, i.e. Eqs. (4–6), are integrated using a fourth-order explicit Runge–Kutta method. Equation (7) is subsequently solved with the newly obtained void fraction and species concentrations to obtain a better temperature profile. Because the equations are solved separately, iteration is required to get a converged solution that satisfies all the conservation equations and boundary conditions.

The governing equations (19–22) for the gas phase are also fully coupled, and solved by an uncoupled-iteration method similar to the subsurface-region solver. Equation (20) is first solved using a fourth-order explicit Runge–Kutta method to get the void fraction and the mass fractions of condensed species. Equations (19), (21), and (22) are then solved using the Chemkin–Premix¹³ package with some modifications since the governing equations have been changed to account for a two-phase system. The grid systems of the two solvers are different, and direct interpolation is used to match the grid information. Iteration is performed to ensure all equations are satisfied simultaneously.

IV. Results and Discussion

The theoretical formulation and numerical method described in the preceding sections have been applied to a broad range of pressure and laser intensity with various RDX/GAP compositions. Model results show good agreement with the measured burning rates at atmospheric pressure. Litzinger et al.¹⁴ have measured the burning rates and species concentration profiles of RDX/GAP pseudo propellants with a mass ratio 8:2 using a triple quadrupole mass spectrometer (TQMS). The measured burning rate is 0.8 mm/s at 1 atm with a CO₂ heat flux of 100 W/cm². The calculated value at the same condition is 0.88 mm/s. The measured rate for 300 W/cm² is 1.9 mm/s whereas the predicted value is 2.18 mm/s. The flame structure observed in experiments¹⁴ is also reasonably well predicted by the

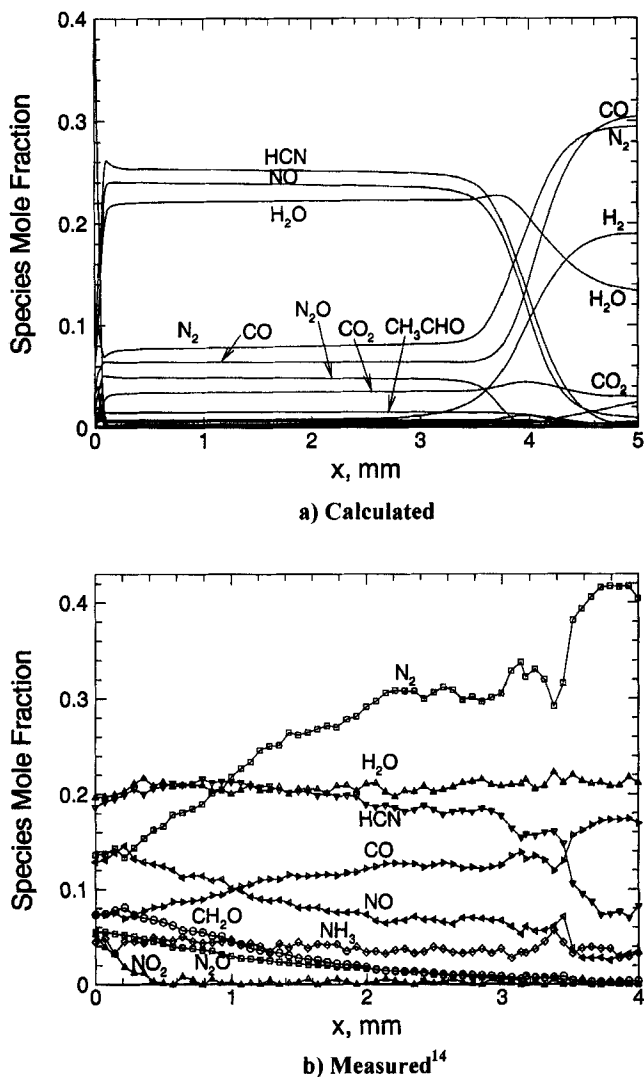


Fig. 4 Species profiles of the gas-phase flame of RDX/GAP pseudo propellant (mass ratio 8:2) at 1 atm and laser intensity 100 W/cm^2 .

model. Figure 4 shows the predicted and measured¹⁴ species concentration profiles in the gas phase at 1 atm and 100 W/cm^2 . It is found that HCN, NO, and H_2O are the major intermediate products in the so-called dark zone. Similar to RDX monopropellant combustion, the conversion of HCN and NO to N_2 and CO dominates the luminous flame whereas the consumption of formaldehyde, NO_2 , and N_2O accounts for the primary flame above the surface. In contrast to RDX combustion, a noticeable amount (1–2%) of CH_3CHO has been observed near the surface. The agreements between the predicted and measured concentration profiles of CO, CO_2 , and formaldehyde are not as good as the others. Chemical equilibrium

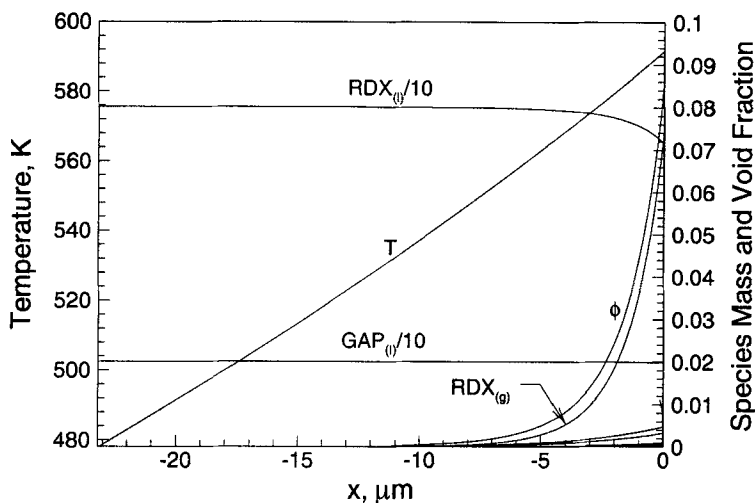


Fig. 5 Predicted flame structure in the foam layer of RDX/GAP pseudo propellant (mass ratio 8:2) at 1 atm and laser intensity 100 W/cm^2 .

calculation has also been performed in this study. The result matches the model output but not the experimental data. Even though the agreement between measured and computed burning rates is reasonably good, further investigations into the combustion wave are suggested to resolve the discrepancy in flame structure.

In the foam layer, Fig. 5 shows that the predicted temperature rises from the melt point of RDX at 478 K to around 590 K at the propellant surface. The mass fraction of liquid RDX originates at 0.8 and decreases slightly, mostly through evaporation and partially through decomposition. The void fraction increases from 0 to almost 9% due to the formation of bubbles containing vapor RDX and a small amount of decomposed gases. Consistent with the condensed-phase kinetics, the extent of GAP decomposition is negligible at temperatures lower than 600 K. The mass fraction of GAP remains at 0.2 throughout the foam layer, and then evolves into the gas phase. Figure 6 shows the predicted temperature, void fraction, and condensed species concentration profiles in the region immediately above the propellant surface. GAP starts to decompose in the gas phase when the temperature reaches 700 K. At this stage, GAP^* is immediately formed because of the elimination of N_2 and reaches its maximum concentration within a short distance (less than 0.004 cm). The peak value of GAP^* mass fraction is less than 10%. The calculated concentration of carbon residue in this case is negligible. If the propellant surface is defined as the location where all condensed species are gasified, the surface temperature would be around 1000 K, consistent with GAP combustion.

Figure 7 shows the predicted pressure dependence of burning rate for a RDX/GAP pseudo propellant with a mass ratio of 8:2. It is found that the burning rate–pressure relation follows a power law that is applicable to many propellants with the exponent $n = 1$, whereas $n = 0.83$ for pure RDX. The exponent value $n = 1$ indicates that the addition of GAP does alter the combustion characteristics of RDX. Figure 8 shows the temperature sensitivity of burning rate at various

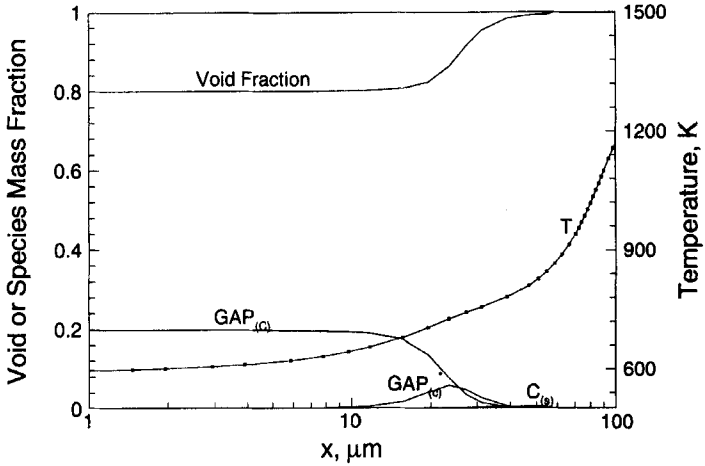


Fig. 6 Predicted temperature, void fraction, and condensed species concentration profiles in the near surface region of RDX/GAP pseudo propellant (mass ratio 8:2) at 1 atm and laser intensity 100 W/cm².

pressures. The sensitivity coefficient is defined as

$$\sigma_p = \left. \frac{\partial(\ln r_b)}{\partial T_{ini}} \right|_p \quad (43)$$

The temperature sensitivity of burning rate decays at high pressures since the heat feedback is more profound than the effect of initial temperature on the burning rate.

Figures 9–12 show the predicted combustion characteristics of RDX/GAP pseudo propellants at various pressures and initial temperatures. Figure 9 shows

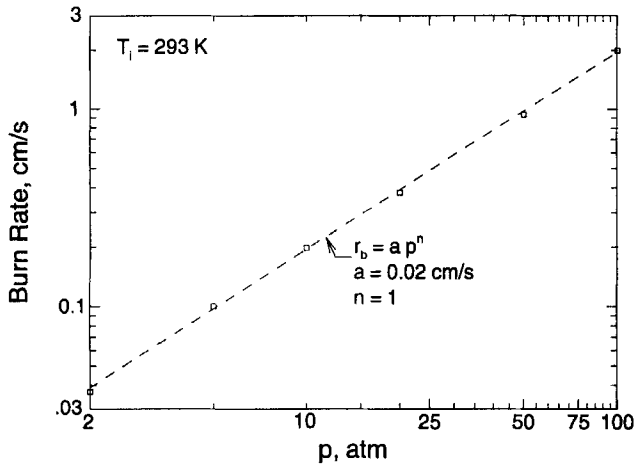


Fig. 7 Predicted pressure dependence of burning rate of RDX/GAP pseudo propellant (mass ratio 8:2).

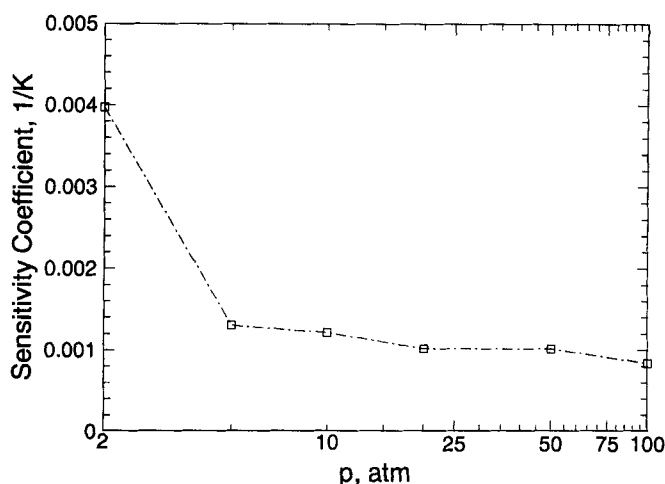


Fig. 8 Predicted temperature sensitivity of burning rate of RDX/GAP pseudo propellant (mass ratio 8:2).

that the surface temperature increases linearly with increasing pressure on the logarithmic scale, but it is not very sensitive to initial temperature. It is understandable because surface temperature is resolved by an energy balance, and the heat flux is strongly dependant on pressure but not initial temperature. Figure 10 shows that the adiabatic flame temperature increases with both increasing pressure and initial temperature. The increase is not linear due to the limitation of grid resolution and the nonlinearity of chemical kinetics. Figure 11 shows that the melt-layer thickness decreases with increasing pressure but is not sensitive to initial temperature. In general, the melt-layer thickness decreases with increasing

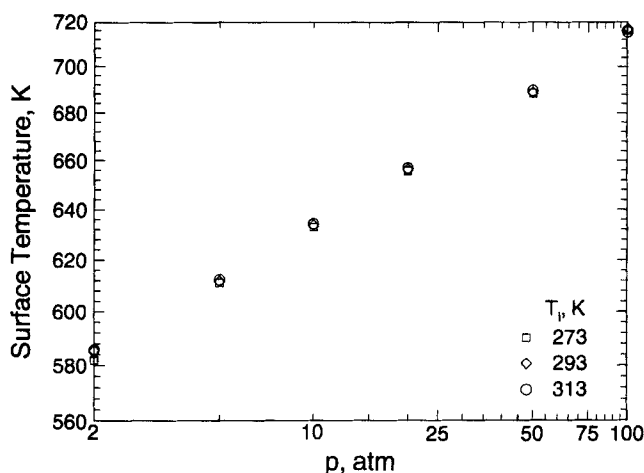


Fig. 9 Predicted surface temperature of RDX/GAP pseudo propellant (mass ratio 8:2) at various pressures and initial temperatures.

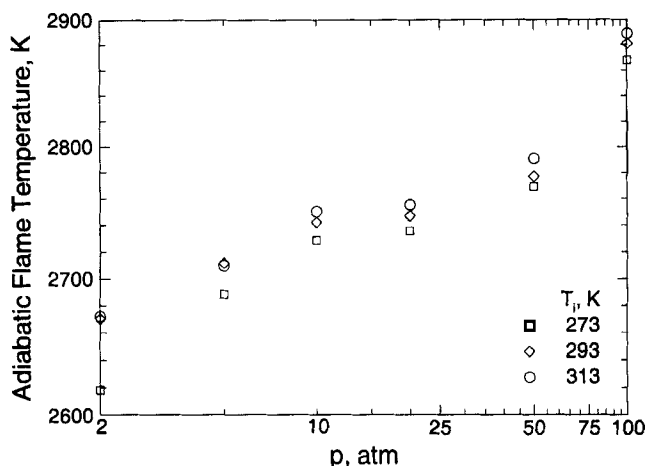


Fig. 10 Predicted adiabatic flame temperature of RDX/GAP pseudo propellant (mass ratio 8:2) at various pressures and initial temperatures.

burning rate, but increases with the higher values of thermal conductivity of the propellant. As shown in Fig. 7, the burning rate is linearly dependant on pressure, and thus the pressure dependence of melt-layer thickness is also linear. The initial temperature of propellant does not exhibit a strong effect on the melt-layer thickness, because both the burning rate and thermal conductivity are not very sensitive to initial temperature. Figure 12 shows that the surface void fraction decreases with increasing pressure, but increases with increasing initial temperature. It is not surprising because the bubble formation strongly depends on the evaporation process, which is retarded at high pressures but enhanced at high initial temperatures.

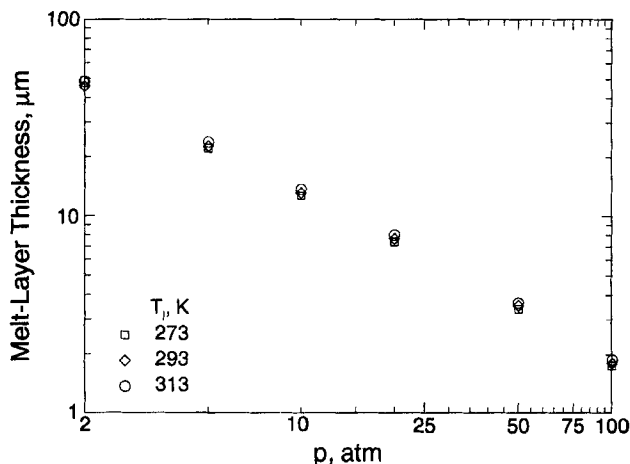


Fig. 11 Predicted melt-layer thickness of RDX/GAP pseudo propellant (mass ratio 8:2) at various pressures and initial temperatures.

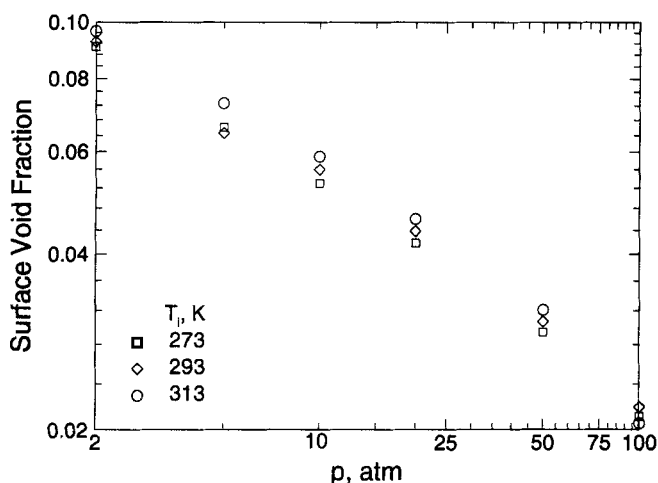


Fig. 12 Predicted surface void fraction of RDX/GAP pseudo propellant (mass ratio 8:2) at various pressures and initial temperatures.

Figures 13 through 17 show the effect of laser heat flux on the burning rate, surface heat flux, surface temperature, melt-layer thickness, and surface void fraction at pressure levels of 1, 10, and 100 atm. The laser represents an external heat flux absorbed by the propellant surface. Therefore, the burning rate and surface temperature increase with increasing laser heat flux. The effect decays with increasing pressure because the heat feedback from the gas phase increases with increasing pressure. The melt-layer thickness exhibits an opposite trend; it decreases with increasing burning rate, and its decreasing rate is consistent with the increasing rate of burning rate. Figure 17 shows the effect of laser heat flux on the surface

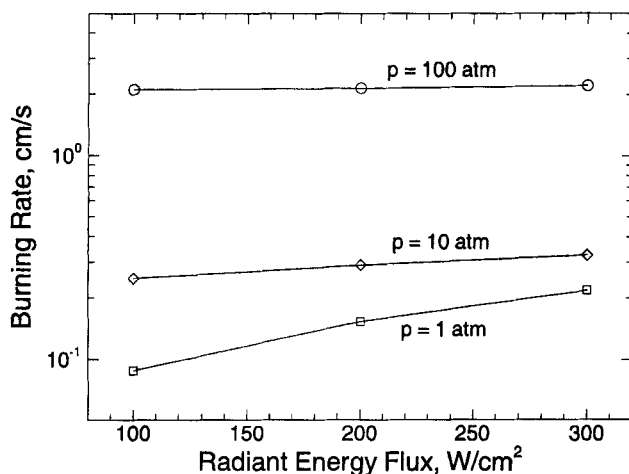


Fig. 13 Predicted effect of laser flux on burning rate at various pressures.

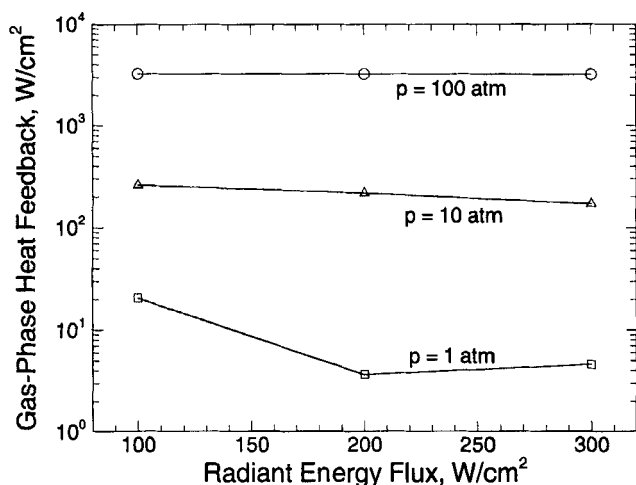


Fig. 14 Calculated gas-phase heat feedback at propellant surface at various laser and pressure levels.

void fraction, which is often visually observed by many researchers. Opposite to the heat feedback from the gas phase at high pressures, the laser heat flux increases bubble formation, up to 50% at the surface at 1 atm and $300 W/cm^2$.

The final set of results shows the predicted effects of binder mass fraction on the combustion characteristics over a broad range of pressure and initial temperature. Here, it is possible to use the model to describe experimental observations. For example, the burning rate of pure GAP is higher than that of HMX, but the addition of GAP into HMX lowers the burning rate.¹⁵ On the contrary, recent measurements¹⁴ show the enhancement of burning rate by adding GAP into RDX or HMX. Both

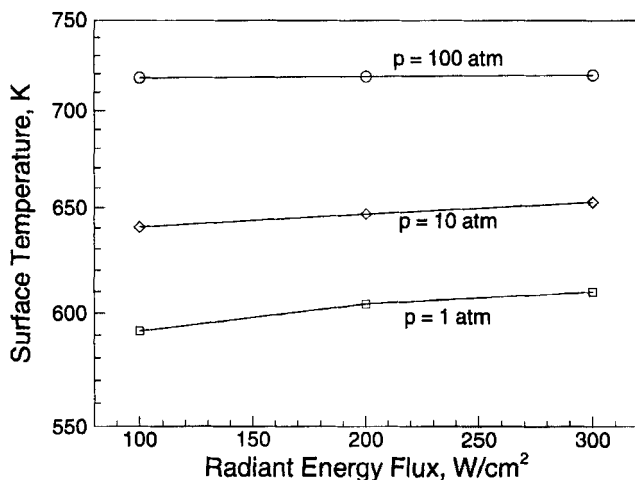


Fig. 15 Predicted effect of laser flux on surface temperature at various pressures.

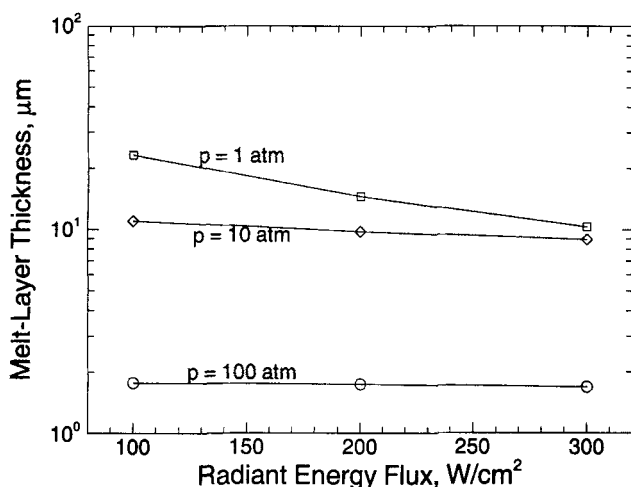


Fig. 16 Predicted effect of laser flux on melt-layer thickness at various pressures.

observations have been reproduced by the model. Figure 18 shows the effects of initial composition and pressure on the burning rate of RDX/GAP pseudo propellants. The burning rate decreases in the case of higher GAP composition because GAP decomposition produces inert gases that dilute the concentrations of surface reactive species, and thus retard the heat feedback from the gas phase as shown in Fig. 19. It is evident that the heat feedback is the controlling factor for the burning rate in all of the cases without laser, because the pressure dependence of burning rate is similar to that of heat feedback. The addition of GAP changes the slopes (pressure dependencies) in Figs. 18 and 19, but not in a consistent trend. A small amount of GAP (10% by weight) increases the slope and makes the system

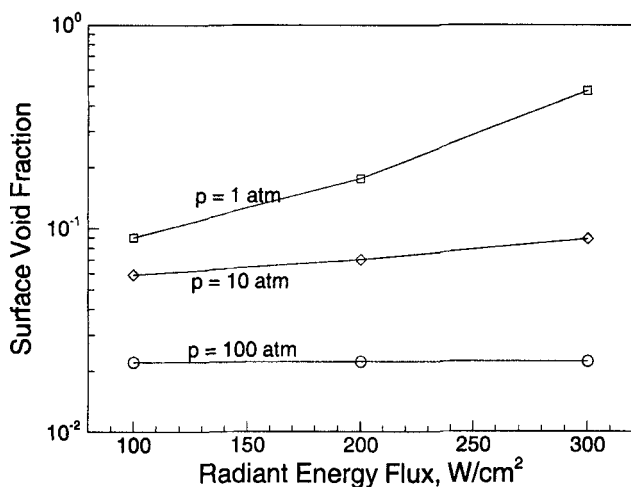


Fig. 17 Predicted effect of laser flux on surface void fraction at various pressures.

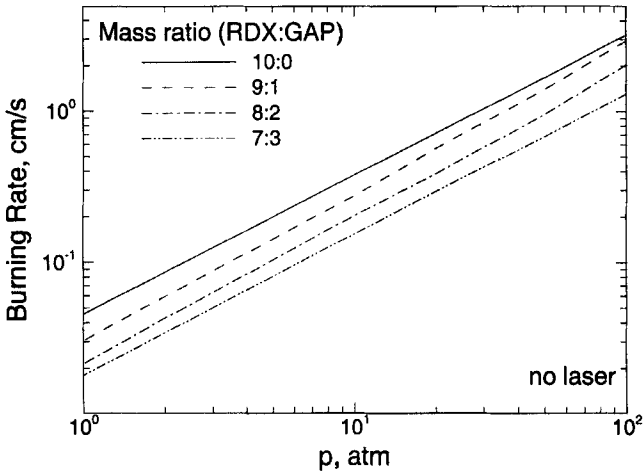


Fig. 18 Predicted effect of propellant formulation on burning rate at various pressures.

unstable, whereas more GAP (30% by weight) restores the slope to the pure RDX case but reduces the burning rate by more than 50%. Figure 20 shows the burning rate at 10 atm with various compositions and laser levels. The profiles of mass ratios 10:0 and 9:1 are very close, indicating the burning-rate change caused by addition of a small amount of GAP is negligible for laser heat fluxes ranging from 100 to 300 W/cm². For higher GAP compositions (20 and 30% by weight), the burning rates decrease at 100 W/cm², but increase at 200 and 300 W/cm². The effect is more profound at low pressures since the conductive heat feedback from the gas phase is of less importance in the case of laser-assisted combustion. However,

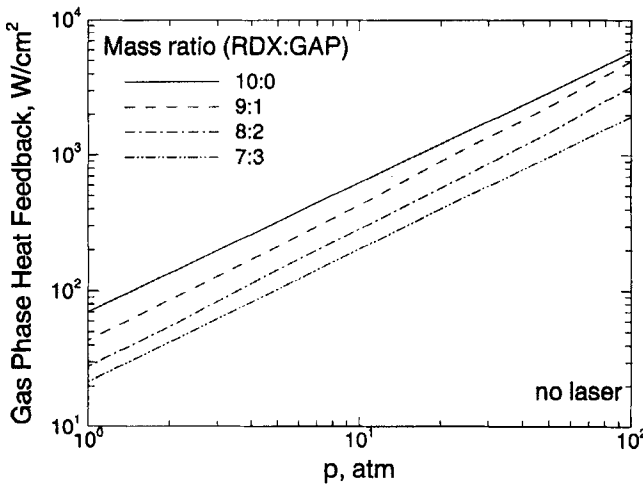


Fig. 19 Calculated gas-phase heat feedback to propellant surface at various composition and pressure levels.

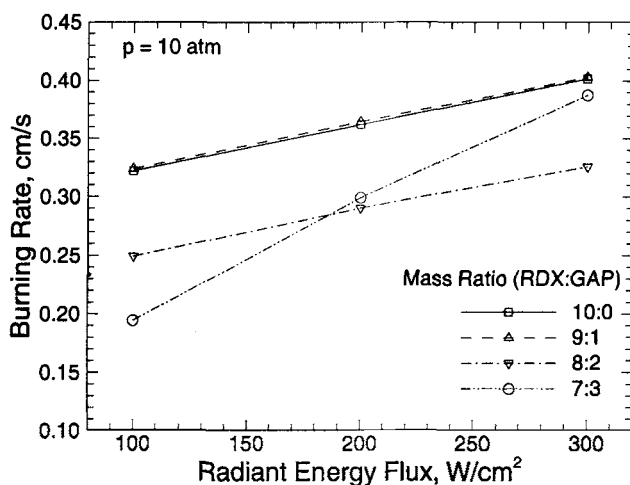


Fig. 20 Predicted effect of propellant formulation on burning rate at various laser and composition levels.

more experimental data are required for model validation as well as an improved chemical kinetics mechanism of GAP decomposition.

V. Conclusions

A numerical analysis has been developed for studying the key physico-chemical processes involved in combustion of RDX/GAP pseudo propellants. The analysis is based on the conservation equations of mass, energy, and species for both the condensed and gas phases, and takes into account finite-rate chemical kinetics and real thermophysical properties. The model has been applied to a broad range of pressure and laser intensity with various binder compositions. Reasonably good agreement is achieved between the predicted and measured burning rate and species concentration profiles at a laser intensity of $100 W/cm^2$ under atmospheric pressure. At low pressures, the laser heat flux exhibits a strong effect on the combustion characteristics such as surface temperature, burning rate, and melt-layer thickness. The effect declines at high pressures since the conductive heat feedback from the gas to the condensed phase becomes stronger. In this work, it is found that the addition of GAP does not enhance the burning rate for the case without external heat flux, even though the burning rate of GAP itself is higher than that of pure RDX. Conversely, with the assistance of external heat flux, the burning rate of pseudo propellants increases with the higher concentration of GAP when the laser intensity is high enough.

Acknowledgments

This work was sponsored partly by Pennsylvania State University, partly by Science Applications International Corporation, and partly by the California Institute of Technology Multidisciplinary University Research Initiative under ONR Grant No. N00014-95-1-1338.

References

- ¹Melius, C. F., "Thermochemical Modeling: I & II," *Chemistry and Physics of Energetic Materials*, Edited by S. N. Bulusu, Kluwer Academic, Norwell, MA, 1990, pp. 21–78.
- ²Liau, Y.-C., and Yang, V., "Analysis of RDX Monopropellant Combustion with Two-Phase Subsurface Reactions," *Journal of Propulsion and Power*, Vol. 11, No. 4, 1995, pp. 729–739.
- ³Davidson, J. E., and Beckstead, M. W., "Improvements to Steady-State Combustion Modeling of Cyclotrimethylenetrinitramine," *Journal of Propulsion and Power*, Vol. 13, No. 3, 1997, pp. 375–383.
- ⁴Davidson, J. E., and Beckstead, M. W., "A Three-Phase Model of HMX Combustion," *Twenty-Sixth Symposium (International) on Combustion*, Combustion Inst., Pittsburgh, PA, 1996, pp. 1989–1996.
- ⁵Prasad, K., Yetter, R. A., and Smooke, M. D., "An Eigenvalue Approach for Computing the Burning Rates of RDX Propellants," *Combustion Science and Technology*, Vol. 124, No. 1-6, 1997, pp. 35–82.
- ⁶Prasad, K., Yetter, R. A., and Smooke, M., "An Eigenvalue Method for Computing the Burning Rates of HMX Propellants," *Combustion and Flame*, Vol. 115, 1998, pp. 406–416.
- ⁷Yetter, R. A., Dryer, F. L., Allen, M. T., and Gatto, J. L., "Development of Gas-Phase Reaction Mechanisms for Nitramine Combustion," *Journal of Propulsion and Power*, Vol. 11, No. 4, 1995, pp. 683–697.
- ⁸Liau, Y.-C., *Numerical Analysis of RDX Monopropellant Combustion with Two-Phase Subsurface Reactions under Steady and Transient Conditions*, Ph.D. Thesis, Pennsylvania State Univ., University Park, PA, 1997.
- ⁹Brill, T. B., "Multiphase Chemistry Considerations at the Surface of Burning Nitramine Propellants," *Journal of Propulsion and Power*, Vol. 11, No. 4, 1995, pp. 740–751.
- ¹⁰Arisawa, H., and Brill, T. B., "Thermal Decomposition of Energetic Materials 71. Structure-Decomposition and Kinetic Relationships in Flash Pyrolysis of Glycidyl Azide Polymer (GAP)," *Combustion and Flame*, Vol. 112, 1998, pp. 533–544.
- ¹¹Sysak, G. S., Kim, E. S., and Thynell, S. T., "Decomposition Rates of Glycidyl Azide Polymer from Confined Rapid Thermolysis/Infrared Spectroscopic Technique," *Proceedings of 35th JANNAF Combustion Meeting*, Tucson, AZ, Dec. 7–11, 1998.
- ¹²Tang, C.-J., Lee, Y. J., Kudva, G., and Litzinger, T. A., "Simultaneous Temperature and Species Measurements of the Glycidyl Azide Polymer (GAP) Propellant During Laser-Induced Decomposition," *Combustion and Flame*, Vol. 116, 1999, pp. 244–256.
- ¹³Kee, R. J., Grcar, J. F., Smooke, M. D., and Miller, J. A., "A Fortran Program for Modeling Steady, Laminar, One-Dimensional, Premixed Flames," Sandia National Lab. Rept. No. SAND85-8240, Albuquerque, NM, 1985.
- ¹⁴Litzinger, T. A., Lee, Y.-J., and Tang, C.-J., "Experimental Study of Nitramine/Azide Propellant Combustion," *Solid Propellant Chemistry, Combustion, and Motor Interior Ballistics*, Vol. 185, edited by V. Yang, T. B. Brill, and W. Z., Ren, Progress in Astronautics and Aeronautics, AIAA, Reston, VA, 2000, Chap. 2.4.
- ¹⁵Kubota, N., and Sonobe, T., "Burning Rate Catalysis of Azide/Nitramine Propellants," *Twenty-Third Symposium (International) on Combustion*, Combustion Inst., Pittsburgh, PA, 1990, pp. 1331–1337.

Energetic-Material Combustion Modeling with Elementary Gas-Phase Reactions: A Practical Approach

Martin S. Miller* and William R. Anderson*

U.S. Army Research Laboratory, Aberdeen Proving Ground, Maryland

I. Introduction

THE past 10 years have seen an important paradigm shift in the modeling of energetic-material combustion. Models for which chemically nonspecific reaction formalisms were used have given way to models that promise to explain the detailed chemical nature of combustion through their explicit elementary-reaction mechanisms. The seminal prototypes for the chemically nonspecific models were developed during the Second World War by Parr and Crawford¹ and Rice and Ginell.² Typically, these models considered a gasification reaction at the surface of the condensed phase and a single overall reaction in the gas phase; burning rates were computed by imposing the energy and species conservation equations in each phase and at the burning surface. A conceptual review of many of these models was given by Miller³ and a review of their application to composite propellants was provided by Ramohalli.⁴ These early models elucidate the interplay between the chemical and the physical phenomena that produce the observed patterns of burning-rate dependence on pressure and initial temperature and provide guidance in the choice of some physical features of composite-propellant formulation, such as oxidizer particle size. By their nature, however, they cannot give guidance for chemical formulation and the effects of chemical additives on performance. This role had to await the development of chemically specific descriptions of the combustion. Models with explicit chemical mechanisms now dominate new development activities and are the subject of this article. We confine ourselves here to steady-state combustion, although some recent work^{5,6} has addressed the role of elementary reactions in ignition.

The transition from overall reactions to detailed elementary reactions in the modeling of energetic-material combustion did not occur suddenly and, in fact, is

This material is declared a work of the U.S. Government and is not subject to copyright protection in the United States.

*Research Physicist, Weapons and Materials Research Directorate.

not yet complete. Thus far, the use of elementary reactions has been limited to the gas phase; our fundamental understanding of the condensed-phase processes does not allow more sophistication at present. In the interim, condensed-phase reactions have been treated as one or more overall reactions. Reaction mechanisms for the gas phase were first developed apart from any attempt to compute the burning rate. As early as 1965, Sotter⁷ assembled a mechanism consisting of 12 species reacting by 17 reversible reactions to describe the secondary reaction zone of double-base propellants. He numerically integrated this mechanism, neglecting transport processes, and found order-of-magnitude agreement with experimentally determined induction times for the visible flame. Ermolin et al., in the early-to-mid-1980s, worked out elementary-reaction mechanisms for NH_4ClO_4 (Ref. 8) and cyclotrimethylenetrinitramine⁹ (RDX), guided by mass spectrometric measurements in the flames of these condensed systems.

Attempts to compute the burning rate of an energetic material by use of realistic chemistry probably began with the treatment by Guirao and Williams¹⁰ of NH_4ClO_4 in 1971. Although the chemical mechanism consisted of 14 species and 10 irreversible reactions, a small problem by today's standards, computational tools at that time did not permit the simultaneous solution of the kinetics and the transport. A simplified simultaneous solution of kinetics and transport for a larger mechanism of 19 species and 60 reversible reactions was reported by Hatch¹¹ in 1986 for nitroglycerine (NG). A significant advance in the computational tools available for work of this type occurred in 1985 with the publication and availability of the PREMIX code,¹² a user-friendly, well-documented, one-dimensional, premixed-laminar-flame code. This code and its later improvements provide a high level of rigor to the description of gas-phase transport, allowing such subtle effects as thermal diffusion and multicomponent transport to be conveniently treated. Moreover, the description of thermodynamic functions, transport parameters, reactions, and reaction rates in this code is also very general, allowing a wide scope of kinetic representations and convenient updating. Melius¹³ was the first to utilize the PREMIX code in a calculation of energetic-material burning rate, addressing the case of RDX. In the United States, as a result of several workshops by the U.S. Office of Naval Research and the U.S. Army Research Office starting in approximately 1987, a concerted effort was directed at understanding the physics and the chemistry of RDX as a prototypical system. This focus resulted in a number of further refinements of RDX modeling.¹⁴⁻¹⁷ Extensions of these general methods have been made to include cyclotetramethylene tetranitramine (HMX)^{18,19} and glycidyl azide polymer²⁰ (GAP). To study the physical aspects of three-phase combustion, Miller²¹ described a detailed chemical model applied to the combustion of frozen ozone as a prototypical energetic material for which very reliable kinetic and thermophysical data exist.

The focus of this chapter is on models that compute the burning rate based on detailed elementary-reaction mechanisms in the gas phase. However, it is worth mentioning a few models that are chemically specific to some degree and utilize overall reactions to describe the gas phase. An early example of this type of model is that of BenReuven et al.,^{22,23} who treated the combustion of RDX by using one overall reaction in the liquid phase, evaporation as the surface-gasification mechanism, and two overall reactions in the gas phase. Another example was advanced by Bizot and Beckstead,²⁴ who considered double-base propellant combustion by using three overall reactions in the condensed phase and two overall reactions in

the gas phase. A recent model attempting to simplify the very complex chemistry involved in double-base propellants is that by Song and Yang.²⁵ Like the model of Bizot and Beckstead, the model of Song and Yang lumps species into categories such as aldehydes and oxidizers. Yet another approach in this vein was taken by Li and Williams,²⁶ who argued for the dissociation of HONO as the rate-limiting step in the primary gas-phase mechanism of RDX and then applied asymptotic analysis to compute the burning rate based on this one reaction. The relative simplicity of these models is appealing, but it will take time to determine the extent to which generality and even understanding is sacrificed.

II. Conceptual Framework

As stated in Sec. I, our primary interest here is in that class of models that strive to describe the gas-phase reactions as true elementary reactions, the rate coefficients for which are determined from independent kinetics experiments, reaction-rate theory, or thermochemical estimation methods. This restriction narrows the number of models to only four.^{14,16,17,21} In this chapter we describe a fifth approach. In developing this new approach, we apply it to RDX. It is therefore helpful to review some of the details of the other RDX models^{14,16,17} (i.e., those in our restricted subset of model types).

All three models^{14,16,17} defer to the experimental work of Brill et al.²⁷ for a description of the condensed-phase reactions in RDX. Brill and his coworkers found that RDX decomposes by two competing channels, R1 and R2 (see Table 1). Unfortunately, their experiment was unable to distinguish among several possible R2 paths, R2a, R2b, and R2c. Both Prasad et al.¹⁶ and Davidson and Beckstead¹⁷ elected to use R2a for the second path. Liao and Yang¹⁴ suggested and used in their model another interpretation of Brill's measurements, R2d. One can see from Table 1 that the degree of endothermicity among the different R2 paths varies dramatically. Unless condensed-phase reactions are unimportant to the deflagration of RDX, one would expect such differences to have a significant effect on the computed burning rate. Because the three models being considered differ in many details other than the condensed-phase reactions just discussed and the burning rates computed by each of the models agree quite well with experimental burning

Table 1 Liquid-phase reactions in deflagrating RDX adopted by various models

Reaction number	Reaction	Heat of reaction at 570 K, ^a kcal/mole	Model
R1	$\text{RDX} \rightarrow 3\text{CH}_2\text{O} + 3\text{N}_2\text{O}$	-47	All ^{14,16,17}
R2a	$\text{RDX} \rightarrow 3\text{H}_2\text{CN} + 3\text{NO}_2$	179	Prasad et al. ¹⁶ ; Davidson and Beckstead ¹⁷
R2b	$\text{RDX} \rightarrow 3\text{HCN} + 3\text{HONO}$	19	
R2c	$\text{RDX} \rightarrow 3\text{HCN} + 3\text{NO}_2 + 3\text{H}$	257	
R2d	$\text{RDX} \rightarrow 3\text{HCN} + \frac{3}{2}\text{NO} + \frac{3}{2}\text{NO}_2 + \frac{3}{2}\text{H}_2\text{O}$	34	Liao and Yang ¹⁴

^aThis is the computed surface temperature at 1 atm.

rates, it is impossible to see the effects of the different liquid-phase reactions in isolation. Nonetheless, it may be significant that the amounts of RDX decomposition reported to occur in the condensed phase vary from as much as 40% (Ref. 16) to 25% (Ref. 17) to a limited amount¹⁴ among these models.

Our intention in this discussion is to highlight the fact that although the computational power now exists to treat condensed-phase reactions, our knowledge of these reactions (even at the level of overall descriptions, let alone an elementary-reaction description) is very limited at the present time. This uncertainty is not confined simply to the rate coefficients but extends to the very identities of both the reactants and the products involved in these reactions. We believe that these difficulties will not soon be resolved, and it is with this prospect in mind that we propose the following new and more practical approach.

A key present difficulty with chemically specific models is the determination of the identity and the mole fractions of chemical species that first emerge from the condensed phase into the gas phase and their rates of formation. We show that, given this knowledge and a reaction mechanism for the gas phase, one can compute the burning rate. One additional requirement is an expression relating the burning rate to the surface temperature; this is discussed in Sec. III. Although there is an element of speculation required in identifying the chemical species emerging from the condensed phase, it is much reduced from having to speculate on the reactions occurring in the condensed phase and the rate coefficients of those reactions. Techniques to measure or calculate those condensed-phase processes are not likely to be realized soon; thus the semiempirical approach described here can be thought of as a practical, interim strategy, pending the development of definitive tools for investigating the condensed phase. With these enabling simplifications, the model can readily be adapted to many worthwhile purposes, including experimental testing of gas-phase reaction mechanisms, computing the burning rate of multi-ingredient propellant formulations, and predicting the effect of chemical additives on the burning rate.

III. Mathematical Framework

We consider the one-dimensional, steady-state deflagration of a condensed substance that is oriented in a coordinate system moving with the linear regression velocity such that the unreacted material at an initial temperature of T_0 extends to $x = -\infty$, the regressing surface is always at $x = 0$ with temperature T_s , and the final gaseous combustion products at temperature T_f are found at $x = +\infty$. The mass conservation equation can be integrated simply to give

$$\dot{m} = \rho u = \rho_s r \quad (1)$$

where \dot{m} is the mass burning rate or mass flux, ρ and u are the mass density and the mixture mass velocity at any point in the interval, respectively, ρ_s is the mass density of the unreacted material at its initial temperature, and r is the linear regression rate of the surface. The continuity equation for each chemical species i is

$$\frac{d}{dx}(\rho Y_i V_i) + \dot{m} \frac{dY_i}{dx} - \dot{\omega}_i W_i = 0 \quad (2)$$

Here Y_i is the mass fraction of the i th species, V_i is the diffusion velocity of the i th species, $\dot{\omega}_i$ is the molar production rate by reactions of the i th species per unit volume, and W_i is the molecular weight of the i th species. Finally, the equation of energy conservation for this system is

$$\frac{d}{dx} \left(\lambda \frac{dT}{dx} \right) - \dot{m} \bar{c}_p \frac{dT}{dx} - \sum_i^N \rho Y_i V_i c_{p_i} - \sum_i^N \dot{\omega}_i h_i W_i = 0 \quad (3)$$

where λ is the mixture thermal conductivity, \bar{c}_p is the mixture specific heat, c_{p_i} is the specific heat of the i th species, h_i is the enthalpy of the i th species, and N is the total number of species being considered.

These equations are to be solved in the condensed and the gas phases and their solutions matched through appropriate boundary conditions at the surface. In the condensed phase the energy boundary conditions are

$$T = T_0 \quad \text{at} \quad x = -\infty, \quad T = T_s \quad \text{at} \quad x = 0 \quad (4)$$

and the species boundary conditions are

$$Y_i = Y_i^{-\infty} \quad \text{at} \quad x = -\infty, \quad Y_i = Y_i^{-0} \quad \text{at} \quad x = -0 \quad (5)$$

In the gas phase the energy-equation boundary conditions are

$$T = T_s \quad \text{at} \quad x = +0, \quad \frac{dT}{dx} = 0 \quad \text{at} \quad x = +\infty \quad (6)$$

and the gas-phase boundary condition on each species is

$$Y_i = Y_i^{+0} \quad \text{at} \quad x = +0, \quad \frac{dY_i}{dx} = 0 \quad \text{at} \quad x = +\infty \quad (7)$$

At the surface between these two regions the continuity of species and energy flux is guaranteed by the following two boundary conditions. Continuity of species flux at the surface is expressed by

$$\dot{m} Y_i^{-0} + \rho_c Y_i^{-0} V_i^{-0} = \dot{m} Y_i^{+0} + \rho_g Y_i^{+0} V_i^{+0} \quad (8)$$

where the superscripts -0 and $+0$ and c and g refer to the condensed and the gas sides of the surface, respectively. Continuity of the energy flux across the surface boundary is expressed by

$$\begin{aligned} & -\lambda_c \left(\frac{dT}{dx} \right)^{-0} + \dot{m} \sum_i^N Y_i^{-0} h_i^{-0} + \rho_c \sum_i^N Y_i^{-0} V_i^{-0} h_i^{-0} \\ & = -\lambda_g \left(\frac{dT}{dx} \right)^{+0} + \dot{m} \sum_i^N Y_i^{+0} h_i^{+0} + \rho_g \sum_i^N Y_i^{+0} V_i^{+0} h_i^{+0} \end{aligned} \quad (9)$$

The preceding, quite general equations are the starting point for our simplifications. In the gas phase these conservation equations are solved numerically with the PREMIX code¹² as a subroutine; thus the gas phase is treated with full rigor in our model. In the condensed phase we assume 1) that there are no in-depth chemical reactions, and 2) molecular diffusion is negligible.

With these assumptions the energy equation in the condensed phase reduces to

$$\frac{d}{dx} \left(\lambda \frac{dT}{dx} \right) - \dot{m} \frac{d}{dx} \left(\sum_i^N Y_i h_i \right) = 0 \quad (10)$$

Integrating this equation from $x = -\infty$ to -0 , one obtains

$$\lambda_c \left(\frac{dT}{dx} \right)^{-0} = \dot{m} \sum_i^N Y_i^{-0} h_i^{-0} - \dot{m} \sum_i^N Y_i^{-\infty} h_i^{-\infty} \quad (11)$$

Substituting Eqs. (11) and (8) into Eq. (9), one obtains

$$\lambda_g \left(\frac{dT}{dx} \right)^{+0} = \dot{m} \sum_i^N (Y_i^{-0} h_i^{+0} - Y_i^{-\infty} h_i^{-\infty}) \quad (12)$$

This is the form of the energy-flux boundary condition used in the model developed in this study. Note that one does not need to know the enthalpies of the species on the condensed-phase side of the surface at T_s , only their mass fractions there. This is important because heats of desorption of the nascent gas-phase species may be difficult to estimate. We are not aware of this form of the energy-flux boundary condition ever having been previously published, perhaps because of the novelty of the present context of a single overall condensed-phase reaction being coupled to a full elementary-reaction description of the gas-phase. This equation enables our treatment. Note also that neither the thermal conductivity, the mass density, nor the specific heat of the condensed phase at temperatures near the surface is required; the values of all these quantities are very uncertain. Only the specific heat and the mass density of the unreacted material over the range of initial temperatures are required, at least for purposes of computing the burning rate. Of course, if one needs the temperature profile through the condensed phase, then a further integration with values for these parameters over the full condensed-phase temperature range will be required.

To compute a burning rate, one must supply the enthalpy and the mass density of the unreacted energetic material over the range of initial temperatures, a set of products (species and mole fractions) of the condensed-phase decomposition, a rate of appearance of these decomposition products as a function of surface temperature, and finally an elementary reaction mechanism through which these decomposition products react in the gas phase. The condensed-phase decomposition products become the initial or nascent gas-phase reactants.

As pointed out in our conceptual-framework discussion, the identities of the condensed-phase reaction products are not known with completeness, even for the relatively well-studied case of RDX. For most other energetic materials, the situation is worse still. The only clear constraint we have in constructing this species set is elemental balance. Therefore, from the universe of possible product sets, that is, those leading to a balanced overall reaction, one must select the plausible ones based on experimental knowledge of these product identities and concentrations, if available, or based on theoretical consideration of likely reaction paths. In general one may expect to confront a multiplicity of such plausible product sets. One might then simply pick the one that best reproduces the experimental burning rate or take an average of the product sets based on the assumption of equal a priori

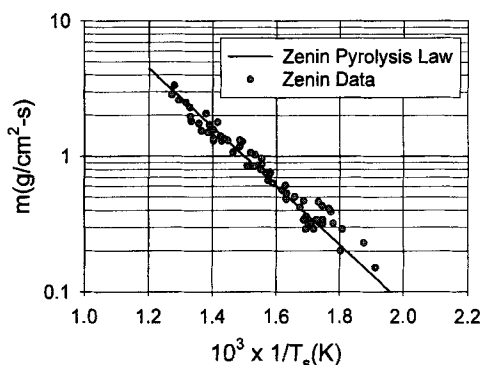


Fig. 1 Demonstration of the universality of the pyrolysis law for double-base propellants based on the work of Zenin.²⁸

probabilities of occurrence. In any case, one can improve the chosen decomposition set as new experimental data or theoretical insights become available.

The final type of information required for computing a burning rate is the rate of appearance of the condensed-phase decomposition products. For this we appeal to the very old notion of an Arrhenius-like expression² relating the burning rate to the surface temperature, that is,

$$\dot{m} = A_s e^{-E_s/RT_s} \quad (13)$$

Such an expression has often been termed a “pyrolysis law” in the propellant-combustion literature. There are other forms of this expression in use,^{28,29} but the aforementioned form preserves the dominant functionality without additional (probably uncertain) data and, in fact, is chosen in preference to others by Zenin²⁸ to represent his experimental determination of surface temperatures vs burning rates for a range of double-base propellants. Zenin found that this form provides a universal representation for double-base propellants of different ingredient proportions (see Fig. 1). It is this universality for a given class of propellants that impels us to adopt it here as a formalism for the rate of appearance of the condensed-phase decomposition products. In the case of double-base propellants, the mechanism for surface regression is likely to be reactive in nature because of the polymeric character of the nitrocellulose molecules. That the pyrolysis law in the form of Eq. (13) also proves appropriate to a purely evaporative surface regression mechanism can be seen in Fig. 2. Here the surface temperature for the three-phase deflagration of frozen ozone was computed based on nonequilibrium evaporation driven by heat feedback from gas-phase reactions.²¹ The steady deflagration of RDX is also believed to be predominately the result of evaporation.¹⁴ A best-fit pyrolysis law (in the least-squares sense) for RDX that uses the surface-temperature and the burning-rate data of Zenin²⁸ is shown in Fig. 3; again, the fit is quite reasonable.

IV. Example: Frozen Ozone

Our first example of the application of this new model is that of the self-sustained deflagration of frozen ozone. Using the pyrolysis law previously determined from

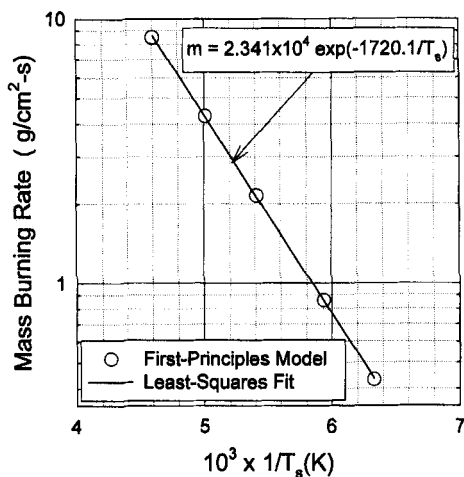


Fig. 2 Quality of fit of a pyrolysis law to an evaporative regression mechanism calculated from a first-principles treatment of frozen-ozon deflagration.²¹

a first-principles model,²¹ we compute the burning rate by the new model and compare it with the burning rate computed by the first-principles model to test for consistency. Such a test is not as trivial as it might seem. The calculational details involving the evaporative surface-regression mechanism of the first-principles model is considerably more complicated than that involved in the new model. However, the evaporation process is characterized by an energy barrier (heat of vaporization) and the assumption of local thermodynamic equilibrium introduces a Boltzmann factor; this suggests that the process may be controlled by an Arrhenius-like term. On the other hand, the evaporation-mechanism equations²¹ do not lead to such a simple expression, although an Arrhenius-like dependence on temperature evidently does have an implicit relevance, given the excellent fit of the pyrolysis law observed in Fig. 2.

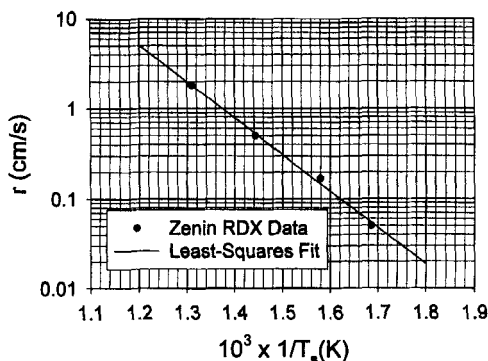


Fig. 3 Pyrolysis law for RDX derived from Zenin's experimental data.²⁸

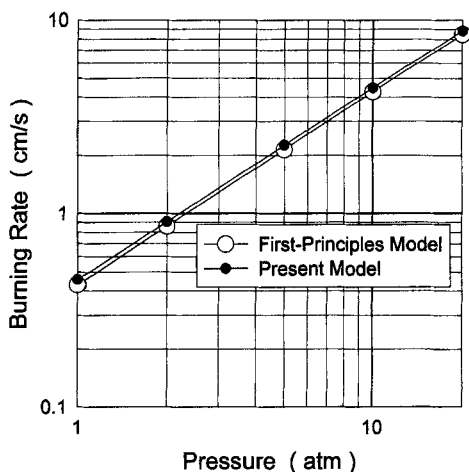


Fig. 4 Comparison of the burning rates for frozen ozone computed by the new model developed here and the previously published first-principles model.²¹

Because any condensed-phase reactions in liquid ozone are too slow to influence the deflagration rate, the mechanism of surface regression is evaporation driven by heat released in gas-phase reactions and conducted back to the surface. In this situation the nascent gas-phase species is evaporated ozone, i.e., $Y_{O_3}^{-0} = 1$. Coupling this with the fitted pyrolysis law just described and the reaction mechanism consisting of three reversible reactions,²¹ we have computed the frozen-ozone burning rate by our new model for comparison with that computed by the first-principles model.²¹ Figure 4 shows that the agreement is excellent. The first-principles model in this case includes thermal diffusion and multicomponent transport, and the numerical grid spacing is fine enough that the burning rates are computed to within a few tenths of a percent accuracy. Also, the central-differencing option was selected. Thus the success of both the pyrolysis law and the new model is based on a high level of computational rigor. The dominant chemical steps occurring in the gas phase for the ozone case are thoroughly discussed in Ref. 21.

V. Example: RDX

As discussed in Sec. II, the condensed-phase decomposition paths for RDX are uncertain. Evaporation was determined to be the overwhelmingly dominant mechanism by Melius,¹³ and Liao and Yang^{14,15} and at least predominant by Davidson and Beckstead¹⁷ and Prasad et al.¹⁶ We therefore examine the consequences of assuming in our model that the surface-regression mechanism is purely evaporative. Thus, by analogy to the preceding ozone case, vapor-phase RDX is assumed to be the sole species emerging from the surface; mathematically this is expressed as $Y_{RDX}^{-0} = 1$. The pyrolysis law is obtained by a linearized least-squares fit to the experimental data of Zenin²⁸ and is illustrated in Fig. 3.

The enthalpy of the solid at the initial temperature is determined as follows. The specific heat of solid RDX is obtained by a least-squares fit of a linear temperature function to the data of Shoemaker et al.³⁰ combined with that of Miller.³¹ The

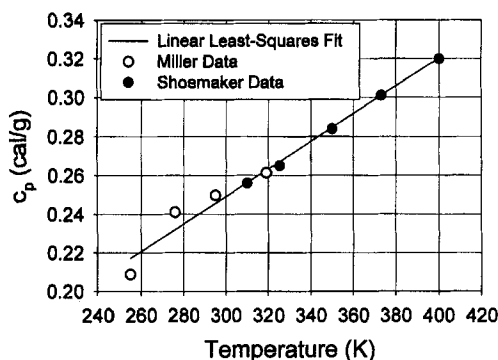


Fig. 5 Linear least-squares fit of the specific heat data of Miller³¹ and Shoemaker et al.³⁰ for solid RDX over a range of initial temperatures.

fit is shown in Fig. 5, and its parameters are in Table 2. This functional form of the specific heat is integrated over temperature to determine the enthalpy of solid RDX, with the value of the heat of formation at 298 K used to obtain the integration constant. This treatment differs from that of Liao and Yang¹⁴ and Liao¹⁵ in that their model assumes a constant value of specific heat.

The reaction mechanism (the second model of Prasad et al.¹⁶), thermodynamic data, and transport data for this case are taken from the work of Liao.¹⁵ The burning rate (Fig. 6), temperature (Fig. 7), and species profiles (Fig. 8) computed by the present model at an initial temperature of 293 K agree very closely with that computed by the Liao model. (Liao kindly made his code available to us for our use. All calculations in this article attributed to the Liao model¹⁵ were made with the code version dated 13 February 1997.) We emphasize that the gas-phase reaction mechanisms, species thermodynamics, and transport parameters in both models are identical; only the treatment of the condensed phase and the surface-gasification mechanism are different. The model burning rates are also seen to compare favorably with the experimental data of Miller (M. S. Miller, U.S. Army Research Laboratory, unpublished data), Zenin,²⁸ Ulas et al.,³² Homan et al.,³³ and Atwood et al.,³⁴ also shown in Fig. 6.

In the RDX case we have sought to minimize nongermane computational differences between the new semiempirical model and that of Liao and Yang. Their choice of the windward-differencing option, numerical-grid options, and

Table 2 Values of condensed-phase parameters used in RDX calculations

Value	Description
$A_s = 6.134 \times 10^5 \text{ g/cm}^2 \cdot \text{s}$	Exponential prefactor in pyrolysis law (see text)
$E_s = 18,539 \text{ cal/mole}$	Activation energy in pyrolysis law (see text)
$\rho_s = 1.66 \text{ g/cm}^3$	Mass density of pressed solid used in experiments ²⁸
$W_{\text{RDX}} = 222.118 \text{ g/mole}$	RDX molecular weight
$\Delta H_f^{298 \text{ K}} = 14,690 \text{ cal/mole}$	RDX heat of formation at 298 K
$c_p^{\text{solid}} = 0.03604$	Specific heat of solid RDX over temperature
$+ (7.105 \times 10^{-4}) T \text{ cal/g} \cdot \text{K}$	range 260–400 K (see text)

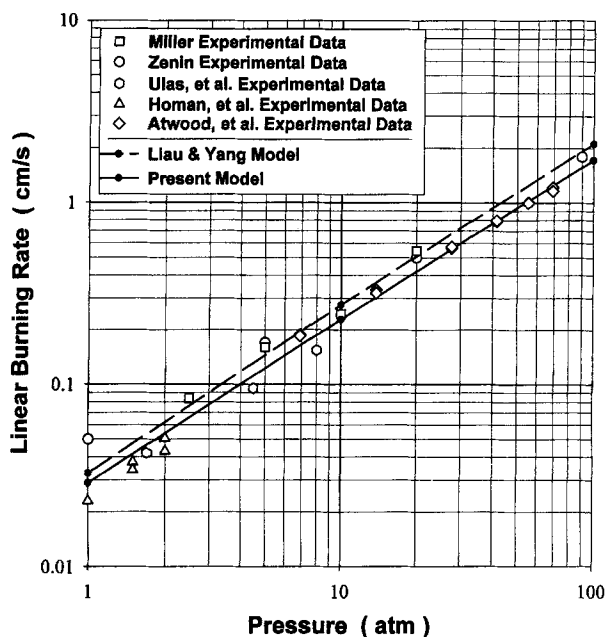


Fig. 6 Comparison of burning rates for RDX computed by the new model with those computed by Liao¹⁵ and with experimental data (see text for experimental data references).

suppression of the thermal-diffusion and multicomponent-transport options in PREMIX were selected for our calculations as well.

The dominant reaction paths for RDX flames have been discussed previously,¹³ and although the reaction mechanism has been expanded and refined since that study, we believe that the conclusions have not changed significantly. Hence, no new dominant-path analysis for RDX is given here. However, a brief explanation is now given for the slight rise in temperature above the adiabatic equilibrium value

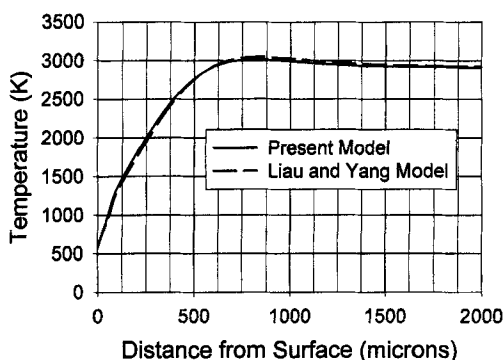


Fig. 7 Temperature profiles for RDX at 1 atm and 293 K computed by the new model compared with those of Liao.¹⁵

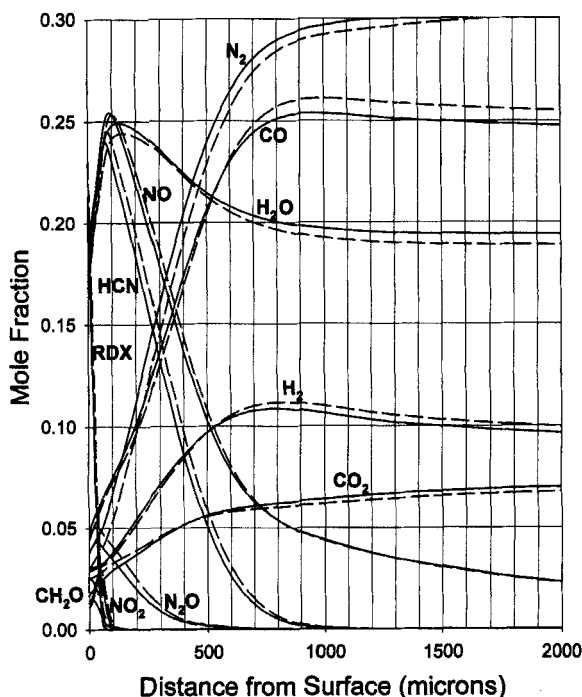
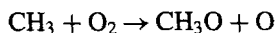
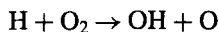


Fig. 8 Species profiles for RDX at 1 atm and 293 K computed by the present model (solid curves) compared with those of Liau¹⁵ (dashed curves).

late in the flame zone, as seen in Fig. 7. This behavior is surprising compared with that of O_2 /fuel combustion in which the temperature rise is monotonic; however, it is quite typical of flames oxidized by N_2O and NO_2 . In O_2 flames, there is typically an overshoot of H, O, and OH concentrations late in the flame zone above their eventual equilibrium values. In OH/O_2 flames, this overshoot is caused by the radical chain-branching reactions:



As this excess of radicals recombines in the burned-gas region, heat is released and the temperature continues to rise to the adiabatic equilibrium value. For N_2O - and NO_2 -oxidized flames, these chain-branching reactions are absent. Toward the end of the flame zone, the radical concentrations are usually somewhat below their eventual equilibrium values. To reach the final equilibrium concentrations of radicals, stable species slowly decompose in the burnt-gas region, absorbing heat in the process and lowering the final temperature to the equilibrium value. For the case in Fig. 7, our calculations show that H, O, and OH concentrations rise by factors of 2–5 between 800 and 2000 μm . Over this same region the temperature drops by ~ 100 K. A similar result was observed in computations for a low-pressure $H_2/N_2O/Ar$ flame.³⁵

VI. Example: Nitroglycerine

Relatively little information is available on the thermal decomposition pathways of nitroglycerine (NG). We examine it here in the context of the new semiempirical burning-rate model because it represents a case of intermediate chemical complexity, it continues to play an important role in gun propellants, and it is a substance for which experimental burning-rate data exist. Vital also is the fact that we could assemble a gas-phase reaction mechanism with relatively few changes from that previously developed for the dark zone of nitrate ester and nitramine propellants.^{36,37} This was accomplished by adding only one additional species, CH_2O , and its associated reactions. The resulting mechanism (labeled DB11 here) is given in the Appendix and consists of 35 species and 178 reversible reactions.

For the pyrolysis law we simply use the universal double-base law determined by Zenin²⁸ and shown in Fig. 1. Double-base propellants, of course, consist primarily of different proportions of NG and nitrocellulose. Although NG is therefore one limiting case of a double-base propellant, there is not necessarily a reason to suppose the double-base pyrolysis law to be applicable to NG solely on this account. However, both NG and nitrocellulose are nitrate esters whose likely first step in decomposition is an NO_2 scission; if this were a rate-limiting step, then one might expect the decomposition rates for NG and nitrocellulose to be similar. This argument may, in fact, be the underlying reason for the apparent universality of the double-base pyrolysis law. In any case, we have to let the results be the ultimate justification for this assumption.

A major source of ambiguity in applying the new model to NG is the identification and the quantification of the condensed-phase decomposition products, which are the nascent gas-phase species. As suggested previously, this is a situation in which one must examine a number of possibilities (consistent with a balanced reaction) and, ideally, arbitrated by broad theoretical reasoning. Again, the results must be the ultimate justification for this choice. We have given values of condensed-phase parameters in Table 3 and have examined the use of three sets of condensed-phase decomposition products for the NG case (see Table 4). The first set is motivated by the only other elementary-reaction treatment of NG of which we are aware. Hatch¹¹ assumed, without attempting justification, that NG decomposed by the path indicated in Table 4. We have not found a way to rationalize this path theoretically, but considered it worthwhile to consider it anyway based on its previous use. A second path, given in Table 4, was hypothesized by J. B. Levy (in personal communication with Eli Freedman, U.S. Army Research Laboratory) based on theoretical considerations. The steps in NG decomposition

Table 3 Values of condensed-phase parameters used in NG calculations

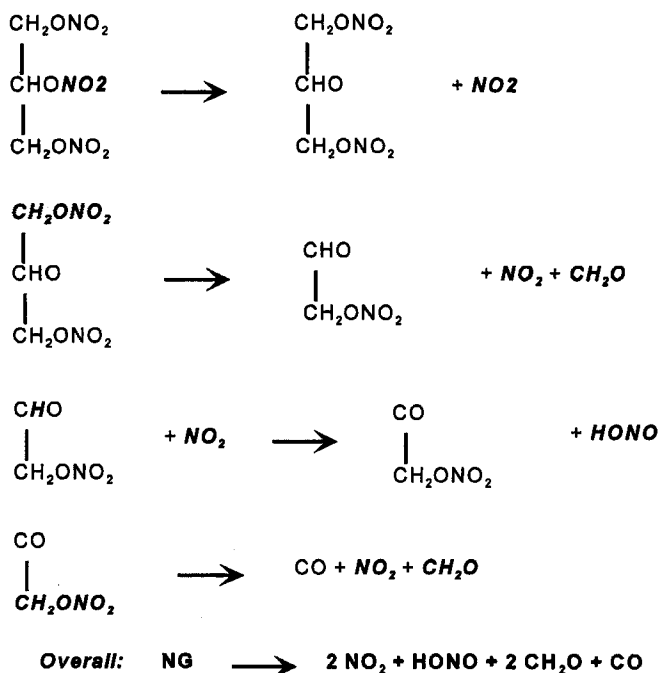
Value	Description
$A_s = 1.8 \times 10^3 \text{ g/cm}^2 \cdot \text{s}$	Exponential prefactor in pyrolysis law (see text)
$E_s = 9935 \text{ cal/mole}$	Activation energy in pyrolysis law (see text)
$\rho_s = 1.59 \text{ g/cm}^3$	Mass density of liquid NG
$W_{\text{NG}} = 227.087 \text{ g/mole}$	NG molecular weight
$\Delta H_f^{298 \text{ K}} = -88,600 \text{ cal/mole}$	NG heat of formation at 298 K
$c_p^{\text{liquid}} = 0.2975 \text{ cal/g} \cdot \text{K}$	Specific heat of liquid NG

Table 4 NG condensed-phase decomposition paths considered

Overall NG decomposition path	Reaction path label
NG ($\text{C}_3\text{H}_5\text{N}_3\text{O}_9$) \rightarrow $3\text{NO}_2 + 2\text{CH}_2\text{O} + \text{HCO}$	Hatch ¹¹
NG \rightarrow $2\text{NO}_2 + \text{HONO} + 2\text{CH}_2\text{O} + \text{CO}$	Levy (see text)
NG \rightarrow $3\text{HONO} + 2\text{HCO} + \text{CO}$	MSM4

proposed by Levy are illustrated in Fig. 9. A third set (MSM4) of decomposition products is also given in Table 4 and used to compute burning rates. No theoretical justification based on a detailed sequence of paths is offered for this set but, as will be seen, it does lead to good agreement with experimental rates. One of our aims in considering a number of condensed-phase reaction paths is to gauge the sensitivity of the computed burning rate to the choice of path.

The results of the burning-rate calculations made with each of the above sets of condensed-phase decomposition products at an initial temperature of 298 K are shown in Fig. 10. Also shown in the figure are the experimental burning rates measured by Andreev^{38,39} and Andreev et al.⁴⁰ The MSM4 decomposition-product set leads to very good agreement with the experimental burning rates over a wide range of pressure. It is also of interest to note that the burning rate can vary by as much as an order of magnitude among the possible decomposition-product sets that we have considered. This finding could be of considerable importance to the

**Fig. 9** Mechanism for condensed-phase decomposition of NG proposed by Levy.

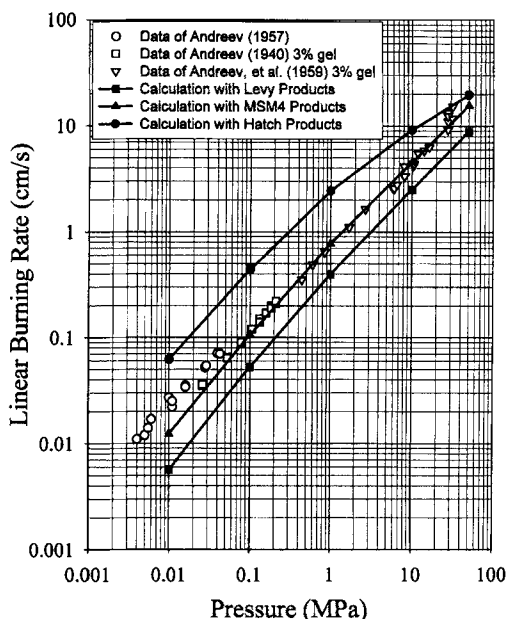


Fig. 10 Computed NG burning rates at 298 K for different decomposition paths by use of new semiempirical model compared with experimentally measures rates of Andreev^{38,39} and Andreev et al.⁴⁰

tailoring of propellant burning rates for specific purposes if one could find a way to actively influence the decomposition pathways in the condensed phase.

In all of the calculations presented here involving NG (including those of Sec. VII) the windward-differencing option and the suppression of the thermal-diffusion and multicomponent-transport options were selected. The numerical grid options were such that the burning rates presented are numerically accurate to $\sim 2\%$ or better.

Because this is the most extensive detailed chemical modeling of NG combustion ever performed, a detailed analysis of the gas-phase flame for one condition is presented. The case chosen is for pure NG at 10 atm and an initial temperature of 298 K, with the assumed MSM4 product set ($3\text{HONO} + 2\text{HCO} + \text{CO}$). This is the product set that yields the best agreement between predicted burning rates and experiment (see Fig. 10). Pathway diagrams, shown in Fig. 11, have been constructed for this case by a postprocessor code, PREAD, written at the U.S. Army Research Laboratory for the PREMIX code. To obtain these diagrams, the rates were first integrated over distance from the propellant surface to 0.030 cm. This region, which we term the primary reaction zone, includes all of the near surface flame up to the leading edge of the dark zone, as determined by plateaus in temperature and key species, e.g., NO, concentration profiles (not shown). Use of the integrated rates gives a concise global picture of the chemistry in this region. We caution the reader, however, that the flame is quite structured in this region, having five separate peaks in the heat release profile! A complete discussion of this structure is outside the scope of this chapter, but some remarks about the structure are contained in the following discussion. The chemistry of the dark zone of NG,

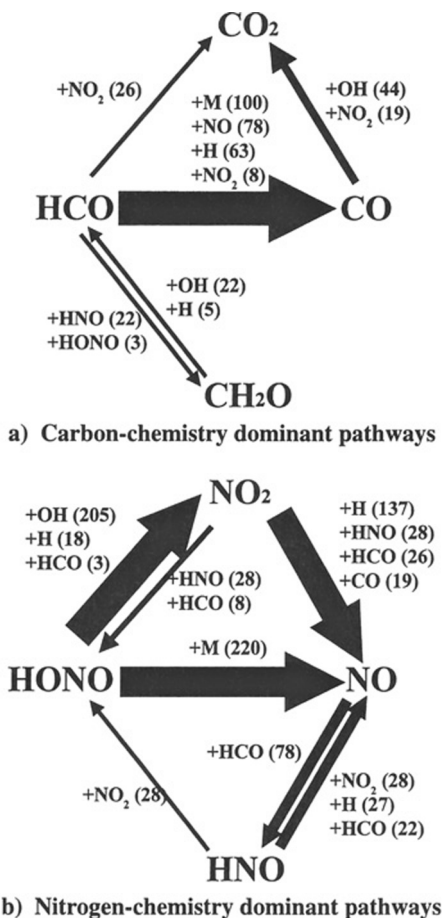


Fig. 11 Identification of dominant chemical pathways for NG at 10 atm and 298 K by use of the MSM4 product set. Numbers in parentheses are the relative rates of each reaction integrated over the primary reaction zone (0–0.030 cm). A value of 100 in relative units equals 8.817×10^{-3} mole/cm² · s. The thicknesses of the lines are proportional to the total, relative, integrated rates for each path.

the region of low gradients in species concentration and temperature between the primary flame and the secondary, or visible flame, is similar to that for double-base propellants. That case has been discussed elsewhere.^{36,37}

The conversion of HCO to other species is very rapid, which is not surprising considering its radical nature. This conversion takes place very close to the surface, occurring within the first 0.001 cm. As shown in Fig. 11a, most of the HCO is converted to CO by unimolecular decomposition or by reaction with NO, H, or NO₂. However, a portion of the HCO is temporarily converted to CH₂O, primarily by reaction with HNO. The CH₂O, being much less reactive than HCO, survives further into the primary flame. Later in the primary reaction zone, the CH₂O is converted by reaction with OH and H back into HCO; the HCO formed in this

way never builds to an appreciable concentration but instead is converted to CO or CO₂ first stage products.

The nitrogen chemistry is considered in Fig. 11b. As with HCO, the conversion of HONO to other species begins rapidly near the surface because of its direct reaction with a portion of the HCO, forming NO₂ and CH₂O. However, only a small portion of the available HONO reacts before the depletion of the HCO. Instead, most of the HONO conversion is delayed, occurring mainly between 0.001 and 0.015 cm. A portion of the HONO is converted directly to NO by means of unimolecular decomposition. However, much of it is first converted to NO₂ by means of reaction with OH, H, or HCO. Curiously, the conversion of NO₂ to NO takes place mainly after the burnout of the HONO. Ordinarily, in combustion involving NO₂ as a major species, it is found that the NO₂ conversion to NO by reaction with H atoms is so fast that it occurs at a very early point and it controls the radical pool concentrations. However, here the HONO + M = NO + OH + M reaction is the major radical source, the HONO concentration in the region is large, and the HONO + OH rate constant is also large. This leads to HONO + M = NO + OH + M and HONO + OH = H₂O + NO₂, rather than NO₂ + H = NO + OH, being the major nitrogen pathways close to the surface. The NO₂ formed early in the flame from HONO reacts higher in the flame, after the HONO is gone. NO₂ is converted to NO primarily by H atom reaction, but there are also important contributions from HNO, HCO, and CO reactions. NO, the only nitrogenous species surviving into the dark zone, may be viewed as the nitrogenous product of the first-stage combustion. The concentration of HNO is small except very close to the surface. It appears that although their concentrations are small, HNO and NO play important roles in a catalytic cycle for the near surface HCO conversion, as is discussed below.

More information concerning the importance of the various reactions to the predicted burning rate may be obtained from sensitivity analysis. The sensitivity coefficient of the temperature at a given spatial grid point to a particular reaction rate is defined as

$$S_i = \frac{A_i}{T_m} \left(\frac{\partial T}{\partial A_i} \right)$$

where A_i is the A factor of the i th reaction, T is the temperature at the point of interest, and T_m is the maximum temperature observed in the entire solution. The second grid point in the solution is chosen as the point of interest because this one has special significance. The burning rate is strongly controlled by the amount of heat feedback from the gas-phase reactions to the propellant. The heat feedback rate is in turn primarily controlled by the temperature gradient at the propellant surface. Thus the magnitude of rate constants for reactions that have a high temperature sensitivity at the second grid point in the solution must have a strong influence on the computed burning rate. In fact, to a good approximation, the sensitivity coefficient of the heat feedback is simply proportional to the sensitivity coefficient of the second grid point. The first-order temperature sensitivities for the second gas-phase grid point of the solution (and the heat feedback) is given in Table 5 for those reactions with relative values above 3. For the coefficient of the second grid point, a relative value of 100 equals an absolute value of 7.769×10^{-4} . A positive temperature sensitivity coefficient indicates that an increase in the reaction-rate coefficient will result in an increase

Table 5 Relative sensitivity coefficients of the temperature gradient at the surface to the most sensitive reactions (in rank order) for NG with MSM4 product set at 10 atm and 298 K initial temperature^a

Reaction number	Reaction	Relative sensitivity coefficient
33	$\text{HCO} + \text{M} \rightleftharpoons \text{H} + \text{CO} + \text{M}$	100
139	$\text{H}_2 + \text{NO}_2 \rightleftharpoons \text{HONO} + \text{H}$	46.2
4	$\text{NO} + \text{OH} + \text{M} \rightleftharpoons \text{HONO} + \text{M}$	29.4
34	$\text{H} + \text{HCO} \rightleftharpoons \text{H}_2 + \text{CO}$	-26.4
178	$\text{HCO} + \text{NO}_2 \rightleftharpoons \text{H} + \text{CO}_2 + \text{NO}$	23.6
175	$\text{HCO} + \text{HNO} \rightleftharpoons \text{CH}_2\text{O} + \text{NO}$	21.3
177	$\text{HCO} + \text{NO}_2 \rightleftharpoons \text{CO} + \text{HONO}$	-21.3
176	$\text{CH}_2\text{O} + \text{NO}_2 \rightleftharpoons \text{HCO} + \text{HONO}$	19.6
128	$\text{H} + \text{HNO} \rightleftharpoons \text{H}_2 + \text{NO}$	-15.9
147	$\text{HCO} + \text{NO} \rightleftharpoons \text{HNO} + \text{CO}$	-4.97
157	$\text{H} + \text{CH}_2\text{O} \rightleftharpoons \text{HCO} + \text{H}_2$	-3.94
64	$\text{NO}_2 + \text{H} \rightleftharpoons \text{NO} + \text{OH}$	3.17

^aPositive values indicate reactions that increase the temperature gradient when the rate coefficient for the reaction is increased.

in temperature at point 2, and such an increase is expected to increase the burning rate. Note that the largest sensitivity is for $\text{HCO} + \text{M} = \text{H} + \text{CO} + \text{M}$. This is not surprising, as the reaction not only converts HCO to a final product, but produces the highly reactive H atom. Sensitivities of most of the other reactions can also be rationalized by their effects on the radical pool or formation of final products with release of heat. The only one whose high, positive sensitivity has been difficult to rationalize is the second one on the list, $\text{H}_2 + \text{NO}_2 = \text{HONO} + \text{H}$. This reaction is reversed throughout the entire calculational domain (see, e.g., Fig. 11b). Its reversal is not surprising because one starts with HONO in the MSM4 decomposition-product set. Ordinarily, because this reversed reaction converts a highly reactive H atom to a comparatively unreactive species, one would expect the corresponding sensitivity would be negative. It seems likely that the explanation for the positive sensitivity is the formation of NO_2 , which in turn leads to NO and HNO formation close to the surface. NO and HNO take part in a catalytic cycle for rapid HCO conversion to CO and CH_2O in this region (see Fig. 11, both parts). This conversion occurs by means of reactions $\text{HCO} + \text{NO} = \text{HNO} + \text{CO}$ and $\text{HCO} + \text{HNO} = \text{CH}_2\text{O} + \text{NO}$, releasing considerable heat near the surface.

Rate constants of most of the highly sensitive reactions in Table 5 are well established. Three exceptions are R175 ($\text{HCO} + \text{HNO} = \text{CH}_2\text{O} + \text{NO}$), R178 ($\text{HCO} + \text{NO}_2 = \text{H} + \text{CO}_2 + \text{NO}$), and R177 ($\text{HCO} + \text{NO}_2 = \text{CO} + \text{HONO}$). The rate-constant expression for R175 has especially large error limits. It is an estimate that is due to Tsang and Herron,⁴¹ who obtained it based on comparison with similar reactions. Rate-constant expressions for R177 and R178 were obtained from Lin et al.⁴² The expressions were computed based on ab initio and transitional state-Rice-Ramsperger-Kassel-Marcus theories. This approach should yield reasonable estimates, but experimentation is desirable.

VII. Effect of Chemical Additives on the Burning Rate

It has always been hoped that theoretical modeling might some day contribute to solving the problem of the effects of chemical additives on the burning rate of propellants. However, only with the relatively recent advent of chemically specific modeling with elementary reactions was there any real prospect for realizing these hopes. In this section we demonstrate that theoretical guidance useful to the propellant formulator, namely, the effect of additives on the burning rate, is becoming feasible.

As a first demonstration of the effects of additives on propellant flames, we took the converged values of burning rate (0.394 cm/s) and surface temperature (628 K) obtained in a calculation of NG at 10 atm by using the Levy decomposition-product set and the DB11 reaction mechanism as our starting conditions for a series of steady premixed flames with several different additives. A 10% mole fraction of NH_3 was then added to the Levy product set (reducing the original product mole fractions proportionately). The flame structure was then computed and compared with the pure NG case. The result is shown in Fig. 12. The two-stage flame structure is known to occur because of the reduction of HONO and NO_2 to NO in the primary reaction zone (next to the surface) and the subsequent, slower reduction of NO to N_2 in the secondary reaction zone (at the end of the dark zone). The secondary reaction zone is also known as the secondary flame or the visible flame. In Fig. 12 one can see that the secondary gas flame for the pure NG case stands off from the surface by ~ 1 cm. (Note that the distance scale is logarithmic.) This is typical of the dark-zone length of double-base propellants. When the NH_3 is added, the dark zone collapses by a factor of ~ 5 . Also, the heat feedback increases by 31%. Normally, when the heat feedback increases, one can expect the burning rate to increase as well. The effect NH_3 has on the dark-zone length may explain why M30 (29% nitrocellulose, 22% nitroglycerine, 47% nitroguanidine, 2% stabilizer) burns with no apparent dark zone, unlike any other gun propellant. A major ingredient in M30 is nitroguanidine (NQ), which may be expected to supply NH_2 on decomposition. The chemical rationale for this effect is discussed later in this section. A case with 10% N_2 added is shown in Fig. 12 for comparison. The N_2 has its expected diluent effect, lowering the heat feedback by

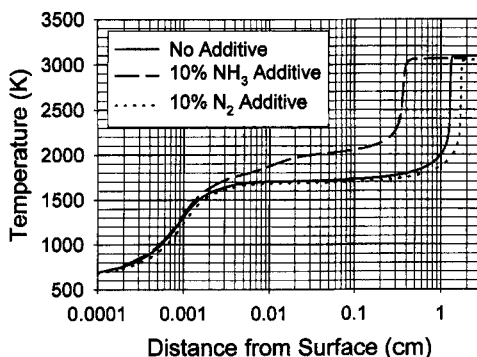


Fig. 12 Effect of two additives, NH_3 and N_2 , on the flame structure of NG at 10 atm and 298 K by use of Levy's decomposition-product set. Surface temperature and mass flux are fixed at 628 K and $0.626 \text{ g/cm}^2 \cdot \text{s}$, respectively, for all cases.

28% but having relatively little effect on the dark-zone length. Liao¹⁵ performed a similar study of the effect of various additives on the dark zone of RDX.

A more systematic approach is needed to compare the effects of one additive with another in a quantitative sense. Adopting a propellant formulation strategy of adding enough additive to bring the mixture to a zero oxygen balance affords a rational method of determining the amount of each additive appropriate for comparison purposes. The oxygen balance is defined as that amount of oxygen one must add or subtract to have all oxygen appear in either H₂O or CO₂. NG has a positive balance of 3.5%, that is, it has an oxygen surplus. Thus we compute that we must add one third of a mole of NH₃ to effect a neutral oxygen balance for each mole of NG. For comparison we examine two other potential additives, CH₂O and H₂. We are, of course, limited here to those fuel molecules that are already in our reaction mechanism.

Additional assumptions are required for modeling the effects of condensed-phase mixtures of ingredients. The mass density of the mixture is computed by the method of additive partial molar volumes, that is,

$$\rho_{\text{mix}} = \frac{W_{\text{avg}}}{\sum_i X_i V_i} \quad (14)$$

where W_{avg} is the average molecular weight, X_i is the mole fraction of ingredient i , and V_i is the molar volume of ingredient i . This quantity is important in calculating the linear burning rate from the mass burning rate. Second, we assume that the starting mixture enthalpy is given by the weighted sum of the ingredient enthalpies. This is a reasonable approximation to make, but it ignores any enthalpy of mixing or solution contributions; there is also some ambiguity as to what state is best to use for the additive enthalpy. Finally, we must, of course, assume that the pyrolysis law is unchanged as a result of these additives. This assumption is reasonable in view of the small amount of each additive.

The results of the additive computations are given in Table 6 for the Levy decomposition-product set and in Table 7 for the MSM4 decomposition-product set. The enthalpies of all the additives in Tables 6 and 7 at 298 K are taken as that for the gas phase. It should be noted that this assumption could have important consequences for the computed burning rate. For example, if the enthalpy for NH₃ liquid at 298 K is used, the linear burning rate increases by only 12%. This smaller increase reflects the additional energy requirement of the heat of vaporization. Clearly the calculation of the unreacted-mixture enthalpy may require a more sophisticated theoretical treatment. In interpreting the small percentage differences shown in these tables, one should bear in mind that the numerical accuracy of these

Table 6 Effect of different chemical additives on the burning rate of NG at 10 atm and 298 K, assuming the Levy decomposition-product set

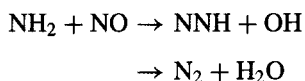
Additive	Weight %	Linear burning rate, % increase	Mass burning rate, % increase	Heat feedback, % increase
NH ₃	2.4	19	15	19
CH ₂ O	3.2	1	-1	-5
H ₂	0.44	1	-8	-6

Table 7 Effect of different chemical additives on the burning rate of NG at 10 atm and 298 K, assuming the MSM4 decomposition-product set

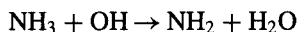
Additive	Weight %	Linear burning rate, % increase	Mass burning rate, % increase	Heat feedback, % increase
NH ₃	2.4	16	12	14
CH ₂ O	3.2	7	5	2
H ₂	0.44	2	-7	-6

calculations is no worse than 2%; thus some of the smaller effects found may not be significant.

Through sensitivity and rate analysis we were able to identify the chemical mechanism for the burning-rate enhancement of NG by NH₃. Essentially, NH₂ reduces NO to final product N₂ by the following two most important paths:



The NNH thus formed rapidly decomposes to N₂ + H. The reaction therefore leads to chain branching, which may be important to the burning-rate enhancement in addition to the increased NO conversion rate to N₂. The NH₂ is formed from NH₃ predominately by the reaction



This mechanism reinforces our speculation that M30 forms no dark zone because of the presence of an amino group on the NQ.

VIII. Speculations on Practical Burning-Rate Modifiers

The mechanism of NH₃ action in Sec. VII invites a further discussion of the M30 case. With NH₃-modified NG we found both a collapse in the dark-zone length and a significant boost in the burning rate. M30 has no dark zone, consistent with our NH₃-modified NG case, but it burns no faster than a single-base propellant and slower than a double-base propellant, a fact that appears to be inconsistent with our model calculation. This apparent inconsistency might be explained as follows. It is likely that the large percentage of NQ present in M30 is responsible for the lack of burning-rate enhancement because it acts to lower the flame temperature of the propellant. Hence the cooling effect might outweigh the rate-acceleration effect for such major proportions of NQ. We would expect that if a small amount of NQ, say 2–5%, were added to either a single- or a double-base propellant, then the burning rate would be increased and the dark-zone length diminished. Of course, some of the benefit of the NH₂ from NQ could be hindered by the energy required either for breaking down its parent molecule or getting it into the gas phase, as could be seen in our model calculation's sensitivity to the NH₃ starting enthalpy state. Nonetheless, here is a concrete, theoretically inspired idea that could easily be tested. Thus, although the model needs to be further refined and expanded, it can already provide insights of potential worth to the propellant formulator.

It should also be remarked that the propellant formulator may find it expedient to tailor decreases in the burning rate as well as increases. For example, it has been found⁴³ that for layered propellants one would like to achieve at least a 3:1 ratio in the rates of the two-layer materials in order to achieve desired performance enhancements. We have conducted preliminary calculations⁴⁴ that show that HNCO is an additive that both decreases the heat feedback (and therefore presumably the burning rate) as well as decreases the visible-flame standoff. As NH_2 proved to be the active molecule in increasing the heat feedback resulting from the addition of NH_3 to NG, so NCO appears to be the active molecule for the HNCO additive. One factor leading to the reduced heat feedback may be that the radical NCO combines with NO and NO_2 near the surface to form relatively stable molecules such as N_2 , N_2O , CO, and CO_2 , thereby diminishing the rate of radical growth. Reduction in the visible-flame standoff (dark-zone length) may be due to the unimolecular decomposition in the dark zone of the N_2O , which is formed in the near surface region by means of the NCO reactions. This decomposition, $\text{N}_2\text{O} \rightarrow \text{N}_2 + \text{O}$, increases the radical growth rate in the dark zone, causing acceleration of the reactions leading to the visible flame. A decrease in the visible-flame standoff may, in fact, be a desirable effect in that it may reduce gun-ignition delays attributable to the slowness of the reactions, leading to the substantial heat release of the visible flame.⁴⁵ Of course, to realize the benefits of these provocative ideas, much work is yet to be done both in searching for suitable active molecules and in finding practical substances that can release these active molecules, but the way is clear for a new and productive partnership between the theoreticians and the formulation chemists.

IX. Conclusions

Models of energetic-material combustion have increased enormously in their sophistication and complexity in recent years. Treatments of the gas phase involving dozens of species and hundreds of elementary reactions are now common. On the other hand, chemically specific descriptions of the condensed phase have not kept pace, largely because of the lack of definitive experiments and theory relating to the reaction paths there. All of the existing treatments of the condensed phase consider several overall reactions at most, and even these suffer from uncertainties in the identities and concentrations of the reactants and products. In the face of these intractabilities, we have developed a new semiempirical model that requires as input a single overall reaction representing the conversion of unreacted energetic material to the nascent gas-phase species and a pyrolysis law expressing the relationship of surface temperature to burning rate. This approach makes the most sense where the pyrolysis law is universal over some class of materials; the existence of such a relation has been previously verified for double-base propellants. We have demonstrated that the simplest form of the pyrolysis law also well describes surface regression that is due to evaporative mechanisms as well as reactive ones. The capability of this model in describing the burning rate as a function of pressure and even species profiles, where available, was illustrated for frozen ozone, RDX, and NG.

A key uncertainty in applying this model to energetic materials is the identity and the concentrations of the products of the condensed-phase decomposition. By examining a number of possible product sets, we found that the computed burning rate could vary by as much as an order of magnitude among these sets. This finding

suggests that it might be possible to influence the burning rate of a material by stimulating decomposition along normally less favored paths.

One of the long-held hopes for chemically specific combustion modeling is to possess the capability to compute the effects of chemical additives on the burning rate in order to rationalize the performance tailoring of propellants. We believe that progress is rapidly being made toward fulfillment of that promise. As a demonstration of this budding capability, we determined the relative effect of three additives on the burning rate of NG in which the amounts of each additive were computed to achieve a neutral oxygen balance for each mixture.

Appendix: Reaction Mechanism (DB11) for Nitroglycerine

CHEMKIN INTERPRETER OUTPUT: CHEMKIN-II Version 3.6 Apr. 1994
DOUBLE PRECISION

		ELEMENTS CONSIDERED		ATOMIC WEIGHT			
		1. H		1.00797			
		2. C		12.0112			
		3. O		15.9994			
		4. N		14.0067			

		C					
		P H					
		H A					
		A R					
SPECIES		S G	MOLECULAR	TEMPERATURE		ELEMENT COUNT	
CONSIDERED		E E	WEIGHT	LOW	HIGH	H	C O N

1. H	G O	1.00797	300.0	5000.0	1	0	0 0
2. H2	G O	2.01594	300.0	5000.0	2	0	0 0
3. O2	G O	31.99880	300.0	5000.0	0	0	2 0
4. H2O	G O	18.01534	300.0	5000.0	2	0	1 0
5. CO2	G O	44.00995	300.0	5000.0	0	1	2 0
6. CO	G O	28.01055	300.0	5000.0	0	1	1 0
7. N2	G O	28.01340	300.0	5000.0	0	0	0 2
8. NO2	G O	46.00550	300.0	5000.0	0	0	2 1
9. N2O	G O	44.01280	300.0	5000.0	0	0	1 2
10. NO	G O	30.00610	200.0	6000.0	0	0	1 1
11. HONO	G O	47.01347	300.0	5000.0	1	0	2 1
12. OH	G O	17.00737	300.0	5000.0	1	0	1 0
13. O	G O	15.99940	300.0	5000.0	0	0	1 0
14. HO2	G O	33.00677	300.0	5000.0	1	0	2 0
15. H2O2	G O	34.01474	300.0	5000.0	2	0	2 0
16. CH2O	G O	30.02649	200.0	6000.0	2	1	1 0
17. CH3O	G O	31.03446	300.0	3000.0	3	1	1 0
18. CH2OH	G O	31.03446	250.0	4000.0	3	1	1 0
19. CH3OH	G O	32.04243	300.0	5000.0	4	1	1 0
20. CH	G O	13.01912	300.0	5000.0	1	1	0 0
21. C	G O	12.01115	300.0	5000.0	0	1	0 0
22. HCO	G O	29.01852	300.0	5000.0	1	1	1 0
23. NH3	G O	17.03061	300.0	5000.0	3	0	0 1
24. NH2	G O	16.02264	200.0	6000.0	2	0	0 1
25. NH	G O	15.01467	200.0	6000.0	1	0	0 1
26. N	G O	14.00670	300.0	5000.0	0	0	0 1
27. NNH	G O	29.02137	250.0	4000.0	1	0	0 2
28. HNO	G O	31.01407	200.0	6000.0	1	0	1 1
29. HOCO	G O	45.01792	300.0	4000.0	1	1	2 0
30. HNNO	G O	45.02077	300.0	5000.0	1	0	1 2
31. N2H2	G O	30.02934	300.0	5000.0	2	0	0 2
32. N2H3	G O	31.03731	300.0	5000.0	3	0	0 2
33. N2H4	G O	32.04528	300.0	5000.0	4	0	0 2
34. NO3	G O	62.00490	300.0	5000.0	0	0	3 1
35. NCO	G O	42.01725	200.0	6000.0	0	1	1 1

REACTIONS CONSIDERED		(k = A T**b exp(-E/RT))		
		A	b	E
1. NO2(+M)=NO+O(+M)		7.600E+18	-1.27	73290.0
Low pressure limit:	0.24700E+29 -0.33700E+01	0.74800E+05		
T&H VALUES	0.95000E+00 -0.10000E-03			
N2O	Enhanced by	1.500E+00		
H2O	Enhanced by	4.400E+00		
N2	Enhanced by	1.000E+00		
CO2	Enhanced by	2.300E+00		
2. N2O(+M)=N2+O(+M)		1.260E+12	0.00	62620.0
Low pressure limit:	0.59700E+15 0.00000E+00	0.56640E+05		
N2O	Enhanced by	5.000E+00		
H2O	Enhanced by	7.500E+00		
N2	Enhanced by	1.000E+00		
CO2	Enhanced by	3.200E+00		
O2	Enhanced by	8.200E-01		
3. H+NO(+M)=HNO(+M)		1.520E+15	-0.41	0.0
Low pressure limit:	0.40000E+21 -0.17500E+01	0.00000E+00		
N2O	Enhanced by	5.000E+00		
H2O	Enhanced by	5.000E+00		
N2	Enhanced by	1.000E+00		
CO2	Enhanced by	1.300E+00		
4. NO+OH(+M)=HONO(+M)		1.988E+12	-0.05	-721.0
Low pressure limit:	0.50800E+24 -0.25100E+01	-0.67600E+02		
T&H VALUE	0.62000E+00			
N2O	Enhanced by	5.000E+00		
H2O	Enhanced by	8.300E+00		
N2	Enhanced by	1.000E+00		
CO2	Enhanced by	1.500E+00		
5. NO+M=N+O+M		1.400E+15	0.00	148430.0
N2	Enhanced by	1.000E+00		
H2	Enhanced by	2.200E+00		
H2O	Enhanced by	6.700E+00		
CO2	Enhanced by	3.000E+00		
N2O	Enhanced by	2.200E+00		
6. N2+M=N+N+M		3.710E+21	-1.60	225000.0
7. N2O+N=N2+NO		1.000E+13	0.00	19870.0
8. NO2+N=N2O+O		5.010E+12	0.00	0.0
9. NO2+N=NO+NO		3.980E+12	0.00	0.0
10. NO2+NO2=NO+NO+O2		1.630E+12	0.00	26120.0
11. NO2+NO2=NO+NO3		9.640E+09	0.73	20920.0
12. NO2+NO3=NO+NO2+O2		1.400E+11	0.00	3180.0
13. HNO+NO=N2O+OH		8.510E+12	0.00	29590.0
14. HNO+O2=HO2+NO		1.000E+13	0.00	25000.0
15. HNO+NO2=HONO+NO		6.000E+11	0.00	1987.0
16. HONO+O=OH+NO2		1.200E+13	0.00	5961.0
17. HONO+OH=H2O+NO2		1.270E+10	1.00	135.0
18. HONO+NH2=NO2+NH3		1.000E+10	1.00	0.0
19. HNO+O=OH+NO		3.610E+13	0.00	0.0
20. NH+O=NO+H		5.500E+13	0.00	0.0
21. NH+O=N+OH		3.720E+13	0.00	0.0
22. NH+NH=N2+H+H		5.100E+13	0.00	0.0
23. NH+M=N+H+M		2.650E+14	0.00	75510.0
24. NH2+NO=N2O+H2		5.000E+13	0.00	24640.0
25. CH+O2=HCO+O		3.300E+13	0.00	0.0
26. CH+O=CO+H		5.700E+13	0.00	0.0
27. CH+OH=HCO+H		3.000E+13	0.00	0.0
28. CH+CO2=HCO+CO		3.400E+12	0.00	690.0
29. CH+H=C+H2		1.500E+14	0.00	0.0
30. C+O2=CO+O		2.000E+13	0.00	0.0
31. C+OH=CO+H		5.000E+13	0.00	0.0
32. OH+HCO<=>H2O+CO		5.000E+13	0.00	0.0
33. HCO+M<=>H+CO+M		1.870E+17	-1.00	17000.0
H2	Enhanced by	2.000E+00		
H2O	Enhanced by	1.200E+01		
CO	Enhanced by	1.500E+00		
CO2	Enhanced by	2.000E+00		
34. H+HCO<=>H2+CO		7.340E+13	0.00	0.0
35. HCO+O=CO+OH		3.000E+13	0.00	0.0

36.	$\text{HCO}+\text{O}=\text{CO}_2+\text{H}$		3.000E+13	0.00	0.0
37.	$\text{HCO}+\text{O}_2\rightleftharpoons\text{HO}_2+\text{CO}$		7.600E+12	0.00	400.0
38.	$\text{CO}+\text{O} (+\text{M})=\text{CO}_2 (+\text{M})$		1.800E+10	0.00	2380.0
Low pressure limit: 0.13500E+25 -0.27900E+01 0.41900E+04					
T&H VALUE 0.10000E+01					
	H2O	Enhanced by	1.200E+01		
	H2	Enhanced by	2.500E+00		
	CO	Enhanced by	1.900E+00		
	CO2	Enhanced by	3.800E+00		
	N2O	Enhanced by	5.000E+00		
39.	$\text{CO}+\text{OH}=\text{CO}_2+\text{H}$		1.510E+07	1.30	-758.0
40.	$\text{CO}+\text{O}_2=\text{CO}_2+\text{O}$		2.530E+12	0.00	47688.0
41.	$\text{HO}_2+\text{CO}=\text{CO}_2+\text{OH}$		5.800E+13	0.00	22934.0
42.	$\text{H}_2+\text{O}_2=2\text{OH}$		1.700E+13	0.00	47780.0
43.	$\text{OH}+\text{H}_2=\text{H}_2\text{O}+\text{H}$		2.160E+08	1.50	3430.0
44.	$\text{O}_2+\text{H}=\text{O}+\text{OH}$		3.520E+16	-0.70	17070.0
45.	$\text{O}+\text{H}_2=\text{OH}+\text{H}$		5.060E+04	2.67	6290.0
46.	$\text{H}+\text{O}_2+\text{M}=\text{HO}_2+\text{M}$		3.610E+17	-0.72	0.0
	H2O	Enhanced by	1.860E+01		
	CO2	Enhanced by	4.200E+00		
	H2	Enhanced by	2.900E+00		
	CO	Enhanced by	2.100E+00		
	N2	Enhanced by	1.300E+00		
47.	$\text{OH}+\text{HO}_2=\text{H}_2\text{O}+\text{O}_2$		7.500E+12	0.00	0.0
48.	$\text{H}+\text{HO}_2=2\text{OH}$		1.690E+14	0.00	874.0
49.	$\text{O}+\text{HO}_2=\text{O}_2+\text{OH}$		1.400E+13	0.00	1073.0
50.	$2\text{OH}=\text{O}+\text{H}_2\text{O}$		6.000E+08	1.30	0.0
51.	$2\text{H}+\text{M}=\text{H}_2+\text{M}$		1.000E+18	-1.00	0.0
	H2	Enhanced by	0.000E+00		
	H2O	Enhanced by	0.000E+00		
	CO2	Enhanced by	0.000E+00		
52.	$2\text{H}+\text{H}_2=2\text{H}_2$		9.200E+16	-0.60	0.0
53.	$2\text{H}+\text{H}_2\text{O}=\text{H}_2+\text{H}_2\text{O}$		6.000E+19	-1.25	0.0
54.	$2\text{H}+\text{CO}_2=\text{H}_2+\text{CO}_2$		5.490E+20	-2.00	0.0
55.	$\text{H}+\text{OH}+\text{M}=\text{H}_2\text{O}+\text{M}$		1.600E+22	-2.00	0.0
	H2O	Enhanced by	5.000E+00		
56.	$\text{H}+\text{O}+\text{M}=\text{OH}+\text{M}$		6.200E+16	-0.60	0.0
	H2O	Enhanced by	5.000E+00		
57.	$\text{O}+\text{O}+\text{M}=\text{O}_2+\text{M}$		1.890E+13	0.00	-1788.0
58.	$\text{H}+\text{HO}_2=\text{H}_2+\text{O}_2$		6.630E+13	0.00	2126.0
59.	$2\text{HO}_2=\text{H}_2\text{O}_2+\text{O}_2$		1.800E+12	0.00	0.0
60.	$\text{H}_2\text{O}_2+\text{M}=2\text{OH}+\text{M}$		1.300E+17	0.00	45500.0
61.	$\text{H}_2\text{O}_2+\text{H}=\text{HO}_2+\text{H}_2$		4.820E+13	0.00	7948.0
62.	$\text{H}_2\text{O}_2+\text{OH}=\text{H}_2\text{O}+\text{HO}_2$		1.750E+12	0.00	318.0
63.	$\text{NO}+\text{HO}_2=\text{NO}_2+\text{OH}$		2.110E+12	0.00	-479.0
64.	$\text{NO}_2+\text{H}=\text{NO}+\text{OH}$		1.300E+14	0.00	361.0
65.	$\text{NO}_2+\text{O}=\text{NO}+\text{O}_2$		3.900E+12	0.00	-238.0
66.	$\text{NCO}+\text{H}=\text{NH}+\text{CO}$		5.400E+13	0.00	0.0
67.	$\text{NCO}+\text{O}=\text{NO}+\text{CO}$		4.520E+13	0.00	0.0
68.	$\text{NCO}+\text{N}=\text{N}_2+\text{CO}$		2.000E+13	0.00	0.0
69.	$\text{NCO}+\text{OH}=\text{NO}+\text{CO}+\text{H}$		2.000E+13	0.00	7500.0
70.	$\text{NCO}+\text{M}=\text{N}+\text{CO}+\text{M}$		1.140E+23	-1.95	59930.0
	N2O	Enhanced by	5.000E+00		
	H2O	Enhanced by	5.000E+00		
	N2	Enhanced by	1.000E+00		
	CO2	Enhanced by	1.500E+00		
71.	$\text{NCO}+\text{NO}=\text{N}_2\text{O}+\text{CO}$		8.800E+17	-1.78	790.0
72.	$\text{NCO}+\text{NO}=\text{CO}_2+\text{N}_2$		1.130E+18	-1.78	790.0
73.	$\text{NCO}+\text{NO}_2=\text{CO}_2+\text{N}_2\text{O}$		1.950E+13	-0.26	-620.0
74.	$\text{NCO}+\text{NO}_2=\text{CO}+\text{NO}+\text{NO}$		1.770E+12	-0.26	-620.0
75.	$\text{NH}+\text{O}_2=\text{HNO}+\text{O}$		4.610E+05	2.00	6500.0
76.	$\text{NH}+\text{O}_2=\text{NO}+\text{OH}$		1.280E+06	1.50	100.0
77.	$\text{NH}+\text{NO}=\text{N}_2\text{O}+\text{H}$		3.500E+14	-0.46	16.1
78.	$\text{NH}+\text{NO}=\text{N}_2+\text{OH}$		2.160E+13	-0.23	0.0
79.	$\text{N}_2\text{O}+\text{H}=\text{N}_2+\text{OH}$		2.530E+10	0.00	4550.0
Declared duplicate reaction...					
80.	$\text{N}_2\text{O}+\text{H}=\text{N}_2+\text{OH}$		2.230E+14	0.00	16750.0
Declared duplicate reaction...					
81.	$\text{NNH}+\text{O}=\text{N}_2\text{O}+\text{H}$		1.400E+14	-0.40	477.0
82.	$\text{NNH}+\text{O}=\text{NO}+\text{NH}$		3.300E+14	-0.23	-1013.0
83.	$\text{N}_2\text{O}+\text{O}=\text{N}_2+\text{O}_2$		3.654E+12	0.00	15900.0

84.	N2O+O=NO+NO	9.985E+13	0.00	28040.0
85.	H+HNO=NH+OH	3.000E+14	0.00	18000.0
86.	NH+OH=N+H2O	5.000E+11	0.50	2000.0
87.	NH+N=N2+H	3.000E+13	0.00	0.0
88.	N+H2=NH+H	1.600E+14	0.00	25140.0
89.	HNO+H=NH2+O	3.500E+15	-0.30	28200.0
90.	NH2+O=NH+OH	6.750E+12	0.00	0.0
91.	NH2+OH=NH+H2O	4.000E+06	2.00	1000.0
92.	NH2+H=NH+H2	4.000E+13	0.00	3650.0
93.	NH2+NH=N2H2+H	1.500E+15	-0.50	0.0
94.	NH2+N=N2+H+H	7.200E+13	0.00	0.0
95.	NH2+O2=HNO+OH	4.500E+12	0.00	25000.0
96.	NH2+NH2=N2H2+H2	5.000E+11	0.00	0.0
97.	NH2+NH2=NH+NH3	5.000E+13	0.00	10000.0
98.	NH2+NH2=N2H3+H	1.790E+13	-0.35	11320.0
99.	NH2+NH2+M=N2H4+M	2.980E+47	-9.44	9680.0
100.	NH2+NO2=N2O+H2O	2.840E+18	-2.20	0.0
101.	NH+NO2=N2O+OH	1.000E+13	0.00	0.0
102.	N2H4+H=N2H3+H2	1.000E+12	0.50	2000.0
103.	N2H4+OH=N2H3+H2O	3.000E+10	0.68	1290.0
104.	N2H4+O=N2H3+OH	2.000E+13	0.00	1000.0
105.	N2H3=N2H2+H	1.200E+13	0.00	58000.0
106.	N2H3+H=N2H2+H2	1.000E+12	0.50	2000.0
107.	N2H3+OH=N2H2+H2O	3.000E+10	0.68	1290.0
108.	N2H3+O=N2H2+OH	2.000E+13	0.00	1000.0
109.	N2H2+M=NNH+H+M	5.000E+16	0.00	50000.0
	H2O	Enhanced by	1.500E+01	
	O2	Enhanced by	2.000E+00	
	N2	Enhanced by	2.000E+00	
	H2	Enhanced by	2.000E+00	
110.	N2H2+H=NNH+H2	5.000E+13	0.00	1000.0
111.	N2H2+O=NH2+NO	1.000E+13	0.00	0.0
112.	N2H2+O=NNH+OH	2.000E+13	0.00	1000.0
113.	N2H2+OH=NNH+H2O	1.000E+13	0.00	1000.0
114.	N2H2+NH=NNH+NH2	1.000E+13	0.00	1000.0
115.	N2H2+NH2=NH3+NNH	1.000E+13	0.00	1000.0
116.	NH2+NO=NNH+OH	9.300E+11	0.00	0.0
117.	NH2+NO=N2+H2O	2.000E+20	-2.60	924.0
118.	NH3+OH=NH2+H2O	2.040E+06	2.04	566.0
119.	NH3+H=NH2+H2	5.420E+05	2.40	9917.0
120.	NH3+O=NH2+OH	9.400E+06	1.94	6460.0
121.	NH3+M=NH2+H+M	2.200E+16	0.00	93470.0
122.	NNH+NO=N2+HNO	2.000E+13	0.00	0.0
123.	NNH+H=N2+H2	1.000E+14	0.00	0.0
124.	NNH+OH=N2+H2O	5.000E+13	0.00	0.0
125.	NNH+NH2=N2+NH3	5.000E+13	0.00	0.0
126.	NNH+NH=N2+NH2	5.000E+13	0.00	0.0
127.	HNO+OH=NO+H2O	1.295E+07	1.88	-958.0
128.	H+HNO=H2+NO	4.460E+11	0.72	655.0
129.	HNO+NH2=NH3+NO	2.000E+13	0.00	1000.0
130.	N+NO=N2+O	3.270E+12	0.30	0.0
131.	O+NO=N+O2	3.800E+09	1.00	41375.0
132.	NO+H=N+OH	1.700E+14	0.00	48800.0
133.	HNO+HNO=N2O+H2O	3.630E-03	3.98	1190.0
134.	N2O+NO=N2+NO2	4.290E+13	0.00	47130.0
135.	NO+NO+NO=N2O+NO2	1.070E+10	0.00	26800.0
136.	HOCO+M=OH+CO+M	2.190E+23	-1.89	35270.0
137.	CO+NO2=NO+CO2	9.040E+13	0.00	33780.0
138.	CH+NO2=HCO+NO	1.010E+14	0.00	0.0
139.	H2+NO2=HONO+H	3.210E+12	0.00	28810.0
140.	NNH=N2+H	3.000E+08	0.00	0.0
	Declared duplicate reaction...			
141.	NNH+M=N2+H+M	1.000E+13	0.50	3060.0
	Declared duplicate reaction...			
142.	HNO+NO+NO=HNNO+NO2	1.700E+11	0.00	2100.0
143.	HNNO+NO=NNH+NO2	3.200E+12	0.00	270.0
144.	HNNO+NO=N2+HONO	2.600E+11	0.00	810.0
145.	HNNO+M=H+N2O+M	2.200E+15	0.00	21600.0
146.	HNNO+M=N2+OH+M	1.000E+15	0.00	25600.0
147.	HCO+NO=HNO+CO	7.230E+12	0.00	0.0
148.	O+CH2O<=>OH+HCO	3.900E+13	0.00	3540.0
149.	O+CH2OH<=>OH+CH2O	1.000E+13	0.00	0.0

150.	O+CH3O<=>OH+CH2O	1.000E+13	0.00	0.0
151.	O+CH3OH<=>OH+CH2OH	3.880E+05	2.50	3100.0
152.	O+CH3OH<=>OH+CH3O	1.300E+05	2.50	5000.0
153.	O2+CH2O<=>HO2+HCO	1.000E+14	0.00	40000.0
154.	H+HCO(+M)<=>CH2O(+M)	1.090E+12	0.48	-260.0
	Low pressure limit:	0.13500E+25	-0.25700E+01	0.14250E+04
	TROE centering:	0.78240E+00	0.27100E+03	0.27550E+04 0.65700E+04
	H2	Enhanced by	2.000E+00	
	H2O	Enhanced by	6.000E+00	
	CO	Enhanced by	1.500E+00	
	CO2	Enhanced by	2.000E+00	
155.	H+CH2O(+M)<=>CH2OH(+M)	5.400E+11	0.45	3600.0
	Low pressure limit:	0.12700E+33	-0.48200E+01	0.65300E+04
	TROE centering:	0.71870E+00	0.10300E+03	0.12910E+04 0.41600E+04
	H2	Enhanced by	2.000E+00	
	H2O	Enhanced by	6.000E+00	
	CO	Enhanced by	1.500E+00	
	CO2	Enhanced by	2.000E+00	
156.	H+CH2O(+M)<=>CH3O(+M)	5.400E+11	0.45	2600.0
	Low pressure limit:	0.22000E+31	-0.48000E+01	0.55600E+04
	TROE centering:	0.75800E+00	0.94000E+02	0.15550E+04 0.42000E+04
	H2	Enhanced by	2.000E+00	
	H2O	Enhanced by	6.000E+00	
	CO	Enhanced by	1.500E+00	
	CO2	Enhanced by	2.000E+00	
157.	H+CH2O<=>HCO+H2	2.300E+10	1.05	3275.0
158.	H+CH2OH(+M)<=>CH3OH(+M)	1.800E+13	0.00	0.0
	Low pressure limit:	0.30000E+32	-0.48000E+01	0.33000E+04
	TROE centering:	0.76790E+00	0.33800E+03	0.18120E+04 0.50810E+04
	H2	Enhanced by	2.000E+00	
	H2O	Enhanced by	6.000E+00	
	CO	Enhanced by	1.500E+00	
	CO2	Enhanced by	2.000E+00	
159.	H+CH2OH<=>H2+CH2O	2.000E+13	0.00	0.0
160.	H+CH3O(+M)<=>CH3OH(+M)	5.000E+13	0.00	0.0
	Low pressure limit:	0.86000E+29	-0.40000E+01	0.30250E+04
	TROE centering:	0.89020E+00	0.14400E+03	0.28380E+04 0.45569E+05
	H2	Enhanced by	2.000E+00	
	H2O	Enhanced by	6.000E+00	
	CO	Enhanced by	1.500E+00	
	CO2	Enhanced by	2.000E+00	
161.	H+CH3O<=>H+CH2OH	3.400E+06	1.60	0.0
162.	H+CH3O<=>H2+CH2O	2.000E+13	0.00	0.0
163.	H+CH3OH<=>CH2OH+H2	1.700E+07	2.10	4870.0
164.	H+CH3OH<=>CH3O+H2	4.200E+06	2.10	4870.0
165.	H2+CO(+M)<=>CH2O(+M)	4.300E+07	1.50	79600.0
	Low pressure limit:	0.50700E+28	-0.34200E+01	0.84350E+05
	TROE centering:	0.93200E+00	0.19700E+03	0.15400E+04 0.10300E+05
	H2	Enhanced by	2.000E+00	
	H2O	Enhanced by	6.000E+00	
	CO	Enhanced by	1.500E+00	
	CO2	Enhanced by	2.000E+00	
166.	OH+CH2O<=>HCO+H2O	3.430E+09	1.18	-447.0
167.	OH+CH2OH<=>H2O+CH2O	5.000E+12	0.00	0.0
168.	OH+CH3O<=>H2O+CH2O	5.000E+12	0.00	0.0
169.	OH+CH3OH<=>CH2OH+H2O	1.440E+06	2.00	-840.0
170.	OH+CH3OH<=>CH3O+H2O	6.300E+06	2.00	1500.0
171.	HO2+CH2O<=>HCO+H2O2	1.000E+12	0.00	8000.0
172.	CH+H2O<=>H+CH2O	1.713E+13	0.00	-755.0
173.	CH2OH+O2<=>HO2+CH2O	1.800E+13	0.00	900.0
174.	CH3O+O2<=>HO2+CH2O	4.280E-13	7.60	-3530.0
175.	HCO+HNO=CH2O+NO	6.000E+11	0.00	2000.0
176.	CH2O+NO2=HCO+HONO	8.020E+02	2.77	13730.0
177.	HCO+NO2=CO+HONO	1.240E+23	-3.29	2355.0
178.	HCO+NO2=H+CO2+NO	8.390E+15	-0.75	1930.0

Note: Units for the rate parameters are centimeters, seconds, and moles and for E , calories per mole. For reactions followed by three numerical parameters, the rate-coefficient expression is $k = AT^b \exp(-E/RT)$. For reactions that appear twice with the phrase "Declared duplicate reaction . . .," the rate coefficient is computed as the sum of the two three-parameter expressions. For reactions involving a generalized collider species M , collider efficiencies different from 1.0 are specified. For reactions involving pressure-dependent rate expressions, that is, those with a collider species specified as $(+M)$, three types of expression are used. If "T&H VALUE" occurs in the output, the Tsang and Herron form was used, as described in Ref. 46, with constants a_0 and a_1 (if the latter is used) appearing, respectively, on the same line. A version of CHEMKIN modified at the U.S. Army Research Laboratory was used to allow this computation. If "TROE centering:" occurs, the TROE form was used with appropriate parameters specified on that line. If neither of these is mentioned, the Lindemann form was assumed. Descriptions of the TROE and the Lindemann expressions may be found in the CHEMKIN manual.⁴⁷

References

- ¹Parr, R. G., and Crawford, B. L., "A Physical Theory of Burning of Double-Base Rocket Propellants," *Journal of Physical and Colloid Chemistry*, Vol. 54, 1950, pp. 929–952.
- ²Rice, O. K., and Ginell, R., "The Theory of the Burning of Double-Base Rocket Powders," *Journal of Physical and Colloid Chemistry*, Vol. 54, 1950, pp. 885–917.
- ³Miller, M. S., "In Search of an Idealized Model of Homogeneous Solid Propellant Combustion," *Combustion and Flame*, Vol. 46, No. 1, 1982, pp. 51–73.
- ⁴Ramohalli, K. N. R., "Steady-State Burning of Composite Propellants Under Zero Cross-Flow Situation," *Fundamentals of Solid-Propellant Combustion*, edited by K. Kuo and M. Summerfield, Vol. 90, Progress in Astronautics and Aeronautics, AIAA, New York, 1984, pp. 409–477.
- ⁵Liau, Y.-C., and Yang, V., "A Time-Accurate Analysis of RDX Monopropellant Combustion with Detailed Chemistry," *Proceedings of the 32nd JANNAF Combustion Subcommittee and 1995 Propulsion Systems Hazards Subcommittee Meeting*, CPIA Publ. 638, Vol. 1, Chemical Propulsion Information Agency, Columbia, MD, 1995, pp. 57–67.
- ⁶Liau, Y.-C., and Yang, V., "An Improved Model of Laser-Induced Ignition of RDX Monopropellant," *Proceedings of the 33rd JANNAF Combustion Meeting*, CPIA Publ. 653, Vol. 2, Chemical Propulsion Information Agency, Columbia, MD, 1996, pp. 529–545.
- ⁷Sotter, J. G., "Chemical Kinetics of the Cordite Explosion Zone," *Proceedings of the Tenth Symposium (International) on Combustion*, The Combustion Inst., Pittsburgh, PA, 1965, pp. 1405–1411.
- ⁸Ermolin, N. E., Korobeinichev, O. P., Tereschenko, A. G., and Fomin, V. M., "Kinetic Calculations and Mechanism Definition for Reactions in an Ammonium Perchlorate Flame," *Fizika Goreniya i Vzryva*, Vol. 18, No. 1, 1982, pp. 61–70.
- ⁹Ermolin, N. E., Korobeinichev, O. P., Kuibida, L. V., and Fomin, V. M., "Study of the Kinetic and Mechanism of Chemical Reactions in Hexogen Flames," *Fizika Goreniya i Vzryva*, Vol. 22, 1986, pp. 544–553.
- ¹⁰Guirao, C., and Williams, F. A., "A Model for Ammonium Perchlorate Deflagration Between 20 and 100 atm," *AIAA Journal*, Vol. 9, 1971, pp. 1345–1356.

¹¹Hatch, R. L., "Chemical Kinetics Combustion Model of the NG/Binder System," *Proceedings of the 23rd JANNAF Combustion Meeting*, CPIA Publ. 457, Vol. 1, Oct. 1986, pp. 157–165.

¹²Kee, R. J., Grcar, J. F., Smooke, M. D., and Miller, J. A., "A Fortran Program for Modeling Steady Laminar One-Dimensional Premixed Flames," Sandia National Lab. Rept. SAND85-8240, Dec. 1985, reprinted, March 1991.

¹³Melius, C. F., "Thermochemical Modeling: II. Application to Ignition and Combustion of Energetic Materials," *Chemistry and Physics of Energetic Materials*, edited by S. Bulusu, NATO ASI 309, 1990, pp. 51–78.

¹⁴Liau, Y.-C., and Yang, V., "Analysis of RDX Monopropellant Combustion with Two-Phase Subsurface Reactions," *Journal of Propulsion and Power*, Vol. 11, 1995, pp. 729–739.

¹⁵Liau, Y.-C., "A Comprehensive Analysis of RDX Propellant Combustion and Ignition with Two-Phase Subsurface Reactions," Ph.D. Dissertation, Dept. of Mechanical Engineering, Pennsylvania State Univ., University Park, PA, May 1997.

¹⁶Prasad, K., Yetter, R. A., and Smooke, M. D., "An Eigenvalue Method for Computing the Burning Rates of RDX Propellants," *Combustion Science and Technology*, Vol. 124, No. 1, 1997, pp. 35–82.

¹⁷Davidson, J. E., and Beckstead, M. W., "Improvements to Steady-State Combustion Modeling of Cyclotrimethylenetrinitramine," *Journal of Propulsion and Power*, Vol. 13, 1997, pp. 375–383.

¹⁸Davidson, J. E., and Beckstead, M. W., "A Three-Phase Model of HMX Combustion," *Proceedings of the Twenty-Sixth Symposium (International) on Combustion*, The Combustion Inst., Pittsburgh, PA, 1996, pp. 1989–1996.

¹⁹Prasad, K., Yetter, R. A., and Smooke, M. D., "An Eigenvalue Method for Computing the Burning Rate of HMX Propellants," *Combustion and Flame*, Vol. 115, 1998, pp. 406–416.

²⁰Davidson, J. E., and Beckstead, M. W., "A Mechanism and Model for GAP Combustion," *Proceedings of the 33rd JANNAF Combustion Meeting*, CPIA Publ. 653, Vol. 2, Chemical Propulsion Information Agency, Columbia, MD, 1996, pp. 91–100.

²¹Miller, M. S., "Three-Phase Combustion Modeling: Frozen Ozone, a Prototype System," *Proceedings of the Materials Research Society Symposium: Decomposition, Combustion and Detonation Chemistry of Energetic Materials*, edited by T. B. Brill, T. P. Russell, W. C. Tao, and R. B. Wardle, Materials Research Society, Pittsburgh, PA, 1996, pp. 169–180.

²²BenReuven, M., Caveny, L. H., Vichnevetsky, R. J., and Summerfield, M., "Flame Zone and Sub-Surface Reaction Model for Deflagrating RDX," *Proceedings of the Sixteenth Symposium (International) on Combustion*, The Combustion Inst., Pittsburgh, PA, 1977, pp. 1223–1233.

²³BenReuven, M., "Nitramine Monopropellant Deflagration and Non-Steady, Reacting Rocket Chamber Flows," Ph.D. Dissertation, Dept. of Mechanical and Aerospace Engineering, Princeton Univ., Princeton, NJ, Jan. 1980.

²⁴Bizot, A., and Beckstead, M. W., "A Model for Double Base Propellant Combustion," *Proceedings of the Twenty-Second Symposium (International) on Combustion*, The Combustion Inst., Pittsburgh, PA, 1989, pp. 1827–1834.

²⁵Song, H., and Yang, D., "Model for Predicting the Burning Rate of Double Base Propellants from Ingredients," *Proceedings of the 28th International Annual Conference of ICT*, Fraunhofer Institut Chemische Technologie, Karlsruhe, Germany, June 1997, pp. 84-1–84-12.

²⁶Li, S. C., and Williams, F. A., "Nitramine Deflagration: Reduced Chemical Mechanism for Primary Flame Facilitating Simplified Asymptotic Analysis," *Journal of Propulsion and Power*, Vol. 12, 1996, pp. 302–309.

²⁷Brill, T. B., Arisawa, H., Brush, P. J., Gongwer, P. E., and Williams, G. K., "Surface Chemistry of Burning Explosives and Propellants," *Journal of Physical Chemistry*, Vol. 99, 1995, pp. 1384–1392.

²⁸Zenin, A., "HMX and RDX: Combustion Mechanism and Influence on Modern Double-Base Propellant Combustion," *Journal of Propulsion and Power*, Vol. 11, 1995, pp. 752–758.

²⁹Ward, M. J., Son, S. F., and Brewster, M. Q., "Steady Deflagration of HMX with Simple Kinetics: A Gas Phase Chain Reaction Model," *Combustion and Flame*, Vol. 114, 1998, pp. 556–568.

³⁰Shoemaker, R. L., Stark, J. A., and Taylor, R. E., "Thermophysical Properties of Propellants," *High Temperatures—High Pressures*, Vol. 17, 1985, pp. 429–435.

³¹Miller, M. S., "Thermophysical Properties of Cyclotrimethylenetrinitramine," *Journal of Thermophysics and Heat Transfer*, Vol. 8, 1994, pp. 803–805.

³²Ulas, A., Lu, Y. C., Kuo, K. K., and Freyman, T., "Measurement of Temperature and NO and OH Concentrations of Solid Propellant Flames Using Absorption Spectroscopy," *Proceedings of the 32nd JANNAF Combustion Meeting*, CPIA Publ. 631, Vol. 1, Chemical Propulsion Information Agency, Columbia, MD, 1995, pp. 461–469.

³³Homan, B. E., Miller, M. S., and Vanderhoff, J. A., "Absorption Diagnostics and Modeling Investigations of RDX Flame Structure," *Combustion and Flame* (to be published).

³⁴Atwood, A., Curran, P. O., Price, C. F., and Winklich, J., "Burning Rate, Radiant Ignition, and Global Kinetics of Cyclotrimethylene Trinitramine (RDX)," *Proceedings of the 32nd JANNAF Combustion Meeting*, CPIA Publ. 638, Vol. 1, Chemical Propulsion Information Agency, Columbia, MD, 1995, pp. 149–159.

³⁵Sausa, R. C., Anderson, W. R., Dayton, D. C., Faust, C. M., and Howard, S. L., "Detailed Structure Study of a Low Pressure, Stoichiometric $H_2/N_2O/Ar$ Flame," *Combustion and Flame*, Vol. 94, 1993, pp. 407–425.

³⁶Anderson, W. R., Ilincic, N., Meagher, N. E., Seshadri, K., and Vanderhoff, J. A., "Detailed and Reduced Chemical Kinetic Mechanisms for the Dark Zones of Double-Base and Nitramine Propellants in the Intermediate Temperature Regime," *Proceedings of the 32nd JANNAF Combustion Subcommittee Meeting and 1995 Propulsion Systems Hazards Subcommittee Meeting*, CPIA Publ. 638, Vol. 1, Chemical Propulsion Information Agency, Columbia, MD, 1995, pp. 197–114.

³⁷Ilincic, N., Anderson, W. R., Seshadri, K., and Meagher, N., "Simplified Chemical-Kinetic Mechanisms for Characterizing the Structure of the Dark Zones of Double-Base and Nitramine Propellants," *Proceedings of the 26th Symposium (International) on Combustion*, The Combustion Inst., Pittsburgh, PA, 1996, pp. 1997–2006.

³⁸Andreev, K. K., "Experimental Investigation on Combustion of Explosives," *Collection of Articles on Theory of Explosives*, Oborongiz, Moscow, 1940, pp. 39–65.

³⁹Andreev, K. K., *Thermal Decomposition and Combustion of Explosives*, Gosenergoizdat, Moscow-Leningrad, 1957.

⁴⁰Andreev, K. K., Glazkova, A. P., and Tereshkin, I. A., "Investigation of Pressure, Temperature, and Density Influence on Combustion, Explosives, and Some Composites," Rept. of Chemical Physics Inst., Moscow, 1959, 1960.

⁴¹Tsang, W., and Herron, J. T., "Chemical-Kinetic Data Base for Propellant Combustion. I. Reactions Involving NO, NO₂, HNO, HNO₂, HCN, and N₂O," *Journal of Physical and Chemical Reference Data*, Vol. 20, 1991, pp. 609–663.

⁴²Lin, C. Y., Wang, H. T., Lin, M. C., and Melius, C. F., "A Shock Tube Study of the $\text{CH}_2\text{O} + \text{NO}_2$ Reaction at High Temperatures," *International Journal of Chemical Kinetics*, Vol. 22, 1990, pp. 455–482.

⁴³Robbins, F. W., and Worrell, D. A., "Fastcore Layered Propellant Study," *Proceedings of the 29th JANNAF Combustion Meeting*, CPIA Publ. 593, Vol. 1, Chemical Propulsion Information Agency, Columbia, MD, 1992, pp. 91–98.

⁴⁴Miller, M. S., and Anderson, W. R., "Detailed Combustion Modeling as a Aid to Propellant Formulation: Two New Strategies," U.S. ARL Memorandum Rept., U.S. Army Research Lab., Aberdeen Proving Ground, MD, 1999.

⁴⁵Kooker, D. E., Howard, S. L., and Chang, L.-M., "Flamespreading in Granular Solid Propellant: Initial Results," *Proceedings of the 30th JANNAF Combustion Meeting*, CPIA Publ. 606, Vol. 1, Chemical Propulsion Information Agency, Columbia, MD, 1993, pp. 241–258.

⁴⁶Tsang, W., and Herron, J. T., "Chemical Kinetic Data Base for Propellant Combustion. I. Reactions Involving NO , NO_2 , HNO , HNO_2 , HCN , and N_2O ," *Journal of Physical and Chemical Reference Data*, Vol. 20, 1991, pp. 609–663. Note that the log expressions used in this source are for base 10 (W. Tsang, private communication).

⁴⁷Kee, R. J., Rupley, F. M., and Miller, J. A., "Chemkin-II: A Fortran Chemical Kinetics Package for the Analysis of Gas-Phase Chemical Kinetics," Sandia National Lab. Rept. SAND89-8009, Sept. 1989.

Chapter 2.13

**Burning-Rate Prediction of Double-Base
Plateau Propellants**

Dong Yang* and Hongchang Song†

*Nanjing University of Science and Technology,
Nanjing, People's Republic of China*

and

Fengqi Zhao‡ and Shangwen Li§

*Xi'an Modern Chemistry Research Institute,
Xi'an, People's Republic of China***Nomenclature**

C_A	= catalytic coefficient of lead salt
C_B	= enhancement coefficient of carbon black on lead salt
C_C	= enhancement coefficient of copper salt on lead salt
C_R	= enhancement coefficient of hexogen on lead salt
C_1	= catalytic coefficient of lead salt, copper salt, and carbon black compound catalyst
C_2	= catalytic coefficient of copper salt
[CH]	= representatives of less reactive hydrocarbon groups
[CHO]	= representatives of splittable free radical/groups
[CH ₂ O]	= representatives of reductive groups
[CO]	= representatives of less reactive groups containing CO
d_H	= size of the particle of nitramine
g	= influence level of catalysts on reaction (5)
g_1	= influence level of lead salt, carbon black, and copper salt compound catalyst on reaction (5)
g_2	= influence level of copper salt on reaction (5)
[NO ₂]	= representatives of oxidative groups

Copyright © 1999 by the authors. Published by the American Institute of Aeronautics and Astronautics, Inc., with permission.

* Associate Professor, School of Chemical Engineering.

† Professor, School of Chemical Engineering.

‡ Associate Professor.

§ Professor.

p	= pressure, MPa
p_a	= pressure at the time when the content of newly produced lead is the maximum
p'_a	= pressure at the time when the content of newly produced catalytic centers from copper salt is the maximum, 17.73 MPa
p^*	= first characteristic pressure, MPa
p^{**}	= second characteristic pressure, MPa
q	= ratio of the quantity of [CHO] to the quantity of [NO ₂]
u	= burning rate, cm/s
v	= pressure exponent
v_1	= pressure exponent contributed by the natural split of [CHO]
v_2	= pressure exponent contributed by compound catalyst
v_3	= pressure exponent contributed by nitramine
w_a	= parameter related to the catalytic effect pressure region, in MPa
w'_a	= parameter related to the catalytic effect pressure region of copper salt, 7.84 Mpa
X	= content of catalysts
X_N	= quantity of [N ₂ O] groups in 1-kg propellant
X_0	= characteristic content
Z_1	= relative total quantity of gaseous products in the initial stage of propellant burning
Z_2	= relative total quantity of gaseous oxide in the initial stage of propellant burning
α	= ratio of the quantity of [CH] to the quantity of [NO ₂]
α'	= quantity of [CH]
α_H	= percentage of nitramine in the propellant
α_N	= ratio of the quantity of [N ₂ O] to the quantity of [NO ₂]
β	= ratio of the quantity of [CO] to the quantity of [NO ₂]
β'	= quantity of [CO]
γ	= ratio of the quantity of [CH ₂ O] to the quantity of [NO ₂]
γ'	= quantity of [CH ₂ O]
δ	= quantity of [NO ₂]
η	= function describing the natural split of [CHO]
θ_0	= mole fraction of [NO ₂] near the burning surface
ξ	= function describing the transference between C—N homolysis and N—N homolysis of nitramine
ρ_H	= density of nitramine
ρ_P	= density of propellant

I. Introduction

THE plateau combustion phenomena of solid rocket propellants, which are very beneficial ballistics of solid rockets, have drawn much attention since they were discovered in 1946.¹ Up to 1980 researchers interpreted the plateau combustion phenomena from various perspectives and developed a large number of catalytic combustion theories, such as gaseous phase, condensed phase, and gaseous-condensed phase theories. Among them, the free radical theory,² the lead-carbon catalysis theory,³ the subsurface photochemical reaction model,⁴ the complex compound theory,⁵ and the stoichiometric ratio theory⁶ are well known

and could qualitatively explain a part or all of the plateau burning process. References 6–8 developed the super-rate combustion model and the catalytic combustion model, respectively. Based on their hypotheses, the calculated results of their models agree well with the experimental results.

In past years the development of solid-propellant combustion models mainly depended on the transmission of energy and mass during burning processes. The mathematical models were derived from physical models based on experimental observations. The chemical processes of burning were little considered. The development of burning-rate expressions did not depend upon chemical composition and combustion reactions, so that there were few combustion models that could predict the phenomena of super rate, plateau, and mesa quantitatively from the composition (including catalysts) of plateau propellants.

Reference 9 provided a method to predict the burning rate of noncatalyzed double-base propellants from the propellant ingredients. Incorporation of mass transport into this model allowed the development of a combustion model based on the analysis of the chemical structure and characteristic combustion reaction of noncatalyzed propellants. The burning rate is a function of pressure and propellant composition. The calculation of burning rate avoids the measurement of physical parameters, such as heat conduction, chemical-reaction activation energy, and heat effects.

In this investigation the site of the catalytic reaction, the form of the catalytic centers and the split reaction of a class of splittable free radical represented by $[\text{CHO}]$ during the catalytic combustion process near the burning surface are assumed. The mathematical model is developed based on experimental results, and the burning-rate equation of noncatalyzed propellants is extended to include the effect of catalysts. Using this equation, the burning rate and pressure exponent of double-base and nitramine-modified double base plateau propellants can be computed as a function of propellant composition.

II. Theoretical Background

The prediction method for noncatalyzed double-base propellant burning rate and its development was introduced in Ref. 10. The basic model is as follows.

1) In the initial stage of noncatalyzed double-base propellant combustion, the main gaseous combustion products are divided into five classes, which are represented respectively by $[\text{NO}_2]$, $[\text{CH}_2\text{O}]$, $[\text{CHO}]$, $[\text{CH}]$, and $[\text{CO}]$. According to their chemical properties and the role they play in the dominant combustion reaction, the gases are also classified respectively as oxidizers, reducers/fuel, splittable/unstable groups, less reactive hydrocarbons groups, and less reactive CO groups in the burning surface of noncatalyzed double-base propellants.

It is almost impossible to measure accurately the quantities of the five gases present under given combustion condition, but the composition of the propellant and the chemical structure of each component are definite. Therefore, the relationship between the gaseous composition and the chemical structure of the propellant or its components can be developed. The five gases can also represent the chemical groups of the propellant and its components. The quantities of the five classes of gases/groups of a propellant can be calculated by adding the quantity of the five classes of gases/groups of each component together.

The splittable free radical [CHO] represents the class of gases that can split. The form of [CHO] is different at different pressures. When the pressure is very low, [CHO] is present in the vicinity of the burning surface in the form of a polymer, such as $(\text{CHO})_n$. When the pressure is very high, [CHO] splits into two groups, [CO] and [H](categorized to [CH]). The natural split process of [CHO] can be described as the following reaction:



The relationship between the natural split process of the free radical [CHO] and pressure can be described by the following equation:

$$\eta(p) = 2 - \exp[0.6931(1 - p/p^*)] \tag{2}$$

When $p = p^*$, [CHO] is present in the form of CHO and $\eta(p) = 1$. p^* is an empirical value, which is 9.81 MPa for double-base propellants. When $p \gg p^*$, $\eta(p) = 2$. When $p \ll p^*$, $\eta(p) = 0$.

At the characteristic pressure the quantities of the five classes of gases are symbolized as δ' , γ' , q' , β' , and α' . They are also called the chemical structure parameters. Then, the molecular formula of 1-kg propellant can be written as $[\text{NO}_2]_{\delta'}[\text{CH}_2\text{O}]_{\gamma'}[\text{CHO}]_{q'}[\text{CH}]_{\beta'}[\text{CO}]_{\alpha'}$.

2) We symbolized the mole fraction of gaseous oxidizer $[\text{NO}_2]$ near the burning surface as $\theta_0(p)$. If $\alpha = \alpha'/\delta'$, $\beta = \beta'/\delta'$, $q = q'/\delta'$, and $\gamma = \gamma'/\delta'$, then, at any pressure,

$$\theta_0(p) = 1/[\alpha + \beta + q \cdot \eta(p) + \gamma + 1] \tag{3}$$

3) The burning rate of noncatalyzed double-base propellants is a function of pressure and propellant compositions. At 20°C the expression for the burning rate is

$$u(p) = 1.709 p \theta_0^2(p) / \rho_P \text{ cm/s} \tag{4}$$

References 9 and 10 calculated the burning rates of various noncatalyzed double-base propellants. Part of the results are shown in Figs. 1 and 2. The calculated

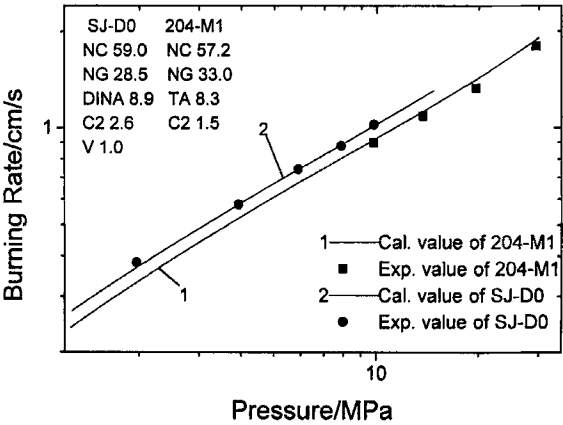


Fig. 1 Burning rate vs pressure for double-base propellants (Chinese propellants).

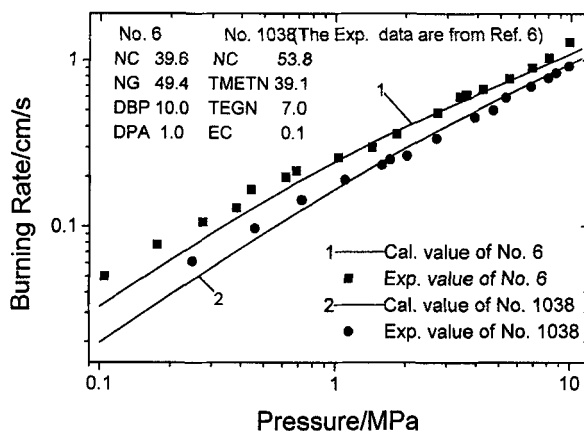


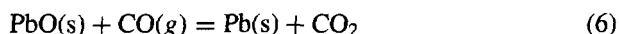
Fig. 2 Burning rate vs pressure for double-base propellants (Kubota's propellants).

burning rates show good agreement with the experimental values in the pressure range from 0.1 to 30 MPa. The burning rates of double-base gun propellants can also be predicted by Eq. (4). References 11–13 give the comparison between the calculated burning rates and the experimental data for various gun propellants. Equation (4) is suitable for calculating the burning rate of double-base propellants even in the range of pressure up to 400 MPa.

III. Mechanism of Plateau Combustion

A. Effects of Catalysts on Burning Surface Physico-Chemistry

To reveal the reaction mechanism of burning-rate catalysts, experiments were conducted to study the interaction among lead salts, copper salts, and carbon black during the decomposition and combustion of double-base propellants. The relationship between the interaction among the catalysts and catalytic combustion was obtained, and results were reported in Ref. 14. The main conclusions are that there are interactions among lead salts, copper salts, and carbon black during propellant combustion. Carbon black and copper salts make lead salts easy to decompose at lower temperatures. At the same time the lead content in the burning surface of propellants increases with an increase in carbon black content, while catalytic activity is promoted by the increase of lead content in the burning surface. That is to say, lead plays the key role in plateau combustion. It is thought that one of the main products of lead salts in the burning surface is PbO, and then PbO produces lead metal through the reactions as follows:



From this lead works in the form of metal, and the microball of lead metal in the burning surface forms the catalytic center.

B. Hypothesis on the Reaction of [CHO] Near Burning Surface

The burning surface of double-base plateau propellants is obviously different from that of a noncatalyzed double-base propellant. A large number of loose carbon structures containing lead appear on the plateau propellant burning surface in the pressure region of catalytic effect, hence make the dividing line between the gas phase and solid phase vague and in the statement of diffusion. When the thermal decomposition products pass through the burning surface, they will definitely be affected by catalytic centers.

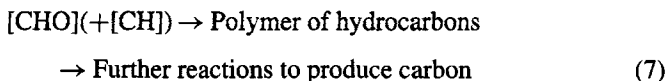
Research on the burning surface structure of double-base plateau propellants³ show that super-rate burning is always related to the appearance of a great deal of carbon in burning surface, whereas carbon disappears gradually upon mesa burning.

No definite theory explains the reason for the production of a great deal of carbon. Kubota et al.⁶ suggest that in the process of plateau propellant combustion the products from the decomposition of lead compound, i.e., lead in metal or lead oxide, change the reaction pathway of nitrate ester degradation in the subsurface zone or burning surface and thus the degradation of a proportion of nitrate ester produces carbon. Ferreira et al.⁷ suggest that the chemical reaction between lead compounds and aldehyde produced from the decomposition of nitrate ester produces carbon. They did not, however, illustrate the mechanism for the production of lead in the burning surface in detail.

The results of fundamental studies¹⁵ on the formation of carbon from gaseous hydrocarbon show that despite the middle products between the primary hydrocarbon and the final products carbon black is produced in polymerization process. The first step is the polymerization of small molecules, and the second is thermal decomposition to produce solid materials through chemical reactions, such as condensation and molecular rearrangement.

For double-base plateau propellants the present paper supposes that the carbons come from certain carbon-containing groups in the nitrate ester whose decomposition is suppressed by catalytic centers and which cannot decompose to gaseous products. They cannot participate in gas-phase combustion reaction but polymerize around the catalytic centers and produce carbon through incomplete combustion.

According to the burning rate prediction model of noncatalyzed double-base propellants, among the five kinds of gases near the burning surface, [CHO] has properties of both polymerization and decomposition. When the propellant has no catalyst, the natural split reaction of [CHO] is as shown in reaction (1). When the propellant has catalysts, the free radical [CHO] conglomerates around the catalytic centers, and its split pathway is changed to



Because [CHO] also is produced in the condensed-phase nitrate ester at the burning surface, chemical reaction (7) indicates that [CHO] can possibly combine the less reactive hydrocarbon groups near it to form a polymer.

Because the decomposition of carbon-containing groups is suppressed by catalytic centers, reaction (7) changes the gaseous composition near the propellant burning surface and reduces the total quantity of gaseous decomposition products.

Hence, if using the function $g(p, X)$ to describe the influence level of catalysts on reaction (7) under different pressures, Eq. (3) is converted to

$$\theta_0(p, X) = 1/\{\alpha + \beta + q \cdot [\eta(p) - g(p, X)] + \gamma + 1\} \quad (8)$$

In normal cases function $g(p, X)$ should possess the following properties:

$$g(p, X) = \begin{cases} 0 & \text{without catalyst} \\ 1 & [\text{CHO}] \text{ all involved in reaction (5)} \\ >1 & [\text{CHO}] \text{ partially involved in reaction (5)} \end{cases} \quad (9)$$

As can be seen from Eq. (8), the mole fraction of oxide gases near the burning surface increases with the effect of catalysts. After the substitution of Eq. (8) into Eq. (3), it can be predicted that the burning rate is higher than that of noncatalyzed propellants. This is the fundamental reason for catalytic combustion.

C. Effect of Nitramines

The experimental results of the effect of hexogen (RDX) on the thermal decomposition of lead salt are given in Ref. 14. The differential scanning calorimeter (DSC) results show the positive effect of RDX on the thermal decomposition of lead salt. The decomposition peak of lead salt shifts to a lower temperature and the heat of decomposition of lead salts in the double-base propellant systems increases with the increase of RDX content in the double-base systems. This phenomenon is similar to the effect of carbon black on the thermal decomposition of lead salt. Reference 16 suggests that RDX combined with the burning characteristics of RDX-composite-modified double-base (CMDB) propellants enhances plateau combustion to a certain extent.

The results of studies of RDX and HMX thermal decomposition¹⁷⁻¹⁹ show that whether the decomposition pathways are C–N homolysis to produce N_2O or N–N homolysis to produce NO_2 depends on temperature. At lower temperature the decomposition reaction begins with C–N bond homolysis, and at higher temperature the N–N bond homolysis is dominant, so there is more NO_2 in the gaseous products at higher temperature than at lower temperature. The temperature of the burning surface of a solid propellant is consistent with pressure in certain regions. The temperature of the propellant burning surface increases with the increase in pressure. Therefore, whether the decomposition pathway of nitramine is C–N bond homolysis or N–N bond homolysis is related to pressure. The following expression can be used to describe the transference between C–N homolysis and N–N bond homolysis:

$$\xi(p) = 1 - e^{-p/p^{**}} \quad (10)$$

where p^{**} is also an empirical parameter and P^{**} is about 40 MPa.

If X_N is the quantity of the $[\text{N}_2\text{O}]$ group that can belong to the $[\text{CO}]$ group in 1 kg of propellant and $\alpha_N = X_N/\delta'$, then Eq. (8) is changed to

$$\vartheta_0(p, X) = \frac{1 + \xi(p) \cdot \alpha_N}{\alpha + \beta + q[\eta(p) - g(p, X)] + \gamma + 1} \quad (11)$$

IV. Burning Rate Equation of DB and RDX-CMDB Propellants

A. Influence Level of Catalysts on the Reaction of [CHO]

From the principle of the effect of catalysts on the burning characteristic of propellants, lead salts play the main catalytic role, copper salts and carbon black play the assistant catalytic role, and copper salts also have independent catalytic effect similar to lead salts. So the $g(p, X)$ function can be expressed as follows:

$$g(p, X) = g_1(p, X) + g_2(p, X) \quad (12)$$

where $g_1(p, X)$ is the influence level of lead salts on reaction (7) and $g_2(p, X)$ is the influence level of copper salts on reaction (7).

According to the experimental results, the lead content of the propellant burning surface is consistent with catalytic activity. On the burning surface of solid propellants, lead catalytic centers are produced, accumulate, and then disappear. Analysis of the data in Refs. 20–22 suggest that the change in lead content of the burning surface with pressure can be described as follows:

$$g_1(p, X) = C_1(X)\exp\{ -[(p - p_a)/w_a]^2 \} \quad (13)$$

The experimental results¹⁹ show that the lead content of the burning surface is higher at lower pressure. $C_1(X)$ is the coefficient of catalytic activity and is related to the variety and the content and species of catalysts in propellants and is one-dimensional. X is the percentage of catalysts and is one-dimensional.

When lead salt is the only catalyst in solid propellants, the coefficient $C_1(X)$ is only related to lead salt, and

$$C_1(X) = C_A \quad (14)$$

Because carbon black promotes the thermal decomposition of lead salt and makes the lead content of burning surface increase when the solid propellant contains lead salt and carbon black,

$$C_1(X) = C_A(1 + C_B) \quad (15)$$

where C_B is the enhancement coefficient, which reflects the effect of carbon black on the catalytic activity of lead salts, and is one-dimensional.

If C_C is the enhancement coefficient, which reflects the effect of copper salt on the catalytic activity of lead salt, when the propellant contains lead salt, copper salt, and carbon black,

$$C_1(X) = C_A(1 + C_B)(1 + C_C) \quad (16)$$

If C_R is the enhancement coefficient, which reflects the effect of RDX on the catalytic activity, according to the mechanism described in Sec. III.C, then

$$C_1 = C_A[1 + C_B(1 + C_R)](1 + C_C) \quad (17)$$

Reference 23 shows that copper compounds play the role of plateau catalysis in the middle- and high-pressure regions (14.7–20.5 MPa). The assumption is made that the catalytic centers formed by copper salt also promote reaction (7), so that the function $g_2(p, X)$ can be written as

$$g_2(p, X) = C_2(X)\exp\{ -[(p - p'_a)/w'_a]^2 \} \quad (18)$$

$C_2(X)$ is related to the variety and content of copper salt, which is one-dimensional, $Pa' = 13.73$ MPa, and $w_a' = 7.84$ MPa.

When the variety of plateau catalysts is defined, the catalytic activity is related to the catalyst content. Based on the experimental results, the expressions of C_A , C_B , C_C in $C_1(X)$ and $C_2(X)$ are the same in form:

$$Y = \begin{cases} \phi \exp[-(x - x_0)/x x_0] & X > 0 \\ 0 & X = 0 \end{cases} \quad (19)$$

where ϕ is the weight, is related to the properties of the catalyst, and is one-dimensional; X is the lead content, carbon to lead ratio (C/Pb), and copper to lead ratio (Cu/Pb); X_0 is the characteristic catalyst content (one-dimension quantity); and the values of ϕ and X_0 can be determined by a series of typical double-base plateau propellants.²⁴⁻³¹

The value of catalytic pressure region parameter w_a is related to the residence time of catalytic centers on the burning surface. Accurate measurements have not yet been carried out, but it can be determined by the analysis of burning laws.

B. Burning-Rate Equation

Considering the effect of the particle size of nitramine on the area of burning surface, Ref. 9 gave the effect of nitramine on the burning rate as the parameter h_H ,

$$h_H = 1 + 1.73(\rho_p/\rho_H)^{\frac{1}{3}}(\alpha_H)^{\frac{1}{3}}d_H \quad (20)$$

Using Eqs. (8-20), Eq. (4) is rewritten as

$$u(p, X) = 1.709 p \theta_0^2(p, X) h_H / \rho_p \text{ cm/s} \quad (21)$$

Equation (21) is the burning-rate formula for double-base plateau propellants and RDX-CMDB plateau propellants. That is, when the particle size of nitramine is increased, the area of the burning surface increases, and the burning rate increases.

C. Burning-Rate Pressure Exponent

Taking the natural logarithm of the two sides of Eq. (21) and calculating the first derivative of $\ln u(p, X)$ with respect to $\ln p$ gives the burning-rate pressure exponent of plateau propellants,

$$v(p, X) = 1 + v_1(p, X) + v_2(p, X) + v_3(p, X) \quad (22)$$

where

$$v_1(p, X) = -2 \frac{pq}{Z_1} \cdot \frac{\partial \eta(p)}{\partial p} \quad (23)$$

$$v_2(p, X) = -2 \frac{pq}{Z_1} \cdot \frac{\partial g(p, X)}{\partial p} \quad (24)$$

$$v_3(p, X) = 2 \frac{p\alpha_N}{Z_2} \cdot \frac{\alpha \xi(p)}{\partial p} \quad (25)$$

$$Z_1 = \alpha + \beta + [\eta(p) - g(p, X)] \cdot q + \gamma + 1 \quad (26)$$

$$Z_2 = 1 + \xi(p) \cdot \alpha_N \quad (27)$$

Table 1 Detail of propellant compositions (wt. %)^a

Number	NC/NG/DEP/C2	Lead flake	Cupric adipate	Carbon black
1	60.0/29.9/7.3/2.8	—	—	—
2	59.5/29.3/7.18/2.7	1.0	0.32	—
3	59.4/29.3/7.08/2.7	1.0	0.32	0.2
4	59.3/29.3/7.08/2.7	1.0	0.32	0.3

^aPropellants manufactured at Xi'an Modern Chemistry Research Institute.

V. Results and Discussion

A. Calculated Results

The propellant compositions investigated here are shown in Tables 1–3. Among them, Nos. 5–7 are from the U.S. Patent as described in Ref. 26. The authors prepared the others. Table 4 shows the catalytic parameters that are used in the calculation. Figures 3–5 are the plots of burning rate vs pressure. The figures show that the burning rates of different propellants of which main compositions and the catalyst contents are different can be computed by means of the formula described here. The results not only model every stage of the plateau combustion, such as super rate, plateau, and mesa of DB and RDX-CMDB propellants, but also have good agreement with the experimental results. Figures 6–8 show the relationships between the pressure and pressure exponents of propellant Nos. 1–11. The pressure exponent does in fact change with the pressure, and the pressure exponents have an extremely low value.

B. Plateau Combustion Phenomena

From Eq. (21) the burning rate $u(p, X)$ is in direct proportion to $p\theta_0^2(p, X)$. In the pressure region where catalysts are effective, the value of $\theta_0(p, X)$ is larger than $\theta_0(p)$ of the noncatalyzed propellant. Therefore, the burning rate of the catalyzed propellant is higher than that of the noncatalyzed propellant, and there are three relationships between $p\theta_0^2(p, X)$ and $(p + \Delta p)\theta_0^2(p + \Delta p, X)$. Correspondingly, there are three combustion phenomena in relation between burning rate and pressure:

- 1) $p\theta_0^2(p, X) < (p + \Delta p)\theta_0^2(p + \Delta p, X)$, super rate combustion.
- 2) $p\theta_0^2(p, X) = (p + \Delta p)\theta_0^2(p + \Delta p, X)$, plateau combustion.
- 3) $p\theta_0^2(p, X) > (p + \Delta p)\theta_0^2(p + \Delta p, X)$, mesa combustion.

Table 2 Detail of propellant compositions (wt. %)^a

Number	NC/NG/TA/C2	Lead stearate	Carbon black ^b
5	58.5/27.0/8.5/4.0	2.0	—
6	58.5/27.0/8.5/4.0	2.0	0.35
7	58.5/27.0/8.5/4.0	2.0	0.75

^aPropellants and burning rate from Ref. 23.

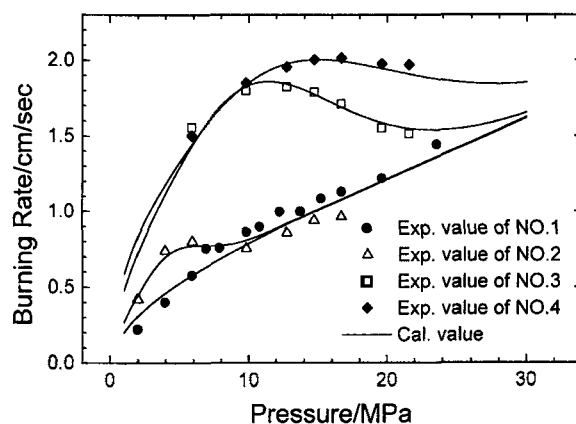
^bAdditional carbon black.

Table 3 Detail of propellant composition (wt. %)^a

Number	NC/NG/DEP/C2	RDX	Lead salt ^b	Copper salt ^c	Carbon black
8	37.5/27.4/3.0/2.0	30.1	—	—	—
9	35.5/25.7/3.0/2.0	30.1	3.0	0.4	0.3
10	35.7/25.7/3.0/2.0	30.1	2.5	0.4	0.6
11	35.5/25.7/3.0/2.0	30.1	2.5	0.4	0.8

^aPropellants manufactured at Xi'an Modern Chemistry Research Institute.^bLead phthalate.^cCupric 2,4-dihydroxybenzoate.**Table 4** Catalytic parameters used in calculation

Number	P_a /MPa	w_a /MPa	$C_1(X)$	$C_2(X)$
2	3.92	3.92	0.55	0.003
3	8.83	11.77	1.25	0.003
4	9.81	16.67	1.25	0.003
5	1.47	1.47	0.50	—
6	8.83	10.30	0.85	—
7	8.83	12.75	0.50	—
9	3.92	5.88	1.60	0.005
10	3.92	8.83	1.80	0.005
11	3.92	9.81	1.90	0.005

**Fig. 3** Burning rate vs pressure for propellants 1–4.

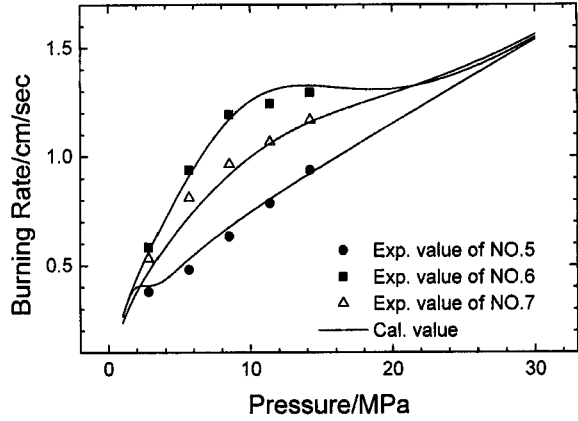


Fig. 4 Burning rate vs pressure for propellants 5–7.

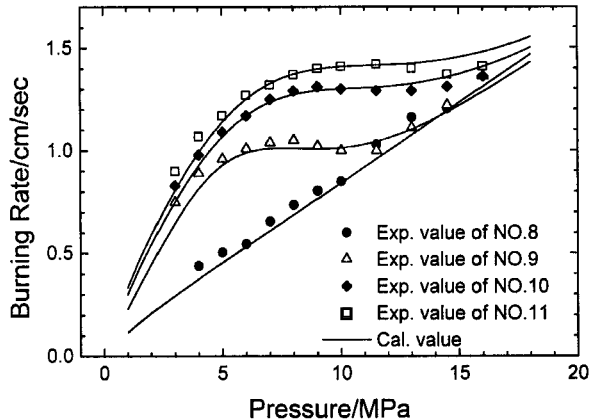


Fig. 5 Burning rate vs pressure for propellants 8–11.

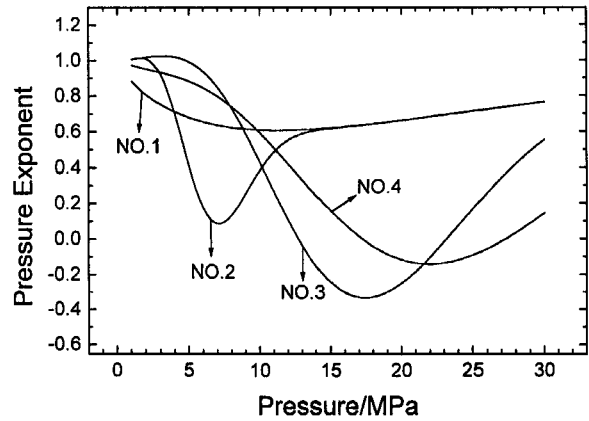


Fig. 6 Pressure exponent vs pressure of propellants 1–4.

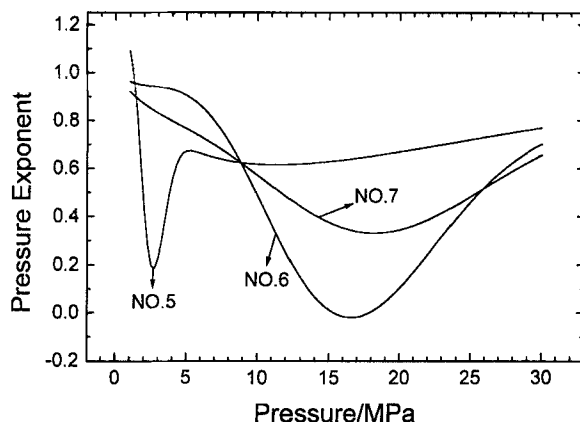


Fig. 7 Pressure exponent vs pressure for propellants 5-7.

When the pressure exceeds the catalytic pressure region and $\theta_0(p, X)$ is approximately equal to $\theta_0(p)$, the burning rate follows the law of the noncatalyzed propellant. This is the reason why the super rate, plateau, and mesa appear in the integral plateau combustion. Sometimes, in the later stage of mesa combustion, the burning rate of the catalyzed propellant is slower than that of the noncatalyzed propellant. It is perhaps because of this that the reduction of the catalytic centers accelerates the split of free radical $[CHO]$. This will be investigated in the future using the model.

C. Effect of Chemical Structure Factors on Plateau Combustion

In the plateau combustion reaction $[CHO]$ free radical is the catalysant. The conclusion is made from Eq. (22) that the pressure exponent is closely related to the value of mole fraction q/Z_1 of $[CHO]$ free radical in the burning surface. The higher the q/Z_1 value is, the lower the pressure exponent is. Therefore, only

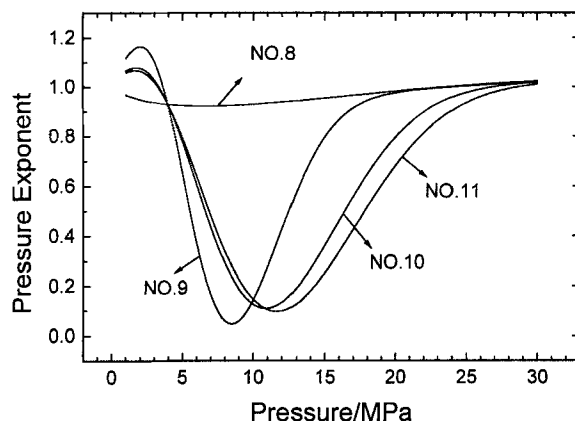


Fig. 8 Pressure exponent vs pressure for propellants 8-11.

when there are sufficient [CHO] in the propellant chemical structure can it guarantee that the catalytic reaction will be fully completed. The ingredients determine the chemical structure parameters of the propellant. Each ingredient of the propellant has its own chemical structure parameters, such as δ' , γ' , q' , β' , and α' . Reference 9 gives the chemical structure parameters of propellants in common use. Among them, the value of q' of nitrocellulose is the largest. If the content of nitrocellulose is reduced, the catalysant [CHO] in the chemical structure of the propellant is reduced too, and when the nitrocellulose content is too small to sustain the catalytic reaction, the plateau combustion will be destroyed. This explains, from the theory, why the quantity of nitrocellulose is one of the vital factors in guaranteeing burning-rate modification and plateau combustion in smokeless propellants.³²

Compared with ester nitrate, the molecular structure of nitramine (HMX or RDX) involves the N-NO₂ and lacks the -CHO group. The main combustion products are NO₂, N₂O, CH₂O, and N₂, among which no catalysant [CHO] is found. [N₂O] increases, and [NO₂] reduces. Adding nitramine to catalyzed propellant causes the value of $\theta_0(P, X)$ of the propellant to decrease (with a tendency to lower the burning rate) and brings down the value of $g(P, X)$ (with a tendency to raise the pressure exponent and lessen the catalytic effect). Therefore, nitramine, on the one hand, by strengthening the effect of catalyst, can promote catalytic combustion, and, on the other hand, because of its intrinsic chemical structure, can play a negative role in plateau combustion.

From Eqs. (21) and (22) one can see that the burning rate in the plateau region has a close relation with the catalytic activity coefficients $C_1(X)$ and $C_2(X)$ and that $C_1(X)$ is dominant. The bigger the value of $C_1(X)$, the higher the burning rate in the plateau region. $C_1(X)$, $C_2(X)$, and w_a affect the plateau region of propellants and its pressure exponent. If w_a remains unchanged while the value of $C_1(X)$ is large, the pressure exponent of the plateau region is comparatively low. If w_a rises, the range of the low-pressure exponent shifts to the higher pressure. Therefore, for a given catalyst its catalytic activity can be predicted by calculating its $C_1(X)$, and the position of plateau region can be predicted by calculating w_a .

VI. Conclusions

This chapter suggests that the reason for plateau combustion is that the natural split process of [CHO] in the area near the burning surface is suppressed by catalytic centers. The suppressing process of occurrence, development, and disappearance is the same as that of catalytic centers in the burning surface. Therefore, it is expressed as super rate, plateau, and mesa in the curve of burning rate vs pressure.

The chemical structure of the propellant exerts an important influence on catalytic combustion. The higher the [CHO] content in the chemical structure of the components of a propellant, the more advantageous it is for the catalysis. Among the general energetic materials nitrocellulose is a good provider of catalysant [CHO]. Hence, guaranteeing enough nitrocellulose in the propellant promises plateau combustion in solid propellants.

Adding nitramine (HMX, RDX) to double-base plateau propellant on the one hand lessens catalysis because of the reduction of [CHO] in the chemical structure of propellant, and on the other hand is more advantageous to plateau combustion because of the strengthening catalytic effect of lead salt. Therefore, with proper nitramine content the plateau effect is attainable.

The variety of catalyst, its content, and the combining style affect the value of the catalytic activity coefficient $C_1(X)$, $C_2(X)$, and the catalytic parameter w_a . Generally, the burning rate of the propellant increases with the increase of $C_1(X)$ and $C_2(X)$, whereas the pressure exponent decreases with the increase of $C_1(X)$ and $C_2(X)$ in the plateau or mesa region. The plateau pressure region is related to the value of w_a . Therefore, it is of vital importance to guarantee the proper match of propellant in designing the burning characteristics of plateau propellants.

A burning-rate formula and pressure exponent formula, which are formally the same and are suitable for catalytic double-base and nitramine-modified double-base propellants, are derived in this chapter. The calculated results indicate that when catalyst content, the proportion, and the combining style change, the calculated results conform in general with real values and can quantitatively and completely remanifest the super rate, plateau, and mesa of plateau propellants and hence confirm the basic validity of the model.

References

- ¹Avery, W. H., Hunt, R. E., and Down, M. N., "Burning Rate Studies in Double Base Powders," Office of Scientific Research and Development, OSRD 5827 ABL/P/1, Jan. 1946.
- ²Singha, H., and Rao, K. R. K., "Platonization in Double-Base Rocket Propellants," *AIAA Journal*, Vol. 15, No. 11, 1977, pp. 1545–1549.
- ³Hewkin, D. J., Hicks, J. A., Powling, J., and Watts, H., "Combustion of Nitric Ester-Based Propellants: Ballistic Modification by Lead Compounds," *Combustion Science and Technology*, Vol. 2, Nos. 5–6, 1971, pp. 307–327.
- ⁴Camp, A. T., Haussmann, H. K., McEwan, W. S., Henry, R. A., Olds, R. H., and Besser, E. G., "A Decade of Progress in the Understanding of Certain Ballistic Properties in Double-Base Propellants," U.S. Naval Ordnance Test Station, White Oak, NAVORD Rept. 5825, Silver Spring, MD, Jan. 1958.
- ⁵Suh, N. P., Adams, G. F., and Lenchitz, C., "Observations on the Role of Lead Modifiers in Super Rate Burning of NC Propellants," *Combustion and Flame*, Vol. 22, Nos. 3–4, 1974, pp. 289–293.
- ⁶Kubota, N., Ohlemiller, T. J., Caveny, L. H., and Summerfield, M., "The Mechanism of Super-Rate Burning of Catalyzed Double Base Propellants," Princeton Univ., Dept. of Aerospace and Mechanical Sciences, Rept. AMS 1087 or AD-763786, Princeton, NJ, March 1973.
- ⁷Ferreira, J. G., Bizot, A., and Lengellé, G., "Model for Double-Base Propellants Combustion, Without and With Additives," AIAA Paper 83-1197, July 1983.
- ⁸Duterque, J., and Lengellé, G., "Combustion Mechanism of Nitramine based Propellants with Additives," AIAA Paper 88-3253, July 1988.
- ⁹Song, H. C., "Combustion Model and Burning Rate Prediction Method for Propellants," Ph.D. Dissertation., Chemical Engineering Dept., Nanjing Univ. of Science and Technology, PRC, April 1986.
- ¹⁰Song, H. C., and Yang, D., "Model for Predicting the Burning Rate of Double Base Propellants from Ingredients," *The 28th International Annual Conference of ICT*, Fraunhofer Inst. of Chemistry Technology, Karlsruhe, Germany, 1997, pp. 84-1–84-12.
- ¹¹Song, H. C., "Burning Rate Prediction for Double Base Gun Propellants," *The Fascicle of Explosives and Propellants of ACTA Armament*, Vol. 9, No. 2, 1987, pp. 7–13.
- ¹²Yang, D., Zhao, B. C., Song, H. C., and He, X. Y., "Modeling for Nitramine (RDX, HMX) Propellant Burning Characteristics," *The Journal of Nanjing University of Science and Technology*, Vol. 21, No. 5, 1997, pp. 415–418.

¹³Yang, D., Zhao, B. C., Song, H. C., Li, X. R., and Li, L., "Modeling for Nitroguanidine Gun Propellant Characteristics," *The 23rd International Pyrotechnics Seminar Tsukuba*, 30 Sept.–4 Oct., 1997, pp. 972–979.

¹⁴Yang, D., Li, S. W., and Song, H. C., "The Interrelation Between the Thermal Decomposition of Lead Salt and the Platonization Mechanism of Double-Based Propellants," *Propellants, Explosives, Pyrotechnics*, Vol. 23, No. 2, 1998, pp. 77–81.

¹⁵Donnet, J. B., and Voet, A., *Carbon-Physics, Chemistry and Elastomer Reinforcement*, Marcel Dekker, New York, 1976.

¹⁶Yang, D., Chen, S. C., Li, S. W., and Song, H. C., "The Enhancement of RDX on Plateau Catalytic Effect," *The Fascicle of Explosives and Propellants of ACTA Armament*, Vol. 17, No. 1, 1995, pp. 15–19.

¹⁷Brill, T. B., and Patil, D. E., "Thermal Decomposition of Energetic Materials 63. Surface Reaction Zone Chemistry of Simulated Burning 1, 3, 5, 5-Tetranitrohera-Hydropyrimidine (DNNC or TNDA) Compared to RDX," *Combustion and Flame*, Vol. 95, Nos. 1–2, 1993, pp. 183–190.

¹⁸Palopoli, S. F., and Brill, T. B., "Thermal Decomposition of Energetic Materials 52. On the Foam Zone and Surface Chemistry of Rapidly Decomposing HMX," *Combustion and Flame*, Vol. 87, Nos. 1–2, 1991, pp. 45–60.

¹⁹Lengellé, G., and Duterque, J., "Combustion des Propergols á Base d'Octogene," AGARD-CP-391, Florence, Jan. 1986.

²⁰Sharama, J., Wilmot, G. B., Campolattaro, A. A., and Santiago, F., "XPS Study of Condensed Phase Combustion in Double-Base Rocket Propellant With and Without Lead Salt-Burning Rate Modifier," *Combustion and Flame*, Vol. 85, Nos. 3–4, 1991, pp. 416–426.

²¹Liu, S. Y., "The Study on the Structure of Double Base Propellant Burning Surface," *Proceedings of Combustion*, Society of Propellants and Explosives, Chongqing, 1979.

²²Yang, D., Dong, C. S., Li, S. W., and Wang, Y., "The Structure of Nitramine Modified double-base Propellant Burning Surface," *Solid Rocket Technology*, Vol. 20, No. 2, 1997, pp. 31–36.

²³Li, S. W., and Zhao, F. Q., "The Study on the Propellants with Non-Lead Catalysts," *The Fascicle of Explosives and Propellants of ACTA Armament*, Vol. 8, No. 1, 1986, pp. 25–32.

²⁴Preckel, R. F., "Gas Producing Compositions for Smokeless Powder and Metal Inhibitor," U.S. Patent 3,009,796, 1962.

²⁵Preckel, R. F., "Gas Producing Propellant for Jet Propellant Devices," U.S. Patent 3,003,716, May 1962.

²⁶Preckel, R. F., "Gas Producing Propellant for Jet Propellant Devices," U.S. Patent 3,003,717, May 1962.

²⁷Preckel, R. F., "Rocket Propellants," U.S. Patent 3,032,972, May 1962.

²⁸Camp, A. T., "Lead Burning Rate Modifiers for Double Base Rocket Propellant," U.S. Patent 3,088,858, May 1963.

²⁹Camp, A. T., and Crescenzo, F. G., "Copper and Lead Burning Rate Modifiers for Double Base Propellants Containing Alumimum," U.S. Patent 3,318,499, June 1964.

³⁰McEwan, W. S., Gordan, A. S., and Cohen, J., "Increasing the Burning Rate of Propellants," U.S. Patent 3,228,338, 1966.

³¹Henry, R. A., and McEwan, W. S., "Double Base Propellants of Increased Burning Rate Containing Benzophenones," U.S. Patent 3,228,815, 1966.

³²Evans, G. I., "Technical Evaluation Report," AGARD-CP-391, Florence, Jan. 1986.

Chapter 2.14

Structure and Stability of Deflagrations in Porous Energetic Materials

Stephen B. Margolis*

Sandia National Laboratories, Livermore, California

and

Forman A. Williams†

University of California at San Diego, La Jolla, California

I. Introduction

THE combustion behavior of porous energetic materials is of increasing interest because even supposedly nonporous materials may develop significant porosities over time due either to aging or to other types of degradation that may arise from exposure to abnormal environments. In such materials, the effects of two-phase flow are especially significant because of the presence of gas flow relative to the condensed material within the unburned porous solid as well as in the exothermic liquid/gas layers that typically form on the surfaces of many types of propellants, such as nitramines.¹⁻⁵ In the presence of confinement, the significance of the convective transport effects due to two-phase flow are enhanced, leading, through gas permeation into the unburned solid, to a preheating of the solid and, consequently, to a strong enhancement of the burning rate relative to that of the unconfined case. Indeed, this type of preheating associated with gas permeation into the unburned solid generally is associated with the onset of specially identified modes of combustion, such as convective burning (cf. Ref. 6 and the additional references therein). However, even in unconfined problems, effects of two-phase flow play an important role, affecting not only fundamental thermodynamic characteristics such as the burned temperature, but also the burning rate and the stability of steady, planar burning.

We synthesize and describe the results of several recent analyses that, by means of asymptotic methods, have been successful in predicting the effects of two-phase

This material is declared a work of the U.S. Government and is not subject to copyright protection in the United States.

*Principal Member of Technical Staff, Combustion Research Facility.

†Professor, Dept. of Applied Mechanics and Engineering Sciences.

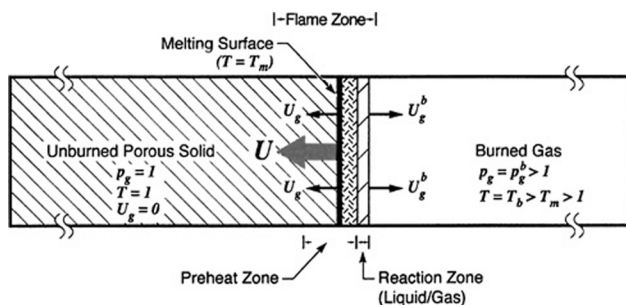


Fig. 1 Schematic of deflagration in porous energetic material with two-phase flow in both the solid-gas and liquid-gas regions, with combustion occurring in the latter. In the unconfined limit ($p_g^b \rightarrow 1$), the gas flow is everywhere in the downstream direction, whereas for sufficiently large overpressures, even the gas flow in the burned region is directed upstream.

flow on the structure, burning rate, and linear stability of a propagating deflagration wave.⁷⁻¹² For the case of a confined or partially confined geometry, a quasi-steady propagation regime can be identified such that, in the limit that the pressure difference, or overpressure, between the burned and unburned regions approaches zero, the combustion wave collapses to that corresponding to an unconfined deflagration. Indeed, a sketch of the geometry for the simplified chemistry adopted here is shown in Fig. 1, which indicates an unburned solid-gas region, a melting surface, a liquid-gas region within which is embedded a thin reaction zone in which burning takes place, and finally, a burned gaseous product region. The primary difference between the unconfined and confined problems is that, in the case of confinement, the direction of gas flow in the unburned region is likely to be negative, resulting in a preheating effect that results in a rapid increase in the burning rate as a function of overpressure. This permeation-enhanced burning generally is referred to, for obvious reasons, as convective burning, and one of the successes of the present model formulation and analysis is the ability to predict the transition from ordinary conduction-controlled burning that is characteristic of unconfined deflagrations to one in which convection plays a significant role.

The model used to investigate the wave structure just described is essentially a simplified version of more general models of two-phase reacting flow (cf. Ref. 13). In particular, the model essentially consists of continuity and energy equations for each coexisting phase, a simplified accounting for momentum conservation appropriate for deflagrations, an equation of state for the gas, and an appropriate set of boundary and melting surface conditions. Although it is critical to the focus of our study to allow for velocity differences between coexisting phases, for simplicity we assume good thermal contact and adopt the single-temperature approximation that the temperature at a given spatial location is the same for each phase. Also, in keeping with our goal of focusing on the effects of two-phase flow, we deliberately simplify the chemistry by postulating the overall process $R(s) \rightarrow R(l) \rightarrow P(g)$, where the first step denotes the melting (assumed to be slightly endothermic) of the solid material, and the second represents a one-step exothermic process in which liquid-phase reactants are converted directly to burned gaseous products. Extensions of the analysis to more complicated global mechanisms have been

given,^{5,10,11} but such extensions are not critical to the examination of the primary effects of two-phase flow of interest.

In what follows, we first present the formulation and nondimensional models that are considered for the analysis of the two types of problems (confined and unconfined) just introduced (Secs. II and III). We then consider the case of steady (unconfined) or quasi-steady (confined) burning, in order to derive, via asymptotic methods, analytical expressions for the respective planar burning rates and other aspects of the deflagration structure (Secs. IV and V). Then, we derive a time-dependent, multidimensional asymptotic model, in which the reaction zone is represented by a reaction sheet (Sec. VI) and use it to examine the stability of a basic planar mode of burning (Secs. VII and VIII). In the Conclusions (Sec. IX), we summarize the results and indications for future investigations.

II. Formulation

A sketch of the physical problem is shown in Fig. 1. The unburned porous solid lies generally to the left, and the burned gas products lie to the right. The two are separated by a deflagration wave that generally moves from right to left, converting the former into the latter. These regions (unburned and burned) in turn are bounded on the left and right, respectively, but these boundaries are assumed to be sufficiently far away (relative to the width of the flame region) that the only significant effect on the combustion wave itself occurs in the case of confinement, where a significant difference develops between the upstream and downstream values of the pressure. In the unconfined problem, the gas flow is unrestricted in the burned region, and pressure gradients remain sufficiently small that they can be neglected on the nonacoustic scales of interest. In the confined case, however, gas flow in the burned region is restricted and hence the continual production of gas via chemical reaction causes the pressure to become greater in the burned region than in the unburned solid. This pressure difference drives at least some of the gas upstream in the direction of the unburned solid, where momentum conservation plays a critical role in reducing the gas velocity far upstream to zero so as to satisfy the ambient conditions there. Depending on the magnitude of the overpressure, the gas velocity in the burned region, on the other hand, may be either positive or negative. Hence, for moderate overpressures, the gas velocity can experience a turning point within the reaction region where the gaseous products are generated.

The structure of the combustion wave thus consists of a solid-gas preheat region that, for the confined problem, contains a gas-permeation boundary layer in which the pressure rises from its ambient value to its larger (possibly much larger) value in the liquid-gas region; the melting surface that marks the left boundary of a liquid-gas preheat region, and the right boundary of the gas-permeation layer if one exists; the liquid-gas preheat zone, a relatively thin exothermic reaction layer in which chemical reaction occurs; and the burned gaseous region that extends to the right boundary. In the limit that the activation energy of reaction is large, the reaction zone asymptotically becomes a propagating surface similar to, but displaced from, the melting surface. In the laboratory-fixed spatial coordinate system $(\tilde{x}_1, \tilde{x}_2, \tilde{x}_3)$, the porous solid extends to $\tilde{x}_3 = -\infty$, where conditions are denoted by the subscript u , and the gas extends to $\tilde{x}_3 = +\infty$, where conditions are identified by the subscript b . The deflagration generally propagates in the $-\tilde{x}_3$ direction, although, in general, the wave motion is allowed to be both nonsteady

and nonplanar. Here and in what follows, a tilde over a symbol (e.g., \tilde{x}_3) denotes a dimensional quantity, and the subscripts s , l , and g denote solid-, liquid-, and gas-phase quantities, respectively. A continuum formulation, in which appropriate gas- and condensed-phase volume fractions α and $1 - \alpha$, respectively, multiply the physical variables associated with each phase, is used to model the physical problem just described.

The governing system of equations that are considered incorporates a number of assumptions that greatly simplify the analysis without compromising the fundamental two-phase-flow aspects of the problems of interest. Two of these include restricting the analysis to the single-temperature limit and considering only weakly nonplanar deflagrations. The first implies sufficiently good thermal contact between coexisting phases such that corresponding temperature differences are small, whereas the latter, which implies that the transverse velocity components are small relative to the component of velocity in the \tilde{x}_3 direction, allows the velocity field (for the gas and liquid phases) to be approximated by $\tilde{u}_{l,g} \sim [0, 0, \tilde{u}_{l,g}(\tilde{x}_1, \tilde{x}_2, \tilde{x}_3, \tilde{t})]$, with the velocity of the solid assumed to be zero. Other assumptions are indicated as they are introduced. We remark that the single-temperature assumption, which can be relaxed readily by considering the limit of sufficiently large, but finite, rates of interphase heat transfer,^{7,14} is quite reasonable for many two-phase-flow problems. In contrast, the corresponding limit of large rates of interphase momentum transfer is not so plausible,^{4,7} and thus it is important to retain velocity differences in the model if one wishes to capture true two-phase-flow effects.

Denoting the melting surface that separates the solid-gas and liquid-gas regions by $\tilde{x}_3 = \tilde{x}_m$, and the gas-phase volume fraction by α , continuity in the region $\tilde{x}_3 > \tilde{x}_m$ is expressed separately for the liquid and gas phases, where the latter may be replaced by an overall continuity equation for the two-phase medium. Consequently, we have

$$\frac{\partial}{\partial \tilde{t}}[(1 - \alpha)\tilde{\rho}_l] + \frac{\partial}{\partial \tilde{x}_3}[(1 - \alpha)\tilde{\rho}_l\tilde{u}_l] = -\tilde{A}\tilde{\rho}_l(1 - \alpha)\exp\left(-\frac{\tilde{E}_l}{\tilde{R}^\circ\tilde{T}}\right) \quad \tilde{x}_3 > \tilde{x}_m \quad (1)$$

$$\frac{\partial}{\partial \tilde{t}}[(1 - \alpha)\tilde{\rho}_l + \alpha\tilde{\rho}_g] + \frac{\partial}{\partial \tilde{x}_3}[(1 - \alpha)\tilde{\rho}_l\tilde{u}_l + \alpha\tilde{\rho}_g\tilde{u}_g] = 0 \quad \tilde{x}_3 > \tilde{x}_m \quad (2)$$

where $\tilde{\rho}$, \tilde{u}_l , \tilde{T} , and \tilde{t} denote density, velocity, the single temperature, and time, respectively. For simplicity, we assume a constant value for $\tilde{\rho}_l$, but not for $\tilde{\rho}_g$. In the reaction-rate expression, \tilde{E}_l is the overall activation energy, \tilde{R}° is the universal gas constant, and \tilde{A} is the exponential reciprocal-time prefactor which, for simplicity, is assumed to be constant. For this type of global kinetic modeling, however, it may be reasonable to assign a pressure, as well as a temperature, dependency to \tilde{A} . In the solid-gas region $\tilde{x} < \tilde{x}_m$, we assume for the solid phase a constant density $\tilde{\rho}_s$ and zero velocity ($\tilde{u}_s = 0$), with $\alpha \equiv \alpha_s$ also constant in this region. Gas-phase continuity for $\tilde{x} < \tilde{x}_m$ thus is independent of the solid phase and is given by

$$\frac{\partial \tilde{\rho}_g}{\partial \tilde{t}} + \frac{\partial}{\partial \tilde{x}_3}(\tilde{\rho}_g\tilde{u}_g) = 0, \quad \tilde{x}_3 < \tilde{x}_m \quad (3)$$

Conservation of energy for each phase in the liquid-gas and solid-gas regions is given similarly by separate equations for each coexisting phase, which, as before, can be summed to give an overall energy equation in each region. In the

single-temperature limit, however, only the overall energy equations remain, and these are given by

$$\begin{aligned} \frac{\partial}{\partial \tilde{t}} [\tilde{\rho}_l(1-\alpha)(\tilde{Q} + \tilde{c}_l\tilde{T}) + \tilde{\rho}_g\tilde{c}_g\alpha\tilde{T}] + \frac{\partial}{\partial \tilde{x}_3} [\tilde{\rho}_l\tilde{u}_l(1-\alpha)(\tilde{Q} + \tilde{c}_l\tilde{T}) + \tilde{\rho}_g\tilde{c}_g\tilde{u}_g\alpha\tilde{T}] \\ = \tilde{\nabla} \cdot [\tilde{\lambda}_l(1-\alpha)\tilde{\nabla}\tilde{T} + \tilde{\lambda}_g\alpha\tilde{\nabla}\tilde{T}] + \alpha \frac{\partial \tilde{p}_g}{\partial \tilde{t}}, \quad \tilde{x}_3 > \tilde{x}_m \end{aligned} \quad (4)$$

$$\begin{aligned} \frac{\partial}{\partial \tilde{t}} [\tilde{\rho}_s\tilde{c}_s(1-\alpha_s)\tilde{T} + \tilde{\rho}_g\tilde{c}_g\alpha_s\tilde{T}] + \frac{\partial}{\partial \tilde{x}_3} (\tilde{\rho}_g\tilde{c}_g\tilde{u}_g\alpha_s\tilde{T}) \\ = \tilde{\nabla} \cdot [\tilde{\lambda}_s(1-\alpha_s)\tilde{\nabla}\tilde{T} + \tilde{\lambda}_g\alpha_s\tilde{\nabla}\tilde{T}] + \alpha_s \frac{\partial \tilde{p}_g}{\partial \tilde{t}}, \quad \tilde{x}_3 < \tilde{x}_m \end{aligned} \quad (5)$$

where Eq. (1) has been used to eliminate the reaction-rate term in Eq. (4). Here, \tilde{c} , $\tilde{\lambda}$, and \tilde{p} denote heat capacity (at constant volume for the liquid, and at constant pressure for the gas, both assumed constant), thermal conductivity, and pressure, respectively; and \tilde{Q} is the heat release for the global reaction at temperature \tilde{T} . We remark that, because of the small Mach number and the small ratio of gas-to-condensed phase densities in the problems to be considered, no terms involving the pressures in the condensed phases appear in these equations. Terms involving \tilde{p}_g , however, arise from the contribution to the rate of change of the internal energy of the gas from the sum of the rate of surface work $-\partial(\alpha\tilde{u}_g\tilde{p}_g)/\partial\tilde{x}$ and the rate of volume work $-\tilde{p}_g\partial\alpha/\partial\tilde{t}$ performed by the gas.

Although analogous equations can be written for momentum conservation, we avoid introducing them explicitly by adopting certain simplifying approximations that often are used in these types of problems. In particular, in place of gas-phase momentum, we adopt, depending on the type of problem, either the assumption of constant pressure throughout or Darcy's law (in the solid-gas region). In the latter instance, which provides a convenient formulation when pressure gradients are not negligible (as in the confined geometry introduced later), it is still reasonable to assume, based on the assumption of small Mach number, that the gas pressure is homogeneous in the liquid-gas region. If it is assumed further that the gas pressure in the burned region varies on a longer timescale than that associated with the flame structure itself (e.g., when the confining boundary is sufficiently remote with respect to the flame), then the upstream and downstream pressures can be regarded as constant in the quasistatic sense. This argument is supported by numerical calculations,¹⁵ which, though based on the assumption of a flame sheet propagating with constant velocity, nonetheless enabled the authors to identify correctly this quasi-steady regime, which they described as a "gas-permeation boundary-layer solution." The latter refers to the fact that the solution is characterized by a relatively thin gas-permeation layer in the solid-gas region, described later in the context of the present model, which arises from the difference, or overpressure, between the upstream and downstream values of the gas pressure. Thus, in place of gas-phase momentum, we adopt either the conditions

$$\tilde{u}_g = -\frac{\tilde{\kappa}(\alpha_s)}{\alpha_s\tilde{\mu}_g} \frac{\partial \tilde{p}_g}{\partial \tilde{x}_3}, \quad \tilde{x} < \tilde{x}_m; \quad \tilde{p}_g = \tilde{p}_g^b > \tilde{p}_g^u, \quad \tilde{x} > \tilde{x}_m \quad (6a)$$

which are appropriate for the confined problem, or

$$\tilde{p}_g = \tilde{p}_g^u, \quad -\infty < \tilde{x} < +\infty \quad (6b)$$

for the unconfined problem. Here, the first of Eqs. (6a) is the planar approximation of Darcy's law, $\tilde{u}_g = -\tilde{\kappa} \tilde{\nabla} \tilde{p}_g / (\alpha_s \tilde{\mu}_g)$, implied by the planar representation of the velocity field introduced earlier. The coefficient $\tilde{\kappa}$ is the permeability of the solid-gas region and $\tilde{\mu}_g$ is the gas-phase viscosity, and the value \tilde{p}_g^u is the specified upstream boundary condition on the gas pressure according to Eq. (9). We observe that Eq. (6b) actually is obtainable from Eqs. (6a) in the limit $\tilde{\kappa} \rightarrow \infty$ (which implies $\tilde{p}_g^b \rightarrow p_g^u$), so that, in the aforementioned quasi-steady burning regime, the solution to the unconfined problem constitutes a limiting case of the corresponding solution obtained from the more general condition given by Eqs. (6a).

The equation of state for the gas is assumed to be ideal, and thus \tilde{p}_g is, in general, coupled to the other field variables through the gas-phase equation of state

$$\tilde{p}_g = \tilde{\rho}_g \tilde{R}^0 \tilde{T} / \tilde{W}_g \quad (7)$$

where \tilde{W}_g is the molecular weight of the product gas. Consideration of condensed-phase momentum, on the other hand, leads in principle to an equation for the liquid-phase velocity \tilde{u}_l . Based on a previous analysis,⁴ a reasonable first approximation is to set the condensed velocity equal to the condensed-mass burning rate divided by the condensed-phase density. In the present context, this implies that, because $\tilde{u}_s = 0$,

$$\tilde{u}_l = -\frac{\partial \tilde{x}_m}{\partial \tilde{t}} \left(\frac{\tilde{\rho}_s}{\tilde{\rho}_l} - 1 \right), \quad \tilde{x}_3 > \tilde{x}_m \quad (8)$$

where $\partial \tilde{x}_m / \partial \tilde{t} < 0$ is the (unknown) propagation velocity of the melting surface. A modification to this expression that introduces a linear dependence of \tilde{u}_l on the gas-phase volume fraction α that qualitatively takes into account viscous and surface-tension-gradient (Marangoni) effects in the liquid-gas region has been proposed,⁴ but in the present work we adopt the simpler result given by Eq. (8).

The preceding equations now constitute a closed set for the variables α , \tilde{u}_g , \tilde{T} , $\tilde{\rho}_g$, and \tilde{p}_g . The problem thus is determined completely once initial and boundary conditions, including interface relations at $\tilde{x}_3 = \tilde{x}_m$, are specified. However, because we are not concerned with the initial-value problem, but only the long-time solution corresponding to a (quasi) steadily propagating deflagration, only the latter are required here. Thus, the required boundary conditions are given by

$$\begin{aligned} \alpha &= \alpha_s & \text{for } \tilde{x} < \tilde{x}_m \\ \tilde{u}_g &\rightarrow 0, & \tilde{T} \rightarrow \tilde{T}_u, \quad \tilde{p}_g \rightarrow \tilde{p}_g^u \quad \text{as } \tilde{x} \rightarrow -\infty \end{aligned} \quad (9)$$

$$\begin{aligned} \tilde{p}_g &= \tilde{p}_g^b & \text{for } \tilde{x} > \tilde{x}_m \\ \alpha &\rightarrow 1, & \tilde{u}_g \rightarrow \tilde{u}_g^b, \quad \tilde{T} \rightarrow \tilde{T}_b \quad \text{as } \tilde{x} \rightarrow +\infty \end{aligned} \quad (10)$$

where the burned temperature \tilde{T}_b , gas velocity \tilde{u}_g^b , and pressure \tilde{p}_g^b are to be determined, except in the unconfined limit where, from Eq. (6b), $\tilde{p}_g^b = \tilde{p}_g^u$. The unburned and burned values $\tilde{\rho}_g^u$ and $\tilde{\rho}_g^b$ of the gas density then follow from the equation of state. We remark that the upstream boundary condition on the gas velocity is, except in the unconfined limit, merely a consistency condition in the present formulation because it is implied by the corresponding upstream condition on pressure and the first of Eqs. (6a). Finally, where the plus or minus superscripts denote the quantities evaluated at $\tilde{x} = \tilde{x}_m^\pm$, the continuity and jump conditions

across the melting surface are

$$\begin{aligned}\alpha^+ &= \alpha^- = \alpha_s, & \tilde{u}_g^+ &= \tilde{u}_g^-, & \tilde{u}_g^- &= -\frac{\tilde{\kappa}(\alpha_s)}{\alpha_s \tilde{\mu}_g} \frac{\partial \tilde{p}_g}{\partial \tilde{x}_3} \bigg|_{\tilde{x}=\tilde{x}_m^-} \\ \tilde{p}_g^- &= \tilde{p}_g^+ = \tilde{p}_g^b, & \tilde{T}^+ &= \tilde{T}^- = \tilde{T}_m\end{aligned}\quad (11)$$

the third of which implies $\partial \tilde{p}_g / \partial \tilde{x}_3 \rightarrow 0$ in the infinite-permeability/unconfined limit $\tilde{\kappa} \rightarrow \infty$. In addition, overall conservation of enthalpy flux across $\tilde{x} = \tilde{x}_m$ is expressed, using Eq. (8), as

$$\begin{aligned}& [(1 - \alpha_s)\tilde{\lambda}_l + \alpha_s \tilde{\lambda}_g] \hat{n}_m \cdot \tilde{\nabla} \tilde{T} \big|_{\tilde{x}=\tilde{x}_m^+} - [(1 - \alpha_s)\tilde{\lambda}_s + \alpha_s \tilde{\lambda}_g] \hat{n}_m \cdot \tilde{\nabla} \tilde{T} \big|_{\tilde{x}=\tilde{x}_m^-} \\ &= (1 - \alpha_s) \tilde{\rho}_s G_m^{-1} \frac{\partial \tilde{x}_m}{\partial \tilde{t}} [\tilde{\gamma}_s + (\tilde{c}_s - \tilde{c}_l) \tilde{T}_m]\end{aligned}\quad (12)$$

where the geometric factor G_m and the unit normal \hat{n}_m are given by

$$\begin{aligned}G_m &= \left[1 + \left(\frac{\partial \tilde{x}_m}{\partial \tilde{x}_1} \right)^2 + \left(\frac{\partial \tilde{x}_m}{\partial \tilde{x}_2} \right)^2 \right] \\ \hat{n}_m &= G_m^{-1} \left(-\frac{\partial \tilde{x}_m}{\partial \tilde{x}_1}, -\frac{\partial \tilde{x}_m}{\partial \tilde{x}_2}, 1 \right)\end{aligned}\quad (13)$$

respectively, and where $\tilde{\gamma}_s$ is the heat of melting of the solid at temperature $\tilde{T} = 0$ ($\tilde{\gamma}_s$ being negative when melting is endothermic).

III. Nondimensionalizations and Further Approximations

The formulation presented in the preceding section is meant to be a reasonable representation of certain classes of materials, such as the nitramine propellant HMX, that satisfy the main assumptions introduced thus far. Typical values associated with the physical properties of two widely studied nitramines, HMX and RDX, are quoted in various places.^{5,16} The only additional primary approximation that is introduced is the assumption, already alluded to in the preceding sections, of gas-phase quasi steadiness.¹⁷⁻¹⁹ This approximation is common in analyzing the stability of deflagrations in nonporous propellants (though it can be relaxed under certain conditions²⁰⁻²²), and, for multidimensional stability analyses, generally has been accompanied by a quasi-planar assumption as well.²³ This notion of gas-phase quasi steadiness, which is discussed in more detail in Ref. 9, thus is extended to the two-phase-flow problems associated with porous materials, and is a particularly convenient approximation for the present study in that both confined and unconfined geometries then can be treated within the same framework. However, we emphasize that even though the velocity field can be approximated as one-dimensional (because of the dominance of the normal component) by restricting the analysis to weakly nonplanar deflagrations, terms representing transverse diffusion of heat remain. As a result, the present formulation retains certain multidimensional gas-phase effects, and thus does not explicitly invoke gas-phase quasi planarity as a simplifying assumption.

In proceeding with a reasonable nondimensionalization for the present class of problems, it is convenient to introduce a characteristic velocity \tilde{U} defined as the

speed of propagation $\tilde{U} = -d\tilde{x}_m/d\tilde{t}$ associated with the special case of a quasi-steady planar deflagration (an explicit expression for \tilde{U} is presented in Secs. IV and V). Assuming constant values for heat capacities and thermal conductivities, we then introduce the nondimensional variables

$$\begin{aligned} x &= \frac{\tilde{\rho}_s \tilde{c}_s \tilde{U}}{\tilde{\lambda}_s} \tilde{x}, & t &= \frac{\tilde{\rho}_s \tilde{c}_s \tilde{U}^2}{\tilde{\lambda}_s} \tilde{t}, & T_{s,l,g} &= \frac{\tilde{T}_{s,l,g}}{\tilde{T}_u} \\ u_{l,g} &= \frac{\tilde{u}_{l,g}}{\tilde{U}}, & \rho_g &= \frac{\tilde{\rho}_g}{\tilde{\rho}_g^u}, & p_g &= \frac{\tilde{p}_g}{\tilde{p}_g^u} \end{aligned} \quad (14a)$$

where $\tilde{\rho}_g^u = \tilde{p}_g^u \tilde{W}_g / \tilde{R}^0 \tilde{T}_u$ denotes the gas density at the unburned temperature \tilde{T}_u and pressure \tilde{p}_g^u . In addition, the nondimensional parameters

$$\begin{aligned} r &= \frac{\tilde{\rho}_l}{\tilde{\rho}_s}, & \hat{r} &= \frac{\tilde{\rho}_g^u}{\tilde{\rho}_s}, & l &= \frac{\tilde{\lambda}_l}{\tilde{\lambda}_s}, & \hat{l} &= \frac{\tilde{\lambda}_g}{\tilde{\lambda}_s}, & b &= \frac{\tilde{c}_l}{\tilde{c}_s}, & \hat{b} &= \frac{\tilde{c}_g}{\tilde{c}_s}, \\ \gamma_s &= \frac{\tilde{\gamma}_s}{\tilde{c}_s \tilde{T}_u}, & Q &= \frac{\tilde{Q}}{\tilde{c}_s \tilde{T}_u}, & \kappa &= \frac{\tilde{\rho}_s \tilde{c}_s \tilde{p}_g^u \tilde{\kappa}}{\tilde{\lambda}_s \tilde{\mu}_g}, & \hat{\pi} &= \frac{\tilde{p}_g^u}{\tilde{\rho}_s \tilde{c}_s \tilde{T}_u} = \hat{r} \hat{b} \chi, & (14b) \\ \chi &= \frac{\gamma - 1}{\gamma}, & N &= \frac{\tilde{E}_l}{\tilde{R}^0 \tilde{T}_b}, & \Lambda &= \frac{\tilde{\lambda}_s \tilde{A}}{\tilde{\rho}_s \tilde{c}_s \tilde{U}^2} e^{-N} \end{aligned}$$

are defined, where γ is the ratio of specific heats for the gas. Note that Λ is the appropriate burning-rate eigenvalue, the determination of which will provide the quasi-steady, planar propagation speed \tilde{U} .

Transforming to the moving coordinate $\xi = x_3 - x_m(x_1, x_2, t)$, whose origin thus is defined to be x_m , and introducing the aforementioned nondimensionalizations, Eqs. (1–12) become

$$\frac{\partial \rho_g}{\partial t} + \frac{\partial}{\partial \xi} \left[\rho_g \left(u_g - \frac{\partial x_m}{\partial t} \right) \right] = 0, \quad \xi < 0 \quad (15)$$

$$\begin{aligned} \frac{\partial}{\partial t} [\alpha (\hat{r} \rho_g - r)] + \frac{\partial}{\partial \xi} \left[r (1 - \alpha) \left(u_l - \frac{\partial x_m}{\partial t} \right) \right. \\ \left. + \hat{r} \alpha \rho_g \left(u_g - \frac{\partial x_m}{\partial t} \right) \right] = 0, \quad \xi > 0 \end{aligned} \quad (16)$$

$$\frac{\partial \alpha}{\partial t} - \frac{\partial}{\partial \xi} \left[(1 - \alpha) \left(u_l - \frac{\partial x_m}{\partial t} \right) \right] = \Lambda (1 - \alpha) \exp \left[N \left(1 - \frac{T_b}{T} \right) \right], \quad \xi > 0 \quad (17)$$

$$\begin{aligned} \frac{\partial}{\partial t} [(1 - \alpha_s + \hat{r} \hat{b} \alpha_s \rho_g) T] + (1 - \alpha_s) \left(-\frac{\partial x_m}{\partial t} \right) \frac{\partial T}{\partial \xi} \\ + \hat{r} \hat{b} \alpha_s \frac{\partial}{\partial \xi} \left[\left(u_g - \frac{\partial x_m}{\partial t} \right) \rho_g T \right] = \nabla_m \cdot [(1 - \alpha_s + \hat{l} \alpha_s) \nabla_m T] \\ + \hat{\pi} \alpha_s \left(\frac{\partial p_g}{\partial t} - \frac{\partial x_m}{\partial t} \frac{\partial p_g}{\partial \xi} \right), \quad \xi < 0 \end{aligned} \quad (18)$$

$$\begin{aligned}
& \frac{\partial}{\partial t} [r(1-\alpha)(Q+bT) + \hat{r}\hat{b}\alpha\rho_g T] \\
& + \frac{\partial}{\partial \xi} \left[r(1-\alpha) \left(u_l - \frac{\partial x_m}{\partial t} \right) (Q+bT) + \hat{r}\hat{b}\alpha \left(u_g - \frac{\partial x_m}{\partial t} \right) \rho_g T \right] \\
& = \nabla_m \cdot \{ [l(1-\alpha) + \hat{l}\alpha] \nabla_m T \}, \quad \xi > 0
\end{aligned} \tag{19}$$

$$\rho_g T_g = p_g \tag{20}$$

$$u_l = -\frac{1}{r}(1-r)\frac{\partial x_m}{\partial t} \tag{21}$$

subject to the boundary and melting-surface conditions

$$\begin{aligned}
\alpha &= \alpha_s, \quad u_g = -\frac{\kappa(\alpha_s)}{\alpha_s} \frac{\partial p_g}{\partial \xi} \quad \text{for } \xi < 0 \\
T &\rightarrow 1, \quad p_g \rightarrow 1 \quad \text{as } \xi \rightarrow -\infty
\end{aligned} \tag{22}$$

$$\begin{aligned}
p_g &= p_g^b \quad \text{for } \xi > 0; \quad \alpha \rightarrow 1, \quad u_g \rightarrow u_g^b \\
T &\rightarrow T_b \quad \text{as } \xi \rightarrow +\infty
\end{aligned} \tag{23}$$

$$\begin{aligned}
\alpha^+ &= \alpha^- = \alpha_s, \quad u_g^+ = u_g^-, \quad u_g^- = -\frac{\kappa(\alpha_s)}{\alpha_s} \frac{\partial p_g}{\partial \xi} \Big|_{\xi=0^-} \\
p_g^- &= p_g^+ = p_g^b, \quad T^+ = T^- = T_m
\end{aligned} \tag{24}$$

$$\begin{aligned}
& [l(1-\alpha_s) + \hat{l}\alpha_s] \hat{n}_m \cdot \nabla_m T|_{\xi=0^+} - [1-\alpha_s + \hat{l}\alpha_s] \hat{n}_m \cdot \nabla_m T|_{\xi=0^-} \\
& = (1-\alpha_s) G_m^{-1} \frac{\partial x_m}{\partial t} [\gamma_s + (1-b)T_m]
\end{aligned} \tag{25}$$

where

$$\nabla_m = \left(\frac{\partial}{\partial x_1} - \left\{ \frac{\partial x_m}{\partial x_1} \right\} \frac{\partial}{\partial \xi}, \frac{\partial}{\partial x_2} - \left\{ \frac{\partial x_m}{\partial x_2} \right\} \frac{\partial}{\partial \xi}, \frac{\partial}{\partial \xi} \right)$$

is the gradient in the moving coordinate system. The limit $p_g^b \rightarrow 1$ and the elimination of the third of Eqs. (24) can be taken in the case of an infinitely permeable material and/or unconfined geometry.

In the quasi-steady gas-phase limit discussed earlier, the gas phase is regarded as steady with respect to $\xi = 0$, and thus time derivatives of gas-phase quantities in the moving coordinate system (viz. $\partial p_g / \partial t$, $\partial(\alpha \rho_g) / \partial t$, and $\partial(\alpha \rho_g T) / \partial t$) can be set to zero, so that with the use of Eq. (21), Eqs. (15–19) become

$$\frac{\partial}{\partial \xi} \left[\rho_g \left(u_g - \frac{\partial x_m}{\partial t} \right) \right] = 0, \quad \xi < 0 \tag{26}$$

$$r \frac{\partial \alpha}{\partial t} + \frac{\partial}{\partial \xi} \left[(1-\alpha) \frac{\partial x_m}{\partial t} - \hat{r} \alpha \rho_g \left(u_g - \frac{\partial x_m}{\partial t} \right) \right] = 0, \quad \xi > 0 \tag{27}$$

$$r \frac{\partial \alpha}{\partial t} + \frac{\partial}{\partial \xi} \left[(1 - \alpha) \frac{\partial x_m}{\partial t} \right] = r \Lambda (1 - \alpha) \exp \left[N \left(1 - \frac{T_b}{T} \right) \right] \quad \xi > 0 \quad (28)$$

$$\begin{aligned} (1 - \alpha_s) \frac{\partial T}{\partial t} - (1 - \alpha_s) \frac{\partial x_m}{\partial t} \frac{\partial T}{\partial \xi} + \hat{r} \hat{b} \alpha_s \frac{\partial}{\partial \xi} \left[\left(u_g - \frac{\partial x_m}{\partial t} \right) \rho_g T \right] \\ = \nabla_m \cdot [(1 - \alpha_s + \hat{l} \alpha_s) \nabla_m T] - \hat{\pi} \alpha_s \frac{\partial x_m}{\partial t} \frac{\partial p_g}{\partial \xi}, \quad \xi < 0 \end{aligned} \quad (29)$$

$$\begin{aligned} r \frac{\partial}{\partial t} [(1 - \alpha)(Q + bT)] + \frac{\partial}{\partial \xi} \left[-(1 - \alpha) \frac{\partial x_m}{\partial t} (Q + bT) \right. \\ \left. + \hat{r} \hat{b} \alpha \left(u_g - \frac{\partial x_m}{\partial t} \right) \rho_g T \right] = \nabla_m \cdot \{ [l(1 - \alpha) + \hat{l} \alpha] \nabla_m T \} \quad \xi > 0 \end{aligned} \quad (30)$$

Equations (20–24), along with the equation of state (20) and boundary/interface conditions (22–25), constitute the final model that is considered.

IV. Burning-Rate Eigenvalue for Steady, Planar Combustion

Time-independent solutions of the final formulation given in the preceding section correspond to either steady (unconfined) or quasi-steady (confined) deflagrations. In either case, the nondimensional propagation speed $\partial x_m / \partial t = -1$ by definition, and the classical problem is to determine the dimensional burning rate \bar{U} by obtaining an expression for the burning-rate eigenvalue Λ . Thus, we first consider the more general case of a confined geometry, to seek a solution for the steady eigenvalue problem

$$\frac{d}{d\xi} \left[\frac{p_g}{T} (u_g + 1) \right] = 0, \quad \xi < 0 \quad (31)$$

$$\frac{d}{d\xi} \left[(1 - \alpha) + \hat{r} \alpha \frac{p_g}{T} (u_g + 1) \right] = 0, \quad \xi > 0 \quad (32)$$

$$\frac{d}{d\xi} (1 - \alpha) = -r \Lambda (1 - \alpha) \exp \left[N \left(1 - \frac{T_b}{T} \right) \right], \quad \xi > 0 \quad (33)$$

$$\begin{aligned} (1 - \alpha_s) \frac{dT}{d\xi} + \hat{r} \hat{b} \alpha_s \frac{d}{d\xi} [p_g (u_g + 1)] = \frac{d}{d\xi} \left[(1 - \alpha_s + \hat{l} \alpha_s) \frac{dT}{d\xi} \right] + \hat{r} \hat{b} \chi \alpha_s \frac{dp_g}{d\xi}, \\ \xi < 0 \end{aligned} \quad (34)$$

$$\begin{aligned} \frac{d}{d\xi} [(1 - \alpha)(Q + bT) + \hat{r} \hat{b} \alpha p_g (u_g + 1)] \\ = \frac{d}{d\xi} \left\{ [l(1 - \alpha) + \hat{l} \alpha] \frac{dT}{d\xi} \right\}, \quad \xi > 0 \end{aligned} \quad (35)$$

subject to the boundary and melting-surface conditions (22–25) which, when

specialized to one dimension, become

$$\alpha = \alpha_s, \quad u_g = -\frac{\kappa(\alpha_s)}{\alpha_s} \frac{dp_g}{d\xi} \quad \text{for } \xi < 0$$

$$T \rightarrow 1, \quad p_g \rightarrow 1 \quad \text{as } \xi \rightarrow -\infty \quad (36)$$

$$p_g = p_g^b \quad \text{for } \xi > 0$$

$$\alpha \rightarrow 1, \quad u_g \rightarrow u_g^b, \quad T \rightarrow T_b \quad \text{as } \xi \rightarrow +\infty \quad (37)$$

$$\alpha^+ = \alpha^- = \alpha_s, \quad u_g^+ = u_g^- = -\frac{\kappa(\alpha_s)}{\alpha_s} \frac{dp_g}{d\xi} \bigg|_{\xi=0^-} \quad (38)$$

$$p_g^- = p_g^+ = p_g^b, \quad T^+ = T^- = T_m$$

$$[l(1 - \alpha_s) + \hat{l}\alpha_s] \frac{dT}{d\xi} \bigg|_{\xi=0^+} - [1 - \alpha_s + \hat{l}\alpha_s] \frac{dT}{d\xi} \bigg|_{\xi=0^-}$$

$$= (1 - \alpha_s)[- \gamma_s + (b - 1)T_m] \quad (39)$$

Here, the alternate expression for the coefficient $\hat{\pi}$ indicated in Eqs. (14b) has been used in the last term of Eq. (34), and the equation of state (20) has been used to give a closed problem for α , p_g , u_g , T , and the eigenvalue Λ .

A. Preliminary Analysis

A partial solution in the region $\xi < 0$, where chemical activity is absent, as well as expressions for T_b , u_g^b , and $u_g(0) = u_g|_{\xi=0}$, are obtained as follows. From Eq. (31) and the boundary conditions (36), we have

$$p_g(u_g + 1) = T, \quad \xi < 0 \quad (40)$$

and hence

$$u_g|_{\xi=0} = T_m/p_g^b - 1 \quad (41)$$

We observe from Eq. (40) that because $T \geq 1$, the gas velocity $u_g > -1$ in the gas-solid region $\xi < 0$. That is, consistent with a quasi-steady mode of burning, the speed of gas permeation into the solid must be less than the propagation speed of the deflagration. Equation (32) and surface conditions (38) and (41) then imply that

$$p_g^b(u_g + 1) = \frac{\alpha + \alpha_s(\hat{r} - 1)}{\hat{r}\alpha} T, \quad \xi > 0 \quad (42)$$

which, upon evaluation at $\xi = \infty$, determines u_g^b in terms of T_b as

$$u_g^b = \frac{1 - \alpha_s + \hat{r}\alpha_s}{\hat{r}} \left(\frac{T_b}{p_g^b} \right) - 1 \quad (43)$$

Turning attention to the energy equations (34) and (35), we can readily perform

a single integration and use the preceding relationships to obtain

$$(1 - \alpha_s + \hat{r}\hat{b}\alpha_s)(T - 1) = (1 - \alpha_s + \hat{l}\alpha_s)\frac{dT}{d\xi} + \hat{r}\hat{b}\chi\alpha_s(p_g - 1) \quad \xi < 0 \quad (44)$$

$$\begin{aligned} & [b(1 - \alpha) + \hat{b}(\alpha - \alpha_s + \hat{r}\alpha_s)]T \\ &= [l(1 - \alpha) + \hat{l}\alpha]\frac{dT}{d\xi} - (1 - \alpha)Q + \hat{b}(1 - \alpha_s + \hat{r}\alpha_s)T_b, \quad \xi > 0 \quad (45) \end{aligned}$$

Thus, subtracting Eq. (44) evaluated at $\xi = 0^-$ from Eq. (45) evaluated at $\xi = 0^+$ and using the jump condition (39), we obtain an expression for T_b given by

$$T_b = \frac{(1 - \alpha_s)(Q + 1 + \gamma_s) + \hat{r}\hat{b}\alpha_s[1 + \chi(p_g^b - 1)]}{\hat{b}(1 - \alpha_s + \hat{r}\alpha_s)} \quad (46)$$

which, from Eq. (43), determines u_g^b as

$$u_g^b = \frac{1}{\hat{r}\hat{b}p_g^b} [(1 - \alpha_s)(Q + 1 + \gamma_s - \hat{r}\hat{b}) - \hat{r}\hat{b}(p_g^b - 1)(1 - \alpha_s\chi)] \quad (47)$$

We note that in the limit $p_g^b \rightarrow 1$, Eqs. (46) and (47) collapse to the results for unconfined burning, where in place of Darcy's law in the solid-gas region, $p_g = 1$ throughout.

It is clear from these results that, because $0 < \chi = 1 - 1/\gamma < 1$, T_b increases linearly with the overpressure $p_g^b - 1$, as shown in Fig. 2. It is readily seen that,

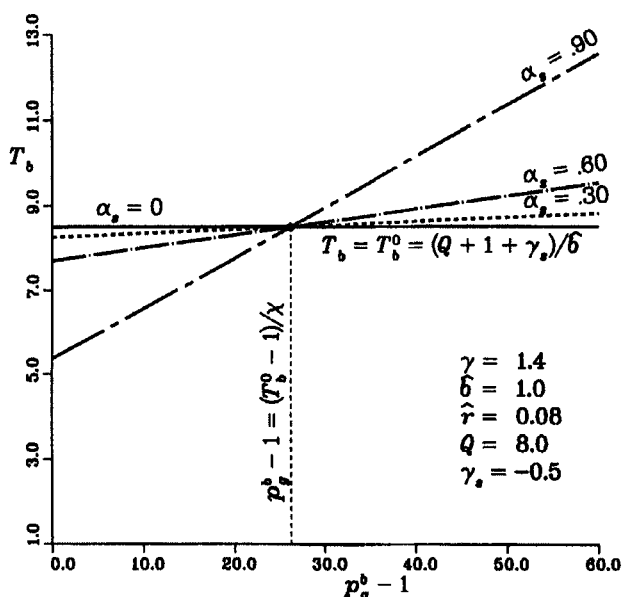


Fig. 2 Final burned temperature T_b as a function of the overpressure $p_g^b - 1$. As the overpressure increases past a critical value, T_b changes from a decreasing to an increasing function of the porosity α_s .

for small overpressures, T_b decreases with increasing values of the porosity α_s , whereas at higher overpressures the opposite trend is observed. Indeed, denoting the burned temperature at zero porosity by $T_b^0 = (Q + 1 + \gamma_s)/\hat{b}$, which is independent of p_g^b , we obtain from Eq. (46) that for $\alpha_s > 0$, $T_b = T_b^0$ at the critical value of overpressure given by $p_g^b - 1 = (T_b^0 - 1)/\chi$. For overpressures greater than this critical value, the preheating effect due to gas permeation is sufficient to overcome that due to a decrease in the amount of solid material, resulting in an increase in burned temperature above T_b^0 . Subsequently, it is clear from Fig. 2 that the magnitude of the difference $T_b - T_b^0$ at a given value of the overpressure is an increasing function of α_s . In connection with this result, we observe from Eq. (47) and Fig. 3 that the burned-gas velocity u_g^b is a monotonically decreasing function of the overpressure. In fact, for sufficiently large overpressures that satisfy the condition

$$p_g^b - 1 > \frac{1 - \alpha_s}{1 - \alpha_s \chi} \left(\frac{Q + 1 + \gamma_s}{\hat{r} \hat{b}} - 1 \right) = \frac{(1 - \alpha_s)(T_b^0 - \hat{r})}{\hat{r}(1 - \alpha_s \chi)} \quad (48)$$

which depends on α_s , we find that u_g^b is negative, implying a gas flow in the upstream direction throughout the multiphase flame. This is illustrated clearly in Fig. 3, which shows the curves for u_g^b as a function of $p_g^b - 1$ crossing the horizontal axis at the aforementioned critical value of the overpressure. Also

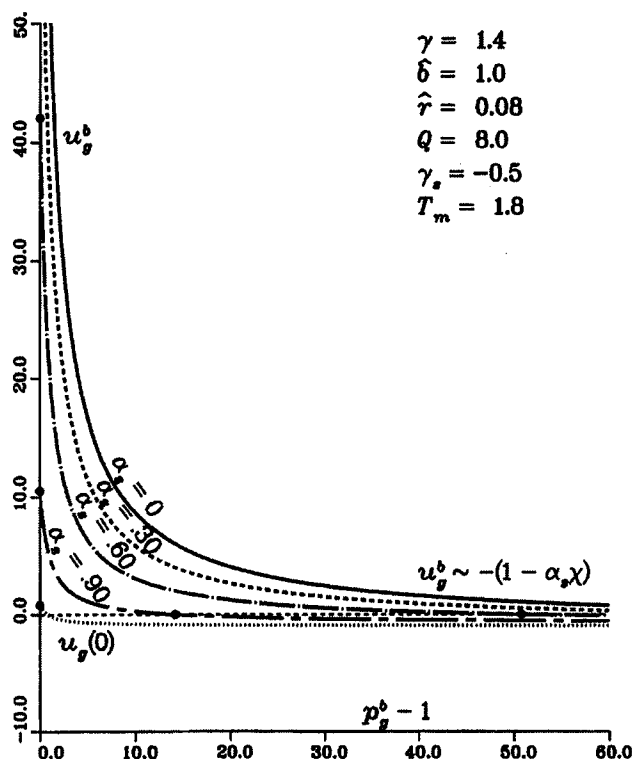


Fig. 3 Burned-gas velocity u_g^b as a function of the overpressure $p_g^b - 1$. Also shown is the gas velocity $u_g(0)$ at the solid-liquid interface. Negative values indicate gas flow in the upstream direction, toward the unburned solid.

shown in Fig. 3 is the value of the gas velocity $u_g(\xi)$ at the solid-liquid interface $\xi = 0$, which is only positive for relatively small values of the overpressure. In particular, from Eq. (41), $u_g(0)$ crosses the horizontal axis at the critical value $p_g^b - 1 = T_m - 1$, beyond which gas flow is directed into the solid-gas region, resulting in the preheating effect due to gas permeation as described earlier. Further solution of the problem in the liquid-gas region, which is necessary for the determination of the burning-rate eigenvalue, is considered in Sec. IV.B.

Before proceeding with an analysis of the liquid-gas reaction region, we observe that the problem in the solid-gas region can be reduced to a scalar problem for the gas pressure p_g . In particular, from Eq. (40) and the Darcy formula for u_g in Eqs. (36), T and thus u_g are given in terms of p_g by

$$T = p_g \left(1 - \frac{\kappa}{\alpha_s} \frac{dp_g}{d\xi} \right), \quad u_g = \frac{T}{p_g} - 1, \quad \xi < 0 \quad (49)$$

Substituting these results into Eq. (44) thus yields a second-order equation for p_g in the region $\xi < 0$ given by

$$\begin{aligned} (1 - \alpha_s + \hat{r}b\alpha_s) \left[p_g \left(1 - \frac{\kappa}{\alpha_s} \frac{dp_g}{d\xi} \right) - 1 \right] \\ = (1 - \alpha_s + \hat{l}\alpha_s) \frac{d}{d\xi} \left[p_g \left(1 - \frac{\kappa}{\alpha_s} \frac{dp_g}{d\xi} \right) \right] + \hat{r}b\chi\alpha_s(p_g - 1) \end{aligned} \quad (50)$$

subject to the boundary conditions

$$p_g = p_g^b, \quad \frac{dp_g}{d\xi} = \frac{\alpha_s}{\kappa} \left(1 - \frac{T_m}{p_g^b} \right) \quad \text{at} \quad \xi = 0 \quad p_g \rightarrow 1 \quad \text{as} \quad \xi \rightarrow -\infty \quad (51)$$

where the second condition follows from the Darcy formula and Eq. (41) for u_g evaluated at $\xi = 0$. We note that the last condition, aside from being consistent with the first of Eqs. (49), is already built into Eq. (50) because Eq. (50) is really a first integral of Eq. (34). Had the preceding expression for T been substituted directly into the latter, a third-order equation for p_g would have been obtained, permitting the specification of the three boundary conditions (51). The problem given by Eqs. (50) and (51), the solution of which will determine T and u_g according to Eqs. (49), are treated in Sec. V.

B. Burning-Rate Eigenvalue

To determine the burning-rate eigenvalue, we must complete our analysis of the liquid-gas region $\xi > 0$. In this regard, Eqs. (33) and (45) constitute two equations for T and α in this region, with u_g then determined by Eq. (42) and the eigenvalue Λ determined by the boundary conditions. To handle the Arrhenius nonlinearity, we exploit the largeness of the nondimensional activation energy N and analyze the problem in the asymptotic limit $N \gg 1$. Because $p_g = p_g^b$ throughout the liquid-gas region, the analysis of the confined and unconfined problems is essentially the same for $\xi > 0$.

In the limit $N \rightarrow \infty$, all chemical activity is concentrated in a very thin region where T is within $\mathcal{O}(1/N)$ of T_b . Denoting the location of this thin zone by $\xi_r > 0$, we see that the semi-infinite liquid-gas region comprises a preheat zone ($0 < \xi < \xi_r$) where chemical activity is exponentially small, the thin reaction zone where the chemical reaction goes to completion, and a burned region $\xi > \xi_r$. Thus, we conclude from Eq. (33) that

$$\alpha = \begin{cases} \alpha_s, & \xi < \xi_r \\ 1, & \xi > \xi_r \end{cases} \quad (52)$$

and from Eqs. (42) and (43) that

$$u_g = \begin{cases} T/p_g^b - 1, & 0 < \xi < \xi_r \\ \hat{r}^{-1}(1 - \alpha_s + \hat{r}\alpha_s)T_b/p_g^b - 1 = u_g^b, & \xi > \xi_r \end{cases} \quad (53)$$

Because T is within $\mathcal{O}(1/N)$ of T_b in the reaction zone, the analysis of this thin region requires the use of a stretched coordinate [see Eqs. (58)]. As a result, T is continuous with respect to the $\mathcal{O}(1)$ outer variable ξ at $\xi = \xi_r$, and thus the gas velocity jumps across $\xi = \xi_r$ by the amount

$$u_g|_{\xi=\xi_r^+} - u_g|_{\xi=\xi_r^-} = (1/\hat{r})(1 - \hat{r})(1 - \alpha_s)(T_b/p_g^b) \quad (54)$$

which is positive, assuming the unburned-gas density is less than that of the solid (i.e., $\hat{r} < 1$). Finally, using Eq. (52), we can integrate Eq. (45) a second time to determine completely the outer temperature profile in the liquid-gas region as

$$T(\xi) = \begin{cases} B + (T_m - B)\exp\left[\frac{b(1 - \alpha_s) + \hat{r}\hat{b}\alpha_s}{l(1 - \alpha_s) + \hat{l}\alpha_s}\xi\right], & 0 < \xi < \xi_r \\ T_b, & \xi > \xi_r \end{cases} \quad (55)$$

where

$$B \equiv \frac{(1 - \alpha_s)(1 + \gamma_s) + \hat{r}\hat{b}\alpha_s[1 + \chi(p_g^b - 1)]}{b(1 - \alpha_s) + \hat{r}\hat{b}\alpha_s} \quad (56)$$

We note that $T(\xi)$ for $\xi < 0$ is still to be determined from Eqs. (49) and the solution of the pressure problem given by Eqs. (50–51), as described in the next section; however, it is not required for the determination of the burning-rate eigenvalue Λ . The location ξ_r of the reaction zone, which appears as a sheet on the scale of the outer variable ξ , thus is determined by Eqs. (55) from continuity of T as

$$\xi_r = \frac{l(1 - \alpha_s) + \hat{l}\alpha_s}{b(1 - \alpha_s) + \hat{r}\hat{b}\alpha_s} \ell_n\left(\frac{T_b - B}{T_m - B}\right) \quad (57)$$

The determination of the burning-rate eigenvalue Λ , as well as the spatial evolution of the variables α and u_g (which are discontinuous on the scale of the outer variable ξ), requires an analysis of the thin reaction-zone region in the vicinity of ξ_r . We thus introduce a stretched inner variable η and a normalized temperature variable Θ defined by

$$\Theta = (T - 1)/(T_b - 1), \quad \eta = \beta(\xi - \xi_r) \quad \beta \equiv (1 - T_b^{-1})N \gg 1 \quad (58)$$

where β is the Zel'dovich number, and seek solutions in the form of the expansions

$$\begin{aligned}\alpha &\sim \alpha_0 + \beta^{-1}\alpha_1 + \beta^{-2}\alpha_2 + \dots \\ u_g &\sim u_0 + \beta^{-1}u_1 + \beta^{-2}u_2 + \dots \\ \Theta &\sim 1 + \beta^{-1}\theta_1 + \beta^{-2}\theta_2 + \dots \\ \Lambda &\sim \beta(\Lambda_0 + \beta^{-1}\Lambda_1 + \beta^{-2}\Lambda_2 + \dots)\end{aligned}\quad (59)$$

The coefficients in the expansion of u_g are determined readily from Eq. (42) in terms of the α_i and θ_i , which themselves are obtained by solving the sequence of inner problems that arise from substituting the above expansions into Eqs. (33) and (45) and matching with the outer solutions for $\xi < \xi_r$ and $\xi > \xi_r$. In particular, at leading order the inner problem is given by

$$\frac{d\alpha_0}{d\eta} = r\Lambda_0(1 - \alpha_0)e^{\theta_1} \quad (60)$$

$$[l + (\hat{l} - l)\alpha_0]\frac{d\theta_1}{d\eta} = \frac{D}{T_b - 1}(1 - \alpha_0) \quad (61)$$

subject to the matching conditions

$$\alpha_0 \rightarrow \alpha_s, \quad \theta_1 \sim E\eta \quad \text{as} \quad \eta \rightarrow -\infty \quad (62)$$

$$\alpha_0 \rightarrow 1, \quad \theta_1 \rightarrow 0 \quad \text{as} \quad \eta \rightarrow +\infty \quad (63)$$

Here, D and E are defined as

$$D \equiv (b - \hat{b})T_b + Q, \quad E \equiv \frac{1}{T_b - 1} \frac{dT}{d\xi} \Big|_{\xi=\xi_r^-} \quad (64)$$

where the latter is calculated from Eqs. (55).

The problem posed by Eqs. (60–63) now is solved readily by employing α_0 as the independent variable. Thus, using Eq. (60), we can write Eq. (61) as

$$r\Lambda_0[l + (\hat{l} - l)\alpha_0]e^{\theta_1} \frac{d\theta_1}{d\alpha_0} = \frac{D}{T_b - 1} \quad (65)$$

which is readily integrated from α_s (at $\eta = -\infty$) to any $\alpha_0 \leq 1$ to give

$$e^{\theta_1(\alpha_0)} = \frac{D}{(T_b - 1)r\Lambda_0} \int_{\alpha_s}^{\alpha_0} \frac{d\alpha_0}{l + (\hat{l} - l)\alpha_0} \quad (66)$$

Evaluating the latter at $\alpha_0 = 1$ (at which $\theta_1 = 0$) thus determines the leading-order coefficient Λ_0 in the expansion of the burning-rate eigenvalue as

$$\Lambda_0 = \begin{cases} \frac{D}{(T_b - 1)r(\hat{l} - l)} \ell_n \left[\frac{\hat{l}}{l + (\hat{l} - l)\alpha_s} \right], & l \neq \hat{l} \\ \frac{D}{(T_b - 1)rl} (1 - \alpha_s), & l = \hat{l} \end{cases} \quad (67)$$

and using this result in Eq. (66) for arbitrary α_0 then determines $\theta_1(\alpha_0)$ as

$$\theta_1(\alpha_0) = \begin{cases} \ell_n \left(\frac{\ell_n[l + (\hat{l} - l)\alpha_0] - \ell_n[l + (\hat{l} - l)\alpha_s]}{\ell_n \hat{l} - \ell_n[l + (\hat{l} - l)\alpha_s]} \right), & \hat{l} \neq l \\ \ell_n \left(\frac{\alpha_0 - \alpha_s}{1 - \alpha_s} \right), & \hat{l} = l \end{cases} \quad (68)$$

The determination of $\alpha_0(\eta)$, and hence $\theta_1(\eta)$, then follows directly from Eq. (60).

From Eqs. (67) and the definition of Λ according to the last of Eqs. (14b) and (59), the leading-order expression for the dimensional propagation speed \tilde{U} is given by

$$\begin{aligned} \tilde{U}^2 &\sim \frac{r(T_b - 1)\tilde{A}(p_g^b)}{\beta D \tilde{\rho}_s \tilde{c}_s} e^{-N} \cdot \tilde{f}(\tilde{\lambda}_g, \tilde{\lambda}_l) \\ &= \frac{r T_b^2}{(b - \hat{b})T_b + Q} \cdot \frac{\tilde{A}(p_g^b)}{\tilde{\rho}_s \tilde{c}_s N_u} e^{-N_u/T_b} \cdot \tilde{f}(\tilde{\lambda}_g, \tilde{\lambda}_l) \end{aligned} \quad (69)$$

where $N_u = \tilde{E}_l / \tilde{R}^0 \tilde{T}_u = N T_b$ is independent of T_b , and the last factor, which contains the complete dependence of the burning rate on the thermal conductivities, is given by

$$\tilde{f}(\tilde{\lambda}_g, \tilde{\lambda}_l) = \begin{cases} \frac{\tilde{\lambda}_g - \tilde{\lambda}_l}{\ell_n(\tilde{\lambda}_g / [\tilde{\lambda}_l + (\tilde{\lambda}_g - \tilde{\lambda}_l)\alpha_s])}, & \tilde{\lambda}_g \neq \tilde{\lambda}_l \\ \tilde{\lambda}_l / (1 - \alpha_s), & \tilde{\lambda}_g = \tilde{\lambda}_l \end{cases} \quad (70)$$

Expression (69) for the burning rate, though virtually identical in form for both the confined problem and the unconfined problem obtained in the limit of constant pressure ($p_g^b = 1$), nonetheless differs implicitly for the two types of problems through the linear dependence of T_b on the overpressure $p_g^b - 1$. In particular, because there is an exponential dependence of the reaction rate on T_b , relatively small changes in T_b can produce significant modifications in the propagation speed.

To analyze explicitly the dependence of the burning rate on the overpressure, it is convenient to define the normalized burning rate $U^* = \tilde{U}(p_g^b) / \tilde{U}(1)$, where the argument denotes the value of p_g^b . Consequently, from Eq. (69), we obtain $U^* = U_n [\tilde{A}(p_g^b) / \tilde{A}(1)]^{1/2}$, where the coefficient U_n is given by

$$U_n = \frac{T_b(p_g^b)}{T_b(1)} \left[\frac{(b - \hat{b})T_b(1) + Q}{(b - \hat{b})T_b(p_g^b) + Q} \right]^{\frac{1}{2}} \exp \left\{ \frac{N_u}{2} \left[\frac{1}{T_b(1)} - \frac{1}{T_b(p_g^b)} \right] \right\} \quad (71)$$

and where T_b as a function of p_g^b is given by Eq. (46). In this form, it is seen readily that, because T_b is a linearly increasing function of overpressure and the nondimensional activation-energy parameter N_u typically is very large [its definition, given after Eq. (69), is in terms of the *unburned* temperature \tilde{T}_u], U_n is exponentially sensitive to T_b and hence to p_g^b . Thus, as the overpressure $p_g^b - 1$ increases from zero, the burning rate increases exponentially (Fig. 4), reflecting the sensitivity to the corresponding increase in the rate of gas permeation into the solid-gas region given by Eq. (41). We remark that this result cannot be predicted

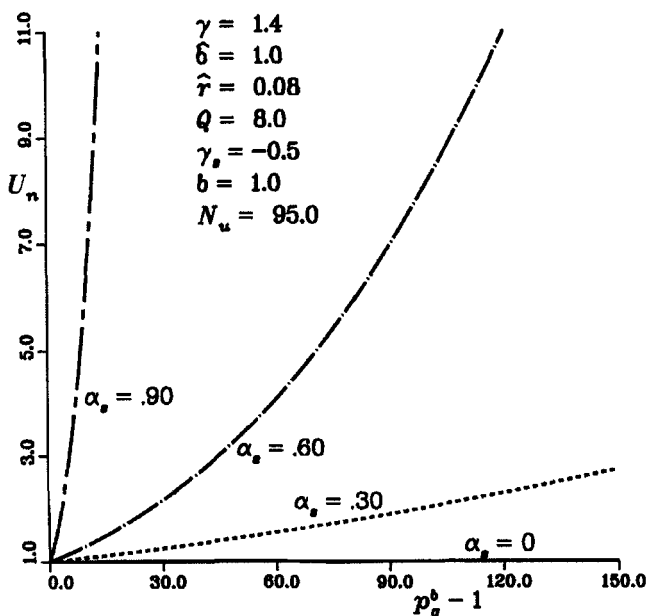


Fig. 4 Normalized burning-rate coefficient U_n as a function of the overpressure $p_g^b - 1$.

with a constant-pressure model appropriate for unconfined deflagrations because in that case, the gas flow is always in the downstream direction (if one imposes the upstream boundary condition that u_g vanish) and an increase in pressure then serves only to decrease T_b because of the increase in the gas density (\hat{r} increases) that absorbs more of the heat of reaction. In the present context, the upstream gas density \hat{r} remains constant, and an increase in overpressure serves to preheat the unburned solid through enhanced permeation of the burned gas into the solid-gas region. In the limit of large overpressures, T_b^{-1} becomes small and the exponential factor in Eq. (71) approaches a constant value. Consequently, in the range of large overpressures, the dependence of U_n on p_g^b becomes algebraic. This also is illustrated in Fig. 4, in which case (because $b = \hat{b}$) the saturated dependence of U_n on p_g^b is linear. We note that this feature (exponential transition to an algebraic pressure-dependent burning rate) is qualitatively consistent with most experiments in Crawford-type (large-volume) bombs that indicate a rapid increase in the burning rate frequently associated with the onset of convective burning,^{6,24,25} followed by a less dramatic pressure dependence that typically is represented in the form Ap^n .

V. Analysis of the Gas-Permeation Layer

The pressure-driven permeation of hot gases into the unburned porous solid has been shown to be a critical factor in causing the rapid increase in the burning rate associated with the onset of convective burning. However, this implies nontrivial pressure and velocity profiles in this region to satisfy the ambient upstream boundary conditions on these variables. Thus, although the calculation of

the burning-rate eigenvalue in the preceding section did not require a detailed knowledge of the actual solution profiles in the solid-gas region, it being sufficient to determine the results (40–41) for u_g , there is nonetheless a strong interest in computing these profiles to better understand the role of convection in these types of two-phase-flow problems. Because gas permeation is clearly a strong function of the pressure difference across the deflagration, it is convenient to define an overpressure variable $p = p_g - 1$, in terms of which the pressure problem posed by Eqs. (50–51) can be written as

$$\begin{aligned} (1 - \alpha_s + \hat{r}\hat{b}\alpha_s) \left[p - \frac{\kappa}{\alpha_s}(p+1) \frac{dp}{d\xi} \right] \\ = (1 - \alpha_s + \hat{l}\alpha_s) \frac{d}{d\xi} \left[p - \frac{\kappa}{\alpha_s}(p+1) \frac{dp}{d\xi} \right] + \hat{r}\hat{b}\chi\alpha_s p \end{aligned} \quad (72)$$

subject to

$$\begin{aligned} p = p_b = p_g^b - 1, \quad \frac{dp}{d\xi} = \frac{\alpha_s}{\kappa} \left(1 - \frac{T_m}{p_b + 1} \right) \quad \text{at} \quad \xi = 0 \\ p \rightarrow 0 \quad \text{as} \quad \xi \rightarrow -\infty \end{aligned} \quad (73)$$

Because our goal is a qualitative understanding of gas-permeation effects, it suffices to obtain approximate solutions using asymptotic methods. In particular, we can introduce a bookkeeping parameter $\epsilon \ll 1$ and consider the realistic parameter regime in which \hat{r} , \hat{l} , α_s , and κ/α_s are all $\mathcal{O}(\epsilon)$, where we note that the permeability κ is usually proportional to some power of α_s that is greater than unity.^{13,26} That is, we scale these small quantities as

$$\alpha_s = \alpha_s^* \epsilon, \quad \kappa = \kappa^* \epsilon^2, \quad \hat{r} = \hat{r}^* \epsilon, \quad \hat{l} = \hat{l}^* \epsilon \quad (74)$$

in terms of which Eqs. (72) and (73) become

$$\begin{aligned} (1 - \epsilon\alpha_s^* + \epsilon^2\hat{r}^*\hat{b}\alpha_s^*) \left[p - \epsilon \frac{\kappa^*}{\alpha_s^*}(p+1) \frac{dp}{d\xi} \right] \\ = (1 - \epsilon\alpha_s^* + \epsilon^2\hat{l}^*\alpha_s^*) \frac{d}{d\xi} \left[p - \epsilon \frac{\kappa^*}{\alpha_s^*}(p+1) \frac{dp}{d\xi} \right] + \epsilon^2\hat{r}^*\hat{b}\chi\alpha_s^* p \end{aligned} \quad (75)$$

$$\begin{aligned} p = p_b = p_g^b - 1, \quad \frac{dp}{d\xi} = \epsilon^{-1} \frac{\alpha_s^*}{\kappa^*} \left(1 - \frac{T_m}{p_b + 1} \right) \quad \text{at} \quad \xi = 0 \\ p \rightarrow 0 \quad \text{as} \quad \xi \rightarrow -\infty \end{aligned} \quad (76)$$

The problem given by Eqs. (75) and (76) has been analyzed¹² for two primary cases of interest: $p \sim \mathcal{O}(1)$ and $p \sim \mathcal{O}(\epsilon^{-1})$, corresponding to two different magnitudes of p_g^b . The results of this analysis are as follows: For $\mathcal{O}(1)$ overpressures, the second condition in Eqs. (76) suggests that there is an $\mathcal{O}(\epsilon)$ boundary layer in the vicinity of $\xi = 0$. Consequently, a stretched coordinate $\eta = \xi/\epsilon$ is introduced to describe the solution within the boundary layer, which then is matched to the outer solution for negative $\mathcal{O}(1)$ values of ξ . In this fashion, the leading-order composite

solution is determined as

$$p \sim p_0(\xi/\epsilon) + (T_m - 1)(e^\xi - 1) \quad (77)$$

where the leading-order inner solution p_0 , which has been expressed functionally in terms of the outer variable ξ , is given implicitly by

$$\frac{\alpha_s^* \xi}{\kappa^* \epsilon} = p_0 - p_b + T_m \ln \left(\frac{p_0 - T_m + 1}{p_b - T_m + 1} \right) \quad (78)$$

The boundary-layer (inner), outer, and composite solutions are illustrated in Fig. 5. From Eq. (77), the gas velocity in the solid-gas region is, in turn, given by

$$u_g = -\frac{\kappa}{\alpha_s} \frac{dp}{d\xi} \sim -1 + \frac{T_m}{p_0(\xi/\epsilon) + 1} - \epsilon \frac{\kappa^*}{\alpha^*} (T_m - 1) e^\xi \quad (79)$$

We observe that $p_0(\xi/\epsilon) \rightarrow T_m - 1$ as ξ approaches $\mathcal{O}(1)$ negative values, and thus, as indicated in Fig. 5, it is clear that gas permeation for $\mathcal{O}(1)$ overpressures is only significant in the thin boundary layer adjacent to the solid-liquid interface, assuming $p_b > T_m - 1$. Although this last qualification is by far the typical case (because $T_m - 1 = \tilde{T}_m/\tilde{T}_u - 1$ is not likely to be larger than unity), it is nonetheless of interest to point out that the structure of the solution will change as p_b approaches the value $T_m - 1$ because the gradient of pressure at $\xi = 0$, which has been scaled as $\mathcal{O}(\epsilon^{-1})$ in Eqs. (76), will cease to be large in that limit. Indeed, for small overpressures ($0 < p_b < T_m - 1$), the pressure gradient becomes negative at $\xi = 0$,

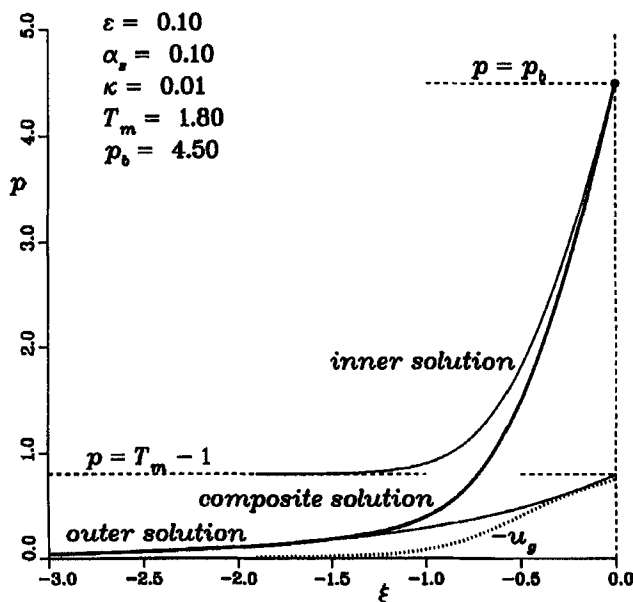


Fig. 5 Pressure profile $p(\xi)$ in the gas-permeation region for $\mathcal{O}(1)$ overpressures. Also shown is the velocity profile $u_g(\xi)$.

indicating, according to Eqs. (36) and (41), a gas flow out of the solid in the downstream direction, as in the case of an unconfined deflagration.

The other primary case of interest in many applications is the limit in which the overpressure itself becomes large. In that case, it is useful to rescale p in Eqs. (75) and (76) by defining the scaled overpressure $P = \epsilon p$. In terms of P , Eqs. (75) and (76) become

$$\begin{aligned} (1 - \epsilon \alpha_s^* + \epsilon^2 \hat{r}^* \hat{b} \alpha_s^*) \left[P - \frac{\kappa^*}{\alpha_s^*} (P + \epsilon) \frac{dP}{d\xi} \right] \\ = (1 - \epsilon \alpha_s^* + \epsilon^2 \hat{r}^* \alpha_s^*) \frac{d}{d\xi} \left[P - \frac{\kappa^*}{\alpha_s^*} (P + \epsilon) \frac{dP}{d\xi} \right] + \epsilon^2 \hat{r}^* \hat{b} \chi \alpha_s^* P \end{aligned} \quad (80)$$

$$\begin{aligned} P = P_b \equiv \frac{1}{\epsilon} (p_g^b - 1), \quad \frac{dP}{d\xi} = \frac{\alpha_s^*}{\kappa^*} \left(1 - \frac{\epsilon T_m}{P_b + \epsilon} \right) \quad \text{at } \xi = 0 \\ P \rightarrow 0 \quad \text{as } \xi \rightarrow -\infty \end{aligned} \quad (81)$$

There is now no reason to suspect a boundary layer near $\xi = 0$, but a straightforward perturbation solution on the ξ scale leads to the approximate solution

$$P \sim P_0 = \begin{cases} (\alpha_s^*/\kappa^*)(\xi + \xi_0), & -\xi_0 < \xi \leq 0 \\ 0, & \xi < -\xi_0 \end{cases} \quad \xi_0 = (\kappa^*/\alpha_s^*) P_b \quad (82)$$

which is valid everywhere except at $\xi = -\xi_0$, where the derivative is discontinuous. This kink in the solution thus suggests the existence of a thin corner layer in that vicinity. Hence, we interpret Eqs. (82) as the leading-order outer solution and proceed to construct an inner solution in a thin region centered about $\xi = -\xi_0$. In particular, it turns out that the proper scales on which to analyze this layer are $P \sim \mathcal{O}(\epsilon)$ and $\xi + \xi_0 \sim \mathcal{O}(\epsilon)$. The result of a matching of the solution in this region with the outer solution (82) is the uniform composite approximation¹²

$$(\alpha_s^*/\kappa^*)(\xi + \xi_0) \sim P + \epsilon \ell_n(P/P_b) \quad (83)$$

The outer and composite solutions (82) and (83) for the scaled overpressure P are illustrated in Fig. 6. It is clear that in this case, gas permeation extends an $\mathcal{O}(1)$ distance into the gas-solid region, although, as in the previous case of $\mathcal{O}(1)$ overpressures, the extent of gas permeation remains, because of the relative smallness of the permeability κ , an order of magnitude less than that of the overpressure itself.

VI. Asymptotic Model for Nonsteady, Nonplanar Burning

The solution analyzed in the preceding sections constitutes the special case of a quasi-steady, planar deflagration, and is not necessarily the only long-time solution of the final model presented in Sec. III. For example, one generally expects that there exist parameter thresholds beyond which such a solution loses stability to one or more nonsteady and/or nonplanar modes of burning. To perform such stability analyses, it is appropriate to extend the previous one-dimensional large activation-energy analysis of the reaction zone to obtain a more tractable flame-sheet type of model. In such a model, the reaction zone is relegated asymptotically

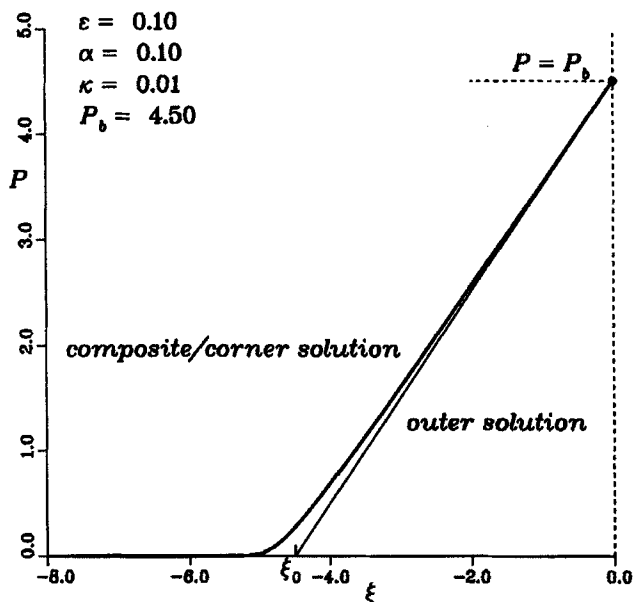


Fig. 6 Scaled pressure profile $P(\xi)$ in the gas-permeation region for large overpressures.

to an infinitesimally thin region, and the (outer) solutions on either side of this reaction front are connected by derived jump and continuity conditions. This effectively simplifies the problem by allowing consideration of a coupled problem for the reactionless outer variables, and is the formulation on which most modern analytical stability analyses are based.

A. Outer Problem

In the limit of large activation energy, the reaction zone collapses to a reaction front located at $x_3 = x_r(x_1, x_2, t) > x_m(x_1, x_2, t)$, and it is convenient to shift the (nonorthogonal) moving coordinate by defining the new coordinate $\zeta = \xi - (x_r - x_m)$, or in terms of the original variables, $\zeta = x_3 - x_r(x_1, x_2, t)$. In this new coordinate system, the origin thus is defined to be at $x_3 = x_r$, and in terms of ζ , the problem defined by Eqs. (15–25) becomes, given the assumption of a quasisteady gas phase with respect to the new coordinate system and expression (21) for u_i ,

$$\frac{\partial}{\partial \zeta} \left[\rho_g \left(u_g - \frac{\partial x_r}{\partial t} \right) \right] = 0, \quad \zeta < -(x_r - x_m) \quad (84)$$

$$r \frac{\partial \alpha}{\partial t} + \frac{\partial}{\partial \zeta} \left\{ (1 - \alpha) \left[\frac{\partial x_m}{\partial t} + r \left(\frac{\partial x_r}{\partial t} - \frac{\partial x_m}{\partial t} \right) \right] - \hat{r} \alpha \rho_g \left(u_g - \frac{\partial x_r}{\partial t} \right) \right\} = 0, \quad \zeta > -(x_r - x_m) \quad (85)$$

$$r \frac{\partial \alpha}{\partial t} + \frac{\partial}{\partial \zeta} \left\{ (1 - \alpha) \left[\frac{\partial x_m}{\partial t} + r \left(\frac{\partial x_r}{\partial t} - \frac{\partial x_m}{\partial t} \right) \right] \right\} \\ = r \Lambda (1 - \alpha) \exp \left[N \left(1 - \frac{T_b}{T} \right) \right], \quad \zeta > -(x_r - x_m) \quad (86)$$

$$(1 - \alpha_s) \frac{\partial T}{\partial t} + \frac{\partial}{\partial \zeta} \left\{ \left[(1 - \alpha_s) \left(-\frac{\partial x_r}{\partial t} \right) + \hat{r} \hat{b} \alpha_s \left(u_g - \frac{\partial x_r}{\partial t} \right) \rho_g \right] T \right\} \\ = \nabla_r \cdot [(1 - \alpha_s + \hat{l} \alpha_s) \nabla_r T] - \hat{\kappa} \alpha_s \frac{\partial x_r}{\partial t} \frac{\partial p_g}{\partial \zeta}, \quad \zeta < -(x_r - x_m) \quad (87)$$

$$r \frac{\partial}{\partial t} [(1 - \alpha)(Q + bT)] + \frac{\partial}{\partial \zeta} \left\{ (1 - \alpha) \left[-\frac{\partial x_m}{\partial t} - r \left(\frac{\partial x_r}{\partial t} - \frac{\partial x_m}{\partial t} \right) \right] (Q + bT) \right\} \\ + \frac{\partial}{\partial \zeta} \left[\hat{r} \hat{b} \alpha \left(u_g - \frac{\partial x_r}{\partial t} \right) \rho_g T \right] = \nabla_r \cdot [l(1 - \alpha) + \hat{l} \alpha] \nabla_r T, \quad \zeta > -(x_r - x_m) \quad (88)$$

subject to the equation of state (20) and the conditions

$$\alpha = \alpha_s, \quad u_g = -\frac{\kappa(\alpha_s)}{\alpha_s} \frac{\partial p_g}{\partial \zeta} \quad \text{for} \quad \zeta \leq -(x_r - x_m) \\ p_g \rightarrow 1 \quad (u_g \rightarrow 0), \quad T \rightarrow 1 \quad \text{as} \quad \zeta \rightarrow -\infty \quad (89)$$

$$p_g = p_g^b \quad \text{for} \quad \zeta > -(x_r - x_m) \quad \alpha \rightarrow 1, \quad T \rightarrow T_b \quad \text{as} \quad \zeta \rightarrow +\infty \quad (90)$$

$$T|_{\zeta=-(x_r-x_m)} = T_m \quad (91)$$

$$[l(1 - \alpha_s) + \hat{l} \alpha_s] \hat{n}_m \cdot \nabla_r T|_{\zeta=-(x_r-x_m)^+} - (1 - \alpha_s + \hat{l} \alpha_s) \hat{n}_m \cdot \nabla_r T|_{\zeta=-(x_r-x_m)^-} \\ = G_m^{-1} \frac{\partial x_m}{\partial t} (1 - \alpha_s) [\gamma_s + (1 - b) T_m] \quad (92)$$

where all variables are implicitly continuous across the melting surface $\zeta = -(x_r - x_m)$ and, analogous to the definition of ∇_m given below Eq. (25), the operator

$$\nabla_r = \left[\frac{\partial}{\partial x_1} - \left(\frac{\partial x_r}{\partial x_1} \right) \frac{\partial}{\partial \zeta}, \frac{\partial}{\partial x_2} - \left(\frac{\partial x_r}{\partial x_2} \right) \frac{\partial}{\partial \zeta}, \frac{\partial}{\partial \zeta} \right]$$

is the nondimensional gradient operator expressed in terms of the moving coordinate system attached to the reacting surface. The final burned temperature T_b that appears in the boundary condition (90) for the general nonsteady, nonplanar problem is the same as that calculated for the special case of steady, planar burning analyzed in Sec. IV, and thus is given by Eq. (46).

As in the special case of steady, planar combustion, we again consider the limit of large activation energy ($N \gg 1$), in which case all chemical activity and heat release associated with the reaction term in Eq. (86) are confined to a thin $\mathcal{O}(N^{-1})$ reaction zone at $\zeta = 0$. In this way, the original distributed-reaction problem is reduced to a pair of reactionless problems in the outer regions $\zeta < 0$ and $\zeta > 0$, the solutions of which must be matched to the reaction-zone solution valid in

the thin inner region $|\zeta| \ll 1$. The result is an asymptotic model for the outer variables, subject to nonlinear jump conditions across $\zeta = 0$ that depend on local conditions there, and an evolution equation for $x_r(x_1, x_2, t)$. With this asymptotic simplification, the outer solution of Eqs. (84–86) for the gas-phase volume fraction and velocity is given by

$$\alpha = \begin{cases} \alpha_s, & \zeta < 0 \\ 1, & \zeta > 0 \end{cases} \quad (93)$$

$$u_g = \begin{cases} -(T/p_g - 1) \frac{\partial x_r}{\partial t}, & \zeta < -(x_r - x_m) \\ -(T/p_g^b - 1) \frac{\partial x_r}{\partial t}, & -(x_r - x_m) < \zeta < 0 \\ (T/p_g^b)g(x_1, x_2, t) + \frac{\partial x_r}{\partial t}, & \zeta > 0 \end{cases} \quad (94)$$

where the first of these indicates that all variation in the volume-fraction variable α is confined to the inner reaction zone analyzed in the next subsection and the second expresses u_g in terms of the local temperature and the instantaneous propagation speed of the reaction zone, with the “constant” of integration

$$g(x_1, x_2, t) = \frac{p_g^b}{T_b} \left(u_g|_{\zeta \rightarrow +\infty} - \frac{\partial x_r}{\partial t} \right)$$

to be determined. The top expression in Eq. (94) may be combined with the expression for u_g in Eqs. (89) (Darcy’s law) to give the additional relation

$$T = p_g \left[1 + \frac{\kappa}{\alpha_s} \frac{\partial p_g}{\partial \zeta} \left(\frac{\partial x_r}{\partial t} \right)^{-1} \right], \quad \zeta < -(x_r - x_m) \quad (95)$$

which is the appropriate generalization of Eq. (49). By use of these results and the equation of state (20) in Eqs. (87) and (88), the outer problem becomes

$$\begin{aligned} (1 - \alpha_s) \frac{\partial T}{\partial t} + (1 - \alpha_s + \hat{r} \hat{b} \alpha_s) \left(-\frac{\partial x_r}{\partial t} \right) \frac{\partial T}{\partial \zeta} \\ = (1 - \alpha_s + \hat{l} \alpha_s) \nabla_r^2 T - \hat{\pi} \alpha_s \frac{\partial x_r}{\partial t} \frac{\partial p_g}{\partial \zeta}, \quad \zeta < -(x_r - x_m) \end{aligned} \quad (96)$$

$$\begin{aligned} rb(1 - \alpha_s) \frac{\partial T}{\partial t} + [rb(1 - \alpha_s) + \hat{r} \hat{b} \alpha_s] \left(-\frac{\partial x_r}{\partial t} \right) \frac{\partial T}{\partial \zeta} - b(1 - r)(1 - \alpha_s) \frac{\partial x_m}{\partial t} \frac{\partial T}{\partial \zeta} \\ = [l(1 - \alpha_s) + \hat{l} \alpha_s] \nabla_r^2 T - (x_r - x_m) < \zeta < 0 \end{aligned} \quad (97)$$

$$\hat{r} \hat{b} g \frac{\partial T}{\partial \zeta} = \hat{l} \nabla_r^2 T, \quad \zeta > 0 \quad (98)$$

subject to boundary and interface conditions (89–92) on T and p_g . From the expression below Eq. (92) for ∇_r , the Laplacian operator ∇_r^2 in the (x_1, x_2, ζ)

coordinate system is given by

$$\begin{aligned} \nabla_r^2 = & \frac{\partial^2}{\partial x_1^2} + \frac{\partial^2}{\partial x_2^2} + G_r^2 \frac{\partial^2}{\partial \zeta^2} - 2 \frac{\partial x_r}{\partial x_1} \frac{\partial^2}{\partial x_1 \partial \zeta} \\ & - 2 \frac{\partial x_r}{\partial x_2} \frac{\partial^2}{\partial x_2 \partial \zeta} - \left(\frac{\partial^2 x_r}{\partial x_1^2} + \frac{\partial^2 x_r}{\partial x_2^2} \right) \frac{\partial}{\partial \zeta} \end{aligned} \quad (99)$$

where

$$G_r^2 = 1 + \left(\frac{\partial x_r}{\partial x_1} \right)^2 + \left(\frac{\partial x_r}{\partial x_2} \right)^2$$

We observe that substitution of relation (95) into Eq. (96) gives a nonlinear partial differential equation for p_g , analogous to the ordinary result (50) for steady, planar burning. These conditions, however, still are not sufficient to determine the solution completely for the outer variables. To do so requires additional jump and continuity conditions across the thin reaction zone located at $\zeta = 0$, as well as an expression for the gas-velocity function $g(x_1, x_2, t)$ in the region $\zeta > 0$, which necessitates an analysis of the inner reaction-zone problem.

The derivation of two of the additional conditions needed to close the outer problem can be obtained directly from an integration of Eq. (88) across the thin reaction region; i.e., from $\zeta = 0^-$ to 0^+ . Using results (93) and (94), and accounting for the fact that quantities such as α , T , $\alpha u_g T$, αT , $(1 - \alpha)T$, $\alpha \partial T / \partial \zeta$, and $(1 - \alpha) \partial T / \partial \zeta$ behave, in the limit of large activation energy, as distributions there, the continuity and jump relations

$$T|_{\zeta=0^-} = T|_{\zeta=0^+} \quad (100)$$

and

$$\begin{aligned} & \left\{ \hat{r} \hat{b} g + [(1 - \alpha_s) r b + \alpha_s \hat{r} \hat{b}] \frac{\partial x_r}{\partial t} + (1 - \alpha_s)(1 - r) b \frac{\partial x_m}{\partial t} \right\} T \Big|_{\zeta=0} \\ & + (1 - \alpha_s) Q \left[r \frac{\partial x_r}{\partial t} + (1 - r) \frac{\partial x_m}{\partial t} \right] \\ & - (l - \hat{l})(1 - \alpha_s) \left(\frac{\partial x_r}{\partial x_1} \frac{\partial T}{\partial x_1} + \frac{\partial x_r}{\partial x_2} \frac{\partial T}{\partial x_2} \right) \Big|_{\zeta=0} \\ & = G_r^2 \left\{ \hat{l} \frac{\partial T}{\partial \zeta} \Big|_{\zeta=0^+} - [l(1 - \alpha_s) + \hat{l} \alpha_s] \frac{\partial T}{\partial \zeta} \Big|_{\zeta=0^-} \right\} \end{aligned} \quad (101)$$

are obtained. The structure of the inner reaction zone, with suitable matching of solutions in that region to the outer solutions, now must be addressed to obtain an additional jump condition across $\zeta = 0$ and an expression for the function g introduced in Eqs. (94). We thus employ the method of matched asymptotic expansions and seek solutions to the coupled outer problems in the form of the expansions $T \sim T^{(0)} + N^{-1} T^{(1)} + N^{-2} T^{(2)} + \dots$, and similarly for the gas-velocity function g . Hence, to leading order, the outer equations obtained thus far are given by Eqs. (89–101) with T and g replaced by $T^{(0)}$ and $g^{(0)}$, respectively.

B. Reaction-Zone Solutions

Spatial variations in the reaction-zone solutions in the normal (ζ) direction occur on a short, of order N^{-1} , length scale relative to that of the outer solutions. Accordingly, it is appropriate to introduce the stretched normal coordinate η defined by

$$\eta = \beta\zeta = \beta(x_3 - x_r) \quad (102)$$

where β is the Zel'dovich number defined in the last of Eqs. (58), and it is also convenient to introduce again the normalized temperature variable $\Theta = (T - 1)/(T_b - 1)$. Solutions to the inner problem then are sought in the form of the expansions

$$\begin{aligned} \alpha &\sim \alpha_0 + \beta^{-1}\alpha_1 + \beta^{-2}\alpha_2 + \dots \\ u_g &\sim u_0 + \beta^{-1}u_1 + \beta^{-2}u_2 + \dots \\ \Theta &\sim 1 + \beta^{-1}\theta_1 + \beta^{-2}\theta_2 + \dots \\ \Lambda &\sim \beta(\Lambda_0 + \beta^{-1}\Lambda_1 + \beta^{-2}\Lambda_2 + \dots) \end{aligned} \quad (103)$$

where the latter represents the appropriate expansion of the burning-rate eigenvalue of the basic solution corresponding to steady, planar burning. We note that because $p_g = p_g^b$ throughout the gas-liquid region, no such expansion is required for p_g and thus, provided that the assumption of gas-phase quasi steadiness remains valid, the development in this section is valid for both unconfined and confined geometries. Substituting these expansions and definitions into Eqs. (85), (86), and (88) and equating coefficients of like powers of β , the leading-order inner problem is derived in the following fashion. Beginning with Eq. (85), we obtain

$$\left(r - \hat{r} \frac{p_g^b}{T_b}\right) \frac{\partial x_r}{\partial t} \frac{\partial \alpha_0}{\partial \eta} + (1-r) \frac{\partial x_m}{\partial t} \frac{\partial \alpha_0}{\partial \eta} + \hat{r} \frac{p_g^b}{T_b} \frac{\partial}{\partial \eta} (\alpha_0 u_0) = 0 \quad (104)$$

Integrating this result and applying the matching conditions $\alpha_0 \rightarrow \alpha_s$ and $u_0 \rightarrow -(T_b/p_g^b - 1)\partial x_r/\partial t$ as $\eta \rightarrow -\infty$, we obtain an expression for u_0 as

$$u_0 = \frac{T_b(\alpha_0 - \alpha_s)}{p_g^b \hat{r} \alpha_0} \left[(\hat{r} - r) \frac{\partial x_r}{\partial t} - (1-r) \frac{\partial x_m}{\partial t} \right] - \left(\frac{T_b}{p_g^b} - 1 \right) \frac{\partial x_r}{\partial t} \quad (105)$$

From the matching conditions $\alpha_0 \rightarrow 1$ and $u_0 \rightarrow (T_b/p_g^b)g^{(0)} + \partial x_r/\partial t$ as $\eta \rightarrow +\infty$, an expression for the outer gas-velocity function $g^{(0)}(x_1, x_2, t)$ in the region $\zeta > 0$ then is found to be

$$g^{(0)}(x_1, x_2, t) = \frac{1 - \alpha_s}{\hat{r}} \left[(\hat{r} - r) \frac{\partial x_r}{\partial t} - (1-r) \frac{\partial x_m}{\partial t} \right] - \frac{\partial x_r}{\partial t} \quad (106)$$

which is needed in Eq. (98).

Utilizing Eq. (105) for the gas velocity, we find that the remaining part of the leading-order inner problem for α_0 and θ_1 is determined from Eqs. (86)

and (88) as

$$\left[r \frac{\partial x_r}{\partial t} + (1-r) \frac{\partial x_m}{\partial t} \right] \frac{\partial \alpha_0}{\partial \eta} = -r \Lambda_0 (1 - \alpha_0) e^{\theta_1} \quad (107)$$

$$\begin{aligned} & \left[r \frac{\partial x_r}{\partial t} + (1-r) \frac{\partial x_m}{\partial t} \right] [Q + (b - \hat{b})T_b] \frac{\partial \alpha_0}{\partial \eta} \\ & = (T_b - 1) G_r^2 \frac{\partial}{\partial \eta} \left\{ [l + (\hat{l} - l)\alpha_0] \frac{\partial \theta_1}{\partial \eta} \right\} \end{aligned} \quad (108)$$

subject to the matching conditions

$$\alpha_0 \rightarrow 1, \quad \theta_1 \sim \Theta^{(1)}|_{\zeta=0^+}, \quad \text{as } \eta \rightarrow +\infty \quad (109)$$

and

$$\alpha_0 \rightarrow \alpha_s, \quad \theta_1 \sim \Theta^{(1)}|_{\zeta=0^-} + \eta \frac{\partial \Theta^{(0)}}{\partial \zeta} \Big|_{\zeta=0^-} \quad \text{as } \eta \rightarrow -\infty \quad (110)$$

where, consistent with the definition of Θ , the $\Theta^{(i)}$ are defined as $\Theta^{(i)} = [T^{(i)} - 1]/[T_b - 1]$. We note that because spatial variations in the normal (ζ) direction are large relative to those in the transverse direction and those with respect to time, as reflected in transformation (102), the reaction-zone problem posed by Eqs. (107–110) is always quasisteady and quasiplanar, independent of the assumption of quasi steadiness for the outer gas-phase equations introduced earlier. Thus, integrating Eq. (108) using Eq. (109), and then transforming to α_0 as the independent coordinate according to Eq. (107), we obtain a first-order equation for θ_1 given by

$$r \Lambda_0 e^{\theta_1} \frac{\partial \theta_1}{\partial \alpha_0} = H_{m,r}^2 \frac{Q + (b - \hat{b})T_b}{T_b - 1} \cdot \frac{1}{l + (\hat{l} - l)\alpha_0} \quad (111)$$

where

$$H_{m,r} = -G_r^{-1} \left[r \frac{\partial x_r}{\partial t} + (1-r) \frac{\partial x_m}{\partial t} \right] \quad (112)$$

Equation (111) then can be integrated with respect to α_0 by using Eq. (110) to give

$$\begin{aligned} r \Lambda_0 e^{\theta_1} &= H_{m,r}^2 \frac{Q + (b - \hat{b})T_b}{T_b - 1} \\ &\cdot \begin{cases} (\hat{l} - l)^{-1} \{ \ell_n [l + (\hat{l} - l)\alpha_0] - \ell_n [l + (\hat{l} - l)\alpha_s] \}, & \hat{l} \neq l \\ l^{-1} (\alpha_0 - \alpha_s), & \hat{l} = l \end{cases} \end{aligned} \quad (113)$$

For the special case of steady, planar burning,

$$\frac{\partial x_m}{\partial t} = \frac{\partial x_r}{\partial t} = -1$$

and $\Theta^{(1)}|_{\zeta=0^+} = 0$ in the matching condition (109). Because Eq. (113) must hold for all solutions, these conditions imply result (67) for the leading-order coefficient Λ_0 in the last of expansions (103) for the burning-rate eigenvalue. Here, T_b was given in Eq. (46), a result that in fact applies to the more general nonsteady, nonplanar problem, given the assumption of a quasi-steady gas phase and the specification of p_g^b .

For the general nonsteady, nonplanar problem, Eqs. (67) and (113) and matching condition (109) yield the local temperature-dependent propagation law

$$H_{m,r} = \exp(\tfrac{1}{2}\Theta^1|_{\zeta=0^+}) \quad (114)$$

Equation (114) introduces the next-order outer variable Θ^1 into the analysis, but this additional complication, which is fundamental to this type of analysis,²² can be circumvented in an approximate fashion by truncating the inner expansion for Θ given in Eqs. (103) after the $\mathcal{O}(\beta^{-1})$ term, so that matching condition (109) implies that $\Theta^{(1)}|_{\zeta=0} = \beta(\Theta|_{\zeta=0} - 1)$. Reverting to the original outer temperature variable T , we find that Eq. (114) can be expressed as

$$-r \frac{\partial x_r}{\partial t} - (1-r) \frac{\partial x_m}{\partial t} = \left[1 + \left(\frac{\partial x_r}{\partial x_1} \right)^2 + \left(\frac{\partial x_r}{\partial x_2} \right)^2 \right]^{\frac{1}{2}} \exp \left(-\frac{\beta}{2} \cdot \frac{T_b - T|_{\zeta=0}}{T_b - 1} \right) \quad (115)$$

where we have used definition (112) for $H_{m,r}$. Substitution of Eq. (115) and expression (106) for g into Eq. (101) then leads to the result

$$\begin{aligned} \hat{l} \frac{\partial T}{\partial \zeta} \Big|_{\zeta=0^+} - [l + (\hat{l} - l)\alpha_s] \frac{\partial T}{\partial \zeta} \Big|_{\zeta=0^-} \\ + (1 - \alpha_s)(l - \hat{l})G_r^{-2} \left(\frac{\partial x_r}{\partial x_1} \frac{\partial T}{\partial x_1} + \frac{\partial x_r}{\partial x_2} \frac{\partial T}{\partial x_2} \right) \Big|_{\zeta=0} \\ = -(1 - \alpha_s)[Q + (b - \hat{b})T|_{\zeta=0}]G_r^{-1} \exp \left(-\frac{\beta}{2} \cdot \frac{T_b - T|_{\zeta=0}}{T_b - 1} \right) \end{aligned} \quad (116)$$

which, if we retain Eq. (115), replaces Eq. (101) as the required jump condition across the thin reaction zone. When the outer solution is approximated (truncated) by setting $T \approx T^{(0)}$ and $g \approx g^{(0)}$, the derived conditions (100) and (101), the propagation law (115), and expression (106) for the outer gas-velocity function g close the outer problem posed by Eqs. (89–92) and (93–98).

C. Summary of Asymptotic Model

The model derived in Secs. VI.A and VI.B constitutes an asymptotic formulation, valid for large activation energies, of deflagration in porous energetic materials for the case of a thermally expansive, quasi-steady gas phase. In this regime, the reaction zone becomes thin relative to the convective–diffusive structure of the deflagration wave, in such a way that both the jump condition across the reaction sheet and the propagation law that governs its motion display a sensitivity to local temperature perturbations. This sensitivity is of a finite, but exponential, form that is induced by the original Arrhenius nature of the reaction rate in the asymptotic limit described earlier. It is helpful to collect the preceding results

for future reference. Hence, the asymptotic model, expressed in nonorthogonal coordinates (x_1, x_2, ζ) attached to the reaction surface ($\zeta = 0$), is given by

$$\begin{aligned}
 (1 - \alpha_s) \left\{ \begin{matrix} 1 \\ rb \\ 0 \end{matrix} \right\} \frac{\partial T}{\partial t} - \left\{ \begin{matrix} 1 + \alpha_s(\hat{r}\hat{b} - 1) \\ rb + \alpha_s(\hat{r}\hat{b} - rb) \\ \hat{r}\hat{b} \end{matrix} \right\} \frac{\partial x_r}{\partial t} \frac{\partial T}{\partial \zeta} \\
 - (1 - \alpha_s) \left[(1 - r) \left\{ \begin{matrix} 0 \\ b \\ \hat{b} \end{matrix} \right\} \frac{\partial x_m}{\partial t} + (r - \hat{r}) \left\{ \begin{matrix} 0 \\ 0 \\ \hat{b} \end{matrix} \right\} \frac{\partial x_r}{\partial t} \right] \frac{\partial T}{\partial \zeta} \\
 = \left\{ \begin{matrix} 1 + \alpha_s(\hat{l} - 1) \\ l + \alpha_s(\hat{l} - l) \\ \hat{l} \end{matrix} \right\} \nabla_r^2 T - \hat{\pi} \alpha_s \left\{ \begin{matrix} 1 \\ 0 \\ 0 \end{matrix} \right\} \frac{\partial x_r}{\partial t} \frac{\partial p_g}{\partial \zeta}
 \end{aligned}$$

$$\zeta < -(x_r - x_m), \quad -(x_r - x_m) < \zeta < 0, \quad \zeta > 0 \quad (117)$$

$$T = p_g \left[1 + \frac{\kappa}{\alpha_s} \frac{\partial p_g}{\partial \zeta} \left(\frac{\partial x_r}{\partial t} \right)^{-1} \right], \quad \zeta < -(x_r - x_m) \quad (118)$$

$$-r \frac{\partial x_r}{\partial t} - (1 - r) \frac{\partial x_m}{\partial t} = G_r \exp \left(-\frac{\beta}{2} \cdot \frac{T_b - T|_{\zeta=0}}{T_b - 1} \right) \quad (119)$$

subject to

$$T \rightarrow p_g \rightarrow 1 \quad \text{as} \quad \zeta \rightarrow -\infty, \quad T \rightarrow T_b \quad \text{as} \quad \zeta \rightarrow +\infty \quad (120)$$

$$T = T_m \quad \text{at} \quad \zeta = -(x_r - x_m) \quad p_g = p_g^b \quad \text{for} \quad \zeta \geq -(x_r - x_m) \quad (121)$$

$$\begin{aligned}
 \left(-\frac{\partial x_m}{\partial x_1}, -\frac{\partial x_m}{\partial x_2}, 1 \right) \cdot \{ [l + \alpha_s(\hat{l} - l)] \nabla_r T|_{\zeta=-(x_r-x_m)^+} \\
 - [1 + \alpha_s(\hat{l} - 1)] \nabla_r T|_{\zeta=-(x_r-x_m)^-} \} = \frac{\partial x_m}{\partial t} (1 - \alpha_s) [\gamma_s + (1 - b)T_m]
 \end{aligned} \quad (122)$$

$$T|_{\zeta=0^-} = T|_{\zeta=0^+} \quad (123)$$

$$\begin{aligned}
 \hat{l} \frac{\partial T}{\partial \zeta} \Big|_{\zeta=0^+} - [l + (\hat{l} - l)\alpha_s] \frac{\partial T}{\partial \zeta} \Big|_{\zeta=0^-} \\
 + (1 - \alpha_s)(l - \hat{l}) G_r^{-2} \left(\frac{\partial x_r}{\partial x_1} \frac{\partial T}{\partial x_1} + \frac{\partial x_r}{\partial x_2} \frac{\partial T}{\partial x_2} \right) \Big|_{\zeta=0} \\
 = -(1 - \alpha_s)[Q + (b - \hat{b})T|_{\zeta=0}] G_r^{-1} \exp \left(-\frac{\beta}{2} \cdot \frac{T_b - T|_{\zeta=0}}{T_b - 1} \right) \quad (124)
 \end{aligned}$$

where the dot in Eq. (122) represents the scalar product of the vector on the left with the operator ∇_r given below Eq. (92), and where expressions for $\nabla_r^2 = \nabla_r \cdot \nabla_r$ and G_r are given in and below Eq. (99). Equations (117–124) constitute a closed boundary-value problem for x_r , x_m , T , and p_g , an equation for the latter being obtained from the combination of Eqs. (117) and (118) in the region $\zeta < -(x_r - x_m)$, and can be solved subject to arbitrary initial conditions. In many applications, however, one is concerned primarily with the long-time basic solution corresponding to a steady, planar deflagration, as described by the formulation derived in the preceding sections, and its stability. We also note that the porosity α has been reduced to a simple step function by the asymptotic formulation and that other quantities of interest, such as the gas velocity (94), are given in terms of x_r , x_m , p_g , and T according to the formulas derived previously.

VII. Basic Solution and Its Linear Stability

As an illustration of the usefulness of the asymptotic model derived above, we consider the stability of a steady, planar deflagration in the unconfined limit $p_g^b = 1$, with $\kappa \rightarrow \infty$ which implies that $p_g = 1$ throughout. A basic solution of the model (117), (119–124) in that case, corresponding to a steadily propagating planar deflagration and denoted by a zero superscript, is given by the solution constructed in Sec. IV, namely,

$$x_m^0 = -t, \quad x_r^0 = x_m^0 + \frac{l(1 - \alpha_s) + \hat{l}\alpha_s}{b(1 - \alpha_s) + \hat{r}\hat{b}\alpha_s} \ell_n \left(\frac{T_b - B}{T_m - B} \right) \quad (125)$$

$$T^0(\zeta) = \begin{cases} 1 + (T_m - 1) \exp \left[\frac{1 + \alpha_s(\hat{r}\hat{b} - 1)}{1 + \alpha_s(\hat{l} - 1)} (\zeta + x_r^0 - x_m^0) \right] & \zeta < -(x_r^0 - x_m^0) \\ B + (T_m - B) \exp \left[\frac{b(1 - \alpha_s) + \hat{r}\hat{b}\alpha_s}{l(1 - \alpha_s) + \hat{l}\alpha_s} (\zeta + x_r^0 - x_m^0) \right] & -(x_r^0 - x_m^0) < \zeta < 0 \\ T_b = \frac{(1 - \alpha_s)(Q + 1 + \gamma_s) + \hat{r}\hat{b}\alpha_s}{\hat{b}[1 + \alpha_s(\hat{r} - 1)]}, & \zeta > 0 \end{cases} \quad (126)$$

where

$$B \equiv \frac{(1 - \alpha_s)(1 + \gamma_s) + \hat{r}\hat{b}\alpha_s}{b(1 - \alpha_s) + \hat{r}\hat{b}\alpha_s} \quad (127)$$

and, from Eqs. (94) and (106), the steady, planar gas-phase velocity u_g^0 is given by

$$u_g^0 = \begin{cases} T - 1, & \zeta < 0 \\ \hat{r}^{-1}[(1 - \hat{r})(1 - \alpha_s) + (T_b - 1)(1 - \alpha_s + \alpha_s\hat{r})], & \zeta > 0 \end{cases} \quad (128)$$

The burning-rate eigenvalue and propagation speed are given by Eqs. (67), (69), and (70), but are not needed explicitly in the stability analysis that follows. Here,

we are interested particularly in the effects of the porosity α_s , in the realistic limit of small gas-to-solid density ratio \hat{r} , on the stability of steady, planar deflagration given by the basic solution (125–128). As shown below, the value of the burned temperature plays a critical role in determining the corresponding neutral stability boundary, in part because the propagation velocity is exponentially sensitive to T_b in the large activation-energy regime. From the last line of Eqs. (128), T_b has the behavior

$$T_b = (1/\hat{b})\{Q + 1 + \gamma_s - \hat{r}[\alpha_s/(1 - \alpha_s)](Q + 1 + \gamma_s - \hat{b}) + \mathcal{O}(\hat{r}^2)\} \quad (129)$$

for $\hat{r} \ll 1$. Because the nondimensional heat release Q typically is significantly larger than unity, whereas the specific heat capacity ratio \hat{b} generally is not significantly larger than unity, the final burned temperature, and hence the steady mass burning rate, decreases with increasing porosity and increasing gas density in the unconfined limit. However, as discussed in Sec. IV (Fig. 3), the opposite trend is predicted for the confined problem once the overpressure achieves a critical value.

When the derived asymptotic model is used, the linear stability analysis of the basic solution (125–128) follows a standard approach.⁹ Briefly, perturbation variables $\phi_m(x_1, x_2, t)$, $\phi_r(x_1, x_2, t)$, and $\tau(x_1, x_2, \zeta, t)$ are defined according to

$$x_m = x_m^0 + \phi_m, \quad x_r = x_r^0 + \phi_r, \quad T = T^0(\zeta) + \tau + \phi_r \frac{dT^0}{d\zeta} \quad (130)$$

These definitions are substituted into the asymptotic model defined by Eqs. (117), (119–124), and the equations are linearized with respect to the perturbation variables to obtain a linear problem for ϕ_m , ϕ_r , and τ given by

$$\begin{aligned} (1 - \alpha_s) \frac{\partial \tau}{\partial t} + [1 + \alpha_s(\hat{r}\hat{b} - 1)] \frac{\partial \tau}{\partial \zeta} - \hat{r}\hat{b}\alpha_s \frac{\partial \phi_r}{\partial t} \frac{dT^0}{d\zeta} \\ = [1 + \alpha_s(\hat{l} - 1)] \left(\frac{\partial^2 \tau}{\partial x_1^2} + \frac{\partial^2 \tau}{\partial x_2^2} + \frac{\partial^2 \tau}{\partial \zeta^2} \right) \quad \zeta < -(x_r^0 - x_m^0) \end{aligned} \quad (131)$$

$$\begin{aligned} rb(1 - \alpha_s) \frac{\partial \tau}{\partial t} + [b + \alpha_s(\hat{r}\hat{b} - b)] \frac{\partial \tau}{\partial \zeta} \\ - \left[\hat{r}\hat{b}\alpha_s \frac{\partial \phi_r}{\partial t} + b(1 - r)(1 - \alpha_s) \frac{\partial \phi_m}{\partial t} \right] \frac{dT^0}{d\zeta} \\ = [l + \alpha_s(\hat{l} - l)] \left(\frac{\partial^2 \tau}{\partial x_1^2} + \frac{\partial^2 \tau}{\partial x_2^2} + \frac{\partial^2 \tau}{\partial \zeta^2} \right), \quad -(x_r^0 - x_m^0) < \zeta < 0 \end{aligned} \quad (132)$$

$$\hat{b}[1 + \alpha_s(\hat{r} - 1)] \frac{\partial \tau}{\partial \zeta} = \hat{l} \left(\frac{\partial^2 \tau}{\partial x_1^2} + \frac{\partial^2 \tau}{\partial x_2^2} + \frac{\partial^2 \tau}{\partial \zeta^2} \right), \quad \zeta > 0 \quad (133)$$

$$-r \frac{\partial \phi_r}{\partial t} - (1 - r) \frac{\partial \phi_m}{\partial t} = \frac{\beta}{2(T_b - 1)} \tau \Big|_{\zeta=0^+} \quad (134)$$

subject to

$$\tau \rightarrow 0 \quad \text{as} \quad \zeta \rightarrow \pm\infty \quad (135)$$

$$\left(\tau + \phi_m \frac{dT^0}{d\zeta} \right) \Big|_{\zeta = -(x_r^0 - x_m^0)^-} = \left(\tau + \phi_m \frac{dT^0}{d\zeta} \right) \Big|_{\zeta = -(x_r^0 - x_m^0)^+} = 0 \quad (136)$$

$$\begin{aligned} [l + \alpha_s(\hat{l} - l)] \left(\frac{\partial \tau}{\partial \zeta} + \phi_m \frac{d^2 T^0}{d\zeta^2} \right) \Big|_{\zeta = -(x_r^0 - x_m^0)^+} \\ - [1 + \alpha_s(\hat{l} - 1)] \left(\frac{\partial \tau}{\partial \zeta} + \phi_m \frac{d^2 T^0}{d\zeta^2} \right) \Big|_{\zeta = -(x_r^0 - x_m^0)^-} \\ = -\frac{\partial \phi_m}{\partial t} (1 - \alpha_s) [-\gamma_s + (b - 1)T_m] \end{aligned} \quad (137)$$

$$\tau|_{\zeta=0^+} = \left(\tau + \phi_r \frac{dT^0}{d\zeta} \right) \Big|_{\zeta=0^-} \quad (138)$$

$$\begin{aligned} \hat{l} \frac{\partial \tau}{\partial \zeta} \Big|_{\zeta=0^+} - [l + \alpha_s(\hat{l} - l)] \left(\frac{\partial \tau}{\partial \zeta} + \phi_r \frac{d^2 T^0}{d\zeta^2} \right) \Big|_{\zeta=0^-} \\ = -\frac{1}{2} (1 - \alpha_s) \left[\frac{\beta Q}{T_b - 1} + (b - \hat{b}) \left(2 + \frac{\beta T_b}{T_b - 1} \right) \right] \tau \Big|_{\zeta=0^+} \end{aligned} \quad (139)$$

where we have used the fact that $dT^0/d\zeta = 0$ for $\zeta > 0$.

From Eqs. (130), steady, planar burning clearly corresponds to the trivial solution $\phi_m = \phi_r = \tau = 0$, whereas nontrivial solutions to the linear stability problem are sought in the form

$$\begin{Bmatrix} \phi_m \\ \phi_r \\ \tau \end{Bmatrix} = \exp[i(\omega t \pm k_1 x_1 \pm k_2 x_2)] \begin{Bmatrix} c_m \\ 1 \\ \sigma(\zeta) \end{Bmatrix} \quad (140)$$

which has been normalized by setting the coefficient of ϕ_r equal to unity. Equations (131–133) and Eq. (135) then determine the function $\sigma(\zeta)$ as

$$\sigma(\zeta) = \begin{cases} c_1 e^{p\zeta} + i\omega(i\omega\hat{b}_1 + k^2)^{-1} b_0 b_1 (T_m - 1) e^{b_1(\zeta + x_r^0 - x_m^0)} & \zeta < -(x_r^0 - x_m^0) \\ c_2 e^{q-\zeta} + c_3 e^{q+\zeta} + i\omega(i\omega\hat{b}_3 + k^2)^{-1} (\hat{b}_0 - b_4 c_m) b_2 (T_b - B) e^{b_2 \zeta} & -(x_r^0 - x_m^0) < \zeta < 0 \\ c_4 e^{\hat{s}\zeta}, & \zeta > 0 \end{cases} \quad (141)$$

where the c_i are constants of integration, and the other quantities that appear in

Eqs. (141) are given by

$$\begin{aligned}
 b_0 &= \frac{\hat{r}\hat{b}\alpha_s}{1 + \alpha_s(\hat{l} - 1)}, & \hat{b}_0 &= \frac{\hat{r}\hat{b}\alpha_s}{l + \alpha_s(\hat{l} - l)} \\
 b_1 &= \frac{1 + \alpha_s(\hat{r}\hat{b} - 1)}{1 + \alpha_s(\hat{l} - 1)}, & \hat{b}_1 &= \frac{1 - \alpha_s}{1 + \alpha_s(\hat{l} - 1)} \\
 b_2 &= \frac{b + \alpha_s(\hat{r}\hat{b} - b)}{l + \alpha_s(\hat{l} - l)}, & \hat{b}_3 &= \frac{rb(1 - \alpha_s)}{l + \alpha_s(\hat{l} - l)} \\
 b_4 &= \frac{b(r - 1)(1 - \alpha_s)}{l + \alpha_s(\hat{l} - l)}, & b_5 &= \frac{\hat{b}}{\hat{l}}[1 + \alpha_s(\hat{r} - 1)]
 \end{aligned} \tag{142}$$

and

$$\begin{aligned}
 p &= \frac{1}{2}[b_1 + \sqrt{b_1^2 + 4(i\omega\hat{b}_1 + k^2)}] \\
 q_{\pm} &= \frac{1}{2}[b_2 \pm \sqrt{b_2^2 + 4(i\omega\hat{b}_3 + k^2)}] \\
 \hat{s} &= \frac{1}{2}[b_5 - \sqrt{b_5^2 + 4k^2}]
 \end{aligned} \tag{143}$$

The remaining conditions embodied in Eqs. (134) and Eqs. (136–139) serve to determine the c_i and the dispersion relation $\omega(k)$, where $k = \sqrt{(k_1^2 + k_2^2)}$.

VIII. Analysis of Dispersion Relation

The linear stability analysis is completed here for a representative case in which $r = b = l = 1$, corresponding to the neglect of differences between the physical properties of the solid and liquid phases of the material. This restriction is introduced to reduce algebraic complexity, but it clearly can be relaxed if there is interest in other values of these parameters. As a result, $b_2 = b_1$, $\hat{b}_0 = b_0$, $\hat{b}_3 = \hat{b}_1$ (which implies that $q_+ = p$), and $b_4 = 0$. Then, from Eq. (133) and Eqs. (136–138), the coefficients in Eqs. (141) are determined as

$$\begin{aligned}
 c_1 &= -(T_m - 1)b_1 \exp[q_+(x_r^0 - x_m^0)] \left[c_m + \frac{i\omega b_0}{i\omega\hat{b}_1 + k^2} \right] \\
 c_4 &= -2i\omega \frac{T_b - 1}{\beta} \\
 c_2 &= (B - 1)b_1 \frac{e^{q_-(x_r^0 - x_m^0)}}{q_- - q_+} \left[c_m(q_- + i\omega) + \frac{i\omega b_0 q_-}{i\omega\hat{b}_1 + k^2} \right] \\
 c_3 &= -b_1 \frac{e^{q_+(x_r^0 - x_m^0)}}{q_- - q_+} \left\{ c_m[(B - 1)(q_+ + i\omega) + (T_m - 1)(q_- - q_+)] \right. \\
 &\quad \left. + \frac{i\omega b_0}{i\omega\hat{b}_1 + k^2} [(T_m - 1)(q_- - q_+) + q_+(B - 1)] \right\}
 \end{aligned} \tag{144}$$

where $x_r^0 - x_m^0$ was given by the second of Eqs. (125) and

$$c_m = \frac{1}{\mathcal{D}} \left[(T_b - 1) \left(b_1 + \frac{2i\omega}{\beta} \right) - (B - 1)b_1 + (T_b - B) \frac{i\omega b_0 b_1}{i\omega \hat{b}_1 + k^2} \right] e^{-q_+(x_r^0 - x_m^0)} \\ + \frac{i\omega b_0 b_1}{\mathcal{D}(i\omega \hat{b}_1 + k^2)} \left[q_-(B - 1) \frac{\exp[(q_- - q_+)(x_r^0 - x_m^0)] - 1}{q_- - q_+} - (T_m - B) \right] \quad (145)$$

$$\mathcal{D} = b_1(T_m - 1) - (B - 1)b_1(q_- - q_+)^{-1} \\ \times [(q_- + i\omega)\exp[(q_- - q_+)(x_r^0 - x_m^0)] - (q_+ + i\omega)]$$

We remark that, in light of the above simplification, all effects due to melting of the solid are embodied in the parameter γ_s . In the limit that the heat of melting becomes negligible ($\gamma_s \rightarrow 0$), we have $B \rightarrow 1$ and hence $c_2 \rightarrow 0$. In that case, the functional form of the temperature function $\sigma(\zeta)$ is the same on either side of $\zeta = -(x_r^0 - x_m^0)$, and the melting surface becomes effectively invisible.

An equation for the dispersion relation $\omega(k)$ now is obtained by substituting the results given thus far into Eq. (139). The result is, in terms of the coefficients defined earlier,

$$\hat{l}\hat{s}c_4 - (1 - \alpha_s + \hat{l}\alpha_s)[q_-c_2 + q_+c_3 + b_1^2(T_b - B)] \\ = -(1 - \alpha_s) \left[\beta \frac{Q + (1 - \hat{b})T_b}{2(T_b - 1)} + 1 - \hat{b} \right] c_4 \quad (146)$$

where s and q_{\pm} depend on $i\omega$ and k according to their definitions given earlier. This is a fairly complicated dispersion relation, but typically, the gas density is small compared with that of the condensed phases, the thermal conductivity of the gas is correspondingly small, and the heat of melting is small compared with the thermal enthalpy. For these reasons, the gas-to-solid and gas-to-liquid density ratio \hat{r} is treated as a small parameter, and the scalings

$$\hat{l} = \hat{l}^* \hat{r}, \quad \gamma_s = \gamma_s^* \hat{r} \quad (147)$$

are introduced for the corresponding conductivity ratio \hat{l} and the nondimensional heat of melting γ_s , where the scaled values \hat{l}^* and γ_s^* are considered to be of order unity. The dispersion relation $\omega(k)$ then is expanded as

$$\omega \sim \omega_0 + \omega_1 \hat{r} + \omega_2 \hat{r}^2 + \dots \quad (148)$$

Associated expansions of all quantities in Eq. (146) that depend on these small parameters then are performed, keeping the overall heat release Q_0 with respect to the solid, $Q_0 = Q + \gamma_s$, a fixed parameter. Under this constraint, there is an expansion of the burned temperature T_b given by

$$T_b \sim T_b^0 + \hat{r}T_b^1 + \dots, \quad T_b^0 = (Q_0 + 1)/\hat{b} \\ T_b^1 = -[\alpha_s/(1 - \alpha_s)](T_b^0 - 1) \quad (149)$$

In addition, the expansions

$$B - 1 \sim \gamma_s^* \hat{r}, \quad \hat{l} \hat{s} \sim \mathcal{O}(\hat{r}^2) \quad (150)$$

$$b_1 \sim 1 + \frac{\alpha_s}{1 - \alpha_s} (\hat{b} - \hat{l}^*) \hat{r} + \dots, \quad \hat{b}_1 \sim 1 - \frac{\alpha_s}{1 - \alpha_s} \hat{l}^* \hat{r} + \dots$$

and

$$q_{\pm} \sim q_{\pm}^0 + q_{\pm}^1 \hat{r} + \dots, \quad q_{\pm}^0 = \frac{1}{2} [1 \pm \sqrt{1 + 4(i\omega_0 + k^2)}] \quad (151)$$

$$q_{\pm}^1 = \frac{1}{2} \cdot \frac{\alpha_s}{1 - \alpha_s} \left[\hat{b} - 2\hat{l}^* q_{\pm}^0 \pm \frac{\hat{b} + \hat{l}^* (2i\omega_0 + 4k^2)}{2q_{\pm}^0 - 1} \right] \pm \frac{i\omega_1}{2q_{\pm}^0 - 1}$$

apply. Substitution of these expansions into Eq. (146) determines the equation for the leading-order dispersion relation $\omega_0(k)$ to be $(2i\omega_0 + \beta)(1 - q_+^0) + i\omega(\beta - 2\hat{b}) = 0$, which, after some manipulation, can be expressed as

$$4(i\omega_0)^3 + (i\omega_0)^2 [4k^2 + 4\hat{b}(1 - \hat{b}) + 2(1 + 2\hat{b})\beta - \beta^2] \\ + 2i\omega_0\beta(\hat{b} + 2k^2) + \beta^2 k^2 = 0 \quad (152)$$

This dispersion relation is identical to the result obtained when a constant density for the gas phase was assumed.⁸ It therefore is concluded that in the absence of confinement and in the first approximation for small values of \hat{r} , the gas-phase thermal expansion has no effect on the stability behavior, a result that might be anticipated on the basis of the small contribution of the mass fraction of gas in this limit.

The neutral stability boundary, corresponding to neither growth nor decay of the infinitesimal perturbations of the form given by Eqs. (140), can be displayed in a plane of the Zel'dovich number β , defined by the last of Eqs. (58), and the nondimensional wave number k . This boundary is obtained by setting the real part of the complex growth rate $i\omega$ to zero. By setting the real and imaginary parts of Eq. (152) separately to zero, the neutral stability boundary at leading order, $\beta_0(k)$, can be obtained as the positive root of the quadratic

$$(\hat{b} + 2k^2)\beta_0^2 + 2[k^2 - (1 + 2\hat{b})(\hat{b} + 2k^2)]\beta_0 - 4(\hat{b} + 2k^2)[\hat{b}(1 - \hat{b}) + k^2] = 0 \quad (153)$$

and the corresponding leading-order frequency $\omega_0(k)$ of the neutral disturbance is

$$\omega_0^2 = \frac{1}{2}\beta_0(\hat{b} + 2k^2) \quad (154)$$

Because $\omega_0 \neq 0$, the stability boundary is of the pulsating type, like that obtained for solid-propellant combustion in the absence of two-phase flow^{17,20,21} (such intrinsic pulsating instabilities also are observable experimentally²⁷). This leading-order stability boundary was obtained and discussed previously⁸ and, for completeness, has been included in Fig. 7 (solid curves), which also exhibits the next-order approximation for a modified Zel'dovich number $\beta^0(k)$ (chain-dash and chain-dot curves) as discussed later. Several curves, corresponding to different values of \hat{b} , are shown, indicating that decreasing values of \hat{b} are destabilizing, which suggests that diminished thermal influences of the gas phase (which convects heat away from the reaction zone in the direction of the burned region) is less able to damp the

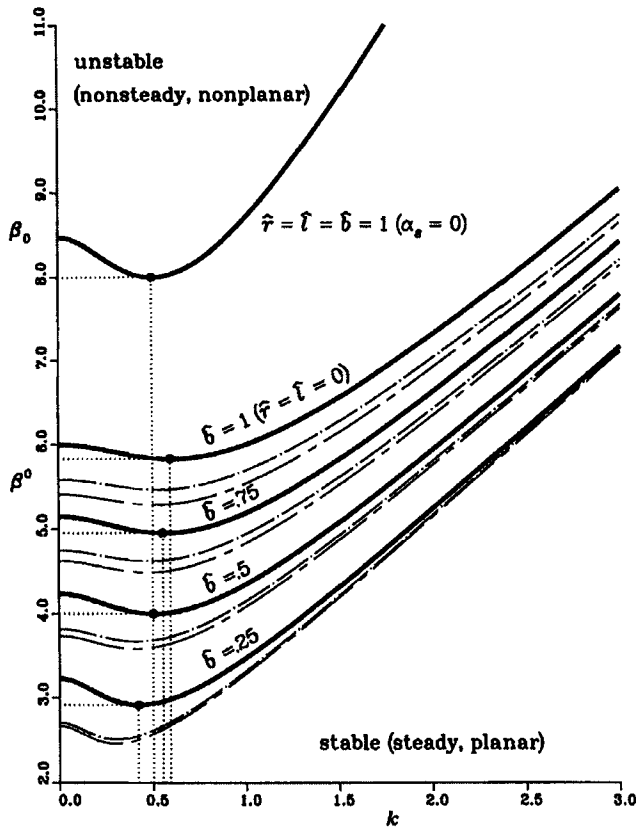


Fig. 7 Leading-order neutral stability boundaries $\beta_0(k)$ (—) for the unconfined problem as a function of wave number for several values of the gas-to-liquid or gas-to-solid heat-capacity ratio \hat{b} . Also shown is the corresponding neutral stability boundary (top curve) for the strictly solid combustion synthesis problem; the remaining curves, which are first-order corrections to the leading-order boundaries, are described in the text.

known thermal/diffusive instability of the condensed phase.²⁸ Indeed, we also show for reference the neutral stability boundary corresponding to strictly condensed-phase combustion (combustion synthesis), which can be recovered from the present analysis by setting $\hat{\tau} = \hat{\ell} = \hat{b} = 1$ and $\alpha_s = 0$ in Eq. (146). This stability boundary, which is determined (in the absence of melting) from the dispersion relation

$$4(i\omega)^3 + (i\omega)^2[1 + 4k^2 + 2\beta - \frac{1}{4}\beta^2] + \frac{1}{2}(i\omega)(1 + 4k^2) + \frac{1}{4}\beta^2k^2 = 0 \quad (155)$$

is qualitatively similar to the stability boundaries obtained from Eq. (152), reflecting the fact that this particular type of instability phenomenon arises from combustion of the condensed phase, with the presence of the gas having a secondary, perturbative effect, as discussed later. The fact that the minimum value of $\beta_0(k)$, given by $\beta_0 = 1 + 2\hat{b} + \sqrt{(8\hat{b})}$, occurs at a nonzero value of $k = (\hat{b}/8)^{1/4} > 0$ (as compared with $\beta_0 = 1 + 2\hat{b} + \sqrt{(1 + 8\hat{b})}$ at $k = 0$) suggests that nonplanar, cellular patterns will be observed at the transition to nonsteady burning as the

stability boundary is crossed. Because the leading-order results for the neutral stability boundary are independent of the porosity α_s , they are also the same as those obtained previously for a nonporous case in which two-phase-flow effects were confined to the liquid-gas region,¹⁴ as well as for a different model in which two-phase-flow effects were suppressed in favor of an intrusive gas flame adjacent to a pyrolyzing solid surface.²⁰ Consequently, these same or very similar results are likely to occur in a variety of different energetic systems.

Because the leading-order results regarding the neutral stability boundary are independent of α_s , the leading-order effects of nonzero porosity are determined by proceeding to the next order with respect to the ratios of gas density and conductivity to those of the condensed phases. With the neutral stability boundary thus represented as

$$\beta \sim \beta_0 + \beta_1 \hat{r} + \dots \quad (156)$$

an expression for $\omega_1(k)$, introduced in Eq. (148), can be obtained from the dispersion relation at $\mathcal{O}(\hat{r})$ given by

$$\begin{aligned} i\omega_1 \left[\beta_0 + 2(1 - \hat{b} - q_+^0) - \frac{2i\omega_0 + \beta_0}{2q_+^0 - 1} \right] + \frac{2i\omega_0}{\beta_0} (q_+^0 - 1 + \hat{b})\beta_1 \\ = \frac{\alpha_s}{1 - \alpha_s} \left\{ \beta_0(1 - q_+^0)\hat{l}^* + \left[\frac{1}{2}\beta_0(2q_+^0 - 3) - i\omega_0(\beta_0 - 1) \right. \right. \\ \left. \left. + \frac{i\omega_0\beta_0(q_+^0 + 1)}{i\omega_0 + k^2} \right] \hat{b} + \frac{1}{2} \cdot \frac{2i\omega_0 + \beta_0}{2q_+^0 - 1} [\hat{b} + (2i\omega_0 + 4k^2)\hat{l}^*] \right\} \\ - \gamma_s^* \left\{ (T_b^0 - 1)^{-1} \left[\beta_0(i\omega_0 - q_-^0) - \frac{q_+^0}{\hat{b}}(2i\omega_0 + \beta_0) \right] \right. \\ \left. + (T_m - 1)^{-1}(i\omega_0 + q_-^0)(2i\omega_0 + \beta_0) \exp \left[(q_-^0 - q_+^0)\ell_n \left(\frac{T_b^0 - 1}{T_m - 1} \right) \right] \right\} \quad (157) \end{aligned}$$

where β_0 and ω_0 were given by Eqs. (153) and (154), respectively. It is observed that Eq. (157) differs from the corresponding result⁸ that assumed a constant gas density, and thus modifications in the neutral stability boundary due to thermal expansion of the gas, as well as those due to two-phase flow, appear at this order in the analysis. Setting $Re(i\omega_1)$ to zero and equating real and imaginary parts of Eq. (157) separately to zero then gives a coupled system of linear equations for β_1 and ω_1 that can be solved and analyzed.⁹ These results are summarized later.

It can be shown that the $\mathcal{O}(\hat{r})$ perturbation coefficient $\beta_1(k)$ with respect to the leading-order stability boundary $\beta_0(k)$ determined by Eq. (153) can be shown to consist of the sum of three contributions arising from the effects of nonzero density and thermal conductivity ratios \hat{r} and \hat{l} , respectively, and the effects of a nonzero heat of melting. In particular,

$$\beta_1(k) = [\alpha_s/(1 - \alpha_s)][\hat{\beta}_r(k) + \hat{l}^*\hat{\beta}_l(k)] + \gamma_s^*\hat{\beta}_\gamma(k) \quad (158)$$

where it is readily seen that for $\gamma_s^* = 0$, the solution for the perturbation coefficient β_1 is proportional to the factor $\alpha_s(1 - \alpha_s)^{-1}$. Positive values of the coefficients $\hat{\beta}_r$, $\hat{\beta}_l$, and $\hat{\beta}_\gamma$ represent an upward, stabilizing shift in the neutral stability boundary from its leading-order position shown in Fig. 2, whereas negative values represent

a downward, destabilizing shift. The magnitude of these perturbations in the stability boundary, whether positive or negative, is seen from Eq. (158) to increase with increasing values of the porosity α_s . In addition, there is a wave-number dependence for each effect, with nonzero values of \hat{l} being destabilizing for small wave numbers and stabilizing for large wave numbers. The effect of nonzero values of \hat{r} , although generally destabilizing, exhibits the opposite trend (increasing destabilization for increasing wave numbers), consistent with the physical expectation that the gas-to-solid or gas-to-liquid thermal diffusivity ratio of the gas to that of the condensed phases, which is equal to $\hat{l}/\hat{b}\hat{r}$, should play a key role in determining the stabilizing or destabilizing influence of the gas phase.

For nonzero values of γ_s^* , the third component $\gamma_s^*\hat{\beta}_\gamma$ to the solution of β_1 provides a correction that is independent of α_s and, assuming an endothermic heat of melting ($\gamma_s^* < 0$), corresponds to the effect of increasing the amount of heat released in the reaction zone by the amount of heat absorbed by the liquid that accompanies the phase change in the preheat region. The effect of melting can be stabilizing or destabilizing,⁸ although in the typical case of endothermic melting, the resulting correction in the stability boundary tends to be destabilizing, especially for smaller, more typical values of \hat{b} and larger wave numbers. This trend can be attributed to the fact that the release of the heat of melting by the liquid-to-gas reaction serves to enhance the heat release in the highly temperature-sensitive reaction zone, and that for $\hat{b} < 1$, a greater proportion of this energy is absorbed by the reactive condensed phase relative to that absorbed by the nonreactive gas. A similar destabilizing result was predicted for low-temperature melting in gasless systems,²⁹ although this effect diminishes and then reverses as the melting temperature increases such that melting occurs within the reaction zone itself.²⁸ Here, too, the effect of increasing T_m (while keeping T_b^0 and all other parameters fixed) is found to be stabilizing, particularly for small-wave-number disturbances.

There is a final $\mathcal{O}(\hat{r})$ effect to be accounted for that is due to the change in the stability parameter β itself that accompanies any variation in the density ratio \hat{r} . Although thus far we have adhered to a conventional definition of the Zel'dovich number as defined by the last of Eqs. (58), this parameter itself varies with \hat{r} through changes in the burned temperature T_b . In particular, for small values of \hat{r} , T_b decreases as \hat{r} increases according to Eq. (149), thereby increasing the effective activation energy. Defining a modified Zel'dovich number β^0 that does not vary with \hat{r} according to

$$\beta^0 = (1 - 1/T_b^0)N^0, \quad N^0 \equiv \frac{\tilde{E}_l}{\tilde{R}^0 T_b^0} \quad (159)$$

where T_b^0 is the leading-order burned temperature defined in Eqs. (149), we calculate an additional correction $-\alpha_s(1 - \alpha_s)^{-1}\hat{\beta}_1\hat{r}$ in the position of the neutral stability boundary with respect to the new parameter β^0 , where $\hat{\beta}_1 = (1 - 2/T_b^0)\beta_0$, and $\beta_0(k)$ is the leading-order neutral stability boundary determined from Eq. (153). That is, analogous to Eqs. (156) and (158),

$$\beta^0 \sim \beta_0 + \left[\frac{\alpha_s}{1 - \alpha_s} \left(\hat{\beta}_r + \hat{\beta}_l\hat{l}^* - \frac{T_b^0 - 2}{T_b^0} \beta_0 \right) + \hat{\beta}_\gamma\gamma_s^* \right] \hat{r} + \dots \quad (160)$$

where $\hat{\beta}_r(k)$, $\hat{\beta}_l(k)$, and $\hat{\beta}_\gamma(k)$ are the same coefficients as those introduced in

Eq. (158). The two-term approximation of β^0 given by Eq. (160) is shown in Fig. 7 (chain-dash curves) for the same values of \hat{b} as the leading-order approximation β_0 and for typical values of the remaining parameters ($\alpha_s = 0.3$, $\gamma_s = 0$, $\hat{r} = 0.1$, $\hat{l}^* = 1.0$, $T_b^0 = 6.0$). Also shown in that figure, for these same parameter values, are the corresponding (chain-dot) curves for the case of a constant gas-phase density,⁸ which, while still indicating an overall destabilizing effect due to gas-phase influences, nonetheless lie above the modified stability boundaries that are obtained when thermal expansion of the gas is taken into account. However, because the constant-density analysis did not assume gas-phase quasisteadiness, it can be argued⁹ that at least part of this difference likely is attributable to the assumption of an instantaneous gas-phase response, because the latter may result in some overstatement of this destabilizing effect. From Eq. (160), it is clear that because the linearized correction to the leading-order result, due to nonzero values of the density and thermal conductivity ratios \hat{r} and \hat{l} , is proportional to $\alpha_s(1 - \alpha_s)^{-1}$, whereas the coefficient $\hat{\beta}_\gamma$ is independent of α_s , the effect of an increase in porosity is destabilizing with respect to steady, planar deflagration, and that this effect is enhanced by gas-phase thermal expansion.

IX. Conclusions

This chapter has summarized recent advances in the application of multiphase-flow theory to the study of deflagrations in porous energetic materials such as degraded nitramine propellants. The focus has been on the investigation of the effects of nonzero porosity and two-phase flow on the structure and stability of steady, planar deflagration. This was facilitated by the application of activation-energy asymptotics and the derivation of an appropriate asymptotic model for the general case of nonsteady, multidimensional propagation in both unconfined and confined materials. This derivation proceeded under the assumptions of a thermally expansive, quasi-steady gas phase, where the latter allowed the reduction of the more general confined problem to an analogous freely propagating combustion wave with a specified pressure difference, or overpressure, between the burned and unburned states.

For the case of steady, planar propagation, it was demonstrated that the existence of an overpressure in the burned-gas region has a significant effect on the burned temperature, gas-velocity profile, and the burning rate of the material. In particular, because of the pressure-driven permeation of the burned gases into the unburned material, a preheating effect is produced. Consequently, the temperature increases linearly, and hence the burning rate initially increases exponentially, with increases in the overpressure, followed by a more modest algebraic pressure dependence of the burning rate that is suggestive of Ap^n -type laws. This rapid increase in the burning rate, an explicit formula for which was derived, is in qualitative agreement with most experimental results on confined materials, which tend to show a sudden and rapid increase in the deflagration speed that generally is associated with the onset of convective burning. Thus, in contrast to the case of an unconfined deflagration, for which the gas flow relative to the condensed material is always in the downstream direction, the flow of gas in the unburned solid is, except in the limit of small overpressures, always directed in the upstream direction, providing an important mechanism for preheating the unburned material and allowing the transition to a convection-enhanced mode of burning.

Because the steadily propagating, planar combustion wave represents a basic solution of the more general nonsteady, nonplanar asymptotic model, its linear stability can be investigated in a reasonably straightforward fashion. This was illustrated for the case of an unconfined (constant-pressure) deflagration, for which it was determined, as in previous studies of nonporous propellants and condensed-phase combustion, that a pulsating stability boundary exists in the plane of activation energy and disturbance wave number. The neutral stability boundary was shown to be especially accessible for realistic parameter values, which, furthermore, permit the effects of porosity on the location of this stability boundary to be handled in a perturbative fashion. Specifically, in the realistic limit of small gas-to-solid and gas-to-liquid density and thermal conductivity ratios, it was shown that shifts in the stability boundary were essentially proportional to $\alpha_s(1 - \alpha_s)^{-1}$ and that the effects of thermal expansion and two-phase flow thus result in a destabilizing shift in the neutral stability boundary relative to the nonporous case. Additional stability results are under investigation for the confined geometry, where two-phase-flow effects associated with burned-gas permeation and the subsequent convective preheating of the material are anticipated to have an even more pronounced effect on the stability of the deflagration wave.

Acknowledgment

The work of the first author was supported by the U.S. Department of Energy under Contract DE-AC04-94AL85000.

References

- ¹Kuo, K. K., and Summerfield, M., "Theory of Steady-State Burning of Gas-Permeable Propellants," *AIAA Journal*, Vol. 12, No. 1, 1974, pp. 49–56.
- ²Ermolayev, B. S., Borisov, A. A., and Khasainov, B. A., "Comments on 'Theory of Steady-State Burning of Gas-Permeable Propellants,'" *AIAA Journal*, Vol. 13, No. 8, 1975, p. 1128.
- ³Gokhale, S. S., and Krier, H., "Modeling of Unsteady Two-Phase Reactive Flow in Porous Beds of Propellant," *Progress in Energy and Combustion Science*, Vol. 8, No. 1, 1982, pp. 1–39.
- ⁴Margolis, S. B., Williams, F. A., and Armstrong, R. C., "Influences of Two-Phase Flow in the Deflagration of Homogeneous Solids," *Combustion and Flame*, Vol. 67, No. 3, 1987, pp. 249–258.
- ⁵Li, S. C., Williams, F. A., and Margolis, S. B., "Effects of Two-Phase Flow in a Model for Nitramine Deflagration," *Combustion and Flame*, Vol. 80, No. 3–4, 1990, pp. 329–349.
- ⁶Asay, B. W., Son, S. F., and Bdzil, J. B., "The Role of Gas Permeation in Convective Burning," *International Journal of Multiphase Flow*, Vol. 22, No. 6, 1996, pp. 923–952.
- ⁷Margolis, S. B., and Williams, F. A., "Effects of Two-Phase Flow on the Deflagration of Porous Energetic Materials," *Journal of Propulsion and Power*, Vol. 11, No. 4, 1995, pp. 759–768.
- ⁸Margolis, S. B., and Williams, F. A., "Influence of Porosity and Two-Phase Flow on Diffusional/Thermal Instability of a Deflagrating Energetic Material," *Combustion Science and Technology*, Vol. 106, No. 1–3, 1995, pp. 41–68.

⁹Margolis, S. B., and Williams, F. A., "Effect of Gas-Phase Thermal Expansion on Stability of Deflagrations in Porous Energetic Materials," *International Journal of Multiphase Flow*, Vol. 22, No. 1, 1996, pp. 69–91.

¹⁰Margolis, S. B., "A Deflagration Analysis of Porous Energetic Materials with Two-Phase Flow and a Multiphase Reaction Mechanism," *Journal of Engineering Mathematics*, Vol. 31, No. 1, 1997, pp. 173–203.

¹¹Ilincic, N., and Margolis, S. B., "Eigenvalue Analysis and Calculations for the Deflagration of Porous Energetic Materials in the Merged-Flame Regime," *Combustion Science and Technology*, Vol. 125, 1997, pp. 201–241.

¹²Margolis, S. B., "Influence of Pressure-Driven Gas Permeation on the Quasi-Steady Burning of Porous Energetic Materials," *Combustion Theory and Modelling*, Vol. 2, 1998, pp. 95–113.

¹³Baer, M. R., and Nunziato, J. W., "A Two-Phase Mixture Theory for the Deflagration-to-Detonation Transition (DDT) in Reactive Granular Materials," *International Journal of Multiphase Flow*, Vol. 12, No. 6, 1986, pp. 861–889.

¹⁴Margolis, S. B., and Williams, F. A., "Stability of Homogeneous-Solid Deflagration with Two-Phase Flow in the Reaction Zone," *Combustion and Flame*, Vol. 79, No. 2, 1990, pp. 199–213.

¹⁵Baer, M. R., and Shepherd, J. E., "A Thin Flame Model for Reactive Flow in Porous Materials," Sandia National Labs., SAND83-2576, Albuquerque, NM, 1984.

¹⁶Mitani, T., and Williams, F. A., "A Model for the Deflagration of Nitramines," *Twenty-First Symposium (International) on Combustion*, Combustion Inst., Pittsburgh, PA, 1988, pp. 1965–1974.

¹⁷Denison, M. R., and Baum, E., "A Simplified Model of Unstable Burning in Solid Propellants," *ARS Journal*, Vol. 31, No. 8, 1961, pp. 1112–1122.

¹⁸Krier, H., T'ien, J. S., Sirignano, W. A., and Summerfield, M., "Nonsteady Burning Phenomena of Solid Propellants: Theory and Experiments," *AIAA Journal*, Vol. 6, 1968, pp. 278–285.

¹⁹De Luca, L., "Nonlinear Stability Theory of Heterogeneous Thin Flames," *Eighteenth Symposium (International) on Combustion*, Combustion Inst., Pittsburgh, PA, 1981, pp. 1439–1450.

²⁰Margolis, S. B., and Armstrong, R. C., "Two Asymptotic Models for Solid Propellant Combustion," *Combustion Science and Technology*, Vol. 47, No. 1–2, 1986, pp. 1–38.

²¹Margolis, S. B., and Williams, F. A., "Diffusional/Thermal Coupling and Intrinsic Instability of Solid Propellant Combustion," *Combustion Science and Technology*, Vol. 59, No. 1–3, 1988, pp. 27–84.

²²Margolis, S. B., and Williams, F. A., "Diffusional/Thermal Instability of a Solid Propellant Flame," *SIAM Journal on Applied Mathematics*, Vol. 49, No. 5, 1989, pp. 1390–1420.

²³Higuera, F. J., and Liñán, A., "Stability of Solid Propellant Combustion Subject to Nonplanar Perturbations," *Dynamics of Flames and Reactive Systems*, Vol. 95, Progress in Astronautics and Aeronautics, AIAA, New York, 1984, pp. 248–256.

²⁴Taylor, J. W., "The Burning of Secondary Explosive Powders by a Convective Mechanism," *Transactions of the Faraday Society*, Vol. 58, 1962, p. 561.

²⁵Boggs, T. L., "The Thermal Behavior of Cyclotrimethylenetrinitramine (RDX) and Cyclotetramethylenetetranitramine (HMX)," edited by K. K. Kuo and M. Summerfield, Vol. 90, Progress in Astronautics and Aeronautics, AIAA, New York, 1984, pp. 121–175.

²⁶Probstein, R. F., *Physicochemical Hydrodynamics*, Butterworths, Boston, 1989, pp. 98–100.

²⁷Zanotti, C., Carretta, U., Grimaldi, C., and Colombo, G., "Self-Sustained Oscillatory Burning of Solid Propellants," *Nonsteady Burning and Combustion Stability of Solid Propellants*, edited by L. De Luca, E. W. Price, and M. Summerfield, Vol. 143, Progress in Astronautics and Aeronautics, AIAA, Washington, DC, 1992, pp. 399–439.

²⁸Margolis, S. B., "The Transition to Nonsteady Deflagration in Gasless Combustion," *Progress in Energy and Combustion Science*, Vol. 17, 1991, pp. 135–162.

²⁹Aldushin, A. P., Vol'pert, V. A., and Filipenko, V. P., "Effect of Reagent Melting on Combustion Stability for Gasless Systems," *Combustion, Explosion, and Shock Waves*, Vol. 23, No. 4, 1987, pp. 408–414.

Chapter 2.15

Modeling of Cook-Off Reaction Violence of Confined Energetic Materials

Sook-Ying Ho*

*Defence Science and Technology Organisation, Salisbury,
South Australia, Australia*

Nomenclature

A_i	= preexponential factor for species i
a_T	= time-temperature shift factor
c	= bulk sound speed
E_i	= activation energy for species i
$E'(T)$	= storage modulus at temperature T
$E(\xi)$	= relaxation modulus
K_C	= critical stress intensity factor
$M(\mu)$	= expected mass of fragments having a mass μ
m_i	= mass of explosive for species i
$N(\mu)$	= expected number of fragments having a mass μ
Q_i	= heat of reaction per unit mass for species i
R	= universal gas constant
r_i	= inner radius of cylinder
r_o	= outer radius of cylinder
S	= average fragment size
s	= heat source term from chemical reaction
t	= time
$\Delta\mu$	= tolerance
ε	= strain
$\dot{\varepsilon}$	= strain rate
$\dot{\varepsilon}_{\theta\theta}$	= hoop strain rate
$\eta(T)$	= viscosity at temperature T
μ	= mass of fragment
μ_{ai}	= mean mass of fragment in cell i

$\bar{\xi}$	= reduced time
ρ	= density
σ	= stress
ω_i	= fraction of undecomposed explosive for species i

I. Introduction

THE development of hazard modeling capabilities to predict the response of munitions to various stimuli, for example, thermal or mechanical, is an area of increasing importance, as a result of the requirement for lower vulnerability munitions and the cost and environmental pressures to reduce full-scale testing. Exposure to high temperatures can initiate violent reactions in confined energetic materials. Thus, it is necessary to develop a fundamental understanding of and predictive models for the thermal explosion or cook-off behavior of munitions.

Until recently, little work has been published on modeling the cook-off behavior of confined energetic materials. Although it is now possible to model/predict cook-off initiation temperatures and times with sufficient accuracy by heat transfer analysis,¹ predicting the violence of cook-off reactions is a much more complex and difficult matter. The modeling of cook-off response requires coupled thermal, chemical, and mechanical analyses to capture adequately the thermochemical and thermomechanical behavior of the energetic material during heating. For example, the constitutive equations used in the stress analysis must account for additional mechanisms such as thermal damage and phase transformations. In the past, most of the work was centered on thermochemical behavior and the onset of thermal runaway reactions, and still relatively little is known about the thermomechanical properties of the energetic materials, damage states of the materials prior to ignition, and the change in geometry of the energetic materials (dependent on the phase/state changes with temperature) during pressure buildup.

The modeling of cook-off reaction response is further complicated by the lack of a quantitative or more scientific basis for defining reaction violence. The level of reaction violence is determined by the competition between the pressure generated from the cook-off reaction and the stress release resulting from breakup of the confinement. Unfortunately, scientifically based burn models are not currently available to predict the overpressure as a function of time. Currently, the level of violence is only defined based on the degree of damage or fragmentation of the test vessel (confinement) after the cook-off experiment. This does not, however, provide a definitive basis for separating the different levels of response (such as burning, deflagration, and explosion) because the boundaries between the various types of responses are not distinct.

Traditionally, the thermal response of energetic materials has been modeled by thermal/chemical analysis. For example, Chidester et al.² used a heat transfer code with multistep chemical decomposition models to treat the thermal process until thermal runaway is reached and then calculated the hydrodynamics of the explosion process using a burn model in a hydrocode. Such an approach, decoupling thermal and mechanical responses, however, could not model the interaction between the thermal/combustion processes and mechanical deformation and may miss important features of the cook-off event.

Although a fully predictive capability for cook-off reaction violence is not yet possible, a few different methods using coupled chemical/thermal/mechanical

analysis³⁻⁷ are currently under development to model cook-off reaction violence. The modeling strategy used by Baer et al.^{3,4} involves coupling massively parallelized computer programs for heat transfer and quasi-static mechanics. At the point of ignition, the stress and temperature fields from the finite element thermal and stress analyses are then mapped to the cells of a finite volume shock physics code. To determine appropriate combustion physics models for cook-off, experiments are conducted to characterize the thermally induced damage of the energetic material.⁵ The breakup of the cook-off confinement is then estimated from a dynamic fragmentation theory, using Lagrangian tracers in the numerical simulations to monitor the hoop and axial stresses of the confinement.

The approach developed by Nichols et al.⁶ at Lawrence Livermore Laboratory involves the transformation of a three-dimensional hydrocode into a three-dimensional coupled thermal/chemical/mechanical code as a single platform for cook-off modeling. Several new capabilities, including implicit thermal transport, thermally driven reactions, models for chemical and mechanical properties of chemical mixtures, second-order species advection, and implicit hydrodynamics were added to the analysis. This code can predict the temperature at which the reaction occurs and qualitatively model the mechanical response, but does not currently have models that will predict the extent of metal fracture or the pressure of the high-explosive products.

A different modeling approach is used in the present study to predict cook-off response. It combines coupled heat (with chemistry included as a source term) and structural analysis (in a single finite element code⁸) with constitutive models of the thermally degrading energetic material, derived from dynamic mechanical thermal analysis experiments, and pressure loading measured from an instrumented small-scale cook-off bomb (SSCB). The thermal and stress fields are calculated at each time step using the material properties at the appropriate thermal state of the material. This method has some advantages over the other approaches. It is comparatively simple and does not require supercomputers or highly parallelized computer systems. Also, real data are used to derive the constitutive equations (which take into account thermal degradation and phase changes) and the combustion models to describe the pressure buildup as a function of time. From the stress-strain states of the confinement, a failure analysis is conducted to assess the likely failure modes of the SSCB. A fragmentation analysis, using the Grady-Kipp dynamic fragmentation model,⁹ is then conducted to assess the level of violence of the cook-off reaction. A hydroxyterminated polybutadiene (HTPB)/cyclotrimethylene trinitramine (RDX) propellant (18:82 wt% and a particle size coarse/fine ratio of 60:40) is used in the SSCB to illustrate how this methodology is applied.

II. Coupled Thermal/Structural Analysis

A commercial general purpose finite element program, STRAND 6, was modified for the coupled heat and structural analysis. A number of new capabilities were added to the program to model cook-off initiation and reaction violence. The modifications have been made to allow a transient analysis to be carried out on the thermal loading of the SSCB, followed by combustion of the propellant. The process of heat transfer and the temporal variations of temperature, stress, and strain are considered.

The transient heat solver was modified to enable the heat source from the electric band heaters and the chemical decomposition of the energetic material in the SSCB to be modeled. The heating rate from the band heaters was calibrated using an inert propellant in the SSCB to obtain a source term for the slow heating rate. The magnitude of the source used for the heater was $9.5 \times 10^6 \text{ W/m}^3$. The chemistry source term, used to describe the heat generation per unit volume of explosive at a given temperature, is similar to that used by Jones and Parker¹⁰ and has the form¹¹

$$s = \sum_{i=1}^N \rho \omega_i m_i Q_i A_i \exp\left[\frac{-E_i}{RT}\right] \quad (1)$$

The thermochemical constants for RDX used in this study are $A_i = 3.162 \times 10^{18} \text{ s}^{-1}$, $\rho = 1.8 \text{ mg} \cdot \text{m}^{-3}$, $Q_i = 2.09 \text{ MJ} \cdot \text{kg}^{-1}$, $E_i = 200 \text{ kJ} \cdot \text{mol}^{-1}$. The nonlinear transient heat analysis solver allows for nonlinear variation of the material properties and heat source with temperature.

A number of modifications were made to the transient stress analysis solver to model cook-off response. First, a capability for nonlinear viscoelastic (NLVE) analysis was implemented in the finite element code. NLVE constitutive models, which are temperature and strain-rate dependent, can be implemented in two forms: 1) three-dimensional interpolation of the Prony series equations, representing the shear and Young's relaxation moduli as functions of time, temperature, and strain level⁸ and 2) the constitutive model described by Eq. (3) (see section on thermomechanical properties). Reference 8 describes in detail the development of this NLVE analysis capability and benchmarking using coupon samples under various mechanical and thermal loading conditions. The accuracy of this code to predict thermally induced stresses has been validated for rocket motors instrumented with miniature normal stress sensors and T-type thermocouples. Second, modifications were made to the program to monitor the temperature distribution in the propellant and begin the time history loading of combustion pressure when the critical temperature in the propellant is reached. The combined thermal and pressure loading is triggered at a user-defined critical temperature (see later section on dynamic combustion). Third, because cook-off reactions span several orders of magnitude in time, the existing solver was modified so that it can capture both the longer time response due to temperature and the short time response due to pressure. The program allows up to 1000 time steps with timescales from seconds (during initial heating) to microseconds (near ignition and during combustion) to be stored.

A schematic diagram of the instrumented SSCB is shown in Fig. 1. The finite element analysis was carried out using eight-node isoparametric plate elements. A single beam element was used to represent the bolt. In the analysis, it was assumed that the change in propellant mass and geometry is small prior to ignition (i.e., no attempt was made to remove elements from the finite-element model as burning takes place) and that an axisymmetric model is still valid when the propellant expands into the air gap in the SSCB. Temperature and von Mises stress σ_{vm} contours in the SSCB at 1360 s (prior to ignition) and 1560 s (during combustion) are shown in Figs. 2 and 3, respectively (see also color reproductions of these figures on p. xxv). The uniform temperature distributions in the propellant before ignition (Fig. 2) are consistent with those from instrumented¹²⁻¹⁴ small-scale cook-off experiments at the slow heating rate ($\approx 0.1^\circ\text{C s}^{-1}$).

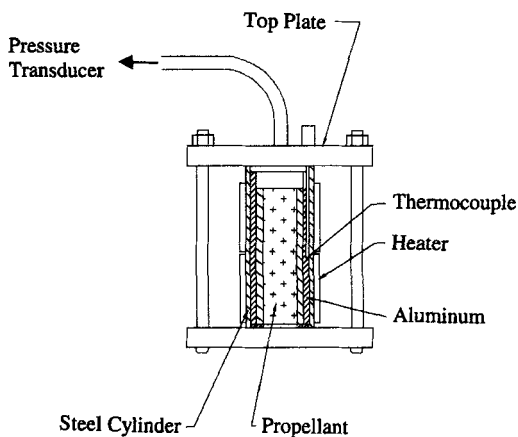


Fig. 1 Instrumented SSCB.

It is evident from Fig. 3 that the stresses in the SSCB are very high during the short time interval over which combustion occurs. The highest von Mises stresses in the different components of the SSCB confinement are listed in Table 1. The most critical stress regions in the confinement during combustion are in the outer steel cylinder. Also note the stress contours in the top end plate that suggests bulging or denting. As expected, the stresses in the propellant are two to three orders of magnitude lower than in the confinement materials.

A. Thermomechanical Properties and Temperature-Dependent Viscoelastic Models

The stress-strain states of the energetic material change with temperature and the degree of damage in the material prior to ignition. Therefore, it is important to have material models that adequately describe the mechanical behavior over

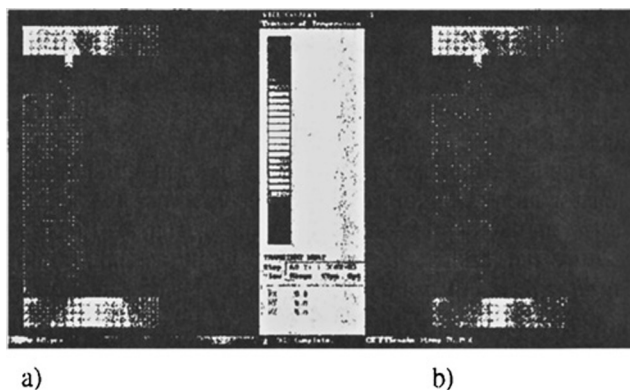


Fig. 2 Temperature distribution in SSCB at a) time = 1360 s (before ignition) and b) time = 1520 s (during combustion) (see also p. xxv).

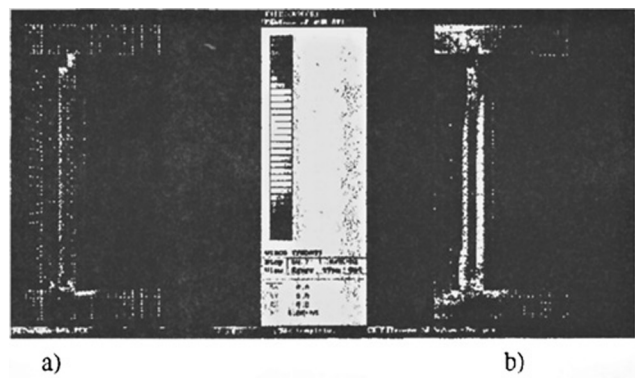


Fig. 3 Von Mises stress contours in SSCB at a) time = 1360 s (before ignition) and b) time = 1520 s (during combustion) (see also p. xxv).

the entire temperature range. Determination of thermomechanical behavior and the damage state of the energetic material are key to predicting cook-off reaction violence.^{3,12,15–17}

NLVE constitutive models are not readily available, in particular in the temperature range appropriate to cook-off behavior. Most NLVE theories handle material nonlinearities (arising from volume change, damage, modulus strain sensitivity, thermal–mechanical coupling, etc.) by including terms (softening functions) in the linear viscoelastic constitutive equation to give observed behavior. For temperature-dependent behavior, the linear viscoelastic constitutive

Table 1 Comparison between predicted von Mises stress and tensile strength of SSCB component materials before and during combustion

Location	Tensile strength, MPa (°C)	Predicted von Mises stress in confinement before and at time ^a of combustion, MPa	
		1360 s	1520 s
Outer steel cylinder (mild steel L1214)	480	130–220	1030 (adjacent to top endplate)
Al liner (Aluminium T6)			550–950
	310 (24)	150–200	260
	234 (150)		
	51 (260)		
	24 (371)		
Inner steel cylinder (mild steel L1214)	480	200	500–980
Base and endplates (mild steel L1214)	480	30–150	210–500 (top endplate) 100–300 (bottom endplate)
Bolt (steel)	400		
Band heater	—	8	20

^aHere $t = 0$ is defined as the time when heating begins, that is, start of the thermal transient from ambient temperature.

equation has the form

$$\sigma = \int_0^{\xi} E(\xi - \bar{\xi}) \frac{d\varepsilon}{d\bar{\xi}} d\bar{\xi} \quad (2)$$

where $\bar{\xi} = t/a_T$ is the reduced time.

In the present study, two different approaches are used for NLVE analysis. In the first method, a three-dimensional interpolation scheme was implemented in the finite element stress analysis to solve the Prony series equations, which represent the Young's and shear relaxation moduli as functions of time, temperature, and strain level. This analysis could be extended to include damage using a cumulative damage model.¹⁸ A second method was developed for modeling mechanical behavior under cook-off conditions because some propellants soften considerably when heated.¹² Empirical constitutive models of degrading energetic materials were developed from the thermomechanical data measured by dynamic mechanical thermal analysis¹⁷ (DMTA). The stress at a given temperature, strain level, and strain rate is described by the equation

$$\sigma = E'(T)\varepsilon + \eta(T) \frac{d\varepsilon}{dt} \quad (3)$$

where η is the viscosity at temperature T and $d\varepsilon/dt$ is the strain rate. The experimental data for E' and η as a function of temperature were fitted to empirical models by a regression analysis for input into the finite element stress solver.

B. Energy Release from Dynamic Combustion

In this study, the measured pressure–time data from small-scale cook-off experiments was used as the pressure loading in the structural analysis because suitable ignition and growth or combustion models are not currently available. An instrumented SSCB (described in detail elsewhere^{7,12,17}) was used to measure the overpressure developed during the dynamic combustion event and the precise temperature and time of energy release from the energetic material during the cook-off reaction. The instrumented SSCB (see Fig. 1) has a pressure transducer connected to the internal volume of the vessel that enables the overpressure developed during dynamic combustion to be measured. An electronic triggering technique was devised to simultaneously trigger data collection of the temperature–time and pressure–time profiles to determine the precise temperature and time when energy was released from the energetic material during the cook-off reaction.

Temperature–time and pressure–time profiles of the HTPB/RDX propellant at the slow heating rate measured using the instrumented SSCB are shown in Figs. 4a and 4b. The temperature and time when the pressure buildup first starts are indicated in Fig. 4a. The overpressure is close to zero until just prior to ignition. The temperature when the initial pressure rise is first detected in the cook-off experiment is used in the structural analysis as a trigger to begin the time history loading of the combustion pressure.

The impulse (area under the pressure–time plot, see Fig. 4b) is a measure of the total energy released during the reaction and is used as the pressure loading in the structural analysis. Combined pressure and thermal loading is switched on in the structural analysis at the critical temperature where pressure buildup is first detected.

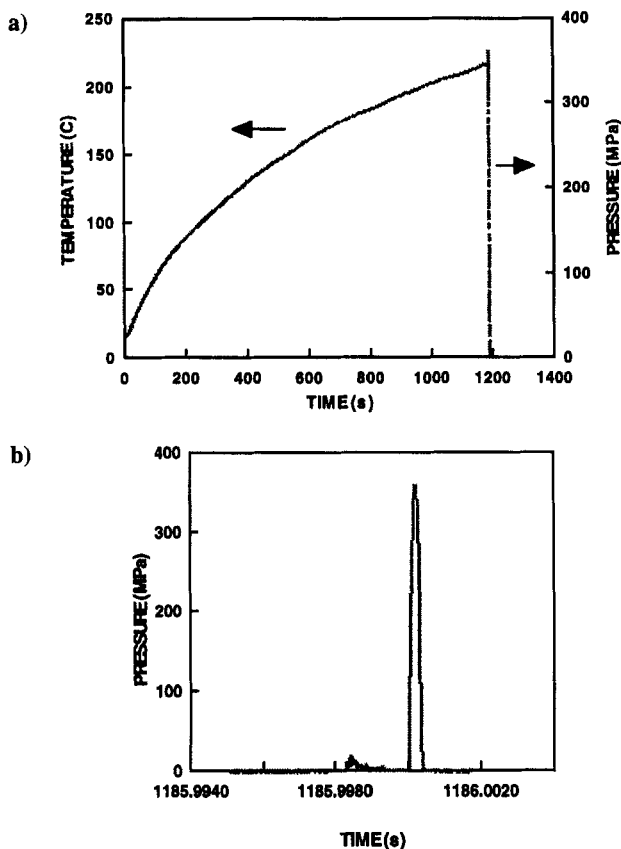


Fig. 4 Time histories for HTPB/RDX (18:82) propellant at slow heating rate of $0.1^{\circ}\text{C s}^{-1}$ of a) temperature at propellant surface and b) pressure. Note: time = 0 is defined as the time when heating begins, that is start of the thermal transient from ambient temperature.

III. Failure Analysis of Confinement

The cookoff behavior in small-scale cook-off tests is usually assessed by visual examination of the damage to the SSCB apparatus after the test.¹⁹ For example, a scale of test responses has been established¹³ as follows: mild burning is little or no damage, SSCB intact; burning is outer cylinder split, inner cylinders undamaged; deflagration is outer cylinder split/fragmented, inner cylinders distorted; explosion is outer cylinder and liner fragmented, inner cylinders split/fragmented, severe bulging of endplates; and detonation is considerable fragmentation, hole in baseplate.

To determine the level of cook-off response in the present study, a failure analysis of the confinement is conducted by comparing the stress/strain states of the confinement during combustion with appropriate failure criteria (such as the tensile strength of the component materials of the SSCB). Failure is predicted when the von Mises stress exceeds the failure criteria. The likely failure mode or damage to the SSCB from the failure analysis is then compared with the scale of test

responses just given, to provide a first approximation of the level of response that can be expected. Although it is often difficult, in cook-off experiments, to distinguish between the different levels of damage to the SSCB (because the delineation of the various types of responses is not sharp) the scale described in the preceding paragraph is used here because at present there are no well-defined demarcations of levels of violence.

A comparison between the predicted von Mises stresses from the coupled thermal and structural analysis before (1360 s) and at the time of combustion (1520 s) and the tensile strength of the component materials is shown in Table 1. It is assumed that the tensile strength of the mild steel material used in the SSCB does not vary significantly with temperature and strain rate because of its linear elastic nature. The tensile strength of the aluminium alloy does, however, vary with temperature as indicated in Table 1.

The results show that the stress levels in the confinement exceed the tensile strength of some of the component materials and that the failure mode is most likely to be splitting/rupture/fragmentation of the outer steel cylinder. Damage/deformation of the aluminum liner and inner steel cylinder are also expected because the predicted stresses in these components exceed the failure criteria. The top and bottom endplates, however, are expected to be undamaged, because the predicted stresses are less than the tensile strength of the mild steel material. The damage to the confinement predicted by the stress and failure analyses appears to be consistent with the damage to the SSCB observed for the HTPB/RDX propellant at the slow heating rate (see Fig. 5). Here the reaction was ranked as a severe deflagration/explosion.

IV. Fragmentation Analysis

A fragmentation analysis was conducted using the Grady-Kipp model^{19,20} to estimate the size of the fragments for each section of the confinement (consisting of a group of plate finite elements with similar stress-strain states) containing fractured material in the SSCB finite element model. For fragmentation mechanisms (dependent on strain rate and temperature at time of failure) where solid

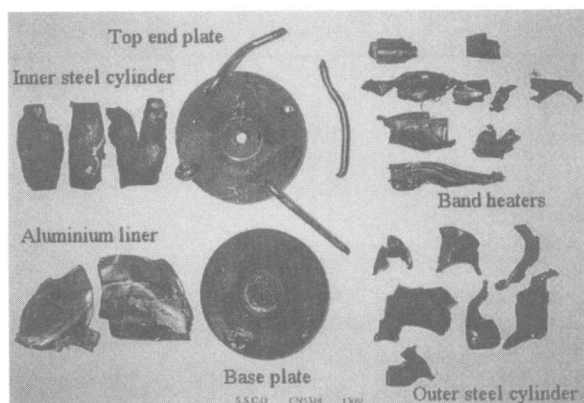


Fig. 5 Damage to SSCB test vessel; HTPB/RDX propellant at slow heating rate.

Table 2 Properties of confinement materials

Material	K_C , $\text{MNm}^{-3/2}$	Bulk sound speed, ms^{-1}	Density, kgm^{-3}
Aluminum liner	37	6320	2700
Inner/outer steel cylinder	50	5960	7750

spall is dominated by fracture toughness, the average fragment size is given by²⁰

$$S = (\sqrt{24}K_c/\rho c\dot{\epsilon})^{\frac{2}{3}} \tag{4}$$

where K_c is measured from fracture mechanics experiments. Detailed descriptions of the development of the Grady–Kipp dynamic fragmentation theory are given in Refs. 9 and 20.

In the small-scale cook-off test, particularly for low-level responses such as deflagration and mild burning, where big fragment sizes are expected, the assumption that the fragments are spherical or cubic may not yield accurate estimates of the average fragment mass. In this study, the fragment mass was calculated by assuming that fracture occurs in the circumferential direction of the cylindrical components of the SSCB confinement. This is a valid assumption because the stress analysis indicates that the hoop stresses are two to three times higher than the axial stresses. Thus, it is assumed that the cross-sectional area of the cylindrical sleeve is unchanged after fracture, the fragment length is S , and the mass of the fragment is $\rho S\pi(r_o^2 - r_i^2)$.

The calculated average fragment size for all of the different sections of the confinement (consisting of plate elements with similar stress and strain states), hoop strain rate at the time of failure $\dot{\epsilon}_{\theta\theta}$, and material properties of the confinement materials are shown in Tables 2 and 3. For this analysis the critical stress intensity

Table 3 Fragmentation analysis of confinement materials

Location	$\dot{\epsilon}_{\theta\theta}$ (from stress analysis) s^{-1} at time of combustion	Average fragment size, m
Aluminum liner		
Cell 1	800	0.056
Cell 2	500	0.076
Cell 3	300	0.10
Inner steel cylinder		
Cell 1	450	0.052
Cell 2	600	0.043
Cell 3	1000	0.030
Outer steel cylinder		
Cell 1	400	0.056
Cell 2	600	0.043
Cell 3	900	0.033

factors at 20°C were used for the mild steel and aluminium alloy materials. As expected, the average fragment size is decreased as the hoop strain rate is increased. Hence, more violent reactions will result in higher loading rates in the confinement and, consequently, in smaller fragment sizes and a larger number of fragments.

To obtain the fragment size distribution, a statistical analysis similar to that described by Kipp et al.²⁰ was applied to each cell (group of finite elements with similar stress and strain states). It is assumed that the fragment size and mass are exponentially (Poisson) distributed. The fragment size calculated from Eq. (4) is now the mean fragment size S_i of cell i . The mean mass μ_{ai} of the fragment in cell i is estimated from the mean fragment size as discussed earlier.

The probability of finding a fragment of mass μ in the interval $(\mu, \mu + \Delta\mu)$ was obtained by multiplying the probability density function^{21,22} $f_i(\mu)$ by $\Delta\mu$ (where $\Delta\mu$ is taken to be unity):

$$f_i(\mu) = (1/\mu_{ai}) \exp(-\mu/\mu_{ai}) \quad (5)$$

Thus, the expected number $N(\mu)$ and mass $M(\mu)$ of fragments in cell i having a fragment mass μ within tolerance $\Delta\mu$ are given by

$$N(\mu) = m_i[f_i(\mu)\Delta\mu] \quad (6)$$

$$M(\mu) = N(\mu)\mu \quad (7)$$

where M_i is the mass of cell i .

Finally, the mass and number of fragments from Eqs. (6) and (7) were summed over all of the cells to obtain the mass and number distributions vs fragment size (or fragment mass). Total mass and number of fragment distributions, after applying statistics, are shown in Figs. 6 and 7. The fragment sizes or masses were grouped into data bins of 2 mm length or 5-g intervals. The expected fragment number and mass distributions are compared with experimental data from eight small-scale cook-off tests of the HTPB/RDX (18:82) propellant. Examples of the frequency (number of fragments) vs fragment mass distributions from three typical experiments are shown in Figs. 8a–8c. Note that the top and bottom endplates were not included in the fragment number because fracture did not occur in these components.

A comparison between the predicted and experimental results indicate that the failure and fragmentation analyses correctly predicted the large spread in fragment sizes (or masses) and the broad tail at the larger fragment sizes, expected from low-level responses. The fragment number distribution also appears to be

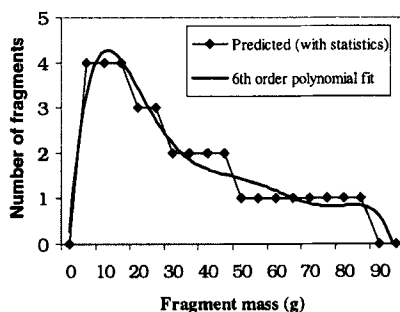


Fig. 6 Expected total number of fragments vs fragment mass.

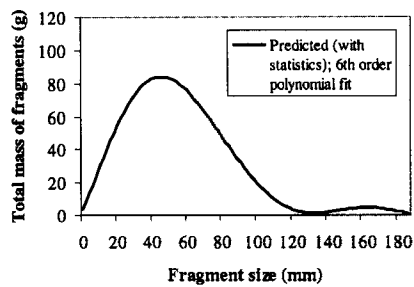


Fig. 7 Expected total mass of fragments vs fragment size.

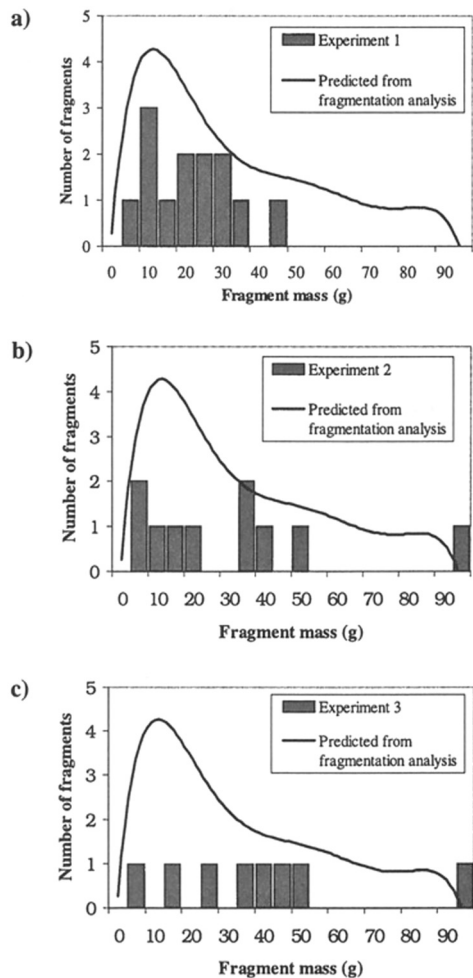


Fig. 8 Comparison between experimental and predicted frequency vs fragment mass for three small-scale cook-off tests.

consistent with experimental data. The approximate correlation between the predicted and experimental fragment mass distributions suggests that the Grady–Kipp fragmentation approach has potential for assessing the level of cook-off violence. More experiments and modeling of different levels of cook-off responses are required to determine if a scale of test responses can be generated to relate the fragment size (or mass) and number distributions to the level of cook-off reaction violence.

A fully predictive capability for cook-off reaction violence is not currently possible. Before the present modeling approach can be applied to full-scale munitions, scientifically based ignition and dynamic burning models, such as the Cook and Haskins model,²³ need to be developed and incorporated into the coupled chemical/thermal/mechanical analyses. This is because the overpressure developed during full-scale cook-off tests can not yet be easily measured. A more quantitative basis for defining the level of reaction violence is also required to guide the fragmentation analysis. For example, the pressurization rate (dP/dt) and impulse during the dynamic combustion event, and/or stress levels and strain rates of the confinement near the onset of failure, are needed to give a better understanding of the cook-off behavior.

V. Conclusions

In this study, an approach for modeling the cook-off response of an energetic material confined in an SSCB was developed, combining coupled thermal and structural analysis of the SSCB and the use of empirical material models and pressure measurements. A dynamic fragmentation analysis was then used to assess the level of violence of the cook-off reaction. The finite element thermal and stress models correctly predicted the temperature distributions and likely failure modes in the SSCB. The expected fragment size and number distributions, predicted from the stress–strain states of the confinement and fragmentation theory, compared reasonably well with the frequency vs fragment mass distributions from eight small-scale cook-off tests.

Acknowledgments

The author would like to thank Gerard Carè of G + D Computing Pty., Ltd., for developing and modifying the STRAND 6P finite element code for this work and David Jones for helpful discussions on the heat flow analysis of explosive materials.

References

- ¹Dimaranan, L. F., Heimdahl, O. E. R., and Covino, J., "Assessment of Cook-off Modelling and Codes," *Proceedings of the Technical Cooperation Program Subgroup W Action Group (WAG)-11 on the Hazards of Energetic Materials and Their Relation to Munitions Survivability*, U.S. Naval Air Warfare Center Weapons Div., China Lake, CA, 1992, pp. 217–227.
- ²Chidester, S. K., Tarver, C. M., Green, L. G., and Urtiew, P. A., "On the Violence of Thermal Explosion in Solid Explosives," *Combustion and Flame*, Vol. 110, 1997, pp. 264–280.

³Baer, M. R., Kipp, M. E., Schmitt, R. G., and Hobbs, M. L., "Towards Assessing the Violence of Reaction During Cook-off of Confined Energetic Materials," *Proceedings of the JANNAF Propulsion Systems Hazards Subcommittee Meeting*, 1996.

⁴Baer, M. R., Hobbs, M. L., Gross, R. J., and Schmitt, R. G., "Cookoff of Energetic Materials," *Preprints of the Eleventh Symposium (International) on Detonation*, Office of Naval Research, Paper 25, 1998.

⁵Schmitt, R. G., Baer, T. A., Renlund, A. M., and Margollis, S. B., "Modelling Burn Rate Phenomena of Damaged Energetic Materials," *Preprints of the Eleventh Symposium (International) on Detonation*, OCNR, Paper 465, 1998.

⁶Nichols, A. L., Couch, R., McCallen, R. C., Otero, I., and Sharp, R., "Modelling Thermally Driven Energetic Response of High Explosives," *Preprints of the Eleventh Symposium (International) on Detonation*, Office of Naval Research, Paper 29, 1998.

⁷Ho, S. Y., "Heat/Structural Analysis of Confined Rocket Propellants for Predicting Cook-off Response," *Preprints of the Eleventh Symposium (International) on Detonation*, Office of Naval Research, Paper 332, 1998.

⁸Ho, S. Y., and Carè, G., "Implementation of a Modified Fracture Mechanics Approach into a Finite-Element Code for Structural Analysis of Solid Rocket Motor," *Journal of Propulsion and Power*, Vol. 14, No. 4, 1998, pp. 409-415.

⁹Grady, D. E., "The Spall Strength of Condensed Matter," *Journal of Mechanical Physics Solids*, Vol. 36, No. 3, 1988, pp. 353-384.

¹⁰Jones, D. A., and Parker, R. P., "Heat Flow Calculations for the Small-Scale Cook-off Bomb Test," Materials Research Lab., MRL TR-91-12, Maribyrnong, VIC, Australia, 1991.

¹¹Bowes, P. C., *Self-Heating: Evaluating and Controlling the Hazards*, Elsevier, New York, 1984.

¹²Ho, S. Y., "Thermomechanical Properties of Rocket Propellants and Correlation with Cookoff Behaviour," *Propellants, Explosives, Pyrotechnics*, Vol. 20, 1995, pp. 206-214.

¹³Parker, R. P., "Establishment of a Super Small-Scale Cookoff Bomb (SSCB) Test Facility at MRL," Materials Research Lab., MRL TR-89-9, Maribyrnong, VIC, Australia, 1989.

¹⁴Dagley, I. J., Parker, R. P., Jones, D. A., and Montelli, L., "Simulation and Moderation of the Response of Confined Pressed Explosive Compositions in a Small-Scale Cookoff Test," *Proceedings of the Technical Cooperation Program Subgroup W, Technical Panel WTP-4*, U.S. Naval Air Warfare Center, China Lake, CA, 1995.

¹⁵Atwood, A. I., Price, C. F., and Curran, P. O., "Combustion Studies of Thermally Damaged Propellants," *Proceedings of the 28th ICT Conference*, Fraunhofer-Institut für Chemische Technologie, Karlsruhe, Germany, 1997.

¹⁶Renlund, A. M., Miller, J. C., Trott, W. M., Erickson, K. L., Hobbs, M. L., Schmitt, R. G., Wellman, G. W., and Baer, M. R., "Characterisation of Thermally Degraded Energetic Materials," *Preprints of the Eleventh Symposium (International) on Detonation*, Office of Naval Research, Paper 341, 1998.

¹⁷Ho, S. Y., Ferschl, T., and Foureur, J., "Correlation of Cookoff Behaviour of Rocket Propellants with Thermomechanical and Thermochemical Properties," Materials Research Lab., MRL TR-91-12, Maribyrnong, VIC, Australia, 1991.

¹⁸Ho, S. Y., "High Strain-Rate Impact Studies of Pre-Damaged Rocket Propellants. I. Characterization of Damage Using a Cumulative Damage Failure Criterion," *Combustion and Flame*, Vol. 104, 1996, pp. 524-534.

¹⁹Pakulak, J. M., and Cragin, S., "Calibration of a Super Small-Scale Cookoff Bomb (SSCB) for Predicting Severity of Cookoff Reaction," U.S. Naval Weapons Center, Rept. NWC TC 6414, China Lake, CA, 1983.

²⁰Kipp, M. E., Grady, D. E., and Swegle, J. W., "Numerical and Experimental Studies of High-Velocity Impact Fragmentation," *International Journal of Impact Engineering*, Vol. 14, 1993, pp. 427–438.

²¹Bury, K. V., *Statistical Models in Applied Science*, Wiley, New York, 1975.

²²Blake, I. F., *An Introduction to Applied Probability*, Krieger Malabar, FL, 1987.

²³Cook, M. D., and Haskins, P. J., "Development and Implementation of an Ignition and Growth Model for Homogeneous and Heterogenous Explosives," *Preprints of the Eleventh Symposium (International) on Detonation*, Office of Naval Research, Paper 252, 1998.

Chapter 2.16

Solid Propellant Combustion Response: Quasi-Steady (QSHOD) Theory Development and Validation

M. Q. Brewster*

*University of Illinois at Urbana-Champaign, Urbana, Illinois***Nomenclature**

A	$= (\bar{T}_s - T_0)(\partial \ln \bar{m} / \partial T_s)_{p,q_r}, (k/r)$
A_c	$=$ condensed phase reaction rate prefactor
A_s	$=$ surface pyrolysis relation prefactor
B	$= 1/[(\bar{T}_s - T_0)(\partial \ln \bar{m} / \partial T_0)_{p,q_r}], (1/k)$
B_g	$=$ gas phase reaction rate prefactor
C	$=$ specific heat, C_p
$E_{c,g}$	$=$ activation energy of condensed or gas phase reaction
E_s	$= E_c/2$
$F_{c,g}$	$=$ steady-state burning functions [Eqs. (19) and (20)]
f	$=$ frequency, Hz
$f_{c,R}$	$= 1/t_{c,R}$
f_r	$=$ fraction of q_r absorbed below surface reaction zone, $\exp(-K_a x_R)$
f_s	$=$ temperature gradient at surface in condensed phase
J	$= \bar{q}_r / \bar{m} C (\bar{T}_s - T_0)$
K_a	$=$ radiation absorption coefficient of condensed phase
k	$= (\bar{T}_s - T_0)(\partial \ln \bar{m} / \partial T_0)_{p,q_r}$
$k_{c,g}$	$=$ thermal conductivity
m	$=$ mass flux, $\rho_c r_b$
m'	$= \Delta m \exp[i(2\pi f t + \phi)]$
n	$= (\partial \ln \bar{m} / \partial \ln \bar{P})_{T_0,q_r}, (v)$
n_q	$= (\partial \ln \bar{m} / \partial \ln \bar{q}_r)_{T_s,p}, (\delta_q/r)$
n_s	$= (\partial \ln \bar{m} / \partial \ln \bar{P})_{T_s,q_r}, (\delta/r)$
P	$=$ pressure
P'	$= \Delta P \exp[i2\pi f t]$

$Q_{c,g}$	= chemical heat release (positive exothermic)
q_c	= conductive heat flux to surface from gas phase
q_r	= absorbed radiant heat flux in condensed phase
q'_r	= $\Delta q_r \exp[i2\pi f t]$
R	= universal gas constant, 1.987 cal/mol-K
R_p	= pressure-driven frequency response function; $(m'/\bar{m})/(P'/\bar{P})$ at constant q_r
R_q	= radiation-driven frequency response function; $(m'/\bar{m})/(q'_r/\bar{q}_r)$ at constant P
r	= $(\partial \bar{T}_s / \partial T_0)_{p,q_r}$
r_b	= burning rate
T_{0a}	= apparent initial temperature [Eq. (15)]
$T_{0,s,f}$	= initial, surface, or final flame temperature
$t_{c,R}$	= characteristic times, $x_{c,R}/\bar{r}_b$
u_g	= gas bulk velocity normal to surface
W	= molecular weight
x	= coordinate normal to surface, positive into gas phase
x_c	= solid convective-diffusive length scale, α_c/\bar{r}_b
x_g	= gas flame characteristic thickness
x_R	= condensed phase reaction zone length scale, $x_c/(E_c/2R\bar{T}_s)$
Y	= acoustic admittance function
$\alpha_{c,g}$	= thermal diffusivity
Δ	= amplitude of fluctuating quantity
δ, δ_q	= Jacobian parameters, $\nu r - \mu k, \nu_q r - \mu_q k$
λ	= $\frac{1}{2} + (\frac{1}{2})(1 + 4i\Omega)^{1/2}$
μ	= $[1/(\bar{T}_s - T_0)](\partial \bar{T}_s / \partial \ln \bar{P})_{T_{0,q_r}}$
μ_q	= $[1/(\bar{T}_s - T_0)](\partial \bar{T}_s / \partial \ln \bar{q}_r)_{T_{0,p}}$
ν	= $(\partial \ln \bar{m} / \partial \ln \bar{P})_{T_{0,q_r}}$ (same as n)
ν_q	= $(\partial \ln \bar{m} / \partial \ln \bar{q}_r)_{T_{0,p}}$
$\rho_{c,g}$	= density
σ_p	= $k/(\bar{T}_s - T_0)$
ϕ	= phase angle
Ω	= dimensionless frequency: $2\pi f/f_c = 2\pi f \alpha_c / \bar{r}_b^2$
ω	= $2\pi f$

Subscripts and Superscripts

c	= condensed phase, convective-diffusive, or conduction
g	= gas phase
R	= reaction zone in condensed phase
r	= radiation
s	= surface
$-$	= steady condition or mean value
$'$	= complex fluctuating quantity

I. Introduction

THE term combustion response for a solid propellant is usually taken to mean the linearized (small amplitude) frequency response function for burning rate or mass flux to harmonic pressure oscillations R_p . Specifically, it is the real part

or in-phase component of the complex frequency response function that is usually meant, $\text{Re}\{R_p\}$:

$$R_p = (m'/\bar{m})/(P'/\bar{P}) = (\Delta m/\bar{m})/(\Delta P/\bar{P}) \exp(i\phi)$$

$$\text{Re}\{R_p\} = |R_p| \cos \phi \quad (1)$$

$$m = \bar{m} + \text{Re}\{m'(t)\} \quad (2a)$$

$$m'(t) = \Delta m \exp[i(\omega t + \phi)] \quad (2b)$$

$$P = \bar{P} + \text{Re}\{P'(t)\} \quad (2c)$$

$$P'(t) = \Delta P \exp[i(\omega t)] \quad (2d)$$

More generally the term combustion response can refer to linear or nonlinear response to any time-varying (harmonic or anharmonic) external parameter including pressure, radiant heat flux, or tangential gas velocity. For example, the linear response to radiant flux can be defined as follows:

$$R_q = (m'/\bar{m})/(q'_r/\bar{q}_r) \quad (3)$$

The present focus will be on linearized response to harmonic oscillations of pressure and radiant flux: pressure because of the primary importance of pressure coupling between propellant combustion and chamber acoustics and radiant flux because of the utility of laboratory laser-driven response measurements for studying combustion mechanisms.

Unsteady combustion response of solid propellants is important for two reasons. First, it is a necessary input for simulating rocket motor performance and predicting combustion instability. The linear pressure-coupled response is related by the quasi-steady mass equation ($m = \rho_c r_b = \rho_g u_g$) to the acoustic admittance Y , which is the boundary condition used in linear acoustic analysis of the motor¹

$$Y \equiv \frac{u'_g/\bar{u}_g}{P'/\bar{P}} = R_p - \frac{\rho'_g/\bar{\rho}_g}{P'/\bar{P}} \xrightarrow[\text{const}]{T_f, W} R_p - 1 \quad (4)$$

The last expression ($R_p - 1$) assumes ideal gas behavior, constant final flame temperature T_f , and molecular weight W . (Isentropic T_f fluctuation is also often assumed, in which case the 1 becomes $1/\gamma$. Either way, in most homogeneous energetic materials, the contribution to Y due to density fluctuations via temperature fluctuations is usually thought to be small. An important, yet relatively unexplored, possible exception is fuel-rich, fine-AP/binder mixtures; see Sec. IX.B at the end of this chapter.) The foregoing discussion relates to linear stability analysis, which is the usual starting point for nonlinear analysis. For nonlinear chamber gasdynamics modeling of a solid rocket motor, a nonlinear, time-dependent propellant regression rate or combustion model must be provided. A second and equally important reason unsteady combustion response is important is that it is a valuable tool for understanding combustion mechanisms of solid propellants. By including much more information than steady state, unsteady combustion allows better verification of physical and chemical modeling assumptions.

The primary focus of this chapter will be the classical, linear, quasi-steady gas and condensed phase reaction zones, homogeneous propellant, and one-dimensional flame(s) and heat transfer (QSHOD) response. Though theoretical development

began much earlier, the designation QSHOD does not appear in the literature until the late 1980s and early 1990s.^{2,3} Note the condensed phase quasi-steady assumption; this tacit assumption has been frequently overlooked in comparison to the gas phase counterpart.

II. Synopsis of QSHOD Theory Development

In 1942 Zel'dovich published a pioneering paper in QSHOD theory development.⁴ Zel'dovich showed that for QSHOD conditions, the unsteady combustion response could be analyzed by solving only the unsteady solid phase heat conduction equation provided one had a knowledge of steady-state burning rate sensitivity parameters, that is steady burning rate as a function of pressure and initial temperature. This approach made use of steady-state burning rate functionalities and the solid phase energy equation to eliminate the need for specific reaction rate information. That is, no assumptions about chemical kinetics were necessary in either the condensed phase decomposition zone or the gas phase reaction zone; it was necessary only that a material particle's transit time through the reaction zones was much less than the characteristic time of an external disturbance. Another way of saying this for the condensed phase is that the decomposition zone must be thin enough to be approximated as a surface phenomenon (the condensed phase decomposition zone is also referred to here as the surface pyrolysis or just pyrolysis zone). This phenomenological approach, which relies on empirical steady-state burning information instead of assumed chemical kinetics, would come to be known as the Zel'dovich–Novozhilov (ZN) method.⁴

In 1959 Hart and McClure⁵ published another foundational paper based on a semiphenomenological approach similar to Zel'dovich's.⁴ In addition to empirical steady-state burning rate information, Hart and McClure⁵ used a simple chemical kinetic expression to describe fluctuating surface temperature (which Zel'dovich⁴ had assumed constant). By assuming a particular chemical kinetic expression for the condensed phase process Hart and McClure⁵ began what would come to be known as the flame modeling (FM) approach. Technically, Hart and McClure's model was a hybrid FM-ZN approach: FM in the condensed phase and ZN in the gas phase. This type of hybrid approach would prove to be popular and practical in later QSHOD modeling, as will be discussed further. One problem with Hart and McClure's sample response calculations was an assumed pyrolysis activation energy, $E_c = 100$ kcal/mol [$E_s = 50$; see Eqs. (27) and (28)], that has since been recognized as being too large. At that point, quantitative comparison between experiment and theory was not possible, as the authors acknowledged; nevertheless, important theoretical groundwork was laid.

In 1961 Denison and Baum published another pioneering paper in QSHOD theory development.⁶ They took the next step in implementation of the FM approach by including a simple gas phase chemical kinetic expression from laminar gas flame theory based on high-activation energy (flame sheet approximation). For the condensed phase they assumed an unsteady Arrhenius pyrolysis relation of the form

$$m = A_s P^{n_s} \exp[-(E_s/RT_s)] \quad (5)$$

with A_s constant and the pressure term absent, that is, $n_s = 0$. Another significant part of their analysis was calculation of intrinsic, linear stability boundaries.

A few years later Novozhilov published the Soviet phenomenological version of QSHOD theory, now known as ZN theory, with Zel'dovich's constant- T_s

assumption relaxed.⁷ Thus, a situation was developing where Russian and U.S. researchers were apparently independently pursuing analyses of the same problem with a common set of underlying assumptions, that is, QSHOD, but by different approaches, ZN and FM, respectively. In these early years, though, the theoretical equivalence of the two approaches was not recognized; at least citations of western FM literature seem conspicuously absent in the Russian papers of the time and vice versa with regard to ZN citations in western papers. For one thing, the FM approach was not even recognized as such yet; rather, a variety of FM models were being developed, all of which looked different due to varying chemical kinetic assumptions and different dependent and independent variables.

One significant example of the FM models appearing in the 1960s, is a paper by Hart et al.⁸ in 1966. They proposed a pressure dependence in the surface pyrolysis relation, that is, specifically, $n_s = 1$ in Eq. (5) (based on autocatalysis kinetics arguments), in an attempt to obtain better agreement with T-burner response measurements⁹ for a double-base propellant, JPN. (They⁸ also included a relatively unimportant term $T_s^{-0.5}$ in the pre-exponential factor.) This theoretical modification succeeded in increasing the magnitude of the response as the experimental data apparently required. However, ironically, those experimental response data would subsequently be adjusted to lower values as the method of data reduction and experimental conditions used in T-burner testing were refined.¹⁰

The next significant contribution on the FM side of QSHOD analysis came in 1968 when Culick¹¹ showed that the various FM models could be expressed in a common form, which has been referred to as the *AB* model [see Eq. (25)]. His paper went a long way toward unifying the various FM models into what is now called the FM approach.

The most recent significant development in QSHOD theory has been recognition of the mathematical equivalence of the FM and ZN approaches. This recognition appears to have come incrementally with contributions being made by various researchers.^{1-3,12-18} The ZN-FM equivalence is noted here as mathematical because of the practical or implementational difference that still remains wherein ZN emphasizes more the use of experimental data, whereas FM emphasizes modeling parameters and assumptions as discussed further subsequently.

In the remainder of this chapter, theoretical QSHOD response formulation is reviewed in more detail. Experimental linear response results are also discussed, particularly those that have contributed to mechanistic understanding by comparison with theory, for example NC/NG and HMX. Finally, a few example studies and issues related to non-QSHOD response are reviewed.

III. Nonlinear QSHOD Response (ZN)

Next, QSHOD theory is reviewed at the most basic level, without any assumptions about chemical kinetics in either the condensed phase decomposition zone or the gas phase reaction zone. This approach is more like ZN than FM in avoiding assumptions about chemical kinetics and allows the equivalence between the ZN and FM to be seen better because the multiplicity of solutions obtained via FM is avoided. In that sense, this treatment is in the same spirit as Culick's¹¹ standard *AB* form; however, here even the condensed phase decomposition kinetics assumption, for example, Eq. (5), is withheld. Details of the derivation can be found in Refs. 16 and 17. The fundamental equation for the QSHOD response is

the unsteady energy equation in the condensed phase that includes the inert solid propellant ($-\infty < x < 0$) and the thin (possibly liquid) decomposition layer on the propellant surface ($x = 0$),

$$\rho_c C \frac{\partial T}{\partial t} + m C \frac{\partial T}{\partial x} = k_c \frac{\partial^2 T}{\partial x^2} + f_r q_r K_a \exp(K_a x) \quad (6)$$

$$m(t) = \rho_c r_b(t) \quad (6a)$$

$$T(-\infty, t) = T_0 \quad (6b)$$

$$T(0, t) = T_s(t) \quad (6c)$$

$$\left. \frac{\partial T}{\partial x} \right|_{0^-, t} \equiv f_s(t) = \frac{1}{k_c} [(1 - f_r)q_r + q_c + m Q_c] \quad q_c = k_g \left. \frac{\partial T}{\partial x} \right|_{0^+, t} \quad (6d)$$

The solution of the unsteady heat equation is a relatively straightforward matter even when, in addition to solid temperature $T(x, t)$, the burning mass flux $m(t)$ is an unknown value to be solved for. What complicates the solution is the question of how to specify the conductive heat feedback to the surface from the gas phase. One approach is to solve gas phase quasi-steady differential equations, based on some sort of kinetics assumptions (usually single step), as in the FM approach. The ZN method provides a convenient alternative for representing the conductive heat feedback from the quasi-steady gas phase as opposed to solving the quasi-steady gas equations. The method consists of using the steady burning laws and integral energy equations to transform the steady burning laws to a form that is valid for unsteady burning. The steady burning laws (overbar represents time-independent or time-mean conditions) can be represented functionally as

$$\bar{m} = \bar{m}(T_0, \bar{P}, \bar{q}_r) \quad (7)$$

$$\bar{T}_s = \bar{T}_s(T_0, \bar{P}, \bar{q}_r) \quad (8)$$

The ZN method assumes as dependent variables \bar{m} and \bar{T}_s and as independent variables T_0 and \bar{P} , as a laboratory measurement would suggest. Other dependent-independent variable choices are possible.¹⁹ [The traditional FM approach uses $\bar{m}(\bar{T}_s, \bar{P})$ and $\bar{T}_s(T_0, \bar{P})$]. Another combination that has been used is $\bar{m}(\bar{T}_s, \bar{P})$ and $\bar{f}_s(\bar{T}_s, \bar{P})$ [see Eqs. (9–11)]. The functionalities indicated in Eqs. (7) and (8) can be in the form of analytic or numerical flame modeling equations (FM approach) or empirical data (ZN approach). Using the steady integral energy equation

$$\bar{f}_s = (\bar{r}_b/\alpha_c)(\bar{T}_s - T_0) - (f_r \bar{q}_r/k_c) \quad (9)$$

the steady burning laws can be transformed to eliminate T_0 in favor of \bar{f}_s ,

$$\bar{m} = \bar{m}(\bar{f}_s, \bar{P}, \bar{q}_r) \quad (10)$$

$$\bar{T}_s = \bar{T}_s(\bar{f}_s, \bar{P}, \bar{q}_r) \quad (11)$$

These functional relationships have been shown to be valid on a time-dependent basis (see Refs. 16 and 20 for formulation without radiation and Ref. 17 for formulation with radiation) under the quasi-steady assumption, giving

$$m = m(f_s, P, q_r) \quad (12)$$

$$T_s = T_s(f_s, P, q_r) \quad (13)$$

Using the time-dependent integral energy equation for surface reaction

$$f_s = \frac{r_b}{\alpha_c} \left(T_s - \left[T_0 - \frac{1}{r_b} \frac{\partial}{\partial t} \int_{-\infty}^0 T \, dx \right] \right) - \frac{f_r q_r}{k_c} \quad (14)$$

an apparent initial temperature T_{0a} can be defined to include the unsteady energy accumulation in the condensed phase region

$$T_{0a} \equiv T_0 - \frac{1}{r_b} \frac{\partial}{\partial t} \int_{-\infty}^0 T \, dx \quad (15)$$

and

$$\left. \frac{\partial T}{\partial x} \right|_{0^-, t} \equiv f_s(t) = \frac{r_b}{\alpha_c} (T_s - T_{0a}) - \frac{f_r q_r}{k_c} \quad [\text{use in place of Eq. (6d)}] \quad (16)$$

and the unsteady burning laws can be written as

$$m = m(T_{0a}, P, q_r) \quad (17)$$

$$T_s = T_s(T_{0a}, P, q_r) \quad (18)$$

The apparent initial temperature T_{0a} has replaced the actual initial temperature T_0 in the steady-state burning laws. These relations are obtained either from a steady model (FM) or steady-state r_b and T_s measurements (ZN). In the case of FM, the solutions generally appear with the two dependent variables m and T_s combined algebraically,

$$F_c(m, T_s; T_{0a}, P, q_r) = 0, \quad F_c(\bar{m}, \bar{T}_s; T_0, \bar{P}, \bar{q}_r) = 0 \quad (19)$$

$$F_g(m, T_s; T_{0a}, P, q_r) = 0, \quad F_g(\bar{m}, \bar{T}_s; T_0, \bar{P}, \bar{q}_r) = 0 \quad (20)$$

with one relation, F_c , coming from analysis of the condensed phase reaction zone and the other, F_g , from the gas phase reaction zone. When combined with the unsteady differential energy equation, these relations allow solution of the unsteady temperature field in the condensed phase $T(x, t)$ and the unsteady burning rate $m(t)$ for a prescribed unsteady $P(t)$ or $q_r(t)$. This solution can be numerical, in which case nonlinear behavior can be simulated, or, in the case of small amplitude linear behavior, analytic representation is possible. The linear analytic solution is more commonly reported; nonlinear simulations have not been reported much outside of the Russian literature. To summarize, the nonlinear problem consists of solving Eqs. (6) and (16), and (17–18) or (19–20).

IV. Linearized QSHOD Response Function (ZN)

In the linear approximation an analytical solution of the QSHOD problem can be obtained. Linearization means that the amplitude of the disturbance (P or q_r) is small enough that nonlinear terms are negligible. The consequence of this condition is that the output is linearly proportional to the input. Consider the case of oscillatory burning and, more specifically, the burning response to a harmonic input. The input is a sine wave with circular frequency ω ($= 2\pi f$) and amplitude Δp or Δq_r ,

$$P(t) = \bar{P} + \text{Re}\{P'(t)\} = \bar{P} + \text{Re}\{\Delta P \exp(i\omega t)\} \quad (21a)$$

$$q_r(t) = \bar{q}_r + \text{Re}\{q'_r(t)\} = \bar{q}_r + \text{Re}\{\Delta q_r \exp(i\omega t)\} \quad (21b)$$

For a linear response, the corresponding mass flux response and temperature field will also be harmonic at the same frequency

$$m(t) = \bar{m} + \text{Re}\{m'(t)\} = \bar{m} + \text{Re}\{\Delta m \exp[i(\omega t + \phi)]\} \quad (22)$$

$$T(x, t) = \bar{T}(x) + \text{Re}\{T'(x, t)\} = \bar{T}(x) + \text{Re}\{\Delta T(x) \exp[i(\omega t + \varphi(x))]\} \quad (23)$$

where Δm is the amplitude of the mass flux response output and ϕ is the phase between the output and input (lead $\phi > 0$ and lag $\phi < 0$). In the linear approximation, $\Delta m \ll \bar{m}$ and $\Delta T \ll \bar{T}$ such that nonlinear terms such as $m' \partial T' / \partial x$ are negligible. This allows analytic solutions of Eq. (6) to be obtained.

The steady-state solution is

$$\frac{\bar{T}(x) - T_0}{\bar{T}_s - T_0} = \left[1 - \left(\frac{f_r J}{1 - \beta} \right) \right] \exp\left(\frac{x}{x_c}\right) + \left(\frac{f_r J}{1 - \beta} \right) \exp(K_a x),$$

$$\beta = K_a x_c, \quad x_c = \frac{\alpha_c}{\bar{r}_b} \quad (24)$$

where $J = \bar{q}_r / \bar{m} C(\bar{T}_s - T_0)$ represents the fraction of energy required to raise the propellant temperature from T_0 to \bar{T}_s that is provided by the radiant flux. Typically most of this required energy is supplied by conductive heat feedback from the gas phase and condensed phase heat release giving $J < 0.1$. Thus, the temperature profile is usually dominated by the first term on the right-hand side, the convective-diffusive term. This equation defines an exponential temperature profile in the inert preheat zone that has a characteristic length scale, x_c .

The oscillatory solution, as in the nonlinear case, relies on the steady-state mass flux and surface temperature laws [Eqs. (7) and (8)] and the integral energy equation [Eq. (9)]. The solution is best obtained using Jacobian transformations.^{16,17} The important practical result is that in the linear case the steady-state information appears as sensitivity parameters, that is, the partial derivatives of Eqs. (7) and (8): k , r , v , δ , v_q , and δ_q (see Nomenclature). The oscillatory solutions for pressure-perturbed burning (constant radiant flux) and radiation-perturbed burning (constant pressure)¹⁷ are

$$R_p = \frac{v + \delta(\lambda - 1)}{\lambda r + k/\lambda - (r + k) + 1 - \frac{k f_r J(\lambda - 1)}{\lambda(\beta + \lambda - 1)}}$$

$$= \frac{nAB + n_s(\lambda - 1)}{\lambda + A/\lambda - (1 + A) + AB - \frac{A f_r J(\lambda - 1)}{\lambda(\beta + \lambda - 1)}} \quad (25a)$$

$$R_q = \frac{v_q + \delta_q(\lambda - 1) - \frac{k f_r J(\lambda - 1)}{\beta + \lambda - 1}}{\lambda r + k/\lambda - (r + k) + 1 - \frac{k f_r J(\lambda - 1)}{\lambda(\beta + \lambda - 1)}}$$

$$= \frac{v_q AB + n_q(\lambda - 1) - \frac{A f_r J(\lambda - 1)}{\beta + \lambda - 1}}{\lambda + A/\lambda - (1 + A) + AB - \frac{A f_r J(\lambda - 1)}{\lambda(\beta + \lambda - 1)}} \quad (25b)$$

Equations (25a) and (25b) assume f_r (the surface reaction layer transmissivity) is a constant parameter. (A recent analysis relaxes this assumption.²¹) The latter form (A , B , n , n_s) was derived under the FM formalism developed in the United

States and Europe,^{6,11} whereas the former (k, r, ν, δ) was derived under the ZN approach in Russia.²¹ The two forms are equivalent mathematically. The relations between the FM and ZN parameters are^{17,18}:

$$A = k/r \quad (26a)$$

$$B = 1/k \quad (26b)$$

$$n = \nu \quad (26c)$$

$$n_s = \delta/r, \quad n_q = \delta_q/r \quad (26d)$$

The ZN definitions are more natural in the sense of being cast as derivatives of the natural dependent variables (r_b and T_s) with respect to changes in the natural independent variables (T_0 , P , and q_r) with the other independent variables held constant, the way a measurement would be conducted.

At this point still no assumption about condensed phase pyrolysis kinetics has been made, although the A parameter is often designated in western literature as $A = (E_s/RT_s)(1 - T_0/\bar{T}_s)$, which depends on Eq. (5) or something similar. However, it is less restrictive to think of A and all of the sensitivity parameters in terms of their mathematical (partial derivative) definitions without introducing a dependence on Eq. (5). In principle, the steady-state sensitivity parameters can be determined completely experimentally if sufficiently extensive and accurate measurements of regression rate and surface temperature are made under steady-state conditions. This would allow at least numerical specification of the functions represented by Eqs. (10) and (11) and from there the sensitivity parameters, k, r, ν, δ, ν_q , and δ_q or A, B, n, n_s, ν_q , and n_q . However, in practice accurate measurement of \bar{T}_s is much more difficult than r_b . In fact, as will be discussed further, in connection with NC/NG propellants, sufficiently accurate measurement of \bar{T}_s to supply the parameters r, μ , and μ_q (or r, δ , and δ_q) is simply not possible. Therefore, it becomes expedient to consider flame models, at least for the surface pyrolysis zone, to replace the need for reliance on empirical data for r, δ , and δ_q (ZN) or A, n_s , and n_q (FM).

V. Condensed Phase Kinetics (FM)

One of the simplest reported kinetic schemes that meets the QSHOD requirement of surface pyrolysis and includes formal consideration of the species equation is a zero-order, single-step, unimolecular decomposition step with large activation energy E_c ($E_c/RT \gg 1$) and frequency factor A_c . This initial, endothermic, rate-limiting step is presumed to be followed by rapid exothermic reactions such that the net converted chemical to sensible enthalpy per unit mass in the condensed phase, Q_c , is possibly exothermic ($Q_c > 0$). The solution for this scheme was first obtained by Merzhanov and Dubovitskii in 1959 and applied to energetic materials.²² In 1970 it was obtained using activation energy asymptotics (AEA) by Lengelle²³ and was applied to endothermic polymer degradation. The following form, which includes radiation, appeared in 1975, is by Ibiricu and William,²⁴ and was also applied to energetic materials:

$$\bar{m}^2 = \frac{A_c \alpha_c \rho_c^2 C R \bar{T}_s^2 \exp[-(E_c/R\bar{T}_s)]}{E_c [C(\bar{T}_s - T_0) - (Q_c/2) - (f_r q_r / \bar{m})]}$$

$$f_r = \exp(-K_a x_R), \quad x_R = \frac{x_c}{(E_c/2R\bar{T}_s)} \quad (27)$$

A commonly used approximation of Eq. (27) is

$$\bar{m} = A_s \exp[-(E_s/R\bar{T}_s)], \quad E_s \cong E_c/2 \quad (28)$$

These equations are commonly called pyrolysis relations, in reference to the thermal (as opposed to a possibly radical chemistry or photonic) nature of the initiating step(s) in the condensed phase decomposition process. It can be seen that although Eq. (28) with constant coefficient A_s preserves the important Arrhenius exponential temperature dependent term, it ignores the effect of initial temperature, condensed phase heat release, and thermal radiation parameters present in the more comprehensive zero-order pyrolysis relation. These terms (T_0 , Q_c , and q_r) make a significant difference when it comes to sensitivity parameter and unsteady combustion considerations [see Eqs. (31–36)].

A popular modification^{8,11,19,25} of Eq. (28) includes an extra pressure-dependent term:

$$\bar{m} = A_s \bar{P}^{n_s} \exp[-(E_s/R\bar{T}_s)] \quad (29)$$

Inclusion of the term \bar{P}^{n_s} in Eq. (29) can be viewed as a means of compensating for the nonconstant, pre-exponential terms in Eq. (27) that are omitted in Eq. (28).

Note that the factor of two that relates the apparent surface activation energy E_s to the actual bulk activation energy E_c is $E_s \cong E_c/2$.[†] Failure to recognize this factor hindered progress in some cases as attempts were begun to relate apparent activation energies, that is, E_s values obtained from Arrhenius plots, to realistic activation energies (E_c values) corresponding to chemical bond energies, for example, the 40 kcal/mol CO–NO₂ bond energy in NC/NG. This can be seen in most early FM papers where it is apparent by the discussion that the difference between the two is not recognized. With the factor of two included, it is reasonable to expect good agreement between apparent activation energies from Arrhenius plots and bond energies, provided the effective activation energy is determined by the energy of the initial bond scission. (Zenin questions this assumption for NC/NG under combustion conditions as discussed further subsequently.²⁶)

Equation (27) is a particular form for the functionality F_c indicated in Eq. (19). It is based on a particular flame model, zero-order, unimolecular, high-activation energy decomposition. It is written in steady-state form but can be put in unsteady form based on ZN theory [see Eq. (19)] by replacing T_0 with T_{0a} and dropping the overbars,

$$m^2 = \frac{A_c \alpha_c \rho_c^2 C R T_s^2 \exp[-(E_c/RT_s)]}{E_c [C(T_s - T_{0a}) - (Q_c/2) - (f_r q_r/m)]} \quad (\text{unsteady}) \quad (30)$$

Similarly, Eq. (28) would become Eq. (5). An obvious feature of Eq. (28) is that it is the same for both steady and unsteady conditions. There is no T_0 term present. The sensitivity of the condensed phase decomposition process to initial temperature has been lost in the approximation of Eq. (28). Because of the important role of T_{0a} in representing unsteady heat accumulation in QSHOD theory [see Eqs. (14) and (15)], the absence of T_0 in Eq. (28) raises a question about the ability of that relation to accurately represent unsteady combustion.

[†]Lengelle, G., informal communication during AGARD visit to ONERA, 1994.

A primary motivation for introducing a condensed phase kinetics model is the difficulty of measuring sensitivity parameters associated with changes in T_s , that is, r , μ , and δ . Useful analytic relations for these difficult parameters can be obtained by differentiating the steady burning laws. Differentiating the general F_c relation [Eq. (19)], with respect to T_0 gives a relation $r(k)$. Similarly, differentiating F_c with respect to pressure gives relations $\mu(\nu)$ and $\delta(\nu, k)$,

$$\left. \frac{\partial [\text{Eq. (19)}]}{\partial T_0} \right)_{P, q_r} \Rightarrow r(k)$$

$$\left. \frac{\partial [\text{Eq. (19)}]}{\partial P} \right)_{T_0, q_r} \Rightarrow \mu(\nu) \quad \text{or} \quad \delta(\nu, k)$$

For zero-order decomposition (assuming constant Q_c), Eq. (27) gives the $r(k)$ and $\delta(\nu, k)$ relations as¹⁸

$$r = \frac{k \left[2 - \frac{Q_c}{C(\bar{T}_s - T_0)} - f_r J \right] - 1}{(1 - T_0/\bar{T}_s) \left(1 + \frac{E_c}{2R\bar{T}_s} \right) \left(2 - \frac{Q_c}{C(\bar{T}_s - T_0)} - 2f_r J \right) - 1} \quad (31)$$

$$\delta = \frac{-\nu}{(1 - T_0/\bar{T}_s) \left(1 + \frac{E_c}{2R\bar{T}_s} \right) \left(2 - \frac{Q_c}{C(\bar{T}_s - T_0)} - 2f_r J \right) - 1} \quad (32)$$

$$\delta_q = \frac{-\nu_q + k f_r J}{(1 - T_0/\bar{T}_s) \left(1 + \frac{E_c}{2R\bar{T}_s} \right) \left(2 - \frac{Q_c}{C(\bar{T}_s - T_0)} - 2f_r J \right) - 1} \quad (33)$$

For most conditions (when values of Q_c , E_c , and T_s thought to be realistic are substituted), the right-hand side denominator in Eqs. (31–33) and the r parameter in Eq. (31) are usually positive. The pressure sensitivity parameter (or pressure exponent) ν is also usually positive (except for plateau or mesa burning regions). Therefore, the Jacobian parameter δ and the n_s parameter are usually negative for zero-order decomposition,

$$n_s = \frac{\delta}{r} = \frac{-\nu}{k \left[2 - \frac{Q_c}{C(\bar{T}_s - T_0) - f_r J} \right] - 1} < 0 \quad (\text{except plateau/mesa}) \quad (34)$$

In contrast, differentiation of Eq. (28) leads to the result that the Jacobian parameters δ , δ_q , and n_s are zero,

$$r = \frac{k}{(E_s/R\bar{T}_s)[1 - (T_0/\bar{T}_s)]}, \quad A = \frac{k}{r} = \frac{E_c}{2R\bar{T}_s} \left(1 - \frac{T_0}{\bar{T}_s} \right) \quad (35)$$

$$\delta = \delta_q = 0 \quad (36)$$

A zero Jacobian parameter results whenever a unique functional relation exists between the two dependent variables, $\bar{m}(\bar{T}_s)$; Eq. (28) is a special case of such a relation. To what degree such a relation might hold for any material is a matter of controversy. Russian investigators have conducted extensive thermocouple measurements, particularly with NC/NG propellant, and concluded that such a relation holds within the uncertainty of the measurement.^{26,27} However, that uncertainty is large enough to allow deviations from zero Jacobian that are significant in terms

of response function prediction. This point is discussed further in connection with experimental NC/NG results.

Differentiation of Eq. (29) is a bit more problematic. The n_s parameter that appears in Eq. (29) is not exactly the same as the ZN n_s parameter $(\partial \ell_n \bar{m} / \partial \ell_n \bar{p})_{T, q_r}$, unless n_s is constant. In general, none of the sensitivity parameters are constant except as an approximation over limited intervals of P , T_0 , and q_r . This ambiguity in n_s definition has resulted in some confusion in the literature²⁸ that can be readily resolved by recognizing the difference between the ZN and FM definitions of n_s . For further elaboration see Ref. 29.

In summary, Eqs. (31–34) are useful for estimating the sensitivity parameters that are difficult to measure accurately (r , δ , and δ_q) from those that are easier to measure (k , ν , and ν_q) and from global parameters for which reasonable estimates can be made (E_c and Q_c). In principle, complex kinetics can also be incorporated into the ZN formalism. Even with a complex kinetics mechanisms it should be possible to obtain mathematical relations (albeit numerical) analogous to Eqs. (30–34) and a functional relation that is the numerical equivalent of F_c in Eq. (19).

VI. Gas Phase Kinetics (FM)

For a more complete FM model and to remove the need for reliance on measured data for k , ν , and ν_q , gas phase kinetics models can be introduced. Gas phase kinetics calculations have progressed further than condensed phase kinetics; calculations with mechanisms involving dozens of species and hundreds of reactions are now done routinely. The motivation for complex kinetics is better accuracy than simple kinetics, i.e., predictions that more closely match experimental observations. Therefore, in principle, it is expected that numerical versions of F_g [Eq. (20)] could be generated from complex kinetics calculations that predict experimental response at least as well as if not better than that with simple kinetics. However, a recent workshop³⁰ on predicting sensitivity parameters and linear quasi-steady response functions for HMX and RDX showed that where reliable response measurements were available, for example, HMX, complex kinetics predictions were still less accurate than those of single-step kinetics. Presumably this situation will change as models with complex chemistry improve. However, even then, as a price for higher accuracy and resolution, complex kinetics calculations will always be more computationally costly than simple kinetics, and there will always be a need for simplified kinetics in large-scale, for example, motor environment, calculations.

To illustrate the procedure for including gas phase kinetics, the example of a single-step, bimolecular reaction is presented with activation energy E_g , prefactor B_g , and chemical-to-sensible enthalpy per unit mass Q_g . In the limit of a high-activation energy reaction the resulting relation for F_g [Eq. (19)] is

$$\bar{m}^2 = \frac{2k_g B_g W^2 C \bar{T}_f^4 \bar{P}^2}{E_g^2 Q_g^2} \exp\left(\frac{-E_g}{R \bar{T}_f}\right)$$

$$\bar{T}_f = T_0 + \frac{1}{C} \left[Q_c + Q_g + \frac{\bar{q}_r}{\bar{m}} \right], \quad \frac{E_g}{RT} \gg 1 \quad (37)$$

This relation is designated here as DBW in reference to its early use in QSHOD analysis by Denison and Baum⁶ and Williams's³¹ subsequent theoretical defense

of its use. The low-activation energy limit gives

$$\bar{m}^2 = \frac{4\bar{P}^2 k_g B_g W^2}{C R^2} \frac{1}{(2/\{Q_g/[C(\bar{T}_s - T_0) - Q_c - \bar{q}_r/\bar{m}] - 1\} + 1)^2 - 1} \quad \frac{E_g}{RT} \ll 1 \quad (38)$$

This limit has recently been proposed as giving closer agreement with burning rate and gas temperature observations for HMX and NC/NG than the high- E_g limit.³²⁻³⁴ Equations (37) and (38) play the role of the function F_g denoted in Eq. (20) for the large and small gas activation energy limits, respectively. They can be differentiated and solved simultaneously with the results from F_c [Eqs. (31-33) or (35)] to obtain analytic expressions for the sensitivity parameters.³⁴ This allows calculation of the linear QSHOD response using fundamental material properties, kinetic ($E_{c,g}$), thermochemical ($Q_{c,g}$), thermophysical (C , $k_{c,g}$, and K_a), and environmental parameters (T_0 , P , and q_r).

VII. Experimental and Theoretical Response for NC/NG

In the 1960s, during the development of the T-burner method for measuring pressure-coupled response at the U.S. Naval Weapons Center (NWC), China Lake, extensive testing was conducted on NC/NG propellants.¹⁰ A family of medium energy NC/NG propellants was tested both with and without catalyst and with two different energy contents (%NG). Comparison with these data was the basis for early development of FM-QSHOD models. Although improvements have been made in T-burner testing methods and data reduction since then, NC/NG propellants apparently have not been revisited for extensive pressure-coupled response measurements. Thus, the original NWC data remain as perhaps the best available for comparison for $\text{Re}\{R_p\}$, in spite of relatively large uncertainties in the data.

Figure 1 shows a comparison of the NWC T-burner data over a range of pressures (15-110 atm, excluding plateau pressures) and linear QSHOD model calculations [Eq. (25)] for a variety of sensitivity parameter sets that have been proposed over the years. [The radiation term in Eq. (25) was not included until the 1990s (see Ref. 17) and so this comparison assumes $J = 0$.] A representative value of pressure exponent for nonplateau double-base burning, $n = \nu = 0.7$, was used for each model for uniformity. The experimental data (shaded region) are represented as a rather wide band ($\text{Re}\{R_p\} \sim 2 \pm 1$, $10 < \Omega < 50$, $1000 < f < 5000$ Hz) due to the variability that exists in those measurements. An early paper⁹ reported response values as high as 3, whereas a later report reduced the earlier values by about a factor of two.¹⁰ The main point is that, in spite of the need for updated measurements, the original data indicate that in the range $1000 < f < 5000$ Hz the response is probably not less than 1 and not greater than 3.

Table 1 lists linear QSHOD model parameters from various investigators who have made comparisons with the NWC NC/NG response data. Where a distinction was made in the original reference with respect to pressure, a nominal value of 50 atm was selected for parameter selection; otherwise, no attempt is made here to distinguish with respect to pressure, as the experimental data do not exhibit obvious, general trends. Apparent inconsistencies that appear between the σ_p and

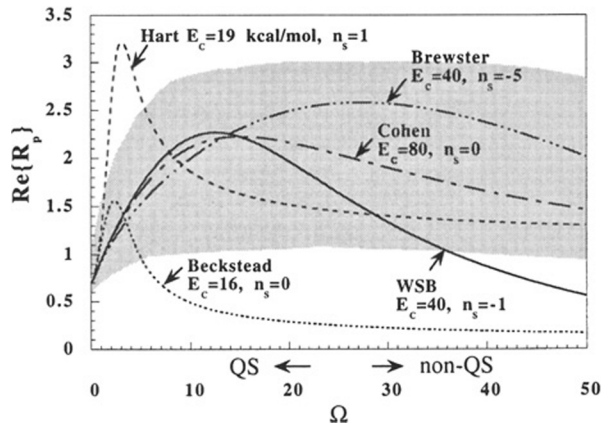


Fig. 1 In-phase component of pressure-coupled response function for NC/NG propellant: shaded region T-burner measurements,^{9,10} and lines QSHOD theory from various investigators^{8,18,34,36,38,39} using parameters in Table 1. Quasi-steady assumption should hold for $\Omega < 25$ for $E_c = 40$ kcal/mol ($\Omega < 10$ for $E_c = 16$ kcal/mol).

$k [= \sigma_p(\bar{T}_s - T_0)]$ values for different investigators in Table 1 are due to different assumptions for surface temperature. Zenin's latest reported measurements suggest 670 K at 50 atm (Ref. 26). (Hart et al.⁸ assumed 750 K.) Still there are noticeable differences in the assumed σ_p (and, therefore, k and B) values. (For more discussion of temperature sensitivity in NC/NG propellants see Ref. 34.) These differences in σ_p are responsible for part of the response differences noted below. However, the assumed values for n_s and E_c also account for a significant part of the differences between response functions discussed subsequently.

The Hart et al.⁸ theoretical curve is one of the first published attempts to apply FM-QSHOD theory to NC/NG T-burner data. Initial attempts using Eq. (28) ($n_s = 0$) gave a response that was generally too low over most of the frequency range measured (similar to Beckstead's curve). In an attempt to increase the response at high frequency, the pressure-dependent term with $n_s = 1$ was added to

Table 1 Linear QSHOD modeling parameters for NWC NC/NG T-burner pressure-coupled response measurements¹⁰ ($n = \nu = 0.7$); see Fig. 1

Reference	Year	k	r	δ	A	B	n_s	E_c , kcal	$r(k)$ Eq.	σ_p , %/K
Hart et al. ⁸	1966	1.69	0.49	0.49	3.5	0.59	1.0	19	(39)	0.38
Butcher and Beckstead ³⁶ and Erikson ³⁸	1979, 1996	1.49	0.44	0	3.4	0.67	0	16	(35)	0.40
Cohen ³⁹	1985	1.0	0.059	0	17	1.0	0	80	(35)	0.29
Brewster and Son ¹⁸	1995	1.0	0.016	-0.084	62	1.0	-5.2	40	(31)	0.28
WSB ³⁴	1997	1.07	0.058	-0.060	18	0.93	-1.0	40	(31)	0.29

the pyrolysis relation [Eq. (29)] justified by the argument of a heterogeneous surface reaction (autocatalysis). A pre-exponential factor of $\bar{T}_s^{-0.5}$ was also included in Eq. (29), making a slight modification in Eq. (35) as follows:

$$A = k/r = [(E_c/2R\bar{T}_s) - \frac{1}{2}][1 - (T_0/\bar{T}_s)] \quad (39)$$

By this change the high-frequency response increased but so did the low-frequency response, to unrealistically high values. An additional possible theoretical problem is that the assumed condensed phase decomposition activation energy $E_s = 9.4$ kcal/mol ($E_c = 19$) is about a factor of two lower than the strength of the CO-NO₂ bond (40 kcal/mol), thermal homolysis of which is now widely believed to be the initiating step for NC/NG decomposition.³⁵ Zenin²⁶ argues that under combustion conditions, the rapid NO₂ recombination reactions that immediately follow the initial bond scission alter the effective E_c value, reducing it by a factor of two to 21 kcal/mol. Lengelle et al.,³⁵ however, presents a comprehensive review of evidence by several researchers, including ignition data, that supports the 40 kcal/mol value. This point seems to require further investigation to explain the various, apparently contradictory, observations.

In 1979 Butcher and Beckstead³⁶ made comparisons with the NWC data using Eq. (28) ($n_s = 0$) and an activation energy $E_s = 8.1$ kcal/mol ($E_c = 16$), even lower than that of Hart et al.⁸ This E_c value is also arguably low as noted earlier. The predicted response falls below the measurements at rather low frequencies ($\Omega \sim 5$: $f \sim 1300$ Hz at 50 atm for propellant JPN, $r_b = 1.3$ cm/s; $f \sim 500$ Hz at 50 atm for propellant N4, $r_b = 0.75$ cm/s). It was suggested³⁶ that this discrepancy was due to breakdown of the quasi-steady assumption, which is expected to occur at some point as frequency increases. However, it now seems clear that the discrepancy in the prediction occurs at lower frequencies than where the quasi-steady approximation should fail. At moderate (not extremely high) pressures, theoretical analysis suggests the quasi-steady assumption breaks down in the condensed phase decomposition layer before (at lower frequency than) it does in the gas phase.¹³ The characteristic frequency of the condensed phase reaction layer from AEA theory is²⁴

$$f_R = f_c(E_c/2R\bar{T}_s), \quad f_c = \bar{r}_b^2/\alpha_c \quad (40)$$

Based on this scaling (with $E_c = 40$ kcal/mol) and with support from laser-recoil measurements,³⁷ it has recently been suggested that a conservative estimate of the beginning of breakdown of the quasi-steady assumption is $f \sim f_R/4$. Thus, for $E_c = 40$ kcal/mol, the quasi-steady assumption should be valid up to a nondimensional frequency of about 25,

$$\Omega_{QSC} = \frac{2\pi(f_R/4)}{f_c} = \frac{\pi}{2} \frac{E_c}{2R\bar{T}_s} \approx 25 \quad (41)$$

(At 50 atm, $f_R/4$ is 6300 Hz for JPN and 2100 Hz for N4.) For $E_c = 16$ kcal/mol, the quasi-steady assumption should be valid up to $\Omega_{QSC} \approx 10$. The drop off in predicted response at $\Omega \sim 5$ in Beckstead's^{36,38} data poses a theoretical problem for this set of parameters if the estimate $f \sim f_R/4$ is accepted. Possibly, the low E_c value does also, depending on the resolution of that question. In 1996 Beckstead and Erickson³⁸ reaffirmed this set of parameters for NC/NG.

The next model comparison chronologically is Cohen's³⁹ in 1985. Cohen thought Beckstead's^{36,38} E_c value was too low and raised it to 80 kcal/mol ($E_s = 40$). By doing so Cohen was able to achieve a much smaller r parameter than the previous

cases. The A parameter is, thus, much larger than that of the previous cases (although use of a smaller k parameter helped reduce an otherwise bigger increase in A). Cohen's reduction of the r parameter is the main reason his calculation fits the experimental data so well and suggests that possibly a smaller r value (<0.1) better represents the actual process. However, because of the use of Eqs. (28) and (35) ($n_s = 0$) this reduction in the r parameter was associated with an unrealistically large E_c . There is no theoretical support in the literature for a value as large as 80 kcal/mol. Although Zenin's argument for E_c less than the CO-NO₂ bond energy (40 kcal/mol) based on ensuing (presumably lower activation energy) exothermic reactions is plausible, no analogous chemically based argument has appeared to support an apparent activation energy E_c higher than the CO-NO₂ bond energy, particularly one so much higher. Nonetheless, Cohen³⁹ indicated that the activation energy and other parameters were "well-supported in the literature." One possible explanation for this apparent contradiction is confusion between E_s and E_c , as noted in Eq. (28). An activation energy of 40 kcal/mol was indeed well supported in the literature at that time (see Table 1 in Ref. 35) but this should have been taken as $E_c (=2E_s)$, not E_s . Still, Cohen's parameters (A , B , n , and n_s) give a good fit of the NWC T-burner data. In fact one might question whether the fit is too good, in light of the expectation that the quasi-steady assumption should begin to fail at $\Omega \sim 50$ (for $E_c = 80$ kcal/mol).

In 1995 Brewster and Son¹⁸ applied the more rigorous zero-order decomposition analysis [Eq. (27)] within the linear QSHOD theory framework and found that it could fit the NWC data over the appropriate frequency range and do so with plausible values for all of the parameters, including E_c . Instead of Eq. (35), Eq. (31) was used as the $r(k)$ relationship. This requires an assumption for the condensed phase heat release Q_c and based on Zenin's thermocouple measurements²⁷ values near 100 cal/g, varying slightly with pressure, were assumed (later Q_c was reduced; see subsequent discussion). Use of the zero-order decomposition relation [Eq. (27)], also suggested the plausibility of a negative Jacobian parameter [Eq. (34)].¹⁸ The idea of negative Jacobian values was subsequently endorsed by De Luca.⁴⁰ Previously, negative Jacobians were generally thought to be physically unrealistic, for example, see equivalent Q_1 parameter in Ref. 19, or at least only small positive n_s values had been considered.¹¹ Negative n_s means that burning rate decreases as pressure increases at constant T_s , not constant T_0 . In Eq. (29), negative n_s means that as pressure increases at constant T_0 , T_s increases enough that the Arrhenius term $\exp(-E_s/RT_s)$ increases faster than the pressure term \bar{P}^{n_s} decreases such that burning rate still increases. Negative n_s also partially explains how linear instability [$\text{Re}\{R_p\} > 1/\gamma$, see Eq. (4)] can happen even in mesa ($\nu < 0$) regions [see Eqs. (25a) and (34)]. In summary, zero-order decomposition, [Eq. (27)] resolves several problems in QSHOD theory and makes possible a better fit of the NWC T-burner data with realistic parameters by allowing smaller r parameters and larger A parameters than had previously been thought possible. As with Cohen's model,³⁹ though, it might be argued that this fit¹⁸ is too good, in light of the expected decomposition layer non-quasi-steadiness (non-QSC) beginning at about $\Omega \sim 25$.

The four QSHOD models discussed are really hybrid FM-ZN models. As noted earlier, a hybrid FM-ZN approach is probably more practical than pure FM or ZN, and this seems to have been recognized early on⁵ as witnessed by the model development. This hybrid FM-ZN approach is FM in the sense of using a pyrolysis or F_c relation for the condensed phase to obtain $r(k)$ and $\delta(\nu, k)$ relations [see

Eqs. (19), (27–29), (31–32), (35–36), and (39)] and ZN in the sense of relying heavily on empirical information for ν and k . However, even from the time of Denison and Baum⁶ there have been numerous attempts to construct complete FM models by including a gas phase flame description. Most investigators who have included a gas phase model^{6,39,41,42} have used a large activation energy, single-step model, equivalent to Eq. (37), usually with the pressure exponent reduced to about 0.7 (by arbitrarily reducing the overall reaction order from 2.0 to 1.4) because, for a bimolecular process, Eq. (37) gives $n = 1$ unless there is a strong component of radiative heat flux to the surface. [Note that Eq. (38) for low E_g gives $n < 1$ without adjustment.]

Recently, Ward et al.^{32,33} found that within the framework of single-step kinetics, the low-activation energy limit [Eq. (38)] matched steady-state HMX temperature profiles better than the large activation energy limit [Eq. (37)]. From this they inferred that the near-surface gas phase process had more the nature of a chain reaction mechanism than thermal decomposition. They also found that the combination of this gas phase model with zero-order decomposition (referred to here as the WSB model) matched steady burning rate data for HMX better than other simple (single-step) kinetics flame models. The WSB model was therefore applied to NC/NG propellant data.

Figures 2 and 3 show a comparison of the WSB model³⁴ with the radiation response function (magnitude and phase) as measured by the laser-recoil method.⁴³ The model parameters for Figs. 2 and 3 are $A = 17$, $B = 0.85$, $\nu_q = 0.29$, $n_q = -0.04$, $J = 0.25$, $\beta = 1.7$, $f_r = 0.9$, $\alpha_c = 8e-4$ cm²/s, and $r_b = 0.23$ cm/s. The comparison is favorable, confirming the basic applicability of the WSB model to NC/NG as well as HMX. An effort was made to preserve the same parameters that had been used in comparing with the NC/NG T-burner data.¹⁸ Because the inclusion of a gas phase model imposes additional constraints, this was not entirely possible; nor is it necessarily desirable because the earlier parameters, like any, are subject to question. One notable change is that the condensed phase heat release Q_c

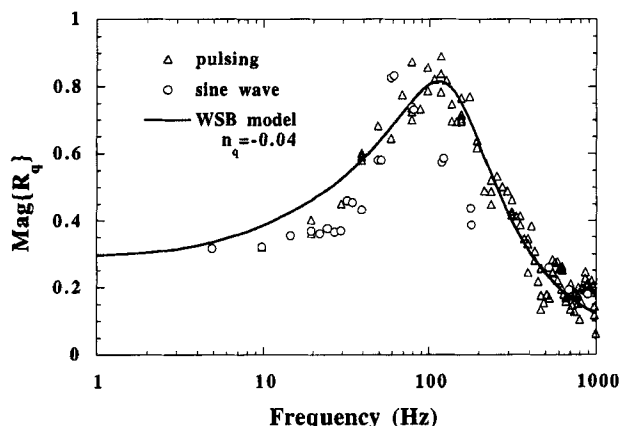


Fig. 2 Magnitude of radiation response function for catalyzed NC/NG propellant N5 (1 atm, 40 W/cm²); CO₂ laser-recoil measurements.⁴³ QSHOD theory with zero-order decomposition and $E_g/RT \ll 1$ (WSB model³⁴). The quasi-steady assumption should hold for $f < 250$ Hz ($f_R = 1000$ Hz).

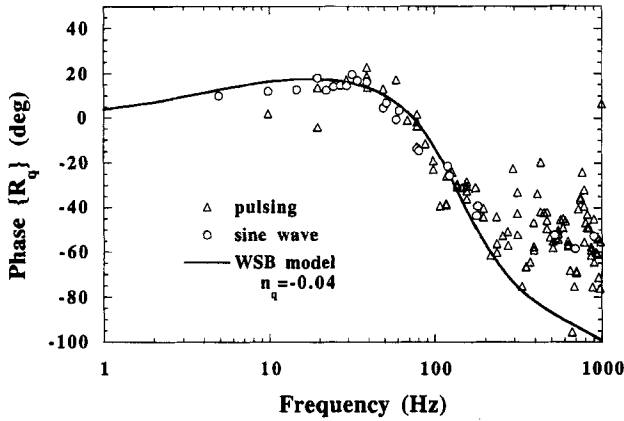


Fig. 3 Phase of radiation response function for catalyzed NC/NG propellant N5 (1 atm, 40 W/cm²); CO₂ laser-recoil measurements.⁴³ QSHOD theory with zero-order decomposition and $E_g/RT \ll 1$ (WSB model³⁴). The quasi-steady assumption should hold for $f < 250$ Hz ($f_R = 1000$ Hz).

was reduced from 100 to 40 cal/g. This may seem a small change, but the calculated response is quite sensitive to it. Figure 3 shows that the quasi-steady prediction of phase begins to deviate from the measurements at about 200 Hz. According to the conservative estimate discussed earlier, the QSC assumption should begin to fail at about $f_R/4 = 250$ Hz. The measurements show that quasi-steady theory over-predicts the actual phase lag. The effect this has on the in-phase (real) component of the response ($\text{Re}\{R_q\} = |R_q| \cos \phi$) is that quasi-steady theory predicts $\text{Re}\{R_q\}$ falls off faster with increasing frequency than it actually does, as shown in Fig. 4. (Note that the model parameters in Fig. 4 are the same as in Figs. 2 and 3.) With this trend in mind, we return to the pressure-response prediction.

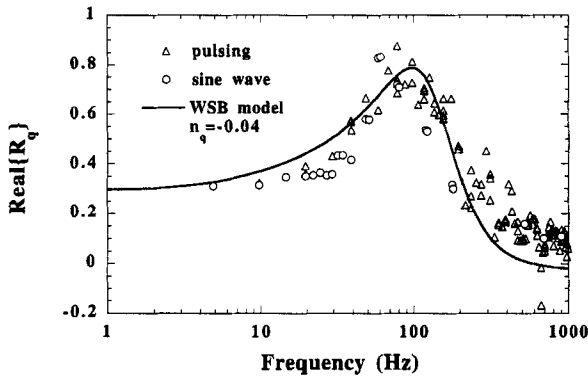


Fig. 4 Real part of radiation response function for catalyzed NC/NG propellant N5 (1 atm, 40 W/cm²); CO₂ laser-recoil measurements.⁴³ QSHOD theory with zero-order decomposition and $E_g/RT \ll 1$ (WSB model³⁴). The quasi-steady assumption should hold for $f < 250$ Hz ($f_R = 1000$ Hz).

The pressure-coupled response based on the new (WSB) NC/NG parameters³⁴ (Table 1) is shown in Fig. 1. This result shows good agreement with the T-burner data for $\Omega < 25$, but underpredicts in-phase response for $\Omega > 25$. This type of discrepancy is what one would expect if breakdown of the quasi-steady assumption had the same effect on pressure response as that observed in the radiation-response measurements (Figs. 2–4). To the degree this interpretation is correct, the newer parameters based on the WSB model (lower Q_c) may be more correct than the older ones even though the pressure response agreement looks worse (Fig. 1). On the other hand, the WSB parameters and the WSB model itself need further scrutiny. Overall, there is a need for further investigation of modeling assumptions, conditions of applicability, and accuracy. New response measurements of NC/NG would be helpful.

Recently researchers at China Lake have been conducting T-burner measurements⁴⁴ for homogeneous energetic materials (HMX, RDX, and AP) to obtain unsteady combustion data for comparison with the complex kinetics models that are being developed. Of these, the results for HMX have been the most reliable. (AP had problems with TCP impurity and RDX results have been scattered, perhaps due to melt layer effects. Attempts to interpret laser-recoil response data for RDX in terms of QSHOD theory at 1 atm (Ref. 37) led to the conclusion that at 1 atm the presence of a thick, bubbly melt layer on the surface invalidated the quasi-steady condensed phase reaction layer assumption.)

VIII. Experimental and Theoretical Response for HMX

T-burner response measurements for HMX made at the end of 1997⁴⁴ provided a unique opportunity to test unsteady combustion models, including linear QSHOD theory. The opportunity was unique because no response function data for HMX had been reported previously that might influence predictions; at the same time several advancements were being reported in HMX combustion modeling, some with complex gas phase kinetics^{45–47} and some with simple kinetics.^{32,33,38,48–50} A workshop³⁰ was organized to take advantage of this situation. One of the workshop objectives was to make blind calculations of the linear pressure-coupled response for HMX and RDX at the same pressures that were planned for T-burner tests and then make comparisons after the measurements were conducted. The WSB model, which had shown promise in describing steady-state burning rate and temperature profile data, was tested for its ability to predict pressure-coupled response.

The strategy used to develop the quasi-steady WSB pressure response prediction was first to compare with measured radiation response at 1 atm, determine model parameters that worked well at 1 atm, and then make any parameter adjustments for higher pressure that seemed warranted based on what was known about HMX flame structure. The first HMX laser-recoil response data that were available for comparison were from the U.S. Naval Air Warfare Center⁵¹ and Pennsylvania State University.⁵² Those data (which did not quite agree between the two sources) were used for comparison until in-house measurements at the University of Illinois, Urbana–Champaign, were available.⁵³ The comparison with laser-recoil radiation response^{50,53} is shown in Fig. 5. The calculated condensed layer characteristic frequency is $f_R = 130$ Hz; therefore, the observed deviation in phase at about 40 Hz is expected as noted earlier. The magnitude is underpredicted, but there was uncertainty about how closely the measurements actually approached

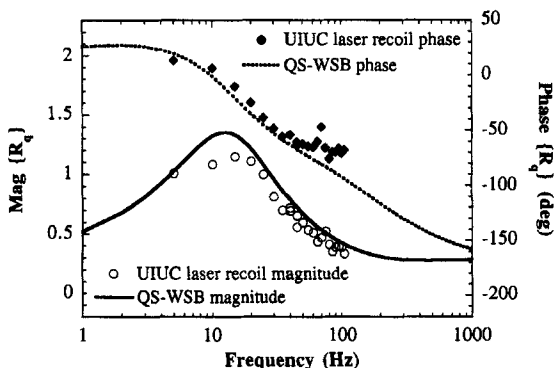


Fig. 5 Radiation response function for HMX (1 atm, 35 W/cm²); CO₂ laser-recoil measurements.⁵³ QSHOD theory with zero-order decomposition and $E_g/RT \ll 1$ (WSB model⁵⁰). The quasi-steady assumption should hold for $f < 32$ Hz ($f_R = 130$ Hz).

the linear limit. The effect of nonlinear response on magnitude is generally to lower the response near the peak. Therefore, the slight mismatch in measured and calculated response magnitude is explainable in terms of uncertainty over the degree of linearity of the measured response. In such a situation, erring on the high side with the response magnitude prediction is better than erring on the low side. The model parameters are $A = 18$, $B = 0.85$, $\nu_q = 0.52$, $n_q = -0.54$, $J = 0.48$, $\beta = 57$, $f_r = 0.03$, $\alpha_c = 8e-4$ cm²/s, and $r_b = 0.08$ cm/s.

To extend the WSB response prediction from radiation response at 1 atm to pressure response at 10 atm and higher, a few flame parameter adjustments were warranted. HMX has a two-stage flame structure that is not readily apparent, that is, noticeable in the temperature profile, at pressures above a few atmospheres (the two-stages merge together) but is apparent at 1 atm with laser augmentation. At 1 atm with sufficient external radiant flux, the second-stage flame is delayed or does not form. Accordingly, the gas phase heat release parameter Q_g in the WSB model (which assumes only a single-step gas reaction) was increased from 250 to 758 cal/g at higher pressures to account for this observed change in flame structure. The condensed phase heat release was increased slightly, from 40 to 60 cal/g (Zenin's thermocouple measurements have suggested an increase in Q_c with pressure⁵⁴), and the gas phase prefactor was adjusted to match steady burning rate. The pressure response prediction was made based on these adjustments.^{30,50} T-burner measurements were made later that year.⁴⁴ The comparisons³⁰ are shown in Fig. 6 for two pressures (nominally 10 and 70 atm). The quasi-steady assumption should hold for $f < 225$ Hz at 10 atm ($f_R = 900$ Hz) and $f < 5500$ Hz at 70 atm ($f_R = 22,000$ Hz). For the low-pressure (14-atm) T-burner data, only the lowest frequency data are within the expected quasi-steady frequency region. The higher frequency data points fall outside the quasi-steady region and, as expected, are underpredicted in magnitude by the QSHOD model, according to the same trend exhibited in Fig. 4 for NC/NG. For the high-pressure (68-atm) T-burner data, all of the measurements fall within the expected quasi-steady frequency range. The model fit is good, perhaps too good, that is fortuitous, but encouraging nonetheless. The highest frequency points appear to be slightly underpredicted. The same comment made in connection with Fig. 5 may be in order here: The tendency with

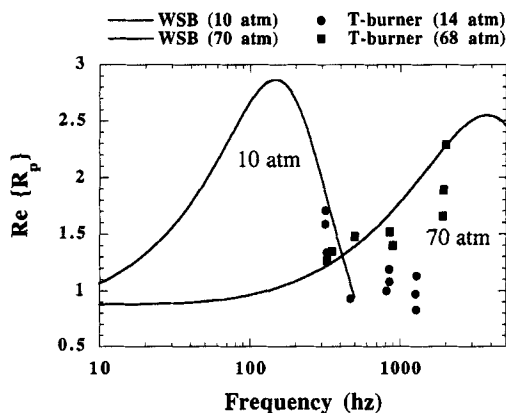


Fig. 6 In-phase component of pressure-coupled response function for HMX. Data points represent T-burner measurements⁴⁴; lines are QSHOD theory with zero-order decomposition and $E_g/RT \ll 1$ (WSB model^{30,50}), predicted before measurements. The quasi-steady assumption should hold for $f < 225$ Hz at 10 atm ($f_R = 900$ Hz) and $f < 5500$ Hz at 70 atm ($f_R = 22,000$ Hz).

linear response measurements, if anything, is to underrepresent the magnitude of the response peak due to nonlinear behavior.

The HMX pressure response data are replotted in Fig. 7 vs nondimensional frequency. To convert dimensional frequency f to nondimensional frequency Ω , a thermal diffusivity value of $8e-4$ cm²/s was used. (Recent measurements of HMX by Parr and Hanson-Parr⁵⁵ indicate a value of $2.5e-3$ cm²/s at room temperature, decreasing to $1.5e-3$ at 170°C. The surface temperature is 400–450°C so that the average temperature in the unsteady solid heated layer is about 250°C.) The only other reported predictions of HMX pressure response made before the 1997 T-burner measurements [Beckstead and Erickson³⁸ (BE)] are also shown in Fig. 7.

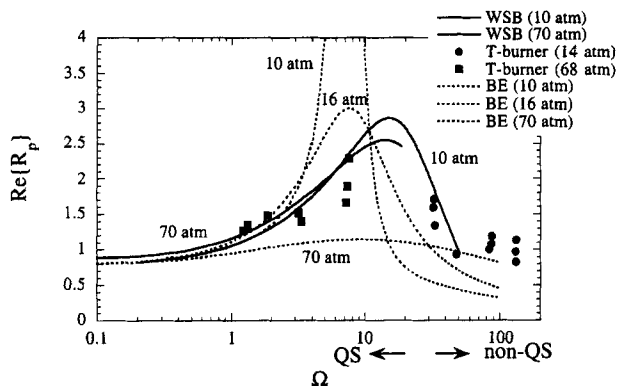


Fig. 7 In-phase component of pressure-coupled response function for HMX. Data points represent T-burner measurements⁴⁴; lines are QSHOD theory predictions made before measurements. —, WSB model^{30,50} and - - -, BE.³⁸ Parameters are listed in Table 2; quasi-steady assumption should hold for $\Omega < 25$.

Table 2 Linear QSHOD modeling parameters for NAWC HMX T-burner pressure-coupled response measurements⁴⁴ ($n = \nu = 0.8$); see Figs. 6 and 7

Method	P , atm	k	r	δ	A	B	n_s	E_c , kcal	$r(k)$ Eq.	σ_p , %/K
BE 1996 ³⁸	10–70	0.5–2.5	0.05–0.27	0	9.3–9.5	0.4–2.0	0	37 ^a	(35)	0.35–0.11
	10	1.6	0.17	0	9.4	0.63	0	—	—	—
	16	1.3	0.13	0	9.4	0.79	0	—	—	—
	70	0.5	0.05	0	9.4	2.0	0	—	—	—
WSB	10	1.07	0.05	−0.061	21	0.93	−1.2	42	(31)	0.26
1997 ^{30,50}	70	0.99	0.046	−0.065	21	1.0	−1.4	42	(31)	0.20

^aThis value of E_c is not compatible with the listed values of A (~ 9.4) for \bar{T}_s of order 700 K, according to Eq. (35) (which relation seems implied by the use of $n_s = 0$); $E_c \sim 46$ kcal/mol would be compatible.

The linear response parameters used for both WSB and BE are listed in Table 2. The BE parameters are based on a hybrid FM–ZN prediction with Eqs. (28) and (35) used for the pyrolysis reaction ($n_s = 0$) and estimates for ν and k based on measurements. The predicted BE pressure variation in Fig. 7 is too strong, with peak response overpredicted at low pressure and underpredicted at high pressure. It is important to note that the predictions of Fig. 7 were made before the response measurements had been conducted. Obviously expectations for agreement cannot be as high when making blind predictions as when the desired result is known beforehand. Nevertheless the exercise of blind prediction is useful. One conclusion that can be drawn from this exercise is that even when experimental data are relied on for temperature sensitivity there is enough uncertainty and possibly even systematic error present to significantly affect the predicted response. A gas phase flame model can be a useful tool in conjunction with sensitivity parameter measurements for predicting unsteady response if the model reflects flame behavior sufficiently well. Another conclusion that carries over from the NC/NG comparisons is that Eqs. (28) and (35) ($n_s = 0$) are not as representative of the process as Eqs. (27) and (31) ($n_s \neq 0$) and not as useful for quantitative linear response prediction.

Predictions relevant to the quasi-steady response of HMX were also made based on detailed chemical kinetics models in connection with the workshop mentioned earlier.³⁰ The results showed that response predictions based on sensitivity parameters from detailed chemistry models underpredicted measurements by about a factor of two over the expected QSHOD frequency range. This was primarily because the predicted temperature sensitivity parameters were outside the range of measured values. Ultimately one would expect detailed chemistry models to be able to predict flame speed or burning velocity (including sensitivity to environmental parameters) at least as accurately as reduced or simplified chemistry models do, as has been demonstrated in the hydrocarbon combustion literature (for example, see Ref. 56). In fact, recent revised calculations⁵⁷ show improvement in calculated pressure response for HMX (although radiation response is off). Development of a new complex chemical mechanism is a formidable challenge. It would seem that the challenge of detailed combustion chemistry modeling for HMX and RDX cannot yet be considered a solved problem.

As for simplified FM–ZN QSHOD response modeling, the results of the WSB model are encouraging. The agreement in Fig. 7 may be partially fortuitous.

However, it seems clear that quasi-steady response modeling is a useful endeavor for investigating and validating combustion mechanisms and modeling assumptions for homogeneous solid energetic materials and propellants.

IX. Non-QSHOD Response

Progress in understanding propellant combustion response under non-QSHOD conditions lags behind that for QSHOD conditions considerably. Nevertheless, a few efforts have been made and some progress can be reported.

A. Homogeneous, Non-Quasi-Steady Response

As perturbation frequency increases, it is expected that the assumptions of QSC zone and QSG zone will break down. What seems not to be generally recognized is that for most propellants at pressures of interest quasi steadiness will probably break down in the condensed phase reaction zone before it does in the gas phase.¹³ (The possibility of condensed phase reaction zone unsteadiness was considered in the early analysis of Ref. 5 and neglected because the assumed $E_c = 100$ kcal/mol value was too high. Ironically, most later analyses that reduced E_c to more realistic values did not revisit the QSC assumption.) The frequency for QSC breakdown has been estimated³⁷ as already noted: $f \sim f_R/4$. This results in a simple relation between nondimensional decomposition activation energy and nondimensional frequency for quasi-steady behavior [Eq. (41)]. For typical E_c and T_s values (40 kcal/mol, 700 K) this corresponds to a nondimensional frequency of about 25.

The effect of breakdown of the QSC reaction zone assumption has been investigated for limited conditions (radiation-driven burning).⁵⁸ The primary effects were to reduce the magnitude of the quasi-steady response near the peak and increase the phase in the high-frequency (phase lag) region. Comparisons between QSHOD modeling and radiation response measurements have manifested the latter behavior (reduced phase lag at higher frequencies) in NC/NG and HMX as already noted. One of the conclusions⁵⁸ was that the criterion (in terms of activation energy) for achieving a certain degree of accuracy in predicting burning rate via AEA, that is, Eqs. (27) and (30), is more stringent for unsteady conditions than steady.

Non-quasi-steady gas calculations have been reported by Tien⁵⁹ and Clavin and Lazimi.²⁵ Both papers assumed a large activation energy single-step gas flame. Tien's method⁵⁹ was numerical and Clavin and Lazimi's²⁵ analytical (AEA). In both cases, gas phase unsteadiness was shown to give a secondary, high-frequency response (above the low-frequency solid thermal relaxation or QSHOD response). Also gas phase unsteadiness was shown to affect the low-frequency response more as the ratio of solid-to-gas density decreased, that is, for increasing pressure. Beyond these similarities, Clavin and Lazimi's paper offers a comparison of their results with Tien's.⁵⁹ In his Fig. 3, Tien claims that for his low-pressure (high ρ_s/ρ_g) case, the low-frequency [quasi-steady (QS)] region of the curve "agrees quite closely with the results of Denison and Baum," which is the quasi-steady case, (although the QS curve is not shown). Such agreement would be expected at high ρ_s/ρ_g , when the two response peaks (the low-frequency solid phase peak and the high-frequency gas phase peak) are widely separated in frequency and relatively

independent. Clavin and Lazimi's²⁵ Fig. 9 includes the QS curve and shows that Tien's curve⁵⁹ is actually not close, whereas their own AEA result,²⁵ for the same parameters, is close at low frequencies. Clavin and Lazimi question such a large discrepancy between the asymptotic results (both QS and non-QS) and Tien's numerical curve,⁵⁶ implying that the assumed nondimensional gas activation energy $E_g/RT_f = 10$ should be large enough to expect good agreement with the AEA analytic results, which are based on only the leading term in the asymptotic expansion. This discrepancy appears to be unresolved and needs further explanation. Perhaps one possible explanation is the idea noted earlier in connection with investigation of non-QSC effects,⁵⁸ extended to the QSG assumption. The idea is that the criterion (in terms of activation energy) for achieving a certain degree of accuracy in predicting burning rate via AEA is more stringent for unsteady conditions than steady. Also note that in both of these papers,^{25,58} although the QSG assumption was relaxed, the QSC assumption was retained. However, other than at extremely high pressures, it is expected that the QSC assumption will break down first, that is, at lower frequency, before the QSG assumption. Therefore if non-QSG effects are to be investigated, non-QSC effects should probably be included.

One other non-QSG analysis that should be noted is that of Hart and McClure.⁵ Hart and McClure's development is semiphenomenological, similar to the ZN method, and makes use of ZN-like variable transformations and assumptions. In particular they treat surface temperature gradient f_s like an independent variable and assume unsteady mass flux to be a function of f_s . No particular gas flame model, for example single-step, high-activation energy, is assumed. Rather, steady-state burning information (pressure and temperature sensitivity) is used. This achieves the unique result of a non-QSG model that does not rely on a particular assumed gas flame model. The analysis is, however, quite complicated mathematically and difficult to compare with the conventional QSHOD model. As noted in the Introduction (and also by Culick¹¹) one problem with Hart and McClure's calculations⁵ was an assumed pyrolysis activation energy $E_c = 100$ kcal/mol ($E_s = 50$) that has since been recognized as being too large. A value of $E_c = 40$ kcal/mol ($E_s = 20$) might have led to different conclusions, in particular the need to relax the QSC assumption before QSG. It also might have resulted in better agreement with double-base propellant T-burner response data. A thorough re-examination of the original Hart and McClure approach in light of recent developments such as negative Jacobians and zero-order decomposition seems in order. (Ironically, Hart and McClure initially considered zero-order decomposition in doing timescale estimates but did not carry the full expression throughout their analysis.)

It is useful to have a criterion for estimating the QSG breakdown, similar to the QSC criterion $\Omega_{QSC} \sim 10-30$. Following the pattern of Eq. (41) the following estimate can be made:

$$\Omega_{QSG} = \frac{2\pi(f_g/4)}{f_c} \approx \frac{f_g}{f_c} = \frac{\bar{u}_g/x_g}{\bar{r}_b/x_c} = \frac{\rho_c}{\bar{\rho}_g} \frac{x_c}{x_g} \sim \frac{\rho_c}{\bar{\rho}_g} \quad (42)$$

The bar over the gas velocity and density terms signifies not only a temporal average but also a spatial average over the gas zone between the surface, T_s , and the burned gas, T_f region. The dominant term is the solid-to-gas density ratio, which can vary from 1000 at low pressures to 10 at high pressures. The ratio x_c/x_g is of order one and is relatively independent of pressure because both x_c and x_g decrease with increasing pressure at about the same rate (at least relative

to the strongly pressure-dependent gas density term). The two limiting single-step models, Eqs. (37) (DBW, $E_g/RT \gg 1$) and (38) (WSB, $E_g/RT \ll 1$) provide useful estimates for x_c/x_g , as well as an interesting contrast. For 10–70 atm, the estimates for x_c/x_g for DBW are 1 to 2 and for WSB, $\frac{1}{4}$ to $\frac{1}{2}$ (Ref. 50). Note that the DBW model predicts QSG breakdown at a frequency that is a factor of four higher than the WSB model. Nevertheless, the QSG breakdown frequency at moderate pressures (for example, density ratio of 100), is significantly higher than the QSC breakdown frequency. Normally, QSC breakdown should be expected to occur before, that is at lower frequency, than QSG breakdown. In attempting to relax the QS assumptions in theoretical analysis if the QSG assumption is relaxed but not QSC, the tacit QSC assumption should at least be acknowledged.

An interesting comparison of non-QSC/non-QSG response with non-QSC/QSG was made⁵⁷ for HMX and RDX. The reported frequencies of breakdown of the QSG assumption agree with the predictions of Eq. (42) to within an order of magnitude and have the same trend with pressure. However, the case of QSC/QSG was not computed numerically. It should be possible to force the QSC condition on the numerical model. The QSC/QSG results should then correspond almost exactly to the ZN-QSHOD results (see Figs. 3 and 4 of Ref. 58) and would be a convincing demonstration of numerical validation of this complex kinetics code.

B. Nonhomogeneous, Quasi-Steady Response

Composite propellants, for example AP/binder, generally have a significant degree of heterogeneity that affects their combustion. Thus, it is questionable as to what degree QSHOD theory will accurately describe their unsteady response. Attempts have been made to interpret composite propellant pressure response in terms of QSHOD theory¹⁹ but the results have not demonstrated the kind of agreement that has been achieved for homogeneous materials. Efforts have also been made using heterogeneous propellant features, for example, multiple QSHOD responses⁶⁰ and heterogeneous flame ideas⁶¹ to model composite propellant response. However, quantitative prediction of observed response behavior has not been reported. A recent such effort⁶¹ acknowledged that failure of the model to correctly predict steady-state sensitivity parameters effectively precluded the possibility of correctly predicting unsteady response. It seems that the next step for advancement with composite propellants is to understand mixtures of binder and fine oxidizer, where the oxidizer particle size is small enough that the gas flame structure is essentially premixed, yet the compositional heterogeneity arising from two components is still present. One example of such an effort is summarized briefly.

In the last few years, measurements of radiation response with binder-rich, monomodal fine-AP/HTPB propellants have demonstrated a prominent secondary (non-QSHOD) response peak.^{43,62} The frequency of this secondary peak decreases with increasing AP particle size, and the peak itself disappears above a certain AP size (around 50 μm at 1 atm). With increasing pressure the second peak frequency increases. The secondary response peak has also been observed in wide distribution bimodal propellants if the pressure is high enough (2 atm). These observations have not been described yet with satisfactory accuracy by any mathematical model, but mechanistic interpretations have been made. The secondary peak has been attributed to time-varying selective or disproportionate pyrolysis of AP ($E_c \sim 29$ kcal/mol) and binder ($E_c \sim 11$ kcal/mol) and the associated

compositional (stoichiometric) fluctuations that occur in the fuel-rich, premixed gas phase reaction zone adjacent to the surface. Low Peclet number (based on AP size) appears to be a requirement of achieving this condition. For AP size below $50\text{ }\mu\text{m}$ (at 1 atm) the Peclet number is small ($Pe < 1$), and the gas flame is premixed (and fuel rich). Flame temperature, flame speed, and conductive heat feedback to the surface are all quite sensitive to perturbations in composition at this off-stoichiometric, fuel-rich condition. Temporal fluctuations in AP/binder decomposition species mass flux result in fluctuations in heat feedback to the surface, creating a feedback loop. This is the basic mechanism for the selective pyrolysis oscillatory response.⁶² The absence of a strong selective pyrolysis response from the fine-AP/binder matrix region in wide distribution bimodal propellant at 1 atm has been attributed to diffusive mixing of gaseous decomposition species between the coarse AP and matrix regions that mitigates the fuel richness of the gas composition issuing from the matrix region. Raising the pressure to as little as 2 atm accelerates the gas phase kinetics enough to restore the necessary fuel richness over the matrix, and the selective pyrolysis response reappears. One important implication of these results is that a strong secondary (non-QSHOD) response peak related to selective or disproportionate ingredient pyrolysis could be expected to occur in wide distribution AP composite propellants even for pressure-coupled response. Another implication is that the normally small density (flame temperature) fluctuation term in Eq. (4) could become significant.

X. Conclusions

For a few homogeneous energetic materials (notably NC/NG and HMX), a convergence of evidence has confirmed the basic applicability of classical ZN-FM QSHOD theory within predictable QSC (or at very high pressures, QSG) frequency limitations. Activation energy values for elementary initiation processes, such as bond energies, for example, CO-NO₂ and N-NO₂, can be used in the common FM single-step surface pyrolysis relation with two conditions. These conditions are 1) the factor of two between the apparent Arrhenius surface pyrolysis activation energy and the actual activation energy $E_s = E_c/2$ [see Eqs. (27) and (28)] must be recognized and 2) the common assumption of zero Jacobian parameter ($n_s = 0$) must be relaxed. Use of the rigorous high-activation energy, zero order decomposition relation [Eq. (27)] satisfies both of these conditions. Recent experimental and theoretical results suggest that the QSC assumption breaks down before (at lower frequency than) QSG. AEA theory (for the decomposition zone) suggests that, for typical E_c and T_s values, QSC breaks down at about $\Omega_{\text{QSC}} \sim 25$ according to Eq. (41), and this seems to be confirmed experimentally by laser-recoil response measurements for both NC/NG and HMX. This Ω_{QSC} criterion is relatively independent of pressure. The QSG criterion [Eq. (42)] typically predicts noticeably higher values for Ω_{QSG} , but it varies inversely with pressure. Presumably at high enough pressure, non-QSG effects could overshadow non-QSC effects in determining the response, but there has been no reported experimental verification (in conjunction with theoretical corroboration) of non-QSG effects. Further corroboration of both non-QSC and non-QSG effects on combustion response of homogeneous materials is needed. Also, numerical flame models with a range of complexity of kinetics are needed. As they are developed, these models should be validated both numerically, for example, by demonstrating recovery of

quasi-steady ZN results, and physically by comparison with not just a wide range of steady-state data but also available response measurements. Expectations for combustion response predictions should be at least as high for complex kinetics flame models as for simplified kinetics models.

For heterogeneous energetic materials (composite propellants), there is not a theoretical framework for combustion response yet established that has the support of a wide variety of experimental evidence such as has been demonstrated for homogeneous materials. Promising developments have been made for quasi-homogeneous mixtures containing fine-AP particles. However, more work, both experimental and theoretical, is needed before a theoretical framework is established that can describe even the low-frequency, quasi-steady response. A worthy goal at this point would be to reproduce computationally the observed two-peak response (low-frequency thermal relaxation peak and the secondary, selective pyrolysis peak), including particle size and pressure effects. The next step would be to do coarse, monomodal AP and then bimodal AP. The latter steps will require breakthroughs in heterogeneous propellant combustion modeling and flame theory.

Development and refinement of any scientific theory takes place in parallel with development of experimental measurements, and solid propellant combustion response theory is no exception. Response measurements are being improved in terms of frequency resolution, accuracy, cost, and convenience. This has the positive effect of generating questions about theory and motivating refinements. As response measurements improve or new ones are developed with improved accuracy and resolution, better agreement with theory can be expected. Response features previously thought to be experimental noise or data scatter can be increasingly examined for physical interpretations. Measured combustion response has the potential to become a detailed signature of the combustion process for any given propellant. To achieve this level of diagnostic capability, however, pressure-response measurements are needed with better accuracy, reproducibility, and frequency resolution. Laser-driven response measurements have been useful in this regard. Radiation-response measurements have been a factor in motivating revisions in theory, such as negative Jacobian parameters, zero-order decomposition, QSC breakdown frequency, and criteria for the onset of nonlinear effects (perturbation amplitudes, frequencies, $E_{c,g}$ values), to name a few. Combustion theory itself has also been useful in achieving better mechanistic response understanding as witnessed by the long-standing confusion between E_s and E_c and the way in which AEA theory clarifies this key point. Future progress in understanding energetic materials combustion through the combustion response function will probably continue to come through a combination of experimental, analytical, and computational advancements and continual comparison of the results of these three tools.

Acknowledgments

Collaborations with several former students (Steven F. Son, Atsushi Ishihara, Maria A. Zebrowski, Matthew J. Ward, Paul S. Loner, and Scott R. Hickman) and Jerry C. Finlinson (U.S. Naval Air Warfare Center) and insightful comments of Guy Lengelle (ONERA) have been instrumental in the development of many of the ideas and work presented in this chapter. Support from the Office of Naval Research, Judah Goldwasser, and Ballistic Missile Defense Organization, Juergen Pohlmann (N00014-97-1-0085) is also appreciated.

References

- ¹Tien, J. S., "Transient Burning of Solid Propellants," *Fundamentals of Solid Propellant Combustion*, edited by K. K. Kuo and M. Summerfield, Vol. 90, Progress in Astronautics and Aeronautics, AIAA, Washington, DC, 1984, Chap. 14.
- ²Cohen, N. S., "Effects of Formulation on the Combustion of Solid Propellants," U.S. Air Force Armament Lab., AFAL-TR-88-090, Sept. 1988.
- ³Price, E. W., "L* Instability," *Nonsteady Burning and Combustion Stability of Solid Propellants*, edited by L. De Luca, E. W. Price, and M. Summerfield, Vol. 143, Progress in Astronautics and Aeronautics, AIAA, Washington, DC, 1992, Chap. 9.
- ⁴Zel'dovich, Y. B., "On the Combustion Theory of Powders and Explosives," *Zhurnal Eksperimental'noi i Teoreticheskoi Fiziki (Soviet Physics—JETP)*, Vol. 12, 1942, pp. 498–510 (in Russian).
- ⁵Hart, R. W., and McClure, F. T., "Combustion Instability: Acoustic Interaction with a Burning Propellant Surface," *Journal of Chemical Physics*, Vol. 30, 1959, pp. 1501–1514.
- ⁶Denison, M. R., and Baum, E., "A Simplified Model of Unstable Burning in Solid Propellants," *ARS Journal*, Vol. 31, No. 8, 1961, pp. 1112–1122.
- ⁷Novozhilov, B. V., "Burning of a Powder Under Harmonically Varying Pressure," *Journal of Appl. Mech. Tech. Phys. (Zhurnal Prikladnoi Mekhaniki i Tekhnicheskoi Fiziki)*, No. 6, 1965, pp. 103–106.
- ⁸Hart, R. W., Farrell, R. A., and Cantrell, R. H., "Theoretical Study of a Solid Propellant Having a Heterogeneous Surface Reaction I—Acoustic Response, Low and Intermediate Frequencies," *Combustion and Flame*, Vol. 10, 1966, pp. 367–380.
- ⁹Horton, M. D., and Price, E. W., "Dynamic Characteristics of Solid Propellant Combustion," *Ninth Symposium (International) on Combustion, Academic*, New York, 1963, pp. 303–310.
- ¹⁰Ibiricu, M. M., "Experimental Studies on the Oscillatory Combustion of Solid Propellants," U.S. Naval Weapons Center, NWC TP 4393, China Lake, 1969.
- ¹¹Culick, F. E. C., "A Review of Calculations for Unsteady Burning of a Solid Propellant," *AIAA Journal*, Vol. 6, No. 12, 1968, pp. 2241–2255.
- ¹²King, M. K., "Composite Propellant Combustion Modeling: Pressure-Coupled Response Functions," AIAA Paper 80-1124, 1980.
- ¹³Kuo, K. K., Gore, J. P., and Summerfield, M., "Transient Burning of Solid Propellants," *Fundamentals of Solid Propellant Combustion*, edited by K. K. Kuo and M. Summerfield, Vol. 90, Progress in Astronautics and Aeronautics, AIAA, Washington, DC, 1984, Chap. 11.
- ¹⁴Beckstead, M. W., "A Review of Soviet Combustion and Combustion Instability Work on Solid Propellants," 28th JANNAF Combustion Meeting, CPIA Pub. 573, Vol. 3, 1991, Chemical Propulsion Information Agency, Laurel, MD, pp. 463–492.
- ¹⁵Barrere, M., "Introduction to Nonsteady Burning and Combustion Stability," *Nonsteady Burning and Combustion Stability of Solid Propellants*, edited by L. De Luca, E. W. Price, and M. Summerfield, Vol. 143, Progress in Astronautics and Aeronautics, AIAA, Washington, DC, 1992, Chap. 2.
- ¹⁶Novozhilov, B. V., "Theory of Nonsteady Burning and Combustion Stability of Solid Propellants by the Zel'dovich-Novozhilov Method," *Nonsteady Burning and Combustion Stability of Solid Propellants*, edited by L. De Luca, E. W. Price, and M. Summerfield, Vol. 143, Progress in Astronautics and Aeronautics, AIAA, Washington, DC, 1992, Chap. 15.
- ¹⁷Son, S. F., and Brewster, M. Q., "Linear Burning Rate Dynamics of Solids Subjected to Pressure or External Radiant Flux Oscillations," *Journal of Propulsion and Power*, Vol. 9, No. 2, 1993, pp. 222–232.

¹⁸Brewster, M. Q., and Son, S. F., "Quasi-Steady Combustion Modeling of Homogeneous Solid Propellants," *Combustion and Flame*, Vol. 103, 1995, pp. 11–26.

¹⁹Brown, R. S., and Muzzy, R. J., "Linear and Nonlinear Pressure Coupled Combustion Instability of Solid Propellants," *AIAA Journal*, Vol. 8, 1970, pp. 1492–1500.

²⁰Novozhilov, B. V., *Nonstationary Combustion of Solid Propellants*, Nauka, Moscow, 1973 (English translation AD-767 945, National Technical Information Service, Springfield, VA).

²¹Lee, C., and Kim, S., "Re-Examination of the Response Function of Solid Propellant with Radiant Flux," AIAA Paper 99-0590, 1999.

²²Merzhanov, A. G., and Dubovitskii, F. I., "The Theory of Stationary Combustion in Powder," *Proceedings of the USSR Academy of Science*, Vol. 129, No. 1, 1959, pp. 153–156.

²³Lengelle, G., "Thermal Degradation Kinetics and Surface Pyrolysis of Vinyl Polymers," *AIAA Journal*, Vol. 8, 1970, pp. 1989–1998.

²⁴Ibricu, M. M., and Williams, F. A., "Influence of Externally Applied Thermal Radiation on the Burning Rates of Homogeneous Solid Propellants," *Combustion and Flame*, Vol. 24, 1975, pp. 185–198.

²⁵Clavin, P., and Lazimi, D., "Theoretical Analysis of Oscillatory Burning of Homogeneous Solid Propellant Including Non-Steady Gas Phase Effects," *Combustion Science and Technology*, Vol. 83, 1992, pp. 1–32.

²⁶Zenin, A. A., "Thermophysics of Stable Combustion Waves of Solid Propellants," *Nonsteady Burning and Combustion Stability of Solid Propellants*, edited by L. De Luca, E. W. Price, and M. Summerfield, Vol. 143, Progress in Astronautics and Aeronautics, AIAA, Washington, DC, 1992, Chap. 6.

²⁷Zenin, A. A., and Novozhilov, B. V., "Single-Valued Dependence of the Surface Temperature of Ballistite on the Burning Rate," *Fiz. Goren. Vzryva*, Vol. 9, 1973, pp. 246–249.

²⁸De Luca, L., DiSilvestro, R., and Cozzi, F., "Intrinsic Combustion Instability of Solid Energetic Materials," *Journal of Propulsion and Power*, Vol. 11, 1995, pp. 804–815.

²⁹Brewster, M. Q., and Son, S. F., "Comment on 'Intrinsic Combustion Instability of Solid Energetic Materials,'" *Journal of Propulsion and Power*, Vol. 13, 1997, pp. 454–456.

³⁰Brewster, M. Q., "Workshop Report on Flame Structure and Combustion Modeling of HMX and RDX," *34th JANNAF Combustion Meeting*, CPIA Pub. 662, Vol. 2, Chemical Propulsion Information Agency, Laurel, MD, 1997, pp. 123–140.

³¹Williams, F. A., "Quasi-Steady, Gas-Phase Flame Theory in Unsteady Burning of a Homogeneous Solid Propellant," *AIAA Journal*, Vol. 11, 1973, pp. 1328–1330.

³²Ward, M. J., Son, S. F., and Brewster, M. Q., "Steady Deflagration of HMX with Simple Kinetics: A Gas Phase Chain Reaction Model," *Combustion and Flame*, Vol. 114, 1998, pp. 556–568.

³³Ward, M. J., Son, S. F., and Brewster, M. Q., "Role of Gas- and Condensed-Phase Kinetics in Burning Rate Control of Energetic Solids," *Combustion Theory Modeling*, Vol. 2, 1998, pp. 293–312.

³⁴Brewster, M. Q., Ward, M. J., and Son, S. F., "Simplified Combustion Modeling of Double Base Propellant: Gas Phase Chain Reaction vs. Thermal Decomposition," *Combustion Science Technology*, 2000 (to be published).

³⁵Lengelle, G., Bizot, A., Duterque, J., and Trubert, J. F., "Steady-State Burning of Homogeneous Propellants," *Fundamentals of Solid Propellant Combustion*, edited by K. K. Kuo and M. Summerfield, Vol. 90, Progress in Astronautics and Aeronautics, AIAA, Washington, DC, 1984, Chap. 7.

³⁶Butcher, A. G., and Beckstead, M. W., "The Effect of Propellant Type on Combustion Response Functions," *16th JANNAF Combustion Proceedings*, CPIA Pub. 308, Vol. 3, Chemical Propulsion Information Agency, Laurel, MD, 1979, pp. 527–558.

³⁷Brewster, M. Q. and Schroeder, T. B., "Unsteady Combustion of Homogeneous Energetic Solids," *Challenges in Propellants and Combustion, 100 Years After Nobel*, edited by K. K. Kuo, Begell, New York, 1997, pp. 1082–1092.

³⁸Beckstead, M. W., and Erikson, W. W., "Combustion Instability of Solid Monopropellants," *33rd JANNAF Combustion Meeting*, CPIA Pub. 653, Vol. 2, Chemical Propulsion Information Agency, Laurel, MD, 1996, pp. 145–157.

³⁹Cohen, N. S., "Combustion Response Functions of Homogeneous Propellants," AIAA Paper 85-1114, 1985.

⁴⁰De Luca, L., Verri, M., Cozzi, F., Jalongo, A., and Colombo, G., "A Survey of Pressure-Driven Burning of Energetic Solids with Arrhenius Surface Pyrolysis," *Challenges in Propellants and Combustion, 100 Years After Nobel*, edited by K. K. Kuo, Begell, New York, 1997, pp. 493–514.

⁴¹Beckstead, M. W., "Model for Double-Base Propellant Combustion," *AIAA Journal*, Vol. 18, No. 8, 1980, pp. 980–985.

⁴²Williams, F. A., *Combustion Theory*, 2nd ed., Addison-Wesley, Reading, MA, 1985, pp. 319–322.

⁴³Son, S. F., and Brewster, M. Q., "Unsteady Combustion of Homogeneous Energetic Solids Using the Laser-Recoil Method," *Combustion and Flame*, Vol. 100, 1995, pp. 283–291.

⁴⁴Finlinson, J. C., and Stalnaker, R. A., "Pure Oxidizer T-Burner Pressure Coupled Response for AP, HMX, RDX from 200 to 1000 PSI," *34th JANNAF Combustion Meeting*, CPIA Pub. 662, Vol. 2, Chemical Propulsion Information Agency, Laurel, MD, 1997, pp. 39–47.

⁴⁵Prasad, K., Tanoff, M. A., Smooke, M. D., and Yetter, R. A., "Modeling the Deflagration of HMX at High Pressures," *33rd JANNAF Combustion Meeting*, CPIA Pub. 653, Vol. 2, Chemical Propulsion Information Agency, Laurel, MD, 1996, pp. 557–568.

⁴⁶Davidson, J. E., Jing, Q., and Beckstead, M. W., "Reasons for the Similarities and Differences in the Combustion of RDX and HMX," *33rd JANNAF Combustion Meeting*, CPIA Pub. 653, Vol. 2, Chemical Propulsion Information Agency, Laurel, MD, 1996, pp. 507–516.

⁴⁷Liau, Y. C., and Yang, V., "An Improved Model of Laser-Induced Ignition of RDX Monopropellant," *33rd JANNAF Combustion Meeting*, CPIA Pub. 653, Vol. 2, Chemical Propulsion Information Agency, Laurel, MD, 1996, pp. 529–546.

⁴⁸Mitani, T., and Williams, F. A., "A Model for the Deflagration of Nitramines," *21st Symposium (International) on Combustion*, Combustion Inst., Pittsburgh, PA, 1986, pp. 1965–1974.

⁴⁹Li, S. C., and Williams, F. A., "Nitramine Deflagration: Reduced Chemical Mechanism for Primary Flame Facilitating Simplified Asymptotic Analysis," *Journal of Propulsion and Power*, Vol. 12, 1996, pp. 302–309.

⁵⁰Brewster, M. Q., Ward, M. J., and Son, S. F., "New Paradigm for Simplified Combustion Modeling of Energetic Solids: Gas Phase Chain Reaction," AIAA Paper 97-3333, 1997.

⁵¹Finlinson, J. C., Parr, T., and Hanson-Parr, D., "Laser Recoil, Flame Emission, and Flame Height Combustion Response of HMX and RDX at Atmospheric Pressure," *25th Symposium (International) on Combustion*, Combustion Inst., Pittsburgh, PA, 1994, pp. 1645–1650.

⁵²Litzinger, T. A., Tang, C. J., Kudra, G., and Lee, Y. J., "A Study of the Combustion Response of HMX Monopropellant to Sinusoidal Laser Heating," *33rd JANNAF Combustion Meeting*, CPIA Pub. 653, Vol. 2, Chemical Propulsion Information Agency, Laurel, MD, 1996, pp. 159–168.

⁵³Loner, P. S., and Brewster, M. Q., "On the Oscillatory Laser-Augmented Combustion of HMX," *27th International Symposium on Combustion*, Combustion Inst., Pittsburgh, PA, 1998, pp. 2309–2318.

⁵⁴Zenin, A. A., "HMX and RDX: Combustion Mechanism and Influence on Modern Double-Base Propellant Combustion," *Journal of Propulsion and Power*, Vol. 11, 1995, pp. 752–758.

⁵⁵Parr, T. P., and Hanson-Parr, D., "Thermal Properties Measurements of Solid Rocket Propellant Oxidizers and Binder Materials as a Function of Temperature," *34th JANNAF Combustion Meeting*, CPIA Pub. 662, Vol. 3, Chemical Propulsion Information Agency, Laurel, MD, 1997, pp. 379–404.

⁵⁶Pitsch, H., Peters, N., and Seshadri, K., "Numerical and Asymptotic Studies of the Structure of Premixed Iso-Octane Flames," *26th International Symposium on Combustion*, Combustion Inst., Pittsburgh, PA, 1996, pp. 73–771.

⁵⁷Erickson, W. W., and Beckstead, M. W., "Modeling Pressure and Heat Flux Responses of Nitramine Monopropellants with Detailed Kinetics," *35th JANNAF Combustion Meeting*, CPIA Pub. 680, Vol. 1, Chemical Propulsion Information Agency, Laurel, MD, 1998, pp. 415–434.

⁵⁸Zebrowski, M. A., and Brewster, M. Q., "Theory of Unsteady Combustion of Solids: Investigation of Quasi-Steady Assumption," *Journal of Propulsion and Power*, Vol. 12, 1996, pp. 564–573.

⁵⁹Tien, J. S., "Oscillatory Burning of Solid Propellants Including Gas Phase Time Lag," *Combustion Science Technology*, Vol. 5, 1972, pp. 47–54.

⁶⁰Murphy, J. J., and Krier, H., "Linear Pressure Coupled Frequency Response of Heterogeneous Solid Propellants," *27th International Symposium on Combustion*, Combustion Inst., Pittsburgh, PA, 1998, pp. 2343–2350.

⁶¹Rasmussen, B., Frederick, R. A., Jr., and Lengelle, G., "Pressure-Coupled Frequency Response Models of Solid Propellants," *34th JANNAF Combustion Meeting*, CPIA Pub. 662, Vol. 2, Chemical Propulsion Information Agency, Laurel, MD, 1997, pp. 263–274.

⁶²Hickman, S. R., and Brewster, M. Q., "Oscillatory Combustion of Fine-AP/HTPB Propellants: Selective Pyrolysis Response," *Journal of Propulsion and Power*, 2000 (to appear for publication); also AIAA Paper 98-0982, 1998.

Burning-Rate Response Functions of Composite-Modified Double-Base Propellants and HMX

Anatoli A. Zenin* and Sergei V. Finjakov†
Russian Academy of Sciences, Moscow, Russia

Nomenclature

c	= heat capacity of solid, cal/gK
$\text{Im}\{U(\omega)\}$	= imaginary part of response function (solid heated layer), dimensionless
$\text{Im}\{U_L(\omega)\}$	= imaginary part of response function (surface melt layer), dimensionless
k	= Zel'dovich criterion of combustion stability, dimensionless
m	= mass burning rate, g/cm ² s
p	= pressure, atm
q_m	= heat of melting, cal/g
r	= sensitivity of burning surface temperature to initial temperature, dimensionless
r_b	= linear burning rate, cm/s
$\text{Re}\{U(\omega)\}$	= real part of response function (solid heated layer), dimensionless
$\text{Re}\{U_L(\omega)\}$	= real part of response function (surface melt layer), dimensionless
T_0	= initial sample temperature, °C
T_s	= burning surface temperature, °C
β	= sensitivity of mass burning rate to initial temperature, %/K
ν	= pressure sensitivity of mass burning rate, dimensionless
μ	= pressure sensitivity of burning surface temperature
ρ	= propellant density, g/cm ³
ω	= dimensionless frequency

Copyright © 2000 by the American Institute of Aeronautics and Astronautics, Inc. All rights reserved.

*Professor, Institute of Chemical Physics.

†Senior Researcher, Institute of Chemical Physics.

$\bar{\omega}$ = frequency, 1/s
 ω_n = resonance frequency, dimensionless

I. Introduction

MANY investigations have focused on nonsteady combustion of solid propellants, including, for instance, the experimental and theoretical works in Refs. 1–6. A first step in the investigations is an attempt to obtain burning-rate response functions to incident pressure oscillations. Experimental response functions have also been measured with radiant fluxes.^{7–10} The first experiments on the determination of response functions by direct measurements (microwave ultrasound and magnetohydrodynamic methods) were discussed recently for HTPB/AP propellants in Ref. 11. Theoretical estimations of the response functions and an analysis of nonlinear effects were suggested by De Luca.¹² Experimental results obtained by T-burner and laser impulses were presented in Refs. 13 and 14. Beckstead and Erikson¹⁵ estimated the amplitudes of response functions for AP, HMX, RDX, and simple double-base propellants based on existing experimental data for burning rates and burning surface temperatures as functions of pressure and propellant initial temperature. In Ref. 16, the amplitudes of RDX response functions at 1 atm were estimated on the basis of full chemical kinetics by the Zel'dovich–Novozhilov (ZN) theory and by numerical simulations; the results of the calculations were compared with the experimentally obtained parameters of RDX combustion.¹⁷

Many investigations have been devoted to the effects of pressure oscillations and pulsed instability inside solid-propellant rocket motors.^{18–24} It is obvious, however, that a full understanding of the phenomena is impossible without an understanding of the physics governing the influence of small pressure oscillations on propellant combustion. Up to now the problem of response function determination by experiments has not been solved, especially at elevated pressures. The aim of this work is to obtain burning-rate response functions of solid propellants on the basis of microthermocouple measurements and by using the ZN approximation.^{2,3} The experimentally obtained pressure and temperature sensitivities of burning rates and burning surface temperatures for HMX and composite-modified double-base propellants were used for calculations of the burning-rate response functions. A part of the response functions was presented in Refs. 25–27. This chapter is a continuation of that work.

II. Investigated Substances and Experimental Results

Two types of modified double-base propellants were used for the investigations: normal double-base propellants with 20% nitroglycerine and “hot” double-base propellants with 34% nitroglycerine. The propellant samples had a cylindrical shape 10 mm in diameter and 20 mm long. Four normal modified propellants were selected for the investigations: A, B, C, and D. Basic normal propellant A (see Table 1) contained 55% nitrocellulose, 20% nitroglycerine, 20% nitrosoamine (1,4,5,8-tetranitrosotetrasamine), and 2% catalyst (Ni) (all percentages are by weight). The density of the propellants was $\rho = 1.6 \text{ g/cm}^3$. The composition of propellants B, C, and D was chosen to check the influence of adding HMX (amount and particle size) and the influence of the catalyst (very small Ni particles). Propellant B had a 10% addition of HMX with relatively large particles ($\sim 40 \text{ }\mu\text{m}$). Propellant C had the same composition as propellant B but without the catalyst. Propellant D had the same addition of HMX as propellant C, but the HMX

Table 1 Propellant compositions

	Propellant					
	A	B	C	D	E	G
Nitrocellulose, %	55	50	50	50	34	35
Nitroglycerine, %	20	20	20	20	34	34
Nitrosoamine, %	20	15	17	17	30	14
HMX, %						
<50 μm /150–300 μm	—	—	—	—	—	15
40 μm	—	10	10	—	—	—
10 μm	—	—	—	10	—	—
Ni, %	2	2	—	—	—	—
Processing additives, %	Up to 100	Up to 100	Up to 100	Up to 100	Up to 100	Up to 100

had a smaller particle size (10 μm). Thus, the comparison of the results obtained for propellants A–D shows the influence of HMX, its particle size, and Ni catalyst additions on the normal modified double-base propellant combustion to be investigated. Two hot modified double-base propellants with 34% nitroglycerine, E and G, differ by nitramine content. Propellant E contained only the nitrosoamine addition, 30%, but propellant G had a 15% HMX addition, mainly instead of nitrosoamine. Thus, the comparison of the results obtained for propellants E and G allows the influence of HMX addition on the hot modified propellant combustion to be studied. The powder HMX in propellant G had two ranges of particle size: less than 50 and 150–300 μm . The propellant density was 1.6 g/cm³. The combustion of pressed 8 \times 8 \times 15-mm pellets of HMX was also investigated. The density of the pellets was 1.7 g/cm³.

Table 2 (see also Refs. 25 and 26) shows the results of measurements of mass burning rate m and burning surface temperature T_s for propellants A–G. The propellant samples were burned in a nitrogen environment of a constant-pressure bomb; the burning surface temperatures were measured by microthermocouples.^{17,25} Table 3 (see also Ref. 28) shows the result of measurements of mass burning rate m and burning surface temperature T_s for HMX. The data analysis shows that the standard deviations of the measurements do not exceed $\pm 5\%$. Thus, it was assumed that $\Delta r_b = \Delta m = \Delta T_s = \pm 5\%$.

III. Pressure and Temperature Sensitivities of Burning Rate and Burning Surface Temperature

The obtained values of burning rate m and surface temperature T_s , which are listed in Tables 2 and 3, were used to obtain the following temperature and pressure sensitivities of the burning rates and the burning surface temperatures:

$$\begin{aligned}\beta &= (\partial \ln m / \partial T_0)_p \text{—sensitivity of mass burning rate to initial temperature;} \\ r &= (\partial T_s / \partial T_0)_p \text{—sensitivity of burning surface temperature to initial temperature;} \\ \nu &= (\partial \ln m / \partial \ln p)_{T_0} \text{—pressure sensitivity of mass burning rate; and} \\ \mu &= (T_s - T_0)^{-1} \cdot (\partial T_s / \partial \ln p)_{T_0} \text{—pressure sensitivity of burning surface temperature.}\end{aligned}$$

Table 2 Mass burning rates m , g/cm²s, and burning surface temperatures T_s , °C, for propellants A–G

Propellant	Property	20-atm p and T_0 , °C			50-atm p and T_0 , °C			100-atm p and T_0 , °C		
		–80 (–70)	+20	+100 (+50)	–70	+20	+50	–80 (–70)	+20	+100 (+50)
A	m	0.64	0.82	1.35	—	—	—	1.20	1.65	2.16
	T_s	350	375	420	—	—	—	410	440	470
B	m	0.64	0.82	1.12	—	—	—	1.12	1.36	1.80
	T_s	350	375	400	—	—	—	400	420	450
C	m	0.64	0.77	1.30	—	—	—	1.02	1.34	2.14
	T_s	350	365	420	—	—	—	390	420	474
D	m	0.61	0.74	1.06	—	—	—	1.02	1.38	1.74
	T_s	350	365	395	—	—	—	390	420	450
E	m	(0.50)	0.66	(0.80)	0.90	0.95	1.20	(1.77)	1.79	(2.05)
	T_s	(330)	355	(374)	380	390	410	(450)	455	(465)
G	m	(0.58)	0.69	(0.78)	0.90	1.07	1.17	(1.23)	1.60	(2.00)
	T_s	(348)	358	(370)	384	400	410	(415)	438	(465)

A smoothing procedure must be used on the experimental data before finite-difference approximations of these derivatives can be made. Otherwise, the error in the results is amplified. The unified dependency $T_s(m)$ for double-based propellants (its validity for the investigated propellants was established) made the smoothing procedure easier. As a rule, the determination of β does not incur any difficulties, because the experimentally obtained functions $m(T_0)$ at constant pressure are smooth enough. For determination of the values of r , it is necessary to use analytic connections between r and β obtained by differentiation of the unified dependencies $T_s(m)$ for double-base propellants¹⁷ and for cyclic nitramines.²⁸ For

Table 3 Mass burning rates m , g/cm²s, and burning surface temperatures T_s , °C, for HMX

Pressure, p , atm	Property	T_0 , °C		
		–170	+20	+100
10	m	0.33	0.47	0.60
	T_s	388	420	442
20	m	0.60	0.77	0.94
	T_s	438	450	470
50	m	1.25	1.42	1.67
	T_s	490	495	500
100	m	2.04	2.20	2.5
	T_s	510	520	522

Table 4 Parameters ν , μ , k , and r for propellants A–D

Pressure, p , atm	T_0 , °C	Property	Propellant			
			A	B	C	D
20	–80	ν	0.40	0.36	0.30	0.34
		μ	0.087	0.073	0.058	0.058
		k	1.07	1.07	0.80	0.86
		r	0.204	0.206	0.510	0.165
	+20	ν	0.46	0.31	0.35	0.39
		μ	0.114	0.079	0.10	0.10
		k	1.47	1.10	0.83	1.07
		r	0.39	0.29	0.22	0.334
	+100	ν	0.29	0.29	0.31	0.31
		μ	0.098	0.104	0.108	0.117
		k	1.98	1.17	2.08	1.33
		r	0.72	0.425	0.75	0.485
100	–80	ν	0.40	0.39	0.30	0.34
		μ	0.077	0.065	0.053	0.053
		k	1.56	0.93	1.36	1.41
		r	0.315	0.186	0.34	0.278
	+20	ν	0.46	0.31	0.35	0.39
		μ	0.097	0.07	0.086	0.086
		k	1.37	1.04	1.68	1.16
		r	0.37	0.278	0.38	0.31
	+100	ν	0.29	0.29	0.31	0.31
		μ	0.083	0.089	0.093	0.098
		k	1.28	1.23	2.18	1.01
		r	0.45	0.43	0.765	0.356

modified double-base propellants, r can be estimated by the formula

$$r = \beta / [E/2RT_s^2 - (T_0/T_s)(T_s - T_0)] \quad (1)$$

The relative standard deviations of r , i.e., Δr , obtained by Eq. (1), and $\Delta\beta$ are practically equal to each other, at $\sim\pm 5\%$.²⁵ The same Δr was obtained for HMX.²⁸ The normal graphical procedure of smoothing gives small standard deviations for ν and μ as well. It can be shown²⁵ that for the substances discussed here the standard deviations $\Delta\nu$ and $\Delta\mu$ are $\sim\pm(2-3)\%$.

Tables 4–6 show the results of the sensitivity determinations. A nondimensional form of the temperature sensitivity parameter is $k = \beta(T_s - T_0)$. This form is used here for propellants instead of β . For HMX, this parameter is designated k_0 (see below). Table 4 presents sensitivities of normal double-base propellants A–D at 20 and 100 atm for $T_0 = -80, 20$, and 100°C . A characteristic feature of the propellants is a relatively small ν range of 0.29–0.46. Table 5 presents the same sensitivities for hot double-base propellants E and G. It can be seen that the values of ν here are significantly higher: from 0.30 up to 1.0. The relatively high values of ν occur also for HMX: Table 6 shows that they are 0.65–0.88. Tables 4–6 show that addition of HMX to the propellants, as a rule, decreases ν . Parameter

Table 5 Parameters ν , μ , k , and r for propellants E and G

Pressure, p , atm	T_0 , °C	Property	Propellant	
			E	G
20	-70	ν	0.65	0.50
		μ	0.134	0.091
		k	1.26	0.79
		r	0.24	0.15
	+20	ν	0.39	0.48
		μ	0.115	0.136
		k	1.3	0.84
		r	0.32	0.22
	+50	ν	0.44	0.45
		μ	0.119	0.138
		k	2.09	1.3
		r	0.62	0.38
50	-70	ν	0.8	0.50
		μ	0.173	0.091
		k	0.225	0.86
		r	0.045	0.17
	+20	ν	0.66	0.54
		μ	0.179	0.131
		k	0.87	0.83
		r	0.23	0.22
	+50	ν	0.61	0.60
		μ	0.164	0.172
		k	2.5	0.27
		r	0.82	0.08
100	-70	ν	1.0	0.5
		μ	0.195	0.093
		k	0.07	1.4
		r	0.015	0.29
	+20	ν	0.93	0.60
		μ	0.216	0.128
		k	0.64	1.69
		r	0.17	0.50
	+50	ν	0.78	0.76
		μ	0.192	0.192
		k	1.87	2.7
		r	0.56	0.91

μ of propellants A–D is equal to 0.05–0.11. The values of μ decrease when the pressure increases, and, as a rule, μ increases with initial temperature. Propellant E has an increased μ (0.12–0.21), and μ quickly increases with pressure. Addition of HMX to the hot propellant significantly decreases μ at 70 and 20°C and does not change μ at 100°C. For HMX μ_0 has high values at 10 and 20 atm (0.2–0.15 for $T_0 = 100^\circ\text{C}$) and quickly decreases with pressure up to 0.06–0.08 at 100 atm.

Table 6 Parameters ν , μ , k , and r for HMX

Pressure, p , atm	T_0 , °C	Property					
		ν	μ_0	μ	k_0	k	r
10	-170	0.85	0.09	0.077	1.05	1.23	0.10
	+20	0.83	0.14	0.113	0.76	0.94	0.12
	+100	0.88	0.20	0.157	0.50	0.64	0.13
20	-170	0.85	0.10	0.087	0.80	0.92	0.11
	+20	0.66	0.12	0.099	0.65	0.79	0.20
	+100	0.68	0.15	0.120	0.96	1.20	0.26
50	-170	0.85	0.06	0.053	0.56	0.64	0.026
	+20	0.66	0.06	0.050	0.40	0.48	0.03
	+100	0.68	0.08	0.065	0.55	0.68	0.10
100	-170	0.65	0.06	0.053	0.56	0.64	0.06
	+20	0.66	0.06	0.051	0.63	0.75	0.07
	+100	0.68	0.08	0.066	0.70	0.86	0.09

The temperature sensitivity of burning rate β , as a rule, decreases with pressure and increases with T_0 ; only propellants E and G at 100 atm have increased values of β , and this increase is especially quick at elevated T_0 . As a rule, β for HMX is less than those of the propellants, and HMX addition to the propellants decreases β (only for propellant E at 100 atm does HMX addition give a significant increase in β). The level of β at a normal temperature is ~ 0.1 – 0.2 %/K for HMX and ~ 0.2 – 0.4 %/K for propellants.

Parameters k_0 for HMX and k for propellants, as a rule, decrease with pressure and increase with temperature. The level of k_0 at a normal temperature for HMX is ~ 0.4 – 0.7 , and the level of k for propellants is ~ 0.8 – 1.4 . The level of r at a normal temperature is ~ 0.03 – 0.25 for HMX and ~ 0.1 – 0.5 for propellants.

Previous work²⁹ has shown that a melted layer on the burning surface decreases the stability of combustion. The parameter k in this case must be calculated by the following expression:

$$k = \beta \cdot (T_s - T_0 + q_m/c) \quad (2)$$

where q_m is the heat of melting and c is the heat capacity. HMX has a melted layer on the burning surface, and therefore expression Eq. (2) was used in further calculations for HMX. Table 6 shows both of the parameters, k and $k_0 = \beta \cdot (T_s - T_0)$. It was assumed for HMX that $q_m = 28$ cal/g and $c = 0.3$ cal/g K. Section IV shows that for the HMX response function calculations, the corrected value of pressure sensitivity of surface temperature in the following equation must be used:

$$\mu = (T_s - T_0 + q_m/c)^{-1} \cdot (\partial T_s / \partial \ln p) \quad (3)$$

Table 6 shows both of the parameters, μ and $\mu_0 = (T_s - T_0)^{-1} \cdot (\partial T_s / \partial \ln p)$.

Previous work^{25,26} has shown that these propellants and HMX have stable combustion under the investigated conditions.

IV. Theory of Burning-Rate Response Functions

A. Solid Layer on the Burning Surface

A full description of propellant burning-rate behavior in a pressure field with low-amplitude pulsations, in the case of a nonmelted layer on the burning surface, can be made in the framework of the ZN theory.^{3,6} Let the pressure have harmonic dependence on time t according to the expression

$$p = p_0 + p_1 \cos \bar{\omega} t \quad (4)$$

where $p_1 \ll p_0$. Then the burning rate in a linear approximation has the following form:

$$r_b = r_{b0} + r_1 \cos \bar{\omega} t \quad (5)$$

where $r_1 \ll r_b$. Novozhilov obtained,^{3,6} using the complex amplitude method, the following expression for the burning-rate response to oscillatory pressure:

$$U = [\nu + (\nu \cdot r - \mu \cdot k) \cdot (z - 1)] / [1 + r \cdot (z - 1) - k \cdot (z - 1)/z] \quad (6)$$

Here $z = (1 + \sqrt{1 + 4i\omega})/2$; $U = v_1/\eta_1$, where v_1 is the complex amplitude of the burning-rate fluctuation and $\eta_1 = p_1/p_0$; and ω is a nondimensional frequency that is equal to the cyclic frequency $\bar{\omega}$, in 1/s, multiplied by the thermal relaxation time of the solid heat layer χ/r_b^2 . Values of ν , μ , k , and r are based on the mean pressure p_0 . It is convenient to derive the response function in a traditional form:

$$U = (A + B \cdot i)/(C - D \cdot i) = (A \cdot C - B \cdot D)/(C^2 + D^2) + (A \cdot D + B \cdot C) \cdot i/(C^2 + D^2) \quad (7)$$

Thus:

$$\text{Re}\{U\} = (A \cdot C - B \cdot D)/(C^2 + D^2) \quad \text{and} \quad \text{Im}\{U\} = (A \cdot D + B \cdot C)/(C^2 + D^2) \quad (8)$$

where

$$A = \nu + \delta \cdot (R_1 - 0.5); \quad B = \delta \cdot (R_1^2 - 0.25)^{0.5} \quad (9)$$

$$C = 1 + r \cdot (R_1 - 0.5) - k \cdot (1 - \frac{1}{2} R_1); \quad \delta = \nu \cdot r - \mu \cdot k \quad (10)$$

$$D = (k/2R_1) \cdot [(2R_1 - 0.5)/(2R_1 + 0.5)]^{0.5} - r \cdot (R_1^2 - 0.25)^{0.5} \quad (11)$$

Equation (6) is based on the supposition that the relaxation time for the solid heated layer is much longer than those for the leading part of the gas phase and reaction layer of the solid. Estimations show that for the investigated substances this supposition is valid. Indeed, values of χ/r_b^2 are at least 10–20 times higher than other relaxation times. This implies that the results obtained in the previous section can be used for calculations of burning-rate response functions.

Estimations also show that the standard deviations of these calculations for $\text{Re}\{U\}$ are equal to 15–20% for HMX and 20–50% for propellants. The accuracy of these calculations allows us to obtain reliable results.

B. Melting Layer on the Burning Surface

Two different layers on the burning surface, liquid and solid, change the physical conditions on the surface. It is necessary to make an additional theoretical analysis of the problem. In Ref. 30, such an analysis was made through the ZN approach.

As in Refs. 3 and 6, it is assumed in Ref. 30 that the thermal inertia of the heated layer is the limiting factor in this nonstationary process, and the burning rate r_b and surface temperature T_s are generally functions of the temperature gradient f_0 on the solid-gas boundary and of the pressure p . The experimentally determined dependencies for steady combustion.

$$r_{b0}(p_0, T_0) \quad \text{and} \quad T_{s0}(p_0, T_0) \quad (12)$$

are in fact the following parametric dependencies:

$$r_b(f_0, p) \quad \text{and} \quad T_s(f_0, p) \quad (13)$$

The burning-rate response function $U = v_1/\eta_1$ was found under conditions of harmonically changing pressure on the burning surface,

$$\eta = 1 + \eta_1 \cdot \cos \bar{\omega} t \quad (14)$$

where $\eta = p/p_0$ and $\eta_1 = \tilde{p}/p_0$; here \tilde{p} is a small harmonic variation of pressure (the tilde indicates a small value), and p_0 is a mean pressure. The corresponding nondimensional equations for the temperature gradient, surface temperature, and burning rate have the following forms:

$$\varphi_0 = 1 + \varphi_1 \cdot \cos \bar{\omega} t \quad (15)$$

where $\varphi_0 = f_0/f_{00}$, $\varphi_1 = \tilde{f}/f_{00}$, and f_{00} is a stationary gradient,

$$\theta_s = 1 + \theta_{s1} \cdot \cos \bar{\omega} t \quad (16)$$

where $\theta_s = \delta T_s/\delta T_{s0}$, $\theta_{s1} = \delta \tilde{T}_s/\delta T_{s0}$, and $\delta T_{s0} = T_{s0} - T_0$,

$$V = 1 + V_1 \cdot \cos \bar{\omega} t \quad (17)$$

where $V = r_b/r_{b0}$, $V_1 = \tilde{r}_b/r_{b0}$, and r_{b0} is a stationary burning rate. Presentation of these expressions in an exponential complex form and substitution into the transient heat conduction equation for the solid phase allow for, after linearization, a solution for the case of a single layer on the burning surface (i.e., no melt layer).

For the case of a melt layer on the burning surface, it is necessary to consider two layers at the surface: liquid and solid. The linearized transient heat conduction equation is then derived for each layer. The solution takes the following functional form:

$$\theta_{s1}(\varphi_1, V_1) \quad \text{and} \quad \varphi_1(\theta_{s1}, V_1) \quad (18)$$

With the use of Eqs. (12) and (13), the following functions are obtained:

$$V_1(\varphi_1, \eta_1) \quad \text{and} \quad \theta_{s1}(\varphi_1, \eta_1) \quad (19)$$

These equations, along with the energy balance between the solid and the liquid layers, serve as a basis for determining the burning-rate response function for melting substances.

1. Determination of $V_1(\varphi_1, \eta_1)$ and $\theta_{s1}(\varphi_1, \eta_1)$

Functions (12) are valid for steady combustion and therefore the steady heat conduction equation is considered here for the liquid layer. It has the following form:

$$L^{-1} \cdot \partial^2 \theta_0 / \partial \xi^2 + \partial \theta_0 / \partial \xi = 0 \quad (20)$$

where $\theta_0 = (T - T_0)/(T_{s0} - T_0)$; $L = \lambda/\lambda_L$, with λ and λ_L being the solid and liquid thermal conductivity, respectively; and $\xi = x/l_0$, with l_0 being the thickness of the thermal layer. Boundary conditions are as follows: $\theta_0 = 1$ at $\xi = 0$; and $\theta_0 = \theta_m = (T_m - T_0)/(T_{s0} - T_0)$ at $\xi = H = x_m/l_0$, where x_m is the thickness of the melt layer and T_m is the melting temperature. The solution to Eq. (20) is

$$\theta_0 = 1 - (1 - \theta_m)(1 - e^{-L\xi})/(1 - e^{-LH}) \quad (21)$$

The heat conduction equation for the solid layer under steady-state conditions is

$$\partial^2 \theta_0 / \partial \xi^2 + \partial \theta_0 / \partial \xi = 0 \quad (22)$$

Boundary conditions are as follows: $\theta_0 = 0$ at $\xi = \infty$ and $\theta_0 = \theta_m$ at $\xi = H$. The solution to Eq. (22) takes the form

$$\theta_0 = \theta_m \cdot e^{-(\xi-H)} \quad (23)$$

The position of the melting section can be found from Eqs. (21) and (23) as follows:

$$H = L^{-1} \cdot \ln[(1 + q)/(\theta_m + q)] \quad (24)$$

where $q = q_m/[c(T_{s0} - T_0)]$. The gradient f_{00} at $x = 0$ can thus be found to be

$$f_{00} = -L \cdot r_b \cdot \Delta_L / \chi \quad (25)$$

where $\Delta_L = (T_{s0} - T_0 + q_m/c)$. Differentiation of f_{00} gives

$$df_{00} = f_{00}(\nu + \mu) \cdot dp/p + f_{00}(k + r) \cdot dT_0/\Delta_L \quad (26)$$

Thus,

$$(\partial \ln r_{b0} / \partial \ln f_{00})_p = k/(k + r - 1) \approx (f_0/r_b) \cdot (\partial r_b / \partial f_0) \quad (27)$$

$$(\partial \ln r_{b0} / \partial \ln p)_{f_{00}} = (\delta - \nu)/(k + r - 1) \approx (p/r_b) \cdot (\partial r_b / \partial p) \quad (28)$$

The final equations of this subsection are as follows:

$$V_1 = k \cdot \varphi_1/(k + r - 1) + (\delta - \nu) \cdot \eta_1/(k + r - 1) \quad (29)$$

$$\theta_{s1} = (1 + q) \cdot r/(k + r - 1) - (1 + q) \cdot (\delta - \mu) \cdot \eta_1/(k + r - 1) \quad (30)$$

Here $k = k_0(1 + q)$, $\mu = \mu_0/(1 + q)$, and $\delta = \nu \cdot r - \mu \cdot k = \delta_0 = \nu \cdot r - \mu_0 \cdot k_0$. Without melting, $q = 0$, $k = k_0$, and $\mu = \mu_0$. Equations (29) and (30) transform into classical equations discussed in Ref. 3.

2. Determination of $\theta_{s1}(\varphi_1, V_1)$ and $\varphi_1(\theta_{s1}, V_1)$

The transient heat conduction equation for the liquid phase is derived as follows:

$$\partial\theta/\partial\tau = L^{-1} \cdot \partial^2\theta/\partial\xi^2 + V \cdot \partial\theta/\partial\xi \quad (31)$$

where $\tau = t/t_0$ and $t_0 = \chi/r_{b0}^2$. Let us present functions θ and V [see Eqs. (16) and (17)] in an exponential form: $\theta = \theta_0 + \theta_1 \exp(i\bar{\omega}t)$ and $V = V_1 + V_1 \cdot \exp(i\bar{\omega}t)$. Substitution into Eq. (31) and linearization of the result give the following expression:

$$\theta_1 + L \cdot \theta_1 - i\bar{\omega} \cdot L \cdot \theta_1 = L^2 \cdot [(1 - \theta_m)/(1 - e^{-LH})] \cdot V_1 \cdot e^{-L\xi} \quad (32)$$

The solution takes the form

$$\theta_1 = iL \cdot (1 + q)V_1 e^{-L\xi}/\bar{\omega} + D_1 \cdot \exp(-a \cdot L \cdot \xi) + D_2 \cdot \exp(-b \cdot L \cdot \xi) \quad (33)$$

where D_1 , D_2 , a , and b are constant values. Hence, at $\xi = 0$,

$$\theta_{s1} = D_1 + D_2 + i \cdot L(1 + q)V_1 \quad (34)$$

After differentiation of Eq. (33) and some assumptions, the following expression can be obtained:

$$\varphi_1 = aLD_1 + bLD_2 + i \cdot L^2(1 + q)V_1/\omega \quad (35)$$

Finally, the condition at the boundary of the melt layer is as follows:

$$D_1[(1 + q)/(\theta_m + q)]^{-a} + D_2 \cdot [(1 + q)/(\theta_m + q)]^{-b} = 0 \quad (36)$$

It can be seen that all the parameters and constant values can be determined by Eqs. (29), (30), and (34–36).

3. Determination of the Burning-Rate Response Function

Thus, a system of the required equations is as follows:

$$V_1 = k \cdot \varphi_1/\chi + (\delta - \nu) \cdot \eta_1/\chi \quad (37)$$

$$\theta_{s1} = (1 + q) \cdot r/\chi - (1 + q) \cdot (\delta - \mu) \cdot \eta_1/\chi \quad (38)$$

$$\theta_{s1} = D_1 + D_2 + i \cdot L(1 + q)V_1 \quad (39)$$

$$\varphi_1 = aLD_1 + bLD_2 + i \cdot L^2(1 + q)V_1/\omega \quad (40)$$

$$D_1 A^{-a} + D_2 \cdot A^{-b} = 0 \quad (41)$$

where $A = (1 + q)/(\theta_m + q)$. The solution of the above system gives an expression for the burning-rate response function in the case of a melted layer at the burning surface: $U_L = V_1/\eta_1$. This expression is as follows:

$$U_L = [\nu + \delta \cdot (z_1 - 1)]/[1 + r \cdot (z_1 - 1) - k - i \cdot [L(1 + q) - z_1]/\omega] \quad (42)$$

where $z_1 = L \cdot (1 + q)[0.5 + 0.5 \cdot z \cdot (A^z + 1)/(A^z - 1)]$ and $z = \sqrt{1 + i \cdot 4\omega/L}$. We assume, in this calculation, that $z_1 \approx z_1^* = L(1 + q)[0.5 + 0.5z(1 + 2/A)]$.

For some calculations it is convenient to have an equation for the response function U_L in a traditional form:

$$\operatorname{Re}\{U_L\} = (A_1 \cdot C_1 - B_1 \cdot D_1) / (C_1^2 + D_1^2) \quad (43)$$

$$\operatorname{Im}\{U_L\} = (A_1 \cdot D_1 + B_1 \cdot C_1) / (C_1^2 + D_1^2) \quad (44)$$

where A_1 , C_1 , B_1 , and D_1 are the following functions (if $z_1 \approx z_1^*$):

$$A_1 = \nu + \delta_0 [L(1+q)(R_{1L} + 0.5) - 1]; \quad B_1 = L \cdot \delta_0 (1+q) (R_{1L}^2 - b_L^2/4)^{0.5} \quad (45)$$

$$C_1 = 1 + r[L \cdot (1+q)(R_{1L} + 0.5) - 1] - k[1 - (1+q)b_L^2/2R_{1L}] \quad (46)$$

$$D_1 = k(1+q)b_L^2(R_{1L} + 0.5)/2R_{1L} (R_{1L}^2 - b_L^2/4)^{0.5} - rL(1+q) (R_{1L}^2 - b_L^2/4)^{0.5} \quad (47)$$

$$R_{1L} = b_L \left\{ \frac{1}{8} [1 + (1 + 16\omega^2)^{0.5}] \right\}^{0.5}; \quad b_L = [1 + 2(\theta_m + q)/(1+q)] \quad (48)$$

In the case that $q_m = 0$ and $T_m = T_0$, Eqs. (43) and (44) convert to Eqs. (8) and (9). In the HMX calculations, it was assumed that $L = 1$.

V. Burning-Rate Response Functions for HMX and CMDB Propellants

A. HMX Response Functions

Figures 1 and 2 present the burning-rate response functions of HMX, calculated at 20 and 100 atm and at $T_0 = 20^\circ\text{C}$ in two ways: by Eq. (6) for the functions $\operatorname{Re}\{U\}$ and $\operatorname{Im}\{U\}$ and by Eq. (42) for the functions $\operatorname{Re}\{U_L\}$ and $\operatorname{Im}\{U_L\}$. It can be seen that melting in the condensed phase changes the HMX burning-rate response functions significantly. The effect of melting decreases the real part of the response functions, approximately 2–3 times at 20 atm and 1.5–2 times at 100 atm. The imaginary part decreases at 20 atm and increases at 100 atm. The effect of melting significantly

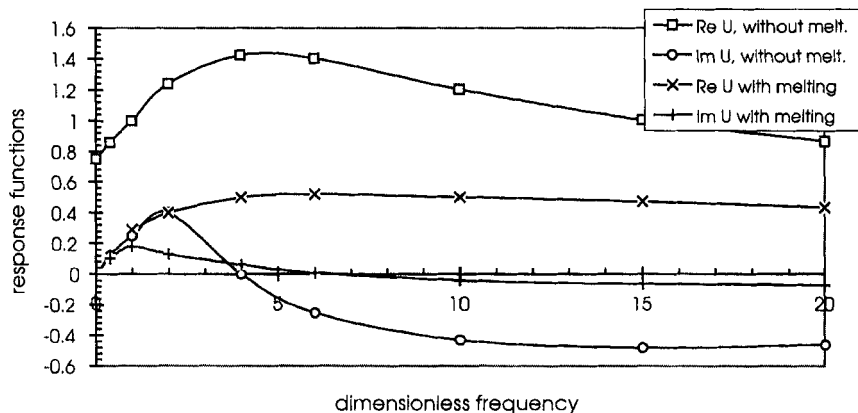


Fig. 1 HMX response functions with and without melting: 20 atm, $T_0 = 20^\circ\text{C}$.

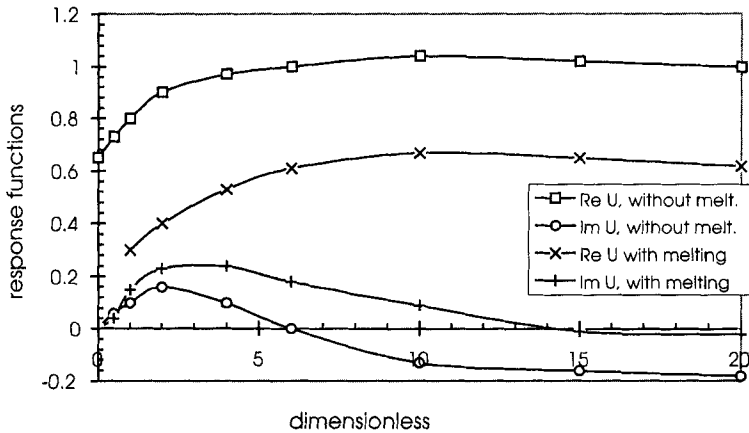


Fig. 2 HMX response functions with and without melting: 100 atm, $T_0 = 20^\circ\text{C}$.

increases the resonance frequency ω_n : at 20 atm, from about 4.5 up to 6.5 and, at 100 atm, from about 6 up to 12.

The observed phenomena have relatively simple physical explanations. A liquid layer on the burning surface plays a damping role that partly blocks the pressure pulsating penetration into the solid part of the HMX heated layer, and therefore the liquid layer decreases the burning rate pulsating. The liquid layer is thicker at 20 than at 100 atm, so that the decrease in the real part of the response function at 20 atm is larger than at 100 atm. As for the resonance frequency, it can be estimated by the expression $\omega_{n,\text{th}} \approx \sqrt{k}/r$ (see below). Obviously, the increase in ω_n , observed above, is connected with the increase in k in the melting case, in comparison with k_0 ; see Eq. (2).

Figures 3–5 show the obtained functions $\text{Re}\{U_L\}$ and $\text{Im}\{U_L\}$ for HMX at 10, 50, and 100 atm and at $T_0 = -170, 20$, and 100°C . It can be seen that burning HMX, as an oscillating system, has a low quality (in filter theory terminology); the response

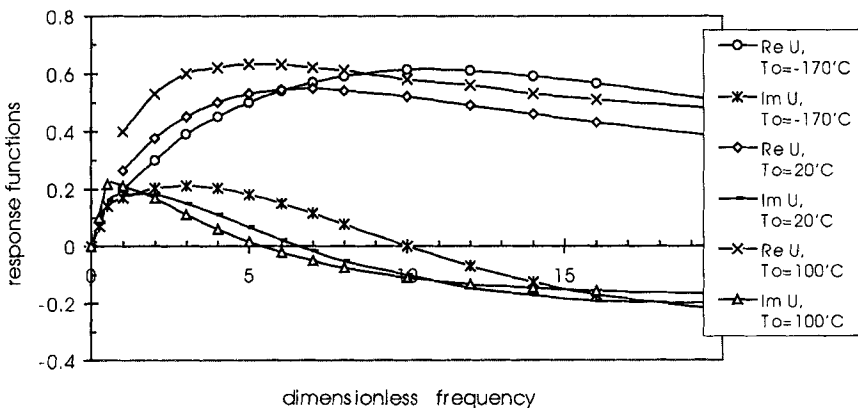


Fig. 3 HMX response functions at 10 atm.

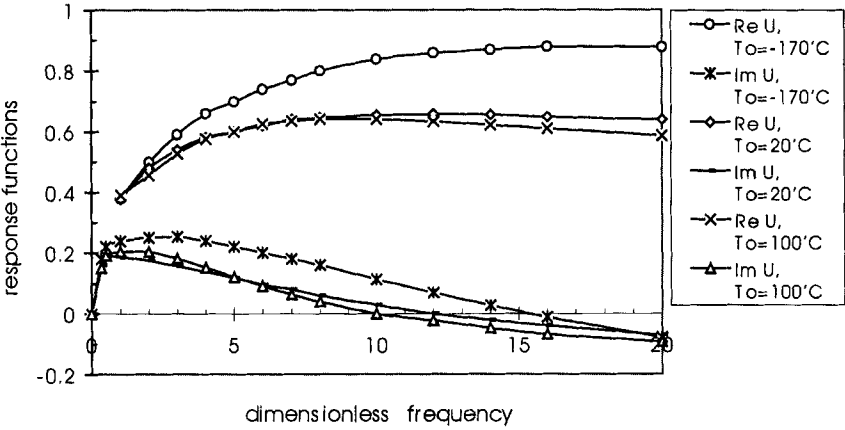


Fig. 4 HMX response functions at 50 atm.

functions close to the resonance frequency ω_n vary only slightly with frequency. Burning HMX has, as a rule, $k < 1$, and therefore its resonance phenomenon is significantly depressed, due to the viscous behavior of the oscillations. HMX combustion is an example of a smoothed resonance phenomenon. It is natural that $\text{Im}\{U_L\}$, presenting the phase of oscillations of the response function, changes the sign at the resonance, at $\omega = \omega_{n2}$.

Table 7 shows the dimensionless characteristics of the HMX burning-rate response functions presented in Figs. 3–5. Here $\text{Re}\{U_{\max}\}$ is the maximal values of $\text{Re}\{U_L\}$, $\sqrt{k}/r \approx \omega_{n,\text{th}}$ is a theoretical expression of the resonance frequency, ω_{n1} is a nondimensional frequency corresponding to $\text{Re}\{U_{\max}\}$, ω_{n2} is a nondimensional frequency corresponding to $\text{Im}\{U_L\} = 0$ (generally $\omega_{n1} \neq \omega_{n2}$), $\text{Im}\{U_{\max(+)}\}$ is the maximal values of $\text{Im}\{U_L\}$ in the positive region of $\text{Im}\{U_L\}$, and $\text{Im}\{U_{\max(-)}\}$

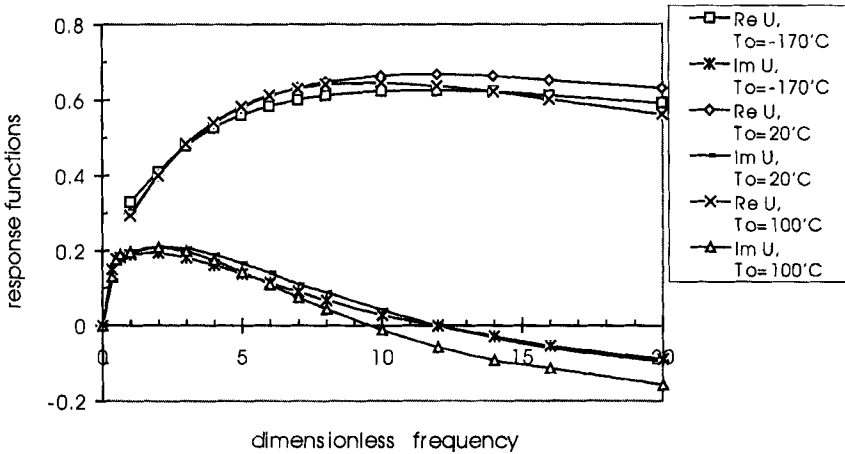


Fig. 5 HMX response functions at 100 atm.

Table 7 Dimensionless characteristics of HMX response functions

Pressure,		Property					
p , atm	T_0 , °C	$\text{Re}\{U_{\max}\}$	\sqrt{k}/r	ω_{n1}	ω_{n2}	$\text{Im}\{U_{\max(+)}\}$	$\text{Im}\{U_{\max(-)}\}$
10	-170	0.61	11	10.5	10	0.21	<-0.23
	+20	0.55	8	7.0	6.5	0.18	<-0.22
	+100	0.63	6	5.5	5.5	0.22	<-0.17
20	-170	0.69	9	9.5	9.5	0.24	<-0.18
	+20	0.52	4	6.5	7.5	0.19	<-0.07
	+100	0.44	4	5.5	6.0	0.16	<-0.10
50	-170	0.89	—	—	—	0.25	<-0.10
	+20	0.66	—	12	12	0.19	<-0.08
	+100	0.64	8	9	10	0.21	<-0.10
100	-170	0.62	13	11.5	12	0.20	<-0.12
	+20	0.67	12	11.5	12	0.21	<-0.13
	+100	0.64	10	9.0	9.5	0.21	<-0.18

is the maximal absolute values of $\text{Im}\{U_L\}$ in the negative region of the functions. The same characteristics appear in Tables 8 and 9.

It can be seen from Table 7 that the formula $\omega_n = \sqrt{k}/r$ gives, as a rule, adequate predictions of regions of ω_{n1} and ω_{n2} . The difference between ω_{n1} and ω_{n2} is small, and, when they differ, $\omega_{n1} < \omega_{n2}$. The above-introduced nomination of $\text{Im}\{U_{\max(-)}\}$ for HMX is the conventional one. The function $\text{Im}\{U_L(\omega)\}$ in the negative region is characteristically monotonic, decreasing with ω . Table 7 contains, in fact, only values of $\text{Im}\{U_L\}$ at the largest values of ω . A characteristic feature of the function $\text{Re}\{U(\omega)\}$ is low values of $\text{Re}\{U_{\max}\}$; it is mainly equal to 0.5–0.7. The values of $\text{Im}\{U_{\max(+)}\}$ and $\text{Im}\{U_{\max(-)}\}$ are close to each other in absolute values and comprise values from 0.05–0.07 up to 0.4–0.7.

A significant peculiarity of response functions of $\text{Re}\{U\}$ (for the case of a single layer) is the fact that $\text{Re}\{U(\omega = 0)\} = v$. Regrettably, Eq. (43) for response functions of $\text{Re}\{U_L\}$ is not valid at frequencies $\omega \leq 1$ for real substances with a melted layer. The problem is that significant increase in energy loss takes place in the melted layer at pressure pulsations. These losses lead to a decrease in response frequencies in comparison with the initial frequencies of the pressure oscillation. This implies that at $\omega \leq 1$ the burning-rate response ceases to pulsate, due to damping, and $\text{Re}\{U_L\}$ cannot be calculated at these small ω . Therefore, the curves of $\text{Re}\{U_L\}$ for HMX in the figures were discontinued at $\omega \leq 1$. At elevated frequencies, the influence of a negative addition to ω of the response due to energy losses is not significant. Of course, in the strict sense, the burning-rate response functions in the case of the melted layer must have a nonharmonic character, and the approach suggested in the previous section is a first approximation.

The comparison of the calculated HMX response functions with those obtained experimentally using a T-burner¹³ shows that the functions calculated here are significantly lower ($\text{Re}\{U_{\max}\} = 1\text{--}1.5$ without melting and $\text{Re}\{U_{\max}\} = 0.5\text{--}0.6$ with melting) than the experimentally obtained response functions ($\text{Re}\{U_{\max}\} = 1.2\text{--}2.0$). The Ward et al. model described in Ref. 13 also predicts elevated values of $\text{Re}\{U_{\max}\}$ in the range of 2.5–2.8.

Table 8 Dimensionless characteristics of propellant response functions:
Propellants A–D

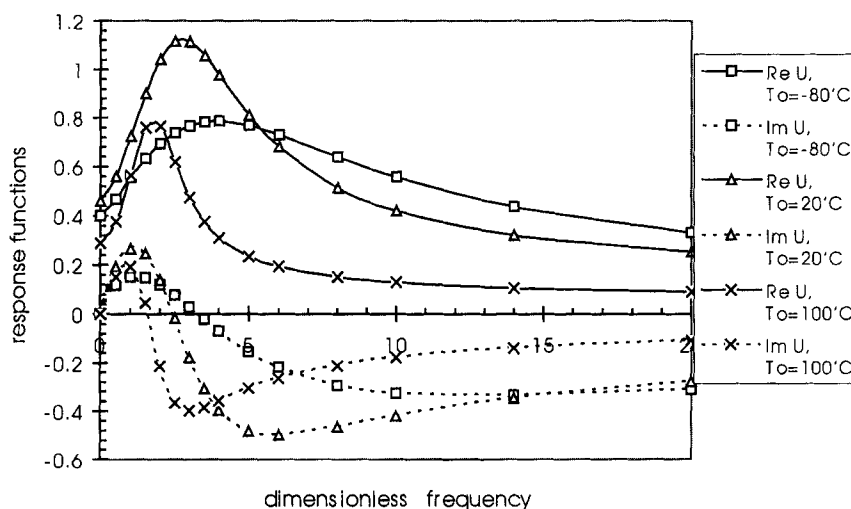
Propellant	Pressure,		Property					
	p , atm	T_0 , °C	$\text{Re}\{U_{\max}\}$	\sqrt{k}/r	ω_{n1}	ω_{n2}	$\text{Im}\{U_{\max(+)}\}$	$\text{Im}\{U_{\max(-)}\}$
A	20	–80	0.79	5	4	3.3	0.15	–0.34
		+20	1.12	3	2.5	2.5	0.27	–0.50
		+100	0.77	2	2	2	0.19	–0.40
	100	–80	1.43	4	3.5	3.5	0.42	–0.68
		+20	1.06	3	3	2.9	0.25	–0.41
		+100	0.53	2.5	2	2	0.09	–0.20
B	20	–80	0.72	5	4	3.5	0.14	–0.29
		+20	0.56	3.6	3	2.5	0.10	–0.22
		+100	0.46	2.5	2	1.5	0.07	–0.19
	100	–80	0.71	5.2	4.3	4	0.13	–0.23
		+20	0.55	3.7	3	2.7	0.10	–0.19
		+100	0.50	2.6	2	1.8	0.08	–0.19
C	20	–80	0.42	2.6	2	2	0.05	–0.07
		+20	0.52	4	3	2.3	0.06	–0.19
		+100	0.88	2	1.5	1.6	0.23	–0.48
	100	–80	0.74	3.4	3	3	0.19	–0.27
		+20	1.25	3.4	3	3	0.34	–0.66
		+100	1.09	2	2	1.7	0.33	–0.55
D	20	–80	0.59	5.6	4.5	4	0.10	–0.19
		+20	0.66	3	2.5	2.3	0.11	–0.23
		+100	0.53	2.4	2	1.5	0.08	–0.24
	100	–80	1.05	4.3	4	3.8	0.30	–0.43
		+20	0.75	3.5	3	2.7	0.15	–0.27
		+100	0.47	2.8	2	1.8	0.06	–0.17

B. Propellant Response Functions

Figures 6–9 present typical dependencies of $\text{Re}\{U(\omega)\}$ and $\text{Im}\{U(\omega)\}$ for propellants A and B. Table 8 shows dimensionless characteristics of the response functions of propellants A–D. The propellants with HMX have only 10% HMX, and nitrosoamine does not melt, so that all calculations for the propellants were performed using Eq. (8). It can be seen that burning propellants A–D, as oscillating systems, have a high quality; the variations in the functions $\text{Re}\{(\omega)\}$ and $\text{Im}\{U(\omega)\}$ with frequency close to the resonance frequency ω_n are rather sharp. In this frequency region, any small perturbation can significantly affect the response functions. It can be seen from Figs. 6–9 and Table 8 that propellant A has elevated values of the response function, in comparison with that of HMX. The same can be seen from, Figs. 10–13 for propellant E. A very important result of the calculations is a significant decrease in the propellant response functions if HMX is added to the propellants. The maximal values of $\text{Re}\{U_L(\omega)\}$ of HMX are relatively close to the response functions of the propellants containing HMX.

Table 9 Dimensionless characteristics of propellant response functions:
Propellants E and G

Propellant	Pressure, p , atm	T_0 , °C	Property					
			$\text{Re}\{U_{\max}\}$	\sqrt{k}/r	ω_{n1}	ω_{n2}	$\text{Im}\{U_{\max(+)}\}$	$\text{Im}\{U_{\max(-)}\}$
E	20	-70	1.58	4.7	4	3.5	0.37	-0.71
		+20	0.80	3.6	3	2.5	0.16	-0.40
		+50	1.87	2.3	2	2.5	0.59	-1.01
	50	-70	0.89	10.5	4.5	3	0.04	<-0.12
		+20	1.01	4	3	2.2	0.13	-0.37
		+50	4.17	1.9	2	2	1.56	-2.3
	100	-70	1.03	—	~5	3.5	0.01	<-0.04
		+20	1.27	4.7	3.5	2.7	0.14	-0.37
		+50	2.59	2.4	2.5	2.4	0.73	-1.22
G	20	-70	0.81	5.9	4.5	3.8	0.13	<-0.27
		+20	0.71	4.2	3	2.5	0.09	-0.27
		+50	0.86	3	2.5	2	0.16	-0.39
	50	-70	0.85	5	4	3.8	0.14	-0.28
		+20	0.82	4	3	2.6	0.11	-0.27
		+50	0.67	6	3	2.4	0.03	<-0.13
	100	-70	1.41	4	3.5	3.4	0.38	-0.61
		+20	1.77	2.6	2.5	2.6	0.49	-0.72
		+50	5.55	1.8	2	2	3.28	-4.33

**Fig. 6** Response functions of propellant A at 20 atm.

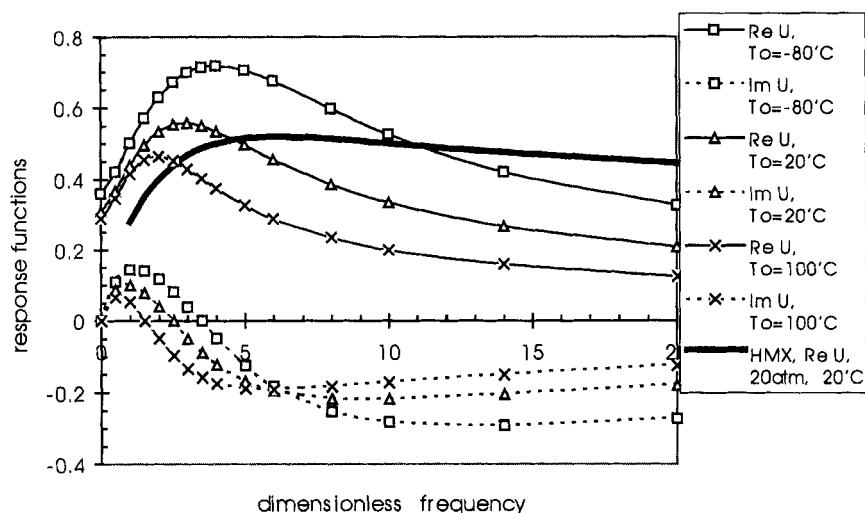


Fig. 7 Response functions of propellant B at 20 atm.

Excluding the Ni catalyst from the propellants leads, as a rule, to an increase in $\text{Re}\{U_{\max}\}$, especially at elevated T_0 (see data for propellant C in Table 8). Decreasing HMX particle size in the propellants without the Ni catalyst leads to a decrease in values of $\text{Re}\{U_{\max}\}$ at elevated pressure and T_0 and to an increase in values of $\text{Re}\{U_{\max}\}$ at 20 atm and low T_0 (see data for propellant D in Table 8). The values of $\text{Re}\{U_{\max}\}$ are about twice as high as the absolute values of $\text{Im}\{U_{\max(-)}\}$, and the absolute values of $\text{Im}\{U_{\max(-)}\}$ are about twice as high as

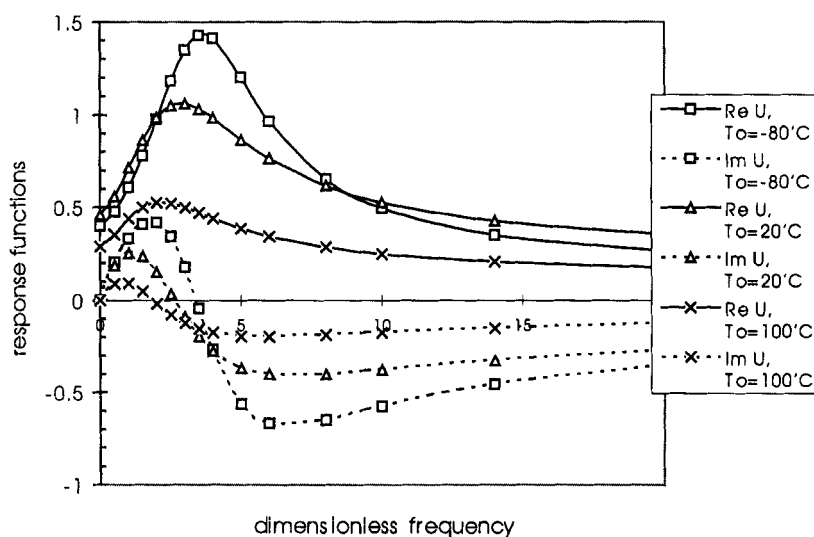


Fig. 8 Response functions of propellant A at 100 atm.

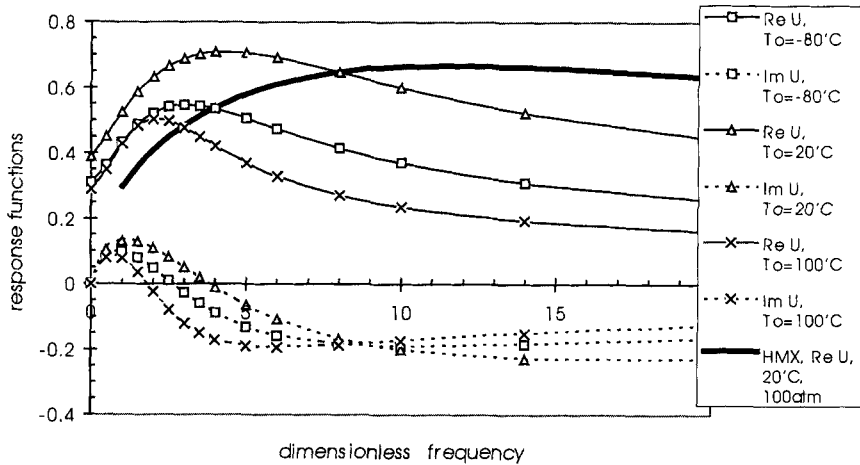


Fig. 9 Response functions of propellant B at 100 atm.

those of $\text{Im}\{U_{\max(+)}\}$. The investigated propellants of relatively low caloric power have, as a rule, decreasing $\text{Re}\{U_{\max}\}$ with T_0 (note that propellant C is an exception).

The formula $\sqrt{k/r}$ gives an adequate prediction for the values of ω_{n1} and ω_{n2} . As a rule, the formula slightly overestimates the real resonance frequencies. The difference between ω_{n1} and ω_{n2} is small, and the following relationship holds for these propellants: $\omega_{n1} \geq \omega_{n2}$. Figures 10–13 present typical dependencies of $\text{Re}\{U(\omega)\}$ and $\text{Im}\{U(\omega)\}$ for the propellants of elevated caloric power, E and D. It can be seen that burning propellants E and G, as oscillating systems, have a very high quality: the variations in the response functions with frequency close

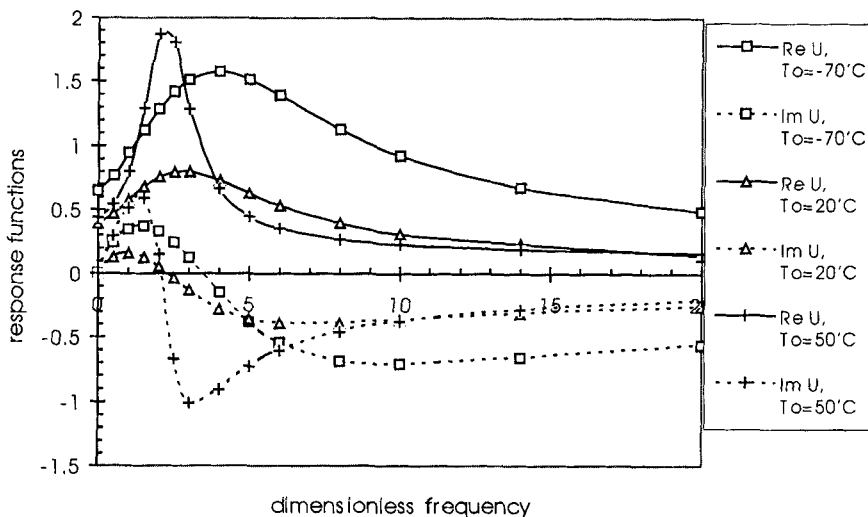


Fig. 10 Response functions of propellant E at 20 atm.

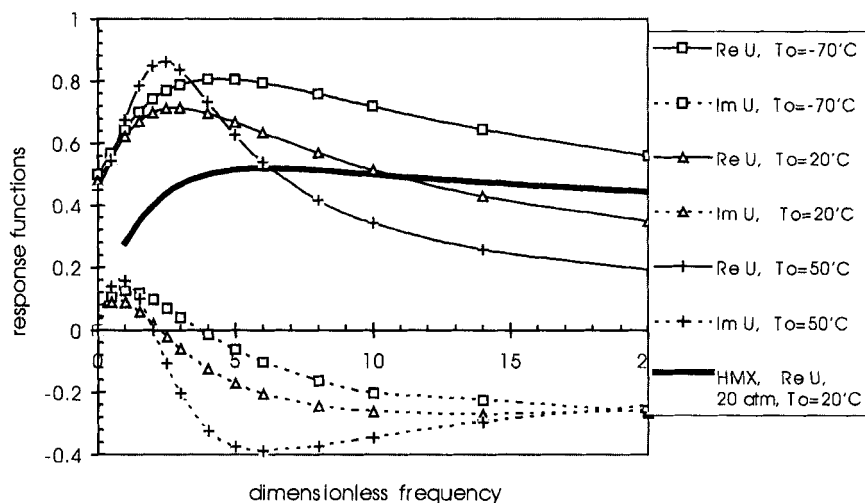


Fig. 11 Response functions of propellant G at 20 atm.

to the resonance frequency ω_n are very sharp. In this frequency region any small perturbations lead to a significant change in the response functions.

Table 9 shows dimensionless characteristics of the response functions of propellants E and G. It can be seen that increasing caloric power leads to significantly increased values of the propellant response functions, especially at 100 atm (up to 3–5.5). The addition of HMX decreases values of $\text{Re}\{U_{\max}\}$, but this decrease is observed only at 20 and 50 atm (see data for propellant G in Table 9, in comparison with those for propellant E). In this pressure region, the values of $\text{Re}\{U_{\max}\}$ practically do not depend on T_0 . At 100 atm, on the contrary, the addition of HMX increases the values of $\text{Re}\{U_{\max}\}$, and at this pressure, the values of $\text{Re}\{U_{\max}\}$ increase with T_0 . Especially quick growth of $\text{Re}\{U_{\max}\}$ is observed here at $T_0 = 50^\circ\text{C}$. Like the case of the low-caloric power propellants, the formula \sqrt{k}/r gives almost-adequate predictions of the resonance frequencies ω_{n1} and ω_{n2} . As a rule, the formula slightly overestimates the real resonance frequencies of propellants E and G. The following relationship also holds here: $\omega_{n1} \geq \omega_{n2}$.

VI. Conclusions

Pressure and temperature sensitivities of burning rates and burning surface temperatures, established for six modified double-base propellants and HMX, were used for calculations of burning-rate response functions to acoustic pulsations. All the propellants contained nitroglycerine and nitrosoamine; the latter was replaced in some propellants by HMX of different particle sizes. A theoretical expression for the burning-rate response function of HMX, having a liquid layer on the burning surface, was obtained and used for the calculations. Burning-rate response functions were found as a function of pulsation frequency at pressures of 10–100 atm and at sample temperatures of from -80 to 100°C . It was shown that a liquid layer on the burning surface significantly decreases the amplitude of the HMX response functions. Also, including HMX in the modified double-base propellants

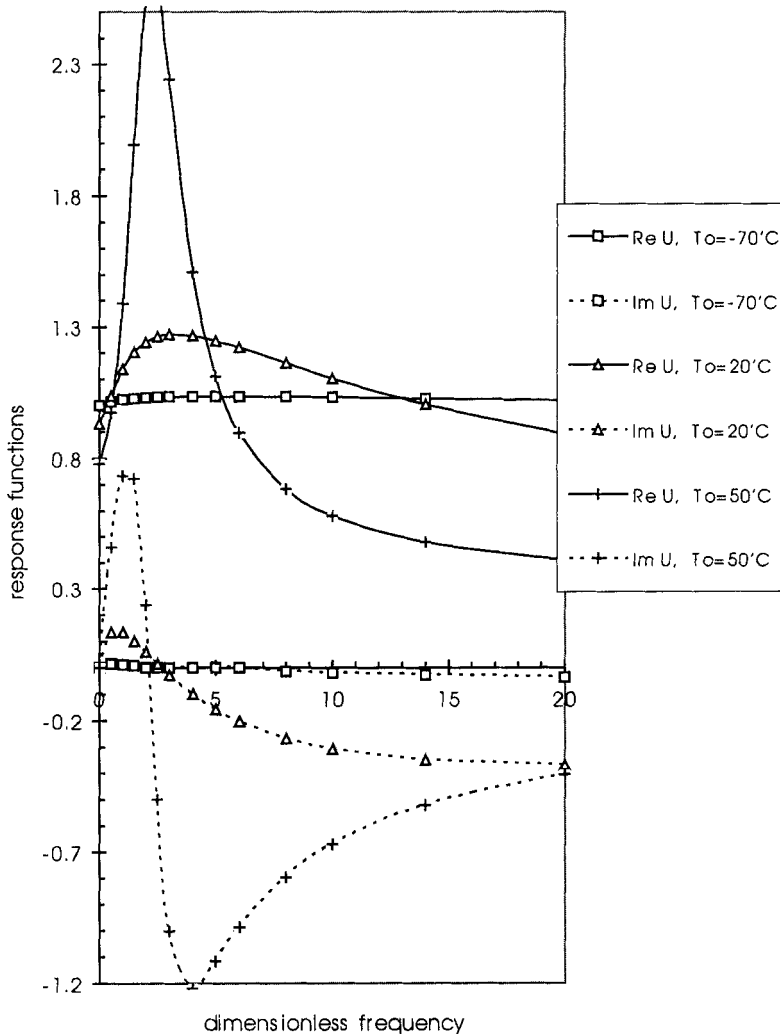


Fig. 12 Response functions of propellant E at 100 atm.

significantly decreases the amplitude of the propellant response functions. The dimensionless characteristics of the response functions were described as functions of pressure and sample temperature. The influence of propellant content on the response functions was investigated.

The following main features of the investigated response functions were found:

(1) Burning HMX has low response-function amplitudes. HMX, as an oscillating system, has a low quality: the response functions are relatively constant with frequency close to the resonance frequencies.

(2) Normal double-base modified propellants have increased response-function amplitudes (relative to HMX). These propellants, as oscillating systems, have a

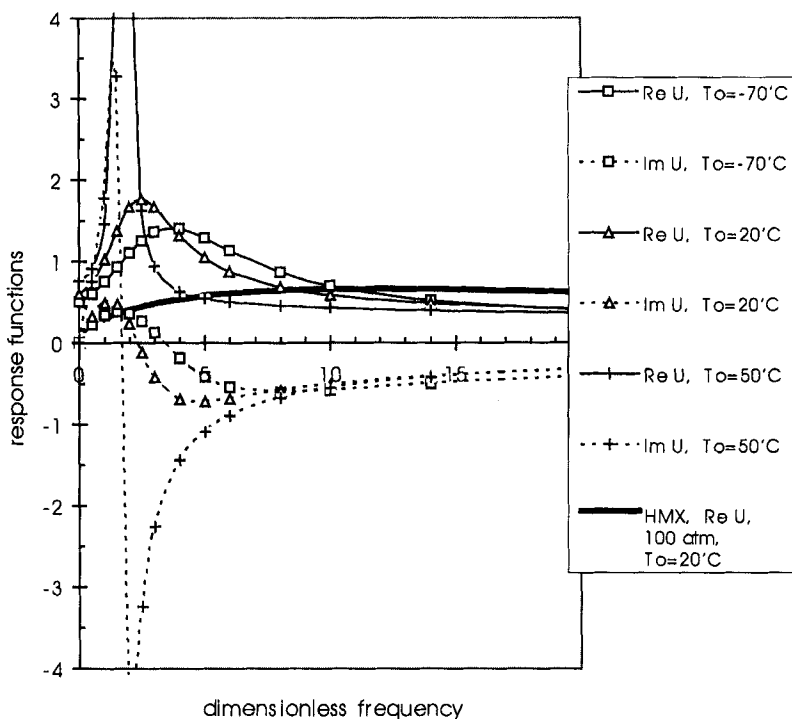


Fig. 13 Response functions of propellant G at 100 atm.

high quality: the response functions vary significantly with frequency close to the resonance frequencies.

(3) Double-base modified propellants with higher concentrations of nitroglycerine have high response amplitudes. These propellants, as oscillating systems, have a very high quality: the response functions vary dramatically with frequency close to the resonance frequencies.

Future work should be devoted to using the methods developed in this work for investigations of combustion of new energetic materials.

Acknowledgment

This work was partly supported by the Russian Foundation of Basic Research under Grant No. 97-03-32076a. This support is much appreciated.

References

- ¹Culick, F. E. C., "A Review of Calculations for Unsteady Burning of a Solid Propellant," *AIAA Journal*, Vol. 6, No. 12, 1968, pp. 2241–2255.
- ²Novozhilov, B. V., "Theory of Nonsteady Burning and Combustion Stability of Solid Propellants, by Zeldovich-Novozhilov Method," *Nonsteady Burning and Combustion Stability of Solid-Propellants*, edited by L. De Luca, E. W. Price, and M. Summerfield, Vol. 143, Progress in Astronautics and Aeronautics, AIAA, Washington, DC, 1992, pp. 601–641.

³Novozhilov, B. V., *Nonstationary Combustion of Solid Rocket Fuels*, Nauka, Moscow, 1973 (Translation AFSC FTD-MD-24-317-74).

⁴Price, E. W., "Experimental Observations of Combustion Instability," *Fundamentals of Solid-Propellant Combustion*, edited by K. K. Kuo and M. Summerfield, Vol. 90, Progress in Astronautics and Aeronautics, AIAA, New York, 1984, pp. 733–790.

⁵T'ien, J. S., "Theoretical Analysis of Combustion Instability," *Fundamentals of Solid-Propellant Combustion*, edited by K. K. Kuo and M. Summerfield, Vol. 90, Progress in Astronautics and Aeronautics, AIAA, New York, 1984, pp. 791–840.

⁶Novozhilov, B. V., Kohno, M., Maruizumi, H., and Shimara, T., "Solid Propellant Burning Rate Response Functions of Higher Orders," Institute of Space and Astronautical Sciences, Rept. No. 661, Kanagawa, Japan, 1996.

⁷Mihlfeith, C. M., Baer, A. D., and Ryan, N. W., "The Response of a Burning Propellant Surface to Thermal Radiation," *AIAA Journal*, Vol. 10, No. 10, 1972, pp. 1280–1285.

⁸Zarko, V. E., Simonenko, V. N., and Kiskin, A. B., "Radiation Driven Transient Burning," *Nonsteady Burning and Combustion Stability of Solid-Propellants*, edited by L. De Luca, E. W. Price, and M. Summerfield, Vol. 143, Progress in Astronautics and Aeronautics, AIAA, Washington, DC, 1992, pp. 363–398.

⁹Finlinson, J. C., Hanson-Parr, D., Son, S. F., and Brewster, M. Q., "Measurement of Propellant Combustion Response to Sinusoidal Radiant Heat Flux," AIAA Paper 91-0204, 1991.

¹⁰Lee, C., and Kim, S.-I., "Re-Examination of the Response Function of Solid Propellant with Radiant Flux," AIAA Paper 99-0590, Jan. 1999.

¹¹Cauty, F., "Solid Propellant Response Functions from Direct Measurement Methods: A Review of ONERA Experience," Materials of International Workshop on Combustion Instability of Solid Propellants and Rocket Motors, June 1997, Milan, Italy.

¹²De Luca, L., "Theory of Nonsteady Burning and Combustion Stability of Solid Propellants by Flame Model," *Nonsteady Burning and Combustion Stability of Solid-Propellants*, edited by L. De Luca, E. W. Price, and M. Summerfield, Vol. 143, Progress in Astronautics and Aeronautics, AIAA, Washington, DC, 1992, pp. 519–600.

¹³Finlinson, J. C., Stalnaker, R. A., and Blomshield, F. S., "HMX and RDX—Burner Pressure Coupled Response from 200 to 1000 Psi," AIAA Paper 98-0556, Jan. 1998.

¹⁴Hickman, S. R., and Brewster, M. Q., "Oscillatory Combustion of Fine-AP/HTPB Propellants," AIAA Paper 98-0557, Jan. 1998.

¹⁵Beckstead, M. W., and Erikson, W. W., "Solid Monopropellant Oscillatory Combustion Instability," Materials of the 2nd International Conference on Combustion, St. Petersburg, Russia, 1996.

¹⁶Erikson, W. W., and Beckstead, M. W., "Modeling Unsteady Monopropellant Combustion with Full Chemical Kinetics," AIAA Paper 98-0804, Jan. 1998.

¹⁷Zenin, A. A., "HMX and RDX: Combustion Mechanism and Influence on Modern Double-Base Propellant Combustion," *Journal of Propulsion and Power*, Vol. 11, No. 4, 1995, pp. 752–758.

¹⁸Culick, F. E. C., and Yang, V., "Prediction of the Stability of Nonsteady Motions in Solid-Propellant Rocket Motor," *Nonsteady Burning and Combustion Stability of Solid-Propellants*, edited by L. De Luca, E. W. Price, and M. Summerfield, Vol. 143, Progress in Astronautics and Aeronautics, AIAA, Washington, DC, 1992, pp. 719–780.

¹⁹Roh, T. S., Tseng, I. S., and Yang, V., "Effect of Acoustic Oscillations on Flame Dynamics of Homogeneous Propellants in Rocket Motors," *Journal of Propulsion and Power*, Vol. 11, No. 4, 1995, pp. 640–650.

²⁰Pivkin, N. M., and Pelikn, N. M., "High Frequency Instability of Combustion in Solid Rocket Motors," *Journal of Propulsion and Power*, Vol. 11, No. 4, 1995, pp. 651–656.

²¹Culick, F. E. C., Burnley, V., and Swenson, G., "Pulsed Instability in Solid-Propellant Rockets," *Journal of Propulsion and Power*, Vol. 11, No. 4, 1995, pp. 657–665.

²²Wicker, J. M., Greene, W. D., Kim, S. I., and Yang, V., "Triggering of Longitudinal Combustion Instabilities in Rocket Motors: Nonlinear Combustion Response," *Journal of Propulsion and Power*, Vol. 12, No. 6, 1996, pp. 1148–1158.

²³Beckstead, M. W., and Blomshield, F. S., "Some Nonlinear Combustion Instability Characteristics of Solid Propellant Rocket Motors," Materials of International Workshop on Combustion Instability of Solid Propellants and Rocket Motors, Milan, Italy, June 1997.

²⁴Blomshield, F. S., Bicker, C. J., and Stalnaker, R. A., "High Pressure Pulsed Motor Firing Combustion Instability Investigations," AIAA Paper 97-3253, 1997.

²⁵Zenin, A. A., Finjakov, S. V., Puchkov, V. M., and Ibragimov, N. G., "Temperature and Pressure Sensitivities of Burning Wave Parameters of Nitramine-Containing Propellants and HMX," *Journal of Propulsion and Power*, Vol. 15, No. 6, 1999, pp. 753–758.

²⁶Zenin, A. A., Finjakov, S. V., Puchkov, V. M., and Ibragimov, N. G., "Temperature Coefficients of Burning Wave Parameters of Propellants with Nitramines," *Chemicheskaja Fizika*, Moscow, 1999 (in Russian; to be published).

²⁷Zenin, A. A., and Finjakov, S. V., "Burning Rate Response Functions of Nitramine-Containing Propellants and HMX Due to Data of Microthermocouple Measurements," *Fizika Goreniya i Vzryva*, Vol. 36, No. 1, 2000 pp. 12–22 (in Russian).

²⁸Zenin, A. A., Puchkov, V. M., and Finjakov, S. V., "Characteristics of HMX Combustion Waves at Various Pressures and Initial Temperatures," *Combustion, Explosion and Shock Waves*, Vol. 34, No. 2, 1998, pp. 170–176.

²⁹Gusachenko, L. K., "Influence of Melting on Combustion Stability of Quasihomogeneous Systems. Method of Zel'dovich-Novozhilov," *Fizika Goreniya i Vzryva*, Vol. 34, No. 4, pp. 26–29 (in Russian).

³⁰Finjakov, S. V., "Influence of Melted Layer at Burning Surface on Burning Rate Response Functions of Condensed Systems," *Chemicheskaja Fizika*, Moscow, 2000 (in Russian; to be published).

Chapter 2.18

Combustion of Aluminized Solid Propellants

E. W. Price* and R. K. Sigman†

Georgia Institute of Technology, Atlanta, Georgia

I. Introduction

ALUMINUM is used as an ingredient in solid rocket propellants because of its high density, high heat release during oxidation, low cost, and relative safety—properties particularly desirable in ballistic missiles and boosters for space launch vehicles. Because most unaluminized propellants are already fuel rich, it would seem that addition of more fuel (aluminum) would be counterproductive, especially when the reaction product (Al_2O_3) is in a liquid state. However, the oxidation reduces the oxidizer vapors (H_2O and CO_2) to H_2 and CO , better propulsive fluids. This, in combination with a large increase in temperature from oxidation of the aluminum, results in increases in specific impulse of around 10%, along with a net gain in propellant mass fraction in the motor of typically 15%. Also, the addition of aluminum in even modest amounts suppresses combustion instability problems that are common in motor development programs.

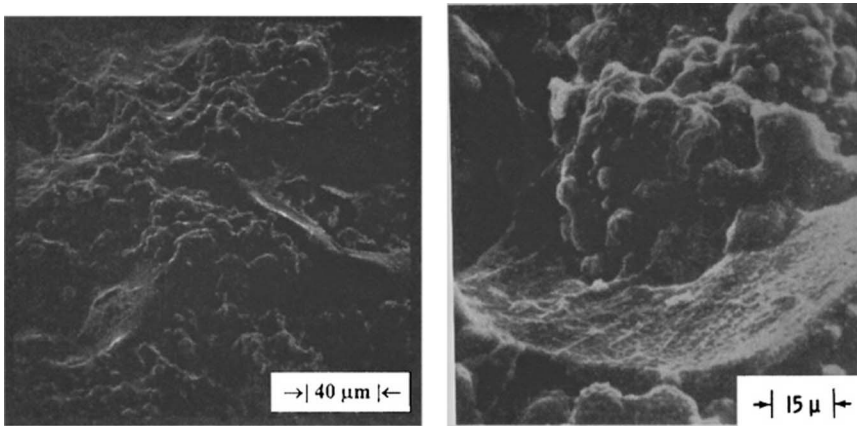
On the other hand, there are problems with use of aluminum, such as smoky, luminous exhaust trails; expected interference with telemetered flight data link and radar-beam guidance systems; contamination of launch sites with Al_2O_3 ; adverse effects on motor components in the extra-hot, two-phase flow; and potential for increased fire damage in the event of launch failure. In some motors accumulation of slag and emission in bursts have been problems. In spin-stabilized motors centrifugal force causes aluminum to linger on the burning surface (affecting burning rate and enhancing slag accumulation). Although the hotter two-phase flow is a more hostile environment for internal motor components, oxidative attack on components is reduced by the reduced oxidizing potential of the modified gas species present in the flow.

For this study the most important aspect of aluminum as a propellant ingredient comes from the fact that aluminum does not generally turn to a vapor at the

Copyright © 1999 by the American Institute of Aeronautics and Astronautics, Inc. All rights reserved.

*Regent's Professor Emeritus, School of Aerospace Engineering.

†Senior Research Engineer, School of Aerospace Engineering.



a) Al particles concentrated in the binder melt b) Concentrated Al particles on the burning surface of an AP particle

Fig. 1 Quenched surface of AP/HTPB propellants with 18% aluminum (quenched from 1000 psi) showing.

propellant burning surface like other primary ingredients, and its reaction or ignition on the surface is inhibited by refractory oxide coatings on the particle surfaces. The particles tend to adhere to the surface in binder melts, leading to concentrations there (concentrations are often observed on oxidizer surfaces as well) (Figs. 1a and 1b). The concentrations of typically 20- μm particles can lead to coalescence into large droplets (e.g., typically 200 μm , containing 10^3 original particles). Large droplets leave the burning surface and burn in the gas flowfield, whereas any original particles that leave the surface individually burn up within 1 or 2 mm of the surface (with a correspondingly greater effect on the propellant burning). In small motors the large droplets may not burn completely, which results in reduced specific impulse. The whole concentration-agglomeration-ignition-burning sequence is dependent on a whole range of propellant formulation and combustion environment variables, such as the 1) size distribution of oxidizer particles, 2) size distribution and amount of aluminum particles, 3) kind of oxidizer and binder, 4) presence of ballistic modifiers such as Fe_2O_3 , 5) pressure and its effect on proximity of hot gas-phase flames to the surface, and 6) state of the gas flowfield seen by the combustion zone.

In general, those mechanisms that decrease agglomeration increase burning rate, leading to a rule of thumb that higher burning rate causes reduced agglomeration. Another related issue is the effect of aluminum on propellant burning rate. Because the aluminum combustion usually occurs primarily outside the normal combustion zone, it does not enhance burning rate much. However, introduction of aluminum is at the expense of the oxidizer, and as a result it is difficult to determine an aluminum effect unambiguously.

This chapter will be concerned primarily with behavior of aluminum in ammonium perchlorate-hydrocarbon binder (AP/HCB) propellants. Further information may be found in earlier reviews (e.g., Refs. 1-4).

II. History

In the mid-1950s when the first experiments with aluminized propellants were made, most of the operational rockets were moderate-size tactical weapons with extruded double-base propellants, charges that were not amenable to addition of aluminum powder. However the age of slurry-mixed (AP/HCB) and solution-cast (double-base) and plastisol propellants in the United States was well started, and incorporating aluminum powder was no longer a major problem. However, nothing was known about how aluminum combustion would proceed. Thermochemical calculations were just beginning and suggested a potential for substantial performance gains, provided the actual combustion attained the thermochemical equilibrium. The first look at the combustion process was done by Waesche,⁵ using high-speed photography of the burning of small samples with low aluminum concentration. The first systematic computations of motor performance were done by Rumbel and Henderson.⁶ There was some hesitancy in the early efforts in that era of tactical rockets because of foreseeable problems such as those just noted. Even the relatively large (for the time) Sergeant⁷ and Hermes⁸ motors used unaluminized propellants. However, all of the then-operating U.S. rocket laboratories and companies (Jet Propulsion Lab, Aerojet, ARC, Thiokol, Allegany Ballistics Lab, Naval Weapons Center, Naval Ordnance Laboratory—Indian Head, Redstone Arsenal, Ballistic Research Lab at Aberdeen) were interested in incorporation of the aluminum ingredient and started motor testing of aluminized propellants in progressively larger motors.

In calculations of potential performance of intermediate- and long-range ballistic missiles (i.e., missiles with solid propellants), use of aluminum became a must if the missiles were to be of practical size.⁹ By then the effect of suppression of combustion instability by aluminum had been established,^{5,10,11} but anxieties remained that the unexplained magic of aluminum might not work in large motors.¹² This concern was soon justified in the development of the SUBROC missile, where a severe combustion instability problem had to be overcome.¹³ The thermal problems were overcome by composite liner materials, graphite nozzle throats, and molybdenum jet deflectors for direction control. In such large (lower-stage) motors the residence time of the aluminum in the combustion chamber was long enough for fairly complete aluminum combustion, but the high content of Al_2O_3 in the combustion products (e.g., 35%) caused some undesirable and difficult to predict two-phase flow effects. Aluminum was also used in several tactical rockets in the early 1960s, but then a major effort was begun in the early 1970s to get rid of the aluminum because the exhaust plume visibility compromised the weapon effectiveness.

In most cases the adoption of aluminum was accomplished without much knowledge about its detailed combustion behavior, but the threat of and encounters with combustion instability motivated relatively intense research starting in about 1958. This paper is concerned primarily with the results of such research.

III. Aluminum

Aluminum is unique among major propellant ingredients in several ways:

- 1) It does not decompose to a vapor at the burning surface. Its boiling point is 2467°C (pressure dependent).
- 2) The usual temperature of propellant burning surfaces is around 600°C , 60 deg below the 660°C melting point of aluminum.

3) The density is around 2.70 (specific gravity), 1.38 times that of AP and 3 times that of typical hydrocarbon (HC) binders.

4) The thermal conductivity is $0.503 \text{ cal/cm s}^\circ\text{C}$, 486 times that of AP and 1400 times that of typical HC binders.

5) The heat capacity is $0.214 \text{ cal/g }^\circ\text{C}$, 0.69 times that of AP and 0.46 times that of typical HC binders.

6) The particle surfaces are coated with an impervious refractory coating of Al_2O_3 (melting point 2072°C) that constitutes about 0.5% of the particle mass (for $25 \mu\text{m}$ particles).

7) Once the Al_2O_3 oxide coating is broken down, Al is extremely reactive in the combustion zone, but its rate is limited by its low vapor pressure (high boiling point).

8) Under most conditions the preceding characteristics cause the aluminum in propellant flames to burn primarily as droplets in the hot gas-phase region in and beyond the usual combustion zone, although some oxidation can occur during the residence time on the burning surface.

9) At high temperatures the droplets contain both aluminum and molten Al_2O_3 , which tend to separate into lobes of the droplets because Al and Al_2O_3 are insoluble.

10) At temperatures between the aluminum and Al_2O_3 melting points, leaking of Al from the oxide coating can lead to sintering in assemblages of particles, referred to here as sintered accumulates. Under progressively more extreme conditions, the leakage may be so great that the aluminum can engulf the assemblage. High aluminum surface tension causes the molten aluminum to produce spherical assemblages referred to here as *agglomerates*.

11) Under the latter conditions in item 10, the exposure of the molten aluminum leads to formation of a hot droplet flame with rapid further rise in temperature. The aluminum flame temperature is around 3800°C .

Most aluminum powder used in rocket propellants is manufactured by atomization of molten aluminum into a low-oxygen gas flow. The droplets become spherical if they do not freeze too quickly, an outcome that is controlled by process control variables, and differs among various suppliers. [Most powders used in propellants are not spherical (Fig. 2)]. While the droplets are cooling, oxidation of the droplet surfaces starts, and oxygen content in the gas flow must be low enough to avoid an aluminum fire. The oxide on the surface is solid. If formed before the aluminum solidifies, then it must experience some modifications during cooling because of the substantial shrinkage of the droplet (about 6% by volume) during freezing. Further surface oxidation no doubt occurs during and after freezing, leading to an oxide skin that becomes impervious to further oxidation. The thin oxide coating constitutes around 0.5% of the particle mass (for $25 \mu\text{m}$ powder). The character of the oxide is dependent on the processing variables to a degree that affects the sintering and agglomeration in propellant combustion. This is not reflected in usual propellant ingredient specifications, but has been a problem in some major weapon systems because of dependence of combustor stability on the details of the sintering behavior in the combustion zone.

IV. Thermal Response of Aluminum Powders

When aluminum powders are heated in inert atmospheres, the individual particles enlarge slightly because of thermal expansion. The coefficient of thermal expansion of the oxide skin is somewhat less so that it must be stressed. At the

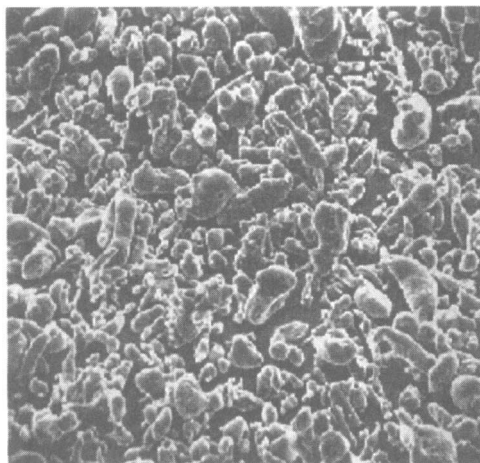


Fig. 2 Particles of aluminum powder widely used in rocket propellants.

melting point of the aluminum, it expands in volume by around 6%, thereby precipitously stressing the oxide skin further, and apparently causing cracks (Ref. 14) and opportunity for leaking of molten aluminum. Heating of Al powders on a hot plate to 1025°C showed that Al contact between particles causes the Al to draw up into large agglomerates (Fig. 3, also Refs. 1 and 2), leaving behind empty oxide debris. When the tests were done in an oxygen-containing atmosphere, the array of particles showed no visible thermal response, but the particles were found to be sintered together. In another series of tests using special spherical aluminum particles scattered on a plate heated to 1400°C in air (Refs. 3, 14, and 15), some coalescence of contacting particles occurred, leaving empty oxide shells. Individual particles showed intensive surface wrinkling, which on close examination

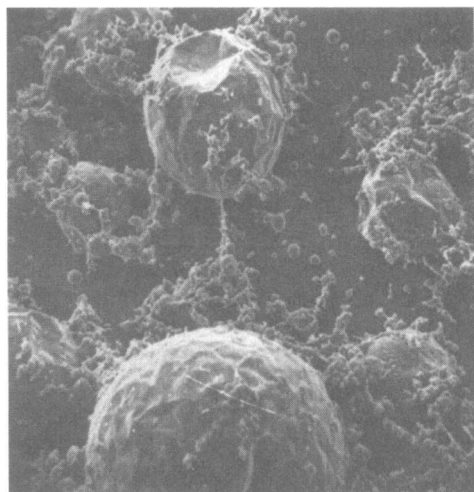


Fig. 3 Agglomeration of aluminum powder when heated abruptly to 1125°C in argon.

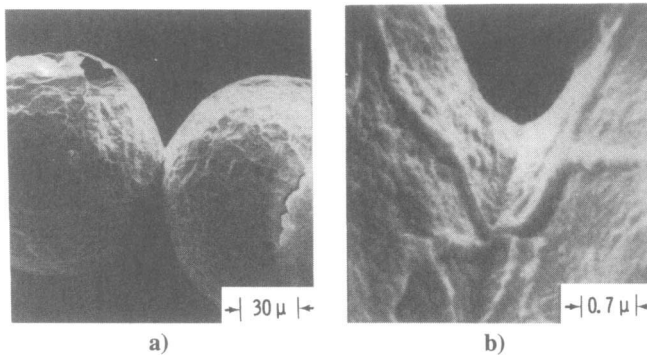


Fig. 4 Oxide skins on particles dropped on a 1400°C flame-heated plate: a) crack pattern with evidence of exuded aluminum oxidized in place and b) bridging between contacting particles.

consisted of cracking of the oxide skin and ridges that reflected oxidation of exuded Al at the cracks. Contacting particles that did not coalesce were sintered together (Fig. 4). The results indicate that Al leakage from cracks apparently can lead to either oxidative sealing, interparticle sintering, or coalescence. Such behavior has not been studied systematically and presumably would depend on properties of the particles, oxidizing atmosphere, and rate of heat-up. References 15 and 16 demonstrated that agglomeration (inert atmosphere) and sintering (oxidative atmosphere) behavior could be modified by heat treatment of the powders in oxidizing atmospheres that either 1) strengthened the oxide skin (prolonged heating at a temperature below the aluminum melting temperature.¹⁵) or 2) prestretched the oxide skin by brief heating above the melting point in an atmosphere with low O₂ concentration.¹⁶

Note that the sintering oxidation necessarily releases heat, and in the propellant combustion zone this heat may contribute to propellant burning rate or at least compensate for the heat expended for heat-up and melting. However the heat-up in the combustion zone progresses rapidly to higher temperatures that lead to agglomeration and intense heat release, in a complex oxide-melting Al agglomeration-inflammation event.

An interesting insight is gained into the sintering-agglomeration-ignition process of aluminum by burning samples prepared by dry pressing mixtures of AP and aluminum powders, e.g., Refs. 2, 16, and 17. At 1000 psi such samples burn at rates comparable to pure AP. High-speed photography of the combustion shows that the aluminum concentrates and sinters on the burning surface and ignites primarily as sections of the sintered layer break loose from the surface. It has been suggested that full ignition is not achieved until the oxide melting temperature is reached, but in a sintered structure it is probable that ignition occurs locally at favorable sites (possibly because of oxide breakage during detachment) and spreads through the sintered structure caused by heating from the already inflamed sites. Such spreading behavior is revealed in the combustion photography as a precursor to agglomerate formation. The most remarkable features of the AP/Al pellet tests are 1) retention-concentration of Al on the burning surface of AP, 2) sintering of the accumulated Al, 3) progressive inflammation leading to burning agglomerates

primarily during or after detachment from the surface; and 4) periodic repetition of this process.^{3,17}

The foregoing gives some idea of physical processes that have been found to be important to explanation of aluminum behavior in propellant combustion. One further area of the overall behavior, somewhat more well studied (at least in laboratory conditions), is the actual burning of aluminum droplets.

V. Droplet Burning

Burning of aluminum agglomerates in the relevant propellant combustion environment is difficult to study because of the smoke obscuration and high pressure, but there have been many studies of the burning of single aluminum droplets in various gaseous environments. Some have been in gas burner flames (e.g., Refs. 18–20), but most have been in room-temperature, room-pressure environments.^{21–25} Increasingly more sophisticated analytical and computational models have been developed.^{26–28} All describe steady burning of spherical droplets. Aside from recognized complications caused by growth of a lobe of oxide on the droplet, the models and experiments indicate that the burning droplet is at a temperature close to the aluminum boiling point and that aluminum vapor reacts with the oxidizing atmosphere in a surrounding flame envelope. Reference 29 noted that an adiabatic reaction to Al_2O_3 would lead to a temperature so high that the Al_2O_3 would dissociate. In the diffusion flame droplets of Al_2O_3 form by their ability to radiate energy, and the rate of formation and growth of droplets (and progress of reaction) is to some extent limited by the rate of this radiant dumping of excess energy (giving rise to the long recognized high luminosity of aluminum flames and pyrotechnics). When droplets burning in Ar/O_2 atmospheres are quenched by impingement on sampling surfaces, the smoke envelope is revealed, along with the parent droplet (Fig. 5a). Also evident [when other oxygen-containing atmospheres are used (Fig. 5b)] is an oxide lobe on the aluminum droplet^{1–3}

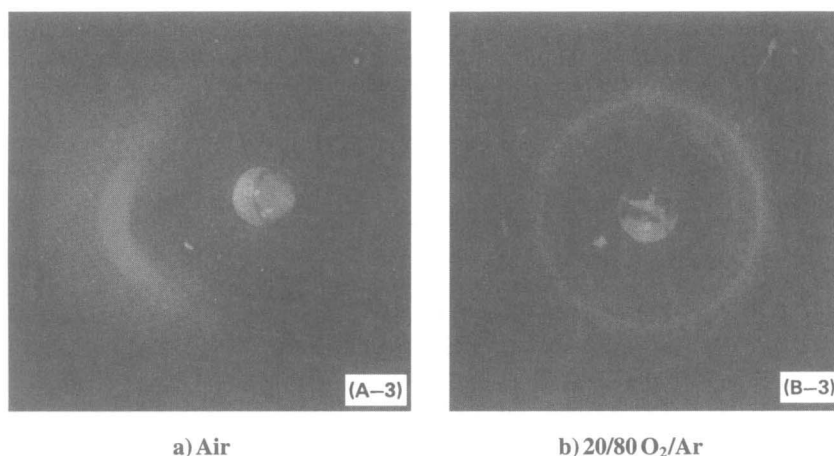


Fig. 5 Aluminum particles intercepted during burning by falling on a quench plate. The halo is oxide smoke (test in 1 atm, room-temperature gas).

indicative of accumulation of Al_2O_3 by either surface reaction or by diffusion from the flame envelope (recent models consider both processes).^{27,28}

The foregoing description of Al droplet burning does not characterize the behavior either late in burning when the oxide lobe dominates the burning or when other atmospheres are used.¹⁸⁻²³ It is not intended to summarize the atmospheric effects here, but to point out further phenomena that occur: 1) spiraling trajectories of free-falling particles, 2) ejection of subsidiary droplets (or bubbles?), 3) fragmentation of the parent droplet into several smaller droplets, and 4) fading of the flame followed by one or more puffs (seen in streak photographs of free-falling droplets).

In most cases these anomalies occur after an initial period of quiet burning and appear to result from increasing effect of the oxide late in burning when it becomes a major part of the droplet. The extent to which it is typical of burning Al droplets and agglomerates in rocket motor-like environments is undetermined. From the practical viewpoint the anomalous behavior is of interest to rocket motors primarily to the extent that phenomenon 1 affects completeness of burning, phenomenon 2 affects the size distribution of oxide droplets in the two-phase flow in the motor, and phenomena 3, 1, and 2 affect motors via heat transfer, slag formation, impulse loss, and damping of flow oscillations.

Given the observed effect of gas environment in the single particle burning experiments, there remains some uncertainty about burning in rocket motors, where the droplets are more complex (agglomerates); the environment is hot, high pressure, and chemically complex; and the droplet is part of a convective, progressive group-burning environment. On the other hand, the single-particle studies provide essential insight into the distinctive burning of aluminum and origin of the oxide droplet population. They also provide data for a droplet burning-rate law, based on observations of burning time vs droplet diameter:

$$t_b = A(D^2 / \sum c_i \chi_i)$$

where A is a constant (dependent on ambient temperature and pressure) and c_i and χ_i are the constants and mole fractions for the individual oxidizing species, respectively.²⁰ The reference suggests values of c_i for H_2O , CO_2 , and O_2 of 0.533, 0.135, and 1.00 based on studies of droplet burning at 1 atm. Burning times of 0.5–2.5 ms are indicated for 20- μm droplets and 60–200 ms for 200- μm droplets, the shorter times corresponded to higher oxygen content in the combustion atmosphere.

VI. Accumulation and Agglomeration

When a particle of aluminum is reached by the propellant burning surface, it is usually not yet melted and is in a pyrolyzing fuel environment, usually a binder melt (binder-dependent). The particle is not immediately carried away because it is temporarily stuck in the binder melt. It is not immediately ignited because of its fuel-rich environment and because it has a protective solid Al_2O_3 coating. In typical composite propellants the aluminum particles are small compared to the oxidizer particles and hence are concentrated in pockets between oxidizer particles. At those sites aluminum particles continue to emerge and collect on the receding surface (Fig. 6) until the changing environment or degree of concentration precipitates ignition and/or detachment from the surface, either singly or collectively.

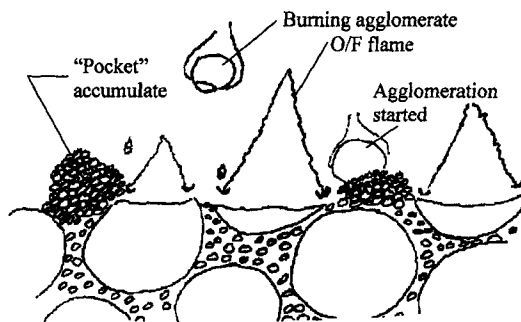


Fig. 6 Progression of the burning front into the propellant.

Some investigators attribute retention of aluminum on the surface to presence of a carbonaceous grid on the binder surface,³⁰ a convenient postulate that is possibly applicable with some binders. The issue of surface retention-concentration is an important one because the observation is made that the bulk of the concentration ends up in the gas phase as large droplets that contain 10–1000 or more original particles, with droplets referred to as agglomerates. As one might suspect, the size distribution of the agglomerates depends on 1) the structural features of the Al particle packing in the propellant, 2) the surface retention characteristics of the binder, 3) the susceptibility of individual particles to ignition, 4) possible connective processes between concentrating particles that lead to group behavior, and 5) evolution of underlying structure and hot overlying gas flamelets that lead to detachment-ignition events. These considerations are examined in some detail here because they affect the propellant burning rate, combustion efficiency, combustor stability, and two-phase flow effects.

A. Particle Packing

The stoichiometry of the AP/HCB system dictates that a maximum achievable content of AP be used consistent with required propellant processing and mechanical properties. To this end a coarse (e.g., 200 μm) AP portion is combined with finer particles selected to fill the spaces left in the coarse particle array. By careful blending of sizes (e.g., using trimodal particle size), formulations can be processed with 86–88% AP by weight, yielding cured propellants with acceptable mechanical properties. Such propellants are still somewhat fuel rich. When aluminum is added to the formulation, it is necessary to reduce the AP content to accommodate the aluminum. The Al particle size is typically 10–30 μm , and a corresponding volume of fine AP is removed to make room for the Al. This leaves a very fuel-rich mixture (Al and binder, some AP) in between the coarse AP particles. Thus, the aluminum particles (Fig. 6) are preconcentrated in pockets in the coarse AP packing pattern,^{1–3,30–34} pockets that are interconnected by bridges that may or may not contain Al particles depending on fineness of the Al particles. When high aluminum content is used, there is not much room left for fine AP.

The foregoing description is oriented around the idea that there are pockets in the AP packing pattern where aluminum particles are already preconcentrated in the mix, pockets that would be occupied by fine AP if no aluminum were used.

However, combinations of AP and aluminum particles sizes can be chosen in which the preconcentrations of aluminum in the packing array are more tenuous and may or may not lead to agglomeration, depending on proximity of ignition sources above the surface (see this subject later). In addition, use of large aluminum particles (e.g., $100\text{ }\mu\text{m}$) leads to sufficient distance between particles to minimize their interaction. The flexibility for choices is limited in practice by considerations of ingredient supply, propellant processing, product mechanical properties, and safety.

B. Retention of Aluminum on the Burning Surface

Once a particle is free of the surface, the vapors from the other pyrolyzing ingredients carry it away with the outward vapor flow. However, there is ample evidence that emergence of the particle is complicated by surface retention forces, leading to aluminum concentration on the surface. It seems reasonable to consider these mechanisms: 1) particle adhesion in a binder melt layer, 2) retention in a carbonaceous surface structure, 3) direct adhesion (sintering) to underlying Al particles, and 4) centrifugal force in spinning motors. Whatever the mechanism(s), it is evident that there is a tendency for surface retention-accumulation for a wide variety of nonvolatile particulate materials (Fe_2O_3 , Cr_2O_3 , Al_2O_3 , Al). The retention mechanisms are matters of speculation because they are inaccessible to measurement. It is evident from interrupted burning samples (Fig. 1) that the binder melt is involved with many butadiene binders. The relative roles of the aforementioned mechanisms probably depend on type of binder, amount of Al, Al particle characteristics, and extent of fine AP or carbon powder in the Al-binder matrix.

C. Susceptibility of Al Particles to Ignition

Aluminum is an extremely reactive material in oxidizing atmospheres, but ignition is impeded by the refractory oxide skin until conditions are reached that cause the skin to break down. Temperatures at the propellant surface are typically 600°C , whereas the melting point of the oxide skin is around 2070°C . Unless an individual particle emerges at a site where oxidizer vapors are present and high heat flow from a close-by hot oxidizer-binder vapor flamelet are present, the particle will not ignite. If it does ignite, its temperature will quickly become so high that residence on the surface will end. Other less favorably located particles tend to reside on the binder surface and to be joined by underlying particles (see Fig. 6). Such behavior is favored by low combustion pressure with correspondingly greater standoff distance of hot flamelets and also by coarse oxidizer size that reduces average proximity of Al to oxidizer vapor and heat sources. The presence of Al/binder-filled pockets gives rise to relatively large areas of concentration with relatively low extent of ignitions of individual particles. On the other hand, the extent of ignition via individual particles is enhanced if the AP and Al particle sizes are selected so that all Al particles are alone, i.e., surrounded by AP (no pockets). For practical reasons this usually can only be achieved by using relatively coarse Al particle size (i.e., $50\text{--}100\text{ }\mu\text{m}$ in typical AP propellants). An alternative strategy to facilitate ignition of Al particles incorporates enough fine AP in the formulation to provide particles in every major pocket, ensuring that most Al particles are near AP particles. This can lead to ignition of a relatively high portion of the Al particles individually, but the effect is strongly pressure-dependent because small AP

particles fail to establish hot near-surface flamelets at low pressures.³² Burning-rate catalysts (like Fe_2O_3) decrease the degree of agglomeration, probably by causing the hot flamelets to stand closer to the surface and facilitating aluminum ignition.

D. Connective Processes Among Concentrating Particles

When aluminum particles concentrate on the burning surface, they eventually establish contact with each other and are then seen to leave the surface as either agglomerates or sintered clusters that form agglomerates after they leave the burning surface. Whatever the uncertainty about how the particles are restrained on the surface during concentration, there must then be connective processes that give rise to the observed group behavior. As concentration progresses on the surface, the uppermost particles presumably become hotter and become oxide shells containing molten aluminum. These are the conditions described earlier that give rise to sintering or agglomeration. Observations of sintered accumulates (e.g., Fig. 7) indicate that there is enough oxidizer present to cause sintering, which is an exothermic process that probably progresses to involvement of emerging particles, and apparently accounts for some of the oxide found in the agglomerates. In effect, the sintered accumulate is an energetic transitory state that progresses to an agglomerate on or above the surface depending on the evolution of its local chemical and thermal environment.

E. Evolution of the Local Environment

An accumulate typically originates from the preconcentration of aluminum in the pockets of the packing pattern. When such sites emerge at the burning surface, binder provides an adhesive surface and a nonoxidizing environment. Only particles on the periphery of the pocket are exposed to oxidizing vapors and high heat flux from hot oxidizer-binder flamelets.

As the surface regresses, the spatial distribution of the surroundings changes, and the oxidizer underlying the pocket eventually emerges. The accumulate is then connected to underlying binder and aluminum only in the their interfacial structures

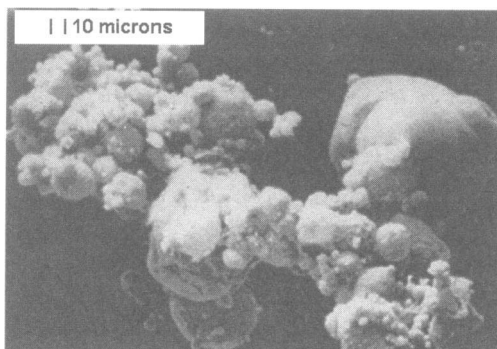


Fig. 7 Sintered accumulate, quenched while in transition to an agglomerate (note spherical structural features where coalescence of liquid aluminum has started) (from Ref. 2).

between pockets, and the accumulate is progressively exposed to an environment of oxidizing vapors and hot oxidizer-binder flamelets. One might expect that an accumulate that has survived to this point would ignite or at least leave the surface. This seems to be the most probable outcome, resulting in a detaching accumulate if the ignition conditions are poor, or a detaching agglomerate if ignition conditions are good. However, this is not always the case.

Under unfavorable ignition conditions, the pocket accumulates do not leave the surface after pocket burnout. Some times accumulates are found on the surfaces of AP particles (quenched sample, Fig. 1b). Sometimes larger agglomerates occur, indicative of interpocket connections. This behavior is evident at low pressure, where the hot oxidizer-binder flamelets either occur further from the surface or fail to be established and are replaced by a more distant premixed flame. Such behavior was illustrated in Ref. 32 by tests on formulations with bimodal oxidizer size distributions, in which the coarse particle packing resulted in pockets that typically contained binder, aluminum, and one intermediate size AP particle. Such formulations lead to large agglomerates at low pressure and small agglomerates at high pressure (Fig. 8). The transition pressure was attributed to the establishment of local oxidizer-binder flamelets on the smaller AP particles, which, at higher pressures, precipitated ignition of the pocket aluminum before the complete pocket sintering. Viewed in a more general sense, these results indicate the importance of the evolution and proximity of the array of hot O/F flamelets near the developing accumulates, which can control the aluminum ignition.^{16,32,35}

F. Formation of Agglomerates

As described in Refs. 1–3, 15, 16, 30–32, and 34–36, accumulates lead to agglomerates by a complex process involving local thermal breakdown of the

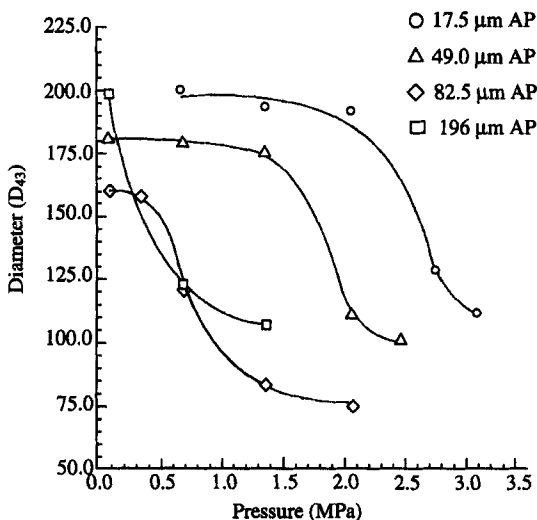


Fig. 8 Effect of pressure on mass-average agglomerate size d_{43} for bimodal propellants with coarse/fine AP of ratio 8/2. Coarse size 390 μm , fine size as indicated (from Ref. 32).

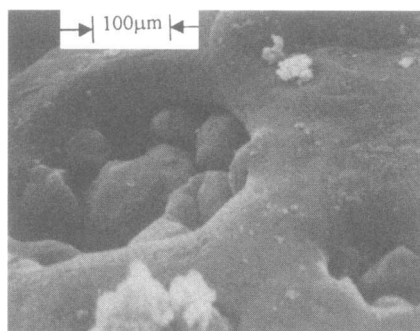


Fig. 9 Agglomerate quenched before complete transition to a molten droplet. Aluminum surface tension had drawn the accumulate into a sphere, but not yet closed the surface. Unmelted oxide shells of original particles are still visible in openings (from Refs. 2 and 16).

protective oxide and progressive inflammation from such local sites. One can only speculate about the initial thermal breakdown, which no doubt starts with cracking of the oxide as described earlier, accompanied leakage and oxidation of aluminum. In the presence of local hot O/F flamelets, this exothermic process goes beyond sintering and probably becomes self-sustaining, spreading through the whole accumulate. The rapid spread very likely involves progressive melting of the oxide structure. This ensures that the molten aluminum will coalesce locally into a burning droplet site (Fig. 7). The resulting heat release further hastens the meltdown of the whole accumulate. Because of the very high surface tension of molten aluminum, it apparently draws up into a single droplet even before all of the oxide shells are melted (Fig. 9), leading to oxide in the interior of the droplet, in addition to the familiar oxide lobe on the agglomerate (Fig 10). At this point the accumulate has become a very complex burning droplet. The transition is revealed in high-speed cinemicrophotography (illustrated in Fig. 11), which is one frame from the motion picture. The figure shows an accumulate that has developed

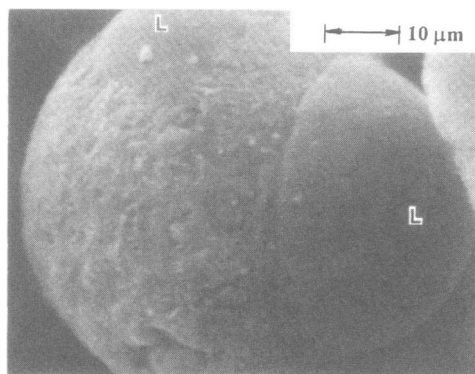


Fig. 10 Agglomerate quenched early in burning showing large aluminum droplet and two small oxide lobes (denoted by L).

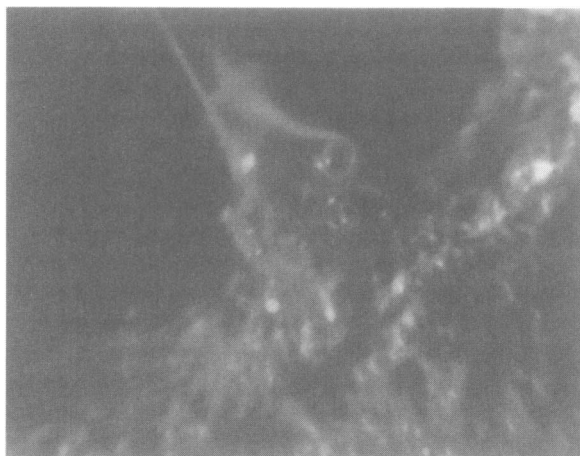


Fig. 11 Formation of an agglomerate from a sintered accumulate. One frame of a high-speed (4000 f/s) cinemicrograph of a burning surface (external illumination). In the movie an edge of an accumulate is seen to rise from the surface, and the whole accumulate draws up into a burning agglomerate. In the frame shown here the accumulate has formed a clump with a burning aluminum droplet near the top. Later frames show the clump being engulfed into a single agglomerate leaving the surface. Field of view is 1 mm high.

burning droplet sites with their typical smoke-oxide plumes. The word *inflammation* seems preferable to the word *ignition* for accumulates because of the complex progressive and propagative nature of the event in the accumulate.

The inner details of the formation of accumulates and their transformation to agglomerates may seem to be incidental in the overall picture of propellant combustion. However, they are important to understanding and controlling the nature and size distribution of the burning aluminum and the oxide droplets in the flow-field, to understanding the energy balance that controls burning rate, and to understanding the potential for effect on combustor stability. In addition, knowledge of the accumulation-agglomeration process holds the key to its modification by change of formulation or by modification of the ingredient aluminum powder. In Ref. 34 some reduction in agglomeration was reported with aluminum particles that were coated with nickel and with fluorine-containing polymers. In other reports agglomeration seemed to be almost eliminated (Fig. 12, Refs. 15, 16, and 37) with preoxidized aluminum having 100% enhanced oxide skin on the particles (achieved by heating the powder in an oxygen-containing atmosphere). In the first case agglomeration was thought to be reduced by earlier ignition of the aluminum, whereas the enhanced oxide method was thought to work by reducing sintering.

VII. Burning Aluminum Agglomerates

The nature and burning behavior of agglomerates are difficult to observe at relevant pressures in the propellant combustion environment because of obscuration by the Al_2O_3 smoke cloud. High-speed photography is effective near the burning surface where there is less smoke, and it is convected away ahead of

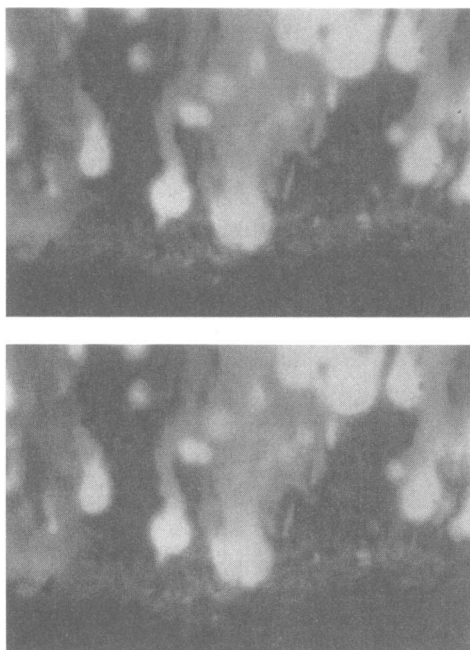


Fig. 12 Frames from a motion picture illustrating the effect of modification of the aluminum powder: on the top is as-received aluminum; on the bottom is preoxidized aluminum (from Ref. 16). Field of view 1 mm high.

the slower moving agglomerates (Fig. 13). Further out in the flow the fine oxide smoke obscures the agglomerates, but the condensed material can be captured in flight by impingement on collection plates or liquid surfaces or by rapid admixture of cold nonreactive gases. In these methods the intention is that burning will be quenched at some describable distance from the propellant surface and that some or all of the particles will be recovered for studies of their nature and size distribution. Usually the fine oxide smoke is separated out and discarded, using



Fig. 13 Agglomerate burning near the surface where smoke obscuration is minimal. Field of view is 1×1.5 mm.

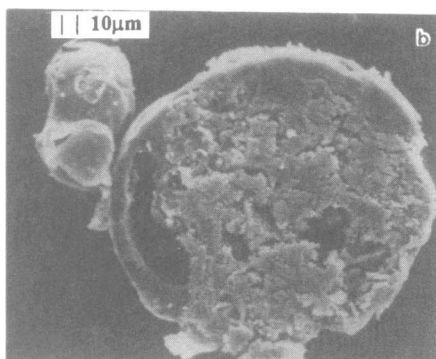


Fig. 14 Cleaved surface of a fully developed agglomerate (quenched in ethanol) (from Ref. 16).

filtering or sedimentation separation methods. Individual agglomerate particles are microtomed and/or broken and examined in scanning electron microscopes or acid etched to remove aluminum and reveal oxide structures (Figs. 14 and 15). Bulk samples are analyzed for aluminum and oxide content (by weighing before and after treatment to dissolve the aluminum). By comparing aluminum content and oxide content with the original aluminum content in the propellant sample, the percent of unburned aluminum and the proportion of oxide that is involved in the agglomerate (i.e., nonsmoke oxide) can be determined (Figs. 16 and 17). Bulk samples are also analyzed for size distribution, and the results are sometimes compared with initial size distributions determined from combustion photography. By repeating quench collection tests at different distances from the propellant surface, the combustion history of the agglomerates can be reconstructed.

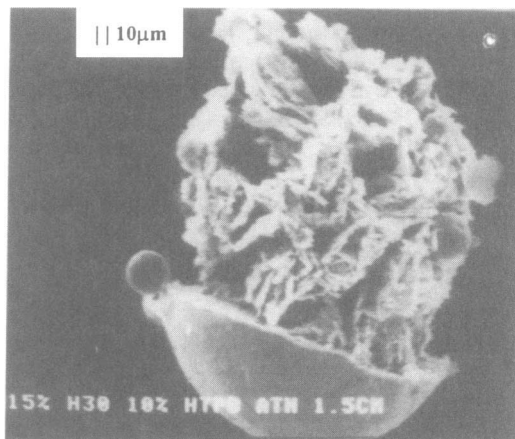


Fig. 15 Fully developed agglomerate, quenched early in its burning in ethanol and acid etched to remove free aluminum. The other structures are believed to be remnants of the preagglomeration oxide films, engulfed during agglomeration, melted, but still suspended in the aluminum droplet (from Ref. 16).

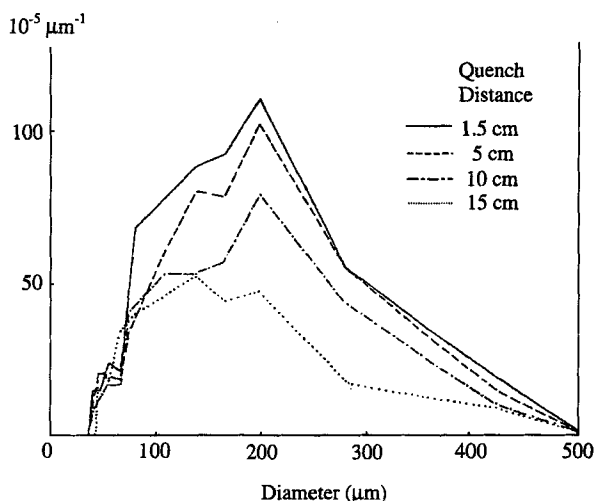


Fig. 16 Mass size distribution of agglomerates at four different quench distances (Thiokol propellant 1780-1, 0.7 MPa test, ethanol pool impingement test). Ordinate scale is mass per micron per initial aluminum mass (from Ref. 16).

Tests of the type just described are very time consuming, and sometimes subject to deceptive results because of poor simulation of rocket motor conditions (associated with small size of the samples) and imprecise establishment of quench distances (different for different quench methods). However the results reveal plausible trends with quench distance and qualitative looks at the effects of variations in propellant formulation and combustion conditions.^{16,34,36,38-40} Because of the large number of formulation and test variables of interest and the strong dependence of aluminum behavior of the variables, it is not safe to make broad

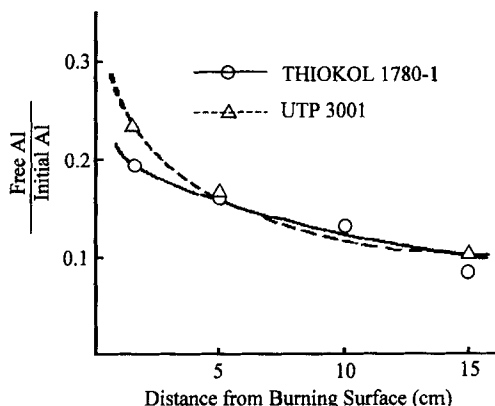


Fig. 17 Mass size distribution of agglomerates at four different quench distances (Thiokol propellant 1780-1, 0.7 MPa test, ethanol pool impingement test) (from Ref. 16).

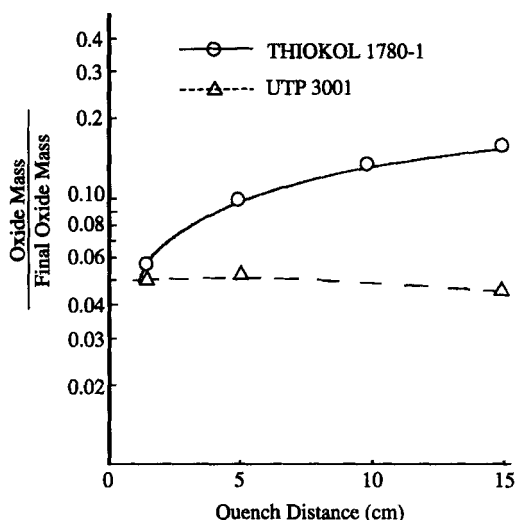


Fig. 18 Mass fraction of final A_2O_3 that is in residual oxide form (nonsmoke) vs quench distance (from Ref. 16).

generalizations regarding effect of variables (some are ventured later, but should be regarded as fallible). Some test results from Ref. 16 are shown next to illustrate by example the kind of data just mentioned.

The size distributions of agglomerates at four quench distances are shown in Fig. 16 (the agglomerates contain aluminum and oxide). Figure 17 shows the mass fraction of original aluminum remaining as a function of quench distance. Note that the initial combustion rate of the aluminum is very high in this example, indicating that much of the aluminum was not agglomerated. Another factor is the low velocity of agglomerates near the surface, with a relatively long time for agglomerate burning before reaching the lower quench distances. Figure 18 shows the mass fraction of residual oxide vs quench distance (determined by weighing the sample residue after acid solution removal of the unreacted aluminum). The propellants in these tests were 18% aluminum and approximately 12.5% butadiene binder (PBAN and HTPB). The downward combustion plume was contained by a quartz tube and quenched by impingement on an ethanol pool. Figure 8 showed mass-average agglomerate size based on combustion photography of the near-surface agglomerates.

It is the combination of results such as those just described that holds the potential for reconstruction of the combustion history of the droplet plume and its relation to the surface processes and propellant formulations. Given the high cost and time for such tests and the almost limitless combinations of formulations and combustion environment variables, *it seems preferable to use the methods to test mechanistic concepts that have potential for applicability over a wide range of variables.* For example, some of the mechanistic issues that need clarification are the following:

- 1) What are the mechanisms for retention of aluminum particles on the burning surface and mechanisms for the adhesion of concentrating particles that are a necessary precursor to transition to agglomerates? Conversely, what conditions lead to particle separation individually, with or without ignition?

2) What conditions in the combustion zone finally precipitate inflammation of sites on accumulates, and how does the inflammation spread through the accumulate?

3) How much aluminum oxidation occurs before agglomeration and surface detachment occur?

4) How fast do agglomerates burn?

5) How much oxide do agglomerates acquire during burning?

6) Do agglomerates fragment later in burning, and if so, why?

7) What is the nature of residual oxide droplets, those remnants of the final burnout phase of agglomerates?

Although the answers to these questions may be dependent on that dreaded myriad of formulation and combustion environment variables, the answers can have broader application than the raw data. What is needed are clever experiments to answer the mechanistic questions.

VIII. Al_2O_3 Product Population

As noted earlier, the presence of the large Al_2O_3 droplet portion in the combustor flow is important to combustor stability,⁴¹⁻⁴⁵ erosion of motor components, slag formation, etc. All of these effects are dependent on the size of the oxide droplets, which in turn is dependent on the aluminum agglomeration-combustion process. This has been the motivation for much of the research described here.

Quench-collection tests that provide a long plume prior to quench (e.g., 50 cm or more) yield only Al_2O_3 particles. The majority of the particles are smoke oxide with mass-average particle size around $1.0\text{--}1.5\ \mu\text{m}$, which is important for damping high-frequency instabilities, but not otherwise important in the interior of the motor and not as dependent on formulation variables as the residual oxide population. In most quench collection tests the smoke oxide is removed, and the properties of the residual oxide population are determined (weight, size distribution). Figure 19 shows a photograph of a sample of residual oxide particles. As noted in Ref. 43,

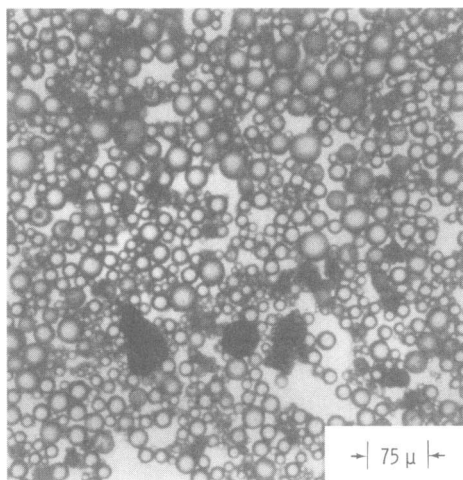


Fig. 19 Example of residual oxide particles.

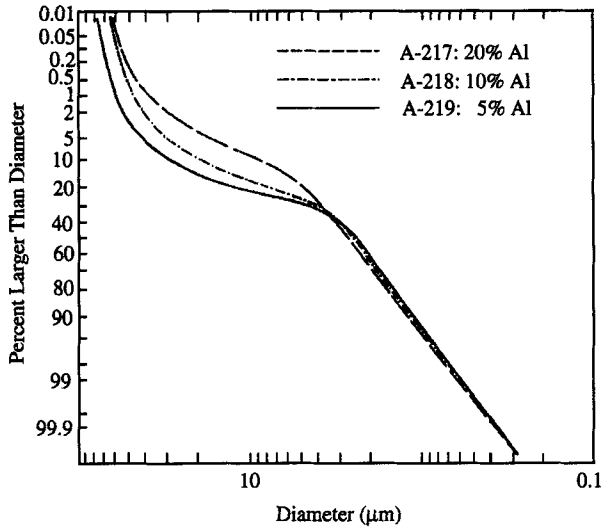


Fig. 20 Example of burn-out residual oxide size distribution (from Ref. 43).

great care is required to get good size distribution measurements when a wide size range (e.g., 2–100 μm) is present.

It is reasonable to expect that the population will contain burn-out residuals from 1) Al particles that did not agglomerate, 2) intermediate and pocket-size agglomerates, 3) large interpocket agglomerates, and 4) smaller products from agglomerate-fragmentation events. Care must be exercised to assure that the largest particles are not incompletely reacted agglomerates.

Because of the strong dependence of agglomerate size on propellant formulation and test conditions, the reported oxide size distributions in the literature are diverse. Total mass fractions (residual oxide/total oxide) range from 0.05 to 0.20. Two examples of measured mass size distribution are shown in Fig. 20 (from Ref. 43) and Fig. 21 (from Ref. 44). From the practical viewpoint a mean size of 10–25 μm

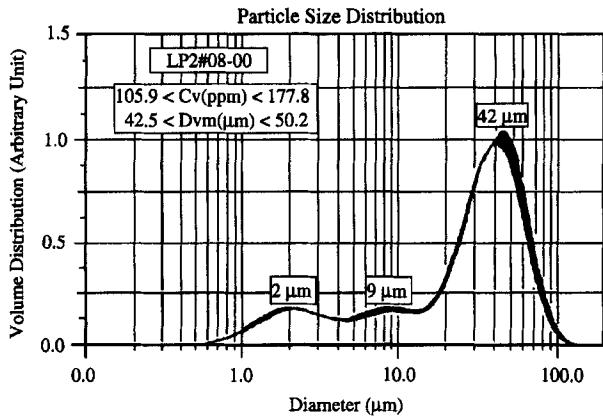


Fig. 21 Example of burn-out residual oxide distribution (from Ref. 44).

would be ideal for stabilizing combustor instabilities in the 200–400 Hz range. From the standpoint of minimizing erosion or slagging of motor components or of two-phase flow losses, residual oxides of all sizes are unwanted. Curiously enough, theoretical computations of slag accumulation usually employ assumptions of mass-average residual oxide droplets in the vicinity of $100\text{ }\mu\text{m}$ (e.g., Ref. 45) in order to get agreement with observed slag accumulations. It is too early to critique available results because of the diversity of test methods and propellants used, but most sources report mass average of residual oxide particle sizes in the 20–60 μm range (for AP composite propellants with 18% aluminum). Smaller sizes result from the pretreated aluminum mentioned earlier.

IX. Conclusions

If the typical aluminum particles that are used in propellants simply ignited individually and burned as they flowed away with the vapors of the other ingredients, there would not be much interest in the combustion (except possibly for its effect on propellant burning rate). Combustion efficiency would be high; there would be plenty of fine oxide droplets to damp high-frequency instabilities, and the larger residual oxide droplets would be near optimum size to damp lower-frequency axial mode instabilities. All oxide droplets would be small enough to ensure low two-phase flow losses, component erosion, and slag accumulation. Unfortunately that is not the way aluminum usually behaves (see exception, Fig. 12). Instead aluminum concentrates on the burning surface and forms slow-burning agglomerates that aggravate those unwanted effects just noted. So a large part of the research has been aimed at understanding and changing the accumulation-agglomeration behavior, which has proven to be very complex and strongly dependent on a host of propellant and combustion environment variables—so many variables that there is no prospect of mapping out all of their combined effects. For example, changing to smaller aluminum particles does not consistently lead to smaller agglomerates because it depends on kind of binder, %Al, AP particle size distribution, pressure, etc.

Collected results to date, for all of their diversity, suggest that the following generalizations have wide applicability for AP/HCB propellants:

- 1) Large agglomerates result in large residual oxide droplets.
- 2) High aluminum content in the propellant leads to large agglomerates.
- 3) Factors that increase burning rate (high pressure, burning-rate catalysts) reduce the amount and size of agglomerates.
- 4) Ingredient particle-size distributions that yield large concentrations of aluminum in the propellant particle-packing pattern give large agglomerates.
- 5) Use of burning-rate suppressants (and binders?) that produce increased melts or carbonaceous residue on the burning surface usually lead to increased agglomeration and agglomerate size.
- 6) Modification of the aluminum particles (e.g., preoxidation or prestretching the oxide skin in such a way as to minimize interparticle sintering) reduces agglomeration, as do certain particle coatings that aid ignition.
- 7) Crossflow environments tend to decrease agglomeration (Ref. 46, and Fig. 22 from Ref. 47).

These generalizations all have mechanistic bases noted in the text of this paper for AP/HCB propellants. Mechanisms and methods that deserve further evaluation (quantification?) and exploitation include the following:

- 1) Determine the role of *agglomerate fragmentation* in determining size of residual oxide droplets.

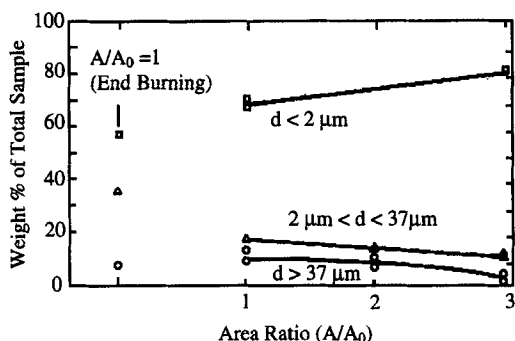


Fig. 22 Comparison of residual oxide particle size for end-burning sample and internal-burning tubular samples of length $\frac{3}{8}$, $\frac{3}{4}$, and $1\frac{1}{8}$ in. Abscissa is ratio of burning surface area to flow channel cross-sectional area (ANB3066 propellant) (see Ref. 47 for details).

2) Give a systematic evaluation of conditions for binder melts (melting temperature viscosity, decomposition temperature, and residue formation) for binders with widely different thermal response characteristics. Then compare their *particle retention behavior* in the combustion zone (several methods).

3) Learn more about sintering of aluminum particles and modification of sintering behavior and evaluate in propellant tests. Then exploit the results to provide low sintering aluminum powders and establish specifications and evaluation tests for acceptance of powder lots used in propellant production.

4) Look for aids to the ignition of aluminum in the propellant combustion zone.

5) Extend propellant studies to include the effect of steady crossflow and oscillating pressure and crossflow (effects on aluminum accumulation and inflammation agglomeration).

The mechanistic aspects involved in the preceding can usually be investigated more definitively and with lower costs using nonpropellant environments (thermal response tests), and then validated selectively in propellant tests. The propellant tests will be more decisive if multiple methods of observation are used (combustion photography, propellant extinguishment tests, plume-quench-collection tests, and some imagination about new methods). However the biggest need is for coordination of the efforts of different investigators to establish a means for comparing results and at the same time covering the combinations of variables of practical or fundamental importance.

Acknowledgments

This work was partially supported by the Cal Tech Multidisciplinary University Research Initiative under ONR Grant N00014-95-1-1338 with Program Manager Judah Goldwasser.

References

- ¹Price, E. W., "Combustion of Metalized Propellants," *Fundamentals of Solid Propellant Combustion*, edited by Kenneth K. Kuo and Martin Summerfield, Vol. 90, Progress in Aeronautics and Astronautics, AIAA, New York, 1984, pp. 478-513.

²Price, E. W., "Combustion of Aluminum in Solid Propellant Flames," *Solid Rocket Motor Technology*, Vol. 259, AGARD, 1979, pp. 14-1-14-15.

³Price, E. W., Kraeutle, K. J., Prentice, J. L., Boggs, T. L., and Sigman, R. K., "Behavior of Aluminum in Solid Propellant Combustion," Naval Weapons Center, Rept. TP 6120, China Lake, CA, March 1980.

⁴Pokhil, P. F., Belyayef, A. F., Frolov, Yu. V., Logachev, V. S., and Krototkov, A. I., *Combustion of Powdered Materials in Active Media*, Nauka, Moscow, 1972, pp. 1-295.

⁵Waesche, R. H. W., "Mechanisms and Methods of Suppression of Combustion Instability by Metallic Additives," *Journal of Propulsion and Power*, Vol. 15, No. 6, 1999, pp. 919-922.

⁶Rumbel, K., and Henderson, C. B., "Design of Propellants for Optimum Propulsion Design," JANNAF Solid Propulsion Meeting, May 1956.

⁷Carroll, P. T., "Historical Origins of the Sergeant Missile Powerplant," Jet Propulsion Lab., Cal Tech, JPL/HR-3, Pasadena, CA, Aug. 1972.

⁸Wiggins, J. W., "The Earliest Large Solid Rocket Motor—The Hermes," Thiokol Chemical Corp., Control U-72-4493, Huntsville, AL, July 1972.

⁹Klager, K., "Early Polaris and Minuteman Rocket Motor History," Aerojet Strategic Propulsion Co., WP-691-12, Sacramento, CA.

¹⁰Lou, R. L., "Suppression of Unstable Burning in Solid Propellants," Aerojet-General Corp., Rept. 1250, Sacramento, CA, April 1957.

¹¹Price, E. W., *Review of Experimental Research on Combustion Instability of Solid Propellants in Solid Propellant Rocket Research*, AIAA Progress Series, Vol. 1, AIAA, New York, 1960, pp. 558, 559.

¹²Ad Hoc Group on Solid Propellant Instability of Combustion, Advisory Panel on Fuels and Lubricants, "Instability of Combustion of Solid Propellants," Office of the Director of Defense, Research, and Engineering, FR, Washington, DC, June 1959.

¹³"Summary Report on Solution of the Combustion Instability Incurred in the Development of the TE260 Rocket Motor," Thiokol Chemical Corp., Rept. E170-60, Elkton, MD, Nov. 1960.

¹⁴Crump, J. E., Prentice, J. L., and Kraeutle, K. J., "Role of Scanning Electron Microscope in Study of Solid Propellant Combustion," *Combustion Science and Technology*, Vol. 1, 1969, pp. 205-223.

¹⁵Kraeutle, K. L., "The Development and Application of Test Methods for the Quality Control of Aluminum Powders Used in Solid Propellants," *Testing Methods for Propellants and Explosives*, Fraunhofer-Inst. fur Trieb-und Explosivstoffe, Karlsruhe, Germany, 1980, pp. 377-398.

¹⁶Price, E. W., Sigman, R. K., Sambamurthi, J. K., and Park, C. J., "Behavior of Aluminum in Solid Propellant Combustion," School of Aerospace Engineering, Georgia Inst. of Technology, Atlanta, GA, June 1982.

¹⁷Price, E. W., Rice, D. W., and Crump, J. E., "Low Frequency Combustion Instability in Solid Rocket Propellants," Naval Ordnance Test Station, NOTS TP 3524 (Unclassified), China Lake, CA, July 1964.

¹⁸Christensen, H. C., Knipe, R. H., and Gordon, A. S., "Survey of Aluminum Particle Combustion," *Pyrodynamics*, Vol. 3, 1965, pp. 91-119.

¹⁹Macek, A., "Fundamentals of Combustion of Single Aluminum and Beryllium Particles," *Eleventh Symposium (International) on Combustion*, Combustion Inst., Pittsburgh, PA, 1967, pp. 203-214.

²⁰Olsen, S. E., and Beckstead, M. W., "Burn Time Measurements of Single Aluminum Particles in Steam and Carbon Dioxide," *Journal of Propulsion and Power*, Vol. 12, No. 4, 1996, pp. 662-671.

²¹Prentice, J. L., "Combustion of Single Aluminum Droplets in Various Oxidizing Gases Including CO₂ and Water Vapor," *10th JANNAF Combustion Meeting*, Vol. 3, Chemical Propulsion Information Agency, Laurel, MD, 1973, pp. 279–296.

²²Dreizin, E. L., "Experimental Study of Stages in Aluminum Combustion in Air," *Combustion and Flame*, Vol. 105, No. 4, 1996, pp. 541–556.

²³Prentice, J. L., and Nelson, L. S., "Differences Between the Combustion of Aluminum Droplets in Air and in an Oxygen-Argon Mixture," *Journal of the Electrochemical Society*, Vol. 115, 1968, pp. 809–812.

²⁴Bucher, P., Yetter, R. A., Dryer, F. L., Vicenzi, E. P., Parr, T. P., and Hanson-Parr, D. M., "Condensed-Phase Species Distributions About Al Particles Reacting in Various Oxidizers," *Combustion and Flame*, Vol. 117, No. 4/5, 1999, pp. 351–361.

²⁵Marion, M., Chauvreau, L., and Goekalp, I., "Studies of the Ignition and Burning Process of Levitated Aluminum Particles," *Combustion Science and Technology*, Vol. 115, Nos. 4–6, 1996, pp. 369–390.

²⁶King, M. K., "Modeling of Single Particle Aluminum Combustion in CO₂–N₂ Atmospheres," *Seventeenth Symposium (International) on Combustion*, Combustion Inst., Pittsburgh, PA, 1998, pp. 1317–1328.

²⁷Bucher, P., Yetter, R. A., Dryer, F. L., Parr, T. P., and Hanson-Parr, D. M., "PLIF Species and Ratiometric Temperature Measurements of Aluminum Particle Combustion in O₂, CO₂, and N₂O Oxidizers, and Comparison with Model Calculations," *Twenty-Seventh Symposium (International) on Combustion*, Combustion Inst., Pittsburgh, PA, Aug. 1998, pp. 2421–2430.

²⁸Liana, Y., and Beckstead, M. W., "Numerical Simulation of Unsteady Single Aluminum Particle Combustion in Air," AIAA Paper 98-3825, June 1998.

²⁹Glassman, I., "Combustion of Metals: Physical Considerations," ARS Progress in Astronautics and Rocketry, *Solid Propellant Rocket Research*, Vol. 1, Academic International Press, New York, 1960, pp. 253–258.

³⁰Babuk, V. A., Belov, V. P., Khodosov, V. V., and Sheluken, G. G., "Investigation of the Agglomeration of Aluminum Particles During the Combustion of Metalized Condensed Systems," *Fizika Goreniya i Vzryva*, Vol. 21, No. 3, 1985, pp. 20–25.

³¹Crump, J. E., "Aluminum Combustion in Composite Propellants," *2nd Combustion Meeting*, Vol. I, Chemical Propulsion Information Agency, Laurel, MD, 1966, pp. 321–329.

³²Sambamurthi, J. K., Price, E. W., and Sigman, R. K., "Aluminum Agglomeration in Solid-Propellant Combustion," *AIAA Journal*, Vol. 22, No. 8, 1984, pp. 1132–1138.

³³Cohen, N. S., "A Pocket Model for Aluminum Agglomeration in Composite Propellants," *AIAA Journal*, Vol. 21, No. 5, 1983, pp. 720–725.

³⁴Babuk, V. A., Vasilyev, V. A., and Sviridov, V. V., "Formation of Condensed Combustion Products at the Burning Surface of Solid Rocket Propellant," *Solid Propellant Chemist Combustion, and Motor Interior Ballistics*, Vol. 185, AIAA Progress in Aeronautics and Astronautics, AIAA, Reston, VA, 2000, pp. 000–000.

³⁵Price, E. W., Sambamurthi, J. K., Sigman, R. K., and Sheshadri, T. S., "Conditions for Inflammation of Accumulated Aluminum in the Propellant Combustion Zone," *20th JANNAF Combustion Meeting*, Vol. I, Chemical Propulsion Information Agency, Laurel, Maryland, 1983, pp. 333–342.

³⁶Price, E. W., Park, C. J., Sigman, R. K., and Sambamurthi, J. K., "The Nature and Combustion of Agglomerates," *18th JANNAF Combustion Meeting*, Vol. III, Chemical Propulsion Information Agency, Laurel, MD, 1981, pp. 121–145.

³⁷Price, E. W., Mathes, H. B., and Zurn, D. E., "Effect of Partial Preoxidation of Aluminum on Oscillatory Combustion Behavior of HTPB-AP Propellants," *9th JANNAF*

Combustion Meeting, Vol. I, Chemical Propulsion Information Agency, Laurel, MD, 1972, pp. 147–168.

³⁸Babuk, V. A., Vasilyev, V. A., and Malakhov, M. S., “Study of Condensed Combustion Products at Burning Surface of Aluminized Solid Propellant,” *Journal of Propulsion and Power* (to be published).

³⁹Babuk, V. A., Belov, V. P., and Khodosov, V. V., “Investigation of Aluminum Particle Agglomeration in Combustion as an Ingredient of Double Base Condensed Systems,” *The Physics of Combustion and Explosion*, Vol. 21, No. 3, 1985, pp. 20–25 (in Russian).

⁴⁰Glotov, O. G., Zarko, V. E., Karasev, V. V., and Beckstead, M. W., “Effect of Binder on the Formulation and Evolution of Condensed Combustion Products of Metalized Solid Propellants,” *Combustion and Detonation*, 28th International Annual Conf. of ICT, Karlsruhe, Germany, 1997, pp. 75-1–75-14.

⁴¹Altman, D., and Berenstein, J., “Study of Detonation Behavior in Solid Propellants: Task II, Resonance,” 1st Quarterly Rept. on U.S. Navy Bureau of Ordnance Contract 17945, Aeronutronics Systems Div. Pub. C-168, Newport Beach, CA, March 1958.

⁴²Price, E. W., “Comments on Role of Aluminum in Suppressing Instability in Solid Propellant Rocket Motors,” *AIAA Journal*, Vol. 9, No. 5, 1971, pp. 987–990.

⁴³Kraeutle, K. J., Mathes, H. B., and Derr, R. L., “The Role of Particulate Damping in the Control of Combustion Instability by Aluminum Combustion,” *Solid Rocket Motor Technology*, Vol. 259, AGARD, 1979, pp. 15-1–15-4.

⁴⁴Scippa, S., Pascal, P., and Zanier, F., “Ariane 5-MPS-Chamber Pressure Oscillations Full Scale Firings’ Results and Analysis and Further Studies,” AIAA Paper 94-3068, June 1994.

⁴⁵Salita, M., “Deficiencies and Requirements in Modeling Slag Generation in Solid Rocket Motors,” *Journal of Propulsion and Power*, Vol. 11, No. 1, 1995, pp. 10–23.

⁴⁶Gany, A., and Caveny, L. H., “Agglomeration and Ignition Mechanism of Aluminum Particles in Solid Propellants,” *Proceedings of the Seventeenth Symposium (International) on Combustion*, Combustion Inst., Pittsburgh, PA, 1978, pp. 1453–1461.

⁴⁷Eisel, J. L., Price, E. W., and Brown, B. G., “ Al_2O_3 Particles Produced During Solid Propellant Combustion,” *AIAA Journal*, Vol. 13, No. 7, 1975, pp. 913–917.

Chapter 2.19

Detailed Studies on the Flame Structure of Aluminum Particle Combustion

P. Bucher,* L. Ernst,* and F. L. Dryer[†]

Princeton University, Princeton, New Jersey

R. A. Yetter[‡]

Pennsylvania State University, University Park, Pennsylvania

and

T. P. Parr[§] and D. M. Hanson-Parr[§]

Naval Air Warfare Center Weapons Division, China Lake, California

I. Introduction

DURING the last decade, there has been renewed interest in the combustion of propellants and explosives. The driving force behind this renewed interest has come, in part, from two emerging areas of energetic materials. The first is the development of fluorine- and oxygen-rich energetic crystals and polymers, which offer high energy densities, and the second is the development of environmentally friendly energetic materials, which are expected to be less polluting and recyclable.¹

Figure 1 illustrates two recently synthesized energetic oxidizers, a polycyclic nitramine, HexaNitroHexaAzalsoWurtzitane (HNIW), and a geminal difluoroaminated analogue of RDX (RNFX). One polymorph of HNIW is the densest and most energetic explosive known. The high density of HNIW is due to the unusually high number and types of cyclic rings in its molecular structure. The geminal difluoroamine group of RNFX is not only dense but rich in fluorine and is the functional group of choice for substitution into polycyclic analogues of HMX and HNIW.¹

The possibility of producing both oxygenated and fluorinated decomposition products from the combustion and detonation of propellants and explosives has

Copyright © 2000 by authors. Published by the American Institute of Aeronautics and Astronautics, Inc., with permission.

*Graduate Student, Department of Mechanical and Aerospace Engineering.

[†]Professor, Department of Mechanical and Aerospace Engineering.

[‡]Professor, Department of Mechanical and Nuclear Engineering.

[§]Chemist, Combustion Diagnostics Laboratory.

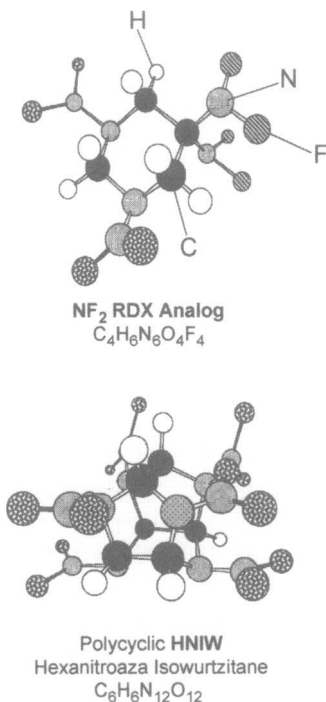


Fig. 1 Two potential energetic oxidizers: HexaNitroHexaAzalsoWurtzitane (HNIW) and a geminal difluoroaminated analogue of RDX (RNFX).

also renewed interest in particulate metal combustion. Fluorinated compounds have already been shown to affect particulate metal ignition delays, burn rates, final product speciation, and overall energetics of several metals.²⁻⁷ Thus, the question of considerable interest to propellant designers is whether propellant decomposition products can be tailored to control the ignition delays/burn times of metal particles and agglomerates and the number density/size distributions of final condensed phase products, thereby improving energy release, plume signature characteristics, and motor stability. By lowering metal ignition temperatures, the addition of fluorine as an element in propellant ingredients may also enable control of particle agglomeration at propellant surfaces.

As part of an effort to investigate the effects of fluorinated compounds on metal combustion, we have been applying modern experimental and numerical techniques to study the detailed flame structure of particulate metal combustion. The experimental measurements include radial distributions of gas-phase species, condensed-phase elements, and temperature about burning particles. The data from these measurements supplement more traditional engineering data, such as ignition delays and burn rates, and enable additional understanding of metal ignition and combustion processes and provide fundamental information for model construction and validation. The importance of detailed numerical models lies in their potential for predicting combustion characteristics under conditions too costly or too difficult to study experimentally and in their use as benchmarks for

developing simplified metal combustion submodels for use in multidimensional engineering systems calculations.

Although we are interested in several metal additives including boron, magnesium, and hafnium, this study is devoted to aluminum particle combustion. A number of excellent reviews on aluminum particle combustion as propellant ingredients and as isolated particles may be found in the literature, with the most recent by Price and Sigman in the current volume.⁸⁻¹¹

Aluminum melts at 933 K and does not have appreciable vapor pressures until heated close to its boiling point of 2750 K. The melting temperature closely corresponds to temperatures normally present on propellant burning surfaces. When nascent surfaces are exposed to ambient air, a surface oxide film 4–5 nm thick forms due to the high reactivity of aluminum.¹² The oxide layer, which forms in the atomization process used for particle manufacturing, is thicker, but significantly below 1 μm .⁹ Protected by their oxide layer, the aluminum particles are heated with the surrounding oxidizer and binder when approached by a regressing propellant burning surface. Subject to interfacial, thermophoretic, and convective drag forces, the emerging particles usually stick to the complex burning propellant surface. Although conditions vary with propellant formulation, mass loading, and size of the ingredient particles, the surface-attached liquid particles are typically joined by other emerging particles and grow either by adhesion or by cohesion into large drops of interconnected particles. Eventually, the resulting agglomerate structures, which can be composed of as many as 10^6 ingredient aluminum particles,⁹ melt down and ignite, either on or after leaving the particle surface. The agglomerate particles experience much of their burning detached from the surface in the equilibrium products of other propellant ingredients, while carried by the flowing gases at a speed of up to 100 m/s through much of the combustor volume.¹³ The gaseous postpropellant flame environment is at a temperature of approximately 2300 K and is composed primarily of H_2O , CO_2 , CO , N_2 , and possibly HCl . The details of particle combustion in practical propellant environments are difficult to observe because of high particle velocities and obscuration of the field of view due to aluminum oxide smoke. It appears, however, that aluminum particles burn with a complex detached envelope flame, in which a bimodal distribution of oxide particles is formed. Typically, 70–95% of the metal oxide mass ends up in particles with diameters of less than 2 μm . The remaining oxide particles, which possess diameters in the range of 2–100 μm , are believed to result from accumulation of oxide layers or lobes on the particle surface during combustion and incomplete particle burnout.¹⁴ The size distribution of the oxide residual particles has been studied extensively, as it is closely linked to the combustion efficiency, combustor stability, nozzle erosion, nozzle efficiency, and exhaust plume signatures.

Figure 2 illustrates the combustion process of aluminum particles in propellant environments.¹⁵ In Fig. 2a, primary particles are shown to accumulate at a propellant surface and typically leave as agglomerates with diameters of between 100 and 200 μm . The propellant was a NASA space shuttle booster propellant (SBP) containing AP, PBAN, and Al, and therefore, HCl was present as a combustion product. In Fig. 2b, an isolated agglomerate is observed to burn with a detached flame zone having an elongated tail and a surface oxide lobe. Here the propellant was a research aluminized nitramine propellant (ANP with 5- μm Al), which had no AP and therefore no chlorine compounds in the flame. Most agglomerates

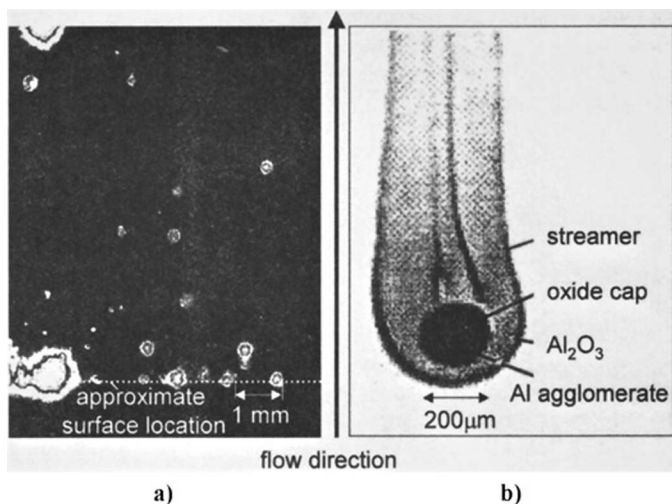


Fig. 2 Aluminum particle combustion: a) image from a small sample of the space shuttle propellant and b) magnified video image from a small sample of a nitramine-based propellant.

do not burn this symmetrically due to influences of the oxide cap, complex fluid dynamics, and interacting multiagglomerates.

It is clear from the foregoing discussion that aluminum particulate combustion in solid propellants is an exceedingly complex phenomenon. There is no doubt that the most relevant of empirical experiments would be those conducted in the gas-phase products from an actual solid propellant flame. Due to the complexity of these environments, however, it is difficult to isolate the individual effects of various oxidizing species on flame structure and particle regression rates. In addition, there are severe experimental limitations associated with object obscuration, limited access, and fast-moving targets in propellant-type experiments. Motivated by these difficulties, a variety of well-controlled bench-top particle combustion experiments has been developed, from which the majority of current macroscopic knowledge of aluminum particle combustion has been obtained.

A. Isolated Aluminum Particle Combustion Experiments

The majority of the present knowledge of aluminum particle combustion has been obtained from ignition and combustion of single aluminum particles, foils, or wires, in well-controlled environments. Ignition has been achieved by laser pulse heating of suspended particles,¹⁶⁻¹⁹ by flash heating of freely falling particles,¹⁹ and by microarc heating,²⁰⁻²² in which particles are simultaneously formed and ignited. Such experiments provide for photographic and quenched sample studies and thus permit monitoring of 1) the instantaneous particle size (burning rate), 2) the extent of the flame zone as macroscopic evidence of the effect of the oxidizing atmosphere and pressure, 3) the distribution and size of product oxide from quenching plate deposits, and 4) time-resolved flame luminosity for characterization of the burning history. Much useful information, particularly with regard to the particle ignition

process, has also been obtained from isolated particle combustion experiments in hot gases²³⁻²⁵ and from bulk aluminum combustion in counterflowing oxidizer environments.²⁶

Collectively, these experiments show that there is a relationship between the melting point of aluminum oxide and the particle ignition temperature, indicating that the oxide film enclosing the aluminum particle loses its protective properties upon melting. Particle ignition is followed by self-sustained combustion, where gaseous aluminum, supplied from a vaporizing aluminum droplet near its boiling point, reacts and forms liquid aluminum oxide particles in a detached flame zone that is located at a distance of 1.5–4 droplet radii from the particle surface. The size of the luminous flame envelope was found to be strongly dependent on the type and concentration of the oxidizing agent. The average burning rate is roughly correlated by $d^n = d_0^n - \beta t$, with $1.5 < n < 2$, indicating that diffusional as well as surface processes are rate controlling. In the above correlation, d_0 denotes the initial particle size, β is the burning-rate coefficient, and n the burning-rate exponent. A burning-rate exponent of $n = 1$ would be expected for kinetically controlled processes, whereas $n = 2$ would result from entirely diffusion-limited processes.

The pressure dependence on the mass burning rate of single particles was measured recently by Marion et al.²⁷ They found an increase in burning rate from 1 to 7 atm and a nearly independent rate above 7 atm. The accumulation of oxide on the aluminum particle surface was observed by many researchers²⁸⁻³¹ and in a variety of combustion situations. Considerable uncertainty exists as to the formation of surface oxide; the proposed mechanisms include surface reactions, suboxide condensation, radial diffusion of flame-generated oxide particles, and convection of flame-generated oxide particles into a recirculating wake. In most cases, the oxide was found to retract to a lobe, causing considerable asymmetry in the combustion event. Depending on the chemical environment, a variety of phenomena such as relatively large bubbles on the droplet surface, puffing, spinning, sudden changes in particle trajectories, and violent fragmentation was observed.

The fragmentary burning behavior, as characterized by sudden ejection of smaller particles, has received considerable attention over the years, as secondary dispersion greatly enhances the particle combustion efficiency and changes the size distribution of the product oxide population. From the available literature, fragmentation appears to be favored with increasing free oxygen content and when nitrogen species are present in the combustion environment. There are almost as many theories on the phenomena as there are experiments. Fragmentation has been attributed to the presence of oxides, oxynitrides, or Al–O–C complexes on the particle surface, to dissolution of hydrogen and oxygen into the molten droplet, and to local superheating of molten aluminum. Mechanistic knowledge of the oxidation process is required to investigate further such subtle, but important details of aluminum particle combustion.

B. Modeling of Single-Aluminum Particle Combustion

Several analytical and numerical models have been developed to gain in-depth understanding of aluminum particle combustion. One of the earliest models was developed in close relationship with familiar analytical hydrocarbon droplet models by Brzustowski and Glassman.³² They assumed that aluminum burns as a vapor-phase diffusion flame because of the lower boiling point for Al, compared to the

final product Al_2O_3 . Fuel and oxidizer were allowed to react in stoichiometric proportions and infinitely fast within a thin flame sheet, assuming that diffusional processes limit the rate of combustion. Recognizing that the flame temperature is exclusively dependent on the metal oxide volatilization,³³⁻³⁶ Brzustowski and Glassman³² constrained the maximum gas-phase temperature to the decomposition temperature (boiling point) of the metal oxide. The combustion of aluminum particles has been found to occur similarly to liquid fuel droplet combustion. In the absence of any rate-limiting chemical processes, the model resulted in a " d^2 law" ($n = 2$) for combustion, which closely correlates with some of the experimentally measured burning rates.¹⁹

There have since been numerous refinements of the original metal combustion model, all of which invoked the thin flame sheet or a thin condensation sheet assumption. For example, Law³⁷ allowed for diffusion of dissociated products from the flame sheet to the particle surface in his analytic model. Heat released from suboxide condensation on the particle surface contributed to the rate of fuel vaporization and to the value of the mass burning-rate coefficient. Law³⁷ later included an extended oxide condensation zone, whereby the outer edge of the flame gained substantially in size. The model by Brooks and Beckstead³⁹ accounts for the accumulation of surface oxide as an inhibition to surface processes. The various models appear to predict qualitatively the previously measured global parameters of aluminum particle combustion, such as the mass burning rate and flame standoff distances. The aluminum particle burning rate coefficient was found to be a strong function of the oxidizer and its concentration but independent of pressure.

In contrast to the analytical models above, King⁴⁰ developed a numerical model, in which rate data have been used for the reaction $\text{Al(g)} + \text{CO}_2 \rightarrow \text{AlO} + \text{CO}$. Aluminum monoxide produced from this reaction was permitted to react infinitely fast with the nascent liquid aluminum surface to form Al_2O . Aluminum oxide condensation was assumed to occur exclusively in a thin flame sheet, whose location was determined by specification of a condensation temperature. Depending on the ambient condition, the burning-rate exponent was predicted to range from 1.35 to 1.9. Thus, King's numerical results indicate that the combustion process may be partially kinetically controlled. It should be noted, however, that although the thin flame sheet assumption has been relaxed, and rate data for one of the elementary reactions have been used, the formation of the condensed-phase Al_2O_3 was permitted within a thin condensation sheet only. While the model of King constitutes a valuable contribution to the capture of true aluminum oxidation characteristics, it is likely limited by the omission of other important elementary reaction steps. In fact, it is the lack of kinetic rate data on gas-phase and heterogeneous reactions, and the lack of experimental data on species and temperature fields (needed for comparison and calibration), that inhibits the development of comprehensive numerical models that are capable of predicting burning rates over a wide range of chemical environments and pressures.

In summary, previous studies have accumulated a very respectable body of knowledge on the macroscopic burning behavior of particulate aluminum. Critical to understanding the combustion process of solid propellants and to the design of rocket motors has been the combination of fundamental studies on isolated aluminum particles burning in well-controlled environments with more complex studies on aluminized propellants. However, due to the lack of understanding of many underlying elementary processes, a comprehensive model for aluminum particle combustion has not yet emerged. As a result, much of the experimental

information remains unconnected and is difficult to utilize for the development of new energetic propellant formulations.

In this chapter we review and present new results on the flame structure of isolated aluminum particles burning in quiescent environments. The measurements, conducted at between approximately 1- and 3-atm pressure, consist of both gas-phase species and condensed-phase elemental profiles as a function of radial distance from the burning particle surface. Condensed-phase elemental analyses are performed on burn-interrupted, quenched particles using electron probe microscopy. Gas-phase species and temperature profiles are obtained using planar laser-induced fluorescence. In particular, flame structure measurements are presented for aluminum particle combustion with the single oxidizers, O_2 , N_2O , CO_2 , CO , H_2O , and SF_6 . These measurements have consisted of radial profiles of temperature, radial profiles of gas-phase AlO , and radial profiles of the condensed-phase elements, Al , O , N , C , F , and S . Finally, the profiles are analyzed with a local equilibrium particle combustion model in which species diffusion is assumed to be rate limiting. The model is then utilized to investigate burning characteristics over the pressure range from 1 to 100 atm.

II. Experimental Approach

The limited ability periodically to produce and ignite particles with uniform diameters in well-characterized environments has often made metal particle research difficult. Central to the present work therefore is the development of an experimental apparatus capable of producing large quantities of isolated, burning metal particles, and the construction of a combustion chamber that permits optical access from multiple directions.

The experimental arrangement was also designed to emulate closely the assumptions that underlie idealized droplet burning theories. Burning particles are generated with near-zero initial velocities and released into a near-stagnant, controlled atmosphere. Both the Reynolds and the Grashof numbers are quite low as a result of the microscopic particle size and the absence of forced convection. Under these conditions, combustion prevails with a spherically symmetric reaction zone.

A. Particle Generation and Ignition

The basic components of the particle generator system are a feeding mechanism, a set of oscillating blades, and a CO_2 laser heat source (Fig. 3).⁴¹⁻⁴⁴ The raw aluminum, in the form of a 127- μm -diameter wire (99.99% pure aluminum obtained from Aldrich Chemicals), is fed from a spool to a chopping mechanism. The chopping blade produces small cylinders by periodically shearing the metal wire. The length of the cylindrical wire fragments is determined by the chopping frequency in relation to the wire-feeding rate. A sequence of cylinders, attracted to each other, end to end, is moved into the densely focused (0.1-mm-beam diameter) radiation from a 100-W CO_2 laser (Synrad Model 57-1). Upon contact with the laser beam, the temperature of the cylinder with a free end rapidly increases above the metal's melting temperature. While exposed to laser radiation, the small cylinder contracts into a spherical particle and ignites. The particles, formed with zero initial velocity, accelerate to Reynolds numbers of the order of 0.1 during ignition and continue to accelerate during free fall through the combustion chamber. The

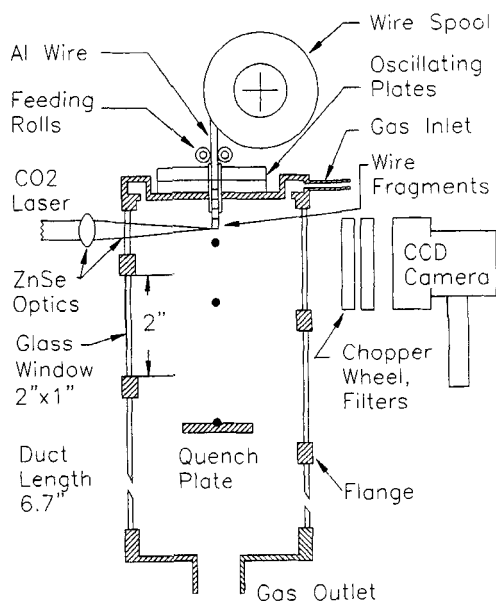


Fig. 3 Particle generator and combustion chamber.

sequence of events is repeated with a frequency of 0.5 Hz, resulting in a highly dispersed stream of monosized burning particles (Fig. 4).

The experimental technique is capable of producing particles from any metal that can be drawn into wire strands. Using a 127- μm -diam aluminum wire, particles of diameters between 100 and 400 μm can be produced. The length of a 5-V DC pulse that activates a miniature wire-feeding motor predetermines the particle size. A series of experiments, in which wire fragments were spherodized by laser heating and dropped into an argon atmosphere, has shown the particle diameter variation (at a given apparatus setting) to be within $\pm 2\%$ of the average diameter.

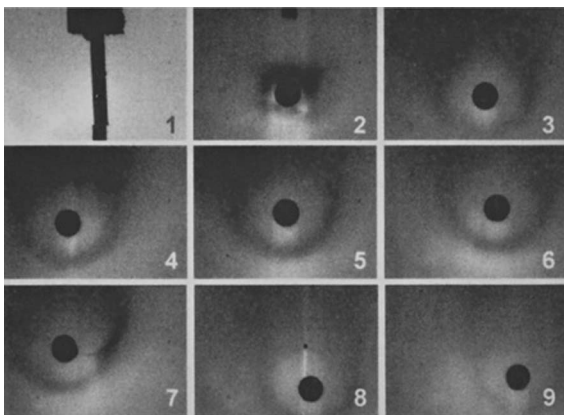


Fig. 4 Backlit images of particle generation and laser ignition in air.

Aluminum particle combustion has been studied in a variety of pure gases and factory-precalibrated gas mixtures, at pressures ranging from 1.1 to 3 atm. The gases entered a combustion chamber, 1.5 in. on a side, and 7.2 in. high, from the top through an annulus (Fig. 3). The chamber was equipped with multiple rectangular windows, made from quartz and zinc-selenide (ZnSe), to allow optical access from four sides and along the entire chamber length. Prior to an experiment, the chamber was purged for 15 min at a flow rate of 3 L/min; the chamber volume of 225 cm³ was displaced 200 times during purging. The flow rate (measured via Matheson 602 and E300 series rotameters) was reduced to 100 ml/min, and the static pressure (measured via Omega Model PX215 and PT602 pressure transducers) was adjusted to the desired value prior to the experiment. As a result of the continuous oxidizer flow, the particles were embedded in a coflowing gas environment of 0.13 cm/s during combustion.

B. Photographic and Emission Measurements

The still images of backlit burning particles shown in Fig. 4 were obtained using a gated CCD camera system in conjunction with a photographic flash unit. The CCD camera and flash unit were mounted on opposite ends of a vertically translating platform. With the particle experiment located between the camera and the flash, the platform was positioned at the height or burn time of interest, and a single image of each particle passing through the focal point of the lens was taken. The luminosity of the backlighting flash was adjusted and a set of imaging filters was chosen such that the particle and surrounding Al₂O₃ condensate, rather than the luminous flame zone, appeared as dark shadows on the digital images. For the purpose of triggering the camera and flash unit, the location of the particle along its trajectory was tracked by a photodiode equipped with a horizontal slit mask.

Multiexposure emission images of burning particles were obtained using a gated CCD camera/frame grabber assembly (Electrim 1000-HR; 753 × 488 pixels in the interlaced mode) in conjunction with a chopper wheel. The rotation speed and the wheel slot width were chosen to multiexpose the CCD camera to the flame luminosity at predetermined time intervals and durations, typically every 3.0 ms for a duration of 0.3 ms. To establish a common time basis between the individual images and the output of other data acquisition devices, the slot position of the chopper wheel was monitored using an emitter-photodiode assembly. The slot position signal, CO₂ laser timing signal, and photodiode trace were recorded using a multichannel data acquisition board and stored on a computer. Both the camera and the chopper wheel assembly were mounted on a vertically translating platform enabling the viewing of different sections of the combustion process along the particle trajectory (Fig. 5).

Particles were viewed by a photodiode (Newport Model 818-UV) from a distance of 50 cm. The placement of the photodiode in the far field permitted continuous monitoring of flame emission during the entire particle burning history (Fig. 6).

C. Condensed-Phase Species Measurements

Particles were quenched 3 mm (equivalent to a burning time of 12–17 ms) below the point of ignition by impacting them on solid plates made from single-crystal silicon wafers (silicon wafers were chosen to ensure substrate purity).^{41,42} It

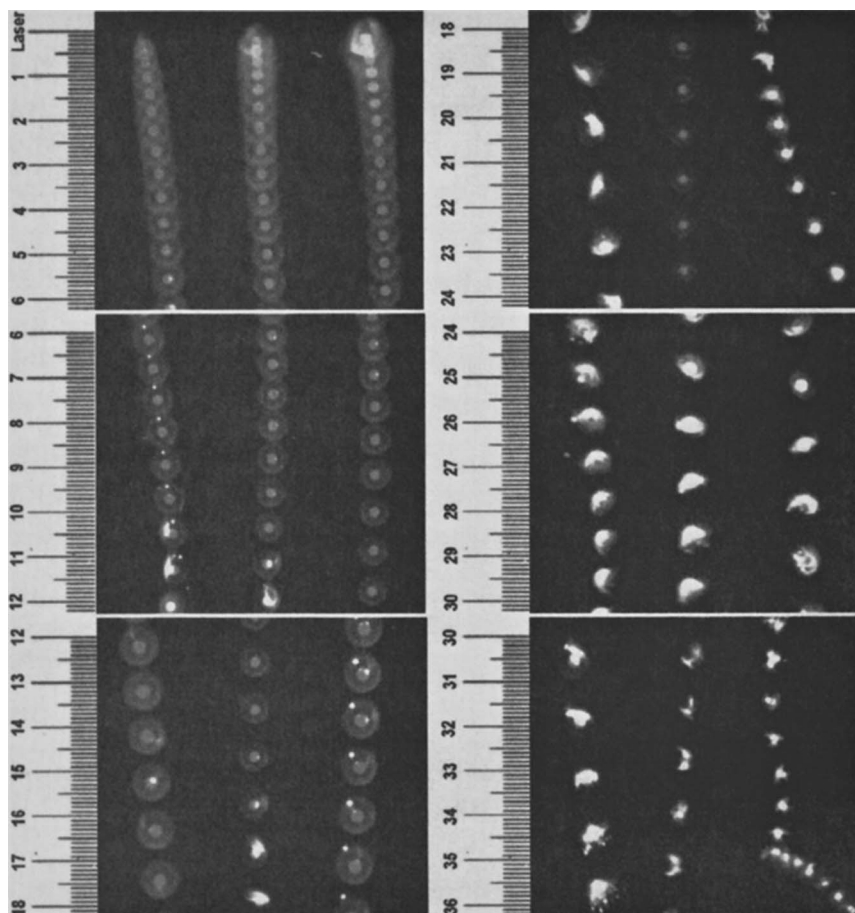


Fig. 5 Chopped natural luminosity images of aluminum particles burning in air as a function of distance from particle generation and ignition in the combustion chamber.

was assumed that the three-dimensional (spherical) flame configuration is rapidly quenched, yielding a relatively undisturbed two-dimensional (planar) projection of the condensate on the quenching plate. Electron probe microanalysis (EPMA) was used to measure relative radial distributions of Al, O, Si, C, N, F, and S on the quenching plate along a line extending from the particle center outward. The results of single-point EPMA measurements are X-ray photon counts, which are linearly proportional to the number of Al, O, Si, C, N, F, and S atoms contained at the probing sight. Along a radial trace, a series of single-point measurements yields relative radial atom distribution profiles. As a result of the particle-plate impact process, these radial atomic profiles correspond to a line-of-sight integration of the condensed phases contained in the three-dimensional flame system prior to impact. Under the assumption of perfect radial symmetry, the cross-sectional distributions of Al, O, C, N, F, and S atoms were reconstructed using a one-dimensional, three-point inverse Abel transform algorithm.⁴⁶ To facilitate a distinction from the

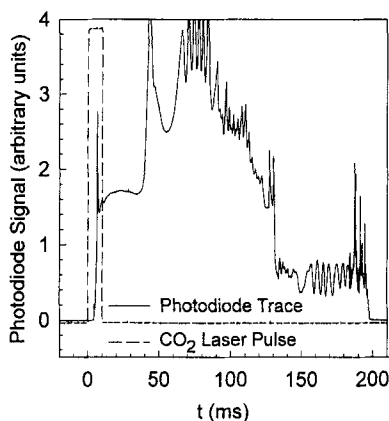


Fig. 6 Luminosity trace vs time for an aluminum particle burning in air.

line-of-sight integrated raw measurements, the Abel recovered cross-sectional elemental profiles are subsequently referred to as relative concentration profiles.

Electron probe microanalysis was conducted on a CAMECA SX50 microprobe equipped with five-wavelength dispersive spectrometers (WDS) and a Princeton Gamma Tech energy-dispersive spectrometer. Automated traverses of the K_{α} X-ray lines of Al, O, Si, C, N, F, and S were performed from near the particle surface to the outer edge of the collapsed condensate cloud. Measurements in close proximity to the particle surface location could not be carried out because the silicon substrate, which melted during particle impact, formed an uneven surface during recrystallization that was unsuitable for x-ray measurements. An accelerating voltage of 7 kV was chosen to maximize the x-ray yield for the light elements (C, N, and O) while minimizing the excitation volume and hence the “oversampling” of Si atoms in the wafer substrate. The electron beam current was regulated at a value of 60 nA. Under these beam conditions and sample densities, the spatial resolution of EPMA is of the order of 800–900 nm³. The aim of microanalysis profiles was to determine the relative differences in x-ray intensities as a function of radial distance throughout the condensate region about the aluminum particles. A typical radial profile consisted of 500 measurements and spanned a length of 500–600 μm , yielding an analytical step size of $\approx 1 \mu\text{m}$. The excitation depth (determined by the electron accelerating voltage of the instrument) was maintained much greater than the deposit (smoke) layer thickness so that the x-ray intensity obtained for each of the K_{α} x-ray lines was always proportional to the number of Al, O, C, N, F, and S atoms present on the silicon substrate at the probing sight. Proportionality factors (x-ray matrix corrections) that link each of the relative x-ray intensities measured to an absolute number of Al, O, C, N, F, and S atoms could not be determined. However, the proportionality factor for each of the atoms is the same constant for all quenched particles studied because the instrument parameters such as electron beam current and accelerating voltage remained unchanged.

Peak/background ratios are reported to distinguish characteristic from continuum radiation. Measurements for C, N, and O were determined by linear interpolation of two backgrounds (on either side of the peak), while a single background and slope method was used for Al and Si measurements. In an effort to mitigate

carbon deposition on sample surfaces during analysis (owing to residual hydrocarbon vapor from pump oils that become cracked by the electron beam), a liquid nitrogen cold trap in the specimen chamber was used.

For the purpose of resolving the condensate structure (oxide particle size) on the quench plates, digital scanning electron microscope (SEM) images were collected with a Philips XL30 field emission gun (FEG) SEM. An accelerating voltage of 10 kV was used in conjunction with working distances smaller than 10 mm to obtain high-resolution secondary electron images. No conductive coating was used on the samples, thereby eliminating the possibility of misinterpreting a film artifact as a specimen feature.

D. Gas-Phase Species and Temperature Measurements

The use of PLIF and planar thermometry as a technique for probing complex reacting flows has been demonstrated.^{47–50} In applying PLIF to metal particle combustion, challenges arise from the presence of condensed phase species in the flame envelope and the high temperatures involved. Single-laser PLIF temperature measurements have shown that the typical laser sheet approach is not applicable because Mie scattering (due to the condensed phases) broadens the distribution of pump energy.^{15,42} At the expense of added noise, cross-sectional fluorescence distributions are reconstructed by applying an inverse Abel transform to line-of-sight measurements in which a broad laser sheet was used to overfill the probing domain.^{42,44} The presence of thermal radiation from hot oxides requires narrow camera gate widths and a laser pumping scheme that results in high LIF-to-background ratios.

Using a two-laser two-camera system for a ratiometric temperature measurement via ALO PLIF, the (0,1) and (0,2) bandheads of the $B^2\Sigma^+ \leftarrow X^2\Sigma^+$ electronic system of AIO were pumped sequentially with laser spectral intensities sufficient to cause saturation, and broadband LIF from the (0,0), (1,1), and (2,2) bands was monitored. Both bandheads are well isolated from other transitions and the common upper laser coupled vibrational state eliminates the assumption of vibrational equilibrium in the B electronic state. A compromise had to be made with regard to the temperature sensitivity and LIF signal level. The energy difference between the absorbing states $\Delta\varepsilon_{12}$, which is one vibrational quanta or, equivalently, ~ 1400 K in the current pumping scheme, resulted in a relatively poor temperature sensitivity. However, based on the observed LIF signal levels and measured contribution from thermal radiation of the condensed phases, the ratio of the two fluorescence signals could be measured to within 1.0%. Because of a decrease in the population fraction, pumping the (0,3) bandhead with $\Delta\varepsilon_{12} \sim 2800$ K or the (0,4) bandhead with $\Delta\varepsilon_{12} \sim 2800$ K instead of the (0,2) bandhead would have resulted in a systematic error of 2.2 and 3.5%, respectively. There is a significant difference in line strength between the vibrational states pumped.⁵¹ Thus, dynamic LIF simulations were necessary to predict the contribution of nonsaturated signal from the frequency and temporal wings of the laser pulse in obtaining a relationship between LIF signal ratios and temperature.

A schematic of the experimental facility is shown in Fig. 7. ALO LIF was excited with a pair of matched Nd:Yag pumped tunable dye laser systems using the dye laser output from coumarin 500. The pump beams were tuned to the (0,1) and

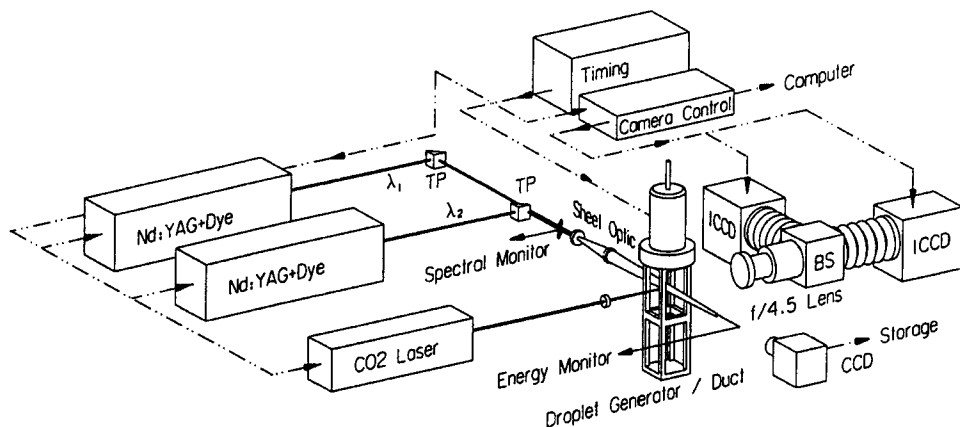


Fig. 7 Experimental arrangement used to acquire instantaneous temperature images of AlO gas-phase diffusion flames around single aluminum particles. TP, turning prism; BS, beam splitter cube; ICCD, intensified, charge-coupled device.

(0,2) bandheads of the $B^2\Sigma^+ \leftarrow X^2\Sigma^+$ electronic system of AlO at 5079.35 and 5336.59 Å, respectively. Including transmission loss, the dye laser beams had pulse energies in excess of 40 mJ, with pulse widths of ~ 6 ns and measured spectral bandwidths of 0.1 cm^{-1} . The two lasers were fired with a time delay of 50 ns. Excitation scans were performed to tune dye lasers to the (0,1) and (0,2) bandheads of AlO. For the purpose of generating AlO molecules without having to run the particle experiment, a vapor plume 5 mm high was produced by focusing a 150-W CO₂ laser pulse of 0.8 ms on a solid sample of sapphire (Al₂O₃).⁵² The dye laser was tuned over a range of frequencies and fired concurrent with the end of the CO₂ laser ablation pulse. AlO LIF was monitored using a gated intensified charge-coupled device (ICCD). The LIF signal was averaged over a 20×5 -pixel region in the most intense region of the plume and stored.

The beams were combined by propagating one beam at a small angle over a right-angle prism, which was used to turn the second beam (Fig. 7). The nearly collinear beams were expanded to overfill the region around the particle using a cylindrical telescope and a $f = 300$ mm spherical lens. The resulting vertical sheet measured $\sim 4.5 \times \sim 8$ mm. The distribution of the energy within the expanded beam was mapped out by translating a pinhole across the sheet and an energy meter. Measurements show the sheet energy to be within 25% of the peak energy in a 2.5×2.5 -mm region (the extent of the flame zone around burning particles is 1 mm). Spatial averages of the sheet energy over the uniform region were recorded for each experimental run (16 particles) and each laser as input parameters for the spectral simulation. A CCD camera was positioned nearly coaxial with the pump sheet to record simultaneous emission images of the burning particles. These images were used to monitor the particle position with respect to the pump sheet. Experiments in which the particle resided outside of the relatively uniform 2.5×2.5 -mm pump sheet region were discarded. The average temporal distribution of power over the laser pulse was measured with a photodetector (350-ps fall time) as the input parameter for the spectral simulation. The saturation behavior of the (0,1) and (0,2) bandheads of AlO generated in the vapor plume was measured by attenuating the

pump beam with various neutral density filters. A slope of ~ 0.22 on a logarithmic plot of laser energy and LIF signal confirmed that nonsaturated signal was sampled from the temporal and frequency wings of the laser pulse.

The broadband AIO LIF from the B-X (0,0), (1,1), and (2,2) bands of AIO was imaged at a right angle to the pump beam with two cooled, intensified detectors (Princeton Instruments; fiber optic-coupled, 576×384 CCD array). The signal was collected with a single $f/4.5$ lens (105-mm focal length) and split using a coated, nonpolarizing beam splitter cube. A 10-nm interference filter centered at 488 nm was used to block elastically scattered laser light. The field of view of both cameras was 4.02×2.68 mm, the spatial resolution [as determined by a measurement of the contrast transfer function (CTF)] was $12 \mu\text{m}/\text{pixel}$. To capture most of the fluorescence signal, but reject the thermal radiation from particle and condensed-phase oxide efficiently, the intensifier gate widths were set to 25 ns. The linearity of detection was verified under operating conditions (microchannel plate gain setting) by attenuating the fluorescence signal with various neutral density filters.

Several image corrections were necessary to determine quantitatively temperatures from fluorescence images.⁵¹ Average background images, which were acquired with the laser operated, were subtracted from raw fluorescence images. For accurate pixel-to-pixel indexing of the two-camera systems,⁴⁸ a geometric transformation (image warp), which involved translation, rotation, and magnification, was applied to images acquired by camera 2. To correct for the relative spectral response between the two cameras on a pixel-to-pixel basis, LIF from one laser was monitored simultaneously using both cameras. In practice, this was done by pumping AIO in the tiny vapor plume and sweeping the plume across the image plane, eventually to fill the entire field of view. By imaging AIO fluorescence from the vapor plume, which was comparable in magnitude to the fluorescence signal of AIO in the particle cloud, the intensifier gain dependence and iris effects in the photocathode were eliminated. The spatial averaging technique utilized the radial symmetry of the combustion system. From each image, the center of the particle was found using a centroid determination, and an averaged radial profile was calculated. A one-dimensional, three-point Abel transform⁴⁶ was performed on all averaged radial profiles to convert the line-of-sight integrated fluorescence signal to cross-sectional profiles. Finally, the ratio of the Abel inverted images corresponding to the same particle was calculated.

The aim of the detailed spectral simulations was to obtain a relationship between predicted LIF signal ratios and temperature. To account properly for the contribution of nonsaturated signal from the frequency and temporal wings of the laser pulse, the rate equations for a two-level system⁴⁸ were integrated over frequency and time using the measured spectral and temporal laser intensity distributions. The two-level fluorescence system was used under the assumption of negligible bleaching and a level-independent, global quenching rate. Band strength and line intensity factors were taken from Partridge et al.⁵¹ A global collisional quenching-rate constant was determined by matching simulated and experimentally measured power saturation behavior of both the (0,1) and the (0,2) bandheads. The best fit was obtained for a quenching rate of $5.6 \times 10^{-11} \text{ cm}^3 \text{ s}^{-1}$. For comparison, Campbell et al.⁵³ measured quenching-rate constants for the $\text{B}^2\Sigma^+$ state of AIO using a pulsed-laser photolysis LIF technique and found CO, NO, N_2 , and CO_2 to have rate constants of 4.8×10^{-12} , 1.8×10^{-10} , 1×10^{-13} , and $1 \times 10^{-12} \text{ cm}^3 \text{ s}^{-1}$, respectively.

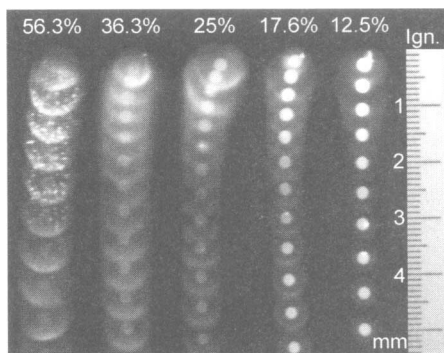


Fig. 8 Multi-exposure emission images of aluminum particles burning in various O_2/Ar mixtures. The percentages at the top denote the volume percentage of O_2 . The scale on the emission image corresponds to the distance from the point of laser ignition (mm).

III. Experimental Results

Multi-exposure luminosity images of $187\text{-}\mu\text{m}$ -initial diameter aluminum particles burning in various O_2/Ar mixtures at room temperature are shown in Fig. 8 at intervals of 2.5 ms for a duration of 0.2 ms . The experiments were conducted at $106 \pm 1.5\text{ kPa}$. For comparison, multi-exposure luminosity images of $215\text{-}\mu\text{m}$ aluminum particles burning in $21\%\text{ O}_2/79\%\text{ N}_2$ and pure N_2O , CO_2 , CO , and H_2O are shown in Fig. 9 at intervals of 3 ms for a duration of 0.3 ms . Combustion prevails, with a bright vapor-phase envelope for all oxidizers studied with the exception of CO . In the O_2/N_2 atmosphere, combustion occurs in different stages, the initial spherically symmetric stage (seen in the image) and a later very violently disruptive stage ($t > 45\text{ ms}$), typical of that shown in Fig. 5 for combustion in air. Generally, no differences were observed between combustion in the air-equivalent controlled mixture of O_2/N_2 and combustion in ambient air. Although the particle rapidly traverses out of the laser radiation field of 0.1-mm diam, a period of approximately 10 ms is needed to establish a quasi-steady, spherically symmetric

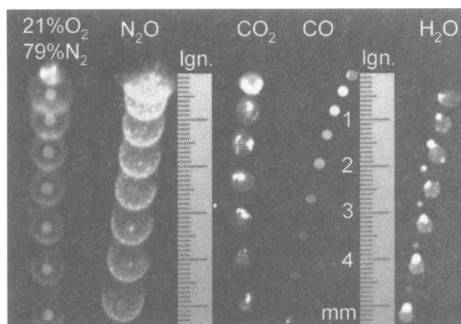


Fig. 9 Multi-exposure emission images of aluminum particles burning in various atmospheres. The scale on the emission image corresponds to the distance from the point of laser ignition (mm).

combustion mode (third luminosity image). Photodiode traces of luminosity show the characteristic staged combustion behavior observed previously in ambient air (Fig. 6) and in the literature.

The O_2/Ar flames (Fig. 8) also exhibited a spherical envelope with a slightly larger luminous zone than the O_2/N_2 flame (Fig. 9). As the O_2 concentration is decreased in Ar, the diameter of the smoke cloud decreases, as does its intensity. For low O_2 concentrations, combustion in O_2/Ar mixtures remained quiescent and no disruptive phase was observed. Both the nonexistence of a disruptive burning phase and a slightly larger luminous flame zone in the O_2/Ar atmosphere are in excellent agreement with the observations of Prentice and Nelson. However, for O_2 concentrations in Ar higher than about 45%, the tendency for disruption and fragmentation increased with increasing O_2 concentration.

In the N_2O atmosphere, the luminous flame envelope was comparable in size to the 21% $O_2/79\%$ Ar atmosphere and slightly distorted. Numerous bright spots, which originate from small particles, appear within the flame envelope. These spots are also visible for the highest oxygen concentration mixture of Fig. 8. The associated photodiode luminosity trace reveals that, at times greater than 50 ms, very violent disruptive events had occurred in the N_2O system.

In CO_2 atmospheres, a gas-phase luminous flame located primarily at 1 nondimensional radius off of the particle surface is observed. The apparent burning time as defined by the presence of a luminosity signal (170–200 ms) was long relative to that of the N_2O (80–110 ms) and the 21% $O_2/79\%$ Ar (145–170 ms) atmospheres, exceeded only by that of the 21% $O_2/79\%$ Ar (200–240 ms) atmosphere. Immediately following ignition, mild disruptions, accompanied by satellite particles at slightly greater burning times, are observed. However, the disruptions are less violent than those seen in O_2/N_2 and N_2O and are periodic, presumably due to particle spin.

No gas-phase formation of condensed-phase Al_2O_3 is observed visually in the CO atmosphere. The luminosity trace is small in magnitude and consistently shows an increase in intensity approximately 45 ms following particle ignition. Vapor-phase combustion was also observed in H_2O atmospheres, with an overall flame size slightly greater than the particle size. Figure 9 shows a typical scenario, in which large luminous satellite particles depart from the main, less luminous flame system, which contains the aluminum droplet. Thus, fragmentation occurred concurrently with ignition, i.e., there was no period of quiescent burning.

Figure 10 shows multi-exposure luminosity images of Al particles burning in pure SF_6 . Each vertical image in the figure shows a different particle recorded at progressively lower locations in the combustion duct. The entire burning lifetime is steady and well behaved, with no sharp jumps in luminosity or jetting of smaller particles as observed with combustion in oxygen bearing environments. Further, no visible cloud of condensed-phase material (smoke) surrounding the particle is observed. As the final product of combustion, AlF_3 has not been observed in the liquid phase and is anticipated to remain gaseous and diffuse far from the burning particle, where its concentration will be considerably less, before sublimating to the solid phase at 1564 K. The bright spot on the particle during the first 1 mm of travel is a lobe of liquid Al_2O_3 , which was the original film of Al_2O_3 solid that had formed on the surface of the aluminum wire due to storage in ambient air. The fluorine appears to reduce the aluminum oxide, and beyond this point, the particle surface is bare Al, as there are no other condensed-phase products formed near the particle to accumulate on the surface.

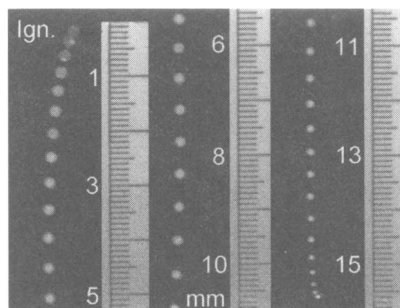


Fig. 10 Multi-exposure emission images of aluminum particles burning in pure SF_6 . The scale on the emission image corresponds to the distance from the point of laser ignition (mm).

With the exception of the 56% O_2 /44% Ar and pure- H_2O mixtures, the flame envelope was nearly spherically symmetric during the initial burning phase ($t < 45$ ms). A nonsymmetric flame structure accompanied by particle fragmentation was observed at longer burning times in some atmospheres. This behavior was attributed to oxide accumulation and participation of aluminum–nitrogen species in the combustion process. Because both the gas-phase and the condensed-phase analysis techniques require spherical symmetry of the flame structure, and to avoid the additional complexity of lobe–particle interaction, all detailed flame structure experiments were taken at a burning time of approximately 15 ms.

Figure 11 shows raw line-of-sight and Abel cross-sectional AIO PLIF images that resulted from pumping the (0,1) bandhead for combustion of aluminum in 21% O_2 and 79% Ar. Both azimuthally averaged radial profiles and single-shot cross-sectional distributions are shown. A slight asymmetry, which arises from a cylindrical shadow of the pump beam to the left of the particle, is noticeable in all raw PLIF images. The cross-sectional profiles clearly show AIO to be a gas-phase intermediate species with nonzero concentrations at the particle surface ($r_0 = 0.11$ mm).

Averages of single-shot radial temperature profiles along with relative AIO concentration profiles, which were calculated from the measured relative population in the pumped rotational states in $v'' = 1$ via the Boltzmann equation, are shown in Fig. 12 for aluminum combustion in mixtures of 21% O_2 /79% Ar, 21% O_2 /79% N_2 , and 100% CO_2 . The relative AIO concentration profile of the 21% O_2 /79% Ar atmosphere was set to 1 at the maximum; all other profiles are scaled accordingly. Although all profiles generally show the temperature to increase in the region adjacent to the particle, the rate of increase is significantly different for the different atmospheres studied. Consistent with the concept of a limiting temperature (which is controlled by the local dissociation temperature of condensed-phase Al_2O_3), the combustion systems appear to have reached a relatively constant flame temperature over significant radial distances in all atmospheres with the exception of CO_2 . Ignoring the data scatter between three and four nondimensional radii (which is due to low PLIF signal levels), the temperature profile of the CO_2 atmosphere is sharply peaked. This trend is in agreement with overall enthalpy considerations, which show that the limiting flame temperature cannot be reached in the Al– CO_2 system.

Relative AIO population profiles were obtained for the 21% O_2 /79% Ar and 21% O_2 /79% N_2 systems at pressures up to 308 kPa. As the pressure increases,

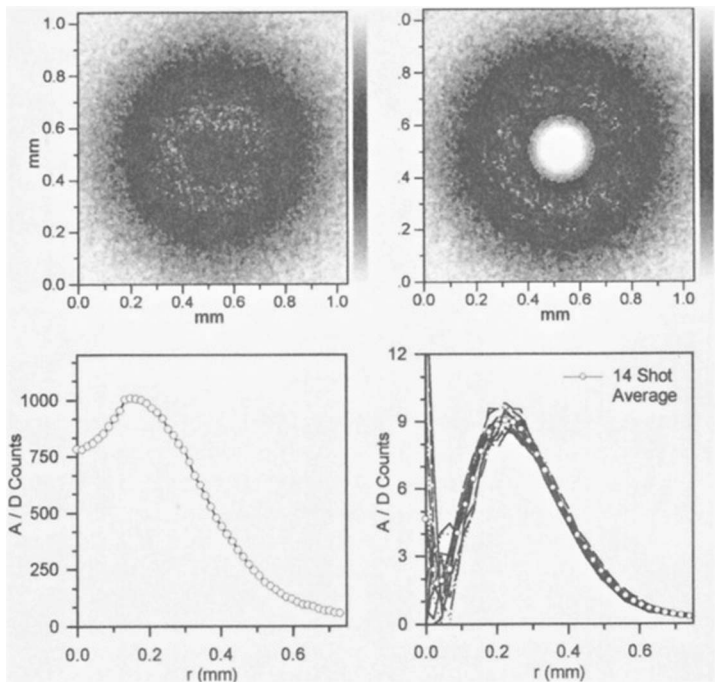


Fig. 11 Raw and cross-sectional AIO PLIF images with corresponding azimuthally averaged raw profiles and single-shot cross-sectional profiles for aluminum particle combustion in 21% O₂ and 79% Ar at 106 kPa.

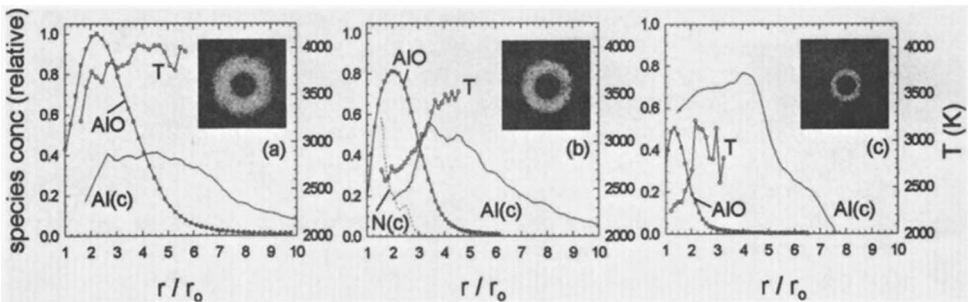


Fig. 12 Nondimensional radial profiles of AIO, Al₂O₃, and N relative concentrations and averaged temperature for 210- μ m aluminum particle combustion at 106 kPa. Profiles were measured at a burning time of 15 ms. Insets are cross-sectional AIO PLIF images. a) 21% O₂/79% Ar; b) 21% O₂/79% N₂; c) 100% CO₂.

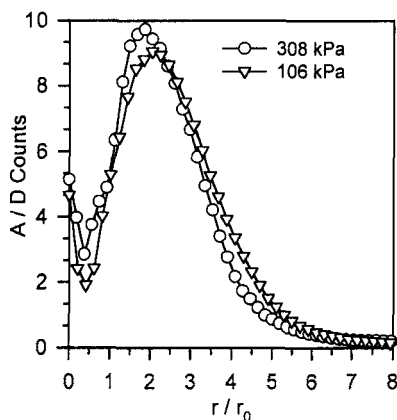


Fig. 13 Pressure dependence of relative cross-sectional AIO $\nu'' = 1$ population for pressures of 106 and 205 kPa for combustion of Al in 21% O_2 /79% Ar.

the width of the Abel inverted profiles (shown in Fig. 13 for the O_2 /Ar system) decreases and the peak moves closer to the particle surface.

In Fig. 14, a typical raw PLIF image obtained from a particle burning in 50% O_2 /50% Ar is shown. As determined from simultaneous emission photography, the area from which little LIF is collected (the circular pattern in the left half of the image) is due to the presence of an oxide lobe at the particle surface. Oxide lobes are observed to exist with great regularity at burning times greater than 15 ms in this gas mixture.

SEM images of 215- μ m-initial diameter particles, quenched by impact on a silicon substrate at 3 mm below the point of ignition, are presented in Fig. 15 for combustion in 21% O_2 /79% N_2 , 100% N_2O , 100% CO_2 , and 100% CO. Because the mechanical chopping system was not compatible with temperatures in excess of 380 K, which were needed to avoid steam condensation, the H_2O experiments could not be executed reliably enough to allow for particle quenching. The quenching distance of 3 mm (equivalent to a burning time of 12–17 ms) was chosen to sample

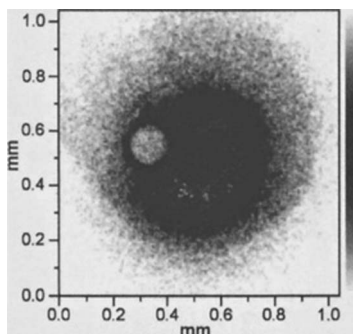


Fig. 14 A raw AIO PLIF image of particle combustion in a 50% O_2 and 50% Ar mixture illustrating the presence of an oxide lobe.

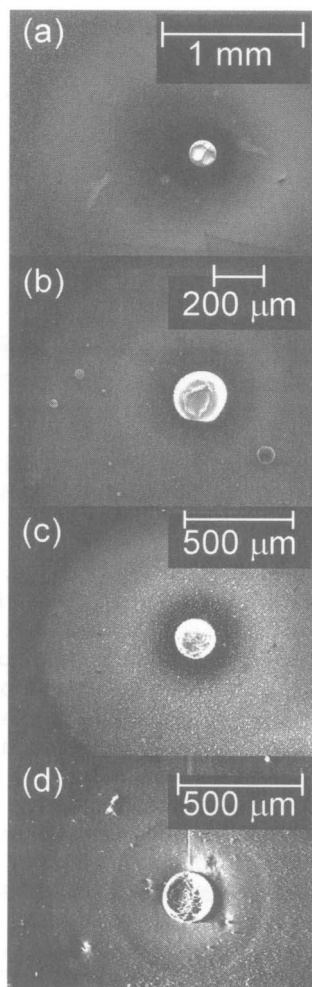


Fig. 15 SEM images of burn-interrupted aluminum particles in 21% $\text{O}_2/79\%$ N_2 , 100% N_2O , 100% CO_2 , and 100% CO . Note the different scales as indicated by the bar within each of the SEM images.

subsequent to the establishment of a quasi-steady burning mode, but within the aforementioned spherically symmetric combustion period ($t < 45$ ms). Common to all of these oxidizers, except CO , is a smoke ring located off the particle surface. The quenched sample for the O_2/N_2 environment was taken during quasi-steady combustion, and no fragments from particle disruption are observed on the plate (satellite particles similar to those found in N_2O appear at greater burning times). Consistent with the particles observed in visual photographs of N_2O combustion (Fig. 9), the parent particle is surrounded by numerous small particles varying in diameter from 5 to $85\ \mu\text{m}$. This also applies for CO_2 combustion with fewer satellite particles and to mixtures with high concentrations of O_2 . In the case of CO , a dual-ring structure is observed, with the inner ring extending to the particle

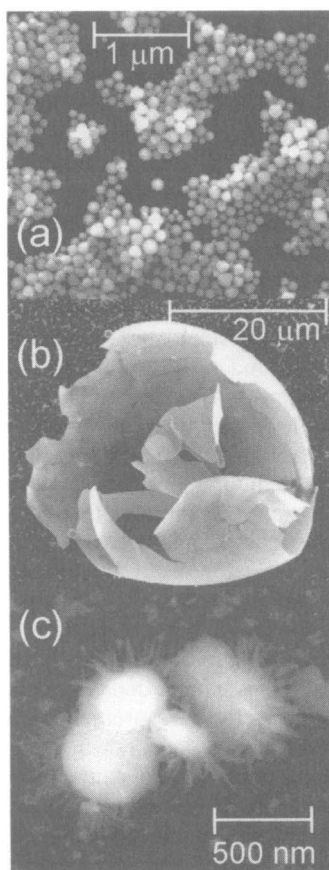


Fig. 16 High-resolution SEM images of the product structure. Experimental conditions and sampling locations: a) O_2/N_2 atmosphere, 600 μm removed from particle surface, 75 μm removed from particle surface; b) N_2O atmosphere, 20- μm satellite particle (hollow shell), found 400 μm removed from particle surface; c) CO atmosphere, typical deposit with attached fibers, found 75 μm removed from particle surface.

surface. Visually, the color of the smoke of the CO atmosphere was gray, compared to the white color found in all other cases.

To classify the product (smoke) structure as a function of the radial distance, high-magnification SEM images (Fig. 16) were taken. For all of the oxygen oxidizers except CO, a common product structure was found. Within the high-density smoke region, small spheres, with diameters of between 100 and 200 nm, were found. The image in Fig. 16a was obtained from the O_2/N_2 quenched particle at a location 600 μm removed from the surface. SEM photographs obtained within the inner dark ring appear to show the deposit as a crystalline, fibrous structure. However, this structure may consist of agglomerates of much smaller, spherical particles. The PLIF flame structural measurements have shown peak concentrations of $\text{AlO}(\text{g})$ to exist at $r/r_0 = 2$. Therefore, the deposit immediately adjacent to

the droplet could have been formed as a result of condensation of AlO or other gas-phase aluminum containing species. Also evident in Fig. 16a are some spherical oxide particles that exist as a consequence of the collapsing three-dimensional flame structure during impact. The low density of these spherical particles is indicative of low particle concentrations in the outer zones before quenching. Hence, the agglomerate structure of the oxide spheres observed in Fig. 16a is most likely a result of the quenching process. Figure 16b is an example of a 20- μm satellite particle formed during combustion in N_2O atmospheres. In this particular case, the particle that remains is a hollow shell approximately 300 nm thick, which is composed of stoichiometric Al_2O_3 . Similar residual particles of between 5 and 60 μm were also found in O_2/N_2 atmospheres at burning times greater than 50 ms (in the aforementioned disruptive burning stage) and by other investigators in flames and solid propellant environments under atmospheric and high-pressure conditions. Large-scale oxide residuals appear to be favored when nitrogen is present in the combustion environment, and two distinct size ranges of oxide particles are formed, greater than $\sim 300 \mu\text{m}$ and less than $\sim 5 \mu\text{m}$, as concluded previously in the literature. The product structure found in CO atmospheres was distinctively different than that found in all other cases. An example of a typical quenching plate deposit (Fig. 16c) consists of a spherical particle between 200 and 400 nm in diameter, with attached fibers. In addition, particles of much smaller size were found.

Aluminum, oxygen, carbon, and nitrogen K_α x-ray relative measurements were made along radial traces from the particle center outward in increments of 1 μm . The SEM in Fig. 15, which shows a particle quenched from a CO atmosphere burn, was acquired after the x-ray analysis and depicts the radial track resulting from charging of the specimen during the measurement. The Abel recovered relative concentration profiles of Al and O (O is shown in terms of the ratio Al/O) in Fig. 17 show a distinct maximum at some distance from the droplet surface in all atmospheres. Although convective drag and thermophoretic forces may distort the condensed-phase oxide distribution, high levels of Al and O are generally indicative of an intense oxide production region. The radial extent of the Al profile, which varies greatly for the different oxidizers studied, indicates the extent of the reaction zone. In the case of O_2/Ar atmospheres (not shown), no C or N was detected, and the ratio of the Al and O x-ray intensities was found to be 1.4 ± 0.15 , independent of the radial position. Because $\text{Al}_2\text{O}_3(\text{s})$ and $\text{Al}(\text{s})$ are the only condensed-phase species in the $\text{Al}/\text{O}_2/\text{Ar}$ system and the formation of $\text{Al}(\text{s})$ [due to condensation of $\text{Al}(\text{g})$ during quenching at regions close to the particle surface] is unlikely to occur at a large radius, the ratio of 1.4 was assumed to correspond to Al_2O_3 . Consequently, all Al/O ratios in Fig. 17 have been rescaled based on the finding that a measured ratio of 1.4 corresponds to 2/3 (the stoichiometry of Al_2O_3). Condensed-phase profiles for the 21% $\text{O}_2/79\%$ N_2 and 100% CO_2 systems, along with the 21% $\text{O}_2/79\%$ Ar system, are also plotted in Fig. 12 to show the relationship between gas-phase species and condensed-phase elements. For example, note that the rise in temperature near the particle surface always coincides with the formation of condensed-phase Al_2O_3 . It is also important to note that the O_2/Ar , O_2/N_2 , and N_2O systems are thermodynamically expected to reach the limit temperature because the enthalpy of the reactants is sufficient to decompose some of the Al_2O_3 . The existence of a plateau region in the temperature profiles experimentally confirms the concept of a limiting temperature.

In both O_2/N_2 and N_2O atmospheres, no carbon was detected, but nitrogen, which must be bound to aluminum to exist as condensed-phase species on the quenching plate, was found in regions smaller than $r/r_0 = 3$ as shown in Fig. 17.

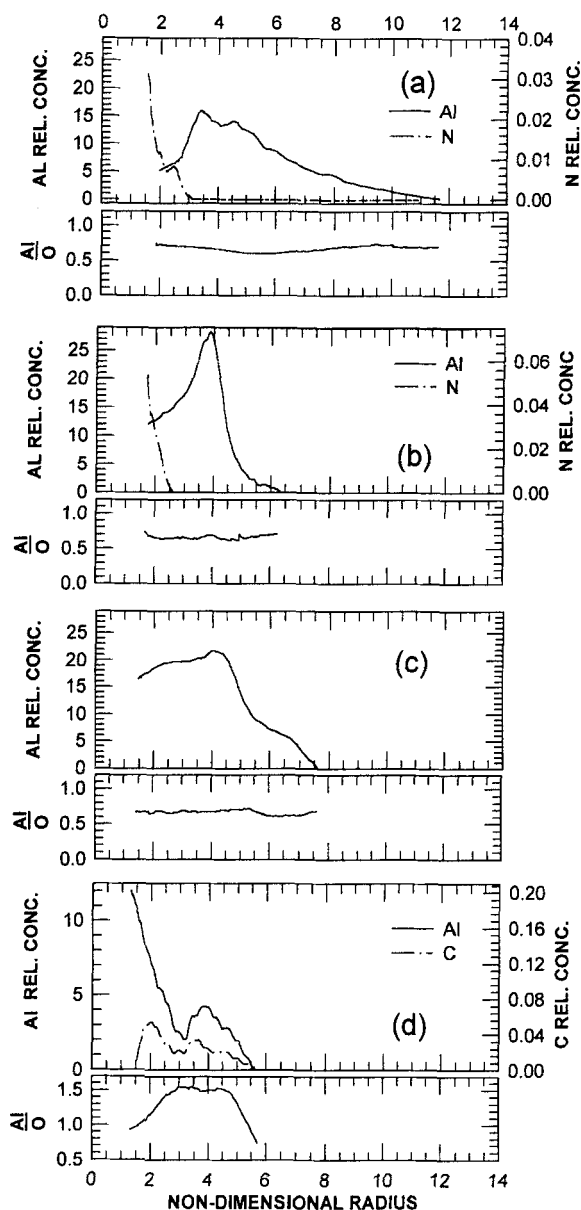


Fig. 17 Abel recovered elemental condensed-phase product distributions for the SEM images in Fig. 15.

Because the ratio of Al/O does not significantly increase in regions where nitrogen is detected, aluminum–nitride species, possibly AlN(s), must constitute a relatively small fraction of the condensed phase. Within the detection limits of the instrumentation, no C or N was found on the quenched samples taken from CO₂ atmospheres. The Al trace taken on the quench plate corresponding to combustion in a CO atmosphere confirms the dual-ring structure seen on the corresponding

Chapter 2.20

Combustion of Aluminum Particles in Solid-Rocket Motor Flows

John C. Melcher,* Rodney L. Burton,[†] and Herman Krier[‡]
University of Illinois at Urbana-Champaign, Urbana, Illinois

Nomenclature

B	= Spalding transfer number of fuel mass fraction
C_D	= drag coefficient
c_{mix}	= total molar concentration, mol/cm ³
D	= droplet diameter, μm
D_0	= initial droplet diameter, μm
\mathcal{D}_f	= fuel diffusion coefficient, cm ² /s
$\mathcal{D}_{\text{ox-mix}}$	= oxidizer diffusion coefficient, cm ² /s
(g)	= gas-phase
$[i]$	= molar concentration of species i , mol/cm ³
k	= burning rate coefficient, $\mu\text{m}^n/\mu\text{s}$
k_i	= reaction rate for oxidizer i , cm ³ /mol-s
(l)	= liquid-phase
L_c	= thermal diffusion layer thickness, μm
$N''_{\text{diff-ox}}$	= molar diffusive flux, mol/cm ² -s
n	= D^n exponent
p	= pressure, atm
Re_D	= Reynolds number
r/r_s	= nondimensional radius referenced to droplet surface
r'	= propellant burning rate, cm/s
t	= time, μs
t_b	= burn time, μs
X_{eff}	= oxidizer concentration expressed as a mole fraction
X_i	= oxidizer concentration of species i

Copyright © 1999 by the American Institute of Aeronautics and Astronautics, Inc. All rights reserved.

*Graduate Student, Dept. of Mechanical and Industrial Engineering.

[†]Professor, Dept. of Aeronautical and Astronautical Engineering.

[‡]Professor, Dept. of Mechanical and Industrial Engineering.

Y_f	= fuel mass fraction
α	= propellant thermal diffusivity, cm^2/s
ρ	= gas-phase density, kg/m^3
α	= propellant thermal diffusivity, cm^2/s
ρ	= gas-phase density, kg/m^3
ρ_l	= droplet density, kg/m^3

I. Introduction and Background

A. Research Motivation and Objective

THIS experimental study focused on one aspect of solid-propellant rocket combustion, that of aluminum droplet combustion. Aluminum is a common metal additive to solid-propellant composition and subsequently affects many performance parameters such as impulse and propellant burning characteristics. To design accurately and predict the performance of a rocket with an aluminized propellant, the combustion behavior of the aluminum droplets in the flow must be accurately described.

Adding lightweight metal particles to the propellant composition is beneficial chiefly because the metal combustion mechanism adds energy to the flow. The high flame temperature of burning metal droplets can impart large amounts of energy through the heat released during combustion and the subsequent formation of metal oxides, a process that occurs in the flow away from the propellant surface.^{1,2} Metal particles have also been shown to help reduce some modes of combustion instability through acoustic particle damping or aerodynamic drag, but the cause of this effect is not fully understood.^{3–7} However, rocket systems that use aluminum additives have historically failed to reach the full potential predicted from the metal combustion, due to performance losses introduced with the two-phase particulate flow of the molten aluminum droplets and smoke oxide particles. Furthermore, the use of aluminum particles for acoustic instability suppression is highly sensitive to particle size, and the control of agglomeration sizes becomes an essential factor in design.⁸

The research objective is to characterize the combustion rate of $\sim 100\text{-}\mu\text{m}$ aluminum particles in solid-propellant gaseous combustion products inside a wind-dowed solid-propellant rocket test chamber. The propellant chamber conditions are generated using an aluminum perchlorate (AP)/Hydroxyl-Terminated Polybutadiene (HTTB) bimodal propellant operating at pressures up to 25 atm, and the aluminum droplet source is a small aluminized propellant sample. An optical technique generates time-resolved images for determining the size of burning droplets as they travel through the chamber. The burning rate is characterized by the variation of droplet diameter with chamber pressure and oxidizer concentration in the gas-phase flow. The quantified effect of the studied parameters is then used to compare with and validate other models for burning rate presented in the combustion literature.

B. Aluminum Particle Combustion

Aluminum droplets burn in a gas-phase reaction where the flame front is at a detached distance away from the droplet surface, as shown in Fig. 1. Aluminum particles have a characteristic oxide coating that must be melted or cracked before

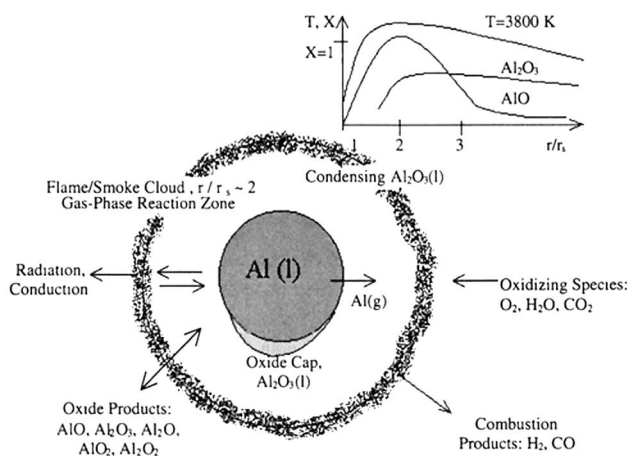


Fig. 1 Simplified description of aluminum droplet combustion^{2,12,27}: the reaction is a gas-phase reaction at a detached distance from the droplet surface, and hot oxide products dissociate outward and Al_2O_3 condenses and forms a smoke cloud that emits thermal radiation at a temperature near 3800 K.

the aluminum particle can ignite.² Because the oxide melting temperature, 2327 K, is higher than the melting temperature of aluminum, 933 K, the aluminum is assumed to be fully melted on ignition. The molten aluminum droplet surface burns at a temperature between the oxide melting temperature, ~ 2300 K, and ~ 2700 K, the aluminum boiling temperature.^{7,9} Although the global oxidation reaction of aluminum produces alumina, Al_2O_3 , many suboxides such as AlO , AlO_2 , Al_2O , and Al_2O_2 exist in the flame zone, with AlO as the most prominent. The condensation of alumina at its estimated boiling point, ~ 3800 K, sets the approximate temperature of the oxide cloud because $\text{Al}_2\text{O}_3(\text{l})$ condenses directly from the association of the suboxides and the idealized gaseous form, $\text{Al}_2\text{O}_3(\text{g})$, immediately dissociates back into AlO and O_2 species.^{10,11}

The submicrometer alumina particles can radially diffuse both outward and inward, where they can accumulate in an oxide cap on the molten aluminum surface.^{2,5} The entire reaction is considered diffusion controlled because the species are reacting much faster than the diffusion rates at the elevated temperatures.⁹ Bucher et al.¹² have made measurements at 1–3 atm pressure showing that the peak in the AlO concentration occurs at a radius close to the droplet surface, $r/r_s \sim 2$, whereas the peak concentration of Al_2O_3 occurs farther away at $r/r_s \sim 3$. The data also show that concentrations of AlO can exist as far out as $r/r_s \sim 6$ and $r/r_s > 10$ for Al_2O_3 . Widener et al.⁹ present calculations showing alumina concentrations out at $r/r_s \sim 20$ in water-containing media at 1 atm. Other experimental and analytical work has shown that the location of the flame front moves closer to the droplet surface as pressure or oxidizer concentration/flux is increased.^{13–17}

The combustion of aluminum droplets is often characterized by the droplet burn time, which has been shown to depend on droplet size, state properties of the medium, and the flow characteristics of the entrained droplet. Classical fuel droplet evaporation/combustion theory states that the diameter of a burning droplet as $D^2 = D_0^2 - kt$, where k is the burning rate or evaporation coefficient. By setting $D = 0$, the classical burn time can be defined as $t_b \equiv D_0^2/k$. The burning rate k

is typically a function of the state properties of the medium including pressure, temperature, and oxidizer concentration.

Past research has shown that the diameter dependence does not necessarily follow the classical D^2 law, but instead follows D^n , where n is typically between 1.5 and 2. It is assumed that n is typically independent of the state properties of the medium and is only a function of combustion mechanism or flow properties. Kuo has shown with classical relations that n should be 1.5 for laminar convective flows around the droplet and closer to 1 for turbulent flow.¹⁸ Experimentally, Belyaev et al.¹⁹ and Friedman and Macek²⁰ found $n = 1.5$ in high-temperature gas flows, and Wilson and Williams found $n = 1.5 \pm 0.5$ in ambient atmospheres.²¹ Davis²² reports $n = 1.8$, and Hartman²³ $n = 2.0 \pm 0.3$, in high-pressure propellant flows, and Turns et al. found $n = 1.77 \pm 0.2$ for slurry agglomerates.²⁴ Analytical models calculated at 1 atm have demonstrated causes of the deviation from the D^2 law. King found $n = 1.4$ – 1.9 due to finite reaction kinetics at high temperatures.²⁵ Brooks and Beckstead found $n = 1.88$ under high convection and temperature conditions and $n = 1.5$ when a surface oxide cap decreased the burning surface area.⁵ Liang and Beckstead found $n = 1.20$ – 1.88 as the oxide cap affected different size droplets in ambient air.¹⁰ Daniel et al. report $n = 1.7$ when modeling droplets in a two-dimensional solid rocket chamber with two-phase flow.¹¹ Lastly, in global burn-time formulas for various conditions, the Hermesen model uses $n = 1.8$ (see Ref. 26) and Widener and Beckstead use $n = 1.9$ in their formula.²⁷

The state properties of the medium affect the burn rate coefficient k , and this study focuses on the effects of pressure and gas composition, more specifically, the oxidizer concentration expressed as a mole fraction X_{eff} . An increase in burning slope indicates a shorter burn time for a given droplet size. Classical theory relates k to X_{eff} through a logarithmic function of mass transfer.^{15,18} Belyaev et al.¹⁹ reported that k was a function of oxidizer concentration by $k \propto X_{\text{eff}}^{0.9}$, where $X_{\text{eff}} = X_{\text{H}_2\text{O}} + X_{\text{CO}_2}$ only, and Hermesen's formula (see Ref. 26) uses $X_{\text{eff}}^{0.99}$, where the concentration of O_2 is also included. Widener and Beckstead²⁷ have improved on their previous work in their formula to include a nonequal weighting to different oxidizing species and a smaller overall oxidizer effect, $X_{\text{eff}}^{0.39}$, where $X_{\text{eff}} = X_{\text{O}_2} + 0.58X_{\text{H}_2\text{O}} + 0.22X_{\text{CO}_2}$, so that oxygen has the strongest effect.^{5,6}

An increase in pressure is considered to increase burning rate by increasing the gas-phase transport of fuel and oxidizer species.^{12,23} At low pressures, oxidizer diffusion to the droplet is reduced by the condensed Al_2O_3 particles surrounding the droplet.¹⁶ Furthermore, the quasi-steady burning rate coefficient k is a function of gas density and diffusion coefficient,¹⁸ two parameters that introduce a pressure dependence into the burning rate. Hartman²³ reported an experimental linear pressure effect and a theoretical $k \propto p^{0.4}$. Foelsche et al.²⁶ found $p^{0.21}$, Hermesen's formula (see Ref. 26) uses $p^{0.27}$, and the Widener–Beckstead²⁷ model uses $p^{0.2}$. However, the effective range of the pressure effect is still in question. Belyaev et al.¹⁹ and Hartman²³ find no effect above 20–50 atm, whereas Foelsche et al. report changes up to 145 atm.²⁶

II. Experimental Apparatus

A. Chamber Design

This experiment studies the aluminum droplets in their environment of true interest, within the rocket motor chamber using a solid-propellant combustion products flowfield. In addition, the aluminum droplet source is an aluminized solid

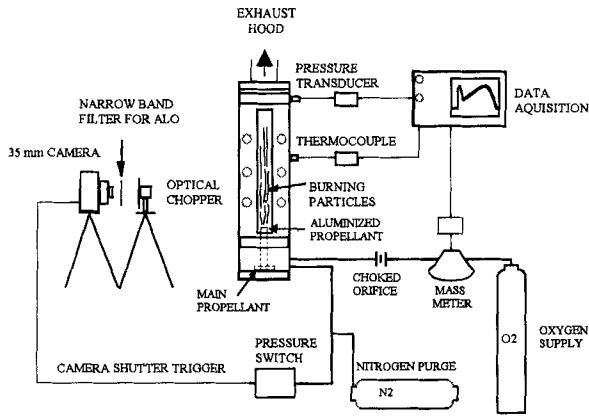


Fig. 2 Schematic of experiment apparatus operation.

propellant, instead of single aluminum droplets typically used in metal combustion experiments. The key to the design is the construction of a chamber with axial observation windows for viewing events in the chamber flow. Figure 2 shows the overall experiment design schematic. The chamber allows for a vertical flow traveling upward from a source propellant in the bottom of the chamber to a discharge at the top through a $2.54 \times 2.54 \text{ cm}^2$ square center channel. The chamber discharge uses a sharp-edged orifice nozzle to choke the flow. The aluminized propellant sample is mounted on a pedestal in the center of the square channel, near the bottom of the window. The 30-cm-long chamber windows were made up of two parts, an outer plastic window and an inner glass window. The outer window was made from 2.5-cm-thick Lexan, a strong plastic that provided the strength necessary to contain the chamber pressure, and a 6.5-mm inner quartz glass window for thermal protection.

Use of the 30-cm-long windows permitted observations over much longer distances at high pressure than is normally possible in metal combustion experiments. This allowed for the tracking of particles through burnout to observe if fragmentation of particles occurred.

The chamber burns two solid-propellant samples during one experiment: a relatively large (22-g) nonaluminized, bimodal propellant to fill the chamber to test conditions, and a much smaller (~ 0.1 -g) aluminized propellant sample to inject aluminum droplets. The main composite propellant is a mixture of 88% AP oxidizer and 12% fuel binder, where percentages are on a mass basis. The oxidizer part is a composite of two sizes of AP: 62% 200- μm AP, and 38% 50- μm AP. The fuel binder is a mixture of 77.4% HTPB fuel, 5.9% dioctyl adipate plasticizer (DOA), and 16.7% isophorone diisocyanate (IPDI) curing agent. The propellant is ignited by applying a 5-A current across a nichrome wire sandwiched between the top of the main propellant and another wafer of propellant of mass ~ 3 g. The aluminized propellant sample is ignited by the hot gases from the main propellant.

The chamber is also configured to allow additional gases to be metered into the chamber to study the effect of oxidizer concentration on aluminum combustion. The additional gas is injected into the bottom plenum of the chamber to allow the gases time to mix and react to equilibrium. By injecting a known mass flux of oxidizer into the chamber, the equilibrium oxidizer concentration from the propellant

products plus injected gas can be calculated. A small flat-plate orifice is installed in-line directly outside of the bottom chamber plenum to choke the oxidizer flow over the pressure range of the chamber. Oxidizer flux is controlled by varying the orifice size and oxidizer supply pressure. To provide accurate measurements of the oxidizer flux, a Micro-Motion Company ELITE CMF Coriolis mass-flow meter is installed in-line.

B. Chamber Conditions

Both pressure and temperature are measured in the center square channel where the aluminum combustion is observed. The thermocouple was mounted at a position ~ 7 cm along the window length. Because of the large temperature range of the chamber, 300–2900 K, a type C (tungsten–rhenium) thermocouple is used, rated up to 3000 K. Because the chamber is only pressurized a few seconds, a fast response time is required, achieved with an Omega open-sheath-type thermocouple with 0.23-mm bead diameter, calculated to have a 125-ms response time at chamber flow conditions.

A typical measurement of pressure and temperature from an experiment is presented in Fig. 3. A linearly rising pressure trace was present in every experiment, with nearly identical slope each time. This ramp in the pressure is useful because it creates a variable pressure condition that can be studied simply by changing the pressure trigger setting for the camera. A quasi-steady chamber model was developed to investigate the cause of the pressure ramp. After determining that the ramp was not caused by an identical linear increase in propellant burning area, a heat transfer model with a chamber wall temperature that increased linearly in time was found to match the data. The steady-state pressure predicted for the chamber with a 0.3-cm discharge orifice is 62 atm, which is well above the measured pressure range. If the wall temperature is held constant in the model, the chamber fills to full pressure in less than 1 s. If the wall temperature is allowed to vary from 300

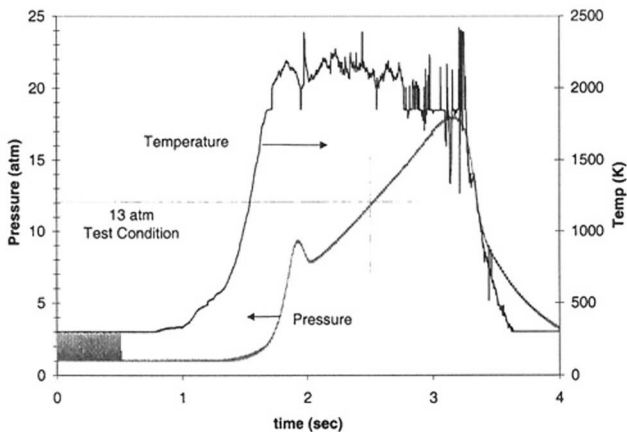


Fig. 3 Chamber experimental conditions, pressure (atm) and temperature (K), through time history of chamber: the temperature of ~ 2200 K can be radiation corrected to ~ 2300 K, and the pressure ramp is a result of a linear wall temperature heat-up, shown by a quasi-steady lumped capacitance model of the chamber.

to 550 K over the 2 s of the burn, the model pressure data matches the experiment data.

Accounting for radiation losses from the thermocouple bead, the measured temperature of ~ 2200 K is corrected to ~ 2300 K. It was also found that the temperature did not change significantly with pressure or additional oxygen gas injected into the chamber. Thus, the temperature was assumed constant in the study of pressure and oxygen effects.

Droplet velocity was measured to be 5–7 m/s on average, which agrees well with a calculated mass-averaged gas velocity of ~ 5.1 m/s across the channel area. There was no measured velocity gradient with axial position in the chamber. The flow velocity increased about 5–20%, or 0.25–1 m/s, across the range of added oxygen flow.

C. Aluminized Propellant Description

A small, aluminized propellant sample of size approximately $3 \times 3 \times 8$ mm³ and mass ~ 0.1 g was mounted on a pedestal in the center of the square channel in an end-burning configuration. The propellant is an AP/HTPB bimodal propellant, similar to the base propellant used to pressurize the chamber. The loaded aluminum is 15% of the propellant mass. Figure 4 is a scanning electron microscope (SEM) image of the propellant surface, where the aluminum appears small and reflective compared to the dull, large boulders of AP. The loaded aluminum particles are near-spherical particles typically specified as 110 μm in diameter. A size analysis of the aluminum particles visible in the propellant SEM shows an average size of 106 ± 20 μm . The raw aluminum used in the propellant, shown in Fig. 5, was measured to have an average size of 107 ± 20 μm .

To predict the likelihood of particle agglomeration, the aluminum behavior near the burning propellant surface must be considered. Because of the intense heat of

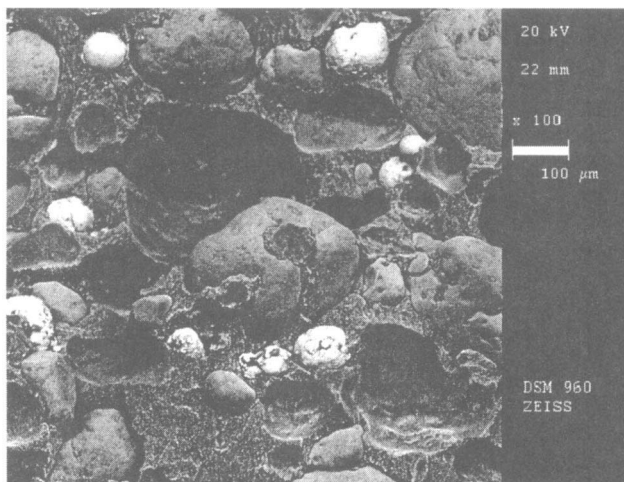


Fig. 4 SEM of aluminized propellant surface: small, reflective particles are aluminum, large boulders are AP, craters from AP particles on opposing face of sampled-capacitance model of the chamber.

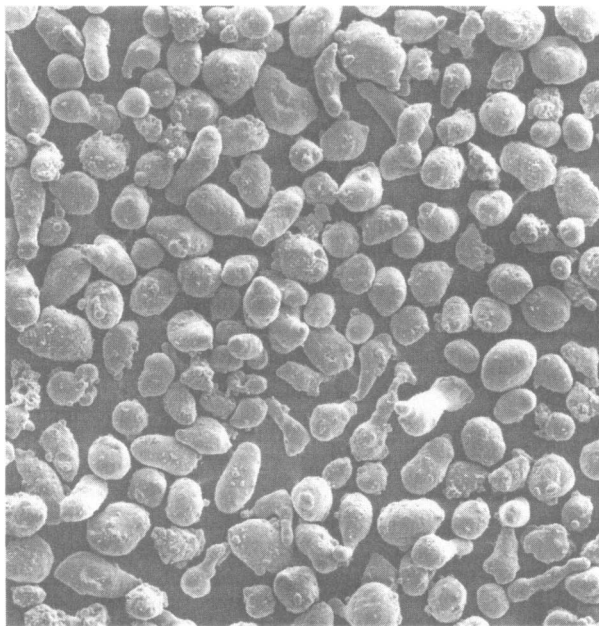


Fig. 5 SEM of H-95 aluminum particles loaded in aluminized propellant, average diameter, 106 μm .

the propellant flame, heat is transferred back into the propellant to a thermal diffusion layer thickness, in which the propellant matrix begins to melt. This thickness can be approximated by $L_c = \alpha / r'$, where α is the propellant thermal diffusivity and r' is propellant burning rate.²⁸ At 13 atm, the experimental baseline pressure condition, the burning rate is roughly 0.4 cm/s, and the thermal diffusivity can be approximated as 0.0006 cm²/s for an aluminized AP/HTPB propellant.²⁸ Thus, the thermal heat-up layer is only 15 μm thick, and the 106- μm particles are an order of magnitude larger than the thermal heat-up layer thickness. As shown by Gany and Caveny, agglomerates are typically formed of particles that are smaller than the propellant reaction layer, which is even smaller than the thermal layer, allowing many particles to collect in the reaction layer to agglomerate together.⁸ The propellant used in the current study falls under the large particle regime in the Gany and Caveny model and would accordingly be expected to show little if any agglomeration.

In real rocket motor applications, 15–20 μm aluminum particles are typically used that can agglomerate in the thermal layer of the burning propellant. The impact on the droplet combustion is that agglomerates have entrained propellant decomposition products and gases and are somewhat porous. This means that the agglomerates can burn from both the exterior and interior and typically have a burning rate greater than pure molten aluminum droplets, such as those used in this study.

D. Particle Quench Tests

Particles were quenched midflight and examined under a light microscope to test for agglomeration and condensed alumina. The test was first conducted in atmospheric ambient air conditions, and particles were quenched on a glass slide.

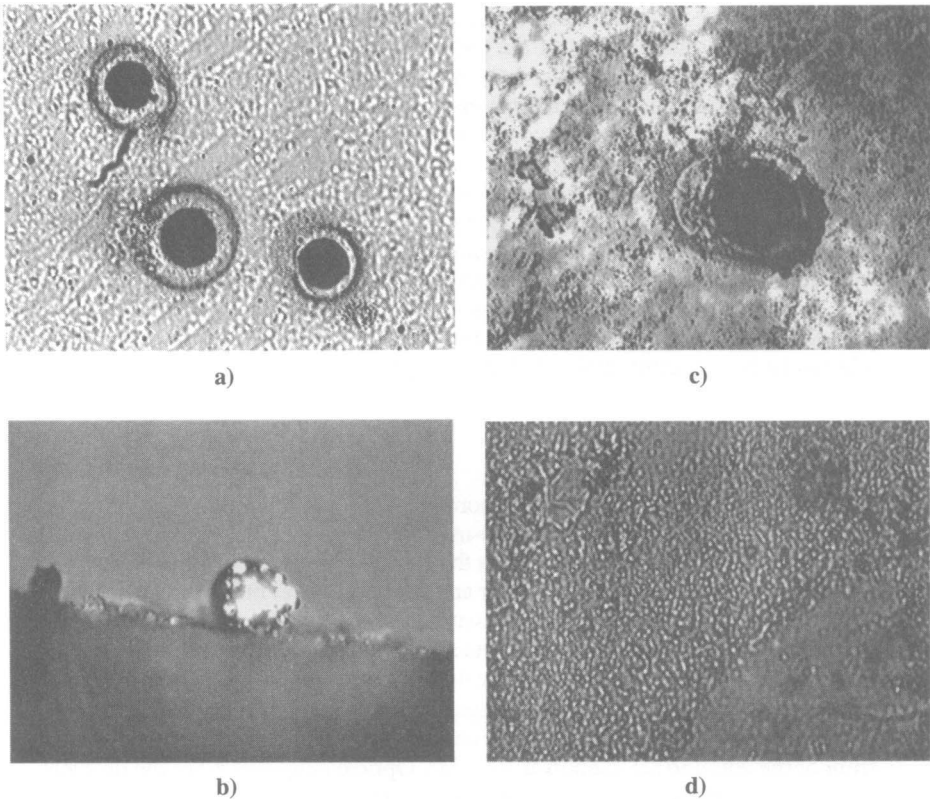


Fig. 6 Light-microscope observations of aluminum particles quenched during burning: a) particles burning in ambient air quenched on glass, $D \sim 140 \mu\text{m}$, smoke at $(r/r_s) \sim 1.6$, b) particle quenched on steel plate during experiment, $D \sim 105 \mu\text{m}$, c) magnification of particle quenched on quartz plate during experiment, $D \sim 110\text{-}\mu\text{m}$, smoke at $(r/r_s) \sim 2.3$, and d) further magnification of particle in Fig. 6c to show oxide smoke particles with $D < 1 \mu\text{m}$.

Figure 6a is a typical image with particle diameter $\sim 140 \mu\text{m}$ and condensed smoke ring at $r/r_s \sim 1.6$. The quenched particles were measured, and the number of loaded particles in an agglomerate N could then be estimated with a simple mass balance, $m_{\text{agglom}} = Nm_{\text{load}}$, resulting in $D_{\text{agglom}} = N^{1/3} D_{\text{load}}$. The majority of the quenched particles from the atmosphere tests were $140\text{--}160 \mu\text{m}$, indicating agglomerations of only 3 to 4 particles. The large quenched particles had the same spherical shape as the small particles, with similar surface roughness at the magnifications used. The ring of condensed oxide was at an average $r/r_s \sim 1.5$, with a finite thickness indicating a finite rate condensation mechanism. The condensed smoke particles typically measured less than a micrometer in diameter, although some were as large as $10 \mu\text{m}$ in size.

Quench plates were mounted inside the chamber $\sim 4 \text{ cm}$ above the aluminized propellant sample to collect particles over the entire burn history of the chamber. Particles were first quenched on a stainless steel strip, and Fig. 6b is a typical image of a $105\text{-}\mu\text{m}$ particle from the metal plate quench test during an

experiment. Most of the particles examined after metal plate quenching are less than $130\text{ }\mu\text{m}$, and the majority of the particles were less than $110\text{ }\mu\text{m}$. The few agglomerates present are typically only two particles worth of agglomeration at most, but some large particles are large enough to be collections of four particles. The reduction in agglomeration compared to the ambient air test is due to the increased propellant burning rate and shorter propellant surface residence time.⁸ Particles were quenched on a quartz slide to observe the smoke cloud, as shown in Figs. 6c and 6d, where the thick oxide ring is at $r/r_s \sim 2.3$ and the smoke particles have diameter $<1\text{ }\mu\text{m}$. For the quenching tests conducted in the chamber, the thick smoke rings had an average outer radius of $r/r_s \sim 1.8$ and smoke size of $<2\text{ }\mu\text{m}$. That quenched smoke rings are typically near $r/r_s \sim 2$ but that the experiment photographs reveal smoke clouds ranging from $r/r_s \sim 2$ – 20 indicates that hot and dense concentrations of alumina exist far away from the droplet surface.

E. Experiment Optics

The burning aluminum streaks are recorded on photographic film using a Canon Eos Rebel G 35-mm camera with a 50-mm $f/1.8$ lens. For the experiments, the largest aperture opening was used so that the camera could pick up more light from the faint droplets passing through a filter and chopper-wheel masking. The camera timing is triggered by a mechanical pressure trigger set at the experimental study pressure. A timing signal is sent to the data acquisition board from the pressure trigger to verify the camera timing. Using the timing mark, shutter delay time, and shutter speed, the pressure condition for an experimental photograph can be determined.

A Thorlabs, Inc., Model MC100 variable frequency optical chopper was mounted in front of the lens and set to chop at 1000 Hz. Optical chopping gives the droplets a streaked appearance so that droplet images can be time resolved to give both droplet velocity and diameter vs time measurements. At a typical droplet velocity of 5 m/s, the droplet tracks are spatially separated 6 mm.

The experimental data come solely from the images captured on film as the droplets burn in the chamber. This introduces a complexity into the data reduction because the captured images are not images of the burning droplets, but instead are images of their flame and condensed oxide smoke clouds. In the design of the experiment, visible spectra bandpass filters were used in front of the camera lens to limit the light observed to the wavelength for AlO emission in the blue–green spectrum. The excited AlO molecules are dropping from the second excited electronic state to the ground electronic state in $B^2\Sigma^+ \rightarrow X^2\Sigma^+$ vibrational transitions.⁷ The largest AlO intensity band is at 484-nm wavelength, where the electronic state drop occurs across the lowest vibrational level of each state.²⁹ To filter the emitted light at the large 484-nm line, a Coherent-Ealing Model 35-3474 bandpass filter, $488 \pm 8.3\text{ nm}$ bandwidth, was used in the experiments.

The second large source of visible light emission from the burning droplets results from the thermal radiation, not only of the molten aluminum droplet surface, but, more important, of the surrounding smoke cloud of condensing Al_2O_3 particles. Many researchers have discovered that thermal emission from both the molten aluminum droplets and the oxide smoke dominated or played a major role in the emitted light signal from burning droplets, causing experimental difficulty with measuring the droplet surface or AlO emissions.^{6,30–32}

To see whether the thermal radiation dominated the signal, two tests were conducted. First, a sample of the aluminized propellant was burned in ambient air

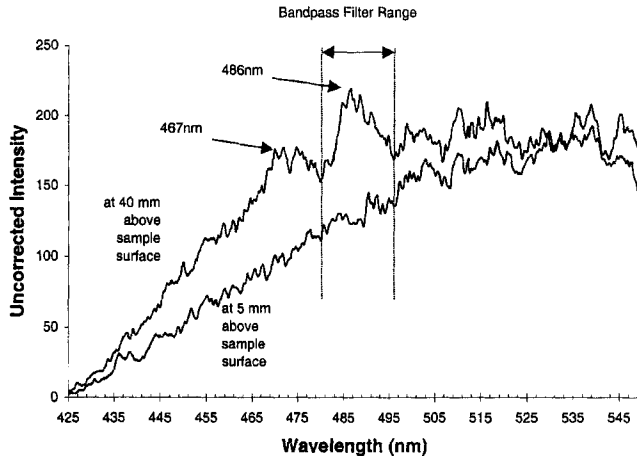


Fig. 7 Results from spectrometer test of aluminized propellant sample: the intensity is not corrected for instrument response, the positive slope of the emission follows a blackbody thermal emission profile, and even at 40 mm above the sample surface where AIO heads are visible, the curve is still dominated by the blackbody shape.

at the focus of an Instruments ISA Model HR-320 Czerny–Turner spectrometer (Fig. 7). The data presented are not corrected for instrument response. The spectrometer was focused at two locations, 5 and 40 mm above the sample surface. At the 5-mm height, the emission was totally dominated by the blackbody emission profile, and no AIO emission bands are discernable. At the 40-mm height, the AIO bands become apparent, but their intensity does not represent a large jump in emission over the broadband blackbody emission that still dominates the signal. It is assumed that the AIO emission lines are visible at the 40-mm distance away from the propellant surface because the droplets are fully ignited and the gas-phase aluminum-combustion flame is more fully developed. Although the test shows that thermal emission still dominates the emitted light, Fig. 7 shows the emission for the 486-nm AIO emission head will be captured in the range of the bandpass filter used in the experiments.

The second test conducted was to examine if a filter would pass light in a region where AIO is not supposed to be present. To get out of the range of emission heads for AIO, a 560 ± 9 nm bandpass filter was used. The image captured for the experiment is shown in Fig. 8, where the lower filter is the typical experiment filter at 490 nm and the upper filter is the 560-nm filter sandwiched with a 50% neutral density filter to compensate for the increase in thermal blackbody emission at the longer wavelength. If the emitted light was AIO dominated, there would be little if any emitted light in the upper filter. Thus, the droplet images captured in the experiments are not primarily AIO emission, but are dominated by thermal blackbody emission.

F. Oxidizer Study Control

The gas composition of the chamber was determined by the combustion products of the main solid propellant. Because of the high temperatures inside the chamber, it is assumed that the product species shift quickly to equilibrium, providing a

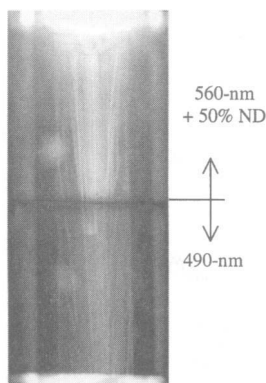


Fig. 8 Experiment with two filters at different wavelengths, showing dominance of thermal emission: the lower filter is the typical experiment filter at 490 nm where AlO bands are present, and the upper filter is a 560-nm yellow filter (where no AlO bands are present) sandwiched with a 50% neutral density filter.

near-constant composition in the upper part of the chamber where the aluminum droplets burn. The small ~ 0.1 -g aluminized propellant sample is assumed to have a negligible effect on the gas composition of the products of the large ~ 22 -g main propellant. Equilibrium concentrations for the experiment were calculated using a thermochemical equilibrium code, Propellant Evaluation Program (PEP).³³ At the baseline condition of 13 atm, the gas composition is calculated to be 40.7% H_2O , 17.6% HCl , 12.3% CO_2 , 9.7% N_2 , 9.4% CO , 4.4% H_2 , 2.1% OH , 1.9% Cl , and 0.8% O_2 . The propellant mixture yields very little excess oxygen, but ample water vapor and carbon dioxide are present for aluminum combustion.

To vary the oxidizer concentration for the experiment, oxygen gas was fed into the chamber at a known mass-flow rate that could easily be added into the PEP program for calculating the new equilibrium concentrations. The measured chamber temperature did not vary significantly with the small amount of oxygen gas added to the chamber, so the high-temperature equilibrium assumption is still valid for the calculations of gas compositions with extra oxygen. This is reinforced by calculating that inert mixing of the cooler oxygen gas would have lowered the chamber temperature to < 2000 K, which was not observed. The calculated equilibrium oxidizer concentrations as a function of oxygen flow rate metered into the chamber are presented in Fig. 9, where the dashed lines represent experimental oxygen flow rates. Note that although the oxygen concentration was varied over a range of 1–11%, the water vapor concentration only changed from 41 to 38%, a 3% difference.

III. Data Reduction Technique

A. Image Analysis

The droplet diameters were measured after scanning and filtering the raw photographs using a Nikon LS-2000 that scans directly from the photograph negative at 2700 dots per inch (dpi). A sample photograph taken of a baseline case experiment is shown in Fig. 10a. As evident in the magnified image, the actual boundary of the image is fuzzy and the background intensity makes the droplets

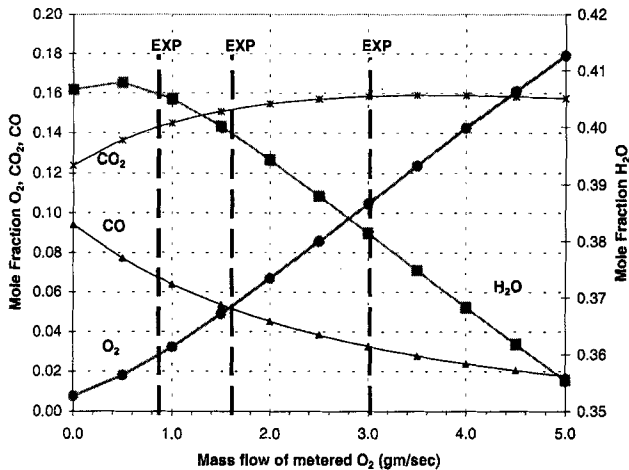


Fig. 9 Equilibrium oxidizer mole fraction concentrations as a function of oxygen flow rate metered into the chamber: concentrations are calculated using the PEP equilibrium code, assuming that the injected oxygen flow quickly reacts and shifts to equilibrium in the chamber; the dashed lines represent the different oxygen flow rates experimentally tested in addition to the baseline oxygen concentration (note that although the oxygen concentration varies over a range of 1–10%, the water vapor concentration only changed from 41 to 38%, a 3% difference).

hard to distinguish in bright regions. The unclear edge of the image makes droplet size measurement prone to user bias, and so a MATLAB[®] procedure was written to clean and contrast the images. After setting the color photos to an 8-bit grayscale, an average-intensity map was made of the image. By subtracting this average-intensity map from the original image, the clutter of background intensity is removed. The new image is then passed through a high-pass intensity filter that effectively removes the remaining noise and leaves a 1-bit intensity map of the droplets, as shown in Fig. 10b. The individual droplet images are at this point characterized by a solid-edged boundary.

To remove any user bias in the diameter measurement, a second MATLAB code automatically measures the image sizes. Because of residual noise at the image boundary, the width of the images is not constant over the length of the image. The code calculates an equivalent ellipse, and the width of the minor axis is recorded as the diameter. The procedure creates a set of diameter calculations for each time-resolved streak of a single droplet, yielding diameter as a function of elapsed time.

B. Mathematical Analysis

As stated earlier, classical fuel droplet combustion theory gives the diameter of a burning droplet as $D^n = D_0^n - kt$, where $n = 2$. By setting $D = 0$, the burn time can be defined as $t_b \equiv D_0^n/k$. The data from the current experiment are the diameter D tracked in time t . To calculate n and k , the data are curve fit in the MATLAB analysis code to a power law of the form $y = ax^b$. The diameter equation is rewritten as $D = k^{1/n}(t_b - t)^{1/n}$ in the power-law format, where $(t_b - t)$ represents the time to

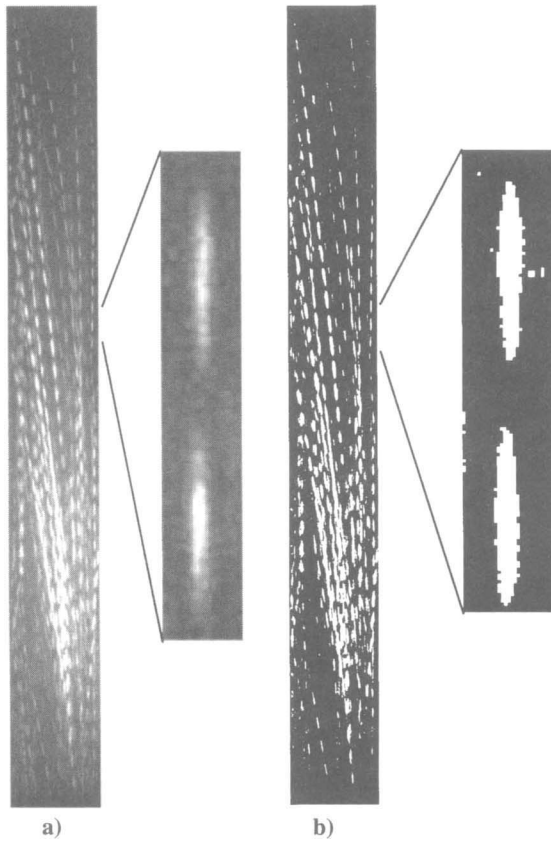


Fig. 10 Image processing technique demonstration: a) raw photo droplet images have fuzzy edges, making diameter measurements subjective to user bias; b) photo is processed in MATLAB[®] to subtract out background intensity image map, then passed through a high-pass intensity filter before the image is set to a 1-bit intensity map, from which droplet size measurements are made.

burnout. To satisfy the definition of t_b in the timescale, a valid data point requires a streak that burns out to zero diameter, eliminating many droplet streaks due to quenching on the walls or visible interference from other droplets.

Because experimental observations are only made of the flame/ smoke cloud diameter in the experiment, changes in flame radius r/r_s greatly influence the outcome of the data. Because $D_{\text{actual}} = D_{\text{image}}/(r/r_s)$, the diameter equation must be rewritten as

$$D_{\text{actual}} = k^{1/n}(t_b - t)^{1/n}$$

$$D_{\text{image}} = (r/r_s)k^{1/n}(t_b - t)^{1/n}$$

Thus the r/r_s value only affects the leading coefficient in the curve-fit form, $a = (r/r_s)k^{1/n}$ and does not affect the calculation of the n power. Accounting for r/r_s , the burning slope is calculated as $k = [a/(r/r_s)]^n$. As shown earlier, particles quenched in the chamber were measured to be in the same size range

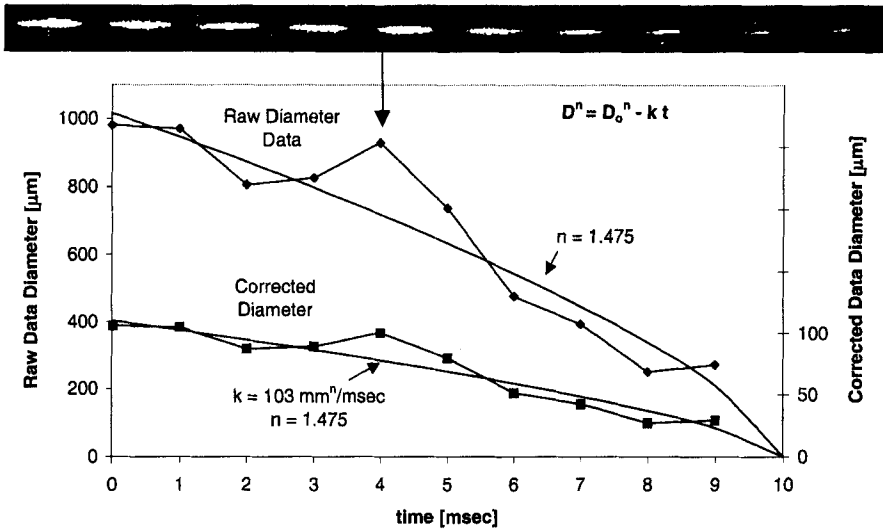


Fig. 11 Sample curve-fit data of measured diameters of a burning droplet at 13 atm: the raw data measurements are in the top curve, the bottom curve diameters have been divided by a (r/r_s) smoke cloud radius ratio of ~ 9 to give an initial streak diameter of $106 \mu\text{m}$, which matches the order of magnitude of the particles quenched in the experimental chamber (note the diameter power n is the same for both cases; it is shown mathematically that the k slope values are equivalent, off by a factor of $(r/r_s)^n$).

as the loaded aluminum. Thus, r/r_s was simply calculated by dividing the initial flame ball diameter by $106 \mu\text{m}$. The critical assumption of the data analysis is that r/r_s remains constant throughout a single droplet burn streak. Figure 11 is a sample of curve-fit data of measured diameters of a burning droplet. The raw data diameter measurements are in the top curve, and the bottom curve diameters have been divided by a (r/r_s) smoke cloud radius ratio of ~ 9 to give an initial streak diameter of $106 \mu\text{m}$. The diameter power n is the same for both cases, and the k slope values are different by a factor of $(r/r_s)^n$.

Quasi-steady models show that flame position r/r_s is a function of pressure and the oxidizer concentration in the flow.^{15,18} The radius ratio r/r_s has also been experimentally observed to be constant during droplet combustion after ignition transients.²¹ In the experiment, we assume that the pressure and oxidizer concentration of the flow are uniform through the length of the chamber, resulting in a constant r/r_s .

Some droplets exhibited a transient ignition in which the smoke cloud size increased with time for the first few milliseconds. No droplet fragmentation, jetting, or exploding was observed. In the droplet burn-time analysis, the droplets are considered noninteracting.

C. Uncertainty Analysis

Uncertainties inherent in the experiment will introduce data scatter into the calculations of r/r_s and k . In addition to the 19% scatter in the loaded aluminum size range, the possibility of two particles agglomerating introduces a 26% increase

in diameter. With no agglomeration, the measured droplets could be $D_0 = 106 \pm 20 \mu\text{m}$, and if two particles agglomerated, the diameter could be $D_0 = 134 \pm 36 \mu\text{m}$. Furthermore, the recorded size of the droplets will be larger because the camera is imaging the smoke cloud surrounding the droplet. It is assumed that variations in diameter are recognized by variations in the imaged smoke cloud diameter.

Scatter is introduced in the pressure and oxygen concentration measurements during the open time of the camera shutter. As the camera shutter is held open, typically for 33 ms, the pressure rises along the pressure ramp, introducing a pressure increase about 0.5–1 atm. Likewise, the mass flux of oxygen drops across the shutter time as the O_2 supply pressure drops by only 1–2%.

IV. Results and Discussion

A. Burn-Time Dependence on Particle Diameter

The droplets do not burn with identical burn times, so a statistical data analysis is used. The results of all experimental data were examined to determine the diameter dependence on droplet burn time because it was found that the diameter dependence of burn time was independent of pressure and oxidizer concentration. Figure 12 is a histogram of the calculated n -power values found from the curve fits for D^n for 63 droplet streaks from 11 experiments. After removing the two points around $n = 4$ as statistical outliers, the average of the data is $n_{\text{av}} = 1.65$, with a standard deviation of $\sigma = 0.55$ and median of 1.51. Double peaks exist in the data around $n = 1.1$ and 1.65. The n power was found to be independent of velocity, initial droplet size, pressure, and oxygen concentration. Therefore, the two peaks in the data distribution could be two modes of droplet combustion or an effect of the aluminum surface oxide cap, which were not characterized by the measurements made in the experiment.

For the baseline condition of 13 atm, the burn time of the burning aluminum droplets was approximated by $t_b = D_0^n / (280 \mu\text{m}^n/\text{ms})$, where $n = 1.65 \pm 0.55$. The deviation of the classical D^2 law can be expected to follow as discussed earlier.

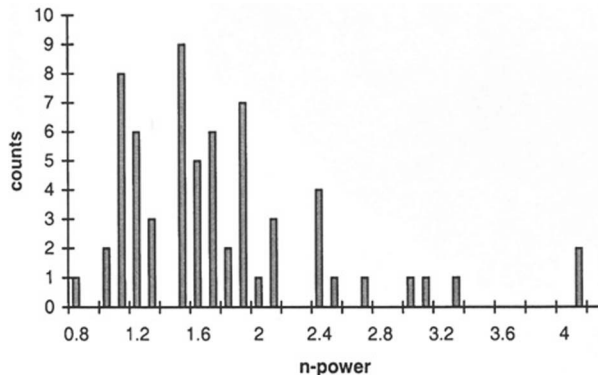


Fig. 12 Histogram of measured values of n power from the curve-fit data: note the double peak in the data around $n = 1.1$ and 1.6, after removing the two points around $n = 4$ as outliers, the average of the data is $n_{\text{avg}} = 1.65$, with a standard deviation of $\sigma = 0.55$.

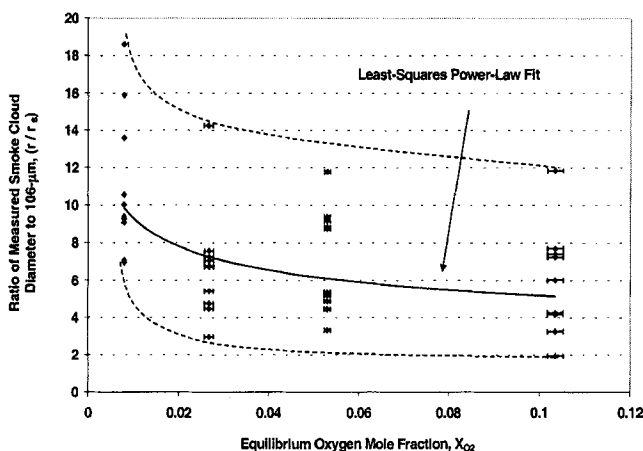


Fig. 13 Effect of equilibrium oxygen concentration at 13 atm on measured apparent smoke cloud image size to an assumed-constant droplet diameter of 106 μm ; the data scatter renders the effect inconclusive.

B. Effect of Oxidizer Concentration

The amount of oxygen gas fed into the chamber was tested at flows of 0, 0.8, 1.6, and 3 g/s, yielding oxygen mole fractions of 0.8, 2.7, 5.3, and 10.4%, calculated at thermochemical equilibrium with the propellant product gases. The addition of oxygen could impact not only the burn time, but also the flame standoff radius, as described earlier. Figure 13 presents the effect of equilibrium oxygen concentration X_{O_2} on the ratio r/r_s of apparent smoke-cloud image size to droplet size of 106 μm . A negative trend is observable through curve fitting, but the data scatter renders the effect inconclusive. Figure 14 plots the effect of calculated equilibrium oxygen mole fraction X_{O_2} on burning rate slope, k -($\mu\text{m}^n/\text{ms}$), from the equation $D^n = D_0^n - kt$. The slope was calculated using the average n power of $n = 1.65$ for all of the data points to normalize the units. Again, the trend is considered negligible given the data scatter.

The lack of an identifiable dependence of X_{O_2} is evidence that oxygen is not the chief oxidizer for aluminum combustion in solid-propellant combustion product gases. As stated earlier, at the baseline condition of 13 atm, the oxidizer components are 41% H_2O , 12% CO_2 , and only <1% O_2 . There is also a concentration of 18% HCl . As shown in Fig. 9, although the oxygen concentration varies over a range of 1–10%, the water vapor concentration only changes from 41 to 38%.

The gas-phase aluminum-combustion mechanism is considered diffusion controlled because of the fast reaction rates at the high temperatures. Using the CHEMKIN transport code³⁴ programmed for the chamber conditions and gas composition (without aluminum combustion products), the mixture-averaged diffusion coefficients for the oxidizers were calculated. As shown in Table 1, the diffusion coefficients for the three oxidizers are the same order of magnitude. Assuming all of the oxidizers are consumed at the flame front and decrease linearly to zero across 10–2 flame radii, the diffusion rates are estimated with the molar diffusive flux, $N''_{\text{diff-ox}} = c_{\text{mix}} \mathcal{D}_{\text{ox-mix}} \Delta X_{\text{ox}} / (8r_s)$, and the results are presented in

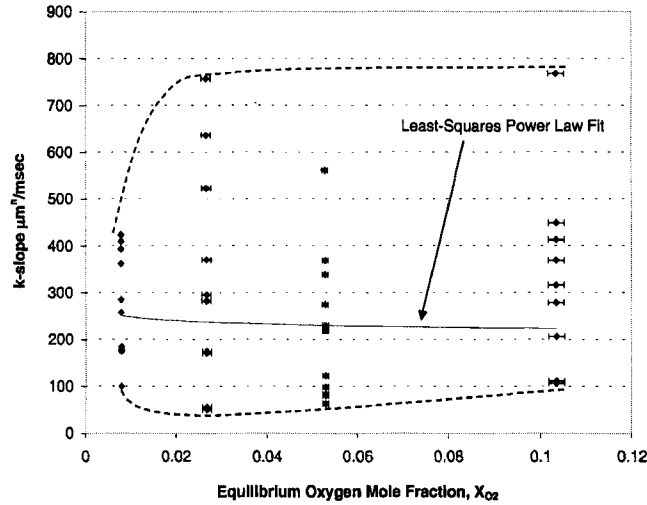


Fig. 14 At 13 atm, effect of equilibrium oxygen mole fraction X_{O_2} on measured burning-rate slope, k -($\mu\text{m}^2/\text{ms}$), from the equation $D^n = D_0^n - kt$; the slope was calculated using the average n power of $n = 1.65$, and the trend is considered negligible given the data scatter.

Table 1. Water diffuses two orders of magnitude and CO_2 one order of magnitude faster than oxygen.

Because the diffusion coefficients for the oxidizers are on the same order of magnitude, reaction rates are also compared. When investigating reaction kinetics, several reaction mechanisms must be considered for the aluminum-combustion reaction because O_2 , CO_2 , H_2O , and even HCl can contribute to the combustion of $\text{Al}(\text{g})$. Table 2 lists second-order reaction rates.³⁵

Although the temperature ranges of most of the reaction rates are lower than the aluminum flame temperature, the rates will be used here for comparison purposes. Evaluated at 3800 K, the H_2O and CO_2 combustion rates are an order of magnitude larger than the O_2 rate, which is two orders of magnitude faster than the HCl rate (Table 3). Similar results were obtained by using reaction rates used by Widener et al.⁹ By describing the combustion of $\text{Al}(\text{g})$ by the forward reactions only, the contribution of the individual reactions can be compared by the product of the

Table 1 Equilibrium oxidizer mole fractions X_{ox} , CHEMKIN calculated mixture-averaged diffusion coefficients $\mathcal{D}_{\text{ox-mix}}$ (without Al combustion products) and estimated molar diffusion flux $N''_{\text{diff-ox}}$

Oxidizer	Equilibrium X_{ox} , %	$\mathcal{D}_{\text{ox-mix}}$, cm^2/s	$N''_{\text{diff-ox}}$, $\text{mol}/\text{cm}^2\text{-s}$
H_2O	41	0.8	5×10^{-4}
CO_2	12	0.4	8×10^{-5}
O_2	0.8	0.6	7×10^{-6}

Table 2 Second-order aluminum combustion reactions from NIST database³⁵

<i>ki</i> (Reference)	Reaction	Rate, cm ³ /mol-s	Data temperature range, K
<i>k1</i> (37)	Al(g) + H ₂ O(g) → AlO + H ₂	60.5 T ^{3.59} exp(525 K/T)	298–1174
<i>k2</i> (38)	Al(g) + CO ₂ → AlO + CO	6.75 × 10 ¹⁵ exp(−10689 K/T)	1500–1880
<i>k3</i> (39)	Al(g) + O ₂ → AlO + O	2 × 10 ¹³	300–2000
<i>k4</i> (40)	Al(g) + HCl → AlCl + H	3.3 × 10 ¹¹ exp(−3925 K/T)	1000–4000

reaction rate by the oxidizer, $ki \cdot [X_{ox,i}]$:

$$\frac{d[Al]}{dt} = -k1[Al][O_2] - k2[Al][CO_2] - k3[Al][H_2O] - k4[Al][HCl]$$

Figure 15 is a plot that compares these reaction contributions to the aluminum combustion where the molar concentrations are calculated at 13-atm pressure. As shown in Table 3, the H₂O and CO₂ contributions are two to three orders of magnitude faster than the oxygen contribution at 3800 K, and the HCl contribution is an order of magnitude less than the O₂ rate.

The heats of combustion for the three main oxidizers at 3800 K are calculated using the JANAF tables³⁶ to be $\Delta h_{c,1} = -3.071$ kJ/mol_{Al} for *k1* (H₂O), $\Delta h_{c,2} = -17.649$ kJ/mol_{Al} for *k2* (CO₂), and $\Delta h_{c,3} = 492.09$ kJ/mol_{Al} for *k3* (O₂). Thus, the water vapor and carbon dioxide reactions are slightly endothermic, and the oxygen reaction is the exothermic reaction that supplies heat. If one mole of aluminum reacts with one mole of the oxidizer mix consisting of 1 part O₂, 15 parts CO₂, and 51 parts H₂O, then *k3* (O₂) would supply 7.38 kJ of heat, *k1* (H₂O) would require 2.34 kJ, and *k2* (CO₂) would require 3.94 kJ.

C. Effect of Pressure

The camera shutter was triggered to image data at chamber pressures of 13, 17, 19, and 22 atm. Although the high-pressure data were collected at the end of the propellant burn as shown in Fig. 3, there should be no significant change in propellant composition at the end of the burn. In addition, thermocouple measurements do not show a significant temperature change for the chamber throughout the propellant burn. As with the oxygen addition tests, the change in pressure could alter both the burn time and the flame/smoke cloud standoff radius. Figure 16 presents the effect of chamber pressure on the radius ratio r/r_s of the apparent smoke-cloud image size to droplet diameter of 106 μm. A power-law curve fit demonstrates

Table 3 NIST reaction rates at 3800 K and contribution to aluminum combustion at 13 atm

Reaction	Rate, cm ³ /mol-s	$ki \cdot [X_{ox,i}]$, 1/s
<i>k1</i> (H ₂ O)	5 × 10 ¹⁴	8 × 10 ¹⁵
<i>k2</i> (CO ₂)	4 × 10 ¹⁴	2 × 10 ¹⁵
<i>k3</i> (O ₂)	2 × 10 ¹³	7 × 10 ¹²
<i>k4</i> (HCl)	1 × 10 ¹¹	9 × 10 ¹¹

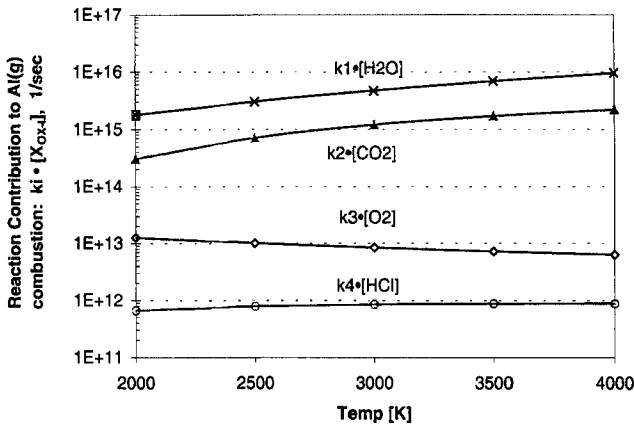


Fig. 15 Reaction contribution to aluminum combustion vs temperature: the reactions are referenced in the NIST database³⁵ and the molar concentrations are at chamber baseline conditions of 13 atm. Note that the water H₂O and CO₂ contributions are two to three orders of magnitude faster than the oxygen contribution at 3800 K.

that $(r/r_s) \propto p^{-2.3}$, that is, that the image size of the apparent smoke cloud shrinks with increasing pressure.

Figure 17 plots the effect of chamber pressure on burning-rate slope, k -($\mu\text{m}^n/\text{ms}$), from the equation $D^n = D_0^n - kt$. The slope was again calculated using the average n power of $n = 1.65$ for all the data points to normalize the units. The curve-fit shows a trend where $k \propto p^{0.98}$ (i.e., the burning rate increases linearly with pressure over the experimental pressure range), which is a larger effect than reported in past literature. The classical formula for burn-rate, or evaporation constant, is $k = 8\rho D_f / \rho_l \cdot \ln(1 + B)$, where $B = (Y_{f-s} - Y_{f-\infty}) / (1 - Y_{f-s})$, the

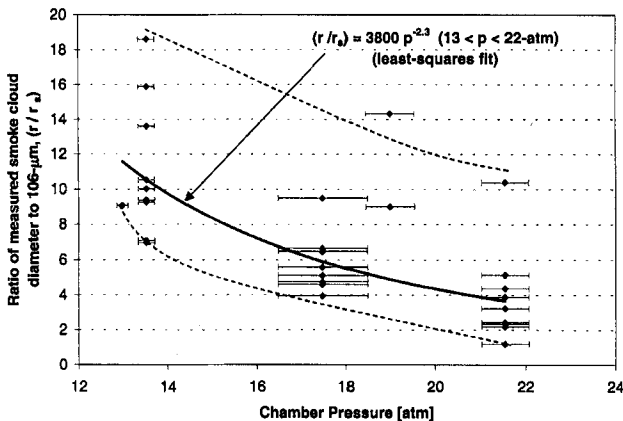


Fig. 16 Effect of chamber pressure on measured smoke cloud size to 106 μm , (r/r_s) : an effect is demonstrated with the curve fit that $(r/r_s) \propto p^{-2.3}$, that is, the image size shrinks with increasing pressure, over the range $13 < p < 22$ atm.

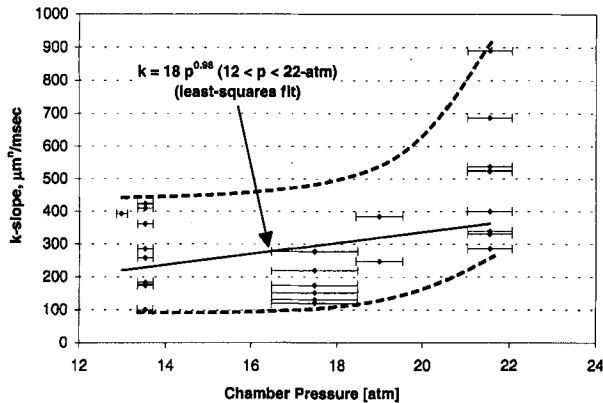


Fig. 17 Effect of chamber pressure on measured burning rate slope, k ($\mu\text{m}^7/\text{ms}$), in the equation $D^n = D_0^n - kt$; the slope was calculated using the average n -power of $n = 1.65$, and the least-squares curve fit shows a trend where $k \propto p^{0.98}$, that is, where the burning rate increases linearly with pressure over the experimental pressure range.

Spalding transfer number of fuel mass fraction.¹⁸ In this classical model, the pressure linearly affects the burning rate through the gas density, $\rho = p/RT$. Typically, the fuel diffusion coefficient is considered inversely proportional to pressure, which would effectively reduce the effect of pressure on burn rate. However, such an effect is not observed here, indicating the gaseous medium transport properties are more important. The cause of this observation is not well understood. Kudryavtsev et al. proposed that the presence of the submicrometer Al_2O_3 on both sides of the flame front interferes with the diffusion of both fuel and oxidizing species at low pressure.¹⁶ Thus, at lower pressures, the diffusion coefficient is lower than expected, but this effect is reduced with increasing pressure, making the diffusion coefficient resemble the expected value at higher pressure. A possible net effect is a diffusion coefficient that appears pressure independent.

V. Conclusions

The combustion behavior of aluminum droplets was studied in a solid-rocket chamber flowfield. Rocket motor chamber conditions were generated directly from the product flow of an AP/HTPB solid propellant. The aluminum droplets were born from a second aluminized solid-propellant sample loaded with $106\text{-}\mu\text{m}$ particles. Chamber conditions were controlled to study aluminum combustion as a function of pressure and oxygen concentration. The experimental test conditions were 13–22 atm pressure and $\sim 2300\text{ K}$ temperature.

Droplets were tracked with an open-shutter 35-mm camera using a narrow band filter and 1-kHz chopper wheel. It was experimentally determined that the thermal emission from the hot oxide smoke particles dominates the emitted light of the burning droplets, instead of excited AlO emission. Burning droplets were quenched in the chamber and found to be typically the same size as the loaded aluminum particles, with thick smoke rings at $r/r_s \sim 2$ and oxide particles $< 2\text{ }\mu\text{m}$ in diameter. Because the data images were considerably larger, $r/r_s \sim 2\text{--}20$, the alumina

concentration must be hot and dense far away from the droplet surface. This apparent smoke size ratio experimentally varies with pressure by $(r/r_s) \propto p^{-2.3}$, but varies weakly with oxygen concentration.

The data show that the diameter dependence on burn time does not strictly follow the classically predicted D^2 , but instead follows D^n , where n is found to be 1.65 ± 0.55 . The burning rate slope k defined in the equation $D^n = D_0^n - kt$, is found to vary little with oxygen concentration, but does increase with pressure over the range of study. The weak dependence of k with oxygen concentration indicates that oxygen is not the primary oxidizer for aluminum combustion in solid-propellant combustion products. This is supported by calculations of reaction rates for H_2O , CO_2 , and O_2 . This contradicts recent literature that shows O_2 as the strongest oxidizer.^{5,6,27} The water vapor and carbon dioxide concentrations and reaction rates are much larger than the corresponding oxygen values. Last, the measured effect of pressure on burn time follows the classical prediction of the linear pressure effect on gas density, indicating the dominance of the gas flow state properties.

In future studies, instrumentation will be developed to allow direct droplet diameter measurement to eliminate error introduced in the current technique of measuring the smoke cloud. Possible techniques are shadowgraph imaging, absorption, and laser-induced fluorescence. Additional experiments should also be conducted with elevated pressures and varying levels of water vapor and CO_2 in the chamber to verify the current conclusions. Finally, the combustion of agglomerated particles should be studied because aluminum particles in real rocket motors typically agglomerate at the propellant surface. The composite nature of the agglomerations introduces complex combustion irregularities such as fissuring and fragmenting.

Acknowledgments

This work was funded by the Ballistic Missile Defense Organization through the Office of Naval Research, Contract N00014-95-1-1339, and is part of the University of Illinois at Urbana-Champaign (UIUC) Multi-Disciplinary University Research Initiative. The program director is J. Goldwasser. SEM images were made with J. Mabon in the Center for Microanalysis of Materials, UIUC, which is supported by the U.S. Department of Energy under Grant DEFG02-91-ER45439. R. Geisler of Geisler Enterprises and T. Parr of China Lake Naval Weapons Center provided technical discussions, and C. Campbell of the Thiokol Corp. provided the formulation of solid rocket propellants used in the experiments. The chamber apparatus was designed and assembled by D. Schneider. Graduate Students J. Murphy and M. Spalding contributed to the data analysis. Undergraduates J. Brzozowski, J. Lim, and M. Abogado assisted in the laboratory experiments.

References

- ¹Pokhil, P. F., Belyayev, A. F., Frolov, Y. V., Logachev, V. S., and Korotkov, A. I., "Combustion of Powdered Metal in Active Media," Rept. FTD-MT-24-551-73, Foreign Technology Div., Wright-Patterson AFB, OH, 1972.
- ²Price, E. W., "Combustion of Metalized Propellants," *Fundamentals of Solid-Propellant Combustion*, edited by K. Kuo and M. Summerfield, Progress in Aeronautics and Astronautics, Vol. 90, AIAA, New York, 1984, pp. 479-513.

³Povinelli, L. A., and Rosenstein, R. A., "Alumina Size Distributions from High-Pressure Composite Solid-Propellant Combustion," *AIAA Journal*, Vol. 2, No. 10, 1964, pp. 1754–1760.

⁴Price, E. W., "Comments on 'Role of Aluminum in Suppressing Instability in Solid Propellant Motors,'" *AIAA Journal*, Vol. 9, No. 5, 1971, pp. 987–990.

⁵Brooks, K. P., and Beckstead, M. W., "Dynamics of Aluminum Combustion," *Journal of Propulsion and Power*, Vol. 11, No. 4, 1995, pp. 769–780.

⁶Olsen, S. E., and Beckstead, M. W., "Burn Time Measurements of Single Aluminum Particles in Steam and CO₂ Mixtures," *Journal of Propulsion and Power*, Vol. 12, No. 4, 1996, pp. 662–671.

⁷Bucher, P., Yetter, R. A., Dryer, F. L., Parr, T. P., Hanson-Parr, D. M., and Vicenzi, E. P., "Flame Structure Measurement of Single Isolated Aluminum Particles Burning in Air," *Twenty-Sixth Symposium (International) on Combustion*, Combustion Inst., Pittsburgh, PA, 1996, pp. 1899–1908.

⁸Gany, A., and Caveny, L. H., "Agglomeration and Ignition Mechanism of Aluminum Particles in Solid Propellants," *Seventeenth Symposium (International) on Combustion*, Combustion Inst., Pittsburgh, PA, 1978, pp. 1453–1461.

⁹Widener, J. F., Liang, Y., and Beckstead, M. W., "Aluminum Combustion in Solid Propellant Environments," 35th JANNAF Meeting, Chemical Propulsion Information Agency, Columbia, MD, 1998.

¹⁰Liang, Y., and Beckstead, M. W., "Numerical Simulation of Unsteady, Single Aluminum Particle Combustion in Air," AIAA Paper 98-3825, June 1998.

¹¹Daniel, E., Basset, T., and Loraud, J. C., "Eularian Approach for Unsteady Two-Phase Reactive Solid Rocket Motor Flows Loaded with Aluminum Particles," AIAA Paper 98-3697, June 1998.

¹²Bucher, P., Yetter, R. A., Dryer, F. L., Parr, T. P., and Hanson-Parr, D. M., "PLIF Species and Ratiometric Temperature Measurements of Aluminum Particle Combustion in O₂, CO₂, and N₂O Oxidizers, and Comparisons with Model Calculations," *Twenty-Seventh Symposium (International) on Combustion*, Vol. 2, Combustion Inst., Pittsburgh, PA, 1998, pp. 2421–2429.

¹³Brzustowski, T. A., and Glassman, I., "Vapor-Phase Diffusion Flames in the Combustion of Magnesium and Aluminum: I. Analytical Developments," *Heterogeneous Combustion*, edited by H. G. Wolfhard, I. Glassman, and L. Green, Progress in Astronautics and Aeronautics, Vol. 15, Academic Press, New York, 1964, pp. 75–115.

¹⁴Frolov, Y. V., Pokhil, P. F., and Logachev, V. S., "Ignition and Combustion of Powdered Aluminum in High-Temperature Gaseous Media and in a Composition of Heterogeneous Condensed Systems," *Combustion, Explosion, and Shock Waves*, Vol. 8, No. 2, 1972, pp. 168–187.

¹⁵Law, C. K., "A Simplified Theoretical Model for the Vapor-Phase Combustion of Metal Particles," *Combustion Science and Technology*, Vol. 7, No. 5, 1973, pp. 197–212.

¹⁶Kudryavtsev, V. M., Sukhov, A. V., Voronetskii, A. V., and Shpara, A. P., "High-Pressure Combustion of Metals (Three-Zone Model)," *Combustion, Explosion, and Shock Waves*, Vol. 15, No. 6, 1979, pp. 731–737.

¹⁷Grigor'ev, V. G., Zarko, V. E., and Kutsenogii, K. P., "Experimental Investigation of the Agglomeration of Aluminum Particles in Burning Condensed Systems," *Combustion, Explosion, and Shock Waves*, Vol. 17, No. 3, 1981, pp. 245–250.

¹⁸Kuo, K. K., *Principles of Combustion*, Wiley, New York, 1986, pp. 371–397.

¹⁹Belyaev, A. F., Frolov, Y. V., and Korotkov, A. I., "Combustion and Ignition of Particles of Finely Dispersed Aluminum," *Combustion, Explosion, and Shock Waves*, Vol. 4, No. 4, pp. 182–185.

²⁰Friedman, R., and Macek, A., "Ignition and Combustion of Aluminum Particles in Hot Ambient Gases," *Combustion and Flame*, Vol. 6, No. 1, 1962, pp. 9–19.

²¹Wilson, R. F., and Williams, F. A., "Experimental Study of the Combustion of Single Aluminum Particles in O₂/Ar," *Thirteenth Symposium (International) on Combustion*, Combustion Inst., Pittsburgh, PA, 1971, pp. 833–845.

²²Davis, A., "Solid Propellants: The Combustion of Particles of Metal Ingredients," *Combustion and Flame*, Vol. 7, No. 4, 1963, pp. 359–367.

²³Hartman, K. O., "Ignition and Combustion of Aluminum Particles in Propellant Flame Gases," *8th JANNAF Combustion Meeting*, Vol. 1, Chemical Propulsion Information Agency, Laurel, MD, 1971, pp. 1–24.

²⁴Turns, S. R., Wong, S. C., and Ryba, E., "Combustion of Aluminum-Based Slurry Agglomerates," *Combustion Science and Technology*, Vol. 54, 1987, pp. 299–318.

²⁵King, M. K., "Modeling of Single Particle Aluminum Combustion in CO₂–N₂ Atmospheres," *Seventeenth Symposium (International) on Combustion*, Combustion Inst., Pittsburgh, PA, 1977, pp. 1317–1328.

²⁶Foelsche, R. O., Burton, R. L., and Krier, H., "Ignition and Combustion of Aluminum Particles in H₂/O₂/N₂ Combustion Products," *Journal of Propulsion and Power*, Vol. 14, No. 6, 1998, pp. 1001–1008.

²⁷Widener, J. F., and Beckstead, M. W., "Aluminum Combustion Modeling in Solid Propellant Combustion Products," AIAA Paper 98-3824, June 1998.

²⁸Zanotti, C., Volpi, A., Bianchessi, M., and De Luca, L., "Measuring Thermodynamic Properties of Burning Propellants," *Nonsteady Burning and Combustion Stability of Solid Propellants*, edited by L. De Luca, E. W. Price, and M. Summerfield, Progress in Aeronautics and Astronautics, Vol. 143, AIAA, Washington, DC, 1992, pp. 145–196.

²⁹Pearse, R. W. B., and Gaydon, A. G., *The Identification of Molecular Spectra*, Wiley, New York, 1976, pp. 41–42.

³⁰Tokui, H., and Iwama, A., "X-Ray Microanalysis on the Surface and Cross-Section of Burning-Interrupted Aluminum Particle and Foil in High Pressure Atmospheres," *Propellants, Explosives, Pyrotechnics*, Vol. 14, No. 4, 1989, pp. 127–132.

³¹Foote, J. P., Lineberry, J. T., Thompson, B. R., and Winkleman, B. C., "Investigation of Aluminum Particle Combustion for Underwater Propulsion Applications," AIAA Paper 96-3086, June 1996.

³²Brewster, M. Q., and Taylor, D. M., "Radiative Properties of Burning Aluminum Droplets," *Combustion and Flame*, Vol. 72, No. 3, 1988, pp. 287–299.

³³Cruise, D. R., "Theoretical Computations of Equilibrium Compositions, Thermodynamic Properties," Naval Weapons Center, TP-6037, China Lake, CA, 1979.

³⁴Kee, R. J., Dixon-Lewis, G. D., Warnatz, J., Coltrin, M. E., Miller, J. A., and Moffat, H. K., "A FORTRAN Computer Code Package for the Evaluation of Gas-Phase, Multi-Component Transport Properties," *The CHEMKIN Collection III, Transport, Reaction Design*, San Diego, CA, 1998.

³⁵Mallard, W. G., Westley, F., Herron, J. T., and Hampson, R. F., *NIST Chemical Kinetics Database—Version 6.0*, NIST Standard Reference Data, Gaithersburg, MD, 1994.

³⁶Chase, M. W., Davies, C. A., Downey, J. R., Frurip, D. J., McDonald, R. A., and Syverud, A. N., "JANAF Thermochemical Tables, Third Edition, Part I, Al-Co," *Journal of Physical and Chemical Reference Data*, Vol. 14, Supplement 1, 1985, pp. 65, 66.

³⁷McClean, R. E., Nelson, H. H., and Campbell, M. L., "Kinetics of the Reaction $\text{Al}(\text{2PO}) + \text{H}_2\text{O}$ over an Extended Temperature Range," *Journal of Physical Chemistry*, Vol. 97, No. 38, 1993, pp. 9673–9676.

³⁸Fontijn, A., and Felder, W., "HTFFR Kinetics Studies, of $\text{Al} + \text{CO}_2 \rightarrow \text{AlO} + \text{CO}$ from 300 to 1900 K, a Non-Arrhenius Reaction," *Journal of Chemical Physics*, Vol. 67, No. 4, 1977, p. 1561.

³⁹Cohen, N., and Westberg, K. R., "Chemical Kinetic Data Sheets for High-Temperature Chemical Reactions," *Journal of Physical and Chemical Reference Data*, Vol. 12, No. 3, 1983, p. 531.

⁴⁰Mayer, S. W., Shieler, L., and Johnston, H. S., "Computation of High-Temperature Rate Constants for Bimolecular Reactions of Combustion Products," *Eleventh Symposium (International) on Combustion*, Combustion Inst., Pittsburgh, PA, 1967, pp. 837–844.

Formation of Condensed Combustion Products at the Burning Surface of Solid Rocket Propellant

V. A. Babuk,* V. A. Vassiliev,[†] and V. V. Sviridov[†]
Baltic State Technical University, Saint Petersburg, Russia

Nomenclature

D	= diameter of agglomerate
d	= diameter of smoke oxide particle
D_{43}	= mass-medium diameter of agglomerates
D_{43}^{AP}	= mass-medium diameter of AP particles
d_{43}	= mass-medium diameter of smoke oxide particles
F	= force
$f_m(D)$	= mass function of agglomerate size distribution density
$f_m(d)$	= mass function of smoke oxide particle size distribution density
P	= pressure
T	= temperature
T_L	= luminance temperature
X	= distance from propellant burning surface
Z_m	= share of unburned metal in agglomerates relative to the original aluminum in the propellant
Z_m^a	= share of original metal in the propellant used to form the agglomerates as a whole
Z_m^{ox}	= share of original metal in the propellant used to form oxide in the agglomerates
η	= mass share of oxide in agglomerates
τ	= time

Copyright © 2000 by the American Institute of Aeronautics and Astronautics, Inc. All rights reserved.

*Professor, Aerospace Division, Dept. of Space Vehicles and Rocket Motors.

[†]Associate Professor, Aerospace Division, Dept. of Space Vehicles and Rocket Motors.

I. Introduction

AN INDISPENSABLE component of a high-energy solid rocket propellant (SRP) is a metal fuel (MF) such as aluminum. An obvious result of the presence of aluminum in a propellant is the formation of condensed combustion products (CCP). This causes a number of essential problems in the functioning of solid propellant motors. A large amount of CCP can deposit on motor parts, which, in turn, leads to slag formation, an increase in rocket mass, and a decrease in rocket range. The presence of CCP in propellant combustion products can also damage motor parts and reduces the specific impulse value. At present, it is commonly acknowledged that the CCP of aluminized solid rocket propellants, even close to the burning propellant surface, consist of agglomerates and smoke oxide particles (SOP). While the size of agglomerates may reach hundreds and even thousands of micrometers, the SOP sizes are of the order of $1\text{ }\mu\text{m}$. Agglomerates resulting from the coalescence of aluminum particles in the propellant surface layer may include aluminum oxide and other condensed products (such as binder residues). The CCP formation in the motor chamber comprises a number of stages. The first stage is the CCP formation at the propellant burning surface. This is the process directly connected with propellant combustion. The key role here is played by agglomeration.

This chapter surveys the authors' previous experimental studies on SRP combustion that consider CCP formation at the propellant burning surface. The paper presents data on experimental techniques and experimentally registered regularities and formulates general physical ideas concerning the CCP formation process. Propellants used in the studies had different compositions, with various types and percentages of components. Granular ingredients were of different particle sizes. In most studies, the aluminum content was in the range of 20–26%.

II. Experimental Technique

The experimental studies were aimed at obtaining information on both micro- and macroscopic regularities in CCP formation. Microscopic regularities are understood as regularities that determine the nature of particle formation, while macroscopic regularities are those that establish the relationship between particle characteristics and propellant compositions as well as their combustion conditions. A set of techniques has been developed to solve the stated problems.

A. Visualization of the Combustion Zone and Temperature Measurements

Visualization of the propellant burning zone was carried out using video recording under natural illumination.^{1,2} The propellant burning surface and the above-surface zone of the gas phase were studied using a high-speed SKS-1M (Russian-made) movie camera. The framing rate varied from 1000 to 4000 frames/s, and the optical system provided for a magnification of 1.5 to 4.5. For the visualization studies, the propellant specimens were burned in a constant-pressure bomb as shown in Fig. 1. The use of inert gas allows us to maintain the desired pressures and to maintain optical transparency. The propellant specimen was cut at a 45 deg angle from the side, facing the camera. To measure the temperature of particles within the observed combustion zone, a video pyrometer was constructed based on the SKS-1M movie camera. Temperatures were taken by the luminance method with photometric registration. The method is simple and highly illustrative, as

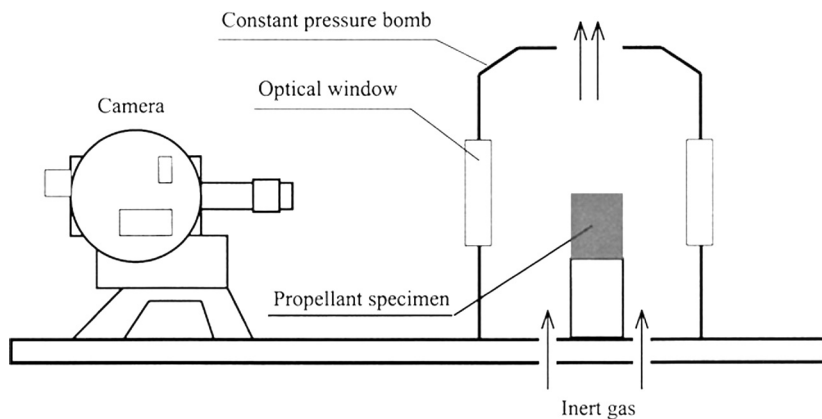


Fig. 1 Experimental setup for visualization studies.

measurement is simultaneous with the visualization of a radiating object. To measure the temperature of an object, its image on the film is used. Using this approach, temperatures of different parts of the object may be measured. In addition, a color spectral pyrometer was constructed for the purpose of measuring temperatures.³ It is a spectrograph with two radiation receivers (germanium photodiodes capable of receiving radiation in two spectral bands) mounted on the focal plane of the spectrograph. The band width is determined by the size of a photodiode light-sensitive area and the spectrograph magnification power. The photodiodes are capable of moving on the focal plane, which ensures the selection of any desirable spectral bands within the spectrograph range. The selected spectral bands were in the visible band, with effective wavelengths of 0.75 and 0.63 μm . Signals from the photodiodes were amplified and then recorded.

The spectrograph inlet tube was equipped with a horizontal slot in addition to an available vertical slot. During the experiments, the flame is projected on the spectrograph slots, and as the burning surface moves, the radiation from all flame zones, beginning with the burning surface, is continuously recorded. The recorded radiation, and consequently the temperature, is averaged for the area cut off by the slots. The vertical slot was 200–300 μm long, and the horizontal slot was 50–100 μm . The dimensions of the slots are smaller than the distances between agglomerates in the gas phase, so that the pyrometer provides measurements of temperature profiles in the gas phase at the propellant burning surface. The pyrometer was also used to measure the temperature of agglomerating particles on the propellant burning surface. Results of the spectral study confirm that the color temperature values of the objects under study are close to the actual values.

B. Surface Layer Study

The surface layer is understood as a three-dimensional area of condensed phase, which is adjacent to the interface between the condensed and the gas phases. Within the surface layer, processes determining the properties of the CCP supplied to the gas phase take place. To understand the nature of these processes, it is vital to know the morphological, chemical, and other properties of the surface layer. One possible method of studying the surface layer is propellant quenching, along

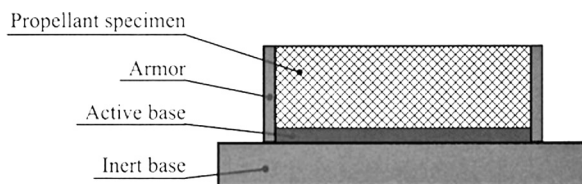


Fig. 2 Propellant specimen on an active base.

with subsequent study of the combustion residues. This method provides a wide range of surface layer characteristics. All quenching methods are based on creating conditions for upsetting the thermal mode of combustion. The most widely used methods are 1) pressure drop and 2) thermal quenching through bases possessing a high heat conductivity.^{4,5} These methods, however, appear to be problematic. A pressure drop causes a sharp increase in the rate of gaseous products leaving the propellant burning surface (through the surface layer). This causes distortion of the surface layer structure due to the increased aerodynamic force and, as a result, removal of agglomerating particles from the burning surface. It is worth noting that agglomerating particles have never been registered on a propellant surface quenched by the pressure-drop method. The second method does not suffer from this problem and is widely used in studies of double-base propellant surface layers.⁶ There is, however, a wide range of high-energy propellants that cannot be quenched with bases having high thermal conductivities.

Two different approaches have therefore been developed.^{1,7} The first is based on the use of active bases (Fig. 2). The active base is made of a substance with a decomposition temperature close to the onset temperature of the binder gasification, and its decomposition products are practically inert to the propellant combustion products. The listed requirements are met largely by ammonium-containing substances, in particular, ammonium carbonate, ammonium oxalate, and others. These substances have comparatively low decomposition temperatures (80–120°C) and a highly endothermic effect and are distinguished by extensive release of gaseous NH_3 . Propellant combustion ceases on the active bases in the following way. When the combustion wave comes to the interface between the propellant and the base, heat is removed from the combustion zone to the base material. An intensive gasification of the base material leads to forced filtration of low-temperature products through pores in the condensed-phase reaction zone and, consequently, to a disturbance of the combustion thermal profile and resultant propellant quenching. After each experiment, a layer of the undecomposed binder with metal and oxide inside remains on the base. The experimental results on propellant specimen combustion with active bases in constant-pressure bombs confirm the reliability of quenching.

The second approach is based on the following considerations. The results of temperature measurements² suggest that there are burning metal particles on the propellant surface. The temperature of those particles is considerably higher than the environmental temperature. Consequently, the surface layer should contain heat-resistant structural elements, which can be decomposed (gasified) only under the effect of a high-temperature active gas flow of the propellant combustion products. After the combustion is completed, there must remain residues representing the upper portion of the surface layer. If these residues are preserved intact, then it is possible to study the surface layer properties. This approach was realized with

the help of inert bases in the following way. The propellant specimen was pressed onto a flat base to ensure good contact of the specimen with the base. Combustion was carried out in a constant-pressure bomb with an inert-gas environment. After the propellant combustion was completed, the surface layer residues remained on the base and were studied afterward.

During the interaction of the combustion wave and inert base, the parameters of the wave underwent some changes. This behavior can also influence the properties of the surface layer. To evaluate the significance of this phenomenon, experiments were carried out with various types of base materials, e.g., copper, quartz glass, and composite materials, which differed considerably in their thermophysical characteristics. The experimental data showed an insignificant effect of the base material type on the residue properties. This result is apparently a consequence of a comparatively high lag of the processes governing the structure of the upper portion of the surface layer. The quenched products and the combustion residues obtained using the active and inert bases were comprehensively studied. Chemical composition parameters and geometric dimensions of the surface layer were determined. Qualitative characteristics of the surface layer structure were studied using an optical microscope. The parameters of the surface layers were found to be approximately the same for both approaches. We consider this fact as clear evidence of reliability of the experimental data obtained.

C. Propellant Structure Study

The propellant structure is understood as a three-dimensional configuration resulting from the presence of the oxidizer powder. The oxidizer particle properties, as well as the structural formations ("pockets" and "interpocket bridges") formed by the oxidizer particles, were carefully investigated by various researchers.⁸⁻¹¹ The general concept of the pocket appeared in the work of Price and Crump⁸⁻¹⁰ in the mid-1960s. For mathematical modeling, the pocket concept was first used in the studies by Cohen¹¹ and Grigoriev et al.¹² The term pocket denotes an enclosed volume composed of binder and MF that is confined from all sides by oxidizer particles and interpocket bridges. The interpocket bridge is understood as a part of the propellant composition confined by two adjacent oxidizer particles taking part in the formation of a common pocket. Experience gained in studying agglomeration showed that it is expedient to introduce the pocket concept, and thus it is necessary to determine characteristics of the pockets for various propellants. The experimental technique for the study of the propellant structure is presented in Refs. 1 and 7. From the general ideas about agglomeration, it was assumed that pocket formation could be realized under the following conditions. The size of oxidizer particles constituting the pocket should be commensurate with each other and with the pocket size and should considerably exceed the original metal particle size. The pocket is a formation of an irregular shape. To make the pocket characteristic more definite we introduce the notion of an equivalent sphere, the volume of which is equal to the pocket volume. The sphere diameter is taken as a geometric characteristic of the pocket.

Because the experimental study of three-dimensional structures is complicated, this problem cannot be practically solved. Therefore, the study is based on plane structures. A similar approach is widely used in the analysis of alloy compositions, the mineralogical composition of rocks, and other things.¹³ In this approach, the

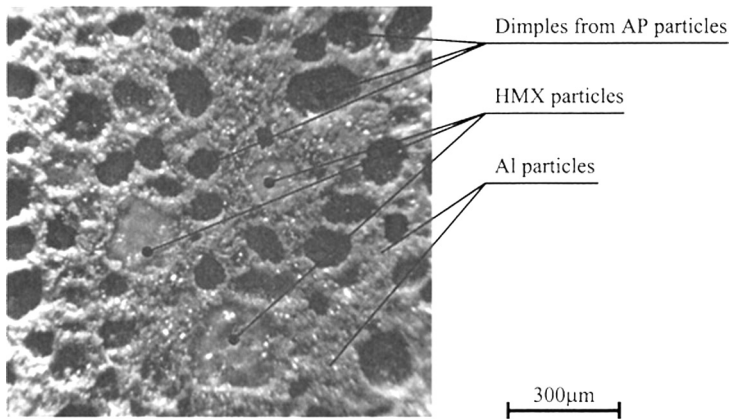


Fig. 3 Cut of a composite SRP containing AP and HMX.

ratio of the specimen volume to the total volume is very low, as a rule, but this factor does not preclude extrapolation of the specimen analysis results to the total volume. A quantitative microscopic analysis generally uses the Deless planimetric method and the Rosival linear method, based on the Cavalieri–Aker principle,^{13,14} which states that “portions of a phase/component of an alloy/mixture are equal within its volume, cross section, and the line running through it.” Random distribution of the oxidizer particles throughout the propellant ensures statistical equality of all the cross sections and, thus, the applicability of the Cavalieri–Aker principle to the propellant structure.

The structure study was carried out using photographs of the cutoff sections of composite SRP as shown in Fig. 3. To obtain clear interfaces between oxidizer particles and pockets, the oxidizer crystals, such as ammonium perchlorate (AP), ammonium nitrate, and ammonium dinitramide (ADN), were dissolved in water. It should be noted that crystals of cyclotetraethylene tetranitramine (HMX) were not dissolved in water. The picture of the cuts was taken with side illumination to increase the degree of contrast. The oxidizer content was measured by the linear method, and the size distributions of the oxidizer particles and pockets were determined by the planimetric method. Pockets were identified heuristically on the basis of the above-mentioned reasons. To measure areas, the method of superimposing equivalent figures (circles) of known areas was used. The function of the oxidizer particle size distribution was found by the Shile–Schwarz–Saltykov method.¹³

D. Quench Collection of CCP Particles

Both the agglomerates and the SOP were sampled using the quench-collection method described in Ref. 15. Sampled particles were subjected to a comprehensive analysis. The function of the particle size distribution and the particle chemical composition was found, and the particle structure was studied. The analysis was carried out separately for two main fractions: agglomerates and SOP. The fractions were separated using screens. It was assumed that particles larger than 30 μm were agglomerates, and those smaller than 30 μm were SOP. In carrying out the size analysis, histograms were measured first, and then average sizes and size

distributions of particles were determined. In addition to these data, the following integral characteristics were found: Z_m^a , Z_m , Z_m^{ok} , and η .¹⁵

III. Agglomeration Behavior

The experimental results allowed us to establish the principal regularities of agglomeration. These regularities involve the conditions of the agglomerate formation and agglomerate properties as functions of various factors.

A. Agglomerate Structure

Analysis and comparison of the data obtained in various experimental investigations allow us to formulate the following ideas about agglomerate structure.^{1,2,16} Agglomerates are systems of aluminum and alumina drops, which may contain gas bubbles. These systems are in a condition close to equilibrium, with the system surface energy striving for a minimum level. Figures 4–11 illustrate evidence of the above statement. Depending on the specific features of their composition, the agglomerates can be divided into two types. The first type includes agglomerates called “matrix” agglomerates. Such an agglomerate presents a spherical alumina particle incorporating separate aluminum drops: as a rule, a few comparatively large and many small drops (Figs. 5 and 6). The metal drops are found largely at the interface between the liquid oxide and the gas phase. Some metal drops can be completely encapsulated with the oxide. The second type of agglomerate has some quantity of oxide at its surface in the form of drops (Figs. 7 and 8). This oxide has been given the name “cap” oxide. Matrix agglomerates are usually larger than agglomerates of the second type.

Taking the aforementioned into account, the agglomerate structure is determined by its type, the quantities of component substances, and their surface properties such as the surface tension at the alumina/gas, alumina/aluminum, and aluminum/gas interfaces. The surface of metal drops in agglomerates is related to



Fig. 4 Agglomerates quenched and collected from the above-surface zone.

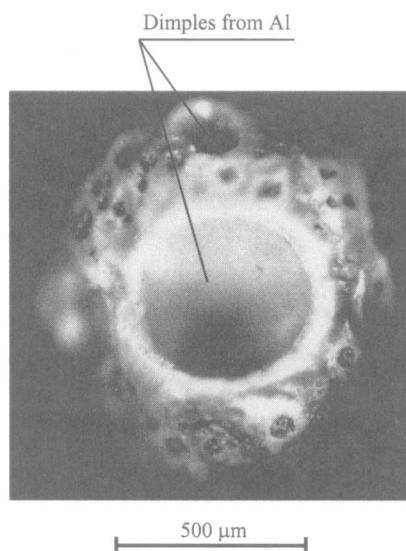


Fig. 5 “Matrix” agglomerate after etching with acid.

the gaseous product flow, which ultimately forms the combustion product trail as shown in Figs. 9–11. It should be noted that video recording without external illumination at low pressures very often does not provide registration of the trail for comparatively small particles, because of a decrease in the radiation from the products forming the trail. This is also confirmed by the temperature measurements and the data obtained from video recording with external illumination.

The temperature of the agglomerating particles is higher than the aluminum oxide melting point. The measurements at atmospheric pressure performed using the

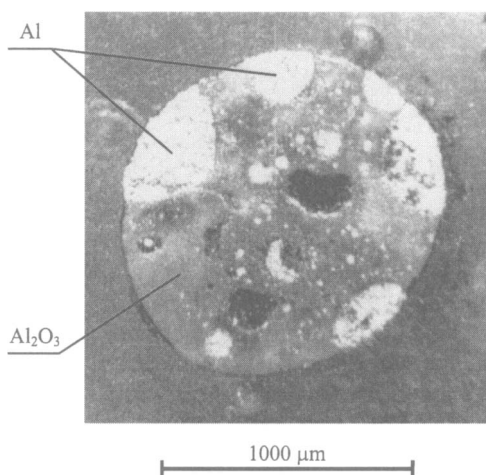


Fig. 6 Microsection of the “matrix” agglomerate.

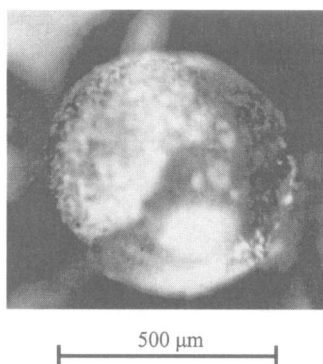


Fig. 7 Agglomerate with an oxide "cap."

color spectral pyrometer show that the temperature is in the range of 2350–2600 K. The luminance temperature T_L of the agglomerating particles (metal and oxide), determined with the video pyrometer, has values in the range of 2100–2200 K for the metal and 2300–2400 K for the oxide as shown in Fig. 9. The difference in those values is an obvious consequence of the difference in optical properties of the metal and oxide.¹⁷ The regularities described are the most general ones. For pressures close to atmospheric, however, and for propellants with a comparatively low burning rate, other formations, referred to as aggregates, are occasionally registered. Aggregates are fragments of the upper portion of the surface layer that include carbonic elements and burning metal particles. At some distance from the propellant burning surface the aggregates take a regular spherical shape. They are analogues of the agglomerates registered in the combustion of double-base metalized propellants.¹⁸ In general, experiments showed that the aggregates do not play a significant role in the combustion of high-energy composite SRP at pressures higher than atmospheric pressure.

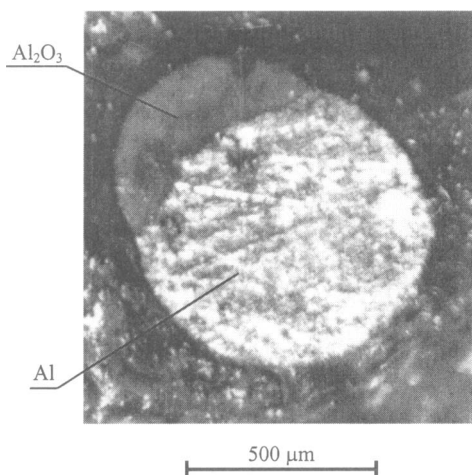


Fig. 8 Microsection of the agglomerate with an oxide "cap."

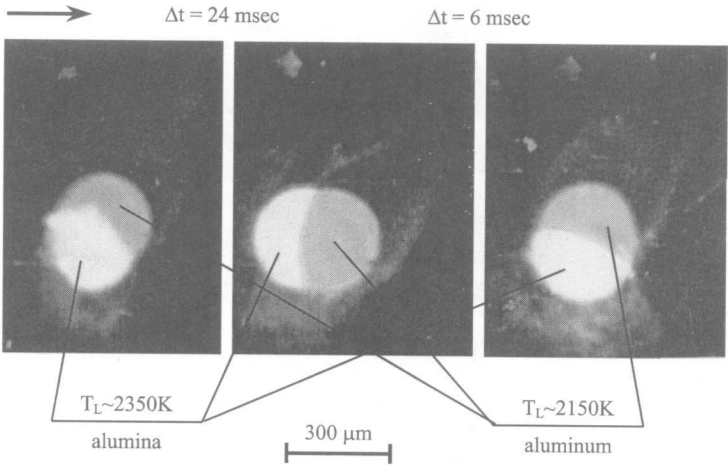


Fig. 9 Agglomerating particle on the propellant burning surface.

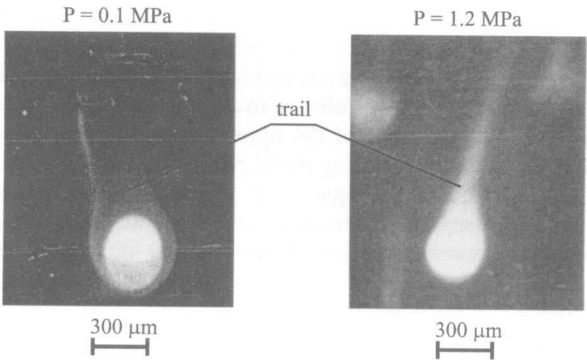


Fig. 10 Agglomerates of the second type in the gas phase.

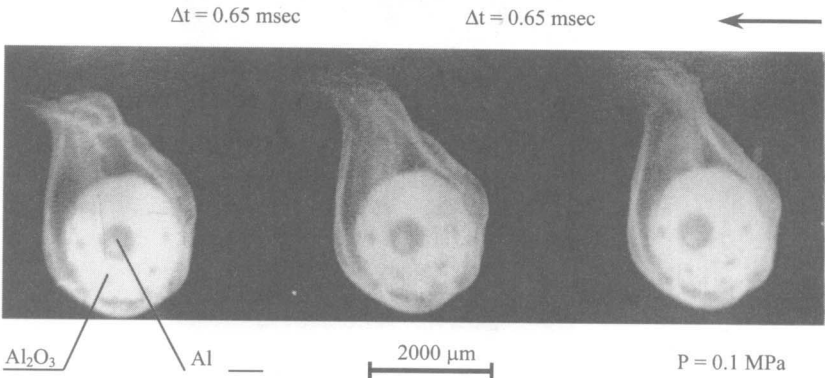


Fig. 11 "Matrix" agglomerate in the gas phase.

B. Agglomerate Formation Conditions

Using a high-speed video camera, the results of visualization based on the light from the propellant burning surface allow us to establish the following.^{1,2} In the process of combustion on the surface, particles appear that are considerably larger than the original metal particles. These particles are retained on the propellant surface for some time. During that time, the particles grow in size (fusion of adjacent particles can be clearly seen). Then the particles break off from the propellant burning surface, i.e., agglomerates are produced and move into the gas phase. The agglomerate properties and specific features of the agglomeration give grounds to assert that the fusion of particles incorporating burning metal drops takes place during the agglomerate formation. The temperature of fusing particles exceeds the oxide melting temperature. This being so, the fusion takes place in accordance with the regularity behavior of liquid under conditions where surface tension is the dominant force. The burning particle may be retained on the propellant surface for a considerable time, which is commensurate with its combustion time. At atmospheric pressure, the residence time reaches ~ 50 ms. Consequently, we cannot assume, based on the results of a number of theoretical models,^{19,20} that particles leave the burning propellant surface just after being ignited. The above-stated observations give grounds to assume that the top part of the surface layer contains a specific structure, ensuring quite long residence of high-temperature particles. The experimental results of the CCP study,^{1,3,7} including study of the combustion residue on various bases and visualization of the burning propellant surface, allowed us to confirm this assumption.

In the combustion of all the propellants being studied, in the upper part of the surface layer we can distinguish the condensed-phase zone, consisting of metal, its oxide, and a small amount of carbonic elements. This zone is called the skeleton layer (SL). It is defined as a gas-permeable three-dimensional structure consisting mainly of the metal and its oxide, as well as thermostable carbonic elements. The combustion zone, where decomposition of the binder into gaseous products and solid-state carbonic elements is largely completed, is considered to be the lower part of the SL. On the upper surface of the SL (facing the gas phase), the coagulating particles, after breaking away from it, form the agglomerate flow.

The SL properties may differ in important ways for different propellants. Depending on the SL properties, we can single out at least two propellant classes, which we designate **A** and **B** (Fig. 12). For class **A** propellants, the basis of SL is the carbon skeleton—an aggregation of thermostable products of unfinished binder decomposition. Pores of the carbon skeleton are filled to a large extent with the liquid metal and oxide (Fig. 13). The pore coherence and presence of the liquid in them have a large effect on the high metal and oxide binding within the SL. The movement of the SL upper surface occurs as a result of the carbon elements burning out. The opening of the pores on the surface leads to the appearance of new particles formed by liquid Al and Al_2O_3 . The binding of these particles (oxide of the particles) with the SL elements (first with the oxide) ensures a high level of adhesion forces.

For class **B** propellants, the SL upper layer consists of the melted original metal particles coated with solid oxide films and bound together in the spots where the film is broken (Fig. 12). Ignition of these particles leads to oxide film melting and particle fusion. As a result, individual fragments of SL form united particles, which

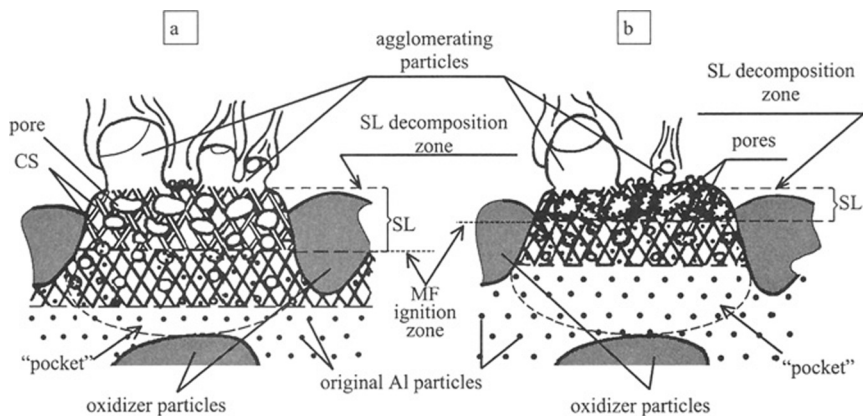


Fig. 12 Sketch of the skeleton layer (SL) in combustion of propellants of a) class A and b) class B. CS, carbon skeleton.

are subsequently retained on the SL upper surface for some time. As SL does not include the liquid oxide in the case of class **B** propellants, it is possible that the adhesion force level is lower than that for class **A** propellants. The ignition and fusion processes of the metal particles in SL determine the movement mechanism of the SL upper surface in the combustion of class **B** propellants.

The peculiarities of class **A** propellant combustion are enhanced by the chemical composition factors leading to earlier ignition of metal particles. In particular, typical representatives of class **A** propellants are propellants containing fine metal particles with a specific surface of about $100 \text{ m}^2/\text{g}$. Class **B** propellants are generally



Fig. 13 Lower part of the skeleton layer for a class A propellant ($P = 0.5 \text{ MPa}$).

Table 1 Propellant compositions of typical representatives of classes A and B

Propellant class ^a	Type and content		Content of aluminum	Specific surface of powdered Al, m ² /g	Ratio of large- to small-size fraction of oxidizer ^b
	Binder	Oxidizer			
SRP-1, A	SR1, 12%	ADN, 68%	20%	100	85/15
SRP-2, B	SR2, 10.8%	AP, 65.2%	24%	0.15	75/25

^aSR1 and SR2—binders based on hydrocarbon polymer plasticized with special oil.

^bThe large-size fraction of granular ADN is about 160 μm , and that of granular AP is 160–316 μm . The small-size fraction of ADN and AP is less than 50 μm .

based on an inert binder, AP, and Al powder with a specific surface less than 1 m²/g. Typical propellant compositions of the two classes are given in Table 1. A number of propellants cannot be unambiguously classified as either A or B. Depending on pressure, the regularities of both class A and class B propellants are observed in their combustion.

SL is of fundamental importance in agglomeration. In fact, the high percentage of the metal and its oxide binding within SL ensures the possibility of the fusion of the original particles, and the presence of adhesion between growing particles and the SL elements provides for their retention on the burning surface and further growth. The breaking-away of the particles from the SL surface takes place when the adhesion forces are weaker than the separation forces. The separation process can be understood in different ways, including by means of cohesion (Fig. 14). An important circumstance is worth noting: SL does not take up all of the propellant burning surface that is free of the oxidizer particles. The SL formation takes place only within “pockets” and does not comprise “interpocket bridges.” The absence of SL on the burning surface means the impossibility of agglomeration. Thus the interpocket bridges supply into the gas phase metal particles that are not involved in agglomeration.

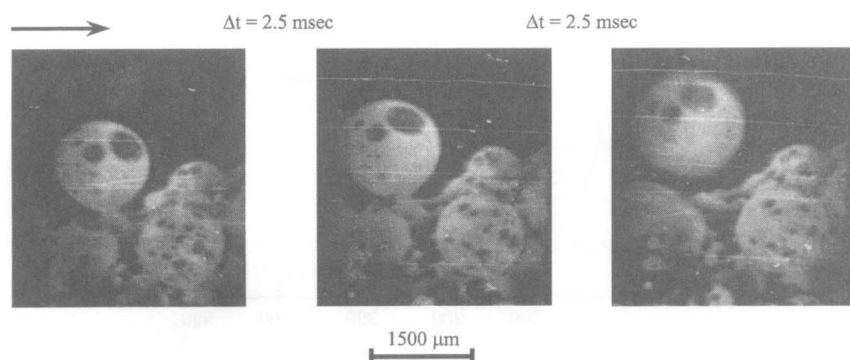


Fig. 14 Breaking-away of agglomerate from the surface of the skeleton layer in combustion of a class A propellant at 0.1 MPa.

C. Influence of Propellant Composition and Combustion Conditions on Agglomeration Behavior

The degree of agglomeration can be characterized in terms of the MF involvement in the agglomeration process. This characteristic can be evaluated by the parameter Z_m^a . It should be noted that the measured values of Z_m^a are lower due to conversion of agglomerate aluminum to SOP while burning in the gas-phase mode on the propellant burning surface as well as in the gas phase (before quenching). A portion of the original MF equal to $(1 - Z_m^a)$ determines the amount of SOP formed at the propellant burning surface.

The relation of Z_m^a to the oxidizer particle sizes, and consequently to the propellant structure, is clearly observed. We can nearly consider the universal statement that the value of Z_m^a increases with an increase in oxidizer particle size. For propellants with comparatively small oxidizer particle sizes, however, this statement is not correct. The above regularities can be illustrated using data obtained in experiments with AP-based propellants in which the oxidizer particle sizes were varied¹⁵ (Fig. 15). With a decrease in AP particle size, the Z_m^a value first decreases to a minimum value and then increases with a further decrease in oxidizer particle size. The effect of pressure on Z_m^a is small. But for the **B** class of propellants, an essential decrease in Z_m^a with increasing pressure is recorded.^{1,7} When the pressure exceeds a certain value, called the critical pressure P^{**} , we observe a comparatively abrupt decrease in the mass of agglomerates (parameter Z_m^a) and an increase in their oxide content (parameter η) (Fig. 16). A further pressure increase does not change these characteristics significantly. The analysis of temperature profiles in the above-surface zone of the gas phase allows us to draw the conclusion that this peculiarity is related to the intensification of metal-agglomerate combustion in this zone.^{3,21} The critical pressure value increases with the growth of agglomerate sizes. Temperature profiles in the above-surface zone of the gas phase are dependent on pressure. Transition from the low-pressure region to the high-pressure one is accompanied by an increase in the maximum temperature in the above-surface zone of the gas phase and an increase in the distance from the burning surface (Fig. 17).^{3,21}

The size and structure of agglomerates depend to a considerable degree on the pressure.^{1,7} Let us examine these dependencies as applied to propellants of various classes.

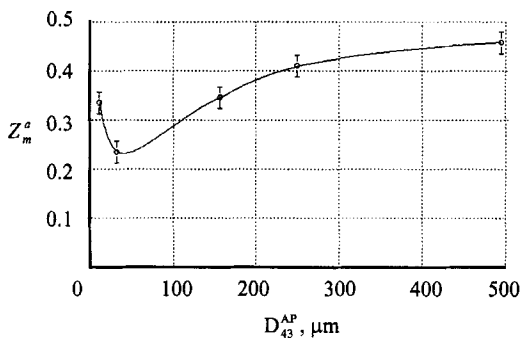


Fig. 15 Dependence of Z_m^a on mass-medium diameter of AP particles for propellants presented in Ref. 14.

Chapter 2.22

Measurements of the Physico-Chemical Properties of Liquid Alumina Using Contactless Techniques

Francis Millot,* Benoît Glorieux,[†] and Jean Claude Rifflet[‡]
Centre National de la Recherche Scientifique, Orléans, France

I. Introduction

A THOROUGH understanding of the properties of liquid alumina is important for the provision of propogol containing aluminum combustion in rockets.

Most of the physico-chemical data on liquid alumina were obtained in the 1960s and 1970s with experimental techniques that involved a contact with a crucible (generally Mo or W).

Although contactless devices have been available for some time for use under microgravity conditions, they have also recently been developed for use in Earth's gravity, at least for oxides.¹⁻⁵ They consist of a levitation system (aerodynamic or aeroacoustic levitation) and of a heating device (CO₂ lasers). Figure 1 presents a schematic example: a gas is flown at about 1 l/mn through an optically polished convergent divergent nozzle made of an Al alloy cooled with a water circuit. A spherical droplet (2–5 mm in diameter) is maintained in the liquid state by impinging two 10.6- μ m wavelength beams produced by two CO₂ lasers. These beams are almost completely absorbed by the alumina and almost completely reflected by the aluminum nozzle.

The temperatures of the two poles of the drop are measured with two pyrometers. It is then possible to adjust the power of the two lasers to have the same luminance temperature within 20 K.

New methods of contactless measurements on levitated liquid oxides have been reported periodically during the few last years; density,^{4,6} surface tension,⁷ viscosity,⁸ electrical conductivity,⁹ liquid structure by nuclear magnetic resonance¹⁰ and x-ray diffraction¹¹ and Extended X Absorption Fine Structure¹² techniques.

Copyright © 1999 by the American Institute of Aeronautics and Astronautics, Inc. All rights reserved.

*Research Director, Centre de Recherche sur les Matériaux à Haute Température.

[†] Ph.D. Student, Centre de Recherche sur les Matériaux à Haute Température.

[‡]Research Scientist, Centre de Recherche sur les Matériaux à Haute Température.

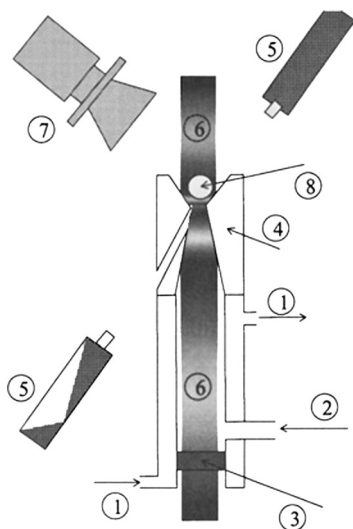


Fig. 1 Schematic view of an aerodynamic levitation device for thermophysical property measurements: 1—water cooling tubes, 2—gas inlet for levitation, 3—NaCl single crystal window, 4—aluminum alloy convergent divergent nozzle, 5—pyrometer, 6—CO₂ laser beam, 7—high-speed digital camera, and 8—liquid sample.

This chapter presents a review of the results on liquid alumina, most of them obtained using techniques that use a crucible, and also the state of the art concerning contactless measurement of the properties of liquid alumina.

II. Physico-Chemical Properties of Liquid Alumina

A. Density

Density has been determined in the past with different experimental techniques that involve contact with a refractory material. Contactless methods consist of measuring the dimensions of a liquid drop of known weight with an optical setup and a camera. The drop could be falling in the older works, and it is levitating in the more recent experiments. The results are shown in Fig. 2. An examination of the results reveals good agreement between data obtained using a given type of crucibles, no matter what the measurement technique. It is, then, reasonable to distinguish three sets of density data—those obtained with Mo or W crucibles, with graphite crucible, and with no crucible.

1) The density of liquid alumina in contact with Mo or W: density was obtained using the sessile drop method,¹³ falling drop method,¹⁴ Archimedean method,^{15,16} maximum bubble pressure method,^{17–19} and menisci method.²⁰ Its value at the melting point of alumina is reported between 2.97 and 3.06 g/cm³. The thermal expansion coefficient deduced from density/temperature variations in the range 2300–3100 K is $3\text{--}4 \times 10^{-4} \text{ K}^{-1}$.

2) The density obtained with a sessile drop on graphite by Zubarev et al.²¹ is characterized by values at the melting point of 2.69 g/cm³ and a thermal expansion coefficient of $3 \times 10^{-4} \text{ K}^{-1}$.

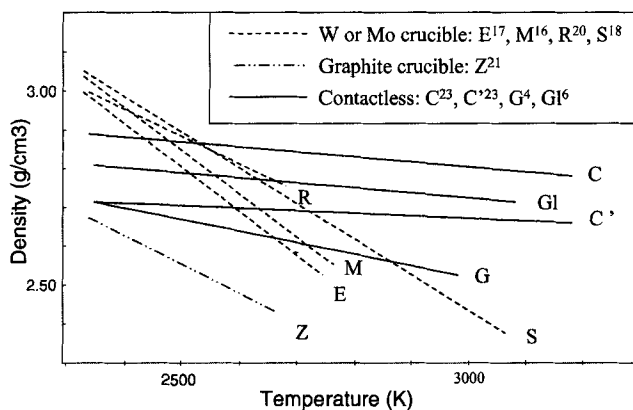


Fig. 2 Density of liquid alumina obtained under different conditions.

3) The results reported in Refs. 4, 6, 22, and 23 obtained with contactless techniques are characterized by a density value for falling drops at the melting point of $2.5 \pm 0.1 \text{ g/cm}^3$ in vacuum²² and $2.6\text{--}2.7 \text{ g/cm}^3$ in argon gas.⁴ The aerodynamically levitated spherical liquid drops have densities deduced from the image recorded from the top of $2.7 \pm 0.1 \text{ g/cm}^3$ in Ar,⁴ 2.7 in O₂ and 2.8 g/cm^3 in Ar,²³ and $2.81 \pm 0.01 \text{ g/cm}^3$ in O₂, Ar and Ar + 10% H₂ (Ref. 6). These last results have a better accuracy than the others because of improved experimental facilities (digitized images from a high-speed camera). The thermal expansion coefficient was reported to be $(1.1 \pm 0.6) \cdot 10^{-4} \text{ K}^{-1}$ between 2300 and 3000 K⁴ and $(4.22 \pm 0.14) \cdot 10^{-5} \text{ K}^{-1}$ between 2000 and 3100 K (Ref. 6). This last result is currently the best available.

The practical conclusions that can be drawn from this set of results is that the chemical pollution from a crucible material, such as molybdenum or graphite, cannot be ignored. For instance, at 3500 K, a typical temperature in rocket technology, density ρ is predicted as follows: alumina in contact with Mo,¹⁸ $\rho = 1.9 \text{ g/cm}^3$, in contact with graphite,²¹ $\rho = 1.8 \text{ g/cm}^3$, no contact,⁶ $\rho = 2.67 \text{ g/cm}^3$.

These results indicate that all of the physico-chemical data on liquid alumina at very high temperatures should be reviewed and remeasured using contactless techniques in the future.

B. Surface Tension

The surface tension ν of alumina has been deduced in the past using various experimental techniques in which surface tension and gravity effects are competing with each other. In some instances (pendant drop, sessile drop, shape of the meniscus, maximum bubble pressure techniques) the ratio ν/ρ is determined, and consequently the value of ν will depend on the choice of ρ . On the other hand, the weight drop technique allows results of ν independent of the density of the liquid. It consists of measuring the weight of falling drops, initially suspended from a capillary having a radius of r and having characteristic values of $rV^{-1/3}$ between 0.6 and 1.2, V being the volume of the drop.

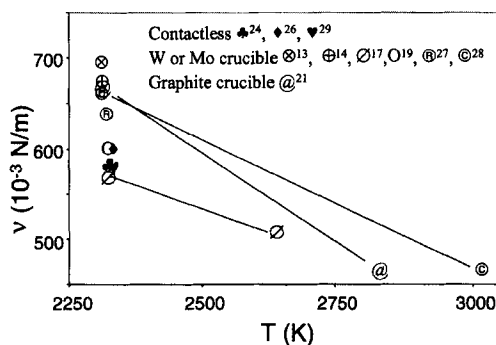


Fig. 3 Surface tension of liquid alumina in vacuum or neutral atmosphere.

Surface tension at the melting temperature was reported between 580 and 705 $\text{mN} \cdot \text{m}^{-1}$ (see Fig. 3).^{13,14,17,19,21,24-30} As we have seen in our preceding discussion of the density measurements, the nature of the crucible must affect the data.

Results on liquid alumina in contact with molybdenum or tungsten were obtained in a neutral atmosphere (argon, helium, or vacuum).^{13,14,17,25,27,28,30} The data of Elyutin et al.²⁵ were obtained by measuring the maximum height of liquid alumina sustained by a molybdenum plate or a hollow cylinder above a liquid alumina bath. This is a method that is quite well known as giving erroneous data with no well-established relation with surface tension. The other data are, generally, in bad agreement with each other at the melting point: 690 $\text{mN} \cdot \text{m}^{-1}$ by a pendant drop method,¹³ 680 $\text{mN} \cdot \text{m}^{-1}$ (pendant drop) and 670 $\text{mN} \cdot \text{m}^{-1}$ (weight drop),¹⁴ 570 $\text{mN} \cdot \text{m}^{-1}$ by the maximum bubble pressure method,¹⁷ 638 $\text{mN} \cdot \text{m}^{-1}$ (in W) and 360 $\text{mN} \cdot \text{m}^{-1}$ (in Mo) from the meniscus shape,²⁷ and 670 $\text{mN} \cdot \text{m}^{-1}$ by the maximum bubble pressure.²⁸ More recently, Ikemiya et al.¹⁹ have reported results for surface tension by the maximum bubble pressure method in an Ar + 10% H_2 atmosphere. They claim that their atmosphere allowed the prevention of an interaction between the molybdenum crucible and the liquid alumina. They obtained a value of $602 \pm 3 \text{ mN/m}$, which they compared favorably with the results reported by Lihrmann and Haggerty with no crucible.²⁹ It is not clear, however, why they obtained a density value of 2.97 ± 0.03 , which compares well with most molybdenum crucible studies.

Results for surface tension near the melting point without pollution by a crucible have been reported^{24,26,29} near the melting point. Wartenberg et al.²⁴ performed a weighting drop measurement from 2 to 3-mm-diam alumina rods under vacuum and reported a value of $580 \pm 30 \text{ mN/m}$. Later, McNally et al.²⁶ made a comparative study using various methods. They reported that the only reproducible method was that of the drop weight. They gave a value of 600 mN/m in argon gas. More recently, Lihrmann and Haggerty²⁹ have determined the surface tension of pendant drops suspended from a polycrystalline alumina rod. They chose a density value of 3.01 g/cm^3 to determine the surface tension. However, we have already seen that the contactless value of the density is 2.81 g/cm^3 at the melting point, whatever the nature of the gas in contact with the liquid. Corrected values of the Lihrmann and Haggerty measurements are therefore $\nu(\text{air}) = 621 \pm 14 \text{ mN/m}$, $\nu(\text{He}) = 583 \pm 13 \text{ mN/m}$, and $\nu(\text{He} + 10\%$

H_2) = 569 ± 12 mN/m. These are in good agreement with the data of Wartenberg et al.²⁴ and that of McNally et al.²⁶

The variation of surface tension with temperature is apparently more consistent with the nature of the solid in contact with the liquid. Alumina in contact with Mo or W has surface tension temperature coefficients of, roughly, $3 \times 10^{-4} \text{ K}^{-1}$ (Refs. 17, 19, and 25) and $5 \times 10^{-4} \text{ K}^{-1}$ (Ref. 28). Rasmussen and Nelson²⁷ claim to have observed no variation of ν in the range 2300–2700°C, but fail to consider the very poor precision of the values of ν ($\pm 100 \text{ mN} \cdot \text{m}^{-1}$). The fact that temperature coefficients of ν are comparable to those of ρ obtained in Mo or W crucibles seems to indicate some consistency between the two sets of results (see Ref. 31, for instance), and consequently it can be deduced that both are wrong by one order of magnitude. The Zubarev results²¹ for alumina in contact with graphite have a temperature coefficient of $7.5 \times 10^{-4} \text{ K}^{-1}$ comparable again with the density temperature coefficient of $3 \times 10^{-4} \text{ K}^{-1}$.

Contactless techniques for surface tension measurements of alumina are still being developed.⁷ Unlike most contact techniques, this is a direct measurement of ν . The principle consists of observing the temporal shape variations of an almost spherical levitating liquid droplet having a homogeneous temperature. In this case the theory³² predicts the existence of a characteristic vibration frequency ω of a drop of mass m related to ν through the relation:

$$\nu = \frac{3m\omega^2}{32\pi}$$

The state of the art in this field is quite advanced for liquid metals. The data considered the best available at high temperature have a precision of 1%. The very first surface tension measurements of liquid alumina using contactless techniques have recently been reported (in oxygen at 2700 K).⁷ The reported value of 575 mN/m is in quite good agreement with available self-contained alumina results at the melting point (620 mN/m). New results may, in principle, become available very soon.

C. Viscosity

The viscosity of liquid alumina has been determined in two distinct ways: 1) from the damping of a torsional oscillation of a W crucible containing the liquid under vacuum^{30,33,34} (The characteristic time allows the determination of kinematic viscosity. Its product with density is the viscosity.) and 2) from the torque exerted on a rotating Mo plate plunging into the liquid in an Ar + 10% H₂ atmosphere.³⁵

The results that are shown in Fig. 4 indicate relatively good consistency between most studies. The results of Bloomquist et al.³⁴ had the form:

$$\eta = 2.55 \cdot 10^{-4} \cdot \exp(22750/RT) \text{ Pa} \cdot \text{s}$$

Contactless techniques to measure the viscosity of high-temperature oxide melts are scarce. Indirect methods have been reported in the recent past.

Temperature variations of kinematic viscosity have been inferred from the width of the Al quadrupolar nucleus peak of nuclear magnetic resonance in calcium aluminates.³⁶

From the relaxation time of a contactless deformed SiO₂ melt, ratios of η/ν have been obtained.⁸

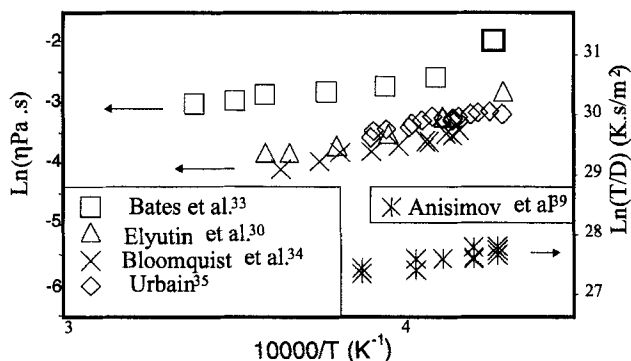


Fig. 4 Variations in viscosity η and aluminum self diffusion coefficient D , represented on a scale that allows a direct comparison via the Stokes–Einstein relation.

It is unlikely that there will be any relevant contactless data on liquid alumina in the near future because of many undesirable artifacts that are difficult to eliminate with the present state of the techniques. The very first data on liquid metal viscosity have been reported using contactless techniques in a microgravity experiment in the NASA TEMPUS project.³⁷

D. Aluminum Self Diffusion

The diffusion of the tracer²⁶ Al was studied by a Mo capillary method in vacuum.^{38,39} The results (see Fig. 4) were obtained between 2335–2575 K. They followed a linear Arrhenius law:

$$D = 2.30 \times 10^{-7} \cdot \exp(-21200/RT) \text{ m}^2/\text{s}$$

Very similar activation energies are obtained for aluminum diffusion and viscosity.

Contactless techniques have not been reported for the measurement of diffusion of liquid alumina. As in the case of viscosity, it appears difficult at the present time to get convincing data with such methods. The main drawback of the contactless experiment is that it is difficult to prevent convection movement in the liquid drop because of the extremely directional character of the laser heating, which induces temperature gradients.

E. Electrical Conductivity

Electrical conductivity has been reported^{40–44} for various pressures and for temperatures from the melting point to 3000 K. The agreement among the various authors is very poor (see Fig. 5), with the conductivity data near the melting point ranging from $0.7 \Omega^{-1} \cdot \text{cm}^{-1}$ to $15 \Omega^{-1} \cdot \text{cm}^{-1}$ and the activation energy being $0 \text{ kJ} \cdot \text{mol}^{-1}$ (Ref. 40), $70 \text{ kJ} \cdot \text{mol}^{-1}$ (Ref. 42), or $160 \text{ kJ} \cdot \text{mol}^{-1}$ (Ref. 44). Although the most recent work by Shpil'rain et al.⁴⁴ tries to relate these large discrepancies to the experimental conditions of the various studies, there are certainly more unknown factors that affect these results.

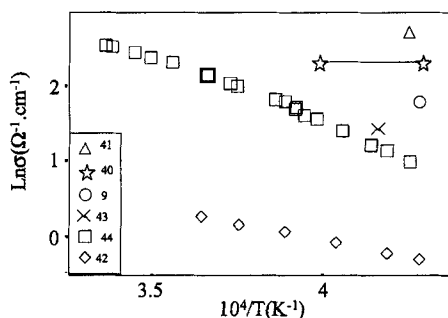


Fig. 5 Electrical conductivity of liquid alumina.

There has been a recent report⁹ of a contactless electrical conductivity measurement on liquid alumina. The principle consists of measuring the inductance L and the quality factor Q of a coil at various rf frequencies, which contain an alumina drop levitating in an aerodynamic device made of boron nitride. The observation was made that the change of Q and L during the solidification of a free cooling liquid drop having a 3.8 mm diameter could be consistently interpreted in spite of the complications induced by the temperature changes of the coil during the measurement sequence. A value of $\sigma = 6 \pm 1 \Omega^{-1} \cdot \text{cm}^{-1}$ for the liquid at the melting point of alumina was proposed. These first data, which fall inside the range of reported data, are very encouraging for the future.

The conclusion that can be drawn from the whole set of atomic transport data in liquid alumina is quite confusing. Apart from the already mentioned similarities of the activation energies of reported aluminum diffusion and viscosity, classical relations, such as the Stokes–Einstein (D_{Al}, η) or Nernst–Einstein (D_{Al}, σ) relations, indicate no consistency between the various sets of results. Roughly calculating η from D is not consistent, because we find a viscosity of $\eta_{\text{calc}} = 0.4 \text{ Pa} \cdot \text{s}$ near the melting point, which is one order of magnitude higher than the experimental η . On the other hand, calculating σ from D_{Al} gives values between 5 and $10 \Omega^{-1} \cdot \text{cm}^{-1}$ near the melting point, depending on the assumptions made on the nature of the migrating Al-bearing ion. This means in practice that this comparison is a relatively good one if we favor the highest reported σ data.^{40,41} However, there is no reason why Al should contribute so strongly to the conductivity.

F. Radiative Properties

The radiative properties of liquid alumina have been examined near the melting point by various authors, with the liquid sample being in contact with solid alumina.^{45–49}

The most important conclusions that are clearly established are as follows:

Liquid alumina emissivity of millimetric drops is higher than 0.9 up to 3500 K at a wavelength of $10.6 \mu\text{m}$ (Ref. 47).

The absorption in the visible region, and particularly at the $0.65 \mu\text{m}$ wavelength, is strongly dependent on the purity of the liquid. These aspects were carefully examined by Weber et al.⁴⁷ Small amounts of impurities like Si, Mg, Fe, or W (5000–10000 ppm) are able to render opaque liquid drops 2.5 mm in diameter that are fairly transparent when they are pure. It also appears quite clearly from this

work that the presence of some gases (H_2 , Ar, N_2 , CO, or HCl) makes the drop opaque. Others, like CO_2 or O_2 , leave the drop transparent under 1 atm pressure. The deduction was then made that opacity is directly related to oxygen pressure. The comparison by Nelson et al.⁴⁸ of the opacity of millimetric drops in oxygen and argon at atmospheric pressure is consistent with these results.

Contrary to these results, results of Weber et al.⁴⁵ obtained at the same wavelength of $0.65 \mu m$ on partially melted sapphire filaments indicated the opposite behavior: liquid alumina was more opaque in oxygen than in argon and also in N_2/H_2 mixtures. Weber et al.⁴⁷ later argued that the temperature of the two studies (2320 vs 2400 K) could explain this difference. It was not noticed, however, that the experiments were performed under quite different pressure conditions: the former work of Weber⁴⁵ was at pressures between 40 and 70 Pa, and the latter⁴⁷ mostly at atmospheric pressure conditions. The role of total pressure on the opacity of liquid alumina was reported incidentally by Weber et al.⁴⁷ for HCl and for a static mixture of H_2 with H_2O . In both cases, opacity is proportional to gas pressure. The conclusions about the influence of the gases in contact with liquid alumina are not so well established. Total pressure of any gas, in addition to oxygen pressure, may be a relevant parameter. However, it is not clear whether this last parameter may influence the state of intrinsic defects or the balance of variously charged extrinsic defects (Fe^{2+} , Fe^{3+}).

The spectral absorption of liquid alumina at $0.65 \mu m$ reported in the previously cited works ranged from 9 to more than $55 cm^{-1}$. This means that liquid drops with diameter less than 4 mm may be more or less transparent.

The reflectivity of liquid alumina in argon at the wavelength of $0.63 \mu m$ has been measured up to 4000 K by Bober et al.⁴⁶ Their technique consisted of heating a small planar surface of Degussa Al23 ceramic to form a liquid about 10μ thick in a few milliseconds and recording the temperature and the reflection of a He-Ne laser beam during the heating. They found a sharp change of the hemispherical reflectance on melting from a value of 0.75 for the solid to a value of 0.11 at the melting point, decreasing linearly with temperature with a coefficient of $1.6 \times 10^{-4} K^{-1}$. They also briefly reported significantly different results on premelted samples. From the already reported results on absorption at the wavelength of $0.65 \mu m$, we should expect a micronic layer of liquid on the ceramic to be transparent and consequently to have no effect on the reflectivity measurement through the melting point. The results of Bober suggest that the liquid is opaque. The suggestion can be made that the porosity of the initial ceramic is not removed from the liquid during the millisecond heating, making the small gas bubbles in the liquid efficient diffusers of the light. This explanation is consistent with the differences observed on the ceramic and on the premelted material. We then expect this result to be correct to some extent.

An indirect method to determine the normal spectral reflectivity R_λ from the refractive index n_λ has been used by Diamond and Drago⁴⁹ through the relation:

$$R_\lambda = \frac{(n_\lambda - 1)^2 + k^2}{(n_\lambda + 1)^2 + k^2}$$

and taking $n_{0.63} = 1.744$, with k being small for a semitransparent material, one gets $R_{0.63} = 0.073$. Note that the index of refraction of liquid alumina is particularly insensitive to the nature of the gas, to the purity and to the temperature.⁵⁰ This result means in practice that a unique value of emissivity of 0.93 can be adopted in

the visible region for opaque liquid alumina, that is, for dimensions equal or higher than 4 mm at or above the melting point. We make no comment on the state of the art of contactless technique for this property because all published data concern self-contained liquid alumina.

III. Conclusions

This rapid glance at the published physico-chemical properties of liquid alumina allows some important conclusions.

The first is that most of the published data obtained with samples in contact with a crucible are increasingly inaccurate as the temperature is increased. The discrepancy between contact and contactless density data is so big at 3500 K that it is hopeless to consider other data, like viscosity or surface tension obtained with a crucible, to be representative of liquid alumina at the highest temperatures.

The examination of the radiative properties generally obtained without contact with a foreign material leads to the following statement: liquid alumina is a fairly transparent medium because opacity is obtained for millimetric size. However, dissolved gases profoundly may modify this conclusion, and efforts should be made to quantify the relationships between the absorption coefficient and the nature and pressures of the gases in contact with liquid alumina. This conclusion could also apply to other physico-chemical properties at high pressures.

References

- ¹Nordine, P. C., and Atkins, R. M., "Aerodynamic Levitation of Laser-Heated Solids in Gas Jets," *Review of Scientific Instruments*, Vol. 53, No. 9, 1982, pp. 1456–1464.
- ²Oran, W. A., and Berge, L. H., "Apparatus and Method for Containerless Melting and Rapid Solidification," U.S. Patent Application 214,360, July 1981.
- ³Coutures, J. P., Rifflet, J. C., Billard, D., and Coutures, J., "Contactless Treatments of Liquids in a Large Temperature Range by an Aerodynamic Levitation Device and Laser Heating," *Proceedings of the 6th European Symposium on Materials Science Under Microgravity Condition*, ESA SP-256, European Space Agency, 1987, pp. 427–430.
- ⁴Granier, B., and Heurtault, S., "Method for Measurement of the Density of Liquid Refractories. Application to Alumina and Yttrium Oxide," *Revue Internationale des Hautes Températures et des Réfractaires*, Vol. 20, 1983, pp. 61–67.
- ⁵Weber, J. K. R., Hampton, D. S., Merkley, D. R., Rey, C. A., Zatarski, M. M., and Nordine, P. C., "Aero-Acoustic Levitation: A Method for Containerless Liquid Phase Processing at High Temperatures," *Review of Scientific Instruments*, Vol. 65, No. 2, 1994, p. 456.
- ⁶Glorieux, B., Millot, F., Rifflet, J. C., and Coutures, J. P., "Density of Superheated and Undercooled Liquid Alumina by a Contactless Method," *International Journal of Thermophysics* (to be published).
- ⁷Glorieux, B., Rifflet, J. C., and Millot, F., "The Measurement of the Surface Tension of Liquid Alumina," *Proceedings du 3ème Colloque CNES R&T Ecoulements Internes en Propulsion Solide*, edited by Y. Fabignon and P. Marion, Vol. 2, 1998, pp. 99–107.
- ⁸Barbé, J. C., Parayre, C., Daniel, M., Papoular, M., and Kernevez, N., "High Temperature Containerless Viscosity Measurement by Gas Film Levitation," *International Journal of Thermophysics* (to be published).

⁹Enderby, J. E., Ansell, S., Krishnan, S., Price, D. L., and Saboungi, M. L., "The Electrical Conductivity of Levitated Liquids," *Applied Physics Letters*, Vol. 71, No. 1, 1997, pp. 116–118.

¹⁰Coutures, J. P., Massiot, D., Bessada, C., Echegut, P., Rifflet, J. C., and Taulelle, F., "An Aluminium 27 NMR Study of Liquid Aluminates in the 1600–2000°C Temperature Range," *Comptes Rendus de l'Académie des Sciences de Paris, série II*, Vol. 310, No. 8, 1990, pp. 1041–1045.

¹¹Ansell, S., Krishnan, S., Weber, J. K. R., Felten, J. J., Nordine, P. C., Beno, M. A., Price, D. L., and Saboungi, M. L., "Structure of Liquid Aluminum Oxide," *Physical Review Letters*, Vol. 78, No. 3, 1997, pp. 464–466.

¹²Launay, X., Gautier, N., Ruffier, D., Landron, C., Coutures, J. P., and Bazin, D., "High Temperature EXAFS in Contactless Conditions at the K-edges of Ga and Y in Solid and Liquid $\text{Ln}_3\text{A}_5\text{O}_{12}$ Garnets ($\text{Ln} = \text{Y}$, $\text{A} = \text{Al}$, Ga)," *Comptes Rendus de l'Académie des Sciences de Paris, série IIB*, Vol. 324, No. 8, 1997, pp. 527–535.

¹³Kingery, W. D., "Surface Tension of Some Liquid Oxides and Their Temperature Coefficients," *Journal of the American Ceramic Society*, Vol. 42, No. 1, 1959, pp. 6–10.

¹⁴Maurakh, M. A., Mitin, B. S., and Roitberg, M. B., "Contactless Measurement of the Density and Surface Tension of Liquid Oxides at High Temperatures," *Zavodskaiya Laboratoriya*, Vol. 33, No. 8, 1967, pp. 984, 985.

¹⁵Kirshenbaum, A. D., and Cahill, J. A., "The Density of Liquid Aluminium Oxide," *Journal of Inorganic and Nuclear Chemistry*, Vol. 14, 1960, pp. 283–287.

¹⁶Mitin, B. S., and Nagibin, Y. A., "Density of Liquid Alumina," *Russian Journal of Physical Chemistry*, Vol. 44, No. 5, 1970, pp. 741, 742.

¹⁷Elyutin, V. P., Mitin, B. S., and Annisimov, I. S., "Surface Tension and Density of Aluminium Oxide-Beryllium Oxide Melts," *Neorganicheskie Materialy*, Vol. 9, No. 9, 1973, pp. 1585–1587.

¹⁸Shpil'rain, E. E., Yakimovich, K. A., and Tsitsarkin, A. F., "Experimental Study of the Density of Liquid Alumina up to 2750°C," *High Temperatures High Pressures*, Vol. 5, 1973, pp. 191–198.

¹⁹Ikemiya, N., Umemoto, J., Hara, S., and Ogino, K., "Surface Tensions and Densities of Molten Al_2O_3 , Ti_2O_3 , V_2O_5 and Nb_2O_5 ," *ISIJ International*, Vol. 33, No. 1, 1993, pp. 156–165.

²⁰Rasmussen, J. J., "Surface Tension, Density and Volume Change on Melting of Alumina Systems, Chromia and Samaria," *Journal of the American Ceramic Society*, Vol. 55, No. 6, 1972, p. 326.

²¹Zubarev, Y. V., Kostikov, V. I., Mitin, B. S., Nagibin, Y. A., and Nischeta, V. V., "Properties of Liquid Aluminium Oxide," *Izvestiya Akademii Nauk SSSR, Neorganicheskie Materialy*, Vol. 5, No. 9, 1968, pp. 1563–1565.

²²Wartenberg, H. V., Wehner, G., and Saren, E., "The Density of Molten Alumina," *Nachricht. Gesellschaft und Wissenschaft Goettingen*, Vol. 2, 1936, pp. 73–75.

²³Coutures, J. P., Rifflet, J. C., Florian, P., and Massiot, D., "Studies of the Solidification of Al_2O_3 Without Heterogeneous Nucleation Using Thermal Analysis and ^{27}Al High Temperature NMR: Effects of the Temperature of the Liquid and the Partial Pressure of Oxygen," *Revue Internationale des Hautes Températures et des Réfractaires*, Vol. 29, 1994, pp. 123–142.

²⁴Wartenberg, H. V., Wehner, E., and Saran, E., "The Surface Tension of Molten Aluminum and Lanthanum Oxides," *Nachricht Gesellschaft und Wissenschaft Goettingen*, Vol. 2, 1936, pp. 65–71.

²⁵Elyutin, V. P., Mitin, B. S., and Nagibin, Y. A., "Method for Measuring the Temperature Coefficient of the Surface Tension of Liquid Aluminium Oxide," *Zavodskaiya Laboratoriya*, Vol. 37, No. 2, 1971, pp. 194–196.

²⁶McNally, R. N., Yeh, H. C., and Balasubramanian, N., "Surface Tension Measurements of Refractory Liquids Using the Modified Drop Weight Technique," *Journal of Materials Science*, Vol. 3, 1968, pp. 136–138.

²⁷Rasmussen, J. J., and Nelson, R. P., "Surface Tension and Density of Molten Alumina," *Journal of the American Ceramic Society*, Vol. 54, No. 8, 1971, pp. 398–401.

²⁸Shpil'rain, E. E., Yakimovich, K. A., and Tsitsarkin, A. F., "Surface Tension of Alumina up to 2750°C and the Wetting Angle near the Melting Point," *High Temperatures*, Vol. 11, 1974, pp. 894–900.

²⁹Lihmann, J. M., and Haggerty, J. S., "Surface Tension of Alumina Containing Liquids," *Journal of the American Ceramic Society*, Vol. 68, No. 2, 1985, pp. 81–85.

³⁰Elyutin, V. P., Mitin, B. C., and Nagibin, Y. A., "Properties of Liquid Aluminum Oxide," *Fizika Aerodispersnykh Sistema*, Vol. 7, 1972, pp. 104–109.

³¹Benz, K. W., Cröll, A., and Tegetmeier, A., "A Formula Describing the Temperature Dependence of Surface Tension for Some Semiconductors Melts," *Journal of Crystal Growth*, Vol. 141, No. 3, 4, 1994, pp. 451–455.

³²Lord Rayleigh, "On the Capillary Phenomena of Jets," *Proceedings of the Royal Society of London*, Vol. 29, 1879, pp. 71–97.

³³Bates, J. L., Mcneilly, C. E., and Rasmussen, J. J., "Properties of Molten Ceramics," *Materials Science Research*, Vol. 5, 1971, pp. 11–26.

³⁴Bloomquist, R. A., Fink, J. K., and Leibowitz, L., "Viscosity of Molten Alumina," *American Ceramic Society Bulletin*, Vol. 57, No. 5, 1978, p. 522.

³⁵Urbain, G., "Viscosity of Liquid Alumina," *Revue Internationale des Hautes Températures et des Réfractaires*, Vol. 19, 1982, pp. 55–57.

³⁶Massiot, D., Trumeau, D., Touzo, B., Farnan, I., Rifflet, J. C., Douy, A., and Coutures, J. P., "Structure and Dynamics of CaAl_2O_4 from Liquid to Glass: A High Temperature ²⁷Al NMR Time Resolved Study," *Journal of Physical Chemistry E*, Vol. 99, No. 44, 1995, pp. 16,455–16,459.

³⁷Egry, I., Lohofer, G., Seyhan, I., Schneider, S., and Feuerbacher, B., "Viscosity of Eutectic $\text{Pd}_{78}\text{Cu}_6\text{Si}_{16}$ Measured by the Oscillating Drop Technique in Microgravity," *Applied Physics Letter B*, Vol. 73, No. 4, 1998, pp. 462, 463.

³⁸Elyutin, V. P., Mitin, B. S., Soldatov, E. A., and Anisimov, Y. S., "Coefficient of Aluminium Diffusion in Molten Aluminum Oxide," *Izvestiya Vysshokii Uchebnykh Zavedenii Tsvetn Metallurgiya*, Vol. 17, No. 3, 1974, pp. 60–62.

³⁹Anisimov, Y. S., and Mitin, B. S., "Diffusion Parameters in Liquid Aluminium Oxide," *Izvestiya Akademii Nauk SSSR, Neorganicheskie Materialy*, Vol. 13, 1977, pp. 1442, 1443.

⁴⁰Aleksandrov, V. I., Osiko, V. V., and Tatarintsev, V. M., "Electrical Conductivity of Aluminum Oxide in the Molten State," *Izvestiya Akademii Nauk SSSR, Neorganicheskie Materialy*, Vol. 8, No. 5, 1972, pp. 956, 957.

⁴¹Van Arkel, A. E., Flood, E. A., and Bright, N. F. H., "The Electrical Conductivity of Molten Oxides," *Canadian Journal of Chemistry*, Vol. 31, 1953, pp. 1009–1019.

⁴²Elyutin, V. P., Mitin, B. S., and Nagibin, Y. A., "Electrical Conductivity of Molten Oxides," *Izvestiya Akademii Nauk SSSR, Neorganicheskie Materialy*, Vol. 7, No. 5, 1971, pp. 880, 881.

⁴³Fay, H., "The Electrical Conductivity of Liquid Al_2O_3 (Molten Corundum and Ruby)," *Journal of Physical Chemistry*, Vol. 70, No. 3, 1966, pp. 890–893.

⁴⁴Shpil'rain, E. E., Kagan, D. N., Barkhatov, L. S., and Zhmakin, L. I., "The Electrical Conductivity of Alumina near the Melting Point," *High Temperatures High Pressures*, Vol. 8, No. 2, 1976, pp. 177–181.

⁴⁵Weber, J. K. R., Krishnan, S., Anderson, C. D., and Nordine, P. C., "Spectral Absorption Coefficient of Molten Aluminum Oxide from 0.385 to 0.780 μm ," *Journal of the American Ceramic Society*, Vol. 78, No. 3, 1995, pp. 583–587.

⁴⁶Bober, M., Karow, H. U., and Muller, K., "Study of the Spectral Reflectivity and Emissivity of Liquid Ceramics," *High Temperatures High Pressures*, Vol. 12, 1980, pp. 161–168.

⁴⁷Weber, J. K. R., Nordine, P. C., and Krishnan, S., "Effects of Melt Chemistry on the Spectral Absorption Coefficient of Molten Aluminum Oxide," *Journal of the American Ceramic Society*, Vol. 78, No. 11, 1995, pp. 3067–3071.

⁴⁸Nelson, L. S., Richardson, N. L., Keil, K., and Skaggs, S. R., "Effects of Oxygen and Argon Atmospheres on Pendant Drops of Aluminium Oxide Melted with Carbon Dioxide Laser Radiation," *High Temperature Science*, Vol. 5, No. 2, 1973, pp. 138–154.

⁴⁹Diamond, J. J., and Dragoo, A. L., "Studies of Molten Alumina in the Arc Image Furnace," *Revue Internationale des Hautes Températures et des Réfractaires*, Vol. 3, 1966, pp. 273–279.

⁵⁰Krishnan, S., Weber, J. K. R., Schiffman, R. A., and Nordine, P. C., "Refractive Index of Liquid Aluminium Oxide at 0.6328 μm ," *Journal of the American Ceramic Society*, Vol. 74, No. 4, 1991, pp. 881–883.

III. Motor Interior Ballistics

Effect of Acoustic Oscillation on Flow Development in a Simulated Nozzleless Rocket Motor

Sourabh Apte* and Vigor Yang†

Pennsylvania State University, University Park, Pennsylvania

Nomenclature

A	= chamber cross section
c	= speed of sound
c_s	= Smagorinsky constant
D	= near-wall damping function
\tilde{e}	= filtered total specific energy per unit volume
E	= turbulence energy
f	= frequency, Hz
G	= spatial filter function
$G_{k,u}$	= amplification factor per time step
h	= chamber half-height, m
I	= turbulence intensity, $\sqrt{u'u' + v'v'}$
I_τ	= number of time steps required for one eddy lifetime
k	= wave number, 1/m
L	= chamber length, m
ℓ	= turbulence length scale, m
\dot{m}''	= injection mass flux, kg/m ² s
M	= mean Mach number averaged over a given cross section
M_c	= mean Mach number at centerline
p	= pressure, Pa
Pr	= Prandtl number
q	= large-scale velocity, m/s
Re	= Reynolds number
S_{ij}	= strain-rate tensor, $((\partial u_i/\partial x_j) + (\partial u_j/\partial x_i))/2 - \delta_{ij}(\partial u_k/\partial x_k)/3$

Copyright © 2000 by S. Apte and V. Yang. Published by the American Institute of Aeronautics and Astronautics, Inc., with permission.

*Ph.D. Student, Dept. of Mechanical Engineering.

†Professor, Dept. of Mechanical Engineering. Associate Fellow AIAA.

T	= temperature, K
t	= time, s
u	= axial velocity, m/s
v	= vertical velocity, m/s
v_w	= injection velocity at wall, m/s
γ	= ratio of specific heats
Δ	= filter width
δ_{ij}	= Kronecker delta
δ	= constant in Eq. (25) ≈ 0.0025
ε_a	= amplitude of imposed pressure oscillation
ε_v	= artificial dissipation coefficient
η	= Kolmogorov length scale, m
κ	= thermal conductivity, W/mK
μ	= dynamic viscosity, kg/ms
ν	= kinematic viscosity, m ² /s
ν_s	= subgrid-scale kinematic viscosity, m ² /s
ρ	= density, kg/m ³
σ	= CFL number
τ	= viscous shear stress, N/m ²
ξ	= grid parameter for LES

Subscripts

b	= bulk mean quantity
c	= centerline
w	= wall

Superscripts

'	= fluctuating component due to turbulence
a	= fluctuating component due to imposed acoustic oscillation
r	= resolved-scale component
s	= subgrid-scale component
\sim	= density-weighted quantity
$-$	= time-averaged quantity

I. Introduction

MUCH of the research in the field of solid rocket propulsion has been directed toward establishing a clear understanding of the combustion instability phenomenon.¹ In an effort to study the detailed coupling between propellant combustion dynamics and local flow oscillations in rocket motors, Yang and coworkers²⁻⁵ conducted a series of numerical studies of homogeneous propellant combustion under conditions representative of practical propulsive systems. Much information has been obtained about the flame structure, heat release mechanism, propellant combustion response, and flow development. In spite of these contributions to the knowledge base on combustion instability, however, existing models provide limited information concerning propellant burning behavior in oscillatory turbulent crossflows. Specifically, the interactions among the mean, acoustic, and turbulent flowfields, and their collective effect on propellant combustion dynamics and motor stability behavior, need to be addressed comprehensively.

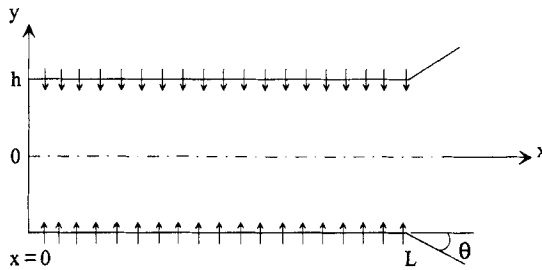


Fig. 1 Schematic diagram of a simulated nozzleless rocket motor.

As an attempt to address these fundamental issues, the present work concentrates on the effect of acoustic oscillation on the flow development in a simulated nozzleless solid rocket motor, as shown schematically in Fig. 1. The evolution of the propellant combustion products in the chamber is simulated by the mass injection through the porous walls. The oscillatory field in a rocket motor consists of three distinct types of waves: acoustic (corresponding to irrotational, compressible flow motions), vortical (arising from rotationality of unsteady flow), and entropy (due to unsteady heat release and viscous dissipation) modes. The three waves, along with the transient combustion response of propellant, collectively dictate the chamber flame dynamics and subsequently the motor stability behavior. Turbulence plays a decisive role in determining the wave characteristics through its influence on the momentum and energy transfer in various parts of the chamber. In particular, the interactions between organized oscillatory motions and random turbulent fluctuations give rise to additional mechanisms of energy production, transfer, and dissipation in the flowfield. These phenomena were studied separately only for simplified configurations in the past. Little effort was made to address their collective effect, especially under conditions representative of real rocket motor environments.

The injection-driven flow in a rocket motor is significantly different from a pipe flow with surface transpiration, because the combustion chamber is closed at the head end. The flowfield is essentially established through a balance between the pressure gradient and inertial forces, in contrast with a pipe flow, wherein the velocity profiles are determined by a balance between viscous and pressure forces. An analytical solution for this category of flows was first developed by Taylor⁶ and later validated by Culick,⁷ revealing a cosine distribution for the axial velocity in the vertical direction. A theoretical analysis of inviscid, rotational, and compressible flowfield in a porous duct with the injection rate varying with local pressure was carried out by Balakrishnan et al.⁸ The effect of fluid compressibility in flattening the radial profile of the axial velocity, in a manner analogous to that arising from turbulence in flows without surface transpiration, was established. Traineau et al.⁹ performed an experimental study of the internal flowfield in a simulated nozzleless rocket motor, indicating three regimes of flow development. The velocity field develops in accordance with laminar flow theory in the upstream region and undergoes turbulence transition in the middle section of the chamber. Transition of the mean axial velocity profile occurs farther downstream, where there appears a fully developed turbulent flowfield with surface mass injection. The experiments were carried out at a high injection Reynolds number (15×10^3)

and elucidated the compressibility effect on the mean velocity profile. Dunlap et al.¹⁰ conducted measurements of flow properties in a cylindrical chamber at low injection Mach numbers (0.0018 and 0.0036). The corresponding injection Reynolds numbers (9×10^3 and 18×10^3) were typical of rocket motor values. The compressibility effect was not observed because of the low Mach number condition. Beddini¹¹ simulated turbulent flows in porous-walled ducts at large injection Reynolds numbers by means of the Reynolds-stress turbulence model. The presence of turbulence fluctuations at the surface, termed "pseudo-turbulence," was noted. Sabnis et al.¹² used conventional single-point turbulence closure schemes to simulate the flowfields in a rocket motor.

Considerable effort has been expended in studying the interactions between acoustic fluctuations and motor internal flows. Flandro^{13,14} established the first analytical model dealing with unsteady vorticity transport in a rocket motor that arises from longitudinal acoustic motions. The work concentrates on cold-flow simulations of laminar flowfields. Vuillot¹⁵ studied the vortex-shedding phenomenon in segmented rocket motors. The unstable-mode frequencies and pressure levels were accurately predicted using a numerical approach. In real rocket environments, turbulence often occurs and exercises strong influence on the gas-phase flow/flame structures and consequently the propellant combustion response. Cai and Yang¹⁶ employed a modified two-layer turbulence closure scheme to investigate the two-phase flow interactions with longitudinal acoustic waves. Roh et al.¹⁷ treated the gas-phase flame dynamics and its coupling with the condensed-phase processes in a turbulent flow environment, following a similar approach of turbulence closure. In spite of their common use and ability to provide useful information, the second-order turbulence closure schemes usually overpredict turbulent flow properties in rocket motors and fail to offer in-depth knowledge of flow evolution. The use of ad hoc assumptions in these models renders them unsuitable for studying unsteady motor internal flows.

High-level turbulence closure schemes based on large-eddy-simulation (LES) techniques provide a new avenue for studying motor internal flows. Although the computational effort required is enormous, this method allows for a comprehensive investigation of the turbulence effect. Piomelli¹⁸ performed an LES analysis of the injection-driven flow in a porous chamber. His work focused on the development of wall-layer models suited for numerical calculations. Liou et al.¹⁹ conducted a two-dimensional LES to achieve a better prediction of turbulence intensity and axial velocity profiles compared with the second-order turbulence closures. The deficiency in applying the wall-function method to injection-driven flows was advocated by demonstrating that the mean velocity profiles away from the viscous sublayer vary along the chamber and cannot be collapsed into a unique universal wall law. The work was recently extended by considering the effect of turbulence intensity at the injection surface on the turbulence evolution.²⁰ In spite of the considerable work conducted in this area, a comprehensive understanding of the physical processes occurring within the motor remains lacking. In particular, the mutual coupling between acoustic and turbulent flow motions needs to be explored.

This chapter attempts to study the internal flowfield in a simulated nozzle-less rocket motor with acoustic excitations. The approach is based on the LES technique. The contribution of large energy-carrying structures to momentum and energy transfer is computed exactly with the effect of small scales of turbulence modeled semiempirically. Various underlying fluid-dynamic mechanisms responsible for driving unsteady motions in a motor are studied. Owing to the limitations of the computational resources and the two-dimensionality of the chamber, a

two-dimensional analysis is carried out herein to provide useful insight into the complex flowfield with acoustic excitation. The present work lacks the vortex-stretching phenomenon commonly observed in turbulent flows but allows for unpredictability and rapid mixing with enhanced momentum and mass transfer, the essential features of turbulent flows. Compared with conventional second-order closure schemes, which are based on ad hoc hypotheses, the present work marks an improvement in predicting turbulence characteristics. A complete three-dimensional simulation is required further to improve and corroborate the results and will be presented in subsequent publications.

In the following sections, a complete theoretical formulation of the motor internal flow is summarized, with a brief description of the numerical implementation. The work starts with calculations of the motor internal flowfield under stationary conditions. Periodic oscillations are then imposed at the head end to simulate traveling acoustic waves in the chamber. The main objectives of the present study are 1) to investigate the internal flowfield in a simulated rocket motor with surface injection, 2) to study the coupling between the imposed periodic fluctuations and turbulent motions, and 3) to explore the energy exchange and turbulence production mechanisms under nonstationary mean flow conditions.

II. Theoretical Formulation

Figure 1 shows the physical model for the problem, which simulates the flow development in a nozzleless solid-propellant rocket motor studied experimentally by Traineau et al.⁹ The chamber is closed at the head end and is connected downstream with a choked divergent nozzle at the exit. Air is injected uniformly through the porous wall to simulate the evolution of propellant combustion products from the surface. The flow accelerates from zero at the head end and becomes supersonic in the nozzle section. The flowfield is governed by the following conservation equations of mass, momentum and energy,²¹

$$\frac{\partial \rho}{\partial t} + \frac{\partial(\rho u_k)}{\partial x_k} = 0 \quad (1)$$

$$\frac{\partial(\rho u_k)}{\partial t} + \frac{\partial(\rho u_k u_l)}{\partial x_l} = -\frac{\partial p}{\partial x_k} + \frac{\partial \sigma_{kl}}{\partial x_l} \quad (2)$$

$$\frac{\partial(\rho e)}{\partial t} + \frac{\partial(\rho h u_k)}{\partial x_k} = \frac{\partial q_k}{\partial x_k} + \phi \quad (3)$$

where ρ is the density, u the velocity vector, p the thermodynamic pressure, h the total specific enthalpy, e the total specific internal energy, and T the temperature. The standard tensor notation with repeated indices implying summation over the axial and vertical components is used. The viscous stress σ_{kl} , the thermal diffusion q_k , and the viscous dissipation ϕ are defined as

$$\sigma_{kl} = -\frac{2}{3}\mu \frac{\partial u_j}{\partial x_j} \delta_{kl} + \mu \left(\frac{\partial u_k}{\partial x_l} + \frac{\partial u_l}{\partial x_k} \right) \quad (4)$$

$$q_k = k \frac{\partial T}{\partial x_k} \quad (5)$$

$$\phi = -\frac{2}{3}\mu \left(\frac{\partial u_k}{\partial x_k} \right)^2 + \mu \left(\frac{\partial u_k}{\partial x_l} + \frac{\partial u_l}{\partial x_k} \right) \frac{\partial u_k}{\partial x_l} \quad (6)$$

where μ is the dynamic viscosity and k the thermal conductivity. The governing equations are supplemented with the equation of state for an ideal gas

$$p = \rho RT \quad (7)$$

where R is the gas constant. The thermodynamic properties are assumed constant for the present case of cold-flow simulation, as the temperature variation within the flowfield of interest is not significant.

Turbulence closure is obtained based on the large-eddy simulation technique in which large, energy-carrying structures are computed exactly and the effect of small-scale motions on large scales is modeled. A spatial filter G is used to decompose the flow variables into large (resolved) and subgrid (unresolved) scales,²²

$$\mathfrak{Z}(\mathbf{x}, t) = \mathfrak{Z}^r(\mathbf{x}, t) + \mathfrak{Z}^s(\mathbf{x}, t) \quad \text{with} \quad \mathfrak{Z}^r(\mathbf{x}, t) = \int_D G(\mathbf{x} - \mathbf{x}', \Delta) \mathfrak{Z}(\mathbf{x}', t) d^3x' \quad (8)$$

where D is the entire domain; Δ the computational mesh size, which determines the size and structure of the unresolved scales; and \mathfrak{Z} any flow property, viz., ρ , p , u_i , or T . The superscripts r and s represent the resolved and unresolved scales of flow properties. The Favre averaging is further used to simplify the governing equations for compressible turbulent flow simulations.²² This density-weighted averaging eliminates complex triple correlations between density and velocity fluctuations in the governing equations and is given as

$$\tilde{\mathfrak{Z}}^r = \frac{(\rho \mathfrak{Z})^r}{\rho^r} \quad (9)$$

Contrary to the more traditional Favre time averaging,²³

$$\tilde{\mathfrak{Z}}^r \neq \tilde{\mathfrak{Z}}^r, \quad \tilde{\mathfrak{Z}}^s \neq 0 \quad (10)$$

The filtered form of the governing equations can be written as

$$\frac{\partial \rho^r}{\partial t} + \frac{\partial (\rho^r \tilde{u}_k^r)}{\partial x_k} = 0 \quad (11)$$

$$\frac{\partial (\rho^r \tilde{u}_k^r)}{\partial t} + \frac{\partial (\rho^r \tilde{u}_k^r \tilde{u}_l^r)}{\partial x_l} = -\frac{\partial p^r}{\partial x_k} + \frac{\partial \sigma_{kl}^r}{\partial x_l} + \frac{\partial \tau_{kl}}{\partial x_l} \quad (12)$$

$$\frac{\partial (\rho^r \tilde{e}^r)}{\partial t} + \frac{\partial (\rho^r \tilde{h}^r \tilde{u}_k^r)}{\partial x_k} = \frac{\partial q_k^r}{\partial x_k} - \frac{\partial Q_k}{\partial x_k} - \frac{\partial (\rho^r \overline{\tilde{u}_l^r \tilde{u}_l^r \tilde{u}_k^r})}{\partial x_k} + \phi^r \quad (13)$$

where $p^r = \rho^r R \tilde{T}^r$ and $\overline{(\quad)}$ represents the filtering operation defined by Eq. (8). σ_{kl}^r and ϕ^r represent the viscous stresses and dissipation of the resolved scales, respectively. The terms τ_{kl} and Q_k are the subgrid-scale (sgs) stresses and heat fluxes, respectively, and are given as

$$\tau_{kl} = -\rho^r \left(\overline{(\tilde{u}_k^r \tilde{u}_l^r)} - \overline{\tilde{u}_k^r} \overline{\tilde{u}_l^r} \right) + \left(\overline{u_k^s \tilde{u}_l^r} + \overline{\tilde{u}_k^r u_l^s} - \overline{\tilde{u}_k^s} \overline{\tilde{u}_l^s} - \overline{\tilde{u}_k^s} \overline{\tilde{u}_l^s} \right) + \left(\overline{u_k^s u_l^s} - \overline{u_k^s} \overline{u_l^s} \right) \quad (14)$$

$$Q_k = C_p \rho^r \left(\overline{(\tilde{u}_k^r \tilde{T}^r - \tilde{u}_k^r \tilde{T}^r)} + (\overline{u_k^s \tilde{T}^r} + \overline{\tilde{u}_k^r T^s} - \overline{\tilde{u}_k^r \tilde{T}^s} - \overline{\tilde{u}_k^s \tilde{T}^r}) \right. \\ \left. + (\overline{u_k^s T^s} - \overline{\tilde{u}_k^s \tilde{T}^s}) \right) \quad (15)$$

The first terms in the small parentheses in Eqs. (14) and (15) can be computed directly once a filter function is defined. The other terms need to be modeled and represent the effect of unresolved scales on the resolved scales of motion. One important feature of any *sgs* model is to provide adequate dissipation. Here, dissipation means transport of energy from resolved scales to unresolved subgrid scales, and the rate of dissipation represents the flux of energy through the inertial subrange of the turbulence spectrum.²⁴ A Smagorinsky model extended to compressible flows is used to model these terms, as suggested by Erlebacher et al.²² Accordingly, the *sgs* terms are modeled by relating the *sgs* stresses to the large-scale strain-rate tensor S_{kl}^r , through the eddy viscosity (ν_T) and the *sgs* kinetic energy (K), as follows:

$$\tau_{kl} - \frac{2}{3} \delta_{kl} K = -2\nu_T \rho^r S_{kl}^r \quad (16)$$

$$S_{kl}^r = \frac{1}{2} \left(\frac{\partial \tilde{u}_k^r}{\partial x_l} + \frac{\partial \tilde{u}_l^r}{\partial x_k} \right) - \frac{1}{3} \delta_{kl} \left(\frac{\partial \tilde{u}_i^r}{\partial x_i} \right) \quad (17)$$

with

$$\nu_T = c_D (D\Delta)^2 (2S_{ij}^r S_{ij}^r)^{\frac{1}{2}} \quad \text{and} \quad K = c_I \rho^r (D\Delta)^2 (2S_{ij}^r S_{ij}^r) \quad (18)$$

where Δ is the average size of the computational cell, and c_D (≈ 0.01) and c_I (≈ 0.007) are the model constants, based on the work of Erlebacher et al.²² The Van-Driest damping function (D) is used to take into account the inhomogeneities near the surface^{20,21} and is expressed as

$$D = 1 - \exp(1 - (y^+)^3 / 26^3) \quad (19)$$

where $y^+ = y \tilde{u}_\tau^r / \nu$. The effect of surface transpiration is indirectly obtained through the wall shear stress τ_w^r , which appears in the computation of the friction velocity \tilde{u}_τ^r . The heat flux is modeled similarly by defining an eddy diffusivity and relating it to the viscosity through the turbulent Prandtl number (Pr_T).

$$Q_k = -\rho^r C_p \frac{\nu_T}{Pr_T} \frac{\partial \tilde{T}^r}{\partial x_k} \quad (20)$$

A standard value of 0.7 is used for the turbulent Prandtl number based on air as the medium.²²

Boundary conditions. The method of characteristics is used to specify the boundary conditions. For the subsonic inflow through the porous surface, three conditions need to be specified. The mass and energy fluxes are kept constant and the injection velocity is assumed to be vertical (i.e., $\tilde{u}^r = 0$). At the head end of the motor, the gradients of axial pressure and vertical velocity are set to zero, along with the adiabatic condition. Application of the slip condition at the head

end is necessary to avoid a numerically induced recirculating flow at the injection surface.²⁵ Symmetry conditions are applied along the centerline of the motor. The supersonic outflow requires no boundary conditions, according to the method of characteristics. The flow variables at the exit are extrapolated from those within the computational domain.

After a stationary flow is obtained, traveling acoustic motions in the motor are simulated by imposing periodic pressure and velocity oscillations at the head end as follows:

$$p^a = \varepsilon_a \bar{p} \sin(2\pi ft) \quad (21)$$

$$u^a = \bar{p}/(\bar{\rho} \bar{a}) \quad (22)$$

where the overbar denotes the time-averaged quantity, and ε_a and \bar{a} represent the percentage of the mean pressure and speed of sound, respectively. No phase difference exists between the pressure and the velocity fluctuations for such a simple wave. The temperature fluctuation is specified according to the isentropic relationship with the pressure.

$$T^a = \bar{T}(1 + p^a/\bar{p})^{(\gamma-1/\gamma)} - \bar{T} \quad (23)$$

III. Numerical Method and Error Analysis

An accurate numerical scheme is essential for resolving various time and length scales of turbulent motions. The issue of a priori estimation of computational errors in turbulence simulations has recently been addressed by several researchers.^{26,27} Ghosal²⁶ analyzed the truncation errors of the various terms in finite-difference equations and compared the contributions of the errors at a given time with the exact terms for incompressible flow equations. A model turbulence spectrum was employed to facilitate the comparison. Results indicated that for finite-difference methods the errors created by approximating the convection terms generally dominate errors introduced by other terms in the governing equation. These convection terms are important in any turbulence computation at large Reynolds numbers, as they represent the dominance of inertial force over viscous force. Fabignon et al.²⁷ and Beddini et al.²⁸ extended the von Neumann stability analysis^{29,30} to assess the importance of the errors associated with convection terms by introducing a reference spectrum obtained from homogeneous, isotropic turbulence theory. This energy spectrum was convected in accordance with the amplification factor of the numerical scheme and then compared with the initial spectrum after one large-eddy lifetime. An estimation of the numerical errors of nonlinear convection terms was made. The fourth-order Runge–Kutta scheme with the sixth-order Padé compact differencing for spatial discretization (RK4-6CP) was shown to resolve the turbulence energy spectrum in the inertial range for a wide range of Mach numbers. A significant reduction in computational time, compared with RK4-6CP, can be achieved by means of an alternative Runge–Kutta scheme presented by Jameson,³¹ which is fourth-order accurate in time and uses fourth-order central differencing in space (RK4-4C). It was shown by Beddini et al.²⁸ that the RK4-4C scheme resolves the energy spectrum with an accuracy comparable to that of the sixth-order Padé scheme over a wide range of Mach numbers. The compromise between

computational time and spatial accuracy facilitates the use of Jameson's method in the present study.

Following the analyses by Fabignon et al.²⁷ and Beddini et al.,²⁸ the effect of computational errors on *sgs* modeling is investigated herein based on the Smagorinsky subgrid eddy-viscosity model. The work extends the previous effort to incorporate the effects of *sgs* models and artificial dissipation, introduced in central-difference schemes for numerical stabilization, on the convection of the turbulence energy spectrum. A thorough investigation is carried out for the RK4-4C method. The transport equation for the energy spectrum function $E(k, t)$ for turbulent flows can be expressed as²⁸

$$\frac{\partial}{\partial t} E(k, t) + (\bar{u}_k)_{AB} \left(\frac{\partial}{\partial x_k} \right)_{AB} E(k, t) = T(k, t) - D(k, t) - P(k, t) \quad (24)$$

where $T(k, t)$ represents the energy transfer between wave numbers, $D(k, t)$ the viscous dissipation, and $P(k, t)$ the production term. A and B represent the points in the flowfield for two-point correlation. For stationary flows, the first term on the left-hand side is zero, and if homogeneity is assumed, the convective term also vanishes. Retention of the convective terms for spectral transport enables the present estimation of convection errors. Convection of the energy spectrum is assumed to take place at a constant mean velocity \bar{u}_k . The main objective of this work is to utilize a representative turbulence spectrum, obtained from the model of the transfer, dissipation, and production terms in the preceding equation, to allow for the estimation of the effectiveness of a numerical scheme. The initial kinetic energy spectrum is introduced using Tennekes and Lumley's analysis.³² It models the production-dominated part of the spectrum at low wave numbers, representing large, energy-carrying structures, and provides the classical $k^{-5/3}$ power law in the inertial subrange, representing equilibrium turbulence. The dimensionless spectrum of turbulent energy is given as²⁸

$$E(k, 0) = \alpha(\delta Re_c)^{-5/4} (k\eta)^{-5/3} \times \exp(-1.5\pi\beta\sqrt{\alpha}(\delta Re_c)^{-1} (k\eta)^{-4/3}) \quad (25)$$

where α is the Kolmogorov constant and η the Kolmogorov length scale. Experimental data show that α and β are 1.5 and 0.3, respectively.^{27,28} An order-of-magnitude estimate relates the turbulent Reynolds number (Re_t) and the Reynolds number at the centerline of the motor (Re_c),

$$Re_t \approx \delta Re_c \quad (26)$$

where $\sqrt{\delta} \approx q/U \approx \ell/L$.

Convection of the initial energy spectrum depends on the numerical scheme and takes the form

$$E(k, \tau) = |G_{k,u}|^{I_\tau} E(k, 0) \quad (27)$$

where $G_{k,u}$ is the amplification factor obtained from the eigenvalue u of the numerical scheme. I_τ is the number of time steps required to reach one eddy lifetime τ , which depends on the grid size and the CFL number σ :

$$I_\tau = \delta^{1/4} \frac{(M+1)}{\xi M \sigma} Re_c^{3/4} \quad (28)$$

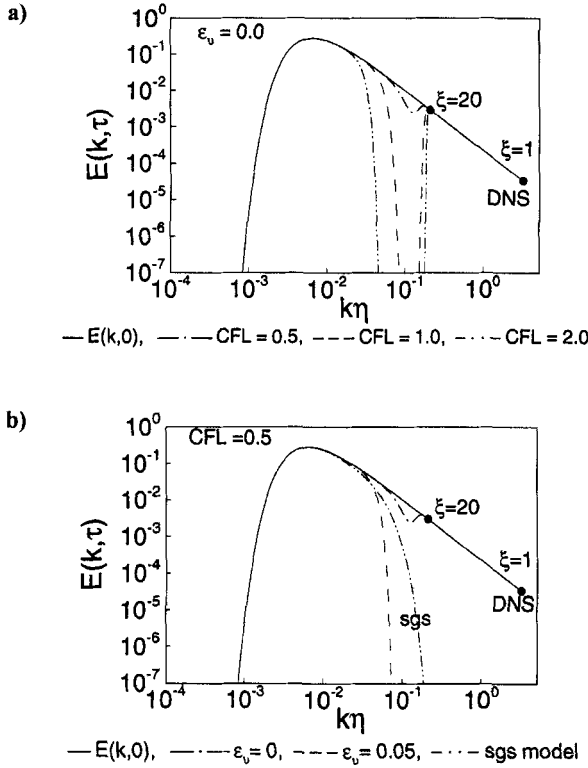


Fig. 2 Dimensionless turbulent energy spectrum of the RK4-4C scheme with $\xi = 20$: a) effect of CFL number for $\epsilon_v = 0$; b) effect of artificial dissipation and *sgs* model for $CFL = 0.5$.

where ξ is the grid parameter ($\Delta x/\eta$). This approach provides a basis for selection of grid size for large-eddy simulation, which requires the cutoff wavenumber to be in the inertial range of the energy spectrum.

Figure 2a shows the spectrum for the RK4-4C scheme for various CFL numbers after one eddy lifetime, at a representative motor condition of $Re_c = 3 \times 10^5$ and $M_c = 0.5$. No artificial dissipation is considered in this analysis, i.e., $\epsilon_v = 0$. The grid parameter ξ of unity implies that the entire range of turbulence scale, up to the Kolmogorov length scale, is modeled as in a direct numerical simulation (DNS). ξ usually varies between 10 and 50 for typical large-eddy simulations and is approximately 15 in the present computation. A decrease in ξ shifts the cutoff point toward the DNS value. $\xi = 20$ is used here to illustrate the range of scale resolved in LES compared with DNS. The numerical scheme becomes neutrally stable at the maximum wave number and the spectrum rises to the cutoff point, as shown in Fig. 2a. An increase in the CFL number reduces the resolution of the energy spectrum owing to the reduction in the cutoff wave number. Since the computational time is inversely proportional to the CFL number, a CFL number of 0.5 is found to be a good compromise between accuracy and computational time.

Artificial dissipation is required to reduce the amplification factor and stabilize the numerical scheme at high wave numbers. Figure 2b shows the effect of the sixth-order artificial dissipation and Smagorinsky's *sgs* model on convection of the energy spectrum. The eddy-viscosity hypothesis gives an estimate of the energy spectrum evolution as³³

$$E(k, \tau) = E(k, 0) \exp\left(-2(k\eta)^2 \sqrt{\delta Re_c} \left(1 + \frac{\nu_T}{\nu}\right)\right) \quad (29)$$

where the eddy viscosity (ν_T) is obtained from the *sgs* model as

$$\frac{\nu_T}{\nu} = 4.11 c_s^2 (\sqrt{\alpha} \beta)^{\frac{1}{4}} \xi^{4/3} \quad (30)$$

The artificial dissipation and *sgs* dissipation are of the same order in the present case, as evidenced in Fig. 2b. Ragab and Sheen³⁴ indicate that the dissipation mechanism in a three-dimensional turbulence simulation is very different from the artificial dissipation, because of the vortex stretching and rolling phenomena. Liou et al.²⁰ showed in their two-dimensional simulation of injection-driven flows that *sgs* stresses have negligible effects on the turbulence characteristics and the artificial dissipation introduced by the numerical scheme can serve as an *sgs* model. The study partly provides a justification for not incorporating *sgs* models and relying on numerical artificial dissipation to produce the *sgs* effect on large energy-carrying structures. Accordingly, the *sgs* terms are neglected herein to save computational effort.

Owing to the enormous computational effort required, only two-dimensional calculations are performed in the present work to study the interactions between acoustic oscillations and motor flow evolution. The analysis, in spite of the lack of a vortex-stretching mechanism, is more accurate than conventional models based on second-order turbulence closure schemes and allows for a systematic investigation into the oscillatory flowfields in a rocket motor. Results will be further corroborated in a subsequent study using full three-dimensional large-eddy simulations.³⁵

IV. Stationary Flowfield

The analysis described above is used to first study the flow development in a simulated nozzleless rocket motor, as shown schematically in Fig. 1. The chamber is two-dimensional and measures 48 cm in length and 2 cm in height. The nozzle at the exit is 3.2 cm long, with a divergence angle of 15 deg. The configuration and the flow parameters studied are based on the experiment of Traineau et al.⁹ Air is injected through the porous surface at a total temperature of 260 K and a total pressure of 3.142 atm. The mean injection mass flux is kept constant at $\bar{m}'' = 13 \text{ kg/m}^2\text{s}$, giving the injection velocity of 3.1 m/s. The numerical calculation is initialized with the analytical velocity profile for an inviscid incompressible flow with surface mass injection,^{6,7}

$$\frac{\bar{u}^r}{\bar{u}_c^r} = \cos\left(\frac{\pi}{2} \frac{y}{h}\right) \quad (31)$$

where the subscript *c* represents the centerline. White noise is introduced in the inflow mass flux to perturb the mean flow for turbulence transition. The magnitude of perturbation is 90% of the mean quantity, as indicated by Traineau et al.⁹ Such a

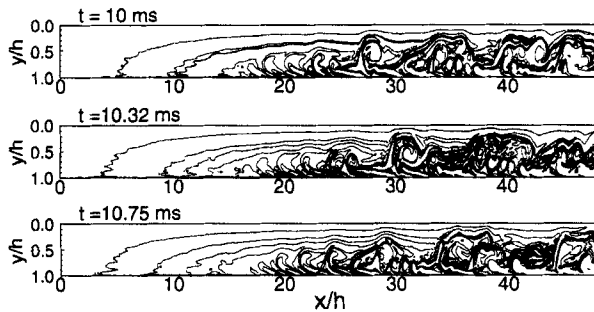


Fig. 3 Time evolution of the vorticity field.

high level of turbulence intensity at the surface is employed to facilitate comparison with experimental data. The computational domain consists of 640×100 cells in the axial and vertical directions, respectively. A uniform grid is used in the x -direction, while the grid is stretched toward the surface in the y -direction with the smallest grid size of the order of $50 \mu\text{m}$. The grid size is based on the studies of Liou et al.^{19,20} and resolves the energy spectrum in the inertial subrange, as shown later. The CFL number is 0.5 and the time step is fixed at 5×10^{-8} s for time-accurate simulations. An outbreak of turbulence occurs at 4–5 ms of the physical time starting from the flow initialization based on Eq. (31). Stationary oscillations are obtained during 8–20 ms, and the mean flow properties are evaluated in this time zone.

A. Vorticity Field

Figure 3 shows the temporal evolution of the vorticity field. To facilitate discussion, only the lower half of the chamber is presented, where $y/h = 1$ corresponds to the injection surface. Vorticity is produced at the propellant surface because the no-slip condition causes the flow to enter the chamber vertically and then turn to align smoothly with the axial axis.^{13,14} Near the head end, turbulent fluctuations appear to be small and the flow is mostly laminar. Transition to turbulence occurs around $x/h = 20$ –25, and the flow becomes highly turbulent farther downstream. Vorticity is rapidly convected away from the surface in this inertia-dominated flow, as evidenced by the presence of large energy-carrying structures. The present two-dimensional computation lacks the vortex-stretching phenomenon responsible for the transfer of energy from the large to the small scales through the energy cascade mechanism and, consequently, leads to lower dissipation and production rates. Nevertheless, it provides much useful insight into the flow development, which was not previously available using second-order turbulence closure schemes.

B. Mean Flow Properties

Figure 4 shows the contour plots of the time-averaged Mach number, pressure, and density fields. The exit Mach number of 2.2 agrees well with the analytical value for an isentropic flow through a divergent nozzle with a known area ratio and given stagnation pressure and temperature upstream. The pressure field is basically one-dimensional, due to the small injection Mach number, with increasing gradient

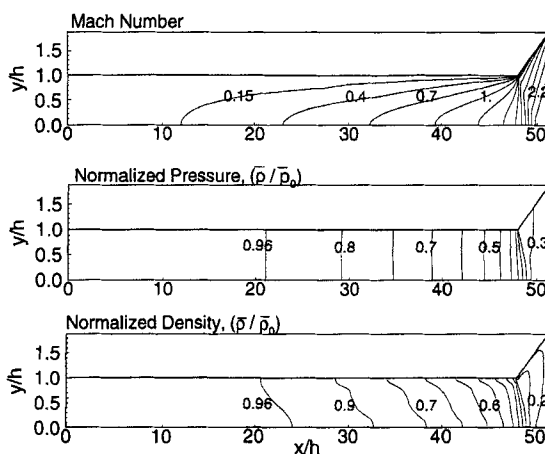


Fig. 4 Contour plots of mean Mach number, pressure, and density.

toward the throat area. Figures 5 and 6 show the axial and vertical variations of the mean axial velocity, respectively. Also included is the analytical solution for an incompressible laminar flow.^{6,7} Good agreement with the experimental data of Traineau et al.⁹ is obtained. The flow is predominantly incompressible and laminar in the upstream region of the chamber. Deviation from the incompressible-flow solution starts between $x/h = 20$ and 30, due to the increasing Mach number and hence the compressibility effect. In the present study, the injection mass flux is kept constant. As a result of rapidly decreasing density toward the throat area, the local flow velocity increases and leads to changes in the velocity profile from its incompressible-flow counterpart. The enhanced momentum transfer due to turbulence also plays an important role. The transition of the mean velocity profile can be characterized in terms of the momentum flux coefficient β , as proposed by Huesmann and Eckert,³⁶

$$\beta = \frac{\int_0^h \bar{\rho} \bar{u}^2 dy}{\bar{\rho}_b \bar{u}_b^2 h} \quad (32)$$

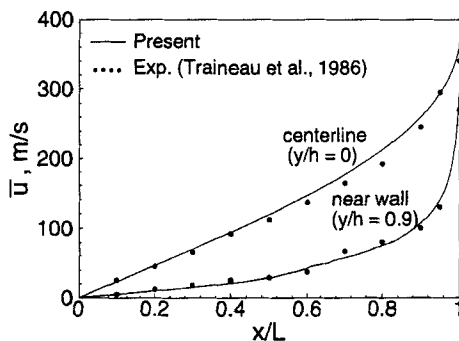


Fig. 5 Variations of mean axial velocity in the axial direction.

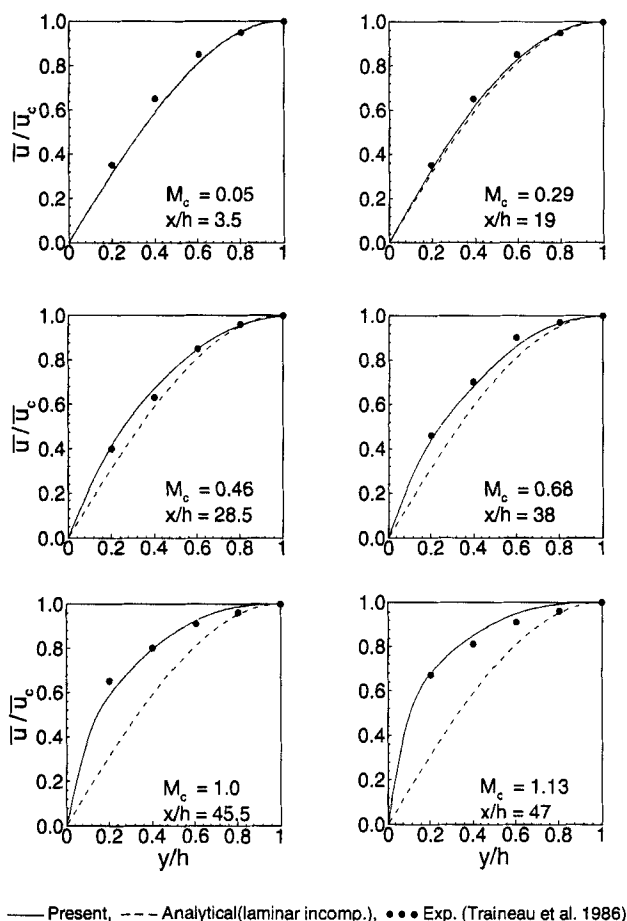


Fig. 6 Variations of normalized mean axial velocity in the vertical direction.

where the subscript b denotes the bulk mean quantity, obtained by averaging the corresponding flow property over a given cross section of the chamber. Figure 7 compares the calculated β with experimental data.⁹ The momentum flux coefficient has a constant value of 1.234 for laminar incompressible flow and can be obtained using Eqs. (31) and (32). The decreasing density and increasing injection velocity toward the nozzle alter the vertical variation of the axial velocity and consequently cause an accelerated decrease in the β value in the downstream region. The experimental value of β at the head end is 1.16 instead of 1.234 as predicted by laminar flow theory, because of the high level of turbulence at the porous wall generated in the experiments.⁹ The agreement of the calculated β in the upstream region with laminar flow theory implies uncertainties in the experimental measurements. Both the numerical and the experimental data show faster variation between $x/h = 20$ and 30 in the turbulent regime. These results are very similar to those obtained by Beddini¹¹ for an axisymmetric duct with a low level of pseudo turbulence at the porous wall.

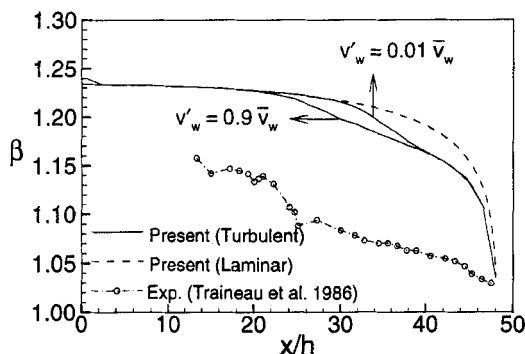


Fig. 7 Variation of momentum flux coefficient in the axial direction.

The effect of surface-generated turbulence on the flow development is also studied. For a high level of wall turbulence (i.e., $v'_w = 0.9\bar{v}_w$), transition of the mean velocity profile occurs upstream of the motor ($x/h = 20$). The transition point shifts downstream ($x/h = 30$) with a lower level of pseudo turbulence (i.e., $v'_w = 0.01\bar{v}_w$) and agrees well with the results of Liou et al.,²⁰ indicating the influence of turbulence on the mean velocity field. Farther downstream ($x/h > 42$), the flowfield is dominated by compressibility effects, and the variation of β closely follows that predicted by laminar compressible-flow theory.

C. Turbulence Energy Spectrum and Transport Properties

To make use of the equilibrium hypothesis generally employed in *sgs* models for estimating the effect of unresolved scales on large-scale structures, the cutoff wave number for turbulence computation should lie in the inertial subrange of the turbulence energy spectrum. This is verified from the energy spectra of the axial velocity fluctuation at various locations, as shown in Fig. 8. The standard 5/3 law of energy spectrum based on the Kolmogorov–Obukhov theory may not be observed in the present two-dimensional simulation. Lesieur et al.^{37,38} indicate in their two-dimensional computation of a temporal mixing layer that the exponent of the wavenumber in the inertial subrange of the turbulence energy spectrum is close to -4 . Gilbert³⁹ proposed that the kinetic energy spectrum results from spiral vortex distributions within the coherent vortices and should follow the $f^{-11/3}$ law, where f is frequency. Figure 8 indicates that the spectrum in the inertial subrange lies between the f^{-3} and the f^{-4} variations. The result ensures that the energy spectrum is well captured in the present computation throughout the chamber, which further confirms the adequacy of the computational grid.

Figures 9a through d show the vertical variations of turbulence intensity ($I = \sqrt{u'^2 + v'^2}$), $\sqrt{u'u'}$, $\sqrt{v'v'}$, and the Reynolds stress ($\overline{u'v'}$) at various axial locations, respectively. The measured turbulence intensity and Reynolds stress⁹ are also included for comparison. The peak in the turbulence intensity increases rapidly and shifts toward the porous wall farther downstream. Since the mass influx is kept constant in the present study, the density decreases and injection velocity increases as the flow accelerates toward the throat. The increasing injection velocity tends to reduce the wall-damping effect, and therefore little change in the vertical

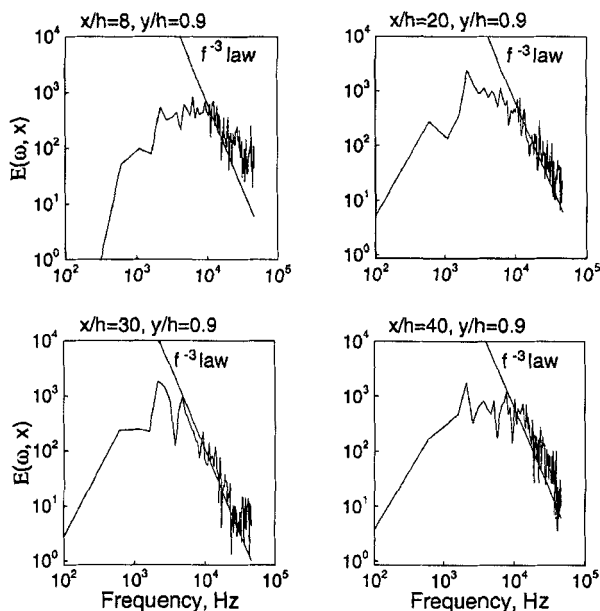


Fig. 8 Turbulence energy spectrum of axial velocity fluctuations at various axial locations.

location of turbulence intensity peak occurs beyond $x/h = 35$. Figures 9b and c show the relative contribution of the axial and radial velocity fluctuations to the turbulence intensity. The internal flowfield is dominated by the strain rates in the axial direction, causing a higher intensity in the axial component. The underprediction of the Reynolds stress may be attributed to the lack of vortex stretching mechanism in the present two-dimensional simulation. The turbulent energy is transferred from large energy-carrying eddies to smaller scales through the energy cascade and is finally dissipated at the molecular level through vortex stretching. The production mechanism in real turbulence is different from that in a two-dimensional simulation, because of the additional spanwise direction. The present approach represents an improvement, however, compared with the conventional two-equation models, which do not predict the Reynolds stress and overpredict the turbulence intensity level.¹²

D. Motor Flow Development

The overall flow development in the motor can be characterized by three distinct regimes—laminar, transitional, and fully turbulent flows—as shown schematically in Fig. 10. Near the head end, the flow is laminar and its velocity profiles can be determined by the laminar similarity theory.^{6,7} The hydrodynamic instability then renders the flow unstable, and turbulence begins to occur in the downstream region (point A). Unlike channel flows without surface injection, the outbreak of turbulence takes place away from the wall, with the region of intensive turbulence production shifting toward the wall as the flow accelerates in the downstream region. Within the initial transition regime, the mean velocity profiles still

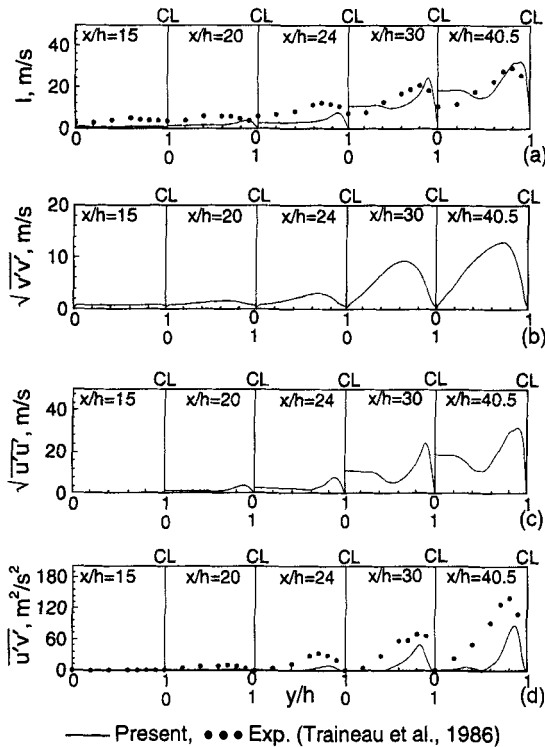


Fig. 9 Vertical distributions of turbulence properties at various axial locations.

correspond to the form predicted by the laminar similarity theory, because of the predominance of the pressure gradient over the viscous stress. As the flow develops further, a strong turbulent flow regime is observed. The deviation of the mean velocity profiles from those predicted by incompressible-laminar flow theory become significant due to the effect of turbulence and fluid compressibility.

Although the entire flowfield is driven by the mass injection through the porous wall, the characteristics of each flow regime are dominated by different physical mechanisms. To facilitate discussion, three key parameters characterizing the flow development are defined here: the injection Reynolds number $Re_w \equiv \bar{v}_w h / \nu$, the mean-flow Reynolds number $Re_m \equiv \bar{u}_b h / \nu$, and the momentum flux coefficient β defined in Eq. (32). The laminar flow regime reaches from the head end to about $x/h = 20$. The turbulence intensity is extremely small, and the velocity profiles can be described by the laminar-flow theory. An analytical study conducted by Hu⁴⁰ indicates that for the injection Reynolds numbers Re_w greater than 500, the velocity profiles are almost identical to the prediction, based on an inviscid rotational-flow analysis, Eq. (31). Significant differences are found, however, between the velocity profiles for inviscid and viscous flows for Re_w less than 100. This observation is consistent with the experimental findings of Dunlap et al.⁴¹ For moderate and high injection Reynolds numbers, the flow is driven mainly by the pressure gradient arising from the mass injection; the viscous shear stress plays a much less important role in determining the flow development. Since the injection Reynolds number

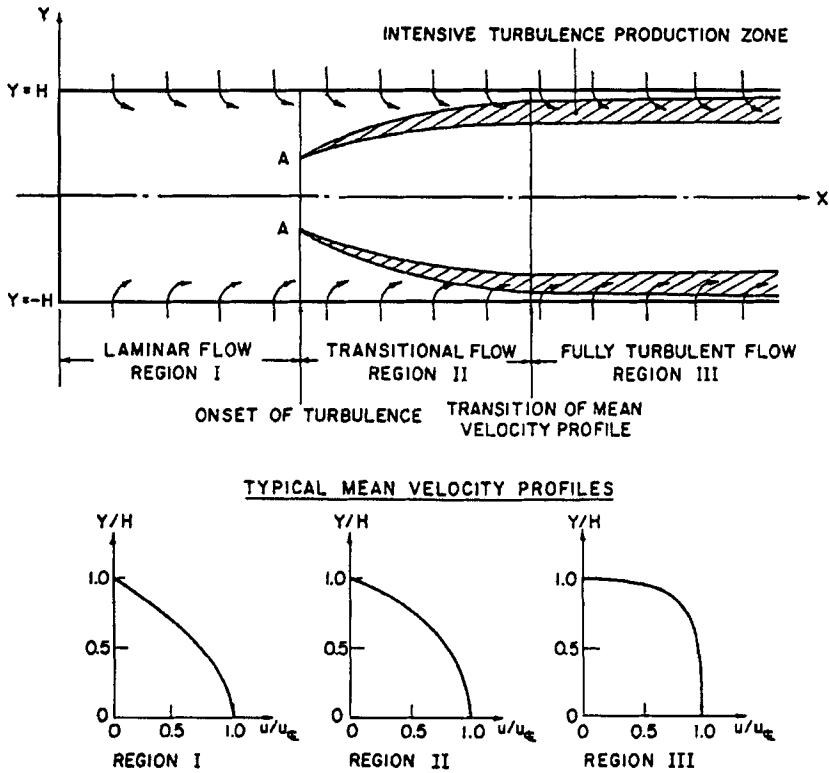


Fig. 10 Schematic diagram of internal flow development in a chamber.

near the head end is about 15×10^3 in the present case, the calculated velocity agrees closely with the cosine profile. A similar observation is made for the distribution of the radial velocity, which can be predicted by the following expression:

$$\frac{\bar{v}^r}{\bar{v}_w^r} = \sin\left(\frac{\pi y}{2h}\right) \quad (33)$$

The second regime is characterized by the onset of turbulence. When the fluid particle moves downstream, the local velocity and Reynolds number increase and eventually reach a point at which turbulent fluctuations occur. The classical hydrodynamic instability analysis of the Poiseuille flow cannot accurately predict the laminar-to-turbulence transition in a porous duct with surface transpiration. Varapaev and Yagodkin⁴² found that the effect of the vertical velocity component must be taken into account in predicting the critical Reynolds number Re^* for the onset of turbulent oscillation. For a small injection Reynolds number, a substantial reduction of Re^* from its counterpart for an impermeable pipe flow is observed, due to the destabilizing effect of the transverse velocity component. For Re_w greater than 300, however, the critical Reynolds number increases linearly with Re_w , due to the stabilizing effect of the resultant favorable pressure gradient. Figure 9 indicates that the turbulent kinetic energy remains at a very low level in the head-end region up to $x/h = 20$ and increases rapidly afterward. The mean velocity profile

only changes slightly, as shown in the transitional region (i.e., $20 < x/h < 25$) in Figs. 6 and 7.

As the flow develops farther downstream, the velocity profile transits into the shape of a fully developed turbulent pipe flow with surface transpiration. The axial velocity gradient becomes much steeper near the wall but smoother in the core region. The value of the momentum flux coefficient β decreases down to 1.04 at the chamber exit. It should be noted that, in addition to the turbulence effect, fluid compressibility might exert more significant influence on the variation of the velocity profile due to the large density gradient in the downstream region.

V. Effect of Acoustic Oscillation on Flow Evolution

After the stationary motor flowfield is obtained, traveling acoustic oscillations are imposed at the head end for two frequencies of 673 and 1346 Hz, corresponding to the second and fourth modes of the longitudinal standing wave in the chamber. The amplitude of the pressure fluctuation is about 5% of the mean pressure at the head end, i.e., $\bar{p} = 3.142$ atm. Computations are performed for 10 cycles of acoustic oscillations in order to obtain statistically meaningful results for data analysis.

A. Decomposition and Averaging

The imposed periodic fluctuations give rise to additional mechanisms of energy transfer between the mean and the turbulent flow. By following the triple decomposition of Hussain and Reynolds,⁴³ each resolved-scale flow property $\tilde{\mathcal{T}}^r(\mathbf{x}, t)$ can be expressed as the sum of the time-averaged $\tilde{\mathcal{T}}(\mathbf{x})$, periodic $\mathcal{I}^a(\mathbf{x}, t)$, and filtered turbulent $\mathcal{I}'(\mathbf{x}, t)$ quantities as follows:

$$\tilde{\mathcal{T}}^r(\mathbf{x}, t) = \tilde{\mathcal{T}}(\mathbf{x}) + \mathcal{I}^a(\mathbf{x}, t) + \mathcal{I}'(\mathbf{x}, t) \quad (34)$$

Both the ensemble- and the time-averaging techniques defined below⁴⁴ are employed to facilitate the decomposition.

Ensemble averaging:

$$\langle \tilde{\mathcal{T}}^r(\mathbf{x}, t) \rangle = \lim_{N \rightarrow \infty} \frac{1}{N} \sum_{n=0}^{N-1} \tilde{\mathcal{T}}^r(\mathbf{x}, t + n\tau) \quad (35)$$

Time averaging:

$$\tilde{\mathcal{T}}(\mathbf{x}) = \lim_{N \rightarrow \infty} \frac{1}{N} \sum_{n=0}^{N-1} \tilde{\mathcal{T}}^r(\mathbf{x}, t_0 + n\Delta t), \quad \text{where} \quad N\Delta t \gg \tau \quad (36)$$

$$\mathcal{I}^a(\mathbf{x}, t) = \langle \tilde{\mathcal{T}}^r(\mathbf{x}, t) \rangle - \tilde{\mathcal{T}}(\mathbf{x}) \quad (37)$$

where τ is the period of the forced oscillation. $\tilde{\mathcal{T}}(\mathbf{x})$ is the long-time average starting from the initial time t_0 , after which steady fluctuations of flow properties are observed. $\mathcal{I}^a(\mathbf{x}, t)$ is the short-time average and represents the periodic fluctuating part. Evaluation of the ensemble average requires calculation and storage of flow quantities over a large number of cycles, to achieve statistical significance. To bypass this computational difficulty, it can be alternatively obtained using time-frequency localization techniques based on the wavelet or fast Fourier transform (FFT) theories. The latter is employed in the present

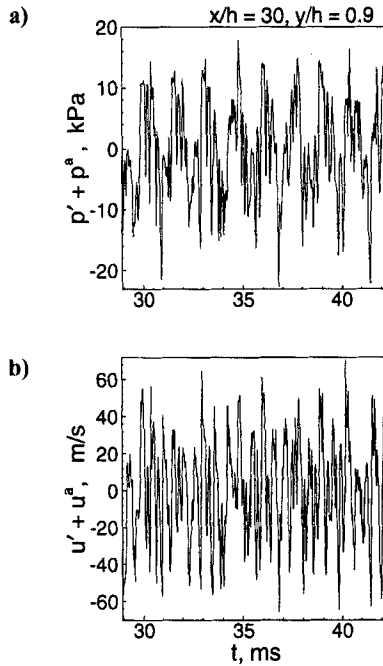


Fig. 11 Time histories of turbulent and acoustic fluctuations: a) pressure; b) axial velocity.

work. The fluctuating part comprising the turbulent and periodic oscillations is first obtained by subtracting the long-time averaged quantity from its instantaneous value. An FFT technique is then applied to transform the data from the physical to the spectral space. The periodic signal is of a known frequency and can be separated from the original signal by using a windowed Fourier transform in the frequency domain. Figures 11a and b show the time evolution of the pressure and axial velocity fluctuations at $x/h = 30$ and $y/h = 0.9$ for $f = 673$ Hz. These signals involve a wide range of frequency corresponding to turbulent fluctuations, in addition to the frequency of the imposed periodic motion. Figures 12a and b show the power density spectra of the pressure and axial velocity fluctuations, exhibiting a distinct peak at 673 Hz. A corresponding power density spectrum for the velocity fluctuation without imposed acoustic motion is shown in Fig. 13. The magnitude of velocity fluctuation with impressed acoustic oscillations is higher than that of the stationary turbulence case indicating enhanced turbulence production due to interactions between periodic and turbulent motions. The qualitative distributions of the power density spectrum are the same for both with and without imposed acoustic oscillations. This facilitates the use of the above procedure to accurately compute the turbulent and periodic fluctuations from the total signal.

B. Vorticity Field

Figures 14 and 15 show the time evolution of the vorticity fields with imposed acoustic motions at frequencies of 673 and 1346 Hz, respectively. Oscillatory

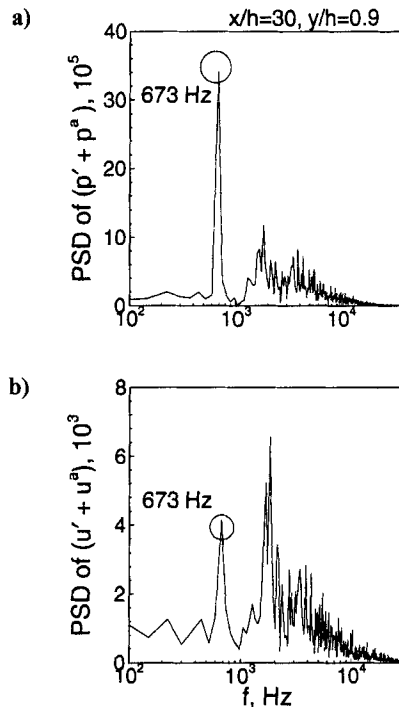


Fig. 12 Power spectral density (PSD) of fluctuating quantity with forced oscillations at $f = 673$ Hz: a) pressure; b) axial velocity.

vorticity is generated at the injection surface because of the no-slip condition.^{13,15} Streaks of vortex lines, which were absent in the stationary case, are clearly observed in the upstream laminar regime. The acoustic fluctuation-induced shear waves undergo transition in the midsection of the motor, giving rise to large-scale motions in the turbulent region. The eddy motions in the acoustic environments appear to be more organized, compared with the case without acoustic waves, and show strong interaction between turbulence and periodic excitations. The

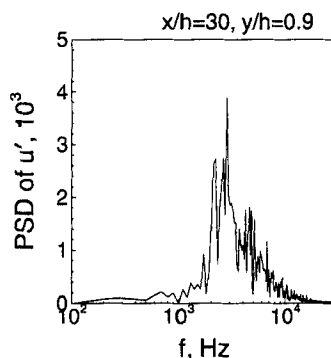


Fig. 13 Power spectral density (PSD) of axial-velocity fluctuation without forced oscillations.

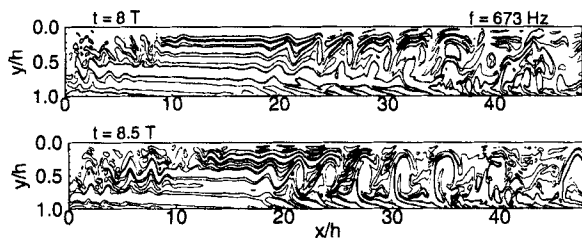


Fig. 14 Time evolution of vorticity fluctuations: $f = 673$ Hz.

fluctuating fields for the two frequencies shown here appear to be drastically different in the upstream regime. For $f = 673$ Hz, the turbulence transition occurs farther upstream, suggesting enhanced turbulence-production mechanisms arising from interactions with acoustic motions. For the higher-frequency case of 1346 Hz, the turbulence level upstream is minimal. Thus, low-frequency acoustic motions in a rocket motor appear to have more significant influence on the oscillatory flow-field.

C. Acoustic Field

Before analyzing the interactions between the acoustic and the turbulent flow-fields, a systematic analysis of traveling waves in a rocket motor is performed. Figure 16 shows the time evolution of the acoustic pressure along the center-line of the motor. A 35% decrease in the magnitude occurs between the head end and the throat. The result is compared with the prediction from quasi one-dimensional analysis, since the pressure field is predominantly one-dimensional. The theoretical model includes the mass influx at the wall as a source term in the governing equations, from which a linearized wave equation is derived. A traveling wave is simulated by imposing periodic boundary conditions at the head end based on the flow parameters used in the present study, *viz.*, $\dot{m}'' = 13$ kg/m²s, $\bar{p} = 3.142$ atm. The resultant differential equations and associated boundary conditions are solved using a space-marching technique. A detailed derivation of the formulation is given in the Appendix.

The analysis focuses on the energy-loss mechanism of acoustic motions resulting from the mass inflow through the lateral boundary of the chamber. The process takes place when a flow particle enters the chamber in a direction perpendicular to

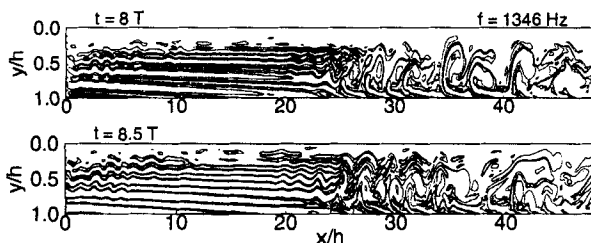


Fig. 15 Time evolution of vorticity fluctuations: $f = 1346$ Hz.

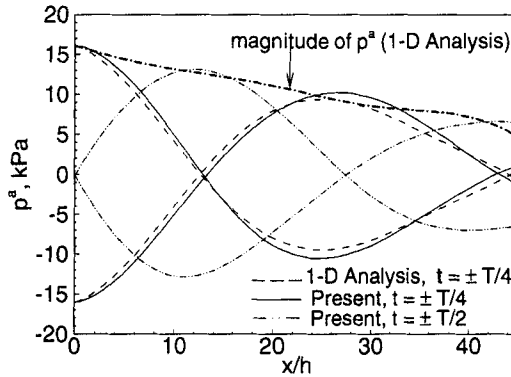


Fig. 16 Axial variations of pressure oscillation compared with analytical results.

the propellant surface and contributes no kinetic energy to the waves in the longitudinal mode. The particle then undergoes a turn into the direction parallel to the chamber axis and eventually participates in the periodic motions, which comprise mainly axial oscillations. During this process, the incoming flow acquires energy from the original acoustic field, representing a redistribution of acoustic energy. The one-dimensional model of Culick⁴⁵ indicates, however, that the acoustic field loses its energy at a rate of twice that actually obtained by the incoming flow. The additional loss can be regarded as the net exchange of energy from the acoustic field to the mean flow field, which is termed “flow-turning loss.” The correct prediction of the decrease in the magnitude of acoustic pressure throughout the combustion chamber indicates the accuracy of the data-deduction procedure employed in this study.

D. Effect of Acoustic Oscillation on Turbulence Properties

The triple decomposition of Eq. (34) enables energy transfer to be viewed as taking place among three participating fields. The turbulent stress in the present case can be expressed as

$$\tau_{kl} = -\overline{\rho u'_k u'_l} - \overline{\rho u^a_k u^a_l} \quad (38)$$

It differs from its form for a stationary flow by virtue of an additional stress due to the “organized” or “periodic” part of the oscillatory motions ($-\rho u^a_i u^a_j$). A set of differential equations describing the transport of the variance of the turbulent and periodic axial velocities may be deduced in the component form, yielding coupled time-averaged energy equations,⁴⁴

$$\begin{aligned} \frac{D}{Dt} (\overline{\rho u^a_\alpha u^a_\alpha}) &= \dots + \overline{\rho u'_i u'_\alpha} \frac{\partial u^a_\alpha}{\partial x_i} - \overline{\rho u^a_i u^a_\alpha} \frac{\partial \bar{u}_\alpha}{\partial x_i} + \dots \\ \frac{D}{Dt} (\overline{\rho u'_\alpha u'_\alpha}) &= \dots - \overline{\rho u'_i u'_\alpha} \frac{\partial \bar{u}_\alpha}{\partial x_i} - \overline{\rho u'_i u'_\alpha} \frac{\partial u^a_\alpha}{\partial x_i} + \dots \end{aligned} \quad (39)$$

where D/Dt denotes the substantial derivative following the mean motion of the fluid, and repeated English alphabets imply summation, while Greek letters imply

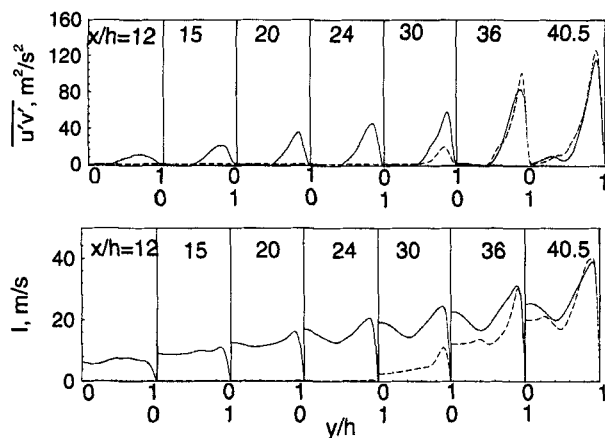


Fig. 17 Vertical distributions of turbulence intensity and Reynolds stress at various axial locations: (—) without forced oscillations; (---) with forced oscillations at $f = 673$ Hz.

no summation on the indices. Additional terms, such as pressure-strain, diffusion, and dissipation, are not explicitly written, as the focus herein is placed on the production terms in these transport equations. For the case of production of $(\rho u'u')$, the important correlations are $\rho u'v'\partial\bar{u}/\partial y$ and $\rho u'v'\partial u^a/\partial y$. While the first term is equally important for stationary turbulence, the latter accounts for the energy exchange between the turbulent and the oscillatory fields, as suggested by Brereton et al.⁴⁴ Figures 17 and 18 show the vertical distributions of the turbulence stress and intensity at various axial locations for two different acoustic frequencies, respectively. The corresponding stationary-turbulence properties are also indicated for comparison. The enhanced level of turbulence in the upstream region of the

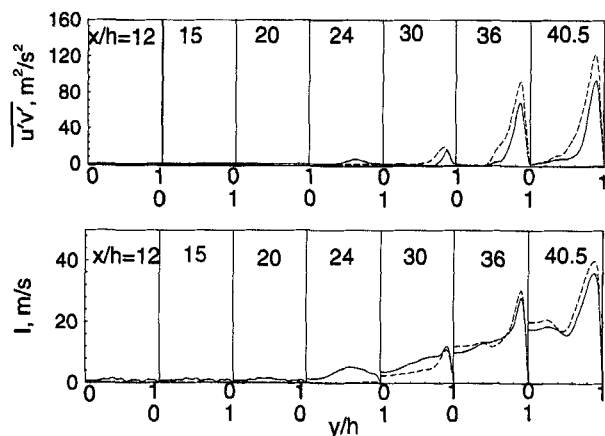


Fig. 18 Vertical distributions of turbulence intensity and Reynolds stress at various axial locations: (—) without forced oscillations; (---) with forced oscillations at $f = 1346$ Hz.

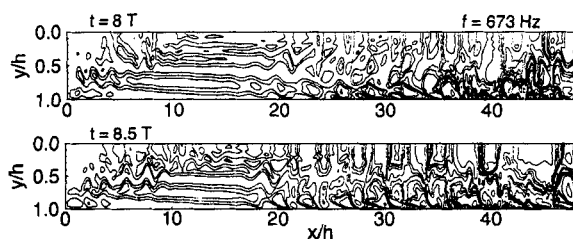


Fig. 19 Contour plots of fluctuating axial velocity with forced oscillations at $f = 673$ Hz.

chamber for the low-frequency excitation of $f = 673$ Hz indicates the transfer of energy from the acoustic to the turbulent field. The acoustic wave indeed can invoke hydrodynamic instability and initiate turbulence in a much earlier stage. The intensity levels off with its value for the stationary-turbulence case in the downstream region. This may be attributed in part to the decreased acoustic energy in the downstream region due to the flow-turning losses. Moreover, the increased mean flow velocity gradient farther downstream causes the effect of $\overline{\rho u'v'}\partial\bar{u}/\partial y$ to override the energy production arising from acoustic excitation. The turbulence intensity and stress levels for the higher-frequency case of $f = 1376$ Hz (shown in Fig. 18) indicate limited change from the case without acoustic excitation in the upstream region. The increased frequency of periodic oscillation reduces the acoustic boundary layer thickness and exerts no influence on turbulence production in the upstream region due to the increased dissipation rate of unsteady vorticity transport.¹⁴

E. Effect of Turbulence on the Acoustic Flowfield

Although acoustic oscillations often enhance turbulence intensity through their interactions, turbulence tends to dissipate organized flow motions due to its induced eddy viscosity. Figures 19 and 20 show contour plots of the axial velocity fluctuation, including turbulent and periodic components, for two excitation frequencies, respectively. Turbulence overrides the periodic fluctuations in the downstream region. The oscillatory velocity field exhibits a multidimensional structure. The acoustic pressure, however, is basically one-dimensional and no discernible variation in the vertical direction is observed. The unsteady flowfield comprises three distinct types of wave motions: acoustic (or irrotational), vortical (or shear),

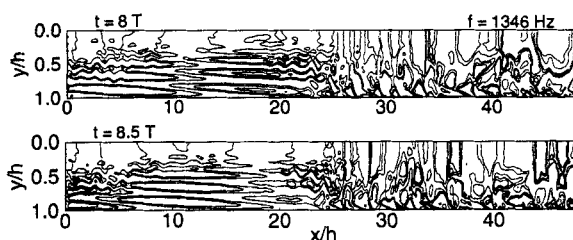


Fig. 20 Contour plots of fluctuating axial velocity with forced oscillations at $f = 1346$ Hz.

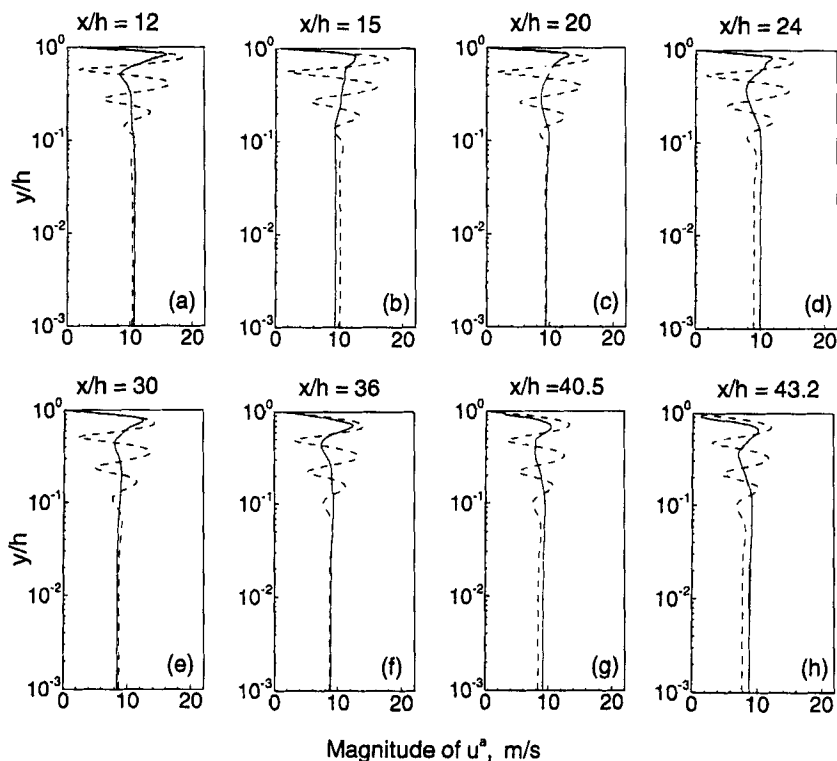


Fig. 21 Amplitudes of fluctuating axial velocity at various axial locations at $f = 673$ Hz: (—) laminar flow; (---) turbulent flow.

and thermal (or entropy) waves. The thermal wave plays a very minor role in the present cold-flow simulation, but may become important in combustion cases. A comprehensive discussion of the acoustic and vortical wave motions in motor environments is given in a companion chapter.⁴⁶ Figures 21 and 22 present the vertical variations of the axial periodic velocity (u^a) at various axial locations for $f = 673$ and 1346 Hz, respectively. Both the laminar and the turbulent flow computations are presented for comparison. The velocity fluctuation in the core-flow region is governed by the isentropic traveling wave relationship with the acoustic pressure. In the laminar-flow case, a velocity overshoot is observed near the porous wall because of the shear wave produced by the no-slip condition.^{13,14} This shear wave travels toward the centerline with the mean vertical velocity and is damped out by the viscous dissipation in the core-flow region. In the present study, the magnitude of the velocity overshoot near the porous wall is smaller than twice the centerline fluctuating velocity, as predicted by Flandro in his theoretical analysis.^{13,14} The high chamber pressure (around 100 atm) considered in Ref. 13 gives rise to a very low surface injection velocity, and hence a prominent acoustic boundary layer is obtained. The strong blowing effect arising from the high injection velocity in the present work, however, extends the acoustic boundary layer and spreads the shear-wave motion through the bulk of the chamber. This

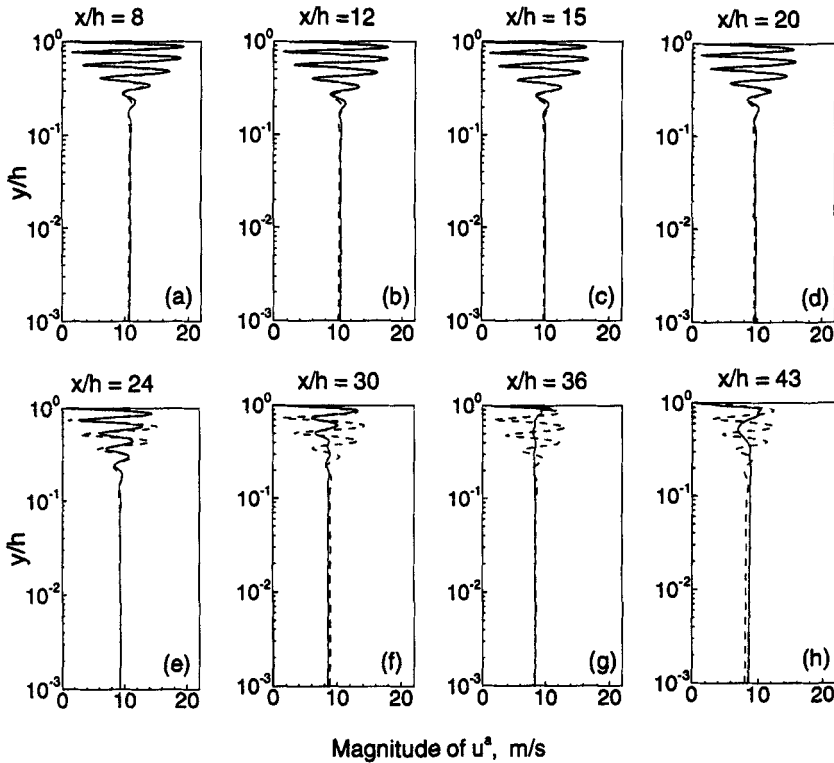


Fig. 22 Magnitude of fluctuating acoustic velocity at various axial locations at $f = 1346$ Hz: (—) laminar flow; (---) turbulent flow.

reduces the magnitude of the axial velocity overshoot near the porous wall. In the turbulent flow case, the shear wave is effectively damped by the enhanced momentum transfer and dissipation rates as soon as it is convected away from the surface. The periodic velocity fluctuation in the upstream region for $f = 673$ Hz appears more suppressed than in the higher-frequency case. This can be attributed to the acoustic wave-induced turbulence and its ensuing increase in the eddy viscosity in that region. The analysis elucidates intricate interactions among the mean, acoustic, and turbulent flowfields in a rocket motor.

VI. Conclusions

A comprehensive analysis of the flow development in a simulated nozzleless rocket motor with acoustic excitations has been performed by means of an LES technique. The flowfield can be characterized with three distinct regimes: laminar, transitional, and fully developed turbulent flows. The effect of turbulence and fluid compressibility on the mean flow structure was examined in depth. The interactions among the mean, turbulent, and periodic oscillatory flowfields were studied by imposing traveling acoustic waves in the chamber at two different frequencies. The acoustic oscillation provides additional mechanisms to

transfer energy from periodic motions to turbulence and, consequently, leads to enhanced turbulence intensity and stresses. The laminar-to-turbulence transition takes place at a much earlier stage under conditions with acoustic waves, especially in the low-frequency range. The influence of turbulence on the periodic oscillatory flowfield arises mainly in the enhanced momentum and energy transfer in the turbulent region. As a result of the acoustic wave-induced eddy viscosity, the shear wave originating from the surface is effectively dissipated as it travels downstream, thereby producing a qualitative change in the oscillatory flowfield, as predicted by the laminar-flow theory. The present work represents a major step toward a complete understanding of the unsteady flow evolution in rocket motors.

Appendix

The quasi-one-dimensional acoustic field in the chamber is formulated by applying the conservation laws to an infinitesimal control volume enclosing the flow passage at a given cross section. The basic assumptions are that

1) the gases obey the perfect-gas law and have constant thermophysical properties,

2) the viscous forces and heat transfer within the gases are ignored,

3) the cross-sectional area of the chamber is assumed constant,

4) the mass inflow at the lateral surface is kept fixed (i.e., $\overline{\dot{m}}_w'' = \text{constant}$), and

5) injection of the fluid is isothermal.

The one-dimensional continuity, momentum, and energy equations take the following form:

$$A \frac{\partial \rho}{\partial t} + A \frac{\partial(\rho u)}{\partial x} = \overline{\dot{m}}_w'' \quad (\text{A1})$$

$$A \frac{\partial(\rho u)}{\partial t} + A \frac{\partial(\rho u^2)}{\partial x} + A \frac{\partial p}{\partial x} = 0 \quad (\text{A2})$$

$$A \frac{\partial(\rho e)}{\partial t} + A \frac{\partial(\rho u e)}{\partial x} + A \frac{\partial(pu)}{\partial x} = h_{0s} \overline{\dot{m}}_w'' \quad (\text{A3})$$

where

$$h_{0s} = C_p T_s + \frac{v_w^2}{2}, \quad e = C_v T + u^2/2 \quad (\text{A4})$$

and A is the cross-sectional area. The gas is injected vertically at the porous surface and thus makes no contribution to the axial momentum balance. The preceding equations can be transformed into the nonconservative form to facilitate derivation of the wave equation. With some straightforward manipulations and the use of the equation of state, Eqs. (A2) and (A3) become

$$\rho A \frac{\partial u}{\partial t} + \rho u A \frac{\partial u}{\partial x} + A \frac{\partial p}{\partial x} = -u \overline{\dot{m}}_w'' \quad (\text{A5})$$

$$A \frac{\partial p}{\partial t} + \gamma p A \frac{\partial u}{\partial x} + u A \frac{\partial p}{\partial x} = \frac{R}{C_v} \left[h_{0s} + \frac{u^2}{2} \right] \overline{\dot{m}}_w'' \quad (\text{A6})$$

Linearization of Eqs. (A5) and (A6) leads to

$$\bar{\rho} A \frac{\partial u'}{\partial t} + A \frac{\partial p'}{\partial x} = -\bar{\rho} A \frac{\partial(\bar{u}u')}{\partial x} - \rho' \bar{u} A \frac{d\bar{u}}{dx} - u' \bar{m}_w'' \quad (\text{A7})$$

$$A \frac{\partial p'}{\partial t} + \gamma \bar{p} A \frac{\partial u'}{\partial x} = \bar{u} A \frac{\partial p'}{\partial x} - u' A \frac{\partial \bar{p}}{\partial x} - \gamma p' A \frac{d\bar{u}}{dx} + \frac{R}{C_v} \bar{u} u' \bar{m}_w'' \quad (\text{A8})$$

Note that the following constitutive relation was used in deriving the preceding equations:

$$c^2 = \left(\frac{\partial p}{\partial \rho} \right)_{\text{entropy}} \Rightarrow \rho' = \frac{p'}{c^2} \quad (\text{A9})$$

For time-harmonic motions, the spatial and temporal dependence of each unsteady flow variable can be decomposed as follows:

$$p' = \hat{p}(x)e^{i\omega t}, \quad u' = \hat{u}(x)e^{i\omega t} \quad (\text{A10})$$

Substitution of Eq. (A10) into Eqs. (A7) and (A8) gives rise to a set of coupled ordinary differential equations for pressure and velocity fluctuations as

$$\begin{bmatrix} \bar{\rho} A \bar{u} & A \\ \gamma \bar{p} A & \bar{u} A \end{bmatrix} \frac{d}{dx} \begin{bmatrix} \hat{u} \\ \hat{p} \end{bmatrix} = \begin{bmatrix} -\bar{\rho} A \frac{d\bar{u}}{dx} - \bar{m}_w'' - \bar{\rho} A i\omega & -\frac{\bar{u} A}{\bar{c}^2} \frac{d\bar{u}}{dx} \\ (\gamma - 1) \bar{u} \bar{m}_w'' - A \frac{d\bar{p}}{dx} & -\gamma A \frac{d\bar{u}}{dx} - A i\omega \end{bmatrix} \begin{bmatrix} \hat{u} \\ \hat{p} \end{bmatrix} \quad (\text{A11})$$

The boundary conditions of $\hat{p} = 1$ and $\hat{u} = \hat{p}/\bar{\rho}\bar{c}$ at the head end ($x = 0$) are specified to simulate traveling acoustic oscillations in the chamber. A simple integration algorithm based on the Euler implicit method is used to solve Eq. (A11) subject to the above boundary conditions.

Acknowledgments

This work was sponsored partly by the Pennsylvania State University and partly by the California Institute of Technology Multidisciplinary University Research Initiative under ONR Grant N00014-95-1-1338. The guidance and suggestions of Dr. Shieh-Yang Hsieh in the development of the computational code are appreciated. Discussions with Dr. Xiyun Lu on subgrid-scale models are also appreciated.

References

- ¹Culick, F. E. C., "A Review of Calculations for Unsteady Burning of a Solid Propellant," *AIAA Journal*, Vol. 6., No. 12, 1968, pp. 2241–2255.
- ²Tseng, I. S., and Yang, V., "Combustion of Double-Base Homogeneous Propellant in a Rocket Motor," *Combustion and Flame*, Vol. 96, 1994, pp. 325–342.
- ³Yang, V., Hsieh, K. C., and Tseng, I. S., "Velocity Coupled Flow Oscillations in a Simulated Solid Propellant Rocket Environment," AIAA Paper 88-0543, AIAA Aerospace Sciences Meeting, 1988.

⁴Roh, T. S., Tseng, I. S., and Yang, V., "Effects of Acoustic Oscillations on Flame Dynamics of Homogeneous Propellant in Rocket Motors," *Journal of Propulsion and Power*, Vol. 11, No. 4, 1995, pp. 2241–2255.

⁵Roh, T. S., Apte, S., and Yang, V., "Transient Combustion Response of Homogeneous Solid Propellant to Acoustic Oscillations in a Rocket Motor," *27th Symposium (International) on Combustion*, Combustion Inst., Pittsburgh, Aug. 1998.

⁶Taylor, G. I., "Fluid Flow Regions Bounded by Porous Surfaces," *Proceedings of the Royal Society London*, Series 234A, Vol. 11199, 1956, pp. 456–475.

⁷Culick, F. E. C., "Rotational Axisymmetric Mean Flow and Damping of Acoustic Waves in Solid Propellant Rocket Motors," *AIAA Journal*, Vol. 4, 1966, pp. 1462–1464.

⁸Balakrishnan, G., Linan, A., and Williams, F. A., "Rotational Inviscid Flow in Laterally Burning Solid-Propellant Rocket Motors," *Journal of Propulsion and Power*, Vol. 8, No. 6, 1992, pp. 1167–1176.

⁹Traineau, J. C., Hervat, P., and Kuentzmann, P., "Cold-Flow Simulation of a Two-Dimensional Nozzleless Solid-Rocket Motor," *AIAA Paper 86-1447*, June 1986.

¹⁰Dunlap, R., Blackner, A. M., Waugh, R. C., Brown, R. S., and Willoughby, P. G., "Internal Flow Field Studies in a Simulated Cylindrical Port Rocket Chamber," *Journal of Propulsion and Power*, Vol. 8, No. 6, 1992, pp. 1167–1176.

¹¹Beddini, R. A., "Injection Induced Flows in Porous-Walled Ducts," *AIAA Journal*, Vol. 24, No. 11, 1986, pp. 1766–1773.

¹²Sabnis, J. S., Madabhushi, R. K., Gibeling, H. J., and McDonald, H., "On the Use of k - ϵ Turbulence Model for Computation of Solid Rocket Internal Flows," *AIAA Paper 89-2558*, July 1989.

¹³Flandro, G. A., "Effects of Vorticity Transport on Axial Acoustic Waves in a Solid Propellant Rocket Chamber," *ASME Annual Meeting*, San Francisco, CA, 1989.

¹⁴Flandro, G. A., "Effects of Vorticity on Rocket Combustion Stability," *Journal of Propulsion and Power*, Vol. 11, No. 4, 1995, pp. 607–625.

¹⁵Vuillot, F., "Vortex Shedding Phenomenon in Solid Rocket Motors," *Journal of Propulsion and Power*, Vol. 11, No. 4, 1995, pp. 626–639.

¹⁶Cai, W. D., and Yang, V., "Two-Phase Turbulent Flow Interactions in a Simulated Rocket Motor with Acoustic Waves," *AIAA Paper 98-0161*, Jan. 1998.

¹⁷Roh, T. S., Apte, S. V., and Yang, V., "Combustion Dynamics of Homogenous Solid Propellants in a Rocket Motor with Acoustic Excitations," *Progress in Astronautics and Aeronautics*, Vol. 185, edited by V. Yang, T. B. Brill, and W.-Z. Ren, AIAA, Reston, VA, 2000, Chap. 3.5.

¹⁸Piomelli, U., "Models for Large Eddy Simulations of Turbulent Channel Flows Including Transpiration," Ph.D. Thesis, Stanford Univ., Palo Alto, CA, 1987.

¹⁹Liou, T. M., and Lien, W. H., "Numerical Simulations of Injection-Driven Flows in a Two-Dimensional Nozzleless Solid-Rocket Motor," *Journal of Propulsion and Power*, Vol. 11, No. 4, 1995, pp. 600–606.

²⁰Liou, T. M., Lien, W. Y., and Hwang, P. W., "Transition Characteristics of Flowfield in a Simulated Solid-Rocket Motor," *Journal of Propulsion and Power*, Vol. 14, No. 3, 1998, pp. 282–289.

²¹Batchelor, G. K., *An Introduction to Fluid Dynamics*, Cambridge Univ. Press, Cambridge, England, UK, 1967.

²²Erlebacher, G., Hussaini, M. Y., Speziale, C. G., and Zang, T. A., "Toward the Large-Eddy Simulation of Compressible Turbulent Flows," *ICASE Paper No. 87-20*, 1990.

²³Hinze, J. O., *Turbulence*, McGraw-Hill, New York, 1975, pp. 321–357.

²⁴Piomelli, U., "Large-Eddy Simulation of Turbulent Flows," TAM Report No. 767, Univ. of Illinois, Urbana-Champaign, 1994.

²⁵Tseng, I. S., "Numerical Simulation of Velocity-Coupled Combustion Response of Solid Rocket Propellants," Ph.D. Thesis, Pennsylvania State Univ., University Park, PA, 1992.

²⁶Ghosal, S., "An Analysis of Numerical Errors in Large-Eddy Simulations of Turbulence," *Journal of Computational Physics*, Vol. 125, 1996, pp. 187–206.

²⁷Fabignon, Y., Beddini, R. A., and Lee, Y., "Analytic Evaluation of Finite Difference Methods for Compressible Direct and Large Eddy Simulations," *Aerospace Science and Technology*, Vol. 6, 1997, pp. 413–423.

²⁸Beddini, R. A., Lee, Y., and Fabignon, Y., "Estimation of Convection Errors of Finite Difference Methods for Compressible Turbulence Simulations," ASME Fluids Engineering Summer Meeting, FEDSM97-3116, Vancouver, June 1997.

²⁹Anderson, D. A., Tannehill, J. C., and Pletcher, R. H., *Computational Fluid Mechanics and Heat Transfer*, Series in Computational Methods in Mechanics and Thermal Sciences, Hemisphere, New York, 1984, pp. 70–118.

³⁰Hirsch, C., *Numerical Computation of Internal and External Flows*, Vol. 1, Wiley, New York, 1992, pp. 238–341.

³¹Jameson, A., "The Evolution of Computational Methods in Aerodynamics," *Journal of Applied Mathematics*, Vol. 50, 1983, pp. 1052–1070.

³²Tennekes, H., and Lumley, J. L., *A First Course in Turbulence*, MIT Press, Cambridge, MA, 1972, pp. 248–287.

³³Beddini, R. A., Lee, Y., and Fabignon, Y., "Effects of Convection Errors on Compressible Turbulence Simulations," *1st AFOSR International Conference on Direct and Large Eddy Simulation*, Paper N-16, Rustin, LA, Aug. 1997.

³⁴Ragab, S. A., and Sheen, S. C., "Large Eddy Simulation of Mixing Layers," *Large Eddy Simulation of Complex Engineering and Geophysical Flows*, edited by B. Galperin and S. A. Orszag, Cambridge Univ. Press, New York, 1993, pp. 255–285.

³⁵Apte, S. V., and Yang, V., "Large Eddy Simulation of Internal Flow Development in Porous Chamber with Surface Mass Injection," *Journal of Fluid Mechanics* (submitted for publication).

³⁶Huesmann, K., and Eckert, E. R. G., "Studies of the Laminar Flow and the Transition to Turbulence in Porous Tubes with Uniform Injection Through the Tube Wall," *Journal of Propulsion and Power*, Vol. 6, No. 6, 1990, pp. 690–705.

³⁷Lesieur, M., Staquet, C., Le Roy, P., and Comte, P., "The Mixing Layer in its Coherence Examined from the Point of View of Two-Dimensional Turbulence," *Journal of Fluid Mechanics*, Vol. 192, 1988, pp. 511–534.

³⁸Lesieur, M., *Turbulence in Fluids*, 3rd ed., Kluwer Academic, Dordrecht, The Netherlands, 1990.

³⁹Gilbert, A. D., "Spiral Structures and Spectra in Two-Dimensional Turbulence," *Journal of Fluid Mechanics*, Vol. 193, 1988, pp. 475–498.

⁴⁰Hu, T. S., "Flowfield and Heat Transfer in the Entrance Region of a Duct with Closed End and Uniform Injection," M.S. Thesis, Dept. of Mechanical Engineering, Pennsylvania State Univ., University Park, PA, 1990.

⁴¹Dunlap, R., Blackner, A. M., Waugh, R. C., Brown, R. S., and Willoughby, P. G., "Internal Flow Field Studies in a Simulated Cylindrical Port Rocket Chamber," *Journal of Propulsion and Power*, Vol. 6, No. 6, 1990, pp. 690–704.

⁴²Varapaev, V. N., and Yagodkin, V. I., "Flow Stability in a Channel with Porous Walls," *Izvestiya Akademii Nauk SSSR, Mekhanika Zhidkosti i Gaza*, Vol. 4, No. 5, 1969, pp. 91–95.

⁴³Hussain, A. K. M. F., and Reynolds, W. C., "The Mechanics of Organized Wave in Turbulent Shear Flow," *Journal of Fluid Mechanics*, Vol. 41, 1970, pp. 241–258.

⁴⁴Brereton, G., Reynolds, W., and Jayaraman, R., "Response of a Turbulent Boundary Layer to Sinusoidal Free-Stream Unsteadiness," *Journal of Fluid Mechanics*, Vol. 221, 1990, pp. 131–159.

⁴⁵Culick, F. E. C., "The Stability of One-Dimensional Motions in a Rocket Motor," *Combustion Science and Technology*, Vol. 7, 1973, pp. 165–175.

⁴⁶Flandro, G. A., Cai, W. D., and Yang, V., "Turbulent Transport in Rocket Motor Unsteady Flowfield," *Progress in Astronautics and Aeronautics*, Vol. 185, edited by V. Yang, T. B. Brill, and W.-Z. Ren, AIAA, Reston, 2000, Chap. 3.3.

III. Motor Interior Ballistics

Effect of Acoustic Oscillation on Flow Development in a Simulated Nozzleless Rocket Motor

Sourabh Apte* and Vigor Yang†

Pennsylvania State University, University Park, Pennsylvania

Nomenclature

A	= chamber cross section
c	= speed of sound
c_s	= Smagorinsky constant
D	= near-wall damping function
\tilde{e}	= filtered total specific energy per unit volume
E	= turbulence energy
f	= frequency, Hz
G	= spatial filter function
$G_{k,u}$	= amplification factor per time step
h	= chamber half-height, m
I	= turbulence intensity, $\sqrt{u'u' + v'v'}$
I_τ	= number of time steps required for one eddy lifetime
k	= wave number, 1/m
L	= chamber length, m
ℓ	= turbulence length scale, m
\dot{m}''	= injection mass flux, kg/m ² s
M	= mean Mach number averaged over a given cross section
M_c	= mean Mach number at centerline
p	= pressure, Pa
Pr	= Prandtl number
q	= large-scale velocity, m/s
Re	= Reynolds number
S_{ij}	= strain-rate tensor, $((\partial u_i/\partial x_j) + (\partial u_j/\partial x_i))/2 - \delta_{ij}(\partial u_k/\partial x_k)/3$

Copyright © 2000 by S. Apte and V. Yang. Published by the American Institute of Aeronautics and Astronautics, Inc., with permission.

*Ph.D. Student, Dept. of Mechanical Engineering.

†Professor, Dept. of Mechanical Engineering. Associate Fellow AIAA.

T	= temperature, K
t	= time, s
u	= axial velocity, m/s
v	= vertical velocity, m/s
v_w	= injection velocity at wall, m/s
γ	= ratio of specific heats
Δ	= filter width
δ_{ij}	= Kronecker delta
δ	= constant in Eq. (25) ≈ 0.0025
ε_a	= amplitude of imposed pressure oscillation
ε_v	= artificial dissipation coefficient
η	= Kolmogorov length scale, m
κ	= thermal conductivity, W/mK
μ	= dynamic viscosity, kg/ms
ν	= kinematic viscosity, m ² /s
ν_s	= subgrid-scale kinematic viscosity, m ² /s
ρ	= density, kg/m ³
σ	= CFL number
τ	= viscous shear stress, N/m ²
ξ	= grid parameter for LES

Subscripts

b	= bulk mean quantity
c	= centerline
w	= wall

Superscripts

$'$	= fluctuating component due to turbulence
a	= fluctuating component due to imposed acoustic oscillation
r	= resolved-scale component
s	= subgrid-scale component
\sim	= density-weighted quantity
$-$	= time-averaged quantity

I. Introduction

MUCH of the research in the field of solid rocket propulsion has been directed toward establishing a clear understanding of the combustion instability phenomenon.¹ In an effort to study the detailed coupling between propellant combustion dynamics and local flow oscillations in rocket motors, Yang and coworkers²⁻⁵ conducted a series of numerical studies of homogeneous propellant combustion under conditions representative of practical propulsive systems. Much information has been obtained about the flame structure, heat release mechanism, propellant combustion response, and flow development. In spite of these contributions to the knowledge base on combustion instability, however, existing models provide limited information concerning propellant burning behavior in oscillatory turbulent crossflows. Specifically, the interactions among the mean, acoustic, and turbulent flowfields, and their collective effect on propellant combustion dynamics and motor stability behavior, need to be addressed comprehensively.

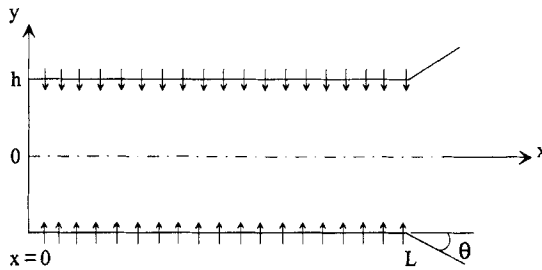


Fig. 1 Schematic diagram of a simulated nozzleless rocket motor.

As an attempt to address these fundamental issues, the present work concentrates on the effect of acoustic oscillation on the flow development in a simulated nozzleless solid rocket motor, as shown schematically in Fig. 1. The evolution of the propellant combustion products in the chamber is simulated by the mass injection through the porous walls. The oscillatory field in a rocket motor consists of three distinct types of waves: acoustic (corresponding to irrotational, compressible flow motions), vortical (arising from rotationality of unsteady flow), and entropy (due to unsteady heat release and viscous dissipation) modes. The three waves, along with the transient combustion response of propellant, collectively dictate the chamber flame dynamics and subsequently the motor stability behavior. Turbulence plays a decisive role in determining the wave characteristics through its influence on the momentum and energy transfer in various parts of the chamber. In particular, the interactions between organized oscillatory motions and random turbulent fluctuations give rise to additional mechanisms of energy production, transfer, and dissipation in the flowfield. These phenomena were studied separately only for simplified configurations in the past. Little effort was made to address their collective effect, especially under conditions representative of real rocket motor environments.

The injection-driven flow in a rocket motor is significantly different from a pipe flow with surface transpiration, because the combustion chamber is closed at the head end. The flowfield is essentially established through a balance between the pressure gradient and inertial forces, in contrast with a pipe flow, wherein the velocity profiles are determined by a balance between viscous and pressure forces. An analytical solution for this category of flows was first developed by Taylor⁶ and later validated by Culick,⁷ revealing a cosine distribution for the axial velocity in the vertical direction. A theoretical analysis of inviscid, rotational, and compressible flowfield in a porous duct with the injection rate varying with local pressure was carried out by Balakrishnan et al.⁸ The effect of fluid compressibility in flattening the radial profile of the axial velocity, in a manner analogous to that arising from turbulence in flows without surface transpiration, was established. Traineau et al.⁹ performed an experimental study of the internal flowfield in a simulated nozzleless rocket motor, indicating three regimes of flow development. The velocity field develops in accordance with laminar flow theory in the upstream region and undergoes turbulence transition in the middle section of the chamber. Transition of the mean axial velocity profile occurs farther downstream, where there appears a fully developed turbulent flowfield with surface mass injection. The experiments were carried out at a high injection Reynolds number (15×10^3)

and elucidated the compressibility effect on the mean velocity profile. Dunlap et al.¹⁰ conducted measurements of flow properties in a cylindrical chamber at low injection Mach numbers (0.0018 and 0.0036). The corresponding injection Reynolds numbers (9×10^3 and 18×10^3) were typical of rocket motor values. The compressibility effect was not observed because of the low Mach number condition. Beddini¹¹ simulated turbulent flows in porous-walled ducts at large injection Reynolds numbers by means of the Reynolds-stress turbulence model. The presence of turbulence fluctuations at the surface, termed "pseudo-turbulence," was noted. Sabnis et al.¹² used conventional single-point turbulence closure schemes to simulate the flowfields in a rocket motor.

Considerable effort has been expended in studying the interactions between acoustic fluctuations and motor internal flows. Flandro^{13,14} established the first analytical model dealing with unsteady vorticity transport in a rocket motor that arises from longitudinal acoustic motions. The work concentrates on cold-flow simulations of laminar flowfields. Vuillot¹⁵ studied the vortex-shedding phenomenon in segmented rocket motors. The unstable-mode frequencies and pressure levels were accurately predicted using a numerical approach. In real rocket environments, turbulence often occurs and exercises strong influence on the gas-phase flow/flame structures and consequently the propellant combustion response. Cai and Yang¹⁶ employed a modified two-layer turbulence closure scheme to investigate the two-phase flow interactions with longitudinal acoustic waves. Roh et al.¹⁷ treated the gas-phase flame dynamics and its coupling with the condensed-phase processes in a turbulent flow environment, following a similar approach of turbulence closure. In spite of their common use and ability to provide useful information, the second-order turbulence closure schemes usually overpredict turbulent flow properties in rocket motors and fail to offer in-depth knowledge of flow evolution. The use of ad hoc assumptions in these models renders them unsuitable for studying unsteady motor internal flows.

High-level turbulence closure schemes based on large-eddy-simulation (LES) techniques provide a new avenue for studying motor internal flows. Although the computational effort required is enormous, this method allows for a comprehensive investigation of the turbulence effect. Piomelli¹⁸ performed an LES analysis of the injection-driven flow in a porous chamber. His work focused on the development of wall-layer models suited for numerical calculations. Liou et al.¹⁹ conducted a two-dimensional LES to achieve a better prediction of turbulence intensity and axial velocity profiles compared with the second-order turbulence closures. The deficiency in applying the wall-function method to injection-driven flows was advocated by demonstrating that the mean velocity profiles away from the viscous sublayer vary along the chamber and cannot be collapsed into a unique universal wall law. The work was recently extended by considering the effect of turbulence intensity at the injection surface on the turbulence evolution.²⁰ In spite of the considerable work conducted in this area, a comprehensive understanding of the physical processes occurring within the motor remains lacking. In particular, the mutual coupling between acoustic and turbulent flow motions needs to be explored.

This chapter attempts to study the internal flowfield in a simulated nozzle-less rocket motor with acoustic excitations. The approach is based on the LES technique. The contribution of large energy-carrying structures to momentum and energy transfer is computed exactly with the effect of small scales of turbulence modeled semiempirically. Various underlying fluid-dynamic mechanisms responsible for driving unsteady motions in a motor are studied. Owing to the limitations of the computational resources and the two-dimensionality of the chamber, a

two-dimensional analysis is carried out herein to provide useful insight into the complex flowfield with acoustic excitation. The present work lacks the vortex-stretching phenomenon commonly observed in turbulent flows but allows for unpredictability and rapid mixing with enhanced momentum and mass transfer, the essential features of turbulent flows. Compared with conventional second-order closure schemes, which are based on ad hoc hypotheses, the present work marks an improvement in predicting turbulence characteristics. A complete three-dimensional simulation is required further to improve and corroborate the results and will be presented in subsequent publications.

In the following sections, a complete theoretical formulation of the motor internal flow is summarized, with a brief description of the numerical implementation. The work starts with calculations of the motor internal flowfield under stationary conditions. Periodic oscillations are then imposed at the head end to simulate traveling acoustic waves in the chamber. The main objectives of the present study are 1) to investigate the internal flowfield in a simulated rocket motor with surface injection, 2) to study the coupling between the imposed periodic fluctuations and turbulent motions, and 3) to explore the energy exchange and turbulence production mechanisms under nonstationary mean flow conditions.

II. Theoretical Formulation

Figure 1 shows the physical model for the problem, which simulates the flow development in a nozzleless solid-propellant rocket motor studied experimentally by Traineau et al.⁹ The chamber is closed at the head end and is connected downstream with a choked divergent nozzle at the exit. Air is injected uniformly through the porous wall to simulate the evolution of propellant combustion products from the surface. The flow accelerates from zero at the head end and becomes supersonic in the nozzle section. The flowfield is governed by the following conservation equations of mass, momentum and energy,²¹

$$\frac{\partial \rho}{\partial t} + \frac{\partial(\rho u_k)}{\partial x_k} = 0 \quad (1)$$

$$\frac{\partial(\rho u_k)}{\partial t} + \frac{\partial(\rho u_k u_l)}{\partial x_l} = -\frac{\partial p}{\partial x_k} + \frac{\partial \sigma_{kl}}{\partial x_l} \quad (2)$$

$$\frac{\partial(\rho e)}{\partial t} + \frac{\partial(\rho h u_k)}{\partial x_k} = \frac{\partial q_k}{\partial x_k} + \phi \quad (3)$$

where ρ is the density, u the velocity vector, p the thermodynamic pressure, h the total specific enthalpy, e the total specific internal energy, and T the temperature. The standard tensor notation with repeated indices implying summation over the axial and vertical components is used. The viscous stress σ_{kl} , the thermal diffusion q_k , and the viscous dissipation ϕ are defined as

$$\sigma_{kl} = -\frac{2}{3}\mu \frac{\partial u_j}{\partial x_j} \delta_{kl} + \mu \left(\frac{\partial u_k}{\partial x_l} + \frac{\partial u_l}{\partial x_k} \right) \quad (4)$$

$$q_k = k \frac{\partial T}{\partial x_k} \quad (5)$$

$$\phi = -\frac{2}{3}\mu \left(\frac{\partial u_k}{\partial x_k} \right)^2 + \mu \left(\frac{\partial u_k}{\partial x_l} + \frac{\partial u_l}{\partial x_k} \right) \frac{\partial u_k}{\partial x_l} \quad (6)$$

where μ is the dynamic viscosity and k the thermal conductivity. The governing equations are supplemented with the equation of state for an ideal gas

$$p = \rho RT \quad (7)$$

where R is the gas constant. The thermodynamic properties are assumed constant for the present case of cold-flow simulation, as the temperature variation within the flowfield of interest is not significant.

Turbulence closure is obtained based on the large-eddy simulation technique in which large, energy-carrying structures are computed exactly and the effect of small-scale motions on large scales is modeled. A spatial filter G is used to decompose the flow variables into large (resolved) and subgrid (unresolved) scales,²²

$$\mathfrak{Z}(\mathbf{x}, t) = \mathfrak{Z}^r(\mathbf{x}, t) + \mathfrak{Z}^s(\mathbf{x}, t) \quad \text{with} \quad \mathfrak{Z}^r(\mathbf{x}, t) = \int_D G(\mathbf{x} - \mathbf{x}', \Delta) \mathfrak{Z}(\mathbf{x}', t) d^3x' \quad (8)$$

where D is the entire domain; Δ the computational mesh size, which determines the size and structure of the unresolved scales; and \mathfrak{Z} any flow property, viz., ρ , p , u_i , or T . The superscripts r and s represent the resolved and unresolved scales of flow properties. The Favre averaging is further used to simplify the governing equations for compressible turbulent flow simulations.²² This density-weighted averaging eliminates complex triple correlations between density and velocity fluctuations in the governing equations and is given as

$$\tilde{\mathfrak{Z}}^r = \frac{(\rho \mathfrak{Z})^r}{\rho^r} \quad (9)$$

Contrary to the more traditional Favre time averaging,²³

$$\tilde{\mathfrak{Z}}^r \neq \tilde{\mathfrak{Z}}^r, \quad \tilde{\mathfrak{Z}}^s \neq 0 \quad (10)$$

The filtered form of the governing equations can be written as

$$\frac{\partial \rho^r}{\partial t} + \frac{\partial (\rho^r \tilde{u}_k^r)}{\partial x_k} = 0 \quad (11)$$

$$\frac{\partial (\rho^r \tilde{u}_k^r)}{\partial t} + \frac{\partial (\rho^r \tilde{u}_k^r \tilde{u}_l^r)}{\partial x_l} = -\frac{\partial p^r}{\partial x_k} + \frac{\partial \sigma_{kl}^r}{\partial x_l} + \frac{\partial \tau_{kl}}{\partial x_l} \quad (12)$$

$$\frac{\partial (\rho^r \tilde{e}^r)}{\partial t} + \frac{\partial (\rho^r \tilde{h}^r \tilde{u}_k^r)}{\partial x_k} = \frac{\partial q_k^r}{\partial x_k} - \frac{\partial Q_k}{\partial x_k} - \frac{\partial (\rho^r \overline{\tilde{u}_l^r \tilde{u}_l^r \tilde{u}_k^r})}{\partial x_k} + \phi^r \quad (13)$$

where $p^r = \rho^r R \tilde{T}^r$ and $\overline{(\quad)}$ represents the filtering operation defined by Eq. (8). σ_{kl}^r and ϕ^r represent the viscous stresses and dissipation of the resolved scales, respectively. The terms τ_{kl} and Q_k are the subgrid-scale (sgs) stresses and heat fluxes, respectively, and are given as

$$\tau_{kl} = -\rho^r \left(\overline{(\tilde{u}_k^r \tilde{u}_l^r)} - \overline{\tilde{u}_k^r} \overline{\tilde{u}_l^r} \right) + \left(\overline{u_k^s \tilde{u}_l^r} + \overline{\tilde{u}_k^r u_l^s} - \overline{\tilde{u}_k^s \tilde{u}_l^s} - \overline{\tilde{u}_k^s \tilde{u}_l^s} \right) + \left(\overline{u_k^s u_l^s} - \overline{\tilde{u}_k^s \tilde{u}_l^s} \right) \quad (14)$$

$$Q_k = C_p \rho^r \left(\overline{(\tilde{u}_k^r \tilde{T}^r - \tilde{u}_k^r \tilde{T}^r)} + (\overline{u_k^s \tilde{T}^r} + \overline{\tilde{u}_k^r T^s} - \overline{\tilde{u}_k^r \tilde{T}^s} - \overline{\tilde{u}_k^s \tilde{T}^r}) \right. \\ \left. + (\overline{u_k^s T^s} - \overline{\tilde{u}_k^s \tilde{T}^s}) \right) \quad (15)$$

The first terms in the small parentheses in Eqs. (14) and (15) can be computed directly once a filter function is defined. The other terms need to be modeled and represent the effect of unresolved scales on the resolved scales of motion. One important feature of any *sgs* model is to provide adequate dissipation. Here, dissipation means transport of energy from resolved scales to unresolved subgrid scales, and the rate of dissipation represents the flux of energy through the inertial subrange of the turbulence spectrum.²⁴ A Smagorinsky model extended to compressible flows is used to model these terms, as suggested by Erlebacher et al.²² Accordingly, the *sgs* terms are modeled by relating the *sgs* stresses to the large-scale strain-rate tensor S_{kl}^r , through the eddy viscosity (ν_T) and the *sgs* kinetic energy (K), as follows:

$$\tau_{kl} - \frac{2}{3} \delta_{kl} K = -2\nu_T \rho^r S_{kl}^r \quad (16)$$

$$S_{kl}^r = \frac{1}{2} \left(\frac{\partial \tilde{u}_k^r}{\partial x_l} + \frac{\partial \tilde{u}_l^r}{\partial x_k} \right) - \frac{1}{3} \delta_{kl} \left(\frac{\partial \tilde{u}_i^r}{\partial x_i} \right) \quad (17)$$

with

$$\nu_T = c_D (D\Delta)^2 (2S_{ij}^r S_{ij}^r)^{\frac{1}{2}} \quad \text{and} \quad K = c_I \rho^r (D\Delta)^2 (2S_{ij}^r S_{ij}^r) \quad (18)$$

where Δ is the average size of the computational cell, and c_D (≈ 0.01) and c_I (≈ 0.007) are the model constants, based on the work of Erlebacher et al.²² The Van-Driest damping function (D) is used to take into account the inhomogeneities near the surface^{20,21} and is expressed as

$$D = 1 - \exp(1 - (y^+)^3 / 26^3) \quad (19)$$

where $y^+ = y\tilde{u}_\tau^r / \nu$. The effect of surface transpiration is indirectly obtained through the wall shear stress τ_w^r , which appears in the computation of the friction velocity \tilde{u}_τ^r . The heat flux is modeled similarly by defining an eddy diffusivity and relating it to the viscosity through the turbulent Prandtl number (Pr_T).

$$Q_k = -\rho^r C_p \frac{\nu_T}{Pr_T} \frac{\partial \tilde{T}^r}{\partial x_k} \quad (20)$$

A standard value of 0.7 is used for the turbulent Prandtl number based on air as the medium.²²

Boundary conditions. The method of characteristics is used to specify the boundary conditions. For the subsonic inflow through the porous surface, three conditions need to be specified. The mass and energy fluxes are kept constant and the injection velocity is assumed to be vertical (i.e., $\tilde{u}^r = 0$). At the head end of the motor, the gradients of axial pressure and vertical velocity are set to zero, along with the adiabatic condition. Application of the slip condition at the head

end is necessary to avoid a numerically induced recirculating flow at the injection surface.²⁵ Symmetry conditions are applied along the centerline of the motor. The supersonic outflow requires no boundary conditions, according to the method of characteristics. The flow variables at the exit are extrapolated from those within the computational domain.

After a stationary flow is obtained, traveling acoustic motions in the motor are simulated by imposing periodic pressure and velocity oscillations at the head end as follows:

$$p^a = \varepsilon_a \bar{p} \sin(2\pi ft) \quad (21)$$

$$u^a = \bar{p}/(\bar{\rho} \bar{a}) \quad (22)$$

where the overbar denotes the time-averaged quantity, and ε_a and \bar{a} represent the percentage of the mean pressure and speed of sound, respectively. No phase difference exists between the pressure and the velocity fluctuations for such a simple wave. The temperature fluctuation is specified according to the isentropic relationship with the pressure.

$$T^a = \bar{T}(1 + p^a/\bar{p})^{(\gamma-1/\gamma)} - \bar{T} \quad (23)$$

III. Numerical Method and Error Analysis

An accurate numerical scheme is essential for resolving various time and length scales of turbulent motions. The issue of a priori estimation of computational errors in turbulence simulations has recently been addressed by several researchers.^{26,27} Ghosal²⁶ analyzed the truncation errors of the various terms in finite-difference equations and compared the contributions of the errors at a given time with the exact terms for incompressible flow equations. A model turbulence spectrum was employed to facilitate the comparison. Results indicated that for finite-difference methods the errors created by approximating the convection terms generally dominate errors introduced by other terms in the governing equation. These convection terms are important in any turbulence computation at large Reynolds numbers, as they represent the dominance of inertial force over viscous force. Fabignon et al.²⁷ and Beddini et al.²⁸ extended the von Neumann stability analysis^{29,30} to assess the importance of the errors associated with convection terms by introducing a reference spectrum obtained from homogeneous, isotropic turbulence theory. This energy spectrum was convected in accordance with the amplification factor of the numerical scheme and then compared with the initial spectrum after one large-eddy lifetime. An estimation of the numerical errors of nonlinear convection terms was made. The fourth-order Runge–Kutta scheme with the sixth-order Padé compact differencing for spatial discretization (RK4-6CP) was shown to resolve the turbulence energy spectrum in the inertial range for a wide range of Mach numbers. A significant reduction in computational time, compared with RK4-6CP, can be achieved by means of an alternative Runge–Kutta scheme presented by Jameson,³¹ which is fourth-order accurate in time and uses fourth-order central differencing in space (RK4-4C). It was shown by Beddini et al.²⁸ that the RK4-4C scheme resolves the energy spectrum with an accuracy comparable to that of the sixth-order Padé scheme over a wide range of Mach numbers. The compromise between

computational time and spatial accuracy facilitates the use of Jameson's method in the present study.

Following the analyses by Fabignon et al.²⁷ and Beddini et al.,²⁸ the effect of computational errors on *sgs* modeling is investigated herein based on the Smagorinsky subgrid eddy-viscosity model. The work extends the previous effort to incorporate the effects of *sgs* models and artificial dissipation, introduced in central-difference schemes for numerical stabilization, on the convection of the turbulence energy spectrum. A thorough investigation is carried out for the RK4-4C method. The transport equation for the energy spectrum function $E(k, t)$ for turbulent flows can be expressed as²⁸

$$\frac{\partial}{\partial t} E(k, t) + (\bar{u}_k)_{AB} \left(\frac{\partial}{\partial x_k} \right)_{AB} E(k, t) = T(k, t) - D(k, t) - P(k, t) \quad (24)$$

where $T(k, t)$ represents the energy transfer between wave numbers, $D(k, t)$ the viscous dissipation, and $P(k, t)$ the production term. A and B represent the points in the flowfield for two-point correlation. For stationary flows, the first term on the left-hand side is zero, and if homogeneity is assumed, the convective term also vanishes. Retention of the convective terms for spectral transport enables the present estimation of convection errors. Convection of the energy spectrum is assumed to take place at a constant mean velocity \bar{u}_k . The main objective of this work is to utilize a representative turbulence spectrum, obtained from the model of the transfer, dissipation, and production terms in the preceding equation, to allow for the estimation of the effectiveness of a numerical scheme. The initial kinetic energy spectrum is introduced using Tennekes and Lumley's analysis.³² It models the production-dominated part of the spectrum at low wave numbers, representing large, energy-carrying structures, and provides the classical $k^{-5/3}$ power law in the inertial subrange, representing equilibrium turbulence. The dimensionless spectrum of turbulent energy is given as²⁸

$$E(k, 0) = \alpha(\delta Re_c)^{-5/4} (k\eta)^{-5/3} \times \exp(-1.5\pi\beta\sqrt{\alpha}(\delta Re_c)^{-1} (k\eta)^{-4/3}) \quad (25)$$

where α is the Kolmogorov constant and η the Kolmogorov length scale. Experimental data show that α and β are 1.5 and 0.3, respectively.^{27,28} An order-of-magnitude estimate relates the turbulent Reynolds number (Re_t) and the Reynolds number at the centerline of the motor (Re_c),

$$Re_t \approx \delta Re_c \quad (26)$$

where $\sqrt{\delta} \approx q/U \approx \ell/L$.

Convection of the initial energy spectrum depends on the numerical scheme and takes the form

$$E(k, \tau) = |G_{k,u}|^{I_\tau} E(k, 0) \quad (27)$$

where $G_{k,u}$ is the amplification factor obtained from the eigenvalue u of the numerical scheme. I_τ is the number of time steps required to reach one eddy lifetime τ , which depends on the grid size and the CFL number σ :

$$I_\tau = \delta^{1/4} \frac{(M+1)}{\xi M \sigma} Re_c^{3/4} \quad (28)$$

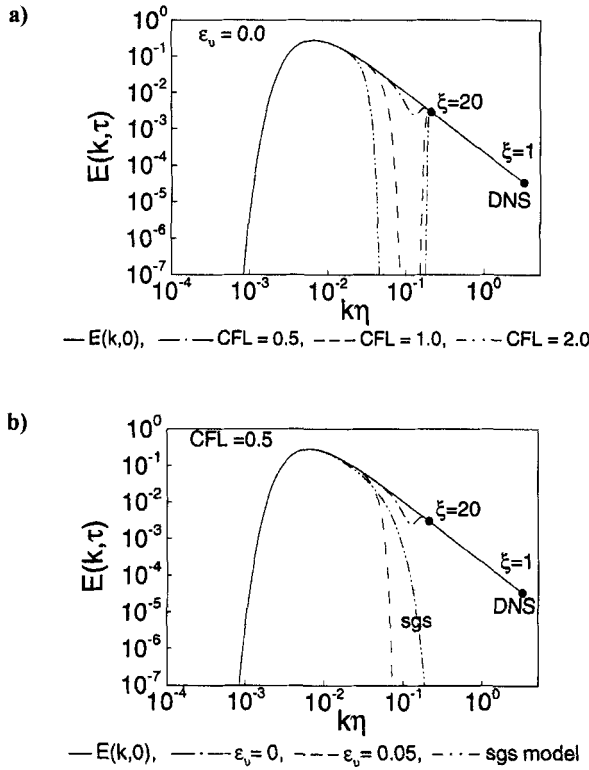


Fig. 2 Dimensionless turbulent energy spectrum of the RK4-4C scheme with $\xi = 20$: a) effect of CFL number for $\epsilon_v = 0$; b) effect of artificial dissipation and sgs model for CFL = 0.5.

where ξ is the grid parameter ($\Delta x/\eta$). This approach provides a basis for selection of grid size for large-eddy simulation, which requires the cutoff wavenumber to be in the inertial range of the energy spectrum.

Figure 2a shows the spectrum for the RK4-4C scheme for various CFL numbers after one eddy lifetime, at a representative motor condition of $Re_c = 3 \times 10^5$ and $M_c = 0.5$. No artificial dissipation is considered in this analysis, i.e., $\epsilon_v = 0$. The grid parameter ξ of unity implies that the entire range of turbulence scale, up to the Kolmogorov length scale, is modeled as in a direct numerical simulation (DNS). ξ usually varies between 10 and 50 for typical large-eddy simulations and is approximately 15 in the present computation. A decrease in ξ shifts the cutoff point toward the DNS value. $\xi = 20$ is used here to illustrate the range of scale resolved in LES compared with DNS. The numerical scheme becomes neutrally stable at the maximum wave number and the spectrum rises to the cutoff point, as shown in Fig. 2a. An increase in the CFL number reduces the resolution of the energy spectrum owing to the reduction in the cutoff wave number. Since the computational time is inversely proportional to the CFL number, a CFL number of 0.5 is found to be a good compromise between accuracy and computational time.

Artificial dissipation is required to reduce the amplification factor and stabilize the numerical scheme at high wave numbers. Figure 2b shows the effect of the sixth-order artificial dissipation and Smagorinsky's *sgs* model on convection of the energy spectrum. The eddy-viscosity hypothesis gives an estimate of the energy spectrum evolution as³³

$$E(k, \tau) = E(k, 0) \exp\left(-2(k\eta)^2 \sqrt{\delta Re_c} \left(1 + \frac{\nu_T}{\nu}\right)\right) \quad (29)$$

where the eddy viscosity (ν_T) is obtained from the *sgs* model as

$$\frac{\nu_T}{\nu} = 4.11 c_s^2 (\sqrt{\alpha} \beta)^{\frac{1}{4}} \xi^{4/3} \quad (30)$$

The artificial dissipation and *sgs* dissipation are of the same order in the present case, as evidenced in Fig. 2b. Ragab and Sheen³⁴ indicate that the dissipation mechanism in a three-dimensional turbulence simulation is very different from the artificial dissipation, because of the vortex stretching and rolling phenomena. Liou et al.²⁰ showed in their two-dimensional simulation of injection-driven flows that *sgs* stresses have negligible effects on the turbulence characteristics and the artificial dissipation introduced by the numerical scheme can serve as an *sgs* model. The study partly provides a justification for not incorporating *sgs* models and relying on numerical artificial dissipation to produce the *sgs* effect on large energy-carrying structures. Accordingly, the *sgs* terms are neglected herein to save computational effort.

Owing to the enormous computational effort required, only two-dimensional calculations are performed in the present work to study the interactions between acoustic oscillations and motor flow evolution. The analysis, in spite of the lack of a vortex-stretching mechanism, is more accurate than conventional models based on second-order turbulence closure schemes and allows for a systematic investigation into the oscillatory flowfields in a rocket motor. Results will be further corroborated in a subsequent study using full three-dimensional large-eddy simulations.³⁵

IV. Stationary Flowfield

The analysis described above is used to first study the flow development in a simulated nozzleless rocket motor, as shown schematically in Fig. 1. The chamber is two-dimensional and measures 48 cm in length and 2 cm in height. The nozzle at the exit is 3.2 cm long, with a divergence angle of 15 deg. The configuration and the flow parameters studied are based on the experiment of Traineau et al.⁹ Air is injected through the porous surface at a total temperature of 260 K and a total pressure of 3.142 atm. The mean injection mass flux is kept constant at $\bar{m}'' = 13 \text{ kg/m}^2\text{s}$, giving the injection velocity of 3.1 m/s. The numerical calculation is initialized with the analytical velocity profile for an inviscid incompressible flow with surface mass injection,^{6,7}

$$\frac{\bar{u}^r}{\bar{u}_c^r} = \cos\left(\frac{\pi}{2} \frac{y}{h}\right) \quad (31)$$

where the subscript *c* represents the centerline. White noise is introduced in the inflow mass flux to perturb the mean flow for turbulence transition. The magnitude of perturbation is 90% of the mean quantity, as indicated by Traineau et al.⁹ Such a

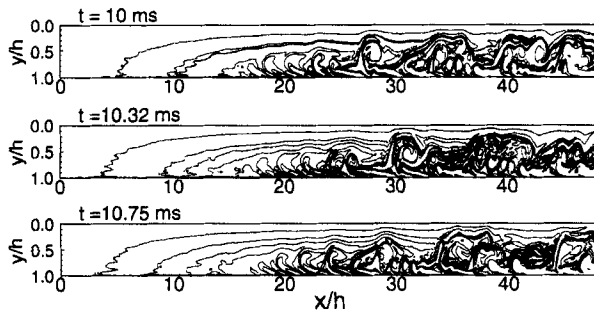


Fig. 3 Time evolution of the vorticity field.

high level of turbulence intensity at the surface is employed to facilitate comparison with experimental data. The computational domain consists of 640×100 cells in the axial and vertical directions, respectively. A uniform grid is used in the x -direction, while the grid is stretched toward the surface in the y -direction with the smallest grid size of the order of $50 \mu\text{m}$. The grid size is based on the studies of Liou et al.^{19,20} and resolves the energy spectrum in the inertial subrange, as shown later. The CFL number is 0.5 and the time step is fixed at 5×10^{-8} s for time-accurate simulations. An outbreak of turbulence occurs at 4–5 ms of the physical time starting from the flow initialization based on Eq. (31). Stationary oscillations are obtained during 8–20 ms, and the mean flow properties are evaluated in this time zone.

A. Vorticity Field

Figure 3 shows the temporal evolution of the vorticity field. To facilitate discussion, only the lower half of the chamber is presented, where $y/h = 1$ corresponds to the injection surface. Vorticity is produced at the propellant surface because the no-slip condition causes the flow to enter the chamber vertically and then turn to align smoothly with the axial axis.^{13,14} Near the head end, turbulent fluctuations appear to be small and the flow is mostly laminar. Transition to turbulence occurs around $x/h = 20$ –25, and the flow becomes highly turbulent farther downstream. Vorticity is rapidly convected away from the surface in this inertia-dominated flow, as evidenced by the presence of large energy-carrying structures. The present two-dimensional computation lacks the vortex-stretching phenomenon responsible for the transfer of energy from the large to the small scales through the energy cascade mechanism and, consequently, leads to lower dissipation and production rates. Nevertheless, it provides much useful insight into the flow development, which was not previously available using second-order turbulence closure schemes.

B. Mean Flow Properties

Figure 4 shows the contour plots of the time-averaged Mach number, pressure, and density fields. The exit Mach number of 2.2 agrees well with the analytical value for an isentropic flow through a divergent nozzle with a known area ratio and given stagnation pressure and temperature upstream. The pressure field is basically one-dimensional, due to the small injection Mach number, with increasing gradient

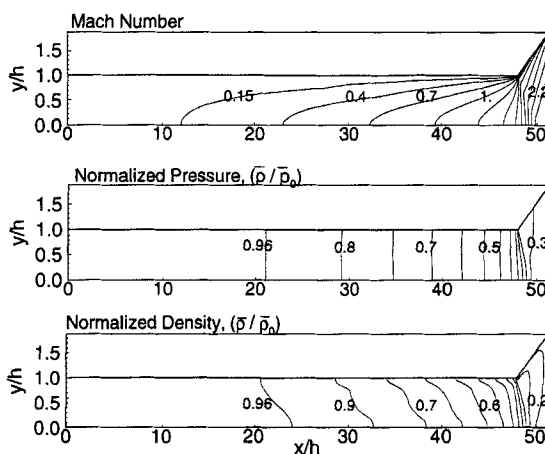


Fig. 4 Contour plots of mean Mach number, pressure, and density.

toward the throat area. Figures 5 and 6 show the axial and vertical variations of the mean axial velocity, respectively. Also included is the analytical solution for an incompressible laminar flow.^{6,7} Good agreement with the experimental data of Traineau et al.⁹ is obtained. The flow is predominantly incompressible and laminar in the upstream region of the chamber. Deviation from the incompressible-flow solution starts between $x/h = 20$ and 30, due to the increasing Mach number and hence the compressibility effect. In the present study, the injection mass flux is kept constant. As a result of rapidly decreasing density toward the throat area, the local flow velocity increases and leads to changes in the velocity profile from its incompressible-flow counterpart. The enhanced momentum transfer due to turbulence also plays an important role. The transition of the mean velocity profile can be characterized in terms of the momentum flux coefficient β , as proposed by Huesmann and Eckert,³⁶

$$\beta = \frac{\int_0^h \bar{\rho} \bar{u}^2 dy}{\bar{\rho}_b \bar{u}_b^2 h} \quad (32)$$

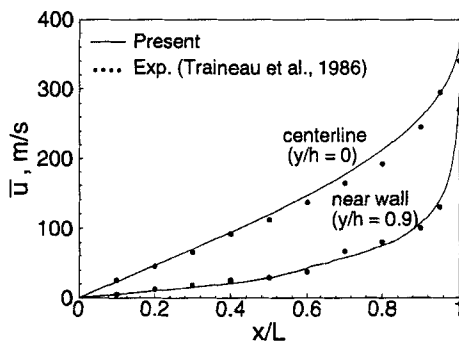


Fig. 5 Variations of mean axial velocity in the axial direction.

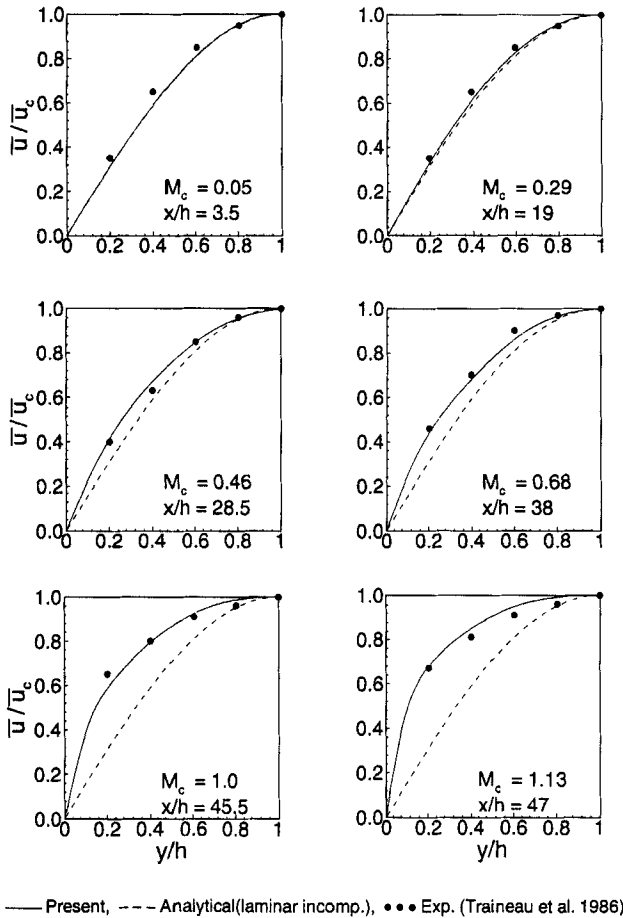


Fig. 6 Variations of normalized mean axial velocity in the vertical direction.

where the subscript b denotes the bulk mean quantity, obtained by averaging the corresponding flow property over a given cross section of the chamber. Figure 7 compares the calculated β with experimental data.⁹ The momentum flux coefficient has a constant value of 1.234 for laminar incompressible flow and can be obtained using Eqs. (31) and (32). The decreasing density and increasing injection velocity toward the nozzle alter the vertical variation of the axial velocity and consequently cause an accelerated decrease in the β value in the downstream region. The experimental value of β at the head end is 1.16 instead of 1.234 as predicted by laminar flow theory, because of the high level of turbulence at the porous wall generated in the experiments.⁹ The agreement of the calculated β in the upstream region with laminar flow theory implies uncertainties in the experimental measurements. Both the numerical and the experimental data show faster variation between $x/h = 20$ and 30 in the turbulent regime. These results are very similar to those obtained by Beddini¹¹ for an axisymmetric duct with a low level of pseudo turbulence at the porous wall.

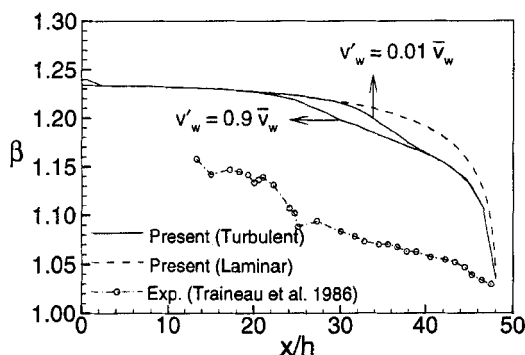


Fig. 7 Variation of momentum flux coefficient in the axial direction.

The effect of surface-generated turbulence on the flow development is also studied. For a high level of wall turbulence (i.e., $v'_w = 0.9\bar{v}_w$), transition of the mean velocity profile occurs upstream of the motor ($x/h = 20$). The transition point shifts downstream ($x/h = 30$) with a lower level of pseudo turbulence (i.e., $v'_w = 0.01\bar{v}_w$) and agrees well with the results of Liou et al.,²⁰ indicating the influence of turbulence on the mean velocity field. Farther downstream ($x/h > 42$), the flowfield is dominated by compressibility effects, and the variation of β closely follows that predicted by laminar compressible-flow theory.

C. Turbulence Energy Spectrum and Transport Properties

To make use of the equilibrium hypothesis generally employed in *sgs* models for estimating the effect of unresolved scales on large-scale structures, the cutoff wave number for turbulence computation should lie in the inertial subrange of the turbulence energy spectrum. This is verified from the energy spectra of the axial velocity fluctuation at various locations, as shown in Fig. 8. The standard 5/3 law of energy spectrum based on the Kolmogorov–Obukhov theory may not be observed in the present two-dimensional simulation. Lesieur et al.^{37,38} indicate in their two-dimensional computation of a temporal mixing layer that the exponent of the wavenumber in the inertial subrange of the turbulence energy spectrum is close to -4 . Gilbert³⁹ proposed that the kinetic energy spectrum results from spiral vortex distributions within the coherent vortices and should follow the $f^{-11/3}$ law, where f is frequency. Figure 8 indicates that the spectrum in the inertial subrange lies between the f^{-3} and the f^{-4} variations. The result ensures that the energy spectrum is well captured in the present computation throughout the chamber, which further confirms the adequacy of the computational grid.

Figures 9a through d show the vertical variations of turbulence intensity ($I = \sqrt{u'^2 + v'^2}$), $\sqrt{u'u'}$, $\sqrt{v'v'}$, and the Reynolds stress ($\overline{u'v'}$) at various axial locations, respectively. The measured turbulence intensity and Reynolds stress⁹ are also included for comparison. The peak in the turbulence intensity increases rapidly and shifts toward the porous wall farther downstream. Since the mass influx is kept constant in the present study, the density decreases and injection velocity increases as the flow accelerates toward the throat. The increasing injection velocity tends to reduce the wall-damping effect, and therefore little change in the vertical

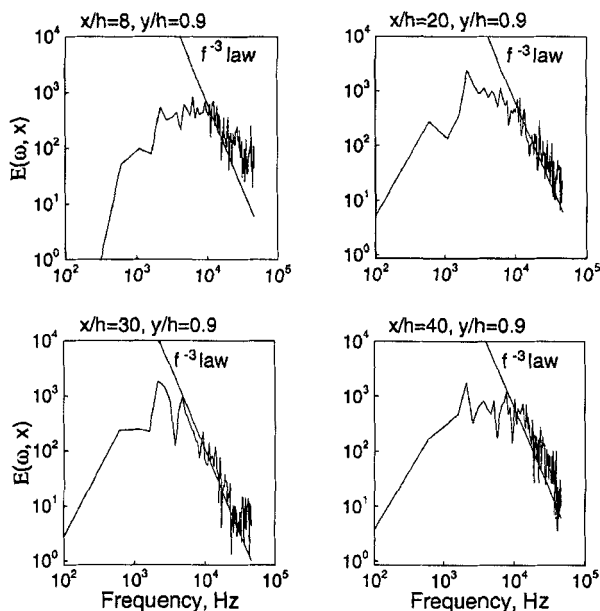


Fig. 8 Turbulence energy spectrum of axial velocity fluctuations at various axial locations.

location of turbulence intensity peak occurs beyond $x/h = 35$. Figures 9b and c show the relative contribution of the axial and radial velocity fluctuations to the turbulence intensity. The internal flowfield is dominated by the strain rates in the axial direction, causing a higher intensity in the axial component. The underprediction of the Reynolds stress may be attributed to the lack of vortex stretching mechanism in the present two-dimensional simulation. The turbulent energy is transferred from large energy-carrying eddies to smaller scales through the energy cascade and is finally dissipated at the molecular level through vortex stretching. The production mechanism in real turbulence is different from that in a two-dimensional simulation, because of the additional spanwise direction. The present approach represents an improvement, however, compared with the conventional two-equation models, which do not predict the Reynolds stress and overpredict the turbulence intensity level.¹²

D. Motor Flow Development

The overall flow development in the motor can be characterized by three distinct regimes—laminar, transitional, and fully turbulent flows—as shown schematically in Fig. 10. Near the head end, the flow is laminar and its velocity profiles can be determined by the laminar similarity theory.^{6,7} The hydrodynamic instability then renders the flow unstable, and turbulence begins to occur in the downstream region (point A). Unlike channel flows without surface injection, the outbreak of turbulence takes place away from the wall, with the region of intensive turbulence production shifting toward the wall as the flow accelerates in the downstream region. Within the initial transition regime, the mean velocity profiles still

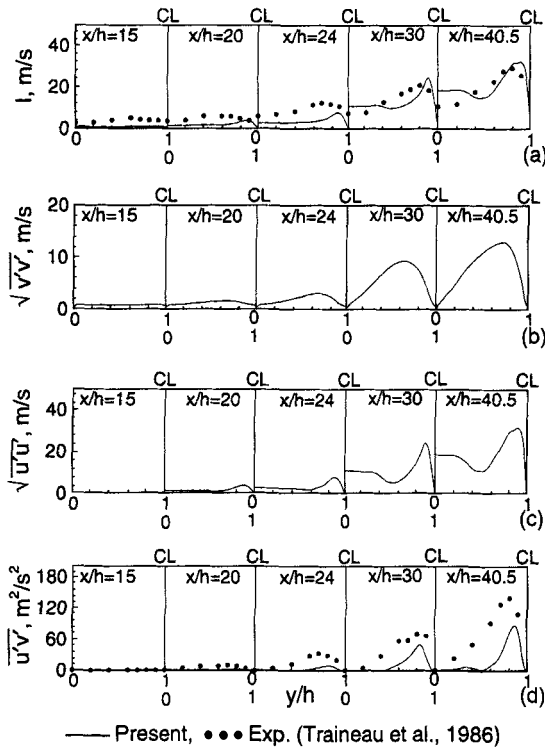


Fig. 9 Vertical distributions of turbulence properties at various axial locations.

correspond to the form predicted by the laminar similarity theory, because of the predominance of the pressure gradient over the viscous stress. As the flow develops further, a strong turbulent flow regime is observed. The deviation of the mean velocity profiles from those predicted by incompressible-laminar flow theory become significant due to the effect of turbulence and fluid compressibility.

Although the entire flowfield is driven by the mass injection through the porous wall, the characteristics of each flow regime are dominated by different physical mechanisms. To facilitate discussion, three key parameters characterizing the flow development are defined here: the injection Reynolds number $Re_w \equiv \bar{v}_w h / \nu$, the mean-flow Reynolds number $Re_m \equiv \bar{u}_b h / \nu$, and the momentum flux coefficient β defined in Eq. (32). The laminar flow regime reaches from the head end to about $x/h = 20$. The turbulence intensity is extremely small, and the velocity profiles can be described by the laminar-flow theory. An analytical study conducted by Hu⁴⁰ indicates that for the injection Reynolds numbers Re_w greater than 500, the velocity profiles are almost identical to the prediction, based on an inviscid rotational-flow analysis, Eq. (31). Significant differences are found, however, between the velocity profiles for inviscid and viscous flows for Re_w less than 100. This observation is consistent with the experimental findings of Dunlap et al.⁴¹ For moderate and high injection Reynolds numbers, the flow is driven mainly by the pressure gradient arising from the mass injection; the viscous shear stress plays a much less important role in determining the flow development. Since the injection Reynolds number

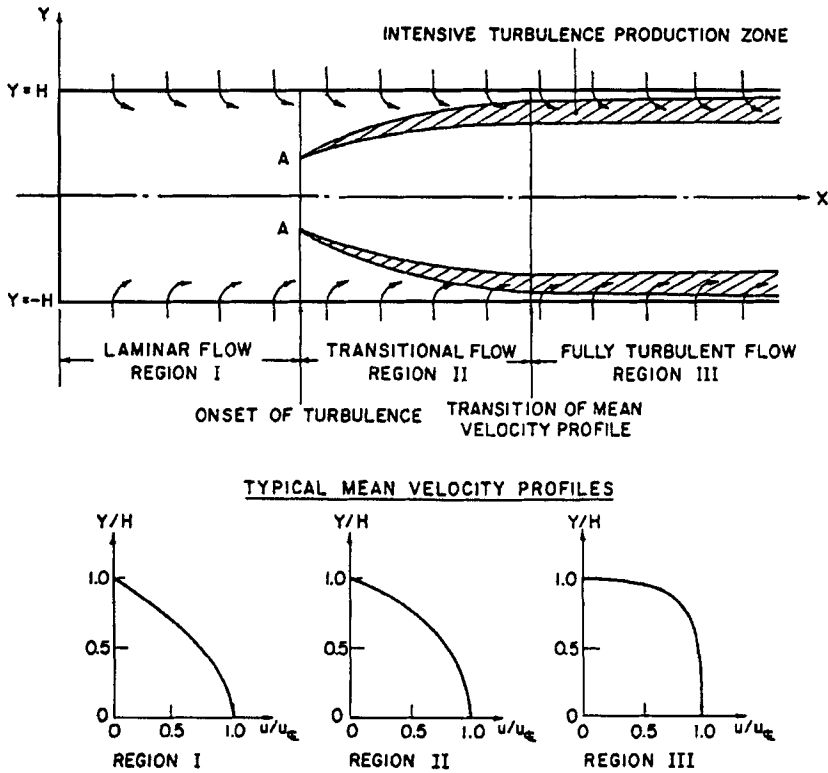


Fig. 10 Schematic diagram of internal flow development in a chamber.

near the head end is about 15×10^3 in the present case, the calculated velocity agrees closely with the cosine profile. A similar observation is made for the distribution of the radial velocity, which can be predicted by the following expression:

$$\frac{\bar{v}^r}{\bar{v}_w^r} = \sin\left(\frac{\pi y}{2h}\right) \quad (33)$$

The second regime is characterized by the onset of turbulence. When the fluid particle moves downstream, the local velocity and Reynolds number increase and eventually reach a point at which turbulent fluctuations occur. The classical hydrodynamic instability analysis of the Poiseuille flow cannot accurately predict the laminar-to-turbulence transition in a porous duct with surface transpiration. Varapaev and Yagodkin⁴² found that the effect of the vertical velocity component must be taken into account in predicting the critical Reynolds number Re^* for the onset of turbulent oscillation. For a small injection Reynolds number, a substantial reduction of Re^* from its counterpart for an impermeable pipe flow is observed, due to the destabilizing effect of the transverse velocity component. For Re_w greater than 300, however, the critical Reynolds number increases linearly with Re_w , due to the stabilizing effect of the resultant favorable pressure gradient. Figure 9 indicates that the turbulent kinetic energy remains at a very low level in the head-end region up to $x/h = 20$ and increases rapidly afterward. The mean velocity profile

only changes slightly, as shown in the transitional region (i.e., $20 < x/h < 25$) in Figs. 6 and 7.

As the flow develops farther downstream, the velocity profile transits into the shape of a fully developed turbulent pipe flow with surface transpiration. The axial velocity gradient becomes much steeper near the wall but smoother in the core region. The value of the momentum flux coefficient β decreases down to 1.04 at the chamber exit. It should be noted that, in addition to the turbulence effect, fluid compressibility might exert more significant influence on the variation of the velocity profile due to the large density gradient in the downstream region.

V. Effect of Acoustic Oscillation on Flow Evolution

After the stationary motor flowfield is obtained, traveling acoustic oscillations are imposed at the head end for two frequencies of 673 and 1346 Hz, corresponding to the second and fourth modes of the longitudinal standing wave in the chamber. The amplitude of the pressure fluctuation is about 5% of the mean pressure at the head end, i.e., $\bar{p} = 3.142$ atm. Computations are performed for 10 cycles of acoustic oscillations in order to obtain statistically meaningful results for data analysis.

A. Decomposition and Averaging

The imposed periodic fluctuations give rise to additional mechanisms of energy transfer between the mean and the turbulent flow. By following the triple decomposition of Hussain and Reynolds,⁴³ each resolved-scale flow property $\tilde{\mathcal{T}}^r(\mathbf{x}, t)$ can be expressed as the sum of the time-averaged $\tilde{\mathcal{T}}(\mathbf{x})$, periodic $\mathcal{I}^a(\mathbf{x}, t)$, and filtered turbulent $\mathcal{I}'(\mathbf{x}, t)$ quantities as follows:

$$\tilde{\mathcal{T}}^r(\mathbf{x}, t) = \tilde{\mathcal{T}}(\mathbf{x}) + \mathcal{I}^a(\mathbf{x}, t) + \mathcal{I}'(\mathbf{x}, t) \quad (34)$$

Both the ensemble- and the time-averaging techniques defined below⁴⁴ are employed to facilitate the decomposition.

Ensemble averaging:

$$\langle \tilde{\mathcal{T}}^r(\mathbf{x}, t) \rangle = \lim_{N \rightarrow \infty} \frac{1}{N} \sum_{n=0}^{N-1} \tilde{\mathcal{T}}^r(\mathbf{x}, t + n\tau) \quad (35)$$

Time averaging:

$$\tilde{\mathcal{T}}(\mathbf{x}) = \lim_{N \rightarrow \infty} \frac{1}{N} \sum_{n=0}^{N-1} \tilde{\mathcal{T}}^r(\mathbf{x}, t_0 + n\Delta t), \quad \text{where} \quad N\Delta t \gg \tau \quad (36)$$

$$\mathcal{I}^a(\mathbf{x}, t) = \langle \tilde{\mathcal{T}}^r(\mathbf{x}, t) \rangle - \tilde{\mathcal{T}}(\mathbf{x}) \quad (37)$$

where τ is the period of the forced oscillation. $\tilde{\mathcal{T}}(\mathbf{x})$ is the long-time average starting from the initial time t_0 , after which steady fluctuations of flow properties are observed. $\mathcal{I}^a(\mathbf{x}, t)$ is the short-time average and represents the periodic fluctuating part. Evaluation of the ensemble average requires calculation and storage of flow quantities over a large number of cycles, to achieve statistical significance. To bypass this computational difficulty, it can be alternatively obtained using time-frequency localization techniques based on the wavelet or fast Fourier transform (FFT) theories. The latter is employed in the present

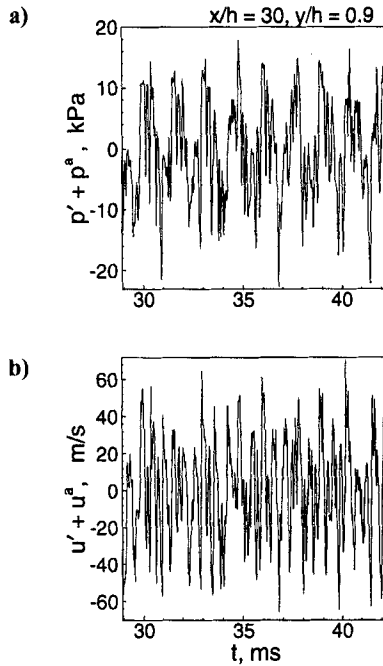


Fig. 11 Time histories of turbulent and acoustic fluctuations: a) pressure; b) axial velocity.

work. The fluctuating part comprising the turbulent and periodic oscillations is first obtained by subtracting the long-time averaged quantity from its instantaneous value. An FFT technique is then applied to transform the data from the physical to the spectral space. The periodic signal is of a known frequency and can be separated from the original signal by using a windowed Fourier transform in the frequency domain. Figures 11a and b show the time evolution of the pressure and axial velocity fluctuations at $x/h = 30$ and $y/h = 0.9$ for $f = 673$ Hz. These signals involve a wide range of frequency corresponding to turbulent fluctuations, in addition to the frequency of the imposed periodic motion. Figures 12a and b show the power density spectra of the pressure and axial velocity fluctuations, exhibiting a distinct peak at 673 Hz. A corresponding power density spectrum for the velocity fluctuation without imposed acoustic motion is shown in Fig. 13. The magnitude of velocity fluctuation with impressed acoustic oscillations is higher than that of the stationary turbulence case indicating enhanced turbulence production due to interactions between periodic and turbulent motions. The qualitative distributions of the power density spectrum are the same for both with and without imposed acoustic oscillations. This facilitates the use of the above procedure to accurately compute the turbulent and periodic fluctuations from the total signal.

B. Vorticity Field

Figures 14 and 15 show the time evolution of the vorticity fields with imposed acoustic motions at frequencies of 673 and 1346 Hz, respectively. Oscillatory

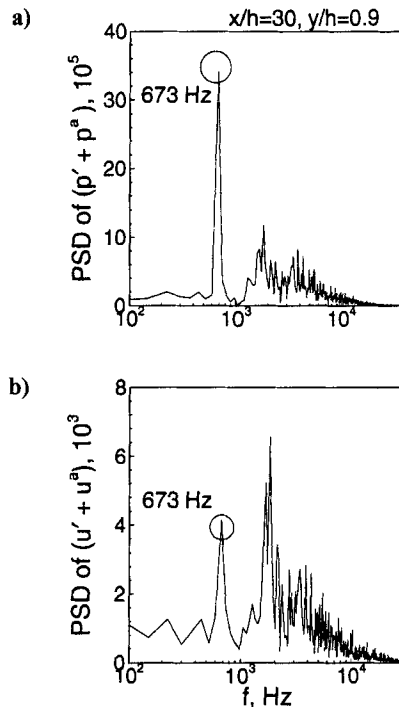


Fig. 12 Power spectral density (PSD) of fluctuating quantity with forced oscillations at $f = 673$ Hz: a) pressure; b) axial velocity.

vorticity is generated at the injection surface because of the no-slip condition.^{13,15} Streaks of vortex lines, which were absent in the stationary case, are clearly observed in the upstream laminar regime. The acoustic fluctuation-induced shear waves undergo transition in the midsection of the motor, giving rise to large-scale motions in the turbulent region. The eddy motions in the acoustic environments appear to be more organized, compared with the case without acoustic waves, and show strong interaction between turbulence and periodic excitations. The

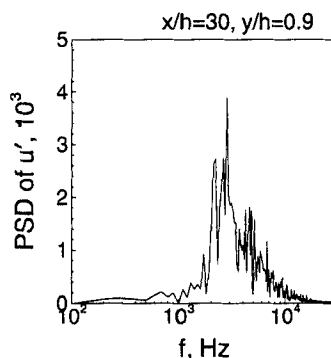


Fig. 13 Power spectral density (PSD) of axial-velocity fluctuation without forced oscillations.

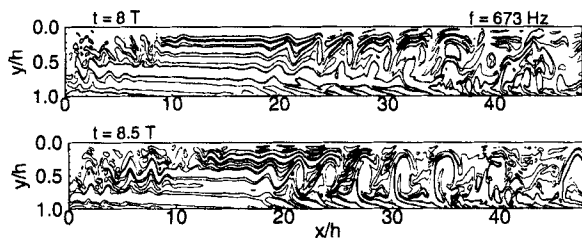


Fig. 14 Time evolution of vorticity fluctuations: $f = 673$ Hz.

fluctuating fields for the two frequencies shown here appear to be drastically different in the upstream regime. For $f = 673$ Hz, the turbulence transition occurs farther upstream, suggesting enhanced turbulence-production mechanisms arising from interactions with acoustic motions. For the higher-frequency case of 1346 Hz, the turbulence level upstream is minimal. Thus, low-frequency acoustic motions in a rocket motor appear to have more significant influence on the oscillatory flow-field.

C. Acoustic Field

Before analyzing the interactions between the acoustic and the turbulent flow-fields, a systematic analysis of traveling waves in a rocket motor is performed. Figure 16 shows the time evolution of the acoustic pressure along the center-line of the motor. A 35% decrease in the magnitude occurs between the head end and the throat. The result is compared with the prediction from quasi one-dimensional analysis, since the pressure field is predominantly one-dimensional. The theoretical model includes the mass influx at the wall as a source term in the governing equations, from which a linearized wave equation is derived. A traveling wave is simulated by imposing periodic boundary conditions at the head end based on the flow parameters used in the present study, *viz.*, $\dot{m}'' = 13$ kg/m²s, $\bar{p} = 3.142$ atm. The resultant differential equations and associated boundary conditions are solved using a space-marching technique. A detailed derivation of the formulation is given in the Appendix.

The analysis focuses on the energy-loss mechanism of acoustic motions resulting from the mass inflow through the lateral boundary of the chamber. The process takes place when a flow particle enters the chamber in a direction perpendicular to

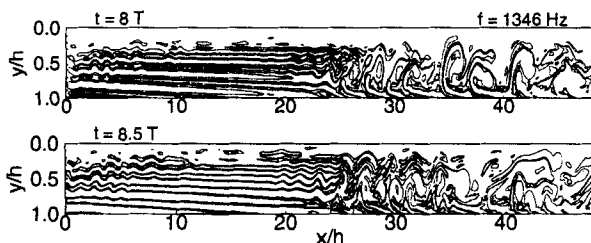


Fig. 15 Time evolution of vorticity fluctuations: $f = 1346$ Hz.

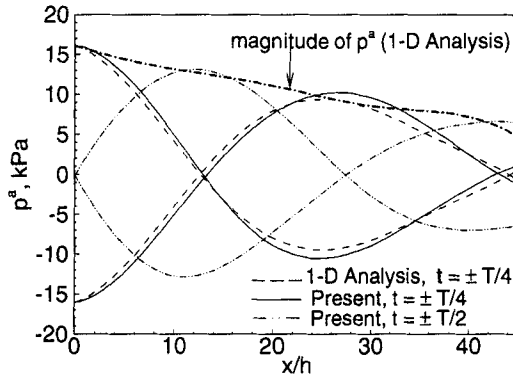


Fig. 16 Axial variations of pressure oscillation compared with analytical results.

the propellant surface and contributes no kinetic energy to the waves in the longitudinal mode. The particle then undergoes a turn into the direction parallel to the chamber axis and eventually participates in the periodic motions, which comprise mainly axial oscillations. During this process, the incoming flow acquires energy from the original acoustic field, representing a redistribution of acoustic energy. The one-dimensional model of Culick⁴⁵ indicates, however, that the acoustic field loses its energy at a rate of twice that actually obtained by the incoming flow. The additional loss can be regarded as the net exchange of energy from the acoustic field to the mean flow field, which is termed “flow-turning loss.” The correct prediction of the decrease in the magnitude of acoustic pressure throughout the combustion chamber indicates the accuracy of the data-deduction procedure employed in this study.

D. Effect of Acoustic Oscillation on Turbulence Properties

The triple decomposition of Eq. (34) enables energy transfer to be viewed as taking place among three participating fields. The turbulent stress in the present case can be expressed as

$$\tau_{kl} = -\overline{\rho u'_k u'_l} - \overline{\rho u^a_k u^a_l} \quad (38)$$

It differs from its form for a stationary flow by virtue of an additional stress due to the “organized” or “periodic” part of the oscillatory motions ($-\rho u^a_i u^a_j$). A set of differential equations describing the transport of the variance of the turbulent and periodic axial velocities may be deduced in the component form, yielding coupled time-averaged energy equations,⁴⁴

$$\begin{aligned} \frac{D}{Dt} (\overline{\rho u^a_\alpha u^a_\alpha}) &= \dots + \overline{\rho u'_i u'_\alpha} \frac{\partial u^a_\alpha}{\partial x_i} - \overline{\rho u^a_i u^a_\alpha} \frac{\partial \bar{u}_\alpha}{\partial x_i} + \dots \\ \frac{D}{Dt} (\overline{\rho u'_\alpha u'_\alpha}) &= \dots - \overline{\rho u'_i u'_\alpha} \frac{\partial \bar{u}_\alpha}{\partial x_i} - \overline{\rho u'_i u'_\alpha} \frac{\partial u^a_\alpha}{\partial x_i} + \dots \end{aligned} \quad (39)$$

where D/Dt denotes the substantial derivative following the mean motion of the fluid, and repeated English alphabets imply summation, while Greek letters imply

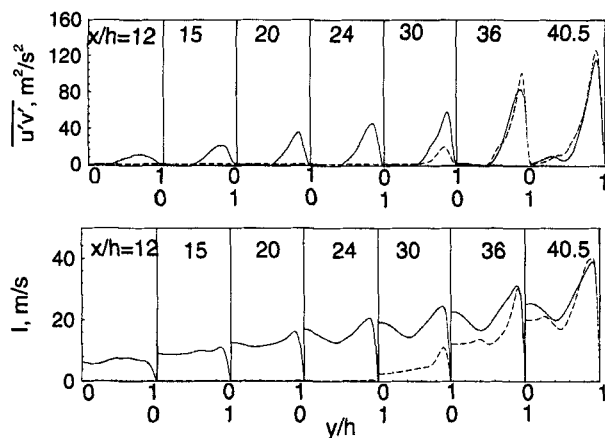


Fig. 17 Vertical distributions of turbulence intensity and Reynolds stress at various axial locations: (—) without forced oscillations; (---) with forced oscillations at $f = 673 \text{ Hz}$.

no summation on the indices. Additional terms, such as pressure-strain, diffusion, and dissipation, are not explicitly written, as the focus herein is placed on the production terms in these transport equations. For the case of production of $(\rho u'u')$, the important correlations are $\rho u'v'\partial\bar{u}/\partial y$ and $\rho u'v'\partial u^a/\partial y$. While the first term is equally important for stationary turbulence, the latter accounts for the energy exchange between the turbulent and the oscillatory fields, as suggested by Brereton et al.⁴⁴ Figures 17 and 18 show the vertical distributions of the turbulence stress and intensity at various axial locations for two different acoustic frequencies, respectively. The corresponding stationary-turbulence properties are also indicated for comparison. The enhanced level of turbulence in the upstream region of the

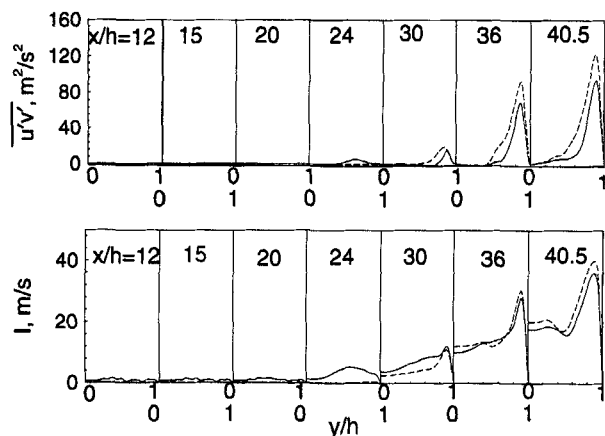


Fig. 18 Vertical distributions of turbulence intensity and Reynolds stress at various axial locations: (—) without forced oscillations; (---) with forced oscillations at $f = 1346 \text{ Hz}$.

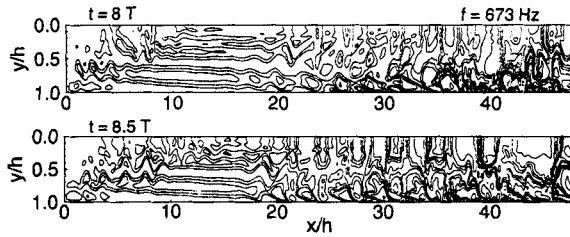


Fig. 19 Contour plots of fluctuating axial velocity with forced oscillations at $f = 673$ Hz.

chamber for the low-frequency excitation of $f = 673$ Hz indicates the transfer of energy from the acoustic to the turbulent field. The acoustic wave indeed can invoke hydrodynamic instability and initiate turbulence in a much earlier stage. The intensity levels off with its value for the stationary-turbulence case in the downstream region. This may be attributed in part to the decreased acoustic energy in the downstream region due to the flow-turning losses. Moreover, the increased mean flow velocity gradient farther downstream causes the effect of $\overline{\rho u'v'}\partial\bar{u}/\partial y$ to override the energy production arising from acoustic excitation. The turbulence intensity and stress levels for the higher-frequency case of $f = 1376$ Hz (shown in Fig. 18) indicate limited change from the case without acoustic excitation in the upstream region. The increased frequency of periodic oscillation reduces the acoustic boundary layer thickness and exerts no influence on turbulence production in the upstream region due to the increased dissipation rate of unsteady vorticity transport.¹⁴

E. Effect of Turbulence on the Acoustic Flowfield

Although acoustic oscillations often enhance turbulence intensity through their interactions, turbulence tends to dissipate organized flow motions due to its induced eddy viscosity. Figures 19 and 20 show contour plots of the axial velocity fluctuation, including turbulent and periodic components, for two excitation frequencies, respectively. Turbulence overrides the periodic fluctuations in the downstream region. The oscillatory velocity field exhibits a multidimensional structure. The acoustic pressure, however, is basically one-dimensional and no discernible variation in the vertical direction is observed. The unsteady flowfield comprises three distinct types of wave motions: acoustic (or irrotational), vortical (or shear),

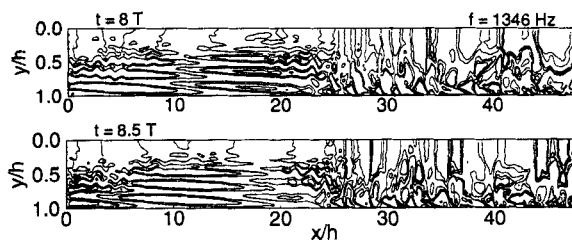


Fig. 20 Contour plots of fluctuating axial velocity with forced oscillations at $f = 1346$ Hz.

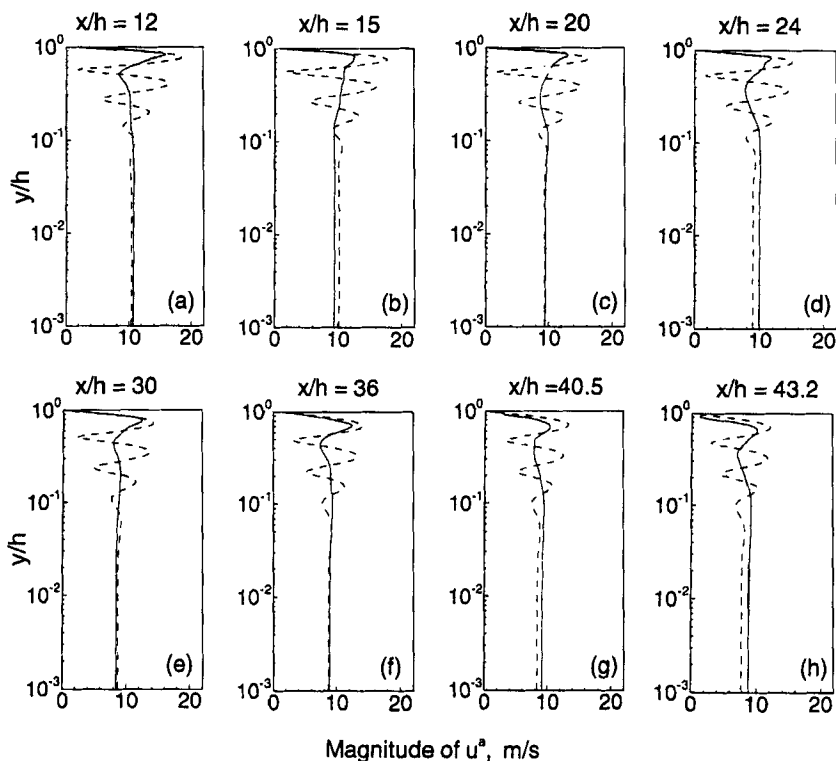


Fig. 21 Amplitudes of fluctuating axial velocity at various axial locations at $f = 673$ Hz: (—) laminar flow; (---) turbulent flow.

and thermal (or entropy) waves. The thermal wave plays a very minor role in the present cold-flow simulation, but may become important in combustion cases. A comprehensive discussion of the acoustic and vortical wave motions in motor environments is given in a companion chapter.⁴⁶ Figures 21 and 22 present the vertical variations of the axial periodic velocity (u^a) at various axial locations for $f = 673$ and 1346 Hz, respectively. Both the laminar and the turbulent flow computations are presented for comparison. The velocity fluctuation in the core-flow region is governed by the isentropic traveling wave relationship with the acoustic pressure. In the laminar-flow case, a velocity overshoot is observed near the porous wall because of the shear wave produced by the no-slip condition.^{13,14} This shear wave travels toward the centerline with the mean vertical velocity and is damped out by the viscous dissipation in the core-flow region. In the present study, the magnitude of the velocity overshoot near the porous wall is smaller than twice the centerline fluctuating velocity, as predicted by Flandro in his theoretical analysis.^{13,14} The high chamber pressure (around 100 atm) considered in Ref. 13 gives rise to a very low surface injection velocity, and hence a prominent acoustic boundary layer is obtained. The strong blowing effect arising from the high injection velocity in the present work, however, extends the acoustic boundary layer and spreads the shear-wave motion through the bulk of the chamber. This

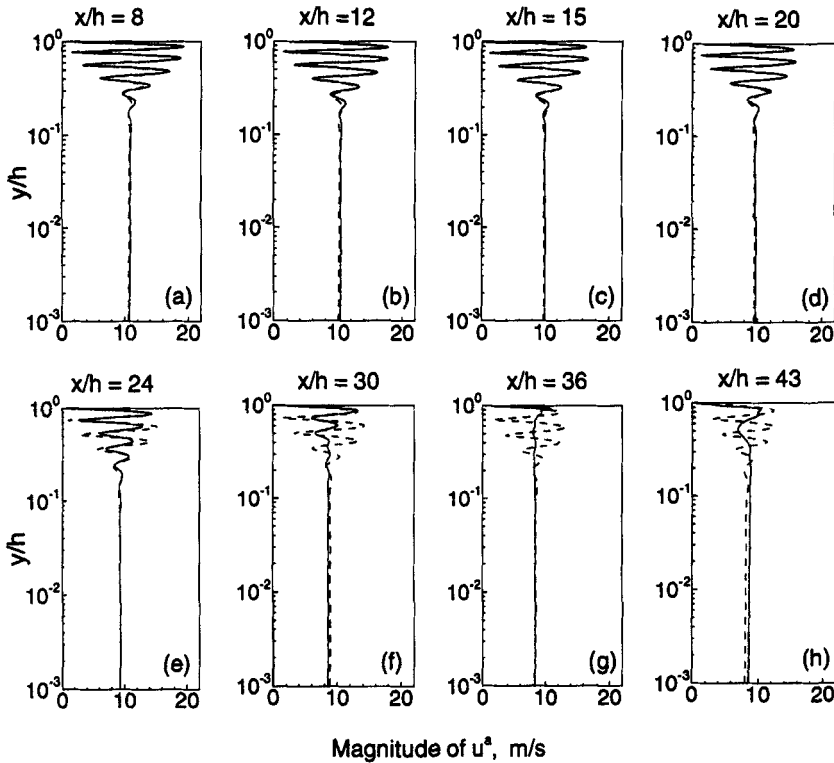


Fig. 22 Magnitude of fluctuating acoustic velocity at various axial locations at $f = 1346$ Hz: (—) laminar flow; (---) turbulent flow.

reduces the magnitude of the axial velocity overshoot near the porous wall. In the turbulent flow case, the shear wave is effectively damped by the enhanced momentum transfer and dissipation rates as soon as it is convected away from the surface. The periodic velocity fluctuation in the upstream region for $f = 673$ Hz appears more suppressed than in the higher-frequency case. This can be attributed to the acoustic wave-induced turbulence and its ensuing increase in the eddy viscosity in that region. The analysis elucidates intricate interactions among the mean, acoustic, and turbulent flowfields in a rocket motor.

VI. Conclusions

A comprehensive analysis of the flow development in a simulated nozzleless rocket motor with acoustic excitations has been performed by means of an LES technique. The flowfield can be characterized with three distinct regimes: laminar, transitional, and fully developed turbulent flows. The effect of turbulence and fluid compressibility on the mean flow structure was examined in depth. The interactions among the mean, turbulent, and periodic oscillatory flowfields were studied by imposing traveling acoustic waves in the chamber at two different frequencies. The acoustic oscillation provides additional mechanisms to

transfer energy from periodic motions to turbulence and, consequently, leads to enhanced turbulence intensity and stresses. The laminar-to-turbulence transition takes place at a much earlier stage under conditions with acoustic waves, especially in the low-frequency range. The influence of turbulence on the periodic oscillatory flowfield arises mainly in the enhanced momentum and energy transfer in the turbulent region. As a result of the acoustic wave-induced eddy viscosity, the shear wave originating from the surface is effectively dissipated as it travels downstream, thereby producing a qualitative change in the oscillatory flowfield, as predicted by the laminar-flow theory. The present work represents a major step toward a complete understanding of the unsteady flow evolution in rocket motors.

Appendix

The quasi-one-dimensional acoustic field in the chamber is formulated by applying the conservation laws to an infinitesimal control volume enclosing the flow passage at a given cross section. The basic assumptions are that

1) the gases obey the perfect-gas law and have constant thermophysical properties,

2) the viscous forces and heat transfer within the gases are ignored,

3) the cross-sectional area of the chamber is assumed constant,

4) the mass inflow at the lateral surface is kept fixed (i.e., $\overline{\dot{m}}_w'' = \text{constant}$), and

5) injection of the fluid is isothermal.

The one-dimensional continuity, momentum, and energy equations take the following form:

$$A \frac{\partial \rho}{\partial t} + A \frac{\partial(\rho u)}{\partial x} = \overline{\dot{m}}_w'' \quad (\text{A1})$$

$$A \frac{\partial(\rho u)}{\partial t} + A \frac{\partial(\rho u^2)}{\partial x} + A \frac{\partial p}{\partial x} = 0 \quad (\text{A2})$$

$$A \frac{\partial(\rho e)}{\partial t} + A \frac{\partial(\rho u e)}{\partial x} + A \frac{\partial(pu)}{\partial x} = h_{0s} \overline{\dot{m}}_w'' \quad (\text{A3})$$

where

$$h_{0s} = C_p T_s + \frac{v_w^2}{2}, \quad e = C_v T + u^2/2 \quad (\text{A4})$$

and A is the cross-sectional area. The gas is injected vertically at the porous surface and thus makes no contribution to the axial momentum balance. The preceding equations can be transformed into the nonconservative form to facilitate derivation of the wave equation. With some straightforward manipulations and the use of the equation of state, Eqs. (A2) and (A3) become

$$\rho A \frac{\partial u}{\partial t} + \rho u A \frac{\partial u}{\partial x} + A \frac{\partial p}{\partial x} = -u \overline{\dot{m}}_w'' \quad (\text{A5})$$

$$A \frac{\partial p}{\partial t} + \gamma p A \frac{\partial u}{\partial x} + u A \frac{\partial p}{\partial x} = \frac{R}{C_v} \left[h_{0s} + \frac{u^2}{2} \right] \overline{\dot{m}}_w'' \quad (\text{A6})$$

Linearization of Eqs. (A5) and (A6) leads to

$$\bar{\rho} A \frac{\partial u'}{\partial t} + A \frac{\partial p'}{\partial x} = -\bar{\rho} A \frac{\partial(\bar{u}u')}{\partial x} - \rho' \bar{u} A \frac{d\bar{u}}{dx} - u' \bar{m}_w'' \quad (\text{A7})$$

$$A \frac{\partial p'}{\partial t} + \gamma \bar{p} A \frac{\partial u'}{\partial x} = \bar{u} A \frac{\partial p'}{\partial x} - u' A \frac{\partial \bar{p}}{\partial x} - \gamma p' A \frac{d\bar{u}}{dx} + \frac{R}{C_v} \bar{u} u' \bar{m}_w'' \quad (\text{A8})$$

Note that the following constitutive relation was used in deriving the preceding equations:

$$c^2 = \left(\frac{\partial p}{\partial \rho} \right)_{\text{entropy}} \Rightarrow \rho' = \frac{p'}{c^2} \quad (\text{A9})$$

For time-harmonic motions, the spatial and temporal dependence of each unsteady flow variable can be decomposed as follows:

$$p' = \hat{p}(x)e^{i\omega t}, \quad u' = \hat{u}(x)e^{i\omega t} \quad (\text{A10})$$

Substitution of Eq. (A10) into Eqs. (A7) and (A8) gives rise to a set of coupled ordinary differential equations for pressure and velocity fluctuations as

$$\begin{bmatrix} \bar{\rho} A \bar{u} & A \\ \gamma \bar{p} A & \bar{u} A \end{bmatrix} \frac{d}{dx} \begin{bmatrix} \hat{u} \\ \hat{p} \end{bmatrix} = \begin{bmatrix} -\bar{\rho} A \frac{d\bar{u}}{dx} - \bar{m}_w'' - \bar{\rho} A i\omega & -\frac{\bar{u} A}{\bar{c}^2} \frac{d\bar{u}}{dx} \\ (\gamma - 1) \bar{u} \bar{m}_w'' - A \frac{d\bar{p}}{dx} & -\gamma A \frac{d\bar{u}}{dx} - A i\omega \end{bmatrix} \begin{bmatrix} \hat{u} \\ \hat{p} \end{bmatrix} \quad (\text{A11})$$

The boundary conditions of $\hat{p} = 1$ and $\hat{u} = \hat{p}/\bar{\rho}\bar{c}$ at the head end ($x = 0$) are specified to simulate traveling acoustic oscillations in the chamber. A simple integration algorithm based on the Euler implicit method is used to solve Eq. (A11) subject to the above boundary conditions.

Acknowledgments

This work was sponsored partly by the Pennsylvania State University and partly by the California Institute of Technology Multidisciplinary University Research Initiative under ONR Grant N00014-95-1-1338. The guidance and suggestions of Dr. Shieh-Yang Hsieh in the development of the computational code are appreciated. Discussions with Dr. Xiyun Lu on subgrid-scale models are also appreciated.

References

- ¹Culick, F. E. C., "A Review of Calculations for Unsteady Burning of a Solid Propellant," *AIAA Journal*, Vol. 6., No. 12, 1968, pp. 2241–2255.
- ²Tseng, I. S., and Yang, V., "Combustion of Double-Base Homogeneous Propellant in a Rocket Motor," *Combustion and Flame*, Vol. 96, 1994, pp. 325–342.
- ³Yang, V., Hsieh, K. C., and Tseng, I. S., "Velocity Coupled Flow Oscillations in a Simulated Solid Propellant Rocket Environment," AIAA Paper 88-0543, AIAA Aerospace Sciences Meeting, 1988.

⁴Roh, T. S., Tseng, I. S., and Yang, V., "Effects of Acoustic Oscillations on Flame Dynamics of Homogeneous Propellant in Rocket Motors," *Journal of Propulsion and Power*, Vol. 11, No. 4, 1995, pp. 2241–2255.

⁵Roh, T. S., Apte, S., and Yang, V., "Transient Combustion Response of Homogeneous Solid Propellant to Acoustic Oscillations in a Rocket Motor," *27th Symposium (International) on Combustion*, Combustion Inst., Pittsburgh, Aug. 1998.

⁶Taylor, G. I., "Fluid Flow Regions Bounded by Porous Surfaces," *Proceedings of the Royal Society London*, Series 234A, Vol. 11199, 1956, pp. 456–475.

⁷Culick, F. E. C., "Rotational Axisymmetric Mean Flow and Damping of Acoustic Waves in Solid Propellant Rocket Motors," *AIAA Journal*, Vol. 4, 1966, pp. 1462–1464.

⁸Balakrishnan, G., Linan, A., and Williams, F. A., "Rotational Inviscid Flow in Laterally Burning Solid-Propellant Rocket Motors," *Journal of Propulsion and Power*, Vol. 8, No. 6, 1992, pp. 1167–1176.

⁹Traineau, J. C., Hervat, P., and Kuentzmann, P., "Cold-Flow Simulation of a Two-Dimensional Nozzleless Solid-Rocket Motor," *AIAA Paper 86-1447*, June 1986.

¹⁰Dunlap, R., Blackner, A. M., Waugh, R. C., Brown, R. S., and Willoughby, P. G., "Internal Flow Field Studies in a Simulated Cylindrical Port Rocket Chamber," *Journal of Propulsion and Power*, Vol. 8, No. 6, 1992, pp. 1167–1176.

¹¹Beddini, R. A., "Injection Induced Flows in Porous-Walled Ducts," *AIAA Journal*, Vol. 24, No. 11, 1986, pp. 1766–1773.

¹²Sabnis, J. S., Madabhushi, R. K., Gibeling, H. J., and McDonald, H., "On the Use of k - ϵ Turbulence Model for Computation of Solid Rocket Internal Flows," *AIAA Paper 89-2558*, July 1989.

¹³Flandro, G. A., "Effects of Vorticity Transport on Axial Acoustic Waves in a Solid Propellant Rocket Chamber," *ASME Annual Meeting*, San Francisco, CA, 1989.

¹⁴Flandro, G. A., "Effects of Vorticity on Rocket Combustion Stability," *Journal of Propulsion and Power*, Vol. 11, No. 4, 1995, pp. 607–625.

¹⁵Vuillot, F., "Vortex Shedding Phenomenon in Solid Rocket Motors," *Journal of Propulsion and Power*, Vol. 11, No. 4, 1995, pp. 626–639.

¹⁶Cai, W. D., and Yang, V., "Two-Phase Turbulent Flow Interactions in a Simulated Rocket Motor with Acoustic Waves," *AIAA Paper 98-0161*, Jan. 1998.

¹⁷Roh, T. S., Apte, S. V., and Yang, V., "Combustion Dynamics of Homogenous Solid Propellants in a Rocket Motor with Acoustic Excitations," *Progress in Astronautics and Aeronautics*, Vol. 185, edited by V. Yang, T. B. Brill, and W.-Z. Ren, AIAA, Reston, VA, 2000, Chap. 3.5.

¹⁸Piomelli, U., "Models for Large Eddy Simulations of Turbulent Channel Flows Including Transpiration," Ph.D. Thesis, Stanford Univ., Palo Alto, CA, 1987.

¹⁹Liou, T. M., and Lien, W. H., "Numerical Simulations of Injection-Driven Flows in a Two-Dimensional Nozzleless Solid-Rocket Motor," *Journal of Propulsion and Power*, Vol. 11, No. 4, 1995, pp. 600–606.

²⁰Liou, T. M., Lien, W. Y., and Hwang, P. W., "Transition Characteristics of Flowfield in a Simulated Solid-Rocket Motor," *Journal of Propulsion and Power*, Vol. 14, No. 3, 1998, pp. 282–289.

²¹Batchelor, G. K., *An Introduction to Fluid Dynamics*, Cambridge Univ. Press, Cambridge, England, UK, 1967.

²²Erlebacher, G., Hussaini, M. Y., Speziale, C. G., and Zang, T. A., "Toward the Large-Eddy Simulation of Compressible Turbulent Flows," *ICASE Paper No. 87-20*, 1990.

²³Hinze, J. O., *Turbulence*, McGraw-Hill, New York, 1975, pp. 321–357.

²⁴Piomelli, U., "Large-Eddy Simulation of Turbulent Flows," TAM Report No. 767, Univ. of Illinois, Urbana-Champaign, 1994.

²⁵Tseng, I. S., "Numerical Simulation of Velocity-Coupled Combustion Response of Solid Rocket Propellants," Ph.D. Thesis, Pennsylvania State Univ., University Park, PA, 1992.

²⁶Ghosal, S., "An Analysis of Numerical Errors in Large-Eddy Simulations of Turbulence," *Journal of Computational Physics*, Vol. 125, 1996, pp. 187–206.

²⁷Fabignon, Y., Beddini, R. A., and Lee, Y., "Analytic Evaluation of Finite Difference Methods for Compressible Direct and Large Eddy Simulations," *Aerospace Science and Technology*, Vol. 6, 1997, pp. 413–423.

²⁸Beddini, R. A., Lee, Y., and Fabignon, Y., "Estimation of Convection Errors of Finite Difference Methods for Compressible Turbulence Simulations," ASME Fluids Engineering Summer Meeting, FEDSM97-3116, Vancouver, June 1997.

²⁹Anderson, D. A., Tannehill, J. C., and Pletcher, R. H., *Computational Fluid Mechanics and Heat Transfer*, Series in Computational Methods in Mechanics and Thermal Sciences, Hemisphere, New York, 1984, pp. 70–118.

³⁰Hirsch, C., *Numerical Computation of Internal and External Flows*, Vol. 1, Wiley, New York, 1992, pp. 238–341.

³¹Jameson, A., "The Evolution of Computational Methods in Aerodynamics," *Journal of Applied Mathematics*, Vol. 50, 1983, pp. 1052–1070.

³²Tennekes, H., and Lumley, J. L., *A First Course in Turbulence*, MIT Press, Cambridge, MA, 1972, pp. 248–287.

³³Beddini, R. A., Lee, Y., and Fabignon, Y., "Effects of Convection Errors on Compressible Turbulence Simulations," *1st AFOSR International Conference on Direct and Large Eddy Simulation*, Paper N-16, Rustin, LA, Aug. 1997.

³⁴Ragab, S. A., and Sheen, S. C., "Large Eddy Simulation of Mixing Layers," *Large Eddy Simulation of Complex Engineering and Geophysical Flows*, edited by B. Galperin and S. A. Orszag, Cambridge Univ. Press, New York, 1993, pp. 255–285.

³⁵Apte, S. V., and Yang, V., "Large Eddy Simulation of Internal Flow Development in Porous Chamber with Surface Mass Injection," *Journal of Fluid Mechanics* (submitted for publication).

³⁶Huesmann, K., and Eckert, E. R. G., "Studies of the Laminar Flow and the Transition to Turbulence in Porous Tubes with Uniform Injection Through the Tube Wall," *Journal of Propulsion and Power*, Vol. 6, No. 6, 1990, pp. 690–705.

³⁷Lesieur, M., Staquet, C., Le Roy, P., and Comte, P., "The Mixing Layer in its Coherence Examined from the Point of View of Two-Dimensional Turbulence," *Journal of Fluid Mechanics*, Vol. 192, 1988, pp. 511–534.

³⁸Lesieur, M., *Turbulence in Fluids*, 3rd ed., Kluwer Academic, Dordrecht, The Netherlands, 1990.

³⁹Gilbert, A. D., "Spiral Structures and Spectra in Two-Dimensional Turbulence," *Journal of Fluid Mechanics*, Vol. 193, 1988, pp. 475–498.

⁴⁰Hu, T. S., "Flowfield and Heat Transfer in the Entrance Region of a Duct with Closed End and Uniform Injection," M.S. Thesis, Dept. of Mechanical Engineering, Pennsylvania State Univ., University Park, PA, 1990.

⁴¹Dunlap, R., Blackner, A. M., Waugh, R. C., Brown, R. S., and Willoughby, P. G., "Internal Flow Field Studies in a Simulated Cylindrical Port Rocket Chamber," *Journal of Propulsion and Power*, Vol. 6, No. 6, 1990, pp. 690–704.

⁴²Varapaev, V. N., and Yagodkin, V. I., "Flow Stability in a Channel with Porous Walls," *Izvestiya Akademii Nauk SSSR, Mekhanika Zhidkosti i Gaza*, Vol. 4, No. 5, 1969, pp. 91–95.

⁴³Hussain, A. K. M. F., and Reynolds, W. C., "The Mechanics of Organized Wave in Turbulent Shear Flow," *Journal of Fluid Mechanics*, Vol. 41, 1970, pp. 241–258.

⁴⁴Brereton, G., Reynolds, W., and Jayaraman, R., "Response of a Turbulent Boundary Layer to Sinusoidal Free-Stream Unsteadiness," *Journal of Fluid Mechanics*, Vol. 221, 1990, pp. 131–159.

⁴⁵Culick, F. E. C., "The Stability of One-Dimensional Motions in a Rocket Motor," *Combustion Science and Technology*, Vol. 7, 1973, pp. 165–175.

⁴⁶Flandro, G. A., Cai, W. D., and Yang, V., "Turbulent Transport in Rocket Motor Unsteady Flowfield," *Progress in Astronautics and Aeronautics*, Vol. 185, edited by V. Yang, T. B. Brill, and W.-Z. Ren, AIAA, Reston, 2000, Chap. 3.3.

Chapter 3.2

Stability and Acoustic Resonance of Internal Flows Generated by Side Injection

B. Ugurtas,^{*} G. Avalon,[†] and N. Lupoglazoff[‡]

ONERA, Palaiseau, France

F. Vuillot[§]

ONERA, Châtillon, France

and

G. Casalis[¶]

ONERA, Toulouse, France

Nomenclature

h	= height of the channel
i	= $\sqrt{-1}$
V_{inj}	= injection velocity
x	= streamwise coordinate
y	= vertical coordinate
α	= complex wave number
ν	= kinematic viscosity
ω	= real circular frequency

I. Introduction

THIS chapter analyzes an unanticipated mechanism leading to instability in large solid propellant boosters for space launchers, such as the Space Shuttle solid rocket booster, the Titan solid rocket motor, and the Ariane 5 MPS P230. Indeed, all of these motors exhibit low-level pressure and thrust oscillations at the frequencies of their first longitudinal acoustic modes, although they

Copyright © 1999 by the authors. Published by the American Institute of Aeronautics and Astronautics, Inc., with permission.

^{*}Ph.D. Student, Applied and Fundamental Energetics Dept.

[†]Research Scientist, Applied and Fundamental Energetics Dept.

[‡]Research Scientist, Computational Fluid Dynamics and Aeroacoustics Dept.

[§]Assistant Director, Computational Fluid Dynamics and Aeroacoustics Dept.

[¶]Research Scientist, Aerodynamics and Energetics Modeling Dept.

are predicted to be stable by classical stability prediction codes based on acoustic balances.

The current explanation for such instabilities relies on vortex shedding from propellant inhibitor rings that couples with the first axial acoustic modes of the chamber. The need to understand the mechanisms leading to this instability has motivated numerous studies, such as those performed in France in the framework of a research program supported by the Centre National d' Etudes Spatiales Direction des Pancours (CNES/DLA).¹⁻⁵ In the course of these studies, it was unexpectedly demonstrated from subscale firings that inhibitor rings were not a necessary condition for the instability.^{2,6} Compressible two-dimensional Navier-Stokes numerical simulations performed to analyze these situations⁷ clearly demonstrated the existence of a strong coupling between the flow's natural instability and the acoustics of the chamber. To understand these new results and to validate the qualitative nature of the numerical simulations, a multifaceted approach has been developed. This approach involves experimental tests performed with a simple cold flow apparatus developed at ONERA, a linear stability analysis,⁸ and computations based on two-dimensional compressible Navier-Stokes equations.⁹ The experimental studies have brought to light the acoustic resonance and the natural instabilities of a two-dimensional planar flow generated by side injection.^{10,11} Note that the first evidence of natural oscillations in a cold flow setup was given by Dunlap et al. with an axisymmetric geometry.¹² However, at the time of their study no information was available on hydrodynamic instability waves, and the link with acoustic instabilities was not considered.

After a description of the experimental setup, the flow stability analysis will be delineated, and comparisons between detailed measurements of the unsteady velocity field and the results of a linear hydrodynamic stability calculation will be shown. Then, a numerical study of the flow instability based on the solution of the full two-dimensional unsteady Navier-Stokes equations will be described, and the results will be discussed in view of the preceding results. Finally, the dynamics of the acoustic resonance will be analyzed, both experimentally and numerically, through imposed variations of the injection velocity.

II. Experimental Facility

The experimental facility is shown in Fig. 1. It is a two-dimensional planar setup, called VECLA (Veine d'Etude de la Couche Limite Acoustique),^{8,10} that is fed with air from high-pressure storage. The internal arrangement of the facility can be seen in Fig. 2. The upper part of the setup is a rectangular channel into which air is injected through a porous plate that serves as its floor. This channel has a length of 603 mm and a width of 60 mm. The porous plate has a length of 581 mm and a thickness of 5 mm and is made of poral, a material obtained by sintering together small spheres of bronze. As can be seen in Fig. 2, the channel has an open exit section that is connected to the ambient air either directly or by an additional choked nozzle. To vary the operating conditions, the height of the channel can be modified. Additional adjustments are possible by varying the nozzle height. The part of the setup located under the porous plate is divided into seven prechambers that are independently fed with air. The goal of the partitioning is to prevent coupling between the longitudinal acoustic modes of this part of the setup and the modes excited in the channel. The tubes linking the feed tube to

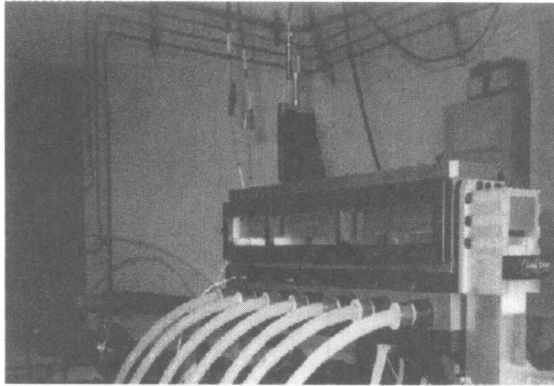


Fig. 1 Experimental setup.

the prechambers are equipped with elementary sonic throats to provide acoustic isolation and to control the mass flow rate in each prechamber.

Various tests were conducted in this experimental facility with and without the nozzle.¹⁰ Without the nozzle, the excited acoustic modes of the cavity are of closed–open type, whereas they are of the closed–closed type when the nozzle is used. Test conditions were chosen to validate the results given by the linear theory, which shows a dual effect of the injection velocity and the channel height on flow stability. To attain this goal, the channel height was adjusted to 10 and 20 mm, and various injection velocities were used: 1.02, 1.36, 1.70, and 2.04 m/s.

The injection velocities are fixed by the pressure in the feeding tube in the configuration without the nozzle, whereas they are fixed by the throat height of the nozzle in the configuration with the nozzle. In the latter configuration, tests are conducted with a prescribed pressure of 1.5 bar at the channel head end, which ensures sonic conditions at the nozzle throat.

Velocity measurements were performed with a single element hot wire probe located at different cross sections of the channel. The hot wire is introduced through the top wall of the channel, its wire being oriented in a direction parallel to the channel width. The probe support has a diameter of 3.2 mm, and the wire has a length of 3 mm and a diameter of 3.8 μm .

To get a description of the flow in the transverse direction, 10 measurement stations, 1 mm apart, have been selected at each longitudinal location. In the first

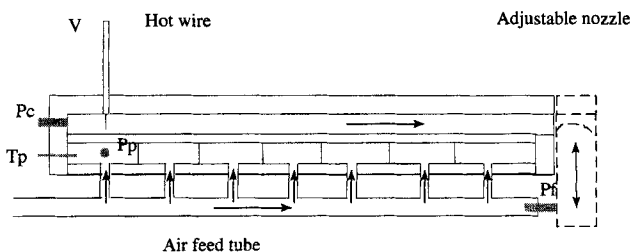


Fig. 2 VECLA setup.

position, the wire is put at a distance of 1 mm from the porous plate. Pressure is measured by means of piezoresistive pressure transducers working in an absolute mode mounted at different locations on the setup: at the end of the feeding tube, P_f , in the first prechamber, P_p , and at the head end of the channel, P_c (Fig. 2). The airflow temperature is maintained at 20°C during the tests by means of an air heater placed at the upstream part of the feeding tube. The temperature is controlled by a thermal probe in the first prechamber, T_p .

The voltages delivered by the pressure transducers and the hot wire probe are numerically recorded at a rate of 10,000 data points per second. For each hot wire position, the signals are recorded during 1 s, the pressure and velocity signals being filtered and amplified before they are digitized. They are later processed to determine their spectral content through power spectral density (PSD) plots. The pressure signals are bandpass filtered, between 50 and 3000 Hz, whereas the velocity signals are low-pass filtered with a cutoff frequency of 3000 Hz.

III. Linear Stability Theory

The linear theory has been fully described in Ref. 8 and is recalled here for completeness. It is applied to the Navier–Stokes equations written for a two-dimensional and incompressible flow, using the channel height h and the injection velocity V_{inj} as parameters of nondimensionalization. The equations are linearized with respect to the amplitudes of the fluctuations and split into a steady part, for which the solution is given by Taylor,¹³ and an unsteady part that governs the behavior of the fluctuations.

The components of the steady velocity are given by

$$\bar{U} = (\pi/2)x \cos(\pi y/2) \quad \bar{V} = -\sin(\pi y/2) \quad \text{with } -1 \leq y \leq 0 \quad (1)$$

in which x and y are dimensionless coordinates evaluated from the head end wall ($x = 0$) and from the upper wall ($y = 0$).

Fluctuations are expressed in normalized form as

$$(\bar{u}, \bar{v}, \bar{p}) = [\hat{u}(y), \hat{v}(y), \hat{p}(y)]e^{i(\alpha x - \omega t)} \quad \text{with } \alpha = \alpha^{(r)} + i\alpha^{(i)}, \quad \omega = 2\pi f \quad (2)$$

where f is the frequency, $\alpha^{(r)}$ the wave number, and $-\alpha^{(i)}$ the spatial growth rate of the fluctuation. This normal mode form is not obvious a priori due to the x dependence of the mean flow. In fact, this problem is related to the question of the nonparallel effects that has been studied for several years in the framework of boundary-layer stability.

An exponential amplification factor that depends on the axial position and the frequency can be linked to the amplitude A of each wave by

$$n(x, \omega) = \int_{x_0(\omega)}^{x(\omega)} -\alpha^{(i)}(\omega, x) dx \quad A(x) = A_0 e^n \quad \text{with } A_0 = A(x_0) \quad (3)$$

In the present study, x_0 is the position where the amplitude of the wave begins to grow and A_0 a constant, independent of the frequency, that will be adjusted to get the best fit with the experimental results.

The system of equations governing the fluctuating quantities is written as follows⁸:

$$\begin{aligned}
 i\alpha\hat{u} + \frac{d\hat{v}}{dy} &= 0 \\
 -i\omega\hat{u} + \frac{\partial\bar{U}}{\partial x}\hat{u} + i\alpha\bar{U}\hat{u} + \bar{V}\frac{d\hat{u}}{dy} + \frac{\partial\bar{U}}{\partial y}\hat{v} + i\alpha\hat{p} &= \frac{1}{Re}\left(\frac{d^2\hat{u}}{dy^2} - \alpha^2\hat{u}\right) \\
 -i\omega\hat{v} + i\alpha\bar{U}\hat{v} + \bar{V}\frac{d\hat{v}}{dy} + \frac{\partial\bar{V}}{\partial y}\hat{v} + \frac{d\hat{p}}{dy} &= \frac{1}{Re}\left(\frac{d^2\hat{v}}{dy^2} - \alpha^2\hat{v}\right)
 \end{aligned} \quad (4)$$

in which $Re = hV_{inj}/\nu$ is the Reynolds number based on the channel height and the injection velocity.

Equation (4) is solved for the following boundary conditions:

$$\hat{u}(-1) = \hat{v}(-1) = \hat{v}(0) = \frac{d\hat{u}}{dy}(0) = 0 \quad (5)$$

which express the intrinsic nature of the eigenresponse at the injection wall ($y = -1$) and the symmetry condition at the upper wall ($y = 0$). To describe correctly the experimental boundary conditions, a no-slip condition is used at the upper wall. Nevertheless, a symmetry condition is adopted because it will be assumed that the viscous boundary layer that is developed at the upper wall has no effect on the stability of the flow in the linear zone.

The problem posed by Eqs. (4) and (5) is an eigenvalue problem: The zero solution is the only one unless the problem becomes singular. The condition is achieved when a certain relation linking the coefficients of Eq. (4) is satisfied. This relation, formally written as

$$\Im(\alpha, \omega, x, Re) = 0 \quad (6)$$

is a dispersion relation and shows that, in particular, the growth rate is a function of x and the frequency.

The described eigenvalue problem has been solved with a fourth-order compact scheme that has been developed and validated in the framework of the stability of the laminar boundary layer.¹⁴ Figure 3 shows the growth factor n in the plane $(x/h, \Omega)$ obtained by computing the integral given in Eq. (3). The computations were performed for $Re = 900$, corresponding to the experimental conditions fixed by $h = 10$ mm and $V_{inj} = 1.36$ m/s. As seen in Fig. 3, the basic flow becomes unstable at a certain critical distance from the head end close to $5h$. The range of amplified frequencies (for which $n > 0$) enlarges toward the higher frequencies as x increases. As the neutral stability curve has been found to have a small dependence on Re (cf. Ref. 8), the results shown in Fig. 3 can be used for other values of h and V_{inj} .

IV. Numerical Approach

Numerical simulations of the flow inside the VECLA setup were performed with a two-dimensional code called SIERRA,^{5,9,15} using a finite volume explicit predictor-corrector Mac Cormack scheme with Jameson artificial viscosities. This

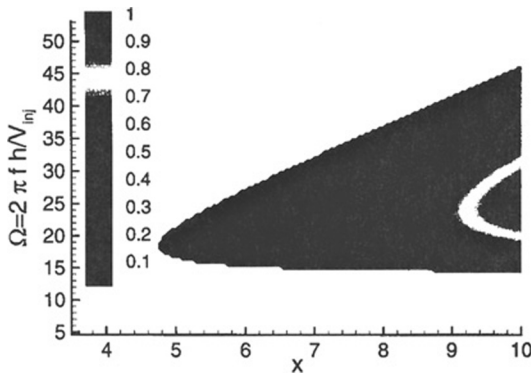


Fig. 3 Iso n factor according to linear theory for $Re = 900$.

is a multidomain code that solves the unsteady compressible Navier–Stokes equations in either an axisymmetric or planar configuration.

The computations were directed toward two main objectives: the description of the development of natural instabilities inside the flow and the prediction of the acoustic levels resulting from an acoustic resonance. The first objective was pursued by computing the flow in the upstream part of the channel on a sufficiently fine grid to capture enough details of the transitional waves to be compared with the previous stability results.⁸ The second objective has led to undertaking computations over the complete geometry of the channel for variable injection conditions, so as to study the interaction between the flow instability and the acoustic field.

Previous numerical simulations⁹ have demonstrated the need to trigger the instability for the unstable waves to grow until resonant conditions are reached. This triggering is obtained by numerically perturbing the flow in part or all of the computational domain. In this study, two methods were used to perturb the flow. The first one, which was applied in the stability computation, consists of adding a noise to momentum quantities ρU and ρV in the entire domain and to refresh it periodically. The level of the noise, relative to the injection velocity, represents only few tenths of a percent, so that velocity fluctuations are always very small compared to the mean flow velocities. In the second method, which was applied in the resonance computation to be presented, the perturbation is obtained by interrupting the injected mass flow rate over a small distance of the wall centered at the middle of the chamber.⁹

To describe properly the experimental conditions, it is necessary to take into account in the computations the response (or acoustic admittance) of the porous wall. This has been done previously⁹ by adjusting the injected mass flow rate as a function of the local pressure, in accordance with a simple unsteady model that couples the motions on the two sides of the porous plate. However, in the present work, and for the sake of simplicity, a zero poral response has been used.

The instantaneous flowfield inside the experimental setup is shown in Fig. 4 (from Ref. 9) through entropy maps that clearly exhibit the vortical structures emitted from the blowing surface. The computations to be presented were performed without the nozzle and for a channel height of 20 mm and $V_{inj} = 1.71$ m/s. A reduced length of 200 mm was used for the stability computations, whereas



Fig. 4 Entropy maps for the VECLA setup for the full length (top) and the downstream section (bottom), $V_{inj} = 1.7$ m/s and $h = 20$ mm.

the full length was adopted for the resonance computations. The computations are started from rest at atmospheric pressure and continued by keeping the exit pressure at ambient value. Convergence toward a steady-state solution is achieved with high levels of artificial viscosity. The subsequent reduction of artificial viscosity values by an order of magnitude allows the development of the instabilities.

V. Discussion of Results

A. Flow Stability

Figure 5 (from Ref. 8) presents a comparison of the results obtained by the linear theory with results deduced from the velocity measurements in the VECLA setup for $V_{inj} = 1.36$ m/s and $h = 10$ mm at $y = 1$ mm. Amplitudes of the streamwise component of the fluctuating velocity are plotted vs frequency for three axial positions: $x = 31$, $x = 81$, and $x = 120$ mm. Because the position $x = 31$ mm is located upstream of the neutral curve, as shown in Fig. 3, only the two latter

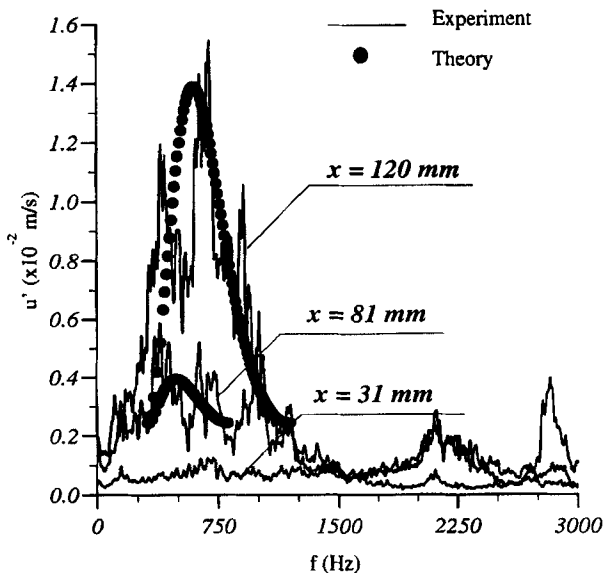


Fig. 5 Comparison between experimental and theoretical results of spatial amplification of fluctuating velocity (from Ref. 8); $V_{inj} = 1.36$ m/s, $h = 10$ mm, without nozzle, and porosity = $18 \mu\text{m}$.

positions are plotted for the theoretical analysis. A spatial amplification in the x direction of the velocity fluctuation amplitude is clear between 300 and 1200 Hz for both sets of results. In Ref. 10, comparisons were presented for other injection conditions and geometries that confirm the theory's accuracy as a predictor.

Results with a reduced porosity injection wall ($8\text{ }\mu\text{m}$) showed lower amplitude (50 times less) for hydrodynamic instability waves. This could result from different injected turbulence and/or wall admittance.

Stability computations using the SIERRA code were performed on a grid of 27,258 points (413×66) having variable spacing in the longitudinal and the transverse directions. The points are more concentrated near the porous wall and in the unstable zone. Two points in this zone are spaced at about $1/100$ of the critical wavelength to ensure correct descriptions of the unstable waves.

The computations were done in two steps, corresponding to the convergence toward a steady state and to the description of the instability. The steady state was reached after 900,000 time steps, and for the description of the instability, 850,000 additional time steps were performed ($dt = 0.34\text{ }\mu\text{s}$). During the second run, the velocity signals were recorded every 100 iterations for five cells (located at $x/h = 4.05, 4.70, 6.55, 7.80,$ and 9.05) of the computational grid at a distance of 1 mm from the porous wall. These signals are analyzed by computing the power spectral density on temporal windows of 8192 points taken at the end of the second step (cf. Fig. 6).

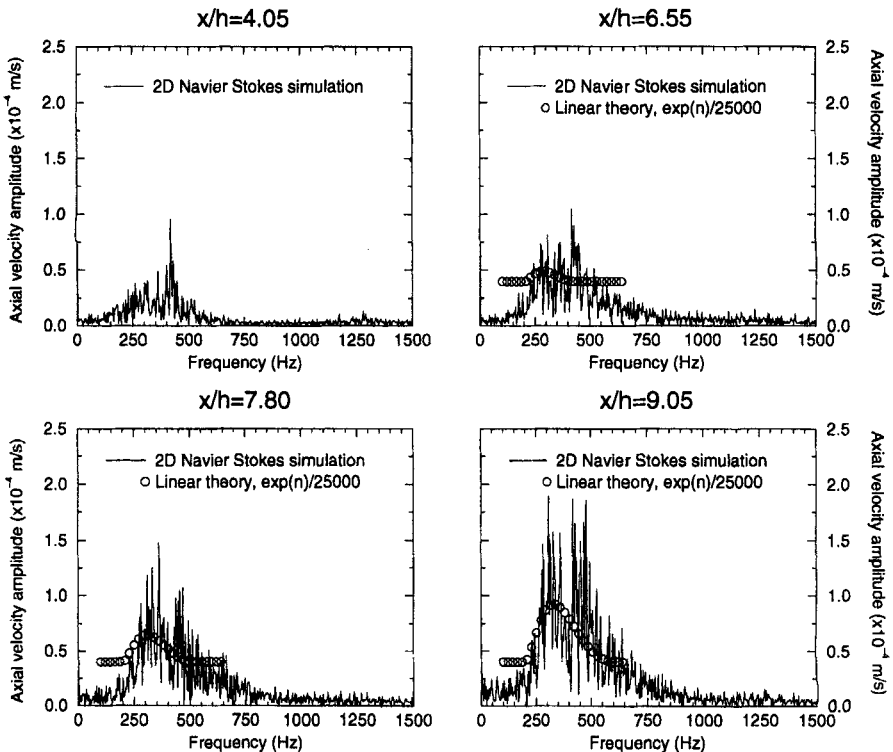


Fig. 6 Comparison between numerical and theoretical results of velocity amplitude levels.

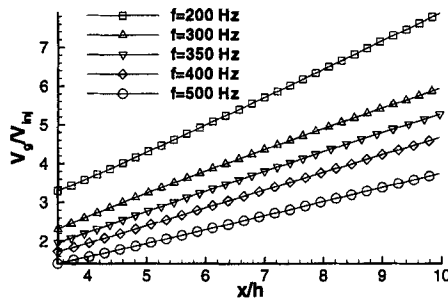


Fig. 7 Group velocity vs x/h according to the linear theory for $V_{inj} = 1.71$ m/s and $h = 20$ mm.

A Gaussian noise of amplitude 0.4% of V_{inj} was applied every 50,000 iterations. This number of iterations corresponds to the time needed for the hydrodynamic instability waves to be evacuated outside the cavity, which can be determined from the group velocity given by the linear theory (cf. Fig. 7).

Numerical and theoretical velocity amplitude levels are plotted vs the frequency for four nondimensionalized longitudinal positions in Fig. 6. It follows from this comparison that the numerical computation predicts fairly well the amplified frequency range and the spatial amplification. This good prediction of the spatial amplification can be seen in Fig. 8, which compares the theoretical and numerical factors n vs the longitudinal coordinate for the most amplified frequency ($f = 300$ Hz).

Fourier coefficients of the unsteady velocity components were computed on the entire domain for a frequency of 350 Hz ($\Omega = 25.72$) over a time interval corresponding to two periods of oscillations. In Fig. 9, theoretical and numerical eigenfunctions, deduced from the Fourier analysis at $x/h = 9.05$, are compared after normalization by the longitudinal velocity amplitude at $y/h = 0$. Good agreement is obtained between the two approaches, except for the levels, which are found to be slightly different. The first maximum of the longitudinal velocity is found at the same transverse location although the positions of the other extrema do not coincide so well. This could be due to a residual presence of

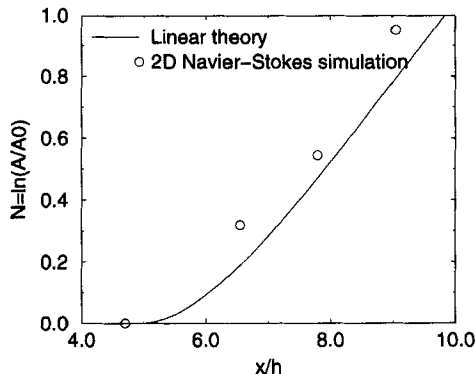


Fig. 8 Numerical and theoretical n factors for a frequency of 300 Hz.

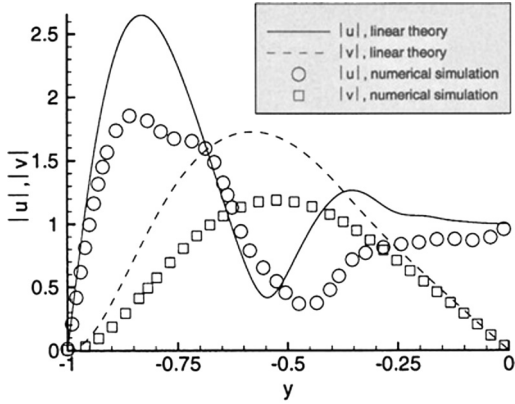


Fig. 9 Theoretical and numerical eigenfunctions for $x/h = 9.05$ and $f = 350$ Hz.

acoustic oscillations in the Navier–Stokes solution. In Fig. 10, where the theoretical and numerical phase angles are compared, the two solutions show very similar behavior.

At this point, the agreement between theoretical and numerical solutions is judged to be very satisfactory. Note that a long temporal exploration is required to get good accuracy in the spectral analysis (in the present case 289 ms was found to be necessary). To conclude, these first results confirm the ability of the numerical method to predict unstable motion inside the flow. Full Navier–Stokes simulations could then be used for a detailed description and to understand conditions leading to acoustic resonance.

B. Acoustic Resonance

Experiments conducted on the VECLA setup have given clear evidence of the influence of the stability of the flow on the acoustic resonance phenomenon. The

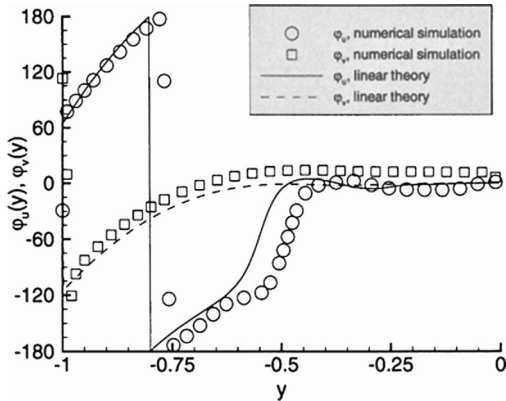


Fig. 10 Theoretical and numerical phases for $x/h = 9.05$ and $f = 350$ Hz.

flow instability leads to the growth of the amplitudes of waves, whose frequencies are inside a range determined by the channel height and the injection velocity. If one acoustic frequency of the cavity lies inside this range, and if its amplification is sufficient, it will grow up to a critical level, above which a resonance will be observed.¹⁰ These conditions seem to be necessary but not sufficient to reach a resonance, as shown from the experimental results. The selection of the acoustic frequency seems also to be conditioned by the position of the acoustic velocity antinodes relative to the amplification zones. In the experiments, it has been found that the resonance is obtained when the acoustic mode has its velocity antinode at a location corresponding to a sufficiently high value of the growth factor ($n = 2.5$ for a frequency of 426 Hz; see Refs. 10 and 11).

To confirm the role played by the injection velocity on the resonance phenomenon, a test was performed with the VECLA setup by slowly varying the injected mass flow rate at the porous wall. Because this variation is operated for constant conditions of pressure in the channel, it is equivalent to varying the injection velocity at the wall. Special acquisition methods were adopted for this test to allow for an appropriate analysis of the signals. Thus, the pressure signal was bandpass filtered between 50 and 1000 Hz, and the velocity signal was low-pass filtered under 1000 Hz. Acquisition has been performed over 7.5 s with a sampling frequency of 2000 Hz. PSD was computed on 29 temporal windows of 512 points decomposed into 7 segments of 128 points. These values correspond to a frequency resolution of 3.91 Hz and a blowing velocity resolution of 0.031 m/s.

Figure 11 shows the contour lines of the head end pressure PSD in the plane (f , V_{inj}). Several lines of maximum amplitude appear on this graph in regions containing the first two longitudinal mode frequencies. These lines are vertical in the low-frequency zone and oblique in the higher frequency zone with constant slopes indicating constant Strouhal numbers. This line shows that f increases with V_{inj} until a jump in frequency is observed. This waterfall in the sequence of dominant frequencies has been seen with other aeroacoustic phenomena and is explained by the presence of an integer number of vortices along the distance separating the point of emission of the vortices from the plane where an acoustic reaction is created.

The test just described was numerically simulated by computing the flow in the entire channel on a mesh having 20,000 cells that were equally distributed

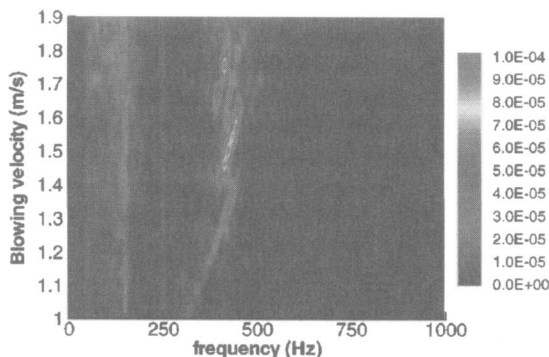


Fig. 11 Isobaric plot of experimental head end pressure amplitudes.

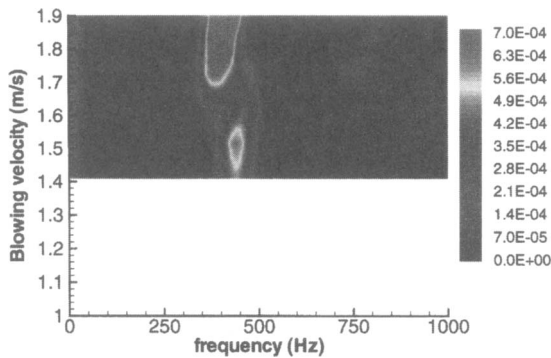


Fig. 12 Isobaric plot of numerical head end pressure amplitudes.

in the longitudinal direction and spatially contracted in the transverse direction at the proximity of the porous wall. A linear variation of the mass flow rate was introduced at the injecting wall during the computation to reproduce the experimental conditions. The pressure was periodically recorded during the computation in a cell located near the head end wall. Figure 12 shows the results given by the spectral analysis of this head end pressure. Despite a limitation in the frequency resolution (9.26 Hz) and in the blowing velocity resolution (0.105 m/s) for the numerical solution, a good comparison is visible. In particular, a frequency shift similar to that obtained in the experiment is observed from these results. As no acoustic response from the wall has been simulated in this computation, the numerical levels are about 10 times greater than the experimental ones.⁹

These results demonstrate the ability of the numerical simulations to reproduce complex aeroacoustic phenomena, such as frequency variation and frequency jumps.

VI. Conclusions

Stability of flows with side injection has been investigated to analyze the mechanisms giving rise to the appearance of parietal vortex shedding and acoustic resonance. Several methods of investigation were used. Among these are tests conducted with a cold flow setup and stability computations of the experimentally studied flow configurations. These computations were performed using two different approaches: a theoretical approach established from a linear analysis of the stability and a numerical approach using a two-dimensional computer code. These approaches produced coherent results that were found to be in good agreement with the measurements.

The stability of flows generated by side injection in closed channels has been found to depend primarily on two parameters: the injection velocity and the transverse dimension of the channel (height for a two-dimensional channel and radius for a cylinder). The theoretical analysis predicts an amplification of the unstable frequencies from an initial point, before which they are stable. A well-delimited range of frequencies is amplified at a given longitudinal location of the channel as a function of the parameters discussed earlier.

Various experimental conditions were examined during the experimental study, especially to check the validity of the theoretical results. Clear resonant conditions were reached on the experimental setup. Frequency shifts and jumps were observed as the injection velocity was varied. These are the signatures of aerodynamically generated resonance. These conditions were also satisfactorily reproduced by the full two-dimensional Navier–Stokes computations.

This chapter presents different and complementary approaches to the study of hydrodynamic instability and illustrates the main properties of the acoustic resonance. This phenomenon, observed in recent experimental¹⁰ and numerical^{7,9} works, is thought to be a powerful mechanism for instabilities that are of particular concern for large motors. Indeed, recent works (e.g., Ref. 6) have shown that inhibitor rings can be significantly bent by aerodynamic forces. This renders possible the appearance of a strong parietal vortex-shedding in the Ariane 5 MPS P230 and perhaps also in the U.S. Titan solid rocket motor unit.¹⁶ Consequently, it is believed that the experimental and numerical tools presented will make possible understanding more completely the acoustic resonance phenomenon in such conditions.

References

¹Vuillot, F., and Kuentzmann, P., "Programme de R&T ASSM (Aero-dynamics of Segmented Solid Motors)," *Proceedings of Colloque CNES/ONERA/CNRS sur les Écoulements Propulsifs dans les Systèmes de Transport Spatial*, Centre National d'Études Spatiales, Paris, Sept. 1995.

²Vuillot, F., Traineau, J. C., Prévost, M., and Lupoglazoff, N., "Experimental Validation of Stability Assessment Methods for Segmented Solid Propellant Motors," AIAA Paper 93-1883, June 1993.

³Vuillot, F., "Vortex-Shedding Phenomena in Solid Rocket Motors," *Journal of Propulsion and Power*, Vol. 11, No. 4, 1995, pp. 626–639.

⁴Prévost, M., Vuillot, F., and Traineau, J. C., "Vortex-Shedding Driven Oscillations in Subscale Motors for the Ariane 5 MPS Solid Rocket Motors," AIAA Paper 96-3247, July 1996.

⁵Lupoglazoff, N., and Vuillot, F., "Numerical Simulation of Vortex-Shedding Phenomenon in Two-Dimensional Test Case Solid Rocket Motors," AIAA Paper 92-0776, Jan. 1992.

⁶Traineau, J.-C., Prévost, M., Vuillot, F., Le Breton, P., Cuny, J., Preioni, N., and Bec, R., "A Subscale Test Program to Assess the Vortex-Shedding Driven Instabilities in Segmented Solid Rocket Motors," AIAA Paper 97-3247, July 1997.

⁷Lupoglazoff, N., and Vuillot, F., "Parietal Vortex-Shedding as a Cause of Instability for Long Solid Propellant Motors. Numerical Simulations and Comparisons with Firing Tests," AIAA Paper 96-0761, Jan. 1996.

⁸Casalis, G., Avalon, G., and Pineau, J.-P., "Spatial Instability of Planar Channel Flow with Fluid Injection through Porous Walls," *Physics of Fluids*, Vol. 10, No. 10, 1998, pp. 2558–2568.

⁹Lupoglazoff, N., and Vuillot, F., "Numerical Simulations of Parietal Vortex-Shedding Phenomenon in a Cold Flow Setup," AIAA Paper 98-3220, July 1998.

¹⁰Avalon, G., Casalis, G., and Griffond, J., "Flow Instabilities and Acoustic Resonance of Channels with Wall Injection," AIAA Paper 98-3218, July 1998.

¹¹Vuillot, F., Casalis, G., Avalon, G., and Lupoglazoff, N., "Mise en Résonance Acoustique d'une Cavité par l'Instabilité Naturelle d'un Écoulement Généré par Injection Pariétale," *Comptes-rendus de l'Académie des Sciences*, Vol. 327, Series II b, 1999, pp. 77–83.

¹²Dunlap, R., Blackner, A. M., Waugh, R. C., Brown, R. S., and Willoughby, P. G., "Internal Flow Field Studies in a Simulated Cylindrical Port Rocket Chamber," *Journal of Propulsion and Power*, Vol. 6, No. 6, 1990, pp. 690–704.

¹³Taylor, G., "Fluid Flow in Regions Bounded by Porous Surfaces," *Proceedings of the Royal Society, Series A: Mathematical and Physical Sciences*, Vol. 234, No. 1199, 1956, pp. 456–475.

¹⁴Airiau, C., and Casalis, G., "Stabilité Linéaire de la Couche Limite par un Système d'Équations Parabolique," *La Recherche Aéronautique*, No. 5, 1993, pp. 57–68.

¹⁵Vuillot, F., "Numerical Computation of Acoustic Boundary Layers in Large Solid Propellant Space Booster," AIAA Paper 91-0206, Jan. 1991.

¹⁶Dotson, K. W., Koshigoe, S., and Pace, K. K., "Vortex-Shedding in a Large Solid Rocket Motor Without Inhibitors at the Segment Interfaces," *Journal of Propulsion and Power*, Vol. 13, No. 2, 1997, pp. 197–206.

Chapter 3.3

Turbulent Transport in Rocket Motor Unsteady Flowfield

G. A. Flandro*

University of Tennessee Space Institute, Tullahoma, Tennessee

and

Weidong Cai[†] and V. Yang[‡]

Pennsylvania State University, University Park, Pennsylvania

Nomenclature

A_b	= pressure coupling admittance function
A_v	= velocity coupling admittance function
a_0	= mean speed of sound
e_r, e_θ, e_z	= unit vectors in r, θ , and z directions
E_m^2	= normalization constant for mode m
k_m	= wave number for axial mode m
L	= chamber length
m	= mode number
M_b	= mach number at burning surface
n	= outward pointing unit normal vector
p	= pressure
P_0	= mean chamber pressure
r	= radial position
R	= chamber radius
S	= Strouhal number, k_m/M_b
t	= time
t	= unit vector tangent to burning surface
u'	= oscillatory velocity vector amplitude
U_r, U_z	= mean flow velocity components
V_b	= mean radial velocity at wall

Copyright © 2000 by the authors. Published by the American Institute of Aeronautics and Astronautics, Inc., with permission.

*Boling Chair Professor of Advanced Propulsion, Dept. of Mechanical and Aerospace Engineering. Associate Fellow AIAA.

[†]Ph.D. Student, Dept. of Mechanical Engineering.

[‡]Professor, Dept. of Mechanical Engineering. Associate Fellow AIAA.

u, w	= unsteady flow velocity components
y	= radial position, $1 - r$
z	= axial position
α	= growth rate, dimensional, sec^{-1}
γ	= ratio of specific heats
λ	= inverse of Strouhal number, M_b/k_m
ν	= kinematic viscosity, μ/ρ
ρ	= density
ψ	= complex exponential argument
ω'	= amplitude of vorticity fluctuation
Ω	= mean vorticity amplitude
Ω_b	= vorticity amplitude at burning surface

Subscripts

b	= combustion zone
m	= mode
0	= zeroth order in M_b
1	= first order in M_b
t	= tangential part
n	= normal part

Superscripts

$*$	= dimensional quantity
(1)	= first order in wave amplitude
$'$	= amplitude of time-dependent

I. Introduction

RECENT work by several investigators using both analytical and numerical methods has clarified some of the details of the rotational flow effects of importance in rocket combustion instability. Although analytical studies have heretofore been limited to laminar treatment of the unsteady viscous flowfield, they have yielded useful information needed in accurate motor stability assessment. In particular, they have revealed the origin of the *flow turning* loss mechanism and other potentially important additions to the system energy gain/loss balance. Numerical solution of similar unsteady flows has verified these analytical solutions in laminar regions of the chamber but indicates that the transition to turbulence markedly influences the results. The purpose of this research is to use information from the numerical calculations in extending the analytical results into the turbulent regime. There are several motives for doing this. Apart from the obvious benefit of enhanced physical understanding inherent in analytical models for complicated flowfields such as those in an unstable rocket chamber, there remain many practical questions related to the precise manner in which turbulent flow processes affect the stability computations.

An approximate method for including the turbulence effects is described. The field is decomposed into two elements. The first is a realistic numerical model of the mean flow that includes the corrections to the transport properties resulting

from transition and growth of random turbulent eddies. The second is a detailed analytical model of organized unsteady motion consisting of the acoustic field and associated rotational waves created by production of vorticity at the chamber inflow boundaries. Information on the mean flow with turbulence is obtained from a detailed computational model by Yang and his coworkers.¹ This provides spatial distributions of the turbulence-modified flowfield and associated transport properties. These are then employed in the analytical flowfield expressions to produce the corrected unsteady field. This procedure is approximate in that the direct interaction between the organized and turbulent fluctuations is neglected. It is believed that in most cases these are not strong interactions, and so the main effect of turbulence on the organized oscillations comes from the changes in transport properties and the mean flow velocity distribution.

Results compare favorably to the complete unsteady simulations. In particular, as the nozzle end of the chamber is approached, the turbulence effects grow rapidly in importance. The organized vortical waves are more rapidly damped, mainly because of the increase in the effective coefficient of viscosity (eddy viscosity), and the motion can then truly be described as an acoustic boundary layer; the organized rotational effects are confined to a thin region near the burning surface. The unsteady vorticity distribution outside this boundary layer does not then contain components directly related to the irrotational acoustic field. Despite this major departure for the laminar description of the unsteady rotational flow, there is little change in the basic effects of vorticity production on the system stability characteristics. That is, important contributions to the system energy gain/loss balance, such as the flow-turning loss, are not strongly affected by turbulence. Direct interactions of the turbulent field with the combustion processes near the propellant are not considered in the present effort, but will be incorporated in developing flame zone models.

II. Analysis

An irrotational (acoustic) unsteady flow is not a sufficiently complete model of the unsteady combustion chamber gas motion. Such a model allows slip flow at the propellant surfaces. Acoustic boundary layer theory, which has been applied to this problem frequently in the past, may not be appropriate since the strong convective field transports vorticity throughout the combustion chamber. Such motion may be laminar near the forward end of the chamber but will naturally transition to fully turbulent motion downstream. It is necessary to determine the effect of this turbulence on the organized wave motion so that a realistic assessment of combustion instability can be carried out. In particular it is required to determine the effects of modifications to the transport properties and mean flow geometry introduced by transition to a fully turbulent flow.

It is not clear at the outset what role, if any, is played by viscosity, since the radial convection tends to discourage formation of highly sheared regions of flow. It is also important to realize that the creation of vorticity does not require the presence of viscous stresses. Crocco's theorem² clarifies the origin of both the steady and unsteady vorticity in the gas particles entering the chamber from the burning zone.

The analysis is carried out in two parts. In the first, a realistic model of the effects of turbulence on the mean flowfield in the rocket chamber is described; numerical results based on this model give the turbulent transport properties needed in assessing the analytical model of the unsteady motion carried out in the second part.

A. Mean Flowfield with Turbulence

The formulation of the mean flowfield is based on the conservation equations of mass, momentum and energy. Full account is taken of variations of thermophysical properties. In vector notation, the governing equations in two-dimensional Cartesian coordinates can be written in the following conservative form:

$$\frac{\partial \mathbf{Q}}{\partial t} + \frac{\partial}{\partial x}(\mathbf{E} - \mathbf{E}_v) + \frac{\partial}{\partial y}(\mathbf{F} - \mathbf{F}_v) = \mathbf{S} \quad (1)$$

Definitions of the variable vector \mathbf{Q} , the convective flux vectors \mathbf{E} and \mathbf{F} , the diffusive flux vectors \mathbf{E}_v and \mathbf{F}_v , and the source vector \mathbf{S} , can be found in Ref. 1.

The $k - \varepsilon$ model is used to achieve turbulence closure. To account for the wall-damping effect on turbulence, a two-layer turbulence model suggested by Rodi³ is employed. In this approach, the standard $k - \varepsilon$ model is applied to regions away from the wall, and a one-equation model is implemented close to the wall. Description of the standard $k - \varepsilon$ model can be found in Ref. 4. In the inner layer, the ε -equation previously described fails, because viscous effect is dominant. Only the k -equation is employed in this region. To achieve turbulence closure, turbulence length scale is empirically introduced to evaluate turbulence dissipation rate and eddy viscosity. Unlike the treatment of high Reynolds number flows, Rodi³ proposed two different turbulence length scales, namely, turbulence dissipation length scale l_ε for quantifying turbulence dissipation rate, and turbulence viscosity length scale l_μ for evaluating eddy viscosity. These two length scales are simulated in a manner similar to the van Driest damping function used in the mixing-length model:

$$l_\mu = c_l y \left[1 - \exp \left(-\frac{Re_y}{A_\mu} \frac{25}{A^+} \right) \right] \quad (2)$$

$$l_\varepsilon = c_l y \left[1 - \exp \left(-\frac{Re_y}{A_\varepsilon} \right) \right] \quad (3)$$

where $Re_y = k^{1/2} y / \nu$ is the local Reynolds number, and the constants A_μ and A_ε are 70 and 5.08, respectively. In conformity with the logarithmic law, the constant c_l is set to be $\kappa c_\mu^{-3/4}$ with κ being the von Kármán constant.

Two modifications are carried out to account for the effects of wall transpiration and flow unsteadiness. As several experimental researchers observed,⁵⁻⁷ turbulence intensity and velocity fluctuation increase with increasing mass injection rate near the wall, as well does the Reynolds shear stress. Surface mass injection tends to reduce the wall damping effect, and the turbulence length scale is less damped by the wall with the increasing injection rate. In the present work, the model modification is based on Kay's experimental work,⁷ which follows directly the concepts developed for the mixing length model. Kay argued that the mixing length is effectively equal to the turbulence length scale. Following the form of the van Driest damping function, A^+ in Eq. (2) is modified by considering the wall injection and pressure gradient effects:

$$A^+ = \frac{A_0^+}{5.51 \left[V_w^+ + \frac{5.86 P^+}{(1 + 5.0 V_w^+)} \right] + 1.0} \quad (4)$$

where A_0^+ is the value of A^+ under conditions without wall transpiration and pressure gradient, and $V_w^+ = V_b/u_\tau$. The influence of pressure gradient is taken into account by introducing

$$P^+ = -K^{\frac{3}{2}}(C_f/2)^{\frac{2}{3}}$$

where

$$K = \nu/U_\infty^2(dU_\infty/dx)$$

This approach was first implemented in Tseng's work with great success.⁸

A variety of experiments have been performed to study turbulence intensity in unsteady flows. Cousteix et al.⁹ reached the following conclusion in the study of turbulent boundary layers with external oscillations. Although the measured turbulence intensity and Reynolds shear stress in various parts may change, the ratio of the shear stress to its component turbulence intensities remains constant at a value equivalent to that of steady flow. Thus, under certain circumstances, such as the oscillation frequency not being too high, a steady flow turbulence model may be used to predict unsteady turbulence behavior. However, it is highly possible that substantial changes in turbulence intensity may occur. As the oscillation frequency increases, a critical value (unfortunately, this value is not available at the present time because of limited experimental and theoretical studies) can be reached above, where significant interactions between oscillatory motions and turbulence structure may occur. Experimental studies by Mizushima¹⁰ and Ramaprian and Tu^{11,12} have proven this phenomenon.

Another noticeable feature is related to the turbulence modeling for unsteady flows. When an external oscillating velocity is imposed on a viscous flow, the flow near the wall responds quite readily to this unsteadiness. In many of the experiments that have been performed, the unsteady viscous reaction to the imposed flow variation is almost confined to the Stokes layer near the wall; the outer region of the boundary layer behaves not as alert as the inner layer. This is very important to researchers whose focus is on the characteristics near the wall. Model modifications, especially near the wall, become necessary. In their study of the performance of low-Reynolds-number turbulence models for unsteady boundary layers without wall transpiration, Fan and Lakshminarayana¹³ pointed out that an instantaneous logarithmic law does not generally exist in the near-wall region, and two treatments may be considered because of the rapid change in the phases of the flow quantities: 1) The local turbulence characteristic velocity, or local Reynolds number, instead of inner variable y^+ should be used in the formulation of near-wall and low-Reynolds-number functions and 2) a more stringent requirement on near-wall and low-Reynolds-number functions for the asymptotic behavior of turbulence quantities is necessary. Although only the turbulence length scales need to be modified, these ideas may be useful in the present two-layer model, such as the use of the local turbulent Reynolds number as a correlation parameter to evaluate the turbulent length scale embodied in Eqs. (2) and (3).

Kovalnogov¹⁴ studied experimentally heat transfer and friction in unsteady turbulent flows with a longitudinal pressure gradient in a chamber. The velocity transient and longitudinal pressure gradient exert an indirect effect by changing the coefficients of turbulent momentum transfer in the flow. This effect can be taken into account by modifying the turbulence length scale, where l_0 is the turbulence

length scale in a steady flow:

$$\frac{l}{l_0} = \left[1 + C_1 \frac{\frac{\partial u_\infty}{\partial t} + u_\infty \frac{\partial u_\infty}{\partial x}}{u_{0\infty} \left(\frac{\partial u}{\partial y} \right)_{y=0}} \right] \quad (5)$$

The subscript ∞ refers to the freestream condition and the subscript 0∞ to the chamber inlet condition. A numerical value of 21.4 was found for C_1 in Kovalnogov's experimental work. In the present study, there is no inlet velocity since the head end of the chamber is closed. Thus, $u_{0\infty}$ is chosen as the average velocity of local section area:

$$u_{0\infty} = \frac{1}{A} \int u \, dA \quad (6)$$

B. Formulation of Unsteady Viscous Flow Model

Much of the literature describing the evolution of oscillatory flow in a rocket chamber is based on the assumption that acoustic waves represent the principal unsteady motion. That is, the time-dependent field is taken to be irrotational. To incorporate turbulence effects it is necessary to incorporate fully the rotational flow effects, including all viscous terms in the unsteady formulation. A method based on that described in Ref. 2 will be used here. However, modifications must be made to explicitly include both the effects of the eddy viscosity and the spatial variability of the viscosity and other mean transport properties. As already described, it is anticipated that a main effect of turbulence will be the modification of the transport properties and thus likely there will be large variations in local values.

The standard assumptions and nomenclature used in combustion stability modeling are employed here for convenience in interpreting the results. Velocities are made dimensionless with respect to the chamber sound speed a_0 to emphasize the central role of compressibility in the oscillating field. Lengths are referenced to the chamber radius R ; the acoustic wavelength expressions then contain the chamber length-to-radius ratio, since longitudinal oscillations will be of primary concern. Time is made dimensionless by dividing by the characteristic time represented by the ratio R/a_0 . Pressure is normalized by γP_0 , and other thermodynamic variables are nondimensionalized with respect to their respective chamber stagnation properties. \mathbf{U} is the mean flow velocity vector. Either a laminar or turbulent form for the mean flow must be accommodated depending on the location within the chamber.

The momentum balance for the first-order unsteady viscous flow is

$$\begin{aligned} \frac{\partial \mathbf{u}^{(1)}}{\partial t} + \nabla p^{(1)} = & -M_b \left[\nabla(\mathbf{u}^{(1)} \cdot \mathbf{U}) - \mathbf{u}^{(1)} \times \nabla \times \mathbf{U} \right. \\ & \left. - \mathbf{U} \times \nabla \times \mathbf{u}^{(1)} \right] \\ & + \left[\begin{aligned} & -\nabla \times \nabla \times \delta^2 \mathbf{u}^{(1)} + \nabla(\mathbf{u}^{(1)} \cdot \nabla \delta^2) \\ & + \frac{4}{3} \nabla(\delta^2 \nabla \cdot \mathbf{u}^{(1)}) - \mathbf{u}^{(1)} \nabla^2 \delta^2 \\ & + \nabla \delta^2 \times \nabla \times \mathbf{u}^{(1)} - \nabla \delta^2 \nabla \cdot \mathbf{u}^{(1)} \end{aligned} \right] \quad (7) \end{aligned}$$

where superscript (1) indicates that terms of first-order in wave amplitude are retained. The first group of terms on the right represents the convective interactions between the mean flow and the oscillatory field. These will be handled as perturbations on the organized fluctuations as they are proportional to the mean flow Mach number at the burning surface M_b , which is used as a second small parameter in

the mathematical strategy. Viscous effects, the second set of terms on the right of Eq. (7), are represented in dimensionless form in terms of the inverse of the Reynolds number δ^2 , based on the chamber size and the sound speed

$$\delta = \delta(\mathbf{r}) = \sqrt{\frac{\nu}{a_0 R}} \quad (8)$$

which must be treated as a function of position since the kinematic viscosity coefficient ν , consists of contributions from both molecular and turbulent diffusion. The turbulent component varies strongly with position. Values for ν and its derivatives must be obtained from the numerical turbulent mean flow calculations.

Conservation of mass requires that

$$\frac{\partial p^{(1)}}{\partial t} + \nabla \cdot \mathbf{u}^{(1)} = -M_b \mathbf{U} \cdot \nabla p^{(1)} \quad (9)$$

Assuming sinusoidal oscillations, $p^{(1)} = p' \exp(-ik_m t)$ and $\mathbf{u}^{(1)} = \mathbf{u}' \exp(-ik_m t)$ where primes denote the complex amplitudes, the equation for the unsteady vorticity amplitude, $\omega' = \nabla \times \mathbf{u}'$, is found by taking the curl of Eq. (7) with the result

$$ik_m \omega' = -M_b \nabla \times [\mathbf{u}' \times \Omega + \mathbf{U} \times \omega'] - \nabla \times \left[\begin{aligned} & -\nabla \times \nabla \times \delta^2 \mathbf{u}' - \mathbf{u}' \nabla^2 \delta^2 \\ & + \nabla \delta^2 \times \omega' - \nabla \delta^2 \nabla \cdot \mathbf{u}' \end{aligned} \right] \quad (10)$$

In the present application to a cylindrical geometry with burning at the sidewall and an axial acoustic wave, the vorticity vector has only an azimuthal component.

The boundary condition that must be satisfied by the vorticity at the burning surface is found by evaluating the axial component of Eq. (7) at $r = 1$ and solving for terms involving the vorticity amplitude. One finds that

$$\omega' + \frac{\delta^2}{M_b} \left[\frac{\partial \omega'}{\partial r} + \left(1 + \frac{1}{\delta^2} \frac{\partial \delta^2}{\partial r} \right) \omega' \right] = -\frac{1}{M_b} \frac{\partial p'}{\partial z} \quad (11)$$

at the burning surface. The no-slip condition has been applied. Several terms in the axial momentum balance are not shown because they are several orders of magnitude smaller than the term representing the effect of the axial pressure gradient. This indicates that the vorticity production at the surface is primarily caused by the axial unsteady pressure gradient across the incoming mean flow streamlines. When turbulence from the main flow stream penetrates to the vicinity of the surface, it is likely that viscous stresses are enhanced because of the modified transport properties. Then the second group of terms on the left of Eq. (11) will play an important role in setting the boundary condition for the organized unsteady vorticity. It is necessary to carefully retain them in the problem solution. At the surface, the scaling parameter δ^2/M_b is the inverse of the injection Reynolds number,

$$R_i = \frac{M_b}{\delta^2} = \frac{V_b R}{\nu}$$

It may be either very small in the laminar case and significantly larger if fully turbulent fluctuations are present near the injection surface.

It is useful to distinguish between rotational and irrotational parts of the velocity field. The latter part will represent the acoustic motions that are not strongly affected in a direct manner by viscous effects. The superimposed rotational part is associated with vorticity production at the boundary and accounts for the viscous

interactions as well as the direct connection to the turbulent fluctuations. Thus, to represent the unsteady velocity as a combination of irrotational and rotational parts, put

$$\mathbf{u}' = \hat{\mathbf{u}} + \tilde{\mathbf{u}} \quad (12)$$

where the circumflex ($\hat{\mathbf{u}}$) indicates the acoustic (irrotational) part whereas the tilde ($\tilde{\mathbf{u}}$) identifies the rotational component.

For a three-dimensional cylindrical chamber, the axial acoustic motion representing longitudinal gas oscillations is the simple plane wave solution

$$\begin{cases} p' = \cos(k_m z) \\ \hat{\mathbf{u}} = \hat{w} \mathbf{e}_z = i \sin(k_m z) \mathbf{e}_z \end{cases} \quad (13)$$

This solution will be used to enable simple assessment of the new turbulence corrections by direct comparison to previous analyses that use this base representation for the chamber oscillations.

C. Unsteady Vorticity

To determine the correct form for the rotational unsteady velocity $\tilde{\mathbf{u}}$, it is first necessary to solve for the unsteady vorticity from Eq. (10) subject to the boundary condition of Eq. (11), which, as has already been noted, is the equivalent of the no-slip condition. Once ω' is known, the momentum and continuity balances, Eqs. (7) and (9), can be solved for the rotational velocity vector. For the assumed cylindrical geometry, Eq. (10) is

$$ik_m \omega' - M_b \left(U_r \frac{\partial \omega'}{\partial r} + U_z \frac{\partial \omega'}{\partial z} - \frac{U_r}{r} \omega' \right) = \left[\begin{aligned} & -\delta^2 \left(\frac{\partial^2 \omega}{\partial r^2} + \frac{1}{r} \frac{\partial \omega}{\partial r} - \frac{\omega}{r^2} + \frac{\partial^2 \omega'}{\partial z^2} \right) \\ & + \frac{\partial \delta^2}{\partial z} \left(\frac{4}{3} \frac{\partial \omega'}{\partial z} - \frac{\partial \omega'}{\partial r} \right) - \frac{\partial \delta^2}{\partial r} \left(r \frac{\partial \omega'}{\partial r} + \frac{\omega'}{r} \right) - \frac{\partial^2 \delta^2}{\partial r \partial z} \omega' \\ & + \frac{\partial^2 \delta^2}{\partial z^2} \omega' + M_b \left[\Omega \left(ik_m p' - \frac{u'}{r} \right) + u' \frac{\partial \Omega}{\partial r} + w' \frac{\partial \Omega}{\partial z} \right] \end{aligned} \right] \quad (14)$$

Though linear, this equation is difficult to solve primarily because of the variable coefficients representing the steady velocity components and vorticity Ω . The latter can be represented in the laminar part of the chamber by the Culick mean flow model as

$$\begin{cases} U_r = -\sin(\frac{1}{2}\pi r^2)/r \end{cases} \quad (15)$$

$$\begin{cases} U_z = \pi z \cos(\frac{1}{2}\pi r^2) \end{cases} \quad (16)$$

$$\begin{cases} \Omega = \pi^2 z r \sin(\frac{1}{2}\pi r^2) \end{cases} \quad (17)$$

In regions with turbulence, the axial velocity profile deepens as in a typical pipe flow, although in the rocket motor flow the profile changes are the result of compressibility corrections. Because the unsteady rotational effects damp rapidly when turbulence is present, no attempt is made here to correct for the changes in the mean flow profile.

The complete solution to Eq. (14) is most readily constructed by recognizing that there are two types of oscillatory behavior involved. The first type is related to the acoustic interaction terms on the right-hand side. These vary slowly with position like the product of the mean vorticity with the acoustic pressure or velocity. The second type of vortical motion involves rapid variations in the radial direction resulting from the production of vorticity waves by the shearing action at lateral boundary of the chamber. Hence, it is useful to separate the two types of behavior by writing

$$\omega' = \hat{\omega} + \tilde{\omega} \quad (18)$$

where the notation is consistent with that introduced earlier. This allows Eq. (14) to be separated into two independent parts:

$$\left\{ \begin{aligned} ik_m \hat{\omega} &= M_b \left[ik_m p' \Omega + \hat{w} \frac{\partial \Omega}{\partial z} \right] \\ \frac{\partial \tilde{\omega}}{\partial r} + \frac{U_z}{U_r} \frac{\partial \tilde{\omega}}{\partial z} - \frac{\tilde{\omega}}{r} - i \frac{k_m}{M_b U_r} \tilde{\omega} &= \frac{1}{M_b U_r} \\ &\left[\delta^2 \left(\frac{\partial^2 \tilde{\omega}}{\partial r^2} + \frac{1}{r} \frac{\partial \tilde{\omega}}{\partial r} - \frac{\tilde{\omega}}{r^2} + \frac{\partial^2 \tilde{\omega}}{\partial z^2} \right) + \right. \\ &\quad \left. - \frac{\partial \delta^2}{\partial z} \left(\frac{4}{3} \frac{\partial \omega'}{\partial z} - \frac{\partial \omega'}{\partial r} \right) + \frac{\partial \delta^2}{\partial r} \left(r \frac{\partial \omega'}{\partial r} + \frac{\omega'}{r} \right) \right. \\ &\quad \left. + \frac{\partial^2 \delta^2}{\partial r \partial z} \omega' - \frac{\partial^2 \delta^2}{\partial z^2} \omega' - M_b \frac{\partial \Omega}{\partial z} \tilde{w} \right] \end{aligned} \right. \quad (19)$$

$$\left. \right\} \quad (20)$$

Terms involving the radial velocity fluctuation in Eq. (14) have been dropped since they introduce terms of only second-order in M_b . The rotational part, Eq. (20), has been written in wave equation form by dividing through by the radial steady velocity at the surface, $M_b U_r$.

The solution of Eq. (19) is straightforward. For a cylindrical chamber the result is

$$\hat{\omega} = \frac{M_b}{k_m} \pi^2 r \sin\left(\frac{1}{2} \pi r^2\right) [k_m z \cos(k_m z) + \sin(k_m z)] \quad (21)$$

for the small part of the vorticity, due to interaction of the mean flow with the irrotational unsteady field.

Solution of Eq. (20) for the rotational part is more involved. It is useful to note first that Eq. (20) is a perturbed first-order wave equation.² This suggests application of the ansatz

$$\left\{ \begin{aligned} \tilde{\omega} &= \zeta \exp[i\psi(r)] \sin[k_m z \sin(\tfrac{1}{2} \pi r^2)] \\ \tilde{w} &= W \exp[i\psi(r)] \sin[k_m z \sin(\tfrac{1}{2} \pi r^2)] \end{aligned} \right. \quad (22)$$

$$\left. \right\} \quad (23)$$

where $\zeta(r)$ and $W(r)$ are functions of radial position to be determined. The sinusoidal factor containing the axial position dependence is based on the $\chi(r, z)$ factor of Ref. 2, which was expressed in series form as

$$\chi(r, z) = (k_m z) \sum_{j=0}^{\infty} \frac{(-1)^j}{(2j+1)!} (k_m z)^{2j} \sin^{2j}(\tfrac{1}{2} \pi r^2) \quad (24)$$

This series can be expressed in closed form^{15,16} as

$$\chi(r, z) = [\sin(\frac{1}{2}\pi r^2)]^{-1} \sin[k_m z \sin(\frac{1}{2}\pi r^2)] \quad (25)$$

showing the origin of the factor used in the trial solutions of Eqs. (22) and (23). The exponential argument

$$\psi(r) = -\frac{k_m}{\pi M_b} \ell_v \tan(\frac{1}{4}\pi r^2) \quad (26)$$

is also based on the findings of Ref. 2.

Inserting Eqs. (22) and (23) into Eq. (20), and simplifying, yields a first-order differential equation for $\zeta(r)$,

$$\frac{\partial \zeta}{\partial r} + i\zeta \frac{d\psi}{dr} - \frac{\zeta}{r} - i\frac{k_m}{M_b U_r} \zeta + \frac{\delta^2}{M_b U_r} \zeta \left(\frac{d\psi}{dr} \right)^2 + \frac{\partial \Omega}{\partial z} \frac{W}{U_r} = 0 \quad (27)$$

where only the numerically significant terms have been retained. For example, the only part of the viscous force that affects the solution is that part arising from the second derivative of ζ with respect to r in Eq. (20). When this second derivative is evaluated, it happens that only the part involving the square of the derivative of ψ gives rise to a significant influence on the solution. That is

$$\frac{d\psi}{dr} = \frac{k_m}{M_b U_r} \quad (28)$$

is inversely proportional to the (small) mean flow Mach number. Hence the square of this term dominates the viscous force, as indicated in Eq. (27).

The axial momentum equation [z component of Eq. (7)] can be used to express function $W(r)$ [which is required to complete the solution of Eq. (27)], in terms of the vorticity. One finds

$$ik_m \tilde{w} = M_b \left[\frac{\partial}{\partial z} (U_z w') - U_r \omega' \right] + \delta^2 \frac{1}{r} \frac{\partial}{\partial r} (r \omega') \quad (29)$$

where the radial velocity terms have been omitted as before since they would introduce corrections of second-order in the mean Mach number. Using Eqs. (22) and (23), the axial vortical velocity function is

$$W = i \left(\frac{M_b}{k_m} U_r - i \frac{\delta^2}{M_b U_r} \right) \zeta \quad (30)$$

to good approximation. Substituting this result yields the first-order differential equation for the vorticity function

$$\frac{d\zeta}{dr} + \left(\frac{\xi}{U_r^3} - \frac{1}{r} - \pi^2 \xi \frac{r^2}{S^2 U_r} - i \frac{\pi^2}{S} r^2 U_r \right) \zeta = 0 \quad (31)$$

where the first term in the brackets is the damping effect resulting from viscosity. The solution is controlled by two dimensionless parameters, the Strouhal number

$$S = \frac{k_m}{M_b} \quad (32)$$

Table 1 Physical parameters for typical motor systems (laminar conditions)

	L , m	R , m	M_b	δ	k_m , first mode	S , first mode	ξ , first mode
Small research motor (Yang and Culick ¹⁷)	0.60	0.025	1.7^{-3}	5.49^{-4}	1.33^{-1}	76.87	1.0309
Tactical rocket (typical geometry)	2.03	0.102	3.1^{-3}	2.74^{-4}	1.58^{-1}	50.84	0.0624
Cold flow experiment (Shaeffer and Brown ¹⁸)	1.73	0.051	3.3^{-3}	6.07^{-4}	9.24^{-2}	28.30	0.0909
Space Shuttle SRM	35.10	0.70	2.3^{-3}	1.04^{-4}	6.27^{-2}	27.24	0.0035

and the viscosity parameter

$$\xi(\mathbf{r}) = \frac{k_m^2}{M_b^3} \delta^2(\mathbf{r}) = \frac{S^2}{M_b} \delta^2(\mathbf{r}) = \frac{S^2}{R_i} \quad (33)$$

which is a combination of the acoustic Reynolds number, Strouhal number, and mean flow Mach number. Table 1 shows values of these key parameters for typical rocket motor configurations when the flow is laminar. Values for the viscous parameter shown in the table are the laminar values applicable in the near vicinity of the burning surface. These correspond to high values of the Reynolds number (typically $Ri > 5000$).

As distance from the surface increases and the flow becomes increasingly turbulent, this reference Reynolds number becomes smaller, indicating that viscous damping of the vortical waves becomes more important than in the laminar case.

Equation (31) is readily solved by simple quadrature. One finds

$$\zeta = rC \exp(\phi) \quad (34)$$

where the complex coefficient C must be found from the boundary condition expressed Eq. (11). The complex argument $\phi(r)$ arises in the integration of the right side of Eq. (31). Part of the integration cannot be carried out in finite form, since it involves the integral

$$I(r) = \int \frac{x}{\sin(x)} dx \quad (35)$$

which can be represented by the infinite series

$$\begin{aligned} I(r) &= x + \sum_{k=1}^{\infty} (-1)^{k+1} \frac{2(2^{2k-1} - 1)}{(1+2k)(2k)!} B_{2k} x^{1+2k} \\ &= x + \frac{x^3}{18} + \frac{7x^5}{1800} + \frac{31x^7}{105840} + \frac{127x^9}{5443200} + \dots \end{aligned} \quad (36)$$

Where

$$x = \frac{1}{2} \pi r^2 \quad (37)$$

Functions B_{2k} are the Bernoulli numbers ($B_2 = 1/6$, $B_4 = -1/30$, etc.).

The remainder of the integration is straightforward, and one finds for the real and imaginary parts of ϕ

$$\left\{ \begin{aligned} \phi^r &= \frac{\xi}{\pi^2} \left[1 - \frac{\pi r^2 \cos(\frac{1}{2}\pi r^2)}{2 \sin^2(\frac{1}{2}\pi r^2)} - \frac{1}{\sin(\frac{1}{2}\pi r^2)} \right. \\ &\quad \left. + \left(1 - \frac{2\pi^2}{S^2} \right) [I(r) - I(1)] \right] \\ \phi^{(i)} &= \frac{\pi}{S} \cos(\frac{1}{2}\pi r^2) \end{aligned} \right. \quad (38)$$

Because this represents the effects of viscous damping of the vorticity wave, it shows that the frictional effect grows rapidly larger as the chamber axis of symmetry is approached. This is both because the vorticity wavelength becomes shorter (spatial frequency becomes higher) and the effective viscosity (eddy viscosity) rapidly increases if turbulence is present. The local axial velocity gradient becomes steeper as r becomes smaller, and the viscous forces become correspondingly more important.

Finally, the vorticity can be written as

$$\tilde{\omega} = Cr \exp(\phi + i\psi) \sin[k_m z \sin(\frac{1}{2}\pi r^2)] \quad (40)$$

where the complex constant of integration must be

$$C = \frac{S^3[(S^2 + \xi) + iS\xi]}{[(S^2 + \xi)^2 + (S\xi)^2]} \quad (41)$$

Figure 1 shows vorticity vs radial position for a typical tactical rocket motor configuration when no turbulence is accounted for. Notice that while the acoustic mode amplitude is symmetrical fore and aft, the vorticity is not. This reflects the influence of the increasing mean velocity and vorticity in the z direction.

Since vorticity transport is also a major feature of the turbulent field, it will be of considerable interest to determine what the relationship between the organized

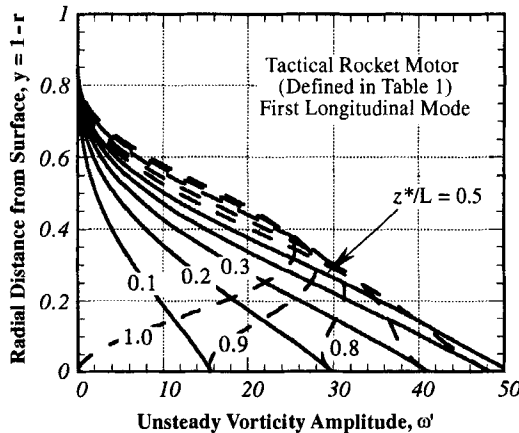


Fig. 1 Laminar vorticity distribution, ω' vs y .

vorticity production just described and the turbulent part. That is, when the part of the field dominated by turbulent motions encroaches on the boundary zone in which the organized vorticity originates, it would appear that the role of the shear layer oscillations must be modified. Vorticity produced at the surface will then be transported mainly by the random fluctuations caused by the enhanced transport mechanisms associated with the turbulent field. Then the organized shear layer oscillations should be rapidly damped as the gas particles produced in the burning zone move into the chamber.

D. Rotational Velocity Vector Corrections

It is now possible to complete the solution for the unsteady velocity field. The axial component is found by inserting the expressions for ζ from Eq. (34) and $W(r)$ from Eq. (30) into Eq. (23). The result is

$$\tilde{w} = iBr \exp(\phi + i\psi) \sin[k_m z \sin(\frac{1}{2}\pi r^2)] \quad (42)$$

where

$$\begin{cases} B^{(r)} = \frac{C^{(r)}}{S} U_r + \frac{\xi}{S^2} \frac{C^{(i)}}{U_r} \\ B^{(i)} = \frac{C^{(i)}}{S} U_r - \frac{\xi}{S^2} \frac{C^{(r)}}{U_r} \end{cases} \quad (43)$$

$$\begin{cases} B^{(r)} = \frac{C^{(r)}}{S} U_r + \frac{\xi}{S^2} \frac{C^{(i)}}{U_r} \\ B^{(i)} = \frac{C^{(i)}}{S} U_r - \frac{\xi}{S^2} \frac{C^{(r)}}{U_r} \end{cases} \quad (44)$$

Figure 2a shows the composite axial fluctuating velocity ($w' = \hat{w} + \tilde{w}$) and Fig. 2b the corresponding phase angle vs radial position for a typical case if no effects of turbulence are accounted for.

It remains to determine the radial velocity correction resulting from the production of vorticity. This velocity must be added to whatever surface fluctuation is present resulting from, for example, pressure or velocity coupled combustion response. It is important to see that this correction is required by continuity since the no-slip condition gives rise to a momentum defect at the surface, as in simple boundary layer theory.

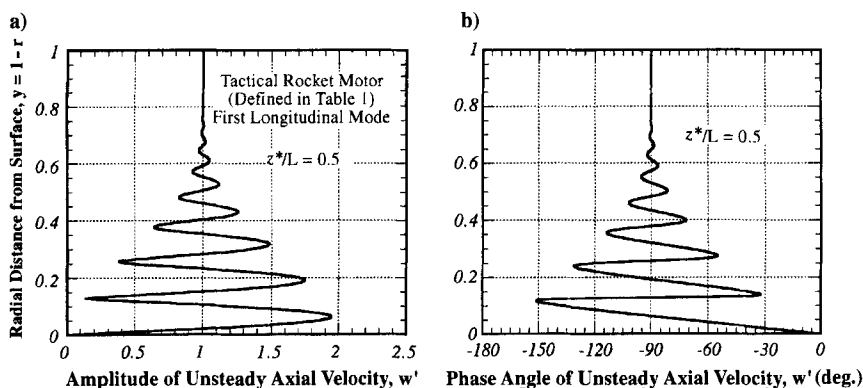


Fig. 2 Laminar axial velocity amplitude and phase angle vs y .

In the present case, the continuity equation that must be satisfied by the rotational part of the unsteady flow is

$$\frac{1}{r} \frac{\partial}{\partial r}(r\tilde{u}) + \frac{\partial \tilde{w}}{\partial z} = 0 \quad (45)$$

The radial velocity can be found directly by setting

$$r\tilde{u} = f(r) \exp(\phi + i\psi) \cos[k_m z \sin(\tfrac{1}{2}\pi r^2)] \quad (46)$$

Using Eq. (42) to represent the axial component. This yields

$$\tilde{u} = M_b B r^2 U_r^2 \exp(\phi + i\psi) \cos[k_m z \sin(\tfrac{1}{2}\pi r^2)] \quad (47)$$

where negligible terms (of order M_b^2) are not shown.

It is important to observe that this radial velocity fluctuation does not vanish at the burning surface. At $r = 1$, one finds for the real part

$$\tilde{u}^{(r)} = -M_b \left(\frac{S^2(S^2 + \xi) + \xi^2 S^2}{(S^2 + \xi)^2 + (S\xi)^2} \right) \cos(k_m z) \approx -M_b \cos(k_m z) \quad (48)$$

where the approximate result corresponds to cases for ξ/S small, which it is in most realistic situations because the flow behavior is nearly laminar in the viscous sublayer.

The surface radial velocity correction must be carefully accounted for in the motor stability calculations and in construction solutions for the gas motions in the combustion zone. Most work on this problem has been based on the assumption of one-dimensional flow normal to the surface. This seems justifiable on the basis of the thinness of the combustion layer. However, as will be demonstrated in what follows, there are strong effects due to parallel wave influence that are eliminated by this and related assumptions (e.g., quasi-steady, one dimensional gas phase). Past failure to demonstrate a consistent model for velocity coupling is also related to this set of limiting assumptions.

III. Effects of Turbulence on Organized Unsteady Flow

It is clear that in real motor chambers there will be two types of unsteady motion when the field is both turbulent and supports acoustic waves (and the associated vortical waves originating at the inflow boundaries). It is necessary to determine how turbulence will affect the organized wave motions. The laminar solution described in the last subsections will be extended by introducing numerically determined turbulent transport properties. As already indicated this is an approximate method for accounting for turbulent effects and does not include direct turbulent flow interactions with the organized wave motions.

Calculations for the development of the turbulent field were carried out for all of the typical motor geometries described in Table 1. For example, Figure 3 shows the evolution of turbulence intensity plotted vs radial position as a function of axial position ($z/L = 1$ corresponds to the nozzle end of the chamber). The turbulence intensity is zero at the chamber axis and peaks at a position that is typically within a distance of 10% of the chamber radius from the burning surface. The turbulent intensity grows in magnitude rapidly as the nozzle end is approached.

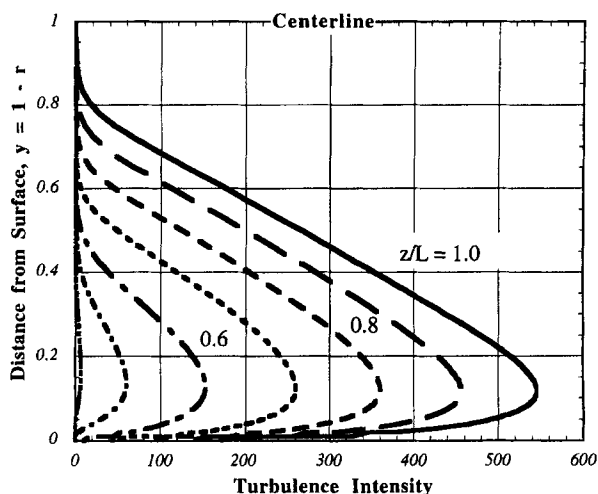


Fig. 3 Turbulence intensity distribution (tactical rocket).

Figure 4 shows the axial velocity profile for the tactical motor configuration indicating transition to a turbulent profile as distance along the chamber increases. The Culick mean flow profile is reproduced for axial positions less than about $z/L = 0.3$. The profile deepens as turbulence further dominates the field with increasing axial distance from the chamber head-end. This is consistent with the usual turbulent pipe flow computations. The turbulent axial velocity profiles near the nozzle end can be fit quite closely with universal pipe flow turbulent profiles such as those devised by von Kármán.

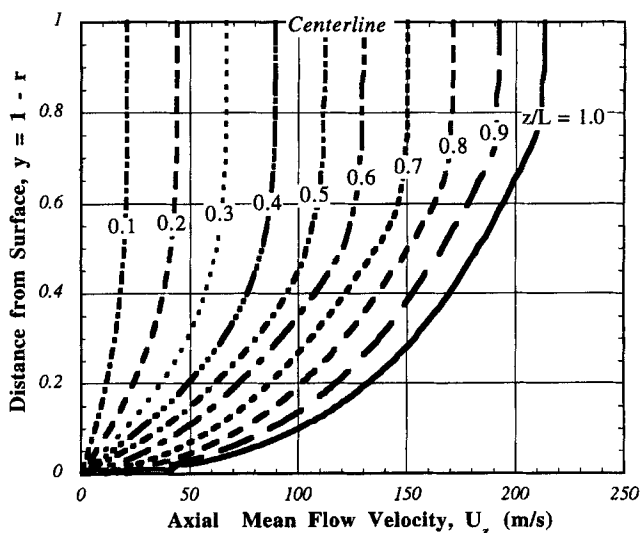


Fig. 4 Effect of turbulence on mean flow velocity profile (tactical motor).

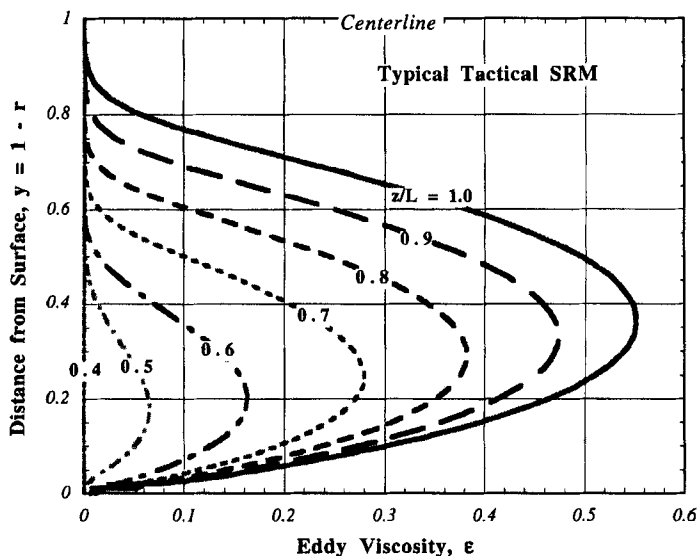


Fig. 5 Eddy viscosity distribution (tactical rocket).

Figure 5 is a plot of the turbulent eddy viscosity distribution as a function of position within the motor. This transport property has a major influence on the organized wave structures, since they are strongly dependent on viscous dissipation. Near the surface, within the laminar sublayer, the laminar solutions are assumed to hold. That is the molecular viscosity dominates the unsteady flow. As distance from the burning surface increases, the effects of turbulent transport become rapidly more important, and dissipation of the energy contained in the organized rotational flow occurs far more rapidly than in the laminar case.

The turbulent transport properties can be used in the expressions developed for the organized unsteady gas motions to approximate the effects of turbulence on the wave structure. The laminar behavior described in Fig. 2 is only maintained near the chamber forward end. As the turbulence dominates the chamber flow as axial distance increases, the laminar motion is replaced by the turbulent organized oscillations.

Figure 6 shows the development of the longitudinal oscillations with axial position. Results shown are for a first mode longitudinal oscillation in the Shuttle SRM. Smaller motors show a more rapid transition to a turbulence-modified solution. The rotational flow effects penetrate deeply into the chamber near the forward end, but rapidly transition to a turbulent form as z/L increases. The turbulent form of the motion closely resembles a typical acoustic boundary layer in which the rotational flow corrections to the longitudinal acoustic wave are confined to a thin zone near the surface. As the nozzle is approached, this effect is enhanced, and it can be seen that this can be thought of as the unsteady analog to the erosive burning situation. In this case, the axial unsteady velocity profiles are deepened in the burning zone. It remains for later study to determine how these changes affect the unsteady combustion characteristics, and in particular, the response function of the combustion layer.

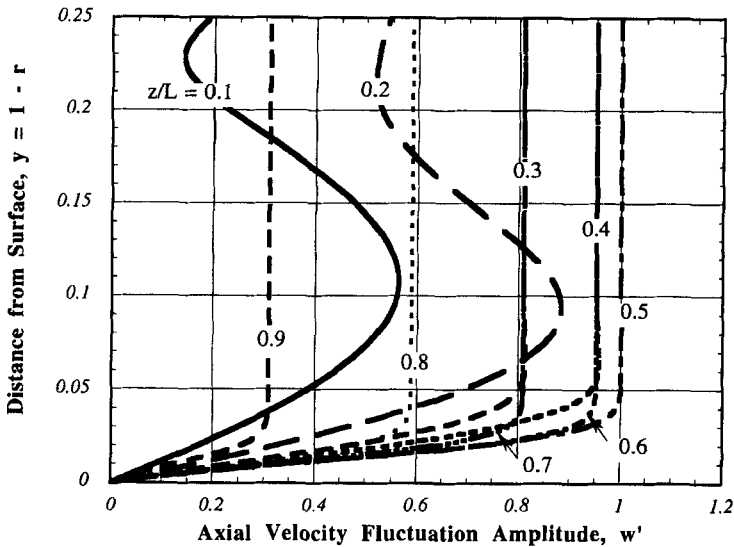


Fig. 6 Effect of turbulence on axial wave amplitude (Shuttle SRM).

To see the strong turbulence interaction with the surface rotational waves, compare the plots for w' in Fig. 6 at a position $z/L = 0.1$ (10% of the chamber length from the head-end) showing the typical laminar behavior and that at $z/L = 0.9$ showing the turbulent behavior. The large overshoot is eliminated, and the profile more closely resembles a classical acoustic boundary layer. It remains to determine the consequences of these changes have on key stability calculations.

A. Effect of Turbulence on Vorticity Production and Transport

We have already demonstrated the important role played by vorticity in accommodating the principal wave motion (assumed to be a longitudinal plane acoustic wave) to the necessary no-slip boundary conditions. In the absence of turbulence, vorticity is produced at the surface and transported as a rotational wave or shear wave as illustrated in Fig. 2. When turbulence is present, the mechanism for vorticity transport is changed because of the enhanced turbulent transport. It is of interest to test the present model to determine if it demonstrates these expected features. Figure 7 compares the laminar and turbulent solutions at a point somewhat less than a third the chamber length from the forward closure. At this location, the turbulent flow has not yet reached a dominant level, and there is only a small difference in the organized vorticity amplitude distribution. As the axial distance increases, the turbulent motion begins to dominate the field. At the location $z/L = 0.4$, only slightly downstream of the position illustrated in Fig. 7, a major modification in the organized unsteady field is apparent.

As shown in Fig. 8, the turbulent fluctuations greatly modify the vorticity distribution, indicating the random motions have taken over in transporting the vorticity produced at the wall into the interior of the chamber. Notice that there is no change in the magnitude of the vorticity at the surface since this is determined entirely by

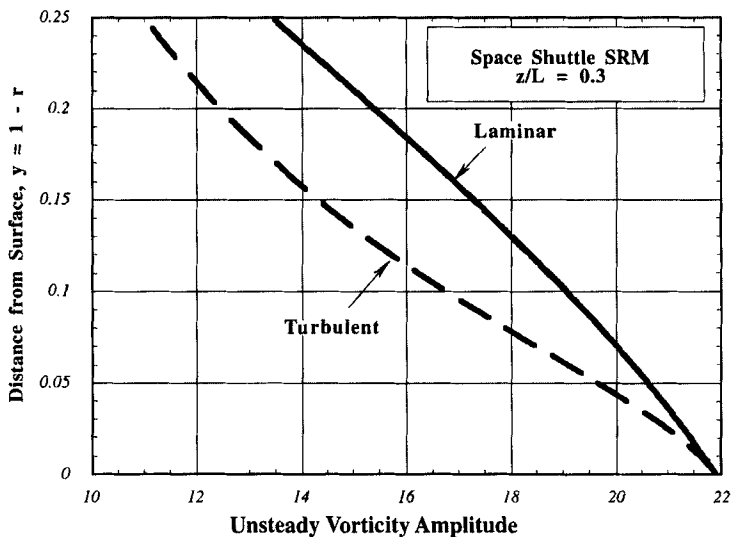


Fig. 7 Effect of turbulence on organized vorticity distribution (Shuttle SRM).

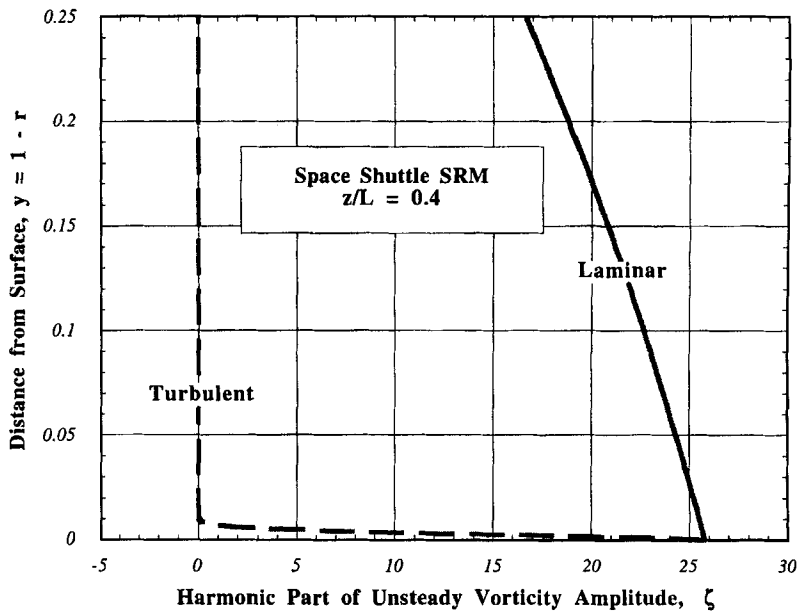


Fig. 8 Effect of turbulence on vorticity distribution (Shuttle SRM).

the pressure gradient across the incoming streamlines. Behavior near the surface is reminiscent of a *laminar sublayer*. The laminar and turbulent solutions are coincident near the inflow boundary.

B. Effect of Turbulence on System Stability Integrals

In estimating the tendency for a given motor to exhibit linear instability, it is necessary to account for many loss/gain effects in determining the net growth rate of an acoustic wave. A very important element is the *flow turning* damping term identified by Culick.¹⁹ The original form of this damping effect was deduced in a one-dimensional analysis. It appeared because the no-slip boundary condition was invoked at the lateral burning surfaces. There followed several years of confusion, since an equivalent term did not appear in the standard multidimensional stability model. It was demonstrated in Ref. 2 that Culick's classical flow turning loss¹⁹ is the one-dimensional equivalent of the volume integral

$$\alpha_{FT} = -\frac{M_b}{2k_m E_m^2} \left(\iiint_V (\mathbf{U} \times \boldsymbol{\omega}') \cdot \nabla p'_m dV \right) \quad (49)$$

where

$$E_m^2 = \iiint_V (p'_m)^2 dV = \frac{\pi L}{2R} \quad (50)$$

is the dimensionless normalization function, evaluated here for a cylindrical chamber with an axial acoustic wave. The first term, Eq. (49), can be written as a surface integral since

$$\boldsymbol{\omega}' = \frac{\partial \mathbf{u}'}{\partial z} - \frac{\partial \mathbf{w}'}{\partial r} \approx -\frac{\partial \mathbf{w}'}{\partial r} \quad (51)$$

The approximate form is valid because the radial velocity fluctuation $O(M_b)$ is small and changes only slowly with respect to z . Figure 8 suggests that both laminar and turbulent results are the same at the surface where the stability integral must be evaluated. Also, the integrand in Eq. (49) oscillates rapidly to zero at the centerline ($r = 0$). Therefore, the value of the volume integral is determined entirely by its upper limit (at $r = 1$). The integrand near the upper limit can therefore be accurately represented as

$$(\mathbf{U} \times \boldsymbol{\omega}') \cdot \nabla p'_m = -k_m \frac{\partial \tilde{w}}{\partial r} \sin(k_m z) = \frac{\partial}{\partial r} (\tilde{\mathbf{u}} \cdot \nabla p'_m) \quad (52)$$

since the derivative of the vortical velocity with respect to r dominates. This is because $\tilde{\mathbf{u}}$ involves ψ , whose derivative is proportional to the inverse of the mean flow Mach number as shown in Eq. (28). Then the flow turning integral reduces to the surface integral

$$\alpha_{FT} = -\frac{1}{2E_m^2} \iint_{S_b} \left(\frac{M_b}{k_m} \tilde{\mathbf{u}}^{(i)} \cdot \nabla p'_m \right) dS_b \quad (53)$$

where the integration is over the burning surface. Notice that only the rotational part of the velocity fluctuation is involved in the flow-turning integral. Therefore, the flow turning stability correction vanishes if one assumes an irrotational unsteady flow as was done in formulating the three-dimensional stability algorithm now in widespread use. Equation (53) is the correct three-dimensional form for the flow turning effect and it is now being incorporated in updated versions of the standard stability prediction code. Of considerable importance is the demonstration given here that this result is not affected by turbulence. This is the result of the independence of this damping effect from viscous processes. It represents the energy loss incurred in the process of transfer of energy from the pressure oscillations (acoustic field) into the complete chamber unsteady flowfield.

There are other surface effects that influence the system stability that are related to satisfying the no-slip boundary condition at the combustion boundary. These results are discussed in Ref. 2, and will not be repeated here. Let it suffice to say that modifications in the fluctuating velocity normal to the surface brought about by rotational flow effects must be accounted for in motor stability computations. What has been demonstrated in this chapter is that these are not affected by the encroachment of turbulence on the inflow boundaries; related modifications to the combustion response function are currently being evaluated.

IV. Conclusions

A fully analytical solution to the Navier-Stokes equations describing the unsteady flow in a cylindrical chamber with sidewall injection has been used in this paper to establish the effects of viscosity on the flow-turning effect in rocket motor combustion instability when strong turbulence is present. The turbulence features are evaluated numerically and the resulting modifications to the chamber transport properties are used in evaluating the analytical expressions describing the unsteady vorticity and velocity distributions.

The results support the findings of earlier fully numerical studies by Yang and his coworkers,¹ which indicated that there is a major influence of turbulence on the unsteady flow features near the combustion zone. The benefits of the present analytical approach are that it 1) enhances physical understanding of the flow processes near the combustion zone, 2) allows ready evaluation of the system linear stability properties in a manner consistent with established stability algorithms, and 3) provides methods that will be useful in further improvement in modeling of the combustion zone in the presence of turbulent fluctuations.

The organized gas oscillations near the burning surface are controlled by two scaling parameters. These are the Strouhal number S , based on the acoustic frequency and the injection velocity at the propellant surface, and the injection Reynolds number Ri . When turbulence is present, the viscous effects are enhanced. There is an apparent decrease in the effective Reynolds number. Then the organized shear waves are rapidly damped and vorticity transport is dominated by turbulent gas motions.

The results demonstrate that the flow-turning can be conveniently represented by a simple surface integral over the chamber boundaries in keeping with other main elements of the stability assessment algorithm. It is demonstrated that turbulence does not modify this result and other related stability affects related to production of vorticity at the chamber inflow boundary.

These stability results are virtually independent of viscosity, although viscous forces greatly influence the unsteady velocity distributions in the volume of the combustion chamber. This is a consequence of the fact that viscous forces are negligible near the injection surface in the laminar sublayer. They are enormously enhanced in strongly turbulent regions because of the modifications to the gas transport properties.

Acknowledgment

This work was sponsored partly by the Pennsylvania State University and the University of Tennessee Space Institute and partly by California Institute of Technology Multidisciplinary University Research Initiative under ONR Grant No. N00014-95-1-1338, Program Manager, Judah Goldwasser.

References

- ¹Cai, W., and Yang, V., "Two-Phase Turbulent Flow Interactions in a Simulated Rocket Motor with Acoustic Waves," AIAA Paper 98-0161, Jan. 1998.
- ²Flandro, G. A., "Effect of Vorticity on Rocket Combustion Stability," *Journal of Propulsion and Power*, Vol. 11, No. 4, 1995, pp. 607–625.
- ³Rodi, W., "Experience with Two-Layer Models Combining the k - ϵ model with One-Equation Model Near the Wall," AIAA Paper 91-0216, Jan. 1991.
- ⁴Wilcox, D. C., *Turbulence Modeling for CFD*, DCW Industries, La Canada, CA, 1993.
- ⁵Yam, C., and Dwyer, H., "Investigation of the Influence of Blowing and Combustion on Turbulent Wall Boundary Layers," *AIAA Journal*, Vol. 27, No. 3, 1989, pp. 370–371.
- ⁶Gibeling, H. J., De Jong, F. J., Sabnis, J. S., and Madabhushi, R. K., *Advanced Flow Field Model*, PL-TR-93-3005, Phillips Laboratory, Edwards AFB, CA, March 1993.
- ⁷Kays, W., "Heat Transfer to the Transpired Turbulent Boundary Layer," *Journal of Heat Mass Transfer*, Vol. 15, 1972, pp. 1023–1044.
- ⁸Tseng, I-Shih, and Yang, V., "Combustion of a Double-Base Homogeneous Propellant in a Rocket Motor," *Combustion and Flame*, Vol. 96, No. 4, 1994, pp. 325–342.
- ⁹Cousteix, J., "Investigation of the Structure and of the Development of a Turbulent Boundary Layer in an Oscillating External Flow," Symposium on Turbulent Shear Flows, Pennsylvania State Univ., University Park, PA, April 1977.
- ¹⁰Mizushima, T., "Structure of the Turbulence in Pulsating Pipe Flows," *Journal of Chemical Engineering of Japan*, Vol. 8, No. 3, 1975, pp. 210–216.
- ¹¹Raamprian, B. R., and Tu, S. W., "An Experimental Study of Oscillatory Pipe Flow at Transitional Reynolds Numbers," *Journal of Fluid Mechanics*, Vol. 100, No. 3, 1980, pp. 513–544.
- ¹²Raamprian, B. R., and Tu, S. W., "Fully Developed Periodic Turbulent Pipe Flow, Part 2: Detailed Structure of the Flow," *Journal of Fluid Mechanics*, Vol. 137, No. 1, 1983, pp. 59–81.
- ¹³Fan, S., and Lakshminarayana, B., "Low-Reynolds-Number k - ϵ Model for Unsteady Turbulent Boundary-Layer Flows," *AIAA Journal*, Vol. 31, No. 10, 1993, pp. 1777–1784.
- ¹⁴Kovalnogov, N., "Unsteady Heat Transfer and Friction in Internal Axisymmetric Flows with Longitudinal Pressure Gradients," *Heat Transfer Research*, Vol. 25, No. 3, 1993, pp. 304–307.

¹⁵Majdalani, J., and Van Moorhem, W. K., "A Multi-Scale Solution to the Acoustic Boundary Layer in Solid Rocket Motors," *Journal of Propulsion and Power*, Vol. 13, No. 2, 1997, pp. 186–193.

¹⁶Majdalani, J., and Van Moorhem, W. K., "Improved Time-Dependent Flowfield Solution for Solid Rocket Motors," *AIAA Journal*, Vol. 36, No. 2, 1998, pp. 241–248.

¹⁷Culick, F. E. C., and Yang, V., "Prediction of Stability of Unsteady Motions in Solid Propellant Rocket Motors," *Nonsteady Burning and Combustion Stability of Solid Propellants*, edited by L. De Luca, E. W. Price, and M. Summerfield, Vol. 143, Progress in Astronautics and Aeronautics, AIAA, Washington, DC, 1992, pp. 719–779.

¹⁸Schaeffer, C. W., and Brown, R. S., "Oscillatory Internal Flow Studies," United Technologies Chemical Systems Division, San Jose, CA, Rept. 2060 FR, Aug. 1992.

¹⁹Culick, F. E. C., "Rotational Axisymmetric Mean Flow and Damping of Acoustic Waves in a Solid Propellant Rocket," *AIAA Journal*, Vol. 4, No. 8, 1966, pp. 1462–1463.

²⁰Nickerson, G. R., Culick, F. E. C., and Dang, L. G., "Standardized Stability Prediction Method for Solid Rocket Motors Axial Mode Computer Program," AFRPL TR 83-017, Edwards AFB, CA, Sept. 1983.

²¹Roh, T. S., Tseng, I. S., and Yang, V., "Effects of Acoustic Oscillations on Flame Dynamics of Homogeneous Propellants in Rocket Motors," *Journal of Propulsion and Power*, Vol. 11, No. 4, 1995, pp. 640–650.

²²Roh, T. S., and Yang, V., "Transient Combustion Responses of Solid Propellants to Acoustic Disturbances in Rocket Motors," AIAA Paper 95-0602, 1995.

²³Roh, T. S., Apte, S., and Yang, V., "Transient Combustion Response of Homogeneous Solid Propellants to Acoustic Oscillations in a Rocket Motor," *Proceedings of 27th Symposium (International) on Combustion*, Combustion Inst., Pittsburgh, PA, 1998, pp. 2335–2341.

Chapter 3.4

Some Aspects of Two-Phase Flows in Solid-Propellant Rocket Motors

J. Dupays,* Y. Fabignon,[†] P. Villedieu,[‡] G. Lavergne,[§]
and J. L. Estivalezes[¶]
ONERA, Châtillon, France

Nomenclature

a, a_0	= speed of sound in the mixture and in the gas
d	= mean droplet diameter
e_b	= web thickness burned
m_{slag}	= slag of aluminum oxide in the aft end of the motor
m_{tot}	= mass of aluminum oxide injected into the chamber
Oh	= Ohnesorge number, $We^{1/2}/Re$
Re	= droplet Reynolds number, $\rho_l V_n d / \mu_l$
V_n	= normal (to the wall) droplet velocity
V_r	= mean relative velocity between two droplets
We	= Weber number, $\rho_l V_n^2 d / \sigma_l$
α, β	= coefficients of attenuation and dispersion of acoustic energy
α_l	= droplet or liquid volume fraction
λ	= heat of vaporization divided by the droplet enthalpy per unit mass
μ_g	= gas viscosity
μ_l	= droplet viscosity
ν_{coll}	= mean collision frequency between two droplets
ρ_l	= droplet density
σ_l	= droplet surface tension
τ_{turb}	= turbulence characteristic time
τ_u	= particle/droplet response time
ω	= pulsation of the acoustic wave

Copyright © 1999 by the American Institute of Aeronautics and Astronautics, Inc. All rights reserved.

*Research Engineer, Fundamental and Applied Energetics Dept.

[†]Project Manager, Fundamental and Applied Energetics Dept.

[‡]Research Engineer, Information Modeling and Processing Dept.

[§]Head of Unit, Aerodynamics and Energetics Models Dept.

[¶]Research Engineer, Aerodynamics and Energetics Models Dept.

II. Aluminum Oxide Formation

Aluminized propellants can be made up of more than 20% aluminum powder. The aluminum particle size lies in the range 5–200 μm , with the range 10–40 μm being the most common.¹⁰ Because of the occurrence of a thin, nonporous oxide skin over the particles and of the relatively high aluminum boiling temperature as compared to the primary flame temperature, the particles do not vaporize immediately on the surface. The heating of the particles leads to the melting of the metal and to the breakdown of the oxide skin due to droplet expansion. Under the influence of surface tension, aluminum can drain out, so that adjacent particles, packed inside microstructures bounded by the coarse ammonium perchlorate (AP), tend to coalesce into large agglomerates whose size is closely related to the propellant burning rate, AP particle sizes, and the ratio of fine to large AP mass fractions.¹ A good estimation of the agglomerate mass fraction for a given composition can be obtained with Beckstead's¹¹ or Cohen and Strand's correlation.¹²

The breakdown of the oxide skin results in an increased oxidation rate and in a rapid temperature rise that leads to the melting of the oxide. The low solubility of the liquid alumina (Al_2O_3) in the liquid aluminum prevents the dissolving of the oxide inside the metal. More precisely, because of the high value of the oxide surface tension and the low interfacial surface tension between the oxide and the metal, the oxide layer tends to retract and expose the metal. Oxidation reactions are intensified, and ignition can occur at this stage.

During combustion, a luminous detached flame surrounds the droplet and a convected Al_2O_3 smoke trail appears behind the droplet (see Fig. 2 and also the color reproduction on p. xxvi). The size of the oxide lobe increases progressively, reducing the vaporization surface, leading to nonsymmetrical combustion and a possible droplet spin. Some jetting processes and disruptive events, probably due to the formation and trapping of gaseous oxide just beneath the oxide lobe, were observed before extinguishment for many experimental conditions in controlled and quiescent atmospheres. Inasmuch as these atmospheres include pure CO_2 or



Fig. 2 Aluminum droplets in combustion immediately above propellant surface, AP/Al/HTPB propellant, chamber pressure = 0.6 MPa (courtesy ONERA; see also p. xxvi).

H₂O, the two main oxidizers with HCl in a propellant environment,^{13–15} these phenomena are likely to occur in a combustion chamber.

One of the general characteristics of aluminum combustion is the production of a condensed phase, consisting mainly (80–90% of mass) of submicron Al₂O₃ smoke, and for the remainder of Al₂O₃ residues ranging roughly from 20 to 200 μm , depending on original aluminum particle size and degree of agglomeration.^{2,16} Another general characteristic is the so-called distributed combustion. Because of their low volatility, the aluminum droplets can burn across a fairly large portion of the chamber. In this case, the energy release does not contribute to an increase in the burning rate, but, according to recent theoretical, experimental, and numerical studies,^{4,17–20} its contribution could be significant to the global acoustic balance of a motor, especially for a high burning-to-residence time ratio. In fact, even in large motor, where this condition is not satisfied, distributed combustion is suspected to be a driving mechanism by amplifying flow disturbances in sheared regions near the propellant surface. Unfortunately, to date, there is no theory allowing the prediction of the intensity of this contribution for a given propellant and motor geometry arrangement.

The process(es) leading to the increase of the oxide lobe is (are) still unknown. Three nonexclusive scenarios can be considered. First, Al₂O₃ smoke is carried out toward the surface by convective and thermophoresis effects, because in the latter case the temperature difference between the smoke and the droplet surface is relatively high.²¹ Second, aluminum-containing species, essentially AlO as well as Al₂O and Al₂O₂, produced at the flame diffuse inward and condense on the cold surface of the droplet. Third, aluminum oxide is produced through heterogeneous reactions between the liquid aluminum and the gaseous oxides surrounding the droplets. Each of these scenarios might be preponderant in different stages of the combustion or depending on the ambient conditions.

In spite of our relative misreading of the physical mechanisms involved, further analytical or semi-analytical models have been proposed.^{22–26} Two of them, namely, Law's model,²³ extended recently by Brooks and Beckstead¹⁸ and Marion et al.,²⁷ and the Greymachin et al.²⁴ model, explain the surface formation of the oxide lobe by assuming the second scenario and the third scenario, respectively. To date, the fragmentation process is omitted from all of the models. Moreover, except for King's model,²⁵ they all assume a diffusion-controlled vapor-phase combustion. The pressure effect is taken into account only by the physical property variations. Law's model²³ and its byproducts have been introduced successfully in further numerical flow or acoustic codes.^{18,28,29} It is also possible to build combustion models from experimental and numerical correlations.^{30–32} In this case, either the fraction of oxide that condenses on the surface is arbitrarily fixed or the combustion is stopped for a fixed diameter.^{33,34}

III. Interactions Between Droplets and Gas Flowfield

There is some experimental evidence that even a small mass fraction of aluminum particles can significantly modify the global acoustic balance of a motor. The distributed combustion can be seen as a powerful driving mechanism, whereas the viscous and thermal lags can be a very efficient damping mechanism. As these two antagonistic effects are not supposed to compensate themselves, a two-phase reactive approach seems to be necessary to achieve a reliable stability prediction.

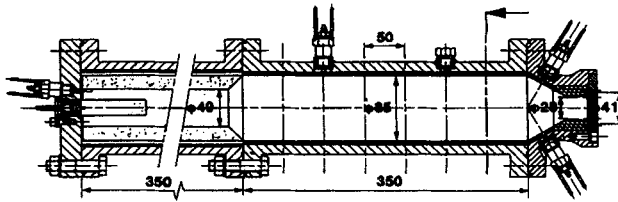


Fig. 3 Schematic of experimental setup (dim in mm).

To illustrate these different interactions, we emphasize three cases: interactions between inert particles and vortex shedding, interactions between vaporizing droplets and acoustic waves, and interactions between burning droplets and mean gas flowfield. Even though the last case is a steady-state study, it can give a first indication of the possible effect of distributed combustion on acoustic-related instabilities.

A. Interactions Between Inert Particles and Vortex Shedding

The experimental setup shown in Fig. 3 is a small, naturally unstable (whistling) motor that was designed to develop a vortex shedding phenomenon locked on the first axial mode, as observed in large segmented motors. This laboratory facility is only partially representative of these motors, because the shear layer is generated from a chamfered edge of the grain located in the middle of the chamber and the vortex does not evolve above an injecting surface. In fact, a very simple internal geometry was retained to facilitate both the interpretation of results and the validation of numerical calculations.

Two experimental programs were conducted at ONERA. The main purpose was to study the effect of an inert particulate phase on the instabilities.^{8,35} Four composite propellants, with close burning rates and flame temperatures, were used to perform parametric studies on mass fraction and particle diameter. The first, a 79% AP–21% hydroxyl-terminated-polybutadiene (HTPB) propellant, was kept free of particles to serve as reference. Two were loaded with small alumina particles (about 5 μm) with mass fractions of 5 and 10%, respectively. Because large spherical alumina particles were not available, the last was loaded with zirconium silicate particles (about 70 μm) with a mass fraction of 5%. In the following discussion, these propellants will be subsequently called Butalite, Butalamine 5%, Butalamine 10%, and Butalazine. The particle sizes and mass fractions were carefully chosen by resorting to the acoustic balance theory.³⁶ For the frequency of the first axial mode, which is roughly 700 Hz, small particles should be far more efficient than large particles in damping the oscillations. Moreover, the mass fraction was chosen to observe both vortex shedding and particulate damping.

Vortex shedding was identified on all of the firings. All tests experienced pressure oscillations with some bursts corresponding to sustained self-excitation phenomenon. Butalite tests exhibited three of them, and the other compounds only two, in the second-half of the burn (Fig. 4). Spectral analysis suggests that they are linked to acoustic mode frequencies, especially the first one, and the frequency shifts observed on the power spectral density plots establish the reality of the coupling between the acoustics and the vortex roll.⁶

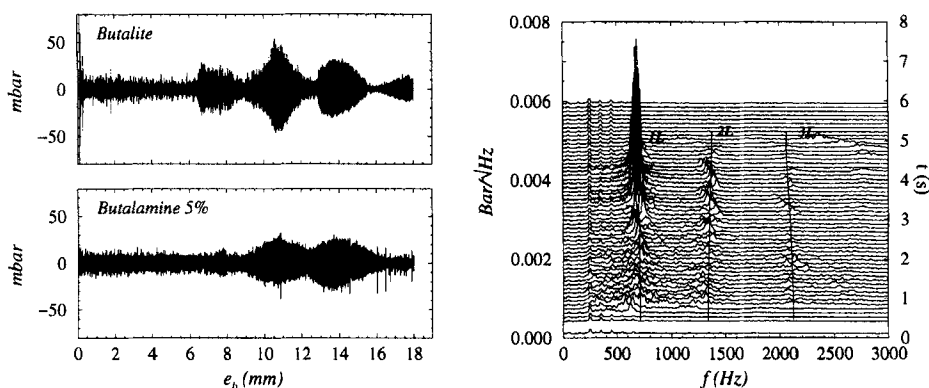


Fig. 4 Unsteady pressure component at the head end and power spectral density vs time and frequency for Butalamine 5% firing.

In addition, pressure oscillation damping was observed for the Butalamine tests (see Fig. 5). More precisely, the first burst is inhibited, as though the particles delay the self-starting, self-sustaining acoustic oscillations, and the second is less pronounced because of viscous and thermal particle gas interaction. The increase of the particulate mass fraction leads to a moderate increase of the damping effect, but only in the second burst. Indeed, the third is barely damped, perhaps because of the occurrence of complex wall–eddy–particulate phase interactions at this point in the burn.

Results obtained for the Butalazine tests are quite different. Large particles seem to modify the energy distribution inside the chamber, as shown in Fig. 6. At the beginning of the firing, the third axial mode and even the fourth are unstable, to the point that oscillation levels are larger than for the Butalite and Butalamine tests. However, when the vortex shedding is set in motion, although the third axial mode

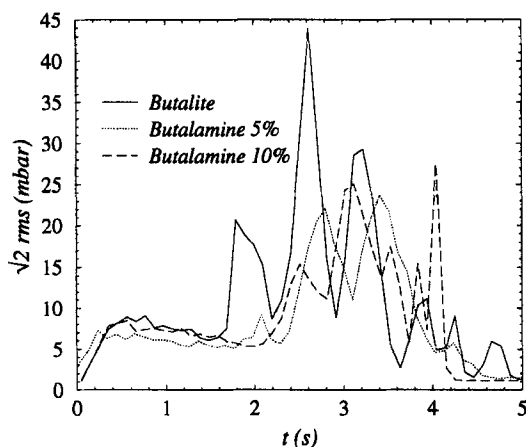


Fig. 5 Oscillation levels vs time.

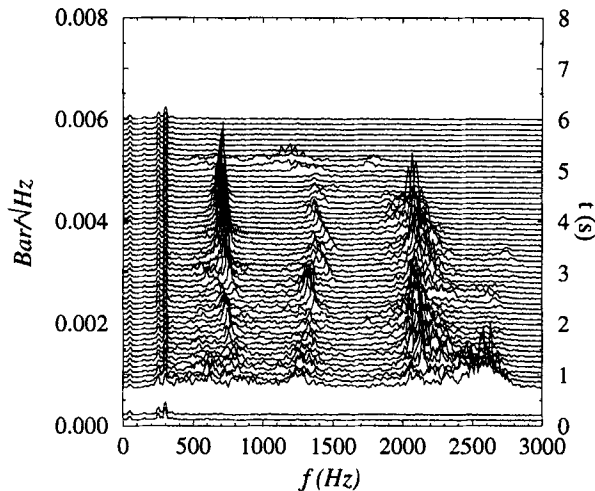


Fig. 6 Power spectral density vs time and frequency for Butalazine firing.

remains important, oscillation levels keep moderate values, similar, as expected, to those measured on the Butalite tests. This amplification of high frequencies by large particles can be explained by the high value of the Stokes number $\omega\tau_u$ (see Sec. III.B), but the mechanisms leading to the coupling with this acoustic mode and then to its amplification are still unknown. Such a phenomenon could not be observed for the Butalamine tests because, assuming the same value of the critical Stokes number, the corresponding frequency would be two orders of magnitude larger, that is, about 200 kHz.

This database was used to validate an unsteady two-phase numerical code. A configuration leading to a sustained self-excitation phenomenon was retained. Computation conditions (such as grid size, numerics, gas and particle properties, and boundary conditions) are described in Ref. 35 and will not be repeated here. The code is based on a two-fluid approach and computations were performed without propellant response models. In spite of this, simulation–experiment comparisons are rather good as shown in Fig. 7 for the Butalamine 5% case (see also the color reproduction of this figure on p. xxvi).

Computations were first conducted for 6- μm particles with three different mass fractions of 5, 10, and 20%. The magnitude and phase of the Fourier coefficient of the first axial mode, along the chamber axis, highlight the form of this mode in the grain port and the presence of four eddies in the second part of the chamber, in agreement with the vorticity contour plot (see Fig. 7). Oscillation levels were found to be larger with a mass fraction of 10% than with a mass fraction of 5%, whereas, with 20%, oscillations are totally damped (not shown). This result is in direct conflict with the linear theory (see Sec. III.B) that, of course, cannot predict this threshold effect, which is probably related to complex, still unknown, particle–eddy–acoustic interactions. By contrast, the frequency shift due to a change in the speed of sound is well recovered by the computations, in agreement with both theoretical and experimental results.

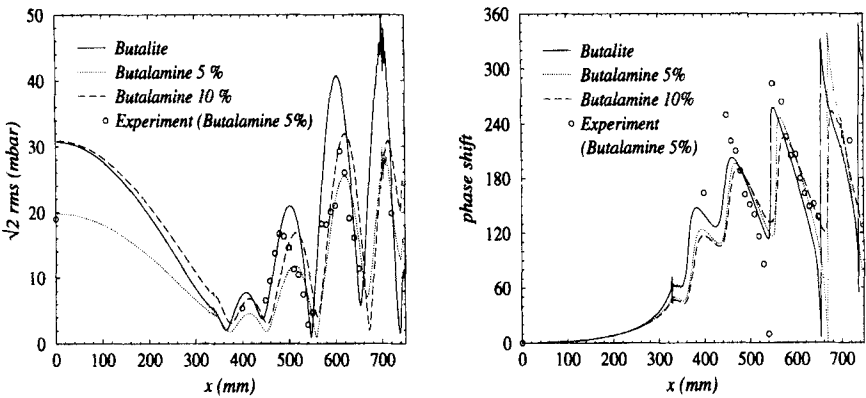


Fig. 7 Vorticity contour plot for the Butalite computation and Fourier coefficients of the first mode along the chamber axis (see also p. xxvi).

A parametric study on the particle size around $6 \mu\text{m}$ highlights the drastic sensitivity of the oscillation levels to the particle size, at least when the Stokes number approaches 1 (see Table 1). Unlike the case for single-phase flow, the ratio of the aft-end to head-end oscillation level is larger than 1. The damping is more significant at the head end because the upstream running pressure wave has to travel a greater distance.

For all of these computations, the signal remains monochromatic and the frequency keeps the same value. For the larger particles, the signal is no longer monochromatic. The first three acoustic modes are amplified, and the frequency of the first mode is slightly increased, in accordance with the experimental results. Coarse particles are swept by the eddies toward the centerline, where the mass concentration increases drastically. As a result, $70\text{-}\mu\text{m}$ particles tend to damp the oscillations with the same efficiency as $6\text{-}\mu\text{m}$ particles, as though the concentration effect, due to a selective repartition mechanism, could compensate the size effect. In fact, these large particles act less on the acoustics than on the flow itself,

Table 1 Parametric study on particle size for 5% mass fraction

Particle diameter, μm	Stokes number, $\omega\tau_u$	Frequency, Hz	Head-end pressure oscillation, mbar	Aft-end pressure oscillation, mbar
—	—	731	31	26
5	0.33	684	30	30
6	0.47	684	20	22
6 and 7	0.56	684	12	15
7	0.64	684	8	11
70	64.4	713 ^a	21	14
5 and 70	—	699	18	21

^aPolychromatic signal.

because, as in single-phase flow, the ratio of the aft-end to head-end oscillation level is larger than 1.

The computation with two classes of particles, 50% each of 5 and 70 μm , also gives a monochromatic signal with a frequency that is exactly the average value between the two monosized computations, whereas, as regards the oscillation levels, intermediate but not average values are obtained. In other words, there are enough small particles to damp the upper acoustic modes, probably with a threshold effect, and the frequency depends linearly on the mass fraction, although the dependance is far more complex for the oscillation levels.

To sum up, the main results deduced from this study are the following:

1) The influence of the dispersed phase must be taken into account to achieve a reliable stability prediction.

2) The particle–gas interactions are extremely complex; some threshold effects can be identified.

3) The increase in the loading does not necessarily accentuate the attenuation of instabilities.

4) The selective repartition mechanism of the dispersed phase by the vortex can lead to a concentration effect that, in practice, can reveal itself as efficient as the size effect.

5) Particle size is a sensitive parameter that may act on the oscillation levels and on the energy distribution, so that the distribution size must be described very precisely.

B. Interactions Between Vaporizing Droplets and Acoustic Waves

Attenuation of sound by suspended droplets in a gas has been treated theoretically by many authors for more than 80 years. The simplified analysis of Temkin and Dobbins³⁷ is among the most popular. An alternative method, developed in the acoustic balance theory framework, is reported in Ref. 36.

Inert droplets are inclined to damp and to disperse the waves by slowing them. The damping is all the more pronounced when the droplet response time is close to the acoustic time period or, in other words, when the acoustic Stokes number $\omega\tau_u$ is close to 1. The damping increases linearly with the droplet mass fraction. The dispersion is highest for relatively small droplets and/or for relatively low frequencies, as shown in Fig. 8, which presents a plot of the nondimensional coefficients of attenuation and dispersion of acoustic energy, namely, α^* , and β^* , defined by

$$\alpha^* = (a_0/\omega)\alpha \quad \beta^* = (a_0^2/\omega^2)\beta = [(a_0/a)^2 - 1] \quad (1)$$

The Temkin and Dobbins³⁷ reasoning was extended by Marble,³⁸ who studied sound attenuation in a condensing vapor by assuming a diffusion-controlled process, and by Dupays and Vuillot,²⁰ who considered a vaporizing droplet cloud by assuming a thermal conductivity-controlled process. With this model,²⁰ the mass transfer process is found to dominate the other interaction processes and, as a result, to amplify acoustic waves ($\alpha^* < 0$) and to increase the phase velocity ($\beta^* < 0$) as shown in Fig. 8. The position of the minimum of the α^* curve, which gives an estimation of the critical frequency–diameter pair, depends mainly on the nondimensional heat of vaporization λ . By knowing that, for the aluminum, λ is close to 1, it is easy to find critical diameters ranging from 25 to 30 μm for a

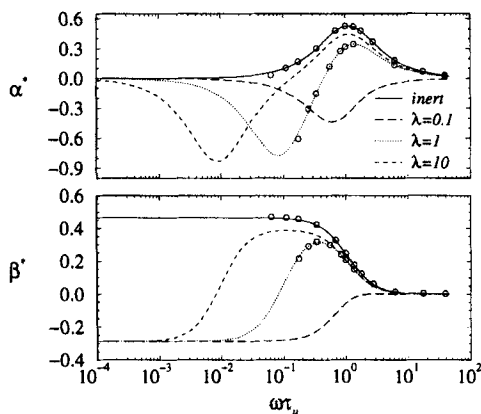


Fig. 8 Nondimensional attenuation α^* and dispersion β^* of an acoustic wave propagating in a two-phase medium with a loading of 0.4 (points correspond to numerical simulations).

typical, large solid rocket motor. It can be shown also²⁰ that even a small mass fraction of vaporizing droplets can amplify acoustic waves.

Even though the generalization of these results to the case of aluminum combustion seems hazardous, this study²⁰ gives arguments for suspecting that distributed combustion may be a powerful source of instability. From a numerical viewpoint, these theoretical developments offer convenient support for defining simple test cases for validating unsteady reactive two-phase flow codes. Results obtained with numerical simulations, for instance, are in good agreement with the theory.²⁰

C. Interactions Between Burning Droplets and Mean Gas Flowfield

This subsection describes the interactions between burning aluminum droplets and the mean gas flowfield in a subscale motor. This small motor was chosen because the residence time is roughly equal to the droplet combustion time. The geometry of this motor is axisymmetric, with a classical converging/diverging nozzle and a cylindrical propellant grain (AP/Al/HTPB), as shown in Fig. 9. Calculations were performed with an Eulerian-Lagrangian approach, with Eulerian gas-phase and Lagrangian liquid-phase modeling.²⁸

Law's model²³ for aluminum combustion was retained because it takes into account the presence and growth of the oxide cap. The original model was improved

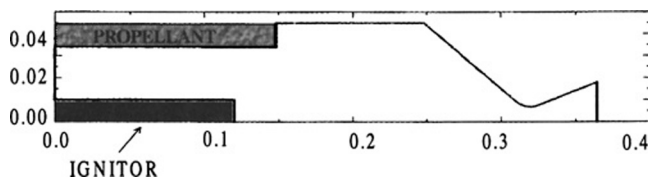


Fig. 9 Schematic of an axisymmetric test motor (dim in m).

with a modified Sherwood number to consider convection effects that can become significant in places where the difference between the gas and droplet velocities is large. The oxidizer concentration was corrected to take into account that, in solid rocket motors, the oxidizer is not pure oxygen but, essentially, a mixture of CO_2 and H_2O . A concentration of an equivalent oxidizer was defined with the correlation suggested by Brooks and Beckstead.¹⁸

Because of the exchange of mass, momentum and energy, the two phases are strongly coupled. The action of the gas phase on the liquid phase was directly taken into account in the droplet behavior models.^{28,39} The effect of the dispersed phase on the mean gas flowfield was modeled by including source terms in the right-hand side of the gas-phase equations.

At the beginning of the calculations, the flowfield was simulated without aluminum droplets but with a propellant surface temperature determined by using results from a complex chemical equilibrium composition code.⁴⁰ The resulting solution is then used as an initial condition for the two-phase flow simulation, and aluminum droplets are injected into this flowfield through 15 injection points uniformly distributed along the propellant surface. The coupling between the two phases was performed by using an unsteady approach: this means that the equations for the two phases are solved simultaneously. In particular, the source terms in the gas-phase equations are evaluated at each time step.

Three gaseous species were considered, namely, an inert propellant gas, an oxidant gas, and a gas produced by the aluminum combustion, as suggested in Ref. 29. Two classes of droplets (125 and 30 μm) were injected, with the same mass fraction, to take into account the agglomeration process on the surface. Gas and droplets were injected at the same temperature, 2317 K, but not at the same velocity. The injection velocity of the droplets was about one order of magnitude smaller than the gas velocity.

The results of this calculation were compared with the results of another simulation, in which combustion was considered as confined to the propellant surface (surfacic combustion). In that case, we considered an equivalent gas that was the result of the mixing of all of the species comprising the combustion products of aluminum. The injection temperature was 3380 K.

Figure 10 shows the temperature field for both cases (see also the color reproduction on p. xxvii). In the case of surfacic combustion, we note that the temperature is homogeneous in the entire combustion chamber. On the other hand, the temperature distribution is very heterogeneous in the case of distributed combustion. It depends essentially on the aluminum droplet concentration, and so it is higher

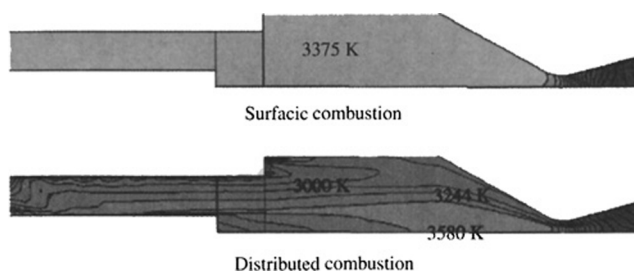


Fig. 10 Temperature fields for the two approaches (see also p. xxvii).

near the axis of the motor, where the dispersed phase is very dense. For the case of distributed combustion calculations, the $30\text{-}\mu\text{m}$ droplets are rapidly burned. Indeed; the mean radial distance traveled by these droplets before their total burning is about 4 mm. The $125\text{-}\mu\text{m}$ droplets that are injected close to the head end of the motor impinge on the ignitor wall, whereas the others are dispersed in the chamber and burn all along their trajectory. Most of them have completely burned before reaching the nozzle. Similar computations using an Eulerian approach for the gas and liquid phases are described in Ref. 29.

This comparison shows that, in the case of a short solid-propellant motor, distributed combustion may have a major influence on the mean gas flowfield. This study may give a first indication of the possible effects of distributed combustion on acoustic-related instabilities.

IV. Slag Accumulation

The slag generation is very complex and may appear in motors with submerged nozzles. This phenomenon involves unsteady two-phase flow with recirculating aluminum oxide droplets, multimodal droplet size distributions, and droplet-wall interactions in motors that may be vectoring, spinning, accelerating axially, or ejecting slag. Slag is generated when Al_2O_3 droplets become trapped behind the submerged nozzle (Fig. 1). This entrapment occurs by impingement on some portion of the backface of the nozzle or by capture in a recirculation zone. Slag may have several consequences on motor performance, on thermal insulation behavior, and on thrust vectoring.

The biggest database of slag weight measured after static firings was published for U.S. solid rocket motors,⁵ but no reliable slag weights in flight motors have been identified. Slag accumulation measurements in a vertically static rocket motor were recently carried out.⁴¹ Real-time radioscopy (RTR) was used to determine slag accumulation. The RTR system consisted of an x-ray radiation source and a camera box. The x-ray source transmitted radiation through the aft end of the motor into the camera box. Results showed that, in this motor, slag moved actively in the aft dome. Significant sloshing of the material at low frequencies (2–3 cps) was evident. Some of this movement is coordinated with step inputs in the nozzle gimbal angle that are sustained over long periods of time.

Such measurements, however, are complex, are costly, and cannot identify the basic physical phenomena involved in the process. Therefore, a continuous effort in modeling and in the development of numerical tools has been under way for some years.^{5,42–46} In France, to understand the slag accumulation phenomenon, some numerical studies were carried out. The following subsections summarize this French contribution. All numerical studies presented concern computations in a large solid rocket motor using a 68% AP–14% HTPB propellant. To simplify calculations no combustion model was used.

A. Two-Phase Flowfields

The first investigation used a combined Eulerian–Lagrangian⁴⁶ approach based on steady solutions of the gas flowfield. The Eulerian gas-phase analysis used a numerical solution of the ensemble-averaged gas equations completed by a low Reynolds number $k\text{--}l$ turbulence model. The motion of the particulate phase was

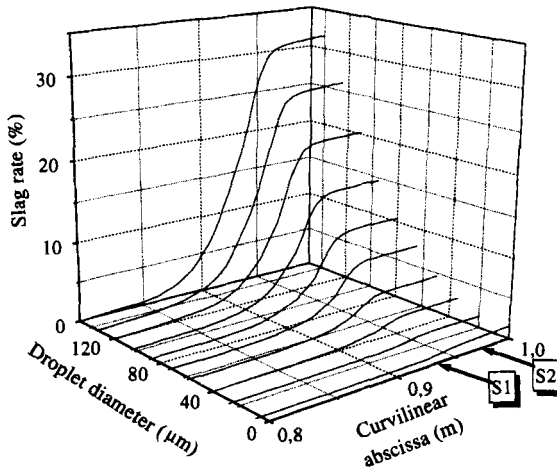


Fig. 11 Slag rate vs droplet diameter and curvilinear abscissa along the motor case walls.

described with a Lagrangian method using different stochastic models to analyze the effect of flow turbulence. The particulate phase consisted only of Al_2O_3 droplets injected with a classical bimodal size distribution^{2,5,16} (80% in mass for the smoke and 20% for the residues). The droplet trajectories were calculated on the steady gas flowfield, and the slag rate was estimated by summing the droplets trapped behind the submerged nozzle. The conditions under which droplets are unable to exit the nozzle are characterized by the capture rules. Two captures rules (see S1 and S2 in Fig. 1) have been considered. S1 corresponds to the break point in the nozzle backside geometry. S2 could be considered as giving the maximum slag accumulation because for any locations $S > S_2$ along the motor case walls, droplets exit the nozzle. An example of the results is shown in Fig. 11 for a large solid rocket motor with submerged nozzle. Figure 11 shows, for one burnback geometry, the slag rate ($m_{\text{slag}}/m_{\text{tot}}$) vs droplet diameter and curvilinear abscissa S along the motor case walls. It can be seen that the slag rate increases with droplet diameters. The increase in slag rate is very abrupt near the two capture points defined earlier. Capture points, thus, seem to be important parameters and need to be defined very accurately. The numerical study also showed that the turbulence flowfield in the chamber seems to be another important parameter for slag accumulation.⁴⁶

It also appears, from these simulations, that classical Al_2O_3 bimodal droplet size distributions could not produce the total amount of slag that has been experimentally observed during static firings. To explain this difference between numerical and experimental results, some new calculations including droplet collisions were carried out.

B. Effect of Droplet Coalescence

The aim of this section is to show that droplet coalescence in the rocket chamber may have a significant influence on the slag accumulation rate in the aft end of the motor and may explain the difference between the experimental and numerical

results just presented. This is plausible, because the coalescence process leads to the formation of larger sized droplets, which are more likely to be trapped behind the submerged nozzle, due to their higher inertia.

Assuming that the droplet collision rate may be calculated as for molecules in a gas, it is possible to estimate the collision frequency order of magnitude. Using arguments of kinetic theory, it can be proved⁴⁷ that the mean collision frequency ν_{coll} is given by

$$\nu_{\text{coll}} \approx \alpha_l V_r / d \quad (2)$$

In the case of a large solid rocket motor, typical values for α_l , V_r , and d are 0.001, 5 m/s, and 10 μm , so that $\nu_{\text{coll}} = 500 \text{ s}^{-1}$. For a residence time of about 0.1 s, this means that a droplet will, on average, participate in 50 collisions while traveling through the combustion chamber. This rough calculation shows that droplet collision may play a fundamental role in a solid-propellant rocket motor and must be taken into account in numerical simulations.

Because of the analogy between droplet collisions in a turbulent gas flow and molecule collisions in a gas, the kinetic theory framework is well adapted to derive a model for droplet coalescence. Let $f^{(1)}(t, x, v, r)$ be the mean droplet density of velocity v and radius r and let $f^{(2)}(t, x, v, r, v', r')$ be the mean density of the droplet pairs. Using classical arguments in the kinetic theory of gases, it is possible to establish an equation of the following form:

$$\left. \frac{df^{(1)}}{dt} \right|_{\text{coll}} = Q_{\text{coll}}(f^{(2)}) \quad (3)$$

where Q_{coll} is a nonlinear integral operator.^{47–51} All of the physical knowledge about the collision process is included in the definition of this operator.

In the present model, following the conclusions in Ref. 52, it has been assumed that a collision may either result in an elastic rebound (for a large impact parameter) without any modification of the droplet sizes or in the coalescence of the two droplets (for a smaller impact parameter). The critical value of the impact parameter separating the two regimes is a function of the radii ratio r/r' of the colliding droplets and of the collision Weber number, defined in Refs. 53–55 by

$$We_c = [\rho_l |v - v'| \min(r, r')] / \sigma_l \quad (4)$$

The main difficulty is to close Eq. (3). The simplest way is the so-called chaos assumption that consists of assuming that

$$f^{(2)}(t, x, v, r, v', r') = f^{(1)}(t, x, v, r) f^{(1)}(t, x, v', r') \quad (5)$$

Actually, because of the correlations induced by the action of the gas on the droplets, this relation is generally not valid and leads to an overestimation of the collision rate. To get a more accurate collision model, Eq. (5) can be replaced by

$$f^{(2)}(t, x, v, r, v', r') = E(t, x, v, v', r, r') f^{(1)}(t, x, v, r) f^{(1)}(t, x, v', r') \quad (6)$$

where $E(t, x, v, v', r, r')$ is a correction factor, called collision efficiency. The general form of E is

$$E(t, x, v, v', r, r') = E_c(t, x, v, v', r, r') E_v(t, x, v, v', r, r') \quad (7)$$

The term E_c takes into account that, when a droplet approaches another one, it does not follow a straight line trajectory, but instead is deflected due to the interaction of

the two droplets with the surrounding gas flow. Thus, it is possible that the smallest droplet may circumvent the largest one and that the collision not occur. Following this mechanism, a typical expression for E_c can be found in Ref. 56.

The term E_v takes into account velocity correlations over a distance larger than the drop radii. It is clear that, due to the drag force exerted by the gas, a small droplet has almost the same velocity as the gas. Thus two small droplets located around the same point would necessarily have almost the same velocity. This yields

$$f^{(2)}(t, x, v, r, v', r') \approx 0 \quad \text{if} \quad v \neq v' \quad \text{and} \quad r, r' \leq r_{\text{crit}} \quad (8)$$

where r_{crit} is the radius of a droplet whose relaxation time is equal to a typical turbulence integral timescale τ_{turb} . On the other hand, it is quite reasonable to suppose that

$$f^{(2)}(t, x, v, r, v', r') \approx f^{(1)}(t, x, v, r) f^{(1)}(t, x, v', r') \quad \text{if} \quad r \gg r_{\text{crit}} \quad \text{or} \quad r' \gg r_{\text{crit}} \quad (9)$$

This reasoning leads to the following expression for E_v :

$$\begin{aligned} E_v(t, x, v, v', r, r') &= 0 & \text{if} & \quad r \leq r_{\text{crit}} \quad \text{and} \quad r' \leq r_{\text{crit}} \\ E_v(t, x, v, v', r, r') &= 1 & \text{if} & \quad r \geq r_{\text{crit}} \quad \text{or} \quad r' \geq r_{\text{crit}} \end{aligned} \quad (10)$$

with

$$r_{\text{crit}}(t, x) = \sqrt{(9\mu_g/2\rho_l)\tau_{\text{turb}}(t, x)} \quad (11)$$

Other possible expressions of the term E_v may be found in Refs. 49 and 57.

To test the influence of coalescence on the slag accumulation rate, this collision model has been introduced in the Eulerian-Lagrangian numerical code mentioned earlier. Several computations were carried out on the same solid rocket motor described earlier. One burnback geometry was chosen for the calculations. The pressure chamber is 45 MPa for this motor configuration. Figure 12 shows the motor chamber and the different droplet trajectories starting on the propellant surface. The particulate phase consisted of Al_2O_3 droplets injected with a classical bimodal size distribution^{2,5,16} (80% in mass for the smoke and 20% for the residues). A complete description of all of these calculations (including numerical algorithms, grid size, and boundary conditions) can be found in Ref. 58.

Two collision models have been tested: the first one (model 1) corresponds to the chaos assumption [$E = 1$ in Eq. (6)]. The second one (model 2), based on the correction factor E [Eqs. (6–11)], takes into account the effect of the surrounding gas on the collision rate. The slag rates obtained, for the second capture rule S_2 (see Fig. 1), are summarized as follows: for slag rate $m_{\text{slag}}/m_{\text{tot}}$, 3.4% for the model without collision, 29.2% for collision model 1, and 6.9% for collision model 2.

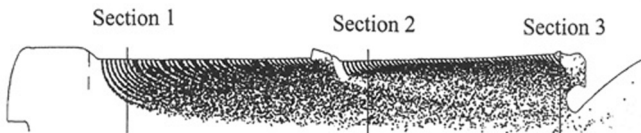


Fig. 12 Position of the sections.

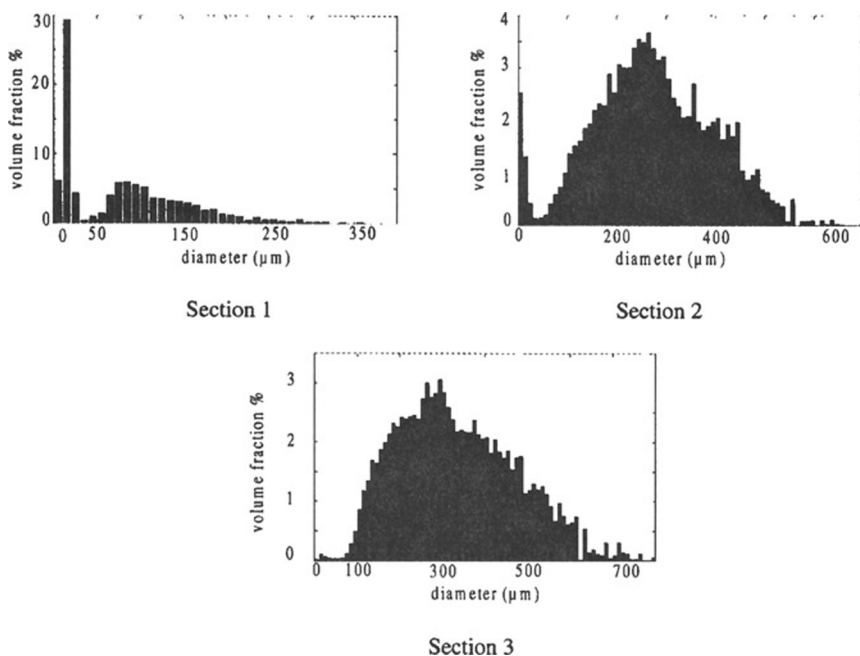


Fig. 13 Droplet size distributions in different sections (model 1) (see also p. xxviii).

These results clearly show the major influence of coalescence on slag calculation and confirm the importance of the correction factor E in the calculation of the collision probability.

Three sections, denoted 1, 2, and 3 in Fig. 12, were chosen to compare the evolution of droplet size distribution in the chamber as computed by model 1 and model 2. Figure 13 shows the results obtained with model 1 (see also the color reproduction on p. xxviii). In this case, almost all of the smallest droplets have coalesced with the larger residues. This explains why the slag rate is so high. Figure 14 shows the results obtained with model 2 (see also the color reproduction on p. xxviii). In this case, the influence of coalescence is significantly reduced. The collision efficiency between the smokes and the residues is much lower than with model 1.

Much work is still necessary to improve and validate this collision model, but these preliminary results indicate that coalescence certainly plays a fundamental role in the slag formation process.

C. Capture Rules, Droplet–Wall Interactions, and Liquid Film Formation

It has been shown that capture rules are one of the most important parameters for the slag calculation. For a better prediction of aluminum oxide slag buildup on the nozzle wall and the motor case walls in the aft end, droplet–wall interactions with and without the presence of a liquid film must be modeled. Because Al_2O_3 is liquid only above 2327 K, direct measurements of droplet–wall interactions and liquid film formation would require expensive motor firings for which no diagnostic techniques are available. If experiments could be conducted at room temperature,

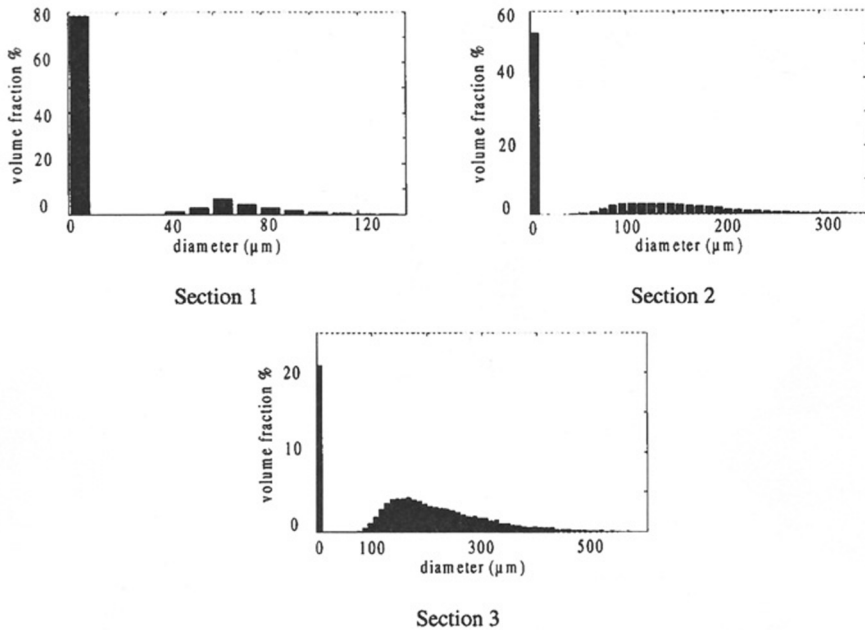


Fig. 14 Droplet size distributions in different sections (model 2) (see also p. xxviii).

measurement and visualization techniques would be available. Ethanol is liquid at room temperature and has been used in several research programs^{59,60} to elaborate models taking into account droplet interaction regimes and both the formation and the behavior of the liquid film. From these studies, several regimes can be identified as regards droplet-wall interactions. Depending on the value of the Ohnesorge number and of the Weber number, rebound, deposition, spattering, and splashing can be observed. The limits between the different zones are given by the parameter $K = \sqrt{[We\sqrt{(Re)}]}$, as shown in Fig. 15 for a dry wall. When a liquid film is present

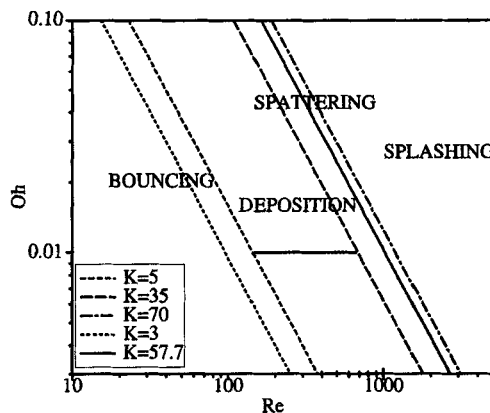


Fig. 15 Regimes of droplet wall interactions, $K = \sqrt{[We\sqrt{(Re)}]}$.

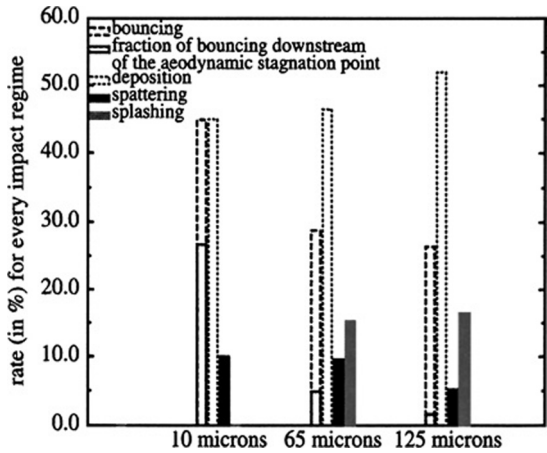


Fig. 16a Impingement rate vs droplet diameter for different regimes.

on the wall, the different regions are only translated. Correlations taking the film thickness into account can be found in Ref. 28.

An example, results for droplet impingement, is shown in Fig. 16a. These calculations were performed by using two-phase flowfields presented earlier on the aft end of a large solid rocket motor. Results present, for the four regimes of interaction, the influence of the droplet size on the impingement rate, as defined by the ratio between the number of impingements for one selected regime and the total number of impingements. The global impingement rate, defined as the ratio between the total droplet impingement and the total injected droplets, is plotted in Fig. 16b. It can be seen in Fig. 16 that most of the impacts concern the larger droplets.

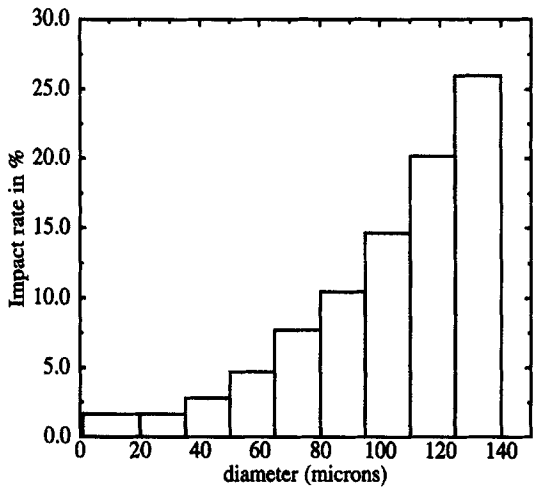


Fig. 16b Global impact rate.

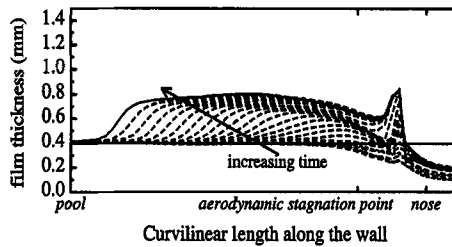


Fig. 17 Evolution of film thickness.

To evaluate the mass flow rate fraction of aluminum oxide supplying the pool in the aft end and the fraction flowing toward the nozzle, the stagnation point of the liquid film must be determined. The liquid film is considered as a laminar⁶¹ one-dimensional flow. The details of the modeling can be found in Ref. 28. Following this approach, computations of the film thickness along the motor case walls (see Fig. 1) were carried out for the case of a continuous injection of aluminum oxide droplets. Figure 17 shows the time evolution of the liquid film thickness. The thick black curve represents the final film thickness obtained after the convergence of the computation. As it can be seen in Fig. 18, the aerodynamic stagnation point is different from the film stagnation point. This fact can induce discrepancies in the slag evaluation if the positions of the two stagnation points are assumed to be similar.

D. Effect of Vortices

The aim of this investigation was to analyze how large coherent structures (due to the vortex shedding phenomenon) can capture droplets and modify slag retention in the aft dome of a large solid rocket motor (mentioned earlier). This numerical simulation used an Eulerian two-fluid model⁹ based on unsteady conservation equations for the gas phase and the dispersed phase. No combustion model was introduced in the model. Calculations were performed, in the entire motor, for three droplet diameters (35, 65, and 110 μm). For each droplet size, the mass flow rate of both phases, on the propellant surface, remained constant. Special care was taken in the refinement of the grid in the regions where the vortex shedding phenomenon occurs.⁶² Figure 19 shows the droplet volume fraction in the aft segment of the

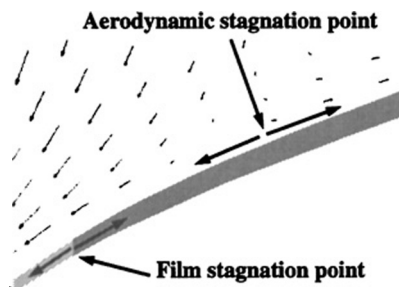


Fig. 18 Closeup of the film.

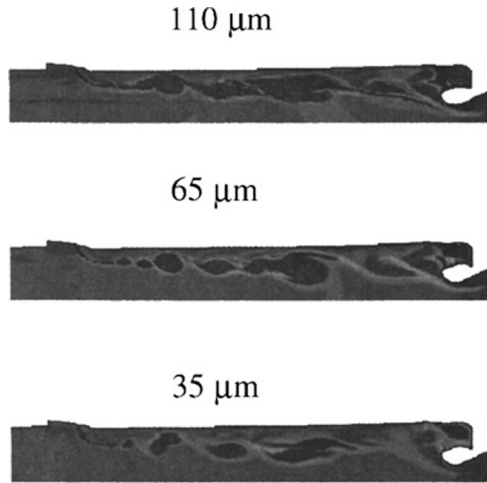


Fig. 19 Droplet volume fraction in the aft segment of the motor for three droplet sizes (courtesy of Société Nationale des Poudres et Explosifs; see also p. xxvii).

motor for the three droplet sizes (see also the color reproductions on p. xxvii). It can be seen that droplets are centrifugated by vortices. An overconcentration of droplets appeared surrounding the vortices. Results have shown that unsteady droplet mass flux enters and exits the aft end of the motor. With this two-fluid model, it was not possible to define a capture rule for calculating the slag rate. Evaluation of the slag rate vs time was carried out by integrating droplet mass flux between two grid lines (Fig. 20) in the vicinity of S1 and S2 (see Fig. 1). Because of the unsteady effect, an integration in time is necessary to obtain the final slag rate ($m_{\text{slag}}/m_{\text{tot}}$). Comparisons with results presented earlier were difficult because the definition of the capture rule was very different. Much work is still necessary to define accurately a base of comparison between unsteady calculations using

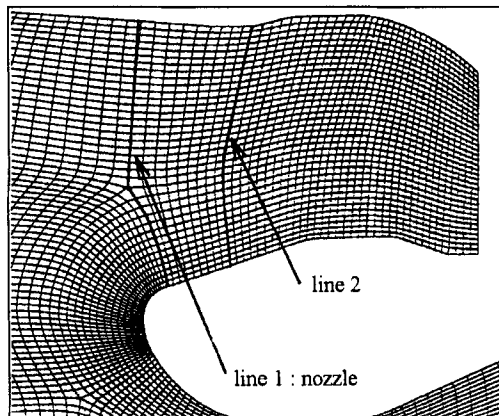


Fig. 20 Lines used in the computation of droplet flows (SNPE picture).

two-fluid model and Eulerian–Lagrangian approach based on steady solutions of the gas flowfield. These calculations, however, reveal the possible important effect of unsteady vortices on slag retention.

V. Conclusions

This chapter summarizes some important results and the current French models of two-phase flows in solid rocket motors. Further work is needed to understand various physical phenomena not clearly identified.

Among them, the mathematical modeling of the distributed combustion effect seems to be the most challenging task. It requires a fine description of the interaction between the combustion process and the acoustic field, whereas the quasi-steady process is still at the beginning stage of understanding. Numerical simulations at a scale of the droplet must be encouraged. In addition, the fragmentation process of aluminum droplets in combustion and the mechanisms responsible for the growth of the oxide lobe need to be explained because knowledge of the droplet size distribution inside the chamber is of primary importance for a correct estimation of slag deposition and for the achievement of reliable stability predictions. Effort is also required to evaluate the role of the turbulence and the large coherent structures on droplet dispersal. Further investigations are necessary to confirm the influence of droplet collisions. Basic experiments must be conducted to validate and to improve the collision efficiency in the motor. Some other points remain to be clarified, including the following: What is the composition of the agglomerates? Do they burn as isolated droplets? Why does the increase of particle loading not necessarily accentuate the attenuation of instabilities? What is the effect of flight acceleration on capture rules? Is the Al_2O_3 slag ejection a source of acoustic mode excitations?

Acknowledgments

The authors would like to emphasize that this synthesis of work on two-phase flows in solid rocket motors would not have been possible without the support of the Centre National d'Études Spatiales, R. Bec) in the framework of the Recherche et Technologies/Direction des Lanceurs research program Aerodynamics of Segmented Solid Motors. The authors would like to thank their colleagues at ONERA, Société Européenne de Propulsion, and Société Nationale des Poudres et Explosifs for their important contributions. These include the agglomeration and combustion testing of J. Duterque and G. Lengellé, the quench bomb testing of H. Ruiz, the helium quench motor and C1xb motor of M. Prévost, the computational fluid dynamics modeling of N. Cesco, K. Gailliègue, J. F. Guéry, F. Godfroy, J. Hylkema, and T. Pevergne. The authors also wish to acknowledge their colleagues in the ASSM program for their helpful discussions.

References

- ¹Duterque, J., "Experimental Studies of Aluminum Agglomeration in Solid Rocket Motors," Challenges in Propellants and Combustion 100 years after Nobel, Begell House, Inc., *4th International Symposium on Special Topics in Chemical Propulsion*, New York, 1996, pp. 693–706.

²Salita, M., "Quench Bomb Investigation of Al_2O_3 Formation from Solid Rocket Propellants (Part 2): Analysis of Data," *Proceedings of the 25th JANNAF Combustion Meeting*, SPIA 698, Vol. 1, 1988, Chemical Propulsion Information Agency, Laurel, MD, pp. 185–197.

³Traineau, J. C., Kuentzmann, P., Prévost, M., Tarrin, P., and Delfour, A., "Particle Size Distribution Measurements in a Subscale Motor for the Ariane 5 Solid Rocket Booster," AIAA Paper 92-3049, July 1992.

⁴Beckstead, M. W., "Evidences for Distributed Combustion," *Proceedings of the 24th JANNAF Combustion Meeting*, CPIA 476, Vol. 1, Chemical Propulsion Information Agency, Laurel, MD, 1987, pp. 1–12.

⁵Salita, M., "Deficiencies and Requirements in Modeling of Slag Generation in Solid Rocket Motors," *Journal of Propulsion and Power*, Vol. 11, No. 1, 1995, pp. 10–23.

⁶Vuillot, F., "Vortex Shedding Phenomena in Solid Rocket Motors," *Journal of Propulsion and Power*, Vol. 11, No. 4, 1995, pp. 626–639.

⁷Morfouace, V., and Tissier, P.-Y., "Two-Phase Flow Analysis of Instabilities Driven by Vortex Shedding in Solid Rocket Motors," AIAA Paper 95-2733, July 1995.

⁸Dupays, J., Prévost, M., Tarrin, P., and Vuillot, F., "Effects of Particulate Phase on Vortex Shedding Driven Oscillations in Solid Rocket Motors," AIAA Paper 96-3248, July 1996.

⁹Godfroy, F., and Guéry, J. F., "Unsteady Eulerian Flow Analysis of Solid Rocket Motor Slag," AIAA Paper 97-2859, July 1997.

¹⁰Price, E. W., "Combustion of Metalized Propellants," *Fundamentals of Solid-Propellant Combustion*, edited by K. K. Kuo and M. Summerfield, Vol. 90, Progress in Astronautics and Aeronautics, AIAA, New York, 1984, pp. 479–513.

¹¹Beckstead, M. W., "A Model for Solid Propellant Combustion," *Proceedings of the 14th JANNAF Combustion Meeting*, CPIA 292, Vol. 1, Chemical Propulsion Information Agency, Laurel, MD, 1977, pp. 281–306.

¹²Cohen, N. S., and Strand, L. D., "A Model for the Burning Rate of Composite Propellants," *Proceedings of the 17th JANNAF Combustion Meeting*, CPIA 329, Vol. 1, Chemical Propulsion Information Agency, Laurel, MD, 1980, pp. 53–97.

¹³Prentice, J. L., "Combustion of Aluminum Droplets in Various Oxidizing Gases Including CO_2 and Water Vapor," *Proceedings of 10th JANNAF Combustion Meeting*, CPIA 243, Vol. 3, Chemical Propulsion Information Agency, Laurel, MD, 1973, pp. 279–296.

¹⁴Brossard, C., Ulas, A., Yeh, C. L., and Kuo, K. K., "Ignition and Combustion of Isolated Aluminum Particles in the Post-Flame Region of a Flat-Flame Burner," *16th International Colloquium on the Dynamics of Explosions and Reactive Systems*, Wydawnictwo, Akapit, Cracow, Poland, 1997, pp. 307–310.

¹⁵Bucher, P., Yetter, R. A., Dryer, F. L., Vicenzi, E. P., Parr, T. P., and Hanson-Parr, D. M., "Condensed-Phase Species Distribution About Al Particles Reacting in Various Oxidizers," *Combustion and Flame*, Vol. 117, No. 1–2, 1999, pp. 351–361.

¹⁶Ruiz, H., and Kratz, J. G., "Granulométrie de la phase condensée, programme ASSM5," Internal Report TR SNPE 4842/96/SNPE/DFP/CER, 1996.

¹⁷Stone, W. C., "Workshop Report: Acoustic Instability in a High Burning Rate-High Pressure Regime," *Proceedings of the 21st JANNAF Combustion Meeting*, CPIA 412, Vol. 2, Chemical Propulsion Information Agency, Laurel, MD, 1984, pp. 113–118.

¹⁸Brooks, K. P., and Beckstead, M. W., "Dynamics of Aluminum Combustion," *Journal of Propulsion and Power*, Vol. 11, No. 4, 1995, pp. 769–780.

¹⁹Micci, M. M., "Linear Acoustic Analysis of Solid Propellant Pressure-Coupled Distributed Combustion," *Journal of Propulsion and Power*, Vol. 12, No. 6, 1996, pp. 1179–1181.

²⁰Dupays, J., and Vuillot, F., "Propagation of an Acoustic Wave in a Two-Phase Reactive Medium," AIAA Paper 98-3696, July 1998.

²¹Bucher, P., Yetter, R. A., Dryer, F. L., Parr, T. P., Hanson-Parr, D. M., and Vicenzi, E. P., "Flame Structure Measurement of Single, Isolated Aluminum Particles Burning in Air," *26th Symposium (International) on Combustion*, Combustion Inst., Pittsburgh, PA, 1996, pp. 1899-1908.

²²Brzustowski, T. A., and Glassman, I., "Vapor-Phase Diffusion Flames in the Combustion of Magnesium and Aluminum: I. Analytical Developments," *Heterogeneous Combustion*, edited by H. G. Wolfhard, I. Glassman, and L. Green, Jr., Vol. 15, Progress in Astronautics and Aeronautics, AIAA, New York, 1964, pp. 75-115.

²³Law, C. K., "A Simplified Theoretical Model for the Vapor-Phase Combustion of Metal Particles," *Combustion Science and Technology*, Vol. 7, No. 3-6, 1973, pp. 197-212.

²⁴Greymachkin, V. M., Istratov, A. G., and Leipunskii, O. I., "Model for the Combustion of Metal Droplets," *Combustion, Explosion and Shock Waves*, Vol. 11, No. 3, 1975, pp. 313-318.

²⁵King, M. K., "Modeling of Single Particle Aluminum Combustion in CO_2 - N_2 Atmospheres," *17th Symposium (International) on Combustion*, Combustion Inst., Pittsburgh, PA, 1977, pp. 1317-1328.

²⁶Bucher, P., Yetter, R. A., Dryer, F. L., Parr, T. P., and Hanson-Parr, D. M., "PLIF Species and Ratiometric Temperature Measurements of Aluminum Particle Combustion in O_2 , CO_2 and NO_2 Oxidizers, and Comparison with Model Calculations," *27th Symposium (International) on Combustion*, Combustion Inst., Pittsburgh, PA, 1998, pp. 2421-2429.

²⁷Marion, M., Chauveau, C., and Gökalp, I., "Studies on the Ignition and Burning of Levitated Aluminum Particles," *Combustion Science and Technology*, Vol. 115, No. 4-6, 1996, pp. 369-390.

²⁸Cesco, N., "Etude et modélisation de l'écoulement diphasique à l'intérieur des propulseurs à poudre," Ph.D. Dissertation, Ecole Nationale Supérieure de l'Aéronautique et de l'Espace, Toulouse, France, Nov. 1997.

²⁹Daniel, E., Basset, T., and Loraud, J. C., "Eulerian Approach for Unsteady Two-Phase Reactive Solid Rocket Motor Flows Loaded with Aluminum Particles," AIAA Paper 98-3697, July 1998.

³⁰Hermesen, R. W., "Aluminum Combustion Efficiency in Solid Rocket Motors," AIAA Paper 81-38, Jan. 1981.

³¹Duterque, J., "Cahier des charges du montage d'étude de la combustion de l'aluminium en ambiance propergol," Internal Rept., RT 1/6274/DMAE/Y/DEFA, ONERA, Châtillon, France, 1998.

³²Widener, J. F., and Beckstead, M. W., "Aluminum Combustion Modeling in Solid Propellant Combustion Products," AIAA Paper 98-3824, July 1998.

³³Sabnis, J., De Jong, F., and Gibeling, H., "A Two-Phase Restricted Equilibrium Model for Combustion of Metalized Solid Propellants," AIAA Paper 92-3509, July 1992.

³⁴Liaw, P., Chen, Y.-S., Shang, H.-M., and Doran, D., "Particulate Multi-Phase Flowfield Calculation with Combustion/Breakup Models for Solid Rocket Motor," AIAA Paper 94-2780, June 1994.

³⁵Dupays, J., "Contribution à l'étude du rôle de la phase condensée dans la stabilité d'un propulseur à propergol solide pour lanceur spatial," Ph.D. Dissertation, Inst. National Polytechnique de Toulouse, Toulouse, France, Nov. 1996.

³⁶Culick, F. E. C., and Yang, V., "Prediction of the Stability of Unsteady Motions in Solid Propellant Rocket Motors," *Nonsteady Burning and Combustion Instability of Solid Propellants*, Vol. 143, Progress in Astronautics and Aeronautics, edited by L. De Luca, E. W. Price, and M. Summerfield, AIAA, Washington, DC, 1992, pp. 719-779.

³⁷Temkin, S., and Dobbins, R. A., "Attenuation and Dispersion of Sound by Particulate-Relaxation Processes," *Journal of the Acoustical Society of America*, Vol. 40, No. 2, 1966, pp. 317-324.

³⁸Marble, F. E., "Some Gasdynamic Problems in the Flow of Condensing Vapors," *Acta Astronautica*, Vol. 14, No. 6, 1969, pp. 585-613.

³⁹Cesco, N., Estivalezes, J. L., and Lavergne, G., "Simulation de l'écoulement diphasique dans le LP2 en combustion distribuée," *Proceedings du 3ème colloque R&T sur les écoulements internes en propulsion solide*, Vol. 2, ONERA, Châtillon, France, 1998, pp. 47-57.

⁴⁰Gordon, S., and Mc Bride, B. J., "Computer Program for Calculation of Complex Chemical Equilibrium Composition Rocket Performance," *Incident and Reflected Shocks and Chapman-Jouguet Detonation*, SP-273, NASA, 1971.

⁴¹Frederick, R. A., Nichols, J. A., and Rogerson, J. A., "Slag Accumulation Measurements in Strategic Rocket Motor," AIAA Paper 96-2783, July 1996.

⁴²Boraas, S., "Modeling Slag Deposition in the Space Shuttle Solid Rocket Motor," *Journal of Spacecraft and Rockets*, Vol. 21, No. 1, 1984, pp. 47-54.

⁴³Haloulakos, V. E., "Slag Mass Accumulation in Spinning Solid Rocket Motors," *Journal of Propulsion and Power*, Vol. 7, No. 1, 1991, pp. 14-21.

⁴⁴Johnston, W. A., Murdock, J. W., Koshigoe, S., and Than, P. T., "Slag Accumulation in the Titan Solid Rocket Motor Upgrade," *Journal of Propulsion and Power*, Vol. 11, No. 5, 1995, pp. 1012-1020.

⁴⁵Chauvot, J. F., Dumas, L., and Schmeisser, K., "Modeling of Slag Deposition in Solid Rocket Motors," AIAA Paper 95-2729, July 1995.

⁴⁶Cesco, N., Dumas, L., Hulin, A., Pevergne, T., and Fabignon, Y., "Stochastic Models to the Investigation of Slag Accumulation in a Large Solid Rocket Motor," AIAA Paper 97-3118, July 1997.

⁴⁷O'Rourke, P. J., "Collective Drop Effects on Vaporizing Liquid Sprays," Ph.D. Dissertation, Princeton Univ., Princeton, NJ, 1981.

⁴⁸Kuentzmann, P., *Aérothermochimie des suspensions*, Mémoires de Sciences Physiques, Gauthier-Villars, Paris, 1973.

⁴⁹Simonin, O., "Continuum Modelling of Dispersed Two-Phase Flows," *Lecture Series 1996-02*, Von Kármán Inst. for Fluid Dynamics, Feb. 1996.

⁵⁰Hylkema, J., and Villedieu, P., "Une méthode particulière aléatoire reposant sur une équation cinétique pour la simulation numérique des sprays denses de gouttelettes liquides," *Note aux Comptes rendus de l'Académie des Sciences de Paris*, Vol. 325, No. 1, 1997, pp. 323-328.

⁵¹Hylkema, J., and Villedieu, P., "Modélisation cinétique et simulation numérique des collisions entre gouttelettes d'alumine dans un propulseur à poudre," *Proceedings du 3ème colloque R&T sur les écoulements internes en propulsion solide*, Vol. 2, ONERA, Châtillon, France, 1998, pp. 119-139.

⁵²Salita, M., "Use of Water and Mercury Droplets to Simulate Al_2O_3 Collision/Coalescence in Rocket Motors," *Journal of Propulsion and Power*, Vol. 7, No. 4, 1991, pp. 505-512.

⁵³Brazier-Smith, P. R., Jennings, S. G., and Latham, J., "The Interaction of Falling Water Drops: Coalescence," *Proceedings of the Royal Society of London, Series A: Mathematical and Physical Sciences*, Vol. 326, 1972, pp. 393-408.

⁵⁴Jiang, Y. J., Umemura, A., and Law, C. K., "An Experimental Investigation on the Collision Behavior of Hydrocarbon Droplets," *Journal of Fluid Mechanics*, Vol. 234, 1992, pp. 171-190.

⁵⁵Estrade, J. P., "Etude expérimentale et modélisation de la collision de gouttelettes," Ph.D. Dissertation, Ecole Nationale Supérieure de l'Aéronautique et de l'Espace, Toulouse, France, Dec. 1998.

⁵⁶Langmuir, I., "The Production of Rain by Chain Reaction in Cumulous Clouds at Temperatures About Freezing," *Journal of Meteorology*, Vol. 5, No. 5, 1948, pp. 175–192.

⁵⁷Pigeonneau, F., "Modélisation et calcul numérique des collisions de gouttes en écoulements laminaires et turbulents," Ph.D. Dissertation, Université de Paris 6, Paris, France, Oct. 1998.

⁵⁸Hylkema, J., "Modélisation cinétique et simulation numérique d'un brouillard dense de gouttelettes—Application aux propulseurs à poudre," Ph.D. Dissertation, Ecole Nationale Supérieure de l'Aéronautique et de l'Espace, Toulouse, France, Jan. 1999.

⁵⁹Hoerter, J., "Development of a Fundamental Experiment to Study the Impact of Monodisperse Droplets on Thin Liquid Films," Diplomarbeit, Univ. of Stuttgart, Stuttgart, Germany, July 1996.

⁶⁰Platet, B., and Lavergne, G., "Caractérisation des phénomènes d'interaction goutte-paroi," *Proceedings du 3ème colloque R&T sur les écoulements internes en propulsion solide*, Vol. 2, ONERA, Châtillon, France, 1998, pp. 231–242.

⁶¹Wittig, S., Himmelsbach, J., Noll, B., Feld, H. J., and Samenfink, W., "Motion and Evaporation of Shear-Driven Films in Turbulent Gases," American Society of Mechanical Engineers, Paper 91-GT-207, June 1991.

⁶²Traineau, J. C., Prévost, M., Vuillot, F., Le Breton, P., Cuny, J., Preioni, N., and Bec, R., "A Subscale Test Program to Assess the Vortex Shedding Driven Instabilities in Segmented Solid Rocket Motors," AIAA Paper 97-3247, July 1997.

Combustion Dynamics of Homogenous Solid Propellants in a Rocket Motor with Acoustic Excitations

Tae-Seong Roh,* Sourabh Apte,[†] and Vigor Yang[‡]
Pennsylvania State University, University Park, Pennsylvania

Nomenclature

A	= preexponential factor
$C_{p,i}$	= specific heat of gas phase species i at constant pressure
C_c	= specific heat of propellant
\mathbf{E}, \mathbf{F}	= convective flux vectors in axial and vertical directions, respectively
$\mathbf{E}_v, \mathbf{F}_v$	= viscous flux vectors in axial and vertical directions, respectively
E_a	= activation energy
e	= specific total internal energy
H	= chamber half-height
h	= specific enthalpy of mixture
h_i	= specific enthalpy of species i
$h_{f,i}^0$	= heat of formation of species i
$\ell_\mu, \ell_\varepsilon$	= turbulent length scales
k	= turbulent kinetic energy
N	= number of species in gas phase reactions
p	= pressure
\mathbf{Q}	= dependent variable vector
Q_s	= specific heat release in condensed phase
r_b	= propellant burning rate
R_u	= universal gas constant
Re	= Reynolds number
Re_t	= turbulent Reynolds number
\mathbf{S}	= source vector

Copyright © 2000 by the authors. Published by the American Institute of Aeronautics and Astronautics, Inc., with permission.

*Currently, Postdoctoral Fellow, Jet Propulsion Center, California Institute of Technology.

[†]Graduate Research Assistant, Dept. of Mechanical Engineering.

[‡]Professor, Dept. of Mechanical Engineering. Associate Fellow AIAA.

t	= physical time
T	= temperature
T_s	= temperature at propellant surface
T_i	= initial temperature in condensed phase
u, v	= bulk velocities in axial and vertical directions, respectively
\hat{u}_i, \hat{v}_i	= diffusion velocities in axial and vertical directions, respectively
\mathbf{v}	= velocity vector
W_i	= molecular weight of species i
x, y	= Cartesian coordinates
X_i	= mole fractions of species i
Y_i	= mass fractions of species i
y_n	= distance from propellant surface
y^+	= nondimensional distance from the wall
\hat{y}	= distance from propellant surface in condensed phase
β	= normalized activation energy
γ	= specific heat ratio
ε	= dissipation rate of turbulent kinetic energy
κ	= von Kármán constant
λ	= molecular thermal conductivity
μ	= molecular viscosity
μ_t	= turbulent viscosity
ν	= dynamic viscosity
ρ	= density
τ	= viscous stress tensor
$\dot{\omega}_i$	= rate of production of species i

Subscripts

a	= acoustic mode
c	= condensed phase
g	= gas phase
i	= i th species or initial condition
p	= propellant
s	= burning surface
v	= vortical mode
w	= wall
σ	= entropy mode

Superscripts

$-$	= time-averaged quantity
$'$	= fluctuating quantity

I. Introduction

THIS study is a sequel to our earlier publications on the transient combustion response of a double-base homogeneous propellant to acoustic oscillations in a solid rocket motor.^{1,2} The previous work focused on the gas-phase flame dynamics¹ and the coupling with the condensed-phase processes in a laminar flowfield.² Much information was obtained about the detailed flame structures and heat-release mechanisms at scales sufficient to resolve the oscillatory motions near the propellant surface. Results indicated that, under laminar-flow conditions,

the motor stability characteristics were governed mainly by the dynamic behavior of the final luminous flame zone. The large thermal inertia in the condensed phase effectively restrains the temperature fluctuations in the near-surface region, and consequently the primary flame dynamics remains unaffected, even with the condensed-phase coupling. The situation in turbulent flowfields, often observed in practical rocket motor environments, is, however, considerably different because of the turbulence-enhanced transport in the flame zone. The present study addresses the effect of turbulence on propellant combustion response in a rocket motor with forced acoustic excitations. The unsteady heat release, arising from the combined influence of turbulent and acoustic motions, as well as its interactions with the condensed-phase processes, is treated in depth.

It is well established that a propellant burning in an acoustic environment can be characterized by its response to the pressure and velocity fluctuations above the propellant surface, phenomena commonly referred to as pressure- and velocity-coupled combustion response, respectively.³ While the former has been extensively studied and the origins of the physical behavior are reasonably well understood, the general problem of velocity coupling remains largely unresolved. This coupling is essentially a local phenomenon, depending on the near-field flow structure, chemical reactions, and imposed acoustic oscillations. Turbulence may drastically alter the gas-phase flame dynamics through its influence on flow motion and, consequently, modify the propellant burning rate. The resultant fluctuations in the mass, momentum, and energy additions to the motor internal flow may trigger unstable modes of acoustic oscillation in the chamber. If the process occurs at proper spatial and temporal phases with respect to the acoustic waves, a feedback loop can be established, and high-amplitude flow oscillations are sustained, leading to combustion instabilities.

To model such a complex phenomenon of unsteady propellant combustion in turbulent flows requires a comprehensive analysis based on complete conservation equations and finite-rate chemical kinetics in both the gas and the condensed phases. In subsequent sections, a theoretical formulation of solid propellant combustion in a rocket motor is developed, followed by a brief description of the numerical technique employed in the present study. The analysis first establishes the steady-state flowfield in the motor. Interactions between acoustic oscillations and propellant burning are investigated by imposing periodic pressure oscillations at the combustor exit, simulating standing acoustic wave motions in the chamber. Various mechanisms driving unsteady heat release and flow motions, as well as their effect on the global stability behavior of the motor, are analyzed in depth.

II. Theoretical Formulation

A. Gas-Phase Process

Figure 1 shows the physical model examined herein, a two-dimensional solid rocket motor loaded with a double-base homogeneous propellant grain. The major ingredients of the propellant are 52% NC, 43% NG, and 5% additives. The formulation follows the model established in Refs. 1 and 2 and is summarized below. In vector form, the governing equations for the multicomponent chemically reacting system of N species can be expressed as

$$\frac{\partial Q}{\partial t} + \frac{\partial}{\partial x}(E - E_v) + \frac{\partial}{\partial y}(F - F_v) = S \quad (1)$$

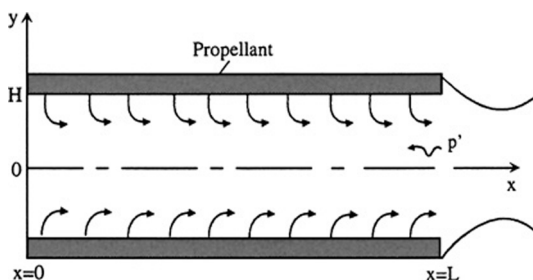


Fig. 1 Schematic diagram of a solid rocket motor.

where x and y represent the axial and vertical coordinates, respectively. The conserved variable vector \mathbf{Q} , convective flux vectors \mathbf{E} and \mathbf{F} , and diffusion-flux vectors \mathbf{E}_v and \mathbf{F}_v are defined as follows:

$$\mathbf{Q} = [\rho, \rho u, \rho v, \rho e, \rho Y_i]^T \quad (2)$$

$$\mathbf{E} = [\rho u, \rho u^2 + p, \rho uv, (\rho e + p)u, \rho u Y_i]^T \quad (3)$$

$$\mathbf{F} = [\rho v, \rho uv, \rho v^2 + p, (\rho e + p)v, \rho v Y_i]^T \quad (4)$$

$$\mathbf{E}_v = [0, \tau_{xx}, \tau_{xy}, u\tau_{xx} + v\tau_{xy} - q_{e_x}, -q_{i_x}]^T \quad (5)$$

$$\mathbf{F}_v = [0, \tau_{yx}, \tau_{yy}, u\tau_{xy} + v\tau_{yy} - q_{e_y}, -q_{i_y}]^T \quad (6)$$

$$\mathbf{S} = [0, 0, 0, 0, \omega_i]^T \quad (7)$$

where the subscript i stands for species i , ranging from 1 to $N - 1$. In these equations, ρ , u , v , Y_i , and τ represent the density, axial and vertical velocity components, mass fraction of species i , and viscous stress, respectively. The thermal diffusion terms q_{e_x} and q_{e_y} consist of contributions from heat conduction and mass diffusion processes. Fick's law is used to approximate the species diffusion terms q_{i_x} and q_{i_y} . For a multicomponent mixture, the pressure and temperature can be calculated iteratively from the following thermodynamic relation and equation of state:

$$e = \sum_{i=1}^N Y_i h_i - \frac{p}{\rho} + \frac{1}{2}(u^2 + v^2) \quad (8)$$

$$p = \rho R_u T \sum_{i=1}^N \frac{Y_i}{W_i} \quad (9)$$

where h_i and W_i are the specific enthalpy and molecular weight of species i , respectively.

Within the pressure and temperature ranges of practical rocket-motor environments, the thermal conductivity and viscosity are basically functions of the temperature alone. They can be well approximated by fourth-order polynomials supplied by McBride and Gordon,⁴ which are valid for temperatures ranging from 300 to

6000 K. Thermal conductivity and viscosity are calculated using Wilke's mixing rule.⁵

B. Chemical Kinetics Model

The chemical kinetics scheme used herein follows the reduced-reaction mechanism established in Ref. 1. In brief, the condensed phase involves two global processes: molecular degradation of the propellant and the ensuing reactions of the decomposed gases, which provide elementary species such as NO_2 , NO , and aldehydes to maintain the gas-phase flames. The gas phase is characterized by five rate-limiting reactions. The NO_2 and aldehyde reactions forming NO , CO , CO_2 , and H_2O occur in the primary flame zone due to their relatively low activation energies. The highly exothermic reduction of NO to N_2 proceeds in the secondary flame zone and provides the major heat source for raising the flame temperature to its final value. The reaction of carbon and NO plays a key role in determining the behavior of the dark zone, giving rise to a two-stage flame structure.

C. Condensed-Phase Process

The condensed phase consists of a preheated zone and a superficial thermal degradation layer, in which thermal decomposition of the propellant and reaction of decomposed species take place simultaneously. If we ignore the bulk motion, mass diffusion, and axial thermal diffusion, and assume constant thermophysical properties, the formulation governing the condensed-phase processes reduces to the following set of one-dimensional equations^{1,2}:

$$\dot{m} = \rho_c r_b \quad (10)$$

$$\rho_c C_c \frac{\partial T}{\partial t} + \dot{m} C_c \frac{\partial T}{\partial y} = \lambda_c \frac{\partial^2 T}{\partial y^2} + \dot{q}_c \quad (11)$$

$$\rho_c \frac{\partial Y_i}{\partial t} + \dot{m} \frac{\partial Y_i}{\partial y} = \dot{\omega}_i \quad (12)$$

where ρ_c denotes the propellant density and r_b the burning rate. The rate of heat release per unit volume \dot{q}_c is determined by the net effect of the endothermic decomposition and exothermic reaction in the condensed phase. The in-depth boundary conditions associated with Eqs. (11) and (12) are $T = T_i$ and $Y_p = 1$, respectively, where T_i is the initial (conditioned) temperature of the propellant. The surface conditions require that the propellant decomposition be completed (i.e., $Y_p = 0$) and $T = T_s$.

D. Interfacial Conditions

The propellant regression rate and the surface conditions of temperature and species concentrations are determined by applying the conservation laws to the gas-solid interface.¹

Mass balance for mixture:

$$(\rho v)_g = -\rho_c r_b \quad (13)$$

Mass balance for species i :

$$[\rho(v + \hat{v}_i)Y_i]_g = -\rho_c r_b Y_{i,s} \quad (14)$$

Energy balance:

$$\begin{aligned} -\lambda_g \left(\frac{\partial T}{\partial Y} \right)_g + \left[\rho \sum_{i=1}^N Y_i h_i (v + \hat{v}_i) \right]_g \\ = -\lambda_c \left(\frac{\partial T}{\partial y} \right)_s - \rho_c r_b \left[C_c (T_s - T_{ref}) + \sum_{i=1}^N Y_i h_{f,i}^0 \right]_s \end{aligned} \quad (15)$$

Subscripts g and s represent conditions at the interface on the gas and solid sides, respectively. Since molecular degradation takes place in an exceedingly thin layer, of the order of a few microns, the corresponding residence time is much shorter than that in the preheated zone, by at least an order of magnitude.⁶ A quasi-steady-state approximation is therefore employed in determining the subsurface pyrolysis behavior. The net heat flux to the preheated zone can be obtained by integrating the energy equation for the superficial degradation layer.^{7,8}

$$\lambda_c \left(\frac{\partial T}{\partial y} \right)_c = \lambda_g \left(\frac{\partial T}{\partial y} \right)_g + \dot{m} [\bar{Q}_s + (C_c - C_p)(T_s - \bar{T}_s)] \quad (16)$$

where \bar{Q}_s and \bar{T}_s are the net subsurface heat release and surface temperature at the steady-state condition, respectively. A matched asymptotic expansion technique similar to that derived in Refs. 9 and 10 is established to relate the propellant burning rate to the local heat fluxes across the superficial degradation layer:

$$r_b^2 = \frac{\alpha_c A_c \exp(-\beta)/\beta}{\{(\lambda_g/\dot{m})(\partial T/\partial y)_g + \frac{1}{2}[\bar{Q}_s + (C_c - C_p)(T_s - \bar{T}_s)]\}/(C_c T_s)} \quad (17)$$

where $\beta \equiv E_{a,c}/R_u T_s$ is the normalized activation energy. Equations (13), (14), (16), and (17) are sufficient to solve for the propellant burning rate and the set of unknowns (v , T , Y_i) at the propellant surface.

E. Turbulence Closure

A well-calibrated two-layer model^{11,12} is used to achieve turbulence closure because its performance is superior to that of conventional low-Reynolds number k - ϵ schemes in terms of numerical accuracy and convergence rate. This model employs the standard k - ϵ two-equation approach for the bulk of the flow away from the wall (i.e., the outer layer) and uses the following equations for turbulent kinetic energy and dissipation rate:

$$\frac{D\rho k}{Dt} = \nabla \cdot \left[\left(\mu + \frac{\mu_t}{\sigma_k} \right) \nabla k \right] + \mu_t G - \rho \epsilon \quad (18)$$

$$\frac{D\rho \epsilon}{Dt} = \nabla \cdot \left[\left(\mu + \frac{\mu_t}{\sigma_\epsilon} \right) \nabla \epsilon \right] + C_{\epsilon 1} \frac{\epsilon}{k} \mu_t G - C_{\epsilon 2} \frac{\epsilon}{k} \rho \epsilon \quad (19)$$

where

$$G = 2 \left[\left(\frac{\partial u}{\partial x} \right)^2 + \left(\frac{\partial v}{\partial y} \right)^2 \right] + \left(\frac{\partial u}{\partial y} + \frac{\partial v}{\partial x} \right)^2 \quad (20)$$

The eddy viscosity can be obtained from the Prandtl–Kolmogorov relation.

$$\mu_t = C_\mu \left(\frac{\rho k^2}{\varepsilon} \right) \quad (21)$$

The empirical constants in the preceding equations have standard values, with $\sigma_k = 1.0$, $\sigma_\varepsilon = 1.3$, $C_{\varepsilon 1} = 1.44$, $C_{\varepsilon 2} = 1.92$, and $C_\mu = 0.09$.

Unlike the low-Reynolds number treatment, which solves two turbulent transport equations all the way to the surface, the two-layer approach solves only the turbulent kinetic energy equation in the near-surface region (i.e., the inner layer) and greatly reduces the complexities associated with the stiff distributions of turbulent transport properties. The dissipation rate of the turbulent kinetic energy is determined by

$$\varepsilon = \frac{k^{\frac{3}{2}}}{\ell_\varepsilon} \quad (22)$$

and the eddy viscosity from

$$\mu_t = C_\mu \rho \sqrt{k} \ell_\mu \quad (23)$$

The near-wall damping effect is modeled through specification of the length scales ℓ_μ and ℓ_ε :

$$\ell_\mu = C_\ell y_n \left[1 - \exp \left(-\frac{Re_y}{A_\mu} \frac{25}{A^+} \right) \right] \quad (24)$$

$$\ell_\varepsilon = C_\ell y_n \left[1 - \exp \left(-\frac{Re_y}{A_\varepsilon} \right) \right] \quad (25)$$

where $Re_y = \sqrt{k} y_n / \nu$ represents the turbulent Reynolds number, with y_n standing for the distance from the propellant surface. The coefficient C_ℓ is given by

$$C_\ell = \kappa C_\mu^{-\frac{3}{4}} \quad (26)$$

where κ is the von Kármán constant. In most cases, A^+ is given a value of 25, but it can be modified to include the effect of pressure gradient and surface transpiration. In the present study, an empirical correlation of A^+ is used^{12,13}:

$$A^+ = \frac{25}{5.15 \{ v_w^+ + [5.86 P^+ / (1 + 5 v_w^+)] \} + 1.0} \quad (27)$$

where

$$v_w^+ = \frac{v_w}{u_\tau} \quad (28)$$

$$P^+ = -K^{\frac{1}{2}} \left(\frac{C_f}{2} \right)^{\frac{2}{3}} \quad (29)$$

$$K = \frac{v}{U_\infty^2} \left(\frac{dU_\infty}{dx} \right) \quad (30)$$

The reference velocity U_∞ is chosen to be the bulk velocity for motor internal flows. Other constants applied here are $A_\mu = 70.0$ and $A_\varepsilon = 2C_\ell$.

The inner and outer layers are matched at locations where viscous effects are negligible, according to the following criteria.¹² First, the minimum y^+ for these matching points must be greater than 120. Second, the local turbulent Reynolds number Re_y must be larger than 200 in strong turbulent regions. The exponential terms in Eqs. (24) and (25) for the length-scale relations have values close to zero at the matching point.

F. Turbulence/Chemistry Interaction

The reaction rates $\dot{\omega}_i$ in the species-concentration equations need to be modeled to capture the effect of turbulence on chemistry. Peters¹⁴ examined the problem of turbulence/chemistry interactions for premixed flames in terms of three nondimensional parameters, viz., turbulent Reynolds number Re_t , turbulent Damkohler number Da , and turbulent Karlovitz number Ka , as defined in Ref. 12. If chemical reactions proceed at rates lower than those of turbulent mixing ($Da < 1$), and the flame stretch is strong enough to cause penetration of small eddies into the flame zone ($Ka > 1$), then the flame structure can be locally modeled as a well-stirred reactor. Tseng and Yang¹² indicated that, for the combustion of homogeneous double-base propellants, the condition of $Da < 1$ and $Ka > 1$ is always satisfied throughout the flame region. Under this situation, turbulence rapidly penetrates into the flame zone through enhanced mass transfer, leaving chemical reactions as the rate-controlling processes. No direct interactions between turbulence and combustion occur in this regime. Accordingly, the reaction rates are computed based on the relations for laminar flows as described in Ref. 1. The preceding observation offers a satisfactory explanation about the accuracy of the present analysis in predicting the burning rate, although no direct coupling between the turbulence and combustion was included in the reaction rate formulae.

G. Boundary Conditions

Boundary conditions are treated carefully based on the method of characteristics to avoid spurious, nonphysical acoustic reflections. A complete description of the exit boundary conditions is given in Ref. 1. Because the outflow is subsonic, only one physical condition needs to be specified. The remaining conditions are obtained by appropriately manipulating the governing and characteristics equations, as suggested by Watson and Myers.¹⁵ At the upstream boundary, the axial

velocity and gradients of pressure and vertical velocity are set to zero along the solid wall. The last condition is required to prevent the occurrence of a numerically produced recirculating flow at the head end. Finally, flow symmetry is assumed at the centerline.

III. Numerical Method

The theoretical formulation summarized in the preceding section presents a stringent challenge for computational efficiency, due to slow convergence and large round-off errors at low Mach numbers, numerical stiffness associated with chemical reactions, and complex coupling of physiochemical processes between gas and condensed phases. A brief summary of various computational problems encountered in the analysis of rocket-motor internal flow is given in Ref. 12. An implicit dual time-stepping integration method was developed and has proven to be quite efficient and robust for reacting flows at all speeds.^{12,16} The algorithm first employs pressure decomposition and preconditioning techniques to circumvent difficulties for low-speed compressible flows, a basic requirement for treating acoustic oscillations in a rocket motor. A fully coupled implicit formulation is then used to enhance numerical stability and efficiency. The scheme has the advantage of achieving a high degree of temporal accuracy with only a modest increase in computational cost. Moreover, since the governing equations are solved implicitly, the numerical method is very stable and allows the selection of the integration time step to be dictated by the physical processes rather than the numerical stability.

IV. Results and Discussion

The combustion chamber considered herein is closed at the upstream end and measures 5.08 cm in height and 1.2 m in length, as shown in Fig. 1. Only the upper half of the volume is treated, due to symmetry of flow properties around the centerline. The propellant is preconditioned at an initial temperature of 300 K. The chamber pressure at the head end is 60 atm. The computational grid for the gas phase consists of 90×90 points in the axial and vertical directions, respectively, while the condensed phase is composed of 90×50 points in respective directions. The grids are clustered near the burning surface to resolve the viscous sublayer and the steep gradients of temperature and species concentrations there. The computational grid for condensed phase extends up to $100 \mu\text{m}$ into the propellant. The smallest grid spacing in the direction normal to the surface are 0.7 and $0.1 \mu\text{m}$ in the gas and condensed phases, respectively.

A. Steady-State Flowfield

A steady-state flowfield is first obtained to provide an initial solution for the analysis of unsteady motions within the motor. Figure 2 shows the contour plots of Mach number, mean temperature, and turbulent kinetic energy. The Mach number along the centerline increases almost-linearly, from 0 at the head end to 0.12 at the exit, revealing a slowly varying mass injection-driven flow. The overall flame structure can be visualized by the isothermal contours. Only the portion close to the propellant surface is presented, to provide good spatial resolution.

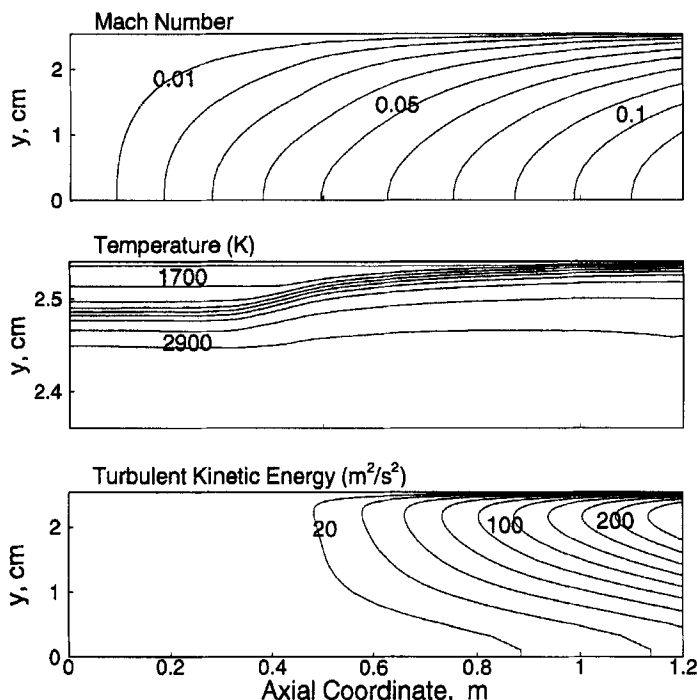


Fig. 2 Contours of Mach number, temperature, and turbulent kinetic energy under steady-state conditions.

The temperature distribution exhibits a laminar two-stage flame in the upstream region. The strong temperature gradient near the surface represents the primary flame zone, with relatively smooth variation around $y = 2.5$ cm characterizing the secondary flame. The secondary flame broadens and merges with the primary flame in the downstream region. This spatial evolution of the flame structure is closely related to the turbulence development, demonstrating the effect of turbulence on propellant combustion. The contours of turbulent kinetic energy exhibit an increase in the turbulence intensity at $x/L = 1/3$, where the Reynolds number based on the centerline velocity is about 12,000. Compared with the boundary layer over a flat plate, the onset of turbulence occurs farther from the surface, due to mass injection by propellant burning. The location of the peak in turbulence intensity moves toward the surface as the flow progresses downstream.

The effect of turbulence on the flame structure can be best described by vertical distributions of temperature and is shown in Fig. 3. The temperature field is characterized by three distinct regimes corresponding to the primary-flame, dark, and secondary-flame zones. The temperature at the propellant surface is about 672 K, and increases rapidly to 1600 K in the dark zone, where a slowdown in temperature increase occurs. The gas particle undergoes another rapid increase in temperature in the luminous flame zone, finally attaining its maximum value of 2950 K. The predicted flame thickness is consistent with most reported measurements under strand-burner conditions.¹ Compared with the corresponding laminar-flow case,^{1,2}

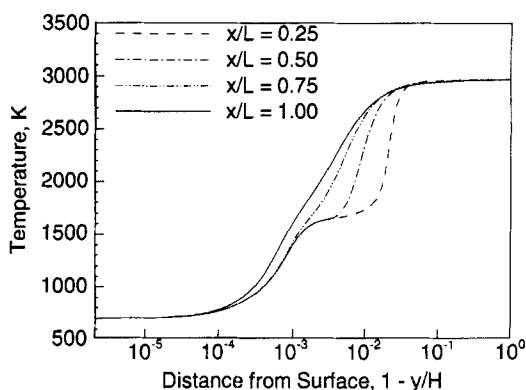


Fig. 3 Vertical distribution of temperature at various axial locations.

the motor internal flow exerts almost no influence on the combustion wave structure in the upstream region. For the temperature development in the downstream, the most significant observation is that the dark zone gradually disappears. Turbulence-enhanced heat transfer in the dark zone facilitates reduction of NO into final products at elevated temperatures. Turbulence penetrates into the primary flame zone and consequently alters the heat transfer to the condensed phase. This leads to an increase in the surface temperature and propellant burn rate in the downstream turbulent region as indicated in Fig. 4. The increase in burning rate due to strong turbulent crossflow near the propellant surface is termed "erosive burning." Figure 5 shows vertical distributions of the ratio of the turbulent eddy (μ_t) to the molecular viscosity (μ) at various axial locations. The peak magnitude of eddy viscosity μ_t lies in the secondary flame zone and increases with the turbulence intensity. Turbulence begins to penetrate into the primary flame at a point in the downstream region, where the mass flow rate over the surface becomes about $700 \text{ kg/m}^2\text{s}$, corresponding to the experimentally determined onset of erosive burning.¹⁷

Figure 6 shows vertical distributions of vorticity in the spanwise direction at various axial locations. Vorticity is produced at the propellant surface because the no-slip condition causes the flow to enter the chamber vertically and then turn to align smoothly with the axial axis.¹⁸ Vorticity increases almost linearly

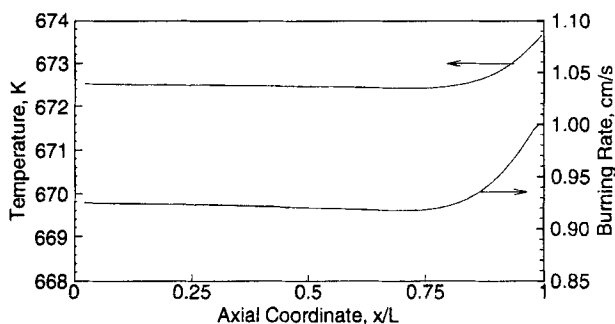


Fig. 4 Distributions of surface temperature and burning rate along centerline.

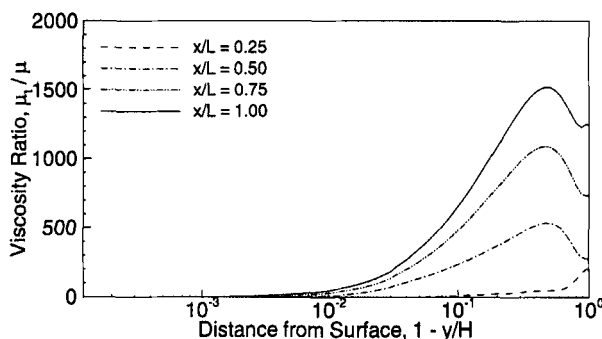


Fig. 5 Vertical distributions of the viscosity ratio at various axial locations.

in the axial direction near the burning surface. In the upstream laminar region, it reaches its maximum in the secondary flame zone. The peak magnitude of vorticity increases and its location shifts closer to the propellant surface further downstream, as the flame structure gets modified due to turbulence effects. For the present two-dimensional simulation, the vortex-stretching mechanism is absent and transport of vorticity is governed by viscous diffusion, volume dilatation, and baroclinicity resulting from the misalignment between the density and the pressure gradients. In the flame zone, the density varies dramatically, so that volume dilatation and baroclinicity become predominant and viscous dissipation gives only negligible contributions to the vorticity evolution.

B. Interaction Between Acoustic Wave and Propellant Combustion

After a steady-state solution is obtained, periodic pressure oscillations are imposed at the exit to simulate a standing acoustic wave in the combustion chamber. The amplitude of pressure oscillation is 1% of the mean pressure at frequencies of 440 and 880 Hz, corresponding to the first and second modes, respectively. Since the chamber is twice as long as the one used in the laminar-flow cases, the second-mode frequency in the present work corresponds to the first longitudinal mode studied in Refs. 1 and 2. Data acquisition and analysis for investigating the

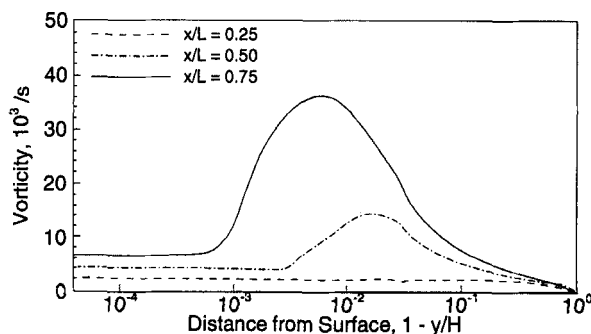


Fig. 6 Vertical distributions of vorticity at various axial locations.

interactions between acoustic motions and propellant combustion are conducted over one cycle after obtaining steady oscillations.

1. Pressure and Velocity Fields

The acoustic pressure field is basically one-dimensional. No discernible variation in the vertical direction is observed, due to the low-Mach number environment under consideration. The oscillatory velocity field exhibits a complex multidimensional structure adjacent to the burning surface within which rapid velocity variations arising from the interactions among acoustic disturbances, unsteady shear waves, flame oscillations and turbulence occur. Figures 7 and 8 show the vertical distributions of the magnitude and phase of the fluctuating axial velocity (u') for the first and second modes, respectively. The most salient feature is the wavy distribution with decreasing amplitude with frequency, a phenomenon commonly observed for nonreacting flows, as reported in Refs. 18 and 19.

The unsteady flowfield can be characterized by three distinct types of wave motions, acoustic (or irrotational), vortical (or shear), and thermal (or entropy) waves, as follows:

$$u' = u'_a + u'_v + u'_\sigma \quad (31)$$

A comprehensive discussion of the acoustic and vortical wave motions in motor environments is given in a companion chapter.¹⁹ The acoustic velocity u'_a is

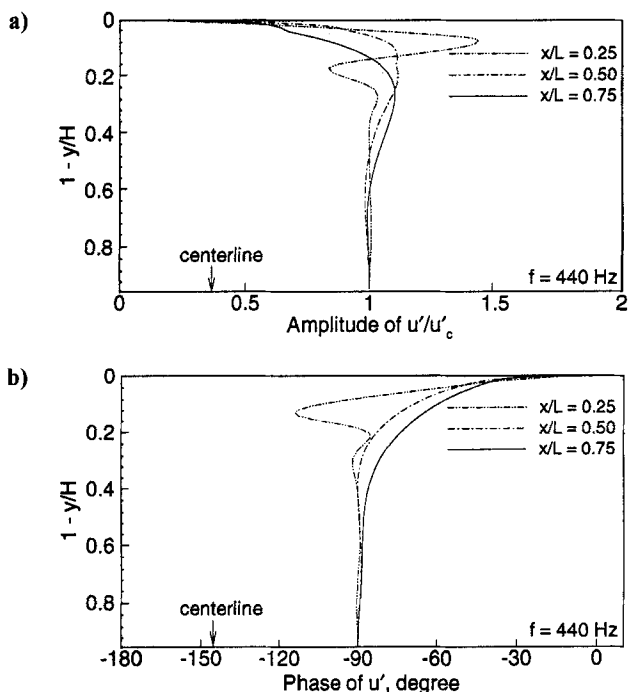


Fig. 7 Vertical distributions of axial velocity fluctuation for the first mode at various axial locations: a) amplitude; b) phase.

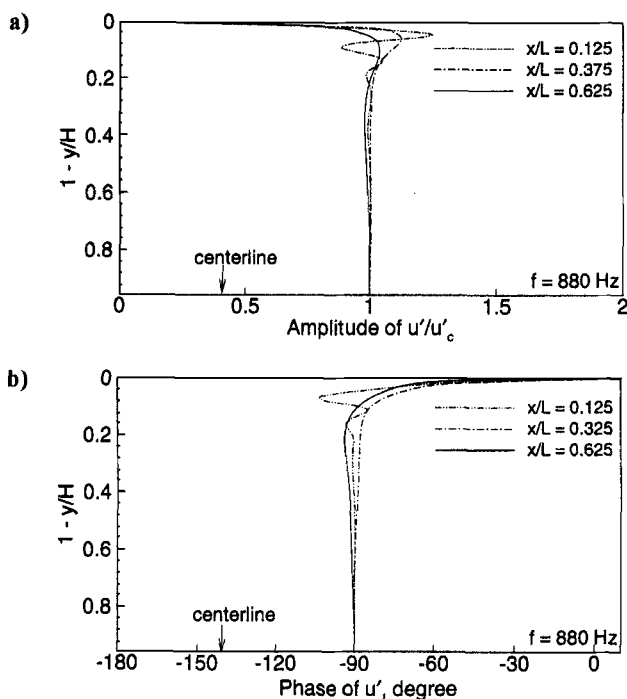


Fig. 8 Vertical distributions of axial velocity fluctuation for the second mode at various axial locations: a) amplitude; b) phase.

directly correlated with the pressure fluctuation through the acoustic impedance, $\bar{\rho}\bar{c}$, which varies rapidly in the flame zone and is proportional to the inverse of \sqrt{T} . The distribution of vortical velocity u'_v exhibits the effect of unsteady vorticity generation and transport. The volume dilatation and baroclinicity in the flame zone tend to diminish the unsteady vorticity and result in decreasing amplitude of the shear wave. In addition, the wavelength of the vortical motion is enlarged in the flame zone due to the increasing wave-propagation speed resulting from volume dilatation. u'_v usually attains its maximum amplitude beyond the major heat-release region. The entropy velocity fluctuation u'_e results from the unsteady heat-release distribution. Since the temperature gradient exists only in the vertical direction in the present configuration, the effect of entropy waves on the axial velocity fluctuation is negligible. Its influence on the vertical velocity fluctuation is, however, usually significant and may excite large oscillations in that direction.²⁰

In the upstream laminar region, a velocity overshoot is observed near the porous wall, because of the shear wave produced by the no-slip condition.¹⁸ This shear wave travels toward the centerline with the mean vertical velocity and is damped out by the viscous dissipation in the core-flow region. In the present study, the magnitude of the velocity overshoot near the porous wall is smaller than twice the centerline fluctuating velocity, as discussed in Refs. 18 and 19. This can be attributed to the damping effect due to strong variations of the acoustic impedance, in the presence of steep temperature gradients in the flame zone. In the turbulent regime, the shear wave is effectively damped by the enhanced momentum transfer

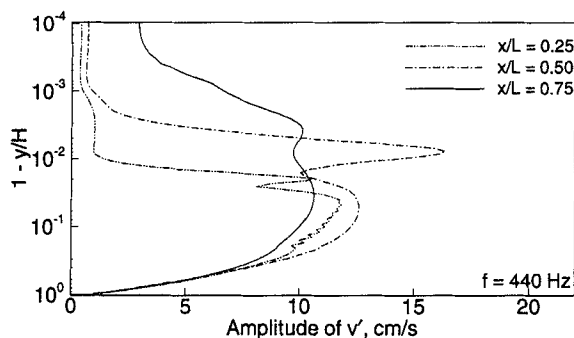


Fig. 9 Distributions of amplitude of vertical velocity fluctuation at various axial locations for the first mode.

and dissipation rate, as it gets convected away from the surface. In the core-flow region, the amplitude of u' reaches a value of 7.01 m/s at the pressure node point ($x/L = 0.5$) for the first mode. The shear wave vanishes and the behavior of u' follows the isentropic relation with the acoustic pressure ($p'/\bar{\rho}\bar{c}$), with a phase lag of 90° with reference to p' .

Figure 9 shows the vertical distributions of the amplitude of the vertical velocity fluctuation v' at various axial locations for the first mode. A logarithmic scale is adopted for the vertical coordinate to portray clearly the variations near the burning surface. The vertical velocity fluctuation is directly related to the surface burning rate, which is a function of the surface temperature. In the laminar region, v' varies slightly near the surface due to density fluctuation associated with the acoustic pressure oscillation. A simple analysis based on the calculated mass burning rate fluctuation yields a value of v' at the surface of about 5 mm/s. A substantial increase in v' occurs in the secondary flame zone due to volume dilatation across the flame. The most noticeable feature is the increase in the fluctuation amplitude inside the primary flame zone in the fully turbulent regime ($x/L > 0.5$). Turbulence penetrates into the primary flame and causes large temperature and heat-release fluctuations close to the propellant surface, altering the burning rate. The magnitude of vertical velocity fluctuation is about 2.5 cm/s at the surface. Turbulence-enhanced momentum transfer induces large v' over the entire flame zone. The peak magnitude is, however, smaller than the corresponding value in the laminar region. This can be partly explained based on the smoother temperature variations in the turbulent regime compared with the two-stage laminar flame. The unsteady mass injection into the chamber may act as a potential source driving combustion instability in a rocket motor, a phenomenon discussed later.

2. Unsteady Turbulent Flowfield

The unsteady velocity field can be decomposed into three components: the time-averaged (or mean), periodic, and turbulent parts. Interactions among the mean, periodic, and turbulent flowfields may enhance the turbulence production rates.²¹ The effect of the periodic velocity field on the fluctuating component of the Reynolds stress gives rise to additional energy exchange mechanisms between the turbulent and the oscillatory motions.³ The enhanced levels of turbulence in the unsteady flowfield can be investigated by computing the fluctuating turbulent

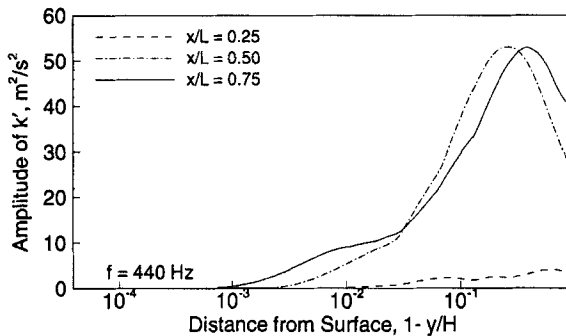


Fig. 10 Vertical distributions of amplitude of turbulent kinetic energy fluctuation at various axial locations for the first mode.

kinetic energy (k'), as shown in Fig. 10. In the laminar regime, k' values as high as $10 \text{ m}^2/\text{s}^2$ are obtained in the secondary flame. These fluctuations grow in the turbulent region and penetrate into the primary flame, drastically changing the gas-phase combustion dynamics. Although acoustic oscillations often enhance turbulence intensity through their interactions, turbulence tends to dissipate organized flow motions due to its induced eddy viscosity. The low value of fluctuating axial velocity (u') near the propellant surface in the upstream region could be due to the acoustic wave-induced turbulence and its ensuing increase in the eddy viscosity.

3. Temperature Field and Heat-Release Distribution

The oscillatory combustion mechanism was investigated in depth by monitoring the temporal evolution of the temperature field and its associated heat-release distribution. Figures 11a and b show the vertical distributions of the amplitude of temperature fluctuation at various axial locations for the first and second modes, respectively. In the upstream laminar region, a large temperature fluctuation occurs in the luminous flame zone, where the major heat-release mechanism is associated with the reduction of NO species. The large activation energy of the NO reaction produces a stiff flame with a steep temperature gradient. Any small variation of the flame location due to local flow disturbances causes substantial oscillations in the temperature field. The large thermal inertia of the condensed phase restrains the temperature fluctuations near the burning surface, keeping the primary flame unaffected. Accordingly, small perturbations of the propellant surface temperatures, about 1 K, are obtained, consistent with the laminar-flow study.² In the turbulent regime, enhanced heat and mass-transfer rates eliminate the dark zone, giving rise to a less stiff flame. Turbulent mixing distributes the temperature fluctuations over the entire flame zone, as opposed to the concentrated peak in the thin secondary flame for laminar region. The increased heat input to the condensed phase leads to surface temperature fluctuations of about 5 K, sufficient to modify the local flame dynamics and ensuing propellant combustion response.

The maximum temperature variation in the core-flow region is about 10 K, following the isentropic relation with the acoustic pressure, because this region has no

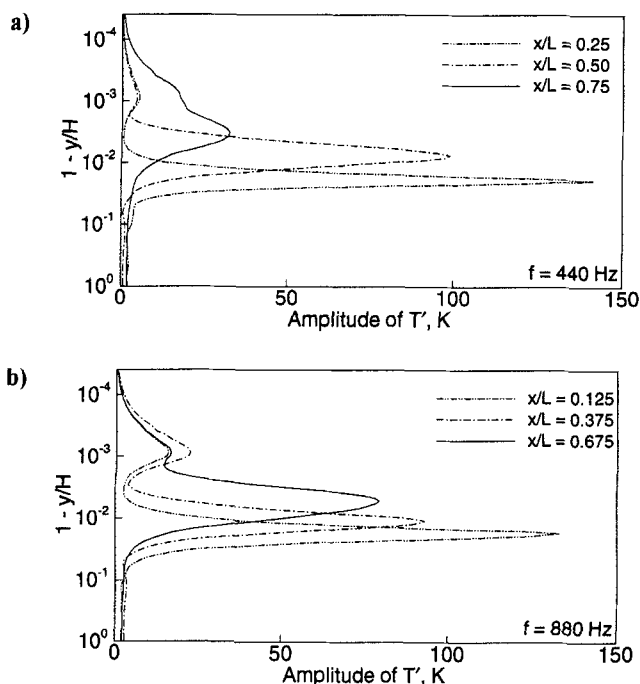


Fig. 11 Vertical distributions of amplitude of temperature fluctuation at various axial locations: a) first mode; b) second mode.

chemical reaction and negligibly low viscous stress.^{1,2} The qualitative differences in the laminar and turbulent regimes substantially alter the heat-release fluctuations, which basically follow the spatial gradient of the temperature oscillations.¹ The vertical distribution of the amplitude of the heat-release fluctuation is shown in Figs. 12a and b for the first and second modes, respectively. It exhibits two peaks with a phase difference of about 180° in the luminous flame zone, a phenomenon commonly observed for flames with steep temperature profiles in laminar flowfields.^{1,2} The heat-release fluctuations are significantly suppressed by turbulence in the secondary flame and enhanced in the primary flame, altering the motor stability behavior.

4. Rayleigh's Criterion

The effect of heat release on motor stability characteristics can be investigated using Rayleigh's criterion,²² which determines the conditions for driving or suppressing flow oscillations when thermal energy is added (or subtracted) periodically to (or from) the acoustic field. This can be investigated by calculating the Rayleigh's parameter ($p'q'$), a time-averaged quantity of the product of acoustic pressure and heat-release fluctuation over one cycle of oscillation. Figure 13 shows the vertical distribution of Rayleigh's parameter for the first and second modes. The transient response of the condensed phase qualitatively modifies the time evolution of local heat release, despite its limited effect on the magnitude of

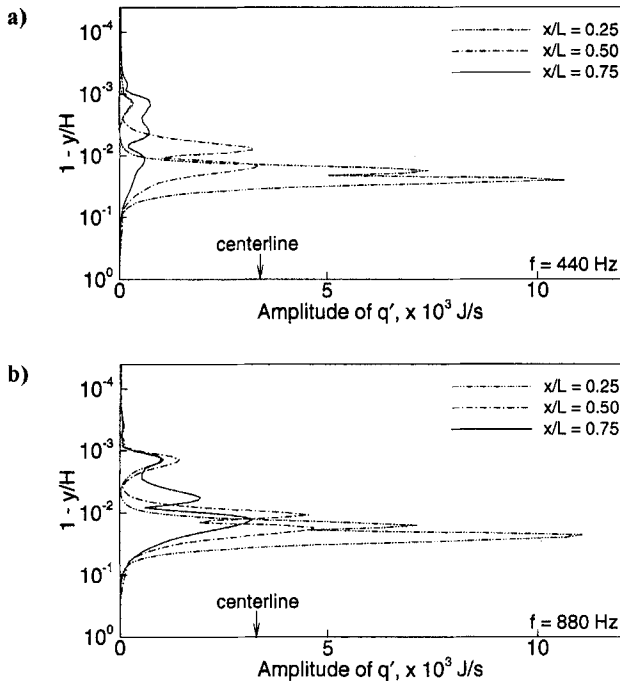


Fig. 12 Vertical distributions of heat-release fluctuation at various locations: a) first mode; b) second mode.

heat release in the laminar flow region, as observed in our previous work.² For both modes, the net value of $\langle p'q' \rangle$ is positive, indicating potential to drive unsteady motions within the motor. In the turbulent regime, the magnitude of $\langle p'q' \rangle$ is significantly reduced. Turbulence suppresses the local flow oscillations in the gas-phase due to enhanced mixing. Unlike laminar flows, the primary flame plays a decisive role in motor stability characteristics in the turbulent regions.

5. Propellant Combustion Response

In addition to the fluctuations in gas-phase heat release, periodic mass addition to the chamber is capable of providing the energy needed to support large-scale pressure oscillations within a rocket motor. In this regard, calculations were made to determine the fluctuations of propellant surface temperature and mass burning rate. Figures 14a and b show the evolution of temperature fluctuations in the condensed phase for the first and second modes, respectively. The temperature fluctuations in the upstream region follow the distribution obtained for laminar flows,² indicating pressure-coupled combustion response. Large surface-temperature fluctuations around 5 K, are, however, observed in the turbulent region with significant penetration of the thermal wave into the condensed phase. The penetration depth δ_p of the thermal wave decreases with increasing frequency and can be estimated using a simple dimensional analysis, $\delta_p = \sqrt{\alpha_p/f}$, where α_p stands for the thermal diffusivity of propellant.

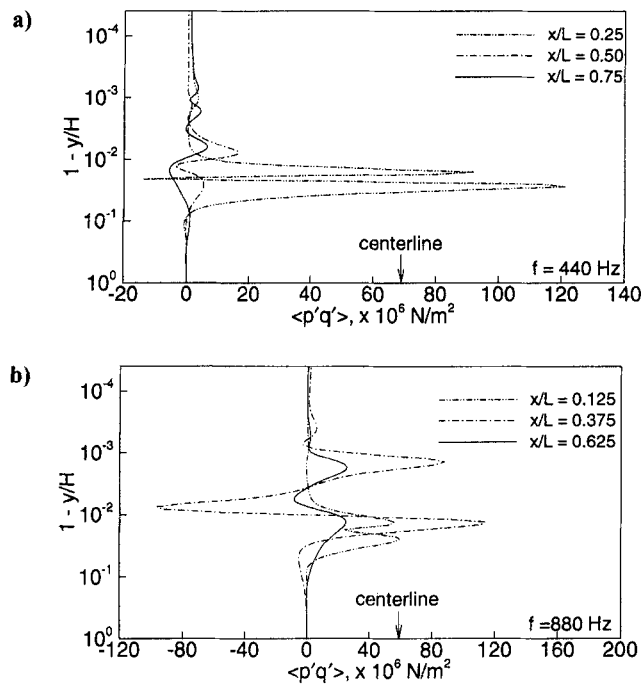


Fig. 13 Vertical distributions of Rayleigh's parameter at various axial locations: a) first mode; b) second mode.

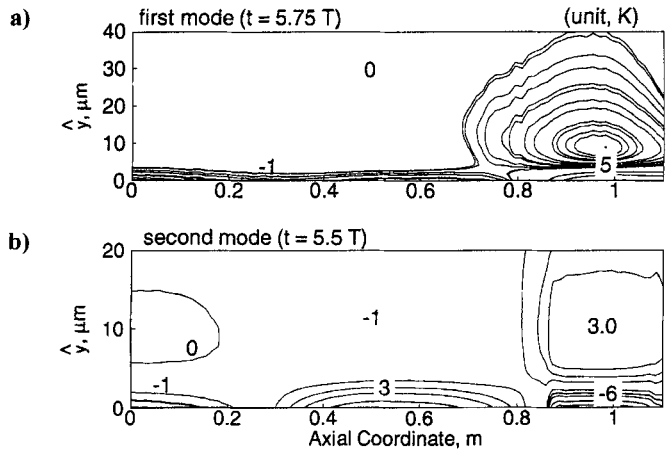


Fig. 14 Time evolution of temperature fluctuation in the condensed phase: a) first mode; b) second mode.

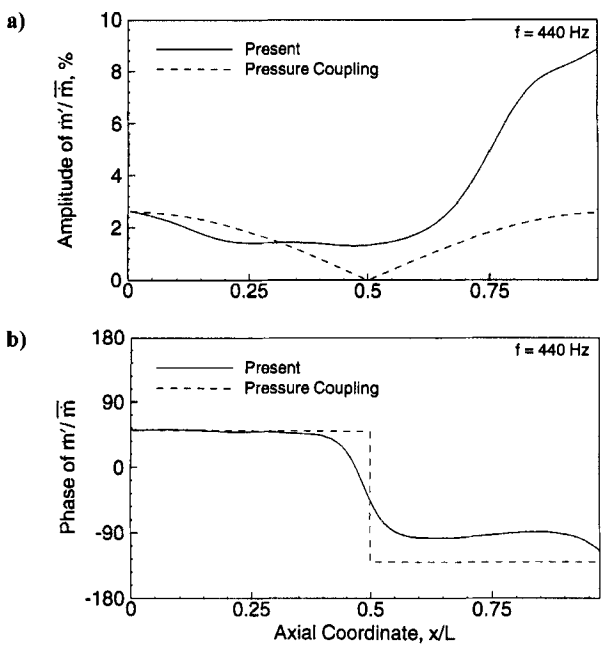


Fig. 15 Axial variation of burning rate fluctuations for the first mode: a) amplitude; b) phase.

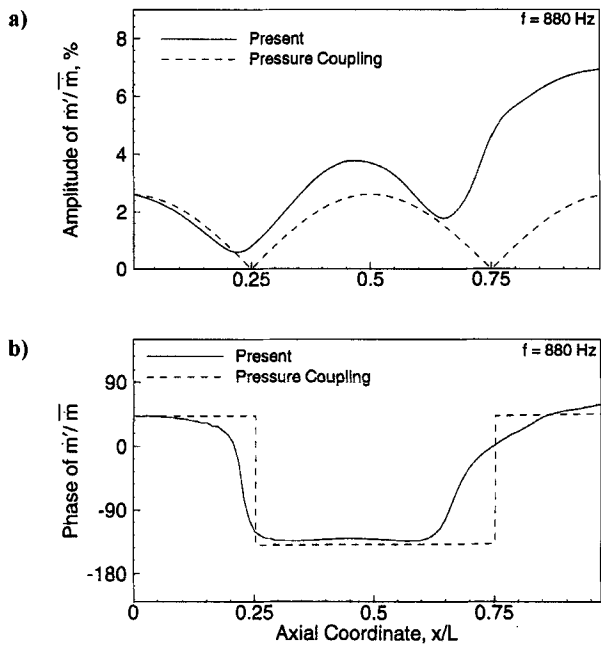


Fig. 16 Axial variation of burning rate fluctuations for the second mode: a) amplitude; b) phase.

To analyze the propellant combustion response to the gas-phase flame dynamics, the distributions of the amplitude and phase of the normalized burning-rate fluctuations (\dot{m}' / \dot{m}) for the first and second modes are presented in Figs. 15 and 16, respectively. The phase of \dot{m}' is obtained relative to the pressure fluctuations at the head end. To facilitate discussion, the amplitude and phase of the pressure-coupled propellant response to the imposed acoustic standing wave are also included. The magnitudes of burning-rate fluctuations at the head end are 2.6 and 2.3% for the first and second modes, respectively. For the first mode, the pressure and mass burning rates are in phase in the first half of the chamber and go 180° out of phase farther downstream. Turbulence drastically alters the gas-phase flame dynamics through its influence on flow motions and, consequently, modifies the propellant burning rate. Distributions of the magnitude and phase indicate that the propellant response is largely pressure-coupled in the upstream laminar region. Effects of velocity coupling and turbulence become significant in the downstream region. The condensed phase behaves as an oscillating piston feeding energy through unsteady mass addition and can be a potential mechanism driving unsteady motions within the chamber.

V. Conclusions

Interactions between acoustic waves and transient combustion response of a double-base homogeneous propellant in a rocket motor have been analyzed. The combined influence of turbulence and acoustic motions on the coupling between gas-phase flame dynamics and condensed-phase physiochemical processes is investigated in depth. The luminous secondary flame expands and eventually merges with the primary flame, due to turbulence-enhanced energy transport, modifying the combustion wave structure significantly. Turbulence penetrates into the primary flame zone and smears out the oscillatory behavior of the shear wave, compared with the laminar flowfield. Large oscillations in heat release and temperature close to the propellant surface increase the burning rate and surface temperatures downstream. Based on Rayleigh's criterion, the primary flame plays a key role in determining the motor stability behavior in the turbulent environment. The propellant combustion response is pressure dominant in the upstream laminar regime and becomes velocity-coupled in the fully developed turbulent region.

Acknowledgments

This work was sponsored partly by the Pennsylvania State University and partly by the California Institute of Technology Multidisciplinary University Research Initiative, under ONR Grant N00014-95-1-1338.

References

- ¹Roh, T. S., Tseng, I. S., and Yang, V., "Effects of Acoustic Oscillations on Flame Dynamics of Homogeneous Propellants in Rocket Motors," *Journal of Propulsion and Power*, Vol. 11, No. 4, 1995, pp. 640–650.
- ²Roh, T. S., Apte, S. V., and Yang, V., "Transient Combustion Response of Homogeneous Solid Propellant to Acoustic Oscillations in a Rocket Motor," *Proceedings of*

Twenty-Seventh Symposium (International) on Combustion, Combustion Inst. Pittsburgh, PA, 1998, pp. 2335–2341.

³Apte, S. V., and Yang, V., “Effect of Acoustic Oscillation on Flow Development in a Simulated Nozzleless Rocket Motor,” *Progress in Astronautics and Aeronautics*, Vol. 185, edited by V. Yang, T. B. Brill, and W.-Z. Ren, AIAA, Reston, VA, 2000, Chap. 3.1.

⁴McBride, B. J., and Gordon, S., *Computer Program for Calculation of Complex Chemical Equilibrium Compositions, Rocket Performance, Incident and Reflected Shocks, and Chapman-Jouguet Detonations*, NASA SP-273, March 1976.

⁵Reid, R. C., Prausnitz, J. M., and Poling, B. E., *The Properties of Gases and Liquids*, 4th ed., McGraw-Hill, New York, 1987, pp. 407–410.

⁶Zenin, A. A., “Structure of Temperature Distribution in Steady-State Burning of a Ballistite Powder,” *Combustion, Explosion and Shock Waves*, Vol. 2, No. 2, 1966, pp. 67–76.

⁷Levine, J. N., and Culick, F. E. C., “Nonlinear Analysis of Solid Rocket Combustion Instability,” AFRPL-TR-74-45, Oct. 1974.

⁸Kooker, D. E., and Nelson, C. W., “Numerical Solution of Solid Propellant Transient Combustion,” AICHE-ASME Heat Transfer Conference, Salt Lake City, Aug. 1978.

⁹Lengelle, G., “Thermal Degradation Kinetics and Surface Pyrolysis of Vinyl Polymers,” *AIAA Journal*, Vol. 8, No. 11, 1970, pp. 1989–1998.

¹⁰Ibricu, M. M., and Williams, F. A., “Influence of Externally Applied Radiation on the Burning Rates of Homogeneous Solid Propellants,” *Combustion and Flame*, Vol. 24, 1975, pp. 185–198.

¹¹Rodi, W., “Experience with Two-Layer Models Combining the k - ϵ Model with a One-Equation Model Near the Wall,” AIAA Paper 91-0216, Jan. 1991.

¹²Tseng, I. S., and Yang, V., “Combustion of a Double-Base Homogeneous Propellant in a Rocket Motor,” *Combustion and Flame*, Vol. 96, 1994, pp. 325–342.

¹³Chen, H. C., and Patel, V. C., “Near-Wall Turbulence Models for Complex Flows Including Separation,” *AIAA Journal*, Vol. 26, No. 6, 1988, pp. 641–648.

¹⁴Peters, N., *Numerical Approaches to Combustion Modeling*, edited by E. S. Oran and J. P. Boris, AIAA, Washington, DC, 1991, pp. 155–182.

¹⁵Watson, W. R., and Myers, M. K., “Inflow-Outflow Boundary Conditions for Two-Dimensional Acoustic Waves in Channels with Flow,” *AIAA Journal*, Vol. 29, No. 9, 1991, pp. 1383–1389.

¹⁶Hsieh, S. Y., and Yang, V., “A Preconditioned Flux-Differencing Scheme for Chemically Reacting Flows at All Mach Numbers,” *International Journal of Computational Fluid Dynamics*, Vol. 8, 1997, pp. 31–49.

¹⁷Osborn, J. R., and Burick, R. J., “Technique for the Measurement of the Erosive Burning Rate of Solid Rocket Propellants,” *Proceedings of Second International Symposium on Nucleonics in Aerospace*, July 1967, pp. 87–94.

¹⁸Flandro, G. A., “Effect of Vorticity on Combustion Instability,” *Journal of Propulsion and Power*, Vol. 11, No. 4, 1995, pp. 607–695.

¹⁹Flandro, G. A., Cai, W. D., and Yang, V., “Turbulent Transport in Rocket Motor Unsteady Flowfield,” *Progress in Astronautics and Aeronautics*, Vol. 185, edited by V. Yang, T. B. Brill, and W.-Z. Ren, AIAA, Reston, VA, 2000, Chap. 3.3.

²⁰Chu, W.-W., *Dynamic Responses of Combustion to Acoustic Waves in Porous Chambers with Transpiration*, Ph.D. Diss., Department of Mechanical Engineering, Pennsylvania State University, University Park, PA, Dec. 1999.

²¹Beddini, R., and Roberts, T., “Turbularization of an Acoustic Boundary Layer on a Transpiring Surface,” *AIAA Journal*, Vol. 26, No. 8, 1988, pp. 917–923.

²²Rayleigh, J. W. S., *Theory of Sound*, Vol. II, Dover, New York, 1954.

Chapter 3.6

Combustion Characteristics of Aluminized HTPB/AP Propellants in Acceleration Fields

Peijuan Yang,* Zhen Huo,[†] and Zhongquan Tang*
*46th Institute of China Aerospace Corporation, Huhhot,
People's Republic of China*

Nomenclature

a	= mean radial acceleration
B_1, B_2	= composite parameters
E, E_1, F, F_1	= burning rate augmentation parameter in empirical formulas
g	= gravitational acceleration
P	= chamber pressure
R	= correlation coefficient
r	= average burning rate
t	= time
t_1	= onset time of burning
t_2	= end time of burning

Subscripts

0	= condition without radial acceleration
a	= condition with radial acceleration a

I. Introduction

S PIN is often employed for attitude stabilization of upper stage launch vehicles, tactical missiles, and gun-launched rocket-assisted projectiles (and base burners). Unfortunately, the deflagration rate of solid propellant is modified in an acceleration field,¹⁻⁷ becoming an orthotropic dyadic,^{4,8} which greatly increases

Copyright © 1999 by the authors. Published by the American Institute of Aeronautics and Astronautics, Inc., with permission.

*Professor, Property Research Laboratory.

[†]Engineer, Property Research Laboratory.

surface regression difficulties. Moreover, when metal additives are present, they are partially retained, altering burning rate and burning surface texture (the effects are dependent upon distance burned), increasing the insulation's thermal load, and reducing performance. In addition, moment of momentum relative to the spin axis is imparted to combustion products departing the burning surface, thereby altering port flow and nozzle characteristics.⁹ The aggregate of these effects complicates motor development^{10,11} and requires knowledge of acceleration-augmented deflagration characteristics.

High-speed cinephotography,¹² and terminated burnings^{4,12} have identified *localized* metal additive agglomerate deflagration interactions as the governing mechanism in the acceleration-augmented deflagration of metallized propellants. The localized nature of the interaction and the agglomerate's mass alter the burning surface's topography. The portion beneath the agglomerate burns at an augmented rate, whereas the remainder (pit walls) seem to burn at the base rate. Because this complex topography cannot be adequately characterized, it is implicitly assumed that the local burning surface is smooth and regressing uniformly at the augmented rate (the rate observed in quasi-steady tests). This assumption is useful for quasi-steady deflagration; it is not useful for dynamic situations where the complex burning surface topography and the multiplicity of local burning rates could be significant. Unfortunately, nothing is currently known about the oscillatory response of acceleration-augmented heterogeneous propellant deflagration, although Greatrix¹³ has made some interesting projections. The distance burned effect is associated with the agglomerates' increasing mass and changing shape. Crowe's unified model¹⁴ provides qualitative functional relationships among burning rate augmentation, base burning rate, acceleration level, and pressure for the initial and final stages of this process. (See King's review of modeling efforts.¹⁵ Greatrix's model,¹⁶ which considers neither explicit AI/deflagration interactions nor distance burned dependency, is the only postreview effort; it seems most applicable to nonmetallized composite propellants.¹⁷)

The mechanism for acceleration-augmented deflagration of nonmetallized propellants is more complex, and has not yet been adequately modeled [the results of Boggs et al.¹⁸ suggest that acceleration augmentation effects in pure ammonium perchlorate (AP) are opposite to those in an AP composite propellant], although Davis et al.¹⁷ have found that the Greatrix/Gottlieb model correlates Broddner's¹⁹ high acceleration level data and extrapolates the effects to similar formulations.

The objective of this chapter is to briefly describe our experimental apparatus and data-reduction procedure, and then present results for systematic formulation changes for $0 < a \leq 60$ g.

II. Experimental Apparatus

A variable speed dc motor drives the spin test apparatus fitted with a subscale test motor. Therefore, the acceleration vector is normal to the grain's bore surface and parallel to the end surfaces. Consequently, augmented burning is expected only on the bore surface.⁴ The subscale test motor's basic parameters are 1) motor, overall length 239 mm, outside diameter 90 mm; and 2) CP grain, outside diameter 80 mm, inside diameter 56 mm, length 146 mm, mass about 650 g (burning on bore and end surfaces).

The pressure instrumentation is strain gauge type. Electrical connections to the spinning motor are through slip rings, and digital data that include motor pressure

and rotational speed are acquired with an ADC equipped microcomputer. Thrust is not measured.

Subscale motors were chosen over strands because 1) a mass balance can be employed to estimate instantaneous mass burning rates; 2) Broddner's results¹⁹ for nonmetallized propellants at high acceleration levels demonstrate that this approach is more reliable than strands (contrast Broddner's results with those of Sturm and Reichenbach²⁰ for strands); and 3) hardware continuity is preserved with conventional ballistic characterizations.

In a typical test, firing the motor is brought to the proper spin rate and ignited, and data are recorded. After the propellant burnout, the motor is disassembled and the retained residue photographed and otherwise examined. Errors in the time-mean, radial burning rate measurements were estimated at less than 2%.

III. Data Reduction

Time-mean burning rates were computed from the expression

$$r = \frac{\text{web}}{t_2 - t_1} \quad (1)$$

The web was determined from pretest measurements. The onset of burning t_1 was defined as the time of the first maximum in dp/dt after sustained pressure rise; the end of burning t_2 was determined by the tangent bisector method.

Time-mean chamber pressure was computed from the expression

$$P = \frac{\text{total pressure impulse}}{t_2 - t_1} \quad (2)$$

When the changes of nozzle throat area and characteristic exhaust velocity and the effect of end surface burning are ignored, the instantaneous burning rate can be estimated from a mass balance as

$$r(t) = \frac{p(t) * \text{web}}{\text{total pressure impulse}} \quad (3)$$

The instantaneous chamber pressure $p(t)$ corresponded to the instantaneous burning rate $r(t)$. In this study, each listed datum is generally an average value of results for three tests.

IV. Experiment

Table 1 presents the propellant formulations examined. Data from each formulation came from a single mix, all tests were conducted at $20 \pm 1^\circ\text{C}$, the average chamber pressure of all tested formulations at zero-acceleration condition was 5.0 ± 0.2 MPa, except formulation 3.

V. Results and Discussion

A. Acceleration Effects: Baseline Formulation

The baseline propellant in the present study is formulation 1 of Table 1. The corresponding pressure histories are presented in Fig. 1. The propellant burning is essentially neutral at the zero-acceleration condition, and, as expected, no residue

Table 1 Propellant formulations

Formulation	Solid content, %	Al content, %	Al size, μm	AP content, %	AP (250 μm / 120 μm /10 μm) fraction ratio	RDX content, %	TB content, %	GFP content, %	r_0 , mm/s	P_0 , MPa
1	85	17	24	68	2/2/1	0	0	0.08	7.66	5.06
3	85	17	5	68	2/2/1	0	0	0.08	8.56	5.27
4	80	12	24	68	2/2/1	0	0	0.08	5.56	4.93
5	85	12	24	73	2/2/1	0	0	0.08	8.27	5.05
7	85	2	24	83	2/2/1	0	0	0.08	8.72	4.85
8	85	17	24	68	5/2/1	0	0	0.08	6.83	5.01
10	85	17	24	68	2/2/1	0	1.5	0	6.66	5.10
11	85	17	24	48	2/2/1	20	0	0.08	6.52	4.99
13	85	0.5	24	84.5	2/2/1	0	0	0.08	8.86	5.06
14	85	17	24	68	2/2/1	0	0	1	10.37	5.06

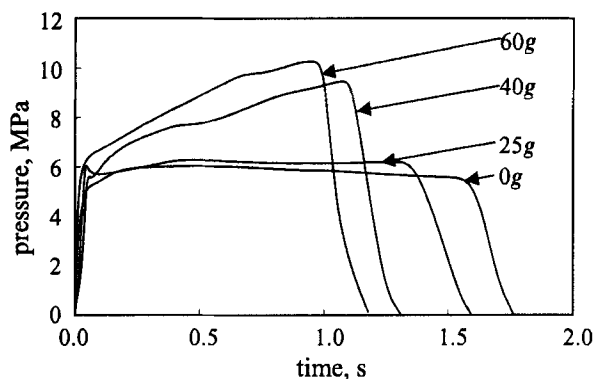


Fig. 1 Time history of chamber pressure; baseline formulation.

retention is observed. There are melted aluminum or alumina globules near the burning surface following ignition, but they are quickly swept away by burning gas. However, as the spin rate increases, the pressure history initially becomes increasingly progressive due to retained aluminum agglomerates and increased burning surface from pitting. Because agglomerate mass is increasing with distance burned but flattening, however, the remainder of the pressure history represents a complex tradeoff between orthotropic grain regression and the transition of the augmented burning phenomena from pit to puddle phases. Figure 1 and the estimated burning rate history shown in Fig. 2 also indicate that, with increasing acceleration, the burning time will shorten, and instantaneous chamber pressure and burning rate augmentation will increase.

Acceleration effects for the baseline formulation are illustrated in Table 2 in terms of the time-mean burning rate. Table 2 shows the following:

1) There is no acceleration effect for the baseline formulation when the acceleration is less than 8 g, but there is a threshold value between 8 and 25 g where acceleration augmentation occurs.

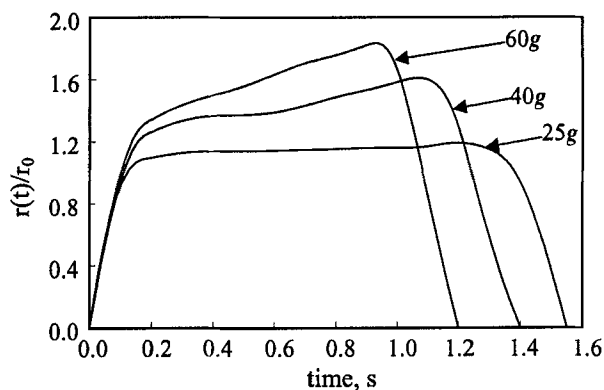


Fig. 2 Time history of propellant burning rate augmentation; baseline formulation.

Table 2 Mean acceleration effects: baseline formulation

a (g)	8	25	40	60
r_a/r_0^a	1.0	1.10	1.30	1.47
P_a/P_0^b	1.0	1.07	1.12	1.40
Sensitive time (ms)	—	180	53	36
Ignition delay (ms) ^c	—	65	57	62

^a $r_0 = 7.66$ mm/s. ^b $P_0 = 5.06$ MPa. ^cStatic ignition delay = 63 ms.

- 2) When the acceleration level is above the threshold, the average burning rate and average chamber pressure are higher than their static values, and increase with increasing acceleration level. Also, the average chamber pressure augmentation is less than the average burning rate augmentation in the same subscale motor.
- 3) The sensitive time (defined as the time corresponding to a burning rate augmentation up to 1.05) decreases with increasing acceleration level.
- 4) There is no acceleration effect on ignition delay.

B. Influence of Aluminum Content

To investigate the influence of aluminum content, the aluminum and oxidizer contents were changed while holding the total solids and other formulation components constant. Table 1 shows that formulations 1, 5, 7, and 13 contain 17, 12, 2, and 0.5% Al, respectively. Results for these formulations are shown in Fig. 3, and can be summarized as follows:

- 1) The average burning rate augmentation and the amount of aluminum or aluminum oxide agglomerates retained close to the burning surface decrease with decreasing aluminum content for hydroxy-terminated polybutadiene (HTBP) propellants containing from 17 to 0.5% Al content.
- 2) The combustion characteristics of the HTPB propellant with 0.5% Al content are insensitive to acceleration for $0 < a \leq 60$ g.

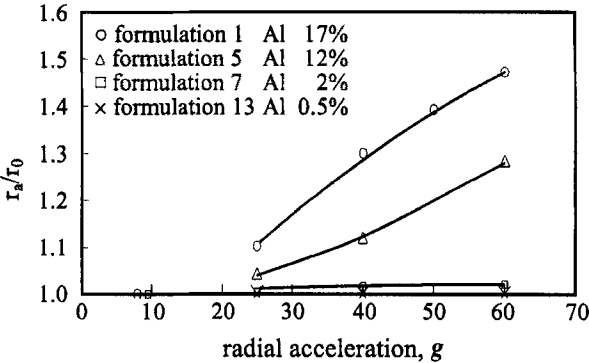


Fig. 3 Influence of aluminum content on burning rate augmentation.

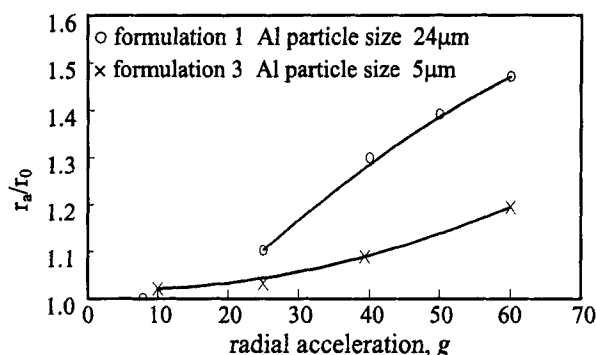


Fig. 4 Influence of aluminum particle size on burning rate augmentation.

C. Influence of Aluminum Particle Size

Formulations 1 and 3 of Table 1 were studied to evaluate the influence of aluminum particle size. Formulation 1 contains 17% Al with a weight-mean diameter of 24 μm , and formulation 3 contains 17% Al with a weight-mean diameter of 5 μm . The other elements of the compositions are identical. Results shown in Fig. 4 indicate that the smaller the aluminum particle diameter, the smaller the burning rate augmentation. Because finely powdered aluminum leads to static burning rate increases of these propellants, agglomerate retention is reduced by reducing Al particle size.

D. Influence of Solid Content

The solid content, defined as the total amount of aluminum and oxidizer, for formulations 1, 4, and 5 of Table 1 are 85, 80, and 85%, and their Al/AP contents are 17/68%, 12/68%, and 12/83%, respectively. Results presented in Fig. 5 show that average burning rate augmentation is increased when solid content is reduced by decreasing either Al or AP content. This occurs because increasing binder content aids agglomeration of aluminum/aluminum oxide near the burning surface.¹¹ For example, at the radial acceleration of 60 g, the burning rate augmentation, r_a/r_0 , reaches 1.89 for formulation 4. However, for formulations 1 and 5, r_a/r_0 are 1.47 and 1.28, respectively.

E. Influence of Oxidizer Particle Size

Formulations 1 and 8 in Table 1 contain 68% trimodal 250/120/10 μm AP, but the ratios are 2/2/1 and 5/2/1, respectively. Therefore, the weight-mean AP diameter is 150 μm for formulation 1, and 188 μm for formulation 8. They are used to investigate the influence of the oxidizer particle size. Results in Fig. 6 show that the larger the weight mean diameter, the greater the burning rate augmentation. The reasons are as follows: 1) the coarser oxidizer reduces static burning rate, thereby reducing the velocity of the debouching gases and increasing Al retention, and 2) according to Cohen's pocket model,²¹ pocket size and therefore agglomerate size, increases with oxidizer particle size. Consequently, as oxidizer

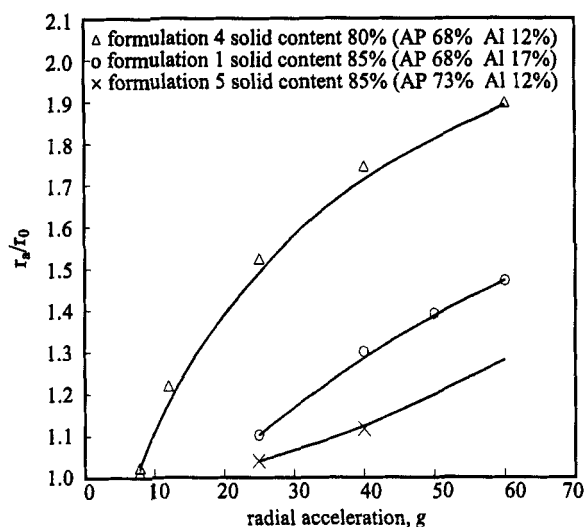


Fig. 5 Influence of solid content on burning rate augmentation.

particle size increases, agglomerate size increases, whereas the gas velocity to carry the agglomerates away decreases, and so Al retention and rate augmentation increase.

F. Influence of Oxidizer Type

In Table 1, formulation 1 contains 68% AP oxidizer and formulation 11 contains 48% AP and 20% RDX oxidizers. These formulations are used to define the influence of the oxidizer type. Results presented in Fig. 7 show that replacing AP with RDX increases average burning rate augmentation. The slab motor tests, however, did not reveal this change.⁶

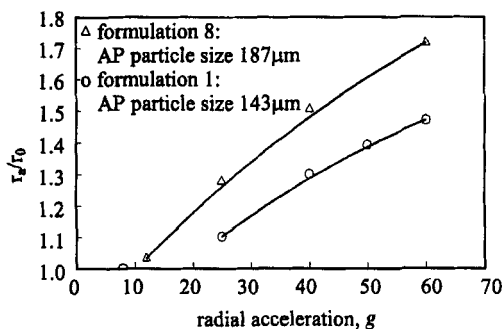


Fig. 6 Influence of oxidizer particle size on burning rate augmentation.

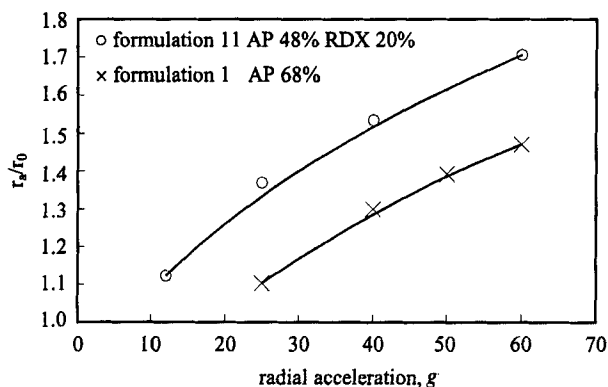


Fig. 7 Influence of oxidizer type on burning rate augmentation.

G. Influence of Static Burning Rate

Adding burning rate modifier to a propellant is an important method of modifying the static burning rate of the propellant. In Table 1, formulations 1, 10, and 14 contain 0.08% GFP, 1.5% TB, and 1% GFP burning rate modifiers, respectively. Their static burning rates at chamber pressure 5.06~5.10 MPa are 7.66, 6.66, and 10.37 mm/s, respectively. These formulations are used to investigate the influence of the static burning rate. The testing results are illustrated in Fig. 8, showing that the average burning rate augmentation increases with decreasing static burning rate. The reason for this is that the lower the burning rates, the smaller the aerodynamic drag of the combustion gases at the same acceleration level; the agglomerates retained close to the burning surface of propellant with lower static burning rate are removed with more difficulty. Therefore, the acceleration effect is more obvious.

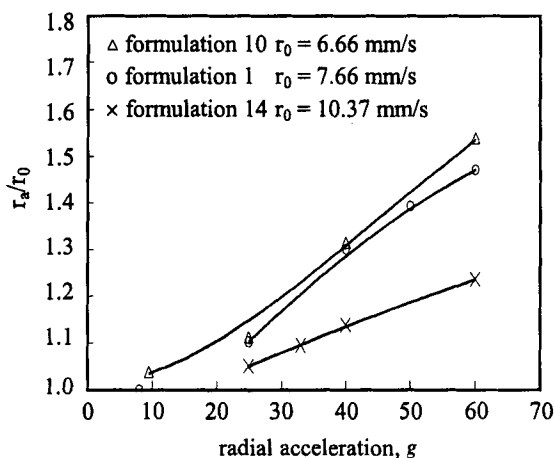


Fig. 8 Influence of static burning rate on augmentation.

Table 3 Influence of static pressure: baseline formulation

P_0 , MPa	r_0 , mm/s	r_a/r_0		
		25 g	40 g	60 g
5.06	7.66	1.10	1.30	1.47
5.67	8.08	1.12	1.27	1.44
8.83	9.28	1.19	1.36	1.51

When the acceleration level is lower than the threshold value of the propellant, the aerodynamic drag of the combustion gas is the dominant of the two forces acting on the agglomerates. Under this condition, there is no acceleration effect. Figures 3–8 indicate that, for all of the formulations in Table 1, the acceleration threshold values are above 5 g, and this value (unequal) for different formulations increases with decreasing acceleration effect of the formulation. For example, the acceleration threshold value of formulation 7 is above 25 g. However, when the acceleration level ranges from the threshold value to certain value, the centrifugal force resulting from the acceleration becomes dominant. Under this condition, the average burning rate augmentation increases with increasing acceleration level (see Figs. 1–8).

H. Influence of Static Pressure

To determine the influence of static chamber pressure, three groups of tests at 5.06, 5.67, and 8.83 MPa were conducted in acceleration fields from 0 to 60 g. Results are listed in Table 3, and show that the influence of pressure level on the average burning rate augmentation is small and somewhat anomalous for the baseline propellant when $5 < P < 9$ MPa and $0 < a \leq 60$ g.

Analysis of these data discloses that the average burning rate augmentation for these formulations are linearly related to Crowe’s composite variable: $B_1(B_1 = [P_0 \cdot a]^{0.25}/r_0)$ and $B_2(B_2 = [P_a \cdot a]^{0.25}/r_0)$. Table 4 shows that every

Table 4 Empirical correlation parameters for burning rate augmentation

Formulation	$r_a/r_0 = E_1 * B_1 + F_1$			$r_a/r_0 = E_2 * B_2 + F_2$		
	E_1	F_1	R	E_2	F_2	R
1	3.443	−0.403	0.999	2.508	−0.009	0.998
3	1.678	0.353	0.958	1.492	0.427	0.970
4	2.774	−0.154	0.997	1.971	0.222	0.997
5	2.426	0.041	0.977	2.083	0.176	0.988
7	0.183	0.934	0.984	0.170	0.937	0.985
8	3.402	−0.368	0.999	2.483	0.017	0.999
10	3.351	−0.575	0.999	2.770	−0.340	0.999
11	2.677	−0.006	0.999	1.920	0.310	0.999
14	2.325	0.297	0.999	1.979	0.410	0.999

Table 5 Comparison of predicted and measured burning rate augmentation

Formulation	Acceleration, <i>g</i>	r_a/r_0		P_a , MPa		Threshold value, <i>g</i>	
		Predicted	Measured	Predicted	Measured	Predicted	Measured
1	50	1.390	1.392	6.647	6.531	18.2	8 ~ 25
4	12	1.229	1.215	5.426	5.477	5.2	5
11	12	1.137	1.122	5.168	5.334	—	—
14	33	1.103	1.095	5.301	5.280	—	—

formulation corresponds to two empirical equations in a 60 *g* acceleration field. Using the static burning rate r_0 in Table 1, the average burning rate augmentation and the average chamber pressure at 60 *g* acceleration level and 5 MPa static pressure for these formulations or similar formulations can be predicted by solving the corresponding equations. The acceleration threshold value also can be predicted. Predicted results approximate the measurements. Examples are presented in Table 5.

I. Residue Retention

After the aluminized HTPB propellant combustion is completed, residue is retained in the chamber and the fore and aft closures. The residue mass increases in an acceleration field as shown in Table 6 (residue mass retained in the throat is small compared to above). Table 6 shows that residue mass is reduced under the following conditions: 1) increasing static burning rate, 2) decreasing aluminum content or particle size, and 3) increasing solid content.

Comparing formulation 11 with 1, the residue mass with AP/RDX is much larger than that with AP alone in acceleration fields from 0 to 60 *g*. It reaches about 5% of grain mass at 60 *g*. Figures 9a–9e show the interior walls of chambers after tests of formulation 10 at 0, 9.5, 25, 40, and 60 *g*, respectively. At 0 and 9.5 *g*, the residue is very small and is in the shape of powder; it is only retained on the aft end of chamber. However, as acceleration level increases, residue mass and size increase. At 60 *g*, the entire chamber wall is covered with residue.

Table 6 Residue retention mass

Formulation	Residue retention mass acceleration, <i>g</i>		Residue retention mass increment, <i>g</i>
	0 <i>g</i>	60 <i>g</i>	
1	5.3	14.8	9.5
3	1.8	7.3	5.5
4	10.5	28.7	18.2
5	6.5	10.4	3.9
10	5.7	16.9	11.2
11	12.1	29.5	17.4

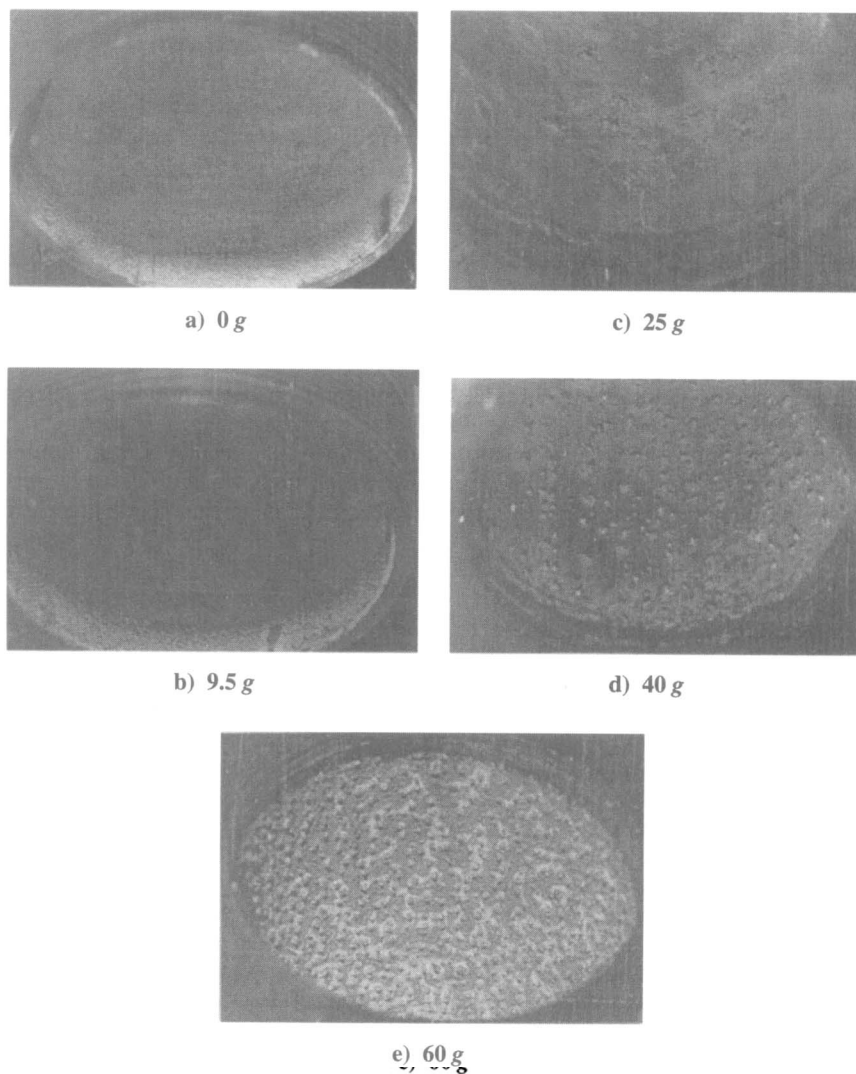


Fig. 9 Residues on chamber wall for various accelerations; formulation 10.

VI. Conclusions

1) The subscale motor method can be more reliably utilized to investigate the combustion characteristics of solid propellants in acceleration fields.

2) Some of the HTPB/AP/Al propellant burning rate augmentation data could be correlated with Crowe's composite independent variable for the acceleration range of 0–60 g in this study.

3) For HTPB/AP/Al propellants with Al content more than 0.5%, acceleration threshold values were above 5 g, and acceleration effects increase with increasing acceleration.

4) For HTPB/AP/Al propellants with Al content up to 0.5%, there is no acceleration effect for $0 < a \leq 60 \text{ g}$.

5) Techniques for reducing the acceleration sensitivity of aluminized HTPB/AP propellant for $0 < a \leq 60 \text{ g}$ are as follows: 1) increase static burning rate, 2) use fine particle size oxidizer and fine particle size aluminum, 3) increase solid content, 4) decrease aluminum content when solid content cannot be changed, and 5) decrease RDX content.

Acknowledgments

The authors thank Robert L. Glick, Yaodong He, and Qingbiao Lin for their assistance.

References

- ¹Sturm, E. J., and Reichenbach, R. E., "Aluminized Composite Solid-Propellant Burning Rates in Acceleration Fields," *AIAA Journal*, Vol. 7, No. 11, 1969, pp. 2087–2093.
- ²Nioka, T., Mitani, T., and Ishii, S., "An Experimental Study on the Accelerated-Produced Burning Rate Augmentation During Transient Period," AIAA Paper 75-1331, Sept.–Oct. 1975.
- ³Northam, G. B., "Effects of Steady-State Acceleration on Combustion Characteristics of an Aluminized Composite Solid Propellant," NASA TN-D-4914, 1968.
- ⁴Northam, G. B., "Effects of the Acceleration Vector on Transient Burning-Rate Augmentation of an Aluminized Solid Propellant," *Journal of Spacecraft and Rockets*, Vol. 8, No. 11, 1971, pp. 1133–1137.
- ⁵Ishii, S., Nioka, T., and Mitani, T., "An Analytical and Experimental Study for Solid Propellant Combustion in an Acceleration Field," *Combustion Science and Technology*, Vol. 8, No. 4, 1973, pp. 177–184.
- ⁶Yang, P. J., "An Experimental Study on the Acceleration Effect of Aluminized HTPB Propellants," ISBN7-5612-0672-0/v.18, 1994, pp. 190–196.
- ⁷Brundige, W. N., and Caveny, L. H., "Low Burning Rate Aluminized Propellants in Acceleration Fields," *AIAA Journal*, Vol. 22, No. 5, 1984, pp. 638–646.
- ⁸Murphy, J. M., and Wall, R. H., "Effects of Grain Configuration upon the Burning Rate of a Spinning Rocket Motor," *Journal of Spacecraft and Rockets*, Vol. 3, No. 2, 1966, pp. 263–264.
- ⁹Norton, D. J., Farquhar, B. W., and Hoffman, J. D., "An Analytical and Experimental Investigation of Swirling Flow in Nozzles," *AIAA Journal*, Vol. 7, No. 10, 1969, pp. 1992–2000.
- ¹⁰Lucy, M. H., "Spin Acceleration Effects on Some Full-Scale Rocket Motors," *Journal of Spacecraft and Rockets*, Vol. 5, No. 2, 1968, pp. 179–183.
- ¹¹Northam, G. B., and Lucy, M. H., "Effects of Acceleration on Solid-Rocket Performance," *Journal of Spacecraft and Rockets*, Vol. 6, No. 4, 1969, pp. 456–460.
- ¹²Willoughby, P. C., Crowe, C. T., and Baker, K. L., "A Photographic and Analytic Study of Composite Propellant Combustion in an Acceleration Field," AIAA Paper 69-173, Jan. 1969.
- ¹³Greatrix, D. R., "Parametric Analysis of Combined Acceleration Effects on Solid-Propellant Combustion," *Canadian Aeronautics and Space Journal*, Vol. 40, No. 2, 1994, pp. 68–73.

¹⁴Crowe, C. T., "A Unified Model for the Acceleration-Produced Burning Rate Augmentation of Metalized Solid Propellants," *Combustion Science and Technology*, Vol. 5, No. 2, 1972, pp. 55–60.

¹⁵King, M. K., "Critical Review: Modeling of Acceleration Effects on Solid Propellant Combustion," *AIAA Journal*, Vol. 14, No. 1, 1976, pp. 18–25.

¹⁶Greatrix, D. R., and Gottlieb, J. J., "Model for Prediction of Normal-Acceleration Augmentation of Composite-Propellant Combustion," AIAA Paper 87-1736, June–July 1987.

¹⁷Davis, F. E., Bowman, N. F., and Glick, R. L., "Burning Rate Augmentation at High Acceleration Levels," 35th JANNAF Combustion Meeting, Dec. 1998.

¹⁸Boggs, T. L., Zurn, D. E., and Netzer, D. W., "Ammonium Perchlorate Combustion: Effects of Sample Preparation; Ingredient Type; and Pressure, Temperature, and Acceleration Environments," *Combustion Science and Technology*, Vol. 7, No. 4, 1973, pp. 177–183.

¹⁹Broddner, S., "Effects of High Spin Rate on the Internal Ballistics of a Solid Rocket Motor," *Acta Astronautica*, Vol. 15, 1979, pp. 191–197.

²⁰Sturm, E. J., and Reichenbach, R. E., "An Investigation of the Acceleration Induced Burning Rate Increase in Nonmetallized Composite Propellants," *AIAA Journal*, Vol. 8, No. 6, 1970, pp. 1062–1067.

²¹Cohen N. S., "A Pocket Model for Aluminum Agglomeration in Composite Propellant," AIAA Paper 81-1585, July 1981.

Chapter 3.7

Pulsed Motor Firings

Fred S. Blomshield*

Naval Air Warfare Center, China Lake, California

I. Introduction

THE Naval Air Warfare Center Weapons Division (NAWCWD) at China Lake has participated in a program to develop an improved understanding of linear and nonlinear combustion instability in solid propellant rocket motors. One primary goal of this program was to develop a systematic database of motor and stability data for future analysis. Earlier papers have reported on previous NAWCWD work on this program.¹⁻⁴ This past work will be briefly reviewed here.

The motors fired in the past program were 12.7 cm in diameter and 170 cm in length. The majority were loaded with an 88% solids, reduced smoke ammonium perchlorate/hydroxy terminated polybutadiene (AP/HTPB) propellant with a nominal burning rate of 0.61 cm/s at 6.9 MPa. In addition, motors were fired that contained 1% by weight 8 μ aluminum oxide, 90 μ aluminum oxide, and 3 μ zirconium carbide as stability additives in place of 1% ammonium perchlorate. Motor pressures ranged from 3.45 to 10.3 MPa. Pressure-coupled combustion response measurements were made with a T-burner at the nominal motor operating pressures for all propellants.

Several motor configurations and propellant variations were included in the program. Twenty-three motors were fired and each motor was typically pulsed three times during burn. The baseline grain geometry was a six-point star in the aft two-thirds of the motor and a cylindrical section in the forward end. Most of these motors were fired using the baseline reduced smoke composite propellant and three were fired with propellants containing stability additives. Three motors with star-forward grains, one motor with a full star grain, two motors with cylindrical cross sections, and four half-length higher frequency motors were fired. The pulsing produced 10 unstable pulses (pulses that grew to a limiting oscillatory amplitude) and 32 stable pulses (pulses that decayed). A complete description of the motors can be found in Refs. 1 and 2. Table 1 summarizes the data produced by these motor firings. Table 2 shows the differences among the propellants for these firings.

This material is declared a work of the U.S. Government and is not subject to copyright protection in the United States.

*Head, Propulsion Research Branch, Research and Technology Dept.

Table 1 Motor test matrix for past program (actual pulse amplitude determined by extrapolated back to zero time²)

Test no.	Geometry	P_{ave} , MPa	NWR propellant no.	Pulse no. 1				Pulse no. 2				Pulse no. 3			
				Time, s	Web, cm	Pulse, kPa	α , 1/s	Time, s	Web, cm	Pulse, kPa	α , 1/s	Time, s	Web, cm	Pulse, kPa	α , 1/s
1	SAFT3	5.52	11	nrd ^b	—	—	—	2.016	1.270	248	+209	osc ^d	—	—	—
2	SAFT3	5.52	11	0.703	0.503	83	-159	1.708	1.092	83	+207	osc ^c	—	—	—
3	SAFT3	5.52	11	0.805	0.566	97	-112	1.790	1.240	345	+161	osc ^c	—	—	—
4	SFWD3	6.21	11	0.970	0.864	262	-190	1.962	1.506	152	+56	osc ^c	—	—	—
5	SAFT3	5.52	11	0.965	0.660	690	-176	npf ^a	—	—	—	npf ^a	—	—	—
6	SAFT3	3.72	11	0.760	0.467	124	-214	2.005	1.092	48	-102	3.010	1.549	41	-75
7	SFUL3	6.21	11	0.748	0.640	262	+639	osc ^c	—	—	—	osc ^c	—	—	—
8a	SAFT3	5.52	11	npf ^a	—	—	—	npf ^a	—	—	—	3.020	1.816	69	+134
8b	SAFT3	3.72	11	0.950	0.559	345	-210	2.216	1.181	138	-89	3.419	1.732	221	+366
8c	SAFT3	10.3	11	0.617	0.538	138	+151	osc ^c	—	—	—	osc ^c	—	—	—
8d	SAFT3	5.52	11	npf ^a	—	—	—	npf ^a	—	—	—	npf ^a	—	—	—
9	CYL3	5.72	11	0.745	0.351	138	+232	osc ^c	—	—	—	osc ^c	—	—	—

Test no.	Geometry	P_{ave} , MPa	NWR propellant no.	Pulse no. 1				Pulse no. 2				Pulse no. 3			
				Time, s	Web, cm	Pulse, kPa	α , 1/s	Time, s	Web, cm	Pulse, kPa	α , 1/s	Time, s	Web, cm	Pulse, kPa	α , 1/s
10	CYL3	4.21	11	0.887	0.406	248	+244	osc ^c	—	—	—	osc ^c	—	—	—
11	SAFT6	3.31	11b	2.067	0.815	276	-143	3.688	1.445	41	-75	5.218	2.507	28	-60
12	SAFT6	5.52	11b	1.374	0.599	83	-182	2.543	1.102	41	-247a ^d	nrd ^b	—	—	—
13	CYL6	4.00	11b	1.261	0.442	55	-185	2.429	0.902	28	nrd ^b	3.445	1.334	28	-71
14	SFWD6	4.55	11b	1.945	0.930	345	-201	3.465	1.631	55	-133	4.898	2.319	14	-33a ^d
15	SAFT3	6.48	12	0.948	0.719	1200	-122	1.764	1.242	276	-84	nrd ^b	—	—	—
16	SAFT3	4.96	13	0.824	0.533	359	-232	1.505	0.899	179	-137	nrd ^b	—	—	—
17	SAFT3	5.72	17	0.866	0.579	483	-188	1.660	1.044	317	-75	2.572	1.542	14	-11a ^d
19	SAFT3	10.1	11b	nrd ^b	—	—	—	1.817	1.247	14	-26a ^d	2.767	1.842	14	-64a ^d
20	SFWD3	5.03	11b	0.984	0.752	110	-193	2.167	1.402	28	-81	npf ^a	—	—	—
21	SFWD3	5.03	11b	1.012	0.770	290	-251	2.195	1.417	69	-143	3.506	2.060	28	nrd ^b

^anpf—no pulse fired. ^bnrd—not reducible. ^cosc—oscillating. ^da—weak pulse.

Table 2 Propellant matrix for past program

Propellant no.	Additive	Size, μ	Rate, ^a cm/s	Response, ^b R_p	Exponent, n
NWR-11	(none)	—	0.605	1.25	0.491
NWR-11b	(none)	—	0.541	2.20	0.461
NWR-12	Al ₂ O ₃	8.0	0.630	0.75	0.493
NWR-13	ZrC	3.5	0.572	0.82	0.493
NWR-17	Al ₂ O ₃	90.0	0.584	0.79	0.413

^aBurning rate at 6.9 MPa. ^bResponse function at 6.9 MPa and 300 Hz.

In this table NWR stands for Naval Weapons Research propellant. Figure 1 contains a sample ballistic pressure trace of Motor 4 from Table 1. In this figure, a stable pulse can be seen around 1 s and an unstable pulse around 2 s. Numerous conclusions were reached from these first 23 motor firings.

A. Pressure

As chamber pressure is increased, the margin of linear stability decreases and higher pressure motors are more susceptible to pulsed instability at lower pulse amplitudes. The severity of the instability appears to be independent of mean chamber pressure.

B. Stability Additives

Stability additives were very effective in preventing nonlinear pulsed combustion instability. However, differences between different stability additives were not evident. Figure 1 shows how effective additives can be. In this figure, both motors are identical except one has 1% ZrC and one does not. In fact, the one with stability additive was actually pulsed harder. Stability additives suppress instabilities by increasing particle damping and/or reducing the propellant response over a broad

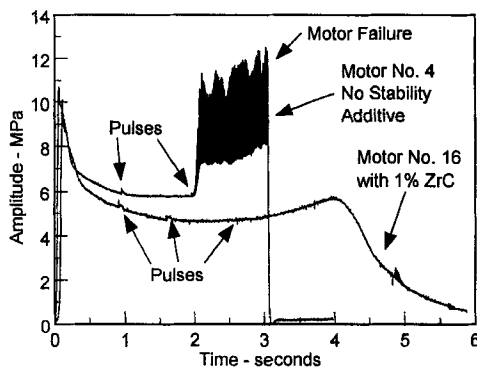


Fig. 1 Comparison of Motor 4 without stability additive and Motor 13 with 1% ZrC stability additive.

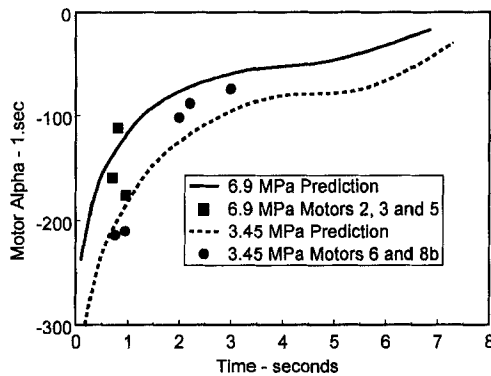


Fig. 2 Measured and predicted star Aft 300-Hz motor alphas comparison with theoretical predictions.

frequency range. These effects reduce nonlinear instability tendencies in motors with additives.

C. Stability Calculations

Stability calculations compared very favorably with motor data, especially for one-dimensional, high length-to-diameter (L/D) motors without metal combustion. An example of this is shown in Fig. 2. It is also important to note that the margin of linear stability decreases with burning time.

D. Geometry

Motor geometry comparisons were made that indicated that a star forward geometry was more stable than a star aft geometry. This conclusion was validated both experimentally and theoretically. This implies that an increase in burning surface area in the aft end reduces the margin of stability. In addition, the constant cross section geometries (full star and full cylinder) were both observed to be very sensitive to pulsing and resulting instabilities.

E. Pulsing

Pulsing motors can give quantitative data, i.e., margin of stability. Routine pulsing of developmental motors is encouraged. High pulse amplitudes can excite instability in an otherwise stable motor. Pulsing a low-pressure motor is easier than pulsing a high-pressure motor, especially at low pulsing levels where the pulser burst pressures are similar to the motor chamber pressures.

F. Nonlinear Effects

Pulsing susceptibility of reduced smoke systems is related to linear, high-frequency combustion response characteristics. Both growth and decay alphas are independent of pulsing amplitude for linear but not nonlinear systems. The susceptibility to pulsed instability increases with decreasing gas mean flow velocity.

Finally, the magnitude of the DC or mean pressure shift is linearly proportional to the limiting amplitude.

II. Motor Firing Details

In the design community, there has been a concerted effort to develop tactical solid rocket systems, which have greatly reduced plume signatures. The combustion instability of these systems is of particular concern because the metal oxide particles are absent that provide acoustic damping. Some of the suggested propellants for these systems have considerably less energy. One way to gain some of the performance lost is to increase the motor operating pressure. Fortunately, many modern rocket motors use composite cases that have excess capacity to support hoop stress and can handle the added pressure without a weight penalty. However, as indicated, some of the data generated and analysis performed during the course of this program indicated a possible increase in instability tendencies at high motor operating pressures. This was also shown in past studies.⁵⁻¹⁰ The loss of particulate damping and the higher operating pressures may cause combustion instability to be a problem in future motors. Therefore, it was decided to fire and pulse additional motors concentrating on pressure effects and stability additives. In addition, one area where the preceding data were lacking was determining the actual pulsing level required to pulse a motor into nonlinear combustion instability. To examine this level it was decided to vary the pulse amplitude. The motor firing results and analysis for varying pressure, stability additive, and pulsing levels for 10 motors fired from 1994 to 1997 are described next.

A. Propellants

Table 3 shows the two different formulations used during these motor firings. Unfortunately, these propellants differ in more than one way, making conclusions

Table 3 Propellants

Ingredient	A, reduced smoke with additive (approximate weight, %)	B, reduced smoke no additive (approximate weight, %)
AP	82.0	86.5
RDX	4.0	—
HTPB	12.5	13.0
Carbon Black	0.5	0.5
ZrC	1.0	—
Burning Rate at 6.9 MPa	0.678 cm/s	0.879 cm/s
Exponent at 6.9 MPa	0.360	0.392
Response at 6.9 MPa	1.55	1.80
Propellant density	1.80 g/cm ³	1.72 g/cm ³
Flame temperature at 6.9 MPa	2713°C	2748°C
Speed of sound at 6.9 MPa	1083 m/s	1077 m/s

about formulation effects difficult. There is one important difference, however, from which conclusions can be drawn. Propellant A contains 1% of the proven stability additive, zirconium carbide (ZrC). In past motor firings it was difficult to pulse a motor containing a stability additive into instability; more on this will be discussed later in this chapter.

B. Test Matrix

Table 4 shows the testing matrix for the 10 motor firings. All motors fired in the program were 12.7 cm in diameter and 170 cm in length. In addition, all motors were typically pulsed two to three times during burn. Motors 1 and 2 both failed during firing. Motors 3–5 were identical except for the nozzle throat size that caused the chamber pressure to vary. These three used the reduced smoke propellant without additive, propellant B, and were full cylinder geometries. The purpose of these motors was to look at the effect of pressure on nonlinear pulsed instability. All three motors were pulsed with similar pulsing levels, three times during burn. Motors 6–9 were star aft motors loaded with propellant A given in Table 3. Motor 10 was a full cylinder motor containing propellant B. The purpose of Motors 6–9 was to see what effect pulsing amplitude would have on the stability of the motors. Motors 6 and 7 were pulsed at 5 and 3% levels at 33 and 66% of the web burned. Motors 8 and 9 were pulsed at 10 and 6% levels. A pulse of 3% means that the desired pulse amplitude was to be 3% of the current chamber pressure in the motor. Because of uncertainties in pulsing motors, the exact desired amplitudes were not always obtained; this will be discussed later. To look at effects of increasing motor pressure, Motors 6 and 7, with the light pulses, were fired at mean chamber pressures of 6.9 and 10.3 MPa, respectively. Likewise, Motors 8 and 9, with the hard pulses, had chamber pressures of 6.9 and 10.3 MPa as well. The Intent of Motor 10 was to repeat the second firing of the previous year's motor firing, Motor 4, but with added instrumentation.³

C. Pulsers

The standard NAWCWD pulsers were used on the firings.^{1–4} By using the results of subscale testing and past motor firings, the pulsers were sized to give the desired pulse amplitude. The subscale results were scaled by knowing the motor volume and pressure and choosing a laboratory pulser baseline that was closest to the test conditions. The pulser was then fine-tuned by adjusting the charge amount to motor pressure, gas density, and volume conditions.² A schematic of the pulser is shown in Fig. 3. The pulser pressure gauges were used on some of the early motor firings and during pulser subscale testing. The final pulser parameters used during these tests are shown in Table 5.

D. Instrumentation

Each motor was instrumented with either two or three water-cooled Kistler 211B2 piezoelectric quartz and one low-frequency strain gauge-type pressure transducer. Also mounted on the motor were two or three pulsers and the igniter. All data were recorded at 20,000 samples/s with a 16-bit A/D converter with a 10,000 Hz antialiasing filter, recorded on FM Wide Band I tape with one

Table 4 Motor test matrix

Motor no.	Firing date	Pressure, MPa	Propellant	Geometry	Case hardware	Comments
1	1994	20.7	RS with additive	Star aft	Light	Motor failed
2	1995	20.7	RS with additive	Star aft	Light	Motor failed
3	1996	3.45	RS	Full cylinder	Heavy	Pressure effects
4		10.3	RS	Full cylinder	Heavy	
5		13.8	RS	Full cylinder	Heavy	
6	1997	6.90	RS with additive	Star aft	Light	Enhanced instrumentation, stability additives, pulsing magnitudes, and geometry effects
7		10.3	RS with additive	Star aft	Light	
8		6.90	RS with additive	Star aft	Light	
9		10.3	RS with additive	Star aft	Light	
10		10.3	RS	Full cylinder	Heavy	

RS—reduced smoke propellant.

Table 5 Pulser details

Motor no.	Pulse no.	Time, s	Orifice, mm	Upstream diaphragm, mm	Downstream diaphragm, mm	Charge amount, g	Estimated pulser amplitude, kPa	Estimated pulser amplitude, % mean P	Estimated motor pressure, MPa
1	—	—	—	—	—	—	—	—	—
2	—	—	—	—	—	—	—	—	—
3	1	1.12	3.66	5.08	5.08	0.2	138	5.0	2.76
	2	2.15	5.05	—	5.08	0.1	93	3.0	3.10
	3	3.13	7.49	—	5.08	0.1	34	1.0	3.45
4	1	0.97	2.51	5.08	5.08	0.1	345	5.0	6.90
	2	1.92	7.49	—	5.08	0.1	259	3.0	8.62
	3	2.90	2.51	—	0.05	0.1	103	1.0	10.3
5	1	0.50	2.51	5.08	5.08	0.11	448	5.0	8.96
	2	1.00	7.49	—	5.08	0.11	310	3.0	10.3
	3	1.50	2.51	—	1.27	0.14	138	1.0	13.8
6	1	1.00	3.66	2.54	2.54	0.1	355	5.0	7.10
	2	2.00	3.66	2.54	2.54	0.1	197	3.0	6.55
7	1	0.865	3.66	2.54	2.54	0.1	535	5.0	10.7
	2	1.715	3.66	2.54	2.54	0.1	306	3.0	10.2
8	1	1.00	2.51	5.08	5.08	0.2	710	10.0	7.10
	2	2.00	2.51	5.08	5.08	0.2	393	6.0	6.55
9	1	0.865	2.51	5.08	5.08	0.2	1069	10.0	10.7
	2	1.715	2.51	5.08	5.08	0.2	612	6.0	10.2
10	1	0.97	2.51	5.08	5.08	0.1	345	5.0	6.90
	2	1.92	7.49	—	5.08	0.1	259	3.0	8.62

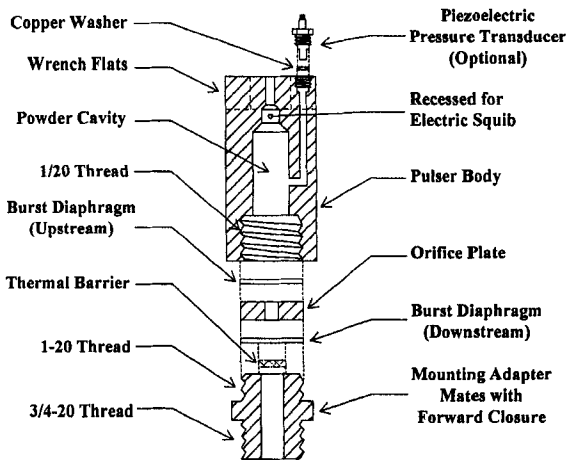


Fig. 3 Pulser schematic.

channel per tape track at 60 inches per second, and recorded on multiplexed FM tape. The digital sample rate per channel was limited by the A/D conversion system by the number of signals recorded and the duration of the test. Each high-frequency gauge was split three ways: 1) DC-coupled data scaled to the maximum expected pressure of the test, 2) low-gain AC-coupled or oscillatory data that was high pass filtered at 80 Hz with a typical gain of two, and 3) high-gain AC-coupled data that was high pass filtered at 80 Hz with a typical gain of 10. The high-gain signal provided good resolution of low level AC signals up to several hundred psi, the low gain gave good resolution of higher level AC signals up to 5000 psi and the DC data provided a comprehensive view of the data from zero to 10,000 psi. It is important to note that the DC pressures obtained by the Kistler gauges are not very accurate because of a slight drifting of the signal with time. The AC component is very accurate. The strain gauge pressure transducer was used for accurate ballistic pressure. The Kistler amplifiers were usually set at sensitivities of either 3.45 or 6.9 MPa/V depending on the expected pressure in the motor. Standard S-Video and 1600 frames/s movies were also taken of each firing at various angles. In addition, flash bulbs went off on the motor test stand coinciding with each pulse and ignition. In the figures that follow, the digital data were used and the data channel providing the highest resolution of the signal of interest was used. All transducers and data channels worked successfully although some of the high gain channels did saturate during oscillations. Signal saturation was expected and is the reason low-gain channels were also recorded.

Motors 1-8 had two high-frequency Kistler gauges mounted in the forward closure. This was identical to past motor firings.¹⁻³ For Motors 9 and 10, three identical Kistler gauges were mounted along the length of the motor. The first was located at the forward closure, like Motors 1-8. The second was located at the middle of the motor and the third was located very near the nozzle entrance at the aft end. The middle and aft gauges were installed by drilling a hole through the 4-cm case wall and on through the propellant. The propellant was then inhibited to prevent burning on the inside the hole. The purpose of these gauges was to examine wave structure and phase relationships of the acoustic oscillations in the motor.

E. Motor Failures

The first two motors fired in the test program ended in failure. Motor 1 failed 35 ms into the motor firing when the aft closure snap ring failed and the forward closure containing all of the instrumentation was injected, destroying all instrumentation, and the pulsers, and ruining the motor firing. The instrumentation worked long enough to show that the motor did reach 28 MPa when the failure occurred and the two Kistler gauges recorded the drop in pressure as the closure flew off the motor. High-speed photography at 1000 frames/s showed the failure. Because the failure occurred so early in burn, the pulser performance could not be verified.

Motor 2 was fired in the summer of 1995. Unfortunately, the pressure exceeded 48 MPa and explosively blew off the forward closure, all retaining hardware, and all pulsers and instrumentation. The structural failure of Motor 1 was caused by a faulty snap ring installation as described in the preceding; however, the poor installation may have only allowed the motor to fail at a lower pressure. The Motor 2 firing had significant reinforcing hardware added to hold the closures on. It is now believed that the added hardware only delayed and made the failure more severe.

The propellant A was initially believed to have a constant exponent up to 28 MPa. Unfortunately, it was later discovered that the burning rate curve at higher pressures was extrapolated data from low pressures. With the constant exponent curve, the motor was predicted to have a peak pressure of 29 MPa immediately after ignition and then return to a mean value of 21 MPa for the remainder of the firing. This pressure profile is now believed to take the propellant ballistics into a higher exponent region of the burning rate curve and the ballistic calculations now show that the motor could easily reach 41 MPa or greater. These two failures forced a lowering of the chamber pressures for future firings and a complete redesign of the motor hardware. This is why the heavy walled cases described next were fabricated. In addition, to minimize the ignition-erosive burning spike at the beginning of burn, the geometry was changed to a full cylinder configuration.

F. Motor Hardware

Reliable motor hardware is essential for successful firing and pulsing of motors, especially at higher operating pressures. Two types of motor cases and end closures were used, although the internal geometry of both types was identical. The difference between the cases was the wall thickness and fastening method of the forward and aft closure. Although both types were very heavy duty and reusable, one is extremely heavy duty. For the purposes of this paper, the really heavy cases that were 20 cm in diameter with screw-on end caps to hold the nozzle and forward closure assemblies were called heavy weight cases; see Table 4. The smaller, 17.8-cm-diam cases with snap-ring closures at both ends were called lightweight cases. The snap rings proved to be unreliable at the high motor chamber pressures. In the heavy weight motors, the threaded end cap design allowed for much greater strength and reusability over the previous snap-ring installation of the forward and aft closures. Table 4 indicates what type of case was used with each motor fired. Both cases had an inside diameter of 12.7 cm with an inside length of 170 cm. Both were made of stainless steel. In addition, the heavy walled cases were heat-treated. The heavy cases are good to 70 MPa whereas the light cases are good to 35 MPa. Both sets of hardware were completely reusable except for the nozzle. Each assembled

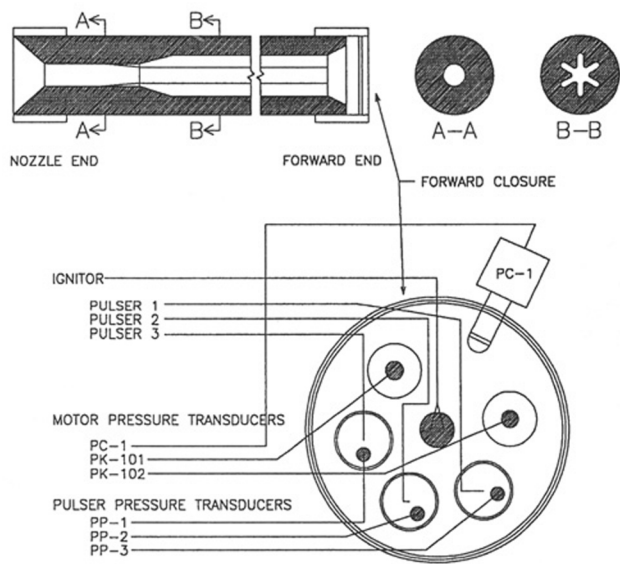


Fig. 4 Motor geometry and forward closure instrumentation.

motor weighed more than 230 kg and the cast propellant weight is approximately 23 kg. The forward closure, which held the instrumentation, pulsers, steady-state pressure gauge and igniter, and the aft nozzle assemblies, were compatible with both motor designs. Figure 4 shows the internal geometry for the star aft motor and a schematic of the instrumentation typically used for each firing. The pulser pressure gauges were only used on some of the firings.

III. Firing Results and Analysis of Motors 3–5

Motors 3–5 were fired in the summer of 1996. The principal intent of these motors was to examine the effect of increasing motor pressure on pulsed nonlinear combustion instability. Figure 5 shows the ballistic pressure traces of the three

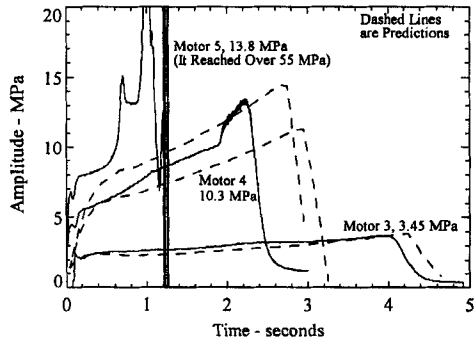


Fig. 5 Ballistic pressure of Motors 3–5 compared with predicted pressure.

motors with the ballistic prediction (dashed line) for each motor. The predicted pressures followed the experimental traces fairly well until the onset of instability. The instability results of each motor firing will be described next.

A. Motor 3

Motor 3 was a low pressure 3.45 MPa motor that was pulsed three times at approximately 25, 50, and 75% of the web burned or at 1, 2, and 3 s. Each of the pulses decayed rapidly and no oscillations were sustained in the motor after the pulses. Movies and video taken of the motor firing showed flashes in the plume during each pulse. In addition, there were two additional unplanned pulses because of debris passing out through the nozzle. The pulse amplitudes and decay rates were measured and will be presented along with the other motor data later in this chapter.

B. Motor 4

Motor 4 was a higher pressure motor whose pressure ranged from 5.5 to 11.7 MPa during a normal burn. It was pulsed twice, at 1 and 2 s, corresponding to 40 and 80% of the web burned. The pulse timing was incorrectly set so that the third pulse was after burnout. Motor oscillations decayed after the first pulse and grew after the second pulse. Figure 6 shows the DC-coupled high-frequency data of the firing. There are several interesting items shown in this figure. The first pulse, which decays, can be seen at around 1 s. Immediately after the decay, some tangential oscillations are observed. The motor is reasonably quiet until the second pulse, which triggers the motor into violent nonlinear combustion instability.

Figure 7 shows the first pulse whose nonlinear peaks match the first longitudinal mode of the motor that is 320 Hz. There is a very interesting observation concerning the high-frequency content of the pulse. Besides showing the nonlinearities of the pulse, it also corresponds to the first tangential mode of the case near the forward closure. These oscillations are observed in the traces of all pulses, both decaying and growing. Similar acoustic content was noted by Harris et al. in a recent work.¹⁰ At the forward end of the motor, the propellant stops 2.5 cm short of the closure containing the instrumentation and pulsers. The propellant face is inhibited. In this region of exposed case wall, the computed tangential mode is around 5000 Hz.

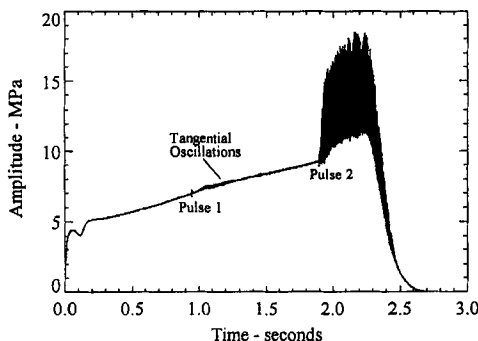


Fig. 6 DC-coupled high-frequency ballistic pressure trace of Motor 4.

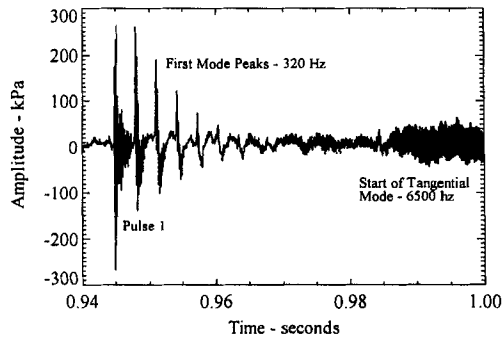


Fig. 7 Details of pulse 1 of Motor 4.

The first tangential mode is computed by

$$\text{Frequency} = \frac{0.586 * (\text{Gas Speed of Sound})}{\text{Diameter of Chamber}} \quad (1)$$

As mentioned, after pulse 1 decays, spontaneous oscillations are observed. Figure 8 shows some details of these oscillations. Frequency analysis of the oscillations (Fig. 9) strongly suggests that these oscillations are the first tangential mode occurring around the inside of the cylindrical propellant surface. The labels on the vertical axis represent time slices whereas the height of the peaks represent the amplitude of the oscillations at a given frequency. In the waterfall plot, the initial pulse can be seen containing many modes from the first longitudinal harmonic up to 7000 Hz. The pure tangential oscillations are seen next. Unlike the tangential oscillations noted, whose frequency is constant, these show the traditional decreasing frequency shift as the oscillation progresses, from 6700 to 6400 Hz. The computed variation in frequency between 0.9 and 1.3 s in burn is from 6847 to 6357 Hz using Eq. (1) and the properties from Table 3.

The second pulse is shown in Figs. 10 and 11. An initial disturbance grows from an initial pulse of around 345 to 6900 kPa in less than 10 cycles. In these two figures the DC component of the signal has been taken out by digitally high passing the data above 80 Hz. This serves two purposes: 1) the DC pressure level

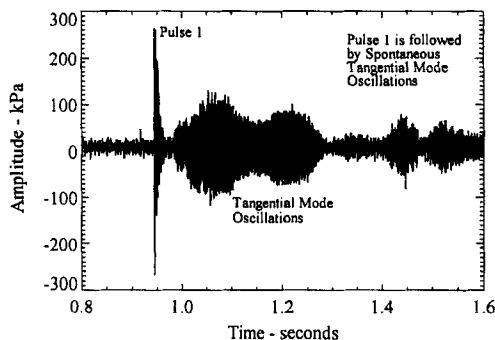


Fig. 8 Details of spontaneous oscillations after pulse 1 of Motor 4.

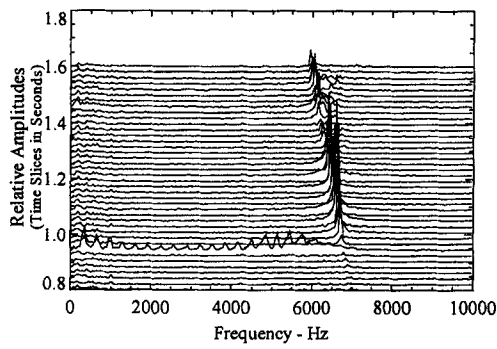


Fig. 9 Frequency analysis of pulse 1 and following tangential oscillations for Motor 4.

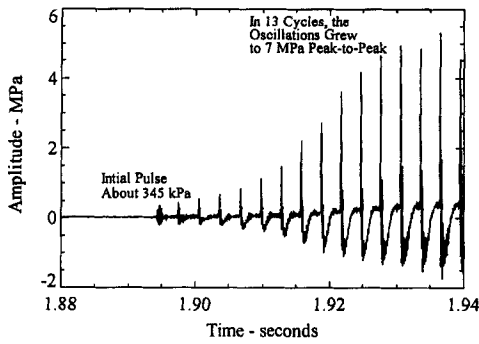


Fig. 10 Details of pulse 2 of Motor 4.

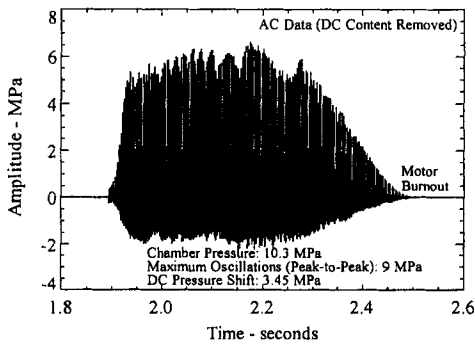


Fig. 11 Limiting amplitude oscillations of pulse 2 of Motor 4.

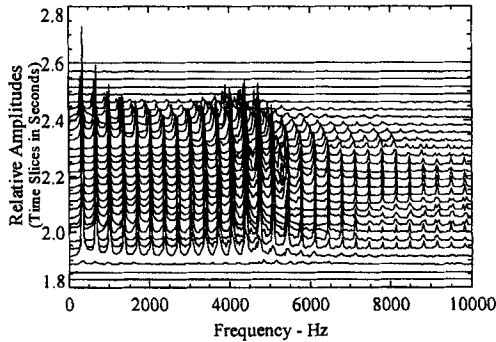


Fig. 12 Frequency analysis of limiting amplitude oscillations of pulse 2 of Motor 4.

is changing very rapidly making determination about the AC component difficult, and 2) it eliminates some minor 60 Hz signal noise that can distort the true data. A frequency analysis of the violent limiting amplitude oscillations of Fig. 11 is shown in Fig. 12. The first mode of 330 Hz is the most dominant and 20 more harmonic modes are present. Notice the larger tangential mode peaks at around 5000 Hz because of longitudinal mode coupling with tangential oscillations around the front closure.

C. Motor 5

Motor 5 was the highest pressure motor whose pressure ranged from 8.3 to 13.8 MPa during a normal burn. Although the motor was scheduled to be pulsed three times, spontaneous tangential oscillations prevented the analysis or detection of any of the pulses. The motor went spontaneously unstable at around 0.5 s and, after some acoustic gyrations, failed at just over 1 s of the planned 2-s burn. Figure 13 documents the probable series of events that led to failure. The oscillations quickly increased to 6.9 MPa peak-to-peak with a 13.8 MPa DC pressure shift. At this point, it is believed that the nozzle partially failed. The resultant nozzle assembly bounced around in the motor until it blocked the nozzle at about 0.95 s. The pressure then increased dramatically to 55 MPa. At this pressure the nozzle

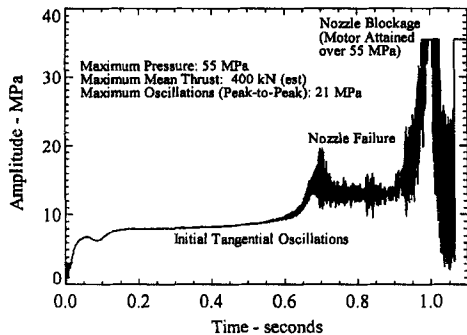


Fig. 13 DC-coupled ballistic pressure of Motor 5.

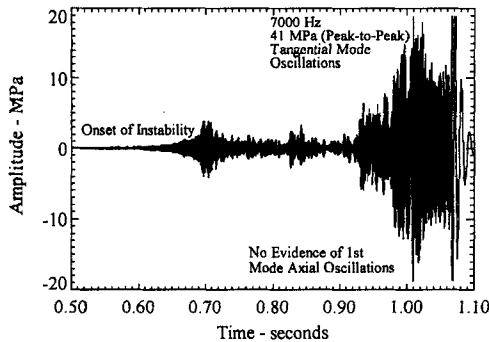


Fig. 14 Details of initial oscillations that led to Motor 5 failure.

blockage was ejected along with the nozzle assembly and the instantaneous large aft end opening with 55 MPa chamber pressure caused the mean thrust of the motor to increase tenfold to around 400 kN. A second possible scenario that caused the massive overpressurization deals with the fluid dynamics of the violent tangential mode oscillations. It is possible that these oscillations caused a “tornado” to form down the axis of the motor. This fluid dynamic vortex prevented the mean flow from escaping the motor through the nozzle because of a reduction of the effective nozzle diameter. The mean chamber pressure increased until the nozzle assembly was ejected from the motor. Like the previous scenario, the instantaneous large nozzle opening with 55 MPa chamber pressure increased the mean thrust of the motor to around 400 kN. Whatever the reason, the acoustic oscillations exceeded 21 MPa peak-to-peak and mean chamber pressure exceeded 55 MPa. The excessive thrust and violent oscillatory behavior sheared the four 16-mm grade five bolts holding the motor to the test stand. The motor left the test stand and traveled about 150 m up over a 15-m-high earthen berm and into the surrounding desert. Amazingly, no damage was done to the test stand and the motor hardware except the forward closure and instrumentation. The motor case and end caps were scratched but undamaged. Figure 14 is the AC component of the oscillations and shows the onset of oscillations and, again, the first tangential mode was the culprit. Figure 15 shows the frequency analysis of the oscillations. The downward trend in

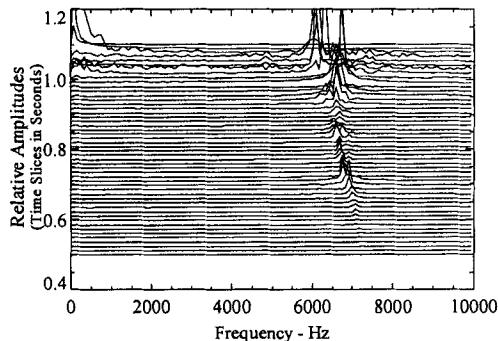


Fig. 15 Frequency analysis of spontaneous tangential mode oscillations of Motor 5.

frequency from 7000 to 6600 Hz at around 1 s is followed by an actual increase in frequency. This occurs when the motor pressure increases dramatically, resulting in increased chamber temperatures and an upward frequency shift. The peaks at 1.1 s are because of the movement of the motor as it launched.

D. Linear Stability

One thrust of the overall program was to develop an improved understanding of nonlinear (pulsed) combustion instability. Linear stability aspects were studied on this program because the nonlinear (pulsed) instability of a motor is believed related to its linear stability. The linear stability of a motor is characterized by its exponential decay (stability) or growth (instability) of pressure oscillations as follows:

$$\hat{P} = P_0 e^{\alpha t} \quad (2)$$

The rate of growth (or decay) is expressed in terms of the alpha in this equation. If a pressure perturbation in the motor is damped, the alpha is negative and the motor is linearly stable. If the perturbation excites a growth of pressure oscillations, the alpha is positive and the motor is linearly unstable. Nonlinear instability, on the other hand, deals with the response to large or finite-amplitude (nonlinear) types of disturbances.⁵⁻¹⁰ Since knowledge of the linear stability was required, this facet of the program presented an opportunity to predict the linear stability of several motors and to make comparisons with linear experimental data that might be obtained under some test conditions. The Solid Propellant Performance computer program (SPP) and the one-dimensional Standard Stability Prediction computer program (SSP) were used to predict the motor performance and linear stability of the motors.^{11,12} The code's inputs include motor geometry, propellant ballistics, and the response of the propellant. The ballistic predictions shown in Fig. 5 were performed using the SPP code. Figure 16 shows the pressure coupled response of the two propellants given in Table 3 at 6.9 MPa as measured by the T-burner.^{13,14} Response measurements were also made at other pressures corresponding to motor conditions.

Figure 17 is a 150–450 Hz digitally band-passed, filtered trace of pulse 1 of Motor 4; see Fig. 7. This signal is used to measure the linear decay of the fundamental

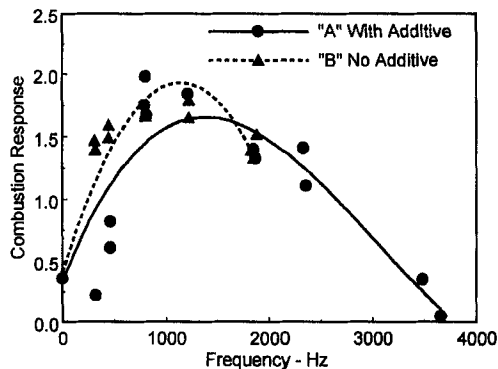


Fig. 16 Combustion response for A and B propellants at 6.9 MPa.

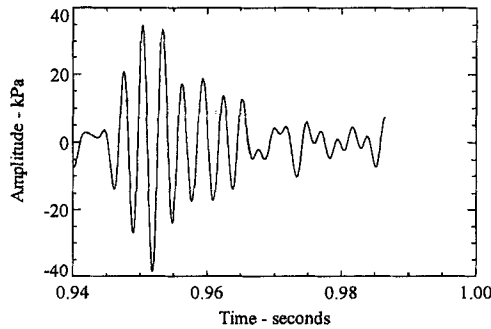


Fig. 17 150–450 Hz bandpassed trace of pulse 1 of Motor 4.

first longitudinal mode produced by the pulse. The top graph in Fig. 18 plots the absolute value of the filtered peaks of Fig. 17 on a log scale vs time. The slope of this line is the decay alpha [Eq. (2)] and can be directly compared to the stability predictions. The bottom part shows the frequency of the decay, 330 Hz. Table 6 contains various parameters measured for firings of Motors 3–5, including the pulsing details, measured values of the decay alphas (like from Fig. 17), linear growth alphas, DC pressure shifts, and limiting oscillatory amplitudes. Figure 19 compares the predicted motor stability computed by the SPP/SSP program with the measured experimental data given in Table 6. The comparison is surprisingly good. The magnitudes of the total stability alphas produced by SPP/SSP and the trend of the data both agree with the predicted values. This type of comparison is similar to that seen in past studies.¹

There is an interesting observation worth noting about the growth rates, both of the first mode longitudinal oscillations in Motor 4 and in the spontaneous first mode tangential oscillations of Motor 5. The growth rate of both is linear. Figures 20 and 21 show this very nicely. Figure 20 is a plot of the growth rate amplitudes, band-pass filtered between 150 and 450 Hz. The linear growth rate is 109 1/s. Figure 21 shows the same for the tangential oscillations except band-pass filtered between 3000 and 9000 Hz. Again the growth rate is linear and has a value of 22 1/s. These data should be of interest to combustion instability modelers trying

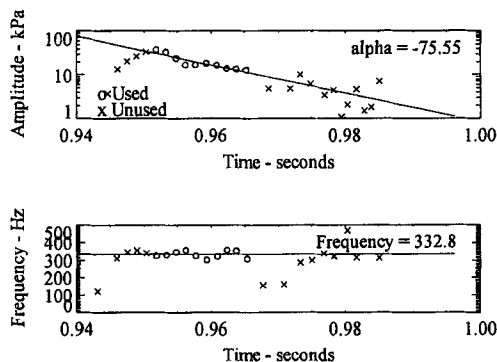


Fig. 18 Decay alpha and frequency determination of pulse 1 of Motor 4.

Table 6 Summary of pulse data for Motors 3–5

Motor no.	Pulse no.	Parameter							
		Chamber pressure, MPa	Estimated pulse, kPa	Pulse amplitude, kPa	Normalized pulse, % (planned)	Time, s	Measured alpha, 1/s	DC pressure shift, MPa	Limiting amplitude, MPa
3	1	.6	138	345	13.3 (5.0)	1.09	−129	—	—
	2	.2	93	172	5.4 (3.0)	2.12	−119	—	—
	2a (Injecta)	3.2	—	62	1.9	2.24	−159	—	—
	3	3.4	34	159	4.7 (1.0)	3.11	−115	—	—
	3a (Injecta)	3.4	—	28	0.8	3.15	−111	—	—
4	1	7.6	345	345	4.5 (5.0)	0.95	−75	—	—
	2	10.0	259	345	3.5 (3.0)	1.89	+109	3.45	9.0
5	Spontaneous	9.0	—	—	—	0.50	+21	6.9	9.0

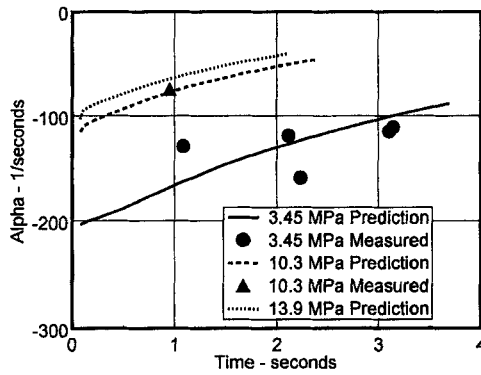


Fig. 19 Stability comparison of stable pulses for Motors 3-5.

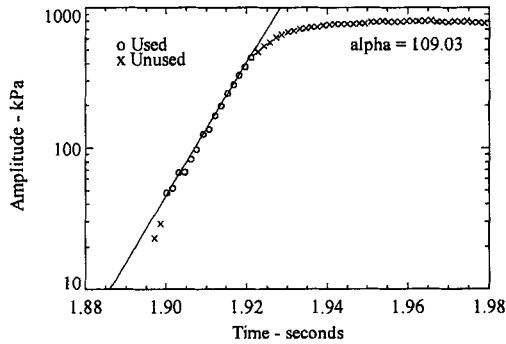


Fig. 20 Growth rate of oscillations from pulse 2 of Motor 4.

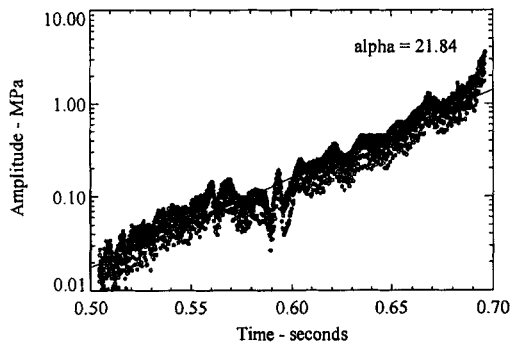


Fig. 21 Growth rate of spontaneous tangential oscillations of Motor 5.

to understand the important mechanisms involved during these important initial periods of instability.

E. Nonlinear Instability

Why does the severity of the oscillations, both the nonlinear longitudinal and tangential, increase as the motor operating pressure is increased? Two possible explanations will be discussed. First, if one examines linear stability theory it is possible to see what driving and damping factors change as pressure is increased in a rocket motor. Table 7 illustrates this point; in this table are the individual terms that make up the linear stability prediction shown in Fig. 19 from the SPP/SSP linear stability computer program.^{11,12} Velocity coupling is not included because it has a small value and varies little in magnitude. Although the driving because of pressure coupling decreases with pressure, the decrease in combined damping from the flow turning, and especially nozzle damping, more than offsets the pressure coupling decreases and result in a motor that has a much lower margin of linear stability. In fact, the 13.8 MPa motor is more than two times less stable than the 3.45 MPa motor. It is widely held that the nonlinear stability is related to the linear stability.¹⁻¹⁰ The damping changes can be explained in large part by a smaller nozzle opening causing a decrease in nozzle damping and a lower mean velocity of the chamber flow when the motor is operated at higher chamber pressures that reduces the flow turning losses.

Another approach at understanding the effect of pressure in the stability of the motors is examining what effect pressure has on the acoustic boundary layer and this interaction with the propellant response. A study undertaken by Beddini and Roberts analyzed the response function produced by both pressure coupling and oscillatory crossflow conditions (velocity response) within the acoustic boundary layer near a propellant surface.¹⁵⁻¹⁷ Their computational results (conducted with several simplifying assumptions) indicated that the velocity response function is of a similar form to that assumed by Baum and Levine^{18,19} and Levine and Culick,²⁰ i.e., negligible response below a threshold velocity or pressure amplitude, followed by a nearly linear dependence on the absolute value of acoustic velocity or pressure amplitude above the threshold. The mechanism producing this response was found to be enhanced thermal diffusivity caused by turbulent transition of the acoustic boundary layer. The velocity response was found to depend on operating conditions such as mean chamber pressure and frequency. As mean chamber pressure was increased, it was found that the local acoustic pressure amplitude required to exceed the threshold condition decreased appreciably (Fig. 22) indicating that a motor that does not exhibit a local velocity response at lower chamber pressures may experience a significant nonlinear response (in comparison with pressure coupling) at elevated chamber pressures. According to Beddini, this type of response might require additional damping sources at elevated chamber pressures to ensure motor stability.¹⁷ Figure 23 shows a representation of the nonlinear response variation with acoustic velocity levels at three motor pressures. The higher the pressure the lower the threshold velocity and the higher the response at a particular acoustic oscillatory level. In addition, as motor pressure is increased the mean velocity in the motor goes down, pushing the operating condition farther to the right and increasing the nonlinear response of the propellant. Increasing pulse amplitude will also cause an increase in the response.

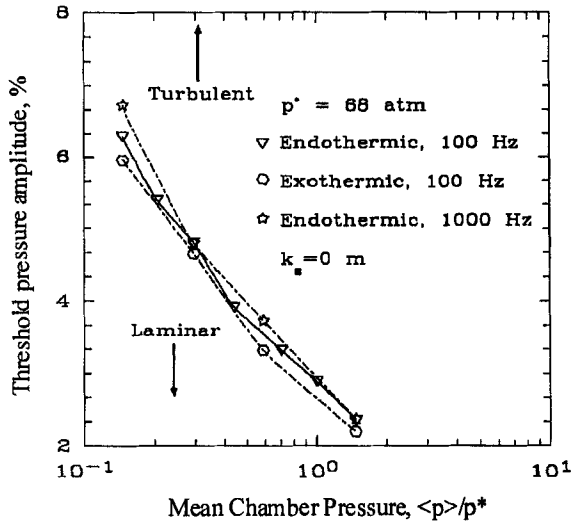


Fig. 22 Threshold pressure amplitude vs mean chamber pressure.

In a recent unpublished study by the author, which applied the nonlinear model of Levine and Baum,^{18,19} increasing pressure did not tend to increase a motor's susceptibility to nonlinear combustion instability. However, in this study the threshold velocity was assumed zero and the nonlinear velocity coupled response was held constant with pressure. It is the understanding of the author that the nonlinear velocity coupled response is a strong function of pressure and not having this dependence in his work yielded incorrect correlations between pressure and combustion instability. Unfortunately, experimental or empirical functional dependencies of threshold velocity and velocity coupling with pressure are currently not available, making exact nonlinear combustion instability predictions difficult. Experiments are needed to evaluate threshold velocities and nonlinear combustion response to apply the nonlinear combustion motor stability models and obtain accurate qualitative data.

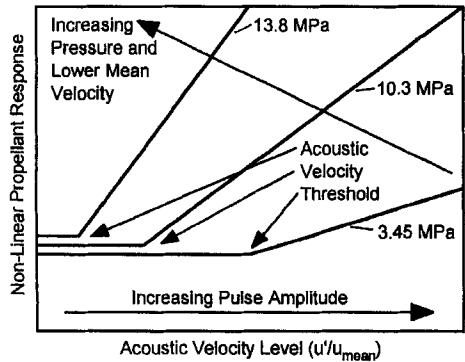


Fig. 23 Nonlinear response variation with acoustic velocity and motor pressure.

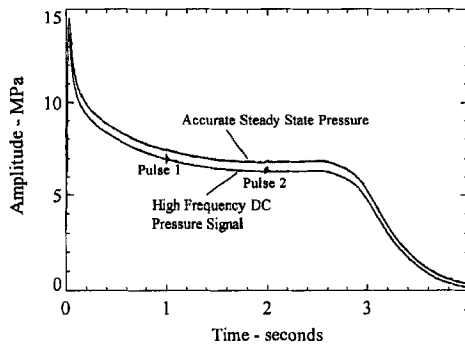


Fig. 24 Motor 6 ballistic pressure.

The preceding discussions are not necessarily opposed to each other and in many cases support each other. They address the problem of instability with differing degrees of sophistication and emphasis. What is important is that they all indicate that increasing pressure can lead to more severe instability in solid rocket motors. It is hoped that by understanding the mechanisms that logical experiments can be performed and parameters can be varied to control combustion instability in motor systems that operate at higher pressures.

IV. Firing Results and Analysis of Motors 6–10

Motors 6–10 were successfully fired during the week of August 1997. Figures 24–28 show the DC-coupled ballistic pressure of each motor. Included on Figs. 24 and 25 are two pressure traces. One is the high-frequency DC-coupled signal recorded from the Kistler gauges; the other is from the low-frequency strain-gauge-type transducer that indicates the actual pressure level in the motor. Both were included to illustrate that although piezoelectric gauges yield excellent AC data, their DC data are not as good because of drifting of the gauge with time. Detailed plots shown later will indicate the true AC noise levels and show much greater detail of the pulses. The behavior of each motor fired is summarized next.

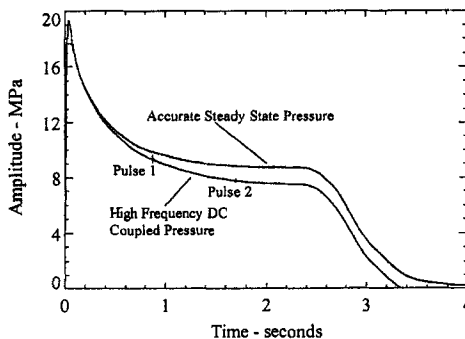


Fig. 25 Motor 7 ballistic pressure.

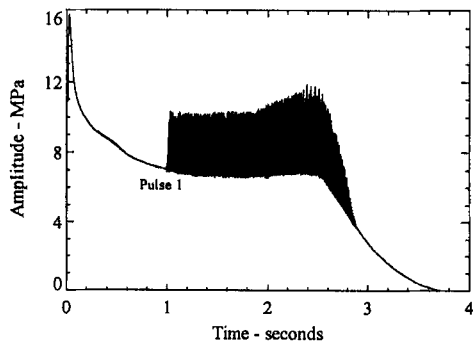


Fig. 26 Motor 8 ballistic pressure.

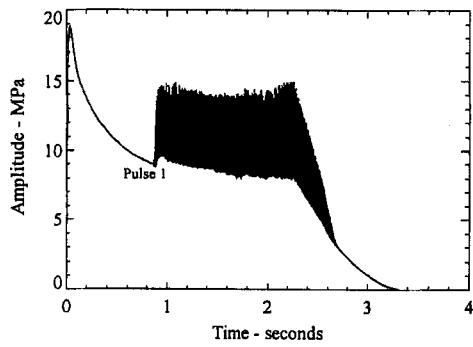


Fig. 27 Motor 9 ballistic pressure.

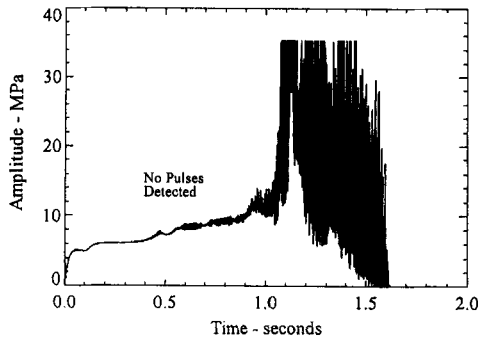


Fig. 28 Motor 10 ballistic pressure.

Motor 6: This motor had a chamber pressure of 6.9 MPa, star aft geometry, and was loaded with propellant A. It was pulsed twice lightly at 3.9 and 3.1% levels (276 and 205 kPa, respectively) and both pulses decayed, i.e., no oscillations resulted.

Motor 7: This motor had a chamber pressure of 10.3 MPa, star aft geometry, and was loaded with propellant A. It was also pulsed twice lightly at 4.7 and 2.9% levels (442 and 220 kPa, respectively) and both pulses decayed.

Motor 8: This motor had a chamber pressure of 6.9 MPa, star aft geometry, and was loaded with propellant A. This motor was pulsed hard at 9.7% or 689 kPa. The motor went into violent nonlinear longitudinal oscillations, i.e., the oscillations grew to a limiting amplitude and the chamber pressure was elevated.

Motor 9: This motor had a chamber pressure of 10.3 MPa, star aft geometry, and was loaded with propellant A. This motor was pulsed hard at 10.2% or 959 kPa. The motor went into violent nonlinear longitudinal oscillations.

Motor 10: This motor had a chamber pressure of 13.45 MPa, full cylinder geometry, and was loaded with propellant B. This motor went spontaneously unstable before pulsing occurred and experienced large DC pressure shifts and reached chamber pressures in excess of 41 MPa before the nozzle insert was injected.

Table 8 contains specifics on the pulsing results. Examining the normalized pulse column, it can be seen that the actual pulsing levels compare quite favorably with the estimated pulse amplitudes. For Motors 3–5 the pulsing agreement was not as good; see Table 6. Figure 29 shows the AC data for pulse 2 of Motor 6. This was an interesting pulse, as it appeared that the motor almost went unstable. In this figure, some of the dark area immediately after the pulse is probably transducer ringing because of the explosive pulse. Figure 30 shows the DC data for pulse 1 of Motor 8. The pulse and resultant oscillations are nonlinear and steep fronted. In around 11 cycles, the oscillations reached a limiting amplitude of around 3.5 MPa. The limiting amplitude eventually increased to a value of 5.5 MPa as can be seen in Fig. 31, showing all AC data for the Motor 8. Figure 32 shows some tangential oscillation detail toward the beginning of Motor 8 and marked in Fig. 31. These oscillations are low in magnitude, but do contain frequencies and frequency shifts indicative of tangential oscillations. The following sections will describe some of the observations of the motor firings, including stability boundaries, stability additives, waveform shape and phase relationships, frequency content, and Motor 10 failure analysis.

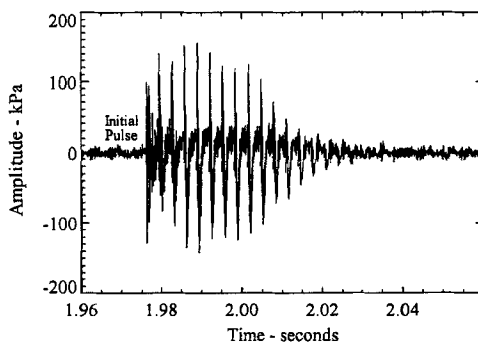


Fig. 29 Details of pulse 2 of Motor 6, AC data.

Table 8 Summary of pulse data for Motor 6–10

Motor no.	Pulse no.	Parameter							
		Chamber pressure, MPa	Estimated pulse, kPa	Pulse amplitude, kPa	Normalized pulse, % (planned)	Time, s	Measured alpha, 1/s	DC pressure, MPa	Limited amplitude, MPa
6	1	7.1	355	276	3.9 (5.0)	1.0	−125	—	—
	2	6.6	197	205	3.1 (3.0)	2.0	−92	—	—
7	1	9.4	535	442	4.7 (5.0)	0.865	−87	—	—
	2	7.6	306	220	2.9 (3.0)	1.715	−50	—	—
8	1	7.1	710	689	9.7 (10.0)	1.0	—	0.69	5.52
9	1	9.4	1069	959	10.2 (10.0)	0.865	—	1.38	6.90
10	1	10.7	345	—	— (3.0)	0.97	—	>28	>35

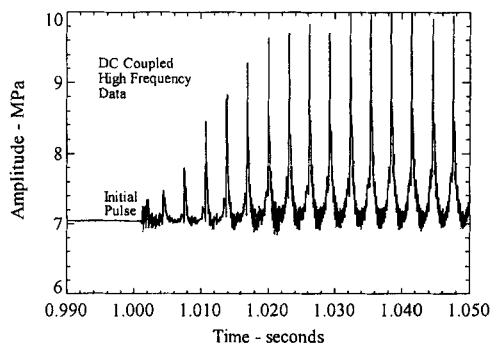


Fig. 30 Details of pulse 1 of Motor 8, DC-coupled data.

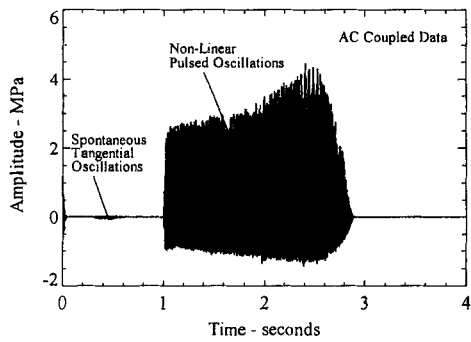


Fig. 31 AC-coupled data of Motor 8.

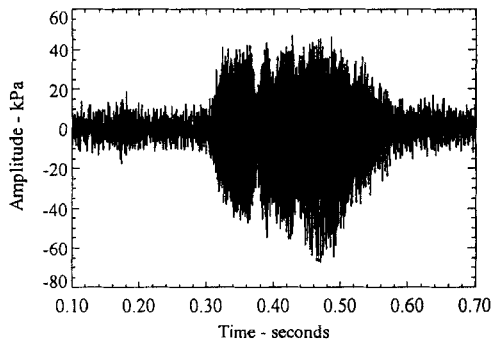


Fig. 32 Low-level spontaneous tangential oscillations of Motor 8.

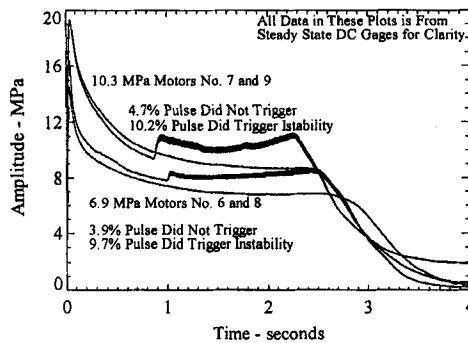


Fig. 33 Examples of pulsing threshold.

A. Stability Boundaries

One aspect looked for in past motor firings was the pulsing level required to trigger a motor into nonlinear instability. In Motor 6, a 3.9% pulse did not trigger the motor. A 9.7% pulse in an identical Motor 8 did. This behavior was repeated in the higher pressure Motors 7 and 9, which had 4.7 and 10.2% pulses, respectively. Figure 33 shows this graphically by comparing the steady-state gauge outputs for Motors 6 and 8, and Motors 7 and 9, respectively. The steady-state strain-gauge-type transducer does not have the frequency response and, hence, the oscillatory levels shown by the gauge are much lower than they actually were, as was indicated in Figs. 26 and 27. These gauges were used in Fig. 33 for clarity, making the effects much easier to see. This type of data is very hard to obtain and will be very valuable in gaining understanding into the physics of combustion instability. A qualitative knowledge of what pulsing level is required to trigger a motor into limiting amplitude nonlinear instability should provide insight into the mechanistic behavior of this form of instability. Figure 34 shows real-time photographs of Motors 7 and 9, taken at the same time during burn after the onset of oscillation of Motor 9. The difference is obvious. The bottom motor in Fig. 34 experiencing instability has a much brighter plume signature.



Fig. 34 Comparison of Motors 7 and 9.

B. Stability Additives

In past motor pulsing activities it was very difficult to pulse motors into nonlinear instability when the propellant contained stability additives.² Motors 6–9 in this study had propellants that did have a stability additive, 1% ZrC. Motors 8 and 9 were both pulsed into instability with approximately 10% pulse levels. Although the exact propellant in the past studies was slightly different, the geometry, pressure, and pulse magnitudes were not. In the past studies, when the motors without additives did go unstable, the resulting oscillations were often very hard with large DC pressure shifts. In motors in this study, the oscillations were hard often exhibiting 5–7 MPa peak-to-peak oscillations. In some of the past motors without stability additives, the oscillatory levels were also near 7 MPa. However, the DC shifts in this study were much smaller, on the order of 1 MPa for the 6.9 MPa motor and 2 MPa for the 10.3 MPa motor. The past motors of similar geometry and operating pressure, but without stability additive, had DC shifts of 5–8 MPa. The presence of a stability additive may have the effect of reducing the DC shift once a motor does go unstable.

The motors in the past study containing stability additives were pulsed with similar and sometimes stronger pulses and yet did not go unstable. Why? As mentioned, one difference was the propellant, although both were AP/HTPB-reduced smoke propellants of similar rate and exponent, there was one important difference. The current propellant contained 4% 1,3,5-trinitro-1,3,5-triazacyclohexane (RDX). The presence of RDX making these motors more susceptible to pulsing is very speculative and more research should be performed.

C. Waveform Shape and Phase Relationships

By installing three gauges along the axis of the motor, it was hoped to gain insight into the phase, waveform shape, and frequency content of the acoustic oscillations. Figure 35 shows some of this detail. The onset of oscillations is shown for Motor 9 for all three high-frequency gauges. All three gauges were mounted very close to the motor cavity with no loss in signal response at the 20 kHz sample rate. To allow more readable comparison of the signals, the middle signal in Fig. 35 has an artificial offset of 3 MPa psi and the aft signal has an offset of 6 MPa. The gauges all use the identical timescale, making phase relationships possible. It is quickly noted

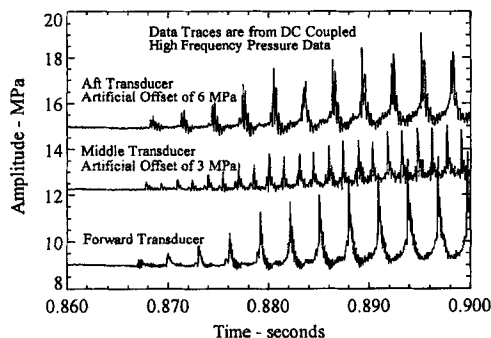


Fig. 35 Waveshape comparison for Motor 9.

that the aft gauge is 180 deg out of phase with the forward gauge. The middle gauge is 90 deg out of phase. The middle gauge also appears to have dominant harmonics at twice the frequency and half the amplitude compared with the forward location. This is expected because the oscillatory wave passes the midpoint twice for each cycle of oscillation. Because most of the longitudinal acoustic energy is conserved for a cycle of oscillation, the energy level or amplitude is half of the amplitudes at the ends of the motor. Also seen in this figure is the relative noise level before the onset of oscillations. Typical noise levels were sometimes less than 7 kPa out of 35 MPa.

D. Frequency Content

The frequency content of acoustic oscillations of Motor 9 can be see in Fig. 36. These plots are fast Fourier transform (FFT) plots of oscillations of the motor at the forward, middle, and aft locations at around 2 s after the onset of pulsed instability. Twenty-eight harmonics of the first longitudinal mode can be seen. The second harmonic and subsequent even harmonics are the dominant ones at the middle location. Also, the level of the oscillations is roughly half that of the forward and aft ends. This is expected based on the observed middle pressure signal in Fig. 35.

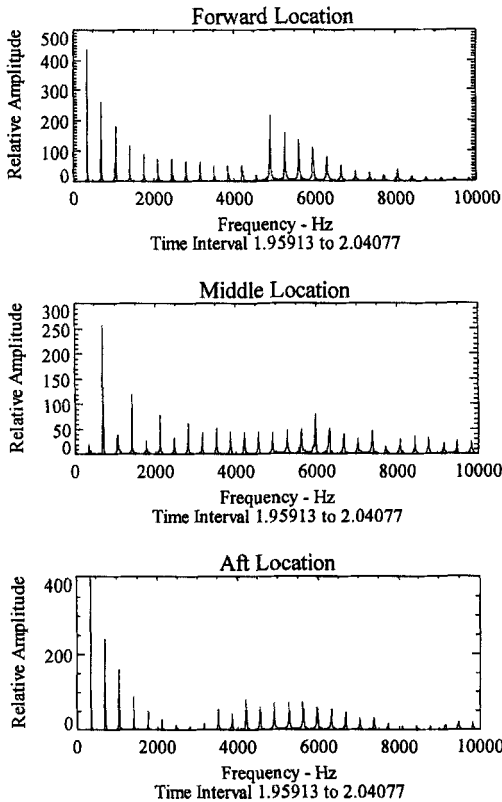


Fig. 36 Frequency analysis comparison of Motor 9.

The increase in magnitude of the modes around 6000 Hz is because of coupling between the longitudinal waveforms and the tangential modes of the motor as has been discussed and shown in Figs. 8 and 9. These have been seen in past motor firings as well.¹⁻⁴ However, the observed frequency content of the tangential modes at the three axial locations is different. In Fig. 36, the forward-end frequency peaks around 5000 Hz corresponds to the tangential mode of the case inner diameter. To explain this more fully, there is a 2.5-cm portion of exposed case wall at the forward end of the motor, which was to allow the pulses to be introduced into the motor chamber. The exposed end face of the propellant was inhibited. The observed frequency at the forward end is approximately the computed first tangential mode of the inner case diameter. Using Eq. (1), a value of 4970 Hz is computed. This mode remains roughly constant as the motor burns. Looking at the tangential oscillations at the middle shows the dominant frequency to be about 6000 Hz. This corresponds to the estimated frequency using Eq. (1) for the inner diameter of the motor at the middle. As expected, this peak does decrease in frequency as the motor burns as the inner diameter of the motor increases. The tangential coupling at the aft end (Fig. 36) is not as distinct. This may be because of effects of the nozzle and more dominant star geometry in the aft end; however, it is still there. The conclusion reached here is that the dominant nonlinear oscillations appear to couple with whatever the local tangential mode happens to be along the length of the rocket motor. In recent work by Harris and Champlain,²¹ the coupling relationships between various local oscillatory modes motors experiencing high amplitude oscillations was also reported by using very sophisticated data reduction techniques.

Figure 37 is an FFT of the oscillations occurring before the pulse of Motor 8 at around 0.5 s. Recalling Figs. 31 and 32, this time corresponds to tangential oscillations. It was originally thought that the tangential modes were excited by the pulses. However, the tangential oscillations shown here occurred without any apparent external stimuli. In Fig. 37, both first and second tangential modes are present. It is interesting to note that the second tangential mode was not observed when the nonlinear longitudinal oscillations occurred (Fig. 36). Finally, Fig. 38 is an FFT of Motor 6 before any pulsing occurs, to examine what low-level oscillations might be present. It shows frequency peaks near the first and second tangential modes. It is assumed that the multiple peaks corresponding to the first tangential mode around 4000 Hz are because the mode is very weak and probably

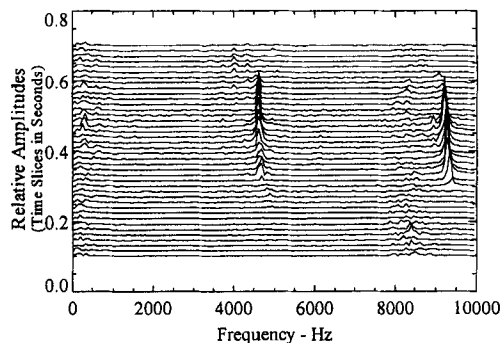


Fig. 37 Frequency analysis of Motor 8 from 0.1 to 0.7 s.

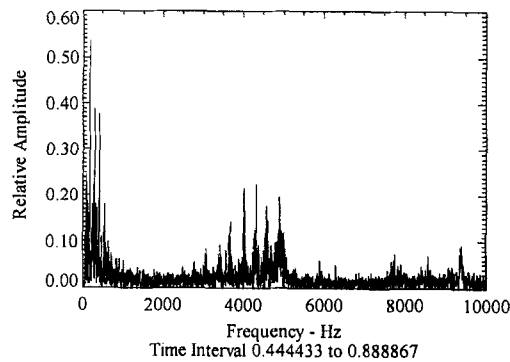


Fig. 38 Frequency analysis of Motor 6 before pulsing.

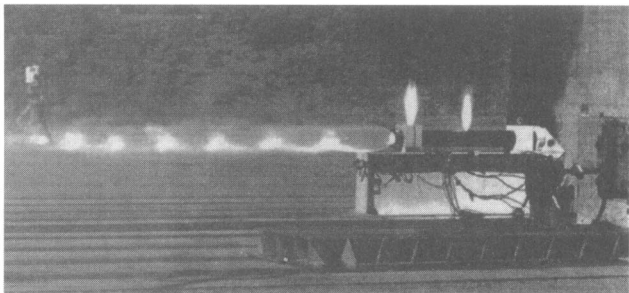


Fig. 39 Motor 10 after gauge failure.

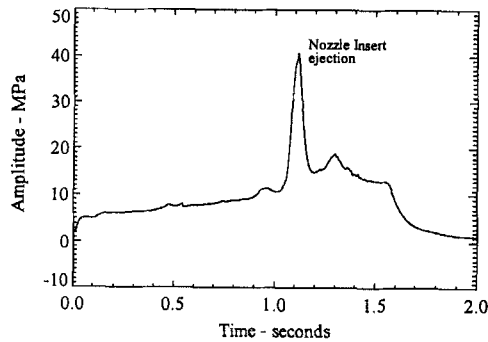


Fig. 40 Steady-state pressure of Motor 10.

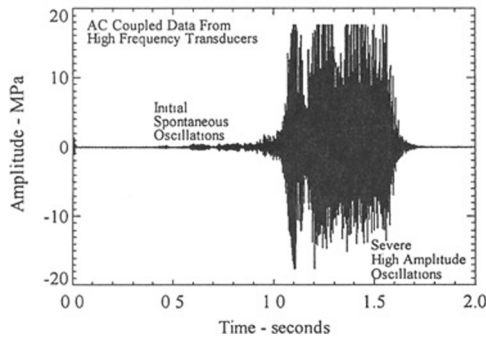


Fig. 41 High-frequency data of Motor 10.

not organized like the stronger tangential modes shown earlier in Fig. 37. Notice that the magnitude of oscillations is much lower than those in Figs. 36 and 37. The bulge around 200 Hz is believed to be caused by some 60-cycle noise causing peaks at 60, 120, 180 Hz, etc.

E. Motor 10 Failure Analysis

Motor 10 was a 10.3 MPa full cylinder with a propellant containing no stability additive and was to be pulsed at 5 and 3% levels. Three high-frequency Kistler gauges were mounted at the forward, middle, and aft end of motor. This was supposed to be a repeat of Motor 4 of the previous year in which the motor was stable to the first pulse and unstable to the second. The difference was enhanced instrumentation with the three gauges. Unfortunately, the motor went spontaneously unstable at about 1 s with the first tangential mode. This was followed by a DC shift in pressure to 41 MPa. At this elevated pressure, the nozzle insert was ejected and the middle and aft gauges blew off and were lost. However, good data were obtained up to this point. Figure 39 is a photograph taken during the firing after the gauges were lost. Notice the two vertical plumes where the transducers were located. Despite the failure, the case will be refurbished and reused. Figures 40 and 41 show the steady-state pressure and oscillatory pressure of the motor, respectively. Figure 42 shows an FFT waterfall plot of the entire firing. It is clearly

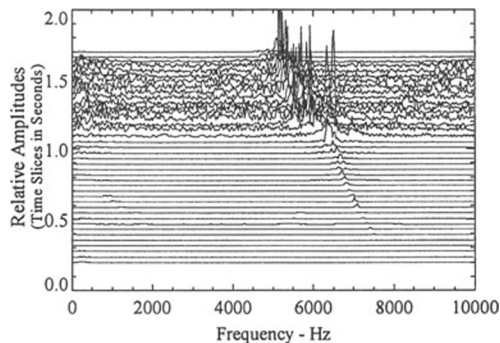


Fig. 42 Frequency analysis of Motor 10.

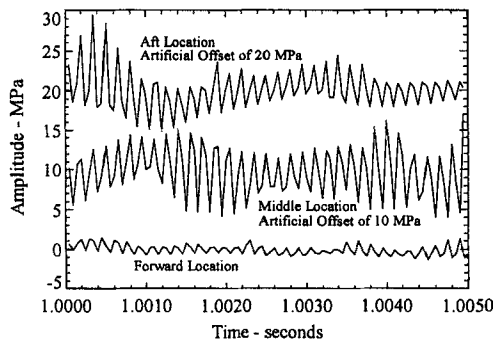


Fig. 43 Waveshape comparison for Motor 10.

seen from this figure that the motor experienced a tangential mode, which led to excessive DC pressure shifts and motor failure. Examining the other two AC gauges mounted at the midpoint and aft end showed similar behavior except they had much higher oscillatory amplitudes. Figure 43 shows this behavior by plotting all three gauges over a very short time period. Artificial offsets were added to the middle and aft pressure traces to allow easier visualization of the data. Although the noise level is very low, the resolution of the signal is poor because of the low sample rate, 20,000 Hz, compared to the frequency of the mode, 6000 Hz. This is only about 3 points per cycle. The long-period oscillations are probably because of dithering of the signal because of the low sample rates. However, it is interesting to note that the magnitude of the oscillations is much higher at the middle and aft locations. It is assumed that this is because the tangential oscillations are combustion driven, and because no propellant is located very near the forward gauge, the oscillations are lower there. Apparently, the magnitude of the tangential oscillations is very dependent on the axial position in the motor.

V. Conclusions

The purpose of this study was to examine the stability of motors as a function of pulse amplitude, geometry, pressure, and propellant formulation. Ten motors were carefully fired and pulsed and had extensive instrumentation to characterize their combustion instability behavior. Several significant observations were made from the data.

- 1) The susceptibility of a motor to go unstable with pressure was shown in a very clear and precise manner. As pressure was increased, it was not only easier to pulse a motor unstable, but also the inherent stability of the motors decreased with pressure.
- 2) Comparisons with the predicted stability were performed with favorable results. Both the magnitude and trends in the data agreed with the theoretical predictions.
- 3) Linear growth rates were observed for both the pulsed longitudinal and spontaneous tangential instabilities.
- 4) The triggering level was bracketed between two pulse amplitudes for two sets of motor firings at different pressures.
- 5) The function of additives to suppress triggered instability was questioned. It was possible to trigger two motors that used stability additives in their propellant.

The motors that did go unstable showed lower than expected DC pressure shifts. This may be because of the additive. In addition, the DC shifts appeared to increase slightly as motor pressure is increased.

6) Detailed acoustic waveform measurements were performed by mounting transducers at three locations along the length of the motor. It showed the expected phase, frequency, and amplitude characteristics as a function of axial location along the motor. Details of this data are available to those who need it. It should also be mentioned that the noise level for some of the data was less than 7 kPa out of 35 MPa (1 psi out of 5000).

7) Extensive frequency analysis was performed on the nonlinear, tangential, and background oscillations. One important conclusion reached here is that the dominant nonlinear oscillations appear to couple with whatever the local tangential modes happen to be.

8) Detailed analysis was performed on Motors 5 and 10, which failed. It was concluded that spontaneous tangential oscillations caused the overpressurization in both motors.

9) Another important lesson learned in this study is the destructive and potentially violent nature of a motor experiencing combustion instability. The motor tiedowns for Motor 5 were designed with a safety factor of 10 times the expected thrust of 35 kN. The actual thrust achieved reached over 400 kN, or nearly 12 times higher. The presence of instability made things even worse. If Motor 5 had merely failed because of nozzle blockage, without combustion instability, it is most likely that the motor would merely have burned to completion after ejecting the blockage. The thrust oscillations acted like a jackhammer to cut the retaining bolts. Motor tiedown hardware was redesigned with limits in excess of the absolute worst-case scenario.

10) An added important result of this work has been a working knowledge of dealing with higher pressure motors in terms of instrumenting, pulsing, and fabricating motor hardware to allow detailed measurements to be made.

It is hoped that the data provided here, and future and past data, will provide other researchers acoustic oscillatory data for model validation purposes and insight into the physical mechanisms that cause this type of combustion instability.

Acknowledgments

The author wishes to thank Jay Levine of the Phillips Laboratory, Edwards Air Force Base, for his help in interpreting the nonlinear modeling results and Bob Beddini of the University of Illinois for his help in understanding acoustic boundary layers. The author also thanks Richard Hoery and Richard Stalnaker of the Naval Air Warfare Center for their help in building, instrumenting, and firing the motors. Their abilities and insight were greatly appreciated. The author also wishes to thank Scott Fuller, Fred Zarlingo, and Tom Loftus of the Naval Air Warfare Center for supporting this effort. A practice has been established that allows full-scale motors to be fired and intentionally pushed to limits, sometimes resulting in failure. This atmosphere fosters a positive research environment.

References

- ¹Blomshield, F. S., Crump, J. E., Mathes, H. B., Stalnaker, R. A., and Beckstead, M. W., "Stability Testing of Full-Scale Tactical Motors," *Journal of Propulsion and Power*, Vol. 13, No. 3, 1997, pp. 349–355.

²Blomshield, F. S., Mathes, H. B., Crump, J. E., Beiter, C. A., and Beckstead, M. W., "Non-Linear Stability Testing of Full-Scale Tactical Motors," *Journal of Propulsion and Power*, Vol. 13, No. 3, 1997, pp. 356–366.

³Blomshield, F. S., Bicker, C. J., and Stalnaker, R. A., "High Pressure Pulsed Motor Firing Combustion Instability Investigations," AIAA Paper 97-3253, July 1997.

⁴Blomshield, F. S., and Stalnaker, R. A., "Pulsed Motor Firings: Pulse Amplitude, Formulation and Enhanced Instrumentation," AIAA Paper 98-3557, July 1998.

⁵Brownlee, W. G., "Non-Linear Axial Combustion Instability in Solid Propellant Motors," *AIAA Journal*, Vol. 2, No. 2, 1964, pp. 275–284.

⁶Jensen, R. C., and Beckstead, M. W., "Limiting Amplitude Analysis," AFRPL-TR-73-61. Hercules, Inc., Magna, UT, July 1973.

⁷Baum, J. D., Levine, J. N., and Lovine, R. L., "Pulse-Triggered Instability in Solid Rocket Motors," *AIAA Journal*, Vol. 22, No. 10, 1984, pp. 1413–1419.

⁸Baum, J. D., and Levine, J. N., "Modeling of Non-Linear Longitudinal Instabilities in Solid Rocket Motors," *Acta Astronautica*, Vol. 13, Nos. 6–7, 1984, pp. 339–348.

⁹Baum, J. D., Levine, J. N., and Lovine, R. L., "Pulsed Instability in Rocket Motors: A Comparison Between Predictions and Experiments," *Journal of Propulsion and Power*, Vol. 4, No. 4, 1988, pp. 308–316.

¹⁰Harris, P. G., Champlain, A., and Bourque, C., "Pulse-Triggered Nonlinear Instability in Solid Rocket Motors: An Experimental Study," AIAA Paper 97-3246, July 1997.

¹¹Hermesen, R. W., Lamberty, J. T., and McCormick, R. E., "A Computer Program for the Prediction of Solid Propellant Rocket Motor Performance (SPP)," Vol. 5, AFRPL-TR-84-036, Sept. 1984.

¹²Nickerson, G. R., Culick, F. E. C., and Dang, L. D., "Standard Stability Prediction Program for Solid Rocket Motors," AFRPL TR-83-017, Sept. 1983.

¹³Culick, F. E. C., "T-Burner Testing of Metallized Solid Propellants," AFRPL-TR-74-28, Oct. 1974.

¹⁴Crump, J. E., "Combustion Instability in Minimum Smoke Propellants," NWC-TP-5936, Nov. 1977.

¹⁵Beddini, R. A., and Roberts, T. A., "Turbularization of an Acoustic Boundary Layer on a Transpiring Surface," *AIAA Journal*, Vol. 26, No. 8, 1988, pp. 917–923.

¹⁶Roberts, T. A., and Beddini, R. A., "A Comparison of Acoustic and Steady-State Erosive Burning in Solid Rocket Motors," AIAA Paper 89-2664, July 1989.

¹⁷Beddini, R. A., and Roberts, T. A., "Response of Propellant Combustion to a Turbulent Acoustic Boundary Layer," *Journal of Propulsion and Power*, Vol. 8, No. 2, 1992, pp. 290–296.

¹⁸Baum, J. D., and Levine, J. N., "Numerical Techniques for Solving Non-Linear Instability Problems in Solid Rocket Motors," *AIAA Journal*, Vol. 20, No. 7, 1982, pp. 955–961.

¹⁹Baum, J. D., and Levine, J. N., "Modeling of Non-Linear Combustion Instability in Solid Propellant Rocket Motors," AFRPL TR-83-058, Feb. 1984.

²⁰Levine, J. N., and Culick, F. E. C., "Non-Linear Analysis of Solid Rocket Combustion Instability," AFRPL TR-74-45, Oct. 1974.

²¹Harris, P. G., and Champlain, A., "A New Methodology for the Analysis of Experimental Data Describing Pulse-Triggered Non-Linear Instability in Solid Rocket Motors," AIAA Paper 98-3558, July 1998.

Transverse Waves in Solid-Propellant Rocket Motors: Pulse-Triggered Unstable Mode

P. G. Harris*

Defence Research Establishment Valcartier, Val Bélair, Québec, Canada

and

A. De Champlain†

Laval University, Québec, Québec, Canada

I. Introduction

DURING the operation of solid-propellant rocket motors, the passage of ejecta through the nozzle will create a small compression wave that can grow into a large-amplitude steep-fronted wave (shock wave). This wave is usually accompanied by an increase in the time-averaged operating pressure of the motor. This type of instability, illustrated in Fig. 1, is often referred to as pulse-triggered instability.

The experimental study of pulse-triggered instability at the Defence Research Establishment Valcartier (DREV) began in the early 1960s with the development of a pulsing technique by Dickinson¹ to overcome the random occurrence of instability. This was followed by the foundational work of Dickinson and Jackson,² Brownlee,³ Roberts et al.,⁴ Roberts and Brownlee,⁵ and the later work of Smith et al.⁶ and Hughes and Smith.⁷ It produced an extensive database of hundreds of pulsed-motor firings that characterize the effects of propellant formulation, propellant burning rate, initial propellant temperature, motor scale, and grain configuration. Early propellant formulations were based on polyurethane (PU) and ammonium perchlorate (AP). However, the work expanded with time to include carboxyl-terminated polybutadiene (CTPB) and hydroxyl-terminated polybutadiene (HTPB) binders. Other formulation variants included the effect of aluminum, burning-rate modifiers, oxidizer particle-size distribution, and binder level. The motors varied in size from 51 mm in diameter and 254 mm long to 432 mm in diameter and 4570 mm long. Grain configurations included full-length cylinders,

Copyright © 1999 by P. G. Harris and A. De Champlain. Published by the American Institute of Aeronautics and Astronautics, Inc., with permission.

*Leader, Propulsion Group, Delivery Systems.

†Professor, Mechanical Engineering.

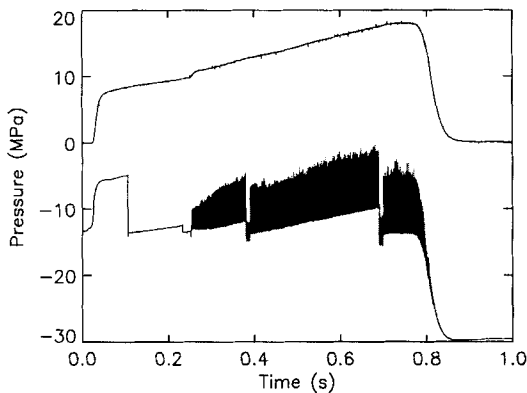


Fig. 1 Time-averaged (top) and high-frequency (bottom) pressure profiles for pulse-triggered instability.

stars, arms, split cylinders, and slotted tubulars. A single grain having both a cylindrical and a slotted tubular cross section was also tested.

These experimental studies illustrated a number of phenomenological trends concerning the behavior of pulse-triggered instability. First, the nonlinearity of pulse-triggered instability with respect to initiation was shown. As such, a finite-amplitude pulse was required for it to be triggered. Second, a correlation between the unstable time-averaged pressure p_{cus} and the restriction ratio K_n , similar to that which exists for the stable time-averaged pressure p_{cs} , was uncovered. Third, regions of intrinsic stability and instability were shown to exist that could be expressed in terms of critical values of p_{cs} and K_n . For values of p_{cs} and K_n below these critical values, a motor could not be pulsed unstably. Fourth, these critical values were shown to depend on motor scale, meaning that comparisons of the intrinsic stability of different propellants could be done only with motors with the same configuration. Finally, the fractional increase in time-averaged pressure (fraction of dc shift) and the value of the critical pressure were shown to be highly dependent on the stable burning rate of a propellant, slower propellants being the more unstable and having the lower critical pressures.

In addition to the parametric studies at DREV, optical techniques were used with windowed motor firings by Brownlee and Kimbell⁸⁻¹¹ and Hughes and Saber¹² to investigate the relationship between the unsteady flow and the combustion processes associated with pulse-triggered instability. Through these techniques, the existence of a traveling shock wave was confirmed and shown to be highly planar during downstream propagation and concave in the direction of propagation when moving upstream. The shock wave was shown to be followed by an attached expansion wave and also a series of compression and expansion waves. Complete flow reversal was observed in the core flow region and combustion zone during the upstream propagation of the shock wave. Finally, increased rates of reaction were also observed on passage of the shock wave.

The most recent experimental investigation of pulse-triggered instability at DREV was carried out by Harris and De Champlain.¹³ This was part of the Canadian contribution to a joint international study also involving Australia, the United Kingdom, and the United States.¹⁴ The U.S. experimental contribution was

supplied by the Aerojet Solid Propulsion Company and by Blomshield et al.^{15,16} at the U.S. Naval Air Warfare Center. This joint study was a follow-up on the extensive experimental and theoretical investigations directed by Levine and carried out by the Aerojet Solid Propulsion Company and Phillips Laboratory.¹⁷⁻¹⁹

In the body of work reviewed, it was clearly demonstrated that the primary transient waveform associated with pulse-triggered instability was a longitudinally propagating shock wave. However, the presence of transverse waves in the pulse-triggered unstable environment was also briefly mentioned. Brownlee³ identified a transverse wave that grew so quickly that it actually suppressed the longitudinal shock wave. Kimbell and Brownlee¹¹ postulated the existence of transversely propagating wave disturbances based on schlieren images, although no final conclusions were ever drawn. More recently, Hughes²⁰ attributed the catastrophic failure of a motor to the coupling between a radial-acoustic mode and the radial propellant/casing vibration driven by the passage of the shock wave. According to Hughes, the propellant/casing system provided a means of transforming longitudinal-acoustic energy into transverse-acoustic energy. Harris et al.²¹ pursued this concept in an experiment that was intended to demonstrate the effect of changing propellant/casing vibrational characteristics on pulse-triggered instability. Although interesting effects were noted, the analysis method used to reduce the data was not capable of clearly identifying the presence of transverse waves in a shock-wave environment.

Given the primary importance of the shock wave in the study of pulse-triggered instability, an initial publication explored the effect of different ballistic parameters on pulse-triggered instability from the perspective of a longitudinal shock wave.¹³ However, continued examination of the data by use of a new analysis method pointed to the presence and the potential importance of transverse pressure waves. These waves are considered to be driven by the propagating longitudinal shock wave either through the conversion of longitudinal-acoustic energy to transverse-acoustic energy, through the movement of the propellant/casing system, or through gasdynamic interaction between the shock wave and the mean flow. The presence of these oscillations, identified here as transverse pressure waves, can be seen in the decay portion of the shock wave in the inset of Fig. 2. Several returns of a

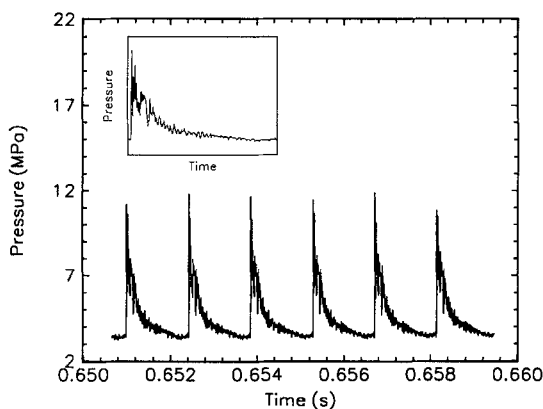


Fig. 2 Typical shock and transverse pressure waves.

shock wave followed by transverse pressure waves are illustrated in the main part of Fig. 2.

The purpose of this chapter is the experimental demonstration of the presence, nature, source, and effect of transverse pressure waves in a pulse-triggered unstable environment. It begins with a brief discussion of the experimental test matrix. A description of the experimental technique follows, with particular emphasis on the geometry of the headend of the motor chamber. This is followed by an introduction to a new data analysis method used to identify the transverse pressure waves. Based on this method, a frequency analysis of the headend pressure signal for a sample motor firing is then presented, identifying the presence and the nature of transverse waves. Frequency analyses of data from eight sample motors of varying propellant formulation, grain configuration, size, and length are then used to generalize the discussion for the present database. This is followed by an analysis that relates the presence of the transverse waves throughout a firing directly to that of the shock wave. Finally, data are presented that suggest that for the present database, part of the fraction of dc shift associated with pulse-triggered instability can be attributed to the presence of transverse pressure waves.

II. Test Matrix

The original experimental test matrix for the Canadian contribution to the joint international study was composed of 45 full-scale motor firings, divided into 11 test cases. The test cases included variations in propellant formulation, operating pressure, grain configuration, motor length, and motor scale. For a complete description of the test matrix, the reader is referred to the initial paper in this series.¹³

For this paper, eight representative motor firings were selected from 7 of the 11 test cases. Motor parameters are described in Table 1, and the time-averaged pressure profiles are shown in Fig. 3. The designation 03031-C identifies a cylindrical grain with a nominal diameter of 3 in. (76 mm) and a nominal length of 31 in. (787 mm); the experiment was designed with the British system of units. Grain configurations SA and SB indicate two different star variations, A and B. The numbers in parentheses, (1), (2), and (3), identify different motors. The letters in parentheses, (B) and (C), designate propellant formulations B and C. The two propellants had differing particle-size distributions of AP, and propellant B contained 0.5% by weight of ZrSiO₄, a stability additive.

Table 1 Selected firings from the experimental test matrix

Test case	Motor number	Diameter, mm	Length, mm	Grain geometry	Propellant formulation	Reference pressure, MPa	Reference K_n
2	03031-C(B)	64.8	777	Cylinder	B	12.4	307.8
3	03031-C(C)	64.8	777	Cylinder	C	12.4	307.8
4	03020-C	64.8	518	Cylinder	A	12.4	307.8
5	03020-SA(1)	64.8	518	Star A	A	12.4	307.8
5	03020-SA(2)	64.8	518	Star A	A	12.4	307.8
6	03020-SA(3)	64.8	518	Star A	A	13.8	331.4
10	05057-C	119.8	1438	Cylinder	A	12.4	307.8
11	05057-SB	119.8	1438	Star B	A	12.4	307.8

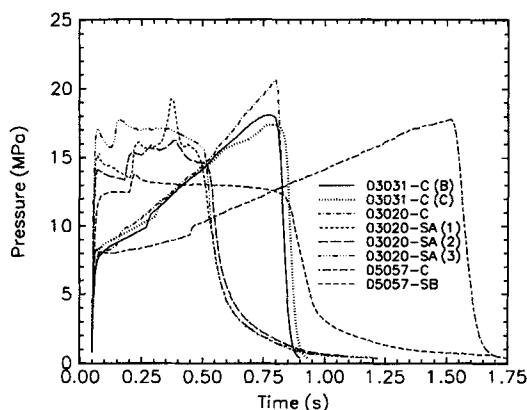


Fig. 3 Time-averaged pressure profiles of eight representative motor firings.

III. Experimental Technique

Both time-averaged and high-frequency pressure measurements were taken at the motor headend. The time-averaged measurements were made through one pressure port with two Baldwin-Lima-Hamilton strain transducers. Two Kistler transducers, covered with a thermal protective layer of room temperature vulcanized (RTV) silicon, 2.54 mm thick, measured the high-frequency pressure. As can be seen in Fig. 4, the Kistlers were positioned off the centerline of the motor headend and at different azimuthal angles in order to best measure multiple modes of the transverse pressure waves.

The signal from the Kistler transducers was reset at various times throughout a given firing (Fig. 1) to maximize resolution. The output from each Kistler went through a low-pass antialiasing filter before being sampled with a 12-bit A/D converter. The signal was filtered at 80 kHz and sampled at a frequency of 250 ksamples/s, thereby ensuring no aliasing in subsequent frequency analyses. Both Kistler 603B2 and 7031 pressure transducers were used. However, only

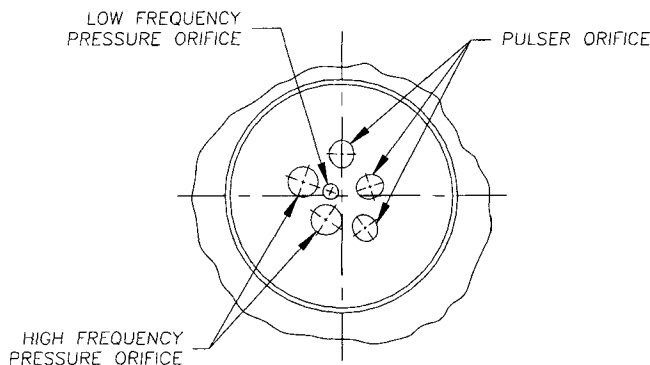


Fig. 4 Placement of the pressure transducers and the pulsers in the motor headend.

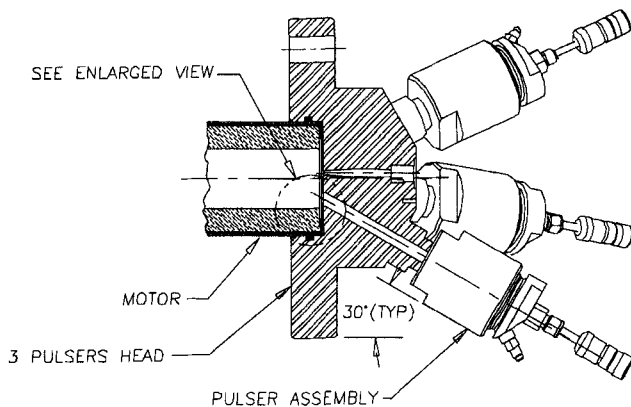


Fig. 5 Cutaway of the motor headend showing pulsers and a pulser channel.

data from the 603B2 are presented in this paper because its resonant frequency (101.6 kHz) was significantly higher than that of the 7031 (74.7 kHz).

Motors were pulsed at the headend with up to three pyrotechnic pulsers. First, a 1% pulse was generated to evaluate the linear stability margin of the motor. The second pulse and, where necessary, the third pulse were of larger amplitude to drive the motor unstable (10% of the chamber pressure). A cutaway of a motor headend showing three pulsers and one of the pulser channels is shown in Fig. 5. The figure indicates that the pulser gases were injected into the chamber at an angle of 30 deg with respect to and off the motor centerline. Figure 6, an enlarged view of Fig. 5, shows a small cavity at the headend of the motor resulting from partial inhibiting of the propellant grain; a full inhibitor would have covered the Kistler transducers. As the propellant burned, the geometry of this cavity changed, as indicated by the dashed line. The significance of the orientation of the pulsers, the presence of the pulser channels, and the existence of the cavity created by the headend inhibitor are described later in this chapter.

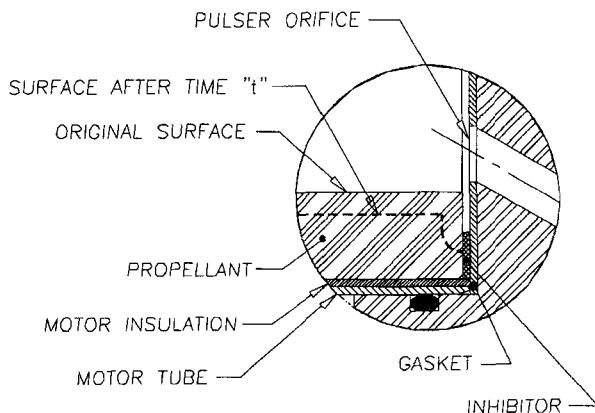


Fig. 6 Enlarged view of the motor headend.

IV. New Data Analysis Method

The standard time-marching frequency analysis method used in the field of combustion instability is not capable of identifying transverse pressure oscillations in a shock environment for two major reasons. First, the harmonics of the shock wave tend to mask the presence of the transverse oscillations. Second, the inclusion of multiple cycles in the fast Fourier transforms (FFTs) obscures the transverse oscillations through the addition of artificial peaks, in the form of sidelobes, at multiples of the fundamental shock frequency. Consequently a new time-marching frequency analysis method was developed that overcame these problems. This method was described and evaluated in a previous publication.²² Therefore it is presented here only in sufficient detail to provide the reader with a working understanding.

The new time-marching frequency analysis method was performed in two steps, the removal of the shock wave from the original signal and the harmonic analysis of the resultant signal. The removal of the shock wave from the original signal is illustrated in Fig. 7. The times corresponding to the wave front of each return of the original signal (top trace) were first identified. These are specified in Fig. 7 as indices. With these indices used as reference points, each shock-wave return was approximated with the actual shock front and a polynomial fit for the decay portion. This step is identified in Fig. 7 as the polynomial fit (middle trace). Finally, the approximation of the shock returns (polynomial fit) was subtracted from the original signal, leaving only the transverse oscillations (resultant signal), bottom trace.

To facilitate an understanding of the harmonic analysis involved in the new method, it is compared in Figs. 8–12 with that of the standard one. The new method was based on the calculation of single-cycle FFTs of the resultant signal. These FFTs were referenced to the indices that located the positions of the shock-wave fronts. This is illustrated in the bottom trace of Fig. 8. The standard method, on the other hand, was based on the calculation of multiple-cycle and overlapping FFTs of the original signal. Each consecutive FFT was advanced by a certain percentage of the FFT length. This is illustrated in the top trace of Fig. 8, where the percentage of overlap was 50% and the FFT length was 1024 points.

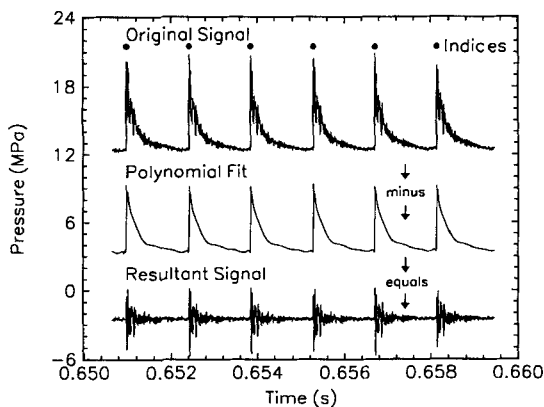


Fig. 7 Illustration of the process of removing the shock wave from the original signal.

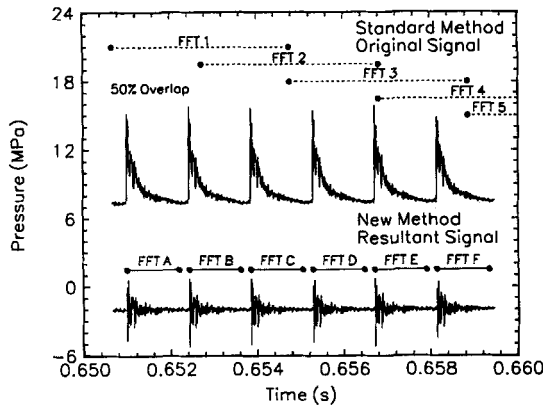


Fig. 8 Illustration of the standard and the new time-marching analyses.

The actual signal included in a given 1024-point FFT is illustrated for the two methods in Fig. 9. For the standard method, the top trace, all 1024 points in the FFT contained the actual signal. However, for the new method, a single cycle of 300 points of actual signal was centered in the FFT with the surrounding points set to zero. Both methods used a 1024-point Hanning window in the calculation of the FFT.

The power of the new method is illustrated through the discussion of Figs. 10–12. In Fig. 10, FFTs for the two methods are compared. The figure demonstrates that the new method is greatly superior to the standard one in identifying transverse oscillations. In Figs. 11 and 12, contour plots of the FFT analyses are shown for the standard and the new methods along with the approximate variation of tangential- and radial-acoustic modes. The results obtained with the new method, Fig. 12, represent a significant improvement over those obtained with the standard one, Fig. 11. Individual frequencies in Fig. 12, which follow the global trends of the transverse modes, are readily discernible.

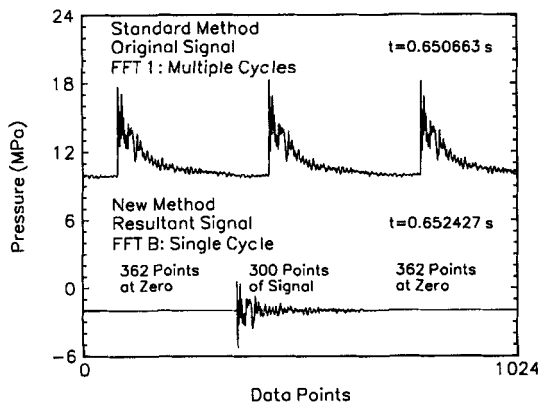


Fig. 9 Calculation of FFTs according to the standard and the new time-marching analyses.

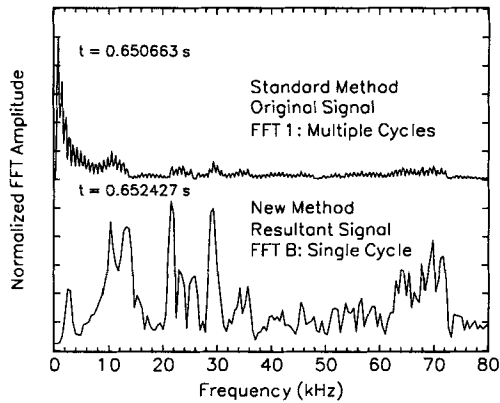


Fig. 10 FFTs calculated according to the standard and the new time-marching analyses.

The new time-marching frequency analysis follows the evolution, throughout a firing, of the frequency content of transverse oscillations averaged over the decay portion of successive shock waves. As such, it is incapable of tracking the temporal evolution of these oscillations over the decay portion of a single shock cycle. This latter task is the domain of time-frequency analysis techniques.²²

V. Transverse Waves: Presence and Nature

Applying the new data analysis method to the resultant signals revealed that in all cases transverse pressure waves were present. In the following discussion, their presence is first demonstrated and their nature discussed through a detailed frequency analysis of one of the motors from Fig. 3, 03031-C(C). This analysis is then generalized through the presentation of results for the remainder of the motors in Fig. 3; these motors were chosen as representative of the trends found in the joint program.

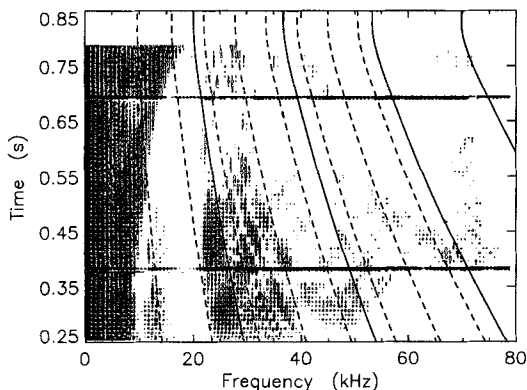


Fig. 11 Contour plot of the FFTs of the original signal obtained with the standard time-marching analysis (---, tangential modes, and —, radial modes).

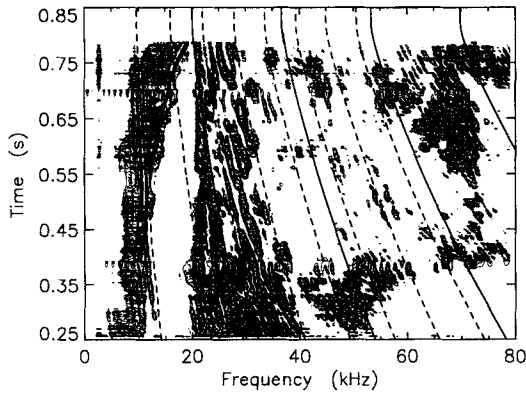


Fig. 12 Contour plot of the FFTs of the resultant signal obtained with the new time-marching analysis (---, tangential modes, and —, radial modes).

A. Detailed Analysis

In this subsection, motor 03031-C(C) is discussed as an example of the different pressure waves that are present in a pulse-triggered unstable environment. As such, the new data analysis method was applied to the resultant signal from one of the Kistler 603B2 transducers in the motor headend. The resulting contour plot is repeated in Figs. 13–15, where it is compared with analytical approximations of the variation with time of the frequency of different modes of acoustic oscillation. The contour plot was also compared with a frequency analysis of the vibrations of the casing, during pulse-triggered unstable operation, of a motor similar to that of 03031-C(C), Fig. 16.

The investigation, which is described in detail in the following paragraphs, showed that the headend pressure transducer measured pure transverse and combined tangential–radial and transverse–longitudinal waves associated with the motor combustion chamber, a radial pressure wave in the combustion chamber

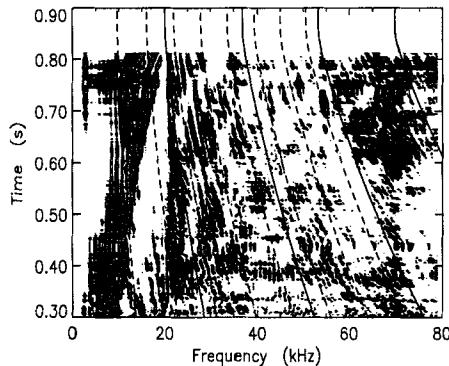


Fig. 13 Contour plot of the FFTs of the resultant signal for motor 03031-C(C) compared with the analytical tangential-acoustic (---) and radial-acoustic (—) modes of the combustion chamber.

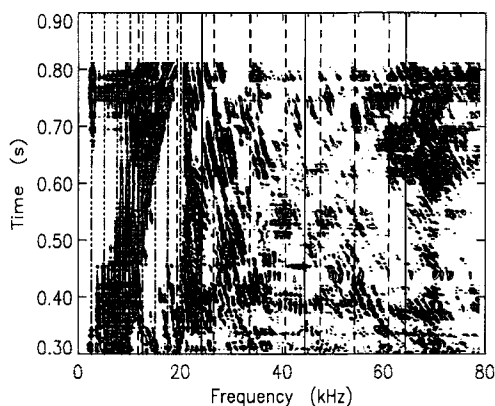


Fig. 14 Contour plot of the FFTs of the resultant signal for motor 03031-C(C) compared with the analytical longitudinal modes for the pulser channels (\cdots) and the analytical tangential-acoustic ($---$) and radial-acoustic ($---$) modes of the constant radius inhibitor cavity.

related to the vibration of the propellant/casing system, and various modes associated with the geometry of the motor headend. These last modes were undesirable in that they tended to mask the modes of oscillation associated with the combustion chamber pressure, the main interest of this investigation.

As was specified above, the contour plots in Figs. 13–15 were based on 1024-point FFTs that contained 300 points of signal, the rest of the FFT being filled with zeros (see Fig. 9). Therefore the effective frequency resolution of the FFTs based on a 250-ksample/s sampling rate was 0.83 kHz.

With the exception of the pulser channel, analytical acoustic frequencies were approximated with the solution for three-dimensional wave propagation in a closed cylindrical cavity with no mean flow; the pulser channel had one open end and

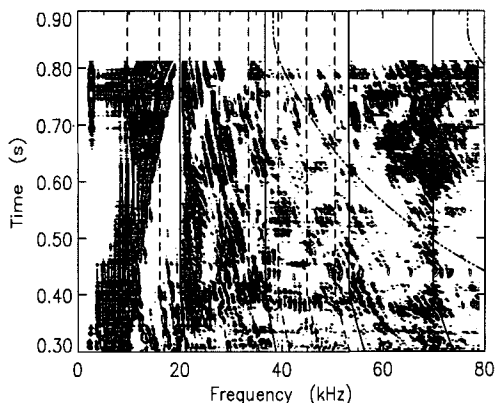


Fig. 15 Contour plot of the FFTs of the resultant signal for motor 03031-C(C) compared with the tangential-acoustic ($---$), radial-acoustic ($---$) and longitudinal-acoustic (\cdots) modes of the expanding propellant cavity at the headend.

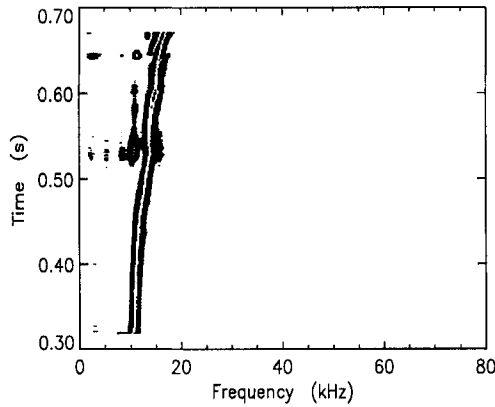


Fig. 16 Contour plot of the FFTs of the hoop strain of a motor similar to 03031-C(C).

therefore a different, but similar, solution was used. The circular frequency (rev/time) for a closed cavity $f_{m,n,q}$ is given by

$$f_{m,n,q} = (a_{\infty}/2)[(\alpha_{mn}/R)^2 + (q/L)^2]^{\frac{1}{2}} \quad (1)$$

where a_{∞} is the acoustic speed in the undisturbed gas, the subscripts m , n , and q are the wave numbers associated with the radial, tangential, and longitudinal modes, respectively, α_{mn} is a constant associated with the transverse modes, and R and L are the radius and the length of the cylindrical cavity, respectively. Pure tangential modes correspond to $m = q = 0$ and $n \neq 0$, pure radial modes correspond to $n = q = 0$ and $m \neq 0$, and pure longitudinal modes correspond to $m = n = 0$ and $q \neq 0$ ($\alpha_{00} = 0$). Combined modes correspond to any two indices' not being equal to zero.

For motor 03031-C(C),

$$\alpha_{mn}/R \gg 1/L \quad (2)$$

Therefore the number of possible combined transverse-longitudinal modes between any pure transverse modes was large. The frequency differential between consecutive combined transverse-longitudinal modes was smaller than the effective frequency resolution of the FFTs, 0.83 kHz. Consequently the frequency analysis was not capable of detecting all potential modes.

The first eight pure tangential-acoustic and first four pure radial-acoustic modes, as approximated with Eq. (1), are compared in Fig. 13 with the contour plot. The tendency of the frequencies of the tangential and the radial modes to decrease with time corresponded well with the general behavior of many of the modes in the contour plot. However, exact frequencies were not reproduced. In addition, many more experimental modes were present than could be explained by pure transverse or combined transverse modes. This discrepancy implied the presence of combined transverse-longitudinal modes, which was consistent with the hypothesis that the presence of transverse waves throughout the firing was related to the longitudinally propagating shock wave. Unfortunately, the frequency resolution of the FFTs, 0.83 kHz, was not sufficient to determine which and how many combined transverse-longitudinal modes were actually present.

In addition to transverse-acoustic waves, Fig. 13 reveals the presence of an oscillation between 10 and 20 kHz whose frequency increased with time. It was proposed that this oscillation was related to the radial vibration of the propellant/casing system; the frequency of vibration increased as the propellant mass decreased. Unfortunately, no casing vibration measurements were taken for any of the motors of the present experimental test matrix. Consequently a motor similar to 03031-C(C) was instrumented with a hoop-oriented strain transducer and pulsed fired. The output from the strain transducer, placed at the midpoint of the motor length, was analyzed, and the contour plot is included in Fig. 16. The correspondence between this contour plot and the oscillation between 10 and 20 kHz in Fig. 13 confirmed that the latter was related to propellant/casing vibrations. It is believed that the passage of the shock wave stimulates radial vibration of the propellant/casing system, which in turn forces radial oscillation of the chamber gases.

In Fig. 14, time-invariant acoustic modes are compared with the contour plot. These modes were calculated based on the particular geometry of the motor head-end and, in the present context, were considered as acoustic noise; they interfered with the measurement of the acoustic modes in the propellant grain cavity. First, eight longitudinal modes associated with the constant length pulser channels, Fig. 5, were calculated and plotted in Fig. 14. The correspondence between these modes and the contour plot indicated that the resonance of the pulser channels was one source of acoustic noise. Second, the first eight tangential and the first three radial modes associated with the constant radius cavity/step created by the headend inhibitor, Fig. 6, were calculated and plotted in Fig. 14. In general, there was very little correspondence between these modes and the contour plot. The one exception was the close proximity of the second tangential mode to the dominant line of peaks at a frequency of approximately 21 kHz in the contour plot. However, as will be described in the next paragraph, this line of peaks was not considered to be the second tangential mode of the cavity.

Throughout motor burn, the cavity created between the propellant grain and the motor headend by the presence of the inhibitor, Fig. 6, increased with time until it reached the motor insulation. The first eight tangential and the first four radial modes associated with this cavity were calculated and plotted in Fig. 15. The close proximity of the first radial mode to the dominant line of peaks at approximately 21 kHz, in addition to the physical feasibility of a radial oscillation's being stimulated by the sudden radial expansion of the shock wave into the cavity, suggested that the peaks corresponded to this radial mode. Longitudinal-acoustic modes associated with this headend cavity were also calculated and compared with the contour plot in Fig. 15. However, there seemed to be no correspondence between the two.

B. Generalized Analysis

The preceding analysis demonstrated the presence and discussed the nature of transverse pressure waves in motor 03031-C(C). However, this behavior was not unique. In fact, as is shown in this section, transverse pressure waves were continuously present in all motors from the Canadian study while operating in fully developed pulse-triggered unstable mode, regardless of propellant formulation, operating pressure, grain configuration, motor length, or motor scale. On the other hand, global qualitative differences in the frequency content were noted, which depended on these ballistic parameters.

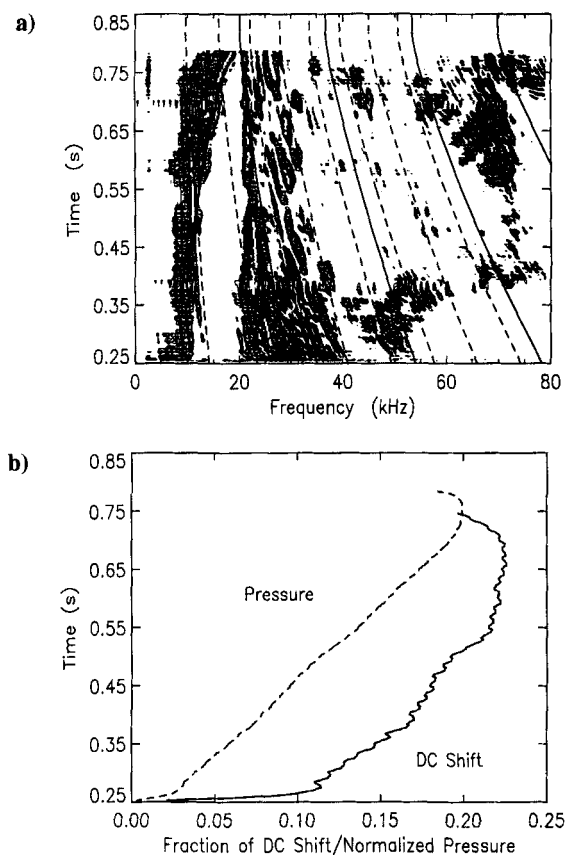


Fig. 17 Motor 03031-C(B): a) contour plot of the FFTs of the resultant signal compared with the analytical tangential-acoustic (---) and radial-acoustic (—) modes of the combustion chamber and b) normalized and translated time-averaged pressure (---) and fraction of dc shift (—).

For discussion of the above points, contour plots of the resultant signals for the eight motors in Fig. 3 and analytically calculated transverse-acoustic modes are presented in Figs. 17–24. It should be noted that only part of the contour plot for motor 03020-SA(1), Fig. 20a, was calculated for reasons that are discussed in a subsequent section. Also, for convenience in data interpretation in a subsequent section, graphs of the fraction of dc shift and normalized time-averaged pressure have been included along with the contour plots.

Several unsuccessful attempts were made at quantitatively characterizing the different contour plots in Figs. 17–24. Therefore the following discussion is qualitative in nature. In particular, six qualitative observations are presented:

- 1) Transverse pressure waves were continuously present in all motors operating in the fully developed pulse-triggered unstable mode. However, the actual transverse modes present varied throughout motor burn. This is illustrated in Fig. 19a,

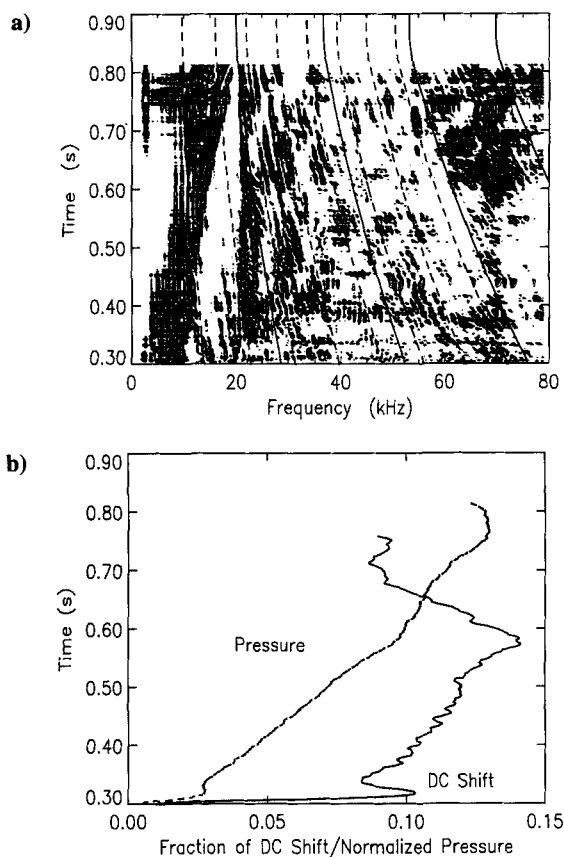


Fig. 18 Motor 03031-C(C): a) contour plot of the FFTs of the resultant signal compared with the analytical tangential-acoustic (---) and radial-acoustic (—) modes of the combustion chamber and b) normalized and translated time-averaged pressure (---) and fraction of dc shift (—).

motor 03020-C, in which high-frequency modes, 60–75 kHz, were dominant at the beginning of instability, only to be replaced with lower-frequency ones, 35–60 kHz, at 0.25 s.

2) A pressure wave related to the vibration of the propellant/casing systems was evident for the majority of the motors. In fact, as would be expected, the frequency for the large-diameter motors, Figs. 23a and 24a, was lower than that for the small-diameter ones.

3) The frequency content for the small-diameter long cylinders, Figs. 17a and 18a, differed from that of the small-diameter short cylinder, Fig. 19a. This difference, which is related to motor length, was consistent with the presence of combined transverse–longitudinal modes.

4) The frequency content for the small-diameter cylinders differed from that for the large-diameter one, Fig. 23a. In this case both the radial and the longitudinal

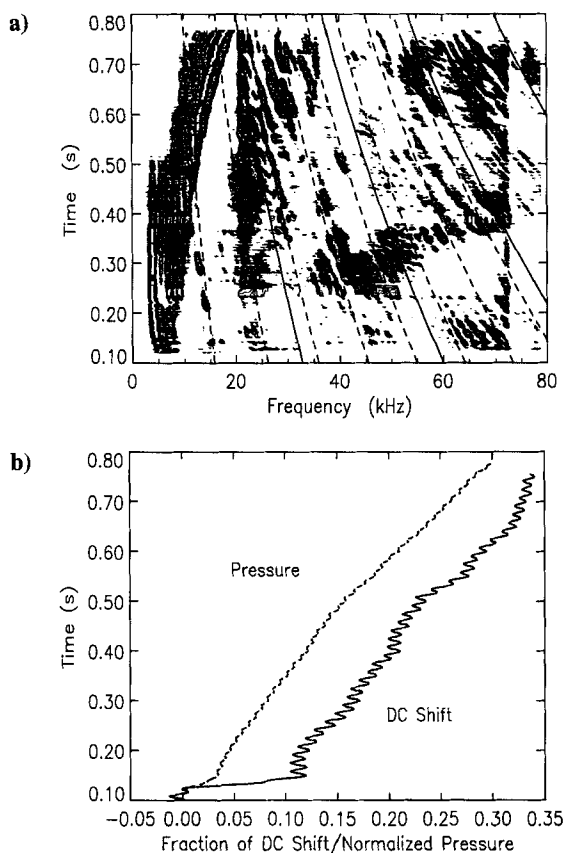


Fig. 19 Motor 03020-C: a) contour plot of the FFTs of the resultant signal compared with the analytical tangential-acoustic (---) and radial-acoustic (—) modes of the combustion chamber and b) normalized and translated time-averaged pressure (---) and fraction of dc shift (—).

dimensions were larger, resulting in lower-frequency pure transverse and combined transverse-longitudinal modes for the larger motor.

5) The frequency content for the small-diameter short cylinder, Fig. 19, differed from that for the small-diameter stars, Figs. 21a and 22a. This was not surprising, given the three-dimensional nature of the oscillations and the drastically different grain shapes. Similarly, the frequency content for the large-diameter star, Fig. 24a, and cylinder, Fig. 23a, differed.

6) Propellant formulation seemed to have an effect in that the frequency content for propellant B, Fig. 17a, was different from that for propellant C, Fig. 18a.

VI. Transverse Waves: Source

The presence and the nature of transverse pressure waves in solid rocket motors operating in pulse-triggered unstable mode were discussed in the preceding section.

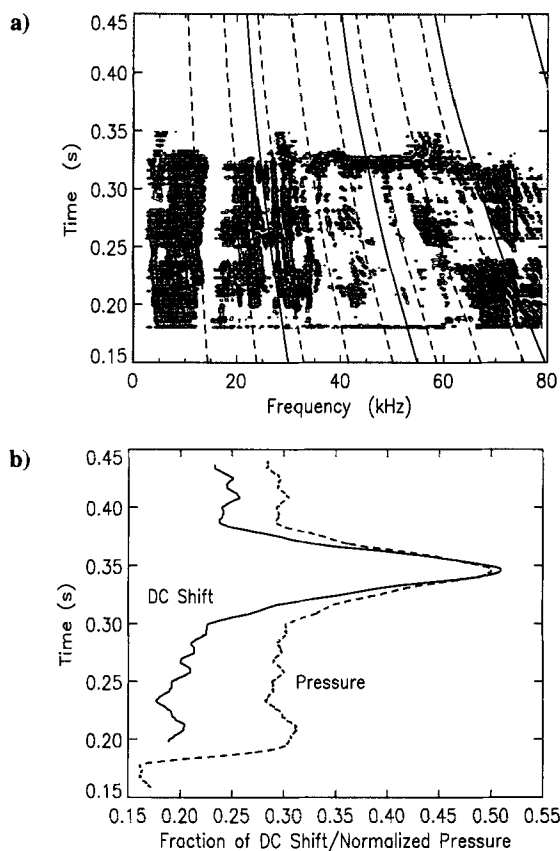


Fig. 20 Motor 03020-SA(1): a) contour plot of the FFTs of the resultant signal compared with the analytical tangential-acoustic (---) and radial-acoustic (—) modes of the combustion chamber and b) normalized and translated time-averaged pressure (---) and fraction of dc shift (—).

However, to this point no substantial proof has been presented that relates to the source of these waves. This is the purpose here.

The initial concern on the discovery of the continuous presence of transverse pressure waves during fully developed pulse-triggered instability was that these waves resulted from the pulsing technique. This was a plausible explanation, given that the pulser channels entered the combustion chamber at an angle of 30 deg and were off the centerline. Suspicion grew when analysis of the pulsing event revealed the dominant presence of tangential waves. However, as will be seen in the following analysis, the tangential waves associated with the pulsing event decayed before the appearance of the transverse waves identified in the preceding section. In fact, it is demonstrated that, after the initial pulsing event, the growth of these transverse waves correlated directly with the steepening of the longitudinal shock wave. In addition, the growth of the amplitude of individual transverse modes correlated with that of the amplitude of the harmonics of the shock wave with similar frequencies.

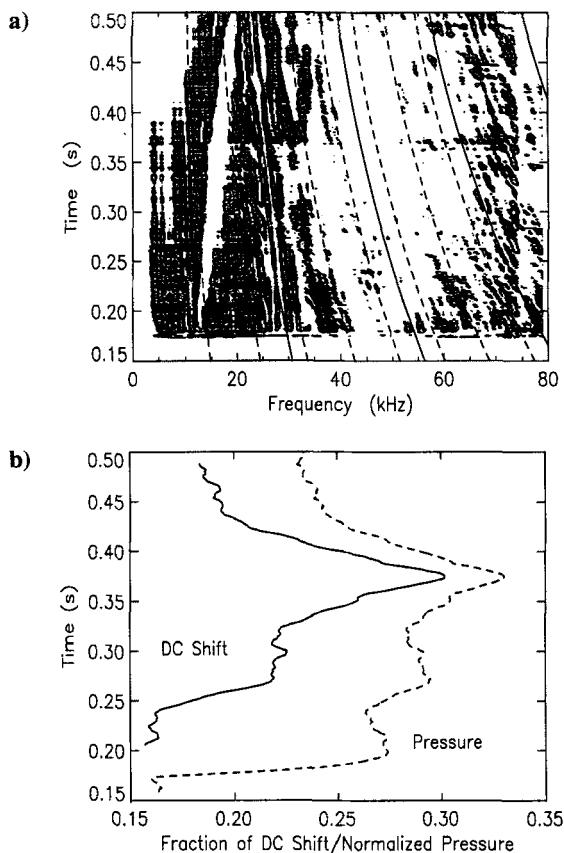


Fig. 21 Motor 03020-SA(2): a) contour plot of the FFTs of the resultant signal compared with the analytical tangential-acoustic (---) and radial-acoustic (—) modes of the combustion chamber and b) normalized and translated time-averaged pressure (---) and fraction of dc shift (—).

The pressure-time trace from the second pulse of motor 03020-SA(3) was chosen for this discussion. The original signal is shown in Fig. 25 along with its polynomial fit and resultant signal based on the new analysis method. Nineteen shock returns were included, with the pulsing event identified as return 0. FFTs of the polynomial fit (shock returns without transverse waves) and the resultant signal (transverse waves without shock returns) were calculated and the results for returns, 0, 3, 5, 7, 10, and 16 were included in Figs. 26 and 27, respectively. In addition, the frequencies associated with the pure transverse-acoustic modes, as calculated with Eq. (1), were included as points of reference in Fig. 27. The returns were chosen because they represented the pulsing event (0), the region of low growth rate of the shock (3, 5), the beginning of the region of high growth rate (7), the region of high growth rate (10), and finally the region where growth leveled off (16).

Figure 26, from the polynomial fit, was calculated with 470 points of signal, two shock returns, centered in 1024-point FFTs; the remaining 554 points were

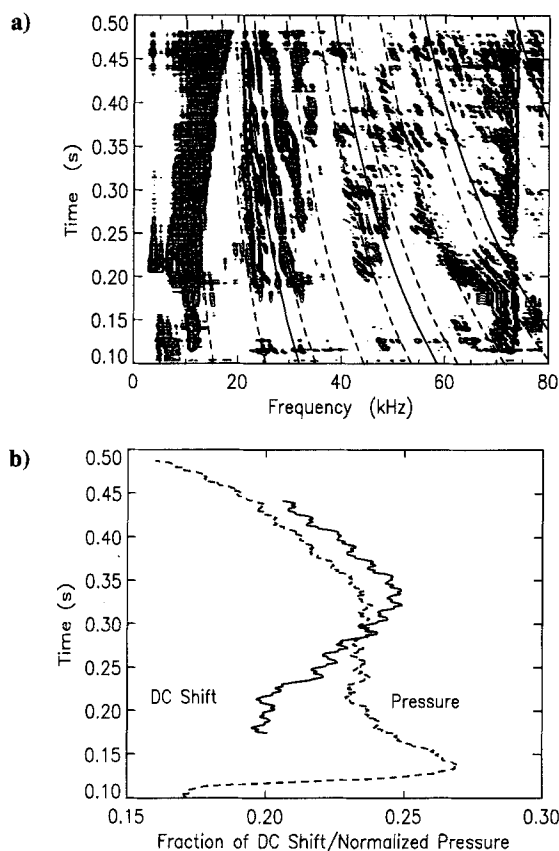


Fig. 22 Motor 03020-SA(3): a) contour plot of the FFTs of the resultant signal compared with the analytical tangential-acoustic (---) and radial-acoustic (—) modes of the combustion chamber and b) normalized and translated time-averaged pressure (---) and fraction of dc shift (—).

set to zero. Consecutive FFTs were located with the indices calculated with the new analysis method. The harmonic content of each FFT was a time average over two shock returns.

Figure 27, from the resultant signal, was calculated according to the new analysis method. As such, it was based on 230 points of signal, single cycles, and centered in 1024-point FFTs, with the remaining 794 points set to zero. The harmonic content of each FFT was a time average of the frequency content of the transverse waves for the decay portion of a single shock return. For the interested reader, the temporal evolution of the amplitude of these transverse waves over the decay portion of a single shock return can be tracked by use of time-frequency analysis techniques.²²

Figure 27 shows that the pulsing event, return 0, was dominated by two transverse waves with frequencies of approximately 11.5 and 35 kHz. It is believed that these were tangential modes. However, their exact identity is not important. Rather, what

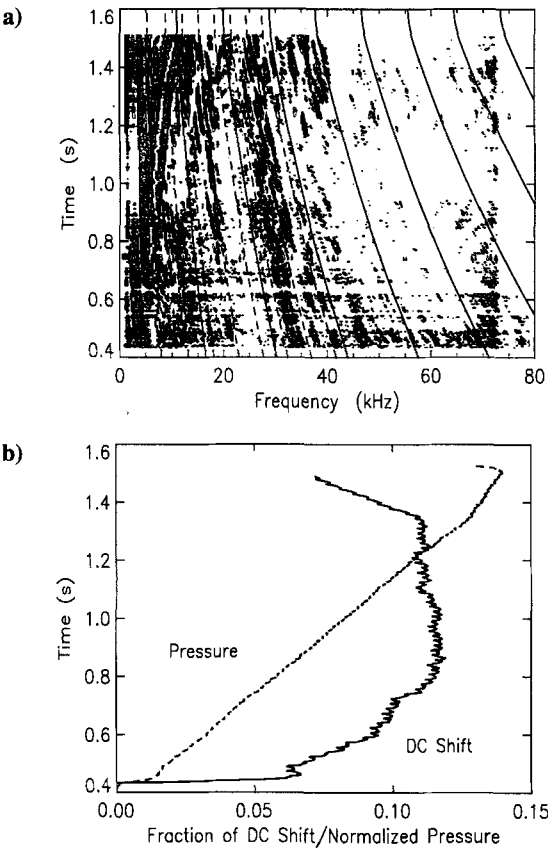


Fig. 23 Motor 05057-C: a) contour plot of the FFTs of the resultant signal compared with the analytical tangential-acoustic (---) and radial-acoustic (—) modes of the combustion chamber and b) normalized and translated time-averaged pressure (---) and fraction of dc shift (—).

is significant is that, by return 5, these dominant waves were no longer evident in the FFT. These waves, which were part of the pulsing event, decayed before the transverse oscillations identified in the preceding section appeared, return 7. Consequently it was concluded that these latter transverse oscillations were not a result of the pulsing event. The oscillations between 4 and 8 kHz in returns 3 and 5 are believed to be directly related to the amplitude of the shock wave and do not represent the nonlinear transfer of energy from the transverse waves identified in return 0. This issue will be pursued in a later paragraph.

The relationship between the growth of the transverse waves and that of the shock wave was investigated by use of two complementary analyses. First, the temporal evolution of the integral of the FFTs of the transverse waves was correlated with that of the steepness of the shock wave, Fig. 28. Second, the temporal evolution of the amplitude of two oscillations from the resultant signal was correlated with that of the amplitude of two harmonics of the shock wave of similar frequency, Fig. 29.

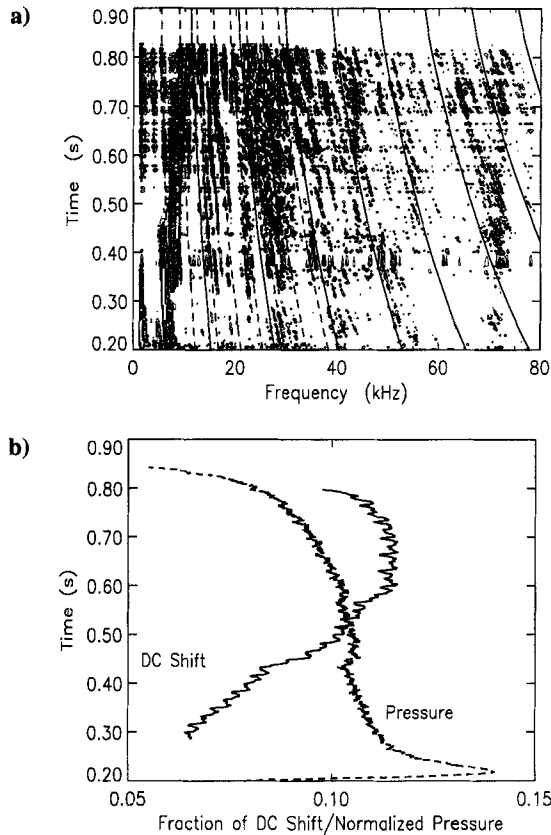


Fig. 24 Motor 05057-SB: a) contour plot of the FFTs of the resultant signal compared with the analytical tangential-acoustic (---) and radial-acoustic (—) modes of the combustion chamber and b) normalized and translated time-averaged pressure (---) and fraction of dc shift (—).

The first analysis provided an indication of the relationship between the total high-frequency energy present in the transverse waves and that in the shock wave. This is because the integral of an FFT of a signal is proportional to its total time-averaged energy and the steepness of a shock wave is proportional to the energy of its high-frequency harmonics. The integral of the FFT of the transverse modes was based on the results in Fig. 27 (from the resultant signal). It was calculated with a discretization of the following continuous integral:

$$\text{IFFTA}(t) = \int_0^{80} a(f, t) df \quad (3)$$

where t is time, f is circular frequency, a is the amplitude of the harmonic analysis (FFT in the discrete form) at a given time and frequency, and IFFTA is the integral of the harmonic analysis at a given time. The steepness of the shock wave, dp/dt , was based on the maximum rate of pressure increase for a given return of the

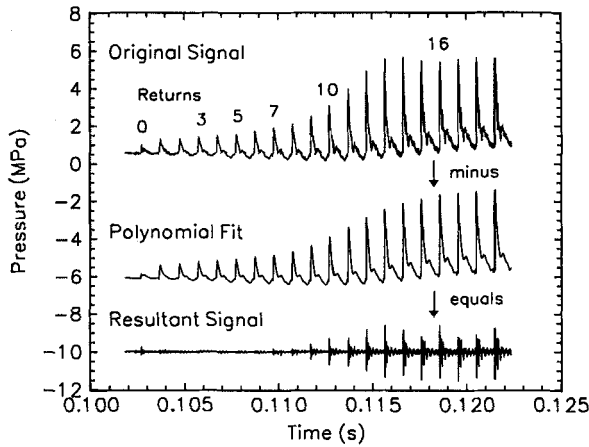


Fig. 25 Original signal, polynomial fit, and resultant signal corresponding to the second pulse of motor 03020-SA(3).

original signal, Fig. 25. Normalized values of the integral of the FFT, IFFTA, and the steepness of the shock wave, dp/dt , were calculated and are shown in Fig. 28. The correlation between the two is very good, indicating a direct relationship between the growth of the transverse oscillations and the shock wave.

The second analysis continued the idea of comparing measures of energy levels. However, instead of time- and frequency-averaged energy levels at a given time step being compared, only time-averaged levels were considered; the growth in amplitude of several oscillations in the resultant signal was correlated with that of harmonics of the shock wave having similar frequencies. Normalized results for two oscillations, the resonating pulser channel at 5.5 kHz and the transverse frequency at 25.1 kHz, are included in Fig. 29 along with two harmonics of the

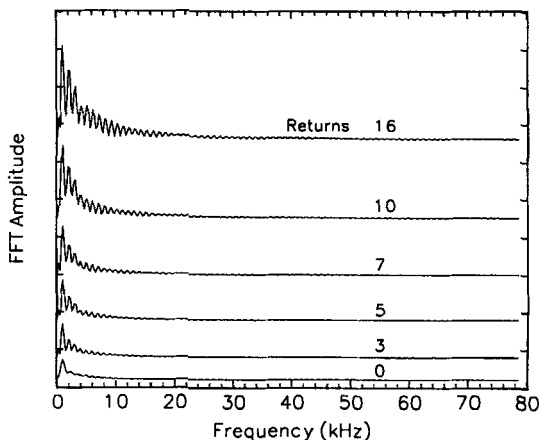


Fig. 26 FFTs of the polynomial fit corresponding to the second pulse of motor 03020-SA(3).

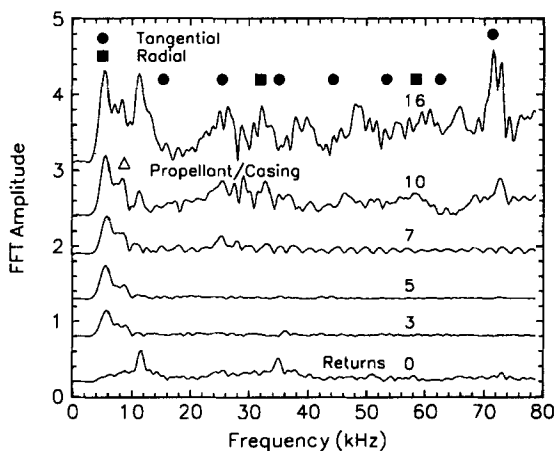


Fig. 27 FFTs of the resultant signal corresponding to the second pulse of motor 03020-SA(3).

shock wave having similar frequencies, the 4th (5.1 kHz) and 24th (25.6 kHz). The amplitudes of the 5.5- and the 25.1-kHz oscillations were based on the results in Fig. 27 (from the resultant signal), whereas the amplitudes of the shock harmonics were based on the results in Fig. 26 (from the polynomial fit). Figure 29 shows that the general increase in the amplitude of the two oscillations is accompanied by an increase in the amplitude of the shock harmonics. In addition, good correlation with respect to much of the detail of the curves was obtained. In particular, the amplitudes of both the transverse oscillation at 25.1 kHz and the 24th shock harmonic (25.6 kHz) remained relatively constant until approximately 0.108 s. However, during this time the amplitudes of the 5.5-kHz signal and the 4th shock harmonic (5.1 kHz) increased continuously. This good correlation reinforces the

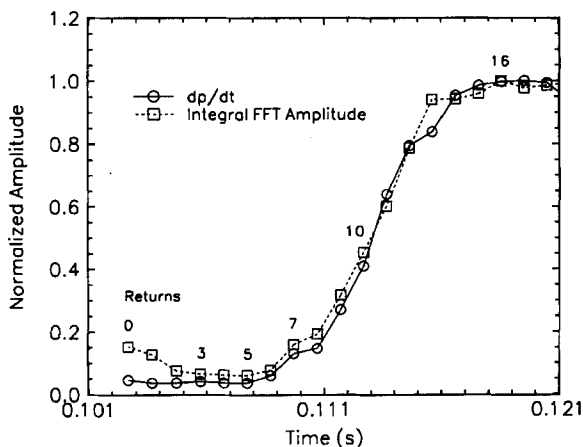


Fig. 28 Steepness of the shock front of the original signal for the second pulse of motor 03020-SA(3) compared with the integral of the FFTs of the resultant signal.

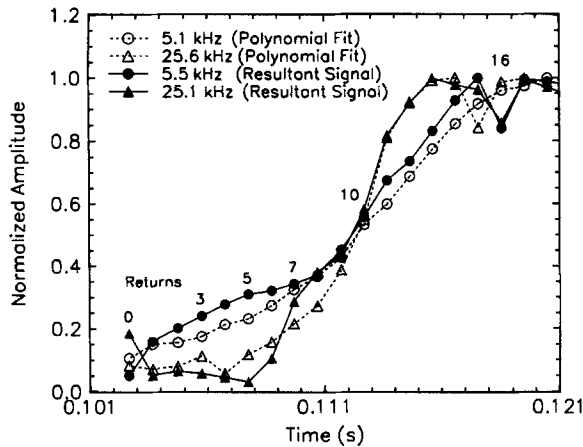


Fig. 29 Comparison of FFT amplitudes of the polynomial fit and the resultant signal for the second pulse of motor 03020-SA(3).

conclusion of a direct relationship between the growth of the transverse oscillations and the shock wave.

The experimental evidence suggests that the transverse waves were driven by the shock wave. It seems to point to a mechanism whereby longitudinal-acoustic energy was converted into transverse energy through the movement of the propellant/casing system. However, gasdynamic interaction between the shock wave and the mean flow could also have been possible. Unfortunately, the present data are not sufficient to identify the mechanism precisely and further work is required.

VII. Transverse Waves: Effect

It is generally accepted that the longitudinally propagating shock wave is responsible for the increase in time-averaged pressure often associated with pulse-triggered instability. This increase in time-averaged pressure can be described in terms of fraction of dc shift. The fraction of dc shift is defined as the ratio of the difference between the unstable and the stable time-averaged chamber pressures, divided by the stable time-averaged chamber pressure $(p_{cus} - p_{cs})/p_{cs}$.

In this section evidence is presented that suggests that for the motors from the Canadian test matrix, part of the increase in time-averaged pressure/fraction of dc shift associated with pulse-triggered instability could be attributed to transverse pressure waves and not simply to the longitudinally propagating shock wave. This hypothesis is consistent with the widely observed time-averaged pressure increases associated with transverse waves during classical acoustic instability. In fact, it was the resemblance of the large increase in time-averaged pressure associated with motor 03020-SA(1) (Fig. 20b) to increases resulting from acoustic instability that provided the initial indication of the effect of transverse pressure waves in the pulse-triggered environment.

The output from one of the high-frequency pressure transducers (original signal) for 03020-SA(1) is shown in Fig. 30. A comparison of Fig. 30 with Fig. 20b shows that the large increase in the fraction of dc shift was accompanied by a significant

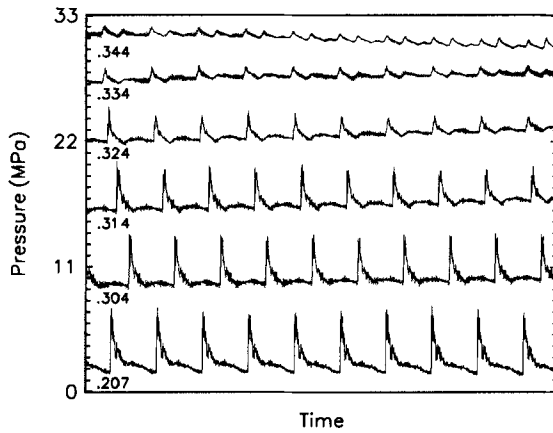


Fig. 30 Evolution of the original signal for motor 03020-SA(1) during the large increase in the time-averaged pressure.

decrease in the amplitude of the shock wave, leaving primarily high-frequency oscillations. Four FFTs of this signal are included in Fig. 31 to illustrate this change from the perspective of the frequency domain. This figure shows that by 0.343 s the shock wave had all but disappeared, leaving only two dominant high-frequency modes. That these were in fact two tangential modes was inferred from the correspondence between their frequencies and those of the third and the seventh tangential modes shown in both Figs. 20a and 31. Therefore it was concluded that the large increase in time-averaged pressure/fraction of dc shift for motor 03020-SA was indeed driven by transverse pressure waves.

It is worthwhile at this point to distinguish between the classical theory of acoustic instability applied to transverse modes and what is potentially taking

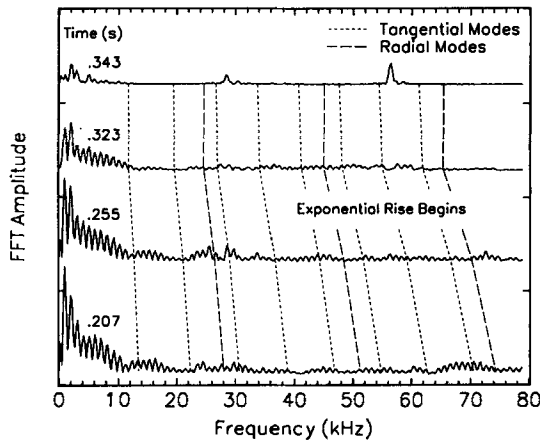


Fig. 31 Evolution of the FFTs of the original signal for motor 03020-SA(1) during the large increase in the time-averaged pressure.

place in a motor operating in the pulse-triggered unstable mode. In classical theory, the acoustic energy balance (sum of the energy sources and sinks) is essentially time averaged. As such, it does not account for transient energy sources such as those associated with the passage of the shock wave. It is therefore entirely possible for transverse waves to exist in the pulse-triggered environment without a motor's being unstable in the classical sense. In addition, the average amount of transverse wave energy existing at a given point along the length of the combustion chamber between consecutive passes of the shock wave depends on, among other things, the period of the shock wave and the classical acoustic decay rate. It is possible to imagine a case in which the additional time-averaged energy added by the passage of the shock wave is sufficient to drive a motor unstable in the classical sense. This is potentially what contributed to the large time-averaged pressure increase for 03020-SA(1). The worst case will occur when a motor is already unstable in the classical sense and transverse wave energy is added through the passage of the shock wave.

The relationship between the amplitude of transverse pressure oscillations and the increase in time-averaged pressure for 03020-SA(1) is illustrated through comparison of the FFTs of the resultant signal (shock wave removed), Fig. 32, and curves of fraction of dc shift and normalized pressures, Fig. 20b. Figure 32 shows that the amplitude of the seventh tangential mode at 0.343 s was between two and three times that of the larger peaks for the FFTs from 0.183 to 0.280 s. This ratio is entirely consistent with fractions of dc shift of approximately 0.50 and 0.20 at 0.343 s and 0.183–0.280 s, respectively. As such, it indicates the plausibility that part of the increase in time-averaged pressure/fraction of dc shift associated with pulse-triggered instability could be attributed to transverse pressure waves. Any more detailed conclusions are questionable, given that this argument considers neither combustion response function nor the variation of transverse wave amplitude along the propellant grain.

In spite of clear evidence indicating that the large fraction of dc shift at 0.343 s for 03020-SA(1) was driven by tangential pressure waves, the correlation between the amplitude of these waves (calculated from Fig. 32) and the fraction of dc shift was poor. Figure 33 shows the amplitude of the third mode to decrease and

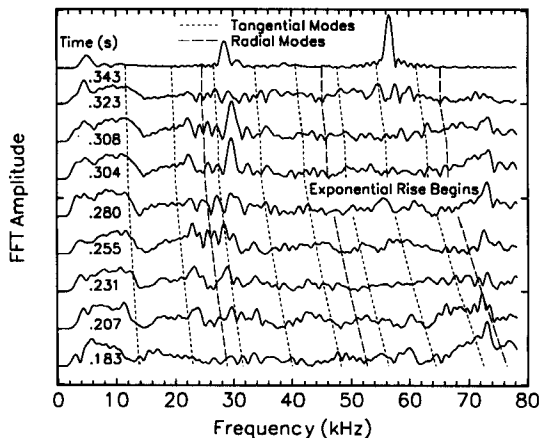


Fig. 32 Evolution of the FFTs of the resultant signal for motor 03020-SA(1) during the large increase in the time-averaged pressure.

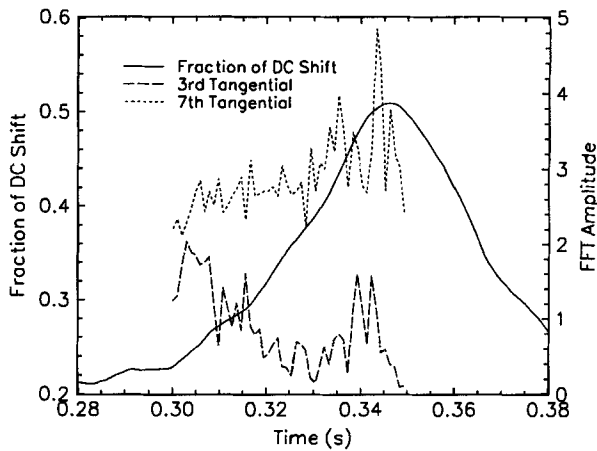


Fig. 33 Correlation between the amplitude of the FFTs of the tangential pressure waves in the resultant signal and the fraction of dc shift during the large increase in the time-averaged pressure for motor 03020-SA(1).

that of the seventh mode to remain constant during a significant portion of the increase in fraction of dc shift. The fact that the correlation improved as the shock amplitude decreased (see Fig. 31) indicated that the poor correlation resulted from the broadband nature of the high-frequency content, including headend resonances, combined with the poor frequency resolution of the FFT.

Originally the effect of transverse pressure waves on time-averaged pressure was to be evaluated through a correlation of their amplitudes. As such, contour graphs and curves of time-averaged pressure/fraction of dc shift have been grouped in Figs. 17–24 for the perusal of the reader. However, because of the poor correlation for motor 03020-SA(1), this line of reasoning was abandoned. Instead, profiles of time-averaged pressure and fraction of dc shift were examined for abrupt changes in level and slope, as was the case for motor 03020-SA(1). These were considered as potential evidence of the effect of transverse waves. This assumed that the continuous change in transverse frequency and acoustic decay α based on the changing radial dimensions of the internal grain geometry were a more probable source of abrupt change in the level of fraction of dc shift than the longitudinally propagating shock wave with unchanging longitudinal dimensions.

The profile of the fraction of dc shift of motors 03020-SA(2) and 03020-SA(3) in Figs. 21b and 22b, respectively, showed tendencies similar to that of 03020-SA(1) near the middle of the firing. This suggested transverse wave driving, with that for 03020-SA(2) being the more pronounced of the two. In addition, the abrupt change in level for 03020-SA(2) at approximately 0.24 s could also suggest transverse wave driving (see also Fig. 3). This type of change in level was identified in a previous paper.²¹ There, the abrupt change in dc shift disappeared when the resonant characteristics of the propellant/casing system were changed by insertion of the motor into a steel tube, 14.1 mm thick, before firing.

The profiles of the fraction of dc shift for the two small-diameter long cylindrical motors, 03031-C(B) and 03031-C(C) in Figs. 17b and 18b, respectively, were significantly different from each other, indicating an effect of propellant formulation. The behavior of motor 03031-C(C), Fig. 18b, was very interesting and is best

visualized with the curve of time-averaged pressure. The curve shows a similar behavior to that of star 03020-SA(2) (Fig. 21b). However, instead of an increase in pressure, the cylinder underwent a decrease in pressure between approximately 0.6 and 0.7 s.

The profile of the fraction of dc shift for the small-diameter short cylindrical motor (03020-C), Fig. 19b, showed abrupt changes in level and slope and was generally similar to that of motor 03031-C(B), Fig. 17b.

In general, the overall shape of the time-averaged pressure curves for the small-diameter stars differed more significantly from what would be expected for unstable operation than that of the small-diameter cylinders. This suggested that the stars were more affected by the transverse pressure waves and in turn illustrated a three-dimensional effect of grain configuration.

Finally, the profiles of the fraction of dc shift for the large-diameter cylinder, Fig. 23b, and star, Fig. 24b, also showed abrupt changes in level and slope. However, they were significantly different from the smaller-diameter motors with the same grain shape. A difference of this type would be expected if transverse waves were in part responsible for the fraction of dc shift; the transverse frequencies in the large-diameter motors were much lower than those in the small-diameter motors.

VIII. Conclusions

In this chapter, the presence of transverse pressure waves in a pulse-triggered unstable environment has been demonstrated and their nature, source, and effect explored for eight representative motor firings selected from the Canadian database generated during a joint international study.

With a new data analysis method, it was shown that transverse pressure waves were always present during fully developed pulse-triggered instability. This result was independent of propellant formulation, operating pressure, grain configuration, motor length, or motor scale. However, qualitative differences in the actual frequency content that depended on these parameters were noted. It was also noted that, although transverse oscillations were always present, the actual modal content changed throughout a firing. The modal content was identified as being composed of both pure transverse and combined transverse-longitudinal-acoustic modes of the combustion chamber. A radial gas oscillation was also identified that corresponded to the vibration of the propellant/casing system. The presence of certain oscillations was also attributed to the motor headend geometry, comprising pulser channels and a cavity created by the inhibitor. Unfortunately, given that only head-end measurements were made, no conclusions could be drawn as to the variation of transverse wave energy along the length of the motors.

It was shown that the presence of transverse waves was not the result of the pulsing event. Rather, their growth, represented by the integral of the FFTs, correlated with the steepening of the longitudinal shock wave. Good correlation was also shown to exist between the temporal evolution of the amplitude of transverse waves and that of the amplitude of shock-wave harmonics of similar frequency. Therefore it was concluded that the transverse waves were driven by the propagating longitudinal shock wave either through the conversion of longitudinal-acoustic energy to transverse-acoustic energy through the movement of the propellant/casing system and/or through gasdynamic interaction between the shock wave and the mean flow.

Evidence was presented that suggested that part of the increase in time-averaged pressure associated with pulse-triggered instability could be attributed to transverse

pressure waves and not simply to the longitudinally propagating shock wave. This evidence was in the form of abrupt changes in level and slope of the time-averaged pressure/fraction of dc shift. This approach was adopted as correlations with the amplitude of transverse waves were masked by the broadband nature of the high-frequency content combined with the poor frequency resolution of the FFT analysis. Abrupt changes in level and slope of the time-averaged pressure were identified for the eight representative motor firings examined. As such, it was noted that small-diameter stars were more affected by transverse pressure waves than were the small-diameter cylinders, indicating a three-dimensional effect associated with grain configuration. The difference in the profiles of fraction of dc shift for small-diameter cylinders with different propellant formulations indicated an effect of propellant formulation. In addition, the significantly different profiles of fraction of dc shift for small- and large-diameter motors indicated an effect of scale. However, numerical modeling, further experimentation, and the development of new data analysis methods are required for demonstrating in a conclusive manner that transverse pressure waves do in fact drive a portion of the dc shift.

Conclusions were drawn with only headend pressure measurements. In addition, no numerical modeling was performed. Consequently no information exists as to the behavior of transverse waves along the length of the motor cavity. This information would be very instructive and as such its generation will be the focus of future experimental and numerical studies.

The implications of the data presented in this chapter for motor design and theoretical modeling are significant. First, the shock wave provides a new, albeit transient, source of transverse wave energy that could be sufficient to drive a motor unstable. As such, testing a motor design for pulse-triggered unstable operation could reserve some undesirable surprises. Second, although one-dimensional models are a good starting point, only three-dimensional models with moving boundaries are sufficient to describe all the significant processes occurring during pulse-triggered instability.

Finally, the longitudinally propagating shock wave is the primary cause of the increase in time-averaged pressure associated with pulse-triggered instability. As such, care should be taken in extrapolating the present conclusions to other databases. In particular, aluminized propellants, which are not favorable to transverse mode oscillations manifest increases in time-averaged pressure that may be totally attributed to the shock wave.

References

¹Dickinson, L. A., "Command Initiation of Finite Wave Axial Combustion Instability in Solid Propellant Rocket Engines," *Journal of the American Rocket Society*, Vol. 32, 1962, pp. 643, 644.

²Dickinson, L. A., and Jackson, F., "Combustion in Solid Propellant Rocket Engines," *Proceedings of the Fifth AGARD Combustion and Propulsion Colloquium*, 1962, pp. 1-14.

³Brownlee, W. G., "Nonlinear Axial Combustion Instability in Solid Propellant Motors," *AIAA Journal*, Vol. 2, No. 2, 1964, pp. 275-284.

⁴Roberts, A. K., Brownlee, W. G., and Jackson, F., "Combustion Instability and the Design of Solid Propellant Rocket Motors," *Canadian Aeronautics and Space Journal*, Vol. 16, No. 1, 1970, pp. 21-27.

⁵Roberts, A. K., and Brownlee, W. G., "Nonlinear Longitudinal Combustion Instability: Influence of Propellant Composition," *AIAA Journal*, Vol. 9, No. 1, 1971, pp. 140–147.

⁶Smith, D. L., Christie, F., and Clark, M. N., "Combustion Instability of Nonaluminized Propellants—The Influence of Propellant Formulation," AIAA Paper 77-900, July 1977.

⁷Hughes, P. M., and Smith, D. L., "Non Linear Combustion Instability in Solid Propellant Rocket Motors—Influence of Geometry and Propellant Formulation," *Solid Rocket Motor Technology*, CP 259, AGARD, 1979, pp. 1–25.

⁸Brownlee, W. G., and Kimbell, G. H., "Optical Studies of Longitudinal Combustion Instability," CARDE TN 1708/66, Canadian Armament Research and Development Establishment Valcartier, Quebec, May 1966.

⁹Brownlee, W. G., and Kimbell, G. H., "Shock Propagation in Solid Propellant Rocket Combustors," *AIAA Journal*, Vol. 4, No. 6, 1966, pp. 1132–1134.

¹⁰Kimbell, G. H., and Brownlee, W. G., "Flow Processes in Solid Propellant Combustor During Unstable Operation," CARDE TN 1783/68, Canadian Armament Research and Development Establishment, Valcartier, Quebec, March 1968.

¹¹Kimbell, G. H., and Brownlee, W. G., "Status Report on Optical Studies of Combustion Instability at CARDE," CARDE TN 1784/68, Canadian Armament Research and Development Establishment, Valcartier, Quebec, March 1968.

¹²Hughes, P. M., and Saber, A. J., "Nonlinear Combustion Instability in a Solid Propellant Two-Dimensional Window Motor," AIAA Paper 78-1008, July 1978.

¹³Harris, P. G., and De Champlain, A., "Experimental Database Describing Pulse-Triggered Nonlinear Instability in Solid Rocket Motors," *Journal of Propulsion and Power*, Vol. 14, No. 4, 1998, pp. 429–439.

¹⁴Blomshield, F. S., Jolley, W. M., Tandy, I. S., Harris, P. G., Lovine, R. L., and Levine, J. N., *Pulsed Nonlinear Combustion Instability*, Vols. 1–4, Technical Cooperation Program, Naval Air Warfare Center, China Lake, CA, 1991.

¹⁵Blomshield, F. S., Crump, J. E., Mathes, H. B., Stalnaker, R. A., and Beckstead, M. W., "Stability Testing of Full-Scale Tactical Motors," *Journal of Propulsion and Power*, Vol. 13, No. 3, 1997, pp. 349–355.

¹⁶Blomshield, F. S., Mathes, H. B., Crump, J. E., Beiter, C. A., and Beckstead, M. W., "Nonlinear Stability Testing of Full-Scale Tactical Motors," *Journal of Propulsion and Power*, Vol. 13, No. 3, 1997, pp. 356–366.

¹⁷Lovine, R. L., Micheli, P. L., and Flandro, G. A., *Nonlinear Stability for Tactical Motors*, Vols. 1–5, AFRPL TR-84-017 and AFRPL TR-85-017, 1985 and 1986.

¹⁸Baum, J. D., Levine, J. N., and Lovine, R. L., "Pulsed Instabilities in Rocket Motors: A Comparison Between Predictions and Experiments," *Journal of Propulsion and Power*, Vol. 4, No. 4, 1988, pp. 308–316.

¹⁹Baum, J. D., and Levine, J. N., "A Critical Study of Numerical Methods for the Solution of Nonlinear Hyperbolic Equations for Resonance Systems," *Journal of Computational Physics*, Vol. 58, No. 1, 1985, pp. 1–28.

²⁰Hughes, P. M., "The Influence of the Elasticity of the Casing and Grain on the Combustion Instability of a Solid Rocket Motor," DREV Memorandum, 2588/81, Dec. 1981.

²¹Harris, P. G., Wong, F. C., and De Champlain, A., "The Influence of Structural Vibrations on Pulse-Triggered Nonlinear Instability in Solid Rocket Motors: An Experimental Study," AIAA Paper 96-3250, July 1996.

²²Harris, P. G., and De Champlain, A., "A Methodology for the Analysis of Post-Shock Oscillations in Solid Rocket Motors Operating in the Pulse-Triggered Unstable Mode," *Journal of Propulsion and Power*, Vol. 15, No. 5, 1999, pp. 719–728.

AUTHOR INDEX

Index Terms

Links

A

Anderson, W. R .	501	
Apte, S .	791	885
Atwood, A. I.	221	
Avalon, G.	823	

B

Babuk, V. A.	749	
Bazaki, H.	439	
Beckstead, M. W.	267	
Blomshield, F. S.	921	
Boggs, T. L.	221	
Brewster, M . Q.	607	
Brill, T. B.	3	
Bucher, P.	689	
Budenz, B . T.	3	
Burton, R .L.	723	

C

Cai, W.	837	
Casalis, G.	823	
Chakraborty, D.	33	
Chan, M. L.	185	
Chen, F.	129	

Index Terms

Links

Ciaramitaro, D. A.

185

D

De Champlain, A.

959

Dryer, F. L.

689

Duo, Y.

129

Dupays, J.

859

Duterque, J.

287

E

Egorshev, V. Yu.

99

Emst, L .

689

Estivalezes, J .L.

859

F

Fabignon, Y.

859

Finjakov, S . V.

639

Flandro, G . A.

837

Fogelzang, A . E.

99

G

Glorieux, B.

777

H

Hanson-Pan, D. M.

381 689

Harris, P. G.

959

Ho, S.-Y.

591

Hou, L.-F.

413

This page has been reformatted by Knovel to provide easier navigation.

Index Terms

Links

Howe, P. M .	141
Huo, Z.	907

K

Kato, K.	455
Kobayashi, K.	455
Kolesov, V. I.	99
Komai, I .	455
Kong, Y.	425
Korobeinichev. O. P.	335
Krier, H.	723

L

Lavergne, G.	859		
Lee, Y. J .	355		
Lei, M.	425		
Lengellé, G .	287		
Li, Shangwen	425	465	533
Li, Shufen	465		
Liau, Y.-C.	477		
Lin, M . C.	33		
Lindfors, A. J.	221		
Litzinger, T. A.	355		
Liu, Z.	425		
Lu, D.	465		
Luk'yanov, O. A.	207		
Luo, Y.	425		
Lupoglazoff, N.	823		

Index Terms

Links

M

Margolis, S .B.	549
Melcher, J. C.	723
Miller, M .S .	501
Millot, F.	777
Mulder, E .J .	221

O

oyumi, Y.	73
-----------	----

P

Parr, T, P.	381	689
Price, E . W.	663	
Pritchard, R . W.	221	

R

Reed R. Jr.	185
Rifflet, J . C.	777
Roh, T.-S.	885

S

Serushkin, V. V.	99
Shan, W.	465
Shao, Y.	425
Sigman, R. K.	663
Sinditskii, V. P.	99
Song, H.	533
Sviridov, V. V.	749

This page has been reformatted by Knovel to provide easier navigation.

<u>Index Terms</u>	<u>Links</u>			
T				
Tan, H.	129			
Tang, C.-J.	355			
Tang, Z.	907			
Tartakovsky, V. A.	207			
Thynell, S . T.	477			
Trubert, J . F.	287			
U				
Ugurtas, B.	823			
V				
Vassiliev, V. A.	749			
Villedieu, P.	859			
Vuillot, F.	823			
W				
Wang, Y.	425			
Williams, F. A.	549			
Y				
Yang, D.	533			
Yang, P.	907			
Yang, V.	477	791	837	885
Yetter, R. A.	689			
Yin, C.	425			

Index Terms

Links

Z

Zenin, A .A .	639		
Zhang, P.	425		
Zhang, X.-P.	413		
Zhao, F.	425	465	533
Zhao, X.-B.	413		